PEM FUEL CELLS: HOW THINGS WORK

Thomas A. Zawodzinski

Department of Chemical Engineering, Case Western Reserve University, 10900 Euclid Ave., Cleveland, OH 44106

Proton exchange membrane (PEM) fuel cells operating on hydrogen are a particularly appealing technology with a wide range of potential applications. This talk will introduce the technology by describing the components of a typical PEM fuel cell system and how they function. After an initial birds-eye overview, the current state of the art of individual materials and the structure and function of central components such as polymer membranes and electrodes will be described. Key aspects of function that have impact at the system level, such as water management and its implications for materials function and properties, will also be discussed. Finally, a few illustrations of the speaker's research group's current efforts on new membranes and electrodes will be presented. Emerging research opportunities at the fundamental level will be touched on, with an emphasis on needed understanding.

CAN AVAILABLE MEMBRANES AND CATALYSTS MEET AUTOMOTIVE POLYMER ELECTROLYTE FUEL CELL REQUIREMENTS?

Mark Mathias, Hubert Gasteiger, Rohit Makharia, Shyam Kocha, Tim Fuller, Tao Xie, and Jason Pisco

General Motors
Fuel Cell Activities
10 Carriage Street
Honeoye Falls, NY

Introduction

Over the past few years, significant R&D efforts have been aimed at meeting the challenging cost and performance targets required for the use of polymer electrolyte fuel cells (PEFCs) in automotive applications. Besides engineering advances in bipolar plate materials and design, the optimization of membrane-electrode assemblies (MEAs) was an important enabler in reducing the cost and performance gaps towards commercial viability for the automotive market. On the one hand, platinum loadings were reduced from several mg_{Pt}/cm^2_{MEA}[1] to values of 0.5-0.6 mg_{Pt}/cm^2_{MEA} in current applications and loadings as low as 0.25 mg_{Pt}/cm^2_{MEA} have been demonstrated on the research level.[2] On the other hand, implementation of thin membranes (20-30 μm)[3,4] as well as improvements in diffusion medium materials, essentially doubled the achievable power density of MEAs to ca. 0.9 W/cm^2_{MEA} (at 0.65 V),[5] thereby not only reducing the size of a PEFC fuel cell system, but also reducing its overall materials cost (controlled to a large extent by membrane and Pt-catalyst cost). In this paper, we evaluate current cost, performance, and durability issues associated with PEFC membranes and catalysts, and we suggest areas where a renewed focus of R&D effort will accelerate the commercialization of PEFCs in automotive applications.

Membrane Requirements

Membrane Cost. The current polymer electrolyte fuel cell membranes of choice are based on poly[perfluorosulfonic acid] (PFSA), and are produced by DuPont, Asahi Glass, Asahi Kasai, and Solvay. PFSA membrane has been commercialized for the chlor-alkali industry, but the market volume is small (<65 metric tons (MT)/year)[6] and the price is high (~$5000/kg), characteristic of a specialty material. This compares with the commodity poly[tetrafluoro-ethylene] which is produced at a volume of 80,000 MT/year and sells in the neighborhood of $10/kg. To assess the high-volume automotive price potential of PFSA membrane, we conducted a study in which we designed for cost estimation purposes, vinyl ether monomer, PFSA polymer, and membrane production plants. The price projections are shown in **Figure 1** and indicate that at 1 million vehicles/yr (100 kW/vehicle at ca. $1kg_{membrane}$/100kW), which would require approximately 1,000 MT/yr of PFSA, the membrane cost would drop to less than $100/kg. This translates to approximately $1/kW, an affordable price against the $50/kW total power system target, and demonstrates that PFSA price should not be prohibitive for automotive application. Whereas there are reasons why alternatives to PFSA membranes are of interest, the high price of PFSA membrane is at best a secondary one.

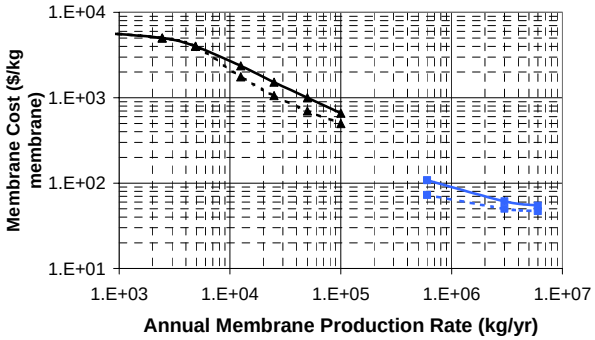

Figure 1. Price projection of PFSA membrane (25 micron thick, 0.05 kg/m^2, 1100 EW) at high volume. Low volume projections provided by DuPont.[7] High volume numbers from GM cost study. Two lines in each case roughly indicate uncertainty on projections.

Membrane Performance. Current PEFCs systems run at a maximum of 80ºC because operation above that temperature requires too much system support of the membrane (e.g. pressure, humidification) to maintain close to 100% relative humidity (RH) required for good proton conduction. Also, current membranes have glass transition temperatures in the range of 80-120ºC and are thus subject to creep and hole-formation at temperatures in that range. **Figure 2** shows the conductivity vs. RH for a Nafion® 1100 EW ($EW \equiv g_{polymer}/mol_{H+}$) membrane at 80ºC, although the conductivity vs. RH response is not very sensitive to temperature up to 120ºC.[8] At the fully humidified condition, the conductivity of ~0.1S/cm translates to a tolerable 25 mV loss for a 25 μm membrane at a current density of $1A/cm^2$. The figure also shows that the conductivity drops off very quickly with RH, thereby requiring the fuel cell system to provide for humdification of the reactant streams. There would be great value in reducing system complexity (and thus cost) from a membrane that maintains good conductivity to low-RH such as shown in the "desired" curve in Figure 2 (0.1 S/cm at 50% RH), even if limited to a maximum of 80-100ºC operation. Indeed developments by manufacturers have shown promising progress in this direction for PFSA membranes. An example is shown on Figure 2, a low (<800) EW PFSA that has conductivity of 0.06-0.07 S/cm at 50% RH and 80ºC.

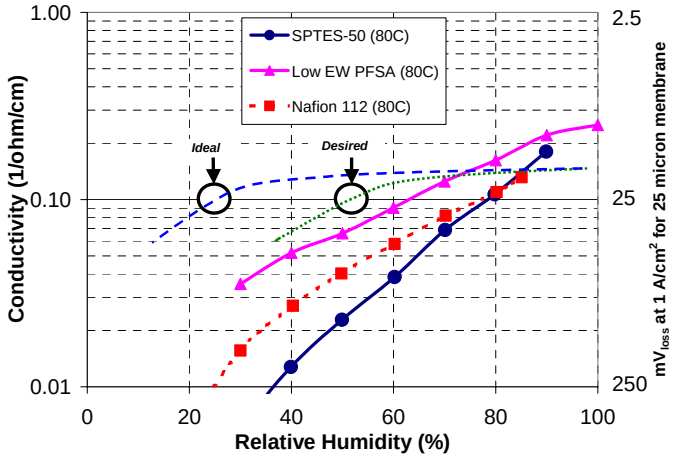

Figure 2. Conductivity vs. RH at 80ºC for Nafion® 112, sulfonated polyarylenethioethersulfone (SPTES),[9] and low-EW (<800) PFSA. Also indicated are desired (50% RH inlet, 150 kPa_{abs}, 80-100ºC) and ideal (0% RH inlet, 120 kPa_{abs}, 100ºC) conductivity characteristics to enable system simplification and vehicle heat rejection.

Also shown in Figure 2 are data from a sulfonated polyarylenethioethersulfone (SPTES-50, 1.6 mEq/gm) from Dang and coworkers.[9] This conductivity vs. RH performance is the characteristic of many hydrocarbon membranes -- it surpasses Nafion® 112 at high RH (>80%) but drops off more sharply than Nafion® 112 as the RH is decreased. Available hydrocarbon membranes do not yet appear competitive with materials in the PFSA family with regards to their low-RH (<75%RH) conductivity.

Unfortunately, it turns out that the heat rejection rate of current automotive radiators is insufficient to reject continuous full power waste heat loads with the 80ºC fuel cell stack temperature. Operation at 80ºC results in significant adjustment in thermal system complexity/cost, vehicle design, and/or negative impact on the high-power vehicle capability (e.g. length of time at full load). Vehicle system analysis indicates that 120ºC high-power operation would enable the use of radiators similar to those available today,[10] and this has driven the need for development of a high-temperature membrane that could operate at temperature of up to 120ºC. We earlier argued that such a membrane would need to have a characteristic conductivity curve like that shown as the "ideal" curve in Figure 2 in order not to increase system-support demands over those of state-of-the art membranes.[5] This has led to development projects focused on high-temperature (120ºC), low-RH (25%) membranes.

Our latest estimates, encompassing the impact of higher temperature on Pt catalyst dissolution rates (discussed below) suggest that extended operation above 80ºC may result in unacceptable Pt cathode catalyst dissolution rates. Operation limited to 80ºC will result in heat rejection systems for fuel cell vehicles that are more complex than in current automotive applications. This in turn drives for a more aggressive simplification of the fuel cell system, achievable for example by the development of low-RH membranes which would enable stack operation at 80ºC without external humidification. Very short excursions of up to 100ºC may be tolerable, but fuel cell stack temperatures above 80ºC risk unacceptably high cathode catalyst degradation rates. In light of these arguments, low-RH (0.1S /cm at 25-50%RH) membranes with a main operating temperature of 60-80ºC and short-time temperature excursions up to ca. 100ºC now appear to be the desired development goal to enable simpler fuel cell systems that could compensate for the increased complexity of the thermal system. The "ideal" curve shown in Figure 2 (0.1S /cm at 25%RH) is an appropriate membrane development target for 100ºC operation – such a membrane would enable a system pressure of 120 kPa_{abs} and no external humidification, a significant simplification over current state-of-the art requirements.

Phosphoric acid doped polybenzimidazole (PBI), first identified by Case Western Reserve University and now under development by PEMEAS GmbH, is a high-temperature membrane that allows operation up to approximately 200°C with very low humidification requirement.[11] However, issues that prohibit its use for automotive are instability in the presence of liquid water and inefficient cathode structures resulting in low areal power density.

Whereas much work is ongoing to develop alternative membranes to PFSA, the vast majority of approaches rely on the sulfonic acid based conduction mechanisms. Fundamental work such as morphological investigations[12] and molecular modeling are needed to determine the physical limits of these materials in terms of conductivity vs. RH characteristic shown in Figure 2. Also, the data in Figure 2 suggest that PFSAs may have an intrinsic morphological advantage at low-RH over the hydrocarbon materials, and this requires investigation at the fundamental level.

Membrane Durability. To be successful in automotive application, membranes must survive 10 years in a vehicle and 5,500 hours of operation including transient operation with start-stop and freeze-thaw cycles. Even though thin polymer electrolyte membranes (20-30 μm) enable high power density operation, the requirements on their chemical and mechanical stability are significantly more demanding compared to the thick membranes (100-200 μm) used in the past. While PFSA membranes are chemically very stable, they are known to degrade in the fuel cell environment[4] via peroxyl-radical attack, strongly enhanced in the presence of trace iron contamination.[13] While the exact degradation mechanism is being actively investigated, its understanding is clearly required to improve the chemical stability of PFSA's.

Less is understood about the mechanical property requirements of polymer electrolyte membranes, but it is clear that dimensional stability as a function water uptake and removal is a critical consideration. For example, membranes expand when wet but sometimes shrink to less than their pre-wet size when dried again due to relief of residual processing stresses in the material. More work is needed to understand the connection between these *ex-situ* properties and *in-situ* failure. Clearly though, dimensional stability and limited water uptake when wet (<100 wt% maximum, <50 wt% preferred) are desired for suitable membranes. To support these efforts, deepened fundamental understanding of the morphology of these materials both through experiments (e.g. SAXS, SANS) and molecular modeling is needed.

Electrocatalyst Requirements

Cost and Performance. In current H_2/air applications, MEA (membrane-electrode assembly) Pt-loadings are on the order of 0.2-0.4 mg_{Pt}/cm^2 on the anode and typically 0.4 mg_{Pt}/cm^2 on the cathode.[3] Owing to the fast H_2 oxidation kinetics on carbon supported platinum catalysts (Pt/C), anode Pt-loadings can be lowered to 0.05 mg_{Pt}/cm^2 without performance loss.[2] At nominal operating conditions with H_2/air (s=2/2) at 150kPa_{abs} and 80ºC, state-of-the-art MEAs with a total Pt-loading of 0.45 mg_{Pt}/cm^2 achieve power densities of $P_{MEA} \approx 0.7$ W/cm^2 at a single cell voltage of 0.65 V.[2,14] As shown in the first row of Table 1, this demonstrated performance equates to Pt-specific power densities, P_{Pt}, of 0.63 g_{Pt}/kW. While being a significant improvement over MEA performance achieved in the 90's,[1] these Pt-loadings still result in noble metal costs of approximately 22 $/kW (assuming ≈35 $/$g_{Pt}$ for a Pt/C catalyst) and do not meet the stringent cost requirements for automotive applications.

Table 1. MEA power densities, P_{MEA} [W/cm^2], and Pt-specific power densities, P_{Pt} [g_{Pt}/kW], in state-of-the-art MEAs and mass-transport optimized MEAs with anode Pt-loadings of 0.05 mg_{Pt}/cm^2.

assumptions	catalyst activity	cathode loading [mg_{Pt}/cm^2]	P_{MEA} at 0.65V [W/cm^2]	P_{Pt} at 0.65V [g_{Pt}/kW]
current MEA	Pt/C	0.4	0.71	0.63
opt. MEA	Pt/C	0.4	0.91	0.48
opt. MEA	2x Pt/C	0.1	0.78	0.19
opt. MEA	4x Pt/C	0.1	0.91	0.17

One approach to reduce the cost per kW is based on improving the mass-transport losses observed at high current densities, resulting from the non-optimized performance of currently used diffusion

media and bipolar plate flow fields. The feasibility of this approach has been demonstrated on the research level, and optimized MEAs can be achieved by improved diffusion media treatments and coatings. This enables the achievement of improved power densities of ≈0.9 W/cm^2, thereby lowering the Pt-specific power density to 0.48 g_{Pt}/kW (see 2nd row in table 1) or ≈17 $/kW of catalyst cost. While being a noticeable improvement, MEA Pt-loadings must be reduced to approximately 0.15 mg_{Pt}/cm^2/MEA without significant performance loss in order to meet the stringent automotive cost requirements.

Contrary to the fast kinetics for H_2 oxidation on the anode catalyst, the oxygen reduction kinetics are very sluggish and a lowering of the cathode Pt-loading by a factor of 2 results in a cell voltage loss of 20 mV,[2] while the required lowering by a factor of 4 which is needed to achieve 0.15 mg_{Pt}/cm^2/MEA would result in a loss of at least 40 mV. For efficiency reasons, a loss of 40 mV is not acceptable and novel cathode catalysts with improved activity are required. Platinum-cobalt alloys (PtCo/C) and other Pt-alloys have been demonstrated to yield an activity improvement by a factor of 2 compared to a conventional Pt/C catalysts[14] and implementation of these catalysts enables a lowering of the cathode Pt-loading to 0.1 mg_{Pt}/cm^2 at an overall performance loss of 20 mV. In this case (see 3rd row of table 1), the Pt-specific power density reduces to 0.19 g_{Pt}/kW, yielding a catalyst cost of ≈7 $/kW. While this is acceptable from a catalyst cost point of view, Pt-alloy catalysts with a 4-fold activity enhancement would be desirable in order to improve the overall MEA power density to ≈0.9 W/cm^2, thereby reducing the cost of the other stack components (membranes, bipolar plates, diffusion media) via reduction of the overall plate area of a fuel cell stack.

In summary, the catalyst and MEA technology demonstrated on the research level is capable to meet automotive costs. Implementation in fuel cell applications, however, requires a renewed focus on the performance optimization of Pt-alloy catalysts and detailed studies on the durability of Pt-based fuel cell catalysts at the targeted anode and cathode loadings of 0.05 and 0.1 mg_{Pt}/cm^2, respectively.

Catalyst Durability. While Pt catalysts are very stable at the low electrode potentials occurring at the anode electrode (0 to 0.05 V vs. the reversible hydrogen electrode potential (RHE)), Pt sintering and dissolution as well as carbon corrosion pose significant concerns at the high electrode potentials occurring in the cathode electrode (≈0.9V vs. RHE at idle conditions where minimal currents are drawn from the fuel cell stack). This has been observed in the past in the development of phosphoric acid fuel cells (PAFC) for stationary power applications, leading to operating strategies which circumvent idle conditions and limit high cell voltages to significantly below 0.9V.[15,16] In automotive applications, a large fraction of a vehicle's operating time will be spent at idle (i.e., cathode potentials of ≈0.9V vs. RHE), and the question arises whether Pt-dissolution at the lower operating temperature of 60-80°C (in contrast to the 200°C for a PAFC) still has deleterious effects on cathode catalyst durability in a PEFC. Although very few data on the occurrence of Pt-dissolution in PEFCs are published, a recent report by Patterson[17] shows that Pt can be found in the membrane after MEA aging in a fuel cell, indicating that Pt-dissolution is indeed an issue even at the low operating temperatures of a PEFC. A subsequent publication by Darling and Meyers[18] models the Pt-dissolution process as the formation of Pt^{+2} and either its diffusion away from the electrode or its redeposition on the catalyst, both effects leading to a loss of Pt surface area concomitant with a loss in fuel cell performance.

In order to estimate the temperature dependence of Pt-dissolution at idle conditions, one might refer to the data by Bindra et al.[19] who measured the Pt-solubility in phosphoric acid at 196°C. As shown in **Figure 3** (solid line), the Pt-solubility reported at 196°C is consistent with Pt being oxidized to soluble Pt^{2+} ions, with the solubility increasing by a decade for every increase in voltage by ≈45mV (i.e., RT/2F). Based on this Nernstian behavior of the Pt-dissolution process, the Pt-solubility at 25°C may be estimated from the Pt/Pt^{+2} equilibrium published by Pourbaix[20] (Figure 3, dashed line). As a rough estimate, one may now calculate approximate activation energies for Pt-dissolution at 0.85-0.95V of ≈85-65 kJ/mol, and use these values to estimate the Pt^{+2} equilibrium concentrations at both 80 and 120°C that are shown in Figure 3 (short-dashed lines). As evident from figure 3, the Pt^{2+} equilibrium concentration at 0.9V increases by two orders of magnitude from 25 to 80°C and an additional order of magnitude from 80 to 120°C.

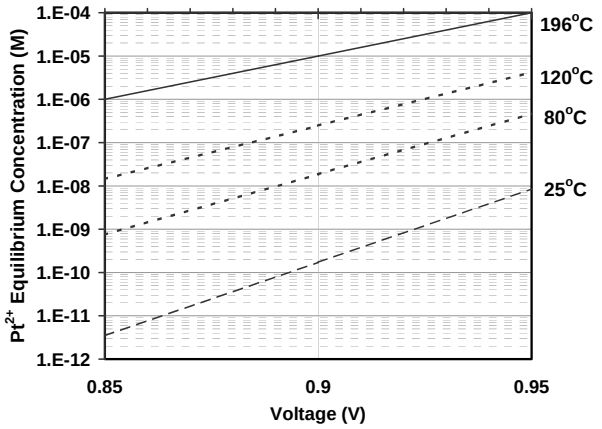

Figure 3. Equilibrium Pt^{2+} concentration in electrolyte as a function of temperature and voltage.

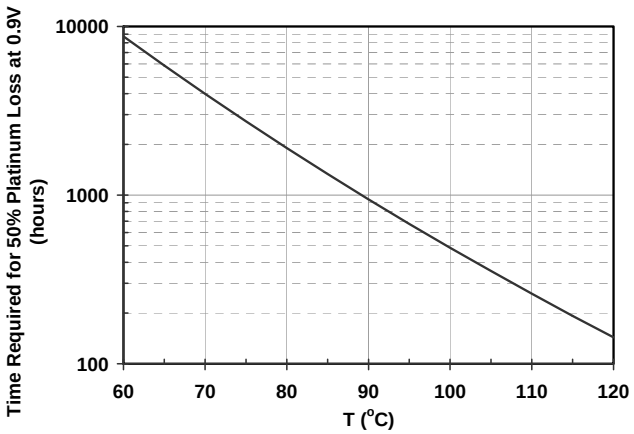

Figure 4. Estimated time required for 50% Pt loss from a Pt cathode catalyst at a loading of 0.1 mg_{Pt}/cm^2 during continuous operation at 0.9V as a function of temperature.

Having estimated the Pt^{+2} equilibrium concentration, c_{Pt+2}, at 0.9V vs. temperature, one can now conduct a back-on-the-envelope calculation of the overall Pt loss as was used previously by Ross[21]

who estimated the Pt-loss from PAFC electrodes by means of a simple Fickian semi-infinite 1D diffusion equation:

$$N_{Pt} \approx D_{eff} \cdot c_{Pt+2}/t$$

where N_{Pt} is the Pt-flux away from the electrode, t is the thickness of the electrode, and D_{eff} is the effective diffusion coefficient of Pt^{+2} in the ionomer phase of the electrode. Assuming that Pt^{+2} diffusion occurs in the aqueous phase of the ionomer, its diffusion coefficient is expected to be on the order of $1 \cdot 10^{5}$ cm^2/s as was used by Ross[21], while the effective diffusion coefficient can be estimated as:

$$D_{eff} \approx D \cdot \varepsilon$$

where ε is the volume fraction of the ionomer in the electrode, with a value of ≈0.2,[Ref 3] resulting in a value of $D_{eff} \approx 2 \cdot 10^{-6}$ cm^2/s. If we now assume an average electrode thickness, t, of 10 μm[Ref 3] and a Pt cathode loading of 0.1 mg_{Pt}/cm^2, we can estimate the total time required to lose 50% of the Pt from the cathode, assuming that Pt^{+2} diffuses into either the membrane or the gas diffusion medium where it becomes essentially inactive for the oxygen reduction reaction. This estimated Pt-loss at 0.9V versus temperature is shown in **Figure 4**. Figure 4 suggests that PEFC operation at idle conditions (i.e., at ≈0.9V) at the currently typical operating temperature of 80°C would lead to a loss of 50% of the active Pt surface area over an operating time (at idle!) of 2000 hours. While significant time at idle conditons are expected in a vehicle driving cycle, a total of ≈40% idling time over the entire service life of a PEFC vehicle is certainly a worst case scenario and unlikely to occur. Therefore, based on the presented back-on-the-envelope calculation, PEFC-vehicle operation at 80°C seems to be quite feasible. On the other hand, if a PEFC vehicle were to be operated at 120°C by means of a previously proposed high-temperature membrane,[5] not more than 150 hours (see Figure 4) at idle conditions would be allowable, a requirement which does not appear feasible for vehicle operation.

In summary, our analysis suggests that fundamental Pt instability may limit the operation of PEFCs in realistic automotive applications to 80°C, with a few allowable excursions to higher temperatures in the vicinity of 100°C. This limit on the upper operating temperature of PEFC vehicles may be even more stringent as previous literature data indicate that voltage cycling (i.e., idle/load cycles) of Pt electrodes may lead to even enhanced Pt-dissolution rates.[17,18,22]

Summary

The currently known material set for PEFCs, i.e., PFSA membranes and Pt-based catalysts, are in principle able to meet the cost requirements for automotive applications. It should be stressed that alternative, non-PFSA based membranes are desirable if they enable low-RH operation, but that they are not required in terms of cost reduction, contrary to frequently made statements in this respect by the scientific community. Nevertheless, significant advances in materials optimization as well as in understanding and mitigating the currently observed degradation mechanisms are needed. Therefore, future R&D efforts should address the following issues:

- Understanding of the physical limits of materials based on the sulfonic acid conduction mechanism in order to enable the development of low-RH membranes operating at 60-100°C.
- Understanding of the fundamental chemical degradation mechanisms of ionomers used both in the electrode and in the membrane.
- Fundamental understanding of the morphology of membranes and its impact on their mechanical properties, particularly in terms of long-term creep and structural changes under cyclic conditions (i.e., cyclic variations of temperature and RH).
- Development of Pt-alloy cathode catalysts with improved activity and durability.
- Catalyst degradation considerations clearly demonstrate that PEFC operating temperatures need to be limited to 60-80°C, only allowing for short-term temperature excursions up to a maximum of 100°C. This is in strong contrast to previously communicated high-temperature requirements for 120°C operation.

Acknowledgment. We would like to thank Cortney Mittelsteadt of Giner Electrochemical Systems, LLC, for providing the conductivity data in Fig. 2.

References

1. Strasser, K.; In *Handbook of Fuel Cells – Fundamentals, Technology and Applications*; Vielstich, W.; Lamm, A.; Gasteiger, H. A. Eds.; John Wiley & Sons: Chichester, UK: **2003**; Vol. 4, Ch. 88, pp 1201-1214.
2. Gasteiger, H. A.; Panels, J. E.; Yan, S. G.; *J. Power Sources*, 127 (2004) 162.
3. Gasteiger, H. A.; Gu, W.; Makharia, R.; Mathias, M. F.; Sompalli, S.; In *Handbook of Fuel Cells* (ibid.): **2003**; Vol. 3, Ch. 46, pp 593-610.
4. Cleghorn, S.; Kolde, J.; Liu, W.; In *Handbook of Fuel Cells* (ibid.): **2003**; Vol. 3, Ch. 44, pp 566-575.
5. Mathias, M. F.; Gasteiger, H. A. In *Proceedings of the Proton Conducting Membrane Fuel Cells III Symposium*; The Electrochemical Society: **2002**, in press.
6. Doyle, M.; Rajendran, G.; In *Handbook of Fuel Cells* (ibid.): **2003**; Vol. 3, Ch. 30, pp 351-395.
7. DuPont Nafion® Fuel Cell Division, Fayetteville, NC.
8. Alberti, G.; Casciola, M.; Massinelli, L.; Bauer, B.; *J. Membrane Science*, **2001**, *185*, 73.
9. Bai, Z.; Williams, L. D.; Durstock, M. F.; Dang, T. D.; *Polym. Prepr.*, **2004**, *45(1)*, 60.
10. Masten, D. A.; Bosco, A. D.; In *Handbook of Fuel Cells* (ibid.): **2003**; Vol. 4, Ch. 53, pp 714-724.
11. Wainright, J. S.; Litt, M. H.; Savinell, R. F.; In *Handbook of Fuel Cells* (ibid.): **2003**; Vol. 3, Ch. 34, pp 436-446.
12. Rubatat, L.; Rollet, A. L.; Gebel, G.; Diat, O.; *Macromolecules*, **2002**, *35*, 4050.
13. LaConti, A. B.; Hamdan, M.; McDonald, R. C.; In *Handbook of Fuel Cells* (ibid.): **2003**; Vol. 3, Ch. 49, pp 647-662.
14. Gasteiger, H. A.; Kocha, S. S.; Sompalli, S.; Wagner, F. T.; submitted to *J. Appl. Catal. B.*
15. Breault, R. D.; In *Handbook of Fuel Cells* (ibid.): **2003**; Vol. 4, Ch. 59, pp 797-810.
16. Landsman, D. A.; Luczak, F. J.; In *Handbook of Fuel Cells* (ibid.): **2003**; Vol. 4, Ch. 60, pp 811-831.
17. Patterson, T.; In *Fuel Cell Technology Topical Conference Proceedings*, 2002 AIChE Spring National Meeting, March 10-14, **2002**.
18. Darling, R. M.; Meyers, J. P.; *J. Electrochem. Soc.*, **2003**, *150*, A1523.
19. Bindra, P.; Clouser, S.; Yeager, E.; *J. Electrochem. Soc.*, **1979**, *126*, 1631.
20. Pourbaix, M.; *Atlas of Electrochemical Equilibria in Aqueous Solutions*, Pergamon Press: Oxford, **1966**.
21. Ross, P.N.; In *Catalyst Deactivation*, Petersen, E.E.; Bell, A.T. Eds.; Marcel Dekker, Inc: New York, **1987**.
22. Kinoshita, K.; Lindquist, J. T.; Stonehart, P.; *J. Electroanal. Chem. Interfacial Electrochem.*, **1973**, *48*, 157.

DIRECT METHANOL FUEL CELLS FOR PORTABLE POWER APPLICATIONS

Shimshon Gottesfeld

MTI MicroFuel Cells
Albany, NY

When it comes to portable power applications, the key merit characteristics of fuel cells are somewhat different than in potential transportation, or stationary power applications. In the latter applications, it is the higher conversion efficiency of a fuel (basically hydrogen) derivable from a variety of potential sources and the low tail pipe emissions associated with such fuel , as well as the lower emission of CO_2 per unit energy consumed. In the case of portable power applications, the central merit characteristic is the high energy density of fuels vs. that of advanced batteries. The need for longer use time of hand held, or laptop devices of increasing functionality, creates market pull for portable power sources of higher energy density. Direct methanol fuel cells emerge as an interesting option, thanks to the high energy density and benign nature of a liquid fuel (100% methanol) stored in a small cartridge. At presently demonstrated conversion efficiencies near ambient conditions (methanol fuel – to – Wh to the load), a volume/weight of 5cc /4g of methanol fuel would provide the same energy as that of a fully charged, Li ion battery of 1300 mAh, typically associated with volume/weight of 20cc/24g.

The challenge of translating such an intrinsically strong advantage in energy density, fuel vs. battery, into a viable power source technology, is, however, non-trivial. Obviously, what replaces the battery in a complete "power-pack" based on a fuel cell, is not the fuel alone, rather the sum total of volumes and weights of: fuel + fuel cell + "balance of plant" (BOP) + hybridizing battery. So, while the advantages of fuel of high energy density look highly attractive for portable power applications, the complete implementation of the power pack requires to both maximize the conversion efficiency fuel-to-electric power and to minimize, at the same time, the weights and volumes of the fuel cell and BOP components to maintain an energy density advantage for the complete power pack.

Minimizing the volume/weight of the fuel cell, requires to achieve high power density and that requirement is made more severe when operating near ambient conditions, i.e., when advantages of enhanced internal cell temperature and/or pressure, cannot be utilized. How high a power density is required for some application, is obviously a function of the power demand in that application, as well as the power demand duty cycle. Applications of relatively low average power demand (average over a full day) with peak power demands limited to short durations, can be accommodated more easily with portable fuel cell technology recently developed. In such cases, the fuel cell would provide the average power over the day and a hybridizing battery would provide the peak power demands, thereby packaging most effectively energy (fuel) and power (battery). In a way, the approach can be then described as replacing a large part of the present battery in a given device, by fuel, of much higher energy content per unit weight/volume, while maintaining a small part of the present battery for purposes of peak power.

As to the BOP component of the fuel cell-based power pack, it has presented significant challenges in terms of both volume/weight and, more importantly perhaps, complexity. Therefore, the new, direct methanol fuel cell (DMFC) –based technology platform developed at MTI Microfuel Cells has very unique combined properties of liquid fuel of high energy density, consumed directly in the fuel cell (no fuel processing upstream the fuel cell), with the BOP reduced to the bare minimum. The latter element required to come up with a rather revolutionary approach to operation of DMFCs, which allows to use direct feed of 100% methanol fuel into the cell anode, eliminating completely the need to dilute the fuel with water on entry to the cell and/or to collect for that purpose water at the air cathode and pump it back to the anode recirculation loop. The result is a highly simple, basically passive system using no liquid pumps and no air blowing. Further discussion of the potential of such a DMFC–based power pack to enter the market of hand held portable power devices, will be provided in this talk

ENZYMATIC BIOFUEL CELLS FOR IMPLANTABLE AND MICRO-SCALE DEVICES

Scott Calabrese Barton[a] *and Plamen Atanassov*[b]

[a]Dept. of Chemical Engineering, Columbia University, New York, NY 10027; [b]Dept. of Chemical and Nuclear Engineering, University of New Mexico, Albuquerque, NM 87131

Introduction

Technology for electrical power generation using enzyme catalysts, established four decades ago, has recently received increased attention associated with demand for micro-scale and implantable power supplies. The main challenges, namely the fragility of enzyme molecules, characteristic low current density, and poor fundamental understanding of redox biocatalysis, are currently being addressed from a variety of research perspectives, to take advantage of enzyme selectivity, low temperature and moderate pH activity, and manufacturability in small-scale devices. Such an effort benefits from four decades of multidisciplinary research in biosensors and related bioelectrochemical fields. This review paper summarizes the current state of enzymatic biofuel cell research in the context of foreseeable applications and assesses the future prospects of the technology. Emphasis is placed on device performance and engineering aspects, with a view toward practical portable power devices based on enzymatic biofuel cells.

Research in biocatalytically modified electrodes, particularly for sensor applications, has provided a significant technological underpinning for current biofuel cell development. There exists significant overlap in technical requirements between sensors and biofuel cells, including chemical and mechanical stability, selectivity, and cost of materials. However, these two technologies diverge in the areas of current density, cell potential and stability.

There exists extensive review literature in the area of biological fuel cells. Notably, Palmore and Whitesides summarized biological fuel cell concepts and performance up until about 1992.[1] More recently, Katz and Willner discussed recent progress in novel electrode chemistries for both microbial and enzymatic fuel cells.[2] We do not duplicate these valuable contributions, but instead focus on the strengths and weaknesses of state-of-art materials in the context of specific classes of applications, and point to areas where additional knowledge is currently needed to exploit biological fuel cells. With some exceptions, we focus on contributions made after 1992.

Biofuel cells have traditionally been classified according to whether the catalytic enzymes were located inside or outside of living cells. If living cells are involved the system is considered to be microbial, and if not it is considered enzymatic. Although microbial fuel cells posses unique features unmatched by enzymatic cells, such as long-term stability and fuel efficiency, the power densities associated with such devices are typically much lower owing to resistance to mass transfer across cell membranes. Thus, microbial fuel cells are expected to find limited application in small-scale electronic devices. This review will focus on enzymatic biofuel cells. While such cells typically demonstrate reduced stability due to the limited lifetime of extracellular enzymes, and are typically unable to fully oxidize fuels, they allow for substantial concentration of catalysts and removal of mass transfer barriers and provide higher current and power densities, approaching the range of applicability to micro- and mini-scale electronics applications.

Applications and Requirements

The range of possible applications for biofuel cells may be broken down into three main subclasses:

1. Implantable power, such as micro-scale cells implanted in human or animal tissue, or larger cells implanted in blood vessels.
2. Power derived from ambient fuels or oxidants, mainly plant saps and juices, but extending to sewage and other waste streams.
3. Power derived from conventional fuels including hydrogen, methanol or higher alcohols.

Classes 1 and 2 are closely related. The fuels available for implantable power, such as blood borne glucose or lactate, are ambient in the sense that they are present in a physiological environment in the absence of a fuel cell device. One major distinction between these two classes is that the ambient-fueled cell need not be implanted, and focuses on plant- or waste-derived fuels, whereas the implantable cell focuses on animal-derived fuels and is present within the physiological system. Class 3 is unique in that this class competes with well-established conventional fuel cell technology. To a greater or lesser extent, all three classes share the fundamental technical requirements of high power density and high activity.

Enzyme Catalyzed Direct Electron Transfer

There are two ways of coupling an electrode process to an enzyme reaction (see Figure 2).[3-5] The first approach is based on the utilization of low-molecular weight redox mediators.[4] The second is to pursue direct (mediatorless) electron transfer.[5] In this case, the electron is transferred directly from the electrode to the substrate molecule (or vise versa) via the active site of the enzyme. Direct (mediatorless) electron exchange between a redox group of protein and the electrode surface has been studied for a number of proteins such as cytochrome c, peroxidase, ferredoxin, plastocyanin, azurin, azotoflavin, glucose oxidase, etc.[6-8] These studies developed an electrochemical basis for the investigation of protein structure, mechanisms of redox transformations of protein molecules, and metabolic processes involving redox transformations. Recently, the ability of oxidoreductase enzymes to catalyze mediatorless electron transfer from the electrode surface to the substrate molecule (or vice versus) has been demonstrated for laccase, lactate dehydrogenase, peroxidase, hydrogenase, p-cresolmethylhydroxylase, methylamine dehydrogenase, succinate dehydrogenase, fumarate reductase, D-fructose dehydrogenase, alcohol dehydrogenase, and D-gluconate dehydrogenase.[3]

Mediated electron transfer

The main purpose of redox mediation is to increase the rate of electron transfer between the active site of enzyme biocatalysts and an electrode by eliminating the need for the enzyme to interact directly with the electrode surface. Depending on the enzyme and reaction conditions, mediated electron transfer rates may exceed by orders of magnitude that of the direct mechanism. However, by introducing an additional transfer step, enzyme-mediator electron transfer is isolated from direct electrode potential control. For typically fast (Nernstian) kinetics between the mediator and electrode surface, the electrode potential merely controls the relative concentration of oxidized and reduced mediator at the surface. The electrode thus provides a boundary condition for electron flux to and from solution via the mediator.

The practical impact of such considerations is that the working potential of a mediated biocatalytic electrode is dominated by the

redox potential of the mediator couple, and the operating potential of a biofuel cell comprising two such electrodes will be primarily determined by the difference in redox potential of the two mediator couples. The differences in redox potential between the mediator and enzyme, and enzyme and substrate, represent driving forces for electron transfer, and therefore must be nonzero. As shown in Figure 2 for a glucose-oxygen biofuel cell,[9] this difference represents an activation overpotential that reduces the observed open circuit potential from a theoretical maximum, given by the potential difference between the substrates. Some examples of diffusional mediators to be discussed are NADH cofactors, ABTS, and redox hydrogels.

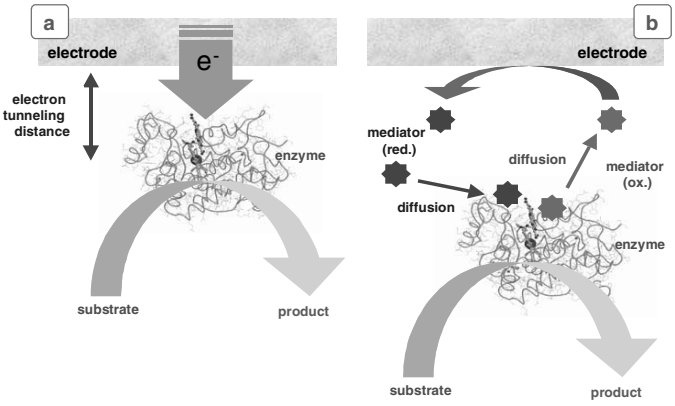

Figure 1. Alternative electron transfer mechanisms. (a) Direct electron transfer (tunneling mechanism) from electrode surface to the active site of an enzyme; (b) Electron transfer via redox mediator.

Engineering of enzymatic biofuel cell Systems

The recent literature in bioelectrochemical technology, covering primarily the electrochemical aspects of enzyme immobilization and mediation, includes few reports describing engineering aspects of enzymatic biofuel cells or related devices. Current engineering efforts address issues of catalytic rate and stability by seeking improved kinetic and thermodynamic properties in modified enzymes or synthesized enzyme mimics. Equally important is the development of materials and electrode structures that fully maximize the reaction rates of known biocatalysts within a stable environment. Ultimately, the performance of biocatalysts can only be assessed by their implementation in practical devices.

Future Outlook

The development of successful power sources has always been driven by specific applications. So it must also be for successful biofuel cells. Therefore, technological paths will be determined by application specifics: Implanted biofuel cells must exhibit biocompatibility, and cathodes for *ex vivo* electronics must take advantage of gas-phase oxygen. That being said, a general statement can be made that for the advantages of biofuel cells to compel adoption, the weaknesses relative to conventional technology must be minimized. It is clear that the advantages of biocatalysts are reactant selectivity, activity in physiological conditions, and manufacturability. The weaknesses are equally clear- modest absolute activity, and low stability, issues of significance, to a greater or lesser extent, in every conceivable application of this technology.

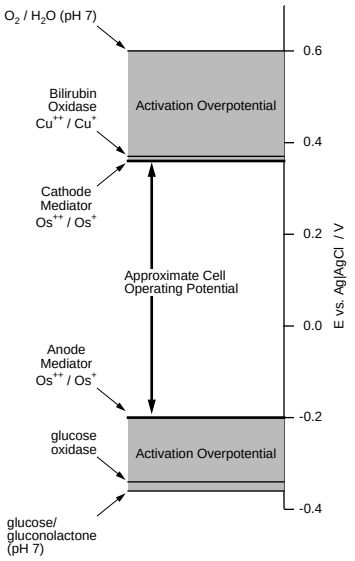

Figure 2. Potential Schematic for a mediated biofuel cell.

References

1. Palmore, G. T. R.; Whitesides, G. M., Microbial and enzymic biofuel cells. *ACS Symp. Ser.* **1994,** 566, (Enzymatic Conversion of Biomass for Fuels Production), 271-90.
2. Katz, E.; Shipway, A. N.; Willner, I., Biochemical fuel cells. In *Handbook of Fuel Cells – Fundamentals, Technology and Applications*, ed.; Vielstich, W.; Gasteiger, H. A.; Lamm, A., Eds., John Wiley and Sons, Ltd.: London, 2003; Vol. 1, pp. 355-381.
3. Ghindilis, A. L.; Atanasov, P.; Wilkins, E., Enzyme-catalyzed direct electron transfer. Fundamentals and analytical applications. *Electroanalysis* **1997,** 9, (9), 661-674.
4. Bartlett, P. N.; Tebbutt, P.; Whitaker, R. G., Kinetic aspects of the use of modified electrodes and mediators in bioelectrochemistry. *Progress in Reaction Kinetics* **1991,** 16, (2), 55-155.
5. Tarasevich, M. R., Bioelectrocatalysis. In *Comprehensive Treatise of Electrochemistry*, Plenum Press: New York, 1985; Vol. 10, pp. 231-295.
6. Hill, H. A. O., Bio-Electrochemistry. *Pure and Applied Chemistry* **1987,** 59, (6), 743-748.
7. Nakamura, K.; Aizawa, M.; Miyawaki, O., *Electro-enzymology, coenzyme regeneration*. Springer-Verlag: Berlin ; New York, 1988; p viii, 166.
8. Guo, L. H.; Hill, H. A. O., Direct Electrochemistry of Proteins and Enzymes. *Advances in Inorganic Chemistry* **1991,** 36, 341-375.
9. Kim, H. H.; Mano, N.; Zhang, X. C.; Heller, A., A miniature membrane-less biofuel cell operating under physiological conditions at 0.5 V. *Journal of the Electrochemical Society* **2003,** 150, (2), A209-A213.

SOLID OXIDE FUEL CELLS: AN OVERVIEW

S. C. Singhal

Pacific Northwest National Laboratory
902 Battelle Boulevard
P. O. Box 999
Richland, WA 99352, USA

Intriduction

Solid oxide fuel cells (SOFCs),[1] based on an oxide ion conducting electrolyte, offer a clean, low-pollution technology to electrochemically generate electricity at high efficiencies. These fuel cells provide many advantages including high efficiency, reliability, modularity, fuel adaptability, and very low levels of SO_x and NO_x emissions. Quiet, vibration-free operation of SOFCs also eliminates noise usually associated with conventional power generation systems. Furthermore, because of their high operation temperature (700-1000^{o}C), some hydrocarbon fuels such as natural gas can be reformed within the cell stack eliminating the need for an expensive, external reformer. This paper reviews the current status of the SOFC technology for use in stationary power systems and transportation auxiliary power units.

SOFCs essentially consist of two porous electrodes separated by a dense, oxide ion conducting electrolyte. Oxygen supplied at the cathode (air electrode) reacts with incoming electrons from the external circuit to form oxide ions, which migrate to the anode (fuel electrode) through the oxide ion conducting electrolyte. At the anode, oxide ions combine with H_2 and/or CO in the fuel to form H_2O (and/or CO_2), liberating electrons. Electrons flow from the anode through the external circuit to the cathode. The overall cell reaction is simply the oxidation of fuel (H_2 and/or CO).

Cell Materials

Oxides such as yttria-stabilized zirconia (YSZ), rare earth doped ceria, rare earth doped bismuth oxide, and doped lanthanum gallates have been widely investigated as electrolytes.[1] Of these, YSZ has been most successfully employed in SOFCs. The yttria dopant serves dual roles: it stabilizes the high temperature cubic phase in zirconia and also generates oxygen vacancies; the high oxide ion conductivity in YSZ is attributed to these oxygen vacancies. Zirconia doped with about 10 mole percent yttria is generally used as the electrolyte. The thermal expansion of 10 mole percent YSZ is about 10×10^{-6}/°C; materials for all other cell components are chosen to have thermal expansion near this value.

Lanthanum manganite suitably doped with alkaline and rare earth elements is generally used as cathode. Lanthanum manganite is a p-type perovskite and shows reversible oxidation-reduction behavior. The material can have oxygen excess or deficiency depending upon the ambient oxygen partial pressure and temperature. The electronic conductivity of lanthanum manganite is due to hopping of an electron hole between the +3 and +4 valence states of Mn. This conductivity is enhanced by doping with a divalent ion such as calcium or strontium. Furthermore, any interactions between doped lanthanum manganite and yttria-stabilized zirconia electrolyte up to 1000^{o}C are minimal. In addition to lanthanum manganite, other perovskites such as doped lanthanum cobaltite, ferrite and nickelite have also been used as cathode materials. These oxides have generally higher activity for oxygen reduction than lanthanum manganite. However, the thermal expansion coefficient of cobaltites is much higher than that of the YSZ electrolyte, and the electrical conductivities of ferrites and nickelites are low.

The reducing conditions present on the fuel side of an SOFC permit the use of a metal such as nickel (alternately cobalt or ruthenium) as the anode (fuel electrode). However, the thermal expansion of nickel is considerably larger than that of YSZ. Nickel can also sinter at the cell operating temperature resulting in a decrease in the fuel electrode porosity. These problems are minimized by using a Ni/YSZ cermet for the anode. The YSZ prevents sintering of the nickel particles, decreases the thermal expansion coefficient bringing it closer to that of the electrolyte, and provides better adhesion of the fuel electrode with the electrolyte. Even though Ni-YSZ cermet remains the most commonly utilized anode material for SOFCs, recently copper-based anodes have also been proposed for intermediate-temperature (< 800^{o}C) SOFCs intended to operate directly on hydrocarbon fuels.

The interconnection should have nearly 100 percent electronic conductivity; stability in both oxidizing and reducing atmospheres at the cell operating temperature; low permeability for oxygen and hydrogen to minimize direct combination of oxidant and fuel during cell operation; a thermal expansion coefficient close to that of the air electrode and the electrolyte; and non-reactivity with other cell materials. To satisfy these requirements, doped lanthanum chromite is used as the interconnection material for cells intended for operation at about 1000^{o}C. Lanthanum chromite is a p-type conductor; its conductivity is due to small polaron hopping from room temperature to 1400°C at oxygen pressures as low as 10^{-18} atm. The conductivity is enhanced as lower valence ions (e.g., Ca, Mg, Sr, etc.) are substituted on either the La^{3+} or the Cr^{3+} sites. In cells intended for operation at lower temperatures (< 800^{o}C), it is possible to use oxidation-resistant metallic materials for the interconnection. Many stainless steels and high temperature chromia-forming alloys are being developed for this application and their successful use will result in substantial reduction in the cost of SOFC stacks.

Cell Designs

The two most common designs of SOFCs are the tubular and the planar. In the tubular cells, as illustrated by the Siemens Westinghouse design shown in **Figure 1**, the cell components are deposited in the form of thin layers on a doped lanthanum manganite cathode tube[1-3] which is fabricated by extrusion and sintering. YSZ electrolyte is deposited in the form of about 40 um thick dense layer by electrochemical vapor deposition[4] or by plasma spraying; and the Ni/YSZ anode is deposited either by nickel slurry application followed by electrochemical vapor deposition of YSZ, by sintering of a Ni+YSZ slurry, or by plasma spraying. The doped lanthanum chromite interconnection strip along the length of the cell is deposited by plasma spraying.[5]

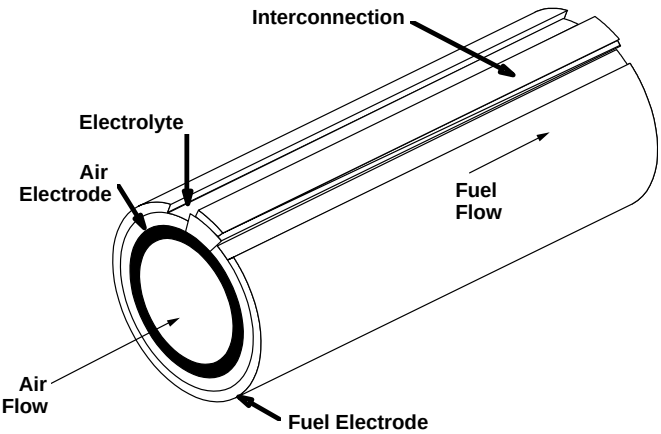

Figure 1. Tubular design solid oxide fuel cell.

Tubular cells perform satisfactorily for extended periods of time under a variety of operating conditions with less than 0.1% per 1000 hours performance degradation and have a power density at 1000°C of about 0.20-0.25 W/cm^2. To date, the tubular design has progressed the most and power generation systems of up to 250 kW size have been produced and operated using such cells. To construct an electric generator, individual cells are connected in both electrical parallel and series to form a semi-rigid bundle that becomes the basic building block of a generator. The cell bundles are arrayed in series to build voltage and form generator modules. These modules are further combined in either series or parallel to form SOFC generators. Using this scheme, Siemens Westinghouse fabricated a 100 kW size and a 250 kW size atmospheric power generation system. The 100 kW system was successfully operated for over two years in the Netherlands and Germany on desulfurized natural gas without any significant performance degradation.

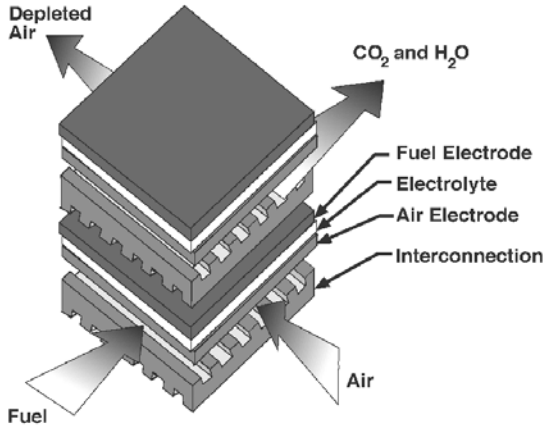

Figure 2. Planar design solid oxide fuel cell.

Even though the tubular SOFCs have progressed the most, their electrical resistance is high, power densities (W/cm^2 and W/cm^3) low, and manufacturing costs high. The low power density (0.20 to 0.25 W/cm^2) makes tubular SOFCs suitable only for stationary power generation and not very attractive for transportation applications. Planar SOFCs, in contrast, are capable of achieving very high power densities of up to about 2 W/cm^2. In the planar design, illustrated in **Figure 2** in its most generic version**,** the cell components are configured as thin, flat plates. The interconnection, which is ribbed on both sides, forms gas flow channels and serves as a bipolar gas separator contacting the anode and the cathode of adjoining cells. The cells are fabricated by low-cost conventional ceramic processing techniques such as tape casting, slurry sintering, screen printing, or by plasma spraying. Different organizations have developed several different variations of the planar design and use different manufacturing processes. In electrolyte-supported cells, the thickness of the electrolyte, typically yttria-stabilized zirconia (YSZ), is 50 to 150 μm, making their ohmic resistance high, and such cells are suitable for operation at ~1000°C. In electrode-supported designs, the electrolyte thickness can be much lower, typically 5 to 20 μm, which decreases their ohmic resistance and makes them better suited for operation at lower temperatures (~800°C). Lower temperature operation results in less degradation of cell and stack components, makes feasible use of inexpensive metallic interconnects, is less demanding on seals, and aids in faster heat up and cool down. The anode (Ni/YSZ cermet) is selected as the supporting electrode, because it provides superior thermal and electrical conductivity, superior mechanical strength, and minimal chemical interaction with the electrolyte. Kim et al[6] have reported power densities as high as 1.8 W/cm^2 at 800°C for such anode-supported SOFCs.

Sizeable cost reductions are possible with the planar design cells through a concept called "mass customization" that is being pursued in the U.S. Department of Energy's Solid State Energy Conversion Alliance (SECA).[7] This concept involves the development of a 3 to 10 kW size core SOFC module, that can be mass produced and then combined for different size applications in stationary power generation, transportation, and military market sectors, thus eliminating the need to produce custom-designed and inherently more expensive fuel cell stacks to meet a specific power rating. Very high power densities of anode-supported planar SOFCs make them very attractive for use in the core SOFC module.

Using planar cells, stationary power systems of up to 25 kW size have been fabricated by various organizations and tested for up to a few thousand hours with only limited success because of the problems with the glass seals that are employed to isolate air from fuel in cell stacks. Another application of the high power density planar SOFCs is in on-board auxiliary power units (APUs) in vehicles. Such APUs, operating on existing fuel base, can supply the ever-increasing electrical power demands of luxury automobiles, recreational vehicles, and heavy-duty trucks. Delphi/Battelle has developed a 5 kW APU using anode-supported SOFCs.[3] Such units operates on gasoline, which is reformed through partial oxidation. APUs require fast heatup and ability to be thermally cycled. Thermomechanical, thermal-fluids, and stress modeling is being conducted to aid in achieving stack designs with such attributes.

Summary

SOFCs provide a highly efficient, low-pollution power generation technology. Performance of tubular SOFCs has been confirmed by successful operation in several power generation systems of up to 250 kW size, though their cost still remains to be reduced. Planar SOFCs, particularly anode-supported, provide much higher power densities and potentially much lower cost than the tubular cells. The challenge in commercializing planar SOFCs offering high power densities requires successful development of seals for isolating oxidant from fuel, development of low-cost oxidation-resistant metallic alloys for use as interconnection, and lower cost. Additionally, for transportation applications, ability for rapid start up and thermal cycling needs to be developed. When fully developed, planar SOFCs will have widespread application in the stationary distributed power generation, transportation and military market sectors. Systems based on both the tubular and the planar SOFCs are ideal power generation systems – reliable, clean, quiet, environmental friendly, and fuel conserving.

References

1. Singhal, S. C. and Kendall, K., *Solid Oxide Fuel Cells: Fundamentals, Design and Applications*, Elsevier, Oxford, UK, **2003**.
2. Singhal, S. C., *Materials Research Bulletin*, **2000**, 25(3), 16-21.
3. Singhal, S. C., *Solid State Ionics*, **2002**, 152-153, 405-410.
4. Pal, U. B. and Singhal. S. C., *J. Electrochem. Soc.*, **1990**, 137, 2937-41.
5. Kuo, L. J. H., Vora, S. D., and Singhal, S. C., *J. Am. Ceram. Soc*., **1997**, 80, 589-93.
6. Kim, J-W, Virkar, A. Fung, K-Z., Mehta, K., and Singhal, S. C., *J. Electrochem. Soc*., **1999**, 46, 69-78.
7. Surdoval, W. A., Singhal, S. C., and McVay, G. L., in *Solid Oxide Fuel Cells VII*, Yokokawa, H., and Singhal, S. C., eds., The Electrochemical Society, Inc., Pennington, NJ, **2001,** PV 2001-16, 53-62.

CHEMICAL SYSTEMS FOR HYDROGEN STORAGE

George J. Thomas

Consultant,
Sandia National Laboratories
Livermore, CA 94551

Hydrogen storage systems for use in hydrogen-fueled vehicles will require high energy density and high specific energy in order to achieve comparable performance to conventional gasoline-fueled vehicles. It is believed that this issue remains as one of the critical barriers to the development of fuel cell powered vehicles. With the president's initiative and increased funding levels in hydrogen and fuel cell development, there are a number of new and exciting areas of research which have emerged aimed at developing high density hydrogen storage media.

At the present time, essentially all hydrogen-fueled vehicles use either compressed gas or liquid hydrogen tanks for onboard storage. Both of these technologies are straightforward, relatively mature and are commercially available. Compressed gas systems have progressed rapidly over the last few years. These cylindrical tanks, constructed with high strength carbon fiber composite materials, are robust, lightweight and have been demonstrated at hydrogen pressures up to 700 bar. However, even at this pressure at ambient temperature, the volumetric density of the hydrogen is insufficient for long-term use. Liquid hydrogen storage has been advocated mainly by BMW and a number of their demonstration vehicles have employed tanks which were developed by Linde. The high energy cost of liquefying hydrogen has been stated as a key issue in its utilization as a fuel.

This presentation will focus on chemistry-based hydrogen storage methods, that is, hydrogen storage materials. Storage materials can be broadly classified as having reversible or non-reversible hydrogen behavior. Reversible materials absorb and desorb hydrogen from the gas phase based on the hydrogen gas overpressure and temperature. These materials can therefore be recharged in-situ onboard the vehicle by supplying hydrogen at the appropriate pressure. On the other hand, non-reversible systems require chemical processing, perhaps including intermediate phases and additional materials, to be recharged. In this case, the spent material (depleted of hydrogen) which could be in liquid or solid form, must be removed from the vehicle and reprocessed elsewhere. These materials are generally referred to as chemical hydrides. Although reversible systems would be the preferred method, both options are currently under consideration.

There are many materials which have reversible hydrogen properties. These include materials where the hydrogen is adsorbed to the surface and those where the material is absorbed into the bulk. Single wall carbon nanotubes and other nanostructured materials, such as metal organic frameworks (MOFs), are examples of adsorbed hydrogen systems being studied. Critical issues which must be answered with adsorbed systems are hydrogen capacity, volumetric density and hydrogen binding energies.

Materials where hydrogen is absorbed and chemically bound in the bulk offer the potential of having the highest volumetric density of hydrogen, surpassing even that of liquid hydrogen. Metal hydrides are the best known class of materials with this property and these have been extensively studied for more than 30 years. Although they exhibit good capacities and good kinetic properties, they are generally too heavy. Lighter weight hydrides typically have stronger covalent or ionic hydrogen bonds and hence require high temperatures for hydrogen release. Emphasis in this area of research has shifted in recent years to other materials. Complex hydrides, particularly those formed with Al-H or B-H complexes, offer higher hydrogen capacities, lighter weight over intermetallic hydrides and reduced hydrogen binding energies over covalent or ionic hydrides. However, only NaAlH4, doped with Ti, has been demonstrated to be reversible at this time. Work on this and other complex hydrides, as well as effective dopant materials and processes to achieve reversible behavior and the desired kinetic and thermodynamic properties, is currently being pursued. A number of other alternative materials have also shown promising early results and are being proposed for further study, including imide-amides and amine borane systems.

In this overview presentation we will discuss inherent limitations of hydrogen storage concepts and briefly describe some of the specific chemical systems mentioned above. Emphasis will be on material performance relative to that required in storage applications.

OVERVIEW OF HYDROGEN PRODUCTION

Carolyn C. Elam and Robert J. Evans

National Renewable Energy Laboratory,
1617 Cole Blvd, Golden, CO 80401

Introduction

Hydrogen, like electricity, can be produced from many sources, including fossil fuels, renewable resources, and nuclear energy. Today, hydrogen is produced primarily from natural gas using well-known commercial thermal processes. In the future, it could be produced directly from renewable resources. In the meantime, we can adapt current technologies to produce hydrogen with significantly reduced CO_2 emissions, through carbon capture and sequestration processes, and by using renewable and nuclear electricity to produce hydrogen with no production-side CO_2 emissions.

The transition to a Hydrogen Economy will progress through the development and commercialization of a range of advanced technologies to produce, store, and use hydrogen. Hydrogen would first be produced by distributed thermochemical and electrolytic means and then eventually via photolytic processes. In the near- to mid-term, on-site production from natural gas or electricity will provide hydrogen for the moderate but growing needs of various energy sectors. Eventually, larger networks of pipelines will permit distribution of hydrogen, produced throughout the country by a variety of means from domestic resources, to urban centers, airports, and seaports.

There are technical and economic hurdles to the implementation of hydrogen energy systems. The cost of hydrogen production from renewable resources (with low or no CO_2 emissions) is not currently competitive with that of production from fossil feedstocks (with high CO_2 emissions). Hydrogen can provide storage options for intermittent renewable technologies such as solar and wind. It can transform base-load technologies such as nuclear, geothermal, biomass, and hydro into load-following systems. When combined with emerging decarbonization technologies, hydrogen could reduce the climate impacts of continued fossil fuel use.

Current Hydrogen Production Processes

Nearly half of the worldwide production of hydrogen is via large-scale steam reforming of natural gas:

$$CH_4 + H_2O \rightarrow CO + 3\,H_2$$
$$CO + H_2O \rightarrow CO_2 + H_2$$

By 2030-2050, world-wide oil production and U.S. production of natural gas are expected to have reached or passed their peak, thereby increasing their costs. In addition, their *value* as feedstocks for chemical production would far exceed their value as fuels. Coupled with carbon constraints, this would require a paradigm shift in the fuels used to produce hydrogen.

There is a need to build on the established steam reforming technology base, which primarily uses natural gas and is accomplished in large, central facilities, to provide low-cost hydrogen for nearer-term hydrogen demonstration projects, while research continues on cleaner fossil- and renewable-based hydrogen production systems.

With continued improvements in renewable power systems (wind, solar, biomass, geothermal, etc), hydrogen would be produced without significant (or any) carbon emissions. Eventually, through continued support of long-term RD&D, direct water-splitting technologies would be available, realizing the ultimate Hydrogen Vision (sunlight + water = hydrogen = electricity + water + usable heat). This feedstock flexibility is an essential and unique feature of hydrogen - with (in some cases, only minor) modification to existing and developing technologies, hydrogen can be produced efficiently and cleanly from nearly any resource, including natural gas, coal, nuclear power, renewable energy and wastes.

It is anticipated that coal gasification combined with sequestration strategies would compete with natural gas, renewables and nuclear to produce hydrogen. Renewable, nuclear and fossil fuel/sequestration systems would lead to the centralized production of hydrogen, transporting it to cities for use in distributed generation systems and as fuels for fuel cell vehicles.

Nearly half of the worldwide production of hydrogen is via steam methane reforming; a catalytic process that involves reacting natural gas or other light hydrocarbons with steam. The primary by-product from this process is carbon dioxide, the majority of which is exhausted to the atmosphere. At the large scale, this is the most energy-efficient and cost-competitive commercial technology available. In order to reduce carbon emissions to the atmosphere, these plants could be engineered to allow the capture and sequestration of the carbon dioxide emissions from the process.

High purity hydrogen is also produced by electrolysis - the use of electricity to split water into its elements, hydrogen and oxygen. Electrolysers are commercially available around the world and any source of electricity can be used. The cost of electricity directly impacts the cost for hydrogen production; however, electrolysis is the nearer-term option for small-scale distributed hydrogen production. The emissions from this production technology are solely from electricity production. Use of renewables, such as wind or solar, can make this a clean and sustainable option for hydrogen production.

Research, Development and Demonstration Status and Needs

Fossil Production Systems

Current RD&D efforts are focused on developing improved processes for smaller-scale hydrogen production systems, based on established industrial production processes or innovative reactor designs. These include industry-led cost-shared development and deployment of small-scale autothermal reformers (ATR) and steam methane reformers (SMR). Process improvements may have limited impact on greenhouse gas (GHG) emissions due to the focus on using conventional fossil fuels to keep costs low. However, well-to-wheels efficiency improvements relative to conventional systems can directly reduce GHG and other emissions.

Fundamental and applied research and development of high-temperature, high-pressure separation and purification processes need to proceed at a rate sufficient to allow significant impact on process efficiency and cost. Such efforts would enable demonstration of large integrated coal gasification plants, such as integrated gasification combined cycle (IGCC) coal plants combined with sequestration. The facilities would co-produce electricity and hydrogen (via water-gas shift of the syngas), depending on power and fuel demands. Support is also needed for accelerated materials research and system development for ceramic/membrane reactors and microchannel reformers to meet the growth in demand for distributed and centralized hydrogen generation at lower capital costs and increased efficiency.

Renewable Production Systems

Current RD&D efforts are focused on a broad range of options to produce hydrogen from biomass (fermentative processes, integrated biomass pyrolysis systems, and supercritical water processes), intermittent renewables (wind and solar), and base-load renewables (geothermal and hydro).

Intermittent Renewables

For intermittent renewables, hydrogen-production efforts are focused on integrating wind-electrolysis systems, reducing the costs of electrolyzers, and on developing small-scale units for home refueling applications. These efforts include industry-led cost-shared development of small-scale electrolyzers, industry-university partnerships to integrate renewable systems, and national lab efforts to develop high-temperature steam electrolyzers. Cost reductions in wind and photovoltaic technologies will have direct impacts on the economic competitiveness of renewable electrolysis.

Nuclear-Based Production Systems

Nuclear power-to-hydrogen is receiving increasing attention as we address the mounting evidence of the greenhouse gas impacts of continued and increased use of fossil fuels. Conventional electrolyzers can be used to produce hydrogen from nuclear power. Waste heat from high-temperature nuclear reactors (Gen IV) or from concentrated solar power could be used for hydrogen production via chemical cycles.

Current R&D efforts are primarily focused on the development of high-temperature steam electrolyzers. Parallel development of next-generation nuclear power facilities are expected to result in systems that can be used to produce hydrogen with no production-side CO_2 emissions.

Additional research areas include development efforts on improved materials, higher temperature and pressure operation of conventional alkaline electrolyzers, polymer membrane electrolyzer development, and optimization of control strategies. Acceleration of the development of high-temperature steam electrolyzers, with their reduced electrical demands and higher efficiencies is also needed.

Direct Hydrogen Production Systems

Current RD&D efforts are focused on fundamental approaches to producing hydrogen using sunlight and water through photobiological, photoelectrochemical, and photochemical means. These long-term processes are "the Holy Grail" of the Hydrogen Economy - they are the ultimate clean, sustainable hydrogen production method. However, the R&D investment these technologies receive is limited. Resources will need to be invested in these technologies over a significant period of time before the required fundamental understanding is achieved and industry invests resources in commercialization.

Accelerated understanding of the fundamental aspects of microbial production systems, including thermophilic, algal, and fermentative approaches, is needed to pursue the applied process development efforts to develop and implement microbial hydrogen systems. Improved fundamental understanding is required to permit development of better semiconductor-based photoelectrochemical systems. Accelerated scale-up and validation of promising photoelectrochemical and photochemical systems, and the development of new photolytic processes is also needed.

Biomass

Biomass has the potential to accelerate the realization of hydrogen as a major fuel of the future. Since biomass is renewable and consumes atmospheric CO_2 during growth, it can have a small net CO_2 impact compared to fossil fuels. However, hydrogen from biomass has major challenges. There are no completed technology demonstrations. The yield of hydrogen is low from biomass since the hydrogen content in biomass is low to begin with (approximately 6% versus 25% for methane) and the energy content is low due to the 40% oxygen content of biomass.

Biomass conversion technologies can be divided into two categories: 1) direct production routes and 2) conversion of storable intermediates. Direct routes have the advantage of simplicity. Indirect routes have additional production steps, but have an advantage in that there can be distributed production of the intermediates, minimizing the transportation costs of the biomass. The intermediates can then be shipped to a central, larger-scale hydrogen production facility. Both classes have thermochemical and biological routes. Of these options, gasification coupled with water-gas shift is the most widely practiced process route for biomass to hydrogen. Thermal, steam and partial oxidation gasification technologies are under development around the world. Feedstocks include both dedicated crops and agricultural and forest product residues of hardwood, softwood and herbaceous species.

Conclusions

Abundant, reliable, and affordable energy is an essential component in a healthy economy. Because hydrogen can be produced from a wide variety of domestically available resources and can be used in heat, power and fuel applications, it is uniquely positioned to contribute to our growing energy demands, particularly in the environmentally- and traditional resource- constrained scenarios facing many communities. By diversifying our energy supply, we will not only reduce our dependence on imported fuels, but will also benefit from cleaner technologies and investment in our communities.

CHARACTERIZATION OF HEAVY, BIODEGRADED CRUDE OILS BY HIGH RESOLUTION ESI FT-ICR MASS SPECTROMETRY

Ryan P. Rodgers[2], Geoffrey C. Klein[1], Lateefah A. Stanford[1], Sunghwan Kim[2] and Alan G. Marshall[1,2]

[1.] Department of Chemistry and Biochemistry, Florida State University, Tallahassee, Florida 32306.
[2.] Ion Cyclotron Resonance Program, National High Magnetic Field Laboratory, Florida State University, 1800 E Paul Dirac Drive, Tallahassee, Florida 32310.

Introduction

ESI FT-ICR MS analysis crude oil achieves sufficient mass resolving power ($m/\Delta m_{50\%} > 300{,}000$, in which $\Delta m_{50\%}$ denotes mass spectral peak full width at half height) and high mass accuracy (< 1 ppm) to allow for the baseline resolution and elemental composition assignment of thousands of heteroatomic species in a single crude oil.[1] The selectivity of the ElectroSpray Ionization (ESI) process limits the observed species to those that both contain one or more heteroatoms (N,S or O) and are acidic (negative ion mode) or basic (positive ion mode). The limitation imposed by ESI is beneficial in that the bulk hydrocarbon matrix is transparent to the analysis, and therefore chromatographic pretreatment for the isolation of polar heteroaromatic species is superfluous. Here we apply ESI FT-ICR MS to a series of heavy crude oils of similar geographic origin that have gone through varying degrees of biodegradation.

Experimental

Crude Oil Samples. Each of six biodegraded crude oils (~20 mg) was dissolved in 10 mL of toluene and then diluted with 10 mL of methanol to a final volume of 20 mL. The samples were further diluted to a final concentration of 0.1 mg of crude/mL of solvent. One mL of the final solution was spiked with 30 µL of ammonium hydroxide to facilitate deprotonation for the ESI FT-ICR mass spectral analysis.

Mass Analysis. The crude oils were analyzed at the National High Magnetic Field Laboratory (NHMFL) with a homebuilt 9.4 Tesla Fourier transform mass spectrometer. Ions were generated externally by a micro-electrospray source and samples were delivered by a syringe pump at a rate of 300 nL/min. Approximately 2.2 kV was applied between the capillary needle and ion entrance (heated metal capillary). The externally generated ions were accumulated in a short (15 cm) rf-only octopole for 30s and then transferred via a 200 cm rf-only octopole ion guide to a Penning trap. Ions were excited by frequency-sweep (100-725 kHz @ 150 Hz/µs at an amplitude of 200 Vp-p across a 10-cm diameter open cylindrical cell). The time-domain ICR signal was sampled at 1.28 Msample/s for 3.27 s to yield 4 Mword time-domain data. One hundred data sets were co-added, zero-filled once, Hanning apodized, and fast Fourier transformed with magnitude computation. Mass spectra were internally calibrated with respect to the most abundant heteroatom containing series over the full mass range. Homologous series were separated and grouped by nominal Kendrick mass and Kendrick mass defect to facilitate rapid identification, as described elsewhere.[2]

Results and Discussion

Variations in the molecular weight distributions are readily observable in the broadband mass spectra shown in Figure 1. As the level of degradation increases (Figure 1, top to bottom) the molecular weight distribution narrows and the average mass shifts to lower m/z.

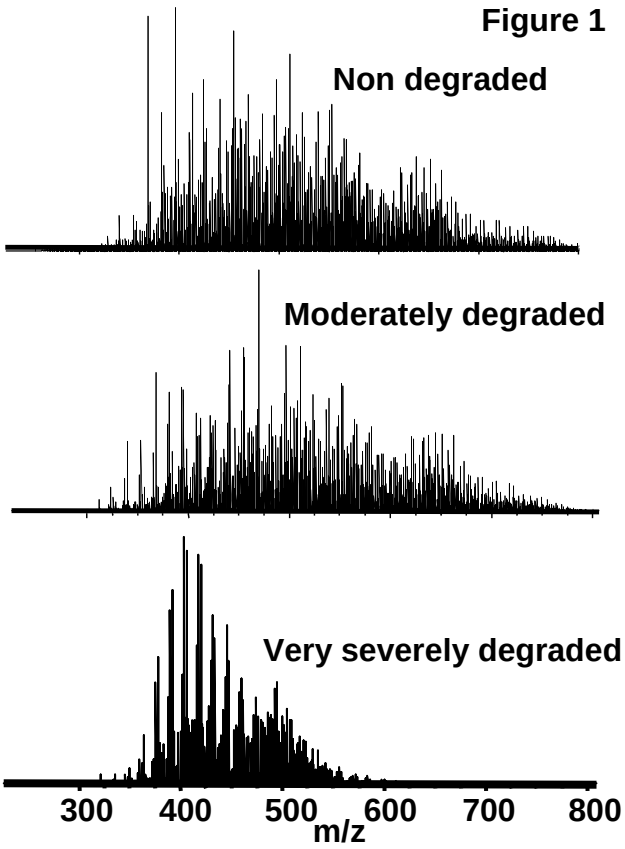

Figure 1. Series of broadband negative ion ESI mass spectra for three (undegraded (top), moderately degraded (middle) and very severely degraded (bottom)) members of a series of biodegraded oil samples.

Such changes in the molecular weight distribution provide little information and are easily obtainable from lower resolution mass spectrometers. FT-ICR MS is unique in that the high resolution coupled with the extremely high mass accuracy (less than 1 ppm) allow for the resolution of very closely spaced isobaric doublets (less than 3 mDa) and elemental composition assignment for observed species. Mass resolution is paramount because each mass spectrum is composed of as many as ~8,000 peaks with as many as 20 peaks at a single nominal mass at an average mass resolving power that exceeds 300,000. The assignment of elemental compositions for the thousands of polar heteroaromatic species observed allows for component-by-component monitoring of the compositional changes in the biodegradation samples.

To highlight the compositional changes, three-dimensional van Krevelen diagrams are constructed from the assigned elemental compositions. The van Krevelen diagram facilitates information retrieval from assigned formulas. The plots, constructed from the assigned elemental compositions of peaks corresponding to oxygen containing compounds in the mass spectra, are displayed in Figures 2 and 3. It is clear that there has been substantial change in molecular compositions as the biodegradation of oil proceeds. For the diagram constructed from the spectrum of the non-degraded sample (Figure 2), O_2 species with double bond equivalence (DBE) value of 1 (which are presumably acyclic fatty acids) dominate in abundance. O_2 species with 6 DBE (likely hopanoic acids) are also abundant. The sample is also rich in highly cyclic or aromatic fatty acid type molecules. The diagram (Figure 3) from the severely degraded oil, shows a shift in dominance of O_2 type abundance from a DBE value

of 1 to a DBE value of 2-4 (presumably mono-, di- and tri- cyclic naphthenic acid). From this pattern of change, we propose that ratio of acyclic to cyclic naphthenic acid can be used as an indicator of biodegradation.

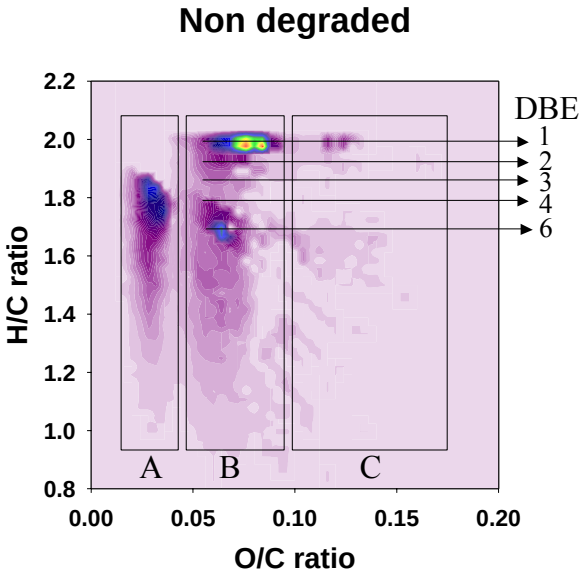

Figure 2. Van Krevelen diagram of O containing compounds in non degraded oil sample. A, B, C each represent O, O_2 and O_3 or more oxygenated species.

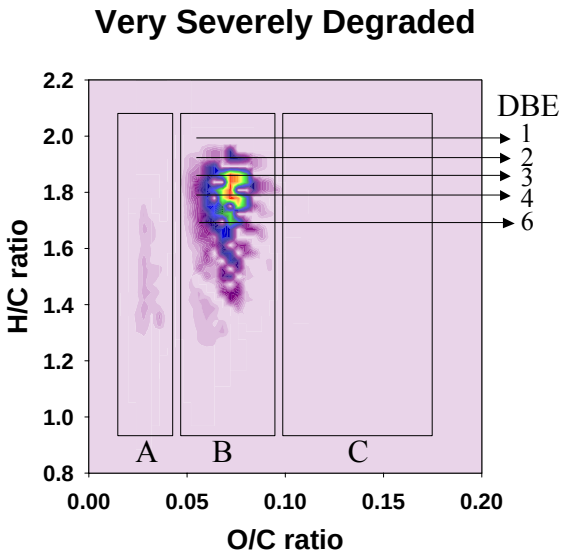

Figure 3. Van Krevelen diagram of O-containing compounds in a very severely degraded oil sample. A, B, C represent O, O_2 and O_3 or more oxygenated species.

The van Krevelen diagrams, constructed from the assigned elemental compositions of peaks corresponding to nitrogen containing compounds in the mass spectra, are displayed in Figures 4 and 5. For nitrogen containing compounds, there is a slight shift in the most abundant species to those with lower H/C ratios as biodegradation proceeds, suggesting that N-containing compounds with more condensed ring type structures are more resistant to biodegradation. A more complete picture, including all classes, types and carbon number distributions will be presented.

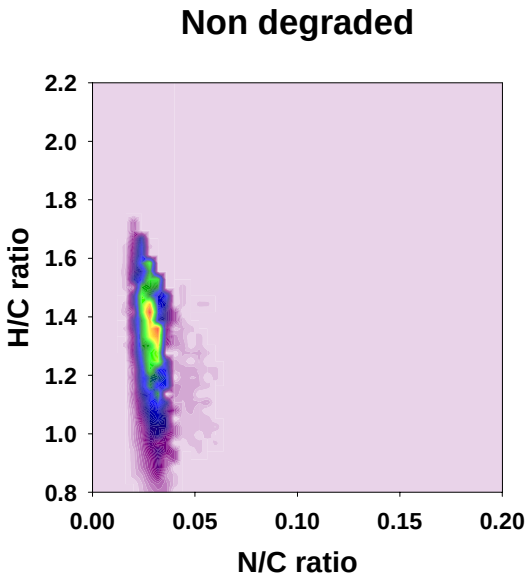

Figure 4. Van Krevelen diagram of N-containing compounds in a non-degraded oil sample.

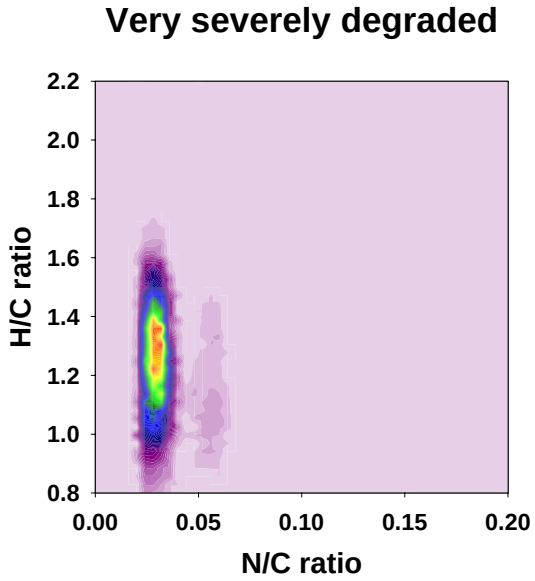

Figure 5. Van Krevelen diagram of N-containing compounds in a very severely degraded oil sample.

Acknowledgments

The authors thank Kuangnan Qian for providing the series of biodegraded oil samples and for his many helpful discussions. This work was supported by ExxonMobil Research and Engineering Co., NSF CHE-99-09502, Florida State University, and the National High Magnetic Field Laboratory in Tallahassee, FL.

References

1. Qian, K; Robbins, W. K.; Hughey, C. A.; Cooper, H. J.; Rodgers, R. P.; Marshall, A. G., *Energy and Fuels,* **2001**, 1505-1511
2. Hsu, C. S.; Qian, K.; Chen, Y. C., *Analytica Chimica Acta,* **1992**, 79-89.

COMPARISON OF THE AVERAGE MOLECULAR WEIGHTS OF HEAVY HYDROCARBONS DETERMINED USING GPC, LD/MS, AND LC/MS

Shinya Sato and Toshimasa Takanohashi

Institute for Energy Utilization
National Institute of Advanced Industrial Science and Technology
16-1 Onogawa, Tsukuba, Ibaraki 305-8569, JAPAN

Ryuzo Tanaka

Central Research Laboratories
Idemitsu Kosan, Co.,Ltd
1280, Kamiizumi, Sodegaura 299-0293, JAPAN

Introduction

Although the molecular weight (MW) is the most basic physical parameter used to characterize heavy hydrocarbons such as asphaltene, no standard method for determining MW has been agreed on. For example, gel permeation chromatography (GPC) is widely used to determine MW, but the value it gives is relative to a polystyrene standard (MWps) and is not regarded as the true MW. Further, asphaltene is considered to form aggregates via the formation of noncovalent bonds, such as intermolecular interactions and hydrogen bonds. It has not been established whether MWps represents the MW of the aggregates or the true MW. By contrast, the MW determined using soft-ionization mass spectroscopy (MWms), such as laser desorption mass spectrometry (LD/MS), is believed to provide a value that more truly represents the MW distribution than does GPC irrespective of molecular aggregation, provided the conditions for ionisation are optimised.

Previously, we used preparative GPC to determine the properties of asphaltene separated into five fractions. We found that the H/C values increased with the average MWps, up to MWps = 1600-1700. At higher MWps, the ratio became constant[1]. We also have used GPC/MS analyses to demonstrate that at MWps < 800, MWps is smaller than MWms[2].

In this report we use the results of LC/MS and LD/MS analyses to examine the correlation between the average MWps and MWms over the entire MW range, including low MWs, from the perspective of an averaged molecular structural analysis.

Experimental

Samples. The samples used in this study were asphaltenes recovered from the vacuum residue distillation of Iranian Light, Khafji, and Maya crude oils (ASIL, ASKF, and ASMY, respectively) (Table 1). Each sample was separated into five fractions using a GPC (JASCO, 980 Gulliver Series) equipped with a preparative column (Shodex KF2003, exclusion limit 70000), and using chloroform as the eluent[1].

Molecular weight. GPC analyses were carried out using a GPC equipped with two series of analytical columns (Shodex K403HQ, exclusion limit 70000) and chloroform as the eluent. LC/MS analyses were carried out using a LC/MS system (Agilent SL-1100) fitted with an ultraviolet (UV) detector and an atmospheric pressure photo ionisation (APPI) mass spectrometer. The original asphaltenes were analysed and the average MWs determined every 0.5 minutes using the APPI detector. LD/MS analysis was carried out using a Voyager-DE STR mass spectrometer (Applied Biosystems Co. Ltd.) at the Central Research Laboratory, Idemitsu Kosan Co., Ltd. The laser irradiation strength was altered within the range 1.45 to 8.57 mJ/pulse in order to select the optimal conditions to minimise any increase in the higher MW range and fragmentation within the lower MW range.

Table 1 Properties of asphaltenes

Source of VR	Maya (MY)	Khafji (KF)	Iranian Light (IL)
Elemental, wt %			
C	82.0	82.2	83.2
H	7.5	7.6	6.8
S	7.1	7.6	5.9
N	1.3	0.9	1.4
H/C	1.10	1.11	0.98
Carbon aromaticity (fa)	0.53	0.50	0.57
Mn (GPC)	787	903	706

Results and Discussion

Molecular weight determined using LC/MS and GPC. All samples showed MWps distributions of up to 20,000, but the MW values determined using LC/MS extended only to 1,500. The LC/MS system lacks any practicable sensitivity at MW values above 1,500. For values around 1,000, the average MW determined by LC/MS (MWmc) was similar to the MWps values, but the differences between them increased as MWps decreased (Fig. 1). For example, for a MWmc of 430, the corresponding MWps was only 150. This means that values of MWps tend to be underestimated compared with the MW determined using LC/MS. No significant difference in this relationship was found among the different asphaltenes and the results suggest that a more reasonable picture of the MW distribution as determined by GPC will become possible only when a new calibration curve has been determined to allow the existing gap to be bridged.

Molecular weight using LD/MS and GPC. The MWms determined using LD/MS highlight three patterns among the MWps results (Fig.2) with no differences in behavior found for the three asphaltenes used. The three patterns show: (1) MWms is larger than MWps for MWps<800, (2) MWms is similar to MWps for MWps = 800-1,600, (3) MWms is almost constant at MWps>1,600. From these results, the average MWs of asphaltene are considered to be no more than 2,000. Hence, it is reasonable to assume that higher values of MW determined by GPC represent the MW of molecular aggregates.

From the properties of the different asphaltene fractions, the structural parameters were estimated using the average molecular structural analysis technique we have developed[3]. Selected structural parameters are summarized in Table 2, along with the properties.

It is clear that for fraction 1, MWps is about 3-4 times larger than MWms. In fraction 5, MWps is less than 250 and its small value should not arise from asphaltenes. In this instance MWms appears

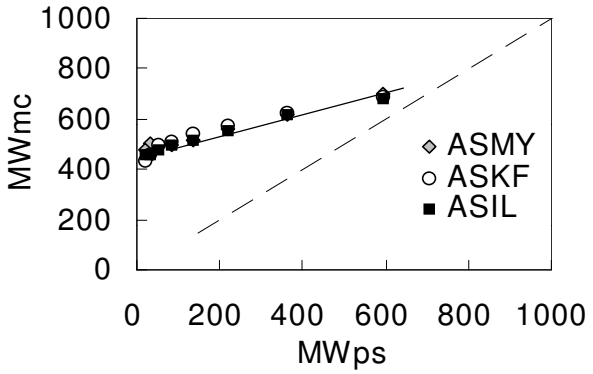

Fig. 1 Relationship between MWps and MWmc

more reasonable and consequently, MWms and MW mc are considered more realistic than MWps.

Formula weight of unit structure. In Table 2, M represents the number of units per molecule consisting of a fused ring system containing aromatic and naphthenic rings. Although MWps and MWms are quite different in the higher MW range, the formula weight per unit (MW/M), calculated from the corresponding MW and M, are similar (Fig. 3). This implies that the average unit size of the asphaltene molecule is the same in each case, and the differences in MW reflect the differences in the number of units contained in a molecule. If all the units in a molecule are linked with bonds etc., then MWms should be the same as MWps.

A reasonable explanation of this phenomenon arises from the fact that LD/MS measures the true mass of a single molecule, whereas GPC measures the mass of a molecular aggregate, and not a single molecule, since chloroform lacks sufficient potential to reduce the aggregates to single molecules. Consequently, given the perspective of an averaged molecular structural analysis, an upper limit is set on the possible molecular size.

Table 2 Properties and structural parametersa of fractionated asphalte

Fraction	1	2	3	4	5
Asphaltene Maya (ASMY)					
H/C	1.18	1.16	1.12	1.07	1.02
fa	0.46	0.47	0.49	0.53	0.57
Mn(GPC)	6984	3318	1677	674	145
Ct	469.2	229.1	97.1	70.1	56.8
M	6.0	3.5	1.7	1.0	1.0
Rt	82.9	19.8	19.8	15.0	12.4
Ra	76.0	15.7	15.7	12.2	10.0
Mn(LD/MS)	2169	1701	1595	634	497
Ct	145.8	117.4	109.9	56.0	45.5
M	1.8	1.8	1.8	1.0	1.0
Rt	26.4	22.0	22.2	12.2	10.2
Ra	23.4	19.0	17.8	9.6	8.4
Asphaltene: Khafji (ASKF)					
H/C	1.12	1.13	1.13	1.08	1.01
fa	0.48	0.48	0.47	0.51	0.56
Mn(GPC)	7856	3617	1712	725	221
Ct	531.9	249.0	117.9	59.5	47.2
M	6.2	4.2	2.3	1.3	1.0
Rt	105.0	48.5	24.2	13.2	11.1
Ra	93.2	38.9	17.5	9.3	8.4
Mn(LD/MS)	1823	1741	1578	710	512
Ct	123.4	119.8	108.7	49.4	49.3
M	1823	1741	1578	710	512
Rt	25.1	23.9	22.3	11.1	11.1
Ra	21.2	18.7	16.2	7.7	8.4
Asphaltene: Iranian Light (ASIL)					
H/C	1.14	1.12	1.12	1.07	0.98
fa	0.48	0.48	0.48	0.53	0.60
Mn(GPC)	5682	3029	1608	658	189
Ct	386.9	211.3	112.3	55.6	40.9
M	6.0	3.3	2.1	1.2	1.1
Rt	73.0	43.2	23.0	12.0	9.5
Ra	62.2	32.3	17.1	9.2	7.6
Mn(LD/MS)	1699	1571	1400	711	475
Ct	115.7	109.6	97.8	49.8	40.9
M	1.8	1.9	2.2	1.1	1.0
Rt	22.5	22.9	20.1	10.8	9.5
Ra	18.4	16.9	14.2	8.1	9.5

Mn: Number averaged MW
Ct: Number of total carbon per molecule
M: Number of unit per molecule
Rt: Number of total rings per molecule
Ra: Number of aromatic rings per molecule

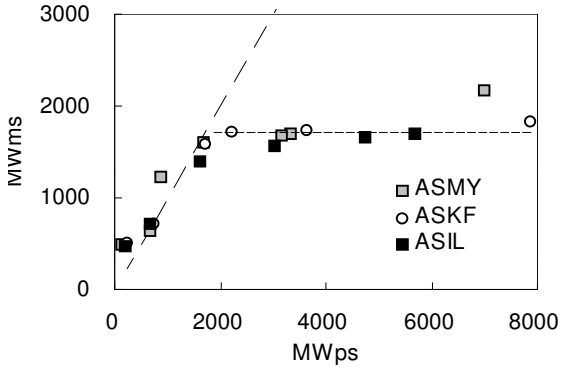

Fig. 2 Relationship between MWps and MWms

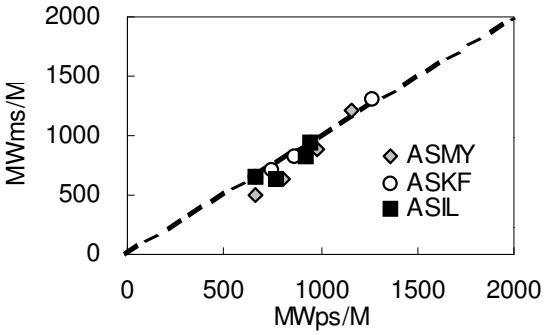

Fig. 3 Relationship between formula weight per unit calculated using MWps and MWms

Conclusion

A comparison of the MW distributions determined using LC/MS, LD/MS and GPC shows that GPC underestimates the MW for MWps<800. However, for MWps>1800, MWms proves to be almost constant, suggesting that GPC detects and measures aggregates of molecules. From the viewpoint of averaged molecular structural analysis, such differences can be explained by the differences in the values of MW. The values of MWps and MWms are similar for MWps = 800-1,800.

Acknowledgement

This study was supported by an International Joint Research Grant Program of the New Energy and Industrial Technology Development Organization (NEDO) and was carried out with the collaboration of the National Institute of Advanced Industrial Science and Technology (AIST), the Central Research Laboratory, Idemitsu Kosan Co., Ltd., the Hokkaido University, the Argonne National Laboratory, the Pennsylvania State University, USA and the Alberta University, Canada.

References

1. Sato, S., Takanohasgi, T., Tanaka, R., *Prep. Pap. Am. Chem. Soc., Div. Fuel Chem.*, **2003**, 48(1), 61
2. Sato, S., Takanohasgi, T., Tanaka, R., *Proceeding, 12th Annual Meeting of Japan Energy Inst.*, **2003**, p61
3. Sato, S., *Sekiyu Gakkaishi*, **1997**, 40, 46

MULTI-DIMENSIONAL HPLC DETERMINATION OF AROMATIC CORE CONTENT, MASS COMPOSTION AND ALIPHATIC SIDE CHAIN DISTRIUBTIONS IN HYDROCARBON FRACTIONS OF HEAVY DISTILLATES

Ashraf Z Khan, Intertek Caleb Brett

Philadelphia Regional Laboratory
327 Erickson Ave, Essington, PA 19029
Telephone: 610 521 1725; akhan@itscb.com

Introduction

In recent years there has been growing interest in refining and asphalt industries for quantitative measurements of hydrocarbon compositions in heavy distillates and solid asphalt materials. The heavy distillates are deep boiling fractions of crude oil separated by multiple refining processes such as atmospheric and vacuum distillations and usually comprise of complex molecules with initial boiling points (IBPs) in the range of 650 - 1300º F. These liquid distillates are widely used as feedstocks for refinery processes including fluid catalytic cracking (FCC), hydrocaracking, dewaxing, coking, lube extraction et al. This is because of their specific values and importance, as well as the refining industries' interests in cutting deep into crude oil barrels [1]. Whatever the means to upgrading the "bottom of the barrel" may be, improved characterization methods for compositional analyses are necessary for process design, operational control and unit optimization. Modern analytical techniques can offer much in this direction.

In spite of the necessity of reliable and affordable techniques, there are only a handful of modern techniques, most notably a specially designed high performance liquid chromatography (HPLC), that can effectively examine heavy distillates [2,3]. Characterization of heavy distillates by conventional techniques like preparative scale liquid or clay-gel chromatography suffers from tedious steps, poor separation capabilities and low repeatability [3]. Although, historically, high resolution mass spectrometry (HRMS) has been an excellent technique, particularly for building refinery process models, it is quite complex, time-consuming and expensive thereby making it difficult for routine analyses [2,4]. Moreover, HRMS involves multiple steps like, first, separation of saturates, aromatics and polar fractions by a preparative HPLC followed by a field ionization mass spectrometry (FIMS) determination of the saturates and a low energy HRMS determination of the aromatics and polars. As a result it takes many hours to analyze a sample. Attempts have been made to update older HRMS methods for use with modern quadrupole mass spectrometers, but it still involves multiple steps for sample preparation and isolation [4].

In this paper attempts have been made to show that a multi-dimensional HPLC, originally pioneered by Robbins and others [2], comprising two detectors and normal phase columns and operating under isocratic and gradient modes offers a number of advantages that makes it an attractive tool for heavy distillate analyses and that no other modern technique can offer.

Experimental

Instrumentation. The multi-dimensional HPLC system, obtained commercially from AC Analytical Controls (Rotterdam, the Netherlands), is based on an HP 1100 unit (Hewlett-Packard, Palo Alto, California) with a module from Alltech (Des Plaines, Illinois). It is operated by a 2D LC Chemstation software with an additional AC software. The system comprises a quaternary pump for isocratic and gradient flows, a vacuum degasser unit for extracting any dissolved air from the solvents, an automatic liquid sampler for sample injection and other accessories. Two normal phase HPLC columns are mounted in series in a thermostated column compartment on separate switching valves (Rheodyne, Rohnert Park, California) that allows a forward flow of solvent to be directed through both or either of the columns independently. An HP photo diode array detector (DAD) is used for determining the aromaticity (% C_a) and an Alltech 500 evaporative light scattering detector (ELSD) for the mass compositions. The DAD spectra are collected over a range of 200 – 430 nm (reference 550 nm) for a maximum coverage of the aromatic π-π absorption [2,3]. A specially designed 1-mm quartz flow cell is used to keep the sensitivities of both the detectors within the working range. The ELSD spectra are obtained using a laser light (650 nm) refractive scattering produced by the sample particles with a nitrogen nebulizer. A dual channel HP 35900E serves as an analog-to-digital interface for the raw ELSD signal, and communicates across the HPIB (IEEE-488) cables.

A preparatory HPLC comprising a 2" diameter silica column and a pre-column with a refractive index detection to monitor cut points was used for comparison of mass. A 500 MHz Varian NMR in $CDCl_3$ with a relaxation agent (TEMPO) was used to record ^{13}C NMR spectra to compare aromaticity.

Separation. The hydrocarbon group-type separation is carried out using two normal phase columns: a propylaminocyano (PAC) column (Whatman, Clifton, NJ) for separation of saturates and mono-aromatics and a dinitroaminopropyl (DNAP) column (ES Industries, Berlin, NJ) for separation of di-, tri-, tetra- and polar (> 5+ ring plus N- and O- functionalities) aromatics. The starting cut points are based on hexadecane (saturates), nonadecylbenzene (1-ring), naphthalene (2-ring), dibenzothiophene (3-ring) and pyrene (4-ring). The valve switching time is determined using a dodecahydrotriphenylene (a 1-ring with a retention in the 2-ring region) solution in n-hexane. The column thermostat temperature is kept at 85ºF.

Calibration. Nonadecylbenzene (1-ring) dissolved in n-hexane is used as a calibration standard with fine tunings done by a certified 'super' heavy distillate (IBP 716ºF) containing no asphaltenes. The calibration procedure is similar to those described [2,3,5]. The DAD response factors for aromaticity are based on the average values determined from the 200-430 nm spectra over 80 model compounds dissolved in n-hexane [2]. The DAD is programmed to measure the absorbance at 210 and 262 nm. The spectra are converted to an energy (meV) basis for each wavelength and the absorbance are integrated over the range 204-430 nm. Because these integrated absorption energies ("oscillator strength") include all transitions between a ground state molecule and its excited states, they count the aromatic carbons [2].

The ELSD is a non-linear detector and does not obey Beer's law, unlike the DAD. Its response (mV) is calibrated using 15 solutions of nonadecylbenzene in n-hexane in the range 0.05 – 12 mg/ml. These 15 solutions are eluted through both the columns and detected by the DAD at 210 and 262 nm followed by the ELSD. The instantaneous concentration (µg/ml) at the chromatographic peak maximum (a pseudo-steady state point) is calculated by applying Beer's law to the absorbance at 210 and 262 nm [2]. Since the ELSD calibration data over the wide concentration range could not be fitted with a single function, the standard levels are divided into two ranges (standards 1 -8 for the low range and 8 – 15 for the high range). The best fit for both sets are plotted in one graph and a 'cross-over point' (the point in the

graph where both fits are closest to each other or actually cross each other) is determined. The calibration curve as established with the calibration procedure is 'scaled' to get a correct calculation of the amount of standard injected. This is done by calculating the Injection and Flow Factors from a nonadecylbenzene standard of 2.000 mg/ml. The Injection Factor and the Flow Factor are related to the DAD and the ELSD responses respectively.

Solvents and Sample Preparation. Three HPLC grade solvents: n-hexane, methylene chloride and iso-propanol (J.T.Baker, Phillipsburgh, NJ) are used as the mobile phase and cyclohexane as the dissolving solvent. Always n-hexane and methylene chloride are treated with activated molecular sieve 4A (J.T.Baker). The sample preparation procedure is simple and involves only one step. A 300 mg of sample is dissolved in a scintillation vial with cyclohexane (10 ml) and sonicated or mildly heated up at 140ºF for 5 min. An aliquot of 1 ml is transferred to a 2 ml vial, from where 10 µl is injected into the system by an autosampler.

Representative samples of refinery process streams are used to illustrate the potential of the technique. These include vacuum gas oils (VGO, 650 to 1050ºF), heavy vacuum gas oils (HVGO, 800 to 1050ºF), vacuum resides (VR, 1050ºF and above) and deep distillates obtained by short-path distillation (DISTACT, 1050 to 1300ºF).

Data Acquisition. The two detectors acquire data at 3 s intervals starting after a dead volume delay (2.1 min) and continuing until the end of the run. The run time is 35 min followed by a regeneration of the columns for 40 min. Each set of samples is initiated with two blanks (cyclohexane) to ensure that each analysis starts from the same condition. This is followed by two quality control standards ('super' heavy distillates) to establish acceptable performance both before and after running the unknown samples. At the end of each run the mass composition, aromatic core content and aliphatic side chain distributions plus the total aromatic core content and mass recovery (in total 20 key parameters) are calculated by the software. The data files can be easily converted to a PDF format for reporting.

Results and Discussion

Chromatographic Profiles. Due to the complex nature of heavy distillates, it takes real efforts to separate and quantitate each of the six key molecular fractions precisely. A proper optimization of the entire system facilitates this separation . After the raw data have been acquired, those are converted into chromatograms, which are automatically plotted - one for the aromaticity in meV and the other for the mass in mV. The DAD and ELSD chromatograms of a heavy distillate standard is illustrated in Figure 1.

The size and shape of the peaks vary from each other with the saturates eluting first and the polars last. The cut points are marked by 5 vertical lines. The saturates show a sharp and tall ELSD peak, no DAD response is to be expected because of its non-aromatic nature. The 1-ring DAD profile shows two distinct peak maxima, presumably, due to the presence of multiple absorption chromophores in the specially refined 'super' heavy distillate standard. Such double peak maxima are absent in any other fractions or in any refinery sample routinely done in this laboratory and, to the best of our knowledge, have not been reported before. The valve-switching time and solvent gradient scheme developed to maximize the resolution of the six groups remain unchanged for subsequent runs. As evident (Figure 1), most of the peaks, particularly the DAD, are asymmetric with some tailing, which is not unusual for a system designed for hydrocarbon group-type separations, rather than any individual compound [3].

Effects of Columns and Flow Modes. Because many previous studies have found that no single column is sufficient to provide the necessary resolution of such a broad range of sample polarities, a two column approach was developed [2]. The standard first gets into the DNAP column, where an initial separation of the saturates and 1-ring from the multi-ring aromatics takes place. After a dead volume delay, the column switching valve transfers these two fractions to the PAC column, where the separation occurs under an isocratic flow of n-hexane. The PAC column, unsuitable for operating with a gradient flow and for a multi-ring separation, completes its separating function with the 1-ring but the flow continues until the valve switches to the DNAP column. In this column the 2-ring aromatics elute first, still under the isocratic flow (Figure 1).

The remaining three groups (3-ring, 4-ring and polar fractions) are separated with gradient flows of n-hexane, methylene chloride and iso-propanol and 'chromatofocussing'. It is a saw-tooth type gradient phenomenon with a successive decrease of methylene chloride after achieving its maximum strength in the gradient. The additional force generated by 'chromatofocussing' is required for the complete elution of the 3-ring and 4-ring aromatics. For a complete elution of the polar fractions, iso-propanol (IPA) is added to the gradient stream. In addition, during the column regeneration cycle an IPA doping is added near the end of the cycle. In spite of all the precautions, some baseline drifts may occur as a non-random error in the gradient region starting from the 3-ring DAD chromatogram (Figure 1). As a result some inconsistency in the aromaticity quantitation of the higher rings may be expected.

Quantitative Results. The HPLC algorithm automatically calculates the quantitative results for the aromaticity, mass and aliphatic side chain distributions, which are tabulated with a statistical evaluation (Table 1). This standard has a low saturates (11.1%), high aromatics (79.0%) and low polars (9.9%). The mass distribution in the aromatics rises from the 1-ring reaching a maximum at the 2-ring (27.1%) followed by a gradual decrease. The aromaticity or aromatic core distribution, however, reaches a maximum (9.8%) at the 3-ring followed by a similar decrease. From the difference between the normalized mass % and aromaticity % for each group, the aliphatic side chain is calculated. Its distribution follows a similar pattern as that for the normalized mass %. The presence of aliphatic side chain across all of the aromatic fraction is favorable to cracking and known to yield more products like gasoline and distillate range materials [6].

The total aromaticity (32.7%) is well below the maximum allowed (70%) by this technique (Table 1). The mass recovery (99.1%) is the ratio of the total measured mass to the injected mass and is strongly dependent on the nature of the heavy distillates. Thus the measurement of both the mass and aromaticity and their distributions in a single step, without any isolation of the fractions, adds a remarkable dimension previously lacking in HPLC analyses of multi-ring aromatics [2,3].

Effects of Initial Boiling Points. The mass recovery (amount recovered/amount injected) of a sample strongly depends on its IBPs, unlike the total aromaticity. For a vacuum gas oil (VGO) at an IBP of 650ºF, the mass recovery is only 65%; whereas for a deep distillate (DISTACT) with an IBP of 1300ºF, the recovery is 104% (Figure 2). The reason for this may be due to the nature of the ELSD detector and the sample itself and also, presumably, sample volatility is an issue for VGO. More volatile compounds evaporate in the ELSD chamber before reaching the light scattering region. A similar observation was made by Robbins and this author

[2,3]. For the total aromaticity, volatility is less relevant since everything passes by the DAD detector and there is no scope for any sample evaporation in the DAD chamber. On going from the VGO to the VR, the aromaticity varies little with IBPs (from 12.6 to 15.7%) but shows a drastic increase for the deep distillates (28.1%). This may be due to the inherently high aromatic contents in the deep distillates, rather than due to the high IBPs. The observation that the mass recovery is strongly dependent on the IBPs, unlike the aromaticity, has some practical relevance. The real world refinery samples have always some lighter fractions (<650ºF) and as a result the mass recoveries are likely to be less than 100%, sometimes as low as 65% (Figure 2). When one is interested only in the total aromaticity or its distributions, which remain unaffected by the presence of the lighter fractions, the mass recoveries may be less relevant. Because these two parameters are determined independently by two detectors with the mass recovery always after the sample has passed through the photo DAD.

Data Validation. A limited number of data validation was made with two other techniques**.** A VGO feed and hydrotreated product were compared with a Preparatory HPLC for saturates and total aromatics mass and with a ^{13}C NMR for total aromaticity (Table 2). There is good agreement between the results obtained by the multi-dimensional HPLC and the preparatory HPLC. The differences between the two techniques either for the saturates or the aromatics in both the feed and product are less than 5%. Given the completely different nature of measurements, these differences are better than expected. Similar agreement was reported earlier [2]. The total aromaticity for the VGO feed measured by ^{13}C NMR is close to the multi-dimensional HPLC, but the hydrotreated product shows a noticeable difference with the HPLC value being lower. A repeated HPLC analysis improved the situation, but was still on the lower side. The problems could be attributed to non-random baseline drifts in the gradient region. Such drifts are inherent in gradient HPLC and are difficult to eliminate entirely [7]. The baseline drifts, usually caused by the different UV absorbance characteristics of the gradient solvents, mostly affect the DAD detector (aromaticity), rather than the ELSD detector (mass).

Refinery Application. The changes in mass and aromaticity distributions that occur in a typical refinery heavy distillate process like hydrotreating is illustrated in Table 3. The purpose of hydrotreating is to reduce the coke-forming, large-ring aromatics with a low conversion of the heavy distillates to lower boiling fractions [2]. On going from the feed to the product, both the mass recovery and total aromaticity dropped from 94 to 82% and 25.5 to 17.8% respectively. The saturates mass increased by 15% and that of 1-ring by almost 12%, whereas those for the remaining 4 fractions decreased. The distribution of $\%C_a$ increased only in the 1-ring by 2.4%, unlike the other 4 fractions. Similar observations were made by Robbins [2].

Thus, apart from being a convenient technique requiring only a single step sample preparation and no isolation of the cuts for separate analyses, the HPLC system equally accommodates both heavy liquid distillates (IBPs > 650ºF) and solid asphalt materials (a subject of recent investigation) using the same technique and procedure by virtue of the materials' excellent solubility in a powerful solvent (cyclohexane) employed and by the sophistication of the technique operating isothermally at room temperature.

Conclusions

The multi-dimensional HPLC has been demonstrated to be an excellent technique for the determination of mass, aromaticity and aliphatic side chain distributions in a wide range of heavy distillates and, also, solid materials. The system provides data for 20 key parameters from a single sample injection, virtually eliminating the tedious sample preparation procedure and reducing the lengthy run times required by other techniques. Being relatively free from noticeable complexity, it is likely to become an affordable and a reliable technique for refining and asphalt industries.

Acknowledgement. The author wishes to thank Intertek Caleb Brett for the permission and financial assistance for this work as well as his colleagues for their comments and suggestions.

References

1. Boduszynski, M.M., Prepr. Pap. – Am. Chem. Soc., Div. Petrol. Chem., **2002,** 47 (4), 329.
2. Robbins, W.K., *J. Chrom. Sci.,* **1998,** 36, 457 and references there in.
3. Khan, A.Z., *Hydrocarbon Engineering,* **2003,** 8 (9), 91.
4. Lubeck, A.L. In *Manual on Hydrocarbon Analysis, 6th ed.,* Drews, A.W., Ed.; ASTM, Philadelphia, 1998, Ch. 6, pp. 34-40.
5. In *HDA Operator and Service Manuals for Refining Analysis,* AC Analytical Controls, Rotterdam, The Netherlands, 1997, Ch. 9, pp. 1-12.
6. Lerner, B.A., and Himpsl, F.L., *Oil & Gas Journal,* **1997,** 1.
7. Dolan, J.W.,Jupille, T.H., and Southern, D. In *Practical HPLC Troubleshooting*, LC Resources, Walnut Creek, California, 2001, Ch. 11, p. 12.

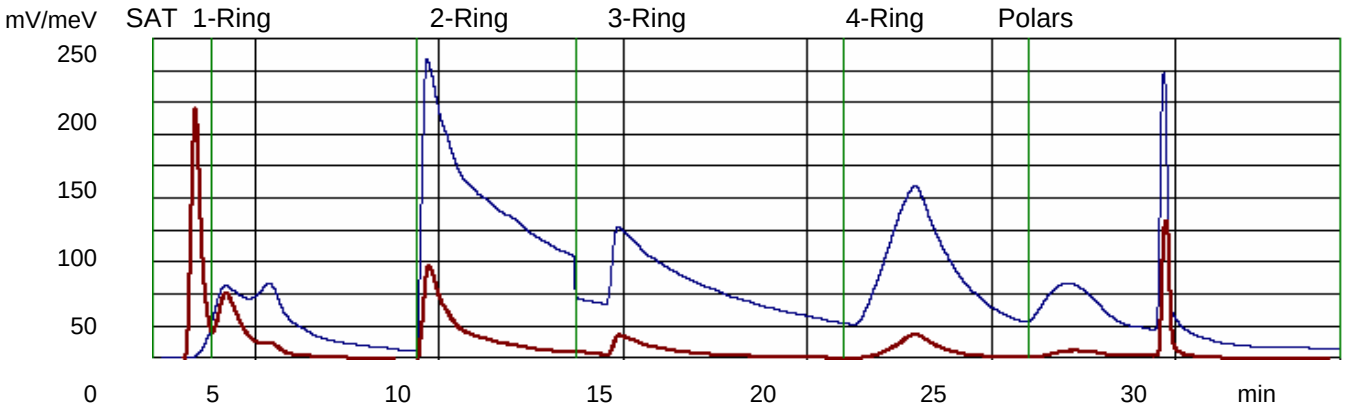

Figure 1. Multi-dimensional chromatograms of a heavy distillate standard obtained by the DAD (thin/blue line in meV) and the ELSD (thick/red line in mV) detectors with the cut points marked by 5 vertical lines (green).

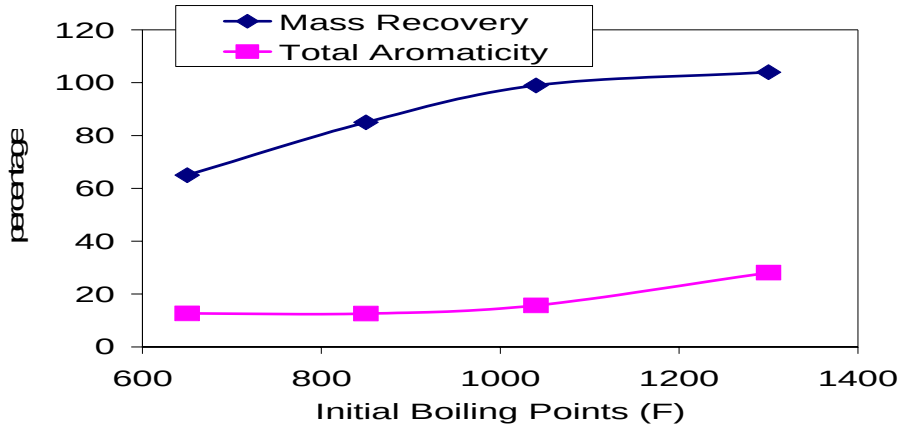

Figure 2. Effects of Initial Boiling Points of Heavy Distillates on Mass Recovery and Total Aromaticity

Table 1. Quantitative Results for Mass, Aromaticity, and Aliphatic Side Chain Distributions in a Heavy Distillate Standard

Group Type	Normalized Mass, %	Standard Deviation	Aromati-city, %	Standard Deviation	Side Chain, %			
Saturates	11.1	0.1	0.1	-0.4	11.1			
1-Ring	18.3	0.7	3.3	-0.2	15			
2-Ring	27.1	1.4	8.8	-0.1	18.3	Total		SD
3-Ring	20.7	0.8	9.8	0.2	10.9	Aromaticity, %	32.7	-0.7
4-Ring	12.9	-1.9	7.5	-1.9	5.4	Mass		
Polars	9.9	-0.5	3.3	-0.1	6.7	Recovery, %	99.1	0.8

Table 2. Data Validation with Preparatory HPLC and ^{13}C NMR

Hydrocarbon Group	Multi-Dimensional HPLC		Preparatory HPLC		^{13}C NMR	
	Feed	Product	Feed	Product	Feed	Product
Saturates Mass, %	42.8	54.2	45.6	56.4	None	None
Aromatic Mass, %	57.2	45.6	53.4	43.6	None	None
Aromatic Core, %	20.2	13.8	None	None	21.0	20.3

Table 3. Comparison of Distributions of Mass and Aromaticity in Hydrotreated Feed with Products

Normalized Mass, %	Feed	Product	Aromatic Core, %	Feed	Product
Saturates	30.1	45	Saturates	0.1	0.1
1-Ring	18.7	30	1-Ring	2.9	5.3
2-Ring	15.7	13.1	2-Ring	6.9	5.8
3-Ring	9.6	3.9	3-Ring	5.8	2.9
4-Ring	12.2	5.2	4-Ring	6.1	2.8
Polars	13.7	2.8	Polars	3.7	0.9
Mass Recovery, %	94	82	Total Aromatic Core, %	25.5	17.8

BIOLOGICAL MARKER COMPOUND TRANSFORMATIONS AS AN EXTREMELY SENSITIVE MEASURE OF CRACKING IN VISBREAKING

Christopher A. Russell[1], Colin E. Snape[1], Simon Crozier[2] Thakor Kikabhai[2] and Ron Sharpe[2]

[1]Nottingham Fuel and Energy Centre, School of Chemical, Environmental and Mining Engineering, University of Nottingham, University Park, Nottingham, NG7 2RD, UK
[2] Advanced Technology Group, Nalco Ltd (Energy Services Division), Block 102, Cadland Road, Hardley, Hythe, Southampton SO45 3NP, UK

Introduction

Visbreaking is an important part of petroleum refining as it converts heavy oil fractions to more useful, lighter distillate fuels. Modelling this process has involved the pyrolysis of petroleum residua in mini- bombs [1]. Usually, examination of these mechanisms is based on changes to the bulk compositions of the product generated from pyrolysis under different conditions. However, these are not necessarily sensitive to small changes in the extent of cracking. In this study, attention is focussed on discrete molecular transformations that occur in the maltene fraction. The transformations involve a suite of compounds more commonly known as biomarkers, which are routinely employed for upstream petroleum exploration purposes, and have been shown to be extremely sensitive and adaptable through a range of thermal regimes [2]. It is anticipated that further development of the biological marker approach outlined here may be able to accurately detect the proximity to coke formation during visbreaking.

Experimental

Pyrolysis Approximately 2 g of feed was used for both anhydrous and hydrous pyrolysis experiments. Prior to anhydrous pyrolysis, the reactor was evacuated using a vacuum pump. For the hydrous pyrolysis experiments, the reactor was evacuated, then refilled with nitrogen. The reactor was placed in a temperature stabilised sand bath, where pyrolysis was allowed to run for 30 minutes, at temperatures of 420, 430 and 440^{o}C. Once complete, the reactor was removed from the sand bath and submerged in dry ice to quench any further reactions. To sample the gas, a 100 ml syringe was attached to the reactor. When the syringe revealed no further expansion of gas, a sampling bag was attached, and the gas was injected, ready for immediate chromatographic analysis. The reactor was then carefully disassembled and the product was collected by extensive washing in toluene.

Asphaltene Precipitation The reactor washings were first evaporated so as to contain a minimum amount of solvent. To this, a 40 fold excess of *n*-heptane was added and mixed using a magnetic stirrer for 20 minutes. The solution was then added to centrifuge tubes and spun for 5 minutes at 2500 rpm. The *n*-heptane supernatant was then removed to a round bottom flask and the remaining asphaltenes were transported back to the beaker using toluene. This process was repeated a further 3 times. The maltenes were combined and evaporated.

Open Column Chromatography Separation of maltene fractions into compound classes were performed using a silica gel column. The aliphatic hydrocarbons were attained by elution with 50 ml *n*-hexane. The aromatic hydrocarbons and polar spices were obtained by elution with a 20% v/v mixture of CH_2Cl_2 (dichloromethane) in *n*-hexane (50 ml), and a 1:1 mixture of CH_2Cl_2 and CH_3OH (methanol) (50 ml) respectively.

Gas Chromatography (GC) Analysis of the gas was performed on a Carlo Erba HRGC Mega Series gas chromatograph with a thermal conductivity detector attached, set at 200^{o}C. Analysis of total aliphatic hydrocarbon distributions were performed on a Carlo Erba HRGC gas chromatograph with the flame ionisation detector (FID) attached. **Gas**

Chromatography – Mass Spectrometry (GC-MS) Analysis of hydrocarbon fractions were carried out on a Carlo Erba / Fisons Instruments 8000 Series (8035) gas chromatograph interfaced to a Fisons Instruments MD 800 mass spectrometer, electron voltage 70 eV with a source temperature of 280^{o}C.

Solution State ^{1}H NMR This was performed on maltene fractions dissolved in deuterated chloroform ($CDCl_3$), using a Bruker 500 MHz spectrometer.

Results and Discussion

Anhydrous Pyrolysis The composition of the petroleum residua before and after various conditions of pyrolysis are displayed in table 1. The series of anhydrous pyrolysis experiments (420 – 440^{o}C) reveal the expected marked decrease in maltene content, which is accompanied by an increase in gas and asphaltene content. The changes in product composition are also reflected in the percentage of aromatic hydrogen as determined by ^{1}H NMR, which increase systematically with increasing pyrolysis temperature. However, these changes occur over a small range of values and are therefore more susceptible to experimental and interpretive error. Further changes to the refinery residua with increasing pyrolysis temperature are also represented by certain aliphatic and aromatic hydrocarbon molecular transformations (table 2).

Normal alkane distributions (figure 1) are particularly useful due to their high relative abundance. Here, the ratio of short to long chain *n*-alkanes increases with pyrolysis temperature as more of the longer chained components are cracked.

Similar thermally induced molecular transformations occur for certain biological marker compounds present in the aliphatic hydrocarbon fractions in the maltenes. One such group of compounds are the steroids. It has been shown that rearranged steranes, or diasteranes, are much more thermodynamically stable than their regular sterane counterparts [2]. Therefore, the diasterane to sterane ratio increases with increasing thermal stress, which has been shown in previous pyrolysis experiments[3].

Table 1. Composition of petroleum residua after various conditions of anhydrous and hydrous pyrolysis.

	Maltenes (%wt)	Asphaltenes (%wt)	Total Gas (%wt)	Losses (%wt)[3]
Initial Feed	94.9	5.1	0	0
420^{o}C	82.7 $^{+}$/-1.1[1]	12.8 $^{+}$/-0.1[1]	0.5	4.0 $^{+}$/-1.1[1]
430^{o}C	74.3 $^{+}$/-0.8[2]	17.5 $^{+}$/-0.3[2]	1.4	6.8 $^{+}$/-1.1[2]
440^{o}C	66.9 $^{+}$/-1.3[2]	17.2 $^{+}$/-0.0[2]	2.2	13.7 $^{+}$/-1.3[2]
430^{o}C + 5 %wt H_2O	61.7 $^{+}$/-0.8[2]	17.8 $^{+}$/-1.0[2]	2.8 $^{+}$/-0.3[2]	17.7 $^{+}$/-0.4[2]
430^{o}C + 1 %wt H_2O	57.4 $^{+}$/-0.1[2]	18.1 $^{+}$/-0.5[2]	3.4 $^{+}$/-0.4[2]	21.2 $^{+}$/-1.0[2]

	Total HC Gas (%wt)[4]	H_2S Gas (%wt)	% H_{ARO}[5]
Initial Feed	0	0	6.4
420^{o}C	0.4	0.2	8.6
430^{o}C	1.1	0.2	10.8
440^{o}C	1.9	0.3	12.3
430^{o}C + 5 %wt H_2O	2.4 $^{+}$/-0.2[2]	0.5 $^{+}$/-0.1[2]	11.0
430^{o}C + 1 %wt H_2O	2.7 $^{+}$/-0.1[2]	0.6 $^{+}$/-0.1[2]	12.0

[1]: Mean of three experimental runs; error is standard deviation. [2]: Mean of two experimental runs; error is standard deviation. [3]: Toluene insolubles, including light ends lost during evaporation of maltene fractions. [4]: Total Hydrocarbon Gas (HC). [5]: Aromatic hydrogen within maltene fractions; error is $^{+}$/-0.2

Table 2. Molecular transformations within the maltene fraction under various pyrolysis conditions.

	n-C_{15-20} / n-C_{25-30} [1]	Dia- / Regular Steranes [2]	Tri- / Pentacyclic Terpanes [3]	Naphthalene / Pyrene [4]
Initial Feed	2.85	0.13	0.02	0.05
420°C	2.17	0.22	0.17	n.d.
430°C	3.88	0.29	0.26	0.48
440°C	5.21	0.38	0.48	1.04
430°C + 5 %wt H_2O	4.15	0.32	0.32	0.95
430°C + 1 %wt H_2O	4.48	0.41	0.41	1.43

[1]: Normal alkane distributions – short chain / long chain. [2]: Steranes – Total Diasteranes / (Total Diasteranes + Total Regular Steranes). [3]: Terpanes – Total Tricyclics (C_{20} – C_{29}) / (Total Tricyclics (C_{20} – C_{29}) + Total 17α (H) Pentacyclics (C_{29} – C_{35})). [4]: Relative Aromatic ring size distributions – Naphthalene / Pyrene.

The results presented here also reveal a gradual increase in the diasterane to sterane ratio. Although undoubtedly this ratio offers an accurate representation of the increasing thermal stress, the actual concentration of these steroid compounds is relatively low. On the other hand, terpanoid compound distributions are present in significant quantities. There is a significant relationship between tricyclic and pentacyclic terpanoids, which is displayed in figure 2.

The initial feed appears to contain virtually no tricyclic terpanes, with the (pentacyclics) hopanes dominating the distributions. After pyrolysis at 420°C, there is a notable decrease in hopanes, especially the longer chain lengths. Coupled with this decrease, the relative abundance of the tricyclics dramatically increases. This phenomenon is repeated for experiments at 430 and 440°C, where the ratio of tricyclics to hopanes is approximately 0.5, which compared to the initial feed (approximately 0), is a significant systematic increase, much more dramatic than that of the bulk aromaticity, as determined by ^{1}H NMR. There are two mechanisms responsible for this pattern. Firstly, the increasing thermal stress causes cracking of the extended side chain hopanes, thus explaining the marked decease of such compounds as C35- αβ S+R. Secondly, the increase in tricyclics is thought to be a consequence of their preferential release from the high molecular mass constituents of the feed relative to the hopanes i.e. the tricyclics migrate faster out of the organic matrix of which the hopanes show a greater affinity [2].

Systematic changes to aromatic hydrocarbon distributions also occur as a function of increasing pyrolysis temperature. Here, the ratio of naphthalene to pyrene is used to represent the overall incorporation of large ring systems into high molecular mass material, leaving relatively more small ring system species.

Hydrous Pyrolysis

The composition of the product after visbreaking with 5 %wt H_2O at 430°C is presented in table 1. Again experimental reproducibility is within acceptable limits, and relative to the corresponding anhydrous pyrolysis experiment, it appears that the level of cracking has been extended. Significantly, there is a dramatic decrease in the maltene content that is coupled by an increase in the gas component. Also, it may be argued that the asphaltene component has not changed significantly, indicating that the stability of the feed may be maintained.

The addition of water to the pyrolysis process has been shown to maintain the stability of feed (asphaltene quantities remain relatively unchanged), whilst promoting the generation of gas and other more useful low molecular mass hydrocarbonsThe promotion of cracking is also represented by certain molecular transformations, reported in table 2. The proportion of long relative to short chain *n*-alkanes appears to have decreased compared to the anhydrous pyrolysis experiment at the same temperature. Similarly, the removal of regular steranes and

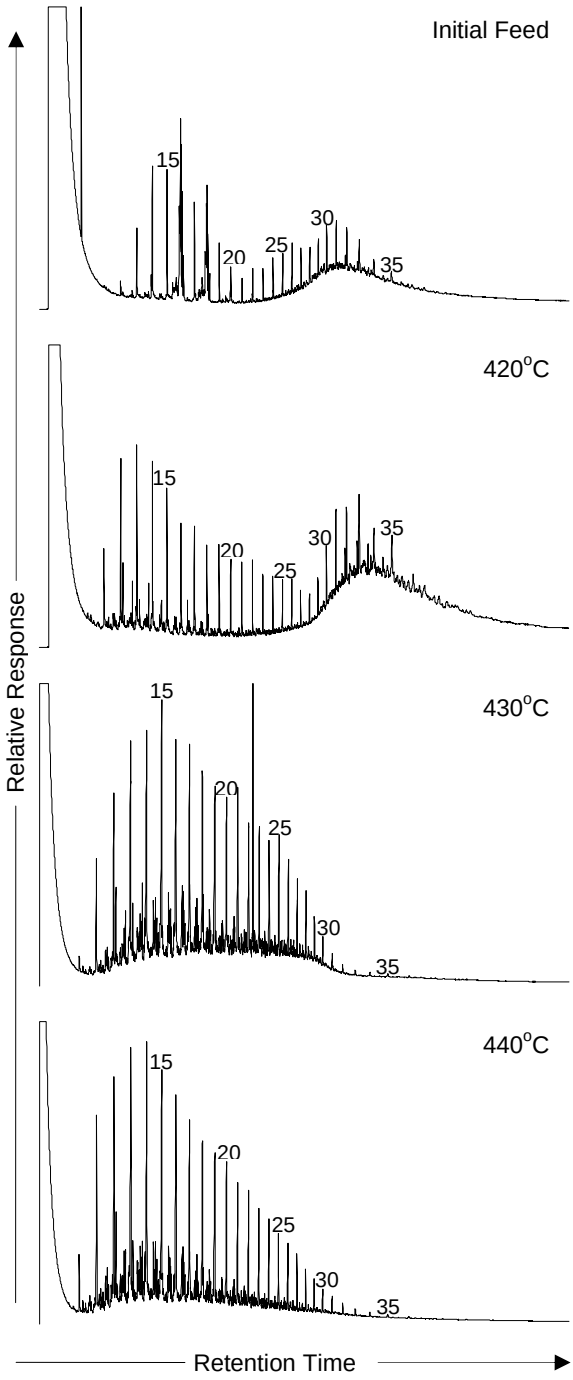

Figure 1. Normal alkane distributions revealed by GC analyses of pyrolysis products.

hopanes relative to diasteranes and tricyclic terpanes respectively also indicates that the addition of water has resulted in an extension to the cracking process. The transformations that have occurred in the aromatic hydrocarbon fraction are again represented by the ratio of naphthalene to pyrene. Assessment reveals that the addition of 5 %wt H_2O promotes further incorporation and condensation reactions, leaving relatively more of the small membered ring compounds. Also, enhanced condensation reactions are reflected by an increase in the percentage of aromatic hydrogen (table 1) as determined by ^{1}H NMR (table 1). Again, however, this measurement does not

appear to be as sensitive as the molecular transformations described previously.

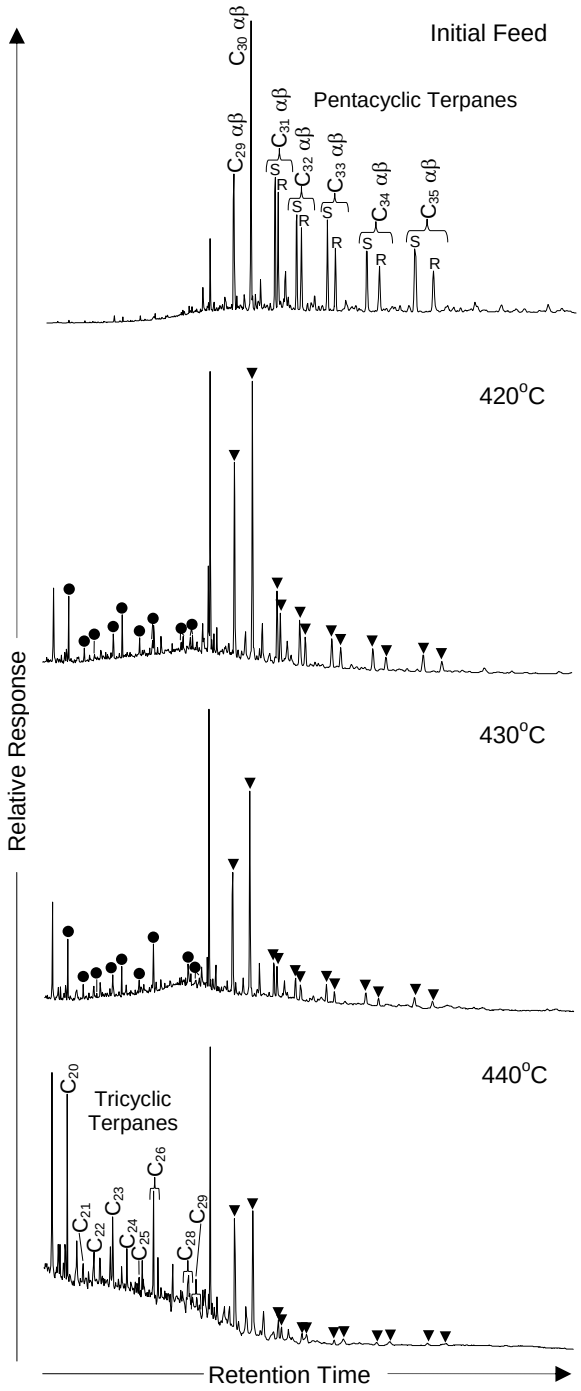

Figure 2. Tricyclic (filled circle) and pentacyclic (filled triangle) terpane distributions (*m/z* 191) generated from various pyrolysis conditions.

The proportion of water was then reduced to 1 %wt of the starting material, which more accurately reflects the mass of water that may be added in a real visbreaker. The composition of the hydrous pyrolysis product is shown in table 1. Once more, the asphaltene component of the products does not appear to have changed a great deal from the anhydrous experiment, or the previous 5 %wt H_2O hydrous pyrolysis experiment. However, the maltene component appears to have slightly decreased, which is coupled with a slight increase in gas content and overall losses (including toluene insolubles) relative to these experiments. The aromatic hydrogen content also appears to have slightly increased. Interestingly, this composition represents an increase to the extent of cracking relative to anhydrous pyrolysis at the same temperature, and importantly, hydrous pyrolysis using 5 %wt H_2O. Therefore, less water in the system appears to promote cracking.

The compositional changes are also reflected in the molecular transformations listed in table 2. The *n*-alkane ratio is again higher than that observed from anhydrous pyrolysis. Interestingly, it is also higher than the 5 %wt H_2O experiment. Further investigation of the distributions revealed that the *n*-alkane ratio of *n*-C_{13-17} / *n*-C_{25-35} provide a more pronounced difference, as these longer chained *n*-alkanes are lower in abundance than their counterparts generated by hydrous pyrolysis using 5 %wt H_2O. Also, the *n*-alkane distributions generated by the 1 %wt H_2O experiments appear to contain a significant proportion of light or short chain length compounds (e.g. figure 4), that do not exist in the aliphatic hydrocarbon fractions for the other experiments. This is further evidence for an increased proportion of cracking.

Aliphatic biomarker distributions also suggest that the extent of cracking has increased (table 2), for example, the ratio of tricyclic to pentacyclic terpanes. Aromatic hydrocarbon ring size distribution, represented by the ratio of naphthalene to pyrene again suggests that the extent of condensation reactions, and therefore cracking, has been furthered relative to the hydrous pyrolysis experiment using 5 %wt H_2O.

Overall, the compositional and molecular changes suggest that a relatively small amount of H_2O is beneficial for cracking. Thus other factors must control reaction rates that are more important than simply hydrogen availability alone. One such aspect that may exert an overriding effect could be that of pressure. For example, the more H_2O present in the system, the greater the pressure in the reactor, resulting in the retardation of reactions. This may have significant consequences for real refinery units.

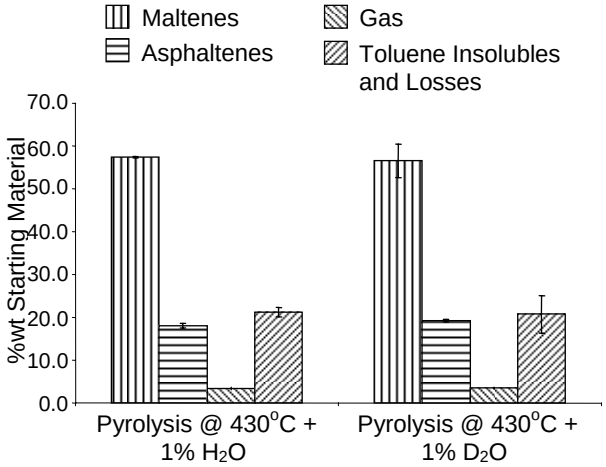

Figure 3. Compositions of hydrous pyrolysis products using 1 %wt H_2O and 1 %wt D_2O. Reported values are an average of duplicate runs, with the error being the standard deviation over this mean.

The fate of hydrogen during hydrous pyrolysis may be examined by utilising deuterium labelled water. However, the introduction of this heavy water can have a subtle effect on the kinetics of reactions, which may result in a slightly different picture to that of the actual fate of hydrogen from water. Therefore, to begin with hydrous pyrolysis at 430°C, using 1 %wt D_2O, was performed to investigate whether these kinetic changes are

significant to the prevalent reactions. Importantly, overall product compositions, displayed in figure 3, do not exhibit significant differences, which suggests that the bulk changes are not effected by the involvement of heavy water.

Detailed molecular transformations, also appear to be relatively unaffected by the presence of D_2O. Preliminary assessment of aliphatic hydrocarbon distributions (figure 4) suggests that the level of cracking is relatively similar. Indeed the extent that the low molecular mass hydrocarbons generated from H_2O pyrolysis are also present for the same experiment involving D_2O. The terpane distributions generated from the hydrous pyrolysis experiments using H_2O and D_2O are also not affected by the differences in reaction kinetics. The ratio of tricyclic to pentacyclic terpanes are relatively similar from the D_2O relative to the H_2O experiments: 0.41 and 0.39 respectively. Further investigations of the fate of the hydrogen, by analysis of deuterium, during the hydrous pyrolysis experiments may be more accurately examined by utilising compound specific stable isotope ratio mass spectrometry (GC-Ir-MS). This will enable compounds that have utilised the deuterium from the heavy water to be distinguished from other compounds that have used hydrogen from the feed itself. It is anticipated that using this analytical technique and thus determining the possible fate of the hydrogen donated by water, we will be able to better understand the mechanisms at work during visbreaking that can only lead to the further development, optimisation and monitoring of the process.

Conclusions

Systematic transformations to biological marker compound distributions during visbreaking are potentially an attractive method for examining the extent of cracking due to their high sensitivity compared to bulk aromaticity measurements and ease of analysis.

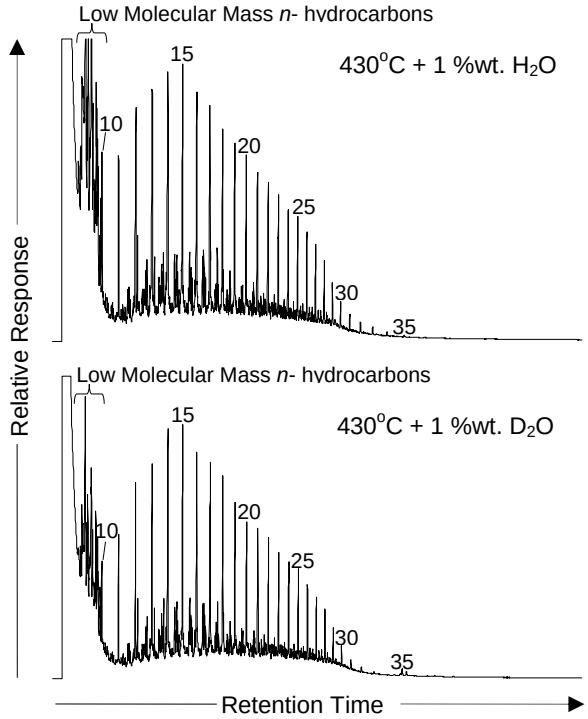

Figure 4. *n*-Alkane distributions generated from pyrolysis of petroleum residua at 430°C using 1% wt H_2O and D_2O.

Acknowledgements

The authors thank Nalco for their financial support.

References

(1) Schabron, J.F., Pauli, A.T., Rovani Jr., J.F. and Miknis, F.P. *Fuel*, **2001** 80, 1435-1446

(2) Peters, K.E. and Moldowan, J.M. *The biomarker guide. interpreting molecular fossils in petroleum and ancient sediments*, 1993, Englwood Cliffs, N. J.: Prentice Hall.

(3) Peters, K.E., Moldowan, J.M. and Sundararaman, P. *Organic Geochemistry*, **1990** 15, 249-265.

CHARACTERIZATION AND STUDIES OF KINETIC AND SEVERITY IN THE VISBREAKING OF HEAVY CRUDE OILS: CASTILLA, RUBIALES AND NARE-JAZMIN

J.A. C*arrillo*

Colombian Petroleum Institute-ECOPETROL
Km 7, Piedecuesta, Colombia.

L.M. Corredor, M.L. Valero

Universidad Industrial de Santander

Introduction

Visbreaking appears like an alternative for the conversion or transportation of heavy crudes. In a refinery, this one process allows to the production of Fuel Oil and feed for the catalytic cracking units. In this work, it is determined the influence of the temperature and the reaction time over the viscosity reduction, the visbreaking bottoms stability, the conversion, and the coke formation. Nevertheless the equivalent severity express the conversion by temperature and residence time, it does no give the difference in some propierties like viscosity reduction [1,2]. On the other hand there are many heavy crude oils, which are classified like that because of their API gravity, but there are many differences among them: sulphur concentration, n-C7 insolubles concentration, Ni and V concentration, etc. These differences determined the best way in wich each crude oil should be processed, and these propierties can be found by chemical analysis, by rection behaviour given by their activation energies and reaction constants.

Experimental

There are some parameters related with the stability wich allow to predict the tendency of a crude oil to form coke. One of these parameters are that of the free solvent volumen [3,4,5], which was applied to the 3 crude oils studied by the following expressions:

$$\varphi_{fs} = 1 - K_s K_F \phi_a \quad [1]$$

$$K_s = \frac{1}{1 - X_{cy}} \quad [2]; \quad K_F = \frac{1}{1 - P_a} \quad [3]; \quad \varphi_a = \frac{X_a}{\rho_a} \quad [4]$$

Where:

φ_{fs} = Free solvent volumen.
K_s = Solvatation factor.
K_f = Floculation factor.
X_{cy} = Weight fracción of heptane-asphaltenes solubles in ciclohexane.
P_a = Asphaltene peptizability (Heithaus parameter)[6].
φ_a = Volumen fraction of asphaltenes present in one crude or in its heavy fractions.
X_a = Weight fraction of heptane-asphaltenes.
ρ_a = Asphaltene density.

Taken in account previous studies to predict the coke formation, it has been determined that as low is the free solvent volumen in the crude oils or in their fraction, as high is the heavy bottoms and the coke production [3,4].

For the determination of soluble Heptane-asphaltenes in ciclohexane, they were carried out three stages: first stage, there precipitates heptane-asphaltenes of each cude. For that there were taken 160 gr of each crude, and they were diluted with n-heptane in a relationship of 6:1, v/v. The precipitation process was carried out to a temperature of 50ºC, maintaining the stirring in 500 rpm, during 150 min. For this purpose it was used a 1500 ml contactor with stirring and temparature control. The solution coming from the contactor was filtered under vacuum (20mBa), using a funnel of 12.5 cm of diameter and whatman filtration paper Nº 41. The obtained cake was washed with n-heptane in a solvent relationship solvent:solids of 6:1 in volume. The washed heptane-asphaltenes were loaded in the extractor soxhlet, with the purpose of moving away the residual maltenes. The process, was carried out during 72 hours, enough time for the total removal of the soluble maltenes, that which was verified by the color loss in the solvent. To the maltenes coming from the filtration stages, laundry of the filtration cake, and extraction was moved away the solvent. In the second stage, the insoluble ones were disolved in toluene to determine the amount of toluene insolubles. For this purpose, the insolubles en n-heptane were disolved in toluene in a relationship solvent:solids of 4:1 in volume. The diluted product was filtered under the same conditions of the filtration with n-heptane. The insoluble material dried off and it was weighed, and the soluble ones were loaded to the rotaevaporator to withdraw the solvent. Third stage: the soluble ones in toluene free of solvent, underwent an extraction process with ciclohexane, during 72 hours in the soxhlet extractor. To the soluble ones in ciclohexane were moved away the solvent. The insoluble material dried off and it was weighed.

Asphaltenes density was calculated by means of the procedure suggested by Rogel [7].

On the other it was carried out a preliminary kinetic study of the process, by means of the calculation of the reaction constants and the activation energy. For the processes of thermal conversion, it is assumed that the reaction kinetics is of first order [8,9,10]:

$$K = \frac{1}{\tau} \ln\left(\frac{Ao}{At}\right) \quad [5]$$

Where:

- k = Kinetic constant, 1/s.
- A_0 = feed, v %
- At = conversión, v %
- t = reaction time, s.

The severity of a thermal process depend of the reaction temperature and the reaction time [10,11]. Therefore, with the purpose of finding a relationship among these two variables, the concept of equivalent severity is applied (S):

$$S = \theta \frac{k_{(T)}}{k_{(427^\circ C)}} \quad [6]$$

Where:

S = Severity, s.
θ = reaction time, s.
$K_{(T)}$ = reaction constant at the temperature T, s^{-1}.
$K_{(427ºC)}$ = reaction constant at the temperature 427ºC, s^{-1}.

To determine the kinetic and the severity it was used the results of [12].

Results and discussion

In the figure 1, its given the crude oil fractions in different solvents.

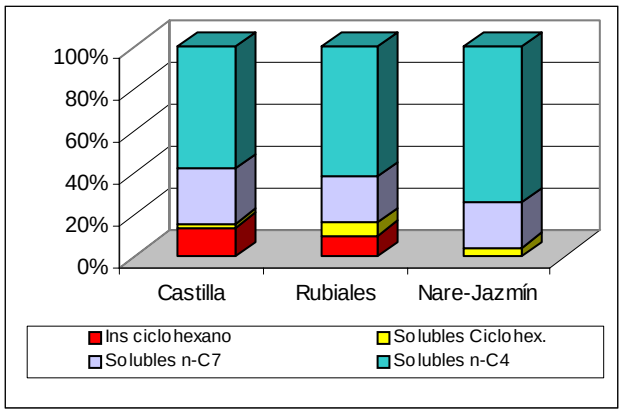

Figure 1. Crude oil fractions.

Castilla crude oil is the one that presents the highest content of insolubles in n-C7 and in ciclohexane, and it is followed by Rubiales and Nare-jazmin crudes. The Nare-jazmin doesn't present any percentage of insoluble in ciclohexane, that which is related with the drop in coke production. Taking in mind the obtained results, the free solvent volume is calculated by means of the equations 1 at 4. The results are presented in table 1.

Table 1. Free solvent volume (ϕfs)

Crudo	Pa	Kf	Xcy	Ks	Xa	ρa, g/ml	ϕa	ϕfs	Coke*, wt %
CCN	0,56	2,29	0,02	1,02	0,16	1,5	0,13	0,75	3,4
CRN	0,42	1,73	0,06	1,06	0,16	1,24	0,14	0,76	1,1
CNN	0,82	5,69	0,05	1,05	0,05	1,33	0,04	0,80	0,3

* Conditions : Reaction temperature = 442ºC and residence time = 1,2 minutes.

According to the free solvent volume values it is establishes that Castilla crude presents the highest tendency to form coke, continued by Rubiales and Nare-jazmin. These results coincide with the content of insolubles in ciclohexane of each crude, that is to say, highest quantity of insoluble, highest coke production. This fact is proven in the runs carried out at pilot plant level, in which under the same severity conditions Castilla crude oil produces the highest amont of coke.

Reaction constants and the severities are calculated by means of the equation [6 and 7] and the results are given in table 2.

By means of Arrhenius equation activation energies are calculated. The found values are 24,6, 56 and 71,9 KJ/mol for the crudes: Rubiales, Castilla and Nare-jazmin respectively.

With the purpose of determining the effect of the equivalent severity on the reduction of the viscosity, there were built a series of figures that correlate these two variables.

Table 2. Reaction constants and severities of each pilot plan run

VBB	K, sg^{-1}	S*, sg	VBB	K, sg^{-1}	S**, sg	VBB	K, sg^{-1}	S***, sg
FC1	0,009	66,4	FR1	0,012	73,566	FN1	0,009	140,758
FC2	0,011	84,8	FR2	0,013	75,780	FN2	0,009	141,689
FC3	0,011	81,8	FR3	0,014	80,179	FN3	0,009	145,662
FC4	0,015	108,6	FR4	0,014	81,059	FN4	0,012	191,633
FC5	0,011	92,1	FR5	0,016	77,762	FN5	0,014	147,605
FC6	0,010	97,8	FR6	0,012	81,429	FN6	0,014	179,377

$K_{427ºC}$ = 0,00973 s^{-1}; ** $K_{427ºC}$ = 0,012 s^{-1}; *** $K_{427ºC}$ = 0,0066 s^{-1}.

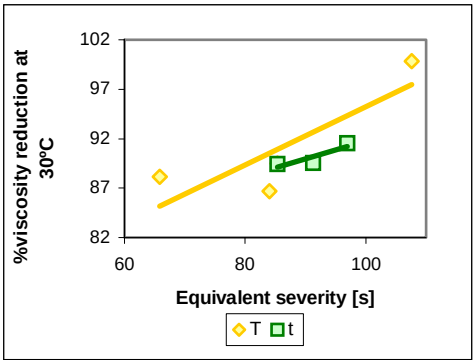

Figure 2. Viscosity reduction vs. equivalent severity of Castilla VBB.

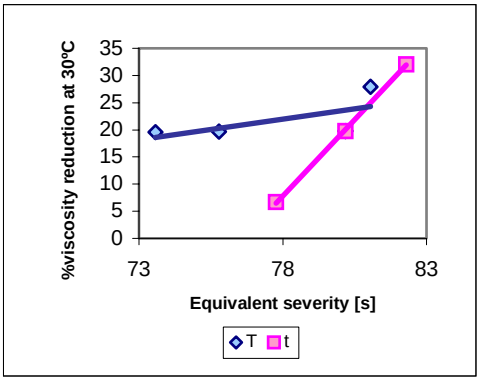

Figure 3. Viscosity reduction vs. equivalent severity of Rubiales VBB.

With the comparison of the equivalent severities reached by the variations in the temperature and in the reaction time, it is observed that for all the VBB, the temperature presents a highest influence over the viscosity reduction. On the other hand, in the figures 5 to 10 are given the influence of the equivalent severity over the yields and the VBB quality.

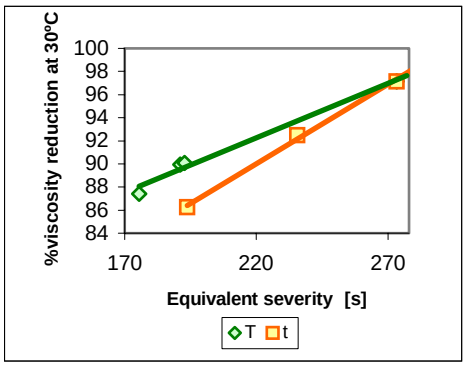

Figure 4. Viscosity reduction vs. equivalent severity of Nare-jazmin VBB.

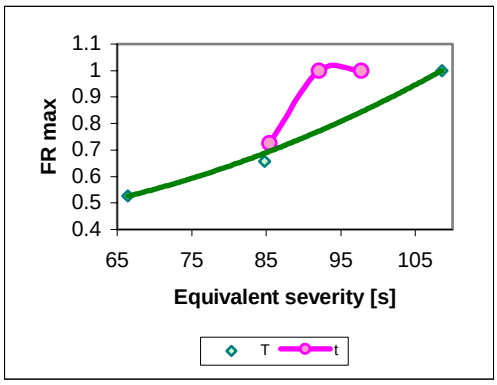

Figure 5. Flocculation factor vs. equivalent severity of Castilla VBB

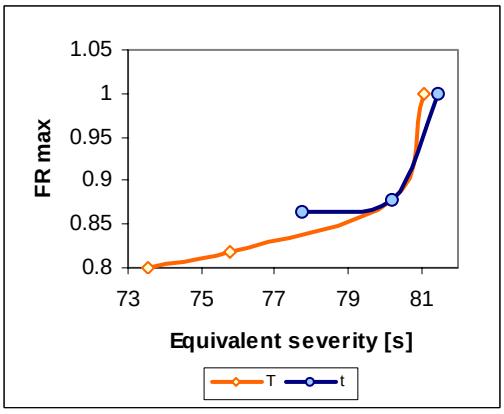

Figure 6. Flocculation factor vs. equivalent severity of Rubiales VBB.

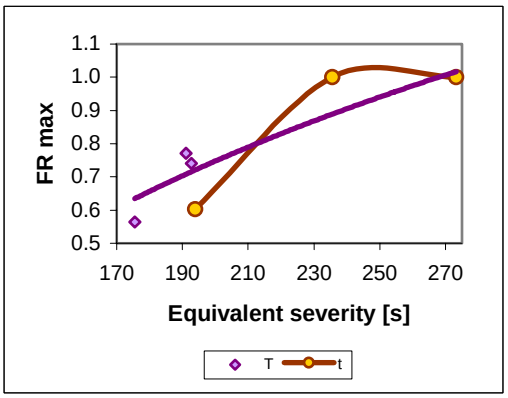

Figure 7. Flocculation factor vs. equivalent severity of Nare-jazmin VBB.

Applying the concept of the flocculation factor (FRmáx), the VBB stability decrease with the increasing in the equivalent severity, in the following order: Nare-jazmin < Castilla < Rubiales. It is observed that the VBB from the Nare-jazmin requires twice the equivalent severity of the other ones two crudes to produce unstable VBB (FRmáx =1).

In the case of the crudes Castilla and Nare-jazmin, for the same values of equivalent severity, the produced VBB are more instable by reaction time.

Nevertheless the equivalent severity by temperature and reaction time, doesn't have great influence on the product yields as it is observed in figures 8, 9 and 10, Castilla and Rubiales crude oils present increases in the conversion (of 5 and 2,7 %, respectively), when it is operated to conditions of severity by reaction time.

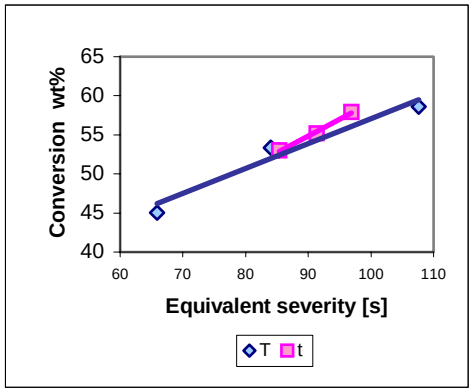

Figure 8. Conversion vs. equivalent severity of the Castilla crude oil.

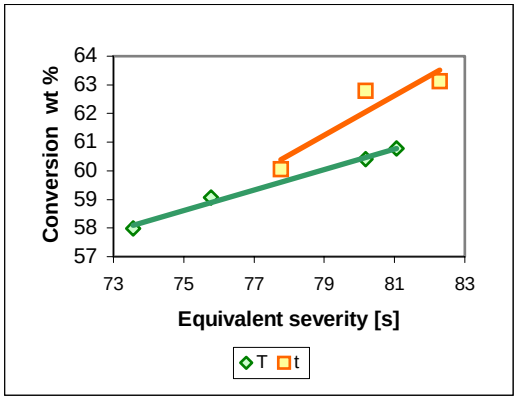

Figure 9. Conversion vs. equivalent severity of the Rubiales crude oil.

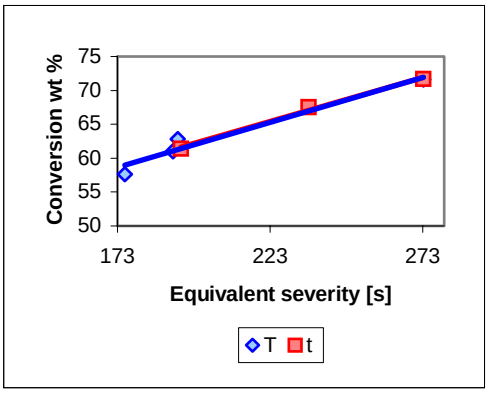

Figure 10. Conversion vs. equivalent severity of the Nare-jazmin crude oil..

In the same way as the product yields, the equivalent severity, doesn't has a significant influence over the coke production, however, for the crudes Castilla and Rubiales there are observed increments of 1 wt% and 0,2 wt% respectively, when it is operated under conditions of severity by temperature.

Conclusions

The concept of equivalent severity (for reaction temperature and reaction time), could be applied to the product yields, but it could not be applied to their qualities.

The low activation energy of the Rubiales crude is possible because of the high concentration of side paraffin chains in the aromatic rings.

By means of the subdivision of the crudes in maltenes and asphaltenes, it was demonstrated that the content of insoluble in ciclohexane is related with the coke production.

The free solvent volume factor allowed to determine the following tendency in the coke formation: Castilla > Rubiales > Nare-jazmin.

Nomenclature

FC1-5: Castilla VBB. Runs from 1 to 5
FR1-6: Rubiales VBB. Runs from 1 to 6
FN1-6: Nare-jazmin VBB. Runs from 1 to 6

Acknowledgment. This work was supported by the Division of No-Catalytic Process of the Colombian Petroleum Institute-ECOPETROL and by Universidad Industrial de Santander, under contract No. 003.

References

[1] Savaya, Z, Al-soufi, H, Al-Azawi, I and Mohammed H. Fuel Science and Technology, 6 (3), 355 (1988).
[2] Al-soufi, H, Shanshool, J and Savaya, Z. Fuel Science and Technology, 5 (5), 543 (1987).
[3] Schabron, J, Pauli, A and Rovani, J. Fuel, 81, 2227(2002).
[4] Schabron, J, Pauli, A and Rovani, J. PRE-PRINTS, Pap. - *Am. Chem. Soc., Div. Fuel Chem.***,** 46 (2),99 (2001).
[5] Schabron, J, Pauli, A and Rovani, J. Fuel, 80, 919 (2001).
[6] Schabron, J, Pauli, A and Rovani, J. PRE-PRINTS, Pap. - *Am. Chem. Soc., Div. Fuel Chem.***,** 44 (2), 187 (1999).
[7] Rogel, E and Carbognani, L. Energy and Fuel, 17, 378 (2003).
[8] WIEHE, I. Ind. Eng. Chem., 32 (11), 2447 (1993).
[9] Krishna, R, Kuchhal, Sarna, S, and Singh, I. Fuel, 67, 379 (1988).
[10] Soodhoo, K, Phillips, C. Fuel, 87, 521(1988).
[11] Yan, Y. Denver meeting, 490 (1987).
[12] Carrillo, J, Corredor, L, and Valero, M. PRE-PRINTS, Pap. - *Am. Chem. Soc., Div. Fuel Chem.***,** 49 (2), (2004).

DISTRIBUTION OF MAIN PRODUCT FRACTIONS IN CO-LIQUEFACTION OF HIGH-SULFUR LIGNITES BLENDED WITH PETROLEUM HEAVY BOTTOMS

Arif Hesenov, Ömer Gül*†, Pervane Gafarova*†, Oktay Erbatur*, Harold H. Schobert†*

*Çukurova Üniversitesi, Fen Edebiyat Fakültesi, Kimya Bölümü, 01330 Adana, Turkey
†The Energy Institute, The Pennsylvania State University, University Park, PA 16802

Introduction

Low rank coals with high sulfur contents liquify comparatively easily (1-4). The type of sulfur in coal structure is an important factor affecting the conversions in catalytic or non-catalytic direct hydrogenations. Pyrite transforms into pyrothite during the process and catalyses the liquefaction reactions (5). Iron sulfate structures are also transformed into pyrothite and contributes to the catalysis of liquefaction reactions (6). When organic sulfur is concerned, the organic sulfide content increases with decreasing rank, although thiophenic sulfur is normally the dominant organic component, regardless of rank (7). In general, aliphatic sulfides are mainly found in lignites whereas thiols, thiophenols, aryl and diaryl sulfides and disulfides are also present in lesser amounts. As the rank goes up, e.g. in sub-bituminous coals aryl sulfides tend to dominate and more heterocyclic structures are also observed. Finally in high-rank bituminous coals almost all organic sulfur is in thiophenic structures with very few of other sulfur fuctional groups (8-11). The aliphatic C-S bonds, other than thiophenics, are thermally less stable (12) and therefore cleave comparatively easily under liquefaction conditions.

In this work, liquefaction of high-sulfur lignites blended with petroleum heavy bottoms has been investigated. This is a continuation of a study in which catalytic direct liquefaction of high-sulfur coals are being evaluated.

Experimental

The analytical data regarding two lignites from Turkey and the petroleum heavy bottoms are given in Table 1 and Table 2, respectively. Petroleum feedstocks were obtained from Izmir Tupras Refinery from Turkey.

Table 1. Analytical Data of the Cayirhan and Kangal Lignites.

	Cayirhan	Kangal
Moisture, wt %	13.76	15.50
Ash, wt % (dry)	32.67	18.14
C, wt % (daf)[a]	73.10	66.58
H, wt % (daf)	4.70	5.94
N, wt % (daf)	1.90	1.88
O, wt % (daf)[c]	12.80	21.55
S_{Total}, wt % (dry)	7.50	5.62
$S_{Pyritic}$, wt % (dry)	2.60	1.07
$S_{Sulphatic}$, wt %(dry)	1.80	0.22
$S_{Organic}$ wt % (dry)	1.30	3.31

[a] daf: dry, ash-free; [b] calculated from difference

The catalyst (1% by wt based on Mo to daf coal ratio) was dissolved in 30 mL of distilled water and added dropwise onto 100 g of dry coal while the coal was effectively mixed with a spatula to achieve a homogeneous mixture. Following addition of the catalyst precursor, the impregnated coal was dried at 50 °C under reduced nitrogen pressure until the moisture content fell below 3 %. A pre-determined amount of catalyst-precursor impregnated coal (50 g daf basis) is charged into a 500 mL PARR model 4575 HP/HT reactor having a magne-drive mixing facility. Also, the petroleum heavy – bottom sample onto which Co/Mo hydrotreating catalyst (CRITERION HDS-22) was added with a weight ratio based on 1% Mo per 100 g organic material has been added to the reactor. Three different weight ratios of blends of petroleum heavy bottoms and lignites were prepared for liquefaction studies. These are 1:1; 2:1; and 3:1 (lignite weight was on daf basis) cases. All liquefaction experiments were carried out at a constant treatment time of 30 min with a constant process temperature of 425 °C.

Following loading the lignite and petroleum heavy bottom blend, the reactor was sealed and air inside the reactor was swept out by successive pressurizing (6.9 MPa cold) and depressurizing twice with nitrogen and twice with hydrogen gases. Finally the reactor was pressurized with hydrogen gas (6.9 MPa cold) and then heated with a rate of 4.7 °C/min upto 425 °C. Following mixing the reactor contents for 30 min continuously via the magne-drive at 425 °C, the reactor was taken out of the heating system and quenched with ice-cold water. Following discharge of the gaseous components, the content of the reactor was withdrawn and transferred into an extraction thimble with the aid of n-hexane. Successive extraction of this material were carried out in a soxhlet apparatus by using n-hexane and tetrahydrofuran. Hexane solubles were called oil and THF solubles were called asphaltene + preasphaltene (AS + PAS). The amount of oil and AS+PAS were determined after removing the solvents under reduced pressure. The char (solid remaining following THF extraction) was also weighed. The difference between the amount of total material charged to the reactor and the total amount of Oil, AS+PAS and Char was accepted as the total amount of gaseous products. Conversion (total) is calculated by taking the per cent ratio: $(W_{oil} + W_{gas} + W_{AS+PAS})*100/W_{total\ charge(organic)}$

Table 2. Analytical Data for Petroleum Vacuum Resid (VR) and Petroleum Asphalt (A).

	VR	A
C, wt %	85.31	84.54
H, wt %	10.17	10.45
N, wt %	0.32	0.34
S, wt %	4.70	5.45
V.M., wt %	86.00	78.16
Ash, wt %	0.17	0.09
[a] FC	13.83	21.75
[b] $\%C_{arom}$	21.25	25.88
[b] $\%C_{alip}$	78.75	74.12
[b] $\%H_{arom}$	5.99	7.90
[b] $\%H_{alip}$	94.01	92.10

[a]FC: Fixed Carbon; [b]From NMR data

Results and Discussion

Elemental analysis of lignites show that Cayirhan lignite has a higher rank than Kangal lignite. The oxygen content of Kangal lignite is much higher than that of Cayirhan. On the other hand the total sulfur content of Cayirhan is higher than that of Kangal lignite. While Cayirhan has higher inorganic type of sulfur, Kangal has higher organic sulfur content.

Analytical data of petroleum heavy bottoms show that although elemental analysis results of both vacuum residue and asphalt are very similar, NMR data indicates that asphalt has a higher content of

aromatics. The higher value of volatile matter in VR is consistent with the NMR data.

The blends of Cayirhan and petroleum vacuum residue gave the highest conversions among all different blends liquefied in this work (Figure 1). Oil fraction was the primary product in all cases. The oil yield increased as vacuum residue component's ratio in the blend was increased. When this ratio was 3/1, the oil yield was 81.1%. Conversely gaseous product yields were higher when the ratio of Cayirhan lignite in the blend was higher; e.g. 17.4% when the ratio of $Wt_{VR}/Wt_{Cayirhan}$ was 1/1 but 11.9% when the corresponding ratio was 3/1. AS+PAS values were rather low (5-6 %) indicating an effective transformation into oil products.

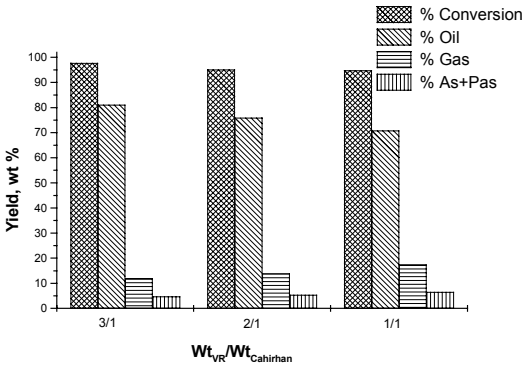

Figure 1. Distribution of the main product fractions formed during co-processing of Cayirhan lignite and petroleum vacuum resid (VR) blends (Wt of coal is on daf basis). Process conditions: 425^0C, 6,9 MPa H_2 (cold), 30 min reaction time.

In Asphalt/Cayirhan blends the trend of change of yields of various fractions with respect to change of the weight ratios of components in the blends are all same but when the corresponding figures in VR/Cayirhan and Asphalt/Cayirhan are compared, oil yields of Asphalt/Cayirhan blends are lower than the corresponding figures in VR/Cayirhan blends (Figure 2). On the other hand, reverse is true for the AS+PAS yields having values around 8-10 %. Gaseous product yields are also a little bit lower in Asphalt/Cayirhan blends compared to the corresponding figures of VR/Cayirhan blends. All these observations are consistent with the structural differences of asphalt and the vacuum residue such that the former has more aromatic structures than the latter whereas reverse was true for the volatile matter content of these petroleum heavy bottoms.

Figure 3 gives the results of co-liquefaction of Kangal lignite with the vacuum residue. The trends of change of yields of various fractions with respect to change of the weight ratios of components in the blends were all similar to the previous observations made for Cayirhan/petroleum heavy bottom blends; i.e. as the ratio of Wt_{VR}/Wt_{Kangal} was increased total conversion and oil yields were also increased whereas the reverse was true for the gas yields. In general, there were differences around 5-6 % from the corresponding figures in VR/Cayirhan with the higher values belonging to the VR/Cayirhan blends. AS+PAS values in all three blends of VR/Kangal are very low (3.2-3.9 %) but the yield of gaseous products are considerably high (26.6%-13.3 %). The high oxygen content of Kangal lignite indicates that the major component in these gaseous products should be carbondioxide in addition to methane.

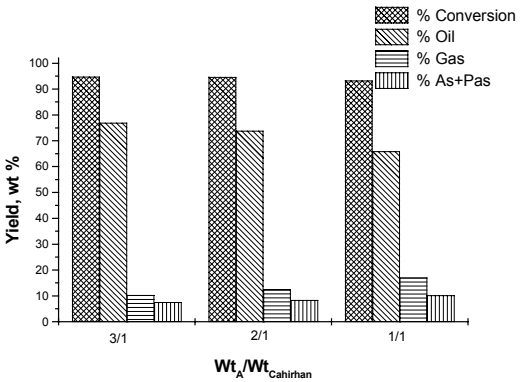

Figure 2. Distribution of the main product fractions formed during co-processing of Cayirhan lignite and petroleum asphalt (A) blends (Wt of coal is on daf basis). Process conditions: 425^0C, 6,9 MPa H_2 (cold), 30 min reaction time.

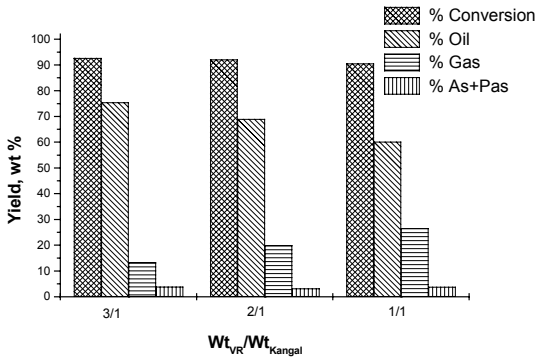

Figure 3. Distribution of the main product fractions formed during co-processing of Kangal lignite and petroleum vacuum resid (VR) blends (Wt of coal is on daf basis). Process conditions: 425^0C, 6,9 MPa H_2 (cold), 30 min reaction time.

Asphalt/Kangal blends gave similar total conversion values to that of VR/Kangal blends upon liquefaction but when the oil yields are investigated, one notes that the values for Asphalt/Kangal blends are about 2-3 % lower than the corresponding figures obtained for VR/Kangal blends. The yield values of gaseous products obtained in the liquefaction of Asphalt/Kangal are very similar to the corresponding values obtained in the liquefaction of VR/Kangal blends. The highest oil yield was obtained in 3/1 Asphalt/Kangal blend with a value of 72.1 %.

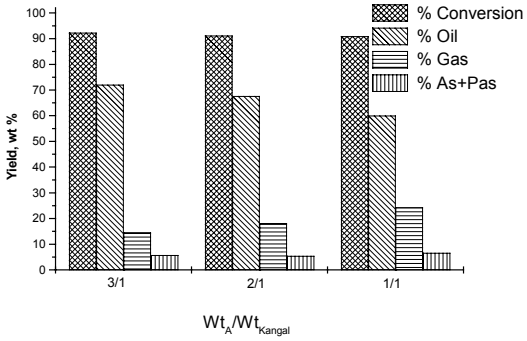

Figure 4. Distribution of the main product fractions formed during co-processing of Kangal lignite and petroleum asphalt (A) blends (Wt of coal is on daf basis). Process conditions: 425^0C, 6,9 MPa H_2 (cold), 30 min reaction time.

A comparison between the corresponding conversion and oil yields obtained in Asphalt/Kangal and Asphalt/Cayirhan blends shows that the latter has higher values of about 5 % for oil yields whereas this difference was less (2-3 %) for the total conversion values. AS+PAS yields in Asphalt/Cayirhan blends are also higher (2-4 %) than the corresponding values for Asphalt/Kangal blends. Gaseous products, as expected are higher (4-6 %) in Asphalt/Cayirhan blends than those corresponding values for Asphalt/Cayirhan blends.

Conclusion

The detailed analysis of oils and gaseous products of this study have not been completed yet. But the distribution of main fractions of products obtained from the liquefaction of the blends of high-sulfur lignites with the petroleum heavy bottoms indicates that such conversions will be beneficial as far as the oil yields are concerned. Of course, the oils obtained at this stage are rather crude and need further treatments such as separation of phenolics and then saturating the aromatics via catalytic hydrogenation by using the appropriate catalysts. In this way, the high-sulfur lignites and low rank coals which cannot be combusted directly due to the creation of extreme pollution will find their ways to be utilized in comparatively acceptable converted forms.

References

(1) Gözmen, B.; Artok, L.; Erbatur, G.; Erbatur, O. *Energy Fuels*, **2002**, *16,* 1040.
(2) Garcia, A. B.; Schobert, H. H. *Fuel*, **1990**, *68*, 1613.
(3) Garcia, A. B.; Schobert, H. H. *Fuel Processing Technology*, **1990**, *24*, 179.
(4) Anderson, R. R.; Bockrath, B.C. *Fuel*, **1984**, *63*, 329.
(5) Attar, A. *Fuel*, **1978**, *57*, 201.
(6) Miller, R. L., Baldwin, R. *Fuel*, **1985**, *64,* 1235.
(7) Huffman, G. P.; Mitra, S.; Huggins, F. E.; Shah, N.; Vaidya, S.; Lu, F. *Energy Fuels*, **1991**, *5*, 574-581.
(8) Gorbaty, M. L. **1989** In DoE Coal Liquefaction Needs-Panel Assessment Final Report, Vol. 2, Chp.4.
(9) Haenel, M. W. *Fuel*, **1992**, *71*, 1211.
(10) Calkins, W. H. *Energy Fuels*, **1987**, *1*, 59.
(11) Rutkowski, P.; Gryglewicz, G.; Mullens, S.; Yperman, J. *Energy Fuels*, **2003**, *17*(6), 1416-1422.
(12) Calkins, W. H. *Fuel*, **1994**, *73*, 475-484.

DEPENDENCE OF THE CONCENTRATION OF ASPHALTENES AND RESINS IN SOLVENTS SOLUTIONS ON DIFFUSION COEFFICIENT MEASUREMENTS USING PULSE FIELD GRADIENT SPIN-ECHO (PGSE) ^{1}H NMR

Hiroyuki Kawashima[1], Toshimasa Takanohashi[1], Masashi Iino[1], and Shingo Matsukawa[2]*

1 National Institute of Advanced Industrial Science and Technology(AIST)
Onogawa, Tsukuba, Japan 305-8569
2 Tokyo University of Marine Science and Technology,
Konan, Minato, Tokyo, Japan 108-8477

Introduction

Asphaltene (AS) is a complex mixture of several molecular weight molecules, and is said to form a micelle aggregate structure by mainly aromatic-aromatic stacking interaction among the molecules in crude oil. Several methods have been used to clarify the AS aggregate structures.[1-4] In the area of polymer solutions, diffusion coefficient (D) measurement using pulse field gradient spin-echo (PGSE) ^{1}H NMR has been widely carried out.[5-8] From the D value, it is possible to estimate the hydrodynamic radius of a molecule.[9] In this study, the D values of some AS and resin (RE) in solutions were measured by PGSE ^{1}H NMR, and the sizes of the aggregates were estimated. The effect of the concentration of the solutions on the sizes of the aggregates is discussed.

Experimental

Samples. Three kinds of crude oil (Khafji, Iranian Light, and Maya) were used. AS fraction and RE fraction were obtained by extraction of vacuum residue (VR) of each crude oil using n-heptane. Table 1 shows the properties of the samples. Polystyrene (PS) with molecular weights (M_n) of 350, 700, 1400, 2000, 2500, and 3000, poly-4-vinylpyridine (PVP) of M_n 1800, poly –2-vinylnapthalene of M_n 1800, pyrene, and coronene were also used as standards.

Table 1. Properties of Asphaltenes and Resin

	Maya AS	Maya RE	Khafji AS	Iranian Light AS
Elemental analysis, wt%				
C	82.0	83.4	82.2	83.2
H	7.5	10.4	7.6	6.8
S	7.1	4.6	7.6	5.9
N	1.3	0.4	0.9	1.4
O	1.2	0.5	1.1	1.5
M_n(VPO)	4000	720	4000	2400
density, g/cm^3	1.1767	1.0367	1.1683	1.1669

PGSE ^{1}H NMR. A Brucker DRX-300 NMR apparatus was used to measure the PGSE ^{1}H NMR spectra. Each sample was dissolved in $CDCl_3$. Concentrations of the solutions were 3% (30g/l), 1% (10g/l), 0.1% (1g/l), and 0.01% (0.1g/l). Each solution was put into a 10 mm in diameter Pyrex glass flat-bottomed type NMR tube. The depth of the solution in the NMR tube was about 10 mm. To avoid convection and vaporization, a plug was inserted into the NMR tube to reach the surface of the solution. The measurements were performed by PGSE pulse sequence (Figure 1). In this case, signal intensities are indicated as following equation.

$$A=A_0 \exp(-\gamma^2 G^2 D \delta^2 (\Delta - \delta/3))$$

In this equation, A is the signal intensity, γ is the gyromagnetic ratio, D is the diffusion coefficient (m^2/s), δ is the pulse width (1ms), and Δ is the diffusion time (10ms). G is a magnetic field gradient (G/cm), and values of G were 8 -16 points in 5 - 1144 G/cm. With the plot between $\gamma^2 G^2 \delta^2 (\Delta - \delta/3)$ and logA, the D value is obtained from the slope. Pulse delay was 3 s. The number of scans was 16 - 4000 depending on the concentration of the solution. In this experiment, the D value was obtained from the change in the aliphatic peak intensity with the change in the G value. There were no large differences in the D values between those obtained from aliphatic and those obtained from aromatic peak intensities. The measuring temperature was 294 K.

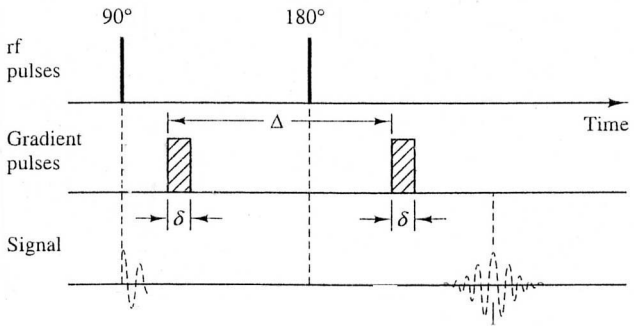

Figure 1. Pulse sequence of PGSE.

Results and Discussion

Table 2 shows the measured D results for the polymers, pyrene, and coronene. In general, for polymer solution, if the polymer and the concentration are the same, the D value decreases with the increase of molecular weight, and if the polymer and the molecular weight are the same, the D value is constant below a critical concentration and decreases with the increase of concentration above the critical concentration. In the concentration range of this experiment, the polymers and pyrene showed few changes in the D values with the change in the concentration. The D of pyrene was large, and the D of coronene was comparatively lower. Compared with the D results for pyrene (molecular weight: 202) and coronene (molecular weight: 300), the D result for PS of M_n 350 was far lower. For PS, there were no differences in the D values between M_n 350 and 700, and the D decreased with the increase of M_n above these values. PVN and PVP of M_n 1800 showed D values different from that of PS. Molecules having sphere structures showed larger D. For structurally similar molecules, the D decreased with the increase in molecular size.

Table 2. D(10^{-10}m^2/s) of each sample in chloroform

Concentration	1%	0.1%
Pyrene	15.4	16.2
Coronene		11.1
PS(M_n:350)	6.2	6.3
PS(M_n:700)	6.1	6.0
PS(M_n:1400)	4.0	4.4
PS(M_n:2000)	3.6	3.7
PS(M_n:2500)	2.7	2.9
PS(M_n:3000)	2.6	2.9
PVN(M_n:1800)	2.7	3.1
PVP(M_n:1800)	3.6	3.8

Table 3 shows the measured D results for the AS and RE. These samples showed different behaviors from those of the polymers. For 3% solutions, the ASs showed similar D values. For 1% solutions, the D value of each AS increased, and the D values were in the order Maya RE > Iranian Light AS = Khafji AS > Maya AS. For 0.1% and 0.01% solutions, two components having quite different D values were observed (In Table 3, percentages of each component obtained from the echo signal intensity are also shown. At 0.01%, signal intensities were very weak, and shimming and phase adjustments for NMR spectra were difficult, so some errors are thought to be contained in obtained D values.).

Table 3. $D(10^{-10}m^2/s)$ of each sample in chloroform

Concentration	3%	1%	0.1%	0.01%
Maya AS	1.0	1.3	2.2(70%),1.3(30%)	5.1(70%),0.9(30%)
Maya RE	2.5	2.7	4.3(62%),2.3(38%)	8.7(69%),2.1(31%)
Khafji AS	1.0	1.6	3.4(87%),1.0(13%)	5.6(88%),1.0(12%)
Iranian Light AS	1.0	1.6	2.6(45%),2.0(55%)	6.5(50%),1.1(50%)

From the relation between the measured D value and the concentration of the solution, the effect of the concentration on the sizes of the aggregates is considered as follows. AS and RE associated themselves originally in the solid state. In higher concentration solutions, AS and RE formed complex aggregates, and the association of the samples was not so greatly dissociated. Consequently, only one component was observed. By VPO measurement, M_n of Maya RE was 720. The D result for the RE was about 2.5×10^{-10} (m^2/s) in higher concentration solutions (3 and 1%), and this value corresponded to that for PS of M_n 2500 or 3000. Therefore, about four or five RE molecules on average were thought to associate in the solutions. By VPO measurement, M_n values of AS samples were in the range of 2400 - 4000. The D results for the AS samples were 1.0 - 1.6×10^{-10} (m^2/s) in higher concentration solutions (3 and 1%), and these values corresponded to those of PS of M_n over 3000. Thus, the average number of AS molecules contained in the aggregates in the solutions was not clear, but, considering the result of the RE, some molecules were thought to associate in the solutions. In lower concentration solutions, some portion of the association was dissociated from the aggregates with solvation by large amounts of $CDCl_3$, and two components were observed. Likely, the dissociated portion consisted of smaller molecules having lower molecular weights.

By using the Stokes-Einstein equation, the average molecular radius (r_{av}) of each sample was calculated for each solution from the D result. The Stokes-Einstein equation is indicated as followed equation.

$$D = kT/(6\pi \eta_S r_{av})$$

In this equation, k is the Boltzmann constant, T is the temperature (K), and η_S is the viscosity of solution. Table 4 shows calculated r_{av} values. The calculated r_{av} values of AS were 2.4 - 3.8 nm in solutions with a concentration above 1 %, and were 3.5 - 4.2 nm (for one component) and 0.6 - 0.7 nm (for the other component) for solutions with a concentration at 0.01%. Tanaka et al. measured some AS aggregates in solutions (decalin, 1-methylnaphthalene, and quinoline) using SANS (small-angle neutron scattering), and showed that the sizes of AS aggregates for 5% solutions were about 5 nm in radius at 298 K.[4] Their results are relatively consistent with ours in the higher concentration solutions. The decreases and the appearances of two components of the r_{av} values with the decrease of the concentration were caused by dissociation of the smaller molecules from the aggregates. The interactions between the aggregates are considered to include aromatic-aromatic stacking, hydrogen bonding, and van der Waals interaction. However, the contribution of each interaction to the aggregates has not yet been clarified. The D measurements using several solvent solutions such as pyridine or toluene and the comparison of the D results among these solutions might be needed to separate the contribution of each interaction to the aggregates.

Table 4. Radius (nm) of each sample in chloroform calculated from the D results

Concentration	3%	1%	0.1%	0.01%
Maya AS	3.8	2.9	1.7, 2.9	0.7, 4.2
Maya RE	1.5	1.4	0.9, 1.6	0.4, 1.8
Khafji AS	3.8	2.4	1.1, 3.8	0.7, 3.8
Iranian Light AS	3.8	2.4	1.5, 1.9	0.6, 3.5

Conclusion

Three kinds of AS and one kind of RE obtained from VR were measured by PGSE ^{1}H NMR, and the D value of each sample was estimated. By using the Stokes-Einstein equation, the r_{av} value of each sample was calculated for each solution from the D result. From the relation between the calculated molecular radius and the concentration of the solution, the effect of the concentration on the sizes of the aggregates is discussed. The differences of the D and r_{av} values with the concentration were caused by the partial dissociation of aggregates.

References

(1) Norinaga, K.; Wargardalam, V.J.; Takasugi, S.; Iino, M.; Matsukawa, S. *Energy Fuels*, **2001**, 15, 1317.
(2) Wargadalam, V.J.; Norinaga, K.; Iino, M. *Fuel*, **2002**, 81, 1403.
(3) Zhang, Y.; Takanohashi, T.; Sato, S.; Kondo, T.; Saito, I. *Energy Fuels*, **2003**, 17, 101.
(4) Tanaka, R.; Hunt, J.E.; Winans, R.E.; Thiyagarajan, P.; Sato, S.; Takanohashi, T. *Energy Fuels*, **2003**, 17, 127.
(5) Callaghan, P.T.; Pinder, D.N. *Macromolecules*, **1980**, 13, 1085; *ibid.*, **1981**, 14, 1334.
(6) von Meerwall, E.D. *J. Magn. Reson.*, **1982**, 50, 409.
(7) von Meerwall, E.D. *Adv. Polym. Sci*, **1983**, 54, 1.
(8) Karger, J.; Pfeifer, H.; Heink, W. *Adv. Magn. Reson.*, **1988**, 12, 1.
(9) Encyclopedia of NMR, Grant, D.M. and Harris, R.K., Eds., Wiley, 1996, p.1615, p.1626.

Commercial Application of TSRFCC technology

Hong-Hong Shan, Jian-Fang Zhang, Chao-He Yang, Gen-Lin Niu, Yong-Shan Tu

State Key Laboratory of Heavy Oil Processing
University of Petroleum, Dongying, 257061, P. R. China

Introduction

In China, the fluid catalytic cracking (FCC) process is one of the most important refining processes, it affords about 80% of gasoline and 30% of diesel oil in market, but now it is faced with a baptism to satisfy the need for producing environmentally-cleaner gasoline and diesel fuels. During the recent decade, almost all the FCC processes became the RFCC (residue fluid catalytic cracking) processes by revamping for processing the heavier feedstock, and RFCC technology got great development around the reaction system, including the feeding atomization, quick separation of oil vapor and spent catalyst, steam stripping of high efficiency, temperature control of reaction, as well as the innovation of riser reactor [1-3].

In order to improve the product distribution, as well as reduce the olefin content and increase the octane number of FCC gasoline, and raise the cetane number of FCC diesel fuel, many technology innovations were proposed and tested in China.

Riser reactor, commonly applied by worldwide FCC (One-Stage Riser, OSRFCC) process, was proved that, in the second half of riser, the activity and selectivity of the catalyst drop dramatically and over-cracking of intermediate products occurs [4], which deteriorate markedly the product distribution and final products properties. Based on this fact, a novel FCC process named TSRFCC had been invented successfully in china. The features of this new process are attributed to catalyst in relay, subsection reaction, short residence time, and high catalyst/oil (C/O) ratio, through which the average activity and selectivity of the catalyst are enhanced and undesirable secondary reaction and thermal reaction are suppressed efficiently. Some former studies proved that TSRFCC process open a fairly good way to optimize product distribution and improve product quality. In this article, the one of Two-Stage Riser FCC technology (TSRFCC-I) was introduced especially for its comercial application.

The Theory of TSRFCC-I technology

The TSRFCC aiming at the disadvantage that the activity of catalyst and the selectivity to ideal products fall greatly at the anaphase of reaction in the traditional one-stage riser FCC (OSRFCC) replaces the present single riser reactor by two modified riser reactors, has two catalyst cycling system. A series of TSRFCC technologies have been developed for various product schemes. TSRFCC-I technology is suitable for enhancing the yield of light oil, especially the ratio of diesel to gasoline. Figure 1 shows the principle flow chart of both OSRFCC and TSRFCC-I processes. For TSRFCC-I technology, the fresh feed is fed into the first riser reactor, after the first stage cracking reaction to a proper extent, diesel distillate as a part of the final product is separated, while heavy oil (or heavy oil and gasoline when olefin reduction of gasoline is needed) enters the second stage riser reactor, contacts with the regenerated catalysts and reacts simultaneously. Therefore, diesel is well protected from non-desired second cracking since it does not take part in the reaction in the second stage after the separation, which increases the yield of diesel. On the other hand, the partial pressure of diesel at the second stage is effectively lowered, so it is optimal for the large molecules of heavy oil breaking down to generate more light oil. The two risers in TSRFCC-I technology are designed to keep the total reaction time less than 2 seconds, this affords a favorable condition for high temperature and short time operation. Compared with the recycle oil, the residue is easier to cracking, but more difficult to atomize, vaporize, and diffuse into the pores of catalyst, so the recycle oil will firstly vaporize and diffuse into the pores of catalyst and cover the active sites when both together enters the riser at the same time, this does affect the effective conversion of residue. The residue and recycle oil entering the two different risers respectively is reasonable for improving the product distribution.

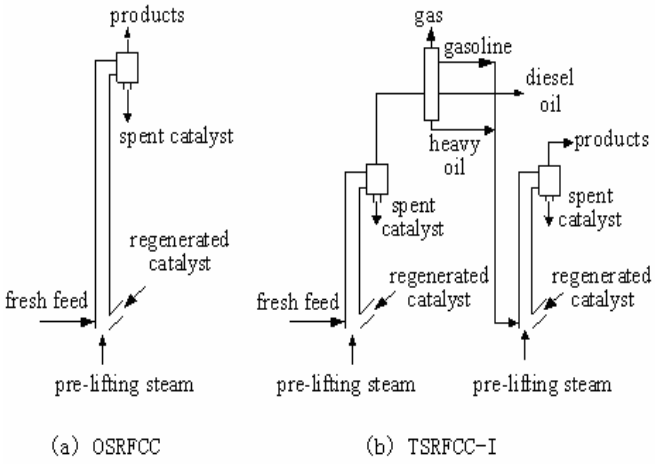

Figure 1. Comparison between OSRFCC and TSRFCC-I

Table 1 Product distribution comparison of TSRFCC-I and OSRFCC processes

	Statistically average of January and February 2002		Calibration on 17-18 June 2002	Changes before and after revamping
	Output data	*Corrected data		
Capacity, 10^4t/a	10.6	10.6	13.9	+3.3
LPG, wt%	11.43	12.18	10.64	-1.54
Gasoline, wt%	40.91	43.6	43.67	+0.07
Diesel oil, wt%	31.06	33.1	36.65	3.55
Decanted oil, wt%	7.74	1.67	1.67	
Coke and gas, wt%	8.86	9.45	4.90	-2.08
**Conversion wt%	92.26	98.33	98.33	+6.07
Light oil wt%	71.97	76.70	80.32	+3.62
Liquid products wt%	83.4	88.88	90.96	+2.08

Note: * corrected to the same yield of decanted oil with TSRFCC-I process
** conversion of heavy oil, equal to (100-yield of decanted oil)

Commercial application of TSRFCC-I technology

In 1994, the TSRFCC technology [5-7] was proposed by the State Key Laboratory of Heavy Oil Processing, University of Petroleum (East China), and was put into industrial test in 2002 at a revamped unit of 100 thousand ton/year capacity. As yet, there are four RFCC units to be modified by the TSRFCC-I technology, including Shenghua refinery, University of Petroleum (East China), Huabei Petrochemical corporation, Liaohe Petrochemical corporation and Changqing Petrochemical corporation.

In 2002, the TSRFCC-I technology was firstly tested in the distillate FCC unit of 100 thousand ton /year capacity, the product distribution comparison of TSRFCC-I process and the conventional OSRFCC before revamping is listed in table 1 with the same FCC feed and catalyst conditions. TSRFCC-I technology increases the yield of desired products, does 3.62 percents for light oil (gasoline and diesel oil) and 2.08 percents for total liquid products. The product distribution is improved obviously, that is, the yield of dry gas and coke decreases 2.08 percents, and the yield of diesel oil increases 3.55 percents. The production capacity is increased over 30%, it imply that the TSRFCC-I has the higher activity of catalyst and the selectivity of product than the OSRFCC process. In addition, the olefin content of gasoline reduces by 7 percents, the cetane number of diesel oil increases 3 units, the sulfur content of light oil decreases by 20-30%, and the reserve stability of gasoline and diesel oil is improved obviously.

Table 2 Product distribution (wt%), Changqing refinery

	LPG	gasoline	diesel oil	Decanted oil	Dry gas
*Statistically average of the first season 2003	14.37	38.46	32.61	0.56	4.4
**Calibration on 30-31 July	14.54	34.41	38.01	0.0	4.2
	coke	losses	Light oil	Desired product	Liquid yield
*Statistically average of the first season 2003	8.6	1	71.07	85.38	85.94
**Calibration on 30-31 July	8.3	0.55	72.42	86.96	86.96

*OSRFCC process; **TSRFCC-I process

In July, 2003, the product distribution result of TSRFCC-I process, Changqing petrochemical corporation, PetroChina, was obtained through calibration. Because the yield of distillates in atmospheric distillation tower increases by 2 percents, this unit processes the atmospheric residue with a higher carbon residue by 0.3-0.5 percents than one used before revamping. The microactivity of catalyst is 52-53, it is 58-60 before revamping. Under the so unfavorable operation conditions for TSRFCC, the comparison of product distribution between TSRFCC-I and OSRFCC was shown in table 2. The yield of diesel oil increases by 5.4 percents, the yield does by 1.35 and 1.58 percents respectively for light oil and the desired product, and the yield of dry gas and coke decreases by 0.95 percents. By the way, the diesel distillate from FCC process is an important product in China, the ratio of diesel oil to gasoline increases from 0.85 to 1.10 by the revamping with TSRFCC-I technology.

In Liaohe Petrochemical Corporation, the key of the RFCC unit running effectively is to produce the low olefin content gasoline according with the specification of GB 17930-1999. The RFCC unit was revamped using TSRFCC-I technology in May 2003. As shown in table 3, the output data were compared before and after revamping at the same operation scheme. The olefin content of gasoline decreases from 37.5v% to 33.5v%, satisfies the requirement of olefin content specification in GB 19730-1999. The yields of light oil and the desired product increase by 2.36 percents and 3.42 percents respectively, and the yield of coke and dry gas decreases by 2.9 percents. The latest output data of TSRFCC-I technology shows that the product distribution is better for producing low olefin gasoline than the best data before revamping and without considering the reduction of olefin in gasoline.

Table 3 Product distribution (wt%), Liaohe Petrochemical Corp

	LPG	gasoline	Diesel oil	Dry gas + coke
*Statistically average in December 2002	12.41	41.70	26.84	16.70
**Statistically average in June 2003	13.48	39.25	31.65	13.80
	Light oil	Desired product	Liquid yield	Olefin content of gasoline,v%
*Statistically average in December 2002	68.54	80.95	83.30	37.5
**Statistically average in June 2003	70.90	84.38	86.20	33.5

*OSRFCC process; **TSRFCC-I process

Conclusions

Compared with the conventional OSRFCC process, TSRFCC technology has great advantages in increasing the yield of desired product, improve the product distribution and product quality for distillate FCC or RFCC.

Acknowledgement. Thanks PetroChina for their financial Support. Thanks Feng Du, Zhong-xiang Han, and Jin-you Wang for their work in this project.

References

(1) Hou Fusheng. *Petroleum Processing and Petrochemicals*. **2001**, 32(1):1-6

(2) Miao Yi, Guan Minghua, Luo Yibin. *Petroleum Processing and Petrochemicals*. **2000**, 31(8):1-7

(3) Xie Chaogang, Zhong Xiaoxiang, and Yang Yinan. *Petroleum Processing and Petrochemicals*. **2001**, 32(1):26-30

(4) Jun-wu Chen and Han-chang Cao, Catalytic Cracking Technology and Engineering, SINOPEC Press, 1991.

(5) Zhang Jianfang, Shan Honghong, and Yang Chaohe. *US Patent*, **2002**, Application Number: 0108887A1

(6) Zhang Jianfang, Shan Honghong, and Yang Chaohe. *Chinese Patent*, **2002**, Application Number: 00134054.9

(7) Zhang Jianfang, Shan Honghong, and Yang Chaohe. Ninth Annual Conference of Catalytic Cracking. **2002.11**, Guangzhou

Advanced Catalyst Technology and Applications for Higher Quality Fuels and Lubes

J. S. Beck, T. F. Degnan, M. C. Kerby, and D. O. Marler

ExxonMobil Process Research Laboratories
1545 Route 22 East
Annandale, New Jersey 08801

Introduction

Catalysts are among our most powerful tools for creating value while meeting the challenges of the petroleum and petrochemical industries [1]. ExxonMobil has continued its long standing tradition of applying industry-leading catalyst technology to enable the conversion of complex molecules in crude oil selectively and efficiently into valuable products needed in fuels, lubricants, and chemicals. The merger of Exxon and Mobil brought together a unique synergy of metal oxide and zeolite catalysis expertise and ExxonMobil continues to be an industry pacesetter in the broad application of catalyst technology.

An overview of our active materials platforms will be reviewed. Emphasis will be given to how zeolitic, mesoporous, and metal oxide catalysts are discovered, developed, and commercially implemented to manufacture higher quality fuels and lubricants within ExxonMobil. Only through a fundamental understanding of how catalysts behave at the molecular level, can innovations in new catalyst platforms continue.

In order to accelerate the pace of catalyst innovation, ExxonMobil is exploiting the use of high throughput experimentation (HTE) to more rapidly discover and implement new catalyst technologies that are critical for future advances. To this end, ExxonMobil Research and Engineering Company and Symyx Technologies, Inc. have entered into a multi-year technology alliance focused on using HTE to enhance downstream and chemicals R&D activities.

ExxonMobil Catalyst Platforms and Applications

Other than a few purely thermal processes, catalysts are used in almost all refining and chemical processes. Catalysts accelerate reactions and lower energy requirements while also improving value by selectively making the desired products. We continue to design a broad array of catalyst platforms ranging from shape selective zeolites to produce world class lubricants, to high activity metal oxide catalysts to manufacture low sulfur transportation fuels.

ExxonMobil's capability spans across the entire catalyst pipeline from the discovery of new catalysts to commercial implementation. A strong fundamental science base drives the discovery of new catalyst systems. Through our internal knowledge of desired hydrocarbon transformations, we can match the molecule size and conversion needs to catalyst design. In the development phase, the most viable catalyst is selected and a process initiated to find a cost effective preparation route for the catalyst of choice. We then set a path to scale-up the catalyst, which could include internal manufacture or joint work with a catalyst vendor. Finally, we commercialize the catalyst with the objective to apply it as broadly as possible across our refinery circuit. This feedback loop provides critical performance information about the performance of the catalyst and allows us to further identify and develop next generation catalyst systems.

Zeolite Catalysts. Zeolites are an important class of molecular sieves and are used to collect, separate, and transform a wide range of organic molecules [2]. They are crystalline aluminosilicate frameworks composed of tetrahedral silica and aluminum atoms linked by oxygen atoms, which can be synthesized into a variety of pore sizes and shapes. Zeolite discovery is a complex science. Components such as silica, alumina, and an organic templating agent, which provides the shape of the material, are combined in a controlled pH and temperature environment to form the crystalline product. The organic template is then removed through calcination. This leaves behind the crystalline zeolite framework with a pore size that matches the organic template. A significant number of experiments (100's-1000's) are required to 'map' the synthesis space. Zeolites can be uni-dimensional or multi-dimensional and exist in a wide assortment of molecular sizes, shapes, and intersecting channels (Figure 1). Unique combinations of pore size, shape, and dimensionality can provide a wealth of new zeolites. ExxonMobil has synthesized well over 50 unique zeolite structures.

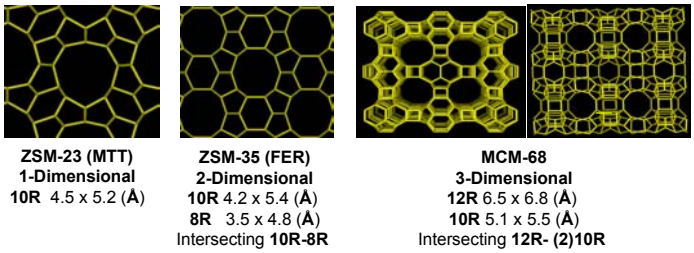

Figure 1. Zeolites can be formed in a variety of molecular sizes and shapes.

With this array of zeolitic materials, it is possible to tailor the catalyst to perform the desired reactions at high rates and selectivity. The ability to match the size of the molecule to the size of the zeolite or molecular sieve is called "shape selectivity" in which ExxonMobil is a leader (Figure 2).

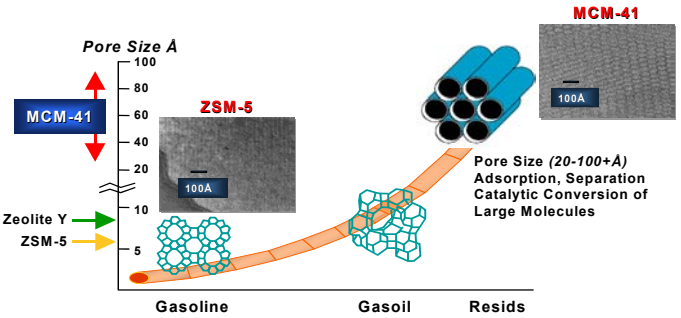

Figure 2. Use of shape selectivity to design catalyst pores for selective conversion of molecular types.

Today, the shape selectivity concept is the basis for ~20 commercial processes with annual hydrocarbon throughput in excess of 70 million metric tons per year. For example, catalytic cracking, a key refinery process used to produce gasoline and diesel utilizes zeolite-Y, which selectively cracks heavier vacuum gas oil molecules. ZSM-5, a smaller pore zeolite, can be added as a co-catalyst to the cat-cracker to promote the selective formation of propylene, a valuable chemical product. Another opportunity for exploiting shape selectivity concepts lies in the modification of mesoporous molecular sieves for reaction or separation of larger molecules. Researchers have functionalized the pores of MCM-41 to selectively adsorb low concentrations of metals such as Hg and Ag while excluding other metals [3, 4].

The zeolitic crystal is formulated into a finished catalyst through the addition of various components such as binders (e.g. silica, alumina, zirconia, titania), modifiers, metals and metal oxides (e.g.

Pt, Pd, Ni, Co, Mo). These components can be added to optimize the finished catalyst's acidity, metals activity, porosity, and physical integrity.

One key application of shape selectivity is ExxonMobil's selective catalysts dewaxing technology. Dewaxing rearranges the structure of primarily straight chain molecules to ensure they have the correct flow properties at the desired temperatures. The MSDW-2 catalyst technology is a medium pore zeolite which applies shape selectivity, proper control of acidity, and a metal driven hydrogenation-dehydrogenation function to selectively convert or 'dewax' the straight chain molecules to a slightly branched molecules as it enters the zeolite pore. More bulky or branched molecules, which already have beneficial lubricant properties, are excluded from entering the zeolite pore. Thus, this catalyst technology only works on the molecules that need to be converted.

Metal Oxide Catalysts. Another important class of catalytic materials that are widely used in the refining industry are metal oxides. These materials, which are typically mixtures of CoMo or NiMo oxides on silica-alumina supports, are primarily used in key refinery processes called hydroprocessing. This technology uses the catalytic addition of hydrogen to selectively remove sulfur and nitrogen from various refinery streams to produce low sulfur gasoline and diesel. More hydrogen intensive hydroprocessing applications can also reduce other components such as olefins and aromatics.

The prime contributor to sulfur in the gasoline pool is from the cat-cracking unit. While it is possible to hydrotreat the sulfur to very low levels, cat naphtha also contains a considerable amount of valuable olefins, which are high in octane. Thus, the challenge is to selectively remove sulfur while minimizing the saturation of olefins. This is particularly an issue for higher sulfur cat naphthas. ExxonMobil's *SCANfining* technology [5] utilizes a proprietary CoMo catalyst, jointly developed with Akzo Nobel, to selectively reduce the cat naphtha sulfur while minimizing the saturation of high octane olefins (Figure 3).

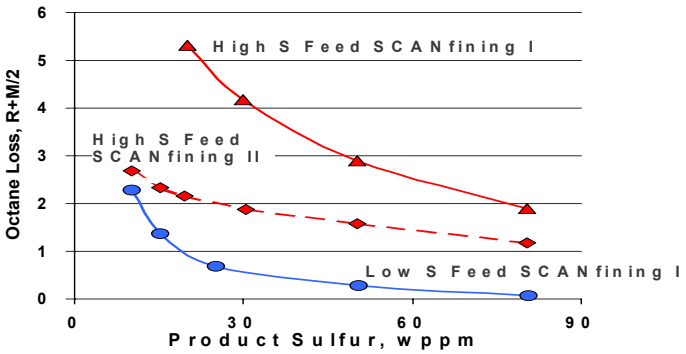

Figure 3. ExxonMobil's *SCANfining* technology selectively removes sulfur while minimizing octane loss.

The CoMo system is characterized by high metals dispersion with special attention given to the support-metal interactions. *SCANfining II*, is even more selective particularly for higher sulfur cat naphthas. *SCANfining* has been rapidly commercialized and will be used in 30 units worldwide to manufacture low sulfur gasoline.

A new generation of ultra-high activity catalysts for nitrogen and sulfur removal was recently discovered by ExxonMobil and jointly developed with Akzo Nobel. This catalyst system called *NEBULA*™ is unique in that it is a bulk mixed metal oxide, which maximizes the number of active sites per volume of catalyst [6]. *NEBULA*™ has shown very high hydrodesulfurization and hydrodenitrogenation activities compared to conventional catalysts (Figure 4). This performance advantage enables the refiner to produce ultra low sulfur diesel in existing units. *NEBULA*™ has been commercialized in a number of distillate hydrotreating and hydrocracking applications.

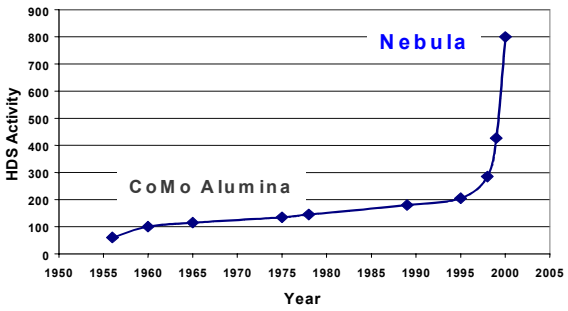

Figure 4. *NEBULA*™ catalyst technology represents a step change in Hydroprocessing catalysts.

Future Advances in Catalysis

Catalysis will continue to play a crucial role in the petroleum and petrochemical industries. Fuel and lube compositions are expected to evolve in response to environmental legislation and advanced engine design. In addition, petroleum feedstocks will become heavier and sourer with time. This will require future catalysts, which are higher in activity and selectivity, more poison tolerant and stable for longer periods.

ExxonMobil is committed to accelerate the pace of innovation and delivery through the use of HTE. ExxonMobil and Symyx Technologies, a leader in the development and application of high-speed materials research methods, have formed a technology alliance focused on the application of HTE technology across ExxonMobil's downstream and chemical portfolio. Implementation of HTE methods will enhance ExxonMobil's core competency in catalyst research and development. This alliance includes high throughput catalyst synthesis, characterization, and evaluation tools coupled with an informatics platform to more rapidly discover and implement future catalyst systems.

References

(1) Kaufmann, T. G.; Kaldor, A.; Stuntz, G. F.; Kerby, M. C.; Ansell, L. L. *Catalysis Today.*, **2000**, *62*, 77.

(2) Chen, N. Y.; Garwood, W. E.; Dwyer, F. G. *Shape Selective Catalysis in Industrial Applications*, *2nd ed.*, Marcel Dekker, New York, 1996.

(3) Beck, J. S.; Vartuli, J. C.; Roth, W. J.; Leonowicz, M. E.; Kresge, C. T.; Schmitt, K. D.; Chu, C. T-W. Olson, D. H.; Sheppard, E. W.; McCullen, J. B.; Higgins, J. B.; Schlenker, J. L. *J. Am. Chem. Soc.* **1992**, *114*, 10834.

(4) Feng, X., Frywell, G.E., Wang, L.Q., Kim, A.Y., Liu, J., Kemner, K.M., *Science*, **1997**, *276*, 923

(5) Riley, K. L.; Kaufman, J. L.; Zaczepinski, S.; Desai, P. H.; Mayo, S. W. *Akzo Nobel Catalyst Symposium, Vol. G-3*, 1998, 1.

(6) Meijburg G.,Brevoord E., Plantenga F., Mayo S., Inoue Y., Fujita K., Lewis W., Sapre A., *NEBULA™ for Hydrocracker Pretreat Operations*, ERTC 2003, London.

SELECTIVE HYDRODESULFURIZATION OF FCC GASOLINE OVER CoMo/Al_2O_3 SULFIDE CATALYSTS

Makoto Toba, Yasuo Miki, Yukio Kanda, Takashi Matsui, Masaru Harada and Yuji Yoshimura

National Institute of Advanced Industrial Science and Technology,
Tsukuba Central-5, 1-1-1 Higashi,
Tsukuba, Ibaraki 305-8565, Japan

Introduction

FCC gasoline is one of the major components of motor gasoline. It contains high level of sulfur derived from heavy gas oil and atmospheric residue used as FCC raw materials. FCC gasoline also contains valuable olefins which contribute to the octane number of the motor gasoline. Therefore, the selective hydrodesulfurization which minimizes octane loss is highly desired to meet the severe limitation of sulfur content (1~3). In this study, the selective hydrodesulfurization (HDS) of FCC gasoline over new sulfide catalysts was investigated.

Experimental

Two kinds of FCC gasoline (full-range and 60 ºC +) were used here. The properties of them are summarized in Table 1.

Table 1. Properties of FCC gasoline

	FCCG (full-range)	FCCG (60ºC +)
Density (g/cm^3@15ºC)	0.733	0.771
Sulfur (wtppm)	158.9	234.1
H/C (mol/mol)	1.93	1.83
Average molecular weight	102	112
GC-RON*[1]	90.5	88.9
Hydrocarbon type (vol%)*[1]		
Paraffins (P)	5.5	4.8
Isoparaffins (I)	37.6	32.4
Olefins (O)	26.3	19.7
Naphthenes (N)	9.2	12.4
Aromatics (A)	21.4	30.8

*1 Research octane number and hydrocarbon type were measured by GC.

Sulfide CoMo and NiMo catalysts were prepared by incipient wetness impregnation of γ-alumina with a mixed solution obtained from molybdenum oxide, cobalt (nickel) carbonate and a special ligand. All catalysts were presulfided in the stream of 5%H_2S/H_2 gas before reaction.

The selective hydrodesulfurization (HDS) of FCC gasoline was carried out in a high-pressure fixed-bed continuous-flow reactor. The reaction conditions were hydrogen pressure of 1~2 MPa, reaction temperature of 220~260 ºC, liquid hourly space velocity (LHSV) of 4 h^{-1}, and a volume ratio of hydrogen (NTP) to feed of 100.

The hydrocarbon composition and research octane number (RON) in feedstock and products were analyzed by using PIONA-GC (Agilent 6890N (JIS K2536)-Yokogawa Analytical Systems Co. GPI system). The contents of total sulfur were measured by elemental analysis (Mitsubishi Chemicals Co., TS-100V). Sulfur compounds were analyzed by a GC-SCD (Agilent6890-Sievers355).

Results and Discussion

Figure 1 shows the time course of HDS percentage, olefin and aromatics hydrogenation percentage during HDS of FCC gasoline (60 ºC+) for 56h. HDS activity showed almost constant, while olefin hydrogenation activity decreases drastically in the first 10h and decreases gradually in the latter 46h. Aromatics hydrogenation activity showed zero except initial stage of reaction.

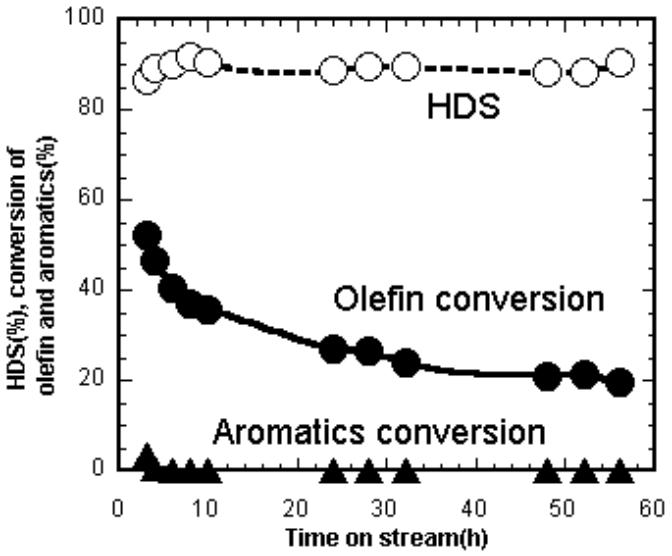

Figure 1. Time course of FCC gasoline (60 °C+) hydrodesulfurization: Reaction conditions: temperature 240 °C; pressure 1MPa, LHSV, 4h^{-1}, H_2/feed ratio 100NL/L: Catalyst: CoMo/Al_2O_3 (CoO 3.1 wt%, MoO_3 11.8 wt%)

Effect of catalyst species on properties of product oil in the hydrotreatment of heavy FCC gasoline is shown in Table 2. Both catalysts showed very high HDS activities. NiMo/Al_2O_3 catalyst gave a much higher olefin hydrogenation activity than CoMo/Al_2O_3 catalyst. This result means that CoMo/Al_2O_3 is more suitable for selective hydrogenation of FCC gasoline than NiMo/Al_2O_3.

Table 2. Effect of catalyst species on properties of product oil in the hydrotreatment of heavy FCC gasoline*[1]

	FCCG (60 ºC+)	NiMo/Al_2O_3*[2]	CoMo/Al_2O_3*[2]
Temperature (ºC)	–	240	240
Time (h)	–	52	52
Density (g/cm^3@15ºC)	0.771	0.766	0.768
Sulfur (wtppm)	234.1	5.6	7.1
HDS (%)	–	97.6	97.0
Olefin conv.(%)	–	80.3	37.2
H/C (mol/mol)	1.83	1.87	1.85
Average molecular weight	112	112	112
GC-RON*[3]	88.9	85.6	87.1
Hydrocarbon type (vol%)			
Paraffins (P)	4.8	9.6	7.3
Isoparaffins (I)	32.4	41.8	36.9
Olefins (O)	19.7	3.8	12.3
Naphthenes (N)	12.4	14.8	13.4
Aromatics (A)	30. 8	30.1	30.1

*1 Reaction conditions: temperature 240 °C; pressure 2MPa, LHSV, 4h^{-1}, H_2/feed ratio 100NL/L
*2 NiO (CoO) 6.1wt%-MoO_3 23.6wt%, sulfidation, 340 ºC for 3h
*3 Research octane number measured by GC

Figure 2 shows effect of sulfidation temperature of catalyst on HDS and olefin hydrogenation activities. The reaction carried out at

220, 240 and 260 ºC. It is noted that olefin hydrogenation activity of the catalyst sulfided at 319ºC is much lower than those of other catalysts, while HDS activity showed almost same level. These results suggest that sulfidation temperature have much larger influence on olefin hydrogenation active sites than the HDS active sites. These phenomena appeared more remarkably at higher temperature. According to the proposed olefin hydrogenation active site, olefin hydrogenation occurs at Mo coordinatively unsaturated sites (CUS) (4). Perhaps, CUS Mo sites of this catalyst may selectively disappear.

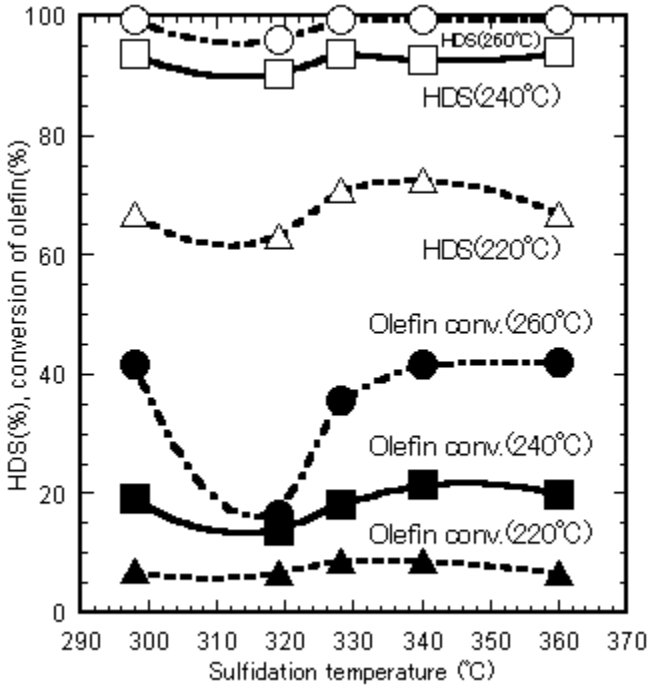

Figure 2. Effect of sulfidation temperature of catalyst on HDS and olefin hydrogenation : Reaction conditions: pressure 1MPa, LHSV, $4h^{-1}$, H_2/feed ratio 100NL/L : Catalyst: $CoMo/Al_2O_3$ (CoO 3.1 wt%, MoO_3 11.8 wt%)

Figure 3 shows HDS and olefin hydrogenation activity in the hydrotreatment of full-range FCC gasoline. Olefin hydrogenation activity of developed catalyst is relatively low and octane (GC-RON) loss is 0.6 to 1.3 in the range of 220ºC to 260ºC. However, olefin hydrogenation activity of commercial catalyst drastically increased at 260ºC, while HDS activities of both catalysts showed almost same. From the analysis of various C5 and C6 olefin reactivity, terminal olefin hydrogenation activity for the developed catalyst (43.6~49.8%) showed slightly lower than the commercial one (48.2~59.6%). However, internal olefin hydrogenation activity at 260 ºC for the developed catalyst (-18.2~5.0%) showed much lower than the commercial one (-17.6~23.6%). These results suggest that internal olefin is less active at olefin hydrogenation active site of developed catalyst. At lower temperature, conversion of internal olefin showed minus value because of formation of internal olefins from terminal olefins by C=C double bond isomerization. These phenomena are effective olefin hydrogenation depression.

Sulfur compounds in full-range FCC gasoline product oils were analyzed by GC-SCD. Benzothiophene and methylbenzothiophene were completely desulfurized. Most of sulfur compounds remaining in the product are thiophene and alkylthiophenes. Slight amounts of sulfur compounds such as 2-pentanethiol which were produced by re-combination reaction between olefins and hydrogen sulfide were observed.

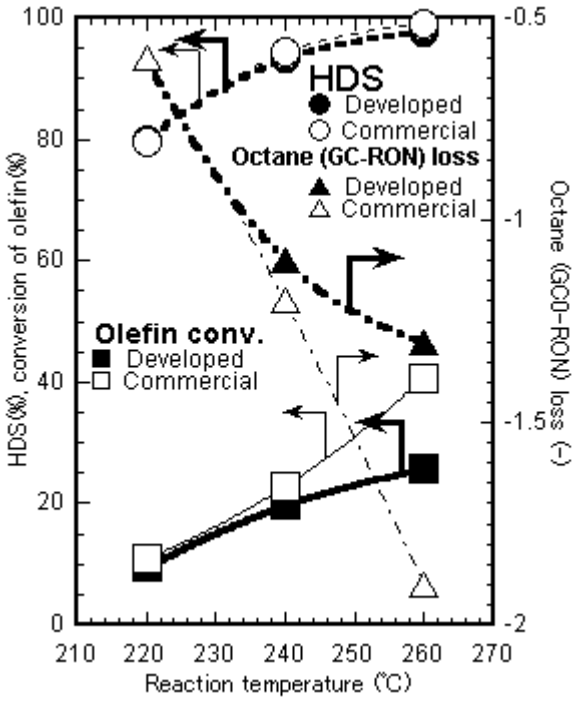

Figure 3. HDS and olefin hydrogenation activity in the hydrotreatment of full-range FCC gasoline: Reaction conditions: pressure 1MPa, LHSV, $4h^{-1}$, H_2/feed ratio 100NL/L: Catalyst: $CoMo/Al_2O_3$ (developed, CoO 3.1 wt%, MoO_3 11.8 wt%; commercial, CoO 4.5 wt%, MoO_3 16.9 wt%)

Conclusions

The developed $CoMo/Al_2O_3$ catalyst showed high HDS activity and depressed olefin hydrogenation. The HDS selectivity of the catalyst depended on their sulfidation conditions. Olefin hydrogenation activity of the catalyst sulfided at 319ºC less increased with increasing operating temperature than those of other catalysts. At higher temperature, internal olefin hydrogenation activity of the developed catalyst was much lower than that of commercial one.

References

(1) S. Hatanaka, M. Yamada, O. Sadakane, *Ind. Eng. Chem. Res.*, **36**, 1519 (1997).

(2) S. Hatanaka, M. Yamada, O. Sadakane, *Ind. Eng. Chem. Res.*, **37**, 1519 (1998).

(3) Rosvoll, J. S., Grande, K., Moljord, K., Skjϕlsvik, P. A., Thorvaldsen, B., Johansen, S., Kuhnle, S., Sϕrum, P. Å., Sapre, A. V., Roundtree, E. M., *Hydrocarbon Processing*, **Feb. 2004**, 55 (2004).

(4) Tanaka, K., Okuhara, T., *Proc. 3rd Int. Conf. on Chem. and Uses of Molybdenum*, Barry H. F., Mitchell, P. C. H. Ed. Climax Molybdenum Company, 1979; p.170.

SELECTIVE SULFUR REMOVAL FROM LIQUID HYDROCARBONS OVER REGENERABLE CeO_2-TiO_2 ADSORBENTS FOR FUEL CELL APPLICATIONS

*Shingo Watanabe, Xiaoliang Ma and Chunshan Song**

Clean Fuels and Catalysis Program, The Energy Institute and
Department of Energy and Geo-Environmental Engineering
The Pennsylvania State University
209 Academic Project Building, University Park, PA 16802
*E-mail: csong@psu.edu

Introduction

In order to improve the air quality, the governments in various countries have announced new regulations to reduce the sulfur contents in transportation fuels. The U.S. Environmental Protection Agency (EPA), for example, has announced a new regulation that mandates refineries to reduce the sulfur content in gasoline to below 30 ppmw from the current average of 300 ppmw and in diesel to below 15 ppmw from the current level of 500 ppmw by year 2006. The interest in the desulfurization of transportation fuels is further motivated by the development of fuel cells to power automobiles, because the fuel-cell-powered vehicles are more efficient energetically and do not emit noxious gases such as SOx, NOx etc. However, for PEMFC applications the sulfur content in the transportation fuels needs to be further reduced to < 1 ppmw.

Catalytic hydrodesulfurization (HDS) is the conventional method that is being employed by the refineries to produce clean transportation fuels. Although HDS process can remove sulfur compounds from gasoline close to 30 ppmw, it is highly inconvenient and more expensive process to produce fuel cell grade gasoline as the process is conducted at high pressure, high temperature with high hydrogen consumption. Several alternative methods such as adsorption, alkylation, oxidation, extraction etc. have been developed in recent years. Among them the adsorptive desulfurization can be accomplished at low temperature and pressure. Since gasoline contains significant amount of olefins and aromatics, the adsorbent should be able to remove selectively organic sulfur compounds in the presence of the olefins and aromatics.

A new concept is being developed in our laboratory at Penn State University known as "Selective adsorption for removal sulfur (PSU-SARS)" for the adsorption desulfurization of gasoline, diesel and jet fuels. Several new adsorbents based on zeolites, mixed oxides, supported metal and metal compounds, and activated carbons are being developed and some of them exhibit excellent adsorption capacity for the desulfurization of gasoline and jet fuels.[8]

Owing to its high oxygen storage capacity, redox properties and good metal-support interactions, CeO_2 has been known as an excellent support for base metals and noble metals in a variety of catalytic processes, including auto exhaust three-way catalyst. The CeO_2-based adsorbents have also been developed in recent years for the removal of H_2S and SO_x from flue gas, natural gas and coal-derived gas. CeO_2 has been evaluated as a high temperature regenerable desulfurization sorbent, which yields elemental sulfur upon regeneration [9-11]. Our recent work on the desulfurization of jet fuel indicated that Ce loaded zeolites and CeO_2-based bimetallic oxides adsorbents exhibit fairly good adsorption properties.

Taking into account of the interesting properties of the CeO_2, the present study aimed at developing CeO_2-based regenerable adsorbents for the removal of thiophenic sulfur compounds present in the gasoline, jet and diesel fuels. High surface area CeO_2-TiO_2 bimetallic oxides with various molar ratios synthesized by coprecipitation have been used as adsorbents for the desulfurization of a model gasoline containing 430 ppmw of sulfur in the form of thiophene, tetrahydrothiophene, benzothiophene and 2-methylbenzothiophene in a fix-bed flow reactor at ambient temperature and pressure. CeO_2-TiO_2 mole ratio was swung to investigate organic sulfur compounds adsorption behavior using model fuel and commercial fuel. Regenerability of the adsorbents by air was also tested.

Experimental

The adsorbents were prepared using cerium ammonium nitrates and titanium oxysulfate sulfuric acid hydrate (Aldrich Chem. Co.) by urea gelation/co-precipitation method.[6] Precipitation was employed at 90~95°C for 8 hours. Precipitants were dried 110°C over night, and calcined at 450°C for 6 hrs in air employing a temperature ramp of 2°C/min. Analysis of the adsorbents was performed by X-ray diffraction (XRD), and surface area was calculated using the BET equation. Pore size distributions were calculated by the Barrett-Joyner-Halender (BJH) method using the desorption branch of the isotherm.

A model gasoline, which contained thiophene, tetrahydrothiophene, benzothiophene and 2-methylbenzo-thiophene (total sulfur concentration: 430 ppmw), toluene and 1-octene in heptane was used in the present study. The composition of the model gasoline is listed in Table 1.

For flow system desulfurization, the powder adsorbent was packed in a stainless steel column with an internal diameter of 4.6 mm and length of 37.5 mm. The adsorbent bed volume was about 0.623 ml. Pretreatment was conducted under the dry airflow at 375°C for 2 hours before adsorption. The model gasoline was fed into the column using a HPLC pump. The feed flow rate was 0.05 ml/min. The adsorption was conducted under ambient temperature and pressure. Antek 9000 Total Sulfur Analyzer (detection limit < 0.5 ppmw) was used to determine the total sulfur concentration of the treated model gasoline. The breakthrough volume and capacity were calculated on the basis of the breakthrough curves considering the sulfur content at the breakthrough point was below 1 ppmw.

Regeneration was conducted under an air flow. Air was flowed through the spent adsorbent bed at room temperature for 5 min. Then, the temperature of the adsorbent bed was increased up to 375°C within 10 min, and kept at 375°C for 45 min. Total time for the regeneration was 60 min. Air was continuously flowing, until temperature was cooled down to room temperature. After the regeneration the adsorptive desulfurization test was conducted again.

Table 1 Model gasoline composition

	FW	d (g/cm^{-3})	b.p. (°C)	mole%	S conc. (ppmw)
C_7	100.2	0.684	98	99.769	-
T	84.1	1.051	-	0.0344	110
THT	88.2	1.000	-	0.0297	95
BT	134.2	1.149	-	0.0359	115
2MBT	148.2	-	-	0.0312	100
Toluene	92.1	0.865	110.6	0.0333	-
1-octene	122.2	0.7515	122	0.0333	-
C_9 (IS)	128.3	0.718	151	0.0333	-
Total				100.00	430

Results and Discussion

The present study was focused on examining the effect of Ti-Ce atomic ratio on the adsorptive performance of the Ti-Ce bi-metal oxide adsorbents (TiO_2-CeO_2) and the regenerability of the Ti-Ce bimetal oxide adsorbents. The breakthrough curves of the model gasoline over the bi-metal oxides with different Ti-Ce atomic ratio are shown in Figure 1. The breakthrough amount of the treated model gasoline (gram of the cumulative treated model gasoline per gram of the adsorbent, g/g) increases in the order of CeO_2 < TiO_2 < $Ti_{0.05}Ce_{0.95}O_2$ < $Ti_{0.1}Ce_{0.9}O_2$ < $Ti_{0.9}Ce_{0.1}O_2$ < $Ti_{0.5}Ce_{0.5}O_2$. It is clear that the bi-metal oxides showed better adsorptive performance than the monometal oxides, CeO_2 and TiO_2, indicating that there is significant synergism of the two metal oxides. It might be because the bi-metal oxides resulte in a morphological change, which was observed in XRD analysis, and/or a change in the electronic structure on the surface. The smaller crystal size for the bi-metal oxides, which were calculated on the basis of XRD data, than those of the mono-metal oxides, TiO_2 and CeO_2, was observed. Figure 2 shows that the breakthrough capacity (milligram of sulfur per gram of adsorbent, mg/g) of the bi-metal oxides at the outlet sulfur level of 1 and 30 ppmw as a function of the Ti-Ce atomic ratio. Adding small amount of TiO_2 into CeO_2 improved the capacity of the adsorbent significantly. The bi-metal oxide with a Ti-Ce atomic ratio of 1:1 showed the highest adsorptive capacity, being 3.8 mg/g.

Adsorptive selectivity of the bi-metal oxides was also examined. The results showed that the bi-metal oxides have good selectivity for the organic sulfur compounds. Further work in characteristics of the bi-metal oxides is necessary for fundamental understanding the adsorptive mechanism.

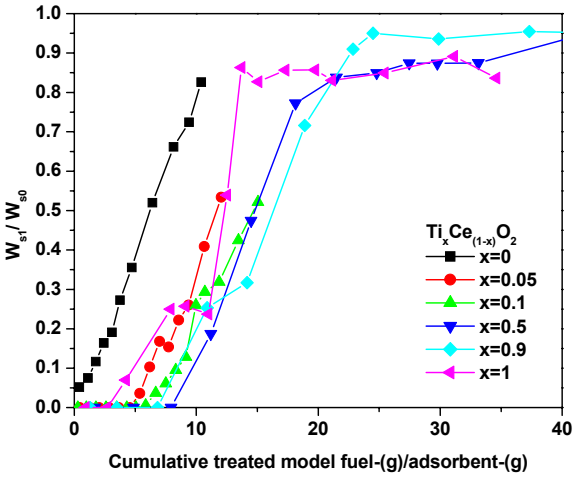

Figure 1 The breakthrough curves of model gasoline over TiO_2-CeO_2 adsorbents

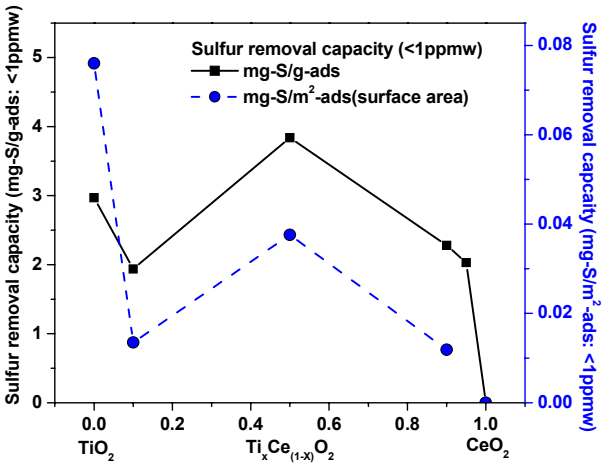

Figure 2 The adsorptive capacities of CeO_2-TiO_2 adsorbents as a function of Ti-Ce atomic ratio in CeO_2-TiO_2 adsorbents

The spent $Ti_{0.1}Ce_{0.9}O_2$ adsorbent was regenerated at 375°C under an air flow. The adsorptive performance of the regenerated $Ti_{0.1}Ce_{0.9}O_2$ adsorbent was shown in Figure 3 in comparison with that of the fresh one. As seen in this figure, the breakthrough curve for the regenerated adsorbent was almost consistent with that for the fresh adsorbent, implying that almost all of the adsorptive capacity of the fresh adsorbent was recovered by the oxidative regeneration with air. More studies are necessary to determine the best regeneration conditions.

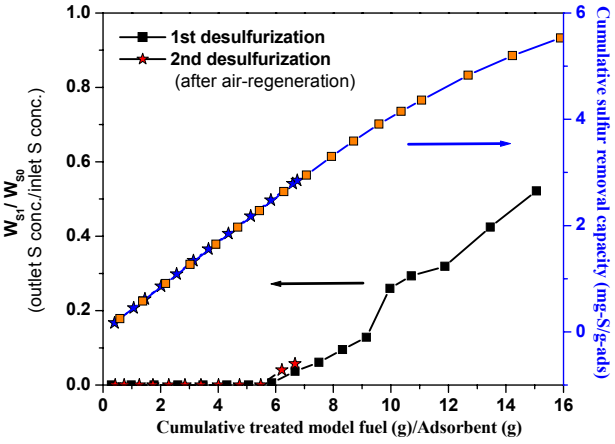

Figure 3 Adsorptive performances of the fresh and regenerated $Ti_{0.1}Ce_{0.9}O_2$ adsorbents

Summary

TiO_2-CeO_2 bimetallic oxides showed higher desulfurization capacity in comparison with the monometallic oxides, TiO_2 and CeO_2. A synergetic effect of the two metal oxides was observed in the adsorptive desulfurization of the model fuel. A potential

advantage of the TiO_2-CeO_2 binary oxides is that they can be regenerated by the oxidation at 375˚C in air.

Acknowledgments

This work was supported in part by the US Department of Defense and in part by the US Department of Energy.

References

(1) Song, C. S. and X.L. Ma, Applied Catalysis B Environmental, **2003,** *41(1-2)* 207-238

(2) Ma, X.L., L. Sun, Z. Yin and C. S. Song, *Preprint Paper – American Chemical Society,* Division Fuel Chemistry **2001***, 46(2),* 648-649.

(3) Ma, X.L., M. Sprague, L. Sun and C. S. Song, *Preprint Paper – American Chemical Society,* Division Fuel Chemistry **2002***, 47(2),* 452-453.

(4) S. Velu, S. Watanabe, X.L. Ma, L. Sun and C. S. Song, *Preprint Paper – American Chemical Society,* Division Petroleum Chemistry **2003***, 48(2),* 56-57.

(5) S. Velu, X.L. Ma and C. S. Song, *Preprint Paper – American Chemical Society,* Division Fuel Chemistry **2002***, 47(2),* 447-448.

(6) M. Kobayashi and M. Flytzani-Stephanopoulos, Industrial and Engineering Chemistry research, **2002**, *41*, 3115-3123

(7) S. Watanabe, S. Velu, X. Ma and C.S. Song **2003**, *Preprint Paper – American Chemical Society,* Division Fuel Chemistry *48(2)*: 695-696.

(8) Song, C. S. **2003**, Catalysis Today, ***86****(1-4)*: 211-263.

(9) Flytzani-Stephanopoulos, M., T. L. Zhu and Y. Li **2000**, Catalysis Today, ***62****(2-3)*: 145-158.

(10) Liu, W., C. Wadia and M. Flytzani Stephanopoulos **1996**, Catalysis Today, ***28****(4)*: 391-403.

(11) Zeng, Y., S. Zhang, F. R. Groves and D. P. Harrison **1999**, Chemical Engineering Science, ***54****(15-16):* 3007-3017.

Vapor-Phase Oxidesulfurization (ODS) of Organosulfur Compounds: Carbonyl Sulfide, Methyl Mercaptans and Thiophene

Sukwon Choi and Israel.E. Wachs

Operando Molecular Spectroscopy & Catalysis Laboratory
Department of Chemical Engineering
Lehigh University, Bethlehem PA, 18015, USA

Introduction

Sulfur in transportation fuels remains a leading source of SOx emissions from vehicle engines and is a major source of air pollution. Significant reduction in the emissions of sulfur compounds has been targeted as one of the highest priorities by the Environmental Protection Agency (EPA) [1]. The conventional technologies to remove S from organosulfur compounds are via catalytic hydrodesulfurization (HDS) or via direct combustion, which operate under severe conditions (elevated temperatures and/or high pressures). During HDS, H_2 is converted to H_2S and subsequently reacted with O_2 in the Claus process to H_2O and elemental sulfur, which is disposed in landfills. Direct combustion leads to the formation of unwanted global warming CO_2, and an undesirable acid rain precursor SO_2.

We have investigated an alternative vapor-phase oxidesulfurization (ODS) of the various organosulfur compounds. Under these initiatives, novel catalytic reaction processes of selectively oxidizing various organosulfur compounds typically found in petroleum streams (CH_3SH, CH_3SCH_3, CH_3SSCH_3, COS, CS_2, thiophene, 2,5-dimenthylthiophene) into valuable chemical intermediates (H_2CO, CO, H_2, maleic anhydride and concentrated SO_2 that can be used for producing H_2SO_4) has been extensively studied. This research has primarily focused on establishing the fundamental kinetics and mechanisms of these selective oxidation reactions over well-defined supported metal oxide catalysts.

Experimental

Catalyst Preparation. The catalysts used in this study were prepared by the incipient wetness impregnation method. This technique is described in detail elsewhere [2-3]. The support materials used in this study are TiO_2 (55 m^2/g), ZrO_2 (39 m^2/g), Nb_2O_5 (55 m^2/g), CeO_2 (36 m^2/g), Al_2O_3 (γ, 180 m^2/g), and SiO_2 (300 m^2/g).

Characterization Methods. *In Situ* Raman spectroscopy was performed with a system comprised of an Ar+ laser (Spectra Physics, model 2020-50) set at 514.5 nm, and a Spex Triplemate spectrometer (model 1877) connected to a Princeton Applied Research (model 143) OMA III optical multichannel photodiode array detector. The reactivities of the catalysts were obtained from an isothermal fixed-bed reactor system operating at atmospheric pressure. The feed gas contained 1000 ppm of the reactant (COS, CS_2, CH_3SH, thiophene), 18% O_2 in He balance, and was introduced into the reactor at a flow rate of 150 ml/min. Sample runs were performed between 200-450 ^oC. Analysis of the reaction products was accomplished using a FTIR, (model #101250 Midac) or an on-line gas chromatograph (HP 5890A) equipped with a thermal conductivity detector (TCD) and a sulfur chemiluminescence detector (SCD 355, Sievers). Temperature Programmed Surface Reaction Mass Spectrometry (TPSR-MS) was carried out with an AMI-100 system equipped with an online mass spectrometer (Dycor DyMaxion). The adsorption was performed between 35-100 ^oC using 200 mg of catalyst and was ramped to 500 ^oC at a heating rate of 10 ^oC/min in 5% O_2/He or He at 30 mL/min. *In situ* FT-IR (Fourier Transform Infrared) studies were conducted with the IRIS[4] setup at TU-Delft, using a Magna-IR spectrometer 550 (Nicolet) under conditions replicating those used for the TPSR experiments.

Results and Discussion

Steady-state reactivity data showed that COS and CS_2 are selectively oxidized to CO and SO_2 over the sulfur tolerant supported vanadia catalysts between 290-330 ^oC and 230-270 ^oC, respectively. CO selectivities as high as 98% and 90% were achieved for COS and CS_2 oxidation, respectively. The major byproduct from CS_2 oxidation is COS, which can be further selectively converted to CO via the ODS of COS. For the selective oxidation of CH_3SH to H_2CO and SO_2 over a series of redox supported metal oxide catalysts (supported vanadia, molybdate, tungstates and niobates) also did not exhibit deactivation and were sulfur tolerant The most selective catalysts for the ODS of COS between 350-400 ^oC were vanadia supported on ZrO_2, TiO_2 and SiO_2 (in the 84-89% range at high conversions). Furthermore, supported vanadia catalysts on various metal oxide supports (CeO_2, ZrO_2, Al_2O3, SiO_2, Nb_2O_5) were found to exhibit high catalytic activity/selectivity for the ODS of thiophene to maleic anhydride.

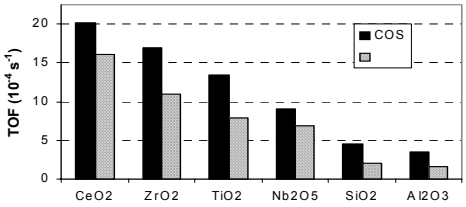

Figure 1. Variation of the TOF with the oxide support for COS and CS_2 oxidation at 330°C and 260°C, respectively, over supported vanadia catalysts with monolayer coverage.

Raman spectroscopy revealed that the supported metal oxide phases were 100% dispersed on the oxide substrate. Thus, the exclusive presence of surface metal oxide species allowed the determination of the number of active sites in the catalyst samples since dispersion was 100 %. As shown in **Figure 1** for monolayer surface vanadia coverage, where the oxide support cations are essentially not exposed to the reactant gases and are covered by the vanadia overlayer, the turnover frequencies (TOF: Activity per surface metal atom based on the yield of CO) for COS and CS_2 oxidation varied about one order of magnitude with the specific oxide support (CeO_2 > ZrO_2 > TiO_2 > Nb_2O_5 > Al_2O_3 ~ SiO_2). A similar phenomenon was observed for TOFs (based on the yield of H_2CO) during CH_3SH oxidation over supported vanadia catalysts at 350 ^oC. The TOFs varied within one order of magnitude (TiO_2 > ZrO_2 ~ Nb_2O_5 > Al_2O_3~SiO_2). These trends are inversely correlated with the electronegativity of the support cation in the bridging V-O-Support bond and suggests the bridging V-O-Support bond being the active site for these reactions since Raman revealed that the terminal V=O bonds were essentially the same in these supported vanadia catalysts[5]. Furthermore, all three reactions exhibited a zero-order dependence on the oxygen partial pressure (0.5-20%) and a first-order dependence on the COS/CS_2 /CH_3SH partial pressures (<1%, due to safety concerns), which suggest that the surface vanadia species is essentially fully oxidized under the investigated reaction conditions.

The desorption spectra of CO and SO_2 are shown in **Figure 2** from the 5% V_2O_5/TiO_2 catalyst following COS adsorption at 100 ^oC. The simultaneous desorption of CO and SO_2 suggests that the

oxidation of COS proceeds via the rate-determining step involving cleavage of the C-S bond.

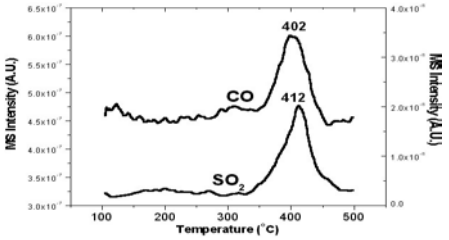

Figure 2. TPSR-MS profiles after *COS* adsorbed at 100 °C on the 5% V_2O_5/TiO_2 catalyst, under 5% O_2/He flow.

The slight delay in the production of SO_2 is consistent with this conclusion since the remaining S(ads) requires the addition of two oxygen atoms. The above suggests the following mechanism for COS oxidation to CO and SO_2 over the 5 % V_2O_5/TiO_2 catalyst.

COS ↔ COS(ads) [1]
COS(ads → CO + S(ads) [2] rds
S(ads) + O(ads) → SO(ads) [3]
SO(ads) + O(ads) → SO_2 [4]

Similarly, the TPSR profiles revealed the reaction mechanisms for the oxidesulfurization of CS_2,CH3SH and thiophene over the 5% V_2O_5/TiO_2 catalyst, as the following given in reaction steps [1]-[16].

CS_2 + O(ads) ↔ CS_2O(ads) [5]
COS_2(ads) → COS + S(ads) [6] rds
S(ads) + O(ads) → SO(ads) [7]
SO(ads) + O(ads) → SO_2 [8]

CH_3SH + O(ads) ↔ CH_3S(ads) + OH(ads) [9]
CH_3S(ads) + O(ads) → CH_3SO(ads) [10]
CH_3SO(ads) → CH_3O(ads) + S(ads) [11]
CH_3O(ads) → H_2CO + H(ads) [12] rds
H(ads) + OH(ads) ↔ H_2O [13]
S(ads) + O(ads) → SO(ads) [14]
SO(ads) + O(ads) → SO_2 [15]

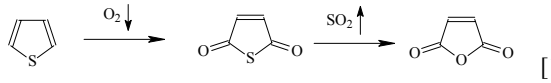

[16]

FT-IR studies were conducted to confirm these reaction mechanisms. And the ODS of thiophene is given as an example. *In situ* FT-IR spectroscopy and steady-state reactivity studies have revealed that for the selective oxidation reactions of thiophene to maleic anhydride over various supported vanadia catalysts proceed via thiomaleic anhydride. *In situ* FT-IR results shown in **Figure 3** indicate that thiomaleic anhydride begins to form even at low temperatures near 100 °C over supported vanadia on titania catalysts. The darkened region indicates the typical IR band regions associated with surface adsorbed anhydride species (C=O vibrations, 1770~1860 cm^{-1}) that appear at relatively low temperatures, while the shifting of these peaks in this region to higher wave numbers with increases in temperature show the transitioning of thiomaleic anhydride to maleic anhydride. These results are consistent with the Temperature Programmed Surface Reaction Mass Spectroscopy (TPSR-MS) results shown in **Figure 4**. In addition, TPSR experiments revealed that the ODS of thiophene over supported vanadia on titania catalyst followed a Langmuir-Hinshelwood reaction path where gas-phase O_2 is involved in the formation of the reaction products. This was in contrast to the ODS reactions of the more simple organosulfur compounds (COS, CS_2, CH_3SH), which exhibited Mars van Krevelen type behavior. Currently we are investigating the ODS of the sterically hindered 2,5-dimethyl thiophene (2,5-DMT) to maleic anhydride. Preliminary results indicate that during the ODS of 2,5-DMT, the two sterically hindering methyl groups are removed in the initial steps of the reaction to form thiophene and subsequently the ODS reaction proceeds via the thiophene ODS reaction pathway.

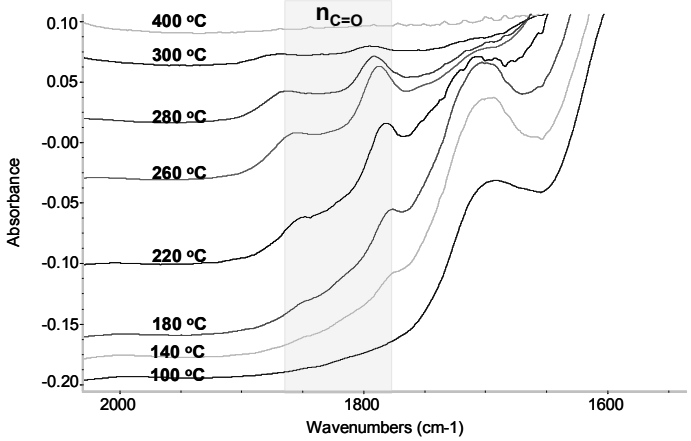

Figure 3. *In situ* FT-IR spectra of thiophene ODS at various temperatures over the 5% V_2O_5/TiO_2 catalyst.

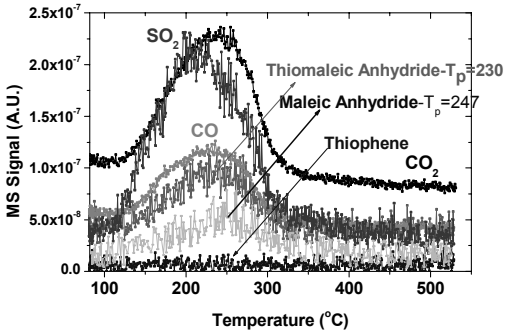

Figure 4. TPSR-MS profiles after thiophene adsorbed at 75 °C on the 5% V_2O_5/TiO_2 catalyst, under 5% O_2/He flow.

Acknowledgement

The authors gratefully acknowledge the National Science Foundation, Grant NSF-CTS-9901643, for financial support of this research, and professors Guido Mul and Jacob A. Moulijn of Delft University of Technology, for their assistance and support.

References

1. EPA-Gasoline, RIA (EPA420-R-99-023), December 1999. EPA-Diesel, RIA (EPA 420-R000-026), December 2000.
2. Deo, G., Wachs, I. E. J. Catal. 146 (1994) 323-334.
3. Wachs, I. E., Deo, G., Juskelis, M. V., Weckhuysen, B. M. in: Froment, G. F., Waugh (Eds.), K. C., Dynamics of Surfaces and Reaction Kinetics in Heterogeneous Catalysis, Elsevier, Amsterdam, 1997, pp. 305-314.
4. Elst, L.P.A.F., Eijsbouts, S., van Langeveld, A. D. Moulijn, J.A., J. Catal. 196 (2000) 95-103.
5. Harcastle, F. D. and Wachs, I. E., J. Phys. Chem. **95** (1991) 5031-5041.

PROCESS FOR THE REMOVAL OF THIOLS FROM A HYDROCARBON STREAM BY A HETEROGENEOUS REACTION WITH A METAL OXIDE

James P. Nehlsen, Jay B. Benziger, and Ioannis G. Kevrekidis

Department of Chemical Engineering
Princeton University, Princeton, NJ 08544

Introduction

The removal of sulfur from gasoline fractions is necessary to prevent the poisoning of Pt reforming catalysts as well as reducing the emission of SO_2 with the combustion products from engines. The process we describe here is a simple, low temperature method for the removal of thiols from a hydrocarbon stream. Thiols are common in hydrotreated gasoline, resulting from the reaction of olefins with H_2S present in the HDS reactor.

In this process, thiols are converted directly to insoluble metal thiolates by a heterogeneous reaction with certain metal oxides or hydroxides. The thiolates are then mechanically filtered from the hydrocarbon stream. The metal and the original thiol can then be recovered in a liquid-liquid extraction step. This process could complement conventional HDS by reducing the sulfur load on an HDS reactor while recovering the thiols for other uses, or to trim refined products that do not meet low-sulfur specifications.

The process is based on thiolate chemistry in which thiols react with metal ions to form metal thiolates. Most work in this area focuses on the reaction of thiols with aqueous solutions of heavy metal salts or with surface reactions on metals and metal oxides. The reaction system applied here is distinct from these works because the reaction removes ions from the surface of the oxide, allowing a dense oxide particle to be completely consumed. An example reaction with PbO is

$$PbO + 2\ RSH \rightarrow Pb(SR)_2 + H_2O \qquad (1)$$

The recovery of the metal is achieved by extraction with a dilute acid. The choice of acid depends on the metal salt desired. An example reaction is

$$Pb(SR)_2 + 2\ HNO_3 \rightarrow Pb(NO_3)_2 + 2\ RSH \qquad (2)$$

This simple process[1] uses inexpensive materials and very little energy compared to conventional desulfurization techniques. The process proposed here, shown as Figure 1, is selective for thiols. No reaction is observed between PbO and disulfide, sulfide, or thiophenic species.

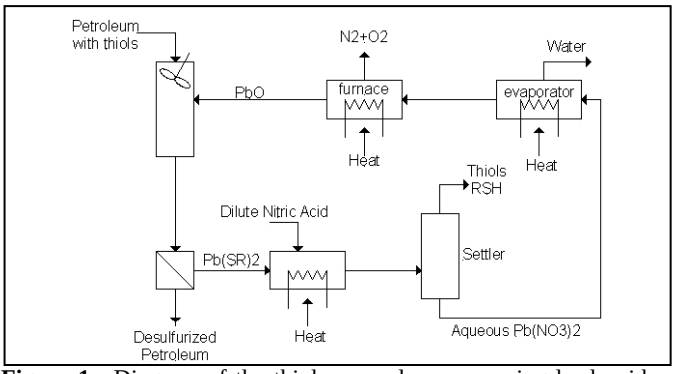

Figure 1. Diagram of the thiol removal process using lead oxides, showing the key operations including reaction, filtration, and extraction.

Experimental

The heterogeneous reaction and the reactive extraction portions of this process were studied. The reaction was carried out in batch mode with various powdered metal oxides including BaO, Bi_2O_3, CaO, CdO, CoO, Cr_2O_3, CuO, HgO, MgO, MoO_3, metallic Pb wire, PbO, Pb_3O_4, PbO_2, $Pb(OH)_2$, $Pb(NO_3)_2$, PbS, SbO, SnO, and $Sr(OH)_2$.

The primary oxide studied was PbO. Powdered PbO (massicot form, Aldrich) of mass between 0.02 and 0.2 g was added to a glass vial. An *n*-alkanethiol, either 1-hexanethiol, 1-octanethiol, or 1-dodecanethiol (Aldrich), was added to the vial. An inert hydrocarbon, usually cyclohexane or toluene, was sometimes added to prevent the reaction product from becoming a paste. The solid product could be suspended in the hydrocarbon by stirring to facilitate filtration. Some samples were stirred using a magnetic stir bar, and some were heated to about 70°C on a hotplate and cooled before filtering.

The reaction product, a wet powder, was gravity filtered (Whatman #50 hardened circles), then rinsed several times with water, acetone, cyclohexane, and then pentane, and dried at room temperature.

Other metal oxides and hydroxides were tested by adding 1-octanethiol to a small amount (approx. 0.15-0.5 g) of the oxide or hydroxide in a glass vial. The formation of thiolates was evidenced by a dramatic increase in apparent solid volume and in some cases, a color change. Reacted mixtures were filtered and dried as above, then weighed to determine conversion. Active oxides were also mixed in the same manner with butyl disulfide (97%, Aldrich), butyl sulfide (96%, Aldrich), tetrahydrothiophene (99%, Aldrich), and thiophene (99+%, Aldrich) to test for reactivity with other sulfur compounds.

The Pb was extracted from the thiolates by liquid-liquid extraction with dilute (0.2-0.3 M) nitric acid. The solid thiolates were added to cyclohexane and the mixture was heated to the melting point of the thiolate, approximately 70ºC. This mixture was added to the nitric acid and agitated by rapid stirring. The hydrocarbon layer was then analyzed for thiol content by gas chromatography (Hewlett Packard HP-1 column, FID). The aqueous layer was evaporated and the Pb was recovered as $Pb(NO_3)_2$ crystals.

Results and Discussion

Reactions. All of the tested oxides and hydroxides of Pb, metallic Pb wire with a surface oxide coating, HgO, $Ba(OH)_2$, and BaO formed stable, insoluble thiolates of the alkanethiols. These oxides did not react with any of the other organo-sulfur compounds tested.

PbO, Pb_3O_4, $Pb(OH)_2$, and PbO_2 reacted quickly yielding an insoluble, yellow thiolate. No other reaction products were detected. Reactions were typically complete in about 1 hour without agitation or heat. The thiolate does not appear to foul the surface of the oxide, allowing the reaction to go to completion without agitation. Yields of $Pb(SC_8H_{17})_2$ were typically 80-90%, including transfer losses. Heating the product above the melting temperature of the thiolate revealed no remaining solid oxide, indicating that some amounts of sub-thiolate, such as $Pb(SC_8H_{17})(OH)$, may have been formed, reducing the yield. Pb^{4+} compounds only reacted with two thiols per Pb, probably resulting in the formation of $PbO(SC_8H_{17})_2$ or $Pb(OH)_2(SC_8H_{17})_2$.

The lead thiolates were solid at room temperature, but became soluble in hydrocarbon solvents at temperatures above about 50°C. In the presence of cyclohexane, a miscible solution of lead dioctylthiolate, $Pb(SC_8H_{17})_2$, was formed at 54-55°C. The melting temperature of dry dialkylthiolates increased with molecular weight and was 70-80°C for the dioctylthiolate. The observed melting point was lower than reported elsewhere,[2] probably due to impurities or incomplete removal of the hydrocarbon solvent. The thiolates were insoluble in cyclohexane, toluene, acetone, and water at room temperature. The thiolate melts were miscible with cyclohexane and toluene, but immiscible with water.

Figure 2 presents a series of photographs demonstrating the reaction of *n*-octanethiol with PbO_2. PbO_2 was used in the photographs for color contrast purposes, since the massicot form of PbO and the thiolate product are both yellow. The reaction is marked by a rapid growth in apparent solids volume as the liquid thiol is converted into solid thiolate. The color change from the black PbO_2 to the yellow thiolate is also evident.

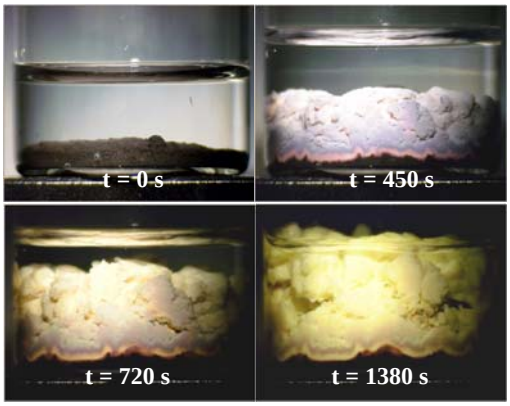

Figure 2. Photographs of the reaction of PbO_2 with *n*-octanethiol. Photographs are chronological, starting from top left, occurring at elapsed times shown. The initial mixture was 0.75 g PbO_2, 4 mL cyclohexane, and 3 mL *n*-octanethiol (added after first picture).

Metallic Pb wire was also active in forming thiolates. The thiol reacted with the natural coating of oxides present on a Pb surface to form an insoluble yellow thiolate. The extent of reaction on a Pb wire was very low when carried out in an inert nitrogen atmosphere. The reaction occurred at the surface of the wire, forming plates of thiolate that were pushed outwards as new thiolate was formed.

An example of this reaction is shown in Figure 3 in which a piece of Pb wire is placed into *n*-octanethiol. The reaction is much slower than the reaction with powdered PbO due to the time required diffusing oxygen to the Pb surface and the lower surface area of the wire compared to the powdered oxides.

Hg(II)O reacted exothermically to generate a white, insoluble thiolate. The yield of $Hg(SC_8H_{17})_2$ was 99%. BaO and $Ba(OH)_2$ also reacted with alkanethiols to generate an insoluble, white thiolate. The reaction was fast and occurred without agitation, but the yield of 54% was lower than for PbO or HgO. The lower yield is again most likely due to the formation of sub-thiolate, $Ba(SC_8H_{17})(OH)$. This reaction is interesting, however, because of the lower environmental and health risks associated with Ba as opposed to Hg and Pb. No other oxides reacted quickly to yield insoluble thiolates.

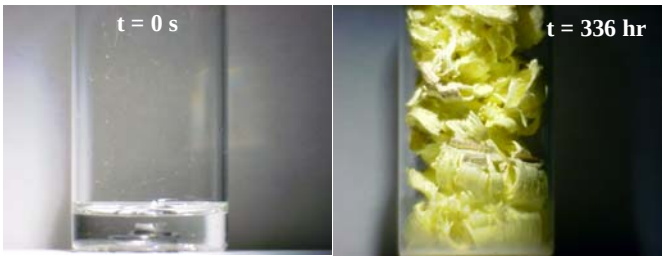

Figure 3. Photographs of the reaction of Pb wire with *n*-octanethiol. Left: Pb wire in cyclohexane before reaction. Right: After reaction with *n*-octanethiol for 14 days. Initial mixture was 2 mL cyclohexane and 4 mL n-octanethiol (added after picture on left).

The thermodynamic limit for the removal of thiols by this reaction can be determined from the heat of reaction. The equilibrium constant K is given by

$$-\Delta G_{rxn} = RT \ln(K) \quad (2)$$

where, from equation 1,

$$K = (a_{Pb(SR)2}\, a_{H2O}) / (a^2_{RSH}\, a_{PbO}) \quad (3)$$

The solids PbO and $Pb(SR)_2$ both have unit activity. Assuming an ideal solution, the activity of the water and thiol are equal to their mole fraction in the hydrocarbon solvent. The value of ΔG_{rxn} estimated previously[3] is -121 kJ/mol. The equilibrium constant for this reaction, assuming unit water activity (present as a second liquid phase), is approximately 1.9×10^{21}, permitting the removal of thiol sulfur to 23 ppt. The thermodynamic limit of this reaction permits desulfurization to extremely low levels, although kinetic and mass transfer limitations may prevent this limit from being practically achieved.

Metal Recovery. Reactive liquid-liquid extraction with a dilute acid can be performed by heating the thiolates to melting, either with or without the addition of a hydrocarbon solvent. Agitating the thiolates with an acid solution (0.1-0.3 M typically) allows the reaction to reach completion in about 2 hours. Improved contacting between the liquid phases and using more concentrated acids can reduce the time required. The result is an aqueous phase containing the metal salt and a hydrocarbon phase containing the original thiols and any added solvent. A reusable oxide can be obtained by roasting most metal salts in air.

Using this technique, thiolates made from reaction with PbO were extracted with 0.21M HNO_3. The yellow diluted melt of $Pb(SC_8H_{17})_2$ changed to colorless as the reaction proceeded. The recovery of Pb as $Pb(NO_3)_2$ was 102%, or essentially all of the lead within experimental error. A second trial with thiolates made from PbO_2 and 0.31M HNO_3 yielded a 95% Pb recovery. Thiol recoveries in the hydrocarbon phase, as measured by GC, for these two runs were 78% and 90%, respectively.

Conclusions

The heterogeneous reaction of thiols with oxides and hydroxides of Pb, Hg(II), and Ba can be used to remove and recover thiols from a petroleum stream. Experimental results suggest that a simple process consisting of reaction, filtration, and extraction is all that is required to separate and recover the thiols. The metal oxide can be recovered by additional evaporation and roasting steps. Most of the required unit operations have low energy requirements and low reagent material costs.

This process can reduce the sulfur content of fuels for environmental benefits. It could also reduce the load on a conventional HDS unit when sour feedstocks are used by removing the thiols before the feed is introduced to the HDS unit, saving costs in hydrogen and catalyst life. The process also recovers thiols which are a valuable feedstock to the food and fragrance industries[4] as well as the pharmaceutical industry.

Acknowledgement. The authors thank Dr. Steffen Berg for his assistance in this work. This work was partially supported by the AFOSR (Dynamics & Control, Dr. B. King).

References

(1) Nehlsen, J. P.; Benziger, J. B. and Kevrekidis, I. G. *Energy Fuels* **2004**, ASAP Article.
(2) Tiers, G. V. D. and Brostrom, M. L. *J. Appl. Crystallogr.* **2000**, 33 (3, Pt. 2), 915-920.
(3) Nehlsen, J. P.; Benziger, J. B. and Kevrekidis, I. G. *Ind. Eng. Chem. Res.* **2003**, 42 (26), 6919-6923.
(4) Naim, M.; Zuker, I.; Zehavi, U. and Rouseff, R. L. *J. Agric. Food Chem.* **1993**, 41 (9), 1359-1361.

PROMOTING EFFECT OF WATER ON COAL HYDROGENATION

Yoshiharu Yoneyama, Aya Kanao, Tatsuya Yamamoto, Yi Zhang , Noritatsu Tsubaki

Faculty of Engineering, Toyama University, Toyama, Japan 930-8555

Introduction

Low-cost hydrogen sources are required for converting coals to liquid or gaseous fuels, and chemicals. Water is a promising candidate among hydrogen sources. Many researchers used water as hydrogen source through water-gas shift reaction or as an effective pretreatment method for hydrogenation and pyrolysis of coals.[1] Water at supercritical state or steam has been used as extraction or pretreatment vehicles of coals as well.[2-5] On the other hand in the catalytic hydrogenation of coals, it is well known that water or steam deactivates hydrotreating catalyst.[6,7] Even if it seems that water exhibited negative effect on coal hydrogenation with or without catalysts, addition of water increased the CO_2 formation and the contents of phenolic compounds in the obtained oils.[3-5] These results strongly suggest that water interacts with coals under hydrogenation conditions.

In this study to clarify the role of water in the coal hydrogenation, Wandoan and Argonne premium coal were non-catalytically hydrogenated at 673 K with water addition. For comparison, experiments under nitrogen, and with addition n-undecane (n-C_{11}) were also carried out. Aliphatic C-O linkages are important linkages between aromatic moieties of coal structures. In addition, dibenzyl ether was used as a coal-model compound containing ether linkage, and was pyrolized with and without water addition in the presence of pyrite in order to determine the cleavage of ether linkages of coal structures under the conditions we used.

Experimental

Basic data of coals are listed in Table 1. The coals were dried at 333 K under vacuum for over 48 h to constant weight before use. Undecane (n-C_{11}) was used without further purification. Super high purity of hydrogen (over 99.999 %) and nitrogen (over 99.999 %) were used to minimize oxidization during the reaction.

Hydrogenation was carried out using coal of 1.5 g with or without adding water of 0.8 g, or adding n-C_{11} of 0.8 g in a 25 ml horizontal microautoclave reactor at 673 K for 60 min under an initial hydrogen pressure of 6.9 MPa. For comparison, similar experiment under nitrogen was also conducted. The gaseous product was collected for analysis by gas chromatograph with thermal conductivity detector. The recovered products were placed into a thimble filter and separated to tetrahydrofuran (THF) soluble product by Soxhlet extraction with THF, followed by rotary-evaporation and dried in a vacuum oven at 333 K. The conversion was defined as the sum of the yields of gases and THF soluble products.

Table 1. Elemental Analysis of Coals (%,daf)

Coal	C	H	N	O + S [a]	Pyrite [b]
Beulah-Zap	72.9	4.8	1.1	21.2	0.2
Wandoan	73.4	6.2	1.1	19.4	-
Wyodak	75.0	5.4	1.1	18.5	0.1
Illinois #6	77.7	5.0	1.4	16.0	5.0
Blind Canyon	80.7	5.8	1.6	12.0	0.4
Lewiston-Stockton	82.6	5.3	2.6	9.6	0.3
Pittsburgh #8	83.2	5.3	1.6	9.8	2.5
Upper Freeport	85.5	4.7	1.6	8.3	3.5

[a] By difference [b]wt%, dry base

Hydrogenation of dibenzyl ether (DE) was carried out using DE of 0.159g and synthetic pyrite of 0.005g with and without adding water of 0.9g in a 25 ml horizontal microautoclave reactor at 350 ºC for 30 min. The products were recovered by washing with acetone. When a residue was present in the reactor, the reactor was washed by ethyl acetate one more to recover the residue completely. After washing the reactor with ethyl acetate, there existed no residual materials in the reactor. After sampling the acetone solution for gc analysis, both the acetone and the ethyl acetate solutions were combined. The combined solution was filtered with a membrane filter, and then the solution was evaporated to weigh the residue.

Results and Discussion

Coal Hydrogenation Figure 1 shows the relationship between the carbon content of original coals and the coal conversions using hydrogen or nitrogen, where water or n-C_{11} was added. In the combination of nitrogen and water, with the increasing the carbon content of original coals, the conversions of coals were enhanced, except for Upprt Freeport coal. Addition of n-C_{11} did not increase the coal conversion, however addition of water enhanced. On the other hand, in the combination of hydrogen and water there existed no clear relationship between the carbon content of original coals and the coal conversions. Addition of water had promoting effect on coal conversions under hydrogen also. It was found that the conversions of both Illinois #6 and Pittsburgh #8 coals were irregularly large. The conversion of Illinois #6 coal increased about 20 % with added water, even though added water in nitrogen did not promote the coal conversion significantly. There existed synergistic effect between hydrogen and water on conversion of Illinois #6 and Pittsburgh #8 coals. Since Illinois #6 and Pittsburgh #8 coals contain more pyrite

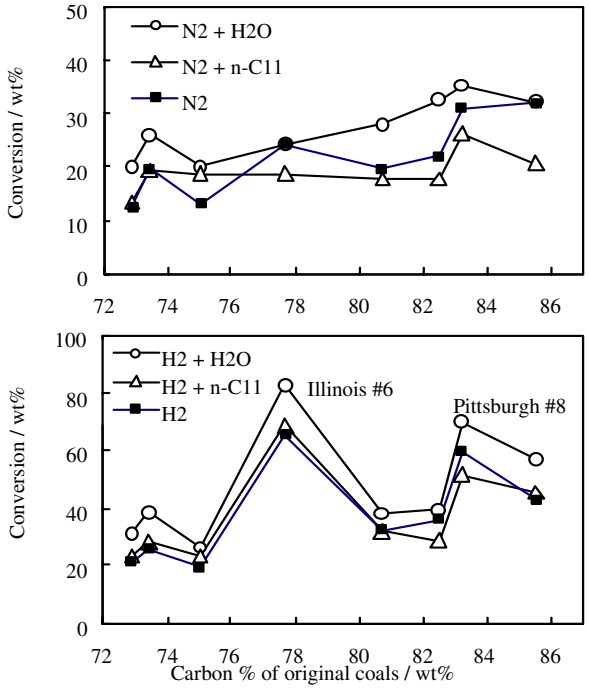

Figure 1. Relationship between carbon % of original coals and the conversion under nitrogen or hydrogen with added water or undecane (n-C11). Temperature, 673 K; time, 60 min.

than other coals as compared in Table 1, it is considered that pyrite plays an important role in the promoting effect of water on coal conversions using hydrogen. It is well known that pyrite in coals acts as catalyst in coal hydrogenation.[7]

Figure 2 exhibits the relationship between the pyrite contents of original coals and the conversions of coals in hydrogen. The conversions of coals containing larger amounts of pyrite were larger except for Upper Freeport coal, while the conversion of coals containing less amount of pyrite were lower. Because Illinois #6 and Pittsburgh #8 coals contain large amount of pyrite, synergistic effect between hydrogen and water is considered to be large. It is referred that pyrite plays an important role in the synergistic effect between water and hydrogen on coal conversion.

Hydrogenation of DE In order to determine the effectiveness of water on the cleavage of ether linkage in coal, DE was hydrogenated with and without water addition in the presence of pyrite. Table 2 summarizes the conversions and the yields of the products of hydrogenation of DE. Since some products did not eluted from the column, both conversions calculated by the sum of the products, and by the unreacted DE are shown. Without pyrite addition, both conversions were close. Water addition was found to inhibit the cleavage of the aliphatic ether linkage. The conversion decreased from 52.8 to 13.8 % with water addition. The yields of benzaldehyde and benzyl alcohol were larger for water addition. On the other hand, without pyrite addition both conversions were close, but with pyrite they were different each other. The residual products, which did not elute from the gc column, formed without water addition in the presence of pyrite. Thus the conversion from the products was lower than that from unreacted DE. The reactions formed the residual products is thought as the retrogressive reactions in the coal hydrogenation. These results suggest that water addition prevents retrogressive reaction occurred in coal hydrogenation using pyrite as a catalyst.

In the hydrogenation with water addition, hydrolysis, pyrolysis and hydrogenation occur. In order to estimate the contribution of hydrolysis and pyrolysis in this hydrogenation, DE was pyrolized in N_2. The conversion and product yields are summarized in Table 3. Under N_2 the residual products were formed in all reactions, however water addition decreased the yield of the residual product. Without pyrite addition, water addition increased the conversion of DE, and promoted hydrolysis reaction. Though pyrite is a hydrogenation catalyst, the conversion of DE increased with pyrite in both reactions with and without water addition. Water addition increased both conversions calculated by the products and by the unreacted DE. Because the yield of benzyl alcohol was increased with water addition, the combination of pyrite and water addition promoted the hydrolysis of DE significantly. It was found that water itself has an inhibitive effect on the formation of the residual product.

These results indicate that the synergistic effect between pyrite and water on coal hydrogenation should be derived from the suppression of the retrogressive reaction occurring in the coal hydrogenations and promoting the cleavage of C-O linkages in coal structures.

References

(1) Ross D. S., *Coal Science*, **3**, 301.
(2) Graff R. A. and Brandes S. D., *Energy Fuels*, 1987, **1**, 84
(3) Desphpande, G. V.; Holder, G. D.; Bishop, A. A.; Gopal, J.; Wender, I. *Fuel* **1984**, *63*, 956.
(4) Kershaw, J. R. *Fuel Process. Technol.* **1986**, *13*, 111.
(5) Artok, L.; Schobert, H. H.; Nomura, M.; Erbatur, O.; Kidena, K. *Energy Fuels* **1998**, *12*, 1200.
(6) Kamiya, Y.; Nobusawa, T.; Futamura S. *Fuel Process. Technol.* **1988**, *18*, 1.
(7) Ruether, J. A.; Mima, J. A.; Kornosky, R. M.; Ha, B. C. *Energy Fuels* **1987**, *1*, 198.
(8) Trewhella, M. Jr.; Grint, A. *Fuel* **1987**, *66*, 1315

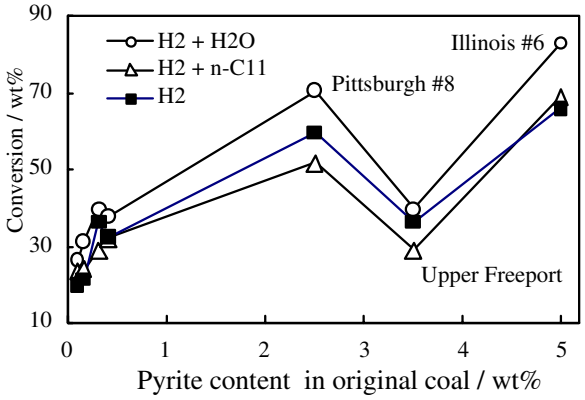

Figure 2. Relationship between pyrite content in original coal and the conversion.

Table 2 Effect of Water Addition on DE hydrogenation

Catalyst	none	none	FeS_2	FeS_2
water addition	no	yes	no	yes
Conversion[1]	51.9	13.8	96.2	68.2
Conversion[2]	52.8	13.8	46.0	68.9
Product (mol%)				
benzene	4.9	0	8.0	5.4
toluene	80.0	12.2	61.3	65.7
benzaldehyde	7.2	8.9	10.4	21.3
benzyl alcohol	4.9	6.5	5.8	34.1
bibenzyl	4.2	0	3.3	5.7
residue[3]	0	0	29.5	0

[1] calculated by the unreacted DE; [2] calculated by the products
[3] polymeric products, wt%; 673K, 6.9MPa H_2, 30 min

Table 3 Effect of Water Addition on DE Pyrolysis

Catalyst	none	none	FeS_2	FeS_2
water addition	no	yes	no	yes
Conversion[1]	42.3	48.2	75.7	81.5
Conversion[2]	6.3	5	25.9	41.1
Product (mol%)				
benzene	0	0	0	0
toluene	3.8	1.7	15.1	9.3
benzaldehyde	6.7	4.2	25.9	10.7
benzyl alcohol	2.1	4.1	7.7	59.5
bibenzyl	0.0	0	1.5	1.3
residue[3]	64.9	60.5	62.9	48.4

[1] calculated by the unreacted DE; [2] calculated by the products;
[3] polymeric products, wt%; 673K, 6.9MPa N_2, 30 min

HYDROTREATING OF DIESEL FUEL OVER EX SITU PRESULFIDED NiW AND NiMoW CATALYSTS

Guoliang Li, Changlong Yin, Huiji Zhao, Chenguang Liu and Yangchu Li

Key Laboratory of Catalysis, CNPC,
State Key Laboratory of Heavy Oil Processing
University of Petroleum, Dongying, Shandong 257061, China

Introduction

The sulfided catalysts for the hydrotreating of petroleum feedstocks have the ability to catalyse hydrogenation and hydrogenolysis reactions in the presence of strong inhibitors such as H_2S and NH_3. The conventional method for presulfurizing hydrogenation catalysts is an in-situ (inside reactor) method of presulfurization, using hydrogen sulfide or a straight fraction oil containing carbon disulfide and dimethyl disulfide to convert the hydrogenation-active metal into sulfurization state. The in-situ method of presulfurization has the disadvantages of higher production costs, prolonged time for presulfurization and flammable and poisonous sulfides being used, thus causing environmental pollution. A process which allows the transformation of an oxide into a stable sulfided intermediate has been developed (1-3) and several related technologies has been patented. These processes consist in wetting ex situ the catalysts with elemental sulfur and/or a hydrocarbon solution of a high molecular weight alkylpolysulfide. The ex situ presulfided catalysts only need to introduce hydrogen or hydrogen and oils simultaneously to start up the presulfurization, and subsequently raise the temperature, thus complete the sulfurization activation process. Therefore, ex-situ (outside reactor) method of presulfurization has advantages of simple operation, high efficiency and non-pollution. In this work, two commercial hydrogenation catalysts NiW/Al_2O_3 and $NiMoW/Al_2O_3$ were presulfided with ex-situ and in-situ method of presulfurization, respectively, and the activities of the catalysts were investigated by the hydrotreating of diesel fuel.

Experimental

Catalyst preparation. The catalysts used in this work are two industrial hydrogenation catalysts: NiW/Al_2O_3 and $NiMoW/Al_2O_3$, the characteristics of which are listed in Table 1. The component of vulcanization agent is: elemental sulfur (60wt%), dimethylsulfoxide (20wt%), tetraethylthiuram disulfide (TETD, 20wt%). The solvent of the vulcanization agent is a mixture of solvent oil and bean oil with weight ratio of 2. The amount of sulfide deposited onto the catalysts was calculated on the basis of the transformation of the oxidic metals phases into sulfided metals, which can be showed as follows:

$$4NiO + 3H_2S + H_2 \longrightarrow NiS + Ni_3S_2 + 4H_2O$$

$$WO_3 + 2H_2S + H_2 \longrightarrow WS_2 + 3H_2O$$

$$MoO_3 + 2H_2S + H_2 \longrightarrow MoS_2 + 3H_2O$$

Catalyst activity. Catalytic activity measurements were carried out in a continuous high pressure reactor unit of 24 mm I.D., 100cm in length. 100 ml of the catalyst extrudates were loaded in the reactor. In situ presulfiding is carried out before the reaction at 100ºC, and 150 ºC for 5 hour, 250 ºC for 5 hours, 340 ºC for 5 hours with a liquid stream containing 1w% CS_2 in straight-run kerosene. The H_2/feed ratio is 350:1 for NiW/Al_2O_3 and 500:1 for $NiMoW/Al_2O_3$ and the LHSV for both catalysts is $2.0h^{-1}$. The total pressure for NiW/Al_2O_3 is 6.4MPa and 4.0MPa for $NiMoW/Al_2O_3$ catalyst. The FCC diesel feed is then admitted at the same conditions as that for presulfiding. The reaction product was cooled and separated into gaseous and liquid products in a high-pressure separator. For ex situ presulfided catalyst presulfiding is performed by heating the catalyst under hydrogen from room temperature up to 220 ºC (heating rate 40 ºC/h), at 220 ºC for 1 hour, and at 340 ºC for 2 hours (heating rate 38 ºC/h). The diesel fuel is then fed at test conditions.

Table 1. Characteristics of the Catalysts

Catalysts	NiW/Al_2O_3	$NiMoW/Al_2O_3$
Pore volume, cm^3/ml	0.25	0.34
BET area, m^2/g	152.0	154.1
Component, wt%		
WO_3	26.0	19.2
MoO_3		9.5
NiO	2.6	2.5

Results and Discussion

Temperature rising during the presulfurization process is a troublesome problem. The heater temperature and sulfurization temperature in catalyst's bed during the process were determined and the curves for the ex situ presulfided NiW/Al_2O_3 and $NiMoW/Al_2O_3$ catalysts were illustrated in Figure 1 and Figure 2, respectively. The temperature curves for the in situ presulfided $NiMoW/Al_2O_3$ catalyst were shown in Figure 3. The experimental results show that no obvious temperature rising appears during the treatment of the ex situ presulfided NiW/Al_2O_3 and $NiMoW/Al_2O_3$ catalysts, while the temperature in catalyst's bed is fluctuant acutely during the in situ presulfurization process. Moreover, the time for the treatment of the ex situ presulfided catalyst is shortened to about 11 hours, much less than that for the in situ presulfurization, the latter is about 24 hours.

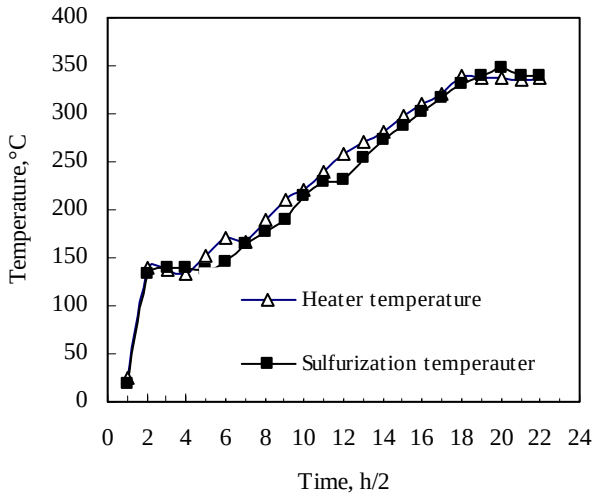

Figure 1. The temperature curve for the ex situ presulfided NiW/Al_2O_3 catalyst.

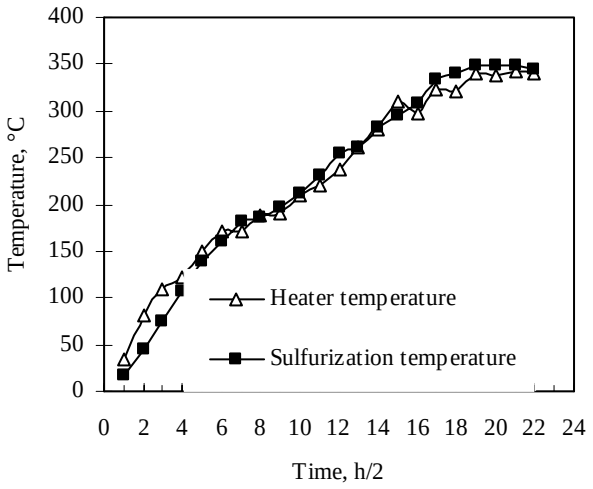

Figure 2. The temperature curve for the ex situ presulfided $NiMoW/Al_2O_3$ catalyst.

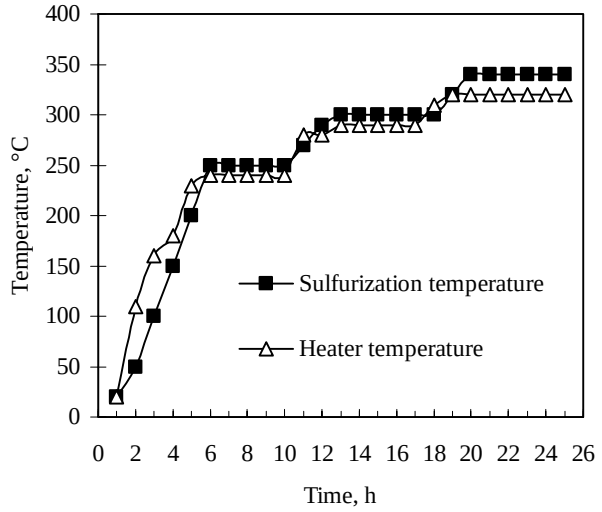

Figure 3. The temperature curve for the in situ presulfided $NiMoW/Al_2O_3$ catalyst.

The activities of the catalysts with different sulfurization method (i.e. in situ and ex situ) were studied according to the characteristics of the hydrotreated products obtained from the hydrotreating of FCC diesel over in situ presulfided and ex situ presulfided catalysts at the same reaction conditions. The characteristics of the hydrotreated products over NiW/Al_2O_3 catalyst and $NiMoW/Al_2O_3$ catalyst were listed in Table 2 and Table 3, respectively. It can be found from the results that the ex situ presulfided catalyst shows the same or even better HDN and HDS activities as/ than in situ presulfided catalyst, and the distillation range of the hydrotreated products over ex situ presulfided catalyst is similar to that over in situ presulfided catalyst. The enhancement of the cetane number of the hydrotreated products indicates that the ex situ sulfurization technology in this work is effective and the activity of the ex situ presufided catalyst is consistent with or even higher than that of conventional in situ presulfided catalyst.

Table 2. The Characteristics of the Hydrotreated Products over NiW/Al_2O_3 Catalyst

	Feed	In-situ	Ex-situ
Sulfur, μg/g	10600.0	3048.0	2399.0
Nitrogen, μg/g	540.0	233.0	186.0
Cetane Number	47.6	50.8	50.4
HDS, %	-	71.3	77.4
HDN, %	-	56.8	65.6
Distillation range, °C			
IBP	205	89	104
10%	244	244	237
30%	281	277	278
50%	307	303	301
70%	329	325	323
90%	360	355	355
95%	>360	>360	>360

Table 3. The Characteristics of the Hydrotreated Products over $NiMoW/Al_2O_3$ Catalyst

	Feed	In-situ	Ex-situ
Sulfur, μg/g	10600.0	2192.0	2019.0
Nitrogen, μg/g	540.0	286.0	286.0
Cetane Number	47.6	50.5	50.5
HDS, %	-	79.3	80.9
HDN, %	-	47.0	47.0
Distillation range, °C			
IBP	205	50	50
10%	244	245	247
30%	281	259	260
50%	307	299	298
70%	329	324	327
90%	360	338	355
95%	>360	359	360

Conclusions

The experimental results reveal that the vulcanization agent with given component in this work can effectively sulfurize NiW/Al_2O_3 and $NiMoW/Al_2O_3$, and it is shown that no obvious temperature rising appears during the treatment of the ex situ presulfided NiW/Al_2O_3 and $NiMoW/Al_2O_3$ catalysts, while the temperature in catalyst's bed is fluctuant acutely during the in situ presulfurization. The time for the treatment of the ex situ presulfided catalyst is half that for the in situ presulfurization, which means energy consuming can be reduced greatly during the sulfurization process. The results of the evaluation for the catalyst's activity disclose that the HDN and HDS activities of the ex situ presulfided catalyst are the same as or even better than in situ presulfided catalyst. The enhancement of the cetane number of the hydrotreated products indicates that the ex situ sulfurization technology in this work is effective and the activity of the ex situ presufided catalyst is consistent with or even higher than that of conventional in situ presulfided catalyst.

Acknowledgement. Financial support from PetroChina Corporation Limited is greatly appreciated.

References

(1) Labruyere F.; Dufresne P.; Lacroix M.; Breysse M. *Catal. Today*, **1998**, *43*, 111.
(2) Murff S. R.; Carliste E.A.; dufresne P.; Rabehasaina H. Prepr. Pap. - *Am. Chem. Soc., Div. Petrol. Chem.*, **1993**, *38*(1), 81.
(3) Neuman D. J.; Klavey H.; Sempey G. K. *NPRA Paper*, **1998,** AM-98-59, San Francisco, California.

POLYBENZIMIDAZOLE BASED SEGMENTED BLOCK COPOLYMERS FOR HIGH TEMPERATURE FUEL CELL MEMBRANES

*Eugene Scanlon and Brian C. Benicewicz**

NYS Center for Polymer Synthesis
Department of Chemistry and Chemical Biology
Rensselaer Polytechnic Institute
Troy, NY 12180
*benice@rpi.edu

Introduction

Polymer electrolyte membrane fuel cells (PEMFC) are the ongoing focus of current research for potential applications ranging from mobile devices such as cell phones and laptop computers utilizing micro fuel cells to automotive applications and stationary devices generating power on the kW scale.

PEMFC's employing polybenzimidazole (PBI) membranes with a phosphoric acid electrolyte have been recognized for their outstanding high temperature performance (>160°C).[1,2] High temperature operation provides favorable electrode kinetics and an increased tolerance to fuel impurities such as carbon monoxide which can poison the Pt catalyst. Conventional perfluorinated ionomers such as Nafion® are limited to temperatures of 100°C or less due their reliance on water to conduct protons. This reliance on water imposes additional hardware requirements to maintain high membrane hydration levels. In general, hydrated perfluorinated ionomers exhibit low tolerance to CO due to their low operating temperatures.

Recently, we have reported the synthesis of different isomers of PBI and their copolymers. A novel technique for film fabrication, called the PPA process, was developed which greatly simplified the PEM preparation and produced membranes with much improved properties as compared to membranes produced from imbibing processes.[3]

In this contribution, we report the synthesis of segmented block copolymers based on PBI and its isomers using the PPA process. The resulting membranes have excellent thermal resistance, high acid content, high conductivity and good mechanical properties. These membranes are promising candidates for high temperature fuel cell applications in mobile and stationary devices.

Experimental

Oligomer Block Synthesis. 4,4'-Sulfonylbis[1,2-benzenediamine] (TAS) and isophthalic acid (IA) were added to a resin flask in equimolar amounts. To this flask polyphosphoric acid (PPA) was added until the weight percent of monomer was between 2 and 7%. In a second resin flask 3,3',4,4'-tetraaminobiphenyl (TAB) and terephthalic acid (TA) were added in equimolar amounts to which PPA was also added until the weight percent of monomer was between 2 and 7%. These two flasks were submerged in an oil bath and outfitted with a nitrogen inlet and outlet and an overhead mechanical stirrer. They were then polymerized under appropriate conditions to control the degree of polymerization of each block (**Scheme 1**).

Segmented Copolymer Synthesis and Membrane Fabrication. After prepolymerization of the starting blocks, the two reactions were combined in a separate resin flask and heated further to complete the polymerization to high molecular weights. After completion of the polymerization, the solution was cast directly on a glass substrate by use of a casting blade with a gap thickness of between 15 and 25mils. The substrate was allowed to stand in a humidity box with a controlled relative humidity of between 25-65% for three to four days. Absorption of water from the atmosphere within the humidity chamber hydrolyzed the PPA to phosphoric acid (PA) and subsequently induced a sol-gel transition that produced membranes with high acid loading.

Blend and Random Copolymer Synthesis. Blends of the two homopolymers were prepared by fully polymerizing each of the "blocks" prior to mixing. Random copolymers were prepared by charging all four monomers at the beginning of the reaction prior to the polymerization procedure.

Polymer and Membrane Characterization. Acid content was determined using a Metrohm 716 DMS Titrino autotitrator with 0.1M standardized NaOH and reported as the average of three samples. After titration, the samples were washed and dried at vacuum at 100°C to obtain the polymer and water content. The inherent viscosity (I.V.) was measured by dissolving the polymer in 96% sulfuric acid at a concentration of 0.2g/dL and measuring the flow times using an Ubblelohde suspended volume viscometer at 30°C. Conductivity was measured with a four point probe impedance method using a Zahner IM6e electrochemical workstation in the frequency range of 1Hz to 100KHz. The experimental data was fitted to a model of a resistor and capacitor in parallel. The conductivity was measured as a function of temperature through use of a programmable oven. Mechanical properties were measured by cutting ASTM type V specimens and tested using a United Testing tensile tester with a 5lb. load cell. All samples were preloaded to 0.1N and the testing speed was 5mm/min.

Fuel Cell Testing. Cells were built with an active area of 44cm^2 using commercially available electrodes. The catalyst was 30 wt% Pt/C with a 1 mg/cm^2 loading on both anode and cathode. Fuel cell tests were carried out using a test station purchased from Fuel Cell Technologies, Inc.

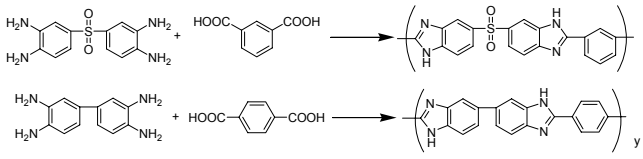

Scheme 1. Synthesis of segmented PBI copolymers using the PPA process.

Results and Discussion.

Previous work in our laboratory had characterized the TAS+IA homopolymer as having high solubility in both PPA as well as PA. The TAB+TA homopolymer was characterized as having lower solubility in both PPA and PA. Films produced from the TAB+TA hompolymer using the PPA process exhibited good mechanical strength. In this work, integration of these characteristics was investigated by preparing and analyzing the properties of the random copolymer, polymer blend and segmented block copolymer containing equimolar amounts of each repeat unit structure.

Table 1 shows the I.V. and titration results comparing a random copolymer, segmented block copolymer and a polymer blend, each containing 50 mole percent of each repeat unit. The I.V.'s listed are for the two separate oligomers or polymers before mixing and the final polymer. For the random copolymer, initial oligomers were not generated. For the homopolymer blend, the two components were fully polymerized and subsequently mixed. The segmented block-copolymer had the highest I.V. and the highest acid content with the lowest polymer content.

Table 1. Initial Polymerization and Titration Results for the Random, Blend and Segmented Block Copolymer Systems

	I.V. (dL/g)			Content (wt%)		
	TAS+IA	TAB+TA	Final	Polymer	Water	Acid
Random	-	-	1.54	17.7	30.4	51.9
Blend	.65	2.24	1.32	5.3	17.2	77.6
Segmented	.49	.24	1.78	3.7	15.7	80.6

Table 2 shows the conductivity and mechanical properties of the three systems. Conductivity measurements were performed twice on each sample. The first heating run showed variable results due to the water contained in each sample and its removal at temperatures above 100˚C. The second heating run was reproducible and is reported in the table. The segmented system had a conductivity of 0.38 S/cm, which is very high compared to the previously reported data for PBI and Nafion®. These high values were due in part to the very high acid content of the membrane. Surprisingly, the segmented membrane also had the highest mechanical properties of the three systems even though the polymer content was the lowest. This combination of properties was attributed to the segmented nature of the block copolymer that combined the excellent mechanical properties of the TAB+TA system with the high acid loading of the TAS+IA system.

Table 2. Conductivity and Mechanical Properties of the Random, Blend and Segmented Copolymer Systems

	Conductivity at 160˚C (S/cm)	Stress (Mpa)	Strain (%)
Random	0.24	0.2-0.3	20-55
Blend	0.06	1-1.4	75-175
Segmented	0.38	1.2-1.8	400-525

Fuel cell performance curves at atmospheric pressure are shown in **Figure 1**. Of interest is the very modest loss when using a reformate containing 40% hydrogen as a fuel compared to pure hydrogen. This is particularly impressive considering the reformate contained 2000 ppm CO. When using hydrogen as a fuel an oxygen gain of 70mV at 0.2A/cm^2 was measured.

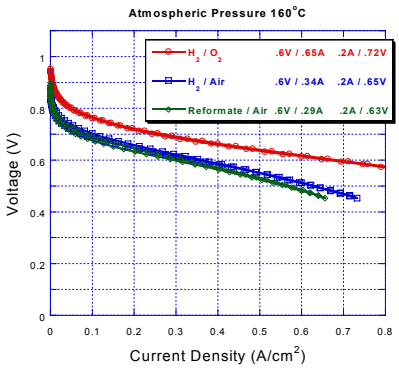

Figure 1. Performance curve for segmented block copolymer membrane at 160˚C and atmospheric pressure. Flow rates were 241 sccm H_2, 602 sccm reformate, 1003 sccm air, and 201 sccm O_2. The reformate composition was 40.0% H_2, 0.2% CO, 19.0% CO_2 and 40.8% N_2.

Fuel cell performance curves at 15psi or approximately 1 atmosphere over pressure are shown in **Figure 2**. A similar effect with regards to the minimal losses associated with reformate are noticed, as well as a similar oxygen gain. Operating at 15psi with hydrogen and air showed the same approximate performance as operating at atmospheric pressure with hydrogen and oxygen.

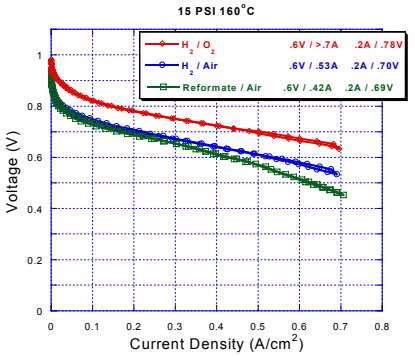

Figure 2. Performance curve for segmented block copolymer membrane at 160˚C and 15 psi. Flow rates were 241 sccm H_2, 602 sccm reformate, 1003 sccm air, and 201 sccm O_2. The reformate composition was 40.0% H_2, 0.2% CO, 19.0% CO_2 and 40.8% N_2.

Conclusions

A novel high temperature electrolyte membrane based on a segmented block copolymer of PBI was synthesized. The membrane displayed a very high acid loading and high conductivity. The membrane also exhibited excellent mechanical properties and fuel cell performance.

Acknowledgements

The authors wish to thank Celanese Ventures, GmbH, Plug Power and NYSTAR for their financial and technical support.

References

(1) Wainright, J.S.; Wang, J.T.; Weng, D.; Savinell, R.F.; Litt, M. *Journal of the Electrochem. Soc.* **1995**, *142*, L121-L123.

(2) Ma, Y.L.; Wainright, J.S.; Litt, M.H.; Savinell, R.F. *Journal of the Electrochem. Soc.* **2004**, *151*, A8-A16.

(3) Xiao, L.; Zhang, H.; Choe, E.-W.; Scanlon, E.; Ramanathan, L.S.; Benicewicz, B.C. *Preprints of Symposia - American Chemical Society, Division of Fuel Chemistry* **2003,** *48*, 447-448.

PROTON CONDUCTING POLYANILINE MOLECULAR SIEVES COMPOSITES

Decio Coutinho, Zhiwei Yang, Fangxia Feng, John P. Ferraris, and Kenneth J. Balkus Jr.

Department of Chemistry and the UTD NanoTech Institute, University of Texas at Dallas, Richardson TX 75083-0688

Introduction

Proton-conducting solid materials have grown in interest due to their potential applications in electrochemical devices, such as batteries, chemical sensors, fuel cells, and supercapacitors. Mesoporous molecular sieves offer many advantages such as thermal, chemical, and mechanical stability as well as significant water uptake at elevated temperatures.[1] The mesoporous molecular sieves pore walls may be easily functionalized with proton conducting groups, which combines the thermal and mechanical stability of the metal oxide framework with proton conducting properties of the organic moieties incorporated into the pores. These materials possess a uniform pore architecture that can be tuned by changing the organic template used or by swelling with the appropriate additives. Another attractive property of mesoporous materials is the compositional variance the can be achieved. In addition to silica, alumina and various transition metals, mesoporous molecular sieves may also be prepared with hybrid organic bridged silyls.[2,3]

The uniform pore architecture of mesoporous materials make them very attractive as hosts for the encapsulation of polymers. In fact, several reports describe the encapsulation of conducting polymers such as polypyrrole, polythiophene, and polyaniline into molecular sieves.[4-6] Polyaniline (PANI) is a widely studied conducting polymer.[7] However, when PANI is placed inside the pores of an insulator, such as MCM-41, several studies has shown that the DC conductivity is close to insulating.[4] The current study describes the preparation, proton and DC conductivity measurements of PANI-SBA-15 composites. In this study, an aniline functionalized mesoporous molecular sieve in which the pore walls are decorated with aminophenylsilane was synthesized (AP-SBA-15) and used for the encapsulation of PANI. All-silica SBA-15 was also used in this study. The aniline monomer tethered to the AP-SBA-15 pore walls functions as the anchor for PANI which then becomes tethered to the walls, while the polymer encapsulated into all-silica SBA-15 could theoretically be extracted from the pores.

Experimental

Aniline containing SBA-15 (AP-SBA-15) was prepared as follows: tetramethylorthosilicate (TMOS) was combined with aminophenyltrimethoxysilane (APTMS) and added to a solution containing 1.2 g of Pluronic 123 (P123) and 40 ml of 2M HCl and heated to 40ºC with stirring for 24 hours followed by heating at 90ºC for 2 days. The amounts of TMOS and APTMS varied (APTMS/Si = 0.05-0.20) while keeping the number of moles of Si at 0.0145 moles. The surfactant was removed by refluxing the as-synthesized material in ethanol for ~24 hours. All silica SBA-15 was prepared as reported in reference 2. Polyaniline containing SBA-15 (PANI-SBA-15) was prepared as follows: Template free AP-SBA-15 (0.2 g) and all-silica SBA-15 (0.2 g) were dried under vacuum at ~100ºC for 24 hours and then placed in a solution containing 0.2 grams of aniline hydrochloride (AHC) and 10 mL of methanol. The dispersion was stirred for ~5 minutes and then allowed to dry at room temperature. The aniline/SBA-15 powder was dispersed in ~20 mL of 1M HCl. To this dispersion, a solution of 0.35 g of ammonium persulfate (APS) in 10 mL of 1 M HCl was and the mixture was stirred at room temperature for ~12 hours. The dark green solids were filtered, washed thoroughly with water and dried at 50ºC. To remove the excess bulk PANI formed outside the mesopores, PANI-SBA-15 composites were first stirred in 0.05 M NH_4OH to convert the green emeraldine salt to the emeraldine base and then Soxhlet extracted in 1-methyl-2-pyrrolidone (NMP) for ~12 hours. After extraction the dark blue powder was stirred in 2 M HCl to produce the emeraldine salt again.

Polyaniline was also polymerized in-situ during the synthesis of SBA-15. In this synthesis, TMOS was combined with APTMS (APTMS/Si = 0.05 and 0.1, total moles of silicon = 0.0145) and added to a solution containing 1.2 g of P123, 0.6 g of AHC, and 40 ml of 2M HCl and stirred at room temperature for 1 hour. Then 0.7 g of APS was added to the mixture, which was stirred at room temperature for ~20 minutes. The dark green gel was aged at 45˚C for 24 hours followed by heating at 90˚C for 48 hours. The as-synthesized samples were Soxhlet extracted with NMP as detailed above. The PANI-SBA-15 materials were also calcined at 550˚C for 24 hours.

The samples were characterized by powder X-ray diffraction (XRD), infrared spectroscopy (FTIR), scanning electron microscopy (SEM), and nitrogen adsorption. The conductivity measurements were made following a published procedure reported previously [10]. Measured amounts of the powder and water added were mixed completely. The resulting wet mixtures were placed into a glass tube with the surface area of 1 cm^2, which was clamped between two stainless-steel pistons as the electrodes. The impedance spectroscopy measurements were conducted on a Voltalab PGZ301 analyzer, using Potential Dynamic EIS method over the frequency range 1–105 Hz at room temperature.

Results and Discussion

Mesoporous SBA-15 containing the conducting polymer, polyaniline, was prepared both in-situ and in a post treatment of the mesoporous aminophenyl functionalized SBA-15. Unlike the aminopropyl functionalized materials prepared with aminopropyltrimethoxysilane, the functionalization of SBA-15 with p-aminophenyltrimethoxysilane by co-condensation under acidic conditions produces very well ordered mesoporous SBA-15 with high APTMS content. As shown in Figure 1, the XRD patterns for the as-synthesized AP-SBA-15 materials display three well resolved reflections typical for hexagonally arranged mesoporous silica., which corresponds to the (100), (200), and (211) reflections. The Surface area for AP-SBA-15 prepared with an APTMS/Si of 0.05 is ~735 m^2/g which is very similar to the surface area of the all-silica SBA-15 (Table 1). However, the pore size for this AP-SBA-15 is substantially larger than that for all-silica SBA-15 (7.8 and 6.5 nm respectively). As the APTMS/Si was increased to 0.2, the surface area decreased to 535 m^2/g and the pore size decreased to 6.5 nm.

SEM images of AP-SBA-15 (not shown) reveal small disks ~1 µm in diameter and 100-200 nm thick. As the APTMS/Si ratio is increased. The morphology changes to less defined shapes. Most of the AP-SBA-15 powder composed of plates, but there are large amounts of small particles.

The post synthesis polymerization of polyaniline in the SBA-15 mesochannels was accomplished by the aniline monomer into the mesopores and then adding the oxidant to complete the polymerization. This process also produced excess bulk PANI on the outside of the SBA-15 particles as seen in Figure 2. The SBA-15 particles are completely covered with fibrous PANI. To remove the excess PANI, the composite powder was stirred in 0.05 M NH_4OH overnight to yield the emeraldine base form of PANI, which is soluble in NMP, and the excess polymer was Soxhlet extracted in NMP. The resulting powder was dark blue. These processes were performed

using template free AP-SBA-15 and all-silica SBA-15 calcined at 550˚C. In the functionalized AP-SBA-15, the polymer should become tethered to walls, because the aniline monomer attached to the pore walls can provide an anchor for the polymer. In this scenario, the polymer would not be extractable. In the calcined all-silica SBA-15, the polymer would be formed in the pores, but it would not be tethered to the walls, and it could be extracted leaving the pores empty again. After extraction, scanning electron microscopy did not show any evidence of bulk PANI among the mesoporous particles (Figure 2). However, it is possible that the outside surface of the SBA-15 particles is coated with PANI. PANI SBA-15 samples prepared with AP-SBA-15 retained its dark blue color, but the sample prepared with all-silica SBA-15 became pale blue.

Polyaniline was also polymerized in-situ during the synthesis of SBA-15. Again, the as-synthesized mesoporous PANI-SBA-15 was dark green, indicating that the emeraldine salt was formed. This synthesis also yielded dark green solids and the XRD patterns (Figure 1) show a well ordered material similar to all-silica SBA-15. The as-synthesized material was also immersed in dilute NH_4OH followed by extraction in NMP. It is clear from the SEM images (Figure 2) that the as-synthesized composites contain a substantial amount of excess PANI as small diameter fibers around the bigger SBA-15 particles. However after extraction there is no evidence of excess bulk polymer.

Nitrogen adsorption studies for the PANI-SBA-15 composites are summarized in (Table 1). The samples prepared by post synthesis encapsulation (samples 4 and 5) using AP-SBA-15 showed a significant decrease in the pore size and surface area, while the samples prepared with all-silica SBA-15 showed a decrease in surface area, but not a significant change in pore size or volume. The composites prepared by in-situ polymerization of PANI (samples 6 and 7) after extraction display a substantially different isotherm from the calcined materials. These materials have a much smaller surface area and pore size (Table 1) than the calcined materials which indicates that the pores are partially filled with polymer.

When a conducting polymer is encapsulated in a zeolite, the electrical conductivity decreases significantly.[8] One of the reasons is that the polymer confined in the zeolite pores cannot create good contact with the electrodes. In this case, this was an advantage, because the main interest of this study was to determine the proton conductivity of PANI encapsulated in the SBA-15 mesopores. Electrical conductivity measurements conducted using the dry emeraldine salt form of aniline doped with hydrochloric acid. The proton conductivities were measured using the same powder at room temperature. During the proton conductivities measurement, water was added to the powder to determine the effect of water content on the conductivity of the composite. PANI-SBA-15 samples exhibited very low electrical conductivities. The as made PANI-SBA-15 samples, which contained a large amount of excess bulk PANI exhibited electrical conductivities in the 10^{-4}-10^{-5} S/cm range. These results compare well with literature reported values for PANI-zeolite composites.[4] After extraction of the excess bulk PANI, the conductivities were not detectable and the material was insulating. The proton conductivity after extraction was in the 10^{-3} S/cm range and it varied significantly depending on the water content. It is worth noting that the PANI in the PANI-SBA-15 composite was doped with HCl. In most cases, stronger acids such as phosphoric acid or triflic acid are used to dope proton conducting membranes such as polybenzoimidazole.

Table 1. Physiochemical properties of AP- and PANI-SBA-15

Sample	APTMS/Si	BET SA (m^2/g)	Pore size (nm)	Pore Vol (cc/g)
1	0	719	6.53	1.09
2	0.05	739	7.78	1.22
3	0.20	575	6.59	1.29
4	0.05	552	3.78	0.81
5	0	461	6.25	1.02
6	0.05	595	3.81	0.68
7	0.10	536	3.79	0.40

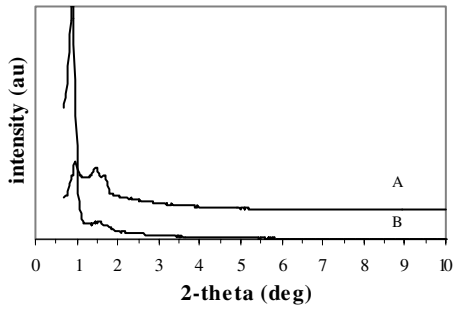

Figure 1. XRD patterns of (A) template free AP-SBA-15 (Sample 2) and (B) PANI-SBA-15 (sample 6) after extraction.

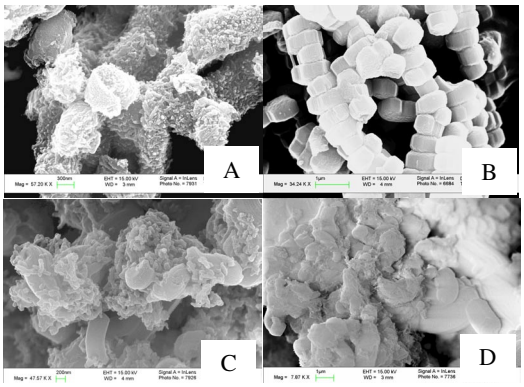

Figure 2. SEM of (A) as prepared PANI-SBA-15 (sample 4), (B) sample 4 after extraction in NMP, (C) as-synthesized PANI-SBA-15 (sample 6) and (D) sample 6 after extraction in NMP.

References)

(1) Kresge, C.T.; Lenowicz, M.E.; Roth, W,J.; Vartuli, J.C.; Beck, J.S.; *Nature* **1992,** 359, 710.
(2) Yang, P.; Zhao, D.; Margolese, D.I.; Chmelka, B.F.; Stucky, G.D., *Chem. Mater.* **1999**, 11, 2813.
(3) Inagaki, S.; Guan, S.; Ohsuna, T.; Terasaki, O., *Nature*, **2002**, 416, 304.
(4) Wu, C-G.; Bein, T.,*Science*, **1994**, 264, 1757.S
(5) Cardin, D.J., *Adv. Mater.* **2002**, 14, 553.
(6) Choi, H.J.; Cho, M.S.; Ahn, W.S., *Synth. Met.* **2003**, 135-136, 711.
(7) MacDiarmid, A.G., Synth. Met. **1997**, 84, 27.
(8) Mikhailenko, S.; Desplantier-Giscard, D.; Danumah, C.; Kaliaguine, S., *Micropor. Mesopor. Mater.* **2002**, 52, 29.

PROTON EXCHANGE MEMBRANE FUEL CELLS: I. SYNTHESIS AND CHARACTERIZATION OF DISULFONATED POLY (ARYLENE ETHER BENZONITRILE) COPOLYMERS

*Mehmet Sankir, William L. Harrison, Kent B. Wiles, Yanxiang Li and James E. McGrath**

Macromolecular Science and Engineering and Materials Research Institute,
Virginia Polytechnic Institute and State University,
Blacksburg, VA 24061, USA
jmcgrath@vt.edu

Abstract

A series of benzonitrile containing sulfonated poly(arylene ether sulfone) copolymers were synthesized by direct nucleophilic substitution copolymerization. The 4,4'-biphenol, 2,6-dichlorobenzolnitrile and 3,3'-disulfonated 4,4'-dichlorodiphenyl sulfone (SDCDPS) were used to produce novel sulfonated copolymers with various degrees of disulfonation (0-45 mol% SDCDPS), yielding ion exchange capacities (IEC's)up to 2.02 mmol/g. NMR analysis coupled with titration of sulfonated moieties confirmed both chemical structure and copolymer composition. GPC and intrinsic viscosity analyses indicated high molecular weight copolymers were synthesized. The copolymers produced ductile films with thin film conductivities reaching 0.12 S/cm, suggesting they are good candidates for proton exchange membranes in fuel cells. Characterizations such as TGA, water uptake, proton conductivity and morphology will be presented

Introduction

Our research group, and others, has been investigating novel, commercially viable proton conducting membranes for polymer electrolyte fuel cells. Polymer electrolyte fuel cell membranes require several qualities, such as good mechanical properties/stabilities, good proton conductivities, and have low permeabilities of the reactant fuels. Currently, expensive perfluorinated sulfonic acid polymers are employed despite their reported limitations. Alternative PEMs are primarily based on aromatic engineering polymers, such as poly ether sulfones and poly ether ketones that have been chemically modified to contain sulfonic acid groups along the main chain. In contrast, our approach has been to control the degree of sulfonation by copolymerizing sulfonated monomers. It has also been demonstrated that exact control (distribution) of sulfonation over the entire sequence is better via direct copolymerization versus post-sulfonation by titration and NMR studies [1-3]. The synthesis and characterization of high molecular weight, nitrile-functional copolymers using SDCDPS, 2,6-dichlorobenzonitrile and hexafluoroisopropylidene diphenol (hexafluorobisphenol A) have recently been reported by our group [4]. In this contribution, we report the systematic study of the synthesis of benzonitrile containing wholly aromatic disulfonated poly (arylene ether) copolymers (PAEB) by directly copolymerizing SDCDPS, 2,6-dichlorobenzonitrile and 4,4'-biphenol. The influence of the pendant nitrile group on this copolymer system is being explored as it may affect properties such as water uptake and proton conductivity by possible hydrogen bonding.

Experimental

Reagents. 4,4'-biphenol was kindly provided by Eastman Chemical, 2,6-dichlorobenzonitrile was purchased from Aldrich and both were used without any purification. The disodium salt of 3,3'-disulfonated 4,4'-dichlorodiphenyl sulfone (SDCDPS) was synthesized through the reaction of 4,4'-dichlorodiphenyl sulfone (Solvay Advanced Polymers) and fuming sulfuric acid, as described previously [5]. All other reagents were obtained from commercial sources and purified, as needed, via common procedures.

Synthesis of Sulfonated Poly (arylene ether benzonitrile). Sulfonated poly (arylene ether benzonitrile) (PAEB) copolymers were achieved with various degrees of disulfonation (0-45 mol% SDCDPS) via direct copolymerization of sulfonated dichlorodiphenyl sulfone (SDCDPS), 2,6-dichlorobenzonitrile and biphenol (BP). 2.2609 g (0.0131 mol) 2,6-dichlorobenzonitrile, 3.4767 g (0.0071mol) SDCDPS and 3.7654 g (0.0202 mol) 4,4'-biphenol and 3.2139 g potassium carbonate (15% mol excess) were transferred to 3-neck flask equipped with a mechanical stirrer, a nitrogen inlet and a Dean Stark trap in order to synthesize 35 mol percent SDCDPS containing copolymer, named as PAEB 35. Dry NMP (20 mL) was used as the polymerization solvent while toluene (10ml) was the azeotrope. The reaction mixture was refluxed for 4 hours at 150 ºC to complete the dehydration process. The reaction temperature slowly increased to 190 ºC for 16 hours just after the removing of the toluene gradually. The viscous reaction product was cooled and diluted with NMP and precipitated in deionized water as swollen fibers. After washing several times with deionized water, the precipitated copolymers were boiled in deionized water for 4 hours to remove the salts. Copolymers were isolated by filtration then dried in vacuum oven at 120 ºC for 24 hours.

Film Casting and Membrane Acidification. Membranes in the potassium sulfonate form were prepared by first redissolving the copolymer in 5-10% (w/v) DMAc, filtered to afford, then cast onto clean glass substrates. The transparent solutions were carefully dried with infrared heat at gradually increasing temperatures (up to ~ 60 ^{o}C) under a nitrogen flow, until the film was dry. The sulfonated poly(arylene ether sulfone) copolymer films were converted to their acid- form by boiling the cast membranes in 0.5 M sulfuric acid for 1.5 hours, followed by 1.5 hour extraction in boiling deionized water, which has been referred to as Method 2 [6].

Characterization

A Nicolet Impact 400 FT-IR spectrometer was utilized on thin films to confirm the functional groups within the copolymers. Proton (^{1}H) NMR analysis were conducted on a Varian UNITY 400 spectrometer. All spectra were obtained from a 10% solution (w/v) in dimethylsulfoxide-d6 solution at room temperature. Gel permeation chromatography (GPC) with polystyrene standards was used to calculate the number average molecular weights (Mn). Intrinsic viscosities were determined in NMP at 25 ºC using an Ubbelohde viscometer. The thermo-oxidative behavior of both the salt-form (sulfonate) and the acid-form copolymers was performed on a TA Instruments TGA Q 500. Dried, thin films (5 to 10 mg in salt form) were evaluated over the range of 30 to 800 ^{o}C at a heating rate of 10 ^{o}C/min in air. Titration of the sulfonic acid groups were performed on acidified membrane samples of known mass by exchanging with sodium sulfate then back titrating with 0.01M NaOH. Thin film conductivity measurements were conducted on acidified membranes while submerged in deionized water using a Hewlett Packard 4129A Impedance/Gain-Phase Analyzer recorded from 10 MHz to 10 Hz.

Results and Discussion

Disulfonated 4,4`- dichlorodiphenyl sulfone (SDCDPS) monomer with a near quantitative conversion was synthesized using a procedure reported by our group [4]. Direct nucleophilic polycondensation was used to synthesize several series of high molecular weight disulfonated poly(arylene ether sulfone) copolymers. The reaction includes two steps; four hours dehydration step, achieved by toluene refluxing at 155 ºC and copolymerization step at 190 ºC for 16 h. Synthetic route was depicted in Figure 1.

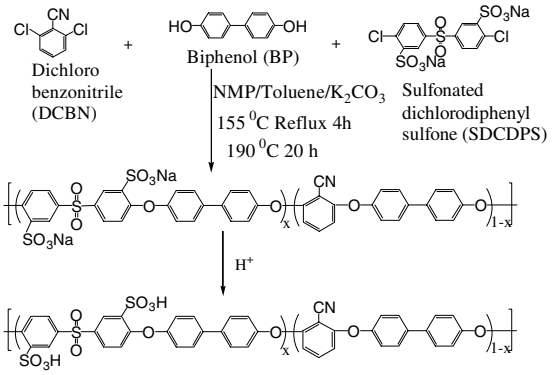

Figure 1. Copolymerization reaction mechanism includes two successive steps: Dehydration and copolymerization

^{1}H NMR was used for compositional and structural determinations (Figure 2). The observed degree of disulfonations from proton NMR was in close agreement with target disulfonations. High molecular weight PAEB

copolymers were synthesized as suggested by intrinsic viscosity, GPC, and film ductility.

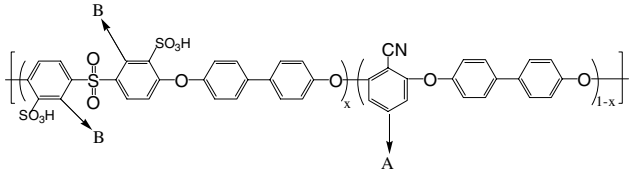

Mole percent disulfonation= (100/(B/2+A/1))*(B/2)

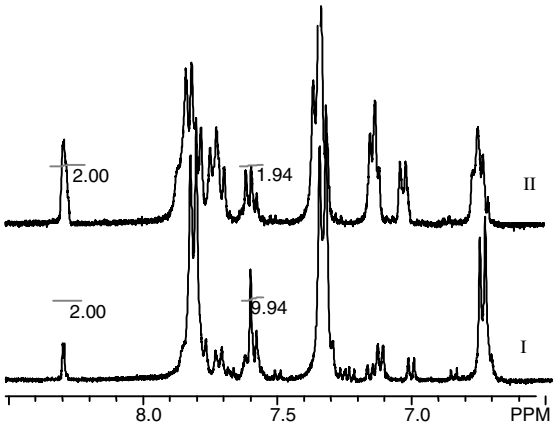

Figure 2. Calculation of mole percent sulfonation based on ^{1}H NMR. I: 9.5 % disulfonation, II: 34 % disulfonation where targets were 10 and 35, respectively.

Copolymers at various percent disulfonation and control copolymer with zero percent disulfonation were compared using FTIR spectra. The two new peaks resulting from sulfonic acid moieties were observed at 1070 cm^{-1} and 1095 cm^{-1}, respectively (Figure 3).

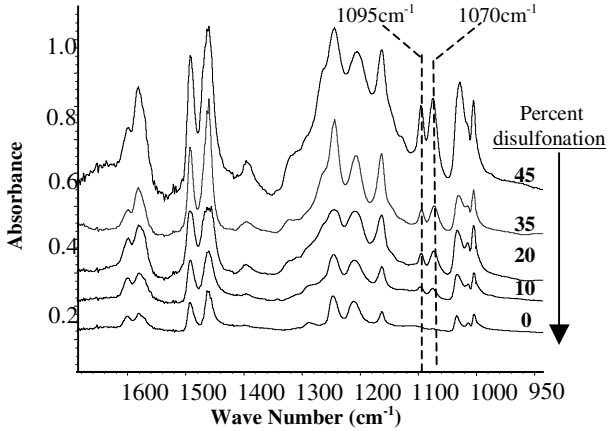

Figure 3. FTIR bands showing incorporation of sulfonic acid moieties into copolymer structure

The control polymer and salt forms of disulfonated copolymers showed very high thermooxidative stabilities (~500 ºC), while the acidified membranes showed good thermooxidative stabilities (>250 ºC), which is sufficient for 120 ºC fuel cell operation (Figure 4). The increase in degree of disulfonation caused decrease in thermooxidative stabilities. The 5% weight loss temperatures for acid form of disulfonated copolymers varied in between 330 and 430 ºC.

The target and actual degree of sulfonation, and intrinsic viscosities and the number average molecular weights of copolymers were shown in Table 1. Table 1 also shows the membrane properties such as water uptake values, proton conductivities at two different temperatures in liquid water, and IEC values as a function of degree of disulfonation.

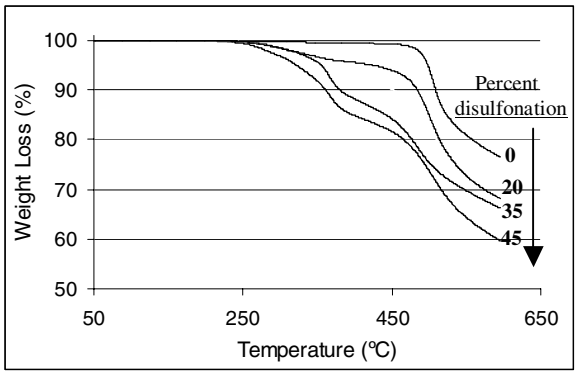

Figure 4. Influence of percent disulfonation on thermooxidative stability of acid form of PAEB copolymers (10 ºC/min in air).

Since the controllable degree of disulfonation strongly influences the membrane properties, it was used as a design parameter for proton exchange membranes in fuel cell applications.

Table 1. Influence of the Percent Disulfonation on Several Features

PAEB XX target	PAEB XX actual	$[\eta]^{NMP}_{25°C}$ dL/g	M_n	Water Uptake (%)	IEC mequiv/g		Proton Conductivity (mS/cm)	
					Cal	Exp	24ºC	80ºC
10	9.5	1.6	50K	6	0.6	0.5	10	14
20	19.7	1.9	80K	10	1.2	1.0	30	50
35	34	1.6	55K	40	1.8	1.8	60	130
45	44	1.2	65K	72	2.2	2.0	120	150

Conclusions

The benzonitrile containing thermally stable, ductile high molecular weight disulfonated copolymers were successfully synthesized. Structural and compositional characterizations showed that all the starting monomers were well incorporated into the copolymer. The spectrum of the physical properties as a function of degree of disulfonation was obtained to provide an input data while fabricating the proton exchange membrane for the desired fuel cell applications. Additional results will be discussed.

Acknowledgement. The authors would like to thank the National Science Foundation "Partnership for Innovation" Program (HER-0090556) and the Department of Energy (DE-FC36-01G01086) for support of this research effort.

References

(1) Wang, F.; Hickner, M.; Kim, Y. S.; Zawodzinski, T. A.; McGrath, J. E. *J. Membr. Sci.* **2002**, 197, 231.

(2) Wang, F.; Hickner, M.; Ji, Q.; Harrison, W.; Mecham, J.; Zawodzinski, T.; McGrath, J. E. *Macromol. Symp.* **2001**, 175(1), 387.

(3) Harrison, William L.; Wang, Feng; Mecham, Jeffery B.; Bhanu , Vinayak A.; Hill, Melinda; Kim, Seung Yu; McGrath, J.E. *J. Polym. Sci.: Part A: Polym. Chem.* **2003**, 42, 2264.

(4) Sumner, M.J.; Harrison, W.L.; Weyers, R.M.; Kim, Y.S.; McGrath, J.E.; Riffle, J.S.; Brink, A.; Brink, M.H. *J. Membrane Science* **2004**, accepted.

(5) Sankir M.; Bhanu, V.A.; Ghassemi, H.; Wiles, K.B.; Hill, M.H.; Harrison, W.; Sumner, M.; Glass, T.E.; Riffle, J.S.; McGrath, J.E. *Polymer Preprints* **2003,** 44, 1.

(6) Kim, Y.S.; Wang, F.; McCartney, S.; Hong, Y.T.; Harrison, W.; Zawodzinski, T. and McGrath, J.E. *J. Polym. Sci.; Part B: Poly. Phys.* **2003**, 41, 2816.

A NEW CLASS OF POLYELECTROLYTES, POLYPHENYLENE SULFONIC ACID AND ITS COPOLYMERS, AS PROTON EXCHANGE MEMBRANES FOR PEMFC'S

*Sergio Granados-Focil, Morton H. Litt**

Department of Macromolecular Science and Engineering, Case Western Reserve University, 10900 Euclid Ave. Cleveland OH, 44106.

Introduction

Polymer membrane electrolyte fuel cells (PEMFC's) have become one of the most attractive alternative power sources for vehicles and portable electronic devices. PEMFC's are the best choice for these applications due to their high power densities and relatively low operating temperatures. The most widely used materials for polymer electrolyte membranes are the perfluorosulfonic acid polymers, like Nafion®. However, these materials present several disadvantages, such as very low conductivities at low relative humidity or temperatures above 80ºC. A considerable amount of effort has been directed towards finding alternative materials that would overcome the disadvantages of Nafion®.[1,2] Among these developments are sulfonated rigid rod liquid crystalline polyimides, where bulky or angled comonomers have been used to generate nanoscale pores lined with sulfonic acid groups. These nanopores increase the water absorption and thus the proton conductivity of the polyimide membranes at low relative humidities and high temperatures.[2]

We have previously reported the application of the structural approach used for the rigid rod polyimides to hydrolytically stable Poly(phenylene sulfonic acid)s.[3] This study extends the same approach to grafted copolymers containing bulky and crosslinkable groups. Their conductivity as a function of temperature and relative humidity surpasses the values reported for Nafion®, the rigid rod sulfonated polyimides and the post-sulfonated PEEK's and poly(4-phenoxybenzoyl-1,4-phenylene)s.[4,5]

Experimental

Materials. All reagents were purchased from the Aldrich Chemical Co. N-methylpyrrolidone (99%), was stirred overnight with calcium hydride, vacuum distilled and degassed prior to use. All the remaining solvents and reagents were used without further purification. Copper bronze was activated according to a previously reported procedure[6] and was used immediately after preparation

Instrumentation. ^{1}H and ^{13}C NMR spectra of the polymers and the monomers were obtained on a Varian Gemini 300 spectrometer using D_2O and DMSO *d-6*. FTIR spectra were recorded on a BOMEM Arid Zone FTIR spectrometer. Intrinsic viscosity of DMSO polymer solutions was measured using a Cannon Ubbelohde viscometer. Proton conductivity was measured using a 4-point probe configuration[7] Solartron apparatus in the AC mode.

Synthesis. The synthetic procedures to obtain 4,4'-dibromo-2,2'-biphenyldisulfonic acid (I), Benzyltrimethylammonium(4,4'-dibromo-2,2'-biphenyl) disulfonate (II) and Poly(phenylene sulfonic acid) (III) have been reported previously.[3] Optimization of the experimental conditions yields now intrinsic viscosities of 0.85dl/g for III.

Synthesis of Poly(phenylene sulfonic acid) grafted copolymers. 5g of polyphenylene sulfonic acid, III, and 15 ml of H_3PO_4 were added to a 50 ml 3-necked round bottom flask under nitrogen flow and stirred at 300 rpm. Once a homogeneous solution was formed, 30g of P_2O_5 were added in batches of 500 mg at a time in order to keep the temperature of the reaction mixture below 100ºC. After addition of the P_2O_5 was complete, a condenser was fitted to the flask, the temperature was raised to 130ºC, and 65meq of the compound to be grafted into the backbone were added to the reaction mixture. The reaction was then allowed to continue for a period of time ranging from 30 to 120 minutes depending on the desired yield for the grafting process. Grafted copolymers containing 5% to 50% of grafted aromatic sulfone can be obtained using this method. The yield of the grafting process was confirmed by ^{1}H NMR and acid base titration of the resulting products.

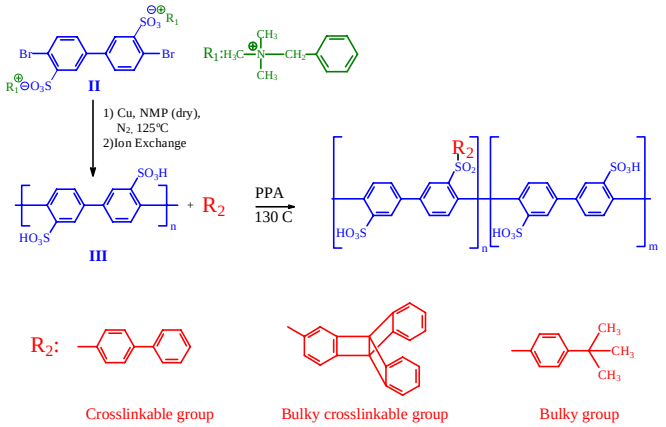

Figure 1. Synthesis scheme for the grafted copolymers.

Thermal Crosslinking of the Poly(phenylene sulfonic acid) copolymers containing grafted biphenyl or triptycene. Copolymer films were placed between Teflon sheets and the assembly was put inside an aluminum box equipped to provide a preheated nitrogen flow. The box was then placed inside a convection oven preheated at the desired crosslinking temperature and kept at a constant temperature for a period of time ranging from 20 to 60 minutes.

Results and Discussion

Synthesis of grafted Poly(phenylene sulfonic acid) copolymers. The grafting of different aromatic compounds had different structural goals. Biphenyl was used as a thermal crosslinker group, while tert-butylbenzene was used to increase the distance between the polymer chains creating more space available for water molecules to be stored within the polymer membrane. The use of triptycene had a dual purpose, to generate crosslinkable films and to increase the intermolecular distance hopefully increasing the water retention capabilities of these crosslinked membranes. The grafting reactions were found to proceed heterogeneously requiring relatively severe conditions, namely the use of high temperature and an excess of the compound to be grafted into the backbone. Table 1 illustrates the conditions used to obtain different copolymer compositions.

Table 1. Experimental Conditions for the Grafting of Aromatic Rings to the Poly(Phenylene sulfonic acid).

Grafted compound	Reaction time (min)	Amount of grafted material (% total sulfonic acids converted to sulfone)
Biphenyl	30	10
Biphenyl	60	20
Biphenyl	120	55
Triptycene	30	6.5
Tert-butylbenzene	60	5
Tert-butylbenzene	120	25

According to the sulfonic acid titration analysis, the amount of sulfone groups present in the grafted copolymer was always found to be approximately 10%-15% lower than the amount expected when calculated based on the amount of aromatic sulfone found by ^{1}H NMR, analysis. This suggests the presence of undesired side reactions most likely due to the vigorous grafting conditions. The use of alternative solvents where the grafting process occurs homogeneously is currently being explored.

Thermal Crosslinking of the Poly(phenylene sulfonic acid) copolymers. The temperature and time required to produce insoluble films depended on the nature of the group being grafted into the polymer backbone but not on the amount present in the polymer. This indicates that a relatively small amount of crosslinker is enough to render the films insoluble, however the amount of swelling upon immersion in water was found to depend on the relative amount of crosslinker present. The conditions required to render the copolymer films water insoluble are summarized in table 2.

Table 2. Experimental Conditions for the Crosslinking of the copolymers containing biphenyl or triptycene.

Grafted compound	Crosslinking time (min)	Crosslinking temperature (ºC)
Biphenyl	25	210
Triptycene	60	250

Proton conductivity of the Poly(phenylene sulfonic acid) grafted copolymers. The proton conductivity of the different copolymers was measured as a function of temperature and relative humidity, see figures 2 and 3. The data show that a small amount of grafted t-butylbenzene or biphenyl (5-10%) decreases the conductivity by a factor of 3, but it is still comparable to or higher than Nafion®'s.

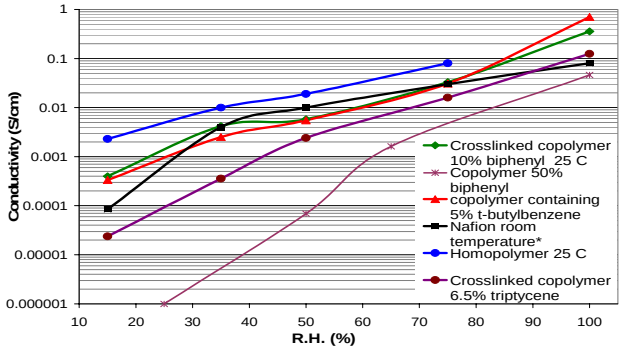

Figure 2. Conductivity vs. relative humidity at room temperature *(the conductivity of Nafion® does not change significantly over this temperature range[8]).

Figure 2 also shows that a large amount of biphenyl grafted into the polymer decreases the conductivity significantly, most likely due to an intrinsic change in the solid state structure of the membrane. In the case of the triptycene inserted membranes, the conductivity is much lower than that of the other copolymers with comparable amounts of grafted aromatic groups. ^{1}H-NMR analysis shows that 6.5% of the sulfonic acids have reacted with the triptycene after the grafting process. However, the amount of sulfone calculated from the titration of the sulfonic acids in the copolymer is approximately 10% mol. This suggests that a second aromatic ring had also reacted. Crosslinking of this copolymer required higher temperatures and longer times than those required by the grafted biphenyl copolymers. This treatment resulted in loss of sulfonic acid due to formation of intermolecular sulfones and possibly thermal degradation of the polymer.

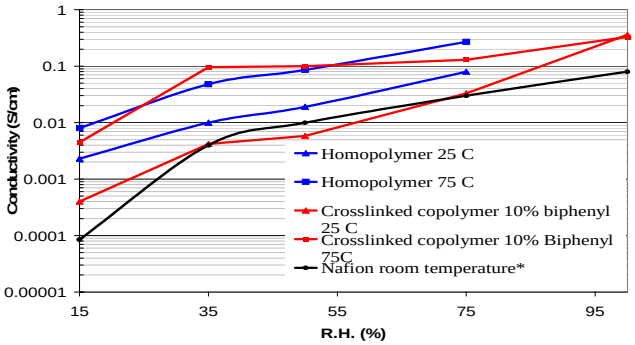

Figure 3. Conductivity as a function of relative humidity and temperature for the crosslinked films.

Dimensional stability and solubility of the copolymer membranes. Grafting of 5% mol tert-butylbenzene into the polymer backbone renders the copolymer insoluble while the grafting of up to 20% of biphenyl or 6.5% of triptycene gave water soluble copolymers. The difference in solubility among these materials may be due to hydrophobic bonding of the bulky non-polar tert-butyl groups, preventing the chains from dissolving in water. Dimensional changes of the copolymers films upon immersion in water occur almost exclusively in the thickness of the films, table 3.

Table 3. Dimensional Change upon immersion in water of films equilibrated at 20%R.H.

Grafted group	Grafted amount (% total sulfonic acids)	Δx (%)	Δy (%)	Δz (%)
Biphenyl	10	2	2	45
Biphenyl	20	1	1	35
Biphenyl	55	~0	1	15
Tert-butylbenzene	5	1	2	85
Tert-butylbenzene	25	1	1	50

Conclusions

Grafted copolymers of poly(phenylene sulfonic acid)s were made by reaction of the backbone's sulfonic acid groups with aromatic compounds in polyphosphoric acid. The grafting of biphenyl produces thermally crosslinkable films that have proton conductivities comparable to or higher than that of Nafion®. Grafting of small amounts of bulky monofunctional groups like tert-butylbenzene produces water insoluble films with proton conductivities similar to those of the thermally crosslinked films. Further work remains to be done in order to obtain dimensionally stable membranes.

References

(1) Rikukawa R. M., Sanui K., *Prog. Polym. Sci.* **2000** *25* 1463
(2) Zhang Y., Litt M.H., *ACS Polym. Prepr. Aug.* **1999**, *40(2)*, 480
(3) Granados-Focil, S., Litt, M.H., *Polym. Mat. Sci. and Eng.* **2003**, 89 438-439.
(4) Bae J.-M. et. al. *Solid State Ionics* **2002** *147* 189
(5) Kobayashi H., et. al., *Solid State Ionics* **1998** *106* 219
(6) Vogel A.I., *Vogel's Textbook of practical chemistry*, **1989**, Longman, London, p. 426.
(7) Cahan, B. D.; Wainright, J. S. *J Electrochem Soc* **1993** *140* L185
(8) Sone Y., et. al.,. *Electrochem. Soc.* **1996**, 143 (4) 1254.

FULLERENE-BASED PEM FOR DRY OPERATION OF POLYMER ELECTROLYTE FUEL CELL

Ken Tasaki[a]†, Arun Venkatesan[a],
Perumal Pugazhendhi[b] ,and Raouf, O. Loutfy[b]

[a]MC Research and Innovation Center,
7127 Hollister Ave. Suite 110, Goleta, CA 93117
[b]MER Corporation, 7960 S. Kolb Rd. Tucson, AZ 85706

Introduction

Water management in polymer electrolyte fuel cells (PEFC) is one of the most difficult issues that require careful attention in designing a reliable fuel cell. A breakdown in water balance at the cathode side results in either drying out or water flood, while the anode side tends to get dry due to the water diffusion across the membrane. Currently dominant water-based proton-exchange membranes (PEM) require not only a humidifier which takes extra space, but also favor an even distribution of water throughout the membrane.

To eliminate the problems associated with water management, a number of efforts have been underway in the development of anhydride PEM.[1-3] Recently, Sony has developed proton-exchange membranes based on functionalized (mainly the OSO_3H and the OH groups) fullerenes for polymer electrolyte fuel cell (PEFC).[4] Fullerenes are very unique in that they have a very low electron affinity and are easy to chemically functionalize; thus their performance (the conductivity, the thermal/chemical/mechanical stability,..) can be fine tuned chemically. Also, fullerenes with multiple acid groups have a high volumetric density of proton conductive groups. The Sony group suggested that the ion conduction in the functionalized fullerene was due to the proton hopping between the functional groups on the fullerene, therefore requiring no humidification, though no detailed examination of the proton transport mechanism was reported.[4] Still, chemical functionarization of fullerenes is well-established; thus their performance (the conductivity, the thermal, the chemical, and the mechanical stabilities) can be controlled and even fine-tuned chemically. Thus, they could be promising materials for a new type of tailored ionic conductors. Yet, so far, it is not clear whether the conductivity of Sony's fullerene membrane is due to the functional groups or C_{60} itself is conductive. Theoretical calculations may provide an insight into the nature of C_{60} as a proton conducting material. In this report, we examine C_{60}'s basic characteristics as a proton conductor primarily through theoretical calculations and report some experimental results on its application in PEFC.

Calculations

The activation energy barriers for proton hopping in fullerene were calculated at the PM3 method since higher levels of calculations are computationally prohibiting due to the size of the molecules. No activation energy barrier of proton transfer has been reported for C_{60}. The activation barrier was obtained by determining the transition state for the proton transfer pathway and then taking the energy difference between the transition state and the equilibrium structure. The transition state and the equilibrium structure were each separately optimized, while the former was further verified by frequency calculations where only one negative frequency was found. Additionally, the internal reaction coordinate calculations were followed to validate the transfer path. All calculations were performed in the gas phase.

Experimental

Preparation of Membranes. A pellet of C_{60} was made for electrochemical performance measurements by mixing the C_{60} powder with 5 wt% of polytetrafluoroethylene as a binder and then pressing the mixed power to yield a pellet with 175 μm thickness. Separately, a Nafion 117 membrane soaked in MeOH was mixed with C_{60}–toluene solution to make a C_{60}–doped Nafion membrane. The loading of C_{60} dopant in the Nafion membrane was approximately 1 wt%.

AC Impedance Measurements. AC impedance measurements were performed for the films at 30 ºC in the frequency range of 1 to 105 Hz without any humidification after operating in a fuel cell under dry gas at 105 ºC for several hours. The resistance associated with the membrane at zero phase angle was used to estimate the proton conductivity of the membrane using the equation, $\sigma = (1/R)\ (L/A)$, where R is the bulk resistance of the membrane, L represents the membrane thickness, and A the membrane area.

Cell Performance Measurements. A membrane-electrode-assembly (MEA) was constructed using each membrane prepared above: the C_{60} pellet, Nafion 117, and Nafion 117 doped with 1 wt% C_{60}. 0.4 mg cm^{-2} of platinum coated on the gas diffusion electrode was applied on each side of the membrane. The cell included highly conducting non-porous graphite plates with grooves to circulate hydrogen gas at the anode and the cathode compartments. The power of the cell was measured at 0.3 A cm^{-2} with dry hydrogen and dry oxygen as fuel under atmospheric pressure at 30 ºC after operating for 33 hrs with dry fuel gases.

Results and Discussion

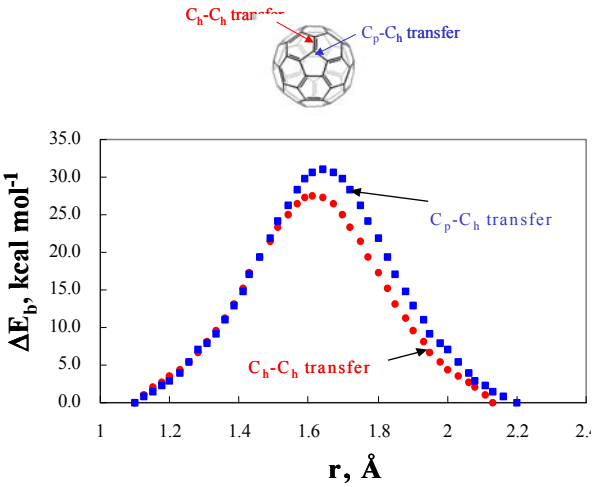

Figure 1. The intramolecular proton hopping potential energies for two possible path ways in C_{60}. r is the distance between the proton and the carbon to which the proton was originally attached.

Figure 1 shows the potential energy profiles for proton hopping on the surface of C_{60} with the activation energy barriers of H^+ transportation along the two paths: 27.8 kcal mol^{-1} along the C-C bond dividing two hexagons (C_h-C_h) and 31.3 kcal mol^{-1} along the bond dividing a hexagon and a pentagon (C_h-C_p) of C_{60}. The distance r refers to the distance between the proton and the carbon to which the proton was originally attached in $C_{60}H^+$. At the distance ~ 2.2 Å, the proton is attached to the adjacent carbon. These values imply a

fast movement of a proton around the C_{60} surface, which is qualitatively consistent with the experimental observation that only a single ^{13}C-NMR spectrum was observed for the $C_{60}H^+$ system at ambient temperature.[5]

Next, the activation barrier of H^+ transportation between two C_{60} molecules was computed for the process illustrated below (the proton shown by a white dot between two C_{60} molecules):

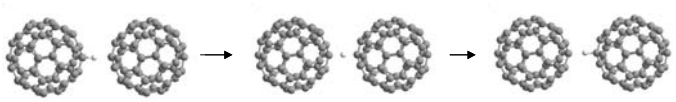

The calculated activation barrier was only 3.29 kcal mol^{-1}. Our calculations suggest that C_{60} itself is highly conductive.

In order to verify the above theoretical results, we assembled an MEA with a C_{60} pellet as the membrane for polarization measurements under dry condition. **Figure 2** presents the polarization curve for the cell measured at 30 ºC with dry hydrogen and oxygen as the fuels under atmospheric pressure. Though the current density is small since there is no acidic proton in the pellet, this is a direct evidence of C_{60}'s proton conductivity. Despite Sony's claim that the proton conductivity is due to the functional groups of fullerene, our finding opens up a possibility of C_{60} as proton conductive material.

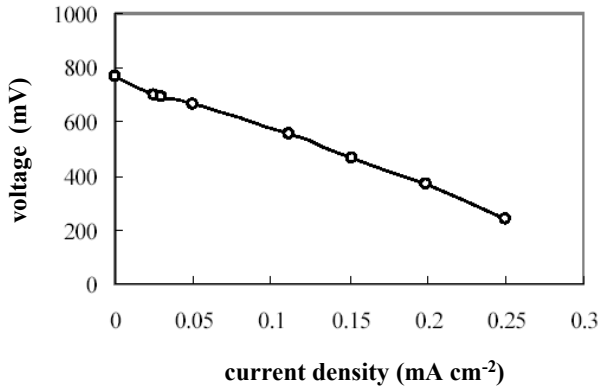

Figure 2. The polarization curve for a fuel cell with a C_{60} pellet.

To examine the effect of C_{60} as an additive to PEM, a Nafion 117 membrane was doped with 1 wt% of C_{60}, and the AC impedance was measured under dry condition. Table 1 lists the proton conductivity of the doped and undoped Nafion.

Table 1. The proton conductivity of doped Nadion films

	σ, mS cm^{-1}
Nafion 117	1.7
Nafion 117 + C_{60}	15

The proton conductivity of C_{60}-doped Nafion shows roughly an order of magnitude improvement over Nafion only under dry condition.

MEA's were also assembled for power measurements using dry H_2 and O_2 gases. Table 2 lists the maximum power density which was normalized by the thickness of the film, thus the unit in mW/cc.

Table 2. Maximum power density of fuel cell with dry Nafion 117 and dry Nafion 117 doped with C_{60}.[a]

	mW/cc
Nafion 117	16
Nafion 117 + C_{60}	200

Nafion doped with C_{60} exhibits the power which is more than an order of magnitude higher than Nafion 117 alone.

Figure 3 shows the transient voltage of a fuel cell with the C_{60}-doped Nafion, a sharp contrast in stability from Nafion alone under dry condition. Our results suggest a promising potential of C_{60} as an additive for Nafion under dry condition.

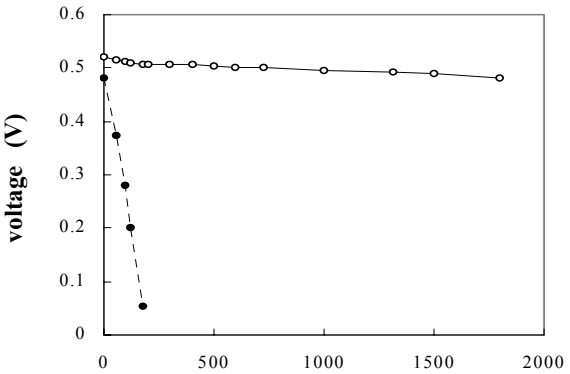

Figure 3. The voltages as a function of time at 30 ºC with dry gases under 0.3 A cm^{-2} of constant current: the Nafion doped with C_{60} (solid line) and Nafion (broken line).

Acknowledgment

This work was supported by the High Temperature Polymer Membrane Program at U.S. Department of Energy.

References

1. Haile, S. M.; Boysen, D. A.; Chisholm, C. R. I.; Merle, R. B.; *Nature*, **2001**, *410*, 910.
2. Wainright, J. S.; Wang, J.-T.; Weng, D.; Savinell, R.F.;Litt, M. H. *J. Electrochem. Soc.* **1995**, *142*, L121.
3. Schuster, M.F.H.; Meyer, W. H.; Schuster, M.; Kreuer, K. D. *Chem. Mater*. **2004**, *16*, 329.
4. K. Hinokuma, J. *Electrochem. Soc.* **2003**, *150*, A112.
5. C. Reed, K.-C. Kim, R. D. Bolskar, L. J. Mueller, *Science*, **289**, 101 (2000).

DESIGN OF POLYMER BLENDS FOR PROTON-EXCHANGE MEMBRANES IN FUEL CELLS

S. Swier, M. T. Shaw and R. A. Weiss

Dept. of Chemical Engineering and Polymer Program
Institute of Materials Science, University of Connecticut
Storrs, CT 06269

Introduction

Proton-exchange membranes (PEM) must have high proton conductivity and sufficient mechanical and chemical stability to withstand the conditions in the fuel cell. Perfluorinated polymer electrolyte membranes such as Nafion™ have been the principal choice in the past for this purpose. However, these materials are expensive, have relatively poor resistance to methanol transport (which is important in direct methanol fuel cells) and have poor mechanical properties when highly swollen by water. Contemporary PEM research involves the development of new polymer electrolytes based on hydrocarbon polymers [1].

Further flexibility in PEM materials design can be achieved by using polymer blends in which each component fulfills a different membrane requirement [2]. One strategy consists of combining a sulfonated aromatic hydrocarbon polymer with an engineering thermoplastic where intermolecular interactions assure a high level of compatibilization. PEKK is a commercial high temperature thermoplastic that has high temperature stability, excellent chemical and solvent resistance and excellent mechanical properties. Because of a higher ketone content, PEKK has a higher glass transition temperature (T_g), melting point (T_m), stiffness and strength than poly(ether ether ketone), PEEK, which has also been used to prepare PEMs.

This paper describes PEMs based on blends of sulfonated PEKK (SPEKK) and pol(etherimide), PEI. The idea of using SPEKK/SPEKK blends for PEMs is also discussed.

Experimental

PEKK (terephthaloyl/isophthaloyl ratio = 8/2) was obtained from Oxford Performance Materials. PEI Ultem 1000 was provided by General Electric. PEKK was sulfonated with a 53/47 (v/v) mixture of concentrated and fuming sulfuric acids. The ion-exchange capacity (IEC) in [meq/g], was determined by titration. Membranes of SPEKK, SPEKK/PEI and SPEKK/SPEKK blends were prepared by solution casting 5% (w/v) solutions in N-methyl-2-pyrrolidone (NMP) or dimethylacetamide (DMAc). Typically, the solvent was allowed to evaporate for about 1 day at 60°C, after which the films were dried at 120°C under vacuum for 3 days.

The blend membranes were characterized using transmission electron microscopy (TEM), atomic force microscopy (AFM), differential scanning calorimeter (DSC) and thermogravimetric analysis (TGA). A frequency response analyzer (Solartron SI 1260) combined with a potentiostat (Solartron SI 1287) was used to measure the proton conductivity of hydrated membranes. Single cell performance curves of the membranes were determined using a membrane-electrode-assembly (MEA) at 80°C and 1 atm. Gasses for the anode and cathode side were hydrogen and oxygen, respectively.

Results and Discussion

Thermal properties of SPEKK and PEI. TGA indicated that PEI was thermally stable up to 460°C, but desulfonation of SPEKK occurred at ca. 260°C. The T_g of dry SPEKK increased linearly from 150°C for PEKK to 215°C for SPEKK-IEC = 2.6 meq/g. The increase was due to hydrogen bonding between sulfonic acid groups that reduces chain mobility. Water, however, plasticizes the SPEKK; e.g., when equilibrated in a 98% R.H. environment, the T_g of SPEKK with IEC = 2meq/g decreased from 200°C to 60°C. PEI had a glass transition of 220°C.

Conductivity and swelling of SPEKK. The room temperature proton conductivities of hydrated SPEKK membranes increased exponentially with sulfonation level (Figure 1). This is due to the increase in the concentration of sulfonic acid sites, which form the locus for proton transport, and the increase in water uptake which plays an important role in increasing the mobility of protons through the membrane. SPEKK with an IEC of 1.9 meq/g. had a conductivity comparable to Nafion™ 112 (IEC = 0.9 meq/g, σ = 60 mS/cm), and its hydration number, $n(H_2O)/n(SO_3H)$at 98% R.H. was 10, which was also comparable to that for Nafion™ [3].

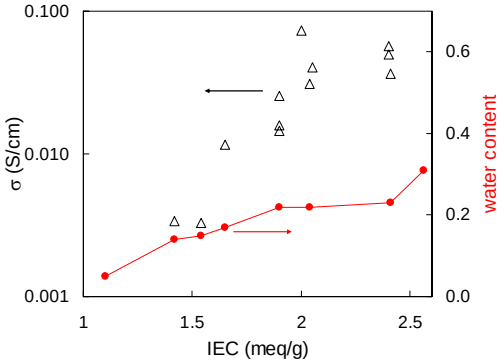

Figure 1. Proton-conductivity, σ in S/cm, and water uptake, $(w_{wet}-w_{dry})/w_{wet}$, of SPEKK in a 98% R.H. environment at 25°C

MEA performance comparable to Nafion™ was obtained (Figure 2) for SPEKK with IEC < 2 meq/g. However, the durability of highly water swollen membranes was poor. The use of SPEKK with a high IEC and corresponding conductivity in a polymer blend with either PEI or a low IEC SPEKK were investigated to remedy this problem.

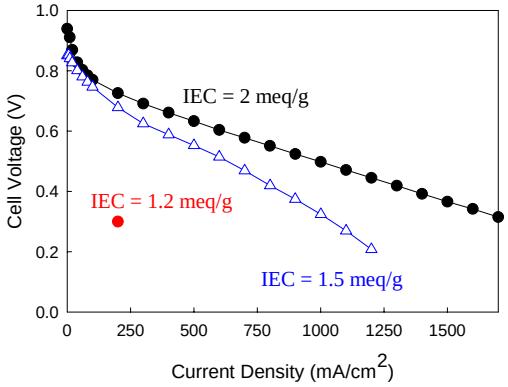

Figure 2. Membrane-electrode assembly (MEA) performance curves of SPEKK membranes at 80°C in H_2/O_2 (1 atm, 75 % R.H.); Nafion™ 112 under these conditions: 0.8 V at 200 mA/cm^2

Ternary phase diagram. The blends were cast from NMP. Unfortunately, the solubility of the SPEKK/PEI mixtures decreased with increasing IEC (Table 1), which is probably due to strong ion-dipole interactions.

Table 1. Cloud points as a function of IEC for SPEKK/PEI in NMP; *DMAc used as casting solvent.

IEC, meq/g	wt% SPEKK/PEI 50/50 in NMP at cloud point
1.1	24
1.5	22
1.7	23
2	17
2	16*
2.6	15

Binary blend morphology and conductivity. The SPEKK/PEI and SPEKK/SPEKK blends cast at 60°C exhibited a two-phase morphology, see Figure 3. DSC analysis indicated that the two phases in the SPEKK/PEI were essentially the pure components, but that some intermixing occurred in the SPEKK/SPEKK blend. This may be due to a combination of a postponed cloud point and the stronger intercomponent interactions in this blend.

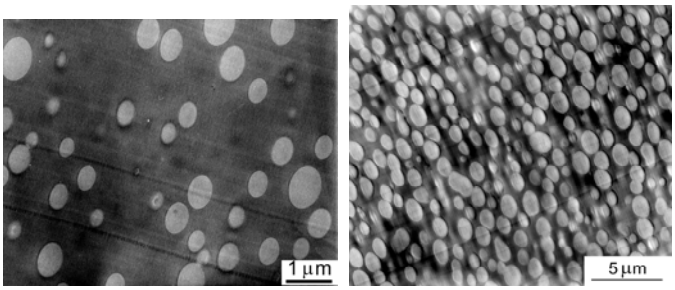

Figure 3. TEM micrographs of blends of SPEKK (IEC = 2 meq/g) with 15 wt% PEI (*left*) and with 50 wt% of SPEKK (IEC = 1.2 meq/g) (*right*); both blends were cast from NMP solutions at 60°C and stained with lead nitrate.

The effect of PEI content on particle size, conductivity and water uptake is summarized in Figure 4 (*left*). Adding the non-conductive polymer reduced the water swelling of these PEMs, but at the expense of a significant drop in conductivity of the SPEKK/PEI blends. The SPEKK/SPEKK blends, however, retained high conductivity, even in a 50/50 blends (see Table 2, cfr.: σ is 8 mS/cm for a 50/50 SPEKK IEC 2 / PEI blend). In that case, the low IEC component, which has relatively low water sorption and conductivity by itself, provided mechanical strength and durability to the membrane. Further investigation of the SPEKK/SPEKK system is currently in progress.

Table 2. Conductivity of 50/50 blends of SPEKK (IEC = 2 meq/g) with SPEKK's of different IEC's at 25°C and 98% R.H.

IEC, meq/g	σ, mS/cm
0.8	24
1.2	32
1.5	34

Effect of casting parameters. High-temperature annealing of the films after casting had no noticeable effect on the morphology, which may be due to low molecular mobility in the blend. A second strategy for controlling the morphology was to vary the temperature during casting. The effect of casting temperature is shown in Figure 4 (*right*). Smaller particle sizes were obtained by increasing the casting temperature. This is probably the combined result of postponed phase separation due to the UCST behavior of the ternary blend and faster solvent evaporation resulting in a frozen-in morphology. Note that the particle size does not significantly affect the conductivity or swelling.

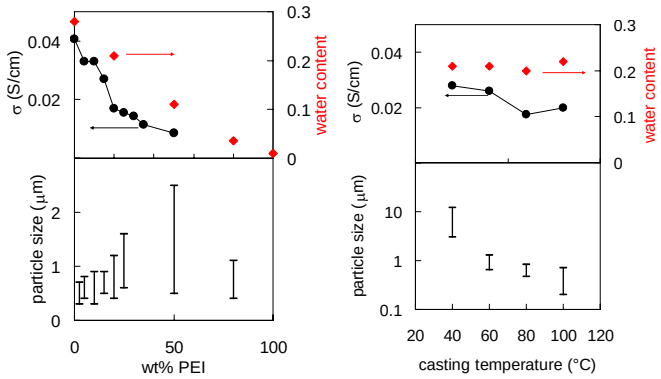

Figure 4. Properties of SPEKK (IEC = 2 meq/g) / PEI blends; cast at 60°C (*left*) and for 15 wt% PEI (*right*); water content and conductivities were determined at 25°C and 98% R.H.; brackets: range of smallest to largest particles

Preliminary results on the use of DMAc instead of NMP as the casting solvent indicate that significant improvements in membrane fuel cell durability can be achieved using this solvent. The reason for this effect might be different SPEKK-solvent interaction and/or a specific chemical reaction involving the DMAc.

Conclusions

Sulfonated poly(ether ketone ketone) (SPEKK) is a potential proton-exchange membrane material for fuel cell applications. Proton conductivities and MEA performance data are competitive with Nafion™ under similar conditions. A large depression in glass transition and significant swelling, however, limits the long term durability of SPEKK membranes. That limitation can be resolved by forming PEMs from blends of SPEKK with poly(ether imide) (PEI), wherein the SPEKK provides conductivity and the PEI improves the mechanical stability of the membrane. A promising alternative approach is the use of blends of SPEKK's with different sulfonation levels.

A specific objective of our work is to achieve a spinodal-like morphology in the membrane, where the interconnected SPEKK phase optimizes proton conductivity and a lower conductivity matrix consisting of PEI or SPEKK with low sulfonation level will provide mechanical stability of the hydrated membranes.

Acknowledgement. The authors wish to thank the Department of Energy (Grant 69797-001-03 3D) and Connecticut Innovations, Inc (Yankee Ingenuity Grant 01Y09) for support of this research, Vijay Ramani and Prof. J. E. Fenton for their help with the MEA tests and Oxford Performance Materials for supplying PEKK.

References

[1] Rikukawa, M.; Sanui, K. *Prog. Polym. Sci.* **2000**, *25*, 1463.
[2] Cui, W.; Kerres, J.; Eigenberger, G. *Sep. Purif. Technol.* **1998**, 14, 145.
[3] Zawodzinski, T.A.; Neeman, M.; Sillerud, L.O.; Gottesfeld, S. *J. Phys. Chem.* **1991**, 95, 6040.

DEVELOPMENT OF NON-PERFLUORINATED POLYMER ELECTROLYTE MEMBRANES

L. Hedhli, K. Adjemian, S. Gaboury, P. Piccione, A.Lemacon

Atofina Chemicals, Inc. 900 First Av.
King of Prussia, PA 19406

Introduction

Intensive work in the area of polymer electrolyte membrane fuel cells (PEMFC) in recent years has lead to enhancements in many aspects of this technology [1,2]. Despite these improvements, the perfluorinated sulfonated ionomer membrane, PFSI, still does not meet several of the major requirements needed to make fuel cell technology commercially viable including: low cost, mechanical strength, dimensional stability at elevated temperatures and low fuel crossover [3]. Atofina has been working on developing a new class of non-perfluorinated polymer electrolyte membranes.

Results and Discussion

As it is increasingly reported, it is possible to control the phase morphology of polymer composites thin films to achieve a unique set of properties [4,5]. Thus, our approach based on a composite polymer structure between a fluoropolymer -Kynar® polyvinylidene fluoride, PVDF - and a proprietary non-perfuorinated polyelectrolyte, enabled us to markedly improve the mechanical properties, fuel crossover resistance and thermal stability compared to PFSI, while meeting the low cost target required by the industry. In this work, Nafion® 112 membrane was used as the commercial PFSI membrane control in all experiments. Mechanical and swelling properties of these membranes - ranging from 17 to 50µm - match or exceed those of the control. At 25 µm thick, the PVDF-based membrane shows superior tear resistance compared to the 50µm control. The inherent strength of the PVDF-based membranes is further demonstrated by comparing axial creep resistance. Figure 1 depicts the gradual linear elongation at 80°C and 120 °C. While the control exhibits relatively large continual deformation with time, the developmental membrane exhibits almost no creep under the same conditions, even at 120°C.

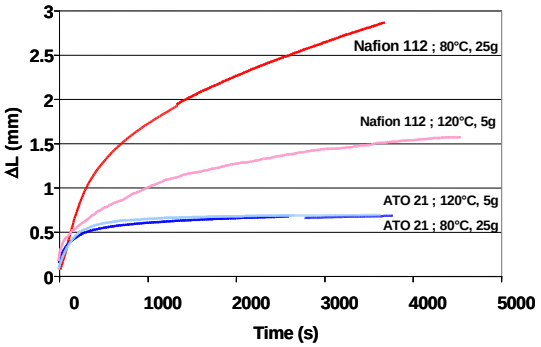

Figure 1. Axial creep data of ATO21 and PFSI membranes at 80°C/25g load and 120°C/5 g load.

A comparison of the electrochemical properties for the PVDF-based membranes and a commercial membrane is shown in Figure 2, where all membrane electrode assemblies (MEAs) were prepared by hot pressing ELAT® electrodes with a Pt loading of 0.4 mg/cm^2 onto the membrane. Resistance values were measured using the current interrupt method. As one can see, the polarization curve of the MEA based on ATO 31C (in blue) is essentially superimposable to the control.

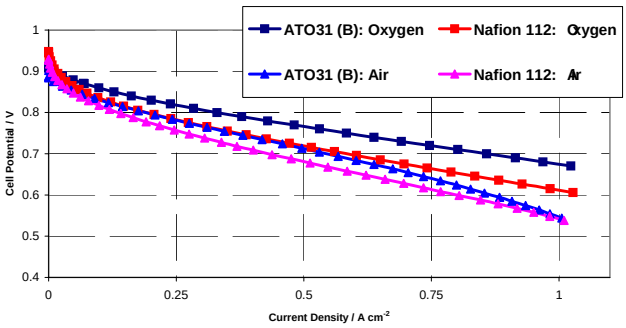

Figure 2. Polarization curve. T= 60ºC, 100% RH, 1 atm.

Furthermore, Figure 3 shows two single-cell runs using ATO27 and ATO31 developmental membranes. Over the 1000 h period showed in this figure, the voltage loss was similar in magnitude to the 20% loss reported by Roelofs *et al.* for a commercial PFSI membrane after 600 hours [6]. Increased stability and overall fuel cell performance during long-term usage may be enhanced with the development of MEAs specifically tailored for our PVDF-based membranes, in particular through optimization of the electrode-membrane interface.

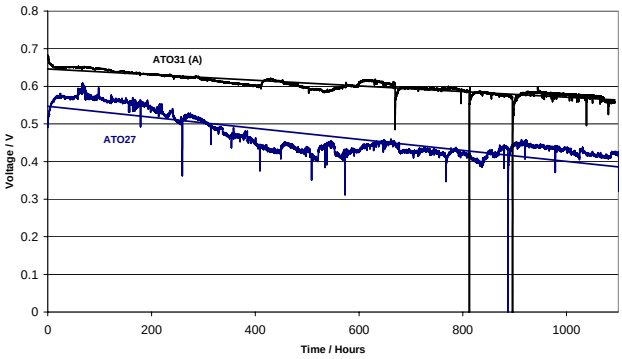

Figure 3. Endurance test. T= 60ºC, 100% RH, 1 atm, H_2/O_2

Conclusions

A unique polymer electrolyte membrane technology has been developed based on alloys of Kynar® PVDF with a proprietary polyelectrolyte. Polarization curves for the 25 µm PVDF-based membranes show similar electrical performance than Nafion® 112 membranes. While optimization of the electrode-membrane interface is expected to yield further improved fuel cell performance, long-term durability testing for these PVDF-based membranes has been demonstrated well over 1500 hours. This new technology has already demonstrated the ability to produce membranes with good physical properties, good electrical properties, and a process that is flexible and easily scaled up.

References

(1) Wheeler, D. J. *J. New Mat. Electrochem. Systems* **2001**, 4, 233
(2) Ralph, T.; Hogarth, M. P. *Platinum Metals Rev.* **2002**, *46* (1), 3
(3) Kerres, J. A. *J. Membrane Science* **2001**, 185, 3-27
(4) Wang, H. ; Composto, R.J. *Europhys. Lett.* **2000**, 50, 622
(5) *Newby Z.; Composto R.* J. *Macromolecules* **2000,** 33, 3274
(6) Roelofs, M.; Reichert, D.; Kourtakis, K. *Fuel Cell Seminar* **2002**.

DIRECT SYNTHESIS OF DISULFONATED POLY(ARYLENE ETHER KETONE)S AND INVESTIGATION OF THEIR BEHAVIOR AS PROTON EXCHANGE MEMBRANE (PEM)

Yanxiang Li, Thekkekara Mukundan, William Harrison, Melinda Hill, Mehmet Sankir, Juan Yang, and James E. McGrath

Department of Chemistry and Materials Research Institute, Virginia Tech, Blacksburg, VA 24061

Introduction

Sulfonated poly(arylene ether ketone)s are promising candidates for proton exchange membranes in fuel cells. These materials have excellent physical properties, including high modulus, toughness, and good thermal and chemical resistance [1]. The method of direct polymerization of sulfonated comonomers has been proven to be better than the post sulfonation method, in that it can control the degree of sulfonation and avoid several side reactions [2, 3]. In this research, two sulfonated ketone type comonomers were synthesized. These comonomers were subjected to nucleophilic aromatic substitution step copolymerization with the unsulfonated monomers and 4, 4'-hexafluoroisopropylidenediphenol (6F-BPA) to obtain two kinds of copolymers containing sodium sulfonated groups. The copolymers were characterized by various methods, and their typical properties as PEM, such as IEC and water uptake, were investigated.

Experimental

Materials. 4, 4'-hexafluoroisopropylidenediphenol (6F-BPA), received from Ciba, was purified by sublimation and dried in vacuo. The ketone type monomers: 4, 4'-difluorobenzophenone (DFBP), and 1, 4-Bis (p-fluorobenzoyl) benzene (PBFB) were purchased from Aldrich and used as received, but all monomers were dried under vacuum prior to use. N- Methyl-2-pyrrolidinone (NMP; Fisher) was vacuum-distilled from calcium hydride onto molecular sieves in vacuo and then stored under nitrogen. N, N-dimethylacetamide (DMAc; Fisher) was used as received. Toluene, sodium chloride, and 30% fuming sulfuric acid were obtained from Aldrich and used as received. Potassium carbonate was vacuum dried before polymerization.

Synthesis of the disodium salt of comonomers. Sulfonated derivatized comonomers (SDFBP, SPBFB) were synthesized according to a modified literature method [2, 4]. A typical procedure was as follows: PBFB (30g) was dissolved in 60 mL of 30% fuming sulfuric acid in a 100mL, three necked flask equipped with a mechanical stirrer and a nitrogen inlet/outlet. The solution was heated to 150 ^{o}C for 6 hours to produce a homogeneous solution. Then it was cooled to room temperature, and poured into 450mL of ice-water. Next, 110.0g of NaCl was added which produced a white solid. The latter was filtered and re-dissolved in 300mL of deionized water. The solution was treated with 2N NaOH aqueous solution to a pH of 6~7 and diluted with deionized water to 500mL. Then, 110.0g NaCl was added to salt out the sodium form sulfonated monomer. The crude product was recrystallized twice from a mixture of isopropyl alcohol and deionized water (3/1 in volume). The anticipated structure was obtained at around 85% yields.

Polymerization. The copolymerization procedures for all ketone monomers were similar. A typical polymerization for PBFB-30 is described as follows: 3.3623 (10 mmol) 6F BPA, 2.2562 (7 mmol) PBFB, and 1.5792 (3 mmol) SPBFB were added to a 3-neck flask equipped with mechanical stirrer, nitrogen inlet and a Dean Stark trap. Next, 1.15 equivalent of potassium carbonate and NMP were introduced to afford a 33% solids concentration. Toluene (NMP/Toluene=3/4, v/v) was used as an azeotropic agent. The reaction mixture was heated under reflux at 150 ^{o}C for 4 hours to remove most of the toluene and dehydrate the system. Next, the temperature was raised slowly to 175 ^{o}C. The solution became viscous after about 7 hours and was subsequently cooled to room temperature and diluted with NMP. The solution product was then isolated by addition to stirred deionized water. The precipitated fibrous copolymer was heated around 50 ^{o}C in deionized water overnight. Then it was filtered and vacuum dried at 120 ^{o}C for 24 hours.

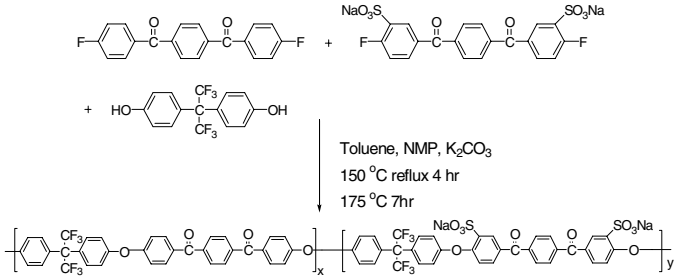

Scheme 1. Synthesis of PBFB copolymer

Membrane preparation. Copolymer 1.0g was dissolved in 20mL of DMAc. The solutions were first filtered with 0.45 μm syringe filters, and then cast onto clean glass substrates. The film was carefully dried with infrared heat at gradually increasing temperature (up to ~ 60 ^{o}C) under a nitrogen atmosphere. The sodium form membranes then were converted into the acid form by boiling in 2N H_2SO_4 for 2 hours, followed by boiling in deionized water for 2 hours. The acid form films were stored in fresh deionized water.

Characterization

FTIR spectra were measured with a Nicolet Impact 400 FT-IR spectrometer with thin homogenous cast films. ^{1}H NMR spectra were obtained with a Varian 400 MHz spectrometer using DMSO-d_6 as a solvent. Intrinsic viscosity (IV) measurements were obtained in NMP at 25 ^{o}C using a Cannon Ubbelohde viscometer. Number average molecular weights (M_n) of obtained copolymers were determined by gel permeation chromatography based on polystyrene standards. Membrane water uptake was determined by a simple weight difference approach: Films were vacuum dried at 85 ^{o}C for 40 hours, weighed and then immersed in deionized water at room temperature for 24 hours. The wet membranes were wiped dry and quickly weighed again. The ratio of weighed gain to initial film weight was expressed as % water uptake. IEC was measured by titration with 0.01 N NaOH standard solution.

Results and Discussion

SDFBP and SPBFB comonomers were synthesized successfully and characterized by ^{1}H NMR. Figure 1 is the representative ^{1}H NMR spectrum for SPBFB comonomer.

Two series of poly(arylene ether ketone) copolymers with high molecular weights were synthesized via step-condensation process as show in Table 1 and Table 2. Copolymers with 0-50 mole % sulfonated comonomer contents were prepared. M_n and Intrinsic viscosity values correlated well. Calculated ion exchange capacity (IEC) and experimental results were shown. FTIR and ^{1}H NMR spectra were used to identify and characterize the two series of sulfonated copolymers. The degree of sulfonation determined by NMR is using the method in reference [3]. Figure 3 shows that in FTIR spectra with increasing of the sulfonation degree, the peak intensity at 1030 cm^{-1}and 1087 cm^{-1} will increase accordingly. Peaks

at 1030 cm^{-1} and 1087 cm^{-1} correspond to symmetric and asymmetric stretching of the sodium sulfonate groups. The IR spectra can thus qualitatively determine the functional groups of the synthesized copolymers.

The influence of sulfonated comonomer content on water uptake of copolymer membranes in the acid form is depicted in Figure 2. The copolymers synthesized using the SPBFB comonomer showed lower uptakes of water relative to the copolymers made with SDFBP comonomer at the same degree of sulfonation. This may be because the structure of PBFB copolymer is more rigid than the structure of DFBP copolymer and the space between sulfonic acid groups in PBFB copolymer is larger than that in DFBP copolymer.

Table 1. Copolymer Characterization at Different Degree of Sulfonation for DFBP/SDFBP Series

Polymer	Degree of Sulfonation by NMR	$[\eta]_{25\ ^oC}$ (dl/g)	M_n	IEC(meq/g)	
				Cal.	Exp.
DFBP-00	0	1.48	148,459	0	0
DFBP-10	9	1.03	76,275	0.36	0.13
DFBP-20	18	0.92	46,901	0.72	0.55
DFBP-30	29	1.00	47,306	1.05	0.94
DFBP-40	40	1.44	59,620	1.38	1.12
DFBP-50	47	0.69	32,580	1.70	1.35

Table 2. Copolymer Characterization at Different Degree of Sulfonation for PBFB/SPBFB Series

Polymer	Degree of Sulfonation by NMR	$[\eta]_{25\ ^oC}$ (dl/g)	M_n	IEC(meq/g)	
				Cal.	Exp.
PBFB-00	0	0.41	39,687	0	0
PBFB-20	22	2.15	89.784	0.62	0.43
PBFB-30	29	1.00	55,630	0.90	0.74
PBFB-40	40	1.00	51,077	1.17	0.87
PBFB-50	48	3.30	134,777	1.43	1.15

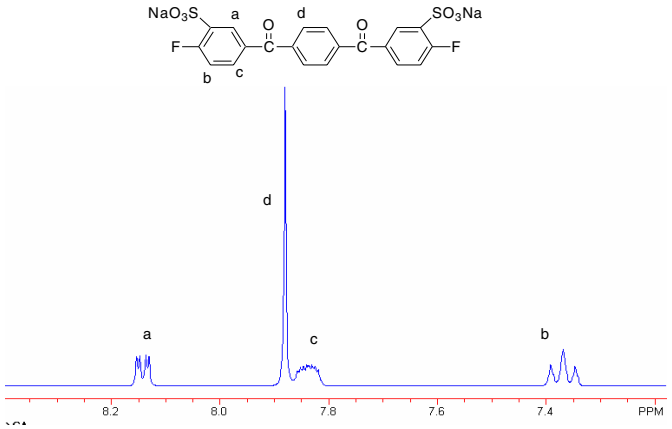

Figure 1. ^{1}H NMR spectrum of SPBFB monomer

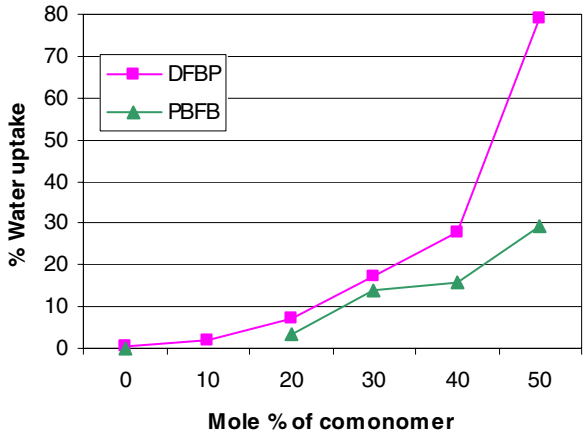

Figure 2. Water uptakes of copolymer membranes

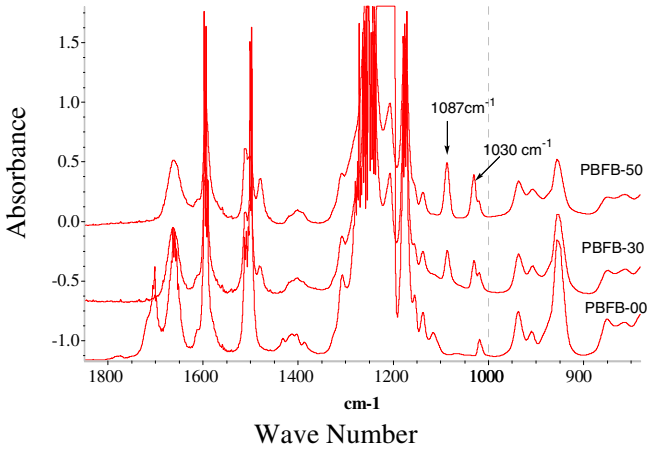

Figure 3. Influence of the degree of sulfonation on the FTIR spectra of PBFB/SPBFB series copolymers

Conclusions

Two sulfonated ketone type comonomers were successfully synthesized, and copolymerized to synthesize poly(arylene ether ketone) copolymers with sulfonation degree from 0 to 50%. PBFB series copolymers showed lower water uptakes relative to DFBP series at the same degree of sulfonation because of the more rigid structure of PBFB copolymer. Further discussion of their properties will be described at the meeting.

Acknowledgement. The authors would like to thank the Department of Energy (contract # DE-FC36-01G011086)

References

(1) J. I. Kroschwitz, Ed; *Encyclopedia of Polymer Science and Engineering.* **1988**, Vol. 12, 313

(2) Shengzhou Liu, Feng Wang, Tianlu Chen; *Macromol. Rapid Commun.* **2001**, 22, No.8, 579

(3) William L. Harrison, Feng Wang, Jeffery B. Mecham, Vinayak A. Bhanu, Melinda Hill, Yu Seung Kim, James E. McGrath; *Journal of Polymer science: Part a: Polymer Chemistry*, **2003**, Vol. 41,2264

(4) Feng Wang, Jianke Li, Tianlu Chen, Jiping Xu; *Polymer*, **1999,** 40, 795

DISULFONATED POLY(ARYLENE ETHER PHENYL PHOSPHINE OXIDE SULFONE) TERPOLYMERS FOR PEM FUEL CELL SYSTEMS

Kenton B. Wiles, Cesar Munoz de Diego, James E. McGrath

Department of Chemistry and Materials Research Institute,
Macromolecular Science and Engineering Program
Virginia Polytechnic Institute and State University
Blacksburg, VA 24061

Introduction

Novel engineering systems based on proton exchange membrane (PEM) fuel cells as an alternate energy source is considered very attractive due to diminishing natural resources, global warming, acid rain and smog producing precursors associated with combustion energy processes. PEM fuel cells produce electrical energy from electrochemical reactions by delivering fuel (H_2) to the anode and an oxidizer (O_2) to the cathode. Limitations of the fuel cell include usable temperature ranges, hydrogen storage, fuel efficiency and cost. Polymer electrolyte membrane fuel cells are limited by the liquid water temperature range. The hydrogen ions are transported across the membranes in an aqueous environment and thus above the boiling point of water, the mechanism becomes severely limited. Temperatures above 100 °C would decrease platinum poisoning by carbon monoxide and would increase reaction kinetics.

PEMs based on Nafion© are limited to membrane performance below 80 °C presumably due to a thermal transition of the hydrated form and loss of water, dehydration. A novel approach[1] could involve the use of heteropolyacids (HPA) as an additive for compatible sulfonated hydrocarbon polymers. Many HPAs have high protonic conductivities but are also water-soluble. HPA composite membranes based on polymers that have a high affinity for the HPA additive can, in principle, make the HPA complex insoluble in water while still retaining high protonic conductivity at elevated temperatures.

Phosphine oxide containing polymers based on poly(arylene ether)s and poly(arylene thioether)s have been reported to be stable at high temperatures while being flame retardant and plasma resistant.[2] Generally these high performance polymers are used as flame retardant materials that also complex with certain metals to help in dispersion and retention of inorganic/organic additives.[3] Furthermore, reports on phosphine oxide containing poly(arylene ether)s that have good interactions with a wide variety of thermoplastics and thermosets like phenoxy, epoxy and vinylester resins has recently been described.[4] It has been proposed that these phosphine oxide containing materials could have an increased interaction with functionalized carbon fibers, glass fibers or inorganic additives due to the very polar phosphine oxide moieties. Synthetic procedures to produce phosphine oxide containing polymers have mainly incorporated 4,4'-bis(fluorophenyl) phenyl phosphine oxide (BFPPO), as the electophile and bisphenols or thiobisphenols as the nucleophilic containing monomers.

By dissolving inorganic heteropolyacids in a dipolar solvent and blending the solution with dissolved ionic polymeric materials, composite membranes that aid in protonic conductivity at high temperatures can be solution cast. The HPAs, in the crystalline form, used in this type of research are protonically conductive inorganic fillers that may have a strong interaction with specific functional groups in the polymeric material. It has been hypothesized that the HPA in PEMs give alternative mechanisms to proton transport at temperatures above 100°C where very little water is present. Composite membranes based on phosphotungstic acid have recently been shown to have higher conductivities and lower water swelling at elevated temperatures as compared to the pure copolymer membranes. Therefore, the present research employs phosphotungstic acid hydrate as an inorganic filler incorporated into 45 mol% disulfonated poly(arylene phenyl phosphine oxide ether sulfone) terpolymers synthesized using nucleophilic aromatic substitution reactions (**Figure 1)** for use in PEM fuel cells at temperatures above 100°C. **Figure 2** indicates the possible interactions present in the 45mol% disulfonated PPO/HPA composite films that retain the water-soluble HPA molecules in the organic soluble PEM. These interactions aid in decreasing extraction of the HPA in aqueous environments, thereby allowing very little, if any, leaching of the ionically conducting HPA.

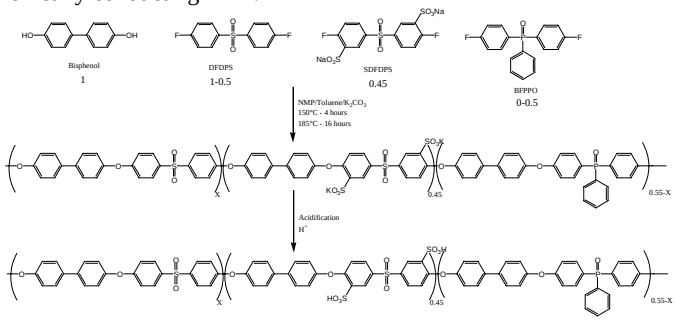

Figure 1. Synthesis of disulfonated poly(arylene phenyl phosphineoxide ether sulfone) terpolymers

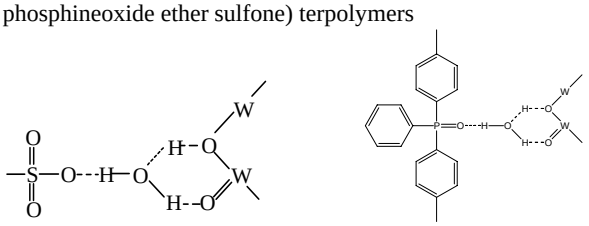

Figure 2. Possible interactions of HPA with sulfonates and phosphine oxide moieties

Experimental

Materials. 4,4′- bis(fluorophenyl) phenyl phosphine oxide (BFPPO) was synthesized using a reported procedure.[5] Anhydrous potassium carbonate and 4, 4′ - difluorodiphenylsulfone (DFDPS) were obtained from Aldrich. NMP and toluene (both from Burdick and Jackson) were dried as follows: NMP was dried overnight over calcium hydride with a nitrogen purge and distilled at reduced pressure; toluene was dried over molecular sieves. Disulfonation of DFDPS was performed in a similar fashion as previously described.[6] Phosphotungstic acid hydrate was obtained from Fluka Chemika and dried at 80°C for 24 hours before use.

Films and Composite Membranes. Neat films of the copolymers were cast from 5 weight% solution in DMAc in a glass casting tray and carefully dried in a vacuum oven. The salt form films were then transformed into the acid form by boiling the films in 0.5M H_2SO_4 for 2 hours to convert the pendant sulfonic salt groups into free acid groups. The residual sulfuric acid was removed by boiling the films in deionized water for 2 hours. The composite membranes were obtained by dissolving both the acid form membranes and 30 weight percent HPA in DMAc in separate containers. The solutions were combined and allowed to mix by stirring for 24 hours. The solution was then cast onto glass casting trays and dried in a vacuum oven. Reacidification was performed by either a room temperature method (M1) or a high temperature boiling

method (M2).[7] HPA extraction was measured by the difference in weight before and after reacidification of the composite membranes. The room temperature method (M1 = method 1) acidified the films using 1.5 M H_2SO_4 in water for 24 hours. The residual H_2SO_4 was removed by immersing the films in D. I. water for an additional 24 hours. The boiling method (M2 = method 2) acidified the films using 0.5 M H_2SO_4 in water at boiling conditions and then removing the residual acid by boiling in water for an additional 2 hours.

Characterization. Membrane water uptake was determined by a weight difference approach as described previously. Proton conductivity of the membranes under fully and partially hydrated conditions was determined at 120°C using a Solatron 1260 Impendence/Gain-Phase Analyzer over the frequency range of 10Hz-1 MHz following the reported procedure.[8] The resistance of the films was taken at the frequency that produced the minimum imaginary response. The conductivity of the membranes was calculated from the measured resistance and the geometry of the cell.

Results and Discussion

Terpolymerizations produced terpolymers with high intrinsic viscosity values ranging from 1.0 to 1.2 dL/g in NMP at 30°C. Successful incorporation of various mole percents of phenyl phosphine oxide (PPO) moieties into the 45mol% disulfonated control poly(arylene ether sulfone) copolymer (BPSH 45) was monitored by FTIR of thin films and ^{1}H NMR of 5wt% solutions in DMSO-d_6. Water uptake measurements of the neat terpolymers are plotted in **Figure 3**.

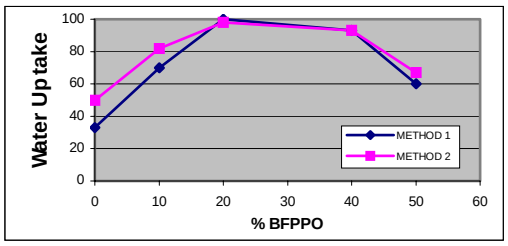

Figure 3. Water uptake measurements of neat terpolymers

Successful incorporation and complex formation of the HPA additive with phosphine oxide moieties were monitored by FTIR and ^{31}P NMR. FTIR indicated significant band shifting for both the sulfonate and phosphine oxide groups when HPA was incorporated. ^{31}P NMR showed a considerable shift of the phosphorous peak when HPA was incorporated into the entire series of terpolymers. Both of these sets of data suggest strong interactions of the HPA additive with the phosphine oxide moieties. Water uptake and extraction of the composite membranes are shown in **Figure 4** and **Figure 5**.

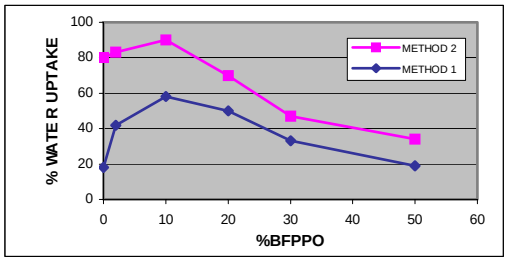

Figure 4. Water uptake of 30wt% HPA composite membranes for Method 1 and Method 2 reacification techniques

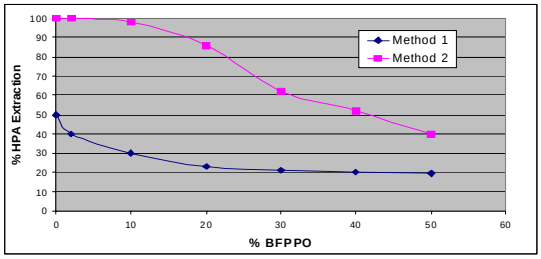

Figure 5. Extraction of HPA additive in 30wt% HPA composite membranes

Table 1 indicates the protonic conductivity and water sorption of both the neat polymers and the composite polymers with reference to the control BPSH 45 copolymer containing no PPO moieties. The selected PPO containing terpolymers indicate that with increasing phenyl phosphine oxide moieties, the conductivity decreases. This is presumably due to the strong interactions of the PPO with the sulfonate moieties. However, when HPA was incorporated, the conductivity increased at high temperatures and water sorption decreased. One might suggest that the strongly interacting nature of the terpolymer functional groups with the surface functionality of the HPA promotes this observation.

Table 1. Conductivity at 120°C and 45% R.H. and water uptake of neat and composite membranes as compared to 45mol% copolymer control containing no PPO moieties

Membrane	Conductivity M2 (mS/cm) Neat Polymer	% H_2O Uptake of Neat Polymer	Conductivity M1 (mS/cm) With 30wt%HPA	%H2O Uptake of Composite M1
BPSH 45	11	50	14	35
10% PPO	9	80	21	58
20%PPO	3.3	95	20	50
30%PPO	3.1	90	15	35
40%PPO	3	88	10	28
50%PPO	2.9	65	7	20

Conclusions

Water sorption measurements indicated lower water sorption was possible in the terpolymer composite films relative to the neat film. Extraction of the HPA filler was found to be minimal for the acidification at room temperature while the acidification at boiling temperatures increased the extraction up to a factor of four. The high temperature/low humidity conductivity measurements indicated increased performance by incorporating HPA into the disulfonated terpolymer membranes using the room temperature reacidification technique.

Acknowledgments. The authors would like to thank Department of Energy for funding under contract sub-56844-FMIJOBDOE-99241.

References

[1] Kim, Y.S., Wang, F., Hickner, M., Zawodzinski, T. A. and McGrath, J. E. *J. Membrane Sci.*, 2003, 212, 263-282.
[2] Riley, D.J.; Gungor, A.; Srinivasan, S.A.; Sankarapandian, M.; Tchatchoua, C.; Muggli, M.W.; Ward, T.C. and McGrath, J.E., *Polym Eng. Sci.*, 1997, 37(9), 1501.
[3] Smith, C.D.; Grubbs, H.J.; Webster, H.F.; Gungor, A.; Wightman, J.P. and McGrath, J.E., *High Perfor. Polym.*, 1991, 4, 211.
[4] Kosmala, B.; Schauer, J. *J. Appl. Polym. Sci.*, 2002, 85, 1118.
[5] Riley, D. J., *PhD. Dissertation*, VPI & SU, 1997.
[6] Wiles, K. B.; Munoz, C. M. and McGrath, J. E. *Polymer Preprints*, **2004**, 45(1), 724.

[7] Kim, Y. S.; Wang, F.; McCartney, S.; Hong, Y. T.; Harrison, W.; Zawodzinski, T. and McGrath, J. E. *J. Polym. Sci.; Part B: Poly. Phys.* **2003**, 41, 2816.
[8] Zawodzinski, T.; Neeman, M.; Sillerud, L. O. and Gottesfeld, S. *J. Phys. Chem*. **1991**, 95, 6040.

Discussion on the shortcoming of conventional RFCC riser reactor

Chao-He Yang, Hong-Hong Shan, Jian-Fang Zhang
Yu-Dong Sun, Feng Du

State Key Laboratory of Heavy Oil Processing
University of Petroleum, Dongying, 257061, P. R. China

Introduction

In petroleum refining industry, the fluid catalytic cracking (FCC) process is one of the most important processes converting heavy oil into light products. Especially in China, it affords about 80% of gasoline and 30% of diesel oil in market. So increasing the yield of desired products and improving the product distribution is the eternal aim pursued by researcher and engineer in this field. But now it is faced with another baptism to satisfy the need for producing environmentally-cleaner gasoline and diesel fuels.

During the recent decade, most FCC processes were revamped into the RFCC (residue fluid catalytic cracking) processes for processing the heavier and heavier feedstock. According to the intuitive knowledge on the disadvantages of conventional FCC reactor, RFCC technology have been got great development around the reaction system, including the feeding atomization (nozzle), quick separation of oil vapor and spent catalyst, steam stripping of high efficiency, temperature control of reaction, as well as the innovation of riser reactor [1-3]. Except for the downer riser technology [4-7] and MSCC technology [8], the studies on the reactor technology of RFCC is scarce. In order to promote the progress of RFCC technology, it is much important to understand the shortcoming of the conventional riser reactor. This problem was discussed in this paper according to the experimental results, industrial test data, as well as literature information.

Experimental

Most researches about the reaction characteristics of RFCC were completed in the fixed fluidized-bed reactors, or with the small riser or downer reactor in laboratory. Because of the complex physical and chemical phenomena occurring in the RFCC reactor, the results obtained in laboratory only afford the limited information about the real situation in commercial unit. For understanding the reality occurring in industrial RFCC riser reactor, a special sampling system was developed, and the treatment and analysis procedure was established. The flow chart of the modified sampling system as shown in figure 1 includes tube sampling probe for catalyst and product (8), the small cyclone for the partial separation of catalyst and oil vapor (2), two stages of cooler of product oil vapor (3A and 3), two liquid product collectors (4A and 4), the wet gas meter for measuring the volume of the noncondensable gas (6), and the gas sample bag for analyzing the composition of the noncondensable gas product (7). The samples obtained from the riser consisted of gas, light liquid, heavy liquid product, and oily catalyst. The gas and liquid were handled and analyzed in a manner to determine their weights and composition. The oily catalyst was treated with different methods including the steam stripping and solvent extraction. The safety measures to be used in the sampling process using this sampling system refers to the previously published papers [9-10].

The sampling work was done in RFCC units of Shengli Petrochemical Factory and Qingdao Petrochemical factory, the sampling points on RFCC riser were selected in terms of the real situation of industrial unit and shown in figure 2.

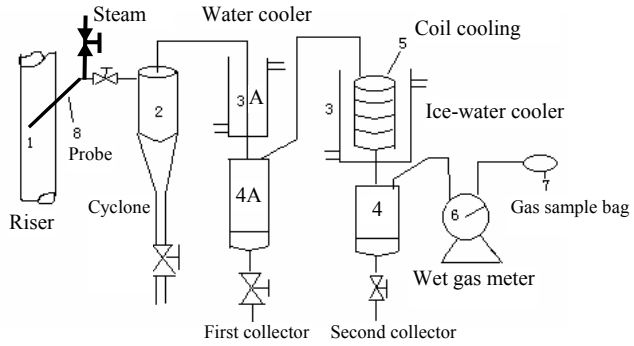

Figure 1. Flow chart of the sampling system for RFCC riser

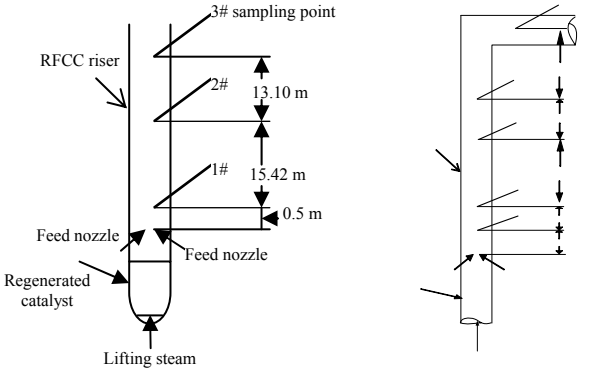

(A) Shengli Petrochemical **(B) Qingdao Petrochemical**

Figure 2. Illustration of sampling points on RFCC riser

Results and Discussion

From the literature, experimental results, and the sampling research of industrial RFCC units, at least three defects could be realized, that is, too long reaction time, too low average activity of catalyst, and the harmful competition of different reactants. These defects resulted in the worse product distribution and the lower once-through conversion.

Too long reaction time. Although the feedstock of RFCC is different from that of distillate FCC because of its high boiling point, high resin and asphaltene content, and high contaminant concentration, the riser reactor is the same for most RFCC with FCC process yet. In general, the distillate FCC is thought to be a gas-solid catalytic reaction, but gas, liquid, and solid exist simultaneously in reactor for RFCC. In catalytic cracking, the chemical bond rupture should mainly occur in the paraffin and naphthene hydrocarbons, the side chains of benzene ring, and the bridge bond between two cyclic structures. The larger the molecule of reactant is, the easier the cracking reaction happens, so the RFCC feedstock is easier to be cracked than distillate feedstock, then the RFCC process should need a shorter reaction time than the distillate FCC. This viewpoint has been accepted in petroleum refining for a long time, so the quick separation of oil vapor and spent catalyst, temperature control of riser reactor, and the MSCC technology were developed, and the downer reactor has been researching.

Gao Yongcan[11] studied the thermal and catalytic cracking of VGO mixed with some AR and VR with ACE-Model-R small fixed fluidized-bed reactor, Xytel corporation. The reaction time, catalyst/oil ratio, and temperature are considered for their contribution to thermal and catalytic reaction, it is concluded that the

short contact time of oil and catalyst may suppress the detrimental thermal cracking reaction obviously.

The riser of 60×10^4t/a RFCC unit in Shengli Petrochemical Factory is 48 m long, the studies on product distribution along the riser of RFCC show that the main conversion of feedstock to gasoline and diesel distillates is completed in the front stage of riser [12]. At 1# sampling point (Figure 2(A)), only 0.5m from the feedstock nozzles, about 60% feedstock was converted into diesel and lighter compounds, the conversion of feedstock reaches about 80% at 2# sampling point. Figure 3 describes the variation of product distribution along the riser length of the RFCC unit. It means that the riser is too long to result in an ideal product distribution at the exit of riser.

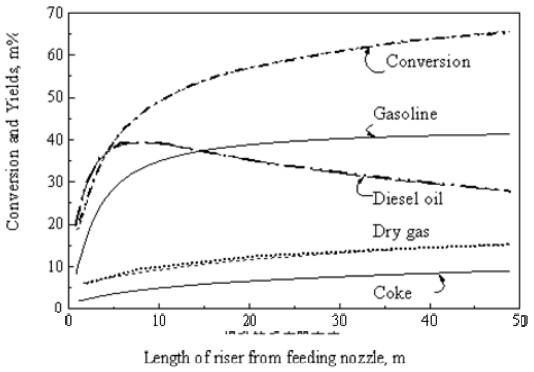

Figure 3. Conversion of feedstock and yields of products versus the length of riser (Simulated result of commercial RFCC unit [13])

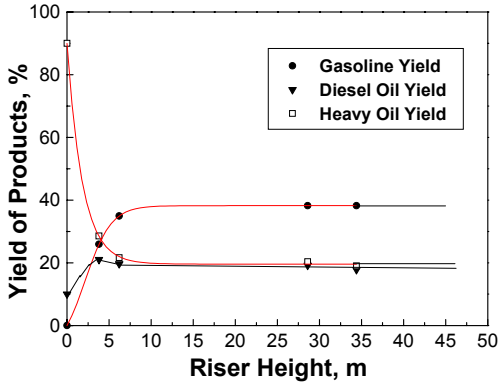

Figure 4. Product yields varies along the riser height

Fortunately the sampling work was perfectly completed in Qingdao Petrochemical Factory. The material balances at every sampling point (Figure 2(B)) were made in terms of gases and liquid products collected in sampling process, as well as the oil absorbed in oily catalysts. The product distribution at different sampling positions was shown in figure 4. The gasoline yield reaches its maximum point at the middle of riser, but the yield of diesel oil reaches its maximum point at the initial stage of riser. The remaining heavy oil (>350°C) deceases along the riser at the bottom of riser, but has no notable change at the later half of riser. In another words, the change of product distribution is drastic in the initial stage of riser and tempered at the later half of riser. In the initial stage of riser, the heavy oil yield decreases from 90m% in feedstock to 28.9m% at the first sampling point (3.8m apart from the nozzles), and nearly 60m% of feedstock are converted into gasoline, diesel oil, gaseous product and coke. This points again that the initial stage play a very important role in RFCC processing, and improving the contacting situation of feedstock with regenerated catalyst is a key method to get satisfied product distribution and maximum refinery profit.

From the results mentioned above, a much short reaction time than the present one (about 3 seconds) is enough for the RFCC riser to complete the conversion of heavy oil into diesel and gasoline distillates, gas and coke. For distillate FCC process, the same viewpoint would be derived from the previous researches. With a continuous, isothermal wall, transfer line catalytic cracking reactor, Paraskos and Shah[14] studied the FCC reaction of mid continent gas oil at the catalyst/oil ratio of 4~8 and temperature of 510~538°C. The conversion of mid continent gas oil into gasoline, gas and coke was plotted with the contact time of oil and catalyst in reactor as shown in figure 5, the contact time is calculated based on zero conversion of gas oil. Before 3 seconds of contact time, the conversion increases quickly, and then closes to a stable level. It could be deduced that 2 seconds of real contact time of oil vapor and catalyst is enough to convert gas oil into gasoline, gas and coke. In china, the diesel distillate in FCC process is also the desired product, a shorter reaction time than 2 seconds should be employed.

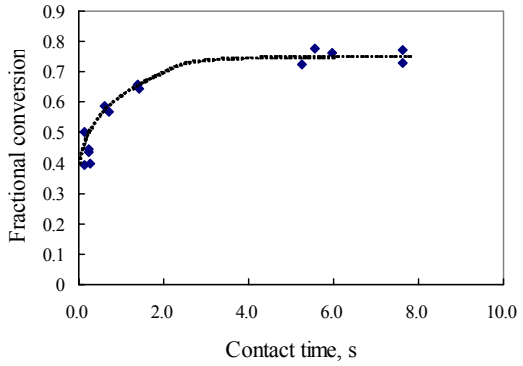

Figure 5. Conversion versus contact time in pilot apparatus

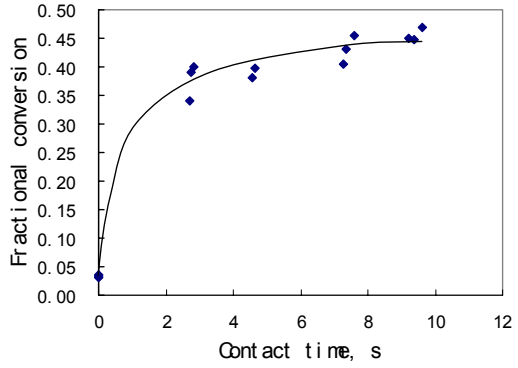

Figure 6. Conversion versus contact time in commercial FCC unit

In a commercial FCC riser of 30 meters long, the sampling was done by Shah and Huling [15] through an open pipe probe using a specialized sampling technique at three probe positions: 8.8, 15.0, and 23.8 miters from the bottom of the riser. In this study, the feedstock is the blend of atmospheric gas oil and vacuum gas oil, the desired product is gasoline, the operation conditions is 6.6~7.1 for catalyst/oil ratio and 480-520°C for reaction temperature. According to the material balance at every sampling point, the similar

relationship between conversion of gas oil and the contact time was obtained as shown in figure 6, the conversion of gas oil cracking increases quickly at the initial stage of riser, and then slowly. It is shown again that the cracking reaction in FCC process occurs at the initial stage of riser.

For distillate FCC process and RFCC process, the conversion of feedstock into desired product is completed in very short time at the bottom of riser reactor, especially the diesel distillate is produced as a desired product in China. If the contact time is too long, the overcracking of diesel and gasoline is inevitable.

Low catalyst activity and poor selectivity. In FCC process, thermal cracking and catalytic cracking exist simultaneously, what is the dominant one depends on the catalyst properties and operation conditions (reaction temperature, catalyst/oil ratio, contact time). The catalytic cracking is the desired reaction for its good product selectivity. Too long contact time and too high reaction temperature will accelerate the thermal cracking, and lead to excessive light gas yield and lower desired product value. At the proper reaction temperature and contact time, the catalyst properties, especially the microactivity, is the key to intensify the catalytic cracking.

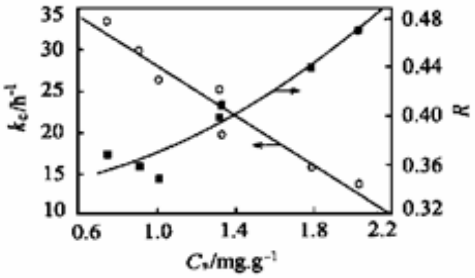

Figure 7. Effect of coke deposition on thermal cracking and catalytic cracking [11]

Gao Yongcan[11] gave the effect of coke deposition in catalyst on thermal cracking and catalytic cracking as shown in figure 7. In figure 7, *C*s is the coke content of catalyst (mg coke/ g catalyst); k_c is the overall reaction rate constant, represents the catalyst activity; and *R* is the ratio of (C_1+C_2) to i-C_4, the criterion of thermal cracking and catalytic cracking. With the increase of coke deposition on catalyst, the catalyst activity decreases gradually, the thermal cracking becomes more and more dominant, so the catalyst selectivity to desired product lowers.

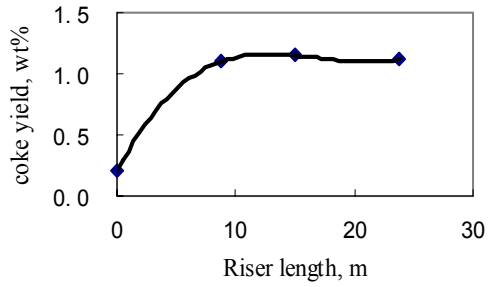

Figure 8. Coke content of catalyst versus riser length in commercial test [15]

For a commercial gas oil FCC process, Shah and Huling [15] obtained the curve of coke content of catalyst along the riser length through the in situ sampling at different position. From figure 8, coke content of catalyst increases rapidly to a stable value at the front section, and then has no obvious change in the rear end of riser. According to the report from Gao Yongcan[11], the catalyst activity will decrease quickly to a low level, and the thermal cracking become a more important reaction at the rear end of riser.

For commercial RFCC process, the changes of catalyst activity with riser length were obtained through the sampling work in Shengli Petrochemical Factory and Qingdao Petrochemical Factory. Figure 9 shows the curves of activity varying with riser height. In figure 9A, the catalyst activity falls down to a low level at the mixing zone of regenerated catalyst and feedstock, then increases slightly to a maximum, finally decreases gradually again. The average microactivity of catalyst in riser reactor is about 50% of the regenerated catalyst. In figure 9B, the microactivity of catalyst decreases to a stable value, and then maintain the level, no maximum exist. The average microactivity of catalyst in riser reactor is only 40% of the regenerated catalyst. Although the feed properties and the operation conditions influence the detail of activity evolution along the RFCC riser, the common result is the drastic fall of catalyst microactivity at the initial stage, the subsequent reactions in riser occur in the catalyst with low activity and poor selectivity.

Therefore, increasing the average microactivity of catalyst in RFCC riser reactor and improving its selectivity is one of the key problems to develop the new RFCC technology.

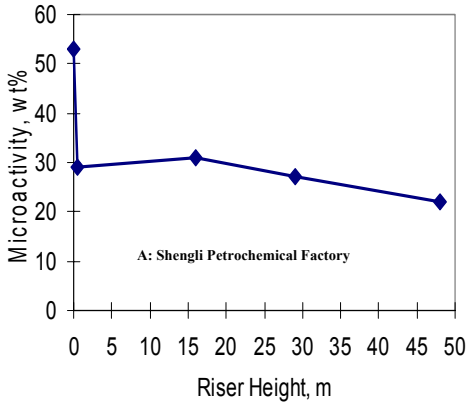

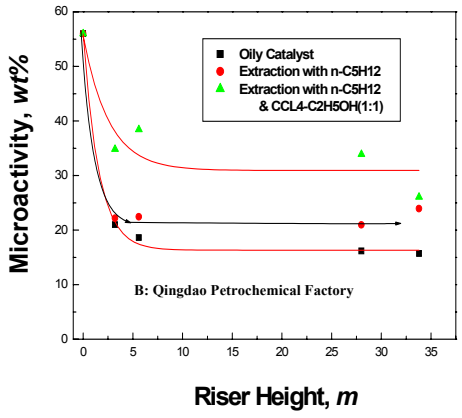

Figure 9. Catalyst microactivity versus riser length for RFCC units

Harmful competition of different reactants. In RFCC process, always there is the recycle oil to be piped into the riser reactor from the bottom of RFCC fractionation tower. The ratio of recycle oil to fresh feed is 0.1~0.8 depending on the feed properties and the

product scheme. The RFCC feedstock has a lot of heavy component with high boiling point, difficult to gasify and move into the interior surface of catalyst, but easy to subject to cracking reactions. Compared with the former, the recycle oil, mainly consisting of aromatics, has a narrow boiling range, so it is easier to gasify and move into the interior surface of catalyst, more difficult to react continuously. In the conventional RFCC process, the fresh feed and the recycle oil exist in one reactor, competition of adsorption on catalyst and chemical reaction will reduces the conversion of fresh feed and results in the unsatisfactory product distribution. So the ideal technology should make the fresh feed and the recycle oil to react respectively in two reactors with different conditions.

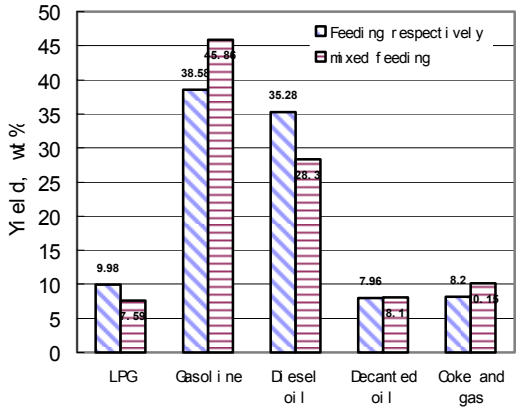

Figure 10. Influence of competition on FCC product distribution

A set of commercial distillate FCC data were shown in figure 10, the Feeding respectively presents the fresh FCC feed and the recycle oil to be injected into two different riser reactor at the different reaction conditions, and the Mixed feeding does the fresh FCC feed and the recycle oil to be injected into one riser reactor as a mixture. Compared with the conventional feeding, the feeding respectively can increase the conversion, obviously increase the ratio of diesel oil to gasoline, and decrease the yield of coke and dry gas.

Conclusions

From the literature, experimental results, and the sampling research of industrial RFCC units, three defects, that is, too long reaction time, too low average activity of catalyst, and the harmful competition of different reactants, were proposed and discussed. These defects resulted in the worse product distribution and the lower once-through conversion.

Acknowledgement . This study was Supported by the Ministry of Education, PetroChina and Sinopec. Thanks Gen-lin Niu, Zhong-xiang Han, De-lian Lin, and Jin-you Wang for their work in this project.

References

(1) Hou Fusheng. *Petroleum Processing and Petrochemicals*. **2001**, 32(1):1-6
(2) Miao Yi, Guan Minghua, Luo Yibin. *Petroleum Processing and Petrochemicals*. **2000**, 31(8):1-7
(3) Xie Chaogang, Zhong Xiaoxiang, and Yang Yinan. *Petroleum Processing and Petrochemicals*. **2001**, 32(1):26-30
(4) Vogiatzis A L. AIChE Symp. Series: Fluidization and Fluid – Particle Systems – Fundamental and Application, **1989**, 85(270):69-76
(5) J. A. Talman, R. Gerier, L. Reh. Chemical Engineering Science, **1999**, (54):2123-2130
(6) Ali G Maadhah, Mohammed Abul-Hamayel, Abdullah M Aitani, et al. Oil & Gas Journal, 2000, 99(33):66-70
(7) Deng Xin. Research on downer reactor in catalytic pyrolysis and catalytic cracking, Doctoral thesis, Tsinghua University, 2001
(8) Kauff D, Bartholic D, Steves C, et al. Successful application of the MSCC process. NPRA Annual Meeting, San Antonio, 1996
(9) Xu Chun-ming, Lin Shi-xiong, Lu Liang-gong. *Petroleum refinery engineering.* **1997**, *27(3)*, 39-42.
(10) Xu Chun-ming, Lu Liang-gong, Lin Shi-xiong. *Journal of the University of Petroleum, China.* **1997**, *21(2)*, 72-75.
(11) Gao Yongcan, Zhang Jiushun. Journal of Chemical Industry and Engineering (China), 2002, 53(5):469-472
(12) Niu Genlin, Yang Chaohe. *Journal of Fuel Chemistry and Technology*. **2002**, 30(3):249-253
(13) Dong Wei. Modelization for the processes in Heavy Oil Catalytic Cracking Riser Reactors and Its Application, Doctoral thesis, University of Petroleum, China, **2001**
(14) Paraskos J A, Shah Y T, Mckinney J D, et al. IEC Process Des. Dev., 1976, 15(1):165-169
(15) Shah Y T, Huling G P, Paraskos J A, et al. IEC Process Des. Dev., 1977, 16(1):89-94

RESIN-ASPHALTENE INTERACTIONS IN VIRGIN AND CRACKED BITUMEN

Parviz M. Rahimi[1], Irwin Wiehe[2], David Patmore[1], Alem Teclemariam[1], and Theo deBrujin[1]

[1]National Centre for Upgrading Technology (NCUT), 1 Oil Patch Drive, Suite A202, Devon, Alberta T9G 1A8 Canada
[2]Soluble Solutions, 3 Louise Lane, Gladstone, NJ 07934 USA

Introduction

The colloidal stability of petroleum can alter significantly as a result of physical or chemical treatment. During crude oil production changes in pressure and temperature can result in asphaltenes precipitation. Addition of diluent or natural gas condensate to crudes to produce piplineable crudes may result in asphaltenes separation and precipitation. To produce synthetic crudes from heavy oils and bitumen these feedstocks have to be upgraded through thermal and catalytic processes resulting in colloidal instability leading to precipitation of asphaltenes. Composition of petroleum particularly the chemical composition of dispersed phase (soluble in n-paraffin) and the peptizing power of the resins plays major role in stabilizing of asphaltenes (1-2). It has been suggested that the resins attach to the asphaltenes provide a steric stabilization and prevent asphaltenes flocculation. Although this qualitative interaction between resin and asphaltenes can be determined by spectroscopic techniques, quantifying it is rather difficult. For this reason, model resins such as alkylbenzene-derived amphiphiles have been used to study the effectiveness of these compounds as asphaltenes stabilizer. A steric stabilization mechanism has been provoked in which amphiphiles adsorbed on the asphaltenes surface and reduce the chances for further asphaltenes-asphaltenes interaction (3).

It is generally accepted that the role of resin in petroleum is to stabilize asphaltenes. However, the mechanism of stabilization is not clear. Although a steric stabilization of resins has been suggested (4), adsorption of multilayer resins on the surface of asphaltenes has been reported (5). More recently León et al., reported the adsorption of native resins on asphaltenes particles (6). Adsorption isotherms of two resins on two different asphaltenes were studied using UV-vis spectrophotometric technique. At the same time the stabilizing power of resins were compared with the known amphiphiles as asphaltenes stabilizer such as nonylphenol. It was shown that resins adsorb and form a multi layer structure on the surface of asphaltenes. Also, when resins were added to the asphaltenes sample immersed n-heptane, a volumetric expansion in asphaltenes was observed that indicated resins penetrated into the microporous structure of asphaltenes. Comparing the stabilizing power of amphiphiles with native resins, it was shown that at the same equilibrium concentration the native resins adsorb in a lower amount than amphiphiles. However, some native resins were capable in dissolving more asphaltenes and were more effective as asphaltenes stabilizer. Based on these results the authors proposed a model for asphaltenes stabilization by resins. According to this model, 1) resins are first adsorb on the surface of asphaltenes; 2) the resins penetrate into the microporous structure of the asphaltenes; 3) breaking microporous of asphaltenes by reins and 4) diffusion of asphaltenes-resins particles in the solvent.

In another study by Wang and Buckley the role of resin in stabilizing asphaltenes was investigated (7). These authors concluded that the role of resin to improve asphaltenes stability is more than just changing the solvent properties. However, there was no evidence of specific interaction between the resins and asphaltenes in this study. Recently González et al., studied the electric characteristic charge of asphaltenes in different solvents. It was shown although asphaltenes dispersed in water showed negative electrophoretic mobility but in organic solvent the mobility was positive (8). Moreover, the addition of resins did not change the electrophoretic mobility and resulted in coprecipitation with asphaltenes i.e., resins failed to stabilize asphaltenes dispersions. The authors concluded that the interaction between asphaltenes and resins exist through some sort of binding interaction (acidic groups) rather that adsorption and this type of interaction does not provide stability to asphaltenes dispersions.

The objective of the present work was to investigate the effectiveness of resins obtained from Athabasca bitumen on stability of thermally cracked bitumen containing unstable asphaltenes prone to precipitation.

Experimental. Athabasca bitumen was subjected to thermal cracking under different severities. Detailed experimental procedure can be found elsewhere (9). For the purpose of the current research we selected a visbroken product that was obtained at a relatively high severity (pitch conversion of 42wt %) and the asphaltenes in this liquid was considered to be relatively unstable.

The resin from Athabasca bitumen was obtained from the +524°C fraction of Athabasca bitumen using a modified ASTM D-2007. In this procedure C_7 asphaltenes were first precipitated and the heptane solubles maltenes were separated into saturates aromatics and resins. For comparison, the visbroken product was also separated into C_7 asphaltenes, saturates, aromatics and resins. The yields of these products are shown in Table 1.

Table 1- SARA analysis of Athabasca bitumen and visbroken products

Source	C_7 Asphaltenes wt%	Saturates wt%	Aromatics wt%	Resins wt%
Athabasca	26.19	5.14	31.51	37.16
Visbroken	19.43	20.85	44.31	15.41

To determine the effectiveness of resins on the stability of visbroken products (VBL), the solubility parameters of VBL as well as those containing different concentration of resins were determined using Wiehe's procedure (10). In this procedure the insolubility (I_N) and solubility blending (S_{BN}) numbers are determined based on n-heptane toluene scale. Similarly, the additions of resins to Athabasca bitumen at different resins concentrations were examined.

Results and Discussions

In the present work the effect of resins separated from Athabasca bitumen was investigated on the stability of unstable asphaltenes present in visbroken liquids (VBL) and on a stable asphaltenes present in Athabasca bitumen. The effectiveness of the resins on asphaltenes stability is shown in Table 2. In this table we report the solubility blending numbers and the P-values (S_{BN}/I_N) as function of resins concentration. The resin concentration changed from 0-20 wt% for both visbroken liquid and Athabasca bitumen. As shown in

Table 1, the visbroken liquid contains approximately 19 wt% C_7 asphaltenes and 21 wt% saturates that can act as non-solvent reducing the effectiveness of asphaltenes in stabilizing asphaltenes. Addition of resins to stable Athabasca bitumen which already contains 37 wt% resins had similar effect and resulted in further stabilization of asphaltenes.

Table 2 - Effect of resins on stability of asphaltenes

	I_N	S_{BN}	P-value
VBL	89.3	104.3	1.17
VBL + 5 wt% Resin	88.9	113.8	1.28
VBL +10 wt% Resin	84.2	118.7	1.41
VBL +20 wt% Resin	82.4	131.3	1.59
AB	34.2	93.0	2.72
AB + 5 wt% Resin	32.9	104.3	3.17
AB + 10 wt% Resin	31.9	110.0	3.45
AB + 20 wt% Resin	31.1	116.7	3.75

In previous work we reported the effect of deasphalted oil (DAO) obtained from Athabasca bitumen on the stability of VB (11). It was shown that the C_7 DAO containing approximately 70wt% polar fractions was only effective in stabilizing VB products at a relatively high concentration. By addition of about 30wt% C_7 DAO to VB the stability index as determined by the ratio of I_N/S_{BN} = P-value increased from 1.18 to 1.56.

The effectiveness of a synthetic amphiphile such as DBSA on unstable asphaltenes of visbroken liquid and stable asphaltenes of Athabasca bitumen were investigated and compared with the natural resin. The results are shown in Table 3.

Table 3 - Effect of DBSA on stability of asphaltenes

	I_N	S_{BN}	P-value
VBL	89.31	104.32	1.17
VBL +5 wt% DBSA	71.82	100.82	1.40
VBL +10 wt% DBSA	62.63	121.64	1.94
VBL +20 wt% DBSA	43.00	213.68	4.97
AB	34.17	92.97	2.72
AB + 0.5 wt% DBSA	30.50	94.46	3.10
AB + 5 wt% DBSA	22.71	71.47	3.15
AB + 10 wt% DBSA	14.35	44.96	3.13

Although the dispersing asphaltenes additives such as DBSA are used in petroleum industry at low concentration, for comparison, in this work we used similar concentrations with natural resins. The data indicate that the addition of 0.5 wt% DBSA was somewhat was effective in further stabilizing the stable asphaltenes in AB and addition of more additive up to 10wt% did not improve stability significantly. In contrast, DBSA was more effective in stabilizing the unstable asphaltenes in visbroken VBL at similar concentrations.

Overall the activity of natural resins to stabilize asphaltenes stability was higher compared with DAO but was significantly lower than expected. The mechanism of stabilization of asphaltenes through steric or salvation model was discussed earlier (11). Since it is expected that unlike synthetic amphiphiles resins and DAO contain molecules with a relatively short chains the improvement in asphaltenes stability may be through mechanism discussed in introduction postulated by León et al., (6).

Conclusions

From the experimental results of this work it is evident that natural dispersants including DAO and resins are not as effective for asphaltenes stabilization as previously thought and significantly lower than synthetic amphiphiles. This result further questions the validity of using synthetic amphiphiles such as DBSA as a model for resins.

Acknowledgement. Partial funding for NCUT has been provided by the Canadian Program for Energy Research and Development (PERD), the Alberta Research Council (ARC) and the Alberta Energy Research Institute (AERI).

References

1- León, O., Rogel, E., Espidel, J. and Torres, J. Energy Fuels 2000, 14, 6.
2- Taylor, S.E., Fuel 1988, 77, 821.
3- Chang, C. L. and Fogler, H.S., Langmuir 1994, 10, 1749.
4- Leontritis, K.J. and Mansoori, G. A., SPE International symposium on oil field chemistry, San Antonio, TX, 1987, SPE 16258.
5- Acevedo, S., Escobar, G., Ranaudo, M. and Gutierrez, L. B., Fuel, 1994, 73, 1807.
6- León, O., Contreras, E., Rogel, E., Dambakli, G., Acevedo, S., Carbognani, L. and Espidel, J., "Adsorption of native resins on asphaltene particles: a correlation between adsorption and activity", Langmuir 2002, 18, 5106 – 5112
7- Wang, J. and Buckley, J.S., "Asphaltenes stability in crude oil and aromatic solvents-The influences of oil composition", Energy & Fuels, 2003, 17, 1445-1451.
8- González, G., Neves, G.B.M., Saravia, S.M., Lucas, E.F., and Anjos de Sousa, M., "Electrokinetic characterization of asphaltenes and the asphaltenes – resins interaction", Energy & Fuels, 2993, 17, 879-886.
9- Rahimi, P.M. and Parker, R.J., "Stability of visbroken products obtained from Athabasca bitumen for pipeline transportation", Preprint, Division of Petroleum Chemistry, San Diego, April 1-5, 2001, Vol. 46, No. 2, 95-98.
10- Wiehe, I.A. and Kennedy, R.J. "The oil compatibility model and crude oil incompatibility", Energy&Fuels, 14, 2000, 56-59.
11- Rahimi, P.M., Teclemariam, T., Patmore, D., Wiehe, I.A., Schabron, J. and de Bruijn, T. "The effectiveness of deasphalted oil in the stability of visbroken bitumen", Preprint, Division of Petroleum Chemistry, Anaheim, March 28-April 1, 2004, Vol. 49, No. 2, 147-149

INCREASE IN EXTRACTION YIELDS OF BEULAH-ZAP LIGNITE BY WATER TREATMENT

Masashi Iino[#1], Toshimasa Takanohashi[1], Chunqi Li[1], and Haruo Kumagai[2]

[1]National Institute of Advanced Industrial Science and Technology (AIST), 16-1 Onogawa, Tsukuba, 305-8569, Japan

[2]Hokkaido University, Kita-ku, Sapporo, 060-8628, Japan

Introduction

, Graff and Brandes[1,2] reported that the treatment of Illinois No.6 coal with 50atm of steam at 340-350°C increased the pyridine extraction yields from 17% for the raw coal to about 30%. Steam treatment of Wiodak coal at 200 °C increased the toluene-solubles conversion in liquefaction at 400°C from 27.3% to 38.4%.[3] However, there are several papers showing that water treatment gave no benefits. Khan et al.[4] reported that steam treatment of Illinois No.6 coal at 330 °C gave only a very small increase in total volatiles of rapid steam pyrolysis, unlike the great increase in total volatiles and tar obtained by Graff and Brandes.[1,2] Ross and Hirschon[5] reported that water treatment of Illinois No.6 coal at 250 °C did not increase toluene solubles in liquefaction in tetralin, though S/C atomic ratio and ash content decreased greatly due to the conversion of pyrite to water soluble sulfate. In the previous paper[6] we have studied on the effect of water treatment on coal extraction yields of Argonne Premium coals, Pocahontas No. 3 (PO), Upper Freeport (UF), and Illinois No.6 (IL) coals. All the coals used show that the water treatments at 600 K increased the extraction yields greatly in the extractions with a 1:1 carbon disulfide / *N*-methyl-2-pyrrolidinone (CS_2 / NMP) mixed solvent, NMP, or 1-methylnaphthalene (1-MN). While, the water treatments at 500 K, and the heat treatments at 600 K without water gave little increase in the yields. It was concluded that the loosening of π–π interactions and hydrogen bonds are responsible for the yield enhancements of PO and UF. While, the yield enhancements of IL may be due to the removal of oxygen functional groups, in addition to the loosening of hydrogen bonds. In this paper water treatment of Beulah-Zap lignite was investigated.

Experimental

Coal Samples. Argonne Premium Beulah-Zap lignite (BZ) with particle size under 100 mesh were used after they were dried in vacuum at 353 K overnight.

Water Treatment. Water treatment of BZ was carried out using a 50 ml autoclave at 500 and 600K. In each run, 10 g of BZ and 20g of water were put into the autoclave, purged with nitrogen three times, and finally pressurized with nitrogen to about 1 Kg/cm^2 at room temperature. Then the autoclave was heated to a fixed temperature at about 10 K/min under stirring at 500 rpm. After the treatment for 1 h the autoclave was cooled down rapidly by immersing in an ice/water bath. The coal/water mixture was filtered, and the treated coal was dried in vacuum at 353 K overnight. The work up of the treated samples including the filtration was carried out without any protection to oxygen exposure. The heat treatment in the absence of water was also carried in the same way as the water treatment.

Characterisation of Water-Treated BZ. FT-IR spectra were measured by a diffuse reflectance method. The difference spectra between raw and treated coal were obtained using the absorption of C=C bond stretching of aromatic rigs at 1610 cm^{-1} as a standard peak.

Extraction yield of the treated coals with CS_2/NMP mixed solvent (1/1 by volume) was determined at the room temperature extraction under ultrasonication, as described previously.[7] Extraction with NMP or 1-methylnaphthalene (1-MN) at 633 K was carried out using a flow-type extractor at various temperatures. The extraction yield was calculated on a dry ash-free basis from the weight of the residue.

Swelling ratio, Q, was determined in methanol by the volumetric method by Green and Larsen.[8] Equilibrium swelling ratio was determined from Q when the change in Q became within 2% variation, and it took 12 – 48 h, depending on the sample and solvent.

Dynamic viscoelastic measurement was carried out using a rheometer, Rheometrics ARES 2K-STD. The coal pellet was heated at a rate of 3 K/min from 573 to 823 K under nitrogen flow, and tan δ, i.e., the ratio of viscous modulus (G'') to elastic modulus (G'), was determined.

Results and Discussion

Weight Loss, and Ultimate and Proximate Analysis. The weight losses accompanying the water treatments of BZ at 500 and 600 K for 1h were 5.5 and 8.9 wt %, respectively. In Table 1 the results of ultimate and proximate analysis are shown. The water treatment at 600K decreased oxygen and VM % due to the loss of oxygen functional groups.

Table 1. Ultimate and Proximate Analyses of the Water Treated BZ Coals

treatment	ultimate analysis (wt%, daf)					proximate analysis (wt%, db)		
temp (K)	C	H	N	S	O[a]	ash	VM	FC
raw coal	69.4	4.8	1.1	0.6	24.1	9.6	42.2	48.2
400	69.3	4.7	1,1	0.6	24.3	9.0	–	–
500	70.4	4.8	1.1	0.5	23.2	8.8	–	–
600	73.1	4.6	1.2	0.6	20.6	9.3	32.6	58.1

[a] by difference

FT-IR Spectra. Figure 1 shows IR spectra of raw and treated coal, and the difference spectra ("water-treated coal" – "raw coal"). The difference spectra show the large decrease in the absorption of hydrogen bonded OH, in agreement to the decease in O %. The decrease in the amount of absorbed water for the treated coal during the IR measurement may be also partly responsible.

Extraction Yield. Table 2 shows that the water treatments at 600 K increased the extraction yield with CS_2/NMP mixed solvent at room temperature by 16.2 %. While, the water treatments at 500 K or the heat treatments without water at 500 and 600 K resulted in a decrease or an only small increase in the extraction yield. Table 3 shows the results for the extraction with NMP and 1-MN. NMP room temperature extraction yield increased from 3.4 % to 9.8 % by the water treatment, but at 633 K extraction the water treatment did not increase the yield, suggesting that the benefit of the water treatment was lost at thigh temperature extraction. 633 K 1-MN extraction shows that the benefit of the treatment was also lost.

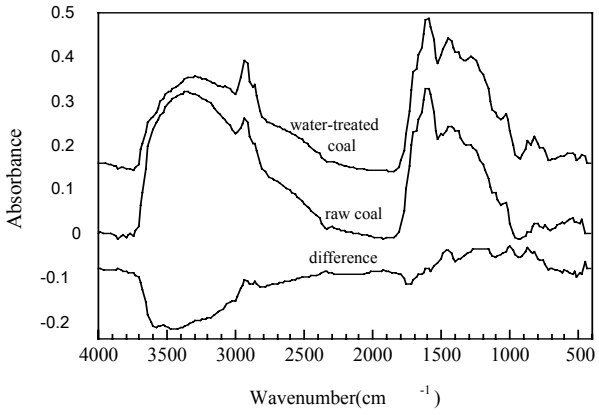

Figure 1. IR spectra of the raw and water-treated BZ coal, and the difference spectrum, in which the spectrum of the treated coal was subtracted from that of the raw coal.

Table 2. Extraction Yields of Water and Heat Treated BZ Coals with CS2/NMP Mixed Solvent

treatment	treatment temp.(K)	extraction yield (wt%)[a]
raw coal	–	5.5
wate	500	4.2
	600	21.7
heat	500	2.5
	600	9.7

[a] under ultrasonication at room temperature

Table 3. Extraction Yields of Water and Heat Treated BZ Coals with NMP and 1-MN

treatment	extraction solvent	extracton yield (wt%) room temp.[b]	633K[c]
raw coal	NMP	3.4	30.5
water	NMP	9.8	30.4
raw coal	1-MN	–	28.8
water	1-MN	–	15.2

[a] 600K, 1h, [b] under ultrasonication, [c]solvent- flow extraction

Swelling Ratio and Dynamic Viscoelasticity. Equilibrium Q value in methanol increased by the water treatment at 600 K to 1.18 from 1.02 of the raw coal, suggesting that crosslinking network became loosened by the treatment. In dynamic viscoelasticity measurement the increase in tan δ indicates the increase in molecular and/or segmental mobility. Tan δ of BZ coal treated with water at 600 K was found to be higher than that for the raw coals at the temperature range from 150 to 300 K. While, above 300 K tan δ of the treated coal is lower than the raw coal, suggesting that at high temperatures the benefit for the water treatment was lost, in agreement to the extraction results, though characteristic temperature ranges are different probably due to the difference in the heating rate.

Mechanisms of the Water Treatment. Like PO, UF, and IL coals, the water treatments of BZ lignite at 600 K increased the extraction yields, but the water treatments at 500 K, or the heat treatments at 600 K without water gave little increase in the yields. Swelling degree in methanol and toluene increased by the water treatment at 600 K, suggesting that cross-links become loosened by the treatment. The decrease in IR absorbance of hydrogen-bonded OH indicates that the loosening and/or breaking of hydrogen bonds is responsible for the extraction yields enhancements, like IL coal. The result that the benefit of the water treatment was lost at 633 K NMP and 1-MN extractions can be explained from that at high temperature extractions almost all the hydrogen bonds were broken resulting in little difference between the treated and raw coals. In addition to the hydrogen bond loosening described above, the removal of oxygen functional groups is considered to be also responsible for the extraction yields enhancements by the water treatments.

Conclusions

The effect of water treatment at 500 and 600 K on solvent extractions of Beulah-Zap lignite (BZ) was investigated. The water treatments at 600 K increased the extraction yields greatly in the extractions with 1:1 carbon disulfide / *N*-methyl-2-pyrrolidinone (CS_2 / NMP) mixed solvent. While, the water treatments at 500 K, and the heat treatments at 500 and 600 K without water gave little increase in the yields. The decrease in O % and hydrogen-bonded OH suggests that the removal of oxygen functional groups such as breaking of ether bonds and the breaking of hydrogen bonds are responsible for the extraction yield enhancements.

Acknowledgement. This work was supported by "Research for the Future " project of the Japan Society for the Promotion of Science (JSPS).

References

(1) Graff, R. A.; Brandes, S. D. *Energy Fuels* **1987,** 1 , 84.
(2) Brandes, S. D.; Graff, R. A.; Gorbaty, M. L.; Siskin, M. *Energy Fuels*, **1989**, 3, 494.
(3) Bienkowski, P. R.; Narayan, R.; Greenkorn, R. A.; Chao, K. *Ind. Eng.Chem.Res.* **1987**, 26, 202.
(4) Khan, M. R.; Chen, W.; Suuberg, E. *Energy Fuels*, **1989**, 3, 223.
(5) Ross, D. S.; Hirschon, A. *Prepr. pap.-Am. Chem. Soc., Div. Fuel Chem*. **1990**, 35(1), 37.
(6) *Energy Fuels*, submitted.
(7) Iino, M.; Takanohashi, T.; Osuga, H.; Toda, K. *Fuel*, **1988**, 67, 1639.
(8) Green, T. K.; Larsen, J. W. *Fuel*, **1984**, 63, 935.

DISPERSED MOLYBDENUM HYDRO PROCESSING CATALYSTS PREPARED VIA FLASHING AND DECOMPOSITION OF MICROEMULSIONS UNDER CONTINUOUS MODE

Pedro Pereira, Rebecca Wang, Josephine Hill

Department of Chemical and petroleum Engineering. University of Calgary. 2500 University Drive. Calgary, AB, T2N 1N4. Canada

Introduction

Due to environmental restrictions as well as to limitations of performance from the traditional fixed bed catalysts for hydro processing extra heavy feedstocks, the generation of micro-nano size catalyst particles within the feed at conditions close to those of the reaction zone results in an important alternative. This idea has allowed the proposition of many different new processes that could be considered the third generation for hydrocarbon heavy ends.

Oil soluble compounds of those transition metals catalytically active for hydro processing yield good results [1] but their preparation is costly. Most of the inorganic forms of these transition metals are much less expensive, for instance, ammonium heptamolibdate is perhaps the least expensive form of Mo with the higher metal proportion within the salt. Nevertheless its insolubility in the reaction media prevents from obtaining a direct good dispersion of the metal, which makes necessary to incorporate significant amounts of the compound to get sufficient catalysis for processing.

Traditionally more considered for transporting heavy crude oils [2] the use of emulsions and micro emulsions are an alternative way of incorporating well-dispersed catalysts for heavy feedstocks hydro processing. In this paper the preparation of micro/nano dispersed Mo particles by thermal decomposition of ammonium heptamolibdate emulsions was studied. A continuous setup for flashing the emulsion and decomposing the precursor salts of the catalyst active phase was used. This setup simulates at laboratory scale the one previously patented [3], for a preparation and demonstration at industrial scale [4]. The effects of the many variables that might have an incidence in the particle diameter and on the nature and quantity of the active sites are being studied by using a methodology for Experimental Design.

Experimental

Emulsions preparation. An oil lubricant base and a Vacuum Gasoil (VGO) were used as different oil phases for the micro emulsions preparation. The aqueous phase was prepared containing ammonium heptamolybdate (7.5% Mo) with or without ammonium sulfide at two different concentrations (3 and 10%). Also different percentages of surfactant were used from 1 to 10%.

Catalyst preparation. The synthesis of the molybdenum catalysts is performed in a continuous mode (Fig. 1). First 6ml of surfactant (Brij 30 from Aldrich) were put in 200g of vacuum gas oil (VGO, boiling point is from 250 to 600ºC). Appropriate amounts of AHM (Ammonium heptamolybdate tetra hydrate from Aldrich, ACS 99.99%) are dissolved in distilled water to produce the desired molybdenum concentration. The AHM solution, VGO and the surfactant were mixed for 6 min until a water-in-oil emulsion was formed. The as prepared water/oil emulsion was pumped through ¼" tubing in a horizontal Linberg furnace. The furnace temperature and flowrate were determined according to a two-level full factorial experimental design. The liquid product was analyzed to determine the size of the suspended particles. Solids are obtained after centrifuging and drying in a vacuum oven at 120 ºC overnight.

Characterization Methods. The particle size measurements of synthesized molybdenum oxide by dynamic light scattering (DLS) was performed on a Malvern Zetasizer Nano series (Malvern, UK) equipped with a 4.0mW He-Ne laser (633 nm) and operated at an angle of 173º and a temperature of 25 ºC with multiple narrow modes. X-ray diffractograms as well as XPS spectras were used to identify the most abundant structural forms of Mo resulting from the preparation and the chemical environment of the surface formed during the preparation process, respectively.

Results and discussion

Dynamic light scattering (DLS) investigation of molybdenum particles. The size of the molybdenum particles depends on experimental variables including decomposition temperature, emulsion flow rate, water/oil ratio and the AHM concentration. Typical results from two experiments are shown in Figure 2. The parameters for these experiments are given in Table 1.

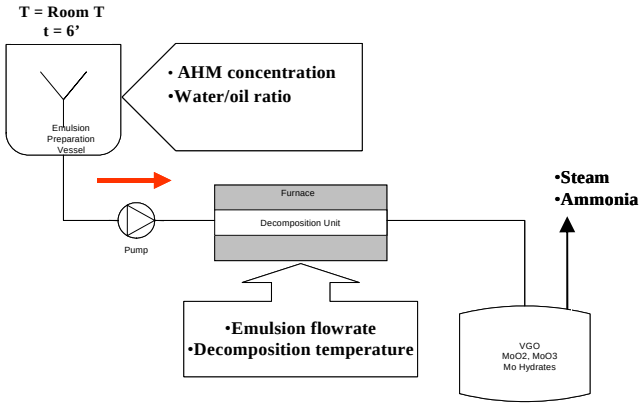

Figure 1. Experimental setup of producing submicron molybdenum catalyst in a continuous mode

The mean particle sizes obtained range from 50nm to 800nm depending on the experimental variables already mentioned. The DLS technique allows to detect suspended particles preexisting in the VGO used for the preparation of the microemulsion In the sequence of figure 3 are shown the results of a series of experiments each one followed of a DLS analysis of the resulting suspended particulate. These particles were presumably traces of asphalthenes based on their significant reduction in quantity when a large addition of n-heptane was used to dilute it. The thermal flashing at 350C of the both the VGO and its emulsion prepared in the absence of Mo salts, shows that these presumed asphalthenes are affected by the thermal treatment. When the emulsion contains the Mo precursor the asphalthene particle signal attributed to them disappears. These presumably asphalthenes are playing a role in the dispersion of Mo. This illustrates that dispersed molybdenum catalysts with sub-micron sizes can be produced by thermal flashing of a micro emulsion containing molybdenum salts, in a continuous mode that simulates the way in which the eventual industrial application has been produced in the past [3-4] for a different demonstration not containing Mo.

BET surface area measurements indicate a good correlation between surface area and particle size, with a surface area of about 60 m^2/g for the smallest 50 nm particle size. X-Ray Diffraction shows the formation of MoO3 as the only significant species formed in the absence of sulphur during the flashing-decomposition process.

Activation with H_2S and reactivity tests of these particles for catalyzing the desulphurization of thiophene are being performed to verify their catalytic activity in a simple and direct way.

Conclusion

Preliminary results indicate that molybdenum particles with sub micron sizes can be synthesized by the thermal decomposition of low cost molybdenum salts in a water-in-oil emulsion in a continuous mode. DLS results show a particle size ranging between 50 and 700 nm as average particle diameter. This synthesis scheme offers potential application for heavy oil upgrading. Of particular relevance is the evidence of the role that asphalthenes might be playing in the flashing-decomposition process to form Mo nano particles when Vacuum Gas Oil is used as the hydrocarbon fraction of the Water-in-Oil microemulsion as shown in recent previous work.

Acknowledgement. We would like to thank NSERC for its financial support for the project. We also would like to thank the support of the Alberta Ingenuity Foundation whose financial support of the Scholar Dr Pedro Pereira Almao in the area of Catalysis for Upgrading and Hydrogen production has also contributed to the deployment of this research at the University of Calgary, Alberta, Canada.

Figures and Tables

Sample Name	AHM concentration	Decomposition temperature	Water/oil ratio	Emulsion flowrate	Mean particle diameter
MC1	0.3	330 °C	0.1	420 ml/hr	617.9 nm
MC2	0.3	220 °C	0.4	420 ml/hr	575.6 nm

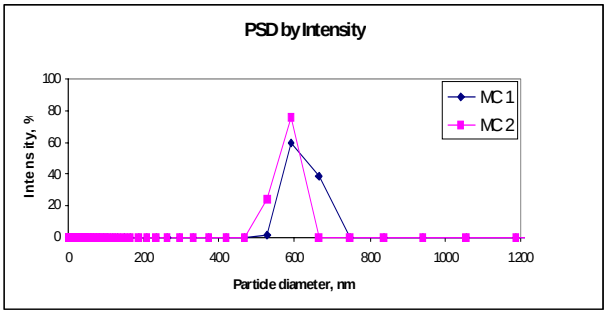

Figure 2. Table 1: Particle size distribution by intensity for the samples MC 1 and MC 2 and preparation variables for the samples MC 1 and MC 2.

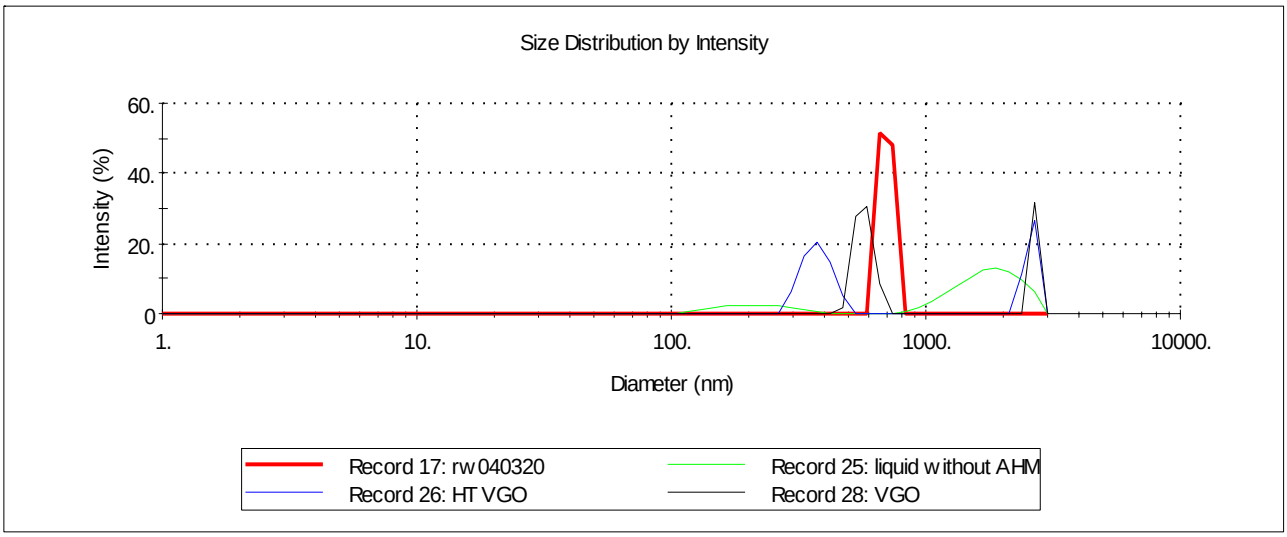

Figrure 3. DLS ANALYSIS OF VGO AND ITS EMULSIONS WITH AND WITHOUT AHM. Record 28: VGO before emulsifying; Record 25: After emulsifying and flashing-decomposition @ 350C in the absence of AHM; Record 26: After heating the VGO @ 350C; Record 17: After emulsifying and flashing-decomposition @ 350C in presence of AHM

References

[1] *Bearden R., Aldridge C. L.*, Energie Progress, **1** (1981) 44
[2] *Ng F.T.T. Rintjema R.T.* Stud. Surf. Sci. Catal., 73 (1992) 51
[3] *Pereira P. et al.* US Patent 5885441
[4] *Pereira P et al***.** Petroleum Technology Quarterly (ISSN 1362-363)V3 N.4 29-30, 33-37 (Winter 1998-99)
[5] *E. Escalona et al.* Memorias VI Congreso Venezolano de Quimica. P 744-747, Nov. 2003. Margarita, Venezuela.

OPTIMUM RESIDUUM TO CLEAN FUELS UPGRADE VIA STRATEGIC RDS/RFCC CATALYST DESIGN

C. J. Dillon,[a] M. J. Armstong,[a] S. W. Davey,[b] W. –C. Cheng,[c] L. J. Hunt,[c] C. J. Schult,[c] M. S. Ziebarth,[c] and S. K. Purnell[c]

[a]ChevronTexaco, Advanced Refining Technologies
Richmond, CA 94802
[b]Grace Davsion, Advanced Refining Technologies
Columbia, MD 21044
[c]Davison Catalysts, Columbia, MD 21044

Introduction

Refiners today are challenged to produce transportation fuels containing a level of contaminants close to zero. The United States, the European Union, and several Asian countries have recently passed legislation for ultra low sulfur diesel and gasoline. These new requirements impose a growing need in the oil industry for more active and selective hydroprocessing and cracking catalysts.

Residuum Hydrotreating (RDS) technology was first introduced to produce low sulfur fuel oil from high sulfur atmospheric residuum to a 1wt% sulfur specification. It became the only technology capable of upgrading vacuum residuum from sour and heavy crude oils into low sulfur fuel oil. Today, developments in both RDS and Fluid Catalytic Cracking (FCC) catalyst technology and reactor design mean that Residuum Fluid Catalytic Cracking (RFCC) is the most popular and economic processing route for the complete conversion of residual oils. Refiners without a pretreating system are limited to processing atmospheric residuum from crudes that are low in metals, carbon residue and sulfur in order to avoid operating problems. Consequently, many refiners chose to combine a residuum hydrotreater upstream of an FCCU allowing them more flexibility in choosing heavier and more contaminated feedstocks, reducing their catalyst consumption in the FCCU and enabling them to achieve higher and cleaner yields of transportation fuels. Indeed many units process mixtures of both atmospheric and vacuum residuum (AR and VR) with high levels of contaminants and nonetheless provide feedstock to an FCCU.

In this paper we examine the impact on sulfur level of RDS catalyst system design with RFCC catalyst selection. Extensive pilot plant testing on both RDS and RFCC processes has been conducted to evaluate the impact of feedstock, process variables and catalyst design on overall system performance. Experiments were conducted in high-pressure, semi-commercial fixed-bed pilot plants to test RDS catalyst systems at ChevronTexaco. The RDS product generated was then processed as FCC feedstock in an ACE fluidized bed pilot plant over new cracking catalyst systems at Grace Davison. Our complimentary studies show that by considering the RDS and RFCC catalyst systems together, we are able to design an optimized system to extract the maximum synergy from RDS and RFCC catalyst systems operating in tandem.

Experimental

RDS pilot plant studies. A typical pilot plant consists of one to three reactors in series which can be run either upflow or downflow. The one to 2.5 inch reactors are equipped with internal thermowells and can accommodate catalyst charges of up to twenty liters in volume. Reactors are temperature controlled by means of six independent heaters, each controlled by feedback from internal catalyst bed thermocouples. This configuration enables realistic adiabatic reactor temperature control representative of commercial operation. Hydrogen is supplied to reactors in either a once thru or recycle gas mode. In this fashion, typical commercial hydrogen partial pressures can be maintained throughout the duration of a test. The product handling portion of the units varies from simple letdown of liquid product with hydrogen sulfide and ammonia stripping to complete product distillation for specific fraction liquid recycle, all on a continuous basis.

ACE pilot plant studies. Testing was conducted in an ACE fluidized bed pilot plant reactor after deactivation by the cyclic propylene steaming (CPS) protocol. Further details can be found in references (1) and (2).

Results and Discussion

Fixed bed RDS catalyst systems are a combination of large pore hydrodemetalation (HDM) catalysts designed to remove contaminant metals such as nickel and vanadium, transition catalysts with dual hydrodemetalation and hydrodesulfurization (HDS) functionalities to provide HDS activity in a relatively high metals environment, and small pore deep desulfurization, denitrogenation (HDN) and Conradson carbon (CCR) removal catalysts. Catalyst systems are designed using kinetic models and constructed in layers with varying ratios of catalyst types depending on feed properties and product specifications.

For this study two RDS catalyst systems were designed: a system optimized for HDM activity heavily weighted with large pore low activity catalyst, and a system designed for optimum HDS activity comprised substantially of high activity conversion catalyst. Table 1 summarizes the feedstock properties (Arab Medium AR/VR blend) and the middle-of-run 650°F+ product properties produced by each catalyst system.

Table 1. RDS Feedstock and Product (650°F+) Properties

	Feedstock	HDM system	HDS system
S, wt%	4.55	0.62	0.50
V, ppm	89	5	11
Ni, ppm	27	3	6
Concarbon, wt%	14.1	4.8	4.5
Nitrogen, ppm	2700	1700	1300
Average MW	–	477	466
1000°F+, wt%	59.5	–	–

The HDM system reduced combined nickel and vanadium levels by 93%, and nitrogen and CCR by 38% and 66% respectively. Sulfur conversion was relatively low at 86% due to the high proportion of large pore demetalation catalyst in the system. The HDS system achieves 89% sulfur conversion but leaves more contaminant metals unconverted: nickel and vanadium were reduced by 77% and 88% respectively, and nitrogen and CCR conversions were 52% and 68%.

The use of residuum feedstocks as described in Table 1 in FCC units has been facilitated by advances in FCC catalyst design. New catalysts, for example *IMPACT* from Grace Davison, are more resistant to poisons such as sodium and vanadium that cause deactivation by neutralizing zeolite acid sites, sintering and destroying the zeolite lattice. Furthermore, cracking catalysts now afford higher bottoms conversion through tuned acidity and increased accessibility and diffusion into the zeolite of large molecules that are abundant in residual feeds. Advances in additive technology are improving sulfur reduction in the FCCU: sulfur additives are effective at reducing sulfur species in the light and intermediate FCC naphtha. These new metals tolerant and sulfur reduction technologies were employed in the testing of the HDM and HDS residuum feedstocks in the following case studies.

RDS sulfur reduction and RFCC metals management. For the cost effective production of high yields of low sulfur gasoline and diesel fuels, the combination of an RDS unit achieving maximum

desulfurization followed by an RFCC is a popular processing route. The HDS RDS catalyst system achieves deep desulfurization, but as a consequence the residuum FCC feedstock contains double the amount of nickel and vanadium contaminants than the feedstock prepared over the HDM RDS catalyst system. Testing of both the HDS and HDM residuum FCC feedstocks in the ACE pilot plant is compared in Table 2. Comparing runs 1 and 2 demonstrates the effect of doubling feed metals on the performance of the RFCC catalyst (changing from HDM to HDS RDS 'mode'): the catalyst-to-oil ratio, selectivities to hydrogen and gasoline, and the amount of coke formed makes this mode of operation impractical for the refiner. The result of increasing catalyst additions to return the catalyst equilibrium (ecat) metal levels to base levels in the RFCC while optimizing HDS in the RDS is shown in run 3. The yields are comparable to run 1; doubling the fresh catalyst addition rate from 0.5 lb/bbl to 1.0 lb/bbl restored the catalyst yields to that of the base case (run 1, HDM RDS system) while giving 25% lower sulfur in the gasoline and 40% lower sulfur in the LCO.

Run 4 shows the effect of employing a new RFCC catalyst (*IMPACT*). Optimizing desulfurization in the RDS and therefore with a high metals RFCC feedstock, the new RFCC catalyst achieves yields comparable with those in run 3, but with half the fresh cracking catalyst additions. The improved coke selectivity and metals tolerance of the new technology is clearly evident, and coke and gas levels are only marginally higher than run 3 at twice the metals level.

Table 2. Comparison of ACE Tests of RFCC Simulation at Constant Conversion (Runs 1-5) and Constant Coke (Run 5a)

Run	1	2	3	4	5	5a
RFCC Catalyst	Base	Base	Base	New	New	New
RDS Catalyst	HDM	HDS	HDS	HDS	HDS	HDS
FCC Cat. Additions, lb/bbl	0.5	0.5	1.0	0.5	0.65	0.65
Ni+V, ppm	5929	12427	6377	12576	9776	9776
Cat-to-Oil Ratio	5.1	18.5	5.4	7.2	4.6	8.9
H_2, wt%	0.33	0.81	0.34	0.5	0.32	0.4
Dry Gas (wt%)	1.95	–	1.65	1.83	1.71	2.82
C_3+C_4, wt%	13.18	–	13.26	13.52	14.32	18.22
Gasoline[a], wt%	46.08	39.61	46.59	45.62	47.85	48.02
RON	89.1	–	88.8	90.2	88.3	90.9
MON	78.8	–	78.4	79.2	78.1	80.3
LCO[b], wt%	20.81	–	20.50	20.94	20.46	16.19
Bottoms[c], wt%	9.19	–	9.50	9.06	9.54	5.46
Coke, wt%	8.84	11.80	8.02	8.87	6.60	8.83

[a]C5-430°F, [b]430-700°F, [c]+700°F

Run 5 demonstrates the yield improvements possible by employing the new FCC catalyst and only a 30% increase in fresh catalyst additions (0.65 lb/bbl) while employing the HDS catalyst system in the RDS. The result is a processing route that achieves the lowest hydrogen yield and the highest gasoline yield, while producing the least coke. Comparing this configuration at constant coke (run 5a) reveals an even greater gasoline yield advantage and therefore benefit of the new FCC technology to the refiner.

Maximizing demetalation in the RDS unit (HDM catalyst system, run 1) means the refiner processes a low metals feedstock in the RFCC, and benefits by maintaining a low cat-to-oil ratio, in addition to producing less coke and achieving higher yields of the desired products. However, maximizing desulfurization in the RDS unit and exploiting the latest RFCC metals-tolerant catalyst technology (at a higher catalyst addition rate) means higher gasoline yields and optimum profitability for the refiner.

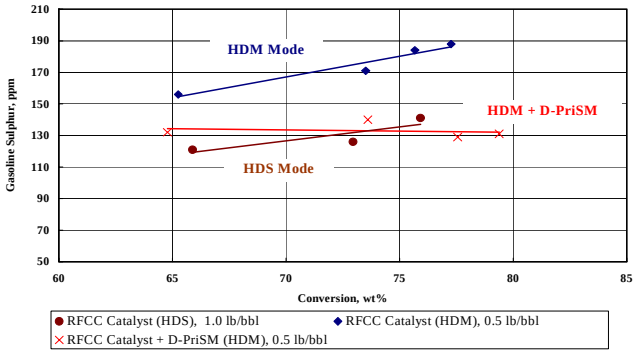

Figure 1. RDS metals management: effect of adding sulfur reduction additive (*D-PriSM*™) to base RFCC catalyst with HDM RDS catalyst on gasoline sulfur level.

RDS metals management and RFCC sulfur reduction. In this case study, the RDS product being fed to the RFCC is low in nickel and vanadium (Table 1) allowing the refiner to operate at a low fresh cracking catalyst addition rate. However, the sulfur content of the RDS product is high (0.62 wt% compared to 0.50 wt% from a HDS RDS catalyst system), which leads to an increase in gasoline sulfur of approximately 25%.

Figure 1 shows the effect of applying recent sulfur reduction additive technology to the base catalyst; Grace Davison's *D-PriSM*™ additive was combined in run 1 (Table 2). The result was to reduce gasoline sulfur from 170 ppm to 132 ppm (22% reduction). The combination of the HDM RDS catalyst system with RFCC sulfur reduction technology was able to achieve a comparable gasoline sulfur level as the HDS RDS catalyst system and base RFCC catalyst alone (Table 2, run 3), allowing the refiner to take further advantage of potential yield improvements and metals tolerance of the HDM system.

Maximum RDS and RFCC sulfur reduction. In order to optimize sulfur removal and achieve the lowest sulfur levels in transportation fuels, a HDS RDS catalyst system is combined with the use of a sulfur reduction additive in the RFCC unit. Relative to RDS operation in 'HDM' mode, this means higher fresh catalyst addition rates in the FCC due to increased contaminant metal levels in the feedstock.

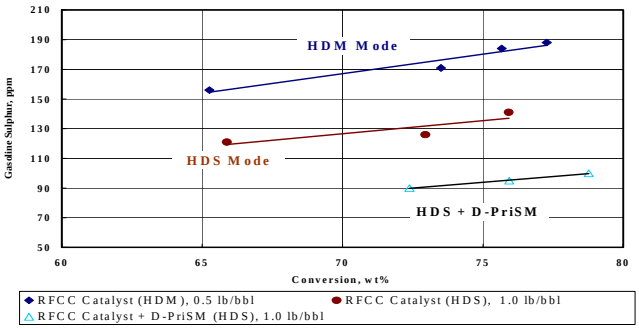

Figure 2. Maximum desulfurization: effect of adding sulfur reduction additive (*D-PriSM*™) to base RFCC catalyst with HDS RDS catalyst on gasoline sulfur level.

The HDS RDS catalyst system alone caused significant reductions in both gasoline and LCO sulfur (25 and 40% respectively). In addition, when the base RFCC catalyst is combined with the new sulfur reduction additive in run 3 (Table 2), the overall sulfur reduction in gasoline was almost 50% (Figure 2).

Conclusions

New developments in RDS catalyst system design and technology, combined with innovations in RFCC catalysts and additives mean refiners can more easily and reliably meet stringent product specifications. Improvements in metals tolerance, catalyst accessibility and sulfur reduction in RFCC catalysts have increased the flexibility and effectiveness of the refinery in processing heavier and more contaminated residual feedstocks in the FCCU.

Through a combination of RDS and ACE pilot plant testing, three processing routes have been demonstrated to optimize the upgrade of residuum to clean fuels. Operation at maximum desulfurization capability in the RDS unit upstream of an FCCU employing the latest sulfur reducing additive technology can deliver a reduction in LCO and gasoline sulfur of 40 and 50% respectively. In addition, an RDS/RFCC optimized system will alleviate the impact of metals on cracking catalyst additions and RFCC product yields with heavier feedstocks.

References

(1) Kayser, J. C., U.S. Pat., No. 6,069,012, **2000**.
(2) Boock, L. T., Petti, T. F., Rudesill, J. A., *Proc. ACS Ann. Meeting*, **1994**, 118.

Visbreaking of the heavy crude oils: Castilla, Rubiales and Nare-Jazmin

J.A. *Carrill*
Colombian Petroleum Institute-ECOPETROL
Km 7 Piedecuesta, Colombia.

L.M. Corredor, M.L. Valero
Universidad Industrial de Santander, Colombia.

Introduction

Visbreaking appears like an alternative for the conversion or transportation of heavy crudes [1,2,3]. In a refinery, this one process allows to the production of Fuel Oil and feed for the catalytic cracking units [4,5]. In the production fields, the reduction of viscosity, offers an alternative for its pipeline transportation. In this work, the obtained results of the thermal conversion of Castilla, Rubiales and Náre-Jazmín crude oils are analyzed. There were found optimal operation condition which correspond to temperature of 442 °C and reaction time of 1.2 minutes for Castilla and Rubiales crudes. For Náre-Jazmín was temperature of 456 °C and reaction time of 1.4 minutes . Under these conditions the reached conversion was 53, 60 and 68 wt %, respectively. On the other hand, the impact of this one process is determined on the reological properties and the stability of the visbreaking bottoms.

The Castilla crude has an API gravity 9.6, its content of insoluble in n-heptano is 15.9 wt %. Its high sulfur content of 2.4 wt % does not allow its use like fuel due to the restrictions imposed by the environmental legislations. Its high viscosity and density don't allow its pipeline transportation. Rubiales and Nare-Jazmin crudes are in similar situation. These heavy crude oils are located far from the refineries and of the export points. Due to all that exposed previously, it is interesting to evaluate their thermal craqueability as alternative for their transportation or as raw matter for Fuel Oil production.

Experimental

The main properties of the Castilla, Rubiales and Nare-Jazmin crude are presented in table 1. These crudes were cut at 171°C, and have been processed in a visbreaking pilot plant of the Colombian Petroleum Institute [6]. The tests were carried out to a constant pressure of 0.1 MPa and different temperatures of (from 420 °C to 456°C) and reaction time of from 1,2 minutes to 1,6 minutes.

Table 1. Characterization of the heavy crude oils cut 171ºC+.

Analysis	Norma	Unit	Castilla	Rubiales	Nare
Insoluble in n-C7	UOP 614	wt %	15,9	13,19	4,5
Insoluble in n-C5	UOP 614	wt %	16,4	13,29	6,35
Conradson carbon	ASTM D4530	w t %	16,6	13,42	9,49
Sulphur content	ASTM D4294	wt %	2,4	1,3	1,6
Acid number	ASTM D664	mg	0,2	0,5	6,68
Density @ 15ºC	ASTM D5002	g/ml	1,0	0,9	0,9
API Gravity	ASTM D1298	°API	9,6	11,9	11,1
Nickel	ASTMD 5863PE	ppm	103,1	49,7	77,5
Vanadium	ASTMD 5863PE	ppm	374,3	141,2	93,2
SARA	IP143/ASTM				
Saturates		wt %	24,0	39	26,1
Aromatics		wt %	41	37	40
Resins		wt %	16,7	9,5	31
Asphaltenes		wt %	14,1	11,4	2,6

Crude oil stability parameters were determined by Heithaus titration, adding a weak solvent such as isooctane to orto-xilene solutions of bottom. The calculations were carried out applying the expressions mentioned in [7,8] and they are presented in table 2.

Table 2. Heithaus parameters.

Crude	FR max	Cmin	Pa	Po	P	IC
Castilla	0,44	0,44	0,56	1,42	3,26	1,27
Rubiales	0,58	0,75	0,42	1,35	2,33	0,56
Nare-Jazmin	0,18	0,24	0,82	0,92	5,24	3,49

The analyzed effluents were: gases up to C4, lights from C5 up to 171 °C; atmospheric gas oil (AGO) 171-371 °C; Vacuum gas oil (VGO) 371-510 °C, and visbreaking bottoms, 510°C+ (VBB). The stability of the VBB was evaluated applying the stability tests: Heithaus titration and Spot test [9]. For the operation conditions the viscosity reduction percentages were calculated by means of the difference between the viscosity of the crude and that of the VBB (or of the bottom-naphtha mixture) about the viscosity of the crude.

Results and discussion

The operation conditions and the obtained yields are given in table 3.

Table 3. Reaction conditions and yields.

Castilla: Severity by temperature, wt %; Tr= residence time, minutes								
T °C	Tr	VBB	AGO	VGO	Naphtha	Gases	Coke	Conversion
420	1.2	53,0	21,2	23,0	0,5	0.3	2.3	45.0
437	1.2	44,0	24,4	27,5	0,9	0.57	2.5	53.3
442	1.2	43,6	26,0	25,1	1,3	0.6	3.4	53.0
456	1.2	35,1	26,8	28,1	2,0	1.6	6.3	58.6
Castilla: Severity by residence time, wt %								
T °C	Tr	VBB	AGO	VGO	Naphtha	Gases	Coke	Conversion
442	1.2	43,6	26,0	25,1	1,32	0,6	3,4	53
442	1.4	41,1	25,9	27,5	1,0	0,7	3,7	55,1
442	1.6	39,0	17,1	37,9	1,4	1,5	4,3	57,9
Rubiales : Severity by temperature, wt %								
T °C	Tr	VBB	AGO	VGO	Naphtha	Gases	Coke	Conversion
430	1,2	40,9	26,0	31,4	0,14	0,40	1,0	58,0
437	1,2	39,8	26,1	32,3	0,31	0,40	1,0	59,0
442	1,2	37,8	27,0	32,7	0,28	0,47	1,1	60,4
448	1,2	37,4	26,8	32,9	0,58	0,53	1,6	60,8
Rubiales: Severity by residence time, wt %								
T °C	Tr	VBB	AGO	VGO	Naphtha	Gases	Coke	Conversion
442	1,0	38,9	27,0	32,3	0,3	0,5	1,0	60,0
442	1,2	37,8	27,0	32,7	0,28	0,5	1,1	60,4
442	1,4	36,8	27,4	33,6	1,7	0,5	1,2	63,1
Nare-Jazmin: Severity by temperature, wt %								
T °C	Tr	VBB	AGO	VGO	Naphtha	Gases	Coke	Conversion
440	1,7	41,3	23,2	33,6	0,3	0,4	0,4	57,5
450	1,7	38,2	24,2	34,6	1,1	1,2	0,7	61,0
453	1,7	37,9	24,0	36,5	1,2	1,4	0,9	62,9
456	1,7	25,5	28,0	39,0	2,3	2,5	2,8	71,7
Nare-Jazmin: Severity by residence time, wt %								
T °C	Tr	VBB	AGO	VGO	Naphtha	Gases	Coke	Conversion
456	1,2	37,7	23,7	35,0	1,3	1,3	1,0	61,4
456	1,4	30,5	25,3	38,0	1,8	2,3	1,7	67,5
456	1,7	25,5	28,0	39,0	2,5	2,5	2,8	71,7

For Castilla and Rubiales crudes, the temperature interval inside which are obtained stable VBB is of from 437°C and 442°C to 1,2 minutes. For these crudes, under severity conditions by residence time of 1.2 minutes, there are obtained stable VBB at 442 °C. Processing the crude Nare-Jazmin at constant residence time of 1,7 minutes, is stable up to 453 °C, and maintaining the temperature constant in 456 ºC, is stable up to 1,4 minutes of residence time.

Table 4. Heithaus parameters and spot test for the VBB.

Castilla: Severity by temperature							
VBB	Spot test	FR max	Cmin	Pa	Po	P	IC
FC1	4	0,53	0,69	0,47	1,29	2,45	0,69
FC2	6,5	0,66	1,44	0,34	1,11	1,69	0,24
FC3	7	0,73	1,80	0,28	1,13	1,56	0,15
FC4	9	1	*	0	*	*	*
Castilla: Severity by residence time							
VBB	Spot test	FR max	Cmin	Pa	Po	P	IC
FC3	7	0,73	1,80	0,28	1,13	1,56	0,15
FC4	8	1	*	0	*	*	*
FC5	9	1	*	0	*	*	*
Rubiales: Severity by temperature							
VBB	Spot test	FR max	Cmin	Pa	Po	P	IC
FR1	6	0,80	0,68	0,20	1,98	2,48	0,30
FR2	6,5	0,82	0,96	0,18	1,67	2,04	0,19
FR3	7	0,88	1,10	0,12	1,68	1,91	0,11
FR4	9	1	*	0	*	*	*
Rubiales: Severity by residence time							
VBB	Spot test	FR max	Cmin	Pa	Po	P	IC
FR5	6	0,86	0,98	0,14	1,74	2,02	0,14
FR3	7	0,88	1,10	0,12	1,68	1,91	0,11
FR6	9	1	*	0	*	*	*
Nare-Jazmin: Severity by temperature							
VBB	Spot test	FR max	Cmin	Pa	Po	P	IC
FN1	3	0,56	0,38	0,44	2,04	3,62	1,14
FN2	4,5	0,74	0,66	0,26	1,87	2,52	0,40
FN3	5	0,77	0,94	0,23	1,59	2,06	0,24
FN4	9	1	*	0	*	*	*
Nare-Jazmin: Severity by residence time							
VBB	Spot test	FR max	Cmin	Pa	Po	P	IC
FN5	4	0,60	0,86	0,40	1,30	2,16	0,46
FN6	7,5	1	*	0	*	*	*
FN4	9	1	*	0	*	*	*

* Unstable product, it cannot be titrated.

The coking index (IC), according to Heithaus titration defines the stability of an atmospheric bottom in the interval of from 0,3 to 1[10], however studies carried out for vacuum bottoms indicate that this value is of from 0,6 to 1[9]. For the heavy crude oils, it was found that the stable interval corresponds at 0,1 - 1.

In figures 1 and 2, there are given the residence time and the temperature incidence over the VBB viscosity reduction with respect to the analyzed crudes.

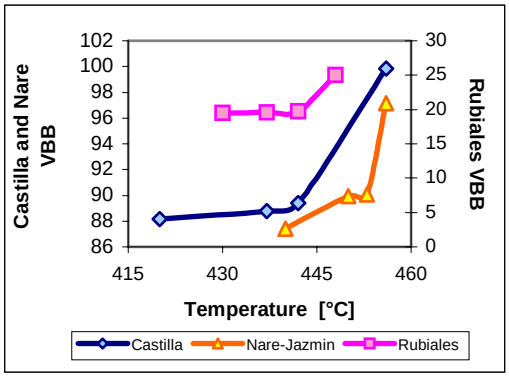

Figure 1. Reaction temperature vs. VBB viscosity reduction at 30°C.

Under conditions of severity by temperature, for the Castilla crude, there were reached VBB viscosity reductions of 88 % under the reaction temperature of 420 ºC, and almost of 100 % under the reaction temperature of 456 ºC. The Rubiales VBB, don't present considerable reductions in their viscosity, for effect of the increase in the temperature. The reduction of the viscosity of the Nare-jazmin VBB, oscillates between 88 and 97%.

Under conditions of severity by residence time, the biggest reduction in the viscosity, is obtained for the Castilla and Nare-Jazmin VBB, being presented a similarity between them although these last ones was obtained to a higher temperature operation. It is observed in the figure 2.

For the Rubiales bottoms, the reduction of the viscosity is smaller than 50% of the one registered for the other bottoms.

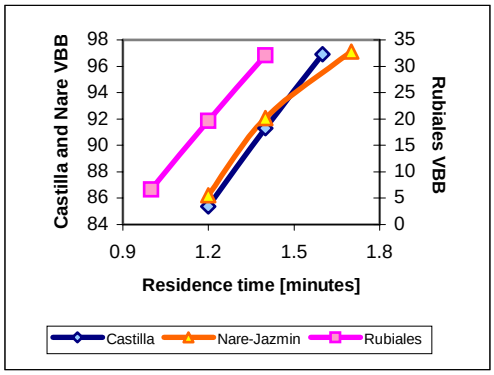

Figure 2. Residence time vs. VBB viscosity reduction at 30°C.

The conditions to be able to transport the crude ones by pipe line are: kinematic viscosity smaller or equal to 100 cSt at deformation velocities of between 10 and 100 s^{-1} at 40°C, and API gravity higher than 18. The FC3, FR3 and FN5, present viscosities of 3784, 3139 and 1171 cSt, respectively, reason why they cannot be transported without the addition of a diluter. One such way is to use naphtha that is usually available onsite, as diluents [11]. For this reason there is carried out a study adding to the VBB the naphtha fraction obtained by visbreaking reaction. These results are presented in the figures 3, 4 and 5.

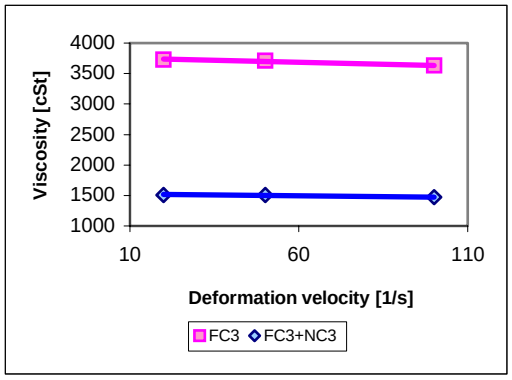

Figure 3. Effect of the naphtha addition over the viscosity of the FC3.

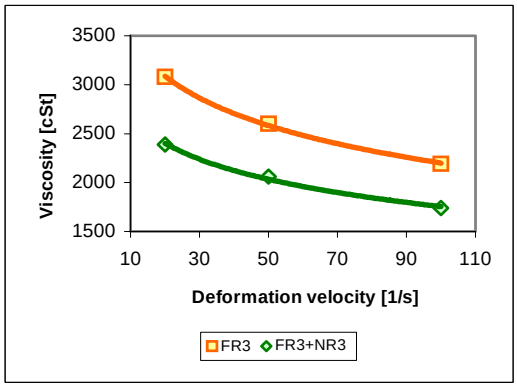

Figure 4. Effect of the naphtha addition over the viscosity of the FR3.

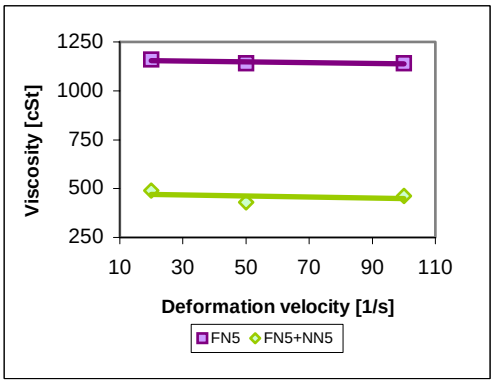

Figure 5. Effect of the naphtha addition over the viscosity of the FN5.

With the addition of visbreaking naphta to the VBB obtained under the best operation conditions, there were reached viscosity reductions of 60% for FC3 and FN5 and of 20% for FR3, however, there are not reached require viscosities that allow their transportation by pipe line. For this reason it required the use of another diluter.

Conclusions

The crude Nare-jazmin 171+ gave high yields of gas oils and light products (naphta and gases) due to its high resin and parafinic hydrocarbon content. Crude Castile 171+, produced great amount of light and VBB because of its more aromatic character. Crude Rubiales 171+ produced gas oils mainly.

At pilot plant level it was determined that the crudes should be processed under conditions of severity by temperature, at the residence time of 1.2 minutes for the crudes Castilla 171+ and Rubiales 171+ and of 1.4 minutes for Nare-jazmin 171+.

The found cocking index stability interval for the analyzed crudes was of from 0.1 to 1.0.

For the transport of the crudes by pipeline, there is not enough the viscosity reduction by thermal conversion, and there is required additional amount of diluents.

Nomenclature

FC1-5: Castilla VBB. Runs from 1 to 5
FR1-6: Rubiales VBB. Runs from 1 to 6
FN1-6: Nare-jazmin VBB. Runs from 1 to 6

Acknowledgment. This work was supported by the Division of No-Catalytic Process of the Colombian Petroleum Institute-ECOPETROL and by Universidad Industrial de Santander, under contract No. 003.

References

[1] Chaparro, M. ECOPETROL- ICP, 7 (1991).
[2] Kuo,C. Oil and Gas Journal, (1984).
[3] González, R. World Focus, (1998).
[4] Treviño, A. Ingeniería Química, 65 (1982).
[5] Speight, J. Taylor & Francis, 27 (1998).
[6]Carrillo, J. PRE-PRINTS, Pap. - *Am. Chem. Soc., Div. Fuel Chem.*, (1998).
[7] Schabron, J., Pauli, A., y Rovani, J. PRE-PRINTS, Pap. - *Am. Chem. Soc., Div. Fuel Chem.*, 44(2), (1999).
[8] Savaya, Z., and *et al.* Fuel, 68, (1989).
[9] Carrillo, J, Pantoja, F and *et al.* ECOPETROL- ICP, CT&F, 1(5), (1999).
[10] Carrillo, J and *et al*. PRE-PRINTS, Pap. - *Am. Chem. Soc., Div. Fuel Chem.*, (1999).
[11] Asomaning, S, Yen, A and Weispfenning, K. PRE-PRINTS, Pap. - *Am. Chem. Soc., Div. Fuel Chem.*, (2001).

THE PARADOX OF ASPHALTENE PRECIPITATION WITH N-PARAFFINS

Irwin A. Wiehe[1], Harvey W. Yarranton[2], Kamran Akbarzadeh[2], Parviz M. Rahimi[3] and Alem Teclemariam[3]

[1]Soluble Solutions, 3 Louise Lane, Gladstone, NJ 07934 USA; [2]Department of Chemical and Petroleum Engineering, University of Calgary, 2500 University Drive N.W., Calgary, Alberta, T2N 1N4 Canada; [3]National Centre for Upgrading Technology (NCUT), 1 Oil Patch Drive, Suite A202, Devon, Alberta T9G 1A8 Canada

Introduction

Hotier and Robin[1] found that the volume of n-paraffin at the onset of asphaltene precipitation of a crude oil with increasing carbon number of the n-paraffin reaches a maximum at carbon number 7 (n-heptane). This suggests that higher carbon number n-paraffins can be poorer solvents for petroleum asphaltenes than lower carbon number n-paraffins even though the solubility parameters of n-paraffins increase continuously with increasing carbon number[2]. However, at high n-paraffin to oil volume ratios and with increasing n-paraffin carbon numbers, lower amounts of more aromatic asphaltenes are precipitated[3]. This indicates that n-paraffins are better solvents for asphaltenes with higher carbon numbers. This contradiction is the paradox of asphaltene precipitation by n-paraffins.

Cimino et al.[4] claimed this maximum is caused by the entropy of mixing of molecules of different sizes and used an approximation to the regular Flory-Huggins model (RF-HM). Other approximations to the RF-HM for petroleum oils have been used by Hirschberg et al[5], Wang and Buckley[6], and Yarranton et al.[7,8]. By including the pseodocomponents: n-paraffin, saturates, aromatics, resins, and associated asphaltenes with a molecular weight distribution, Yarranton et al. quantitatively described the fractional precipitation of asphaltenes from Athabasca and Cold Lake bitumens with volume fraction of n-paraffin from n-pentane through n-hexadecane.

The oil compatibility model[9] has proven to be useful in predicting incompatibility of oil mixtures for fouling mitigation. This model is based upon the assumption that the onset of asphaltene precipitation occurs at the same solubility parameter of the mixture that is dubious because of the data of Hotier and Robin.

Experimental

The onset of asphaltene precipitation for two crude oils and two bitumens were determined at room temperature for n-paraffins from n-pentane through n-hexadecane. Using the same procedure, one laboratory performed measurements on Maya crude and Cold Lake bitumen while a different laboratory performed measurements on an Alberta crude, an Athabasca bitumen, and a much different Cold Lake bitumen sample. The procedure used an optical microscope for detecting asphaltene precipitation. The recorded volume of n-paraffin at the onset of asphaltene precipitation was the average of the maximum volume of n-paraffin added without observing precipitation and the minimum volume of n-paraffin added when precipitation was observed. The volume fractions of n-paraffin at the onset of asphaltene precipitation are shown in Table 1 with properties of the oils in Table 2.

Results and Discussion

Maximum. Table 1 establishes that the volume of n-paraffins going through a maximum with n-paraffin carbon number at the onset of asphaltene precipitation is a general phenomenon for petroleum oils. However, where the maximum can be distinguished, it occurs at n-paraffin carbon numbers of 8, 9, or 10 (for this study) rather than at carbon number 7, as observed by Hotier and Robin[1].

Table 1. Volume Fractions of n-Paraffin at the Onset of Asphaltene Precipitation for Five Oils

n-Paraffin Carbon No.	Cold Lake1	Cold Lake2	Athabasca Bitumen	Maya Crude	Alberta Crude
5	0.587	0.645	0.650	0.412	0.587
6	0.608	0.669	0.669	0.438	0.618
7	0.623	0.669	0.671	0.462	0.640
8	0.636	0.669	0.669	0.474	0.645
9	0.649	0.669	0.673	0.474	0.653
10	0.636	0.669	0.669	0.462	0.667
11	0.623	0.669	0.669		0.645
12	0.608	0.645	0.669	0.438	0.640
13	0.592	0.632	0.660	0.438	0.624
14	0.574	0.621	0.645		0.618
15	0.556	0.612	0.630		0.600
16	0.550	0.590	0.618	0.412	0.590

Table 2. Properties of the Five Oils in This Study

Property	Cold Lake1	Cold Lake2	Athabasca Bitumen	Maya Crude	Alberta Crude
Saturates – wt%	19.5*	19.5	16.4		38.4
- Density (g/ml)	0.882*	0.882	0.885		0.882*
- Molecular Wt.	508*	508	524		508*
Aromatics – wt%	38.2*	38.2	40.1		37.9
- Density (g/ml)	0.995*	0.995	1.003		0.995*
- Molecular Wt.	522*	522	550		522*
Resins – wt%	26.8*	26.8	28.7		12.1
- Density (g/ml)	1.037*	1.037	1.04		1.037*
- Molecular Wt.	930*	930	976		930*
C_5-Asphaltenes – Yield (wt%)	15.5*	15.5	14.8		11.6
- Density (g/ml)	1.203*	1.203	1.203		1.203*
- Molecular Wt.	2850*	2850	2910		2600
Density (g/ml)	0.991	1.001	0.9952	0.876	0.9327
Toluene Equiv.	19	19.5	18.5	38	21.0
Insolubility No.	28.5	33	31.4	47	34
Sol. Blend. No.	76	99.7	95.5	71	94.5

* Not measured but assumed to be as same as Cold Lake Bitumen 2.

Yarranton Approximation to RF-HM. By approximating the RF-HM, Yarranton et al.[6,7] determined that the ratio of the equilibrium mole fractions of each of the asphaltene and resin species in light (L) and heavy (H) phases is given by:

$$\frac{x_i^H}{x_i^L} = \exp\left\{\ln\frac{v_i^L}{v_M^L} + 1 - \frac{v_i^L}{v_M^L} + \frac{v_i^L}{RT}\left(\delta_i - \delta_M^L\right)^2\right\} \quad (1)$$

where: x_i = mole fraction of component i
v_i = molar volume of component i
R = gas constant
T = absolute temperature
δ_i = solubility parameter of component i
δ_M = solubility parameter of the mixture = $\sum\phi_i\,\delta_i$
$v^L_M = \sum x_i\, v^L_i$

Yarranton et al.[8] calculated solubility parameters for n-paraffins from a correlation based on heat of vaporization and molar volume data while Wang and Buckley[5] used a correlation with refractive index data. As is shown in Figures 1-3, the model of Yarranton et al.

correctly predicts the volume maximum with carbon number of n-paraffins at the onset of asphaltene precipitation (calculated for 0.5% precipitation) for three different oils with either the solubility parameters of Yarranton et al. or of Wang and Buckley. Therefore, this volume maximum is definitely a result of low entropy of mixing molecules of much different sizes.

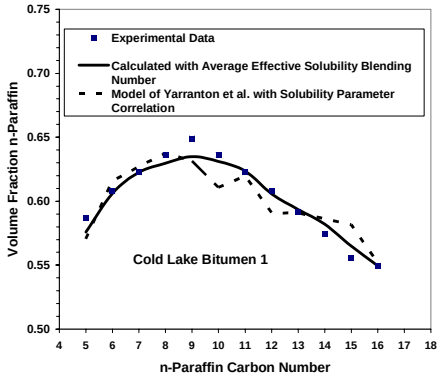

Figure 1. Volume fraction of n-paraffin at the onset of asphaltene precipitation for Cold Lake bitumen 1.

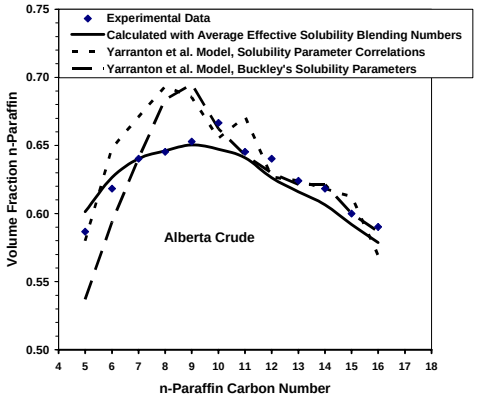

Figure 2. Volume fraction of n-paraffin at the onset of asphaltene precipitation for Alberta Crude.

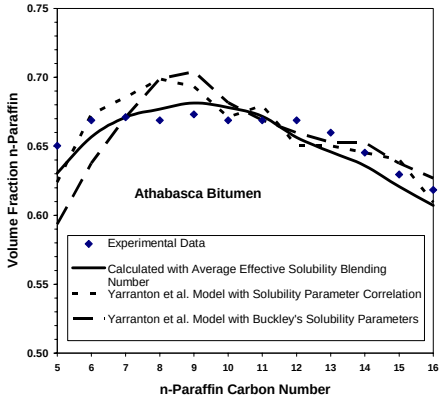

Figure 3. Volume fraction of n-paraffin at the onset of asphaltene precipitation for Athabasca Bitumen.

Oil Compatibility Model Approximation. When the Oil Compatibility Model[9] is applied to an oil without asphaltenes, this unknown oil is blended with five times the volume of a standard oil containing asphaltenes for which the insolubility number (I_N) and the solubility blending number (S_{BN}) have been determined. If this blend is found to contain insoluble asphaltenes, the oil is termed a nonsolvent oil. The maximum volume (V_{NS}) of the nonsolvent oil that can be blended with 5 ml of the standard oil without precipitating asphaltenes is determined and compared with a similar test previously run on the standard oil using n-heptane rather than the nonsolvent oil (called the heptane dilution test with result, V_H). From the assumption of equal solubility parameter of the mixture at the onset of asphaltene precipitation, the solubility blending number of the nonsolvent oil is calculated by:

$$S_{NS} = I_N\left[1 - \frac{V_H}{V_{NS}}\right] \qquad (2)$$

This equation is applied to the five oils in Table 1 using the insolubility numbers in Table 2 and treating all n-paraffins as nonsolvent oils except n-heptane. The calculated effective solubility blending numbers are in Table 3 along with the average values. These average effective solubility blending numbers of the n-paraffins are used to calculate the volume of n-paraffin at the onset of asphaltene precipitation using Eq. 2. As shown in Figures 1-3, the average effective solubility blending numbers can describe well the asphaltene onset data. This demonstrates why the oil compatibility model with compatibility numbers measured by asphaltene onset titrations has been successful at predicting oil compatibility even though the onset does not strictly occur at the same solubility parameter of the mixture. The effective solubility parameter (solubility blending number) of the oil measured with toluene and n-heptane is a good approximation of the effective solubility parameter of the oil when blended with other oils.

Table 3. Effective Solubility Blending Numbers for n-Paraffins

n-P. CNo	Cold Lake1	Cold Lake2	Athabasca Bitumen	Maya Crude	Alberta Crude	Average Eff. S_{BN}
5	-4.62	-3.63	-3.04	-10.7	-8.62	-6.13
6	-1.84	0.00	-0.31	-4.82	-3.36	-2.07
7	0.00	0.00	0.00	0.00	0.00	0.00
8	1.63	0.00	-0.31	2.09	0.75	0.83
9	3.08	0.00	0.30	2.09	1.81	1.46
10	1.63	0.00	-0.31	0.00	3.74	1.01
11	0.00	0.00	-0.31		0.75	0.11
12	-1.84	-3.63	-0.31	-4.82	0.00	-2.12
13	-3.93	-5.76	-1.62	-4.82	-2.46	-3.72
14	-6.33	-7.65	-3.80		-3.36	-5.28
15	-9.12	-9.19	-6.26		-6.35	-7.73
16	-10.05	-13.29	-8.14	-10.7	-8.03	-10.05

References

1. Hotier, G.; Robin, M., *Revue de l'IFP*, **1983**, 38, 101-110.
2. Hansen, C.M.; Beerbower, A., "Solubility Parameters", in Encycl. of Chem. Tech., Suppl. Vol., 2nd ed., Wiley, New York, **1971**.
3. Speight, J.G., The Chemistry and Technology of Petroleum, 3rd ed., Marcel Dekker: New York, **1999**, 412-464.
4. Cimino, R.; Correra, S.; Del Bianco, A.; Lockhart, T.P., in *Asphaltenes Fundamentals and Applications*, E.Y.Sheu and O.C. Mullins, Ed.; Plenum Press: New York, 1995, pp. 97-130.
5. Hirschberg, A.; deJong, L.N.J.; Schipper, B.A.; Meijer, J.G., *SPEJ.*, **1984**, 6, 283-293.
6. Wang, J.; Buckley, J.S., *Energy Fuels*, **2003**, 17, 1445-1451.
7. Yarranton, H.W.; Masliyah, J.H., *AIChE J.*, **1996**, 42, 3533-3543.
8. Alboudwarej, H.; Akbarzadeh, K.; Beck, J.; Svrcwk, W.Y.; Yarranton, H.W., *AIChE J.*, **2003**, 49, 2948-2956.
9. Wiehe, I.A.; Kennedy, R.J., *Energy Fuels*, **2000**, 14, 56-63.

CATALYTIC DIRECT LIQUEFACTION OF HIGH SULFUR LIGNITES: TEMPERATURE AND SOLVENT EFFECT ON PRODUCT DISTRIBUTIONS

Ömer Gül[†]*, Pervane Gafarova*[†*]*, Arif Hesenov**,
Harold H. Schobert[†]*, Oktay Erbatur**

**Çukurova Üniversitesi, Fen Edebiyat Fakültesi,
Kimya Bölümü, 01330 Adana, Turkey
[†]The Energy Institute, The Pennsylvania State University,
University Park, PA 16802

Introduction

The world's population and energy consumption are continuing to increase. While new energy resources are being developed, utilization of the present fossil resources in a clean and efficient way should also be evaluated.

The low-rank coal reserves are around 8.1 billion tonnes in Turkey[(1)]. However, the use of most of these low-rank coals was abondoned because of their high sulfur content (5-10% wt). On the other hand, liquefaction of these high-sulfur lignites via direct catalytic hydrogenation is quite straightforward.[(2)] This paper reports a continuation of a study in which catalytic direct liquefaction of high-sulfur coals is being evaluated.

In this study, two lignites (Mengen from Bolu and Kangal from Sivas) having high sulfur contents were hydroliquefied. In the liquefaction experiments, coal samples impregnated with ATTM as catalyst precursor were used.

Experimental

The proximate and ultimate analysis data of lignites are given in Table 1. The coals were ground to pass 60 mesh, dried at 50 °C under reduced nitrogen pressure until moisture contents fell below 3%, sealed in glass ampules under nitrogen gas and kept at -20 °C until utilization in the liquefaction experiment. All solvents and chemicals were bought from Merck and used as received.

Ammonium tetrathiomolybdate (ATTM: $(NH_4)_2MoS_4$) is used as the catalyst precursor. It was synthesized in our laboratory as described by Naumann et al.[(3)]. The catalyst (1% by wt based on Mo to daf coal ratio) was dissolved in 30 mL of distilled water and added dropwise onto 100 g of dry coal while the coal was effectively mixed with a spatula to achieve a homogeneous mixture. Following addition of the catalyst precursor, the impregnated coal was dried at 50 °C under reduced nitrogen pressure until the moisture content fell below 3 %.

In liquefaction experiments, mini bombs of 25 mL volume were used. Following loading the coal and the solvent, the reactor was sealed, and air inside the reactor was swept out by successive pressurizing (6.9 MPa cold) and depressurizing twice with nitrogen and twice with hydrogen gases. Finally the reactor was pressurized with hydrogen gas (6.9 MPa cold) and submerged into a eutectic salt bath after attaching it to a horizantally oscillating system. The horizantally oscillating system shakes the reactor with an amplitude of 2 cm at 400 cycles/min. In all of the liquefaction experiments, the duration of operation was 30 minutes. All liquefaction experiments were repeated at least three times. Therefore, the numerical quantitative data relevant to liquefied material were the mean of three corresponding values. When the standard deviations of three replicate values for the conversion exceeded 2% of the mean, a fourth replicate experiment was performed.

Table 1. Proximate and Ultimate Analytical Data of Coals

	Coals	
	BM	SK
ASTM classification	Lignite A	Lignite B
Calorific value (kj/kg)	24586	20753
Ash (wt % dry)	20.96	18.14
V.M. (wt % dry)	45.42	53.37
F.C. (wt % dry)	31.33	20.75
Elemental analysis (wt % daf) [a]		
C	74.72	66.58
H	5.91	5.94
N	1.86	1.88
S	10.34	4.05
O [b]	7,17	21,55
Forms of sulfur (wt % dry)		
Total	13.02	5.62
Pyritic	1.98	1.07
Sulfatic	0.14	0.22
Org [b]	8.18	3.31

[a] daf: dry, ash-free
[b] calculated from difference

When the liquefaction reaction time was over, the reactor was taken out of salt bath and immediately plunged into a cold water bath. The slurry content of the reactor was removed with *n*-hexane into an extraction thimble and successively extracted in a Soxhlet apparatus by using *n*-hexane, toluene and tetrahydrofuran. **O**il, asphaltene (AS) and pre-\asphaltene (PAS) were the materials solubilized in these three solvents, respectively. The mass of oil + gas products was calculated by subtracting the total mass of asphaltene + preasphaltene + char (residue) from the mass of original dry coal subjected to liquefaction.

Results and Discussion

The high-sulfur lignites Bolu-Mengen (BM) and Sivas-Kangal (SK) were hydroliquefied in the presence of catalyst and in the presence of solvents. Two different liquefaction temperatures were investigated, namely 400°C and 450°C. Ammonium tetrathiomolybdate (ATTM) was used as a catalyst precursor. Reactions were carried out with different liquefaction solvents and the results were compared regarding temperature and solvent effects.

Tetralin, being a good hydrogen donor and showing good solvation behavior, has been used widely in coal liquefaction studies.[(4-8)] Therefore, in this study, tetralin was the solvent of main choice. In liquefaction experiments with tetralin, the ratios of solvent:coal were 2:1 and 1:1. Tetrahydroquinoline

(THQ), and coal-derived oil were also used in 1:1 ratio of solvent to coal in liquefaction experiments done with BM coal. The coal-derived oil was obtained from liquefaction of Cayirhan lignite in the presence of molybdenum catalyst. Figure 1 shows catalytic liquefaction results of BM coal at 400°C.. When tetralin was used as solvent, total conversion was around 90%, regardless of solvent-to-coal ratio. The oil+gas yield and the yield of asphaltene were slightly higher when equal amounts of tetralin

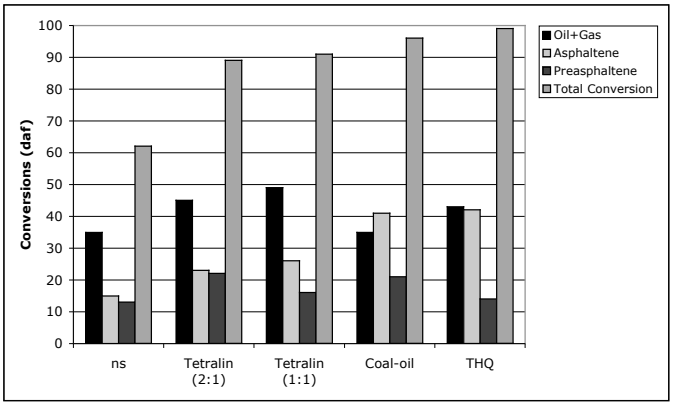

Figure 1. Main product distribution of catalytic liquefaction of BM coal at 400°C in the presence of different solvents.

and coal were used. Overall conversion was highest when THQ was used as solvent, but the yield of oil+gas was lower than the case with tetralin. At this temperature it seems that THQ was more effective than tetralin as far as total conversions were concerned. Similar observations by other researchers led them to conclude that THQ had more solvating power and also more effective in quenching radicals[9-11] compared to tetralin. Coal-derived oil as solvent mainly activated reactions towards asphaltene formation but the oil+gas yield was less than the corresponding value obtained with tetralin. This coal-derived oil had less hydrogen donation ability compared with tetralin and therefore could not quench the radicals formed as efficiently as tetralin. It rather plays the role of offering a liquid medium as discussed by others.[12]

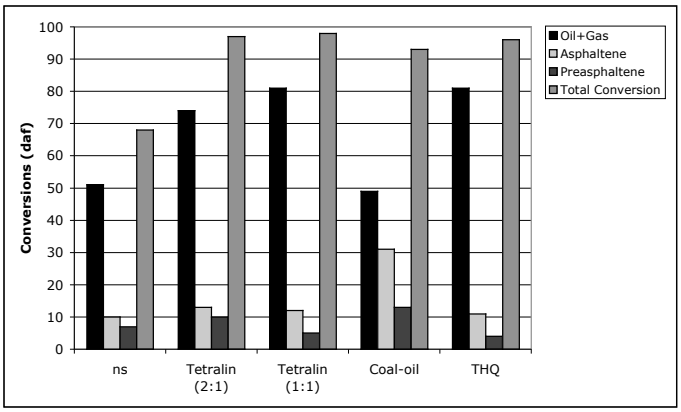

Figure 2. Main product distribution of catalytic liquefaction of BM-coal at 450°C in the presence of different solvents.

When the BM coal samples were liquefied at 450 °C the overall conversions were all higher in all solvents compared to the corresponding values obtained at 400 °C (Figure 2). Again 1:1 tetralin-to-coal ratio yielded higher oil+gas and asphaltene yields compared to the 2:1 case. With this coal overall conversion and all specific yields in 1:1 tetralin case were almost identical to the corresponding values obtained with THQ though the yield of gas+oil was a little higher in tetralin. At this temperature and pressure, tetralin could be in supercritical phase, but since there were relatively considerable amount of heavy components from coal in the same medium, this would not be a high possibility. Nevertheless, tetralin should be more mobile at this temperature compared to THQ since the latter has relatively strong interactions with coal structures via its -NH functional moiety, and in this way tetralin might be balancing the advantage of –NH in quenching radicals faster than –CH.

Tetralin has been used as the only solvent in the liquefaction experiments done with the other lignite, namely Sivas Kangal (SK). The results obtained with the liquefaction experiments done at 400 °C are given in Figure 3.

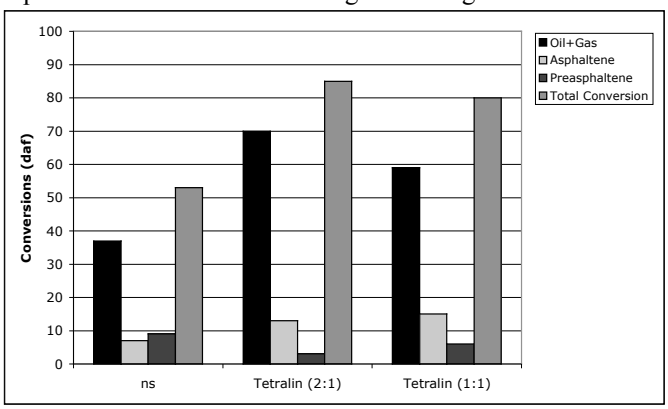

Figure 3. Main product distributions of catalytic liquefaction of SK-coal at 400°C in the presence of solvents.

Here, both the total conversion and the oil+gas yield were highest in the run where the tetralin-to-coal ratio was 2:1. Oil+gas yield reached 70 % whereas the corresponding value for BM coal was only 45 %.

When the results obtained in liquefaction experiments done at 450 °C are investigated one can notice that again total conversion and the oil+gas yield are highest in the run where tetralin-to-coal ratio was 2:1. Actually, in this experiment there was no preasphaltene, and only very little asphaltene had formed, the remainder being oil+gas fraction where the yield approaches 90 %.

One important observation regarding liquefaction behaviour of two lignites in tetralin was that 2:1 ratio of tetralin to coal had some detrimental effect in the liquefaction of BM coal when compared to 1:1 ratio case, but the reverse was true with the other coal (SK). The reason should lie in the structural differences in these two coals. BM has a higher rank than SK, i.e. more condensed aromatic structures are likely present in BM, while SK has more aliphatic structures that are probably in substituted forms on aromatic ring systems . These differences in structures determine the extent of

interaction of tetralin molecules with the coal structures, such that tetralin would interact with the aromatic ring systems in BM more effectively than in SK. With 2:1 tetralin:coal ratio, too many tetralin molecules will solvate aromatic moieties from BM and hinder the interaction of coal structures with the active hydrogen sites on catalyst particles. On the other hand, the radical cleavage reactions in SK would be faster than in BM and more tetralin molecules (2:1 case) this time will be an advantage to quench more radicals compared to the 1:1 case.

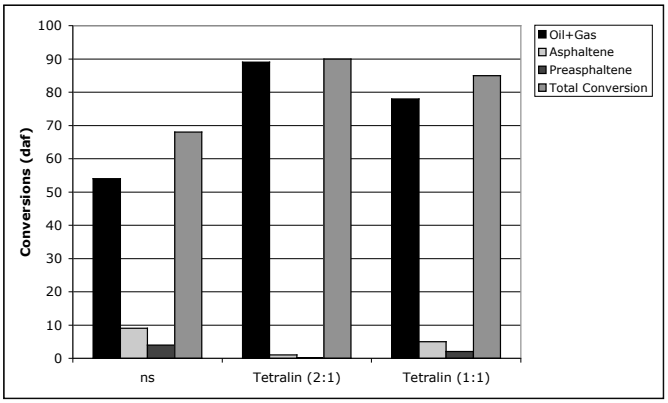

Figure 4. Main product distributions of catalytic liquefaction of SK-coal at 450°C in the presence of solvent.

Conclusions

The liquefaction characteristics of a series of high-sulfur lignites of Turkey with high volatile matter and high mineral matter contents are being investigated, and this work here constitutes a part of these investigations. These lignites show quite different responses to similar liquefaction conditions due to the structural differences in the main organic framework and also due to the differences in mineral matter composition. The two lignites whose liquefaction results are given here have quite different structural characteristics. BM has a considerable sulfur content (much more than SK) and most of these are part of the organic structures. The other lignite (SK) has a high oxygen content. The portion of the heteroatoms which are on the peripheries of aromatic ring systems in the form of carboxyls, phenolics, or other functional groups could cleave easily in the beginning stages of liquefaction reactions. Possibly the 2:1 ratio of tetralin to coal effectively stabilized the radical sites formed due to these fast cleavages. On the other hand, these types of cleavages of oxygen functionalities and short alkyl chains from the periphery of aromatic systems mainly produce gaseous products and do not help much in the formation of oils and asphaltene/preasphaltene products. This also explains why more tetralin was necessary to hydrogenate and quench the radical sites being formed in the main reactions leading to the formation of oil, asphaltene and preasphaltenes during liquefaction of SK lignite.

Acknowledgement

This work was funded by Turkish Scientific and Technical Research Council (TUBITAK). HHS also thanks NATO for funding for a visit to Çukurova University and this collaborative interchange.

References

(1) Birön, C. In *International Coal Technology Seminar*; ITU: Istanbul, **1983;** pp 23-52.
(2) Gözmen, B.; Artok, L.; Erbatur, G.; and Erbatur, O. *Energy Fuels*, **2002**, *16,* 1040
(3) Naumann, A. W. **1981;** US Patent No. 4243554.
(4) Curran, G. P.; Struct, R. T.; and Gorin, E. Prep. Pap.-*Am. Chem. Soc., Div. Petroleum Chem*., **1966,** 130.
(5) Curtis, C. W.; Tsai, K. J.; Guin, J. A. *Fuel Processing Technology*, **1987,** *16*, 71.
(6) Derbyshire, F. J.; Davis, A.; Epstein, M. J.; and Stansberry, P.G. *Fuel*, **1986a.** *70*, 372.
(7) Derbyshire, F. J.; Davis, A.; Epstein, M. J.; and Stansberry, P. G. *Fuel*, **1986b,** *65*, 1233.
(8) Yoon, E.M.; Selveraj, L.; Song, C.; Stallman, J.B.; and Coleman, M.M. *Energy Fuels*, **1996,** *10*, 806
(9) Yoon, E.M.; Selveraj, L.; Eser, S.; and Coleman, M.M. *Energy Fuels*, **1996,** *10*, 812
(10) Davies, G. O.; Derbyshire, F. J.; and Price, R. J. *Inst. Fuel*, **1977,** *50*,121.
(11) Bockrath, B. C. In *Coal Science*,; Vol. II. Gorbaty, M. L.; J. W. Larsen; J. Wender, Eds.; Academic Press: N. Y., 1983**;** p. 65.

Primary Studies on Reaction Mechanism of TSRFCC Technology

Jian-Wen Wang, Yu-Dong Sun, Hong-Hong Shan, Chao-He Yang and Jian-Fang Zhang

State Key Lab of Heavy Oil Processing, University of Petroleum, 271 North Second Road, Dongying 257061, China

Introduction

Fluid catalytic cracking process (FCC) is one of the most important processes for converting heavy oil into light fuels, and it provides nearly 85% of gasoline and 30% of the diesel oil in China. But the FCC feedstock becomes heavier and heavier and requirements of the environmentally-cleaner fuels are larger and larger, especially, the olefin, sulfur and benzene contents of gasoline are greatly limited. So it is a challenge to residue fluid catalytic cracking (RFCC) technology which has been developed in the recent decades. The RFCC technology has got great development around the reaction system [1-3], such as feeding atomization and stream stripping of high efficiency, fast separation of gas (oil vapor) and solid (spent catalyst) and reaction termination technology, and so on.

Although the feedstock of RFCC is different from that of distillate FCC and many technologies attached to the reactor have appeared, the reactor, riser, is the same for RFCC and FCC process yet. The disadvantages of the conventional riser reactor become more obvious, including too long reaction time, low catalyst activity and poor selectivity and harmful competition of different reactants [4]. In order to improve the product distribution, as well as reduce the olefin content and keep or raise the octane number of FCC gasoline and increase light oil yield and diesel oil/gasoline ratio, the two-stage riser FCC (TSRFCC) technology which is one of the advanced technologies in China was put into industrial test in May, 2002. The reaction mechanism of the commercial TSRFCC riser is studied according to commercial production data and analysis of products including oily catalyst, gas and liquid obtained by a special sampling system [4-5].

The Features of the TSRFCC-I technology

For the TSRFCC technology, the two optimized riser reactors replace the conventional single riser reactor, and the features are described as catalyst in relay, short reaction time, subsection reaction and high catalyst/oil (C/O) ratio. It can be classified by the different configurations and production schemes. For TSRFCC-I technology, the fresh feedstock is put into the first riser and react with the regenerated catalyst to a proper extent. The diesel distillate as the final product is separated from the first riser, and then the heavy oil (or the mixture of heavy oil and gasoline which need reduce the olefin content) is fed into the second riser reactor. Thus this operation can reduce over-cracking reactions of diesel oil and raise the ratio of diesel/gasoline. Because the regenerated catalyst replaces the spent catalyst, the average activity of catalyst can be enhanced, which results in increase of cracking, hydro-transfer and isomerization reactions of the olefin of gasoline. The olefin of gasoline decreases to a required criterion. If the olefin reduction of gasoline is not exigent, the recycling heavy oil as the feedstock of the second stage contacts with high activity catalyst. The reaction result can increase the yield of light oil and the processing capacity of equipment.

There are five RFCC units modified by the TSRFCC-I technology, including the RFCC units of Shenghua refinery, Huabei, Changqing, Jinxi and Liaohe Petrochemical factories (ShRFCCU, HbRFCCU, CqFCCU, JxRFCCU and LhRFCCU).

Experimental.

For studies on reaction mechanism of the TSRFCC technology and understanding the true reaction behavior of the commercial riser reactor, a special sampling system is developed by the State Key Laboratory of Heavy Oil Processing, University of Petroleum. The configurations and work principle are offered by a few published papers [6-7]. So the oily catalyst, liquid and gas products of TSRFCC units are obtained from CqFCCU, JxRFCCU and LhRFCCU. From commercial production data and analysis of experiment results, the yields of exit products of the riser, production distribution and composition of gasoline are obtained.

The pressure-measuring points of the unit are used as the sampling points of the commercial TSRFCC riser. In general the sampling points are located near to the exit of riser. The sampling points of JxRFCCU and LhRFCCU are located on the horizontal section of the exit for the two-stage riser reactor. But for CqFCCU, the sampling point of the first stage is located one meter under the horizontal stage of the exit, and the sampling point of the second stage on the horizontal section.

For CqRFCCU, the atmospheric residue, AR, is the RFCC feedstock. The feedstock of the first stage riser (FSCq) is AR and a part of recycle oil, 2610 ton/day and 60 ton/day respectively, the second (SSCq) is recycle oil, 1179.7 ton/day. The oil vapor from two risers enters into the same settler. LhRFCCU processes the AR of the mixture of 70% Daqing crude oil and 30% Liaohe crude oil. The feedstock of the first stage (FSLh) is AR, 1857.21 ton/day, the light recycle oil (LRO), the heavy recycle oil (HRO) and recycle gasoline, 344.4, 119.52 and 480.96 ton/day, are injected into the second stage riser. The first stage feed of JxRFCCU (FSJx) is the atmospheric wax oil, 2422 ton/day, and the second stage feed is LRO and HRO, 1364.88 and 63.12 ton/day. Properties of the Different Feedstock are shown in Table 1.

Table 1 Properties of the Different Feedstock

	FSCq	SSCq	FSLh	SSLh		FSJx	SSJx	
				LRO	HRO		LRO	HRO
ρ_{20} kg/m^3	913.0	988.3	898.6	935.1	957.6	908.7	985.8	1012.2
carbon residue m%	3.65	2.30	4.42	0.50	2.69	0.27	0.16	6.55
Saturate m%	84.25	64.74	50.53	39.74	46.70			
Aromatics m%	10.76	31.42	17.47	26.10	37.50			
Resin m%	3.65	3.51	30.83	34.14	14.94			
Asphaltene m%	1.34	0.33	1.17	0.02	0.86			

The sampling products are oily catalyst, liquid and gas. The methods of treating the sampling products and calculating the product yields are shown in Reference 8.

Analysis of the sampling products

Composition of the gaseous products. The composition of gaseous product in the riser reactor reflects the cracking types and extent, which can be obtained from the dry gas. As the too large deviation of product distribution between sampling and unit material balance for CqRFCCU, only the results for JxRFCCU and LhRFCCU were obtained.

It is well shown in Table 2 that the ratio of $(C_1+C_2)/(C_3+C_4)$, which describes the capacity of thermal cracking and catalyst cracking, increases a little at the second stage of JxRFCCU. This means that the extent of thermal cracking at the second stage is more exquisite. At the same time the ratio of $(C_3^{=}+C_4^{=})/(C_3+C_4)$ also increases. The main reason is that the reaction temperature of the second stage is 10K higher than that of the first stage. It is helpful for cracking reaction and bad to hydro-transfer reaction at high temperature. Thermal cracking reaction produces much (C_1+C_2) and olefin, as shown in Table 2.

Table 2 Composition of the gaseous products for JxRFCCU

Components	1st stage	2nd stage
C_1+C_2, m%	9.59	10.16
C_3+C_4, m%	71.82	69.29
$C_3^{=}+C_4^{=}$, m%	55.19	55.56
$(C_1+C_2)/(C_3+C_4)$	0.135	0.145
$(C_3^{=}+C_4^{=})/(C_3+C_4)$	0.77	0.80

Table 3 describes gaseous products' composition of LhRFCCU. For the main aim of the second stage of LhRFCCU is reducing the olefin content of gasoline, the reaction condition is a little tempered. Recycle gasoline possesses a large proportion of the feedstock of the second stage riser. The olefin cracking reaction of gasoline is very marked. So a lot of (C_3+C_4) and a little (C_1+C_2) are produced, which cause the enormous increase of LPG and $(C_3+C_4)/(C_1+C_2)$. As the same time, a part of gasoline is consumed. This makes the actual production of gasoline smaller.

Table 3 Composition of the gaseous products for LhRFCCU*

Components	1st stage	2nd stage
C_1+C_2	9.19	3.55
C_3+C_4	68.62	64.05
$(C_3+C_4)/(C_1+C_2)$	7.47	18.04

* Except recycle gasoline yield at the second stage, the yield of dry gas decreases by 1.13 percents from 3.13% to 2.00%, while the yield of LPG increases 6.98 percents from 9.27 to 16.25.

Composition of gasoline. From the theories mentioned above, the TSRFCC-I technology can reduce the olefin content of gasoline at the second stage riser obviously when the gasoline is recycled. The analysis results of sampling products of LhRFCCU are representative. Table 4 describes the result of olefin reduction of LhRFCCU after using TSRFCC-I technology. Compared with the first stage riser, the olefin content of gasoline at the exit of the second stage riser reduces by 7.96 percents from 35.66% to 27.70%, and the contents of aromatics, naphthalene and paraffin increase by 1.93, 0.76 and 5.16 percents respectively. Most of all, the content of iso-paraffin increase by 5.86 percents from 31.69% to 37.55%. The reasons are summarized as follows: (1) The function of olefin reduction of gasoline is not marked at the second half of the conventional riser reactor because of the low activity and selectivity catalyst. But for the TSRFCC technology the gasoline contacts with the regenerated catalyst at the second stage riser, the olefin cracking, hydro-transfer and isomerization reactions of gasoline are promoted. (2) The feeding nozzle of gasoline is in the front of that of heavy oil at the second stage riser, which means that the gasoline firstly enters into the riser reactor and contacts with the fresh catalyst. Thus this operation avoids adsorption influence of the big molecular components on the reactions of gasoline. The environment is clean to make gasoline reduce olefin. What's more, the hydro-transfer and isomerization reactions of gasoline induce the increase of iso-paraffin in gasoline. In spite of a big extent of the olefin content reduction, there is no significant change in RON, MON and anti-knock index of gasoline. The results can be explained by the increase of aromatics and iso-paraffin that make up the loss of octane number because of olefin reduction.

Table 4 Properties of Gasoline for LhRFCCU

		FSLh,m%	SSLh,m%
Paraffin	n-	6.21	3.80
	iso-	31.69	30.90
Naphthene		9.28	10.04
Aromatics		17.10	19.03
Olefin		35.66	27.70
RON		92.0	92.3
MON		78.9	79.2
Anti-knock index		85.8	85.8

However, the olefin content of gasoline at the second stage exit is a little more than that of the first stage exit for JxRFCCU (Table 5). This is result of the higher reaction temperature (by 10K), low catalyst/oil ratio and no recycle gasoline in the second stage riser.

Table 5 Properties of Gasoline for JxRFCCU*

		FSJx, m%	SSJx, m%
Paraffin	n-	4.25	3.80
	iso-	31.87	30.90
Naphthene		9.81	7.50
Aromatics		16.38	17.56
Olefin		37.98	40.76
RON		93.9	94.6
MON		80.6	81.2
Anti-knock index		87.2	87.9

*Temperature of the first stage: 777K, Pressure: 300.97KPa,C/O=4.01; Temperature of the second stage: 787K, Pressure: 267.33KPa, C/O=3.74

Comparison of product distribution with the conventional riser. The product distribution has been improved by TSRFCC technology. The commercial production data and the sampling analysis data can account for the advantages of TSRFCC. The production data of the conventional riser FCC (OSRFCC) and TSRFCC are shown in Table 6 for CqRFCCU and LhRFCCU.

Table 6 Material balances of CqRFCCCU and LhRFCCU

Product Distribution	CqRFCCU		LhRFCCU	
	OSRFCC*	TSRFCC	OSRFCC**	TSRFCC
Dry gas, m%	5.40	4.92	***	3.63
LPG, m%	14.37	14.55	11.89	13.33
Gasoline, m%	38.46	34.41	40.57	38.10
Diesel oil, m%	32.61	38.41	31.92	34.44
Heavy oil, m%	0.56	0.00	2.21	1.63
Coke, m%	8.60	8.11	***	8.88
Light oil, m%	71.07	72.42	72.49	72.54
Liquid products, m%	85.38	86.96	84.38	85.87

(*statistically average production data of Jan-Mar of 2003, ** statistically average production data of Aug-Oct of 2002, *** (C1+C2+Coke+ Loss=13.5m%)

For two RFCC units of CqRFCCU and LhRFCCU, the contents of both dry gas and coke decrease while the yields of LPG, light oil and liquid products increase after the revampment. The studies on reaction mechanism of the conventional RFCC technology suggested that the change of product distribution was drastic at the initial stage of the conventional riser reactor [8], that is to say, most of the heavy oil are cracked into gas, liquid and coke, and most of gasoline and diesel oil produced at the initial stage, especially at the mixing zone of feedstock and catalyst. So at the later stage the over-cracking reactions of the intermediate products deteriorate the product distribution. By the revampment with TSRFCC-I technology, the high activity and selectivity regenerated catalyst used at the second stage riser strengthens the catalytic cracking reaction while reduces the disadvantageous reactions efficiently. In the meanwhile, the diesel oil is separated as part of the final products after the first stage riser, which avoids the over-cracking reactions and enhances the yield and selectivity of the diesel oil. In CqRFCCU, the diesel oil yield increases by 5.8 percents. The dry gas yield decreases by 0.48 percents and coke yield decreases by 0.49 percents, while LPG yield increases by 0.18 percents from 14.37m% to14.55m%. In LhRFCCU, the yields of diesel oil and LPG increase by 2.52 and 1.44 percents respectively. The gasoline yield reduces a little. But although the diesel oil yield increases and the light oil yield doesn't reduce, the liquid products yield increases by 1.5 percents.

Conclusion

From analysis of the sampling products, the product distribution, conversion and composition of gasoline for two riser reactors were achieved respectively. The olefin reduction of the gasoline and the increase of LPG content are very obvious when the gasoline was recycled at the second stage riser. TSRFCC technology could enhance the diesel oil and liquid yields compared with the conventional FCC.

Acknowledgements. This work was supported by the PetroChina and the Ministry of Education. Thanks Zhong-xiang Han, Jin-you Wang, Yong-shan Tu, Jun-sheng zheng for their work in analysis of products.

References

(1) Gen-Lin Niu, Xin-Yuan Wang. *Petrochemical Technology&Application*, **2001**, 19(3): 169-173

(2) Ting-Zhao Yan. Oil and gas processing, **1997**, 7(3): 40-44

(3) ZhanYou Cao, ChunXi Lu, MingXian Shi. *Petroleum Refinery Engineering*, **1999**, 29(3):14-18

(4) Chao-He Yang, Hong-Hong Shan, Jian-Fang Zhang, Feng Du and Yu-Dong Sun. *2nd International Symposium on Better Understanding and Utilization of Havy Oil*, **2003**, Beijing

(5) Chun-Ming Xu, Shi-Xiong Lin, Liang-Gong Lu. *Petroleum Refinery Engineering*, **1997**, 27(3): 39-42

(6) Jian-Fang Zhang, Hong-Hong Shan, Chao-He Yang. *US Patent*, **2002**, Application Number:0108887A1

(7) Hong-Hong Shan, Wei Zhao, Chang-Zheng He, Jian-Fang Zhang and Chao-He Yang. Preprints, Division of Petroleum Chemistry, ACS. **2003**, 48(2): 710-711

(8) Jun-Sheng Zheng, Chao-He Yang, Gen-lin Niu, Feng Du, Hong-Hong Shan and Jian-Fang Zhang. Preprints, Division of Petroleum Chemistry, ACS. **2003**, 48(2): 704-705

The Influence of FCC Catalyst with Different Coke Deposition on the Reaction Mechanism of Olefins in Gasoline

Yu-Xia Yuan, Chao-He Yang, Hong-Hong Shan, Jian-Fang Zhang, Zhong-Xiang Han

State Key Lab of Heavy Oil Processing, University of Petroleum, 271 North Second Road, Dongying 257061, China, Fax: 86-546-8391971

Introduction

With the increasing attentions to global environment, the olefin content in specifications of gasoline product is limited. Because a lot of gasoline is produced by FCC process, so it becomes a new subject to reduce the olefin content and increase the content of isoalkane and aromatics with high Octane Number in catalytic cracking gasoline.

The key of reducing olefin is to favor H-transfer, isomerization and aromatization reactions. H-transfer can obviously reduce the olefin content, with the loss of the Octane Number of gasoline. Isomerization and aromatization reactions just could compensate the reduction of Octane Number. But compared with cracking reaction, the reaction rates of these three are slower. Because olefins in gasoline are middle products of FCC process, the catalysts in riser have partly lost selectivity and activity after initial reactions, which will handicap the secondary reactions of olefins [1]. Therefore studying the mechanisms of olefins reactions on the regenerated and spent catalysts with different coke deposition is very important to the developments of catalysts and technologies aiming reducing olefins.

Experimental

In this paper, pulsating reaction system (Fig 1) and a mini reactor with 1.5 mm i.d. (Fig 2) were employed to investigate the reaction of FCC gasoline. FCC gasoline was obtained from Shenghua Refinery, the catalyst is ZC-7300, which is produced in Zhoucun Catalyst Factory and also obtained from FCC unit of Shenghua Refinery.

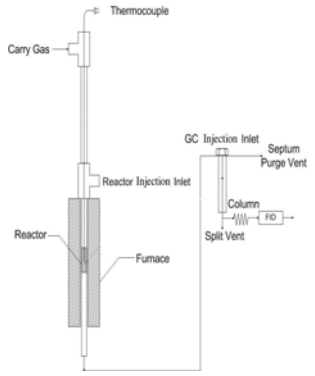

Figure 1. Reaction System

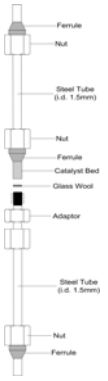

Figure 2. Structure of reactor

Results and Discussion

FCC reactions over ZC-7300 catalyst were carried on the fixed bed reactor, and spent catalysts with different coke deposition (0.5wt%,1.2wt%,2.5wt%) have been prepared previously. The data of gasoline cracking results on different catalysts were given in Table 1.

Firstly, the results showed that olefin content was all reduced more or less after reaction on different kinds of catalyst. When the coke content in catalyst is less 0.5wt%, the olefin content was reduced by 17 percent (compared with that of feed gasoline); while when coke content on catalyst is 1.2wt% or 2.5wt%, olefin content reduced by about 10 percents.

Table 1 The reaction results of FCC gasoline at 773K

Cok content on catalyst /wt%	C3+C4 /wt%	Alkanes /wt%		Naphthene /wt%	Olefin /wt%	aromatics/wt %	Other compounds /wt%	Total
		Normal alkane	Isoalkane					
feed	0.00	3.71	19.09	11.91	39.16	16.14	10.53	100.0
0.0	8.24	*4.98*	*26.21*	11.95	20.24	24.47	3.91	100.0
0.5	8.60	*4.57*	*26.71*	11.92	21.65	24.67	1.88	100.0
1.2	4.28	4.23	23.88	11.31	29.72	23.19	3.39	100.0
1.9	3.65	4.07	24.26	11.75	27.85	23.91	4.51	100.0

Note: C3,C4 ,which are not gasoline components, were not included in the olefin content.

Secondly, the content of naphthenes has nearly not changed after reactions, while isoalkane content and aromatics content have increased greatly. But the coke content on catalyst has no obvious influence on the latter both. The increase of contents of isoalkanes, aromatics and C3+C4, as the result of the processes of hydro-transfer, aromatization and cracking reaction, caused the reduction of olefins.

Selectivity of reactions. Selectivities are defined in order to analyze the influence of the coke in catalyst on the different reactions of olefins. Here, the ratio of the yield of C3+C4 to the reacted olefin fraction was defined as the cracking selectivity (S_C), and the increase of alkanes to the reacted olefin fraction was selectivity of hydro-transfer (S_H), and the increase of aromatics to the reacted olefin fraction was aromatization selectivity (S_A). Then the curves of the selectivities versus the coke content on catalyst were given in Fig 3.

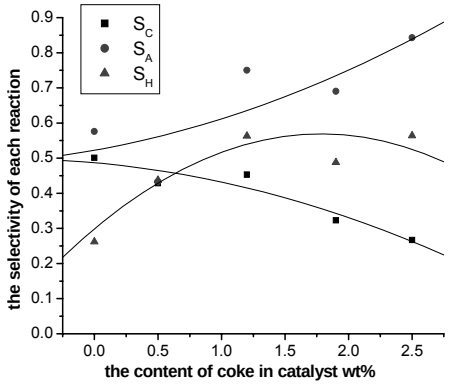

Figure 3**.** Changes of Selectivity with the Content of Coke

From Fig 3, with the increase of the coke in catalyst, the selectivity of cracking reaction decreases gradually, those of H-transfer and aromatization increase, and the selectivity of H-transfer reaches in a relatively stable level over 1.0% coke content on catalyst. The C3, C4 hydrocarbons in products can be looked as the outcome of straight cracking of olefins with above 7 carbons. The process of hydrocarbon reactions includes monomolecular and double-molecular reactions, and the ratio of the two kinds of reaction determines the distribution of products.

According to the Rideal's Mechanism [2], the double-molecular reactions in cracking process occur between the Carbonium Ions adsorbed on the active sites and hydrocarbon molecules in gas phase, so it happens on single acid site. The ratio of monomolecular and double-molecular reactions is relative to the characters of acid centers and the concentration of hydrocarbons in gas phase. With coke deposition on catalyst, the concentration of active centers decreased, which caused the decrease of monomolecular cracking selectivity. But because of coke deposition, the smaller pores in catalyst were jammed, which caused the average pore radius of catalyst increase. As large pores are propitious to double-molecular reactions, so the selectivity of hydro-transfer and aromatization reactions increased.

It is a perfect reducing olefin result to farthest kill olefins, and keep high gasoline yield and high Octane Number at the same time. At the current reaction conditions (reaction temperature is 773K), the catalyst activity had better not be too high, as the higher the activity is, the higher the cracking selectivity is, this will result in the high yield of C3, C4 will be high, and the serious loss of gasoline yield. According to the primary research, using catalyst with 0.5-1.0(wt)% coke deposition, higher ratio of olefin reduction can be kept and high gasoline yield and high selectivity of hydro-transfer and aromatization reactions obtained.

Rules of olefin molecules reaction. It is important to study the mechanism of olefin molecules reaction for clearing olefins conversion process and selecting proper operation conditions. As the activation energy of H-transfer increases with the chain length of olefins, while that of cracking reactions decreases. Then the cracking activity increased with the carbon number of olefins. However, it can be seen from the results (Table 2) that the reduction extent of C_6-C_8 olefins is little, but that of C_5 olefins is the largest.

According to Corma [3], Carbonium Ions formed from the straight chain olefins bellow C_6 will crack in β site directly before isomerization or rearrangement. While Carbonium Ions larger than C_6 will isomerize or rearrange before β-Scission. This explains the dramatic decrease with carbon number of the cracking rates of C5-C8 olefins, as indicated by Buchanan et al. What's more, the retaining time of this experiment is very short, and it has no time to isomerizes and rearrange. And the test result just proved the Corma's conclusion.

And that, the ratio of $C_4^=/C_3^=$ (wt) (it's 2.12 in products) indicated that C_3, C_4 were not all formed by direct β-Scission of heptene, then part of C_3, C_4 should be from direct β-Scission of olefins above C_9, or from olefins' cracking after polymerization. At the same time, there is no C_1 or C_2 in products, which proved that pentenes can not straightly crack. And in olefins reaction study of pure compounds, there was no β-Scission for pentenes. All these phenomena suggested that pentenes should first polymerize with themselves or other olefins, and then crack.

The result of study to 1-heptene proved that 1-heptene mainly cracked at 773K, with more than 47(wt)% of yield of propylene and iso-butylene[4]. While in this experiment, $C_7^=$ in gasoline only decreased by 0.7 percent after reactions, much less than that for 1-heptene. And the change of alkanes and aromatics of C_7 in gasoline also suggested that it is impossible for $C_7^=$ to directly aromatize and H-transfer, the same is $C_6^=$. In a word, the coexistence of hydrocarbons will obviously influence the mechanisms of hydrocarbon molecules reaction, at least affect the product distribution. As it is impossible to reduce olefins in gasoline in molecule circumstance, then studying the mechanism of interactions among hydrocarbons has obviously realistic meanings.

Table 2 The hydrocarbons composition of upgraded gasoline

Carbon number	alkanes/wt%		naphthenes/wt%		olefins/wt%		aromatics/wt%	
	before	after	before	after	before	after	before	after
C_3	0	0	0	0	0	1.37	0	0
C_4	0	0.05	0	0	0	2.91	0	0
C_5	1.21	1.9	1.09	0.87	13.18	7.06	0	0
C_6	6.63	6.1	2.17	2.39	9.33	8.92	1.92	1.63
C_7	4.37	5.63	1.8	2.28	8.84	8.14	1.86	2.66
C_8	4.53	6.36	2.59	3.37	5.06	4.71	4.55	7.04
C_9	2.94	3.52	3.23	1.83	2.66	0.93	4.79	7.3
C_{10}	2.38	2.69	0.85	0.3	0.38	0.21	2.47	3.88
C_{11}	0.73	1.85	0.19	0.27	0	0	0.56	0.67
C_5-C_{12}	22.8	28.06	11.91	11.31	39.46	29.97	16.14	23.19

Note: 773K, coke on catalyst 1.2%(wt)

Quality of upgraded gasoline. It is the most ideal result to convert olefins in gasoline to **i**so-alkanes above C_5 and aromatics, because they have high Octane Number and will not influence the gasoline yield. So the content of **i**so-alkanes and aromatics in gasoline is also one of aspects to upgrade. Fig. 4 gave the mutative curves of the content of **i**so-alkanes , aromatics and naphthene in upgraded gasoline with temperature on different catalysts.

The three hydrocarbon in products should be the outcomes of straightly H-transfer or H-transfer following isomerizations of olefins, and the yield will be influenced by H-transfer and isomerization reactions. From the Figure 4, the lower the coke content on catalyst is, the higher their content in upgraded gasoline is. And the content of them in upgrade gasoline increases with temperature increasing, reaching the culmination (about at the temperature of 673K), and then declines.

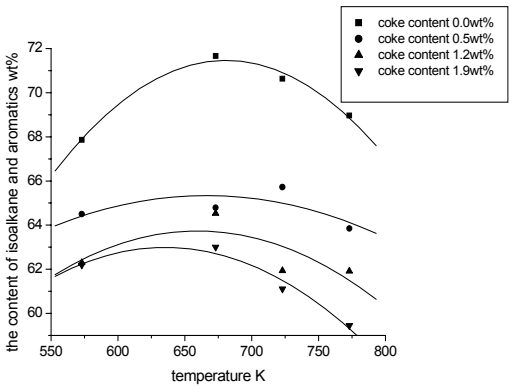

Figure 4. The content of iso-alkanes , aromatics and naphthene in upgraded gasoline influenced by temperature

As shown in Fig3, the selectivity of H-transfer increased with the coke content on catalyst increased, it seems that this phenomenon of these curves in Fig 4 is in conflict with that conclusion. But it is because that the content of isoalkane, naphthene and aromatics is the integrated result of H-transfer, aromatization, isomerization reactions. Although higher coke content could favor H-transfer and aromatization, which also causes the increase of normal alkanes, it will restrain cracking reaction at the same time. Then the yield of gasoline increases, and the relative content of **i**so-alkanes, aromatics and naphthene in upgraded gasoline decreases with coke content.

In a word, in terms of gasoline yield and quality, Using the spent catalyst with 0.5~1.0(wt)% coke, and at lower temperature (673K-773K), we can effectively reduce the content of olefins, and keep high gasoline yield and high selectivity of H-transfer and aromatization**.**

Conclusions

Under the conditions of very short contact time between the gasoline and catalyst, naphthenes in gasoline hardly react, and olefins decrease mainly via cracking reactions, H-transfer and aromatization.

High temperature and low coke content in catalyst can favor the cracking activity of olefin. Using the spent catalyst with 0.5~1.0(wt)% coke, we can effectively reduce the content of olefins, and keep high gasoline yield and high selectivity of hydro-transfer and aromatization. And lower temperature (673K-773K) will improve the distribution of hydrocarbons in the upgrading gasoline.

The obvious interaction of different hydrocarbon compounds in the upgrading process was found, the mechanism does not agree with that of pure olefin compounds.

Acknowledgements. We greatly appreciate the financial support given by the Ministry of Education, PetroChina and Sinopec to the research of this subject.

References

(1) Jun-wu Chen, Han-chang Cao; Catalyst Cracking Technology and Engineering, Sinopec Press: Beijing, **1995**.

(2) Wojciechowski B.W. The Reaction Mechanism of Catalytic Cracking:Quantifying Activity, Selectivity and Catalyst Decay. Catalysis Review, **1998**,40(3):209-328.

(3) Corma A, Orchilles A.V., Current views on the mechanism of catalytia cracking Microporous and Mesoporous Materials 35-36 (**2000**) 21-30.

(4) Zheng-Li, Mechanistic Studies on Solid Acidic Catalyzed Reactions of Alkenes and Its Application in TSRFCC Technology, Ph.D. Dissertation, University of Petroleum, **2003**.10.

FUTURE CHALLENGES OF HYDROTREATING CATALYST TECHNOLOGY

Henrik Topsøe, Ramus G. Egeberg, and Kim G. Knudsen

Haldor Topsøe A/S, Nymøllevej 55, DK-2800 Lyngby, Denmark

Summary

In this presentation we will discuss the advent of tighter fuel specifications and in particular how the very low sulfur content allowed in transportation fuels has set a new agenda for the refining industry. Each refiner must decide how to most cost-effectively implement the needed technology upgrading, whilst also being able to shift the product slate composition as demand for different fuels grows. The decision on e.g. whether to revamp an existing HDT unit or build a grassroots unit requires a detailed analysis of the whole refinery and a deep understanding of the detailed kinetics of the hydroprocessing reactions.

In recent years, several scientific advances have provided new fundamental insight into HDS catalysis. Recent scanning tunneling microscopy (STM) experiments and density functional theory (DFT) calculations have shed light on the atomic-scale structure of Co-Mo-S catalysts, the origin of the high-activity Type II sites, and the detailed molecular reactions that take place. We will also discuss the discovery of a metallic edge state on the active catalyst nanoparticles that has spurred the development of a new series of high-activity catalysts based on the so-called BRIM^{TM} technology.

Challenges in Catalyst Technology

The demand for low sulfur transportation fuels requires that refiners evaluate the many different options for reaching the target. Selection of catalyst types is one of the important decisions. As sulfur conversion increases, we are left with the most refractory species – alkylated dibenzothiophenes. Under idealized conditions, the conversion of these molecules that are sterically hindered mainly proceeds via a prehydrogenative route instead of direct desulfurization (1-5). Since NiMo catalysts are generally more active for the indirect hydrogenative route and CoMo catalysts more active for the direct route, one should think that NiMo is the preferred option for ultra deep desulfurization. However, at low hydrogen pressures and high space velocities CoMo catalyst are often seen to outperform NiMo catalysts (4). It has been observed that nitrogen compounds may inhibit the hydrogenative pathway (6-9), and by conducting detailed studies into the influence of such effects under real feed conditions (9) it was found that specific basic nitrogen compounds have a profound effect on HDS and HDN activity. This is presumably a result of competitive adsorption. These nitrogen compounds inhibit both direct and indirect desulfurization but the effect is largest for the latter. Thus, selection of catalyst depends on both feedstock and operation conditions. In addition, issues such as hydrogen availability and other product properties may play a role (10).

Besides the issues related to the legislative drive for removing sulfur the refiners are also faced with a growing demand for diesel fuels. Such a demand may partly be met by producing less low value products such as heating oil. This can be done by converting heavy fractions by hydrocracking or 'mild hydrocracking' processes or one may adopt upgrading processes e.g. for light cycle oil. The latter alternative requires new technology that not only removes refractory sulfur species in the presence of high amounts of nitrogen but also perform a certain degree of ring opening to reach a reasonable product cetane number.

The development of new catalysts no longer proceeds by trial-and-error but goes hand in hand with the insight gained from fundamental desulfurization studies. Some recent developments are highlighted below.

Support Interaction and Origin of Type I/II Sites

The role of support interactions in desulfurization catalysts has been an important topic for a number of years. Most studies have dealt with alumina-supported NiMo or CoMo sulfides that are predominantly used in the industry. By using alumina as a support, the dispersion of MoS_2 edges is quite high due to the formation of small stable nanoclusters. A high edge dispersion is important since it increases the amount of Co (Ni) that can be accommodated at the edges forming the active Co(Ni)-Mo-S structure (1). However, the support interaction also has important implications for the intrinsic activity of the active sites. Several years ago we observed (11) that increasing the sulfiding temperature from 673 K to 873 K resulted in modified Co-Mo-S structures (Type II Co-Mo-S) with substantially higher activity per active site than those formed at the lower temperature (Type I). The existence of these two different structures is related to the interaction between Mo and surface alumina OH groups during preparation leading to monolayer type structures that are difficult to sulfide. Other studies (12,13) also show some evidence for Mo-O-Al linkage in Type I structures and thus corroborate the idea that a weak support interaction is needed to create Type II sites. The linkages can be broken by high temperature sulfiding but this decreases the MoS_2 edge dispersion and it is therefore preferable to find alternate procedures. This may occur by introduction of additives or chelating agents or by using weakly interacting supports (14-18).

The formation of multi-stack MoS_2 structures has been observed in catalysts containing Type II sites. However, multi-stacking may only be a by-product of weaker support interactions and it is also possible to produce single slab Type II Co-Mo-S samples (1). Furthermore, as discussed below, only the top layer of multi-stacks will expose the special brim sites that seem to play a critical role in hydrogenative desulfurization.

Recently, the origin of intrinsic activity differences between Type I and Type II structures has been the subject of a DFT study (19). Here the direct connection between the presence of linkage to the alumina and HDS activity was addressed by calculating the difference in Mo-S bond strength when oxygen linkages are introduced. It was shown that Mo-O linkages are most probably located on the S edge and the presence of such oxygen linkages was seen to increase the energy required to form sulfur vacancies significantly. Since the sulfur vacancies are necessary for sulfur extraction reactions, this provides us with a consistent picture of the influence of support interaction on the Type I and Type II reactivity.

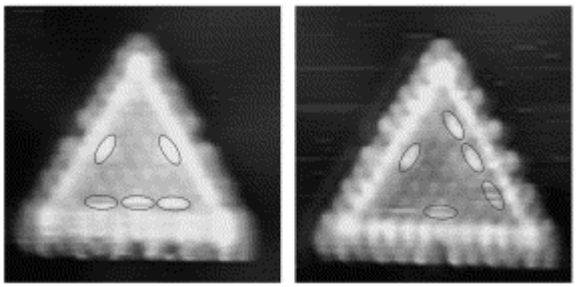

Figure 1. Consecutive STM images of thiolate species adsorbed on the brim sites of a MoS_2 nanocrystal. The time lapse between the images recorded at room temperature is *ca.* 1 min showing a high mobility of the adsorbed molecules along the brim. Adapted from (20).

BRIM™ Technology

The existence of both direct and prehydrogenative desulfurization routes has been known for many years, yet very little information on the precise molecular reaction steps has been available. STM studies have provided interesting clues as to how these reactions proceed. MoS_2 nanoparticles with a triangular geometry posses special brim sites with metallic character. By combining these studies with DFT calculations, it was found (20) that thiophene can be hydrogenated and ring opened on the brim sites, whereafter the butenethiolates diffuse to sulfur vacancies on the cluster edge, where the second sulfur-carbon bond is broken. Consecutive STM images (**Figure 1**) show how the hydrogenated species are highly mobile supporting the outlined two-step reaction pathway.

In parallel with these findings, Haldor Topsøe has developed a new preparation procedure that provides high activity hydroprocessing catalysts. This new BRIM™ technology not only optimizes the brim site hydrogenation functionality but also increases the direct desulfurization pathway. The first two commercial catalysts based on this technology are Topsøe's TK-558 BRIM™ (CoMo) and TK-559 BRIM™ (NiMo) for FCC pretreatment service. They show superior activity (**Figure 2**) and have very recently been successfully adopted by many refiners.

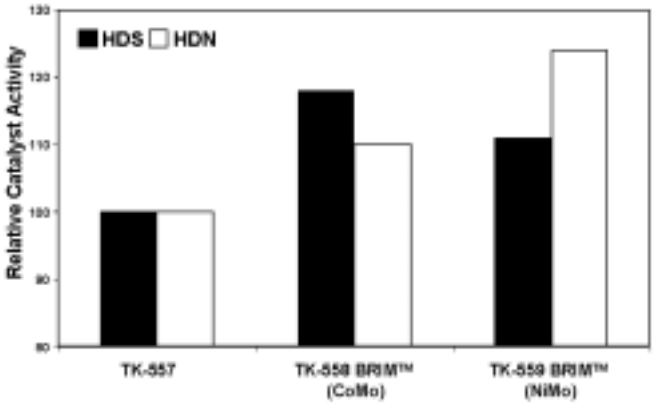

Figure 2. Relative activities of Haldor Topsøe's new BRIM™ technology catalysts for FCC pretreatment service. These catalysts rely on the highly active brim sites present on catalyst nanoparticles.

Conclusions

The challenges that the refining industry is facing now and in the years to come call for major developments within hydroprocessing catalyst technology. To assess how a specific refinery successfully adjusts to the new legislation and market demands, a detailed knowledge of reaction kinetics and catalyst reactivity and selectivity is required. The progress in fundamental HDS studies on support interaction, catalyst morphology and reaction pathways is expected to continue to provide new opportunities for the development of improved commercial catalysts.

References

(1) Topsøe, H.; Clausen, B.S.; Massoth, F.E. *Hydrotreating Catalysis – Science and Technology*,,Vol 11, Ed. Anderson, J.R and Boudart, M.; Springer Verlag Berlin, 1996.
(2) Landau, M. V.; *Catal. Today* **1997**, 36, 393.
(3) Whitehurst, D. D.; Isoda, T.; Mochida, I. *Adv. Catal.* **1998**, 42, 345.
(4) Knudsen, K. G.; Cooper, B. C.; Topsøe, H. *Appl. Catal. A* **1999**, 189, 205.
(5) Song, C. *Catal. Today* **2003**, 86, 211.
(6) Nagai, M.; Kabe, T. *J. Catal.* **1983**, 81, 440.
(7) Nagai, M; Sato, T.; Aiba, A *J. Catal.* **1986**, 97, 52.
(8) van Looij, F.; van der Laan, P.; Stork, W. H. J.; DiCamillo, D. J.; Swain, J. *Appl. Catal. A* **1998**, 170, 1.
(9) Zeuthen, P.; Knudsen, K. G.; Whistehurst, D. D. *Catal. Today* **2001**, 65, 307.
(10) Tippet, T.; Knudsen, K. G.; Cooper, B. C. *Proc. NPRA Annual Meeting* **1999**, Paper AM-99-06.
(11) Candia, R.; Clausen, B. S.; Topsøe, H. *Proc. 9th Iberoamerican Symposium on Catalysis* **1984,** Lisbon, Portugal, 211.
(12) Leliveld, R. G.; van Dillen, A. J.; Geus, J. W.; Konigsberger, D. C. *J. Catal.* **1997**, 165, 184.
(13) Diemann, E.; Weber, Th.; Müller, A. *J. Catal.* **1994**, 148, 288.
(14) Topsøe, H.; Candia, R.; Topsøe, N.-Y.; Clausen, B. S. *Bull. Soc. Chim. Belg.* **1984**, 93, 783.
(15) van Veen, J. A. R.; Gerkema, E., van der Kraan, A. M.; Knoester, A. *J. Chem. Soc. Chem. Commun.* **1987**, 22, 1684.
(16) Vissers, J. P. R; Scheffer, B.; de Beer, J. H. J.; Moulijn, J. A.; Prins, R. *J. Catal.* **1987**, 105, 277.
(17) Medici, L.; Prins, R. *J. Catal.* **1996**, 163, 38.
(18) Coulier, L.; Kishan, G.; van Veen, J. A. R.; Niemantsverdriet, J. W. *J. Phys. Chem. B* **2002**, 106, 5897.
(19) Hinnemann, B.; Nørskov, J. K.; Topsøe, H. *submitted*.
(20) Lauritsen, J. V.; Nyberg, M.; Nørskov, J. K.; Clausen, B. S.; Topsøe, H.; Lægsgaard, E.; Besenbacher, F. *J. Catal*. **2004**, 224, 94.

Nature of active sites on sulfided $CoMo/Al_2O_3$ and its connection with catalyst selectivity in FCC gasoline hydrodesulfurization

[1]Jae-Soon Choi, [2]Françoise Maugé, [1]Christophe Pichon, [3]Josette Olivier-Fourcade, [3]Jean-Claude Jumas, [1]Carine Petit-Clair, and [1]Denis Uzio

[1]IFP, Solaize BP n°3, 69390 Vernaison, France
[2]Laboratoire Catalyse et Spectrochimie, UMR-CNRS 6506, ENSICaen, 6 Boulevard du Maréchal Juin, 14050 Caen Cedex, France
[3]Laboratoire des Agrégats Moléculaires et Matériaux Inorganiques, UMR-CNRS 5072, Place Eugène Bataillon, Case Courrier 015, 34095 Montpellier Cedex 5, France

Introduction

Gasoline from Fluid Catalytic Cracking unit (FCC gasoline) has a high sulfur concentration and may contribute alone more than 90% of the sulfur contained in a total gasoline pool. Therefore, sulfur present in FCC gasoline is a key target in order to meet future sulfur specifications on gasoline. One of the viable technological options is the hydrodesulfurization (HDS) of FCC gasoline[1].

Main sulfur compounds present in FCC gasoline are thiophenes and benzothiophenes, which are relatively easy to remove by conventional HDS catalysts[2]. However, hydrodesulfurization with conventional catalysts is accompanied by the hydrogenation (HYD) of olefins, which are also abundantly (25-50%) present in FCC gasoline. To preserve the octane number of FCC gasoline during HDS process by avoiding simultaneous olefin hydrogenation, it is necessary to improve the selectivity of the conventional catalysts (*e.g.*, sulfided $CoMo/Al_2O_3$). One of possible ways to achieve this goal is to modify catalyst active sites distribution, if different sites are responsible for HDS and HYD, respectively. However, contradictory views still exist on the nature of active sites for HDS and HYD[2-4].

The objective of the present work was to get a better insight into the relationship between different sites on sulfide and catalyst selectivity (HDS/HYD). Tin was added to sulfided $CoMo/Al_2O_3$ and the resulting reactivity variations were studied. The surface organometallic chemistry (SOMC) was used for tin deposition and the local structure of Sn on sulfided $CoMo/Al_2O_3$ was characterized by a multi-technique approach consisting of ^{119}Sn Mössbauer and infrared spectroscopies, as well as EXAFS.

Experimental

Catalyst preparation and characterization. Tin deposition on CoMo sulfide was carried out by reacting tetraallyltin ($Sn(C_3H_5)_4$, +95%, STREM CHEMICALS) with the surface of freshly sulfided $CoMo/Al_2O_3$. First, an oxide precursor (3 wt% CoO-10 wt% MoO_3/Al_2O_3) was sulfided at 673 K in flowing 15 vol% H_2S/H_2 under atmospheric pressure and then the sulfided sample was transferred, without air contact, to the reactor designed for the SOMC treatment. This reactor, containing the solution (complex + solvent), had been purged by Ar flow before catalyst introduction. The reaction was done at RT in flowing H_2 for 2 h. After reaction, the catalyst was washed with pure solvent (n-heptane) under Ar flow. To ensure complete decomposition of the anchored complexes, a post-treatment was performed by reduction under pure H_2 flow at 473 K.

^{119}Sn Mössbauer spectroscopy analyses were carried out at RT using an EG & G Novelec constant acceleration spectrometer in transmission mode. A fresh Sn-containing sample was placed in the specific Pyrex cell, which was sealed under vacuum and then transferred to the spectrometer to avoid air contact. The recorded spectra were fitted with Lorentzian profiles by a least-squares method and the isomer shifts were determined relative to the center of the $BaSnO_3$ spectrum recorded at RT.

For the infrared (IR) spectroscopy measurements, the sulfide sample previously kept under Ar was taken out in air and pressed into a self-supporting disc (10 mg, 2 cm^2). It was then placed into the IR cell and re-sulfided *in situ*. First, IR spectra of fresh sulfide were obtained at RT and 100 K, then small calibrated pulses of carbon monoxide (CO) were introduced into the IR cell at 100 K up to an equilibrium pressure of 133 Pa. IR spectra were recorded after each CO introduction with a Nicolet Magna 550 FT-IR spectrometer equipped with a liquid-nitrogen-cooled MCT detector. The spectrometer operated at 4 cm^{-1} resolution collecting 512 scans.

EXAFS experiments were performed at LURE (Laboratoire pour l'Utilisation du Rayonnement Electromagnétique, Orsay, France) using DCI, a storage ring operated with an electron energy of 1.85 GeV and a current between 260 and 360 mA. The samples were loaded under inert atmosphere and data were collected at RT for the Mo and Co K-edges.

Catalyst performance evaluation. Catalytic test were performed in an autoclave under constant hydrogen pressure with a model FCC gasoline feed. This feed was composed of 1000 ppm sulfur as 3-methylthiophene (> 98%, Fluka), 10 wt% olefin as 2,3-dimethyl-2-butene (> 97%, Fluka) or 1-hexene (~ 98%, Fluka), and solvent as *n*-heptane (> 99%, HPLC grade, Fluka). Fresh catalyst was introduced under argon (Ar) flow into the reactor containing *n*-heptane, which was also previously purged by Ar flow to prevent any air contact of the catalyst. The reactor was purged again by nitrogen (N_2) stream, prior to the injection of reactants consisting of 3-methylthiophene and 2,3-dimethyl-2-butene or 1-hexene. Then, the temperature was increased up to the reaction temperature of 473 K under N_2 atmosphere. After introducing hydrogen (H_2) to have a total reaction pressure of 2.5 MPa, the reaction was started by stirring the reaction mixture. The composition of the reaction mixture was monitored during the reaction, by analyzing the liquid samples using a gas chromatograph (Varian, CP-3800) equipped with a flame ionization detector and a 50-m-long and 0.2-mm-diameter (I.D.) capillary column (HP PONA, 0.5 μm film thickness).

Results and Discussion

Tin doping and structure changes. Tin deposition on $CoMo/Al_2O_3$ sulfide by surface organometallic chemistry of tetraallyltin seems to have taken place maintaining the initial morphology of sulfide slabs, as EXAFS spectra at the Mo and Co K-edges did not show any noticeable change with tin doping even up to 2.4%. Moreover, very high Sn dispersion seems to have been achieved, as indicated by the absence of Sn-Sn environment in ^{119}Sn Mössbauer spectra. Mössbauer spectroscopy also showed that the tin environment was rich in sulfur and oxygen. It suggests that tin-complex anchoring have proceeded through the hydrogenolysis of Sn-C bonds on SH and/or OH groups. The SH groups might be linked to Mo or Co-promoted Mo sites, H-bonded to support OH groups, or located at Al^{3+} sites. As a result, tin doping could have led to the blocking of different sites on sulfide catalysts, according to the Sn loading. Information related to site blocking could be obtained by infrared spectroscopy analysis of CO species chemisorbed on catalyst surface at 100 K (Figure 1) or of catalyst OH groups at RT without CO chemisorption (Figure 2). The introduction of 0.5 wt% Sn decreased the numbers of support sites (OH groups, Al^{3+} sites) and sulfide slab sulfur vacancies. Higher Sn loadings (1.6 or 2.4 wt% Sn) continued to decrease the number of sulfur vacancies but the decreasing rate was considerably lowered. On the other hand, the number of free OH groups and Al^{3+} sites did not change any more significantly at 1.6 or 2.4 wt% Sn. On the contrary, the number of support OH groups H-bonded with sulfide slabs (which we call here

"interfacial sites") decreased drastically at these high Sn loadings, while much less effect was observed at 0.5 wt% Sn. The site blocking by tin seems to have proceeded without significant strength change of residual sites, as no evident band shift trend was observed.

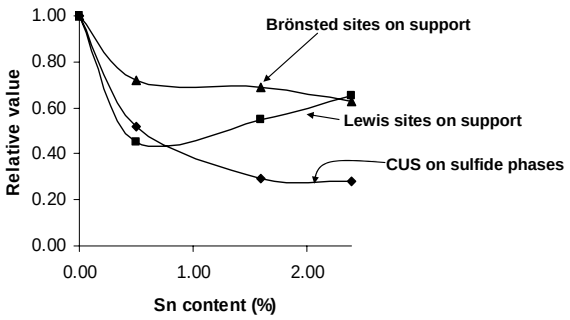

Figure 1. Site blocking caused by tin doping on sulfided $CoMo/Al_2O_3$. Number of sites (relative values) estimated from IR bands of different CO species adsorbed at 100 K.

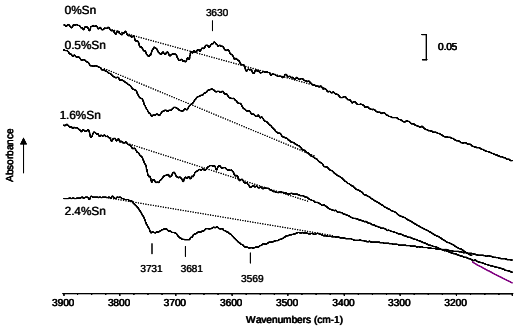

Figure 2. IR spectra of the OH band region of the sulfided $CoMo/Al_2O_3$ with different Sn loadings, after subtraction of sulfided alumina contribution. Band at 3630 cm^{-1} is attributed to the support OH groups H-bonded with sulfide phases[5].

Reaction networks and active sites. The conversion of 3-methylthiophene proceeded via pre-hydrogenation of thiophenic ring and showed an apparent first-order kinetic behavior on $CoMo/Al_2O_3$ sulfides with or without Sn-doping. Hydrogenation of 2,3-dimethyl-2-butene was a consecutive reaction involving intermediate isomerization to 2,3-dimethyl-1-butene. Hydrogenation of 2,3-dimethyl-1-butene started when equilibrated isomer composition was attained and had apparent zero-order kinetics. The conversion of 1-hexene involved isomerization and hydrogenation in parallel. The isomer concentration was again quickly equilibrated and hydrogenation of 1-hexene followed apparent zero-order kinetics. To assess the impact of tin doping on catalyst performance, the rates of three major reactions involved (hydrodesulfurization of 3-methylthiophene, olefin isomerization, and olefin hydrogenation) were compared in terms of tin loading (Figure 3). We could get some interesting information about active sites for the reactions involved, by analyzing the patterns of activity drop for these three reactions (see Figure 3) in connection with the site blocking patterns of different sites (see Figures 1 and 2). Tin-doping did not affect the double-bond isomerization of olefins and as it was only the number of support sites which was not decreased drastically by tin-doping, the support sites seem to play an important role in this reaction. Hydrodesulfurization and olefin hydrogenation were significantly inhibited by tin-doping. According to infrared spectroscopy, the decreased hydrodesulfurization activity could be nicely explained by the decreased number of sulfur vacancies on sulfide phases and activity drop in hydrogenation by the disappearance of support hydroxyl groups in interaction with sulfide phases thus interfacial sites. Therefore sulfur vacancies on sulfide phases seem to play as active sites in hydrodesulfurization, having little influence on olefin hydrogenation or isomerization. The interfacial sites appear to play an important role in olefin hydrogenation reaction pathway. Further studies will however be required to examine the possible role of interfacial sites in hydrodesulfurization.

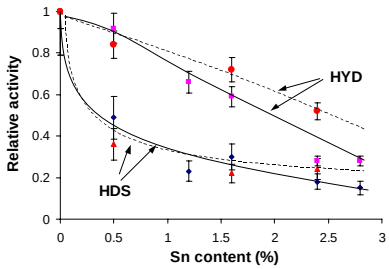

Figure 3. Evolution of 3-methylthiophene HDS and olefin HYD activities as a function of Sn loadings. Dashed lines correspond to the mixture of 3MT and 2,3-dimethyle-2-butene and solid lines to that of 3-methylthiophene and 1-hexene.

Conclusions

In this work, we have investigated the nature of active sites responsible for the sulfide catalyst selectivity in FCC gasoline hydrodesulfurization process, by studying catalyst structure changes and selectivity evolution brought by tin doping via surface organometallic chemistry. Main findings can be summarized as follows:

- Tin doping of sulfided $CoMo/Al_2O_3$ by surface organometallic chemistry proceeded with little change in catalyst bulk structure.
- Finely dispersed tin led to the blocking of different sites (sulfur vacancies on sulfide slabs, support sites, and interfacial sites) without significant change of site strength.
- Sulfur vacancies on sulfide slabs are essential for the conversion of 3-methylthiophene but of much less importance for olefin conversion.
- Support sites seem to play a major role in olefin isomerization with little impact on HDS or HYD.
- Interfacial sites (support hydroxyl groups H-bonded with sulfide phases) appear important in olefin hydrogenation reaction pathway. Further studies are, however, necessary to understand the exact role of interfacial sites in HDS.

References

(1) Baco, F.; Debuisschert, Q.; Marchal, N.; Nocca, J.L.; Picard, F.; Uzio, D., Prime G+ Process Desulfurization of FCC Gasoline with Minimized Octane Loss, AIChE Spring National Meeting, 10-14 March 2002, New Orleans.

(2) Topsøe, H.; Clausen, B.S.; Massoth, F.E. In *Catalysis, Science and Technology*; Anderson, J.R.; Boudart, M. Ed.; Vol. 11, Springer-Verlag: Berlin, 1996.

(3) Miller, J.T.; Reagan, W.J.; Kaduk, J.A.; Marshall, C.L.; Kropf, A.J., *J. Catal.* **2000**, *193*, 123.

(4) Hatanaka, S.; Yamada, M.; Sadakane, O., *Ind. Eng. Chem. Res.* **1997**, *36*, 5110.

(5) Topsøe, N.-Y.; Topsøe, H., *J. Catal.* **1993**, *139*, 641.

DEVELOPMENT OF HYDRODEMETALLIZATION CATALYST FOR DEEP DESULFURIZATION OF ATMOSPHERIC RESIDUE

Takeshige TAKAHASHI, Hidehiro HIGASHI and Takami KAI

Department of Applied Chemistry and Chemical Engineering,
Kagoshima University, Kagoshima 890-0065 JAPAN

Introduction

The deep hydrodesulfurization (HDS) of an atmospheric residue (AR) has been the most important processes to produce low sulfur vacuum gas oil (VGO) for an FCC process. However, when the deep HDS (sulfur content is below 0.3 wt%) of the AR was carried out over a catalyst combination employed in commercial process, that is, demetallization catalyst (HDM), metal tolerant HDS catalyst and high active HDS catalyst, it was found that the high active HDS catalyst was easily deactivated due to the deposition of coke from an asphaltene (ASP) decomposition (1). The detailed study revealed that since the ASP and a maltene as higher reactive heavy residue than the former simultaneously decomposed on a commercial high active HDM catalyst under severe reaction conditions, a large amount of coke was deposited on the HDM surface. As the result, the pore mouth of the HDM catalyst was plugged by the coke at early operation period. In the present study, new HDM catalyst with low activity was prepared and applied to pilot plant scale (catalyst volume is 500ml) fixed bed reactor. The HDS catalyst supported on medium pore (11 nm) was supplied in the rest of the reactor. The effect of metal composition of new type HDM catalyst on catalyst deactivation has been discussed for deep HDS operation. Furthermore, the effect of reaction temperature of HDM catalyst on the catalyst life has also been discussed.

Experimental

In the present study, two kinds of catalysts were used. CDS-R2 is the HDS catalyst (MoO_3=12.0wt%, CoO=1.0wt%, NiO=1.5wt%) supported on γ-alumina with 10.4 nm of average pore size. CDS-DM1 is new HDM catalyst (MoO_3=3.3wt%, NiO=0.7wt%, V2O5=4.0wt%) developed in the study. The sulfur and ASP contents in Khafji AR are 3.95 and 8.2 wt%, respectively. The half of sulfur in the AR is presented in the ASP. The Conradson Carbon Residue (CCR) in the AR is 13.0wt%.

The HDS reaction was carried out in a fixed bed type reactor operated at high H2 pressure. The schematic diagram of the experimental apparatus and experimental procedure were reported in a previous paper (2).

Results and Discussion

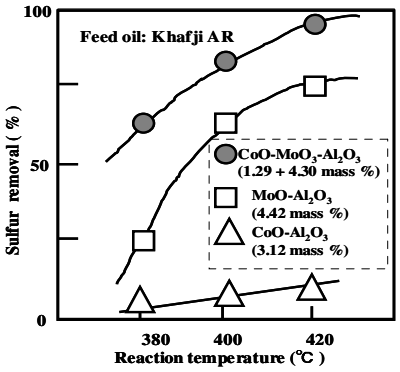

Fig.1 Effect of reaction temperature on sulfur removal over low active catalysts.

Figure1 shows the effect of reaction temperature on sulfur removal over catalysts stipulated as an HDM catalyst for the reaction of Khafji AR. The sulfur removal activity of the Co-alumina and Mo-alumina catalysts was very low and the activity of catalyst simultaneously modified with Mo-Co supported on alumina was high as reported in a literature (3). Furthermore, it was found that molybdenum was active metal for the HDS reaction from the figure.

Figure2 demonstrates the effect of extent of asphaltene cracking on vanadium removal over the same catalysts as shown in Figure1. The vanadium removal rate increases with asphaltene cracking rate. Although 50wt% of vanadium was removed at the 25wt% of asphaltene decomposition, the vanadium removal rate over 50% is proportional to the asphaltene removal rate. Furthermore, the relationship between vanadium removal rate and asphaltene removal rate is laid down on the straight line as shown in Figure 1. This result indicates that vanadium removal activity over the catalysts is almost the same as each other.

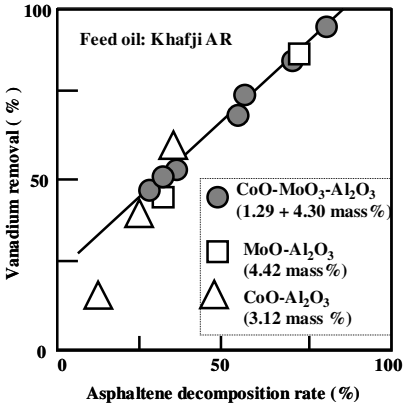

Fig.2 Effect of asphaltene decomposition rate on vanadium removal over low active catalysts.

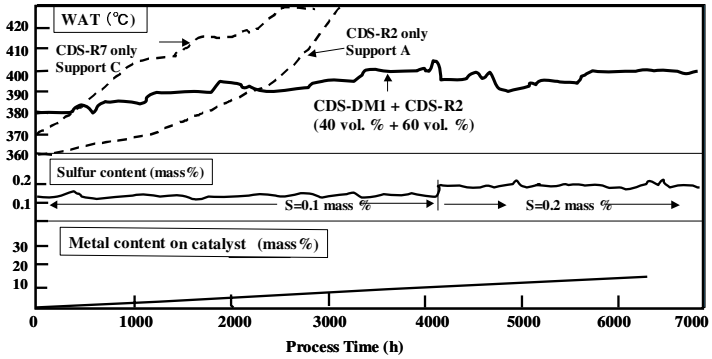

Fig.3 Relationship between WAT, sulfur content and metal on catalyst, and process time.

Figure 3 shows the relationships between reaction temperature to maintain 0.1 wt% sulfur in the product oil (Weight Average Temperature = WAT), sulfur content in the product oil, metal content on the HDM catalyst and process time (time on stream). The relationship between WAT and process time over CDS-R2 and CDS-R7 catalysts are also demonstrated in Figure3. The WATs obtained from two HDS catalysts steeply increased with process time and reached at 683K as the temperature called as the end of reaction. On the other hand, The WAT obtained from the combination catalysts was below 673K after 4000h of process time.

The combination of low active HDM catalyst and high active HDS catalyst is effective to the deep hydrodesulfurization of atmospheric residue. The effect of reaction temperature at HDM zone on CDS-DM1 life was also discussed

References

(1) Higashi,H., Takahashi,T. and Kai,T., *J.Jpn Petro.Inst.*, in print
(2) Higashi,H., Takahashi,T., Kai,T., *Catalysis Survey from Japan*, **5**,111 (2002)
(3) Japan Petroleum Institute ed., "Petroleum Refining Process", Kodansha Scientific, pp.37-99 (1998)

Characteristics of Maya crude hydrodemetallization and hydrodesulfurization catalysts

Mohan S. Rana, J. Ancheyta, S. K. Maity and P. Rayo*

Instituto Mexicano del Petroleo, Eje Central Lazaro Cardenas 152, Mexico City, 07730, Mexico; **msingh@imp.mx*

Abstract

It was found that supports prepared by ammonium carbonate and urea hydrolysis methods have improved pore size distribution (PSD) as well as pore volume. The HDM activity increases while the HDS activity decreases with increasing the average pore diameter (APD). The results of HDM and HDAs activities of catalyst protrude distinct contribution of PSD of support which has more capabilities to retain metal deposition and better diffusion of complex organo-chelating metals. It has been also proposed that deposited vanadium sulfide may act as auto-catalytic activity for HDM and HDAs.

Introduction

The challenging task in hydrotreating of heavy oils is the hydrodemetallization (HDM) which ends up in the metal sulfide accumulation on the catalyst surface and as a result blocking of the active sites and pores [1-3]. This becomes more complicated since virtually infinite number of complex hydrocarbon like asphaltenes together with the molecules containing heteroatom; mainly S, N, V and Ni etc are present in high concentration. The available information using PSD, TEM and XRD suggests that V and Ni exist as crystallite sulfides [4]. In order to draw the concept governing the effect of support preparation in HDT catalysts performance, different γ-Al_2O_3 support preparation methods were employed to vary the porosity and PSD which play an important role in stability as well as in metals retention capacity on the surface of catalyst. The different characterization of the catalysts before and after reaction provides important information about the role of textural properties on metal deposition.

Experimental

γ-Al_2O_3 supports were prepared by using different precipitation agents such as urea (γ-Al_2O_3-u), ammonium carbonate (γ-Al_2O_3-acs) and ammonia (γ-Al_2O_3-am). The details of the preparation of support are given elsewhere [5]. The Co-Mo promoted catalysts were prepared by the sequential incipient wetness impregnation method. The compositions and textural properties of catalysts are reported in Table 1.

The specific surface area (SSA), pore volume (PV) and PSD were carried out using N_2 adsoption-desoption at -196°C. X-ray power diffraction (XRD) patterns were collected on a Siemens D500 diffractometer using CuK_α radiation. The TEM experiments were carried out in Jeol 100CX-II equipment.

The catalytic activities were carried out with a mixture of Maya crude and diesel 50/50 (w/w) at high pressure up-flow micro reactor [5]. The diesiel was used as diluent to avoid precipitation and gum formation during the feed processing. The properties of the feed are presented in Table 2. The Metals (Ni, V), S and N were analyzed in the feed and products by flame atomic adsorption spectrometry, UV-fluorescence, chemiluminescence respectively. Asphaltene is defined as the insoluble fraction in n-C_5. 10 ml of catalyst was sulfided *in-situ* with a mixture of DMDS and SRGO containing ≈2 wt. % ´S´ and wet the catalyst bed at RT. The final conditions of sulfidation were 320°C, 2.8 MPa for 5h. After sulfidation, the flow was switched to the real feed and the following operating conditions were adjusted: temperature of 380° C, LHSV of $1h^{-1}$, H_2/HC of 356 m^3/m^3 and pressure of 5.4 MPa [5].

Table 1. Catalyst characterization and composition

Catalysts	Textural properties and composition					PSD % (nm)					
	SSA m^2/g	PV ml/g	APD nm	Mo wt.%	Co(Ni) wt.%	5	10	20	50	100	200
CoMo/Al_2O_3–u	136	0.39	12.9	7.5	2.5	3.3	15	34.8	34.9	11.8	0.2
CoMo/Al_2O_3–acs	160	0.47	17.3	6.8	2.5	7.6	4.8	19.2	32.8	29.7	5.0
CoMo/Al_2O_3–am	169	0.27	6.5	7.5	2.5	32.1	59	7.0	1.0	0.0	0.0
CC	175	0.56	15.2	10.6	(2.8)	4.6	15	61.9	5.2	12.8	0.0

Table 2. Feed composition

Properties	
Elemental analysis	
C, wt. %	84.2
H, wt. %	8.8
N, wt.%	0.18
S, wt. %	2.21
Metal, wppm (Ni+V)	151
Asphaltene, wt. %	8.43
Physical properties	
Density, 20/4°C	0.88
Pour point, ° C	-15
Ramscarbon, wt. %	5.45
Viscosity,g/cms,100° C	9.45

Results and Discussion

Characterization

γ-Al_2O_3 supports were prepared by aqueous solutions of aluminum nitrate and urea or amm. carbonate in which precipitant is obtained by *in-situ* hydrolysis. However, the different parameters such as aging time, pH, precipitating agents, concentration of solution etc. play an important role to generate the textural properties of support. A plausible explanation for high APD is that during the precipitation the CO_3 is trapped in a bulk between the aluminum oxyhydroxide, which escapes during the calcinations and provides larger porosity and improved PSD. The ammonia prepared alumina exhibited a *Type IV* isotherm, indicative of meso-porosity. The other two supports exhibited a *Type II* isotherm suggesting almost no micro- or meso-porosity. The CoMo/γ–Al_2O_3-acs and CoMo/γ–Al_2O_3-u supported catalysts showed greater number of pores toward macro size diameter, while CoMo/γ–Al_2O_3-am catalyst exhibits only meso-pores after active metal impregnation.

In figure 1, XRD pattern of promoted catalyst does not give any information about the active metal crystallization, which might be due to the low loading of Mo on high SSA support. Spent catalyst (after 60 h time-on stream) XRD carried out in order to see the metal deposition (Ni and V) on the outer surface of catalyst is also shown in the figure. Deposited metals exist as the sulfide compounds and are attributed to the V_3S_4, V_2S_3 and Ni_3S_2 phases [6]. These sulfided phases can be compared with the standard values (symbols in figure 1) of the Joint Committee on Powder Diffraction Standards (JCPDS).

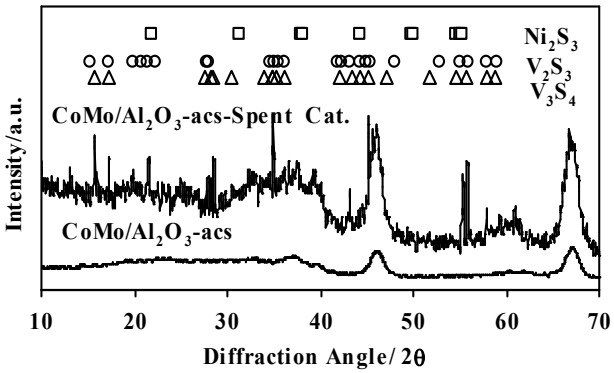

Fig. 1. XRD pattern of supported and spent catalysts

XRD results were further confirmed by spent catalysts TEM (Figure 2) which shows that V_2S_3 phase exists in rod shaped crystallites. It is also possible that nickel may associate with vanadium [Ni(V_3S_4)] which grew perpendicular on the surface of support. Similar kind of TEM results were obtained by Smith and

Wei [4] for the HDM of model molecules. The MoS_2 slabs/stacks reduce drastically in spent catalysts due to the deposition of contaminants and crystals [3]. However, greater number of acicular or rode shaped crystallites were observed in case of $CoMo/Al_2O_3$-acs compared with commercial catalyst as shown in Figure 2. These results indicated that $CoMo/Al_2O_3$-acs is having higher capacity to retain metals (Ni, V) due to the higher amount of >50nm pores (62 %) which is less in the CC (18 %) as shown in Table 1.

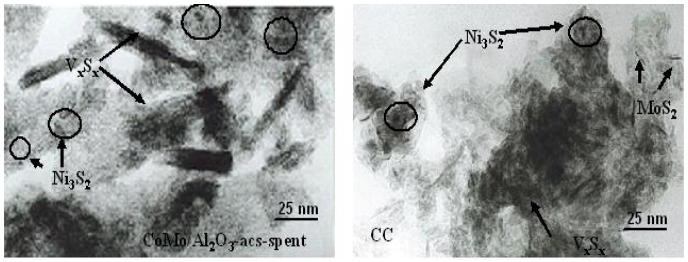

Fig.2: TEM micrographs of lab prepared and commercial catalysts

Catalytic Activities

The catalytic activities after 60h time-on-stream (TOS) are reported in Figure 3. In general, activities decrease with time-on-stream in similar magnitude for all catalysts including commercial one. The activity decrease is due to the metal poisoning on the catalyst surface. The results of the commercial catalyst (CC) are shown in the figure, which contain higher amount of Mo as well as 3.5 wt. % of TiO_2.

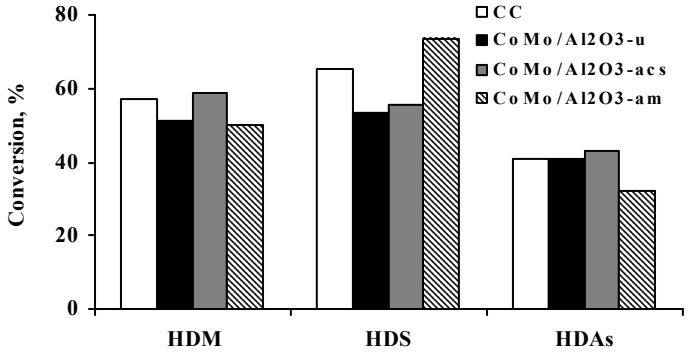

Fig. 3. Activities comparison between the catalysts after 60h TOS

The HDM activity among all lab prepared catalysts containing Co-Mo is slightly better for $CoMo/\gamma\text{-}Al_2O_3$-acs while smaller pore catalyst ($CoMo/\gamma\text{-}Al_2O_3$-am) showed lower activity for HDM. Thus, the PSD are in good agreement with HDM conversion. The low conversion in the case of $CoMo/\gamma\text{-}Al_2O_3$-am is due to its pore distribution in the range of 5-15 nm while the other catalysts have macro pore size profile in the range of 20-200nm.

In figure 3, the comparison between HDM and HDS showed opposite trends which revealed that HDM catalyst should be essentially macro porous in nature. Thus, HDM conversion is limited in the case of $CoMo/\gamma\text{-}Al_2O_3$-am due to the penetration of porphyrins or metal chelating compounds into the pores. The Maya crude contains significant amount of asphaltene, which are responsible for catalyst deactivation in hydroprocessing along with metal deposition. It is observed that the HDM as well as hydrodeasphaltening (HDAs), significantly depend on the catalyst pore structure while the HDS activity showed different behavior in figure 3. This means that the HDS activity distinctively differ from the HDM and HDAs. Most probably the HDS activity appreciably depends on the surface area and the active sites. $CoMo/Al_2O_3$-am showed the lowest activity for HDM and HDAs while maximum activity can be seen for HDS, therefore, HDM and HDAs conversions are limited due to the diffusional limitations of complex metalloid and asphaltenes molecules less than 10nm pore diameter. Thus, performance of heavy oil HDT process with regard to different functionalities, such as HDM, HDS, and HDAs, is clearly linked to the porosity and nature of the heavy crude oil.

To further asses the PSD affect on different activities conversion after 60 h TOS. HDS, HDM and HDAs activities are shown in Figure 4 against average pore diameter along with metal (V+Ni) deposition on the catalyst. The HDM activity increases while the HDS activity decreases when increasing the APD. The expected reasons of decreasing HDS activity is the blocking of active sites and the deposition of carboneous and metallic impurities in the interstices between the catalyst particles. Different catalyst results show that the metallic deposition on the catalyst surface is more of the V metal sulfides that deposited as larger crystallite than Ni as shown by the TEM micrographs. The XRD and TEM results indicate that Ni is subtlety distributed on the catalyst surface in comparison with V.

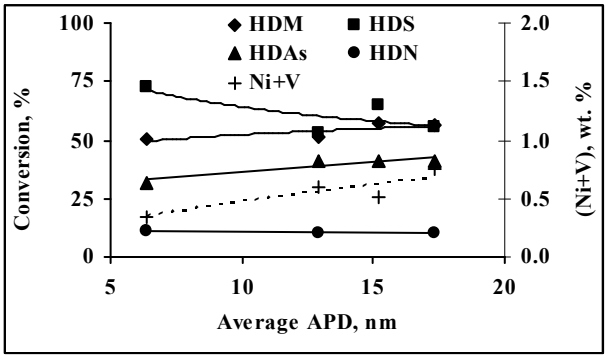

Fig. 4. Effect of average pore diameter on catalysts activity

In conclusion, the TEM and XRD results showed higher deposition of metal on bigger pores with a rod-shape crystalline phases while low porosity catalysts are randomly oriented and overlapping irregular shape of crystallites. Other characterization results of spent catalyst showed that the higher APD the greater the carbon deposition and S/Mo ratio, and hence the greater the stability or metal retention capacity of catalyst. It is also strongly expected that the deposited V_xS_x phases provide some auto-catalytic activity on the surface of the catalyst. Thus, HDM catalyst should be essentially macro porous in nature while HDS conversion is hardly effected by porosity.

Conclusion

The effect of support preparation on the pore size distribution and average pore diameter apparently controls the catalytic activities of heavy crude oil. HDM and HDAs activities significantly depend on the catalyst pore size distribution while the HDS activity may depend on the metal dispersion and surface area of supported catalysts.

References

1. E. Furimsky, F. E. Massoth, Catal. Today 52 (1999) 381.
2. E.Y. Sheu, Energy Fuels 16 (2002) 74.
3. S. Eijsbouts, Stud. Surf. Sci. Catal. 127 (1999) 21.
4. B.J. Smith, J. Wei, J. Catal. 132 (1991) 21.
5. M.S. Rana, J. Ancheyta, P. Rayo and S.K. Maity, Catal. Today, Accepted.
6. I. Kawada, M.N. Onoda, M. Ishii, M. Nakahira, J. Solid Satate, Chem., 15 (1975) 246.

ADSORPTIVE DESULFURIZATION OF TRANSPORTATION FUELS OVER NICKEL BASED ADSORBENTS DERIVED FROM LAYERED DOUBLE HYDROXIDES

*Jennifer Clemons, Subramani Velu, Xialiang Ma and Chunshan Song**

Clean Fuels and Catalysis Program
The Energy Institute and
Department of Energy and Geo-Environmental Engineering
The Pennsylvania State University
209 Academic Projects Building,
University Park, PA 16802
* E-mail: csong@psu.edu

Introduction

Upcoming environmental regulations are pushing towards cleaner fuels for various uses. The Environmental Protection Agency (EPA) has mandated that the sulfur content of gasoline to be below 30 ppmw by 2006, down from the current average of 300 ppmw. At the same time, the diesel fuel will be required to contain sulfur content well below 15 ppmw. Due to the current interest in fuel cells, ultra clean fuels are needed, because of the low tolerance of contaminates. The PEM fuel cell, which many consider as a good possible fuel cell for automotive applications, requires a transportation fuel with less than 1 ppmw sulfur.

Deep desulfurization has become a more difficult problem as restrictions become tighter and available crude oils contain more sulfur[1]. Traditionally hydrodesulfurization (HDS) has been the most common method of sulfur removal. This process is inconvenient to produce ultra-clean fuels, especially for fuel cell applications[2] because of the high temperature and pressure requirements[1, 3], which increases the overall system cost[4]. To reduce the sulfur concentration of a gas oil from 500 ppmw to 10 ppmw, the hydrogen pressure in a traditional HDS is needed to be increased by1.5 to 2 times [5].

The aromatic sulfur compounds such as 4, 6-Dimethyldibenzothiophene (4,6-DMDBT) are the most difficult ones to remove by the traditional HDS systems[4]. Transportation fuels also contain a significant amount of aromatic compounds, so any type of sulfur removal system should selectively remove only the sulfur compounds without removing aromatics[2].

Recently, our group has been working on the development of a new process termed as "Selective adsorption for removing sulfur (PSU-SARS)" to produce ultra-clean transportation fuels for fuel cell applications[2, 3, 6]. New adsorbents based on zeolites, supported metals, mixed oxides, metal sulfides, etc are being developed, Among them, Ni-based adsorbents perform better in removing sulfur from gasoline and jet fuels.

The object of the present study was to develop new Ni-based adsorbents derived from hydrotalcite-like layered double hydroxide (LDH) precursors. The LDH materials are represented by a general formula: $[M(II)_{1-x}M(III)_x(OH)^2]^{x+}[(A^{n-})_{x/n}yH_2O]^{x-}$, where M(II) = Mg, Ni, Zn, Cu, Co, Mn, etc; M(III) = Al, Fe, Cr, etc, A^{n-} is an interlayer anion such as CO_3^{2-} [7]. These materials upon calcinations offers highly active mixed metal oxides with high metal surface area and high metal dispersion, and employed as catalysts and adsorbents in various chemical processes[8]. A new series of NiZnAl-mixed oxides with different Ni:Zn:Al atomic ratios were synthesized and their adsorption performance in removing organo sulfur compounds from transportation fuels is being investigated for the first time and the preliminary results are reported here.

Experimental

A series of NiZnAl-LDHs with different Ni:Zn:Al atomic ratios were synthesized by co-precipitation at a constant pH, around 10[8]. For simplicity the adsorbents are labeled as NiZnAl-A through NiZnAl–E for the Ni:Zn:Al atomic ratios 2:5:1, 3:4:1, 4:3:1, 5:2:1, and 5.5:5.5:1, respectively. A mixed aqueous solution of $Ni(NO_3)_2$ * $6H_2O$, $Zn(NO_3)_2$*$6H_2O$ and $Al(NO_3)$ * 3.9 H_2O of appropriate atomic concentrations and an aqueous solution containing a mixture of KOH/K_2CO_3 were added dropwise by maintaining a constant pH. The precipitate was aged at 65°C for 30 min, filtered, washed with distilled water, dried overnight and then calcined in air at 400°C for 6 hours. The calcined samples were reduced in H_2 flow in a continuous flow reactor at 500°C for 6 h, cooled down to the room temperature in H_2 flow and then sulfu-free n-hexane was passed through the reduced samples. The samples were then retrieved from the reactor and stored in the sulfur-free n-hexane for adsorption experiments. The reduced materials under this condition are non-pyrophoric and could be exposed to air during characterization and adsorption experiments.

Two different model fuels, representative of diesel and jet fuel were used in the present study. The model diesel contained 100 ppmw each of benzothiophene (BT), dibenzothiophene, (DBT) 4-methyldibenzothiophen (4-MDBT) and 4,6-dimethyldibenzothiophene (4, 6-DMDBT), with a total sulfur content of around 400 ppmw. On the other hand, the model jet fuel contained 130 ppmw each of benzothiophene (BT), 2-methylbenzothiophene (2MBT), 5-methylbenzothiophene (5-MBT) and dibenzothiophene (DBT) with a total sulfur content of around 520 pppmw. The model fuels also contained equimolar amounts of Naphthalene, 1-methyl naphthalene and about 10 wt % of n-butylbenzene as aromatics. The adsorbent experiments were performed 200°C using a fixed-bed flow system as described elsewhere[2, 6] The reduced samples stored in n-hexane were dried in vacuum or at room temperature and then packed in a stainless-steel adsorption column as reported earlier.[2, 6] The materials were treated with H_2 gas at 200°C for 1 h, and then cooled down to the adsorption temperature (room temperature or 200°C). Model fuels with 0.2 cc/min were pumped through the adsorption bed. The treated fuels were collected periodically every 15 min and analyzed using an Antek 9000 Series Sulfur Analyzer, with a detection limit of 0.5ppmw sulfur.

Results and Discussion

Figure 1 shows the break through curves for the adsorptive desulfurization of the model jet fuel over NiZnAl-C and NiZnAl-E adsorbents. It can be seen that under the present experimental conditions, the breakthrough capacity at 15 ppmw outlet sulfur content is about 10 ml/g of adsorbent in both cases, indicating that both adsorbents behave more or less similarly in removing sulfur compounds from the jet fuel although their chemical compositions are different. The saturation capacity was over 35 ml of the fuel/ g of the adsorbent.

Figure 2 shows the breakthrough curves for the adsorptive desulfurization of a diesel fuel over the same adsorbents tested for the model jet fuel. The breakthrough capacity at 15 ppmw outlet sulfur level over NiZnAl-C is about 8 ml/g while that over NiZnAl-E, it is 6 ml/g. These values are significantly less than that observed in the desulfurization of model jet fuel. Interestingly, the outlet sulfur content does not reach the saturation value even after 30 ml/g of the fuel treatment, which suggests that the adsorbent continue to adsorb the sulfur compounds without reaching the saturation. The early breakthrough observed in the desulfurization of model diesel fuel

compared to model jet fuel is likely due to the presence of 4, 6-DMDBT, in the former, which is more difficult to remove because of the steric hindrance exerted by the methyl groups at the 4-, and 6-positions of the Dibenzothiophene ring.

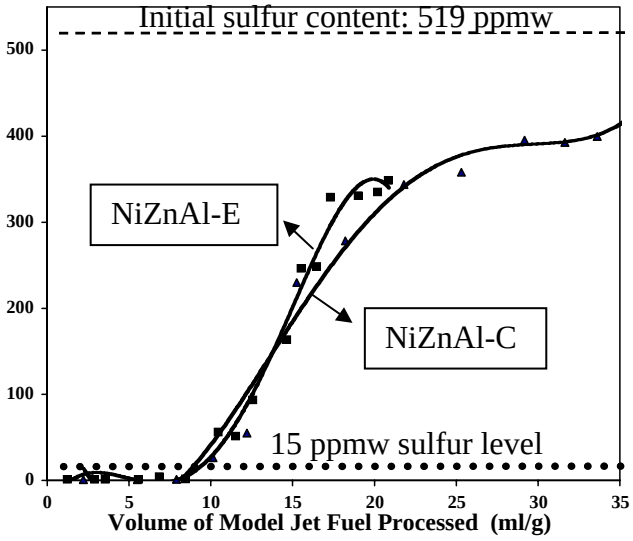

Figure 1. Breakthrough curves for the adsorptive desulfurization of a model jet fuel over NiZnAl-LDH based adsorbents

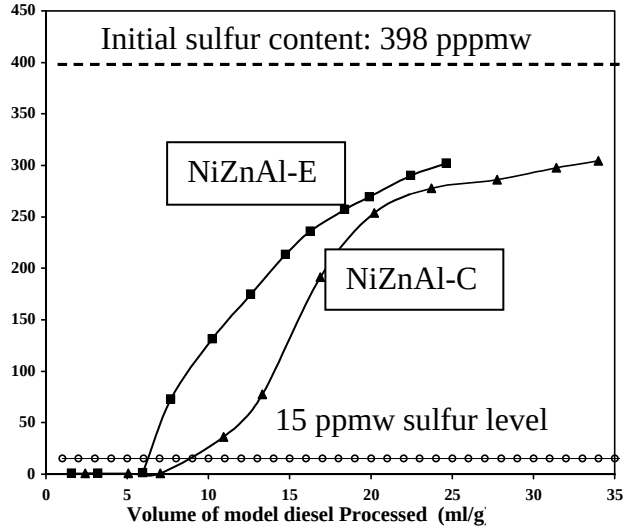

Figure 2. Breakthrough curves for the adsorptive desulfurization of a model diesel over NiZnAl-LDH based adsorbents

Further work on the optimization of chemical composition and experimental conditions in order to improve the adsorption performance is currently in progress and detailed results will be reported.

Conclusions

New series of Ni-based materials derived from hydrotalcite-like layered double hydroxides are synthesized and their performance in the adsorptive desulfurization of model jet fuel and diesel fuel are studied using fixed-bed adsorption. Under the experimental conditions employed in the present study, these adsorbents exhibit better performance in the desulfurization of jet fuel compared to diesel fuel as the later consists of 4,6-DMDBT, which is more difficult to remove because of the steric hindrance of the methyl groups.

Acknowledgements

The authors are grateful to the US EPA for the award of NSF/EPA STC grant.

References

1 C. Song and X. L. Ma, *Applied Catalysis B-Environmental*, 2003, **41**, 207.

2 S. Velu, X. L. Ma, and C. S. Song, *Industrial & Engineering Chemistry Research*, 2003, **42**, 5293.

3 X. L. Ma, L. Sun, and C. S. Song, *Catalysis Today*, 2002, **77**, 107.

4 S. G. Zhang, Q. L. Zhang, and Z. C. Zhang, *Industrial & Engineering Chemistry Research*, 2004, **43**, 614.

5 M. Breysse, G. Djega-Mariadassou, S. Pessayre, C. Geantet, M. Vrinat, G. Perot, and M. Lemaire, *Catalysis Today*, 2003, **84**, 129.

6 S. Velu, X. Ma, and C. Song, *American Chemical Society, Division of Fuel Chemistry*, 2003, **48**, 693.

7 F. Cavani, F. Trifiro, and A. Vaccari, *Catalysis Today*, 1991, **11**, 173.

8 S. Velu, N. Satoh, C. S. Gopinath, and K. Suzuki, *Catalysis Letters*, 2002, **82**, 145.

OXIDATIVE DESULFURIZATION: A NEW TECHNOLOGY FOR ULSD

Ron Gatan, Paul Barger, and Visnja Gembicki

UOP LLC
Des Plaines, Illinois, USA

Agostino Cavanna

Eni S.p.A. Refining and Marketing Division
Rome, Italy

Daniele Molinari

EniTecnologie S.p.A.,
Milan, Italy

Abstract

Oxidative desulfurization is an innovative technology that can be used to reduce the cost of producing ultra-low sulfur diesel (ULSD). The key to successful implementation of this technology in most refinery applications is effectively integrating the oxidative desulfurization unit with the existing diesel hydrotreating unit in a revamp situation.

The economics of applying oxidative desulfurization technology are dependent on the operating pressure of the existing hydrotreating capacity. A case study has been developed to illustrate how this innovative new route can be effectively utilized as an alternative to revamping existing hydrotreaters.

Introduction

Regulations regarding the sulfur content of motor fuels continue to be enacted worldwide in response to the need for cleaner air. Today, most industrialized countries have regulations in place to reduce diesel fuel sulfur to either 15 or 10 ppm by 2009. Developing countries are progressing environmental quality improvement programs as well, with most electing to enact fuel quality regulations similar to those in place in Europe.

Refiners will meet the challenge of these new regulations at a significant cost. Technology licensors and catalyst manufacturers have continued to progress conventional hydro-desulfurization technology to reduce the capital and operating expense required. Revamping existing intermediate and lower pressure units will typically require addition of significant catalyst volume and equipment modifications to increase the hydrogen purity and circulation rate. However, there is a limit to the cost reduction that can be achieved as hydro-desulfurization (HDS) chemistry requires elevated temperature and pressure for deep desulfurization and, of course, consumes hydrogen in the process. Hydro-desulfurization also cannot readily achieve the very low sulfur levels envisaged for future "zero sulfur" fuels.

There are alternatives to using conventional hydrotreating technology for producing ULSD, including biodesulfurization, physical separation, and oxidative desulfurization. Both biodesulfurization and physical separation processes have not been shown to be economically viable on a commercial scale. Oxidative desulfurization technology, however, has progressed to the state where it is nearing commercialization. Oxidation chemistry represents an alternative route to diesel desulfurization that complements HDS chemistry. The integration of an oxidative desulfurization unit with a conventional hydrotreating unit can improve the economics of these regulations-driven projects relative to current HDS technology.

Eni S.p.A. recognized the advantages of lower capital and operating cost that oxidative desulfurization can offer and started research efforts to develop new catalysts. UOP LLC had previously developed process technology for integrating oxidative desulfurization units with hydrotreating units that could be applied to the new catalysts.[1,2] In 2002, EniTecnologie S.p.A. and UOP LLC embarked on a collaborative research effort that combined each company's catalyst and process technology expertise to develop the UOP/Eni Oxidative Desulfurization Process, a new sustainable oxidative desulfurization technology that is targeted for commercialization in 2005.

The question that needs to be addressed is how best to meet future low sulfur fuel regulations such as the upcoming off-road diesel specifications in the United States and the potential for "zero sulfur" fuels at some point in the future. The preference has been to make the most with what is available, and a revamp solution is preferable to building new units. Hydrotreating is expensive, particularly for an existing low pressure unit. These units generally have been revamped to meet ULSD specifications by adding a large quantity of catalyst and reducing the available operating cycle. Hydrogen consumption is increased at the higher severity needed for ULSD, which can result in product quality give-away in some instances. The spent catalyst from these units represents a solid waste disposal issue, which combined with the additional CO_2 emissions associated with increased hydrogen demand, points to the need for a more sustainable technology.

A typical feedstock will contain about 30% LCO or other cracked blendstocks, with the balance being straight run diesel. Substantially higher severity is required to produce ULSD in intermediate and low pressure units. A summary of the process conditions typically required for modern HDS catalysts is shown in Table 1. Generally, a significant increase in catalyst volume is required, combined with a shorter process cycle and higher hydrogen circulation.

Table 1. Process Conditions Required for ULSD

	Intermediate Pressure Original vs. New Specifications		*Low Pressure Original vs. New Specifications*	
Product S, ppm	**500**	**<10**	**500**	**<10**
LHSV, 1/hr	**3.0**	**1.0**	**1.5**	**0.5**
Gas/Oil Ratio, SCFB	**1500**	**2000**	**1000**	**1500**
Cycle Length, months	**36**	**18**	**24**	**8**

Installation of a new high pressure (750$^+$ psi) hydrotreating unit is expensive, which is generally avoided unless there is no other option. Typical capital costs for a new 30,000 BPD diesel hydrotreating unit for ULSD will be $35-$45 MM on a US Gulf Coast (USGC), inside battery limits (ISBL) basis. High pressure units can typically be easily revamped to make ULSD by changing to a modern HDS catalyst and installation of improved reactor internals, such as UOP's Ultramix™ internals, for better flow distribution. Intermediate pressure (600 psi) units may require a significant revamp depending on the difficulty of the feedstock. A major revamp in these cases will typically include a new reactor for additional catalyst, modification or replacement of the compressors, a hydrogen purification system, and a recycle gas scrubber. This is a relatively high cost revamp, $10-$25 MM for a 30,000 BPD unit on the USGC, ISBL basis used by UOP. Operating cost is also higher, ranging from $0.25/bbl to $0.50/bbl or higher. The largest cost element is increased

hydrogen consumption in these units. The revamped unit generally operates with a shorter catalyst cycle which translates into higher catalyst cost.

Low pressure (450 psi) units will require either a major revamp or replacement with a new high pressure hydrotreating unit depending on the feedstock available. A major revamp for such a unit will include a new, much larger reactor, new recycle gas compressors, a recycle gas scrubber, and equipment to increase make-up hydrogen purity such as a Polybed™ PSA unit. These are high cost revamps, ranging from $15-$30 MM for a 30,000 BPD unit. Operating costs are significantly increased, ranging from $0.50/bbl to $0.75/bbl. As in the intermediate pressure case, the operating cycle is typically dramatically shorter in the revamped units and hydrogen consumption is increased. The difficulty of processing cracked feedstocks at low pressure also decreases the flexibility of the unit.

It is clear in this discussion that while hydrotreating is relatively expensive, a new technology has to be cost-effective to be considered as an alternative to revamping existing HDS units to meet ULSD specifications. It is easier to justify a new technology in those instances where the competitive option is a new grassroots unit, but that is only a consideration in about 25% of refineries. UOP and Eni have set development targets for the UOP/Eni Oxidative Desulfurization Process at a capital cost of $15 MM or less for a 30,000 BPD unit and an operating cost of $0.25/bbl or less in order to be competitive as an alternative to a major revamp of moderate to low pressure hydrotreaters. Oxidative desulfurization is not a competitive option for high pressure units where only a minor revamp or a simple catalyst replacement is required.

Oxidative Desulfurization Technology

Oxidative desulfurization is not a new concept and has been discussed for several years in previous publications.[3,4] The advantage that oxidative desulfurization has over conventional HDS is that the difficult-to-desulfurize, refractory-substituted dibenzothiophenes (DBT) are easily oxidized under low temperature and pressure conditions to form the corresponding sulfones. This reaction is shown in Figure 1. The oxidant can be supplied by either hydrogen peroxide/peracid[4] or organic peroxide. Note that there is no hydrogen consumed in this reaction. The sulfones are highly polar compounds and are easily separated from the diesel product by either extraction or adsorption.

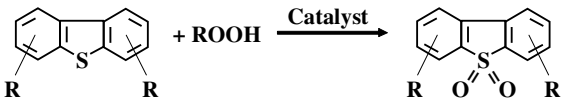

Figure 1. Dibenzothiophene Oxidation Chemistry

This oxidation chemistry is complementary to hydrotreating, as other sulfur compounds such as disulfides are easy to hydro-desulfurize, but oxidize slowly. For this reason, oxidative desulfurization is best utilized as a second stage after an existing HDS unit, taking a low sulfur diesel (~500 ppm) down to ULSD (<10 ppm) levels. In this situation, the diesel product has been depleted of difficult-to-oxidize sulfur species and has a high concentration of the more refractory DBT constituents.

The UOP/Eni Oxidative Desulfurization Process is shown schematically in Figure 2. The process consists of three process steps; an oxidant supply section, a sulfur reaction section, and finally a sulfone separation section. The UOP/Eni technology uses an organic peroxide as an oxidant. The oxidant supply section can consist either of the handling equipment associated with purchased organic peroxide such as t-butyl-hydro-peroxide, or the peroxide can be generated internally via direct oxidation of a hydrocarbon with air.

The oxidant from the oxidant supply section is first mixed with hydrotreated diesel and then sent to the sulfur reaction section. The sulfur reaction section operates at low temperature and pressure, less than 200°F and less than 100 psig. The reaction occurs in the presence of a proprietary heterogeneous catalyst in a conventional fixed bed reactor. The use of an organic peroxide as the oxidant avoids the need to recycle corrosive organic acid catalysts that are needed when hydrogen peroxide is used. Very high conversion is obtained in the sulfur reaction section, in excess of 98% conversion of organic sulfur compounds.

The final step is the sulfone separation section. The sulfones are polar molecules so they are easily separated by either extraction or adsorption. UOP and Eni have evaluated both routes, and have concluded that the adsorption route is more cost-effective. The adsorption section also serves to remove any trace by-products formed during the oxidation and reaction steps. The sulfones that are separated can either be processed in a coker or can be blended directly into the heavy fuel oil pool in some locations.

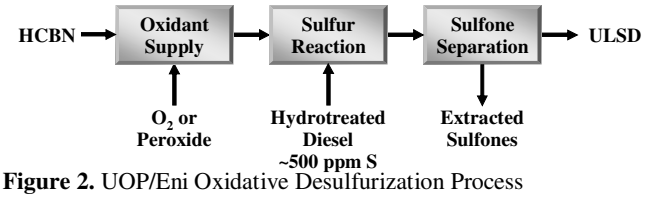

Figure 2. UOP/Eni Oxidative Desulfurization Process

During development of the process flow scheme, a number of key economic issues surfaced that are essential for the oxidative desulfurization process to compete with revamping conventional hydrotreating units for ULSD production. The major hurdles addressed were:

- Oxidant cost
- Minimize equipment
- Minimize operating costs
- Maximize ULSD yield
- Disposition of the sulfone extract

An engineering analysis of the operating and equipment costs for all sections was conducted that highlighted where innovations were needed to meet the development targets of <$0.25/bbl operating cost and <$15 MM capital cost. The sections that have the largest impact on cost of the unit are the oxidant supply and sulfone separation sections. This was not too surprising, as these sections have the largest number of equipment items and require product fractionation. Efforts were then focused on reducing the cost of these two sections.

There are a number of issues associated with using purchased organic peroxides in the process, the chief being the high cost and limited availability of these materials. The purchase cost adds $0.30 to $0.40/bbl to the operating expense, in excess of the required target operating cost. Other safety issues associated with handling and storage of organic peroxides on-site can be addressed technically but will add significant capital cost to the unit. Eni and UOP have decided that the best solution to this problem is to generate the peroxides in situ using an easily oxidizable hydrocarbon and air. We have identified catalysts that are active for the oxidation reaction and are completing the process development necessary for commercialization.

A number of different designs were evaluated for the sulfone separation section, including liquid-liquid extraction and several different adsorber configurations. Extraction is technically viable, but

has a high capital and operating cost, and can be difficult to operate. A high capacity adsorbent was identified that made the adsorption section technically feasible. UOP based the adsorber design on our commercial experience with similar separation applications in other technologies. The configuration used has a low capital cost, low diesel yield loss, and nearly complete sulfone removal from the diesel product.

Oxidative Desulfurization Economics

UOP and Eni conduct extensive techno-economic feasibility studies as part of the development process to ensure that the technologies in development are competitive with alternatives that are available to refiners. A case study was selected to illustrate how oxidative desulfurization can be effectively applied as an alternative to revamping conventional hydro-desulfurization technology. The utility and product values used in this analysis were based on energy pricing current in 4Q03.

The value of hydrogen is critical in any comparisons of hydroprocessing technology options. In the case studies considered here, the hydrogen value used was $2.25/MSCF. This value was calculated based on a 4Q03 Henry Hub natural gas price of $4.50/MM BTU.[5] Typical hydrogen plant operating costs were used to calculate the hydrogen value used based on this assumed natural gas feedstock price.

Case Study

The scenario assumed is an existing diesel hydrotreater, designed for processing 30 MBPD of a 70% straight run/30% LCO blend at 600 psi, producing 400 ppm low sulfur diesel. The unit design parameters are listed in Table 1 for intermediate pressure revamps. The changes required are:

- Decrease LHSV from 3 to 1 hr^{-1}
- Reduction in process cycle from 36 to 18 months
- 33% increase in hydrogen consumption (Δ 150 SCF/bbl)
- Requires new reactor, compressors, and recycle gas scrubber

The critical performance parameters and economic values are summarized in Table 2 for both the base case operation at 400 ppm sulfur and the requirements for ULSD. A capital cost estimate for this revamp was $18.5 MM on a USGC, ISBL basis. The operating cost increased $0.45/bbl over the base case operation, nearly all due to the increased hydrogen consumption.

Table 2. 600 psi Diesel Hydrotreater Revamp Case Study

Parameter	*Base Operation*	*Conventional Revamp*	*Oxidative Desulfurization*
Diesel Sulfur, wt-ppm	**400**	**<10**	**<10**
Diesel Yield, lv-%	**98.5**	**97.0**	**97.0**
Capital Cost, $MM	**—**	**18.5**	**16.0**
Hydrogen Cost, $MM/yr	**10.0**	**13.4**	**10.0**
Utilities Cost, $MM/yr	**0.8**	**1.0**	**2.5**
Catalyst Cost, $MM/yr	**0.3**	**1.3**	**1.5**
Total Operating Cost, $MM/yr	**11.1**	**15.7**	**14.0**
Delta Product Value, $MM/yr	**1.7**	**2.0**	**1.7**
Total Operating Cost, $bbl	**0.97**	**1.42**	**1.28**
ΔNPV, (10%, 10 yr), $MM	**—**	**<41>**	**<31>**

The alternative to the conventional revamp is to install an oxidative desulfurization unit. In this case, the original HDS unit continues to produce 400 ppm sulfur product, with the oxidative desulfurization unit used to make ULSD. A capital cost of $16 MM was estimated for the unit, which is equivalent to $533/bbl. The operating cost was estimated at $0.31/bbl over the base case operation. While both values are slightly above the development target values, the economics are attractive relative to the conventional revamp. The calculated incremental net present value (10% interest rate and 10 year project life) was $10 MM higher for the oxidative desulfurization case. This significant improvement in economics is due to eliminating the additional hydrogen consumption by installation of the oxidative desulfurization section.

The Future of Oxidative Desulfurization

The study presented in this paper has demonstrated that oxidative desulfurization can play an important role in future technical strategies to produce ULSD. This technology can be considered to be a viable option for new ULSD projects that will be implemented in 2006 and beyond. Oxidative desulfurization technology also holds promise for both reducing operating cost and improving the sustainability for low pressure units where substantial investments have already been made. The key to success is that the oxidative desulfurization process must be cost-effective versus the HDS revamp alternatives available to refiners.

Over this coming year, UOP and Eni will continue to conduct studies in our continuous pilot plants to fully demonstrate the UOP/Eni Oxidative Desulfurization Process. The key aspects to be demonstrated include long-term catalyst stability in an integrated operation over a range of commercial feedstocks. We will continue to optimize our engineering design to improve the cost-effectiveness of the process.

Eni is considering implementation of an oxidative desulfurization unit as an alternative to revamping an existing intermediate pressure hydrotreater at an Eni refinery in Italy. The basic design of this unit is scheduled to start at the end of 2004, with construction starting in the second half of 2005. This will be a full scale commercial unit to produce ULSD meeting the 2009 regulations in Europe.

Summary

Oxidative desulfurization technology offers a non-hydrogen consuming, lower capital cost, more sustainable alternative to conventional hydrodesulfurization technology. The technology can be applied as part of an effective strategy for both an alternative to revamping intermediate and low pressure HDS units to produce ULSD, or as a means to reduce the operating cost of low pressure units that have already been revamped. Oxidative desulfurization can also be considered as an attractive revamp opportunity for any existing unit where construction of new high-pressure HDS units is the alternative.

References

(1) Cabrera, C.A.; Imai, T., US Patent 6,171,478 assigned to UOP LLC.

(2) Kocal, J.A.; Brandvold, T.A., US Patent 6,638,495 assigned to UOP LLC.

(3) Liotta, F.J.; Yuan, Z.H., "Production of Ultra-low Sulfur Fuels by Selective Hydroperoxide Oxidation," AM-03-23, NPRA 2003 Annual Meeting.

(4) Levy, R.E.; Pappas, A.S.; Nero, V.P.; DeCanio, S.J., "Unipure's ASR-2 Diesel Desulfurization Process: A Novel, Cost-Effective Process for Ultra-low Sulfur Diesel Fuel," AM-01-10, NPRA 2001 Annual Meeting.

(5) *Oil and Gas Journal*, Vol. 101, Number 41, October 27, 2003, "Industry Scoreboard," pg. 4.

REMOVAL OF HYDROGEN SULFIDE AND CARBONYL SULFIDE FOR PURIFICATION OF BIOMASS-GASIFIED SYNTHETIC GAS USING ACTIVE CARBONS

Kinya Sakanishi[1)], Akimitsu Matsumura[1)], Ikuo Saito[1)], Toshiaki Hanaoka[2)], and Tomoaki Minowa[2)]*

1) Institute for Energy Utilization, National Institute of Advanced Industrial Science and Technology (AIST) Tsukuba Center West, Tsukuba, Ibaraki 305-8569, Japan
2) Biomass Technology Research Laboratory, AIST Chugoku Center, Kure, Hiroshima 737-0197, Japan

Introduction

Removal of sulfur-containing compounds is one of the most important technologies for the utilization of gasified products derived from various feedstocks such as biomass, waste, and solid fossil fuels. Especially, gaseous sulfur compounds of H_2S and COS are severe catalyst poisons against the following processes of steam reforming for hydrogen production or FT-synthesis.[1,2]

Various researches for H_2S removal have been already reported in details for the purification of gasified products derived from various feedstocks,[3-5] however, removal of COS is not concerned yet as much as H_2S, because COS are not the major sulfur compounds produced from the gasification of biomass and other wastes feedstocks.[6,7] In addition, the removal of COS is more difficult than H_2S, since COS is inactive compared to H_2S, probably resulting from its neutrality and similarity to CO_2. What is worse, COS is sometimes produced through the reaction of H_2S with CO_2.

Carbon-based adsorbents such as active carbons and activated carbon fibers have been widely applied for the purification procedures of gas and water, and the selective adsorption of a specific compound from various gaseous mixtures produced from gasification and other conversion processes.[8-10] Although gaseous sulfur compounds such as H_2S and COS contaminated in the synthetic gas products have been conventionally removed by cold and wet procedures, recently, hot gas cleaning procedures are required to be developed for the utilization of highly purified synthetic gas for F-T synthesis and hydrogen of high purity for fuel cell application. For the complete removal of H_2S, higher temperatures around 500 are preferred because H_2S is captured completely by the reaction with catalytic materials such as ZnO and Fe_2O_3 in a absorption manner.[3-5]

In the present study, the adsorption behaviors of H_2S and COS are investigated using active carbon adsorbents in the middle range of temperatures(300 – 400), because tarry compounds produced from biomass gasification have been reported to be effectively removed in this temperature range.[11,12] Sulfur-containing and other contaminants such as vaporized alkali metals are expected to be captured with the tarry byproducts at the same time. Another advantage is that the following catalytic processes of F-T synthesis are operated around 300 , hence a directly coupled gasification process of biomass can be designed by the combination of such hot gas cleaning with catalytic F-T synthesis.

Experimental

100 ppm of H_2S and COS standard gases in N_2 balance was used for the adsorption treatments.

Two types of commercially available active carbons(abbreviated as AC-1 and AC-2) were used in the present study. Their surface areas and average pore diameters are 1120 m^2/g, 1.7 nm and 490 m^2/g, 0.97 nm, respectively.

Figure 1 illustrates the adsorption equipments applied to the present experiments.

The adsorption amounts of H_2S and COS were quantified with the sampled gas out of the bottom of adsorption column by using their detector tubes which are commercially available for the detection and quantification of H_2S and COS.

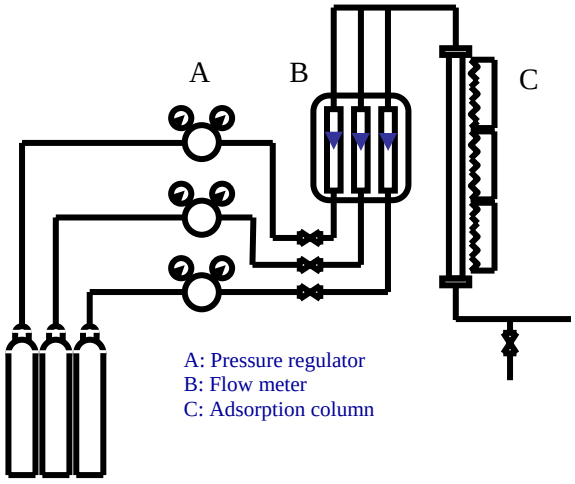

Figure 1. Adsorption apparatus for removal of H_2S and COS

Results and Discussion

Adsorption behaviors of H_2S. Figure 2 illustrates the adsorption results of 100 ppm H_2S in N_2 with glass beads as a blank test for H_2S adsorption at variable temperatures in the temperature range from 100 to 400 . In the temperature range between 100 and 200 , about 20 % of H_2S was adsorbed with glass beads, however, at the higher adsorption temperatures, about 40 % and 70 % of H_2S were removed at 300 and 350 , respectively. It is noted that 100 ppm of H_2S was completely and stationarily removed at the higher temperature of 400 even with glass beads. These results suggest that H_2S may not only adsorb on the glass beads, but also react with each other or with some other materials at the higher temperatures in the adsorption column system.

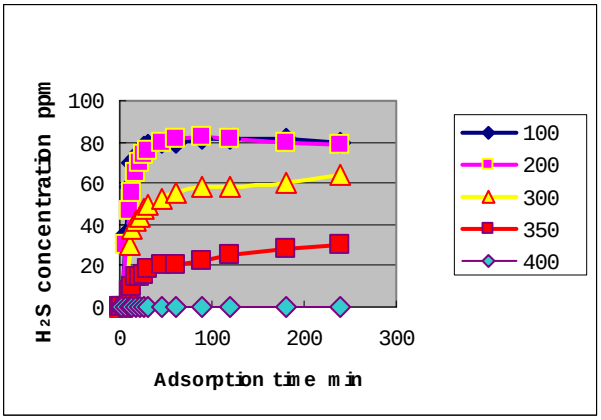

Figure 2. Blank adsorption test of 100 ppm H_2S with glass beads at variable temperatures(50 ml/min H_2S)

In the adsorption of H_2S with active carbons of AC-1 at 300 , 100 ppm of H_2S was completely and stationarily removed for the longer adsorption time of 80 h even with the higher flow rate of 150 ml/min of H_2S.

AC-2 of the smaller surface area and pore diameter exhibited the similar adsorption behavior and capacity of H_2S at 300 to those of AC-1, while AC-1 of the larger surface area and pore diameter showed the much higher performance in the dry removal of tarry compounds produced from biomass gasification.[11,12] The larger surface area and pore diameter may be essential to the efficient capture and removal of both gaseous sulfur-containing compounds and tarry by-products, although they should be carefully optimized depending upon the gasified feedstock, gas composition, and adsorption conditions.

Adsorption behaviors of COS. Figure 3 illustrates the adsorption breakthrough curve of COS over AC-1 at 300 . Unlike with the case of H_2S, about 30 % of COS was eluted from the starting point, and the eluted amount of COS drastically increased in the first 500 min adsorption, being saturated to the level around 85 % from the adsorption time over 1000 min.

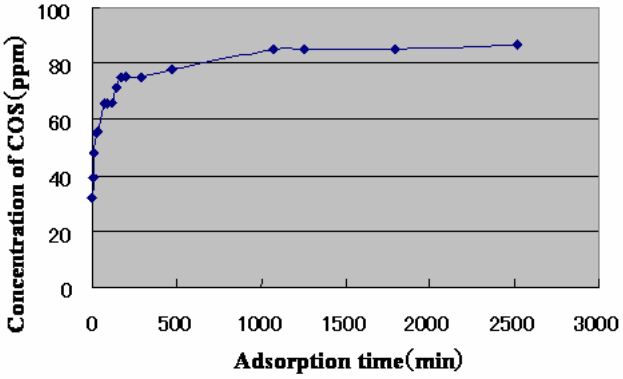

Figure 3 Adsorption treatment of COS with active carbon at 300℃ (AC 2 g, H2S: 100ml/min)

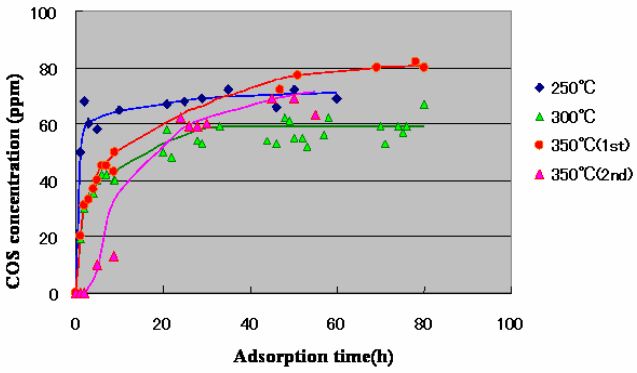

Fig. 4 Adsorption treatment of COS with active carbon at variable temperatures

(COS initial conc.: 100 ppm, 50 ml/min, Active carbon: 5g)

Figure 4 illustrates the adsorption breakthrough curves of COS over AC-1 at variable temperatures. The breakthrough profiles were similar regardless of the adsorption temperatures, showing prompt breakthrough points within the initial 20 h, followed by gradual saturation at the longer adsorption times of 20 to 80 h. However, the stationary adsorption levels of COS with AC-1 after the saturation were different depending upon the adsorption temperatures, showing the order of 250 350 < 300 . It is interesting to note that the adsorption capacity of COS with AC-1 is higher at 300 than that at 350 , suggesting that COS adsorption may be most favorable at around 300 probably because of the balanced chemical adsorption and physical desorption at 300 .

It is also pointed out that the repeated adsorption(2nd in Figure 4) profile of COS at 350 was similar to the initial breakthrough curve, although the breakthrough points looked like shifted to the longer adsorption time.

Conclusion

The present study revealed that contrast adsorption profiles of H_2S and COS over active carbon were obtained in the temperature range from 200 to 400 , showing the much higher adsorption capacity of H_2S probably due to the stronger acidity and polarity of H_2S than those of COS. The stationary adsorption capacities of H_2S and COS seem to be optimized at around 400 and 300 , respectively, of which temperatures may balance the chemical adsorption and physical desorption regardless of their contrast adsorption levels. The adsorption mechanisms of H_2S and COS are not clear yet, however, the possibility of chemical decomposition of H_2S and COS is suggested to produce H_2 and CO, respectively by the direct desulfurization over the active carbon adsorbent at around 300 .

Acknowledgment. The authors are grateful to JFE Engineering Co. for their financial support and providing the active carbon samples.

References

1. Ahmed, M.A., Garcia, E., Alonso, L., Palacios, J.M., *Appl. Surf. Sci.*, **2000**, 156, 115.
2. P. Hasler, P. and Nussbaumer, T., *Biomass & Bioenergy*, **1999**, 16, 385.
3. Ikenaga, N., Ohgaito, Y., Matsushima, H., Suzuki, T., *Fuel*, **2004**, 83, 661.
4. Slimance, R.B. and Abbasian, J., *Ind.Eng.Chem.Res.*, **2000**, 39, 1338.
5. Sasaoka, E., Hatori, M., Yoshimura, H., Su, C., Uddin, M.A., *Ind.Eng.Chem.Res.*, **2001**, 40, 2512.
6. Svoronos, P.D.N. and Bruno, T.J., *Ind.Eng.Chem.Res.*, **2002**, 41, 5321.
7. Ferm, R.J., *Chem.Rev.*, **1957**, 57, 621.
8. Cal, M.P., Strickler, BW, Lizzio, A.A., *Carbon*, **2000**, 38, 1757.
9. Bandosz, T.J., *Carbon*, **1999**, 37, 486.
10. Cal, M.P., Strickler, BW, Lizzio, A.A., *Carbon*, **2000**, 38, 1767.
11. Hanaoka, T., Sakanishi, K., Minowa, T., *Proc. 2nd World Conf. Tech. Exhibit. Biomass for Energy, Industry and Climate Protection*, Rome, Italy, 10-14 May **2004**.
12. Hanaoka, T., Sakanishi, K., Minowa, T., J. Inst. Energy Jpn. in submission.

MORPHOLOGY CONTROL OF POLY(PHENYLENE OXIDE) BY IONOMERIC POLY(STYRENESULFONIC ACID SODIUM SALT) COPOLYMERS FOR FUEL CELL MEMBRANE

Sung-Guk An, Jung-Kyu Woo, and Chang Gi Cho

Dept. of Fiber & Polymer Engineering
Hanyang University
Seoul 133-791, Korea

Abstract : Well-defined block copolymers of poly(styrene-b-styrenesulfonic acid sodium salt) were synthesized via living radical polymerization. Blends of various compositions of block copolymer/polyphenylene oxide were prepared, and their properties for proton exchange membrane were studied. Blend film showed well-defined two phase morphology. The molecular architecture of the block copolymer and the content of the block copolymer in the blend were important factors in controlling the properties of the film for proton exchange membrane. Also graft copolymers of poly(phenylene oxide-g-styrenesulfonic acid sodium salt) were prepared and their properties for proton exchange membrane were studied.

Introduction

Proton exchange membrane (PEM) is a key component in solid polymer electrolyte fuel cells [1]. Generally, proton exchange membrane (PEM) contains cationic exchange groups such as SO_3^- group. For PEM materials, poly(styrene sulfonic acid) (PSSA) and its copolymers have been widely studied because of their synthetic easiness and higher conductivities [2], and many studies utilized PSSA in the forms of random copolymers, block or graft copolymers. But poor physical properties of PSSA such as brittleness and relatively low Tg, discouraged many researcher from studying PSSA compared to engineering plastics (EP) such as polyimide, polysulfone, polyketone, and poly(2,6-dimethyl-1,4-phenylene oxide) (MPPO), etc. as possible PEM materials. Blends of these EP polymers with PSSA look desirable but they have been rarely studied because of poor miscibility of the ionomer in hydrophobic EP. In this work, poly(styrenesulfonic acid sodium salt) (PSSNa) was converted to PS-b-PSSNa block copolymers and MPPO-g-PSSNa graft copolymers. The block copolymers were blended with MPPO because of its good mechanical, chemical, and thermal properties. PEM performance of the blends and graft copolymers were studied.

Experimental

Synthesis of polystyrene-b-poly(styrene sulfonic acid) sodium salt (PS-b-PSSNa). Preparation of block copolymer and polymer blending are shown as in the S**cheme 1**. TEMPO terminated polystyrene macroinitiators were synthesized by reported method. For the block copolymerization, a 100 mL round bottom flask equipped with a reflux condenser was charge with styrenesulfonic acid (SSNa) and macroinitiator in DMAc. The flask was purged with high purity N_2 gas for 30 minute, and polymerization was conducted for 6 h at 125°C. The polymerization solution was cooled to room temperature and precipitated into 60/40 ether/methanol mixture. Precipitate was collected by filtration and dried in air. The product was washed with hot water in order to remove any possible homopolymerized SSNa, then PS-b-PSSNA was obtained by drying under vacuum. For the preparation of a blend membrane, MPPO and PS-b-PSSNa were dissolved in NMP. The polymer solution was casted on glass plate and solvent was evaporated slowly in vacuum at 100°C. Acid treatment of the membrane was followed for proton conductivity measurement.

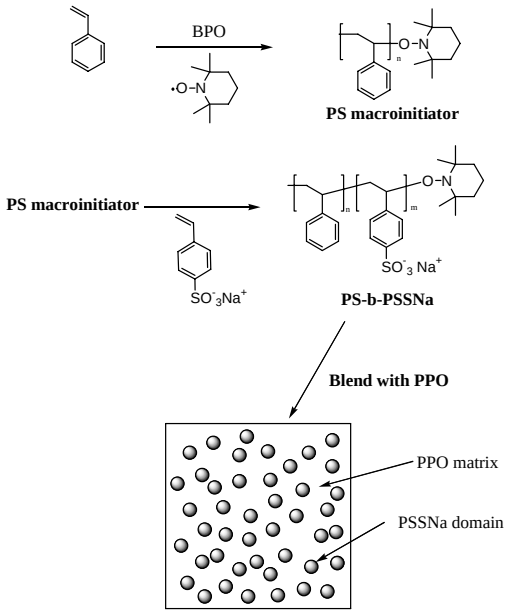

Scheme 1. Synthesis of PS-b-PSSNa and membrane preparation from polymer blend

Results and Discussion

The PS macroinitiator and block copolymers were characterized by GPC and ^{1}H-NMR. **Figure 1** shows the NMR spectra of the PS macroinitiator and block copolymer. TEMPO terminated macromer shows NMR spectrum of a typical polystyrene, and the block copolymer shows a new peak at 7.5 ppm originated from aromatic resonance absorption of PSSNa. The absorption peak at ca. 3 ppm of PS-b-PSSNa is originated from NMR solvent. The molecular weight of PS-b-PSSNa was characterized by FT-IR spectra as reported by other workers [2] (**Figure 2**) as well as by titration. Molecular weight determined by titration agreed well with that of theoretical, and agreed reasonably well with that by IR.

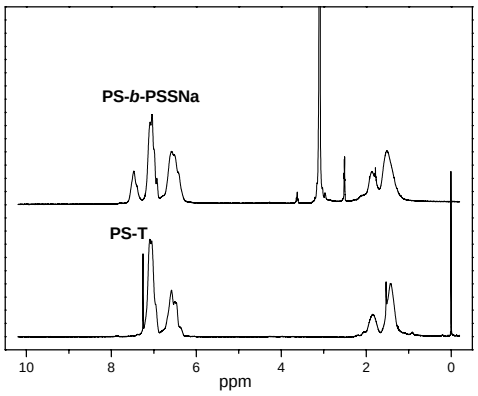

Figure 1. ^{1}H-NMR spectra of macroinitiator and block copolymer

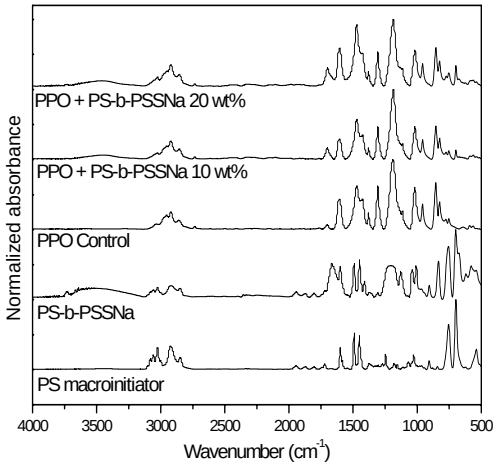

Figure 2. FT-IR spectra of blends and synthesized copolymers

Morphology of polymer films obtained from the blend was examined by atomic force microscopy (AFM). As in the **Figure 3** two phase morphology was developed well for the blend containing 20wt% block copolymer, and the size of dispersed domain is less than 100 nm. Proton conductivity, water uptake, and methanol permeability were measured, and these values showed good relationship with the wt% and the molecular weight of the block copolymer in the blends. Proton conductivity of the blends increased with the content of block copolymers. Some membranes showed high proton conductivities quite comparable to Nafion film. For a blend containing 50wt% of PS-PSSNa with molecular weight of 10K-5K, proton conductivity value of 5.27×10^{-2} S/cm was obtained. When the molecular weight of the block changed to 10K-10K, conductivity value changed to 1.24×10^{-2} S/cm. Detailed phase behavior and conductivity data will be presented.

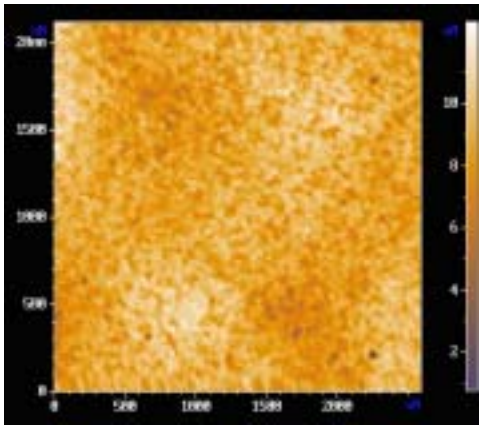

Figure 3. Atomic Force Microscopy of blend

Conclusions

Well-defined block copolymer was synthesized via stable free radical polymerization (SFRP) by using TEMPO. Blends of various compositions of block copolymer/MPPO were prepared, and their properties for proton exchange membrane were characterized. Blend film showed well-defined two phase morphology. The molecular architecture of the block copolymer and the content of the block copolymer in the blend are important factors in controlling the properties of the film for proton exchange membrane.

Acknowledgment

This work was supported by Korea Research Foundation Grant (KRF-2003-41-D00207).

References

1. Appleby, A.J; Foulkes, R.L. Fuel Cell Handbook, Van Nostrand, New York, **1989**.
2. Ding, J; Chuy, C; Holdcroft, S. *Macromolecules* **2002**, *35*, 1348.

SYNTHESIS AND CHARACTERIZATION OF SULFONATED POLY(ARYLENE ETHER SULFONE)/ZIRCONIUM PHENYLPHOSPHONATE COMPOSITE MEMBRANES FOR PROTON EXCHANGE MEMBRANE FUEL CELL APPLICATIONS

Melinda L. Hill[1], Brian R. Einsla[1], Yu Seung Kim[2], and James E. McGrath[1]

[1]Department of Chemistry and Institute for Polymeric Materials and Interfaces, Virginia Polytechnic Institute and State University, Blacksburg, VA 24061
[2]Los Alamos National Laboratory
Los Alamos, NM 87545

Email: jmcgrath@vt.edu

Introduction

High temperature hydrogen and methanol based fuel cells are of increasing interest due to environmental concerns and of the availability of fossil fuels. The proton exchange membrane (PEM), a protonically conductive polymer film, is an integral component of the fuel cell. New polymer materials are needed for these membranes because of the high cost and low conductivity at high temperatures (> 80°C) of the membranes currently in use. Sulfonated poly(arylene ether sulfone)s have good potential for use in fuel cells because of their excellent thermal stability, moderate water sorption, and sufficient conductivity at high temperatures. Addition of inorganic components to these membranes may enhance the high-temperature performance as well as other important properties of the membranes, such as water sorption.[1,2] The *in-situ* formation of inorganic components results in small particle size and preservation of original membrane morphology.[3] Herein we present the synthesis and characterization of disulfonated poly(arylene ether sulfone)/zirconium phenylphosphonate *in-situ* composite membranes for use as proton exchange membranes.

Experimental

Materials. The synthesis of the disulfonated poly(arylene ether sulfone)s with 35 mole % disulfonated moiety (BPSH-35) used for this work has been previously reported.[4] The random copolymer structure is shown in Figure 1. Zirconyl chloride (30% solution in hydrochloric acid) and phenylphosphonic acid were obtained from Aldrich as used as received. HPLC-grade methanol was obtained from EMD Chemicals and used without further purification. Platinum-ruthenium and platinum black were used as received from Johnson-Matthey, and 5 wt. % Nafion dispersion with an equivalent weight of 1100 was obtained from Solution Technologies.

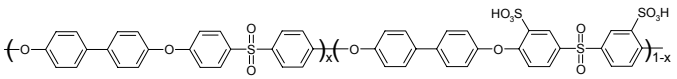

Figure 1. Structure of BPSH-35.

Synthesis of Composite Membranes. Copolymer membranes in the acid form were boiled in deionized water for one hour before use. The membranes were then immersed in zirconyl chloride solution at 80 °C (the concentration of the zirconyl chloride and the soaking time were varied). Upon removal from the zirconyl chloride solution, the membranes were briefly rinsed with deionized water and immersed in 0.2 M phenylphosphonic acid for 24 hours at room temperature. Finally, the membranes were thoroughly rinsed with deionized water and dried in a vacuum oven at 110 °C.

Characterization. The amount of zirconium phenylphosphonate (ZrPP) in the membranes was determined by weight difference after drying as follows: $(W_c-W_p)/W_c \times 100$ where W_c and W_p refer to the dry weights of the composite membrane and the pure copolymer membrane, respectively. The water uptakes of membranes are reported in weight percent as follows: water uptake = $(W_{wet}-W_{dry}) / (W_{dry}) \times 100$ where W_{wet} and W_{dry} are the weight of the wet and dry membranes, respectively. Thermogravimetric analysis (TGA) of dried, thin-film samples (10-15 mg) was performed on a TA Instruments TGA Q500 in air with a heating rate of 10 °C/min. Proton conductivity measurements were performed on the acid form of the membrane using a Hewlett-Packard 4192 Impedance/Gain-Phase Analyzer. The resistance of the film was taken at the frequency that produced the minimum imaginary response. The conductivity of the membrane was calculated from the measured resistance and sample dimensions. Magic angle spinning (MAS) ^{31}P NMR spectroscopy was obtained on a Bruker MSL 300 instrument. The spectra were obtained using 100-200 scans using a spinning rate of 6.0-6.5 kHz. Membrane-electrode assemblies (MEA's) were prepared by painting using a 5 wt. % Nafion dispersion, water, and catalyst (platinum-ruthenium on the anode and platinum black on the cathode). The catalyst loadings were approximately 10 mg/cm^2 on the anode and 6 mg/cm^2 on the cathode. Direct methanol fuel cell (DMFC) performance was measured using a Fuel Cell Technologies fuel cell test stand using a standard 5 cm^2 test cell with 0.5 M methanol and a cell temperature of 80 °C.

Results and Discussion

The incorporation of zirconium phenylphosphonate was found to be dependent on the soaking time in the zirconyl chloride solution. The dependence of soaking time on incorporation is shown in Figure 2 for a zirconyl chloride concentration of 5%. The concentration of the zirconyl chloride solution may also be varied, and it was found that at constant time, varying the concentration resulted in a similar trend as that shown in Figure 2.

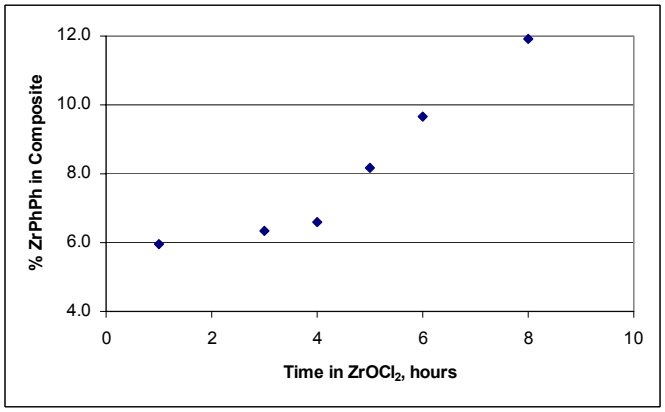

Figure 2. Incorporation versus soaking time in zirconyl chloride for a $ZrOCl_2$. concentration of 5%.

Solid-state ^{31}P NMR was used to confirm the structure of the ZrPP in the membrane. The ^{31}P NMR spectra of ZrPP and a BPSH-35/ZrPP composite membrane are compared in Figure 3.

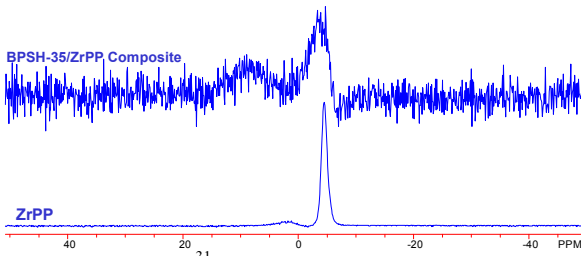

Figure 3. Solid-state ^{31}P NMR of BPSH-35/ZrPP composite and ZrPP powder.

The water uptake of the composite membranes was also studied as a function of ZrPP concentration at room temperature after three days of equilibration in liquid water. Figure 4 shows that the water uptake decreases with increasing ZrPP concentration.

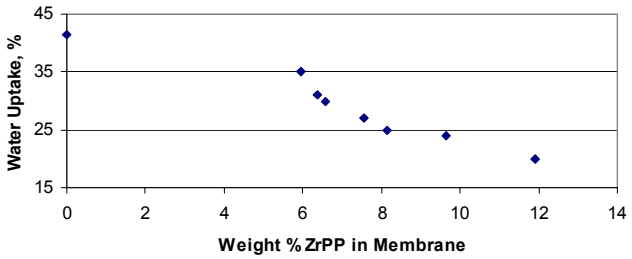

Figure 4. Water uptake as a function of ZrPP concentration in the composite membranes.

The TGA results in air at 10 °C/min showed that the incorporation of ZrPP resulted in an increase in the decomposition temperature (T_d) and the char yield. These results are shown in Table 1.

Table 1. Thermal Behavior of BPSH-35/ZrPP Composites

	T_d, °C	Char Yield at 800 °C, %
BPSH-35	304	1.5
BPSH-35/6.6% ZrPP	324	5.2
BPSH-35/7.6% ZrPP	348	7.3

Since this ZrPP additive is non-conductive, the proton conductivity of the composite membranes decreased with increasing ZrPP content, as shown in Figure 5.

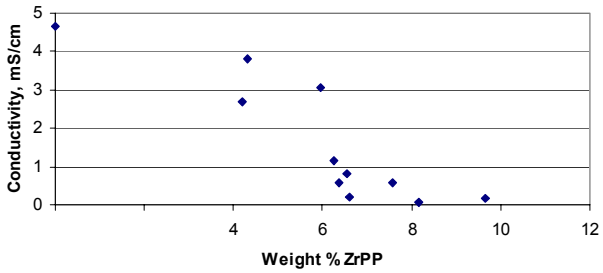

Figure 5. Proton conductivity of BPSH-35/ZrPP composite membranes.

The DMFC performance of several BPSH-35/ZrPP composites is shown in Figure 6. The composite membrane containing 3% of ZrPP exhibits improved performance over pure BPSH-35. The thickness of the BPSH-35 and BPSH-35/ZrPP membranes was approximately 3 mil.

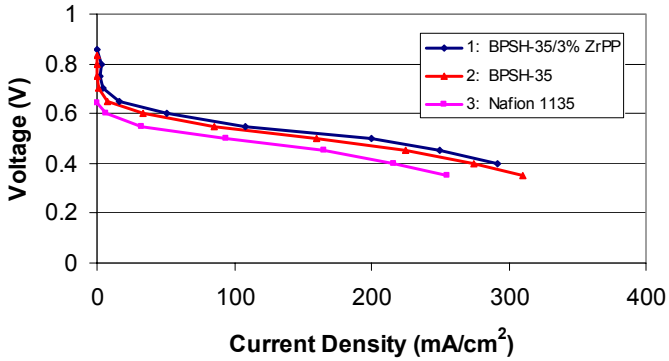

Figure 6. DMFC performance of virgin BPSH-35 and BPSH-35/ZrPP composite membranes.

Conclusions

Composite membranes of a disulfonated poly(arylene ether sulfone) and zirconium phenyl phosphonate were synthesized, and it was shown that the incorporation of the inorganic additive decreased the water uptake, although the conductivity decreased as well. The thermal stability, measured by TGA, was also improved after the ZrPP was added. The amount of ZrPP in the membrane can be controlled by varying the concentration of the zirconyl chloride solution and the amount of time the membrane is immersed in that solution. A composite membrane with 3% of ZrPP showed improved performance over pure BPSH-35 and Nafion 1135.

Future Research. The investigation of other additives, especially those exhibiting good proton conductivity, as well as blending with other polymer membranes is underway in cooperation with the research group of G. Alberti of the University of Perugia.[5]

Acknowledgement. The authors would like to thank the National Science Foundation "Partnership for Innovation" Program (HER-0090556) and the Department of Energy (DE-FC36-01G01086) for their support of this research effort.

References

[1] Yang, C.; Srinivasan, S.; Arico, A. S.; Creti,P; and Baglio, V. *Electrochemical and Solid State Letters*, 2001, *4*, A31.
[2] Zaidi, S. M. J.; Mickailenko, S. D.; Robertson,G. P.; Guiver, M. D.; Kaliaguine, S. *J.Membrane.Sci*. **2000**, *173*.
[3] Tchicaya -Bouckary, L.; Jones, D. J.; Roziere, J. *Fuel Cells* **2002**, *2*, 40.
[4] Wang, F.; Hickner, M.; Kim, Y. S.; Zawodzinski, T. A.; and McGrath, J. E. *J. Mem. Sci.* **2002**, *197*, 231.
[5] Alberti, G.; Casciola, M. *Annual Rev. Mater. Res.* **2003**, *33*, 129.

SYNTHESIS OF SUBSTITUTED POLY(P-PHENYLENE)S BY NICKEL (0) CATALYZED COUPLING REACTION AND DERIVED MULTIBLOCK COPOLYMERS FOR PROTON EXCHANGE MEMBRANE FUEL CELLS

Hang Wang, William Harrison, Juan Yang, James E. McGrath

Department of Chemistry, Virginia Polytechnic Institute and State University, Blacksburg, VA 24061

Introduction

Poly(p-phenylene) (PPP) derivatives are a promising class of high-performance polymers because of their excellent thermal and mechanical properties. One main obstacle in synthesis of high molecular weight poly (1,4-phenylene) is the low solubility of the rigid-rod chains during polymerization. Lateral substituents afford substituted, high molecular weight PPPs with excellent solubility in polar, aprotic solvents[1].

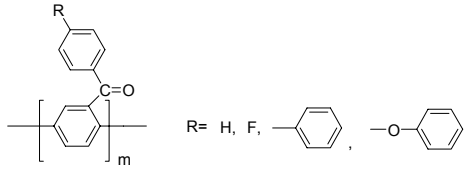

Figure 1. Structure of Poly(2,5-benzophenone) Derivatives

We have previously reported synthesis of poly(2,5-benzophenone) derivatives (shown in Figure 1) via nickel-catalyzed coupling polymerization of 4'-substituted 2,5-dichlorobenzophenones[2]. These polymers were proven to be highly thermo-oxidative stable materials with good solubility and excellent mechanical properties. However, they do not form good films due to their extremely rigid rod-like chains. As an extension to our work, more flexible, film-forming, thermally stable terechelics, such as poly(arylene ether sulfone), poly(arylene ether ketone) oligomers were copolymerized with these PPPs to form multiblock copolymers which had both excellent thermo-oxidative stability and good film-forming ability.

Experimental

Materials. The synthesis of monomers via Friedel-Craft benzoylation of 1,4-dichlorobenzene has been previously reported[3]. N-methyl-2-pyrrolidone (NMP) were dried over calcium hydride, distilled under vacuum and stored under nitrogen before use. Triphenylphosphine (Aldrich) was recrystallized from Et_2O. Zn powder (Aldrich) was washed with acetic anhydride, filtered, washed with dry Et_2O, and dried under vacuum at 150°C. 2,2'-Bipyridine (BPY; Aldrich) and nickel (II) chloride (Aldrich) were used as received.

Polymerization. In a typical polymerization, a 100mL Schlenk flask was charged with $NiCl_2$, PPh_3, Zn, 2,2'-Bipyridine, monomer and a magnetic stir bar. The flask was sealed with a rubber septum, evacuated under flame for 10 minutes, and placed under an N_2 atmosphere by filling with N_2 followed by three evacuation-fill cycles. NMP (5mL) was added via syringe through the rubber septum. The mixture was stirred and heated at 67°C for 24 h. After cooling to room temperature, the reaction mixture was poured into 100mL methanol acidified with 25mL concentrated HCl. The resulting precipitate was collected by filtration and washed with 10% sodium bicarbonate solution (3 times) and deionized water (3 times). After drying in a vacuum oven at 100°C overnight, the light yellow polymer was isolated and gave a yield of 85%.

The synthesis of hydroxyl terminated sulfonated poly (arylene ether sulfone) was same as reported earlier [2c].

Characterization

^{1}H-NMR experiments were performed using a Varian 400MHz instrument in deuterated chloroform. The intrinsic viscosity (IV) of the polymers was measured in NMP at 25°C using a Cannon Ubbelohde viscometer. Number average molecular weights (Mn) and molecular weight distributions (MWD) of polymers were determined by gel permeation chromatography based on polystyrene standards.

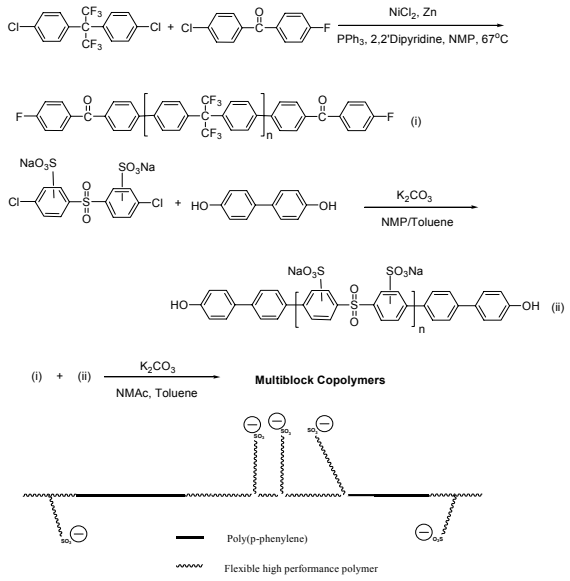

Scheme 1. Synthetic Scheme for Sulfonated Multiblock copolymers

Results and Discussion

As shown in Scheme 1, very rigid PPPs can be copolymerized with poly (arylene ether sulfone)s or poly(arylene ether ketone)s by nucleophilic aromatic reaction. Either the rigid PPP chains or relative soft poly (arylene ether sulfone)s or poly(arylene ether ketone)s can be sulfonated by directly polymerization of sulfonated monomers. In other words, PPP segments can either be a hydrophilic or hydrophobic phase. Besides, the degree of sulfonation can be controlled by varying composition of two macromoleculars in the multiblock copolymers. We also expect that water uptake and conductivity of resulting multiblock copolymers can also be properly controlled.

Furthermore, since PPP molecules have extremely rigid chains and are reluctant to move, they may force some interesting morphology structures in the multiblock copolymers. The swelling properties and conductivity of the resulting membrane are expected to be greatly influenced by the morphology. The results will be discussing at the meeting.

Acknowledgements

The authors would like to thank the National Science Foundation "Partnership for Innovation" Program (HER-0090556) and the Department of Energy (DE-FC36-01G01086) for support of this research effort.

References

[1] (a) Schluter, A. D. *J Polym. Sci Part A: Polym Chem* 2001, 39, 1533-1556; (b) Phillips, R. W.; Sheares, V. V.; Samulski, E. T.; DeSimone, J. M. *Macromolecules* 1994, 27, 2354-2356; (c) Wang, Y.; Quirk, R. P. *Macromolecules* 1995, 28, 3495-3501; (d) Percec, V. Zhao, M.; Bae, J.; Hill, D. *Macromolecules* 1996, 29, 3727-3735; (e) Bloom, P. D.; Sheares, V. V. *J Polym. Sci Part A: Polym Chem* 2001, 39, 3505-3512

[2] (a) Ghassemi, H.; McGrath, J. E. *Polymer* 2004**,** accepted; (b) Ghassemi, H.; Ndip, G.; McGrath, J. E. *Polymer* 2004, accepted. (c) Ghassemi, H.; Harrison, W.; Zawodzinski, T. A., Jr.; McGrath, J. E. *Polymer Preprints* (American Chemical Society, Division of Polymer Chemistry) (2004), 45(1), 68-69; (d) Ghassemi, H.; Ndip, G.; McGrath, J. E. *Polymer Preprints* (American Chemical Society, Division of Polymer Chemistry) (2003), 44(1), 814-815.

[3] Wang, Y.; Quirk, R. P. Macromolecules 1995, 28, 3495-3501

SYNTHESIS, CHARACTERIZATION AND FUEL CELL PERFORMANCE OF POLY (2,2'-(P-PHENYLENE) - 5,5'-BIBENZIMIDAZOLE) AS A HIGH TEMPERATURE FUEL CELL MEMBRANE

*Haifeng Zhang, Ru Chen, L. S. Ramanathan, Eugene Scanlon, Lixiang Xiao, Eui-Won Choe and Brian C. Benicewicz**

NYS Center for Polymer Synthesis
Department of Chemistry and Chemical Biology
Rensselaer Polytechnic Institute
Troy, NY 12180
benice@rpi.edu

Introduction

Polymer electrolyte membrane fuel cells (PEMFC) are receiving attention for their potential application in both stationary and mobile devices. Traditional perfluorinated ionomers, such as Nafion@ rely on water to conduct protons which results in cell operation temperatures lower than 100 ºC and subsequent low carbon monoxide (CO) tolerance. Additional concerns are the high cost of the membrane and extra hardware related to water management issues.

Anhydrous proton-conducting polymers have the potential to extend the cell operation temperature of fuel cell devices. Phosphoric acid (PA) doped polybenzimidazoles (PBI) have been reported to be promising candidates for high temperature fuel cell membranes. The doped membranes exhibited good proton conductivity, low gas permeability and excellent thermal stability at elevated temperatures.[1,2]

In our extensive evaluation of the PBI-PA system, we synthesized the homopolymer poly(2,2'-(p-phenylene) 5,5'-bibenzimidazole) (p-PBI) in polyphosphoric acid (PPA). Membranes were prepared using a novel membrane fabrication technique, called the PPA process, which produced acid-doped films with an excellent balance of thermal, mechanical and electrochemical properties. In this paper, we report on the polymer synthesis, membrane fabrication, composition, conductivity and cell performance based on the p-PBI homopolymer.

Experimental

Polymer Synthesis and Acid Doped Membrane Fabrication. As shown in **Scheme 1**, 3,3',4,4'-Tetraaminobiphenyl (TAB), terephthalic acid (TPA) and polyphosphoric acid (PPA) were added into a round bottom flask equipped with an overhead stirrer and nitrogen inlet/outlets. The monomer concentration was kept below approximately 4.5 wt %. The maximum temperature and polymerization time were varied to study the effects of polymerization conditions on ultimate molecular weight, as measured by inherent viscosity. After polymerization, the solution was cast directly onto a glass substrate using a casting blade with a 20 mil gap (510 µm). The substrate was allowed to stand in the laboratory atmosphere or controlled humidity glovebox for one to three days. Absorption of water from the atmosphere and subsequent hydrolysis of the PPA to phosphoric acid induced a sol-gel transition that produced gel membranes with a high acid doping level. These membranes were readily fabricated into MEAs and subjected to cell performance tests.

Characterization. Inherent viscosity was measured by a Ubblelohde viscometer in 96 % sulfuric acid at a concentration of 0.2 g/dL at 30 ºC.

The acid content was determined by titrating three pieces of membranes using a standard base solution. After titration, the polymer film was washed and dried in a vacuum oven and weighed to obtain the polymer content. Conductivity was measured by a four-probe ac impedance method using a Zahner IM6e electrochemical station in the frequency range of 1 Hz to 100 KHz at a temperature from 20 to 160 ºC. The conductivity was calculated by fitting the experimental data with a model of a resistor in parallel with a capacitor.

Fuel Cell Testing. The cells were constructed with an active area of 44 cm^2 using commercially available electrodes. Pt catalyst loading was 1.0 mg/cm^2 on both anode and cathode.

The long-term tests were carried out on a test station constructed by Plug Power. Other performance tests were performed on a test station purchased from Fuel Cell Technologies.

Scheme 1 Synthesis of Poly (2,2'-(p-phenylene) 5,5'-bibenzimidazole in PPA solution

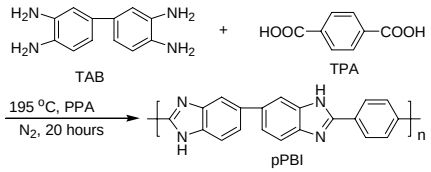

Results and Discussion

The low solubility of p-PBI in various solvents was reported previously.[3] To obtain the high molecular weight polymer, the monomer concentration effect was investigated. **Figure 1** shows the effect of monomer concentration on the final polymer molecular weight. The polymer inherent viscosity increased with the increase of monomer concentration until around 4.5 wt%. At higher monomer concentrations, the solution was too viscous to stir and the solution became immobilized on the stirrer shaft. The polymerization was terminated early and only low molecular weight polymer was obtained due to the low mobility of the polymer chains. The inherent viscosity of p-PBI was approximately 3.0 $(g/dL)^{-1}$ at concentrations just below this critical concentration.

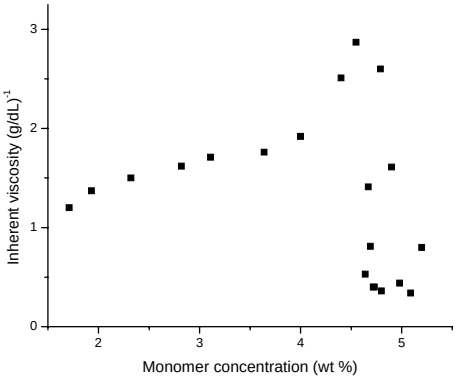

Figure 1. Effect of the monomer concentration on the polymer molecular weight.

Figure 2 shows the temperature dependent conductivity of phosphoric acid doped p-PBI membrane. Because the membrane initially contained water from the hydrolysis process, the first test run reflected the loss of water above 100 ºC. To obtain the reliable and consistent data, the second conductivity test was performed after the first run or the preheating treatment. The conductivity measured on

the second heating run was about 0.23 S/cm at 160 ºC, which is very high compared to the published data, usually reported at ~0.1 S/cm at 160 ºC.[4] This was attributed to the high acid content of this membrane. This membrane originally contained 70 (±3) wt % of acid, 24 (±2) wt % of water and 3.2 (±0.5) wt % of polymer.

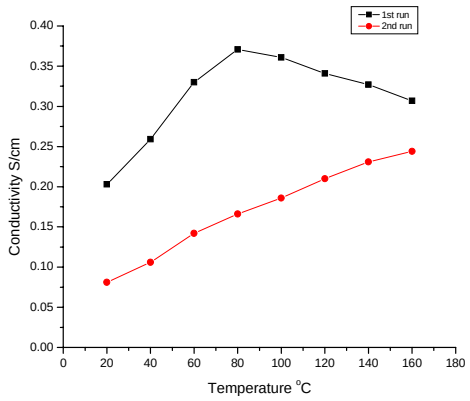

Figure 2. Temperature dependent conductivity of p-PBI membrane.

The cells based on the acid doped p-PBI membrane from the PPA process showed good performance at both low and high temperatures as shown in **Figures 3** and **4**. Cell temperatures ranged from 80 to 160 ºC and cells were tested on hydrogen/air and hydrogen/oxygen gases at 1 or 2 atm (absolute) at fixed flow rates. As expected, performance and power densities increased with increasing temperature. **Figure 5** shows the results of a long-term test using hydrogen and air at ambient pressure and 160 ºC. This preliminary test showed a drop of 53 mV, from 0.648 V to 0.595 V, after 2,500 hours' running at 160 ºC and a current density of 0.2 A/cm^2.

Conclusions

A para-oriented PBI, poly (2,2'-(p-phenylene) 5,5'-bibenz-imidazole), was synthesized at high molecular weights in polyphosphoric acid. Membrane fabrication using a novel sol-gel process produced films with high acid doping levels without isolation and redissolution of the polymer. The membrane showed high acid content (7,000 mole % acid per repeat unit), high conductivity (0.23 S/cm at 160 ºC) and good mechanical and thermal properties. Fuel cells based on this acid doped membrane showed excellent performance and long-term durability at 160 ºC for over 2,500 hours.

Acknowledgment. The authors thank Celanese Ventures, GmbH, Plug Power and NYSTAR for the financial and technical support.

References

(1) Wainright, J. S.; Wang, J. T.; Weng, D.; Savinell, R. F.; Litt, M. *J. Electrochem. Soc.* **1995**, *142*, L121-L123.
(2) Ma, Y. L.; Wainright, J. S.; Litt, M. H.; Savinell, R. F. *J. Electrochem. Soc.* **2004**, *151*, A8-A16.
(3) Delano, C. B.; Doyle, R. R.; Miligan, R. J. *AFML-TR-74-22* **1974**.
(4) Xing, B.; Savadogo, O. *J. New Mat. Electrochem. Systems* **1999**, *2*, 95-101.

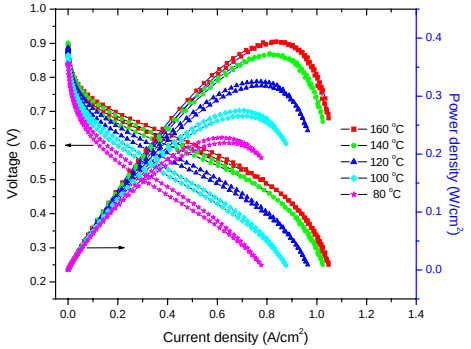

Figure 3. Performance curves for a hydrogen/air fuel cell based on p-PBI/PA membranes at different temperatures at ambient pressure. (Fuel cell operating conditions: constant flow rate, H_2 @ 400 sccm, air @ 1,000 sccm, no humidification.)

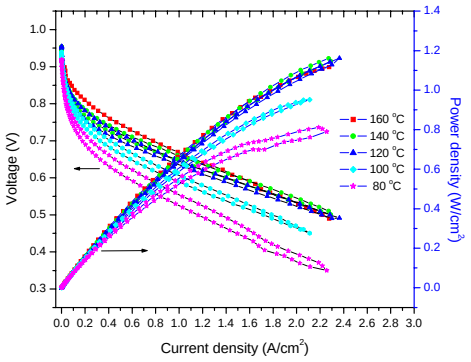

Figure 4. Performance curves for a hydrogen/oxygen fuel cell based on p-PBI/PA membranes at different temperatures at 30 psi(abs). (Fuel cell operating conditions: constant flow rate, H_2 @ 400 sccm, O_2 @ 400 sccm, no humidification.)

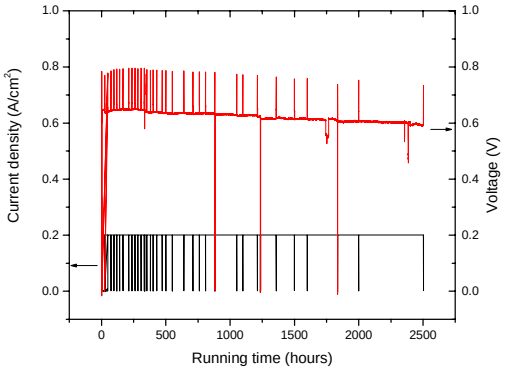

Figure 5. Long-term cell performance test (hydrogen/air) of a phosphoric acid doped p-PBI membrane at 160 ºC, ambient pressure and no humidification. The cell voltage was recorded at a current density of 0.2 A/cm^2 with 1.2 stoic flow of hydrogen and 2.5 stoic flow of air.

THE USE OF HETEROPOLY ACIDS IN COMPOSITE MEMBRANES FOR ELEVATED TEMPERATURE PEM FUEL CELL OPERATION; LESSONS LEARNT FROM THREE DIFFERENT APPROACHES

Andrew M. Herring,[1] John A. Turner,[3] Steven F. Dec,[2] Mary Ann Sweikart,[1, 3] Jennifer L. Malers,[1, 3] Fanqin Meng,[1] F. John Pern,[3] James Horan[2] and David Vernon.[3]

Department of Chemical Engineering[1] and Chemistry and Geochemistry[2]
Colorado School of Mines
Golden, CO 80401-1887

Hydrogen and Electricity, Systems and Infrastructure Group[3]
National Renewable Energy Laboratory
Golden, CO 80401-3393

Introduction

There is increasing interest in using the heteropoly acids, HPA, as proton conducting components in PEM fuel cells for elevated temperature operation, 120 – 200 °C.[1-6] Operation of a PEM fuel cell at these elevated temperatures will allow the integration of the stack into existing vehicular cooling systems, as well as stationary CHP, and use of hydrogen with an elevated CO content, simplifying the overall design of the reformer needed to generate hydrogen from hydrocarbons. The heteropoly acids are a large and structurally diverse class of inorganic proton conducting materials[7] with extremely high room temperature proton conductivities, as high as 0.2 S cm^{-1} for 12-phopshotungstic acid.[8] importantly, for elevated temperature PEM fuel cell operation, the HPA are structurally stable to temperatures in excess of 600 °C and incorporate water molecules and protons to temperatures in excess of 300 °C depending on the system.

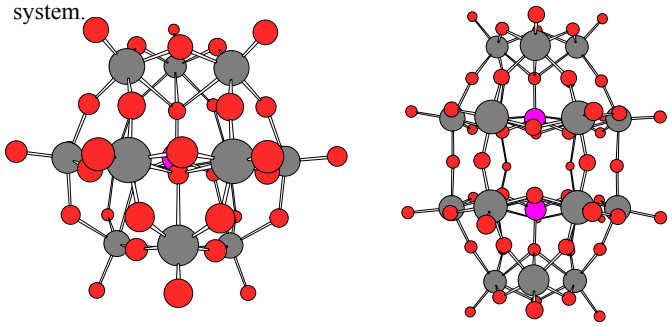

Figure 1. Structures of the Keggin anion, $H_3PW_{12}O_{40}$, 12-HPW , left and Dawson anion, $H_6P_2W_{18}O_{62}$, 18-HP2W, right.

Most studies to date have only considered the commercially available Keggin structures, consisting of a tetrahedral arrangement of three tungsten or molybdenum oxygen octahedral surrounding a central heteroatom, Figure 1. Many other structures are possible including the more thermally Dawson structure, Figure 1 and structures of increasing complexity. Importantly Lacunary structures may be derived from the parent Keggin or Dawson by the removal of 1,2 or 3 metal oxygen octahedral leaving a vacant site that may be used as a covalent attachment point for the synthesis of hybrid materials or a coordination site for another metal center.

Because of their structural diversity these materials are particularly suitable for incorporation into a wide variety of membranes materials for which they can be specifically tailored. In addition, the HPA have interesting redox and catalytic properties that can be exploited for PEM fuel cell applications and must also be fully understood before a practical system incorporating HPA can be developed. We have studied HPA in three systems: HPA cast in inert matrices such as polyvinylidenedifluoride, PVDF, HPA infused into sulfonatedperfluorinated polymers such as Nafion® and in polymer/silicate nanocomposites. All of these membranes were characterized by solid state NMR, IR, XRD and SAXS. Membrane electrode assemblies, MEAs, were constructed using standard E-tek electrodes, so that electrochemical measurements could be made, but the MEAs were not optimized for fuel cell operation.

Experimental

The HPA having the Keggin structure, 12-phosphotungstic acid, $H_3PW_{12}O_{40}$, 12-HPW, and 12-sillicotungstic acid, $H_4SiW_{12}O_{40}$, 12-HSiW, were purchased (Aldrich) and used without further purification. All other HPA, 18-diphosphotungstic acid, $H_6P_2W_{18}O_{62}$, 18-HP2W, and 21-diarsenotungstic acid, $H_6As_2W_{21}O_{69}$, 21-HAs2W21 and the lacunary HPA $H_8SiW_{11}O_{39}$, 11-HSiW,[9] were prepared by literature methods.

The PVDF/HPA membranes were formed by refluxing the PVDF-HFP co-polymer (Aldrich) and the HPA in acetone until dissolution was complete and casting the solution on Teflon blocks and allowing the solvent to evaporate.

Nafion® was cleaned by standard procedures, i.e. by boiling sequentially in concentrated nitric acid, deionized water, and hydrogen peroxide solution. The polymer was then doped by heating in a concentrated solution of the HPA at 80°C overnight.

Polymer/silicate/HPA nanocomposites were synthesized via a method[3] based on Honma's reported method.[2] A Polyethyleeneglycol400, PEG400, /SiO_2 sol-gel precursor was prepared by reacting PEG400 with a stoichiometric amount of 3-isocyanatopropyltriethoxysilane at 60-70 °C for 5 days under a N_2 atmosphere. The molecularly-hybridized precursor thus-obtained was then hydrolyzed and condensed with the addition of 11-HSiW, which served as a catalyst as well as a proton dopant. Monophenyltriethoxysilane, MPhTEOS, was added to the above mixture immediately under rapid stirring. Relative to the weight of the PEG400 precursor, 30 % of 11-HSiW and 60 % of MPhTEOS were added. The transparent and slightly brownish free-standing membranes were obtained and stored in air before further tests.

Membrane electrode assemblies, MEAs were fabricated by a standard hot press method[10] using catalyzed E-TEK ELAT® electrodes with 0.35 mg Pt/cm^2 loading of 20 wt% Pt on Vulcan XC-72 carbon on carbon cloth gas diffusion backings with an active area of 5 cm^2. For the Nafion® MEAs, the electrodes were pretreated by brushing with one coating of 5 % Nafion® solution in mixed alcohols (Electrochem Inc.) and allowed to dry for 45 minutes under ambient conditions. The 5 cm^2 electrodes were hot pressed onto the membranes at 130 °C with a force of 360 psi for 90 seconds.

Results and Discussion

The most convenient method of studying the HPA in inert supports in fuel cell environments is to cast composite films of HPA in PVDF- HFP from acetone solution. These HPA/PVDF membranes can show very high current densities at ambient temperatures, a limiting current over 1 A cm^{-2}, with no external humidification has been achieved with 12-HPW. The polarization curve obtained with 18-HP2W at room temperature using dry O_2 and H_2 is shown in Figure 2. The open circuit value is poor, 0.7 V, as these membranes are quite porous and exhibit excessive cross-over. Attempts to achieve high current densities at elevated temperatures with a very limited set of HPA have so far failed. At 120 °C, similar membranes only exhibit a limiting current of 2 mA cm^{-2}, but as the lattice has shrunk on dehydration cross-over is expected to

deteriorate at these higher temperatures. Excess hydrogen applied to these porous membranes results in the reduction of the HPA and short circuiting of the cell as the reduced HPA can be electronically conducting in this system. As the library of HPA that we study increases we hope to discover HPA that are better suited to high temperature operation.

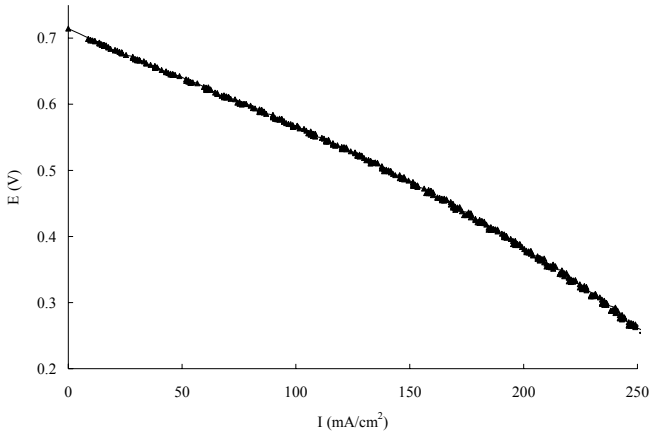

Figure 2. Typical polarization curve obtained for the PVDF-HFP/18-HP2W MEA using dry H_2 and O_2 and no back pressure at room temperature.

In contrast the addition of small amounts of HPA to sulfonated perfluornated polymers such as Duponts Nafion® by infusion from aqueous solution dramatically increases the performance of the membranes at temperatures up to 150 °C depending on the HPA. The polariazation for Nafion® doped with four different HPA at 120 °C with *ca.* 25% RH are shown in Figure 3. All doped samples show improved performance relative to te control, membrane, the best performance is seen with 21-HAsW21, but it is currently unclear what the exact moiety involved in this system is as this HPA equilibrates in to an number of HPA species under the conditions of the experiment. These membranes have been studied in terms of understanding the interaction of the HPA with the polymer to enable a full understanding of this beneficial interaction. The HPA do not appear to be chemically reduced by hydrogen in these systems but are not immobilized and so may be leached from the membrane over time.

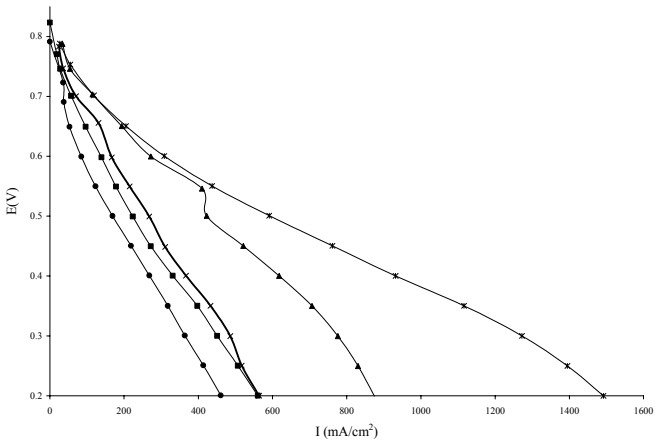

Figure 3. Polarization curves for HPA doped Nafion® at 120 °C using H_2 and O_2 humidified at 80 °C. • - control, ■ - 12-HPW, ▲ – 12-HSiW, x -18-HP2W, * - 21-HAs2W21.

One approach to the leaching problem is to immobilize the HPA in a nanocomposite membrane using silicate sol-gel chemistry.[1-3] A number of polymer backbones have been investigated by us and ion exchange capacities, higher than 3 moleq $g^{-1,}$ and diffusion coefficients as high as 1.2×10^{-6} cm^2 s^{-1} have been achieved with these materials with excellent *exsitu* mechanical and thermal properties. The HPA are stable in these systems to leaching in boiling water. Tem analysis indicates that there is no ordering of proton conducting channels in these systems. In addition, preliminary data from MEA testing of these materials, Figure 4, indicates that significant optimization of the membrane/electrode interface will be required for these membranes to exhibit their full potential. This is manifested in the polarization curves, Figure 4, which lacks a clear kinetic loss region and show little improvement with the addition of Nafion® paint to the electrode surface.

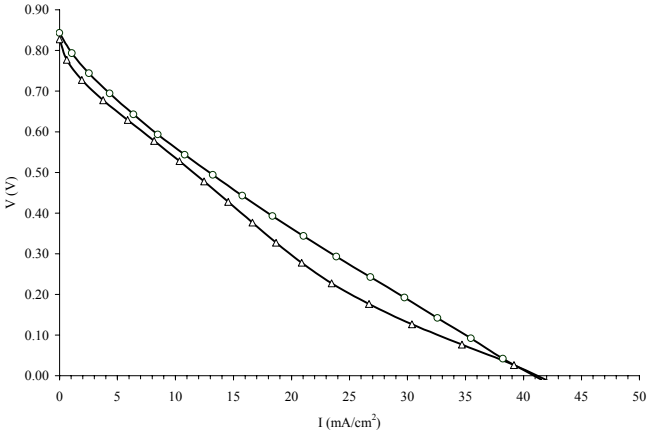

Figure 4. Polarization curves for a membrane with a ratio of PEG400 precursor:11-HSiW :MPhTEOS, of 100:40:100. △ - plain E-tek electrodes, ○ - E-tek electrodes painted with Nafion solution. Fuel cell at 47 °C, humidifier bottles at 80 °C.

Conclusions

HPA proton conducting systems hold much promise for PEM fuel cell operation at low humidity and elevated temperature, but challenges still exist in the development of fuel cell ready materials.

Acknowledgement. This work was supported by the US DOE science initiative, DE-FC02-0CH11088.

References

(1) Honma, I.; Nakajima, H.; Nishikawa, O.; Sugimoto, T.; Nomura, S. *Journal of The Electrochemical Society* **2003**, *150*, A616.
(2) Honma, I.; Takeda, Y.; Bae, J. M. *Solid State Ionics* **1999**, *120*, 255.
(3) Vernon, D.; Meng, F.; Dec, S. F.; Williamson, D. L.; Turner, J. A.; Herring, A. M. *Journal of The Electrochemical Society* **2004**, *submitted*.
(4) Kim, Y. S.; Wang, F.; Hickner, M.; Zawodzinski, T. A.; McGrath, J. E. *Journal of Membrane Science* **2003**, *212*, 263.
(5) Ramani, V.; Kunz, H. R.; Fenton, J. M. *Journal of Membrane Science* **2004**, *232*, 31.
(6) Staiti, P. *Journal of New Materials for Materials for Electrochemical Systems* **2001**, *4*, 181.
(7) Pope, M. T.; Müller, A., Eds. *Polyoxometalate Chemistry: From Topology Via Self-Assembly to Applications*; Kluwer Academic Publishers: Dordrecht, 2001.
(8) Nakamura, O.; Kodama, T.; Ogino, I.; Miyake, Y. *Chemistry Letters* **1979**, *1*, 17.
(9) Tourne, C. M.; Tourne, G. F.; Malik, S. A.; Weakley, T. J. R. *Journal of Inorganic and Nuclear Chemistry* **1970**, *32*, 3875.
(10) Mehta, V.; Cooper, J. S. *Journal of Power Sources* **2003**, *114*, 32.

ELECTRIC-FIELD-STRUCTURED PROTON EXCHANGE MEMBRANES

Jeffrey V. Gasa[1], R. A. Weiss,[1,2] and Montgomery T. Shaw[1,2]

[1]Polymer Program and [2]Department of Chemical Engineering
Institute of Materials Science, University of Connecticut, Storrs, CT 06269-3136

Introduction

Recent advancements in direct methanol fuel cell technology are quite dramatic and have placed this technology on the brink of commercialization. While there are several bottlenecks in current art, many regard the membrane, which must separate the methanol fuel and oxidant yet transport hydrogen ions, as the key polymer challenge because of the need for higher temperatures and greater chemical resistance for operation with methanol as the fuel.[1]

This study has focused on methods for making highly acidic membranes based mainly on the high-performance polymer poly(ether ketone ketone) (PEKK), and its blends with poly(ether imide) (PEI).[2] We have reported recently that proton conductivities and MEA performance comparable to Nafion®, which is the benchmark, can be achieved with membranes based on sulfonated PEKK and its blends with PEI.[2,3] In the case of blends, we have focused on the organization of the domain structure in the blend using mainly electric fields.[4] An important factor for creating structures of high proton conductivity and low methanol permeability was the application of electric fields of selected magnitude and frequency during the formation of the membrane. We have also reported recently that the structured membranes have, in some cases, exhibited significantly increased conductivity relative to the equivalent isotropic material.[5] The discussion in this paper is focused mainly on the influence of the magnitude and frequency of the applied field on the morphology of the resulting membranes.

Experimental

Materials. The acid polymer of principal focus in this study was sulfonated PEKK (SPEKK). The PEKK used was OXPEKK-SP (Oxford Performance Materials, New Britain, CT), which has a T/I ratio of 6/4. Sulfonation was achieved by dissolving the polymer (5% w/v) in a mixture of 53/47 (v/v) concentrated sulfuric acid and fuming sulfuric acid at room temperature. The sulfonation time and temperature were varied to achieve different levels of sulfonation, expressed here in terms of ion-exchange capacity (IEC).

Membrane Preparation. SPEKK and PEI were dissolved together (at various weight ratios) in N-methyl pyrrolidone (NMP) to form 7.5 wt% polymer solutions. These solutions were cast onto clean glass plates at 70 ^{o}C and air dried in a hood until most of the solvent had evaporated. The resulting membranes were dried in vacuum at 110-120^{o}C for 48 h. After drying, the membranes were soaked in de-ionized water at 20^{o}C for 48 h to remove residual solvent.

Electric-field-structured Membranes. The polymer solutions were cast under AC electric fields between two copper electrodes (2 x 3 x 50 mm) mounted on a microscope slide. This casting cell design was adopted from an earlier study conducted by Wnek and coworkers.[4] In this cell, the field is applied along the plane of the membrane (in-plane). The solutions were cast at elevated temperatures (85 ^{o}C) for 1 h to evaporate most of the solvent and freeze in the morphology. The solutions were cast at various magnitudes and frequencies of the applied AC field.

Optical Microscopy. The morphology of the blend membranes was studied using a Nikon Labophot optical microscope in transmission mode. The size of the phase domains was distinct and large enough to be seen easily with the optical microscope.

Impedance Spectroscopy. The proton conductivity of the membranes was measured by impedance spectroscopy using a Solartron® 1260 impedance analyzer over a frequency range of 1-10^{6} Hz. The applied voltage was 50 mV. Membrane conductivities were measured using a cell described by Zawodzinski et al.[6]

Methanol Permeability. The methanol permeability was measured using a permeation cell. One side of the membrane was subjected to 50 wt% methanol solution in water, while pure water was put on the other side. The concentration of methanol was monitored as a function of time. Methanol concentrations were measured using gas chromatography. The methanol permeability was calculated using Fick's law of diffusion.

Results and Discussion

Proton Conductivity. The conductivities of the pure SPEKK membranes exhibited an exponential dependence on IEC, at 20 °C and 98 % humidity (Figure 1). In water, the higher IEC membranes dissolved, pointing to the need for modification by blending.

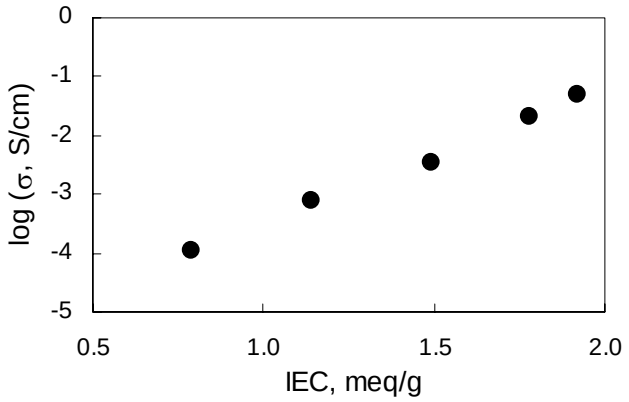

Figure 1. Proton conductivity of pure SPEKK membranes at various sulfonation levels. The measurements were made at 98% relative humidity and 20 ^{o}C.

Methanol Permeability. As shown in Figure 2, the methanol permeability increased with increasing IEC. The blend membranes containing 50% PEI had lower permeabilities than the pure SPEKK membranes.

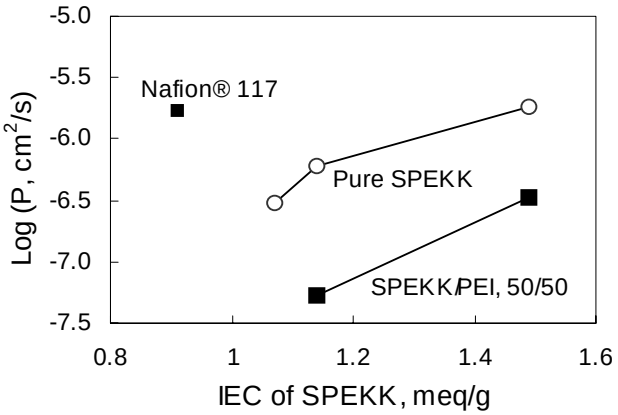

Figure 2. Methanol permeabilities of the membranes at room temperature

Morphology of Structured Membranes. Figure 3 shows the morphology of SPEKK-PEI blends cast at various field magnitudes and at a constant frequency of 10 kHz. Results clearly show that there is a threshold field magnitude (E_p) required to produce

structures that are preferentially aligned (anisotropic) along the direction of the applied field. Figure 5 suggests that E_p increases with increasing frequency. The E_p values for this blend system are much lower than those used by Wnek et al. (1 kV/mm) to align blends of non-sulfonated polymers.[4] This is probably due to the increase in either the dielectric constant or the conductivity of PEKK upon sulfonation, which in effect increases the dielectric or conductivity contrast between the two phases. According to theory, the mutual attractive force due to interfacial polarization between the droplets decreases with increasing dielectric or conductivity contrast.[7]

At field magnitudes below E_p, the size of the dispersed phase was found to increase with increasing field magnitude (Figure 3). Above E_p, the diameter of the columnar structures was found to decrease when the frequency was increased (compare Figures 4B and 4C) and when the sulfonation level was decreased (compare Figures 4B and 4D). Application of DC field caused dielectric breakdown of the membrane as indicated by the presence of electrical trees (Figure 4A).

Conclusions

It has been demonstrated in this study that structured membranes for proton transport can be achieved by the application of electric fields during casting of these blend membranes. The size of the phase domains was found to depend on the magnitude and frequency of the applied field as well as the sulfonation level of the proton-conducting phase. With many other variables available (component structure and MW, temperature, composition, etc.) it is reasonable to imagine that membranes with superior properties can be made.

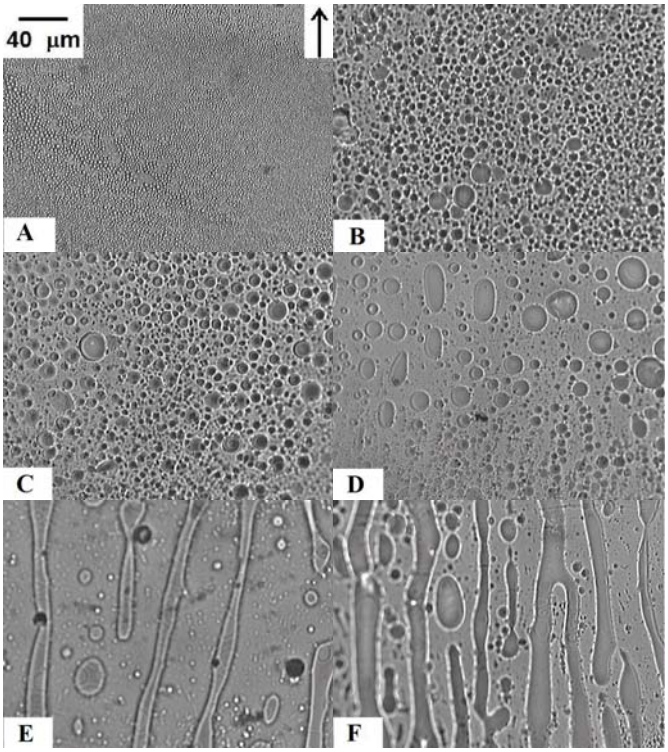

Figure 3. Optical Micrographs of SPEKK-PEI blends solvent cast at 85 °C under AC field with a frequency 10 kHz and at various field amplitudes: A) 5, B) 10, C) 15, D) 20, E) 25, and F) 30 V/mm. The arrow indicates the direction of the applied field. The weight fraction of SPEKK in the membrane was 0.2 with an IEC of 2.67 meq/g.

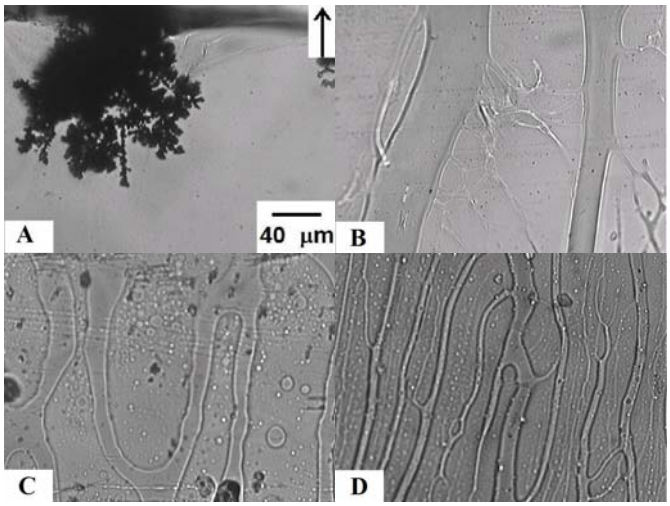

Figure 4. Optical Micrographs of SPEKK-PEI blends solvent cast at 85 °C under 50 V/mm AC electric field at various frequencies: A) DC, B) 10 Hz, and C) 10 kHz. The IEC of SPEKK was 2.67 meq/g. In D, the conditions were similar to B but the IEC of SPEKK was lower (1.26 meq/g).

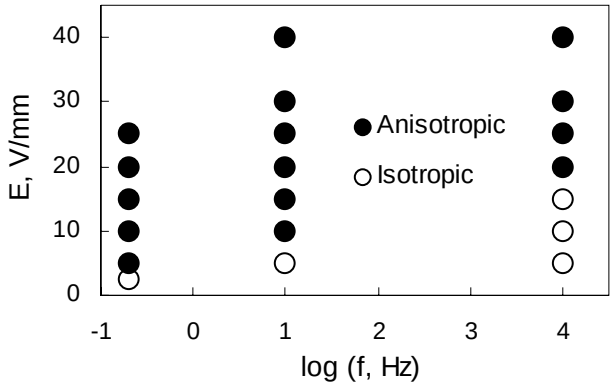

Figure 5. Influence of frequency on the threshold field magnitude required to produce structured (anisotropic) membranes.

Acknowledgement. The authors gratefully acknowledge financial support through the Connecticut Global Fuel Cell Center.

References

1. Hoogers, G. *Fuel Cell Technology Handbook*. CRC Press LLC, 2003.
2. Chun, S., Shaw, M.T., Weiss, R.A., "Sulfonated Poly(ether ketone ketone) Membranes," Asilomar Conference on Proton Exchange Membranes, February (2003).
3. Swier, S., Gasa, J., Shaw, M.T., Weiss, R.A. "Proton-exchange membrane materials based on blends of of poly(ether ketone ketone) and poly(ether imide)," Annual APS March Meeting, Montreal, Quebec, Canada, March (2004).
4. Venugopal, G., S. Krause and G. Wnek, *Chem. Mater.*, **1992**, 4(6), 1334-43
5. Gasa, J.; Shaw, M.T., "Conductivity enhancement of sulfonated poly(ether ketone ketone) blends using electric field structuring techniques," Annual APS March Meeting 2004, Montreal, Quebec, Canada, March (2004)
6. Zawodzinski, T.A., M. Neeman, Jr., L.O. Sillerud and S. Gottesfeld, *J. Phys. Chem.*, **1991**, 95(15) 6040-6044.
7. Pohl, H. A., *Dielectrophoresis*; Cambridge University Press: Cambridge, 1978.

MOLECULAR DESIGN OF RIGID ROD POLYELECTROLYTES: EFFECT OF STRUCTURE ON WATER RETENTION AND CONDUCTIVITY

Morton H. Litt, Sergio Granados-Focil, Yue Zhang and Thomas Young*

Macromolecular Sci. Dept., Case University, 10900 Euclid Ave., Cleveland, OH 44106-7202, U. S. A.

Introduction

My group has been working on polymers of the types shown below because they offer a unique opportunity to define molecular structure more precisely than is possible for most systems (1, 2, 3, 4, 5). The linear rigid rod structure causes the molecules to pack parallel to each other as liquid crystals. A small amount of co-monomer with a large cross-section, or one whose bonds are angled, forces the chains apart along their whole length, generating long pores lined with sulfonic acid groups that hold water very tightly. At low humidities the extra water raises conductivity over that of sulfonated flexible polymers. Recently, we have been studying rigid rod poly(p-phenylene sulfonic acids) **(PPSA**) polymers and copolymers to determine the effect of backbone structure on water retention and conductivity (6). A combination of TGA measurements with ^{1}H NMR for exact determination of the relative humidity dependence of the polymer water content enabled us to correlate the data and compare the two systems.

The polyimide structure is shown below. Comonomer nomenclature is detailed in **Experimenta**l.

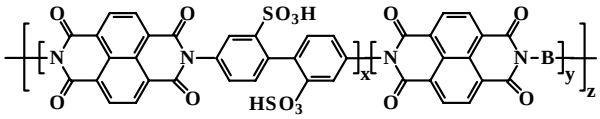

NTDA **DAPS**

Polyimide di sulfonic acid copolymer structure.

The synthesis and properties of some **PPSA**s were reported earlier (6). The basic structure is given below. Here, copolymers were synthesized by post-reacting aromatic moieties with acid groups, creating sulfone links. Other preprints discuss the copolymers (6, 7).

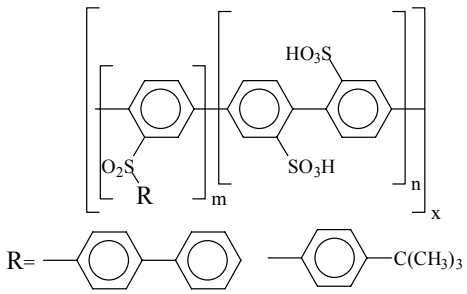

Experimental

The following co-monomers were used as the **B** group: **1**. p **phenylene** diamine (**P**), **2**. **o**xy-dianiline (**O**), **3**. 9,9-**f**luorenyl di-aniline (**F**), **4**. 2', 3' 5', 6'-tetra**p**henyl 1, 4''-diamino p-**t**erphenyl (**4PT**) and 2', 3'-**di**(**bi**phenyl) 5', 6'-**di**phenyl 1,4''-diamino p-**t**erphenyl (**D(BP)DPT**) (4). **O** and **F** are angled while the others are linear. R in the acronym means random copolymer, B block, and the number is the mole% of co-monomer.

Water uptake measurements. Polyimide films in the acid form were dried at 80^{o}C under vacuum for 72 hours. After weighing, they were equilibrated with LiCl solutions at given relative humidities until the weight was constant. One set of films, after equilibration at 50% relative humidity, was dried more thoroughly by heating under vacuum at 80^{o}C for 72 hours, 100^{o}C for 24 hours and at 150^{o}C for 1 hour, and then weighed. Thermogravimetric analyses (TGA) were run at 20^{o}C per minute under nitrogen using a T. A. Instruments TGA. Polyimide films were allowed to dry under a nitrogen stream at RT to get an initial weight and then heated. For PPSA, a film was equilibrated in the TGA pan with humidified nitrogen until its weight stabilized (Weight = 100%). Dry nitrogen was then passed over it at room temperature until the weight no longer changed, about one hour. It was then heated at 20^{o}C/min. to 600^{o}C. ^{1}H NMR measurements (Varian 300 MHz) were run on equilibrated PPSA films dissolved in D_2O, comparing the area from the aromatic H's to that of HDO.

Results and Discussion

Polyimides. Water retention for the polyimide sulfonic acids was determined using the TGA scans, showing the amount of water held by the polymers after nitrogen drying, Fig. 1. The trace derivative determined the maximum water loss rate temperature, Tmax. As Tmax rose, the activity coefficient of the bound water decreased. The bound water ranged from a minimum of 12% for the homopolymer to 21% for RO5, a calculated starting λ of 2 for homopolymer to 4.5 for RO5. Tmax, Table 1, confirms this, it increased with increasing water retention, from 84^{o}C for the homopolymer to 110^{o}C for RO5. The water activity for RO5 is about 40% that of the homopolymer.

Normally, polymer was dried at 80^{o}C for three days under vacuum. Stronger drying conditions, ending with one hour's heating at 150^{o}C under vacuum, removed more water and gave values that agreed with the TGA values. Recalculation showed that homopolymer retained 1 water and the copolymers ~2.4 waters per acid group even after 3 days of drying at 80^{o}C under vacuum.

Ionic conductivity showed a similar response; conductivity at 15% RH for the homopolymer was 0.4 mS/cm; rising to ~1.4 mS/cm. for the best copolymer (Nafion ~0.04 mS/cm.)(1,2,4). Interchain distances (WAXD), also increased for the bulky comonomers(1,4).

Poly(p-phenylene sulfonic acids). When the above approach was used for poly(phenylene sulfonic acids) the results were confusing. The weight loss up to 230^{o}C by TGA, assumed to be water, was much smaller than the water content found by other methods. We needed an unequivocal way to measure water content. The best method used ^{1}H NMR. A solution of sodium acetate in D_2O was used to calibrate the system and to determine the amount of HDO in it. Weighed, equilibrated PPSA was dissolved in a measured volume of D_2O. The ratio of HDO to aromatic hydrogens could be measured easily. In addition, the acetate CH_3 group could be used to calculate an independent measure of water content. (The second method must be used when water insoluble films are measured.) The two approaches gave essentially identical results. These results could then be compared to the TGA data after conditioning at different RHs. For runs at 20^o/min, much of their water was lost with N_2 drying at room temperature. After that, all the curves could be superimposed. Figure 2 shows TGA curves (equilibrated at 22% RH) run at different scan rates. The 20^o/min. run is typical for the set used for the water determination. The TGA and NMR methods agreed only if the TGA transition at 335^{o}C was taken as the end point for water loss. For PPSA Tmax was 108^{o}C, as high as that of the best polyimide homopolymer, Table 1, though less water was sequestered.

TGA water loss up to 250°C was analyzed using the thermodynamic concepts given in Ref. 5. Eq. 1, below, was used. ΔH_λ is the heat of vaporization of water from the polyelectrolyte. It is an average of the normal heat of vaporization at that temperature with the heat of solvation of the last water molecule evaporating under these conditions. B is the bulk modulus of the polymer. Water expands the volume and there is a compressive restoring force. **a** is the equilibrium amount of water held in the polymer free volume with no compressive stress. Minimizations for both 2 and 20°/min gave perfect fits with values of 60 KJ/mole for the heat of vaporization, B=~1.4 Gpa and **a**=~0. The data from four scans at 2, 5, 10 and 20°C/min. (ln(wt. loss rate) vs. 1/TK in this weight loss range) also gave a water heat of vaporization of 60 KJ/mole..

$$d(H_2O)/dt = -k_0 * K * T * \left(\frac{\lambda}{\lambda+1}\right) \exp\left(-\frac{\Delta H_\lambda}{R*T} + \frac{18*(\lambda-a)}{100+18*\lambda} * \frac{(18E-6)*B}{R*T}\right) \quad 1$$

Conductivities of homo- and copolymers at different temperatures showed the expected behaviors. Copolymers held water tightly and were highly conducting at low RHs and elevated temperatures (7).

Conclusions

The water absorption data for two series of rigid rod, liquid crystalline polymers, were analyzed. The molecular design concept for building in free volume was validated for these linear, liquid crystal, rigid rod polymers. Water was held strongly; polyimides dried at room temperature had λs of 2-4. PPSA homopolymer lost some water easily but held one water strongly (stable at RT but completely lost by 150°C) and two more waters so strongly that they were only removed at very high temperatures (200 to 335°C at 20°/min.) where one expects degradation. We are studying weight loss in this temperature range. Higher temperature weight loss is certainly from degradation.

Acknowledgements. We thank Drs. J. Wainright and R. Savinell for helpful discussions and the use of the TGA. This work was supported by DARPA.

References

1. Zhang, Yue; Litt, Morton H.; Savinell, Robert; Wainwright, Jesse. *Polymer Preprints* **40**(2), 480 (1999)
2. Zhang, Yue; Litt, Morton H.; Savinell, Robert; Wainwright, Jesse; Vendramini, Jerome. *Polymer Preprints* **41(2)** 1561 (2000)
3. Kim, H.-J.; Litt, M. H.; *Polymer Preprints (ACS)*, **42(2)**, 486, (2001)
4. Zhang, Yue. *Ph. D. thesis Case Western Reserve University*, 2001
5. Litt, Morton H.; Zhang, Yue. *Polymeric Materials Science and Engineering* (2003), 89 21-22.
6. Granados-Focil, Sergio; Litt, Morton H; *Polymeric Materials Science and Engineering* (2003), 89 438-439.
7. Granados-Focil, Sergio; Litt, Morton H, *Fuels, (ACS Preprints)* Aug. 2004

Table 1. Temperatures of maximum water loss rate, Tmax

Polyimide	Tmax, °C
Homopolymer	84
BP10	94
R(4P)T5	102
RF5	104
RO5	110

Table 2. Water content for PPSA as a function of RH, determined by NMR and TGA

Relative Humidity (%)	λ (TGA)[a]	NMR
22	4.6	3.7
42	5.0	4.7
58	5.9	5.2
75	6.7	6.6

a. Calculated after equilibrating at different RHs, (Wt. = 100%), 1 hr. dry N_2 flow at RT, and then heating at 20°/min.to 600°C. Weight loss at 335°C (end of a transition) agrees with NMR results.

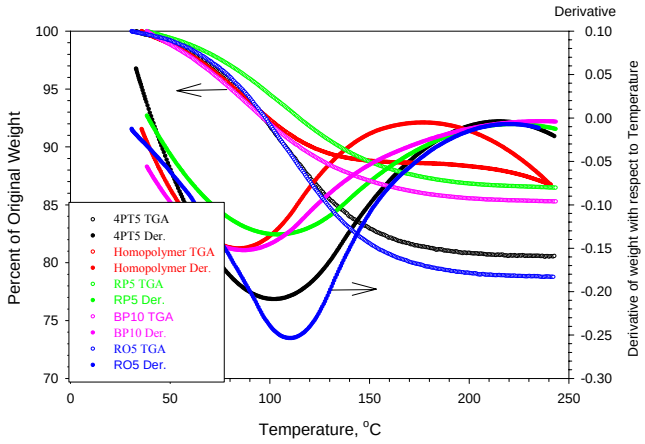

Figure 1. TGA weight loss (20°C/min.) and derivative curves for selected polyimides.

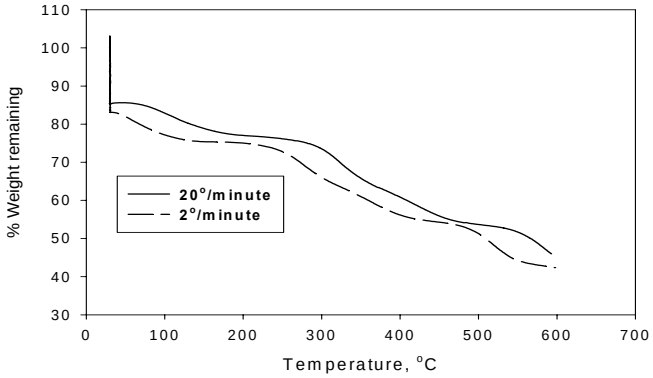

Figure 2. TGAs of PPSA after conditioning at 22% RH: Effect of heating rate on weight loss

New polymeric proton conductors for water-free and high temperature fuel cells

Xiao-Guang Sun, John B. Kerr, Gao Liu, Craig L. Reeder

Lawrence Berkeley National Laboratory, MS 62R0203, One Cyclotron Road, Berkeley, CA 94720

Introduction

Due to the considerable interest in PEM fuel cells for transportation purposes there has arisen a need to examine the feasibility of proton conducting membranes that do not depend on the presence of water for their performance. The most attractive option would involve a true solid-state material that contains no free solvent, can tolerate the presence of water, is conductive at low temperatures as well as high temperatures and can be tailored to provide desired gas permeabilities for both the separator and the membrane-electrode assembly. To accomplish this a somewhat complicated polyelectrolyte structure is necessary but an example of a candidate structure is shown in Figure 1 that illustrates some of the principles involved in proton transport in a solid polymer electrolyte.

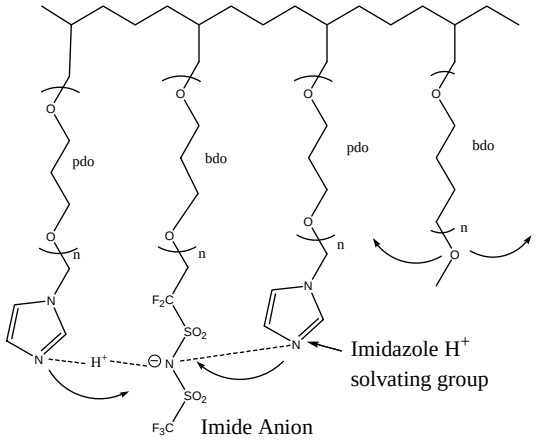

Figure 1. Schematic structure of polyether polyelectrolyte with attached imidazole groups showing mode of proton solvation.

Figure 1 shows the attachment of proton-solvating groups (imidazole) and acid groups (fluoroalkylsulfonylimide) to a backbone by means of flexible side chains. The imidazoles are shown attached via an N-alkyl tether but they can easily be attached via one of the carbons (e.g. C2) so that both nitrogens would be available for proton solvation and to participate in a Grotthuss-type mechanism of proton transfer[1]. The structure that is shown in Figure 1 is completely dependent on polymer side chain segmental motion which is dependent upon the flexibility of the side chains. The figure shows some modifications of the side-chain structure that can be easily made to achieve this and has already been reported for lithium ion transport in polymer electrolytes for lithium batteries. The nature of the backbone can be modified to provide a flexible structure (low T_g) with high gas permeability or a rigid chain with a high T_g (e.g. polystyrene) with low gas permeability. The structural changes that are possible in such a structure are virtually infinite if one considers side chain length, backbone flexibility concentration of proton solavion groups and acid groups, the nature of the acid groups and the role of cross-linking to provide improved mechanical properties.

The object of this work is to devise an easily modified polymer structure that will allow rapid elucidation of the role of these structural features in the determination of the properties of the membrane, bearing in mind that the needs are different in the separator and the MEA. We have chosen to study imidazole as the proton solvating group due to the successful development of the Polybenzimidazole-phosphoric acid system[2], the recent advances reported by Kreuer et al.[3,4] and reports of remarkable stability of imidazole-containing polymer membranes that have been used for oxygen separation[5,6]. The base polymer structure has been under development for use in lithium polymer batteries and uses a grafting chemistry that is shown in Figure 2 for lithium conductors. The grafting chemistry allows easy modification of the nature and length of the side chains, the nature of the backbone, the nature and concentration of the anions and the nature and density of cross-links. This chemistry has been recently reported[7,8] and the strategy is extended to include proton conducting units in this work. The concentration of imidazole groups relative to that of the acid groups is critical not only for the possible operation of a Grotthuss-type mechanism but also to control possible poisoning interactions with the platinum electrocatalysts. Our experimental plan is to dope various acid polyelectrolytes such as Nafion® and the polyether polyelectrolytes shown in Figure 2 with imidazoles at different concentrations to determine the proton mobility and catalyst interactions and use the results as a guide to prepare the fully tethered polyelectrolyte proton conductors

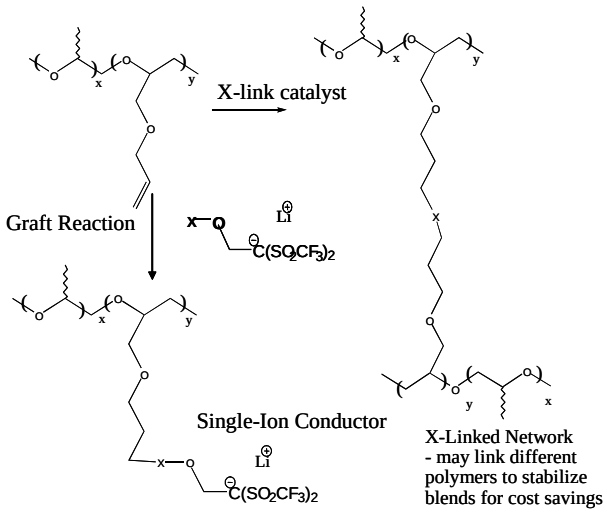

Figure 2. Grafting chemistry used to attach different acid groups (alkyl SO_3H, $-CF_2SO_3H$ and imide $-CF_2SO_2NHSO_2CF_3$) and imidazole groups to the polymer matrix.

Experimental

The basic prepolymer synthesis and grafting chemistry for the lithium forms of polyether polyelectrolytes has been described previously[7] and is also described in another article in this issue[8]. The acid forms were obtained by treatment with DOWEX^R HCR-W_2 ion exchange resin. Anion groups were prepared from tetramethyl-disilylyethane (Gelest,Inc), CH_2=$CHCH_2OC_2H_4OC_2H_4SO_3Li$ and CH_2=$CHCH_2C_2F_4OC_2F_4SO_3Li$ to give a nonfluorinated aand a fluorinated acid group. The equivalent weights(EW) were about 1600-2000. Nafion (EW 1100) in the acid form was obtained from Aldrich as a dispersion in alcohols. The polyelectrolytes were prepared as solutions in alcohol with varying amounts of imidazole

added to the solution. The polymer solutions were then cast of Teflon sheets and dried over P_2O_5 dessicant to provide membranes suitable for conductivity and mechanical measurements. Conductivity measurements were carried out using ac impedance with membranes sandwiched between two stainless steel electrodes. The temperature was controlled by means of convection ovens and ambient humidity conditions were used. Mechanical measurements were carried out on a Rheometrics RSAII solids analyzer and DSC was performed using a Perkin-Elmer DSC7. The thermal and mechanical analysis showed that the presence of imidazole in the membrane lead to an increase in the main glass transition temperature.

Results and Discussion

The conductivities of the Nafion® membranes doped with imidazole and N-methylimidazole as a function of temperature are shown in Figures 3 and 4. These are all carried out in the absence of water and the conductivity of undoped Nafion® is shown for comparison. It is clear that the best conductivities occur at imidazole:acid ratios of 6-7 and that there is an apparent change in dependence once the imidazole is in excess over the acid group. The N-methylimidazole doped membranes, however, show a lower conductivity and the temperature dependence is similar to that of the low imidazole concentration system.

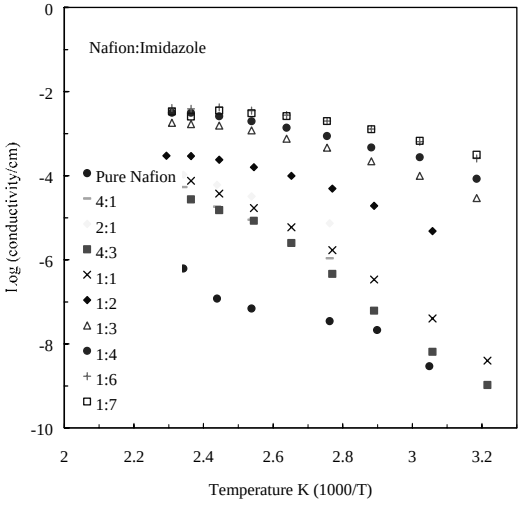

Figure 3. The conductivity of Nafion® doped with imidazole at different concentrations relative to the concentration of acid groups.

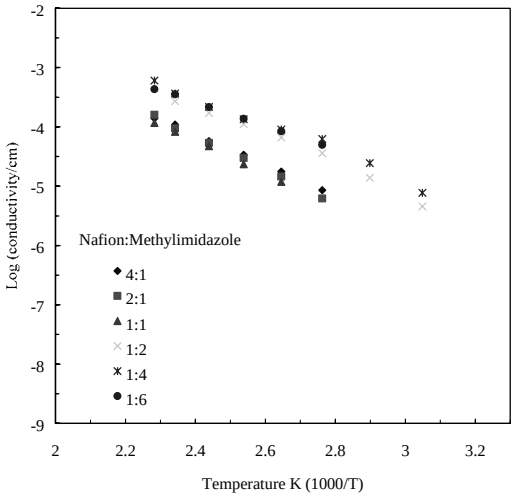

Figure 4. The conductivity of Nafion® doped with N-methyl imidazole at different concentrations relative to the concentration of acid groups.

Conductivities of the two polyether polyelectrolytes doped with imidazole are shown in Figure 5. These results illustrate the effect of the acid group. The alkyl sulfonate polymer has distinctly lower conductivities than the fluorinated alkylsulfonate, illustrating the effect of acid strength. At this time no data is available on the effect of EW. Cyclic voltammetry experiments carried out on a platinum electrode in sulfuric acid in the presence of imidazole shows no poisoning of the platinum activity until the imidazole is present in excess indicating that the imidazole base strongly interacts with platinum but the protonated form does not. This indicates that the polymer in the MEA must be completely protonated to avoid problems with catalyst activity.

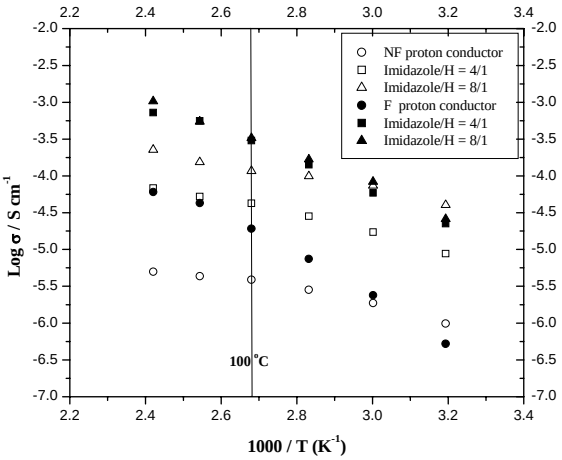

Figure 5. Proton conductivities of the proton conductors based on both non-fluorinated and fluorinated sulfonic acid with different amount of imidazole.

Conclusions

Conductivities of imidazole-containing polyelectrolyte membranes are sufficiently high to be of interest for fuel cell operation. The conductivity of membranes swollen with unsubstituted imidazole is higher than that of the N-methyl imidazole which may provide support for the participation of a Grotthuss mechanism of proton transport. Tethering of the imidazoles to the polymer matrix results in a solid state membrane with no mobile solvent that has lower conductivity than the solvent swollen systems. The polyelectrolyte structures are presently under construction and their conductivities will be reported on. The preliminary indications are that the stronger imide acid will provide higher conductivities and that optimization of the imidazole:acid ratio will provide conductivities that are of interest to fuel cell engineers.

Acknowledgement. This work was supported by the DOE Office of Hydrogen, Fuel Cells and Infrastructure and by NASA Glenn PERS program.

References.

1. Agmon, N. The Grotthuss Mechanism. *Chemical Physics Letters* **244**, 456-462 (1995).
2. Wang, J. T., Savinell, R. F., Wainright, J., Litt, M. & Yu, H. A H-2/O-2 Fuel Cell Using Acid Doped Polybenzimidazole as Polymer Electrolyte. *Electrochimica Acta* **41**, 193-197 (1996).
3. Herz, H. G. et al. New fully polymeric proton solvents with high proton mobility. *Electrochimica Acta* **48**, 2165-2171 (2003).
4. Schuster, M. F. H., Meyer, W. H., Schuster, M. & Kreuer, K. D. Toward a new type of anhydrous organic proton conductor based on immobilized imidazole. *Chemistry of Materials* **16**, 329-337 (2004).
5. Suzuki, Y., Nishide, H. & Tsuchida, E. Membranes of the picket fence cobalt porphyrin complexed with poly(vinylimidazole and -pyridine)s: Selective optical response to oxygen. *Macromolecules* **33**, 2530-2534 (2000).
6. Nishide, H., Tsukahara, Y. & Tsuchida, E. Highly selective oxygen permeation through a poly(vinylidene dichloride) cobalt porphyrin membrane: Hopping transport of oxygen via the fixed cobalt porphyrin carrier. *Journal of Physical Chemistry B* **102**, 8766-8770 (1998).
7. Sun, X. G., Reeder, C. L. & Kerr, J. B. Synthesis and characterization of network type single ion conductors. *Macromolecules* **37**, 2219-2227 (2004).
8. Sun, X. G., Reeder, C. L., Kerr, J. B. & DesMarteau, D. D. Synthesis and characterization of comb shape single ion conductors based on polyepoxide ethers and perfluorinataed lithium salts, in *Polymer Preprints* (2004). This issue.

NOVEL INORGANIC/ORGANIC HYBRID ELECTROLYTE MEMBRANES

Zhiwei Yang, Decio Coutinho, Fangxia Feng, John P. Ferraris, Kenneth J. Balkus Jr.**

Department of Chemistry and The UTD Nanotech Institute,
University of Texas at Dallas
Richardson, Texas 75083-0688, USA

Introduction

Proton exchange membrane fuel cells (PEMFCs) hold promise as next generation clean energy sources for transportation as well as small-scale stationary power generation. The advantages of PEMFCs include high power density, fast startup and immediate response for power demand change.[1] Recently, the interest in high temperature (>130 ^{o}C) PEMFCs has grown because of possible advantages over low temperature PEMFCs. These include the enhanced ability of the FC system to directly use reformed fuels by increasing catalyst tolerance of impurities in the fuel feed stream, simplification of water-management for PEMFC systems, and reduction of radiator size in automotive applications due to enhanced rejection of heat by the FC system.

A key part of a PEMFC is the membrane that conducts protons and insulates electrons. Perfluorosulfonic acid (PFSA) polymers, such as Dupont's Nafion®, have been used as PEMs in PEMFCs for decades because of their superior performance and durability. The conduction of protons in the PFSA polymer is realized through the mobility of H^+-nH_2O clusters among the -SO_3^- end groups, called the vehicular mechanism,[2,3] which requires the PFSA polymers to be fully hydrated to perform well. This limits their applications under ambient atmosphere and elevated temperature (>100 ^{o}C) conditions. The previous efforts for high temperature PEM development mainly include modifying PFSA by compositing with hygroscopic materials and developing novel aromatic-based polymers, which directly incorporate sulfonic acid groups. Since H^+ conduction in these membranes still depends on water (vehicular mechanism), they always suffer from low H^+ conductivity at elevated temperature and low to zero humidity conditions because of the water loss, and/or swelling in the presence of water.

In recent years, Brønsted acid-base systems such as organic amine/ trifluoromethanesulfonimide (HTFSI) melting salts have been reported to be highly proton conducting at elevated temperatures (100–200 ^{o}C) and water-free conditions. The H^+ conduction of these electrolytes could result from hopping of H^+ from one amine/acid active site to another without transport of small molecules (Grotthuss mechanism).[3,4]

In this study, novel inorganic/organic hybrid membranes containing immobilized amine/HTFSI groups were explored. Considering the activation energy of proton transport could depend upon the distance between the active sites as well as nature of electrolytes, a higher density of the active functional groups was introduced into the membranes to reduce the distance among active sites. The membranes are comprised of a 3-dimensional cross-linked silicon-oxygen backbone and organic amine groups. The silicon-oxygen backbone, which is stable to free radical attack, provides the PEM with the necessary thermal/chemical/mechanical properties. The organic amine groups were doped with HTFSI to form H^+ conducting sites. The thermal stability and proton conductivities of these novel membranes were studied using TGA and ac impedance.

Experimental

Preparation of membranes.

HTFSI-doped PEI/SiO_2 membranes: Polyethylenimine (PEI) (linear, M.W. = 215K, prepared according to literature method[5]) was dissolved in absolute ethanol to form 10wt% solution. 3-glycidyl-oxypropyltrimethoxysilane (GLYMO) (97%, Fluka, 1:1 weight ratio vs. PEI) was added and stirred for ½ hour at room temperature. The desired amount of HTFSI (50wt% in ethanol) was added dropwise and stirred for another ½ hour at room temperature. The resultant solution was cast on a level PTFE surface, air dried at room temperature for 1 day, and then annealed at 80 ^{o}C, ambient atmosphere overnight to form a freestanding, flexible membrane.

Polysilsesquioxane membranes with amine/HTFSI groups: Three kinds of membranes comprising different types of organic amines were prepared through sol-gel processes by using N-[3-(trimethoxysilyl)propyl]-ethylenediamine (EDATMS) (97%, Aldrich), N-[3-(triethoxysilyl)propyl]-4,5-dihydroimidazole (IPTES) (Gelest Inc.) and N-[3-(trimethoxysilyl)propyl]-polyethylenimine hydrochloride (PEITMS) (Aldrich), respectively. In a typical membrane preparation, 0.5 g of IPTES was dissolved in 1 ml of methanol. 0.1 g of (GLYMO) (97%, Fluka) was added and stirred for overnight at room temperature. 1.3 g of HTFSI solution (50wt% in dry ethanol) was added and stirred for ~2 hours at room temperature. The resultant mixture was cast on a glass paper (HOVOSORB®, Hollingsworth & Vose Company), then dried in air for 2-3 days and annealed at 80 ^{o}C overnight to form a flexible membrane.

Thermal stability. The thermal decomposition of the membranes under O_2 atmosphere was evaluated by thermogravimetric analysis (TGA) using a Perkin Elmer Pyris 1 TGA. The heating rate was 10^{o}C/min until no further weight loss was detected.

Proton conductivity measurements. Pt black (fuel cell grade, E-TEK) was symmetrically deposited on both sides of the membrane with a loading of ~5 mg/cm^2, followed by hot-pressing at ~ 85 ^{o}C and ~300 psig for 1-2 min to form crude MEA. The proton conductivities of MEA were measured by AC impedance using a PC controlled VoltaLab® PGZ301 (Radiometer Analytical S.A.) over the frequency range of 100 KHz to 0.1 Hz, using a 10 mV amplitude ac single. All measurements were carried out under ambient atmosphere. The experimental temperature and humidity were well controlled using a fuel cell testing station and 5 cm^2 single cell (Fuel Cell Technologies Inc.). The relative humidity of the cell was calculated from humidifier temperature against the cell temperature.

Results and Discussion

HTFSI-doped PEI/SiO_2 membrane. PEI has been chosen in this study because PEI has the highest amine density among the other polyamine polymers. Since the prepared linear PEI (cal. M.W.=215k) has a soft point of ~ 80 ^{o}C, GLYMO was used to cross-link PEI to increase its heat resistance. When mixed with PEI in alcohol solution, the epoxy ends of GLYMO covalently bonded to the anime groups of PEI, and the trimethoxysilane ends of GLYMO hydrolyzed and condensed together to form inorganic silica clusters through so called sol-gel processes, which greatly improved thermal stability of the composite membranes (Figure-1).[6]

Under water-free conditions, the proton conductivity of the membrane increased with increasing temperature, indicating that the proton conduction here follows Grotthuss mechanism only. Increasing relative humidity of the fuel cell operating atmosphere leads to an increase in the membrane's proton conductivity by introducing additional proton conduction through the vehicle mechanism (Figure 2).

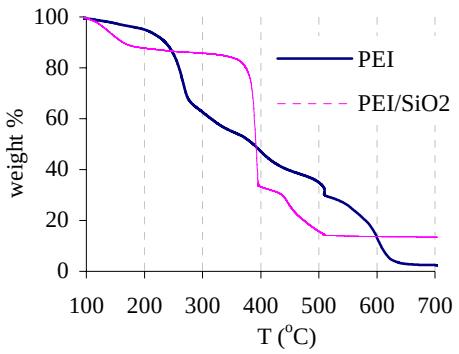

Figure 1. TGA of PEI polymer and GLYMO cross-linked PEI

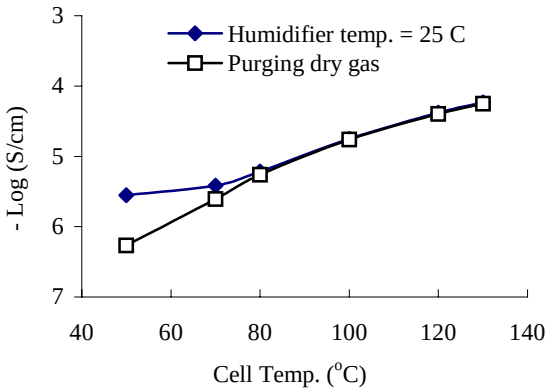

Figure 2. Proton conductivity of HTFSI doped PEI/SiO_2

Polysilsesquioxane membranes with amine/HTFSI groups. The membrane precursors were organosilanes, which hydrolyze and condense to form a 3-dimensional cross-linked Si-O network with pendant organic amine groups that were doped with HTFSI to form proton-conducting sites. The mechanical properties of the membranes, especially flexibility and swelling in hot water, were greatly improved by adding GLYMO to increase the level of cross-linking. In this case, the epoxy end of GLYMO reacts with the amine groups to form covalent bonds, while the trimethoxysilane end of GLYMO hydrolyzes and condenses with the silane through a sol-gel process. The prepared membranes exhibited good thermal stability in an O_2 atmosphere (Figure 3), and hot water.

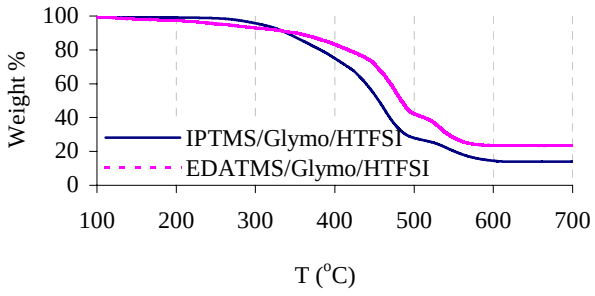

Figure 3. TGA of polysilsesquioxane hybrid membranes

Figure 4 shows the proton conductivities of an IPTES/GLYMO/HTFSI membrane with the corresponding molar ratio of 1.0 / 0.1 / 0.6 (per nitrogen site / GLYMO / HTFSI). Under water-free conditions, the membrane showed excellent proton conductivity, which increases with temperature, reaching a maximum of 10^{-3} S/cm at 130°C, while under fully hydrated conditions, the proton conductivity increased by ~1 order of magnitude. The proton conductivity of the membranes was also affected by GLYMO content and doping level. An increase of GLYMO content results in better mechanical strength but less proton conductivity. An increase in HTFSI content results in an increase in the doping level of organic amine groups, and a better proton conductivity but less mechanical strength. Membranes made from EDATMS/GLYMO/HTFSI and PEITMS/GLYMO/HTFSI showed similar behavior as IPTES/GLYMO/HTFSI membranes.

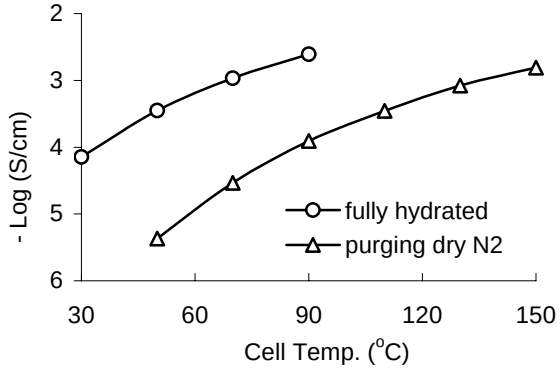

Figure 4. Proton conductivity of polysilsesquioxane membrane comprising IPTES/GLYMO/HTFSI in molar ratio of 1.0 / 0.1 / 0.6

Acknowledgment. We would like to thank *R.A. Welch Foundation,THECB-ATP, DOE, LANL, SPRING,* and the *Clark Foundation* for funding.

References

1 Cleghorn, S. J. C.; Ren, X.; Springer, T. E.; Wilson, M. S.; Zawodzinski, C.; Zawodzinski, T. A. and Gottesfeld, S. *Int. J. Hydrogen Energy*, **1997**, *22*, 1137.

2 Eikerling, M.; Kornyshev, A. A.; Kuznetsov, A. M.; Ulstrup, J. and Walbran, S. *J. Phys. Chem. B*, **2001,** *105*, 3646.

3 Hogarth, M. and Glipa, X. In *High Temperature Membranes for Solid Polymer Fuel Cells*, ETSU F/02/00189/REP DTI/Pub URN 01/893

4 Susan, Md. A. B. H.; Noda, A.; Mitsushima, S. and Watanabe, M. *Chem. Commun.*, **2003**, *8*, 938.

5 Tanaka, R.; Ueoka, I.; Takaki, Y.; Kataoka, K. and Saito, S. *Macromolecules*, **1983**, *16*, 849-853

6 Honma, I.; Takeda, Y.; Bae, J. M. *Solid State Ionics*, **1999**, *120*, 255-264

NOVEL SULFONATED PROTON EXCHANGE MEMBRANES FOR FUEL CELL APPLICATIONS: PARTIALLY FLUORINATED COPOLYMERS

Charles Tchatchoua, William Harrison, Brian Einsla, Mehmet Sankir, Yu Seung Kim, Bryan Pivovar*, James E. McGrath*

Department of Chemistry, Virginia Polytechnic Institute and State University, Blacksburg, VA 24061
* MST -11, Los Alamos National Laboratory, Los Alamos, New Mexico

Introduction

Currently there is great interest in cost effective and efficient fuel cells[1,2]. Proton exchange membranes (PEMs) are essential to the operation and the advancement of the of fuel cell technology [3,4]. The perfluorosulfonic acid polymer Nafion(DuPont) is the current state-of-the-art membrane, however, it is presently expensive, losses proton conductivity at low humidities, and has high methanol permeability. Our research group, and others, has developed alternative PEMs aimed to address noted short-comings of perfluorinated membranes—especially cost. In this presentation, we describe a two series of partially fluorinated, disulfonated poly(arylene ether sulfone) copolymers. The disulfonated copolymers were directly polymerized using the disulfonated monomer SDCDPS, dichlorodiphenyl sulfone (DCDPS), and either 3F bisphenol or 6F bisphenol A.

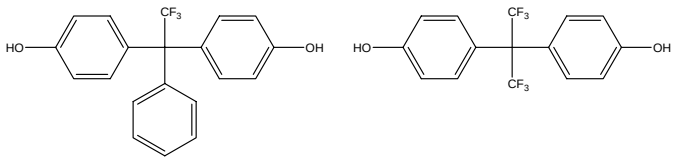

Figure 1. Structure partially fluorinated bisphenols

Experimental

Materials. All reagents were purified using typical laboratory procedures. The synthesis of 3F bisphenol and disulfonated dichlorodiphenyl sulfone have been reported previously by our group.

Copolymer Synthesis Direct syntheses of the copolymers were conducted using a 1:1 stoichiometry of each respective bisphenol to various ratios of activated dihalide monomers. As an example: In a three-necked flask, equipped with a nitrogen inlet, mechanical stirrer, a Dean-Stark trap and condenser, 10mmol of 3F bisphenol and a stoichiometric amount DCDPS and SDCDPS (the molar ratio was varied from 0 to 40%) were added to the flask, followed by K_2CO_3 in 20%molar excess (based on bisphenol). Polymerization was conducted at 20%solids concentration in dry NMP and toluene was used as azeotropic agent. The solution was allowed to reflux at 150^{o}C for 4 hours to dehydrate the system then heated at 190^{o}C overnight, for ~16 hours. The resulting solutions were diluted with NMP to reduce viscosity and then filtered to remove salt and finally precipitated in deionized water. The copolymers were isolated by filtration, washed with water and dried in the vacuum oven at 150^{o}C overnight. All copolymers were isolated in high yields (>95%).

Characterization

^{1}H-NMR experiments were performed using a Varian 400MHz instrument in deuterated chloroform. The intrinsic viscosity (IV) of the polymers was measured in NMP at 25°C using a Cannon Ubbelohde viscometer.

Membrane preparation. Membranes in the sodium sulfonate form were prepared by first redissolving the copolymer in DMAc to afford 5-10% transparent solutions followed by casting onto clean glass substrates. The films were carefully dried with infrared heat at gradually increasing temperatures (up to ~ 60 ^{o}C) under a nitrogen atmosphere, and then vacuum-dried at temperatures up to 150 ^{o}C for two days.

Acidification of Sulfonated Copolymers Membranes. The sulfonated poly(arylene ether) copolymer films were converted to their acid- form by boiling the cast membranes in 0.5 M sulfuric acid for 1.5 hours, followed by 1 hour extraction in boiling deionized water. The acidified membranes were either dried under vacuum at 90 ^{o}C in 48 hours or stored in deionized water at 30 ^{o}C.

Characterization Methods

Fourier Transform Infrared (FTIR) Spectroscopy Thin films of the copolymers were solvent cast from DMAc (~5%, w/v) and spectra were recorded for both the disodium-salt and diacid forms using a Nicolet Impact 400 FT-IR spectrometer to confirm the functional groups concentration of the copolymers.

Nuclear Magnetic Resonance (NMR) Spectroscopy ^{1}H and ^{13}C NMR analyses were conducted on a Varian UNITY 400 spectrometer. All spectra were obtained from a 10% solution (w/v) in dimethylsulfoxide-d_6 solution at room temperature. Monomer purity as well as copolymer compositions were analyzed via NMR spectroscopy.

Intrinsic Viscosity, Solution Properties and Water Uptake Homo- and sulfonated copolymer solubilities were determined at 10% concentration (w/v) in a number of solvents, including NMP, DMAc, DMSO, and chloroform. Intrinsic viscosities were determined in NMP at 25 ºC using an Ubbelohde viscometer.

Water uptake was determined on films for all of the poly(arylene ether) copolymers in both the sulfonate and acidified forms. The films were first thoroughly dried at 150 ^{o}C under vacuum to a constant weight which was recorded. The dried film was then immersed in water at 30 ^{o}C and periodically weighed on an analytical balance until constant water uptake weight was obtained. Typically, the apparent equilibrium water sorption occurred within 48 hours. The water uptake is reported as a percentage and determined by taking the weight difference between the wet film and the dry film and dividing by the dry film weight.

Non-Aqueous Potentiometric Titration Non-aqueous potentiometric titrations were conducted using a MCI Automatic Titrator Model GT-05. The acidified membrane dissolved solutions in DMAc were titrated by standard tetramethyl ammonium hydroxide in isopropyl alcohol solution (TMAH). Quantitative determination of pendent sulfonic acid groups along the copolymer chain via titration confirmed the spectroscopic values and also allowed for the direct measurement of the ion exchange capacity (IEC, meq/g).

Thermogravimetric Analysis (TGA) The thermo-oxidative behavior of both the salt-form (sulfonate) and the acid-form copolymers was performed on a TA Instruments TGA Q 500. Samples were pieces of thin films and totaled a weight of 10 to 15 mg. The films were dried under vacuum for at least 12 hours prior to analysis to remove absorbed water. The samples were evaluated over the range of 30 to 800 ^{o}C at a heating rate of 10 ^{o}C/min in air.

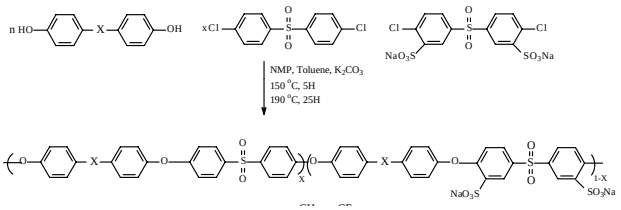

Scheme 1 General synthesis of disulfonated poly(arylene ether sulfone) copolymers.

Results and Discussion

Nucleophilic aromatic substitution step polycondensation long been successfully employed to synthesize high molecular weight poly(arylene ether). Using typical polymerization conditions one may dehydrate the aprotic dipolar reaction system with toluene until a final polymerization temperature of 190 °C is reached. The high molecular weight sulfonated copolymers were isolated as swollen "strings" by precipitating in stirred deionized water after first diluting the viscous reaction solutions from 20 percent solids to ~10 percent solids with DMAc and filtering through filter paper to remove the salts. The copolymers demonstrated exceptional solubility in common polar, aprotic solvents. Interestingly, some of the 3F bisphenol based copolymers were soluble or swollen by chloroform, depending on degree of sulfonation.

.

Table 1. General characterization of selected partial fluorinated disulfonated poly(arylene ether sulfone) copolymer

Copolymer Type	$[\eta]^{NMP,30C}$	IEC (mmol/g)
3FS-0	0.7	--
3FS-20	0.9	0.5
3FS-30	1.4	0.81
3FS-40	1.4	1.0
6F-0	0.6	--
6FS-20	0.8	0.59
6FS-30	1.4	0.87
6FS-40	1.7	1.16
6FS-50	1.6	1.50

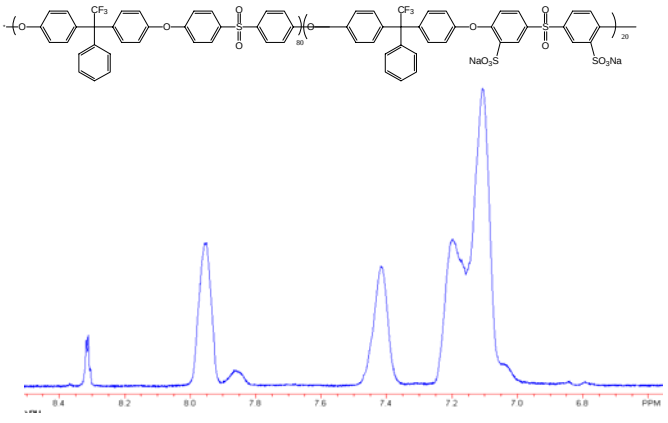

Figure 2. Proton NMR of 20mol% disulfonated 3F bisphenol based sulfonated poly(arylene ether sulfone) copolymer

Separate research from our group have shown that 6F bisphenol A containing membranes produced membrane electrode assemblies with lower high frequency resistance (HFR) than comparable wholly aromatic (biphenol based) membranes. The lower interfacial resistance was attributed to the partially fluorinated copolymer surface having better adhesion with the Nafion based electrodes. The 3F bisphenol was investigated to allow for insight on the 'amount' of fluorination needed in the copolymer composition (bulk and surface) to produced the observed performance enhancement.

Conclusion

New 3F bisphenol-based sulfonated poly(arylene ether sulfone) copolymers were synthesized and characterized. The sulfonated copolymers produced tough, ductile films.

Acknowledgements. The authors would like to thank the Department of Energy and the National Science Foundation for funding.

Polymer Electrolyte Membranes: Blends of Sulfonated Polystyrene and Poly(vinyl alcohol-co-ethylene)

Sarjit Kaur, Ryan Callery, Sarah Tighe, Glenn Dale*

*Chemistry Department, Vassar College, 124 Raymond Ave., Poughkeepsie, NY 12604-0287

INTRODUCTION

Many polymer electrolyte membranes, PEM, are obtained through post sulfonation of aromatic polymers with the goal to obtain both high ionic conductivity and mechanically strong films. This approach has some drawbacks that include difficulties in attaining high enough sulfonation, variability in sulfonation between batches and random sulfonation of aromatic rings. Sulfonated polystyrene (SPS), sodium salt, is available commercially and contains a para-substituted sulfonate group on each benzene. However, SPS is useless as a PEM because it is soluble in water. The goal of this work was to blend SPS with hydroxyl containing polymers to see if solubility of SPS can be reduced in water. Intermolecular polymeric interactions between hydroxyl groups and sulfonate groups can be expected to give miscible blends, with the added advantage that the polar environment will also contain OH groups that could endow a certain degree of inherent hydration. Blends of SPS were attempted using polyvinyl alcohol (PVA), 27 mol % PVACE (poly(vinyl alcohol-co-ethylene)) and 44 mol % PVACE. Three solvents systems were tried to cast the blends, and these included NMP, NMP/water and isopropanol/water. The blends were characterized by physical appearance before and soaking in water, thermal gravimetric analysis (TGA), differential scanning calorimetry (DSC), FTIR spectroscopy, SEM and water uptake studies.

EXPERIMENTAL

All materials were purchased from Sigma Aldrich Co, and used as received. PVACE is a copolymer, and 27 mol. % and 44 mol. % values correspond to the amount of the ethylene component in the polymer. FTIR spectra were collected using a Nexus FTIR model number 670 with an Attenuated Total Reflectance (ATR) thunderdome accessory. Spectra were collected using 32 scans and 2 cm^{-1} resolution. Thermal gravimetric analysis (TGA) and differential scanning calorimetry (DSC) were collected on Shimadzu TGA-50 and DSC-50 model instruments, respectively. The second runs on the DSC are reported .

Blends of SPS and PVA were cast from 5 wt. % polymer solutions to give a range of blends from 25 to75 wt. % SPS. As expected, clear intact films were obtained upon evaporation of solvents, though these membranes absorbed water easily. The 75 wt. % blend came close to dissolving when soaked in water at room temperature (RT) for 24 hours, while the 25 wt. % and 50 wt. % SPS blends became gelatinous. Blends were also cast using 27 mol. % and 45 mol. % PVACE using a co solvent system (50/50 water/isopropanol). In this case, the polymers solutions were heated to 60 °C to allow dissolution, and different combinations of the two polymer solutions were mixed, warmed to 60 ° to obtain a homogenous solution, allowed to cool slowly to room temperature and left to evaporate at room that generally took a day. (The stock solutions remained clear at room temperature for about 24 hours before becoming increasingly cloudy). All the blends from 44 mol % ethylene PVACE were opaque, while 25 wt. % SPS in 27 mol% PVACE was intact and slightly hazy (the higher wt.% SPS blends were significantly more cloudy, though remained intact). Following these results, lower SPS wt. % blends of 10, 15, 25 and 35 were cast using 27 mol% PVACE. The blends were also cast from polymer stock solutions in NMP and 50/50 NMP/water. Sodium SPS in NMP was obtained by dissolving the polymer in water, addition of an equal amount of NMP, followed by removal of water at room temperature using high vacuum (0.2 mmHg).

RESULTS/DISCUSSION

Blend Appearance. Blends from PVA and sodium SPS were clear and intact upon casting but, not unexpectedly, absorbed water readily at RT. The 50 and 25 wt. % SPS blends did not completely dissolve but gave a slimly gelatinous material. To improve the mechanical integrity of the blends in water, copolymer PVACE were blended next with sodium SPS. PVACE was selected because it is readily available and the ethylene component lends a certain degree of hydrophobicity to the blends that would be expected to reduce solubility. The degree of hydrophobicity could be varied using different mol. % PVACE (the 27 % and 44% were selected for this study). Polymer blends in the range of 25 and 75 wt/ % of sodium SPS were cast from three different solvent systems (50/50 water/isopropanol, NMP and 50/50 NMP). Blends cast from 50/50 water/isopropanol solvent gave fairly brittle and opaque samples. It was thought that the solvent may have dried too quickly. Therefore, blends were cast from the other two solvent systems. All the blends from the 40 mol. % PVACE were opaque and initially intact films-became brittle upon standing, presumably when the blends are drier. With the 27 mol. % PVACE that has a higher content of hydroxyl groups, blends $\geq$ 50 wt % SPS were relatively opaque but intact films. The 35 and 25 wt. % blend sample were less opaque, with the latter only showing slight haziness. The results indicated increasing miscibility with lower wt. % sodium SPS in the blends. As a result, blends containing 10 and 15 wt. % SPS blends were also cast, and these were clear and intact films, suggesting miscibility. Water uptake studies were carried on the reasonably clear and intact blend films, the 10 and 15 wt. % samples absorbed 30-32 wt. % water, while the 25 wt. % SPS blend absorbed slightly higher (38%). The clear blends were also evaluated by soaking in water overnight at room temperature; blends remained intact, though become slightly cloudier that could be the onset of phase separation or development of crystallinity.

FTIR Studies. The blends that appeared to be miscible based on visual inspection were also characterized by FTIR ATR analysis (see OH region in Figure 1). There is an apparent decrease in the absorbance of the OH band with increasing wt. % of SPS, which is expected because of the varying OH concentration in the blends. However the OH region of the blends do not show any apparent shift or broadening upon blending, leading to the conclusion that the hydrogen bonding interactions in the blends are qualitatively comparable to intermolecular interactions present in PVACE. Given that the sulfonic acid form of SPS is most relevant for PEM applications, the 25 wt. % sodium SPS blend was converted to the acid form by soaking in 2 M sulfuric acid overnight at room temperature, followed by careful washing in distilled water and dried overnight at room temperature under high vacuum. Figure 2 shows the FTIR spectra of the 27 mol. % PVACE, and the sodium and acid forms of the 25 wt. % SPS blend. The sodium form of the blends shows a S=O asymmetric stretch at 1136 cm^{-1} (corresponding to salt form of sulfate) in addition to the expected PVACE peaks. Upon acidification, there are several changes: broadening of OH region; new peaks at 1389 and 1194 cm^{-1} corresponding to asymmetric S=O asymmetric and symmetric stretches; doublet at 861 and 898 cm^{-1}. The presence of the latter doublets is suggestive of S-O-C, which implies that there could be some condensation of OH and sulfonic acid.[2] Further studies are underway to clarify between organic sulfonate and sulfonic acid groups.

Thermal Studies. The thermal properties of the blends that appear miscible are reported in Table 1 and Figure 3 (peaks going

down are endothermic). TGA analysis showed some water loss about ~100 °C, followed only by degradation at higher temperatures. In terms of onset of degradation, the blends show a slightly earlier degradation (335- 366 °C) in contrast to 374 °C for PVACE copolymer. Presumably the presence of sulfonate groups appears to hasten degradation. DSC analysis showed two transitions, a glass transition that is fairly broaden (relatively difficult to discern in Figure 3) and a melting endoterm. The same two transitions are also observed in the blend samples. While no apparent change in T_g was observed, there is a decrease in the melting endotherm by about 7 °C that can be correlated to blending of the two polymers. The results indicate that SPS is being incorporated into the polar hydroxyl component of PVACE, and the hydrophobic is relatively undisturbed upon blending of the sodium SPS, as inferred by the lack a change in the T_g. Percent crystallinity and SEM studies are currently in progress to obtain further insight into the morphology of the blends.

CONCLUSION

Miscible blends containing between 10 to ~35 wt. % SPS were obtained with 27 mol. % PVACE. These blends remain intact when soaked in water, though became slightly more opaque, which could be attributable to phase separation or increasing crystallinity. Impedance studies will be conducted in future work to evaluate conductivity of membranes. For the most part, the higher hydrophobic content of 44 mol % in PVACE did not favor miscibility.

Table 1. Thermal Analysis of 27 mol% PVACE and Blends.

	Polymers		Blends (wt, % SPS)			
°C	PVACE	SPS	10	15	25	35
Degradation	**374**	**395**	**351**	**335**	**366**	**346**
T_g	**58**	**-**	**59**	**58**	**58**	**-**
T_m	**187**	**-**	**182**	**181**	**181**	**-**

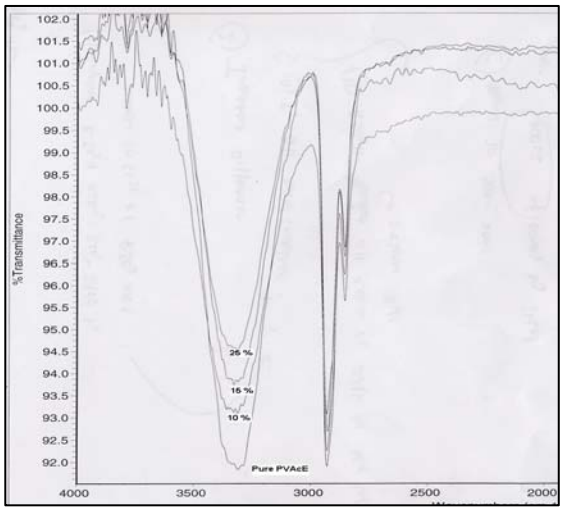

Figure 1. FTIR spectra of PVACE and 10, 15, 25 wt.% SPS blends.

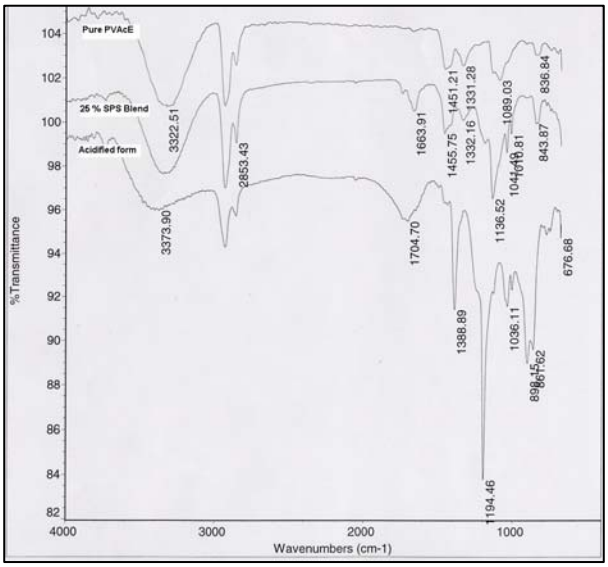

Figure 2. FTIR spectra of PVACE copolymer, 25 wt. % sodium SPS blend and acid form of 24 wt.% SPS blend.

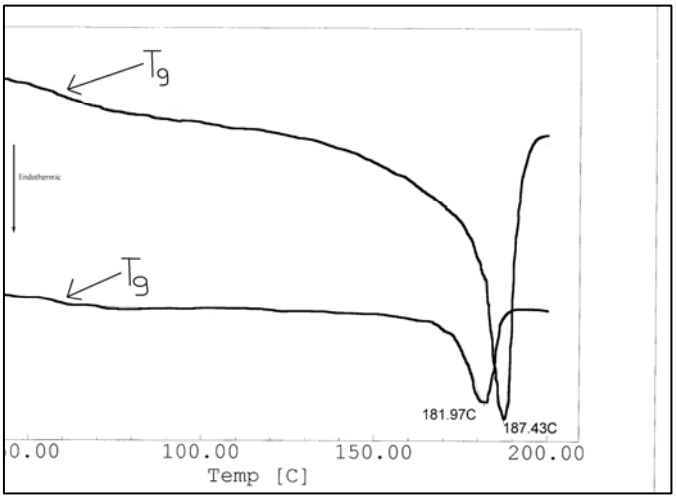

Figure 3. DSC scan of 27 mol. % PVACE (top scan) and 10 wt. % SPS blend (bottom scan)

References

(1) Young, T.; Hsieh, C., Chen L.; Huang, Y. *Journal of Membrane Science*, **1999**, *159* (1-2), pp 21.

(2) Silverstein, R. M.; Bassler, G. C.; Morrill, T. C. *Spectrometric Identification of Organic Compounds*, 5th Edition Wiley: New York, 1991.

Sulfonated diels-alder polyphenylenes: Synthesis and properties of a novel polyelectrolyte

Chris J. Cornelius and Cy H. Fujimoto

Chem and Bio Technologies. Sandia National Laboratories, Albuquerque, New Mexico 87185-0888.

Introduction

The physical property limitations of perfluoronated polymer electrolyte membrane (PEM) such as Nafion are represented by its poor mechanical properties at temperatures above 80°C, high methanol flux in DMFCs, proton conductivity at elevated temperatures, and material cost has driven research in the area of alternative polymer electrolytes.[1,2,3]

Polyphenylenes represent a promising class of thermoplastics, which demonstrate the potential of being used as a PEM within a fuel cell. Furthermore, polyphenylenes synthesized though Diels Alder (DA) polymerizations have the advantages of thermal stability, while maintaining organic solubility making it possible to form mechanically robust films.[4,5,6] The chemistry afforded by the parent DA polyphenylene represents a system that has tunable chemical structure and the potential of adding six sulfonic acid moieties per repeat unit.

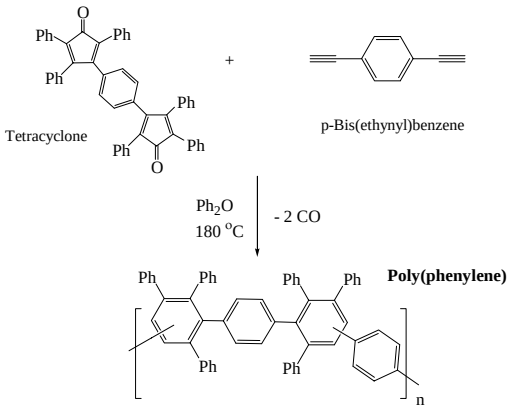

Scheme 1. Preparation of DA Polyphenylene.

We report here some of the physical properties and preliminary hydrogen and methanol fuel cell performance data of this sulfonated Diels-Alder polyphenylene (SDAPP).

Experimental

Membrane Preparation. 0.5 g of sulfonated DA polymer was casted on a clean glass plate as the sodium salt form in 10 mL of NMP. The cast was left to evaporate at 80 °C under a constant flow of N_2 for 12 hrs. The film was then dried at 100 °C under vacuum for 24 hrs and acidified (soak in 2M H_2SO_4 for 24 hrs)

Ion-Exchange Capacity. 0.2 g of acidified polymer was dried and weighed. The sample was then treated with 10 mL of 0.1 M NaOH and stirred for 24 hrs. The sample was then filtered and titrated against 0.01 M HCl.

Water Uptake. The acidified films were immersed in DI water for 24 hrs. at 25 °C. They were then blotted dry and weighed (W_s). The films were then dried and weighted until a constant weight was achieved (W_d). Water uptake was calculated by:

$$\text{Water uptake} = [W_s - W_d / W_d] \times 100\%$$

Proton Conductivity. The conductivities were determined in fully hydrated films by AC impedance spectroscopy over a frequency range of $1x10^3$ Hz to $1x10^6$ Hz using a Solartron 1260 gain phase analyzer and Solartron 1287 potentiostat at 25°C in deionized water.

Fuel Cell Testing. Polarization curves of the membranes were taken on a Fuel Cell Technologies instrument using ulta-pure H_2 and O_2 as reactant gases.

Results and Discussion

Sulfonated DA polymers were readily cast into films from NMP. These films were mechanically robust and were creasable after drying in a vacuum oven.

The films displayed proton conductives ranging from 10-80 mS/cm while still maintaining mechanical stability.

IEC (meq/g)	Water uptake (weight %)	λ (H_2O/SO_3H)	Conductivity (mS/cm)
0.98	21	12	8
1.4	36	14	52
1.6	75	19	78
2.2	137	30	115

Fuel cell performance data indicted that the sulfonated DA polymers could obtain high power levels and current densities of 1000 mW/cm^2 at 2000 mA/cm^2 at 80°C with pure oxygen.

Acknowledgement. Sandia is a multiprogam laboratory operated by Sandia Corporation, a Lockheed Martin Company, for the United States Department of Energy's National Nuclear Security Administration under contract DE-AC04-94AL85000.

References:

1. Savadogo, O. J. New Mater. *Electrochem. Syst.* **1998**, 1, 47.
2. Rikukawa, M.; Sanui, K. *Prog. Polym. Sci.* **2000**, 25, 1463.
3. Steck, A.; Stone, C. Proceedings of the Second International Symposium on New Materials for Fuel Cell and Modern Battery Systems.
4. Stille, J. K. *J. Macromol. Sci. Chem*. **1969**, 3, 1043.
5. Neenan, T. X.; Kumar, U. *Macromolecules*. **1995**, 28, 124.
6. Fujimoto, C. H.; Loy, D. A.; Wheeler, D. R.; Jamison, G. M.; Cornelius, C. J. *Polymer Preprints*. **2002**, 43, 2, 1376.

Composite Membrane-Based PEMFCs for Operating at Elevated Temperature and Reduced Relative Humidity

Serguei N. Lvov, Mark V. Fedkin, Elena Chalkova, and Michael B. Pague

The Energy Institute & Department of Energy and Geo-Environmental Engineering, The Pennsylvania State University, 207 Hosler, University Park, PA 16802, lvov@psu.edu

Introduction

Proton exchange membrane fuel cells (PEMFCs) offer high promises as environmentally clean and highly efficient electric power sources for stationary and mobile applications. While the present-day PEMFCs are operated at temperatures below 100 °C, extension of the operating temperature range to 120-150 °C is desired for a number of technological reasons. Elevated temperature conditions are expected to reduce the need for noble metal catalysts, suppress CO poisoning, and eliminate water flooding at the cathode. High temperature fuel cell operation would also enhance the electrode reaction kinetics and thus boost the fuel cell efficiency. However, perfluorosulfonic acid polymer membranes (Nafion®), currently used in PEMFCs experience severe dehydration at temperatures above 100 °C, resulting in a descrease in proton conductivity and consequent drop of performance.

One of the approaches to suppress membrane dehydration is to impregnate the polymer with hygroscopic particles, e.g. metal oxides[1-3]. Such composite solid oxide/Nafion membranes are known to have an increased water retention[4,5] which helps the Nafion to preserve its functionality at high temperatures. In this study, we describe the properties of TiO_2/Nafion composite membranes and explore the limits of their applicability in PEMFCs over ranges of temperature and relative humidity (RH).

Experimental

TiO_2 properties. The TiO_2 (rutile) powder (Kronos Inc. 4020, Lot #60170) was sieved and cleaned under hydrothermal conditions (220°C) prior to use. The powder preparation was carried out at the Oak Ridge National Laboratory according to the procedure that was described in detailed elsewhere[6,7]. Analytical characterization of the powder revealed the following properties: specific surface area - 2.914±0.004 m^2g^{-1} (BET); aggregates (3-50 μm in size) of anhedral or subhedral micron-size grains (SEM); phase - pure TiO_2 (rutile) with no detectable crystalline contaminants (XRD).

The Kronos TiO_2 was previously studied with respect to surface properties from 25 to 200 ^oC using the high temperature microelectrophoresis technique developed in our laboratory[6,8]. According to these studies and also proton adsorption data obtained for a similarly treated TiO_2 powder sample[7,9], the TiO_2/water interface is positively charged under acidic conditions (pH<5.5 at 25 ^oC and pH<4.7 at 120 ^oC) and is characterized by a very high concentration of adsorbed protons. Based on several studies of the electrical double layer (EDL) at the TiO_2(rutile)/water interface including Multisite Complexation (MUSIC) modeling[6,9,10] the terminal oxygen surface sites of rutile can accept up to two protons and are mainly protonated at the pH of the pore solution in the Nafion (~2-2.5). Since protons in the adsorption layer have hydration spheres of water molecules, TiO_2 is expected to be much more efficient water retainer compared to SiO_2, which remains virtually uncharged in acidic solutions.

Preparation of composite membranes and MEAs. The composite TiO_2/Nafion membranes were prepared using a procedure similar to that described elsewhere[11]. An appropriate amount of commercial 5% Nafion solution (Aldrich) was mixed with a particular amount of TiO_2 powder (0, 5, 10, and 20 mass %), ultrasonicated, and cast in a Teflon dish. After solvent evaporation at 80 °C, resulting TiO_2/Nafion films were detached from the dish and hot-pressed at a pressure of less than 2 bars. The final treatment was at 150 °C for 10 minutes. The resulting membrane thickness was around 80 μm.

The membrane-electrode assemblies (MEAs) were prepared using a commercial gas diffusion solid polymer electrolyte electrode of Los Alamos type (ELAT) with double-side coatings. Electrode specifications were as follows: Pt loading 0.5 $mg\cdot cm^{-2}$ with 20% Pt on Vulcan XC-72 as a catalyst, Nafion loading 0.8 $mg\cdot cm^{-2}$, and standard PTFE loading. MEAs were prepared by pressing the electrodes onto the membrane in a Carver hot press at 130 ^oC and 50 bar for 40 seconds.

Membrane testing. The composite TiO_2/Nafion membranes were tested for proton conductivity and fuel cell performance.

The proton conductivity of the composite membranes fully hydrated in water was determined in a temperature range from 20 to 140 °C using four-electrode AC impedance spectroscopy (Gamry Instruments). Each sample was mounted in an electrochemical cell and submerged in deionized water inside a Parr Autoclave. The impedance measurements were carried out after the membrane was fully saturated with water, and the water was equilibrated with the vapor phase. The details of the experimental method are described elsewhere[12]. The membrane conductivity, σ, was calculated as $\sigma=l/rS$, where l is the distance between the electrodes, r is the measured resistance of the membrane (at 1 kHz), and S is the cross-sectional area of the membrane perpendicular to the current flow.

The fabricated MEAs were tested in an ElectroChem H_2/O_2 fuel cell, which is capable of operating at temperatures up to 130 ^oC and at pressures up to 3.5 bar. To ensure the consistency of fuel cell operation, temperature, gas flow rate, H_2 and O_2 pressures, RH, and compaction force used for fuel cell arrangements were kept the same in parallel tests. The fuel cell tests were performed at 80 and 120 ^oC, at 26, 50, 80, and 100% RH with the total pressure (reactant gas and water vapor) of 3 bar.

Results and Discussion

The highest proton conductivity was obtained for the 5 mass % TiO_2/Nafion membrane. The conductivity value obtained for this membrane exceeded the conductivity of the unmodified Nafion membrane by 5-60% in the temperature range 20 to 140 ^oC (Fig. 1). The conductivity of the unmodified Nafion membrane was still higher than the conductivity of membranes with 10 and 20 mass % of TiO_2 at temperatures below 110 °C. For all studied membranes, the conductivity started to decrease as temperature was increased above 110 °C, however composite membranes showed much less degradation compared the unmodified Nafion membrane. The observed improvement in membrane conductivity is attributed to (1) hygroscopic effect of the TiO_2 particles (since the water retained in the EDL at the TiO_2/water interface can be used for proton solvation inside Nafion) and (2) surface proton conductivity of TiO_2 under the conditions of complete protonation[13] .

The performance of the TiO_2/Nafion composite membranes in the H_2/O_2 PEMFCs was evaluated based on cell voltage vs. current density (polarization) curves. The effects of the TiO_2 content and RH on the PEMFCs performance were studied at temperatures of 80 and

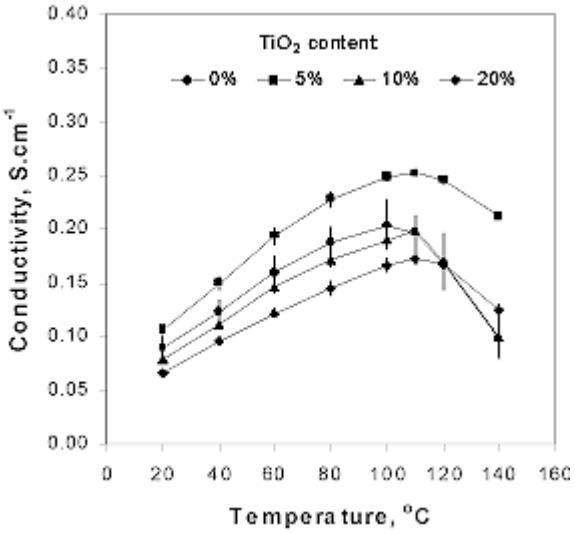

Figure 1. Proton conductivity of bare Nafion and TiO_2/Nafion composite membranes in water as a function of temperature.

120 °C. At 80 °C, the TiO_2 content had no significant effect on the PEMFC performance over the entire range of RH used (from 26 to 100%). However, the situation apparently changed when the same membranes were tested at 120 °C. In this case, the fuel cell performance was significantly affected by both TiO_2 content and RH (Fig. 2). When the TiO_2 content increased from 0 to 20%, the current density delivered at cell voltage of 0.6 V was increased, respectively, 3, 5.8, 1.6, and 1.1 times at 26, 50, 80, and 100% RH. The effect of RH (26 to 100%) was significant for the unmodified Nafion membrane, while the performance of the TiO_2/Nafion composite membranes was not affected by RH reduction within 50-100%. For the unmodified Nafion membrane, the maximum power density progressively dropped with decreasing RH from 100 to 26%. For the 10%-TiO_2/Nafion and 20%-TiO_2/Nafion membranes, the maximum power density stays on a plateau down to RH=50%. These results show that composite membranes are able to operate at RH 50% as efficiently as Nafion operates at RH 100%. This advantage can be attributed to the enhanced water retention properties of TiO_2 particles. Hydrophilic TiO_2 evidently improved the water retention properties of the membranes and, therefore, their hydration, which in turn favors the Nafion proton conductivity. Improvement of membrane water retention becomes more important at reduced relative humidity, when the Nafion polymer readily loses water.

Conclusions

The composite membranes showed a significant advantage over unmodified Nafion membranes, confirming that hydrophilic TiO_2 particles dispersed in the membrane provide better water retention than bare Nafion polymer at a reduced RH. The performance of the composite Nafion/20% TiO_2 membrane at 120 °C and 50% RH was comparable to the performance of the unmodified Nafion membranes at 80 °C and 100% RH, which means that the use of the new composite membrane allows increasing the operating temperature of the PEMFC from 80 to 120°C (at 50% RH) without significant performance loss.

Acknowledgement. This study was supported by DOE (Contract #DE-FC36-01GO11085). The authors thank David Wesolowski for providing TiO_2 powder and useful discussions.

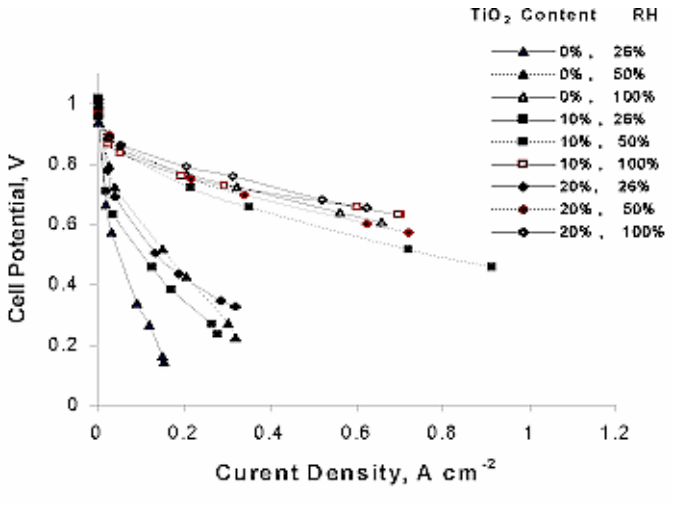

Figure 2. Performance of PEMFC operated with TiO_2/Nafion composite membranes at different relative humidities at 120°C.

References

(1) P.L. Antonucci, A.S. Arico, P. Creti, E. Ramunni, V. Antonucci, *Solid State Ionics,* **1999**, *125*, 431.
(2) N. Miyake, J.S. Wainright, R.F. Savinell, *J. Electrochem. Soc.* **2001,** *148,* A898.
(3) K.T. Adjemian, S.J. Lee, S. Srinivasan, J. Benziger, A.B. Bocarsly, J. Electrochem. Soc. **2002,** *149,* A256.
(4) A.S. Arico, V. Baglio, A. Di Blasi, P. Creti, P.L. Antonucci, V. Antonucci, *Solid State Ionics* **2003,** *161,* 251.
(5) Li, Q., He, R., Jensen, J.O., and Bjerrum, N.J., *Chem. Mater*. **2003**, *15*, 4896.
(6) M.V. Fedkin, X.Y. Zhou, J.D. Kubicki, A.V. Bandura, S.N. Lvov, M.L. Machesky D.J. Wesolowski, *Langmuir* **2003,** *19,* 3797.
(7) M.L. Machesky, D.J. Wesolowski, D.A. Palmer, K. Ichiro-Hayashi, *J. Colloid Interface Sci.* **1998,** *200,* 298.
(8) X.Y. Zhou, X.J. Wei, M.V. Fedkin, K.H. Strass, S.N. Lvov, *Rev. Sci. Instrum*. **2003,** *74,* 2501.
(9) M.L. Machesky, D.J. Wesolowski, D.A. Palmer, M.K. Ridley, *J. Colloid Interface Sci.* **2001,** *239,* 314.
(10) K. Bourikas, T. Hiemstra, W.H. van Riemsdijk, *Langmuir* **2001,** *17,* 749.
(11) A.S. Arico, P. Greti, P.L. Antonucci, V. Antonucci, Electrochem. *Solid-State Lett*. **1998,** *1,* 66.
(12) X.Y. Zhou, J. Weston, E. Chalkova, M.A. Hofmann, C.M. Ambler, H. Allcock, S.N. Lvov, *Electrochim. Acta* **2003,** *48,* 2173.
(13) Lvov, S.N., Fedkin, M.V., Chalkova, E., Jayabalan, D.K., and Wesolowski, D.J., *Electrochim. Acta*, **2004** (submitted).

Degradation of PEMFC : sulfonated polyimides

Gilles Meyer, Carine Perrot, Laurent Gonon, Gérard Gebel, and Jean-Luc Gardette

Groupe Polymères Conducteurs Ioniques, DRFMC/SI3M UMR 5819 CEA-Grenoble, 17 rue des Martyrs, 38054 Grenoble cedex 9, France
* LPMM, UMR 6505, 63000 Aubière, France

Introduction

For the last decade Proton Exchange Membrane Fuel Cell (PEMFC) are of great interest for automotive and portable applications. Perfluorosulfonic acid membranes like Nafion are the reference materials because of their high ionic conductivities and chemical stability[1]. On the other hand, these materials are too expensive, do not allow high temperature FC operation and exhibit a poor resistance to cycling FC conditions. As a consequence alternative nonfluorinated hydrocarbon membranes are developed, essentially by introduction of sulfonic acid groups on thermostable aromatic polymers[1,2]. However, the chemical, electrochemical or physical evolution limits the lifetime in FC conditions. It is worth noting that the operating times are not always specified and never correlated to the ageing extent of the membrane.

Sulfonated polyimides (sPI) are considered as promising ionic conductive polymers for fuel cell applications[3]. While most sulfonated polymers are prepared by post-sulfonation[2] sPI used in this study were obtained by direct polymerization using sulfonated monomers. It allows the control of the quantity and distribution of ionic groups along the polymer chains.

To take into account the influence of the molecular structure of the macromolecules, a series of sPI membranes were studied in FC under stationary operating conditions. The membrane lifetimes were determined and the chemical modifications induced on the macromolecule were quantified by IR spectroscopy. In addition, after *ex-situ* ageing experiments, IR and mechanical analyses were performed to confirm the degradation mechanism involved in FC.

Experimental

Materials. The synthesis of sPI block copolymers (**Figure 1**) is described in details elsewhere[4]. These polymers are characterized by X=5 as sulfonated block size and the size of the hydrophobic sequence (Y) is adjusted to control the Ionic Exchange Capacity (IEC) of the membrane. IEC is defined as the molar amount of sulfonated groups per gram of polymer. The membranes tested have a Y value of 5, 12 or 21 to reach an IEC of 2, 1.3 and 0.9 meq.g^{-1}, respectively. The membrane will be referenced as follow : IEC/X-Y.

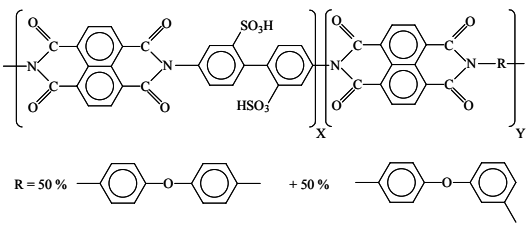

Figure 1. sPI chemical structure

Fuel cell experiments. The lifetimes of sPI in FC were determined using a specially designed bench and a 25 cm^2 active area single cell. The electrodes were provided by Sorapec, and the catalyst loading was 0.1 mg.cm^{-2} at the anode and 0.2 mg.cm^{-2} at the cathode. A gasket of 0.28 mm surrounded each electrode to avoid leaks of gazes. The cell was pressed with a couple of about 7 N.m to enhance the electrode-membrane contacts and therefore to minimise the ohmic drops at the interface. The gas inlets were 27 cm^3/min for hydrogen and 42 cm^3/min for oxygen. The tests were performed under a constant current density of 200 mA.cm^{-2}, at 3 bar absolute gas pressure and a cell temperature ranging from 60 to 90°C. The end of each test corresponded to the mechanical rupture of the membrane evidenced by an abrupt potential drop to 0 V due to a H_2/O_2 gas mixing.

Characterization methods. The mechanical properties were determined on test pieces 0.95 mm width and 4.25 mm long using an Instron 4301 tester, with a traction speed of 3 mm per minute. The samples were studied soaked in water at room temperature in order to control the swelling degree of the membrane. Plastic extensions were calculated as the difference between extensions at rupture and at the beginning of the plastic zone.

FTIR-ATR spectra were recorded on a Nicolet 5SXC spectrometer, with a Thunderdome accessory and a germanium crystal. The surface analysis was about 5 mm^2.

Ionic conductivities of membranes equilibrated in water were measured by impedancemetry using a cell equipped of mercury electrodes.

Results and Discussion

The properties of the polymer membranes tested in the present study and their performances in FC are summarized in **Table1**. As expected, the cell voltages are directly connected to the ionic conductivity of the membrane. The cell voltage thermal dependence observed for the sPI 1.3/5-12 can be attributed to a non optimized water management. Both the lifetime and performances are strongly related to the IEC value, but in opposite ways. Based on the three studied samples, the lifetime dramatically decreases for IEC values larger than 1.3. Correlatively, the FC performances drops for IEC values lower than 1.3. As a consequence, the IEC value of 1.3 appears as the best compromise for FC operation.

sPI	Thickness (µm)	Conductivity (S/cm)	T (°C)	U (mV) (200 mA.cm-2)	Lifetime (hours)
0.9/5-21	87	$0.6.10^{-2}$	80	400	600
1.3/5-12	75	$1.9.10^{-2}$	70	670	600
			80	640	300
			90	580	150
2/5-5	60	$2.6.10^{-2}$	60	700	270
			70	700	100
			80	690	30
			90	695	10

Table 1. Results of ionic conductivity and fuel cell measurements

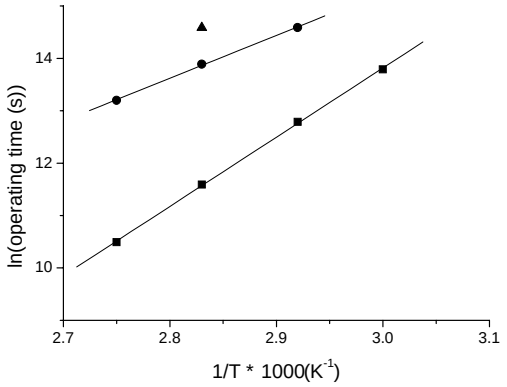

Figure 2. Evolution of the operating times with temperature on an Arrhenius graph for sPI 0.9/5-21 (▲), 1.3/5-12 (●) and 2/5-5 (■) membranes.

The lifetimes represented in an Arrhenius plot exhibit a linear trend **(Figure 2**) characteristic of a thermo-activated process. The activation energies are 72 and 111 kJ.mol^{-1} for an IEC of 1.3 and 2 meq.g^{-1} respectively. From **Figure 2**, the lifetime of the membrane can be extrapolated to lower temperatures (4000 hours at 40°C for a IEC = 1.3 meq.g^{-1}). ion of the curve at low temperatures suggests that these polymers can be used for low temperature PEMFC since it gives an operating time of sPI.

The water produced after fuel cell operation is lyophilized and the residues were analyzed by IR spectroscopy. The absence of the characteristic absorption bands from the hydrophobic sequence suggests the degradation mainly occurs on the sulfonated blocks.

FTIR-ATR analyses were performed on both sides of the 0.9/5-21 sPI tested 600 hours at 80°C. Difference spectra (aged – reference) for both anode and cathode sides are reported on **Figure 3.** Significant differences appear between the two spectra. On the cathode side, the major phenomenon is a decrease of the absorption bands characteristic of the polymer, particularly the one at 1350 cm^{-1} revealing a hydrolysis of imide functions. Assuming that hydrolysis is limited to the ionic segments, the loss of imide groups of these blocks can be estimated to 74%. On the anode side, the same phenomena is detected. However one can notice the appearance of new absorption bands in the carbonyl region suggesting either an oxidative process or a partial hydrolysis of the imide rings.

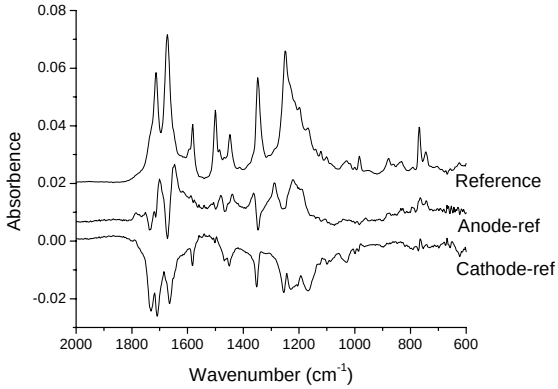

Figure 3. Infra-red spectra (ATR, crystal Ge) of the sPI 0.9/5-21 before and after 600 hours at 80°C of operation in fuel cell.

IR determination of the IEC from the absorption at 1580 cm^{-1} revealed a quasi total disappearance of the sulfonic groups at the cathode side, whereas it is nearly unchanged at the anode one. As water is produced at the cathode, an elution process of the degradation products can take place.

The mechanical properties of sPI membranes were determined after *ex-situ* ageing in water at 70 an 90°C. The plastic extensions measured as function of degradation time are given in **Figure 4**. As expected, the hydrolysis of the imide functions leads to chain scissions and as a consequence to a loss of the mechanical properties.

The evolution of the mechanical properties versus IEC and temperature exhibits the same trend than the results obtained in FC tests and *ex-situ* degradation kinetics by IR.

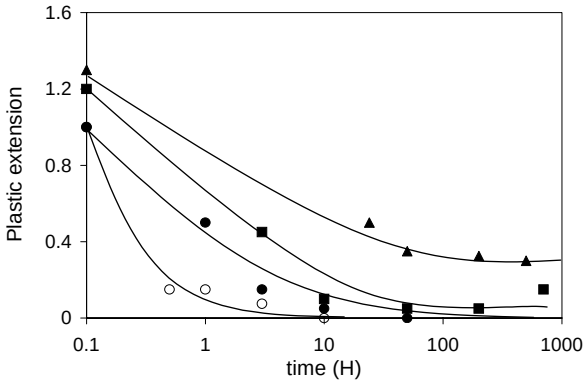

Figure 4. Evolution of the plastic extension with hydrolysis time : sPI 0.9/5-21 at 70°C (▲), 1.3/5-12 at 70°C (■), 2/5-5 at 70°C (●) and 90°C (❍)

Conclusions

The stability of sPI was studied in FC and *ex-situ* conditions. While a good correlation between an in-situ and ex-situ experiments was established, ageing appears accelerated in FC. IR and mechanical experiments have pointed out that hydrolysis of the imide ring leading to polymer chain scissions is the major degradation process. Therefore, the sPI stability can be significantly improved by reducing hydrolytic sensitivity.

Acknowledgements. The authors would like to acknowledge the LMOPS (R.Mercier) for the polymer synthesis, the CEA-Le Ripault/DMAT for the membrane preparation and the CEA Grenoble /DTEN for their help in membrane FC testing.

References

(1) Savadogo, O.; *J. Power Sources*, **2004**, *127*, 135.
(2) Rozière, J., Jones, D.J., *Annu. Rev. Mater. Res.,* **2003**, *33*, 503
(3) Besse, S., Capron, P., Diat, O., Gebel, G., Jousse, F., Marsacq, D., Pinéri, M., Marestin, C., Mercier, R., *J. New Mat. Electrochem. Syst.*, **2002**, *5*, 109
(4) Genies, C.; Mercier, R.; Sillion, B.; Cornet, N. ; Pineri, M. *Polymer*, **2001**, *42*, 359

PROTON EXCHANGE MEMBRANES BASED ON COMPOSITES OF SULFONATED POLY(ETHER KETONE KETONE) AND CROSSLINKED SULFONATED POLYSTYRENE PARTICLES

Jeffrey V. Gasa[1], S. Boob[1], R.A. Weiss,[1,2] and Montgomery T. Shaw[1,2]

[1]Polymer Program and [2]Department of Chemical Engineering
Institute of Materials Science, University of Connecticut, Storrs, CT 06269-3136

Introduction

An elegant solution to the fueling problem of proton-exchange membrane (PEM) fuel cells running on hydrogen is to modify the cell design for operation on a liquid fuel, for example, methanol. This is of particular importance to transportation and portable power supply applications. For portable fuel cells, polymers can provide simplicity of design and reliable performance, in addition to the usual attributes of light weight and low cost. The main polymer challenge for fuel cells operating on methanol is the improvement of the methanol/oxygen barrier properties of the proton-exchange membrane without compromising other essential properties, specifically, proton conductivity.[1]

We have reported recently that proton conductivities and MEA performance comparable to Nafion®, which is the benchmark, can be achieved with membranes based on the high-performance polymer poly(ether ketone ketone) PEKK, and its blend with poly(ether imide).[2,3] At present, our research has focused mainly on improving the transport and mechanical properties of sulfonated PEKK (SPEKK) membranes. The approach of the research presented herein was to use relatively low sulfonation levels of SPEKK (about 1 meq/g) to minimize water uptake and maintain low methanol/oxygen permeability of the membrane. However, SPEKK with low sulfonation level also has low proton conductivity.[2,3] To enhance proton conductivity, crosslinked sulfonated polystyrene (XLSPS) particles that have very high sulfonation levels (about 5 meq/g) were used as an additive. It has been demonstrated in the past by Chen et al. that non-conductive polymer blends can have excellent proton conductivities when mixed with XLSPS microspheres.[4,5] However, they did not include sulfonated matrices in their study. Our hypothesis is that the sulfonic acid groups in the matrix will tend to cluster around the particles to reduce interfacial energy, and provide a highly acidic path for proton movement.

Experimental

Materials. The acid polymer of principal focus in this study was sulfonated PEKK (SPEKK). The PEKK used was OXPEKK-SP (Oxford Performance Materials, New Britain, CT), which has a T/I ratio of 6/4. Sulfonation was achieved by dissolving the polymer (5% w/v) in a mixture of 53/47 (v/v) concentrated sulfuric acid and fuming sulfuric acid. The sulfonation time and temperature were varied to achieve different levels of sulfonation, expressed here in terms of ion-exchange capacity (IEC). Crosslinked sulfonated polystyrene (XLSPS) beads used were Dowex Marathon® C (Aldrich Chemical Company, Inc). These 380-500 μm beads were thoroughly washed with de-ionized water to remove residual sulfuric acid. After drying these beads at 100 °C in vacuum for 1 day, they were ground in a mill and sifted. Particle sizing was done in a 400 mesh sieve to obtain particles of size 37 μm and smaller. The ion exchange capacity of the particles was measured by titration and was found to be about 5.2 meq/g.

Membrane Preparation. SPEKK and XLSPS particles (at various weight ratios) were mixed using N-methyl pyrrolidone (NMP) as a solvent to form 5% polymer solutions. The SPEKK dissolved while the XLSPS particles remained in suspension. These solutions were cast onto clean glass plates at 60 °C and air dried in a hood until most of the solvent had evaporated. After drying, the membranes were soaked in de-ionized water at 60°C for 6 h to remove residual solvent.

Impedance Spectroscopy. The proton conductivity of the membranes was measured by impedance spectroscopy using a Solartron® 1260 impedance analyzer over a frequency range of 1-10^6 Hz. The applied voltage was 50 mV. Membrane conductivities were measured using a cell described by Zawodzinski et al.[6]

Water Uptake Measurements. The membranes were kept in a controlled humidity environment and weighed every 24 h until the mass of the membranes reached equilibrium values. The membranes were then dried in vacuum at 100 °C for 24 h and weighed. The water uptake values reported were calculated on a wet basis.

Electron Microscopy. The morphology of the composite membranes was studied using an environmental scanning electron microscope (ESEM). The composite membranes were cryo-fractured in liquid nitrogen and micrographs of the cryo-fractured section through the thickness were taken.

Results and Discussion

Proton Conductivity. The conductivities of the SPEKK-XLSPS composite membranes at 20 °C and 98 % relative humidity (Figure 1) exhibited a sigmoidal dependence on XLSPS weight fraction for both sulfonation levels of the SPEKK matrix.

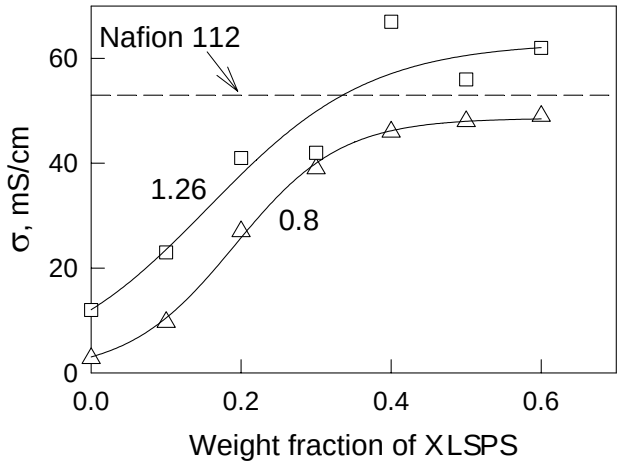

Figure 1. Proton conductivity of the membranes at 98% relative humidity and 20 °C. The values indicated in the graph pertain to the IEC of the SPEKK matrix in meq/g. The solid lines represent 3-parameter sigmoidal fits of the data.

Water Uptake. As shown in Figure 2, the relationship between water uptake and XLSPS weight fraction is almost linear, although there is a slight curvature. The slopes of the λ values (proportional to the second derivatives of the water uptake curves) for both sulfonation levels were significant ($P<0.01$) and were statistically the same. As expected, the composites containing higher-IEC SPEKK (1.26 meq/g) matrix have higher water uptakes than the lower-IEC (0.8 meq/g) counterpart but there was no significant difference in the λ values, which is the water to sulfonic acid mole ratio. Figure 4 compares the water uptakes of the pure SPEKK membranes with those of the composite membranes. The IEC of the composites shown in Figure 4 are weight-average values calculated from the ion-exchange capacities of the pure components. At low IEC values

(below 1.5 meq/g), the water uptake of the composites is almost identical to that of pure SPEKK. However, at IEC values above 1.5 meq/g, the slope of the latter increases with increasing IEC while the slope for the former has an opposite trend.

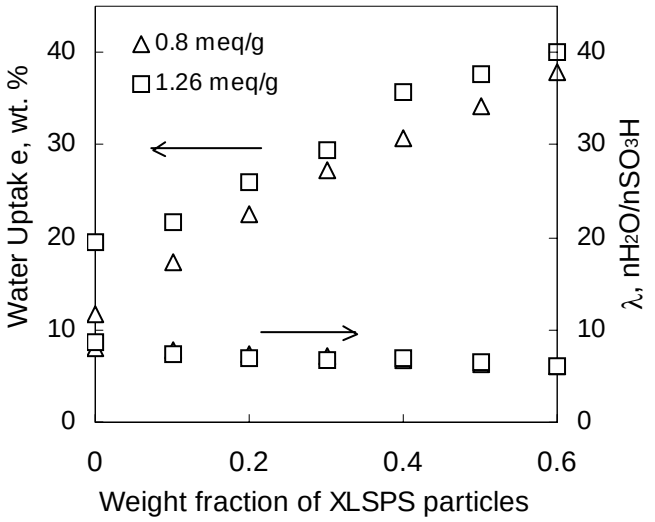

Figure 2. Water uptake of the SPEKK-XLSPS composite membranes at 98% relative humidity and room temperature. The IEC values indicated in the graph pertain to the IEC of the SPEKK matrix.

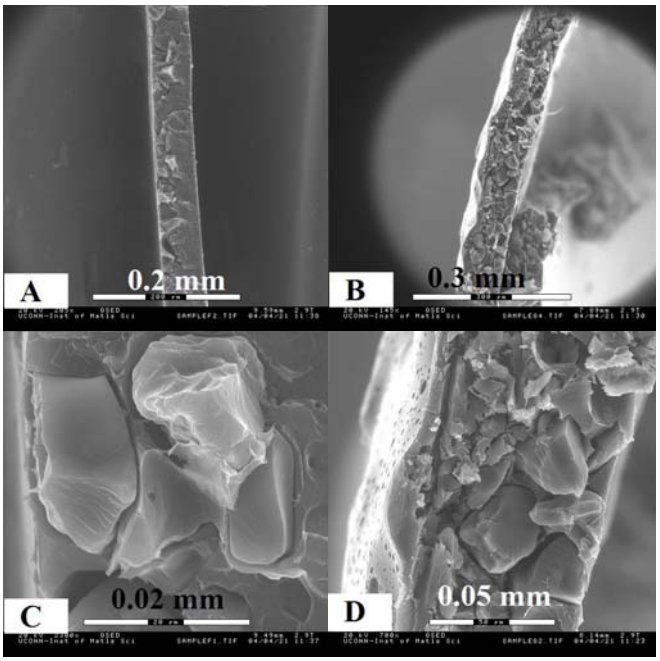

Figure 3. ESEM micrographs of a cryo-fractured section of SPEKK-XLSPS composite membranes at two different weight fractions of XLSPS: A) 0.2 and B) 0.5. The micrographs labeled C and D are the same micrographs as A and B, respectively, but at a higher magnification.

Morphology of the Composite Membranes. ESEM micrographs of cryo-fractured sections of the composite membranes are shown in Figure 3. For high weight fractions of particles (above 0.2), the dispersion of the particles in the SPEKK matrix was fairly uniform. However, at low weight fractions, the particles settled and accumulated on one side of the membrane. This can be beneficial if it is desired that the particles be concentrated on just one side (cathode or anode) of the fuel cell. For example, if the particles are less stable in oxygen environment than the SPEKK matrix, it is desirable that the particles concentrate on the side opposite to the oxygen side.

Conclusions

It has been demonstrated in this study that conductivity of low-IEC SPEKK membranes can be enhanced dramatically by the addition of highly acidic polymeric particles (XLSPS). We are presently investigating the mechanical properties of these composite membranes, as there are some indications of increase in toughness upon addition of the particles.

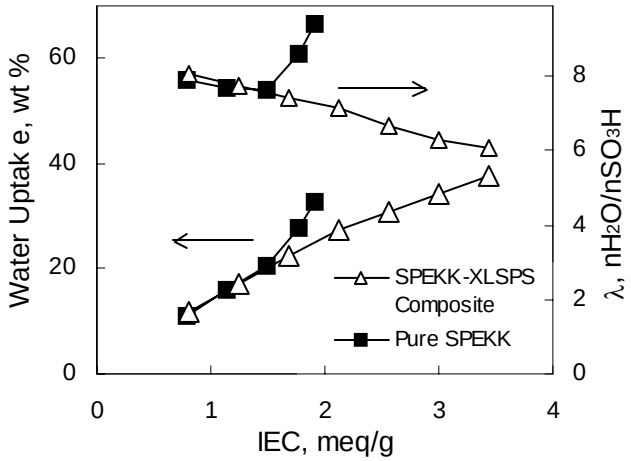

Figure 4. Comparison between the water uptake of pure SPEKK and that of the SPEKK-XLSPS composite membranes. The IEC of XLSPS was 5.2 meq/g while the SPEKK was 0.8 meq/g.

Acknowledgement. The authors gratefully acknowledge financial support from the Army through the Connecticut Global Fuel Cell Center.

References

1. Hoogers, G. *Fuel Cell Technology Handbook*. CRC Press LLC, 2003.
2. Chun, S., Shaw, M.T., Weiss, R.A., "Sulfonated Poly(ether ketone ketone) Membranes," Asilomar Conference on Proton Exchange Membranes, February (2003).
3. Swier, S., Gasa, J., Shaw, M.T., Weiss, R.A. "Proton-exchange membrane materials based on blends of of poly(ether ketone ketone) and poly(ether imide)," Annual APS March Meeting, Montreal, Quebec, Canada, March (2004).
4. Chen, N.; Hong, L. *Solid State Ionics* **2002**, *46*, 377–385.
5. Hong, L.; Chen, N. *J. of Polym. Sci.: Part B: Polym. Phys.* **2000**, *38*, 1530-1538.
6. Zawodzinski, T.A., M. Neeman, Jr., L.O. Sillerud and S. Gottesfeld, *J. Phys. Chem.*, **1991**, 95(15) 6040-6044.

PROTON-CONDUCTING COMPOSITE MEMBRANE DERIVED FROM SULFONATED POLY (ETHER ETHER KETONE) AND POLYACRYLONITRILE

Jinwen Wang, Zhongren Yue, and James Economy

Department of Materials Science and Engineering
University of Illinois at Urbana-Champaign
1304 West Green St.
Urbana, IL 61801

Introduction

Up to now perfluorinated membranes from Dupont, Dow and Asahi Chemical companies have been used exclusively as proton conductors in membrane fuel cells. They possess outstanding chemical and mechanical stability and high proton conductivity (10^{-2} S/cm) and perform excellently not only in PEMFCs but also in direct methanol fuel cells (DMFCs).

However, they have two major drawbacks: 1) high cost due to the toxic and complicated production process and 2) high methanol cross over in DMFCs reducing the fuel utilization efficiency and the cathode performance. These limitations have prompted research into alternative membranes based on partially fluorinated ionomers and hydrocarbon polymer.

A large number of arylene mainchain polymers with chemical and mechanical stabilities approaching the fluorinated polymers have been sulfonated in order to obtain proton-conducting membranes. These included polyethersulfone (PSU) and poly (ether ether ketone) (PEEK). The general problem of homogeneous sulfonated aromatic polymers is that they begin to swell too easily and thus lose their mechanical stability. This happens when the degree of sulfonation exceeds 1.4–1.6 meq SO_3H/g or the operating temperatures are in excess of 60–80°C. Therefore, it is essential to reduce the swelling of the membranes without lowering their proton conductivity[1].

In this study, composite membranes from sulfonated PEEK (sPEEK) and polyacrylonitrile (PAN) were prepared by heating under nitrogen at 380°C. Methanol permeability and the swelling in hot water of the membranes were significantly reduced by the treatment.

Experimental

Sulfonation of PEEK. PEEK Victrex® was sulfonated according to procedures described in the literature[2]. The polymer (60 g) was dissolved in 95–97% H_2SO_4 (330ml) at room temperature for 24hrs and raised to 70°C for 20mins. The reaction temperature was decreased to 60°C and the reaction mixture stirred for a further 6 hrs. The sulfonated polymer was precipitated in 5 l water, filtered off and washed in (1) 1 M HCl at 80°C and (2) H_2O at 50–60°C until a pH of 7 was attained. The polymer was dried to constant weight at 80°C.

Preparation of composite membrane. The sPEEK was converted from acid form to salt form (KPEEK) in 0.5MKCl solution for 24 hrs according to $–SO_3H$: KCl = 1: 10 (molar ratio). KPEEK and PAN were solution blended in DMF at 80-90°C to get a homogenous solution. The resulting solution was spread on a smooth glass plate and kept at 40°C for 24hrs and 150°C for 1hr to form a membrane. Hereafter the temperature was increased to 200°C and PAN in the membrane was pre-oxidized in air for 24 hrs. Finally the membrane was heated at 380°C for 1hr in the furnace under N_2. The $–SO_3H$ was recovered from $–SO_3K$ by heating the membrane in 1M HCl at 80°C and H_2O at 50–60°C for several hours.

Characterization Methods. Proton conductivities of membranes were measured in a two terminal configuration along the membranes rather than perpendicular to them[3]. Before measurement Nafion 117 was refluxed in 1M HNO_3 and the composite membrane in 1M HCl for 1hr and then both in DI water for another hour. The humidity was kept 100% using a sealed bottle in which membranes were suspended above the water surface. The ends of the membranes were connected to an HP4284A analyzer through stainless steel clamps. The frequency range was 20Hz-1MHz and the voltage amplitude 10mV. The impedance (R) with the minimum imaginary part was used to calculate the proton conductivity:

$$\text{Conductivity} = \text{length} / (\text{width} * \text{thickness} * R)$$

Methanol permeability of the membranes was determined using the diaphragm diffusion cell described in the literature[4]. Concentration of methanol in the initially pure water cell was measured versus time using 5890 Series II GC with crosslinked methyl siloxane capillary column and helium as carrier. The temperature of the injection and FID was kept at 120°C and the oven temperature at 35°C for 25mins and 100°C for 2mins.

Results and Discussion

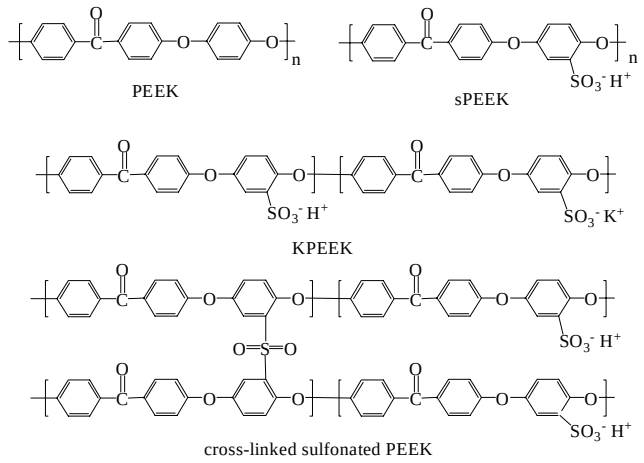

Figure 1. Repeat units of PEEK, sPEEK, KPEEK, cross-linked sulfonated PEEK

In **Figure 1** the chemical changes in PEEK in the composite membrane are described. During sulfonation the $–SO_3H$ was introduced into the diether benzene ring and most $–SO_3H$ groups were converted to $–SO_3K$ after soaked in 0.5MKCl solution. According to thermal analysis about 15% -SO_3H formed sulphone crosslink in the membrane when treated at 380°C[5]. If the temperature were below 360°C, the membrane would dissolve in hot water (60°C) showing that 360°C was the minimum temperature the crosslinking reaction could occur. The $–SO_3K$ was stable even at 400°C and provided protection for the remaining 85% -SO_3H at 380°C. The

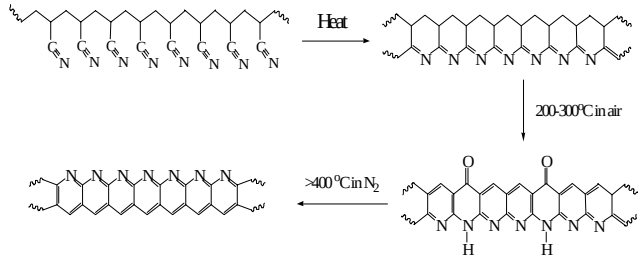

Figure 2. Heat treatment of PAN

-SO_3H groups could be easily recovered by ion exchange with 1MHCl after the thermal treatment. The other reason to choose 380°C is related to the reaction of PAN at this temperature shown in **Figure 2**[6]. By heat treatment the stable ladder structure of PAN could be obtained, in which nitrogen atoms may interact with $–SO_3H$. Some sections within the ladder chains even have structure very similar to imidazole and pyrazole that could act as a vehicle to transport proton in anhydrous membranes[7].

The incorporation of thermally treated PAN could also reduce the swelling of membranes in water. We swelled membranes completely in 80°C water and cut the wet membranes into small disks with the same diameter. After drying, the diameter increased with the increase of PAN in membranes. This could be observed clearly from **Figure 3**.

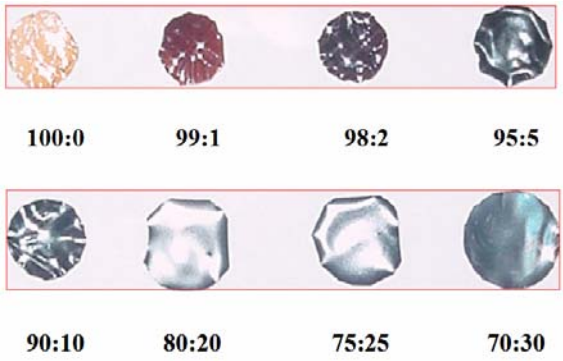

Figure 3. Changes in the diameter of composite membranes with increasing PAN after drying

In **Figure 4** proton conductivities of composite membranes first increased with the addition of PAN. This may result from the interaction between nitrogen atoms in PAN and protons in sPEEK. At 5% there was a maximum (0.52S/cm), which was similar to that of Nafion 117 (0.053S/cm). This is promising because sPEEK has 1/4 of the thickness of Nafion. As shown in **Figure 4**, above 5%, the conductivities decreased quickly. This could be due to larger PAN region in composite membranes blocking the proton transport. When PAN exceeded 10%, there was phase inversion between PAN and sPEEK, i.e., PAN became the continuous phase. Therefore, proton conductivity would be further reduced.

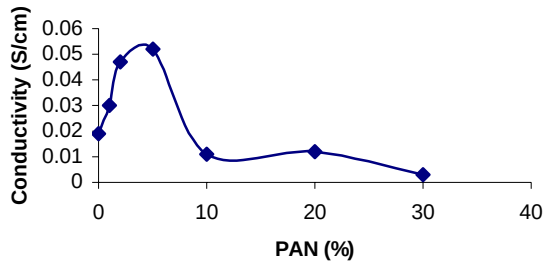

Figure 4. Proton conductivity versus PAN in composite membranes

A typical diffusion curve derived from GC is illustrated in **Figure 5**. Methanol permeability was calculated from the slope of the linear fit line in **Figure 5** based on the equation: methanol permeability = (flux / thickness) /concentration difference, where flux = (slope / cell volume)/membrane area. In **Table 1** methanol permeability of these membranes are listed and compared to Nafion 117. The sPEEK membrane without PAN displayed methanol permeability of 39% of Nafion 117. The composite membranes with thermally treated PAN resulted in lower methanol permeability because the micro-sized dispersion of rigid ladder PAN chains prevented methanol from transferring through the membrane. The membrane (95:5) had 20% methanol permeability compared to Nafion 117 while the proton conductivity was similar to Nafion 117. These properties would make it a possible low cost alternative to Nafion 117 in DMFCs.

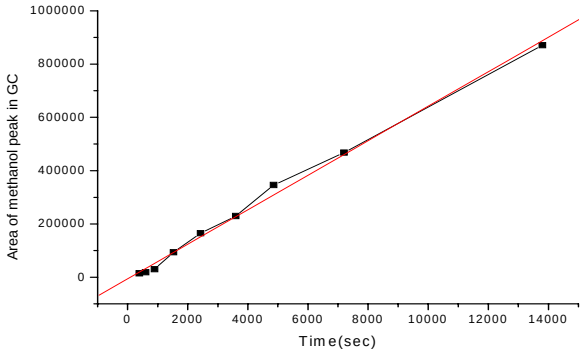

Figure 5. Typical diffusion data at room temperature: the methanol-water solution was 50vol%.

Table 1. Methanol permeability of membranes

Membranes	Thickness (cm)	Slope	Methanol permeability ($10^{-7}cm^2/s$)
Nafion	0.022	2051	27.4
100:0	0.0027	6474	10.6
95:5	0.0035	2562	5.4
80:20	0.0047	1588	4.5
70:30	0.0047	595	1.7

References

1.Kerres, J.A., *J. Membr. Sci.*, **2001**, *185*, 3-27
2.Cui, W.; Kerres, J.A.; Eigenberger. G., *Separation and Purification Technology* **1998,** *14*, 145–154
3.Fontanella, J.J.; McLin, M.G.; Wintersgill, M.C.; Calame, J.P.; Greenbaum, S.G., *Solid State Ionics*, **1993,** *66*, 1-4
4.Pivovar, B.S.; Wang, Y.; Cussler, E.L., *J .Membr. Sci.*, **1999,** *154*, 155-162
5.Yen et al., *US 5795496*, **1998**
6.Memetea, L.T.; Billingham, N.C.; Then, E.T.H., *Polymer Degradation and Stability*, **1995,** *47*, 189-201
7.Kreuer, K.D.; Fuchs, A.; Ise, M.; Spaeth, M.; Maier, J., *Electrochimica Acta*, **1998,** *43(10-11)*, 1281-1288

SYNTHESIS AND CHARACTERIZATION OF HYDROQUINONE BASED DISULFONATED POLY (ARYLENE ETHER SULFONE)S VIA DIRECT COPOLYMERIZATION

Abhishek Roy, Brian R. Einsla, William L. Harrison and James E. McGrath(jmcgrath@vt.edu)

Department of Chemistry, Virginia Polytechnic Institute and State University, Blacksburg, VA 24061

Introduction

The integral part of the fuel cell is considered to be proton exchange membrane (PEM). There has been enormous ongoing research for the development of suitable candidates for PEM fuel cells. Among the promising candidates, [1]poly(arylene ether sulfone)s are the well noted.Poly(arylene ether sulfone)s are important engineering thermoplastics possessing excellent thermal and chemical resistance. [1,2,3]Our group has reported the synthesis of sulfonated poly(arylene ether sulfone)s based on biphenol and other bisphenol systems via direct copolymerization. This paper is focused on the synthesis and characterization of hydroquinone based poly(arylene ether sulfone)s.

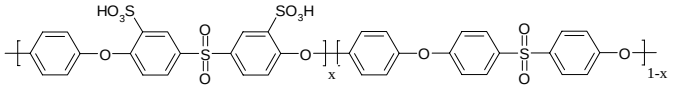

Figure 1. Structure of Hydroquinone-Based Poly(arylene ether sulfone)s (HQSH-x)

Experimental

Materials. Highly purified, commercially available, 4,4` dichlorodiphenyl sulfone (DCDPS) and hydroquinone were obtained from Solvay Advanced Polymers and Eastman Chemical Company, respectively. DCDPS was dried at 60 ^{o}C under vacuum for 12 h and hydroquinone was dried under vacuum at room temperature for 12 h. The preparation SDCDPS was previously reported. The reaction solvent n-methyl-2-pyrrolidone (NMP) was distilled from calcium hydride under vacuum before use. Potassium carbonate was obtained from Aldrich and was dried under vacuum at 120 ^{o}C for 12 h.

Polymerization. A typical direct copolymerization of DCDPS, SDCDPS and hydroquinone was conducted in a three necked round bottomed flask. The reaction was carried out in presence of nitrogen inlet, overhead stirrer, a Dean-Stark trap fitted with condenser and thermocouple sensor. For the 25% sulfonated copolymer, 3.24 g (6 mmol) of SDCDPS, 2.79 g (25 mmol) of hydroquinone, 5.47 g (19 mmol) of DCDPS and 4.037 g of potassium carbonate was charged into the flask. Distilled NMP (38 mL) was added as solvent and 20 mL of toluene was added as refluxing solvent. The Dean-Stark trap was filled with toluene and the reaction flask was heated to 150 ^{o}C and allowed to reflux for 4 h. After that the toluene was gradually removed, the reaction temperature was raised to 190 ^{o}C. The reaction was continued for about 20 h, cooled to room temperature and then the copolymer was precipitated into deionized water. The fibrous precipitate was collected by filtration and dried under vacuum for 2 days at 100 ^{o} C.

Membrane Preparation. The dried copolymer was dissolved in 10 weight % solution of DMAC and casted onto clean glass plates. The films were dried under a infrared lamp in a nitrogen atmosphere. The film formed was removed from the plate by submersion in deionized water. The membranes were treated with 0.5 M boiling sulfuric acid to convert the sulfonate salt of the copolymer to proton conductive acid form.[3]To remove the residual sulfuric acid, the membrane was extracted with boiling water for 2 h and then dried under vacuum at 100 ^{o}C for 16 h.

Characterization. The Proton NMR spectrum of the copolymers was obtained using a Varian 400 MHz instrument in deuterated dimethylsulfoxide. ATR-FTIR analysis was done in DuraSamplR instrument. Intrinsic viscosity measurements were measured in NMP at 25 ^{o}C using a Cannon Ubbelohde viscometer. To determine the water uptake of the membranes, the dry weights of the membranes was taken and then the membranes were immersed in deionized water for 48 h at room temperature. The wet membranes were blotted dry and weighed immediately. The ratio of the weight gain to initial weight was taken as the water uptake. Thermogravimetric analysis was conducted in air at a heating rate of 10 ^{o}C per min using a TA instrument. DSC measurements were performed on a TA instrument in presence of nitrogen at a heating rate of 10 ^{o}C per min. Proton conductivity of the acid form membranes was determined using a Solatron 1260 Impedence /Gain-Phase Analyzer.

Results and Discussion

Hydroquinone based disulfonated poly(arylene ether sulfone)s copolymers were successfully synthesized by nucleophilic aromatic substitution. A series of copolymers (Table I) were prepared with varying degrees of disulfonation (SDCDPS content) and were characterized by ^{1}H NMR, intrinsic viscosity (IV), thermogravimetry (TGA), differential scanning calorimetry (DSC),IR ,water uptake and proton conductivity measurements.

Table 1. Properties of Disulfonated Poly(arylene ether sulfone) Copolymers

Copolymer	Yield (%)	% DS by ^{1}H NMR	IV (dL/g)	IEC	Water Uptake(%)	σ (S/cm)
20	94	19.5	0.75	1.12	19	-
25	97	23.4	1.12	1.37	35	0.05
30	93	30.3	1.60	1.61	46	0.06
35	95	33.2	1.50	1.84	68	0.07

The high IV values suggest formation of high molecular weight disulfonated copolymers. From the water uptake values, it is apparent that water uptake increases with increased degree of sulfonation. Also it was noted that there was a huge jump in water uptake from the 30% disulfonation level to the 35% sulfonation level, which may be associated with a change in morphology (i.e., percolation threshold).[1-3]As apparent from the conductivity data, the conductivity increases with increase in percent sulfonation and water uptake. The structure of copolymers was confirmed by ^{1}H NMR as shown in the Figure 2. The degree of disulfonation was calculated from ^{1}H NMR spectra, and agreed with the theoretical values. ATR-FTIR analysis (Figure 3) confirmed the successful incorporation of sulfonate groups. The strong characteristic peaks at 1030 cm^{-1} and 1098 cm^{-1} were assigned to symmetric and asymmetric stretching of the sulfonate group.

Thermogravimetric analysis (Figures 4 and 5) showed the increased thermo-oxidative stability of the salt form copolymers compared to their sulfonic acid form. Also, it can be concluded that the thermo-oxidative stability of the polymer decreases with increased sulfonation level. The initial drop in weight around 300 ^{o}C is attributed to the loss in sulfonic groups. DSC measurements (Figure 6) conducted on acid form membrane (25% sulfonation) showed a high dry glass transition temperature (~240 ^{o}C).

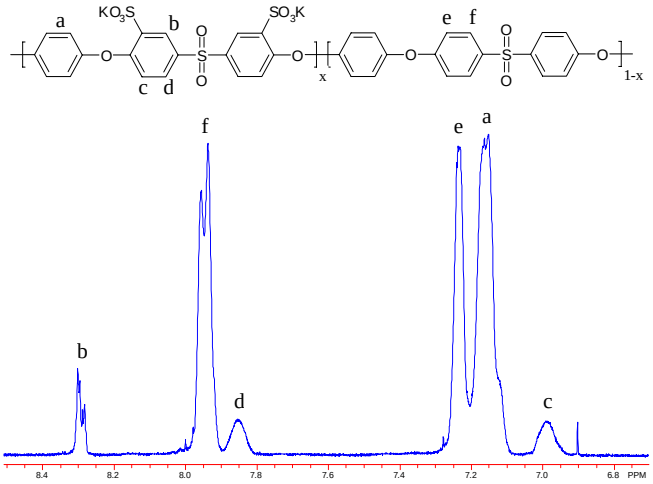

Figure 2. ^{1}H NMR of HQS25 copolymer.

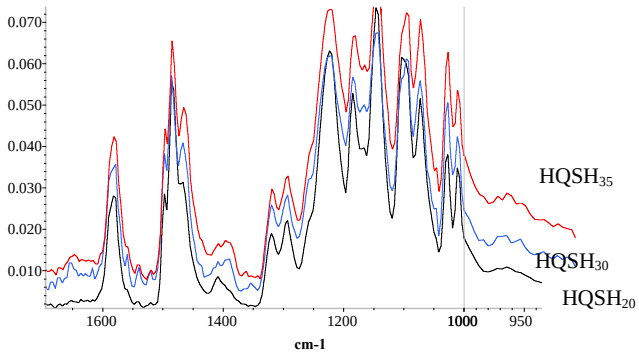

Figure 3. ATR of $HQSH_{xx}$ copolymers.

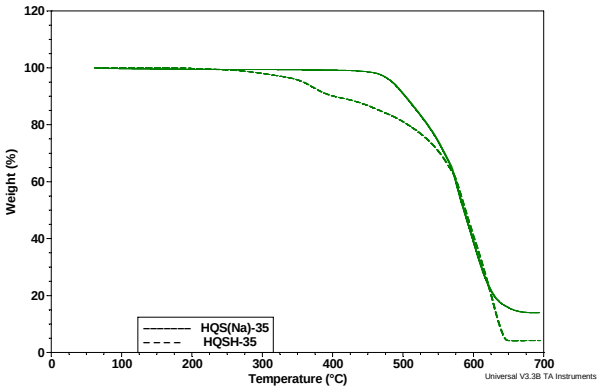

Figure 4. TGA of HQS-35 salt form (⁻⁻) and HQSH-35 acid form (--)

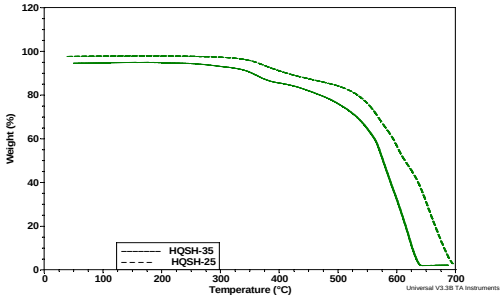

Figure 5. Influence of copolymer composition on thermo-oxidative stability (acid form membranes).

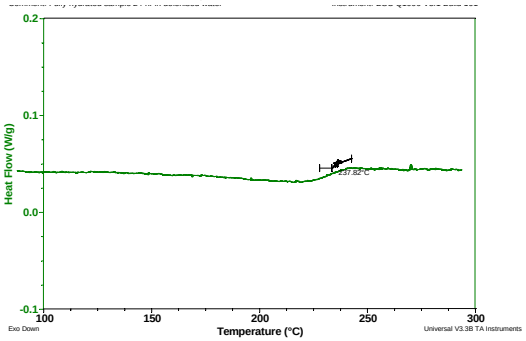

Figure 6. DSC of the acid form HQSH-25 membrane (2nd heat).

Conclusions

Hydroquinone bases sulfonated poly(arylene ether sulfone) copolymers were successfully synthesized and characterized. The structure was confirmed by ^{1}H NMR analysis. Water uptake values demonstrate an increase in water uptake with increased degree of disulfonation, as expected. The proton conductivity value was found to increase with increase in degree in sulfonation. From the TGA, it can be concluded that the salt form membranes are more stable than their corresponding acid form. The high glass transition of the membrane may be for high temperature fuel cell applications.

Acknowledgement. The authors would like to thank the National Science Foundation "Partnership for Innovation" Program (HER-0090556) and the Department of Energy (DE-FC36-01G01086) for support of this research effort.

References

1. W. L.Harrson, F. Wang, J.B. Mecham, V. A. Bhanu, M. Hill,Y. S. Kim, J. E. Mcgrath.; Influence of the Bisphenol Structure on the Direct Synthesis
of Sulfonated Poly(arylene ether) Copolymers; Journal of Polymer Science: Part A: Polymer Chemistry, Vol. 41, 2264–2276 (2003)
2. F. Wang, M. Hickner, Y.S. Kim, T. Zawodzinski and J.E. McGrath, "Synthesis and Characterization of Sulfonated Poly(arylene ether sulfone) Random (Statistical) Copolymers Via Direct Polymerization: Candidates for New Proton Exchange Membranes," *Journal of Membrane Science*, 197 (2002), 231-242
3. ; Y. S. Kim ,F. Wang, M. Hickner, S.Mccartney, Y. Taik Hong,W. Harrison, T. A. Zawodinski, J.E Mcgrath; Effect of Acidification Treatment and Morphological Stability of Sulfonated Poly(arylene ether sulfone)
Copolymer Proton-Exchange Membranes for Fuel-Cell Use above 100 °C Journal of Polymer Science: Part B: Polymer Physics, Vol. 41, 2816–2828 (2003)

SYNTHESIS AND CHARACTERIZATION OF HYDROXY-FUNCTIONALIZED POLY(ARYLENE ETHER SULFONE)S AND CONVERSION TO PROTON CONDUCTING MEMBRANES FOR FUEL CELLS

Brian R. Einsla and James E. McGrath

Institute for Polymeric Materials and Interfaces, Virginia Polytechnic Institute and State University, Blacksburg, Virginia 24061
jmcgrath@vt.edu

Introduction

Recently, there has been considerable interest in the development of high performance and potentially lower cost proton exchange membrane (PEM) fuel cells for transportation, stationary and portable power applications.[1,2] The interest in fuel cells is largely due to their ability to continuously convert chemical energy into electric energy and heat with high efficiency and low emission of pollutants.[3] In PEM fuel cells, the membrane must transport protons from the anode to the cathode, and act as a barrier to oxygen and the hydrogen-rich fuel. At the anode, hydrogen is oxidized to protons and electrons by platinum or platinum/metal catalysts. The resulting protons are transported across the electrolyte to the cathode. Useful electrical energy is harnessed by moving the electrons through an external circuit before allowing them to reach the cathode. At the cathode, gaseous oxygen from the air is reduced and combined with the protons and electrons to form water.[4]

Promising PEM fuel cell systems include high temperature hydrogen/air and direct methanol fuel cells (DMFC). In hydrogen/air-based fuel cells, high temperature (>120 ^{o}C) provides benefits such as faster electrode kinetics and greater tolerance to impurities in the fuel stream.[5] To operate at these high temperatures, new and improved mechanisms for conductivity above the boiling point of water are needed.[6] DMFC's offer reasonably high fuel energy density, readily stored liquid fuel, ease of refueling, and direct and complete electro-oxidation of methanol at moderate temperatures.[7] Nafion® perfluorosulfonic acid copolymers are the state-of-the-art membranes for DMFC and hydrogen/air fuel cells due to their high conductivity when hydrated and chemical stability. However, there is much interest in alternative PEM's because of Nafion's reduced performance above 80 ^{o}C, significant methanol crossover and cost.[8,9,10]

One method to achieve proton conductivity in PEM's is to incorporate sulfonic acid sites along the polymer chain. As an example, sulfonated poly(arylene ether sulfone)s (PAES) can be synthesized via post-sulfonation of the parent polymer, or direct copolymerization of sulfonated monomers. The properties of the resulting copolymer membrane depend on the preparation method as well as the processing steps.[11,12,13] Direct copolymerization of sulfonic acid-containing monomers allows for improved control of the ion-exchange capacity (IEC), and therefore control over the proton conductivity, water sorption, and morphology of the membrane.

It is well known in the area of nonlinear optics (NLO) that polyimides with NLO chromophore side chains can be incorporated into the polymer chain by direct copolymerization or post-derivatization. A common synthetic route for nonlinear optical polyimides is the condensation polymerization of dianhydrides with diamines containing an NLO chromophore via a poly(amic acid) prepolymer.[14] This method, however, often involves a tedious synthesis of the chromophore-containing diamine monomers. Sometimes, the fact that few chromophores can survive the relatively harsh chemical conditions of the monomer synthesis limits the kind of chromophores that are incorporated in the polyimide backbone.[15] To avoid the synthesis of chromophore-containing diamine compounds, an alternate synthetic route was devoped by Chen *et al.*[9,16] A one-pot preparation of a preimidized, hydroxy-containing polyimide was developed, followed by the covalent attachment of a chromophore to the backbone of the polyimide.

This post-derivatization method may also have an application in the synthesis of proton exchange membranes for fuel cells. Instead of bonding the NLO chromophore to the polymer backbone, ion-conducting sites could be introduced. Unfortunately, the hydrolytic stablility of sulfonated polyimides under fuel cell conditions is unsatisfactory. On the other hand, sulfonated poly(arylene ether sulfone)s have attracted much attention as suitable membranes for PEM fuel cells. Herein, we report the synbthesis of hydroxyl-functionalized PAES and derivatization to sulfonated copolymers.

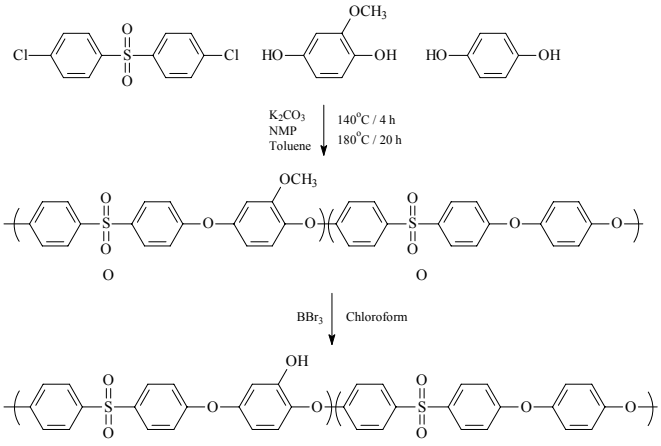

Figure 1. Copolymerization of Methoxy-PAES and Conversion of Methoxy Groups to Hydroxyl.

Experimental

Materials. 4,4'-Dichlorodiphenylsulfone (DCDPS, Solvay Advanced Polymers) was used as received. Hydroquinone, methoxyhydroquinone, potassium carbonate, toluene, boron tribromide, and chloroform were used as received from Aldrich. N-methylpyrolidone (Aldrich) was distilled from calcium hydride under vacuum before use.

Methoxy-Poly(arylene ether sulfone) Copolymerization. A typical copolymerization of a methoxy-PAES with 50 mol % methoxy groups is discussed (MHQS-50). DCDPS (4.000 g, 14 mmol), hydroquinone (0.7669 g, 7 mmol), and methoxyhydroquinone (0.9760 g, 7 mmol) were introduced to a 250-mL, three neck flask equipped with a mechanical stirrer, Dean-Stark trap, condenser, and a nitrogen inlet/outlet. Potassium carbonate (2.22 g, 16 mmol) and 29 mL of NMP were added to the reaction flask to afford a 20% (w/v) solid concentration. Toluene (15 mL) was added to the flask as an azeotroping agent. The Dean-Stark trap was filled with toluene and the reaction mixture was heated to 140 ^{o}C to dehydrate the system. After 4 h at 140 ^{o}C, the Dean-Stark trap was emptied and the oil bath temperature was heated to 180 ^{o}C for 20 h. The resulting viscous solution was cooled to room temperature and precipitated into an excess of deionized water. The precipitated copolymer was collected by filtration and purified in a Soxhlet extractor with deionized water for 2 days. The resulting white, fibrous copolymer (MHQS-50) was dried under vacuum at 110 ^{o}C for at least 24 h.

Conversion of Methoxy to Hydroxyl Groups. A typical reaction for converting MHQS-30 to HOHQS-30 is given. MHQS-30 (1.000 g) was dissolved into 20 mL of chloroform in a 100-mL, three neck flask equipped with a stirbar and nitrogen purge. BBr_3 (0.5 mL in 10 mL chloroform) was added dropwise to the reaction via a syringe. The reaction mixture was allowed to stir overnight at room temperature. The copolymer was isolated by filtration, washed with methanol (2x) and deionized water (2x), and finally dried under vacuum at 120 ^oC.

Preparation of Sulfonated Poly(arylene ether sulfone) Copolymer. HOHQS-30 (1.0000 g) and 4-nitrophenylsulfonic acid sodium salt (0.6100 g) were introduced to a 100-mL, three neck flask equipped with a mechanical stirrer, Dean-Stark trap, condenser, and a nitrogen inlet/outlet. Potassium carbonate (0.48 g) and 10 mL were added to the reaction flask to afford a 15% (w/v) solid concentration. The reaction mixture was heated to 80 ^oC 72 h. The resulting viscous solution was cooled to room temperature and precipitated into an excess of deionized water. The precipitated copolymer was collected by filtration and purified in a Soxhlet extractor with deionized water for 2 days. The resulting white, fibrous copolymer (MHQS-30) was dried under vacuum at 110 ^oC for at least 24 h.

Characterization. ^1H NMR spectra were recorded on a Varian Unity 400 instrument operating at 399.952 MHz in deuterated dimethylsulfoxide (DMSO-d_6). Intrinsic viscosity (IV) measurements were conducted in NMP at 25 ^oC using a Cannon Ubbelohde viscometer.

Results and Discussion

PAES's with pendant methoxy groups were synthesized by nucleophilic substitution reactions (Figure 1). The high molecular weight copolymers were characterized by intrinsic viscosity (Table 1) and ^1H NMR (Figure 2). The incorporation of the methoxyhydroquinone was found to be quantitative through integration of the peak at 3.6 ppm with respect to one in the aromatic region (7.9 ppm) (Table 1). All of the MHQS-XX copolymers were soluble in chloroform; therefore the conversion of the methoxy groups to hydroxyl groups using BBr_3 was conducted in chloroform. Due to the polar nature of the hydroxyl groups, the subsequent HOHQS-XX copolymers were not soluble in chloroform allowing for straightforward isolation. The intrinsic viscosity of the HOHQS-XX copolymers was higher than the MHQS-XX copolymers in all cases. Perhaps this effect is due to hydrogen bonding of the hydroxyl groups. The quantitative conversion of methoxy groups to hydroxyl groups was determined by ^1H NMR. The complete disappearance of the protons of the methoxy group (3.6 ppm) and appearance of a peak at ~10 ppm (due to –OH) was observed for all three copolymers. Additionally, an increase in the glass transition temperature of the HOHQS-XX copolymers with respect to the MHQS-XX copolymers can be attributed to hydrogen bonding which decreases chain mobility (Table 1).

As an example, HOHQS-30 was reacted under nucleophilic conditions with 4-nitrobenzenesulfonic acid sodium salt (NBS) to prepare a 30% sulfonated copolymer. The derivatization reaction was heated to 80 ^oC to reduce the ether-ether interchange that could possibly lower the molecular weight of the copolymer. The resulting high molecular weight sulfonated copolymer formed a tough, ductile membrane when solution cast from N,N-dimethylacetamide. The ^1H NMR of the sulfonated copolymer is shown in Figure 4. The incorporation of the NBS was shown by the ^1H NMR peaks at 7.85 ppm and 8.4 ppm.

Table 1. Copolymer Properties

Copolymer	I.V. (dL/g)*	^1H NMR		T_g (^oC)**
		%-OCH_3	%-OH	
MHQS-30	0.83	31.4	-	195
MHQS-40	0.84	39.5	-	195
MHQS-50	0.81	52.3	-	-
HOHQS-30	1.09	-	29.2	211
HOHQS-40	1.02	-	40.8	216
HOHQS-50	1.30	-	52.2	-

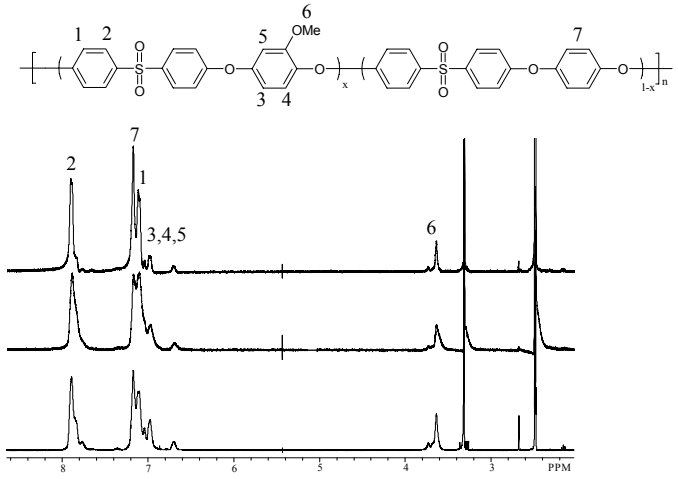

Figure 2. ^1H NMR of MHQS-XX Copolymers in DMSO-d_6

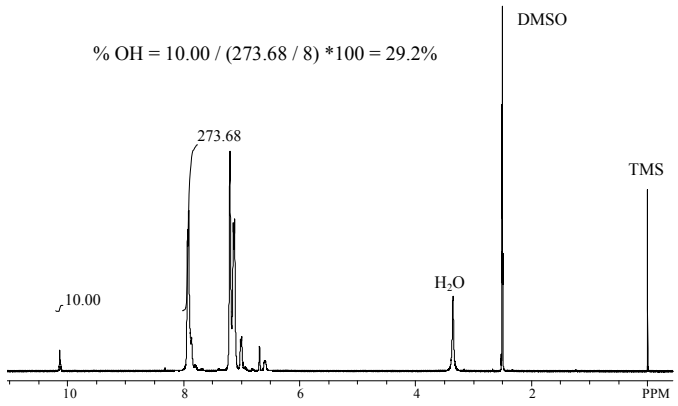

Figure 3. ^1H NMR of HOHQS-30 to Determine the % Hydroxyl Groups

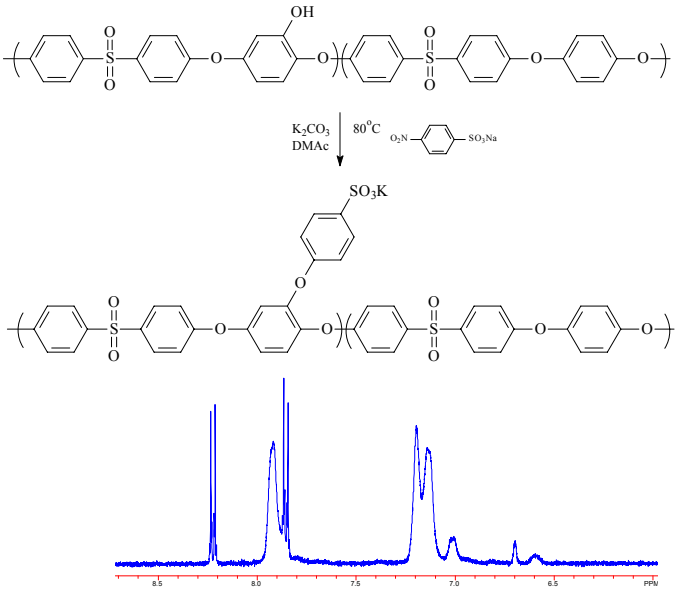

Figure 4. Preparation and [1]NMR of Sulfonated PAES.

Conclusions

A series of high molecular weight PAES's were synthesized with pendant methoxy groups which were completely converted to reactive hydroxyl groups. The hydroxyl functionalized copolymers showed higher intrinsic viscosities and T_g's due to hydrogen bonding. A 30% sulfonated copolymer was prepared by post-derivatization of the 30% hydroxyl copolymer, and this sulfonated copolymer formed a tough, ductile film after solution casting. Further work is ongoing to study the properties of these sulfonated copolymers for use as PEM fuel cells and this will be discussed at the meeting.

Acknowledgements. The authors would like to thank the Department of Energy (DE-FC36-01G01086) for support of this research effort.

References

[1] G.J.K. Acres, Recent Advances in Fuel Cell Technology and its Applications, J. Power Sources 100 (2001) 60-66.
[2] B.C.H. Steele, A. Heinzel, Materials for Fuel-Cell Technologies, Nature 414 (2001) 345-352.
[3] L. Carrette, K.A. Friedrch, U. Stimming, Fuel Cells: Principles, Types, Fuels, and Applications, Chem. Phys. Chem. 1 (2000) 162-193.
[4] M. Jacoby, Fuel Cells Heading For Sale, C&E News, June 14, 1999, 31.
[5] G. Alberti, M. Casciola, L. Massinelli, B. Bauer. J. Membrane Sci 185 (2001) 73-81.
[6] S. Thomas, M. Zalbowitz, Fuel Cells: Green Power, Los Alamos National Laboratory, Los Alamos, NM.
[7] A.S. Arico, S. Srinivasan, V. Antonucci. Fuel Cells 1 (2001) 133-161.
[8] F. Wang, M. Hickner, Q. Ji, W. Harrison, J. Mecham, T.A. Zawodzinski, J.E. McGrath. Macromol. Symp. 175 (2001) 387-395.
[9] F. Wang, M. Hickner, Y.S. Kim, T.A. Zawodzinski, J.E. McGrath. J. Membrane Sci. 197 (2002) 231-242.
[10] W.L. Harrison, F. Wang, J. Mecham, V.A. Bhanu, M. Hill, Y.S. Kim, J.E. McGrath. J. Polym. Sci.: Part A: Polym. Chem. 41 (2003) 2264-2276.
[11] F. Lufrano, I. Gatto, P. Staiti, V. Antonucci, E. Passalacqua. Solid State Ionics, 145 (2001) 47-51.
[12] W.L. Harrison, K. O'Connor, N. Arnett, J.E. McGrath. Polym. Prepr. (Am. Chem. Soc. Div. Polym. Chem.) 43 (2002) 1159.
[13] Y.S. Kim, L. Dong, M.A. Hickner, B.S. Pivovar, J.E. McGrath. Polymer 44 (2003) 5729-5736.
[14] S. Yang, Z. Peng, L. Yu. Macromolecules 27 (1994) 5858-5862.
[15] T.-A. Chen, A.K.-Y. Jen, Y. Cai. J. Am. Chem. Soc. 117 (1995) 7295-7299.
[16] T.-A. Chen, A.K.-Y. Jen, Y. Cai. Macromolecules 29 (1996) 535-539.

PROMISING COMPONENTS FOR HIGH-TEMPERATURE PEM FUEL CELLS: THERMALLY STABLE AND HIGHLY PROTON CONDUCTING HETEROPOLY ACIDS

Fanqin Meng,[1,3] Jennifer L. Malers,[1,3] James Horan,[2] Steven F. Dec,[2] Andrew M. Herring,[1] John A. Turner.[3]

Department of Chemical Engineering[1] and Chemistry and Geochemistry[2]
Colorado School of Mines
Golden, CO 80401-1887

Hydrogen and Electricity, Systems and Infrastructure Group[3]
National Renewable Energy Laboratory
Golden, CO 80401-3393

Introduction

Heteropoly acids (HPAs) have attracted attention of PEM fuel cell community because of their exceptionally high proton conductivities, for example, 0.2 S cm^{-1} for 12-phopshotungstic acid at room temperature.[1,2] Studies conducted in our laboratory as well as by other researchers have revealed the high thermal stabilities of these materials. Moreover, we have found that proton diffusion coefficients of various HPAs increase with temperature till 100 °C or higher. These discoveries are especially encouraging for the use of HPAs in PEM fuel cells operating at desirable elevated temperatures (120 – 200 °C). Besides the many well-know advantages in terms of economy, high temperature operation actually minimizes, if not eliminates, the conventional obstacle to implementing solid acids in fuel cells: at temperatures above 100 °C, H_2O is in the form of steam and is thus harmless to the otherwise water-soluble electrolyte.

The family of HPAs adopts a wide variety of compositions and structures. The central heteroatom has been located in a large area of the periodic table, from transitional metals to main group elements. Diverse molecular structures have been discovered, including the most common Keggin and Dawson types, their lacunary structures, and derivatives by various condensation of the lacunary moieties. However, only the four commercially available Keggin-type HPAs, 12-phosphotungstic, 12-phosphomolybdic, 12-sillicotungstic, and 12-sillicomolybdic acids have been studied to any great extent and the study of proton conduction in these materials has been limited. There is, therefore, a need to correlate proton conducting properties of the HPAs with the vast number of structures and hydration states available in order to choose or design the best materials for fuel cell applications. To this end, our group has been using TGA, DRIFTS, MAS and PFGSE NMR techniques to investigate a variety of HPAs with respect to their thermal stability, hydrogen bonding, proton acidity and proton diffusion coefficients.

Experimental

The Keggin-type HPAs, 12-phosphotungstic acid, $H_3PW_{12}O_{40}$ (12-HPW) and 12-sillicotungstic acid, $H_4SiW_{12}O_{40}$ (12-HSiW), were purchased from Aldrich and used as received. All other HPAs, such as 18-diphosphotungstic acid, $H_6P_2W_{18}O_{62}$(18-HP2W), and 21-diarsenotungstic acid, $H_6As_2W_{21}O_{69}$(21-HAs2W) etc, were prepared by literature methods.[3-6]

All TGA data were taken on samples that had been heated in an oven at *ca.* 120°C for several days. The temperature was run from ambient to 600 °C (heating rate 5 °C/min) under helium flow of 162 mL/min.

All MAS ^1H spectra were recorded on a two-channel Chemagnetics CMX Infinity 400 NMR spectrometer operating at 400.0 MHz, using a Chemagnetics 5mm double-resonance MAS probe equipped with a Pencil spinning module, sample spinning at 10 kHz. Proton diffusion measurements were obtained with the use of a 5mm Doty Scientific, Inc. #20-40 z-gradient pulsed-field gradient NMR probe. The stimulated-echo pulse sequence[7] was used and The gradient coil was calibrated using water at 25 °C. The resulting NMR spectra were integrated and fit to a two-Gaussian decay using Spinsight® software available from Varian, Inc.

DRIFTS samples were heated *in situ* (ambient temperature to 350 °C) under constant helium flow, the spectra were recorded on a Thermo Nicolet Nexus 670 FT-IR spectrometer using the Omnic®6.0 software package and with a specially designed Harrick Praying Mantis diffuse reflection attatchment (DRA).

Results and Discussion

TGA measurements indicate the HPAs in interest maintain a considerable amount of water and proton up to >400 °C. The remarkable observation here is the high temperatures to which some of the HPAs retain water in their secondary structure. Should water presence be required for high temperature proton conduction a great many of these materials would be suitable candidates. Temperature-dependent DRIFTS spectra are consistent with TGA results. Figure 1 shows that the heteropoly anions keep intact above 300 °C, and more importantly, water molecules are present in the structure at temperatures appreciably higher than 100 °C.

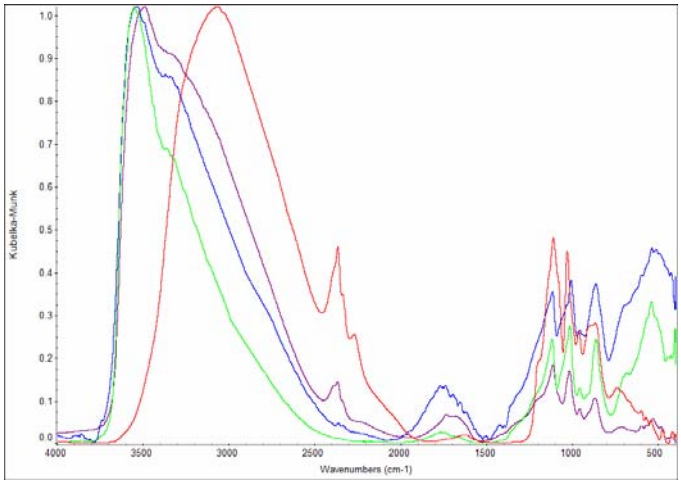

Figure 1. DRIFTS spectra of 18-HP2W at 50(blue), 100(green) 200(purple), and 300(red) °C.

MAS ^1H chemical shifts of HPAs are in the range of 8-11, compounds with main group elements in the center consistently showing lower values than those with transition metal elements as the heteroatom. Diffusion coefficients of the HPAs are mostly in the order of 10^{-6} cm^2/sec, much higher than those of other types of proton conducting solids. As shown in Figure 2, all the HPAs in this work showed increasing proton mobility with temperature until a maximum was reached. Interestingly, while the maxima for most of the materials are at approximately 100 °C, the proton diffusion coefficients for 12-HZnW kept rising till 140 °C, and 21-HAs2W repeatedly showed a second peak around 150 °C although at a lower value.

Conclusions

Highly proton conducting HPAs are promising components for PEM fuel cells operating at elevated temperatures. Certain compositions and structures seem to exhibit higher proton acidity and favor proton diffusion.

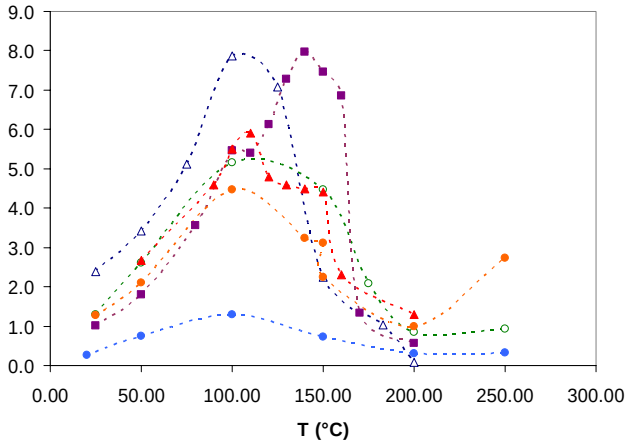

Figure 2. Diffusion coefficients as a function of temperature, 21-HB3W (navy), 11-HSiW (green), 18-HP2W (blue), 21-HP2W (orange), 12-HZnW (purple), and 21-HAs2W (red).

Acknowledgement. This work was supported by the US DOE science initiative, DE-FC02-0CH11088.

References

(1) Nakamura, O.; Kodama, T.; Ogino, I.; Miyake, Y. *Chemistry Letters* **1979**, *1*, 17.
(2) Pope, M. T.; Müller, A., Eds. *Polyoxometalate Chemistry: From Topology Via Self-Assembly to Applications*; Kluwer Academic Publishers: Dordrecht, **2001**.
(3) Brown, D. H., Mair, J. A., *J. Chem. Soc.* **1958**, 2597-9.
(4) Tourné, C. M., Tourné, G. F., Malik, S. A., Weakley, T. J. R., *J. Inorg. Nucl. Chem.* **1970,** *32*, 3875-90.
(5) Tézé, A., Michelon, M., Herve, G., *Inorg. Chem.* **1997,** *36*, 505-9.
(6) Jeannin, Y., Martin-Frere, J., *Inorg. Synth.* **1990**, *27*, 111-2.
(7) Tanner, J. E. *The Journal of Chemical Physics* **1970**, *52*, 2523.

Synthesis of proton conducting tungstosilicate mesoporous materials (WMM) and organic/WMM composite membranes for high temperature PEM fuel cells

Fangxia Feng, Decio Coutinho, Zhiwei Yang, John P. Ferraris and Kenneth Balkus Jr.

Department of Chemistry and
The UTD NanoTech Institute
The University of Texas at Dallas
P O Box 830688 MS BE26
Richardson, TX 75083-0688

Introduction

Proton-conducting solid materials have grown in interest due to their potential applications in electrochemical devices, such as batteries, chemical sensors, fuel cells, and supercapacitors. Heteropolyacids (HPAs) are one of the more promising inorganic based ionic conductors (1,2). The direct application of HPAs as solid proton conductor is somewhat limited by highly solubility in water and alcohols (1,3). This is further complicated by the fact that the proton conductivity is significantly influenced by the relative humidity. In order to overcome these limitations, there have been attempts to disperse HPAs in polymers as inorganic/organic composite membranes for high temperature fuel cells (1,3). However, high proton conductivity normally required high relative humidity (mostly 100%). Additionally, the HPAs are mobile and could partially diffuse out of the membrane.

An alterative strategy for immobilizing HPAs is to construct nanoporous frameworks based on the HPA composition. Mesoporous molecular sieves have several promising properties, such as uniform pore size (in the range of 20 – 500 Å), high specific surface area (≥ 1000 m^2/g), large dimension open channels, and relative high thermal stability.

In this paper, we report the synthesis of tungsten-containing mesoporous materials (WMM) and an evaluation of their proton conductivity. The surfactants employed in the study include the ionic template CTMABr, and the non-ionic Brij surfactants, $C_{12}E_{10}OH$, $C_{16}E_{10}OH$, and $C_{18}E_{10}OH$. The effect of different acids including HCl, H_3PO_4, and CF_3SO_3H was also studied. Additionally, the influence of the surfactant type on the synthesis and the proton conductivity of WMM product was investigated. A free-standing film grown from the $C_{12}E_{10}OH$ - H_3PO_4 system was prepared but too brittle to employ a membrane-electrode-assembly (MEA) for fuel cell test. Therefore, a WMM/PEI-Glymo-HTFSI composite membrane was prepared and evaluated.

Experimental

Materials. Cetyltrimethylammonium bromide (CTMABr, Aldrich), hydrochloric acid (37 wt.%, Mallinckrodt), phosphoric acid (H_3PO_4, 85%, EM), triflormethanesulfonic acid (CF_3SO_3H, 98%, Aldrich), sodium tungstate dihydrate ($Na_2WO_4 \cdot 2\ H_2O$, 99%, Aldrich), tetraethyl orthosilicate (TEOS, 99%, Aldrich), polyoxyethylene 10 lauryl ether (Brij 56, $C_{12}EO_{10}OH$, Sigma-Aldrich), polyoxyethylene 10 cetyl ether (Brij 56, $C_{16}EO_{10}OH$, Sigma-Aldrich), polyoxyethylene 10 stearyl ether (Brij 76, $C_{18}EO_{10}OH$, Sigma-Aldrich), tungstosilicic acid hydrate ($H_4SiW_{12}O_{40} \cdot$ aq, Fluka), poly(2-ethyl-2-oxazoline) (average Mw = 500,000, Aldrich), 3-glycidy—oxypropylmethoxysilane (GLYMO, 97%, Fluka), trifluoromethanesulfonimide (3M company), methanol (98%, Aldrich), Pt black (fuel cell grade, E-TEK), and carbon layer (ELAT®, E-TEK Div. of De Nora N.A., Inc) were used as received.

Synthesis of mesoporous tungstosilicates. The syntheses of tungsten-containing mesoporous materials (WMM) were based on a modification of the method reported by Piquemal et al. (5). The molar composition of the final reaction mixture was SiO_2 : 0.2 T : A : (0 ~ 30) WO_3 : 150 H_2O, in which T = CTMABr, $C_{12}EO_{10}OH$, $C_{16}EO_{10}OH$, and $C_{18}EO_{10}OH$, respectively; A = HCl, H_3PO_4, and CF_3SO_3H, respectively. A typical procedure involved combining 2.19 g of CTMABr in 81 ml of deionized water, with 2.4 ml of concentrated HCl. To this clear solution, 0.25 g of $Na_2WO_4 \cdot 2\ H_2O$ and 6.69 ml of TEOS were added. A light yellow gel was formed and was stirred vigorously at room temperature for 1 ~ 6 days. At elevated temperature, the dense WO_3 was easily formed as an impurity. The resulting product was filtered, washed with deionized water, and then dried at 50°C overnight. Some samples were calcined in air at 500°C for 2 days to remove the surfactant. For the samples obtained in the CTMABr - H_3PO_4 system, the template was removed by ethanol extraction under reflux for 44 hours (0.1 g of as-synthesized material per 100 ml of ethanol).

Preparation of composite membrane. Linear polyethyleneimine (PEI) was prepared by a published procedure (6). Trifluoromethanesulfonimide (HTFSI) was also prepared according to a reported procedure (7).

A typical preparation of a composite membrane was conducted as follows: 0.087 g of linear PEI was dissolved into 0.5 g of methanol, followed by mixing with a mixture of desired amount of as-synthesized (or calcined) tungstosilicate (FF40) dispersed in 0.5 g of methanol. To the above mixture, 0.093 g of Glymo was added and stirred 30 mins. Then, 1.145 g of 50 wt.% HTFSI in methanol was added and stirred until a viscous gel was formed. The gel was casted on Teflon and dried for 12 hours at room temperature and then annealed at 50°C for 12 hours.

Fabrication of Membrane-Electrode-Assembly (MEA). Before the fabrication of MEA, the thickness of the membrane was measured using Mitutoyo IP 54 digimatic micrometer. 20-25 mg of Pt black (fuel cell grade, E-TEK) was dispersed into ~3 mL of hexanes by sonication. Then the Pt was symmetrically deposited on both sides of the membrane with a loading of ~5 mg/cm^2, followed by hot-pressing at ~ 85 ^oC and ~300 psig for 2 mins.

Characterization. X-ray powder diffraction (XRD) patterns were collected using a Scintag XDS 2000 X-ray diffractometer, using CuK_α radiation. Scanning electron microscopy (SEM) images were recorded on a LEO 153VP electron microscope from samples coated with Au/Pd.

The conductivity measurements were made following a published procedure (8). Measured amounts of the dry solid powder and water were mixed completely. The water was added until a maximum conductivity was observed. The water content was calculated by the percentage of the water to the total of the water and the dry solid powder. The resulting wet mixture was placed into a glass tube with the surface area of 1 cm^2, which was clamped between two stainless-steel pistons as the electrodes.

For the proton conductivity measurement of the composite membrane, the MEA was sandwiched between two pieces of gas-diffusion carbon layers and placed into a 5 cm^2 single cell (Fuel Cell Technologies Inc.). A fuel cell testing station (Fuel Cell Technologies Inc.) was used to control the single cell's temperature and humidity. The relative humidity of the cell was calculated from humidifier temperature against the cell temperature. The humidifier temperature was kept at 22°C. The cell temperature was varied. The relative humidity varied in the range of 35 to 95%.

The AC impedance measurements were carried out using a PC controlled frequency response analyzer--VoltaLab® PGZ301 (Radiometer Analytical S.A.) over the frequency range of 100 KHz to 1 Hz, using a 10 mV amplitude AC single throughout the experiments.

Results and Discussion

CTMABr template. Using CTMABr as a template, the product obtained with H_3PO_4 was not stable after calcination at 500°C. The dense WO_3 impurity was detected in the calcined products prepared with HCl and CF_3SO_3H, respectively. The proton conductivities for these samples are given in Table 1. The proton conductivity increased with an increase in water content and finally reached a maximum value of 10^{-2} S/cm. The as-synthesized product showed a higher proton conductivity than the calcined product, which could be attributed to acid trapped in the micelles. The order of the conductivity for as-synthesized products in acid was CF_3SO_3H > H_3PO_4 > HCl.

Table 1. Proton conductivity of WMM using CTMABr.

Acid	Water content (%)		Conductivity (x10^{-2} S/cm)	
	as-made	calcined	as-made	calcined
HCl	50.4	58.4	1.00	0.50
H_3PO_4	33.8	-	1.78	-
CF_3SO_3H	42.4	64.1	2.24	1.38

Brij template. Using non-ionic Brij surfactants, all of products except the one obtained in C_{18}/H_3PO_4 system were thermal stable and no dense WO_3 impurity was detected. The proton conductivities are list in Table 2. The conductivity was influenced by the acid type and the length of the chain of Brij template. The product synthesized in C_{18}/CF_3SO_3H system showed the highest conductivity of 4.0 x 10^{-2} S/cm.

Table 2. Proton conductivity of WMM using Brij.

T.	Acid	Water content (wt%)		Conductivity (x 10^{-2} S/cm)	
		As-made	Calcined	As-made	Calcined
C_{12}	HCl	50.4	58.3	0.07	0.26
C_{12}	H_3PO_4	23.4	28.1	0.19	0.31
C_{12}	CF_3SO_3H	40.5	51.8	3.31	0.30
C_{16}	HCl	42.4	46.5	0.57	0.30
C_{16}	H_3PO_4	34.0	25.5	0.03	0.20
C_{16}	CF_3SO_3H	39.8	63.2	0.03	0.08
C_{18}	HCl	43.9	53.1	0.06	0.35
C_{18}	H_3PO_4	35.7	a.	0.09	a.
C_{18}	CF_3SO_3H	38.8	61.1	3.98	0.66

a.= amorphous

Composite membranes. The composite membrane was continuous as shown in Figure 1 by the SEM image of the cross-section. At 100% relative humidity, the composite membrane with 10 wt.% WMM showed higher conductivity the PEI-Glymo-HTFSI membrane. The difference in conductivity decreased with an increase in the cell temperature, shown in Figure 2. The conductivity increased with increasing the relative humidity.

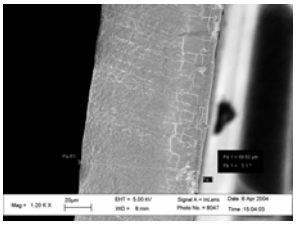

Figure 1. SEM image of the cross-section of the composite membrane.

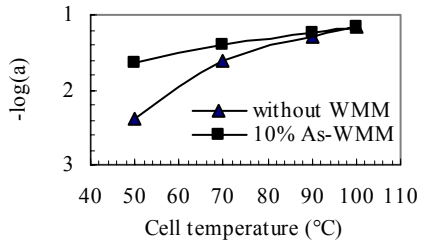

Figure 2. Effect of WMM on the conductivity.

Conclusions

Using CTMABr, $C_{12}EO_{10}OH$, $C_{16}EO_{10}OH$, or $C_{18}EO_{10}OH$ as the structure-directing agent, tungstosilicate mesoporous materials (WMMs) were synthesized with HCl, H_3PO_4 or CF_3SO_3H. Compared to CTMABr, the samples synthesized with the non-ionic surfactant showed higher tungsten incorporation, showed much thicker wall structure (34 ~ 39Å), higher thermal stability, and higher proton conductivity (4.0 x 10^{-2} S/cm). In CTMABr-H_3PO_4 system, the conductivity was found to increase with an increase in the W/Si molar ratio. The preliminary results of the composite membrane suggest tungstosilicates are promising additives for high temperature PEM fuel cell applications.

Acknowledgements. We thank the DOE, THECB/ATP and SAMSUNG for financial support

References

(1) Nakamura, O.; Kodama, T.; Ogino, I.; and Miyake, Y. *Chem. Letts.*, **1979**, 17.
(2) Alberti, G. and Casciola, M. *Solid State Ionics*, **2001**, *145*, 3.
(3) Kim, Y. S.; Wang,F.; Hickner, M.; Zawodzinski, T. A.; and McGrath,J. E. *J. Membr. Sci*., **2003**, *212*, 263.
(4) Tazi, B.and Savadogo, O. *Electrochim. Acta* **2000**, *45*, 4329.
(5) Piquemal, J.Y. ; Briot, E. ; Chottard, G. ; Tougne, Manoli, P. J. M. ; and Brégeault, J. M. *Micropor. Mesopor. Mater.,* **2003,** *58,* 279.
(6) Tanaka, R.; Ueoka, I.; Takali, Y.; Katapka, K.; and Saito, S. *Macromolecules*, **1983**, *16*, 849.
(7) Desmarteau, D. D. and Witz, M. J. Fluorine Chem. **1991**, *52*, 7.
(8) Mikhailenko, S.; Desplantier-Giscard, D.; Danumah, C; and Kaliaguine, S. Micropor. Mesopor. Mater.; **2002**, *52,* 29.

Eastman Chemical Company's "Chemicals From Coal" Program: The First Quarter Century

Joseph R. Zoeller

Eastman Chemical Company
Research Laboratories, B-150B
P.O. Box 1972
Kingsport, TN 37662

Introduction

Part of the driving force for starting Eastman Chemical Company in Kingsport, TN was proximity to a large reservoir of wood and mid-Appalachian coal which provided raw materials and energy, respectively, for the new facility. Throughout Eastman's history, coal has continued to constitute the major energy source for the very large, diversified chemical production facility in Kingsport. However, during the mid-1970's, Eastman Chemical Company recognized the value of turning to coal not only as an energy source, but as a feedstock in place of natural gas. Work began in 1975 on a process to convert its ethylene based largest acetic anhydride process, which represented its largest volume, most energy intensive chemical, with a coal based process. This resulted in the start-up of the first modern chemicals from coal facility in 1983, which generated four chemical entities: methanol, methyl acetate, acetic acid, and acetic anhydride entirely from coal.

Work on additional chemicals from coal has not ceased with the realization of the acetic anhydride process. Eastman's overall philosophy from the outset was that, in principle, methods could be developed to use coal based synthesis gas to generate the full menu of C-1 through C-4 oxygenated products currently generated from natural gas components. Eastman's continued efforts have resulted in potentially commercially viable, coal based, processes for acetaldehyde, vinyl acetate, propionic acid, methacrylates, acrylates, propionic acid. Key breakthroughs which allowed access to earlier acetic anhydride product and the key technologies enabling these new processes will be discussed below.

Acetic Anhydride Process (Methanol, Methyl Acetate, Acetic Anhydride)[1-3]

The generation of acetic anhydride from coal required a series of advances in coal gasification, esterification, and carbonylation. The chemical transformations are shown below:

$$\text{Coal} + H_2O + O_2 \longrightarrow CO + H_2 + CO_2 + H_2O$$
$$CO + 2\,H_2 \longrightarrow MeOH$$
$$AcOH + MeOH \longrightarrow MeOAc + H_2O$$

(AcOH recycled from esterification processes)

$$MeOAc + CO \longrightarrow Ac_2O$$

An excellent overview of the development of the process is provided by Agreda, et. al.[1] As described below, it entailed a multitude of breakthroughs.

Gasification. The gasification of coal using Texaco gasifiers had only been demonstrated for a period of several days. Subsequent work over the last 25 years has resulted in a design that can stay on-line for months before maintenance. Further, the gasifier was designed to allow isolation of carbon dioxide (which can permit sequestration if desired) and for the complete removal of heavy metals, including mercury.

Methanol. Although the original plant used a Lurgi methanol plant, a second methanol plant has been installed using a licensed Air Products Liquid Phase Methanol® process which permits coproduction of dimethyl ether and methanol if desired. This represents the first demonstration of this technology on a commercial scale.

Methyl Acetate. Using technology available at the outset of this project, the esterification of acetic acid would have required 7 units of operation due to the presence of multiple azeotropes. Reactive distillation of methanol with acetic acid reduced the process to a single unit of operation. Although reactive distillation had been a theoretical concept in engineering for some time, no large scale application was demonstrated until this process was brought on-line and it is now a common practice.

Acetic Anhydride. The subsequent carbonylation of methyl acetate to acetic anhydride entailed carbonylation using a homogeneous Rh-Li catalyst. Although this resembles the earlier Monsanto Rh catalyst, the catalyst described by Monsanto fails to accomplish the transformation because the process requires two components. The first component, Li, is required to activate methyl acetate to generate a methyl iodide intermediate. In its absence the reaction proceeds very slowly and generates excessive amounts of tar. The second component, Rh is present as $Rh(CO)I_2^-$ and effectively catalyzes the subsequent transformation of methyl iodide to generate acetic anhydride. A further modification was required.

In the Monsanto system, Rh is continually reduced by water gas shift and remains active. In the anhydrous system, there is no access to this reduction and the Rh deactivates by oxidation to Rh(3+). Small amounts of hydrogen are required to maintain the reduced state.

A third complication is the generation of tar. The generation of high molecular weight by-products (tar) is inherent to operating an acetic anhydride process at high temperature but unfortunately the Rh catalyst has a very high affinity for this tar. Eastman devised a proprietary process for the continuous separation and recovery of Rh from the tar rendering a process which consumes negligible amounts of Rh.

The acetic anhydride generated from the process is used in various esterification processes in the facility, including cellulose acetate, and produces an acetic acid by-product. The by-product acetic acid is recycled to the esterification facility. The facility has been a resounding success and has been in operation for 21 years.

Acetaldehyde (AcH) and Vinyl Acetate (VAM) Processes.[4]

Several companies have attempted the generation of vinyl acetate from synthesis gas but have failed commercially based on a conceptual flaw. Earlier attempts utilized a reaction scheme entailing

$$2\,CO + 4\,H_2 \longrightarrow 2\,MeOH$$
$$2\,MeOH + 2\,AcOH \longrightarrow 2\,MeOAc + 2\,H_2O$$
$$MeOAc + CO + H2 \longrightarrow Ac_2O$$
$$Ac_2O + AcH \longrightarrow EDA$$
$$EDA \rightleftharpoons VAM + AcOH$$

(EDA = ethylidene diacetate (1,1-diacetoxy ethane),
VAM = vinyl acetate monomer)

The very large acetic acid recycle stream in these processes led to enormous plant sizes, which translates to untenable capital requirements. Eastman's concepts were directed at eliminating this excessive recycle stream. Several concepts were developed in parallel. The best process emerging from this work started with dimethyl ether and took advantage of the easy access to dimethyl ether afforded by Liquid Phase MeOH® and consisted of the following steps:

$$2\,CO + 4\,H_2 \longrightarrow Me_2O + H_2O$$
$$Me_2O + CO \longrightarrow Ac_2O$$
$$Ac_2O + AcH \longrightarrow VAM + AcOH$$
$$AcOH + H_2 \longrightarrow AcH \text{ (to feed prior step)}$$

This approach is less capital intensive since it is shorter and eliminates the massive acetic acid recycle loop, but required the development of a new acetic acid hydrogenation procedure and an improved process for the acetylation of acetaldehyde to VAM. To address these needs. Eastman was able to develop a unique Pd-Fe_2O_3 catalyst for the hydrogenation of acetic acid which can produce >2000 g/L-h of AcH at 40% conversion with 77% selectivity when operated at 18 atm. and 300ºC. (The remaining by product is primarily over reduction to EtOH. The ethanol can be either back oxidized or sold as a by-product.) It was critical that the hydrogenation be operated without excessive hydrogen, as prior carboxylic acid catalysts did, in order to recover the AcH product.

The esterification of acetaldehyde with acetic anhydride also required breakthrough technology and to address this need, Eastman developed a reactive distillation of AcH with Ac_2O, which represented a significant breakthrough since it entailed several key features which reactive distillation had never dealt with before including a more volatile starting material than product, two equilibria, and a high boiling intermediate (EDA) which is the most favored product. However, with proper feed ratios (an excess of acetaldehyde) in the presence of a sulfonic acid catalyst, VAM can be produced directly in a single column, in very high yields, although pure VAM requires a second distillation column to remove the excess acetaldehyde and a small amount of acetic acid. The reactive distillation reduced the earlier known conversions of acetaldehyde and acetic acid from 5-6 units of operation to just 2 units of operation.

The process was nearly competitive with Gulf Coast based VAM processes in the mid-1990's and likely represents a viable process for the future as natural gas based ethylene processes become increasingly expensive.

Propionic Acid, Methacrylic Acid, and Acrylic Acid Processes.[5]

Acrylic and methacrylic acids and esters are critical components in emulsion polymers and plastics. Eastman originally targeted methacrylic acid because the existing process, hydrocyanation of acetone, was not only a petroleum based process, but generated a stoichiometric ammonium waste stream and involved a hazardous reagent (hydrogen cyanide.) The methodology is shown below:

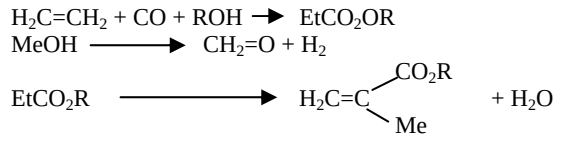

Although Eastman had developed proprietary technology for the homologation of acetic acid to propionic acid, the technology was not superior to using ethylene either generated from methanol or syngas or derived from petroleum resources. To conduct the carbonylation of ethylene, Eastman developed a low pressure, highly efficient low cost $Mo(CO)_6$ based catalyst which operates under a unique free radical mechanism that converts normally inactive $18e^-$ Mo complexes to highly active $17e^-/19e^-$ Mo species and represents a general method for the acid, ester, and anhydride derivatives of propionic acid.[6, 7]

The subsequent condensation was accomplished of the propionate intermediate was found to be achievable over Nb supported on silica. The process is normally run in the presence of excess propionate at temperatures of 300ºC and 2 atm. of pressure. Methyl propionate, propionic acid, and propionic anhydride were tested as feedstocks and it was found that the free carboxylic acid was slightly superior to the anhydride and both were markedly better than the ester. The catalyst is prone to deactivation by coking but can be reactivated by oxidizing the coke off the surface. In principle, acrylic acid can be generated by substituting acetic acid for propionic acid in this process.[8]

Economics are similar to processes entailing the oxidation of isobutylene. Consistent with this claim is the announcement by Davy/Lucite that they intend to build a plant based on this reaction scheme, albeit with different catalysts for the carbonylation and condensation steps.[9]

Conclusions: The Future

As these 3 processes indicate, it is feasible to displace large volume organic chemicals currently produced from natural gas or natural gas liquids with coal based synthesis gas. As natural gas becomes increasingly more expensive relative to more abundant coal and as the United States seeks a hydrogen based economy and energy independence, Eastman Chemical Company believes that coal gasification should play a critical role in the transition and continues to research improved gasification and chemical generation using coal as a feedstock. Improvements in coal gasification that Eastman has made over the course of its 21 years of gasifier operation indicate that coal gasification is a clean process with the potential of allowing access to energy with reduced greenhouse gases since the gasification process permits ready sequestration of CO_2 as a part of its operation. In a parallel to the petrochemical industry, where large scale oil refineries directed primarily directed toward fuel production for transportation and heating gave birth to a dependent petrochemical industry, one can easily envision an analogous emergence of a "coal chemical" industry wherein widespread, large scale coal gasification units dedicated primarily to the production of electrical power and transportation fuels would provide the economies of scale for the synthesis gas feedstocks that can make chemicals from coal a realistic, widespread alternative to most of the chemicals now derived from natural gas components and petroleum resources.

Acknowledgement. The support of the US Dept. of Energy for funding the work on vinyl acetate, acetaldehyde, propionic acid, and methacrylic acid is thankfully acknowledged.

References

(1) Agreda, V. H., Pond, D. M, Zoeller, J. R. *Chemtech*, **1992**, *22*, 172.
(2) Zoeller, J R., Agreda V. H., Cook, S. L., Lafferty, N. L., Polichnowski, S. W., Pond, D. M., *Catalysis Today*, **1992**, *13*, 73.
(3) Zoeller, J. R., Cloyd, J. D., Lafferty, N. L., Nicely, V. A., Polichnowski, S. W., Cook, S. L., *Adv. In Chem.*, **1992**, *230*, 377.
(4) Tustin, G. C., Colberg, R. D., Zoeller, J. R., *Catalysis Today*, **2000**, *58*, 281.
(5) Spivey, J. J., Gogate, M. R., Zoeller, J. R., Colberg, R. D., *Ind. & Eng. Chem. Res.*, **1997**, *36*, 4600.
(6) Zoeller, J. R., Blakely, E. M., Moncier, R. M., Dickson, T. J., *Catalysis Today*, **1997**, *36*, 227.
(7) Zoeller, J. R., Buchanan, N. L., Dickson, T. J., Ramming, K. K., *Catalysis Today*, **1999**, *49*, 431.
(8) Gogate, M. R., Spivey, J. J., Zoeller, J. R., *Catalysis Today*, **1997**, *36*, 243.
(9) Kane, L. Romanow, S., *Hydrocarbon Processing*, **2003 (August)**, 25.

CO-COKING: DISTILLABLE OIL ANALYSIS

María M. Escallón and Harold H. Schobert

The Energy Institute, The Pennsylvania State University,
University Park, PA 16802

Introduction

Advanced jet fuels need to be resistant to degradation at temperature above 450°C where the pyrolytic regime occurs. Thermal stability is crucial because the degradation of the fuel lead to the formation of solid deposition [1]. This problem is magnified at higher speeds [2].

It has been reported that coal-derived components bring more pyrolytic stability to the jet fuel compared to the traditional petroleum-derived fuels. The compounds that provide stability are cycloalkanes and hydroaromatics [3,4].

The strategies to produce coal-derived and coal-based liquids are coal conversion and use of coal/petroleum blends. Coal conversion (e.g.. direct liquefaction) produces *coal-derived* liquids, meaning that the liquids are produced entirely from coal; while coal and petroleum blends (i.e. coal tar and petroleum stream blends, co-processing and co-coking) form *coal-based* liquids, meaning that the liquids are not produced entirely from coal but also contain petroleum components.

Butnark[5] reported a high production of tetralin yields by blending hydrotreated light cycle oil (LCO), a product of catalytic cracking and refined chemical oil (RCO), a fraction from coal tar. The results show a great improvement in the thermal stability.

Direct liquefaction and co-processing are processes that need hydrogen, thus having the disadvantage of an increase in the cost. Co-coking involves the simultaneous thermal treatment of a bituminous coal and a petroleum product, such as decant oil. Co-coking has been developed at our Institute; although the liquid yield is low, the by-product credit for a high-value carbon could help pay for the processing of the jet fuel.

The current paper provides additional analytical data for the liquids present in the co-coking process, extending the information published in a previous paper [6]. The aim is to show the change of the liquid as a function of reaction time.

Experimental

Samples. The decant oil was obtained from Seadrift Coke in Texas and was selected because it is a material used to make premium coke. A number of compatible coals with regard to thermoplastic properties, ash and sulfur values were evaluated in past investigations;[7] that work led to the selection of Powellton coal. Powellton coal was mined in Boone County, West Virginia. It is hypothesized that the interaction between decant oil and coal is facilitated by the fluid state that coal undergoes at its maximum fluidity. Therefore, at temperatures of the coking process the coal-petroleum interaction occurs between two liquid phases rather than one liquid and one solid.

Procedure. The reactor was described in previous work [6]. Approximately 20 g of the decant oil / coal (2:1) mixture, decant oil (100%), or coal (100%) was added to the tubing bomb. The purpose of the experiments with only coal or only decant oil was to establish the coal's contribution to the total liquids. Experiments were conducted by varying the reaction time from 2 to 12h in 2-hour increments.

When the reaction was completed at each specific time interval, the tubing bomb was cooled to room temperature and the apparatus was disconnected. Each test was run in triplicate to provided sufficient material for necessary analytical procedures and report accurate yield values.

Simulated distillation by gas chromatography (SimDist GC) was utilized to determine the boiling-cut distributions of the distillates from co-coking decant oil alone and coal alone. A Hewlett Packard HP 5890GC Series II model was used.

GC/MS was utilized to observe the main differences between decant oil and coal distillable oils.

^{1}H NMR was carried out on a Bruker AMX 360 NMR. Distillates were dissolved in $CDCl_3$ for analysis.

Results and Discussion

GC/MS. The results obtained by a chromatogram comparison give a general view of the co-coking distillable oils. The fact that the decant oil contains hundreds of compounds results in a chromatogram in which peaks of individual compounds overlap, making the identification difficult. Table 1 shows approximately the main differences in composition among the three distillates at produced at 6h: from coal, decant oil and blend.

Table 1: Main differences in composition among the three distillates at 6 hours: Coal, decant oil and blend

	Coal 100%	Decant oil 100%	Blend DO/coal 2:1
Small ring aromatics (i.e. toluene, phenol)	High amount. Presence of di-aromatics	Traces	Moderate
Polyaromatic and long chain alkanes region	Not observed.	High amount	Moderate
Alkanes/alkenes	Alkenes (one or two double bonds) (C_8-C_{14})	Alkanes (C_8-C_{26})	Alkanes (C_6-C_{14})

^{1}H NMR. Since GC/MS alone could not provide enough information about the coal contribution to the total liquid due the overlapping of the peaks, NMR was used to establish differences between decant oil and blend distillable oils.

The ∑poly/single aromatic ratio with reaction time for the blend and decant oil was obtained and is shown in Figure 1. The chemical shift information was obtained by following the peaks integration suggested by Rodriguez et al [8].

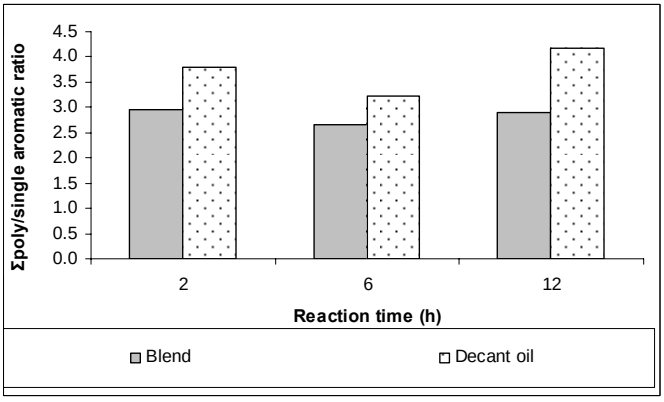

Figure 1. Σ poly/single aromatic ratio (^{1}H NMR) comparison for the blend and decant oil's distillable oil at different reaction times

It is observed in Figure 1 that poly/single ring aromatic ratio is higher for the decant oil than for the blend at the three different reaction times. This shows that coal and/or coal-decant oil interaction provides less heavy fractions to the total distillable oil (co-coking).

Evidence of the decant oil/coal interaction by analyzing the product yield distribution. By calculating the actual amount of products, based on boiling point and co-coking yields, the experimental value and theoretical value for the distillable oil were compared.

Calculation example: To determine the amount of products, a basis of 1 metric ton distillable oil –DO, 1 metric ton distillable oil – COAL and 1 metric ton distillable oil –BLEND was used to obtain the actual amount of products present in the different boiling point ranges. The calculation was done in order to determine the possible contribution from the coal to each boiling point range.

If no interaction takes place, the following linear combination equation would determine the yield of the blend:

EQ: Decant oil (0.67) + Coal (0.33%) = Blend (theoretical value)
Blend (theor.)= {[1*(0.01*0.2061)]*0.33}+
{[1*(0.608*0.1659)]*0.67}*1000
= 68.3 kg

Table 2 shows an example for the jet fuel fraction at 12h reaction time. The actual amount was calculated based on the yield (wt%) and the percentage of compounds present in any given boiling point range.

Table 2: Calculation example. 12h reaction time (co-coking) for the jet fuel fraction (175-300°C)

Sample	Yield (Wt %)	175-300°C (%) (simulated distillation)	kg
Decant oil (exp.)	60.8	16.59	100.9
Coal (exp.)	1.0	20.0	2.0
Blend (exp.)	40.7	19.72	80.3
Blend (theor.)	---	---	68.3

exp.=experimental; theor=theoretical

Theoretical value and experimental value of the blend were compared. A higher experimental value compared to the theoretical suggests that coal being in the process stream is giving coal-derived compounds to the total distillates. Figure 2 was plotted to indicate coal's contribution to the final liquids, based on these calculations

Summary and conclusions

- In some boiling point cuts, the blend's experimental value is higher than the blend's theoretical value; this suggests that coal and/or the result of coal and decant oil interaction produces coal-based liquids. The contribution from coal is mainly in the <175°C and 175-300°C (jet fuel) fractions. No coal contribution has been observed at 300-500°C. This is shown in Figure 2.
- Based on NMR it is observed that there is more polyaromaticity present in liquids from the decant oil than from the coal.

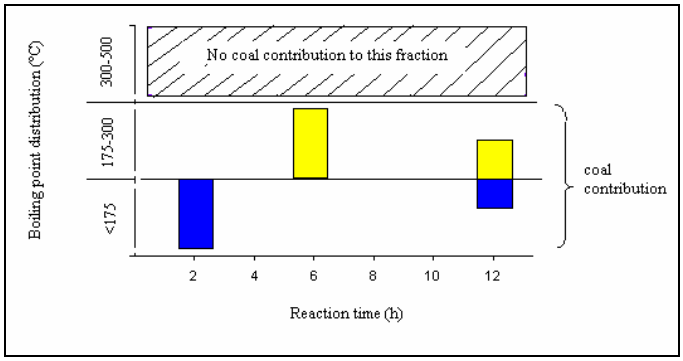

Figure 2. Coal contribution to the boiling point cuts in the distillable oil fraction

Acknowledgements. The authors are pleased to acknowledge the financial support for this work provided by the Air Force Office of Scientific Research. We thank Seadrift Coke for the sample of decant oil used in this work. Thanks to David Clifford and Brian Senger for his help with the GC/MS. We also thank Dr. Leslie Rudnick for useful scientific discussions.

References

(1) Strohm, J. J.; Butnark, S.; Keyser, T. L.; Andrésen, J. M.; Badger, M. W.; Schobert, H. H.; Song, C. *Fuel Chemistry Division Preprints* **2002**, *47*, 177-178.
(2) Chin, J.; Lefebvre, A.; Sun, F.-Y. *Journal of Engineering for Gas Turbines and Power* **1992**, *114*, 353.
(3) Song, C.; Eser, S.; Schobert, H. H.; Hatcher, P. G. *Energy and Fuels* **1993**, *7*, 234-243.
(4) Butnark, S. MSc Thesis, The Pennsylvania State University, 1999.
(5) Butnark, S. PhD Thesis, The Pennsylvania State University, 2003.
(6) Escallon, M. M.; Venkataraman, R.; Clifford, D. J.; Schobert, H. H. *Petroleum Chemistry Division Preprints* **2003**, *48*, 147-149.
(7) Fickinger, A. E. Master Thesis, The Pennsylvania State University, 2000.
(8) Rodriguez, J.; W, T. J.; Irving, W. *Fuel* **1994**, *73*.

COAL EXTRACTION USING LIGHT CYCLE OIL: A FACTORIAL DESIGN STUDY OF PROCESS PARAMETERS

Josefa M. Griffith, Caroline E. Burgess Clifford, Leslie R. Rudnick, Harold H. Schobert, Pedro D. Martín†

The Energy Institute, The Pennsylvania State University, University Park, PA 16802
† Centro de Petróleo y Catálisis, Escuela de Química, Facultad de Ciencias, Universidad Central de Venezuela.

Introduction

Researchers at Penn State University have been involved in the development of a jet fuel JP-900 for the last ten years.[1] The JP-900 program has three components: production, stabilization and combustion. The focus of fuel production is to incorporate coal or coal-derived materials into existing oil refinery operations.[2] Currently, there are two processes under investigation, and the most advanced involves the blending of coal tar distillates with petroleum refinery streams.

Refined Chemical Oil (RCO) is a distillate produced from the refining of coal tar (a by-product of metallurgical coke industry) and it represents around 10% of the coal tar yield. RCO consists mainly of a mixture of naphthalene (70%), indene and their derivatives. It is of special interest to current research at PSU as it is blended with Light Cycle Oil (LCO) coming from catalytic cracking of petroleum, for further processing. Upon hydroprocessing, it is converted to tetralin and decalin, streams that are used to formulate a thermally stable jet fuel.[3,4] Unfortunately, the problem is that by-product coke ovens are being closed down in the United States, and it is very unlikely that any new ones will be built to replace the older unit, thus creating a shortage of RCO.

It is important to consider alternative ways to produce RCO from coal in a very inexpensive process. Direct coal liquefaction would not be considered as an option, because there is no indication that this process would be economically competitive with petroleum processes. In order for the process to be economic, it should be able to be integrated into a refinery. Therefore, it should use operation units, chemical reagents and/or solvents that are used or produced in a refinery. In this sense, the processes expected to be used are those that do not require expensive chemical reagents (in particular catalysts and consumption of hydrogen) and do not consume high quantities of energy. The processes that could possibly produce useful two-ring compounds from coal and meet these criteria are some form of solvent extraction of coal.

This study shows the results of coal extraction using LCO as a solvent. The LCO/coal extractions were carried out in on a relatively large-scale using a 165-mL stirred batch reactor. In order to determine the best conditions to extract the coal, it was decided carry out the LCO/coal extractions following an experimental design. An experimental design is a series of tests in which deliberates changes are made to the input variables of a process or system so that it may observe and identify the reasons for changes in the output response[5] The previous classical approaches used before rely upon a strategy to alter one factor at a time. All factors except the one under investigation are fixed, and the factor under investigation is varied along some predetermined grid.

Experimental

Samples. Pittsburgh coal ground at to –60 mesh (250 µm) was used in this work, with the ultimate and proximate analyses shown in Table 1. The LCO to be used as a solvent to extract organic components from this coal was obtained from PARC Technical Services (100 William Pitt Way, Pittsburgh, PA, 15238). The properties of this solvent are listed in Table 2.

Experimental Design. Factorial designs permit estimation of factor and higher-order (interactions) effects of several factors simultaneously. These designs are widely used in the cases where it is necessary to study the joint effect of the several factors on a response or where it is known or assumed that the response is approximately linear over the range of the factor levels chosen, thus, only a few levels for each factor are needed. The LCO/coal extractions were studied by means of a Four-Factors Two-Levels Factorial Design (2^4). The four factors of this experimental design were temperature, LCO/coal ratio, time and pressure. The two levels of this experimental design are shown in the Table 3.

Table 1. Ultimate and Proximate Analyses for Pittsburgh

	Pittsburgh
Ultimate Analyses (dry)	
% Carbon	74.8
% Hydrogen	5.1
% Nitrogen	1.2
% Sulphur	1.1
Proximate Analyses (dry)	
% Ash	10.3
% Volatile matter	36.0
% Fixed Carbon	53.7

Table 2. LCO Properties

Properties[a]		
API Gravity @ 60 °F, ASTM D-287	10.3	
Specific Gravity (gr/mL), ASTM D-1298	0.9979	
Sulfur (wt %), ASTM D-5453	1.92	
Nitrogen (ppm), ASTM D-5762	535	
Distillation (° C)	ASTM D-86	ASTM D-2887
IBP	220	146
10	266	249
20	277	271
30	286	279
50	296	301
70	313	324
80	324	341
90	336	359
FBP	354	396

[a] Received from PARC Technical Services

Table 3. Two Levels for the Factorial Design

	Temperature (°C)	LCO/coal Ratio	Time (h)	Pressure (psi)
Low Level	150	5	1	100
High Level	350	10	3	1000

The pattern and the code of this design are shown in the Table 4. It can be noticed that the high numbered factors have long sequences where they were at their low or high levels. This pattern is poor because of the potential time-related bias error. There are two strategies to deal with this, randomization and blocking. For randomization, the order is scrambled so that any bias present will become a part of the random variation. For blocking, the test

sequence is broken into smaller groups, each of which is reasonably short, so that bias within a block is negligible.

In this case, the blocks were built into the design to take into account that the experiments were carried out daily during a two week period. Each week represents a block in the experimental design. After this, a randomized sequence was taken from the charts published for this purpose.

Table 4. Pattern and Coding of the Experimental Design

	Pattern Design				Code Design				Randomized and Blocked Design	
Trial Nº	X_1	X_2	X_3	X_4	X_1 Temperature (°C)	X_2 LCO/coal Ratio	X_3 Time (h)	X_4 Pressure (psi)	Block	Random Order
1	-	-	-	-	150	5	1	100	2	10
2	+	-	-	-	350	5	1	100	1	3
3	-	+	-	-	150	10	1	100	1	5
4	+	+	-	-	350	10	1	100	2	14
5	-	-	+	-	150	5	3	100	1	1
6	+	-	+	-	350	5	3	100	2	16
7	-	+	+	-	150	10	3	100	2	13
8	+	+	+	-	350	10	3	100	1	8
9	-	-	-	+	150	5	1	1000	1	6
10	+	-	-	+	350	5	1	1000	2	9
11	-	+	-	+	150	10	1	1000	2	11
12	+	+	-	+	350	10	1	1000	1	7
13	-	-	+	+	150	5	3	1000	2	12
14	+	-	+	+	350	5	3	1000	1	4
15	-	+	+	+	150	10	3	1000	1	2
16	+	+	+	+	350	10	3	1000	2	15

Procedure. The extractions were carried out according to the Scheme in Figure 1. The coal was dried in a vacuum oven overnight at 100 °C and 30 mmHg and cooled down for one hour in a desiccator. Appropriate amounts of coal and LCO were weighed and placed into the reactor. The reactor was sealed and then placed in the heater. The sealed reactor was purged three times with 1000 psi (7 MPa) of ultra-high-purity N_2 (UHP, 99.999%) and finally pressurized at a determined pressure of N_2. When the temperature reached 70-80 °C below the reaction temperature, the stirrer was started and set at 1500 rpm. After the reaction, the reactor was brought to room temperature by immersing it in a cold water bath for 1 hour.

The LCO/coal dispersion was filtered using a Millipore type filter with previously weighted PTFE filter. The reactor and the solid were washed with dichloromethane (DCM) until the supernatant became almost colorless. The resulting solid material, which is called the residue hereafter, was quantitatively transferred to a previously weighed Petri dish and then dried in a vacuum oven at 110 °C and 30 mmHg for at least 4 hours, cooled to room temperature in a desiccator for an hour and then weighed. This was repeated until a constant weight was obtained. The resulting solution, which is called the extract hereafter, was rotary evaporated in a water bath at 60 °C until all the dichloromethane was separated. In order to eliminate the remaining dichloromethane, the solution was dried in a vacuum oven without heating. This was repeated until the loss of weight was less than 200 mg.

The extraction yields were calculated from the weight of initial amount of coal and residue on a dry ash free basis according to Equation 1.[6] The extract yields were calculated to know how much organic material is being dissolved in the LCO. These can be calculated with respect to the initial amount of coal according to Equation 2.[7]

Equation 1:

$$Extraction\ Yield = \frac{1 - \mathrm{Re}\ sidue_{weight}(gr) / Coal_{weight}(gr)}{1 - ash(wt\%, db)/100} * 100$$

Equation 2:

$$ExtractYield = \frac{Extract_{weight}(gr) - LCO_{weight}(gr)}{Coal_{weight}(gr) - Coal_{weight}(gr) * ash(wt\%, db)/100} * 100$$

Figure 1. Experimental Procedure

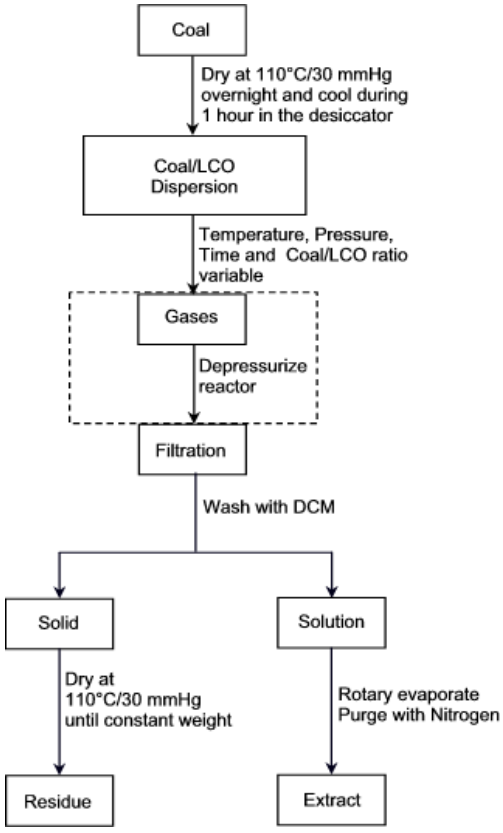

Results and Discussion

The extraction and extract yield results are shown in the Table 5. It was observed that in the condition where all factors had their lowest levels (----) the extraction and extract yields were 0 and -4 wt % respectively, while in the condition where all factors had their highest levels (++++) the extraction and extract yields were 36 and 23 wt % respectively.

These results demonstrate that pressure and reaction time do not have important effect in the extraction process. While the temperature seems to have a consistent and positive effect in both the extraction and extract yields. On the other hand, the LCO/coal ratio also see

to have a positive effect at high level of temperature, thus, there must be some interaction between the temperature and the LCO/coal ratio.

It can be noticed that at the lowest level of temperature the extraction and extract yields are negligible for both levels of LCO/coal ratio. However, at the highest level of temperature, both extraction and extract yields are higher at the higher LCO/coal ratio. The greater the amount of LCO available in the process, the better extraction and extract yields.

The experimental design provided significant insight into the best extraction conditions. While the extraction and extract yields at the most severe conditions are 36 and 23 wt%, respectively, there are two intermediate conditions where the yields are even higher. For trial 4, the extraction and extract yields are 39 and 33 wt% , respectively, and for trial 6, 33 and 28 wt%. These extraction and extract yields are a significant amount, and accomplished at low nitrogen pressure (100 psi). Conditions such as these, at relatively low severity, may be the basis for an economic extraction process.

Table 5. Extraction and Extract Yields.

Trial N°	Temperature (°C)	LCO/coal Ratio	Time (h)	Pressure (psi)	Extraction Yield, % wt	Extract Yield, % wt
1	150	5	1	100	-0.16	-3.69
2	350	5	1	100	14.37	10.26
3	150	10	1	100	2.76	-2.40
4	350	10	1	100	39.36	32.74
5	150	5	3	100	-1.37	-2.75
6	350	5	3	100	32.53	28.35
7	150	10	3	100	0.26	-14.31
8	350	10	3	100	27.23	25.39
9	150	5	1	1000	2.84	-2.23
10	350	5	1	1000	27.79	20.81
11	150	10	1	1000	-1.07	-4.92
12	350	10	1	1000	32.26	28.57
13	150	5	3	1000	0.61	-4.59
14	350	5	3	1000	24.63	20.50
15	150	10	3	1000	-0.09	0.74
16	350	10	3	1000	35.57	23.16

Conclusions

In the experiments evaluating temperature, LCO/coal ratio, time and pressure, under the condition where all factors had their lowest levels (----) the extraction and extract yields were 0 and -4 wt % respectively, while under the condition where all factors had their highest levels (++++) the extraction and extract yields were 36 and 23 wt % respectively.

The only factor that is having a significant effect on the extraction process is the temperature. At high temperature, the LCO/coal ratio starts to have a positive interaction with the temperature. At the highest level of temperature, both extraction and extract yields are higher at the higher LCO/coal ratio. The interaction between others factor are negligible.

The highest extraction and extract yield obtained was at 350 °C, 100 psi N_2, 10/1 LCO/coal ratio, and 1 hr reaction time. Conditions such as these, at relatively low severity, may be the basis for an economic extraction process.

Acknowledgement. The authors want to thank Orlando Pérez for his invaluable contribution in the statistical analysis.The authors are pleased to acknowledge the financial support for this work provided by the Air Force Office of Scientific Research. We thank PARC Technical Services for the sample of LCO used in this work.

References

(1) Schobert H., Badger M., Santoro R., *Prepr. Pap. - Am. Chem. Soc., Div. Pet. Chem.*, **2002**, *47*(3), 192-194.
(2) Maurice L.Q., Lander H., Edwards T., Harrison III W.E., Fuel, 2001, 80,747-756.
(3) Badger M., Butnark S., Wilson G., Schobert H., *Prepr. Pap. - Am. Chem. Soc., Div. Pet. Chem.*, **2002**, *47*(3), 198-200.
(4) Badger M., Butnark S., Wilson G., Schobert H., *Prepr. Pap. - Am. Chem. Soc., Div. Pet. Chem.*, **2002**, *47*(3), 201-203.
(5) Montgomery Douglas, In *Design and Analysis of Experiments*, John Wiley & Sons, New York, 1991; pp. 1-12.
(6) Takanohashi T., Xiao F., Yoshida T., Saito I., *Energy&Fuels*, **2003**, *17*, 255-256.
(7) Guillén M., Blanco J., Canga J., Blanco C., *Energy&Fuels* **1991**, *5*, 188-192.

CO-COKING OF HEAVY SOLUBLE FRACTIONS FROM COAL LIQUEFACTION AND PETROLEUM VACUUM RESID: GAS, LIQUID AND SOLID DISTRIBUTION

Parvana Gafarova[†], Arif Hesenov[*], Omer Gul[†], Harold H. Schobert[†] Oktay Erbatur[*],*

[†]The Energy Institute, The Pennsylvania State University, University Park, PA 16802
[*]Cukurova Universitesi, Fen-Edebiyat Fakultesi, Kimya Bolumu. 01330 Adana, Turkey

Introduction

With the price of oil currently at an all time high, alternative fuels from coal have again come to the forefront. Direct catalytic coal liquefaction can be achieved technically, but has not been shown to be an economic process[1]. One attempt to render liquids from coal economically is to co-process coals and petroleum resids in delayed cokers already present in petroleum refineries. Not only could a liquid product be made, but it is also expected that high-grade carbon could be produced, thus contributing to the economic feasibility[2,3,4]. One of the problems with using raw coal in the coker is that it still contains mineral matter that is not desirable in coke. One way to eliminate the mineral matter is to pre-process the coal using direct catalytic hydrogenation. The present study focuses on catalytically hydrogenating coal and using the heavier liquid products in a delayed coking process. By using this process, the mineral matter is removed and the coal has begun to depolymerize. Use of this material as a feed to the coker could enhance the quality of the carbons produced from the coker because of the relatively high content of aromatics and polycondensed structures in the heavy oil fractions.

Experimental

Material. Two coals were liquefied in this work. The first coal selected was a Pennsylvania coal from the Pittsburgh seam. This coal was selected from Penn State Coal Sample Bank and Database and was denoted as DECS 12. The second coal chosen was Cayirhan lignite from Beypazari, Turkey. This coal was selected because of its high liquefaction yield[5,6]. The ultimate analysis data are given in Table 1. Following catalytic hydrogenation of coals (details were given elsewhere[5,6]), oil fractions were removed by Soxhlet extraction using n-pentane and the heavier fraction was removed by extracting with tetrahydrofuran (THF). The material extracted by THF was called asphaltene + preasphaltene fraction and coded as ap. Specifically, the fraction obtained from Pittsburgh coal was coded as Pap and from Cayirhan as Cap. These materials, following removal of THF under reduced pressure were used in co-coking experiments.

Petroleum vacuum resid was received from the Aliaga-Izmir Petroleum Refinery of the Turkish Petroleum Refineries, Co. and has been coded as VR in this study. The elemental analysis of VR together with the elemental analysis of Pap and Cap are given in Table 2. NMR data for VR are also given in Table 3.

Coking experiments. All coking experiments were performed in a small tubing reactor system (25 mL volume). In a typical experiment, approximately 2.0 g of sample was charged into the reactor. After sealing the reactor, air inside the reactor was swept out by pressurizing (6.9 MPa) with nitrogen gas and then depressurizing the system. This procedure was repeated four more times and then the reactor was left at atmospheric pressure prior to coking treatment. While the reactor was under pressure, a leak test was performed. The reactor was then placed in a temperature controlled pre-heated fluidized sand bath. The duration in all coking experiments was two hours.

Table 1. Analytical data of coals.

	DECS 12	Cayirhan
Rank	hVAb	Lignite
Location	USA-PA	TURKEY-Beypazari
Moisture	2.4	13.8
Ash	10.0	32.7
Elemental	Analysis	(wt % Daf[a])
%C	83.3	73.1
%H	5.7	4.7
%N	1.4	1.9
%S	1.3	7.5
%O[b]	8.4	12.8

[a] Daf: dry, ash-free. [b] Calculated from difference

Following the two-hour treatment, the reactor was removed from the sand bath and quenched in a cold water bath. The weight of the tubing bomb reactor before and after discharging the gaseous products in a gas bag were recorded so as to determine the mass of gaseous products.

Table 2. Elemental analysis of petroleum vacuum resid and the heavy soluble fractions of hydrogenated coals, daf[a].

	VR	Cap	Pap
%C	85.31	82.40	85.05
%H	10.17	9.20	7.58
%N	0.32	2.48	1.50
%S	4.70	2.88	0.53
%O[b]	0.0	3.04	5.34
H/C	1.43	1.34	1.07

[a] Daf: dry, ash-free. [b] Calculated from difference: VR:Vacuum Resid, Cap: Cayirhan asphaltene + Preasphaltene, Pap: Pittsburgh asphaltene + preasphaltene.

Table 3. NMR results of petroleum vacuum resid.

	VR
Aromatic C	21.25
Aliphatic C	78.75
Aromatic H	6.00
Aliphatic H	94.23
f_a	0.21
f_a^H	0.060

The reactor was rinsed out with *n*-pentane into an extraction thimble and successively extracted in a Soxhlet apparatus with *n*-pentane and tetrahydrofuran. Oil and ap were the material solubilized in these two solvents, respectively. The solid part remaining in the ceramic thimble after THF extraction was denoted as the solid product. The mass of oil products was calculated by subtracting the total mass of gas+ap+solid from the mass of original reactant.

The blends of VR:Pap and VR:Cap (with the mass ratios of 1:1, 1:2, and 2:1) and the individual VR, Pap, and Cap samples were coked as described above. Three different temperatures (450°C, 475°C and 500°C) were applied in the coking experiments. Coking of each type of sample was run in triplicate.

Results and Discussion

Coking of VR alone. Figure 1 shows the distribution of gaseous, liquid and solid products following coking at three different temperatures. Total liquid yield in the graph represents the total amount of both oil and ap fractions.

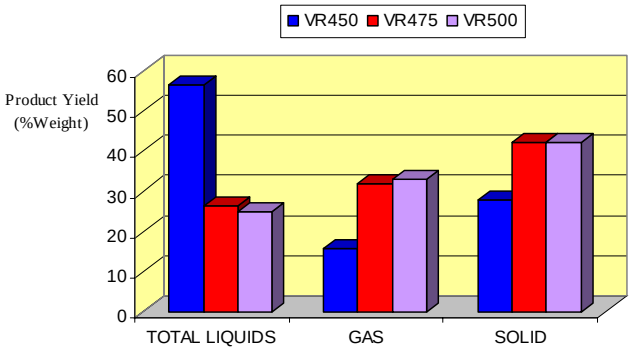

Figure 1. Product distribution following coking of vacuum resid (VR) at three different coking temperatures.

The behaviour of VR at 450°C is quiet different than its behaviour at two other temperatures. At 450°C, a significant portion of the sample is liquid, 56.4 %, while 27.8 % is in the solid form and the rest was gaseous products. A 25°C temperature increase results a dramatic change in percent distribution of products. At 475 °C solid yield is increased to 41.9 %, gaseous products to 31.9 % and the liquid product percentage is 26.2 %. On the other hand, when another 25°C temperature increase was applied, almost no change in percent product distribution was observed; i.e. following coking at 500°C, the percentages of liquid, gaseous and solid products were almost identical to the corresponding figures obtained at 475°C. This shows that the main reactions in the VR towards carbonization and gas formation take place in the temperature range 450-475°C. One other point to be made was that the oils accounted for about 80 % of the total liquid product yields regardless of the treatment temperature.

Coking of Cap alone. The product distribution following coking of Cap at three different coking temperatures is shown in Figure 2.

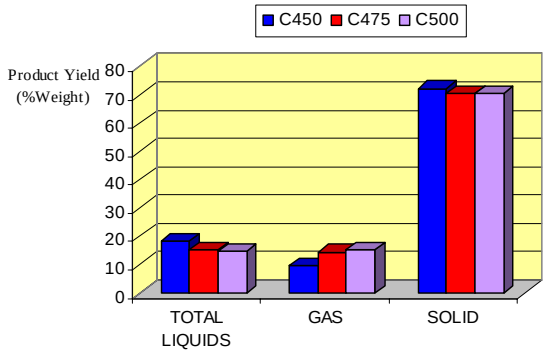

Figure 2. Product distribution following coking of Cap at three different coking temperatures.

As can be seen, the behaviour of the heavy soluble fraction from the liquefied Cayirhan lignite is completely different than the petroleum vacuum resid. First, the major products at 450°C were the solid. Second, there is not much difference in the product distribution following thermal treatment at three different temperatures as far as distribution to three phases is concerned. As treatment temperature is increased, small decreases in quantities are observed both in liquid and solid products whereas these decreases are counterbalanced with increases in gaseous products.

Coking of Pap alone. When one observes the product distribution following coking of Pap at three different temperatures, one can note that both coals, heavy soluble fractions from liquefaction respond very similarly toward heat treatment at these temperatures. Some slight differences are observed in liquid and gaseous product distributions; e.g. there is a very slight increase in liquid content whereas the reverse was true with the liquid products obtained from Cap. Gaseous product formation is a little bit higher in the Cap case.

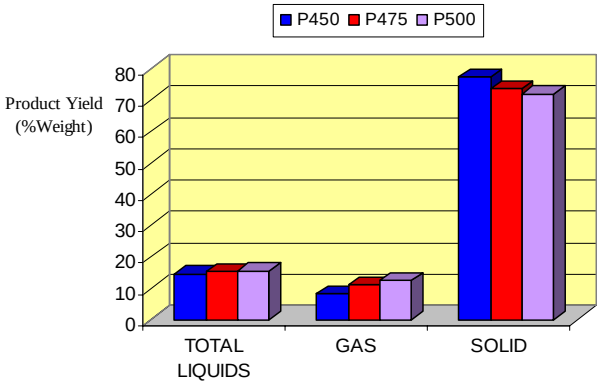

Figure 3. Product distribution following coking of Pap at three different coking temperatures.

Both observations are consistent with the composition differences between Pap and Cap, such that aromaticity is a little bit higher in Pap as can be deduced from the H/C atomic ratio values given in Table 2.

Co-coking of VR + Cap: Three different combinations of VR + Cap (1:2, 1:1, 2:1) were treated at three different temperatures. As can be seen from Figure 4, solid formation is highest when coal derived material dominates in the blend and the reverse is true when VR dominates in the blends.

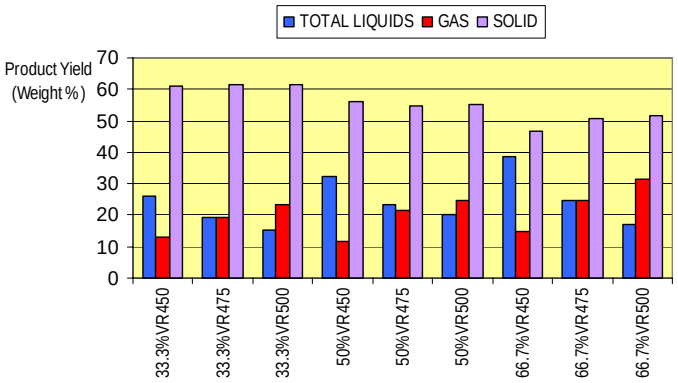

Figure 4. Product distribution following co-coking of VR + Cap in three different compositions and at three different temperatures

One other important observation is that the decrease in solid percentage as the ratio of VR increases in the blends is not as

dramatic as expected. As usual, higher treatment temperatures result in higher gas yields and this change is mainly counterbalanced with lower liquid yields.

Co-coking of VR + Pap: The general trend of product distribution changes following coking of VR + Pap is similar to that of VR + Cap. The solid products ratios following the heat treatments at 450 °C and 475 °C are a little higher than the corresponding values obtained from VR + Cap, but at 500 °C the corresponding values are almost identical.

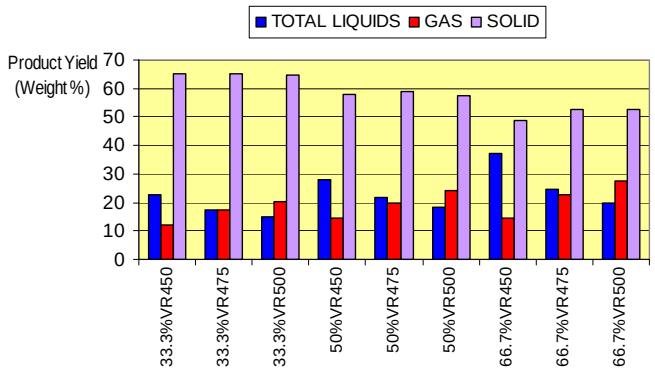

Figure 5. Product distribution following co-coking of VR + Pap in three different compositions and at three different temperatures

The relationship between gaseous and liquid products is almost the same for both VR + Pap and VR + Cap except in a few cases. When the liquid yield is compared with the corresponding liquid yield obtained from co-coking of original Pittsburgh coal with petroleum resid[7], one can notice a higher yield in the former case. This is consistent with the differences of the original coal and its hydrogenated heavy soluble fraction, such that there are certainly more hydrogen-donating moieties in the latter case which can quench radicals and increase the formation of liquid products.

Conclusions

This research is a work in progress. The best conclusions can be derived following investigating the compositions of liquid products and the structure of the carbons (solid products) that are formed under different conditions and with different blend compositions.

Acknowledgement. This study has been supported by The Scientific and Technical Research Council of Turkey (TUBITAK). The authors are pleased to acknowledge the financial support for this work provided by the U. S. Air Force, Office of Scientific Research for portions of this work. HHS also acknowledges financial support from NATO for a collaborative visit to Çukurova University.

References

(1) Elliot, M.A.(Ed.), in "Chemistry of Coal Utilization Secondary Supplementary Volume", Wiley-Interscience Publication, New York, (1981).
(2) Olmstead, W.N., and Bearden, Jr., R., US Patent 5228981, July 20, 1993.
(3) Goval, S.K.; Kolstad, J.L.; Hauschildt, F.W.; Venardos, D.G.; Joval, C.L.M. *US Patent 5286371*, 1994.
(4) Moore, A.W.; Volk, H.F.; Merrow, J.K. *US Patent 4061600*, 1977.
(5) Gözmen, B.; Artok, L.; Erbatur, G.; Erbatur, O. Energy & Fuels **2002**, *16*, 1040-1047.
(6) Hesenov, A. Master Thesis, The Çukurova University, 2000.
(7) Fickinger, A.E. Master Thesis, The Pennsylvania State University, 2000.

EXFOLIATION OF ANTHRACITE: INDUSTRIALLY ACHIEVABLE?

Caroline E. Burgess Clifford, Amy Beil, Erin Boland, and Laurie Grove

The Energy Institute, The Pennsylvania State University, University Park, PA 16802

Introduction

Anthracite is an abundant and inexpensive natural resource that has not been fully exploited as a useful material. Historically, anthracite coal has been used as a slow-burning, high heating value fuel that had a use for domestic heating and cooking as well as industrial applications in iron smelting.[1] More recently, anthracite has found a market as a water filter medium, but only anthracite obtained as-mined is used because of the difficulty (and expense) in grinding.

Anthracite is an intriguing feedstock for premium carbon materials. Most anthracites contain 92–98% carbon, virtually all of which is present as aromatic carbon in large polycyclic sheets.[2] These sheets may contain thirty or more fused aromatic rings,[3,4] resulting in extraordinary properties such as highly ordered carbon that also exhibits a high ultra-microporosity pore volume. Exploiting one or more of these properties of anthracite to produce value-added products offers the potential for developing new markets for this resource.

Because anthracite has potential to be a valuable resource, research initiatives at PSU focused on exploiting the carbon properties of anthracite. Several projects explored graphitizing anthracite for use as feedstock in electrodes.[2,5-7] Pappano et al. examined the potential of anthracite as a filler for graphite production, to determine if it behaved similarly to petroleum coke (i.e., graphitization behavior, if material produced has properties suitable for industrial applications).[2,5] Atria et al. examined the graphitization of several Pennsylvania anthracites mixed with hydroaromatic hydrogen donor compounds (i.e., dihydrophenanthrene). The hydrogen donor was used to help break crosslinks in the anthracitic structure to enable the aromatic sheets to rearrange more easily into a graphitic structure.[6,7] Atria et al. suggested the hydrogen donor hydrogenated anthracite; therefore, another project explored the hydrogenation of small particles of anthracite for transforming coal into a pitch like material.[8] Several projects explored making activated carbons from anthracite.[9-13] Most recently, anthracite was investigated as a feedstock in an aluminum-smelting anode.[15] While the anode made from anthracite exhibited superior properties in most instances, the anode did not meet industrial standards due the mineral matter incorporated from coal. In all of these applications, a common factor was the anthracite was required to have a small particle size distribution and low mineral matter content, something not easily and inexpensively achieved by conventional methods.

Recently, the exfoliation of anthracite, a method to cause "flaking", "expansion," or "breaking apart" of the anthracite, was explored. The expectation is that exfoliation will open up the pores, reduce the particle size, and liberate mineral matter that is "trapped" in the organic matter of coal that cannot be liberated by conventional methods.

Previous investigations have demonstrated anthracite exfoliation.[16-19] Perchloric acid and perchloric/nitric acid mixtures have been intercalated into the anthracite; the resulting intercalated carbons were thermally shocked in order to produce a precursor for activated carbons.[16-19]

So, if anthracite can be exfoliated, why isn't exfoliation of anthracite occurring at the same level as other carbons? There are a few problems that must be examined and solved to exfoliate this extraordinary material and add value to it.

One major problem is the explosive nature of perchloric acid.[20] Perchloric acid can be extremely explosive, and very small quantities can cause extreme damage. For an industrial process to be developed to exfoliate anthracite, a safer way must be found to do so. While perchloric/nitric acids are the only materials to date to demonstrate anthracite exfoliation, there are several compounds that have been intercalated into graphites that produce exfoliation upon additional treatment.

In the literature, several methods have been reported for graphite exfoliation.[16-19,21,22] The most common method required intercalation of a mixture of concentrated nitric and sulfuric acids, followed by a thermal shock in an atmospheric muffle furnace to cause exfoliation.[23] Reversible exfoliation of graphite was achieved using bromine gas.[23] Recently, graphite was exfoliated using potassium metal as the intercalate and reacting the resulting intercalated material with ethanol.[24] Alkali metals, such as Li and Na, can be intercalated into carbon, but have not been shown to exfoliate upon reaction with water.[25-28] However, molybdenum and tungsten sulfide exfoliation was accomplished using *n*-butyllithium as the substrate to intercalate lithium, followed by reaction in water to cause exfoliation.[29-32] Very recently, graphite was exfoliated using supercritical CO_2 extraction.[33]

Even if exfoliation of anthracite can be achieved, safely, for what applications is it best suited? Exfoliated carbons are used to produce a specialized gasket material. Anthracites were exfoliated to produce a precursor for activated carbons.[16-19] Historically, anthracites along with metallurgical coke and petroleum coke were used as the main material in cathodes for aluminum and steel smelting.[34] Anthracites were attractive because of their abrasion resistance, but semi-graphite and other materials replaced anthracite because of superior electrical properties. The carbon materials used have evolved in recent years to using electrically calcined anthracites, electrographite, semi-graphite, and a variety of mixtures using these materials, mainly to reduce the electrical resistivity and increase the thermal conductivity of the electrode. Future electrodes will most likely include these carbons mixed with hard metals in order to continue lowering the electrical resistivity and increasing the thermal conductivity.[33] An exfoliated anthracite may have improved electrical properties compared to a raw anthracite, while still maintaining its abrasion resistance. Exfoliation, which ix expected to open up the pore structure, will certainly improve the possibility of making anthracite a medium to make activated carbons or an adsorption material.

The overall goal of the project is to develop a method of exfoliation that would be less explosive than the nitric/perchloric acid method. The following describes the methods of exfoliation tested and the extent of exfoliation achieved.

Experimental

Materials. Two coals have been chosen to test in this application. Proximate analysis information is provided in Table 1. The rank of these coals is semi-anthracite. Hongay coal was the coal shown to exfoliate in the literature, and is of semi-anthracite rank.[16-19] The other coal was chosen because it was shown to graphitize and was characterized extensively here at PSU.[5]

Acids were purchased from Sigma-Aldrich. *n*-Butyllithium in hexane, $LiBH_4$ in THF, and $NaBH_4$ in THF were also purchased from Sigma-Aldrich.

Acid Intercalation/Exfoliation. Coals were mixed with 50/50 mixtures of perchloric/nitric acids for 2 hours at room

temperature.[16-19] The mixture was filtered and the resulting paste was loaded into crucibles. The intercalated coal was then heated to 700ºC for about ~2 minutes. For the Summit coal, exfoliation was achieved, but for the Hongay coal, sample spontaneously combusted and the majority of the sample was lost.

Table 1. Properties of Hongay and Summit Anthracites

Coals	Rank	Moisture (wt %)	Ash (wt %)	Volatiles (wt %)	Fixed Carbon (wt %)
Hongay	Semi-anthracite	3.0	2.7	5.6	91.7
Summit	Semi-anthracite	2.6	17.6	11.1	71.2

Alkali Intercalation/Exfoliation. Dried glassware was assembled under an inert atmosphere. One gram of the anthracite was added to a round bottom flask; the reaction vessel was sealed for the remainder of the reaction. The alkali solution (10 mL) was added using the Sure/Seal technique to avoid exposure to air. The reaction was then stirred (or sonicated) for 4-5 days, with water flowing through the condenser to minimize solvent evaporation. After reaction, the sample was rinsed with solvent and filtered. The "intercalated anthracite" was then placed in water, and stirred/sonicated for several hours if needed. Table 2 is a summary of the reaction conditions used for each trial.

Table 2: Reaction conditions for alkali intercalation; for each reaction, the alkali was intercalated and then sonicated in water for several hours.

Sample ID	Reaction Time	Alkali Substrate	Solvent	Type of Mixing	Temperature (°C)
BG-1	4 days	*n*-butyllithium	Hexane	Stirring	25
BG-2	4 days	*n*-butyllithium	Hexane	Stirring	70
BG-3	4 days	*n*-butyllithium	Hexane	Sonication	40
BG-5	4 days	*n*-butyllithium	Hexane	Sonication	25
BG-6	4 days	$NaBH_4$	THF	Stirring	25
BG-7	4 days	$LiBH_4$	THF	Stirring	25

Characterization. To date, only scanning electron microscopy (SEM) has been used to characterize the coals before and after reaction. SEM is a useful qualitative method to detect exfoliation.[16-19] SEM was done on a Philips XL20 with a filament gun. The magnification range for the instrument is 20 to 50000X.

Results and Discussion

Acid Intercalation/Exfoliation. SEM micrographs were taken of the anthracite that was reacted. SEM was the method used to detect any obvious visual changes. Figure 1 shows the SEM micrographs of untreated Hongay coal and the slightly exfoliated Hongay coal. While it appears slight exfoliation occurred, this procedure did not fully exfoliate the coal. Most of the sample was lost, so very little characterization could be done on this sample. Figure 2 shows SEM micrographs of untreated Summit coal and the exfoliated Summit coal. Exfoliation did occur, but it took several attempts to accomplish exfoliation, with a fairly low amount of material yielded. We demonstrated that Summit coal, another semi-anthracite, exfoliated. Not all anthracites will exfoliate.[16-19]

Alkali Intercalation/Exfoliation. Several reactions were done with an alkali intercalation procedure, using a condenser and reacting the sample for 4 days with a lithium or sodium compound dissolved in a solvent, followed by reaction in water (see Table 2). Each sample was intercalated with the alkali metal, then reacted in water before doing any analytical tests on the material.

Figure 3 shows the SEM micrographs for samples BG-2 and BG 5. In all cases, the main visual change seemed to be to the surface of the anthracite. There appeared to be striations on the surface, probably due to the reaction of lithium with water, forming a strong base that may have etched the anthracite surface. In a few reactions, particularly BG-2, there appeared to be "fuzzy" particles on the surface, clumps of "puffy" particles, and some porous areas on some of the particles. Initially, we thought we had achieved exfoliation, but preliminary elemental examination by SEM indicated the "fuzzy" and "puffy" particles might in fact be silica based.

We will continue to analyze to see if these are indeed silica based particles and determine the source of the silica. Coals can contain silica based mineral matter; when enough coal is available, we will test the mineral matter content coal before and after reaction. Another source of silica could be the reaction vessels, which were glass. In this case, we would use a different type of reaction vessel, either alumina based or standard steel, as these materials are not affected by strong base.

(a)

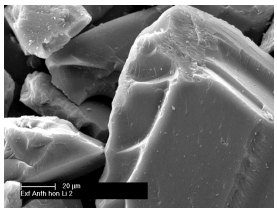

(b)

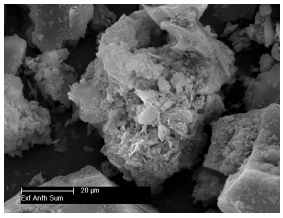

Figure 1. SEM micrographs of (a) untreated Hongay coal and (b) slightly exfoliated Hongay coal.

Conclusions

Exfoliation of anthracite has been achieved with two coals, but only using the perchloric/nitric acid method. We expected exfoliation of Hongay coal as this was reported in the literature.[16-19] Exfoliation of Summit coal was also achieved. We will continue to characterize the exfoliated coal by the following analytical methods: BET surface area, ash content, and particle size distribution. We will continue to explore alternative methods of exfoliation. We hope to produce enough exfoliated anthracite to make a small test electrode. To make exfoliation of anthracite useful in industry, an alternative method to the perchloric/nitric acid method must be developed.

Acknowledgement. Funding for this project was provided by the Consortium for Premium Carbon Products from Coal. We would like to thank Dr. Isao Mochida for a sample of Hongay anthracite.

(a)

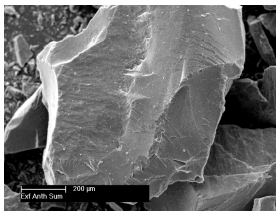

(b)

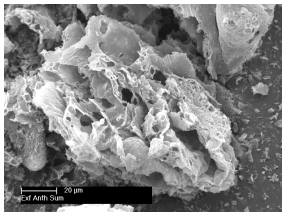

Figure 2. SEM micrographs of (a) untreated Summit coal and (b) exfoliated Summit coal.

(a)

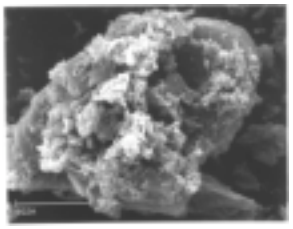

(b)

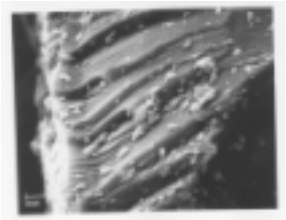

Figure 3. SEM micrographs of Hongay anthracite after reaction (a) "puffy" particles and (b) striations.

References

(1) Wallace, A.F.C., *St. Clair: A Nineteenth Century Town's Experience with a Disaster Prone Industry.* Alfred Knopf, New York, 1987.

(2) Pappano, P.J., Mathews, J.P., Schobert, H.H., *Preprints, Amer. Chem. Soc. Div. Fuel Chem.* **1999**, *44*, 567.

(3) Gerstein, B.C., Murphy, P.D., Ryan, L.M., In: *Coal Structure.* Academic Press, New York, 1982, Chapter 4.

(4) van Krevelen, D.W., *Coal: Typology–Chemistry–Physics–Constitution.* Elsevier, Amsterdam, 1981.

(5) Pappano, P.J., *M.S. Thesis.* The Pennsylvania State University, University Park, PA, 2001.

(6) Atria, J.V., *M.S. Thesis.* The Pennsylvania State University, University Park, PA, 1995.

(7) Atria, J.V., Zeng, S., Rusinko, F., and Schobert, H.H., *Preprints, Amer. Chem. Soc. Div. Fuel Chem.* **1994**, *39*, ??.

(8) Zengel, J.J., Schobert, H.H., Burgess, C.E., Andrésen, J.M., *Proc. 17th. Int. Pittsburgh Coal Conf.,* **2000**, Paper 11-03.pdf (CD-ROM).

(9) Walker Jr., P.L., Almagro, A., *Carbon*, **1995**, *33*, 239.

(10) Walker Jr., P.L., Imperial, G.R., *Fuel*, **1995**, *74*, 179.

(11) Gergova, K., Eser, S., Schobert, H.H., *Energy Fuels,* **1993**, *7*, 661.

(12) Gergova, K., Eser, S., Schobert, H.H., Klimkiewicz, M., Brown, P.W., *Fuel*, **1995**, *74*, 1042.

(13) Maroto-Valer, M.M., Andrésen, J.M., Schobert, H.H. *Proc. 1st World Conf. Carbon,* **2000**, *1*, 115.

(14) Maroto-Valer, M.M., Taulbee, D., Schobert, H.H.. *Preprints, Amer. Chem. Soc. Div. Fuel Chem.*, **1999**, *44*, 101.

(15) Badger, M., Mitchell, G., Katacen, O., Herman, N., Senger, B., Adams, A., and Schobert, H.H., "Co-coking Process for Anodes for Aluminum Electrolysis," DOE/CPCPC Final Report, June, 2001.

(16) Pettijean, D., Klatt, M., Furdin, G., and Hérold, A., *Carbon*, **1994**, *32* (3), 461.

(17) Albiniak, A., Furdin, G., Begin, D., Mareche, J.F., Kaczmarczyk, J., and Broniek, E., *Carbon*, **1996**, *34* (11), 1329.

(18) Furdin, G., *Fuel*, **1998**, *77* (6) 479.

(19) Daulan, C, Lyubchik, S.B., Rouzaud, J-N., and Béguin, F., *Fuel*, **1998**, *77* (6), 495.

(20) http://www.auburn.edu/administration/safety/crcperchloric.html and references therein.

(21) Toyoda, M., Katoh, H., and Inagaki, M., *Carbon*, **2001**, *39*, 2231-2237.

(22) Frackowiak, E., *Polish J. Chem.*, **1993**, *67*, 469-474.

(23) Chung, D.D.L., *J. Mat. Sci,* **1987**, *22* (12), 4190 and reference therein.

(24) Viculis, L.M., Mack, J.J., Kaner, R.B., *Science*, **2003**, *299*, 5611.

(25) Xheng, T., Xing, W., and Dahn, J.R., *Carbon*, **1996**, *34*(12), 1501-1507.

(26) Flandrois, S. and Simon, B., *Carbon*, **1999**, *37*, 165-180.

(27) Sandi, G., Winans, RE and Carrado, KA, *J. Electrochemical Soc.*, **1996**, *143* (5), L95-L98.

(28) Mochida, I., Kim, Y-J., Ku, C-H., Yoon, S-H. and Korai, Y., *Preprints, Amer. Chem. Soc. Div. Fuel Chem.,* **2001**, *46*(2), 584.

(29) Dines, M.B., *Mat. Res. Bull.,* **1975**, *10*, 287.

(30) Murphy, D.W., Di Salvo, F.J., Hull, G.W., and Waszczak, J.V., *Inorg. Chem.,* **1976**, *15* (1), 17.

(31) Kosidowski, L. and Powell, A.V., *Chem. Commun.,* **1998**, 2201.

(32) Golub, A.S., Shumilova, I.B., Zubavichus, Y.V., Jahncke, M., Süss-Fink, G, Danot, M, Novikov, Y.N., *J. Mater. Chem.,* **1997**, *7* (1), 163.

(33) Kaschak, D.M., Reynolds, III, R.A., Krassowski, D.W., Ford, B.M., U.S. Patent, "Graphite intercalation and exfoliation process," #20040033189, February 19, 2004.

(34) Sørlie, M. and Øye, H.A., *Cathodes in aluminum electrolysis,* Aluminum-Verlag GmbH: Dusseldorf, 1994, pp. 1-20.

COMPARISON OF ALTERNATIVE COAL DERIVED BINDER PITCHES FOR CARBON MATERIALS

Uthaiporn Suriyapraphadilok, Colin Jennis-McGroarty and John M. Andresen

The Energy Institute, Pennsylvania State University
407 Academic Activities Bldg., University Park, PA 16802

Introduction

Carbon anodes are manufactured from calcined petroleum coke, butt fillers and coal tar pitch. Since the demand of the coal tar pitch in the aluminum industry accounts for about 75% of the pitch market [1] and the production of coal tars is rapidly decreasing in the United States as well as throughout the world [2], the development of alternative binders were considered in this work. Coal tar binder pitches are traditionally obtained from coal tars that are the by-product of bituminous coal coking process used to make coke for blast furnaces in iron production. During the manufacturing of carbon anodes coal tar pitch is mixed with calcined petroleum coke, where petroleum coke is the by-product from the delayed coker in a refinery. Remaining parts of spent anodes from the aluminum production, namely butts, are also crushed and used as filler [3].

This work is focused on the development of alternative binders from various sources of pitches, namely, petroleum pitch (PP), coal-extracted pitch (WVU), and gasification pitch (GP). Petroleum pitch is a residue produced from heat-treatment and distillation of petroleum fractions. A production of coal-extracted pitch involves a prehydrogenation of coal followed by extraction using a dipolar solvent. Gasification pitches are distilled by-product tars produced from the coal gasification process. Each alternative pitch was mixed with a standard coal tar pitch (SCTP) at various mixtures and laboratory-scale test anodes were formed and studied.

Experimental

Materials. Four types of pitch were used in this study: two standard coal tar binder pitches (SCTP1 and -2), a petroleum pitch (PP), a coal-extraction pitch (WVU5), and a gasification pitch (GP1). The properties of each pitch are summarized in Table 1. Petroleum coke and recycled anode butts were crushed and aggregated into three different sizes: (i) Fines: >200 Tyler mesh size; (ii) Intermediate: 60-200 Tyler mesh size; and (iii) Coarse: <60 Tyler mesh size

Table 1. Properties of pitches

Property	SCTP1	SCTP2	PP	WVU5	GP1
Softening Point (°C)	112.5	111.9	111.9	112.2	115
Quinoline Insol. (wt%)	13.6	15.9	0.1	N.A.	<0.1
Toluene Insol. (wt%)	27.8	30.9	3.2	N.A.	N.A.
Coking Value (wt%)	N.A.	57.9	47	50.3	N.A.
Ash Content (wt%)	N.A.	0.29	0.08	0.2	N.A.
Specific Gravity @ 25°C	N.A.	1.34	1.246	1.25	N.A.

Compositions. All experimental-scale anodes in this work were made using the following compositions:

Pitch:Butt:Coke = 22:29:49

Fine:Intermediate:Coarse = 40:35:25

Mixing and Forming. The aggregate fillers and binders, which weighed about 15 grams in total, were mixed at about 50°C above the softening point of the pitch mixture. The CARVER cylindrical mold with an inside diameter of 28.58 mm was preheated to about 10°C above the softening point of the pitch mixture. The hot mix was placed into the mold and rapidly pressed at 9,000 psi for 2.5 minutes. The final green anode was cylindrical in shape with typically 28.60 mm. in diameter and 13.00-14.00 mm in height.

Baking. The green anodes were baked with a low heating rate to about 1075°C over a period of 5-6 days prior to cooling. The temperature profile was 25°C/hr from 25°C to 125°C; 3.5°C/hr from 125 to 575°C; 100°C/hr from 575 to 1075°C; hold at the temperatures between 950 and 1075°C for 6 hours; and cool down in the furnace to room temperature.

Measured Properties. The green and baked anodes were weighed to the nearest 0.001 gram and their dimensions were measured by a caliper to the nearest 0.01 millimeter. The apparent densities of both green and baked anodes were calculated by a ratio of mass and volume. The amount of pitch loss after baking was calculated by assuming that all the weight loss was resulting from the pyrolysis of pitch. Finally, the volume change of the baked anodes relative to the green ones was calculated.

Results and Discussion

Each type of pitch was mixed with the standard coal tar pitch (SCTP) at various percentages while maintaining the total pitch content of 22 wt% for the anode aggregate. Figures 1-3 show the apparent and baked densities of the green and baked anodes, %pitch loss and %volume change of the experimental-scale anodes of the SCTP2+PP, SCTP2+WVU5 and SCTP1+GP1 mixtures, respectively. The addition of PP gives an improvement in apparent densities for both green and baked anodes (Figure 1(a)). For PP the green apparent density increases from 1.719 g/cm^3 for the SCTP2 only to 1.736 g/cm^3 for the PP only, while the baked apparent density increases from 1.542 g/cm^3 for the SCTP2 only to 1.561 g/cm^3 for the PP only. However, these trends do not keep up for the addition of WVU5 and GP1. The addition of WVU5 gave slightly poorer densities of the green anode and the baked anodes (Figure 2(a)) and . The green apparent density of the SCTP2+WVU5 decreases from 1.719 g/cm^3 for the SCTP2 only to 1.703 g/cm^3 for the WVU5 only, while the baked apparent density decreases from 1.542 g/cm^3 for the SCTP2 only to 1.491 g/cm^3 for the WVU-5 only. For GP1, the green apparent density of the SCTP1+GP1 increases from 1.71 g/cm^3 for the SCTP1 only to 1.73 g/cm^3 for the GP1 only, while the baked apparent density decreases from 1.60 g/cm^3 for the SCTP1 only to 1.54 g/cm^3 for the GP1 only.

The main factor for the reduction in baked density is due to the increased loss of binder during baking as shown in Figures 1(b), 2(b) and 3(b). The pitch loss is defined as a reduction in anode weight over initial pitch content (22%) since the weight loss of the coke material can be neglected. The addition of GP1 to the SCTP1 tends to give the highest pitch loss among all three mixtures (Figure 3(b)), while the addition of PP gives a slightly increase in pitch loss compared to the SCTP2 only (Figure 1(b)). Also, for all SCTP + alternative pitch studied here, the addition of the alternative pitch gives a lower volume change of the baked anodes compared to the baked anodes with SCTP only as shown in Figures 1(c), 2(c), and 3(c).

Of all pitch mixtures studied here, the addition of an alternative pitch shows quite similar trends, i.e. SCTP gives a lower pitch loss and higher volume change compared to the pure alternative pitches. Among all three alternative pitches, the addition of WVU5 and GP1 shows poorer properties of the anodes among all three mixtures, i.e. high pitch loss and low baked densities, while the addition of PP shows little impact on the properties of the anodes for most SCTP-PP compositions. The addition of GP1 and WVU5 also gives

comparable anode properties when the SCTP:WVU5/GP1 ratio is greater than 50:50.

Conclusions

The results of this study show that the petroleum pitch and coal-derive pitch offer a potential to be used as additives to the standard coal-tar pitches for use as binders in aluminum anode production. Further work should be conducted to study the causes of improvement of adding alternative pitches to better understanding the roles of the binders from various types of pitches.

Acknowledgement. The authors would like to thank Kopper Industries for the coal tar and petroleum pitches; Sasol CarboTar for the gasification pitches; West Virginia University for the coal-derived pitches; and Alcoa for the calcined petroleum coke and recycled carbon anode butt materials.

References

[1] CRU International, Carbon Products – Aluminum Raw Materials, London, U.K., May 2002.
[2] Rusinko F, Andresen JM, Adams A, Chapter 13 in Great Lakes Carbon Corp. 6th Carbon Conference (Houston. USA): 2000.
[3] Schmidt-Hatting W, Kooijman AA, Perruchoud R, Light Metals, 705-720, 1991.

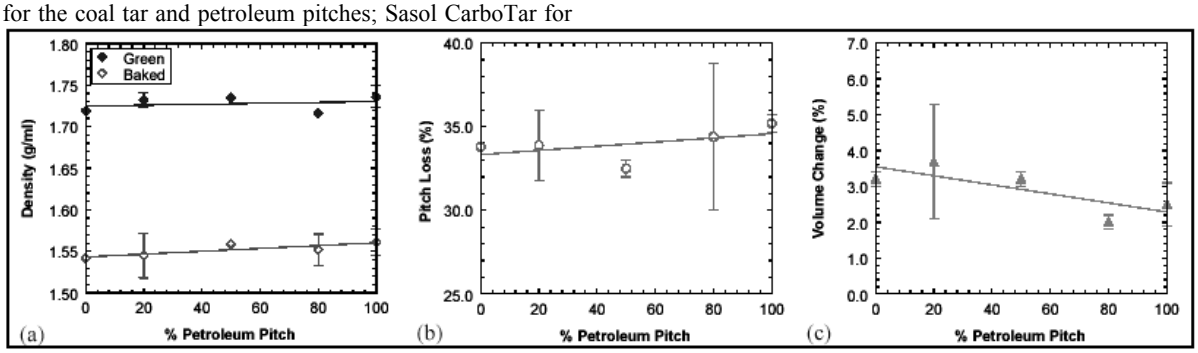

Figure 1. Properties of green and baked anodes of various compositions between SCTP-2 and PP: (a) apparent densities of green and baked anodes, (b) % pitch loss, and (c) % volume change. The error bars show the standard deviations of each experimental set. The dashed lines show the linear relationship of the mixtures.

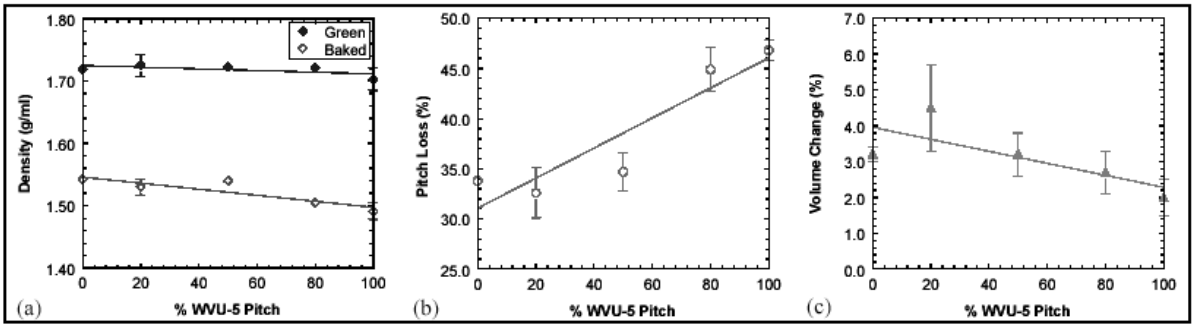

Figure 2. Properties of green and baked anodes of various compositions between SCTP-2 and WVU-5 Pitch: (a) apparent densities of green and baked anodes, (b) % pitch loss, and (c) % volume change. The error bars show the standard deviations of each experimental set. The dashed lines show the linear relationship of the mixtures.

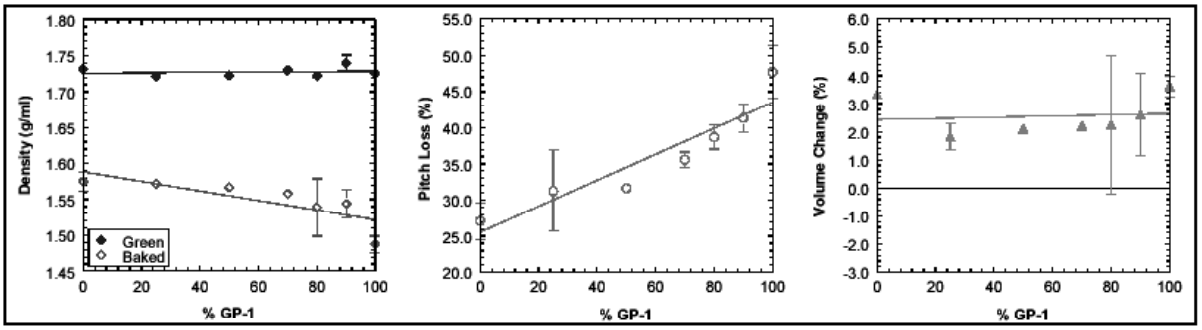

Figure 3. Properties of green and baked anodes of various compositions between SCTP-1 and GP-1: (a) apparent densities of green and baked anodes, (b) % pitch loss, and (c) % volume change. The error bars show the standard deviations of each experimental set. The dashed lines show the linear relationship of the mixtures.

SEQUENTIAL EXTRACTION OF COAL TO OBTAIN SPECIFIC RAW MATERAILS FOR CHEMICALS

Kouichi Miura, Hiroyuki Nakagawa, Ryuichi Ashida, and Kyosuke Nakagawa

Department of Chemical Engineering, Kyoto University
Kyoto Daigaku Katsura, Nishikyo-ku
Kyoto 615-8510, JAPAN

Introduction

The authors have recently presented a new coal solvent extraction method that enhances the extraction yield dramatically[1-4]. The method extracts coal using a flowing stream of non-polar solvent such as tetralin or 1-methylnaphthalene, or inexpensive coal derived oils: carbol oil or creosote oil, under 10 MPa at around 350°C. When tetralin was used as the solvent, the extract yield reached 65 to 80% for bituminous coals at 350°C, and the extract was separated into about 25 to 40% of soluble fraction at room temperature (soluble) and about 40% of solid fraction which precipitated from the extract at room temperature (deposit). The soluble and deposit obtained through the extraction were almost free from inorganic materials. Thus, this method was found to be effective for recovering clean fuels from various kinds of coals under rather mild conditions. Similar researches have been performed in Japan for producing ashless coal, so-called HyperCoal[5,6].

To utilize these clean carbonaceous materials for specific purposes, however, their fractionation and more detailed characterization are essential. Then the deposit obtained at 350°C from two bituminous coals were further extracted by tetralin at different temperatures below 350°C to fractionate the coal into 6 to 8 fractions, and the fractions were characterized by various analyses.

Experimental

Coal Samples. A subbituminous coal, Prima coal from Indonesia, and a bituminous coal, Gregory coal from Australia, were used in this study. The ultimate analyses of the coal samples used are given in Table 1.

Table 1. Analyses of coals used.

Coal	Ultimate analysis [wt%, d.a.f.]				Atomic ratio [-]		Ash
(Abbreviation)	C	H	N	O (diff.)	H/C	O/C	[wt%, d.b.]
Prima (PR)	76.3	5.5	1.4	16.7	0.87	0.16	5.4
Gregory (GR)	83.0	5.3	1.6	10.1	0.77	0.09	6.4

Experimental Procedure for Solvent Extraction. First, the coal samples were extracted at 350°C under 10 MPa by tetralin as stated in previous papers[1,2]. About 0.2 to 4 g of coal samples were charged on a filter (11.2 mm OD and 0.5 μm opening) in an extractor made of Swagelok®. Tetralin was supplied continuously using a high-pressure pump at the flow rate of 1 ml/min. The extractor was heated at the rate of 10°C/min to 350°C, where it was kept for 90 min. The coal fractions extracted and solubilized in the solvent at the extraction temperatures came out from the extractor with the flowing solvent, but a part of the solubilized components precipitated as solid when the solvent flow was cooled to room temperature. The solid that precipitated was called deposit in this paper. The soluble components are called "soluble" here. The deposit thus obtained is judged to be the coal fraction extracted between 25°C and 350°C. From this point of view, we call the deposit obtained by the 350°C extraction "Frac.+25-350". Then the residue and the soluble obtained by the 350°C extraction are, respectively, referred to as "Frac.+350" and "Frac.-25". Next, Frac.+25-350 was subjected to the extraction at 150°C, which separated Frac.+25-350 into Frac.+25-150 and Frac.+150-350. By subjecting Frac.+150-350 at a higher temperature the fraction can be separated into another two fractions. By repeating this sequential extraction procedure, GR coal and PR coal were, respectively, separated into 7 and 5 fractions. All the fractions except Frac.-25 were obtained as solids. Frac.-25 which was still soluble in tetralin at room temperature was mixed with an excessive amount of n-hexane to precipitate a part of it as solid. The solid fraction obtained by this operation is called "TS-HI" hereafter. Through these procedures GR coal and PR coal were, respectively and finally, separated into 8 and 6 fractions.

Analyses of the Products. The fractions obtained were characterized through various analyses. Ultimate analyses of the solid fractions were performed using a CHN analyzer (Yanaco, CHN-500). The laser desorption time-of-flight mass spectrometry (Shimadzu/Kratos KOMPACT-MALDI-II) was used to estimate the molecular mass distributions of the fractions obtained and the parent coal. Thermal analysis of each solid sample was performed using a thermobalance type reactor (Shimadzu; TGA50) a thermomechanical analyzer (Shimadzu; TMA50) during whichthe sample was heated in a nitrogen flow at the rate of 10°C/min up to 900°C.

Results and Discussion

Table 1 lists the yield of each fraction obtained for both PR and GR coals. For PR coal, the yield of Frac.-25 was as large as 0.31 kg/kg-coal daf, whereas that of Frac.+25-150 was only 0.04 kg/kg-coal daf. The sum of the yields of Frac.-25, Frac.+250-350, and Frac.+350 reached as large as 0.88 kg/kg-coal daf, indicating that PR coal mainly consists of two discrete fractions, Frac.-25 and Frac.+250 (Frac.+250-350 and Frac.+350). For GR coal, the yield of Frac.-25 was 0.37 kg/kg-coal daf, even larger than that in the case of PR coal. The yields of the fractions obtained at the fractionation temperature of between 25°C and 300°C were less than 0.05 kg/kg-coal daf. The main constituents of GR coal can be said to be Frac.-25, Frac.+300-350, and Frac.+350.

Figures 1 shows the molecular mass distributions of the fractions obtained from GR coal. The parent coal had a distribution consisting of a sharp peak at around 300 and a very broad peak at around 4000 in molecular mass (MM). Frac.-25 consisted solely of the compounds less than 600 in MM, corresponding to the smaller molecular mass peak in the distribution of the parent coal. For Frac.+25-150, the larger molecular mass peak in the distribution of the parent coal appeared a little. The peak of Frac.+150-200 at around 4000 in MM was more distinct than that of Frac.+25-150. The position of larger molecular mass peak in the distribution of the fraction gradually shifted to larger molecular mass with the increase of fractionation temperature and that of Frac.+350 was at around 4500 in molecular mass. These results show that the parent coal is a mixture of different molecular mass compounds and the proposed fractionation method actually separated the coal into different molecular mass compounds. The results also supports the so called "host-guest theory" for coal structure.

Next, the solid fractions obtained were characterized by ultimate analysis as given in Table 2. The atomic H/C ratio decreased with the increase of the fractionation temperature range, implying that the fraction obtained at the lower fractionation temperature range was richer in aliphatic components. The contents of carbon and hydrogen for all the fractions except for Frac.-25 roughly decreased with the increase of the fractionation temperature. The oxygen content increased with the increase of the fractiona-tion temperature range except that the oxygen contents of Frac.-25. Thus, it was found that

this method could separate coal into the fractions which have different elemental compositions and so might have different chemical structures. Most of ash in the parent coal was retained in Frac.+350 as reported in the previous papers [1-4]. The other fractions, containing less than 0.6wt% ash for PR coal or less than 1.4wt% ash for GR coal, were rather clean, suggesting that these fractions could be utilized as starting materials of various carbon materials.

The solubility parameter, δ, is calculated by using Painter's correlation[7] given for each fraction for GR coal as reference. It increased with increasing fractionation temperature as expected.

Figure 2 shows TG curve for each fraction for GR coal. The volatile yield decreased with the increase of the fractionation temperature range and the volatile yields of the Frac.-25 (TS-HI) and Frac.+25-150 were larger than the yield of the parent coal. Figure 3 shows thermomechanical analysis curve of each fraction obtained from GR coal. The softening temperatures can be estimated from these curves to be 240ºC for Frac.-25, 268ºC for Frac.+25-150, 318ºC for Frac.+150-200, and 349ºC for Frac.+200-250. The softening temperature of the fraction increased with the increase of the fractionation temperature, which means that coal was well fractionated in terms of fusibility by the proposed method. curves of Frac.-25 and Frac.+25-150 were rather close to the displacement curve of a naphthalene-based anisotropic pitch synthesized for producing high per-formance carbon mate-rials. This result suggests a possibility of uti-lizing the fraction as a feedstock of high performance carbon materials.

Acknowledgement. The supports from the Ministry of Education of Japan (Grant No.737) and Kobe Steel, Ltd. are acknowledged.

References

1. Miura, K.; Shimada, M.; Mae, K., *15th Pittsburgh Int. Coal Conf*., Paper No.30-1, Pittsburgh, 1998.
2. Miura, K.; Shimada, M.; Mae, K.; Huan, Y.S., *Fuel*, 2001. **80**, 1573-1582.
3. Miura, K.; Mae, K.; Shindo, H.; Ashida, R.; Ihara, T., *J. Chem. Eng. Japan*, 2003, **36**, 742-750.
4. Miura, K.; Nakagawa, H.; Ashida, R.; Ihara, T., *Fuel*, 2004, **83**, 733-738.
5. Okuyama, N.; Inoue, Y.; Shigehisa, T.; Shinozaki, S., *Proc. 39th Conf. Coal Science* (in Japanese), p.93, 2002.
6. Yoshida, T.; Takanohashi, T.; Sakanishi, K.; Saito, I.; Fujita, M.; Mashimo, K., *Fuel*, 2002, **81**, 1463-1469.
7. Painter, P.C.; Graf, J.; Michael, M.C., *EnergyFuels*, 1990, **4**, 379-384.

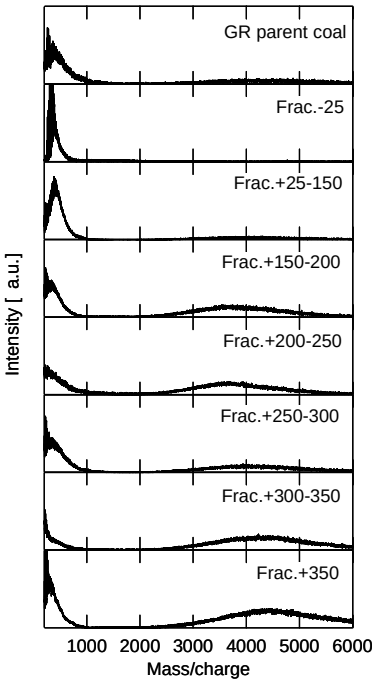

Figure 1. Molecilara mass distribu- tion of each fraction for GR coal.

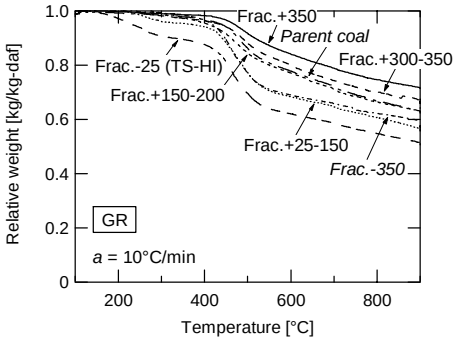

Figure 2. TG curve of each fraction for GR coal.

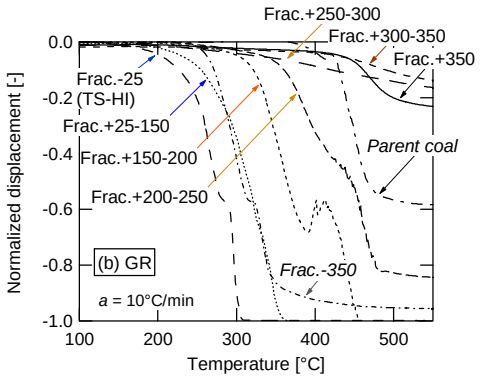

Figure 3. TMA curve of each fraction for GR coal.

Table 2. Yield, ultimate analysis, and solubiliuty parameter of each fraction

Coal	Fraction	Yield	δ	Ultimate analysis [wt%, d.a.f.]				Atomic ratio [-]		Ash
		[kg/kg-coal daf]	[MPa**0.5]	C	H	N	O (diff.)	H/C	O/C	[wt%, d.b.]
PR	Frac.-25 (calc.)	0.31		74.7	6.4	0.3	18.6	1.02	0.19	-
	Frac.+25-150	0.04		80.9	6.2	2.1	10.8	0.92	0.10	0.6
	Frac.+150-250	0.06		80.2	5.7	2.0	12.0	0.85	0.11	0.3
	Frac.+250-350	0.21		80.4	5.4	2.1	12.0	0.81	0.11	0.3
	Frac.+350	0.36		78.9	4.9	1.9	14.3	0.74	0.14	8.8
	Parent coal			76.3	5.5	1.4	16.7	0.86	0.16	5.4
GR	Frac.-25 (calc.)	0.37	22.46	81.1	5.4	0.8	12.7	0.80	0.12	0.2
	Frac.+25-150	0.01	23.21	85.4	5.9	2.1	6.5	0.82	0.06	0.3
	Frac.+150-200	0.05	24.44	84.5	5.5	2.1	7.9	0.78	0.07	0.6
	Frac.+200-250	0.02	24.42	84.1	5.5	2.2	8.2	0.78	0.07	1.2
	Frac.+250-300	0.01	25.19	83.5	5.3	2.0	9.2	0.75	0.08	1.1
	Frac.+300-350	0.10	25.57	84.0	5.1	2.0	8.9	0.73	0.08	1.4
	Frac.+350	0.44	25.46	84.0	5.2	2.1	8.7	0.74	0.08	12.9
	Parent coal		25.06	83.0	5.3	1.6	10.1	0.76	0.09	6.4

DISTRIBUTION OF POLYCYCLIC AROMATIC HYDROCARBONS (PAHS) AND INORGANIC TRACE ELEMENTS IN LIME SPRAY DRYER (LSD) ASH

Ping Sun, Panuwat Taerakul, Linda K. Weavers, Harold W. Walker, and Danold W Golightly

Department of Civil and Environmental Engineering and Geodetic Science, The Ohio State University
470 Hitchcock Hall
2070 Neil Avenue
Columbus, OH, 43210

Introduction

Flue gas desulfurization (FGD) by-product is a residual material from processes used to remove sulfur dioxide from flue gas in coal combustion processes. Approximately 26 million metric tons of FGD by-products are produced in the United States every year with more than 18 million metric tons (72% of total production) sent to landfills[1,2]. To minimize landfilling, studies have been conducted to examine applications of FGD by-product, such as in construction, agriculture and mine reclamation[3,4]. Prior to reuse, FGD by-product must be characterized for potential environmental hazards.

The lime spray dryer (LSD) system is the most common dry FGD technique[1]. A fine spray of slaked lime ($Ca(OH)_2$) is injected into the scrubber, reacting with sulfur oxides resulting in the formation of calcium sulfate or calcium sulfite. Moisture in the reacted lime is lost due to heat from the flue gas. The resulting dry calcium sulfite/sulfate mixture, along with fly ash, is later collected as "LSD ash" by electrostatic precipitation or a baghouse[1].

PAHs are a class of organic compounds that are persistent in the environment[5]. Many PAHs are carcinogenic and/or mutagenic[6]. A major source of PAHs in the environment is from fossil fuel combustion processes (i.e., coal burning)[7]. Our previous work showed that PAH concentrations were related to organic carbon content in the LSD ash[8]. Studies on PAHs in fly ash samples also show that PAHs are mainly associated with carbonaceous materials, which was believed to be the dominant factor for adsorption of PAHs in fly ash[9]. High carbon content material such as unburned carbon has also been suggested to be an effective material for capturing volatile trace elements, such as As, Se and Hg in flue gas[10].

The purpose of this study was to examine the hypothesis that PAHs and trace inorganic elements mainly partition to carbonaceous material in LSD ash. If this hypothesis is true, the concentration of PAHs and trace inorganic elements in LSD ash in the absence of carbonaceous material will be much lower and the environmental impact of LSD ash utilization will be correspondingly less.

Experimental

LSD ash sampling. LSD ash was sampled at boiler #8 at the McCracken Power Plant on The Ohio State University. Multiple grab samples were collected and subsequently stored at 4°C until the chemical measurements were performed.

LSD ash fractionation. A 140 mesh (106 μm) sieve was used to separate LSD ash samples into two fractions: >140 mesh and <140 mesh. Of the initial 10 g LSD ash sample, 1.5 g was retained on the top of 140 mesh sieve. This >140 mesh fraction was further separated using a lithiumheteropolytungstate (LST) solution with a specific gravity of 1.84 g/mL. 0.5 g of >140 mesh sample and 10 mL of LST solution were mixed in a glass centrifuge tube. The unburned carbon floated to the top of the centrifuge tube. The solids were decanted, collected on filter paper, and washed with 50 mL high purity water to remove the LST solution. Unburned carbon samples were then dried in an oven at 60 ºC for 12 hours. Organic carbon content was measured as described elsewhere[8].

PAH analysis. An ultrasonic probe with a 1.90 cm diameter titanium tip (Fisher Scientific), operating at 20 kHz, was used for ultrasonic extraction. In all experiments, the output control knob was set at 10 (full power) and pulse mode (energy on 50% of time and off 50% of time). Effective sonication time was 1.5 minutes. A 20g sample was weighed into the beaker and mixed with 100 mL toluene and spiked with a 16 PAH standard containing 1 μg of each PAH. The end of the probe tip was located 1.3 cm below the surface of the liquid but above the solid. After extraction, the extract was decanted, filtered through a Whatman GF/B filter in a Buchner funnel and then collected in a filtration flask. The ultrasonic extraction was repeated twice with two additional 100 mL aliquots of solvent. After the third extraction, all extracts were poured into the Buchner funnel and rinsed with 20~30 mL solvent. The collected extract was then condensed using a Kuderna-Danish (K-D) concentrator to less than 10 mL. High purity nitrogen gas (Praxair) was used to further blowdown the extract to 1mL for GC/MS analysis. Details of the GC/MS analysis method are stated elsewhere[8]. Twenty grams of LSD by-product sample without adding the PAH standard were also extracted by ultrasound (this is not a blank). Duplicate experiments were conducted to ensure reproducibility.

Inorganic analysis. Inorganic analyses were accomplished by digesting approximately 150 to 300 mg samples by a microwave heating method with a combination of 10 mL deionized water, 6-mL nitric acid, 2 mL hydrochloric acid, and 2 mL hydrofluoric acid. This was followed by a second microwave heating with 20 mL boric acid.

A Vista Pro simultaneous inductively coupled plasma optical emission spectrometer system was used to determine selected metals in sample solutions. As and Se were analyzed by a SpectrAA 880Z Zeeman graphite furnace atomic absorption (AA) spectrometer and Hg was determined by AA with a vapor generation accessory. All analyses included controls such as duplicates, blanks, and check standards for every fifteen samples or less.

Results and Discussion

Fractionation and characterization of LSD ash. Inorganic element concentration and organic carbon content of LSD ash on a weight percent for separated fractions are listed in Table 1. The results show that the organic carbon content of >140 mesh fraction was much higher than the parent LSD ash sample (e.g. 48.5% vs 7.0%), which indicates that sieving effectively enriched the carbonaceous fraction above the 140 mesh sieve. Compared to the >140 mesh fraction and parent LSD ash sample, the <140 mesh fraction had a much lower organic carbon content of 2.0%. Similar to organic carbon, the distribution of Al, Fe and Si concentrations was larger in the >140 mesh fraction which indicates enrichment of fly ash constituents. On the other hand, the Ca and S concentrations in the >140 mesh were much less than in the parent LSD ash, and the <140 mesh fraction was enriched in Ca. Results in Table 1 also show that unburned carbon was separated from the >140 mesh fraction using LST solution. The LST extract had an even higher carbon content (88.7%) compared to 48.5% for the >140 mesh fraction.

PAH Distribution in LSD ash. The concentration of total PAHs in parent LSD ash and the separated >140 mesh and <140 mesh fractions are listed in Table 2. The total PAH concentration was 78.7 μg/kg in >140 mesh fraction, which was higher than 14.1 μg/kg in parent LSD ash and 18.9 μg/kg in <140 mesh fraction. Since the mass percentage of the >140 mesh fraction was about 15% of the total LSD ash, the high concentration of PAHs in carbon-enriched fraction demonstrates that PAHs were mainly associated with the carbonaceous material in LSD ash.

Table 1. Major Constituents in Different Fractions

Elements /Parameter	Unit	Parent LSD Ash	<140 mesh	>140 mesh	>140 mesh	
					>1.84 g/mL	<1.84 g/mL
Ca	%	30.9	30.5	11.7	15.2	0.4
S	%	13.7	13.4	3.6	6.0	0.2
Si	%	4.2	1.9	3.8	9.7	6.8
Fe	%	2.6	2.1	6.3	10.5	1.2
Al	%	1.6	1.0	2.8	4.9	2.4
Org.C	%	7.0	2.0	48.5	26.2	88.7
Spec. S.A.	m^2/g	7.1	6.5	4.3	15.0	7.5

The preferential sorption of PAHs to the >140 mesh fraction may be attributed to surface area, pore size, and surface chemistry of this fraction. The surface area of LSD ash and different fractions are shown in Table 1. The >140 mesh fraction had slightly lower surface area compared to the <140 mesh fraction perhaps since the particle size was larger. However, the SEM results of >140 mesh samples showed a lot of partially burned carbon with pores, which may have provided more adsorption sites for PAHs.

Table 2. PAHs, As, Se and Hg in Different Fractions

Inorg /Org Comp.	Unit	Parent LSD Ash	<140 mesh	>140 mesh	>140 mesh	
					>1.84 g/mL	<1.84 g/mL
As	mg/kg	38.8	46.4	94.8	N/A	N/A
Se	mg/kg	27.6	31.9	3.7	N/A	N/A
Hg	µg/kg	507	552	615	550	540
Tot.PAHs	µg/kg	14.1	18.9	78.7	N/A	N/A

N/A: not available

The <140 mesh fraction had lower organic carbon content, which should result in a lower PAH concentration if PAHs were mainly associated with carbon. However, the results show that PAH concentration on this fraction was approximately the same as that in the parent LSD ash. Thus, besides organic carbon content, other factors might affect PAHs on <140 mesh fraction. Mastral *et al*. showed that limestone helped to control the PAHs emission in gas phase by adsorption[11]. In LSD system, the fine spray of $Ca(OH)_2(s)$ may sorb PAHs in flue gas and result in PAH presence in the < 140 mesh fraction.

Inorganic Composition in LSD Ash. Hg concentrations in the three fractions were similar at around 500-600 µg/kg as shown in Table 2. $Hg^0(g)$ and $HgCl_2(g)$ have been reported to be captured on carbon surfaces via chemisorption[12]. It has also been found that $Ca(OH)_2(s)$ can effectively capture $HgCl_2(g)$ by physisorption[13]. Thus, both carbon and $Ca(OH)_2(s)$ are able to sorb Hg, which may be the reason that the Hg concentration in all three fractions were similar.

The concentration of As in the >140 mesh fraction was 94.8 mg/kg, which was much higher than concentrations in either the parent LSD ash or in the <140 mesh fraction, 38.8 and 46.4 mg/kg, respectively. A reason that As was preferentially associated with the >140 mesh fraction may due to the sorption of As onto fly ash particles prior to reaction with hydrated lime[14].

Se is completely vaporized during combustion and could be removed in ash as oxides and sulfates[15]. Therefore, Se would be expected to be primarily in the >140 mesh fraction. However, our study showed Se in the >140 mesh fraction was 3.7 mg/kg, much lower than found in both parent LSD ash and the < 140 mesh fraction. A previous study showed that Se was effectively captured by hydrated lime at temperature of 400 to 600 °C, forming calcium selenite[16]. This might explain why Se concentration was high in calcium enriched <140 mesh fraction.

Conclusions

In this study, the collected LSD ash samples were separated into several fractions having different carbon contents. The results show that the concentration of PAHs and As were higher in >140 mesh fraction with high organic carbon content, while concentration of Se was high in <140 mesh fraction with a low organic carbon content. Hg was found at similar concentrations in all fractions including the unburned carbon fraction. In addition, the significant concentrations of PAHs, As, Se and Hg in the <140 mesh fraction showed that $Ca(OH)_2(s)$ may also sorb these compounds from the flue gas.

Acknowledgement. The authors would like to thank the Ohio Coal Development Office (OCDO) and The Ohio State University for funding. Help from Mr. Kevin Jewell and C. M. Cheng are gratefully acknowledged.

References

1. U.S. Environmental Protection Agency. Wastes form the Combustion of Fossil Fuels, Volume 1 and 2- Methods, Findings, and Recommendations, Report to Congress, EPA 530-S-99-010, March 1999.
2. Kalyoncu R. Coal combustion products, U.S. Geological Survey Minerals Yearbook-1999, U.S. Geological Survey, Reston, VA., 1999.
3. Walker, H.; Taerakul, P.; Butalia, T.; Wolfe, W.; Dick, W.; Minimization and Use of Coal Combustion By-Products: Concepts and Applications. In: Ghassemi A. editors. The Handbook of Pollution Control and Waste Minimization, New York: Marcel Dekker, 2002.
4. Lamminen, M.; Wood, J.; Walker, H. W.; Chin, Y-P.; He, Y.; Traina, S.; *J. Env. Quality* **2001**, 30, 1371.
5. Henner, M.; Schiavon, M.; Morel, J.; Lichtfouse, E.; *Analusle* **1997,** 25, M51.
6. Denissenko, M.; Pao, A.; Tang, M-S.; Pfeifer, G.; *Science* **1996**; 274, 430.
7. Mastral, A.; Callen, M.; *Environ Sci Technol* **2000**, 34, 3051.
8. Sun, P.; Weavers, L. K. preprint of 225th American Chemical Society Annual Conference, New Orleans, LA, March 23-27, 2003.
9. Low, G.K.C.; and Batley, G.E.; *Environ. Sci. Technol*. **1988**, 22, 322
10. Hower, J.; Trimble, A.; Eble C.; Palmer C.; and Kolker A.; *Energy Sources* **1999**, 21:511
11. Mastral, A..M.; Garcia, T.; Callen, M.S.; Lopez, J.M.; Murillo, R.; and Navarro, M.V.; *Energy & Fuels* **2001**, 15, 1469.
12. Huggins, F.E; Huffman, G.P.; *Energy& Fuel* **1999**, 13, 114.
13. Galbreath, K.C; Zygarlicke, C.J.; *Fuel Proc. Tech.* **2000**, 65-66, 289.
14. Sterling, R.O.; Helble, J.J.; *Chemosphere* **2003**, 1111.
15. Querol, X.; Fernández-Turiel, J.L; López-Soler, A.; *Fuel* **1995**, 74, 331.
16. Ghosh-Dastidar A.; Mahuli, S.; Agnihotri, R.; and Fan L-S.; *Environ. Sci. Technol*. **1996**, 30, 447.

CARBON DIOXIDE REFORMING OF METHANE OVER SUPPORTED MOLYBDENUM CARBIDE CATALYSTS

D. Treacy and J.R.H. Ross

Centre for Environmental Research, University of Limerick, Ireland

Introduction

CO_2 reforming of CH_4 is a subject of considerable interest due to the ability of the reaction to produce synthesis gas with low H_2/CO ratios (~1); higher ratios can be obtained by combining the process with steam reforming or partial oxidation. Ni-based catalysts are commonly used for reforming reactions but suffer from problems due to carbon deposition. Noble metal catalysts, in particular Pt-ZrO_2, have been shown to have high activities for CO_2 reforming while resisting significant C deposition [2,3]; however, because of their relatively high cost, their potential for use as CO_2 reforming catalysts is limited. The group VI transition metal carbides, WC and Mo_2C, have been reported to have catalytic properties similar to those of the noble metals and York *et al.* [4,5,6] have shown that unsupported Mo_2C and WC have good activities as CO_2 reforming catalysts. However, they found that these catalysts deactivated after short periods of use at ambient pressures. We have shown that the deactivation of the carbides is caused by the formation of the corresponding oxides [7]. In this paper, we show that when Mo_2C is supported on a variety of supports, the resultant catalysts are somewhat more stable.

Experimental

Catalyst Preparation. The supports used in this study, ZrO_2 (Norton), Al_2O_3 (Alkan) and SiO_2 (Alfa), were calcined at 800°C for 15 h in a flow of 50 cm^3min^{-1} of air. The support was then impregnated with a solution of heptamolybdate (Johnson Matthey) with, when appropriate, the nitrates of the promoter species (Co, Ni or Bi) and calcined once more before carbiding) in flow of 20 %v/v CH_4/H_2 following a procedure outlined by Lee *et al.* [8], ramping the temperature to 750°C at a ramp rate of $1Kmin^{-1}$.

Catalyst Testing. The CO_2 reforming of CH_4 was carried out in the quartz plug flow reactor used for carbiding. The reactants compositions were typically $CO_2/CH_4/N_2$ = 50/50/5 $cm^{-1}min^{-1}$. The N_2 was included as an internal standard.

Characterisation by Raman Microprobe Spectroscopy. The 514.5 line of an Ar^+ ion laser was used for excitation. Measurements were made at room temperature.

Results and Discussion

Catalyst Activity. Fig. 1. shows the results of CO_2 reforming of CH_4 at 950°C and atmospheric pressure using the 5 wt% Mo_2C-Al_2O_3, 5 wt% Mo_2C-ZrO_2 and 5 wt% Mo_2C-SiO_2 catalysts. The performance of a sample of unsupported Mo_2C under similar reaction conditions is also shown for comparison. The Mo_2C-Al_2O_3 sample gave the highest initial activity, with a CO_2 conversion of 63%, while Mo_2C-ZrO_2 also gave a relatively high CO_2 conversion of 48%. Mo_2C-SiO_2 was a poor CO_2 reforming catalyst, giving a CO_2 conversion of 18%. However, the Mo_2C-Al_2O_3 deactivated almost completely after 4 h of operation whereas the ZrO_2- and SiO_2-supported materials remained comparatively stable over the period of the test; indeed, the Mo_2C-ZrO_2 sample was active even after 80 h at

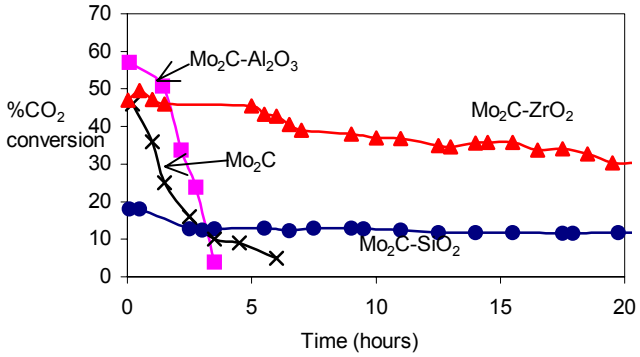

Figure 1. CO_2 reforming of CH_4 using (1) Mo_2C, (2) 5wt% Mo_2C-Al_2O_3, (3) 5wt% Mo_2C-ZrO_2 and (4) 5wt% Mo_2C-SiO_2. [950°C, $CO_2/CH_4/N_2$: 50/50/5 ml/minute, 0.33g catalyst].

950°C (not shown). The unsupported Mo_2C sample deactivated after 7 h. We have previously shown [7] that the deactivation of the unsupported carbide catalyst was due to the formation of the inactive MoO_2 phase under conditions where re-oxidation by CO_2 was thermodynamically favoured. Naito *et al.* [9] have argued that the deactivation of Mo_2C-supported catalysts is due not to MoO_2 formation but to C deposition on the catalyst surface. TG analysis showed that the level of C deposition on the Mo_2C- ZrO_2 material during CO_2 reforming was relatively insignificant in comparison with that on the Mo_2C-Al_2O_3 material [10]. These results are similar to those which we have reported previously [3] for Pt supported on Al_2O_3 and ZrO_2; coke was not deposited to any significant extent on the Pt-ZrO_2 sample while large amounts of coke were detected during CO_2 reforming on the Pt-Al_2O_3 sample. The reaction on the Pt-ZrO_2 appeared to take place at the interface between the Pt and the support and to involve an oxidation-reduction mechanism in which the zirconia takes part in the reaction [11]. There may be a similar explanation for the beneficial effect of the zirconia as a support for the Mo carbide phase.

Raman Spectroscopy. Raman spectroscopy was used to examine whether there was any difference in the surface interactions between the support and the MoO_3 prior to the formation of the carbide phase. Fig. 2 shows the Raman spectrum for the 5wt%MoO_3-Al_2O_3 material prior to reduction/carburisation. Although the spectrum has a poor signal to noise ratio, it is similar to that reported by Cheng and Schrader [12]. The bands at 590 and 943 cm^{-1} are due

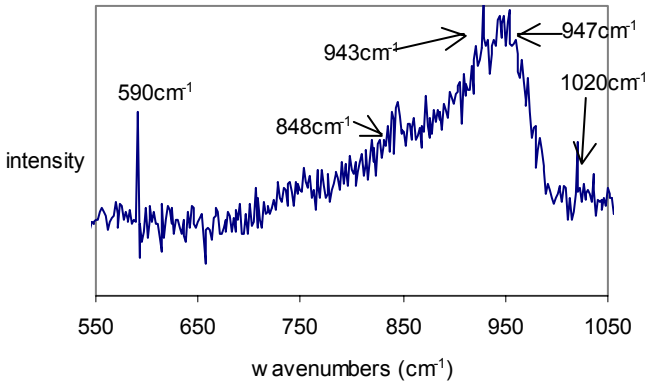

Figure 2. Raman spectrum of 5wt% Mo_2C-Al_2O_3.

to the presence of the polymolybdate species, $Mo_7O_{24}^{6-}$, while the broad band centred at around 970cm^{-1} is due to the presence of a different polymolybdate species, $Mo_8O_{26}^{4-}$. The weak bands at 1020 and 848cm^{-1} also indicate the presence of crystalline MoO_3 [13]; these bands are significantly smaller than that due to the $Mo_8O_{26}^{4-}$ species. In agreement with the results of Cheng and Schrader, there was no evidence for the formation of any aluminium molybdate compounds for the sample used here (calcined at 600^{o}C). Abello *et al.* [14] also showed, using XRD, TPR and NH_3-TPD, that $Al_2(MoO_4)_3$ formation was prevented when MoO_3-Al_2O_3 was calcined at 600^{o}C. We therefore conclude that the predominant species on the surface of the alumina prior to carburisation are adsorbed polymolybdate species and that no amorphous $Al_2(MoO_4)_3$ is formed.

Fig. 3 shows the equivalent Raman spectrum for the 5wt% MoO_3-ZrO_2 catalyst prior to carburisation. The band at 953cm^{-1} indicates the presence of adsorbed polyoxomolybdate while the bands at 749, 942 and 1000cm^{-1} can be ascribed to the presence of bulk $Zr(MoO_4)_2$ species. There was no evidence of the presence of crystalline MoO_3 species [15]. A Raman spectrum of the precarbided MoO_3-SiO_2 catalyst (not shown here) shows that the predominant molybdenum species on the surface of the catalyst was a silicomolybdate species [10]. Polymolybdate surface species do not interact strongly with the support and are therefore highly polarized and easily reduced [16]. The strong interactions created when Mo reacts with the support material decreases the covalency of the Mo-O bonds and therefore stabilises the Mo species; this in turn decreases the reducibility of any such compounds [17]. The presence of the

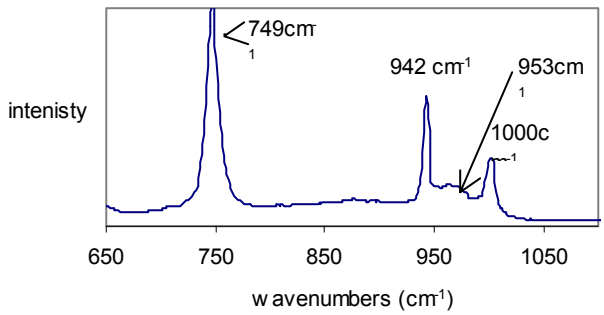

Figure 3. Raman spectrum of 5wt% MoO_3-ZrO_2.

easily reducible polymolybdate species on Al_2O_3 and, to a lesser extent, on ZrO_2 enables a significant quantity of Mo_2C to be produced during the temperature programmed reduction/carburisation step of the preparation. This in turn leads to the formation of a larger number of active sites on the surface of the resultant catalyst. On the other hand, the Mo-Si material is difficult to reduce; the amount of Mo_2C produced during the temperature programmed reduction/ carburisation step for this sample (and to a lesser extent with the zirconia-supported material) is therefore probably less than that with the most active Mo_2C-Al_2O_3 catalyst. TPO experiments [10] support this conclusion: with the Mo_2C-Al_2O_3 sample, 46% of the total possible amount of carbide was formed during the TPR preparation step while, with Mo_2C-ZrO_2 sample, the amount of carbide formed was only 35%.

Optimisation of the Mo_2C-ZrO_2.sample and the effect of promoters. We have examined a series of Mo_2C-ZrO_2 catalysts doped with 1wt% metal oxide promoters (Ni, Bi, Co) to investigate their potential improvement to the activity of the catalyst. The results of this study are summarised in Table 1. The presence of Ni and Co did not significantly change the % CO_2 conversion relative to that with the unprompted Mo_2C-ZrO_2 catalyst. However, the 1wt%Bi-5wt%Mo_2C-ZrO_2 catalyst gave a CO2 conversion of 74.6%, this representing an increase of 16.6% relative to the unpromoted material. An explanation of this promotion is as yet unclear and further characterisation needs to be done; however, it has been suggested by Lietti *et al.* [18] that Bi changes the redox properties of the surface Mo and an effect of this sort may have a role here.

Table 1. Results for the CO_2 reforming of CH_4 using different supported Mo_2C catalysts. [950^{o}C, 50/50/5 ml/minute $CO_2/CH_4/N_2$, 0.33g catalyst]. All the catalysts were calcined at 400^{o}C prior to carburisation. Results recorded after 3 hours of testing.

Mo phase	Promoter	Support	%CO_2 conversion
Mo_2C	-	ZrO_2	58
Mo_2C	Bi	ZrO_2	74.6
Mo_2C	Ni	ZrO_2	59.4
Mo_2C	Co	ZrO_2	55.6

Conclusions

Of all the catalysts tested Mo_2C-ZrO_2 was the most promising due to its stability and reasonably high activity. The activity of this catalyst can be improved by increasing the reducibility of the precarbided MoO_3 surface material. This could be achieved using a number of methods, including low calcination temperatures and the addition of small amounts of a Bi promoter to the catalyst.

References

[1] K. Seshan, H.W. ten Barge, W. Hally, A.N.J. van Keulen and J.R.H. Ross, Stud. Surf. Sci. Catal., 81 (1994) 285.
[2] A.M. O'Connor and J.R.H. Ross, Catal. Today, 46 (1998) 203.
[3] J.R.H. Ross, A.N.J. van Keulen, M.E.S. Hegarty and K. Seshan, Catal. Today, 30 (1996) 193. 65.
[4] A.P.E. York, J.B. Claridge, C. Marquez-Alvarez, A.J. Brungs, S.C. Tang and M.L.H. Green, Stud. Surf. Sci. Catal., 110, (1997) 711.
[5] J.B. Claridge, A.P.E. York, A.J. Brungs, C. Marquez-Alvarez, J. Sloan, S.C. Tsang and M.L.H. Green., J. Catal. 180 (1998) 85.
[6] A.J. Brungs, A.P.E. York and M.L.H. Green, Catal. Lett., 57 (1999).
[7] D. Treacy, E. Xue, J.R. H. Ross, paper presented at 6th NGC Symposium, Alaska, June (2001).
[8] J.S. Lee, S.T. Oyama, M. Boudart, J. Catal. 103 (1987) 125.
[9] S. Naito, M. Tsuji, T. Miyao, Catal. Today, 77 (2002) 161.
[10] D. Treacy, J.R.H. Ross, *in preparation.*
[11] A.M. O'Connor, F.C. Meunier, J.R.H. Ross, Stud. Surf. Sci. Catal., 119 (1998) 819.
[12] C.P. Cheng, G.L. Schrader, J. Catal. 60 (1979) 276.
[13] D.S. Kim, K. Segawa, I.E. Wachs, J. Catal. 136 (1992) 539.
[14] M.C. Abello, M.F. Gomez, O. Ferretti, Appl. Catal. A: Gen., 207 (2001) 421
[15] B. Zhao, Z. Wang, H. Ma, Y. Tang, J. Mol Catal. A, 108 (1996) 167.
[16] M. Del Arco, S.R.G. Currazan, V. Rives, V.J. Llambias, P. Melet, J. Catal. 141 (1993) 48.
[17] J.L Brito, J. Laine, J. Catal. 139 (1993) 540.
[18] L. Lietti, G. Ramis, G. Busca, F. Bregani, P. Forzatti, Catal. Today, 61 (2000) 187.

A STUDY OF THE EFFECT OF DOPANTS WITH PD/CERIA IN THE WGS REACTION

Sufang Zhao and Raymond J. Gorte

Department of Chemical Engineering, University of Pennsylvania, Philadelphia, PA, 19104

Introduction

There is a need for better water-gas shift (WGS) catalysts for the development of efficient fuel processors for fuel-cell applications [1,2]. Materials that are typically used for the WGS reaction in large-scale operations, such as Cu/ZnO, are not applicable for many fuel-cell applications due to the fact that they are sensitive to start-up/shut-down cycles and may be pyrophoric [1,2]. Ceria-supported, precious-metal catalysts are one class of materials that have been identified as exhibiting very interesting properties for the WGS reaction with fuel cells [1-5].

One of the most intriguing scientific aspects of ceria catalysis is that its properties depend strongly on pretreatment conditions and on doping with other oxides. In recent work from our laboratory [6], the effect of a large number of promoters was investigated on Pd/ceria catalysts. The majority of these "promoters" (Tb, Gd, Y, Sn, Sm, Pr, Eu, Bi, and Cr) had minimal effect on the catalytic activity. However, two kinds of "promoters" (Fe and Mo) had dramatic effect over Pd/ceria in the WGS reaction. Small amount of Fe or Mo would affect the activity by one order of magnitude.

In the present study, we set out to investigate the reason for the decrease and enhancement in the WGS activity found on Pd/ceria caused by Mo and Fe respectively. In the presentation, what we will show is that the enhanced activity associated with adding Fe_2O_3 to Pd/ceria is due to formation of a Fe-Pd alloy. And about the Mo modified catalyst, we will show Mo ions react with surface hydroxyls on ceria and that the reducibility of the ceria surface is effectively poisoned by coverages less than 2.0 Mo/nm^2.

Experimental

Sample preparation. The ceria used for all of the measurements in this study was synthesized by decomposition of $Ce(NO_3)_3{\cdot}6H_2O$ (Alfa Aesar, 99.5%) in air at 873 K. For most experiments, Fe or Mo was added to the ceria support by aqueous impregnation with $Fe(NO_3)_3{\cdot}9H_2O$ or $(NH_4)_2MoO_4$ (Alfa Aesar, 99.997%).The samples were again dried at 383 K overnight and calcined in air at 873 K for 4 h. The precious metal Pd was also added to the oxide supports by wet impregnation using aqueous solutions of $Pd(NH_3)_4(NO_3)_2$ (Aldrich, 99.99%). Following impregnation of the precious metal salts, the catalysts were dried at 383 K and calcined at 873 K.

Catalyst Characterization. The WGS reaction rates were measured in a ¼-inch, Pyrex, tubular reactor using 0.10 g of catalyst. Water was introduced by saturation of a He carrier gas flowing through a bubbler with de-ionized water. While the reactor pressure was always atmospheric, the partial pressures of CO, H_2O and He were controlled by adjusting the relative flow rates of each component. All of the reaction measurements in this study were collected with partial pressures for CO and H_2O of 25 torr. All the reaction rates were measured under differential conditions, with the conversions of CO and H_2O kept below 10%. To avoid potential transients associated with catalyst oxidation and reduction, we always allowed the reaction to run for at least 30 min before analyzing the products. To ensure that the results were reproducible, the rates at each point were measured at least three times. The concentration of the effluent from the reactor was determined using an on-line gas chromatograph, SRI8610C, equipped with a Hayesep Q column and a TCD detector.

The transient-pulse experiments were performed on a system that has been described previously. Computer-controlled switching valves allowed the composition of reactants admitted to a tubular reactor to undergo step changes. The product gases leaving the reactor could be analyzed by an on-line quadruple mass spectrometer. Integration of the partial pressures as a function of time allowed accurate determination of the amounts of oxygen that could be added or removed at different temperatures. The carrier gas was pure He, with relatively dilute amounts of CO (5% in He), O_2 (7% in He), and H_2O (2% in He) added in the pulses. The amount of catalyst used in the pulse studies was 1.0 g.

Phase identification in the samples was performed via x-ray diffraction with a Rigaku X-ray diffractometer, using Ni-filtered, Cu Kα radiation (λ = 1.54184 Å). The diffraction measurements were performed in the range of 2θ = 30˚ - 50˚ with a scanning speed of 2˚ 2θ/min.

Results and Discussion

The first evidence that the addition of Fe to the ceria support must do more than simply modify the properties of the ceria support came from WGS rate measurements with various Fe:Pd ratios, with representative data for the Fe-impregnated ceria catalysts reported in **Fig. 1**. Fig.1 summarizes the activity measurements at 453 K for the catalysts with different Fe loading. The activities of the Pd catalysts prepared with Fe-doped ceria were higher than that with undoped ceria; and there is an optimal Fe content for maximizing the rates. The catalyst shows the highest activity with Fe:Pd molar ratio 3:1. It indicates the possibility of the alloy formation between Fe and Pd.

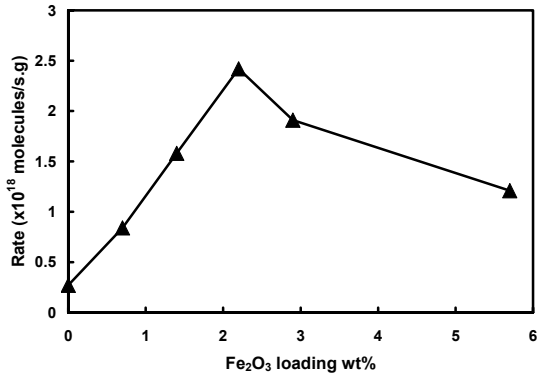

Figure 1. The activity rate measurements for Fe-modified Pd/ceria in WGS reaction at 453K.

To identify the phases responsible for the high activity in the Pd-Fe/ceria catalyst, we prepared the following catalysts: 6 wt% Pd on ceria; 13 wt% Fe_2O_3 on ceria; and 6 wt% Pd, 13 wt% Fe_2O_3 on ceria. Each sample was then exposed to the same WGS reaction conditions at 473 K for 2 h, then cooled in He to room temperature. Because initial experiments showed that the samples were re-oxidized when exposed to air at room temperature, we first passed 1-butene over the catalysts for 30 min at room temperature, before taking the samples out of the reactor, since the carbon-covered catalysts are not as susceptible to re-oxidation. **Figure 2** shows a comparison of XRD patterns on the three catalysts in the range of 30 to 50 degrees 2θ. The metallic Pd peak at 40.12 degrees 2θ was clearly observed for 6 wt% Pd/ceria. On the Fe_2O_3/ceria sample, the peak at 36.85 degrees 2θ shows that Fe remains in an oxidized form, but as Fe_3O_4. The 6 wt% Pd, 13 wt% Fe_2O_3 sample still shows the peak that we associate with Fe_3O_4, but now the peak associated with Pd has shifted upward to near 41.22 degrees 2θ, which would be associated with the (111) plane of the alloy, FePd.

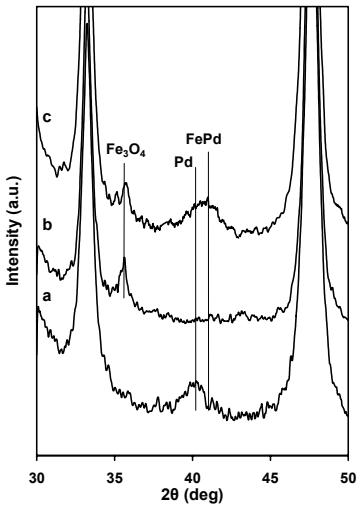

Figure 2. XRD data for (a) 6%Pd/ceria, (b) Fe/ceria (13wt% Fe_2O_3) and (c) 6%Pd/Fe-ceria (13wt%Fe_2O_3)

The effect of added Mo on the water-gas-shift rates is shown in **Figure 3**. Clearly, the Pd/ceria catalyst without added Mo showed the highest rates, with Mo-containing samples exhibiting rates that decreased with increasing Mo content. It is also interesting to consider that the addition of 1.25 wt% Mo decreased the WGS rate by almost a factor of 10. This coverage of Mo corresponds to $1.8x10^{18}$ Mo/m^2, a specific coverage that is less than one would normally associate with a monolayer capable of blocking the surface of ceria.

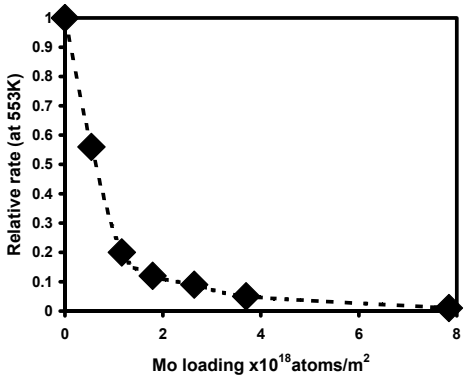

Figure 3. Relative activity rate for the Mo-modified Pd/ceria at 553 K in the WGS reaction.

To understand how Mo modifies the properties of ceria, CO-O_2 pulse studies were performed on catalysts with 1 wt% Pd on the ceria and 1-wt% Mo-ceria samples. Typical data for these two catalysts are shown in **Figure 4** for measurements at 473 K. For Pd/ceria, Fig. 4a), the initial CO pulse (m/e=28) partially reduces the catalyst, forming 135 μmol/g CO_2 (m/e=44,28). A subsequent pulse of CO on this reduced catalyst forms only negligible amounts of additional CO_2. More CO_2 is formed (115 μmol/g) in a sharp peak when the reduced sample is exposed to O_2 (m/e=32). In the previous study, it was shown that the CO_2 formed during the O_2 pulse is due to decomposition of a surface carbonate that is stable only with Ce^{3+}, an assignment that was confirmed by FTIR measurements. The data for Pd on 1-wt% Mo-ceria, shown in Fig. 4b), have a similar appearance to that for Pd/ceria, with the exception that much less CO_2 (38 μmol/g) is formed during the O_2 pulse. According to the FTIR results, the surface carbonate is not formed on the Mo-containing sample and most of this CO_2 is likely formed by reaction of O_2 with CO adsorbed on Pd. The total oxygen transfer in the redox process can be quantified by summing CO_2 formed in the CO and O_2 pulses. We interpret the CO-O_2 pulse results as showing that Mo prevents oxidation and reduction of the ceria surface.

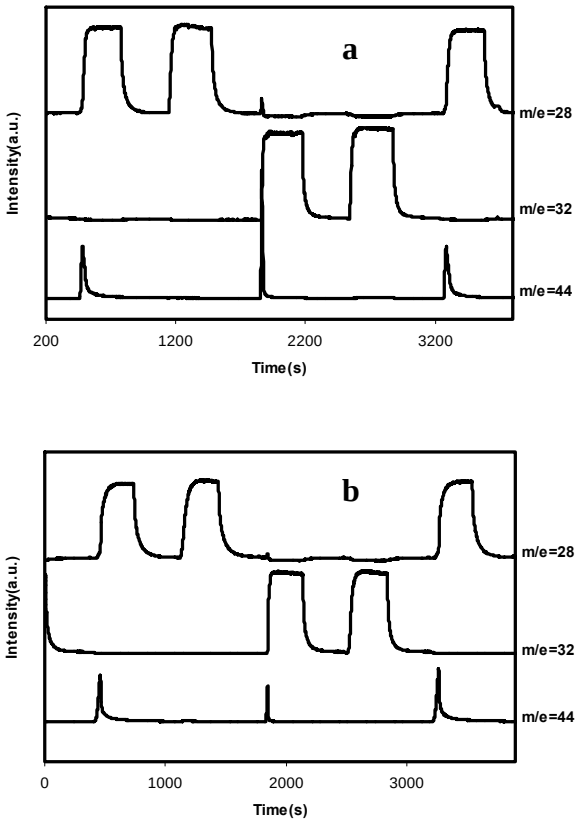

Figure 4. Pulse measurements on (a) 1%Pd/ceria and (b) 1%Pd/1wt%Mo-ceria at 473 K.

Conclusions

We have demonstrated that the enhanced WGS activity observed upon the addition of Fe to Pd/ceria catalysts is probably due to the formation of a Fe-Pd alloy. Our study shows that Mo affects the activity by blocking the surface redox ability of ceria.

Acknowledgement. This work was supported by the DOE, Basic Energy Sciences, Grant #DE-FG03-85-13350.

References

(1) Ghenciu, A.F. *Crrrent Opinion in Solid State and Materials Science*, **2002**, *6*, 389.
(2) Ladebech, J.R.; and Wagner, J.P. In *Handbook of Fuel Cell Technology-Fundamentals, Technology, and Applications*; Vielstich, W., Ed.; Wiley, 2003, chapter 17.
(3) Fu, Q.; Saltsburg. H.; and Flytzani-Stephanopouls, M. *Science*, **2003**, *301*, 935.
(4) Swartz, S.L.; Seabaugh, M.M.; Holt, C.T.; and Dawson, W.J. *Fuel Cell Bull.* **2001**, *4*, 7.
(5) Hilaire, S.; Wang, X.; Luo, T.; Gorte, R.J.; and Wagner, J. *Appl. Catal. A* **2001**, *215*, 271.
(6) Wang, X.; and Gorte, R.J. *Appl. Catal. A* **2003**, *247*, 157.

DEVELOPMENT OF BIMODAL COBALT CATALYSTS FOR FISCHER-TROPSCH SYNTHESIS

Yi Zhang, Yoshiharu Yoneyama, Noritatsu Tsubaki

Department of Applied Chemistry, School of Engineering, Toyama University, Toyama 930-8555, Japan

Introduction

Metallic cobalt is an excellent catalyst for CO hydrogenation, yielding higher hydrocarbons in F-T synthesis. The activity of supported cobalt catalyst in the F-T synthesis should be proportional to the area of the exposed metallic cobalt atoms. For F-T synthesis, the reaction performance of the supported metal catalysts was controlled by a number of factors, such as support property, metal precursor identity and calcination temperature. Among these factors, support pore size has great effect on the mass transfer of reactants and products. The bimodal catalyst where both large pore and small pore coexist can guarantee high diffusion efficiency and large supported metal area meantime, as theoretically proved by Levenspiel. [1]

Until now, several preparation methods were reported to form bimodal catalyst support. But these methods used very corrosive reagents such as aqua regina, and the size of large pore of the obtained bimodal structure was as high as several hundred nanometer that the effect of bimodal structure was not obvious. Furthermore, all the reported methods are only effective for one specific oxide support, such as Al_2O_3 or SiO_2. A general method to prepare bimodal structure, especially containing hetero-atom structure, is expected.

To find a simple, clean, and general preparation method to form tailor-made bimodal structure, it is proposed here a new method to introduce silica or zirconia sols into large-pore silica gel directly, to realize high catalytic activity through higher diffusion efficiency in large pore and higher metal dispersion via the increased surface area. As an application of this kind of bimodal support, it was used for liquid-phase FTS reactions where cobalt was supported. Meanwhile, as a promoter of Co/SiO_2 FTS catalyst, zirconia should promote the catalytic activity as well.

Experimental

The bimodal support was prepared by incipient-wetness impregnation of a commercially available silica gel (Cariact Q-50, Fuji Silysia Chemical Ltd., specific surface area: 70 m^2 g^{-1}, pore volume: 1.2 ml g^{-1}, pellet size: 74-590 μm and mean pore diameter: 50 nm), with zirconia sol (Seramic G 401, Nibban Institute Co., particle size: 1.7~2.4nm, content: 21wt%, alcohol solution) or silica sol (Snowtex XS, Nissan Chemicals Industry Ltd., particle size: 5nm, content 20wt%, aqueous solution), where the volume of zirconia or silica sol was the same with the silica gel support pore volume. After the impregnation, the support was calcined in air at 673 K or 873 K for 2 h directly without drying, for zirconia or silica bimodal, respectively.

Cobalt-supported catalyst with 10wt% metal loading was prepared by incipient-wetness impregnation of different supports, including the bimodal support, with cobalt nitrate aqueous solution. The catalyst precursors were dried in air at 393 K for 12 h, and then were calcined in air from room temperature to 673 K with a ramping rate of 2 K min^{-1} and kept at 673K for 2 h. After calcination, the catalysts were activated in flowing hydrogen at 673 K for 10 h and at last, passivated by 1 % oxygen in nitrogen.

FTS reaction was carried out in a semi-batch autoclave, slurry-phase reactor with the inner volume of 80 ml. The passivated catalyst (1.0 g, under 149 μm) and 20 ml liquid medium (n-hexadecane) were loaded in the reactor. During the reaction, effluent gas released from the reactor was analyzed by on-line gas chromatography. CO and CO_2 were analyzed by using an active charcoal column equipped with a thermal conductivity detector (TCD). The hydrocarbons were also analyzed on-line using FID for C_1-C_5 (Porapak Q) and for C_6-C_{20} (SE-30, uniport), respectively. Argon was employed as an internal standard with concentration of 3 % in the feed gas. The reaction conditions were P (total) = 1.0 MPa, CO/H_2 = 1/2, W/F (CO + H_2 + Ar) = 10 g-cat. h mol^{-1}, T = 513 K.

Pore size distribution, BET surface area and pore volume were determined by using Shimadzu ASAP 2000, where nitrogen was used as absorbent. Supported cobalt crystalline size of the passivated catalysts was detected by TEM (TOPCON EM-002B, acc.volt: 200kV, Point resolution: 0.18nm, line resolution: 0.14nm) and XRD (Rigaku, RINT2000).

In-situ DRIFT spectra were collected on a Nexus 470 FT-IR spectrometer supplied with a diffuse reflectance attachment and with a MCT detector. In-situ absorbance spectra were collected with collecting 32 scans at 2 cm^{-1} resolution.

Temperature-programmed reduction (TPR) experiments were carried out in a quartz-made microreactor using 0.2g calcined catalysts. The gas stream, 5 % H_2 diluted by nitrogen as reducing gas, was fed via a mass flow controller. After the reactor, the effluent gas was led via a 3 A molecular sieve trap to remove the produced water.

Results and Discussion

The characteristics of obtained bimodal supports and silica gel Q-50 were shown in **Table 1**. It is clearly proved that the obtained bimodal support contains distinctly-distributed two kinds of pores, according to the bimodal structure. The increased BET surface area and the decreased pore volume indicated that the particles from sols entered the large pores of Q-50, and deposited on the inner wall of Q-50 to form the small pores. If the sol particles deposited the entrance of large pores of Q-50, the large pores of bimodal support would be blocked, and the BET surface area of the bimodal support would decrease significantly. These data provided evidences that particles from the sols indeed entered the large pores of Q-50 gel and the bimodal support was formed. Based on these findings, it is able to conclude that the obtained bimodal support formed according to the designed route, as introducing the sols into the large pores of silica gel directly.

Table 1. Characteristics of various supports

Support	SiO_2 or ZrO_2 loading [wt%]	BET [m^2/g]	Pore diameter [nm]	Pore volume [ml/g]
Q-50	0.0	70	50.0	1.20
Q-3	0.0	546	3.0	0.30
Silica bimodal	11.2	106	6.0-45	0.46
Zirconia bimodal	16.8	201	3.2-45	0.41

Meanwhile, a lot of oxides, such as zirconia or alumina, were used as promoter to synthesize highly active silica-base catalyst .[2, 3] By introducing different sol other than SiO_2 sol into silica pellet, it is considered that the multi-function bimodal support can be formed, where besides spatial effect of bimodal structure, new chemical phenomenon or effect might appear with the hetero-atom formation between different oxides. In this study, the zirconia-silica bimodal was formed by using zirconia sol and silica pellet to obtain the multi-function bimodal support.

Table 2. Characteristics and reaction performance of various catalysts

Catal.	CO Conv [%]	Sel. [%]		Co Crystal size [nm]		Red. Deg.[a] [%]	TOF[b] [s^{-1}]	α
		CH_4	CO_2	XRD	TEM			
Q-50	17	7.1	3.2	35.0	37.0	98.6	0.035	0.86
Silica bimodal	33	10.1	2.7	20.2	22.6	86.2	0.044	0.86
Zirconia bimodal	86	11.0	3.2	23.6	21.6	88.1	0.134	0.87
Q-3	26	22.0	20.5	4.5	1.4	62.3	0.009	0.84

Reaction conditions: 513 K, 1.0MPa, W/F = 10 g-cat.h/mol, H_2/CO = 2, cobalt loading: 10wt%
a: reduction degree was calculated by TPR from 373 K to 1073 K.
b: used the reduction degree from TPR.

In this study, both the bimodal catalysts, which derived from silica or zirconia sol, showed the best properties such as higher activity and lower methane selectivity, as compared in **Table 2**. For the catalyst prepared from silica bimodal support, the CO conversion was higher than that of catalyst derived from Q-50 and Q-3, and meanwhile selectivities of CH_4 and CO_2 were as low as to those of the catalyst prepared from Q-50. For the zriconia bimodal catalyst, the CO conversion was significantly increased from that of silica bimodal catalyst as the highest in this study, and the selectivities of

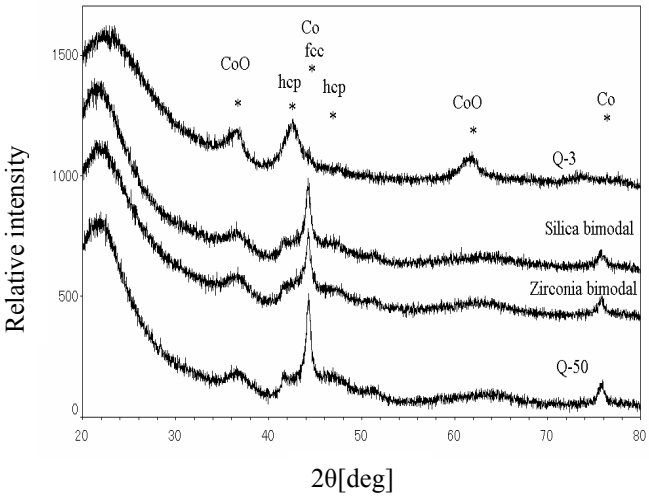

CH_4 and CO_2 were almost the same as that of silica bimodal catalyst.
Figure 1. The XRD patterns of various reduced catalysts

The supported cobalt crystalline size was detected by TEM and XRD. In **Table 2**, the metal particle size calculated by XRD data is generally in accordance with that from TEM. The XRD spectra of various catalysts were shown in **Fig 1**. This clearly displays that the catalysts prepared from bimodal supports had smaller particle sizes than that of the catalyst prepared from silica gel Q-50. Based on these findings, it was proved that the dispersion of the supported cobalt was improved by the bimodal structure of bimodal supports.[4] The TOF of different catalysts was calculated. As shown in **Table 2**, the TOF of zirconia bimodal catalyst was significantly higher than that of silica bimodal catalyst, even though their reduction degree and crystalline size of supported cobalt were almost the same. Hence, the results suggest that the activity of Co sites might be increased due to the presence of ZrO_2 in zirconia bimodal catalyst. ZrO_2 might form an active interface with Co, which was responsible to some extent for the enhancement in Co activity.[5]
Figure 2. In-situ DRIFT spectra of various catalysts.

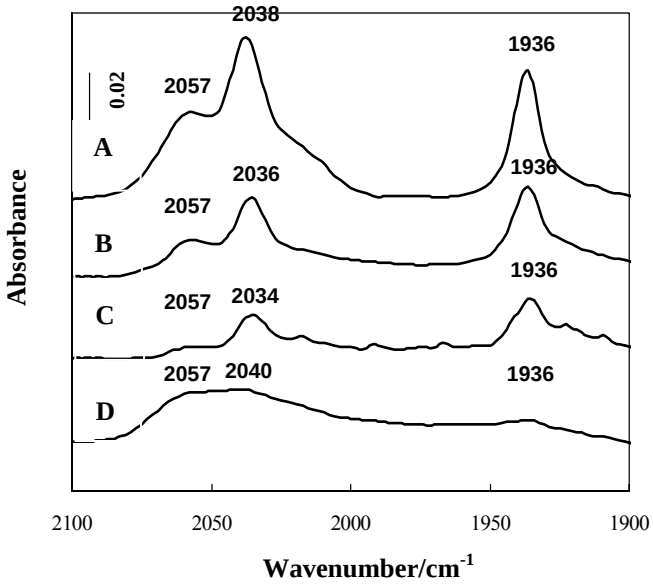

A: Zirconia bimodal pore catalyst; B: Silica bimodal pore catalyst; C: Q-50 catalyst; D: Q-3 catalyst.

As in-situ DRIFT spectra illustrated in **Fig 2**, for both of silica and zirconia bimodal pore catalysts, the peaks of bridged adsorbed CO, which was easily dissociated, were stronger than that of Q-50. The high activity of bimodal catalysts could be attributed to the increase in bridge-type adsorbed CO, which was easily dissociated to carbon and oxygen, contributing to higher reaction rate of FTS.

Conclusions

From described above, it is clear that building up micropores using zirconia particles inside silica large pores realized two functionality, chemical promotion and spatial promotion, at the same time to enhance the activity for liquid phase FTS reaction. These results indicate that a new, simple and general method for preparing bimodal support is developed by manipulation of zirconia nano-particles from its sol inside the pores of silica gel. By this method, the multi-functional bimodal support with both large pore of the desired size and micropore can be easily prepared and the large pore size of the bimodal structure is successfully controlled.

References

(1) Levenspiel, O. *Chemical Reaction Engineering*, 2nd ed., Wiley, New York, 1972; pp. 496.
(2) Withers, H. P.; Eliezer, Jr., K. F.; and Mitchell, J. W. *Ind. Eng. Chem. Res.* **1990**, 29, 1807.
(3) Takahashi, R.; Sato, S.; Sodesawa, T.; Yabu, M. *J. Catal.* **2001**, 200, 197.
(4) Tsubaki, N.; Zhang, Y.; Sun, S.; Mori, H.; Yoneyama, Y.; Li, X.; Fujimoto, K. *Catal. Comm.* **2001**, 2, 311.
(5) Zhang, Y.; Yoneyama, Y.; Tsubaki, N. *Chem. Comm.* **2002**, 1216.

Leaching Studies of a Highly Active Cu-Pd Bimetallic Catalyst Supported on Nanostructured CeO_2 for Oxygen-Assisted Water-Gas-Shift Reaction

*Elise S. Bickford**+, Subramani Velu and Chunshan Song*

Clean Fuels and Catalysis Program, The Energy Institute
*Intercollege Graduate Program in Materials
Department of Energy and Geo-Environmental Engineering
Pennsylvania State University
209 Academic Projects Building
University Park, PA 16802, USA
+Presenting Author

Introduction

Fuel Cell technology is rapidly on the rise. With an increased demand for fuel and energy efficiency over the modern combustion engine, fuel cells are a viable alternative.[1] There is also an added benefit of being more environmentally friendly by reducing exhaust emissions. With the introduction of proton exchange membrane fuel cells (PEMFCs) for the use in automotive technology, it has become increasingly important to decrease the CO concentration of the feed gas to less than 10 ppm. In an early study by Sekizawa et al.[2] on the catalytic activity of Cu on alumina-mixed oxides supports, it was found that Cu(30)/Al_2O_3-ZnO had the highest activity for the water-gas-shift reaction. They also found that if half the stoichiometric amount of oxygen/carbon monoxide was added to the gas feed, the CO removal in the system was greatly enhanced.

However, CuZn-based catalysts are highly pyrophoric and less stable during on stream operation. Thus, new catalysts that are non-pyrophoric, more active, selective for the conversion of CO in the H_2-rich atmosphere and less expensive are required for the down-stream CO clean-up of the reformed gas for fuel cell applications.[3] Since CeO_2 has oxygen storage and release properties, it is anticipated that base metals such as Cu supported on CeO_2 would be less pyrophoric than the CuZn-based catalysts. The pyrophoricity of the Cu/CeO_2 catalyst may be further improved by the addition of a small amount of noble metal due to the synergistic interaction between them. Thus, a new series of Cu-Pd bimetallic catalysts containing various amounts of Cu and Pd supported on a high surface area CeO_2 obtained by urea gelation method have been developed recently in our laboratory for the oxygen-assisted water-gas shift reaction.[4, 5] Among the catalysts tested, the one containing 30 wt % Cu and 1 wt % Pd (Cu(30)Pd(1)/CeO_2) exhibited the best performance with a CO conversion exceeding 99 % under H_2-rich conditions around 210°C. Scanning electron microscopic studies of the catalyst showed the existence of separate Cu-rich and CeO_2-rich regions. This raised a question if the bulk CuO or small CuO clusters dispersed on CeO_2 are active in the OWGS reaction.

In the present study, leaching of CuO by HNO_3 and NH_4OH has been undertaken in order to investigate the nature of active species involved in the OWGS reaction over a highly active CuPd/CeO_2 catalyst identified in our laboratory. The unleached as well as leached catalysts are characterized by XRD, TPR, XPS and SEM techniques. This study is also expected to help developing a new, highly active and more stable catalyst containing less Cu metal supported on CeO_2 for the deep removal of CO from the reformed gas for fuel cell applications.

Experimental

Catalyst Preparation and characterization:

The support CeO_2 was prepared by urea gelation method as described elsewhere and had a BET surface area of about 215 m^2/g.[5] Cu and Pd metals were deposited on the support surface using an incipient wetness impregnation (IWI) method, dried at 120°C overnight and calcined at 400°C for about 4 h using a heating rate of 2°C/min. TPR data were acquired on a Micromeritics AutoChem 2910 instrument. About 0.1 g of the catalyst was loaded in the reactor and heated in 5% H_2/Ar gas (25 cc/min) between room temperature and 500°C at a heating rate of 5°C/min. The H_2 consumption due to the reduction of constituent metal ions is monitored by a TCD detector equipped in the instrument.

Catalytic Studies:

Oxygen-assisted water-gas shift reaction was performed at 240°C in a fixed-bed down-flow reactor. A gas mixture containing 4% CO, 10% CO_2, 2% O_2 and balance (about 84%) H_2 was used as reactants. The CO/H_2O molar ratio was kept at 1/10. The effluent of the reactor was analyzed on-line using an Agilent 3000 A Micro GC equipped with thermal conductivity detectors with a CO detection limit of below 10 ppm. Prior to the reaction, the catalyst was reduced *in situ* at 225˚C for 1h in H_2 flow.

Results and Discussion

Our recent study on the OWGS reaction over Cu-Pd/CeO_2 catalyst containing 30 wt % Cu and 1 wt % Pd indicated that Cu forms bulk-like CuO particles.[5] The bulk CuO can be easily dissolved in nitric acid.[6] Thus, the catalyst, Cu(30)-Pd(1)/CeO_2 was immersed in equivalent amounts of H_2O and HNO_3 for 5, 10 and 15 h. For comparison, the same catalyst was also immersed in aqueous 30% free NH_3 solution (NH_4OH) for 15 h as Cu can also be leached by using NH_4OH.[7]. The leached catalysts were filtered, washed with de-ionized water and dried around 400°C for 3-4 h. The catalytic performance of leached catalysts in the OWGS reaction under H_2-rich conditions is compared with that of the unleached catalyst. As can be seen from Fig. 1, under the present experimental conditions, the unleached catalyst exhibited a CO conversion over 99 %. Interestingly, the catalyst leached in HNO_3 for 15 h shows a CO conversion even slightly higher than that of the unleached catalyst although there is a small drop in conversion for catalysts treated for 5 and 10 h. The inlet CO content of about 4 % has been reduced to below 40 ppm in a single step under the H_2-rich condition over the catalyst leached in HNO_3 for 15 h. On the other hand, the CO conversion drops to below 60% over the catalyst treated with NH_4OH.

TPR experiments are performed over the leached catalysts in order to understand the effect of HNO_3 and

NH_4OH treatments on the redox properties, and the results are shown in Fig. 2. For comparison, the profiles of $Cu(30)Pd(0)/CeO_2$ catalyst without Pd and that of $Cu(0)Pd(1)/CeO_2$ catalyst without Cu are also presented. The catalyst $Cu(0)Pd(1)/CeO_2$ without Cu shows a single reduction peak centering at 153°C, which can be attributed to the reduction of PdO interacting with the CeO_2 support. On the other hand, the 30% Cu/CeO_2 catalyst exhibits reduction peaks at two different temperature regions, one below 200°C, with a doublet centering at 159 and 179°C, and the other above 200°C. The peak below 175°C has been generally assigned to the reduction of dispersed CuO clusters while the peak above 200°C has been attributed to the reduction of CuO particles, similar to that of bulk CuO. Interestingly, the catalyst, $Cu(30)Pd(1)/CeO_2$ possesses an intense peak centering around 160°C together with a broad envelop up to 310°C, indicating the formation of at least two different CuO clusters dispersed on the CeO_2 support together with some bulk-like CuO particles. No separate peak for the reduction of PdO could be seen, suggesting that the presence of Pd along with Cu makes the CuO and PdO reduction as a single broad peak. This reveals that in addition to the Pd-Ce and Cu-Ce interactions, a Cu-Pd interaction also exists in the catalyst. The synergistic interaction between Cu and Pd further improves the reducibility of Cu and Pd species. In fact, a recent *in situ* XANES (X-ray absorption near edge structure) study on the similar $Cu\text{-}Pd/CeO_2\text{-}ZrO_2\text{-}Al_2O_3$ catalyst confirmed the formation of Cu-Pd alloy and this significantly improved the catalytic performance of $CO\text{-}O_2\text{-}NO$ reaction.[9]

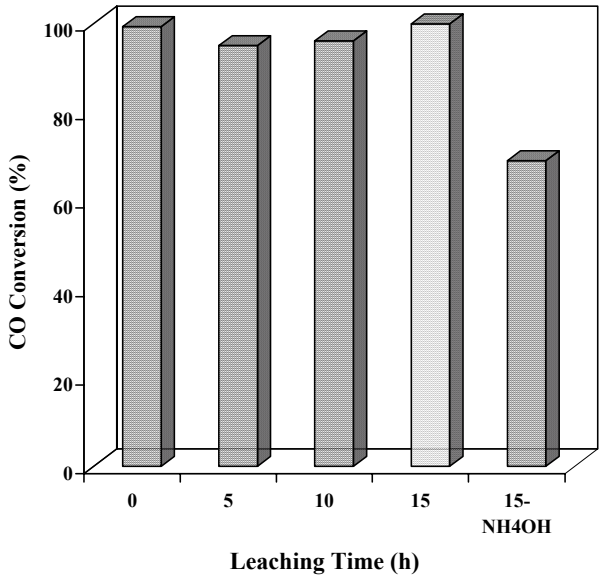

Figure 1. Conversion of 4% CO under H_2-rich conditions over leached and unleached $Cu(30)Pd(1)/CeO_2$ catalysts in the oxygen-assisted water-gas shift reaction .

A comparison of the TPR profiles of unleached and leached samples offers several interesting results. The peak positions are shifted towards lower temperature in the leached samples, suggesting that the metal ions become easily reducible after leaching treatments. In addition, the peak width is narrowed down and the area under the curve decreased dramatically indicating that there is a significant loss in the quantity of reducible cations. This also reveals that the nature of reducible species are identical, particularly in the catalyst leached by HNO_3 as only a sharp reduction peak centering around 130°C is noticed in contrast to a broad H_2 consumption peak around 190°C together with a sharp peak centering at 140°C are observed in the NH_4OH treated sample.

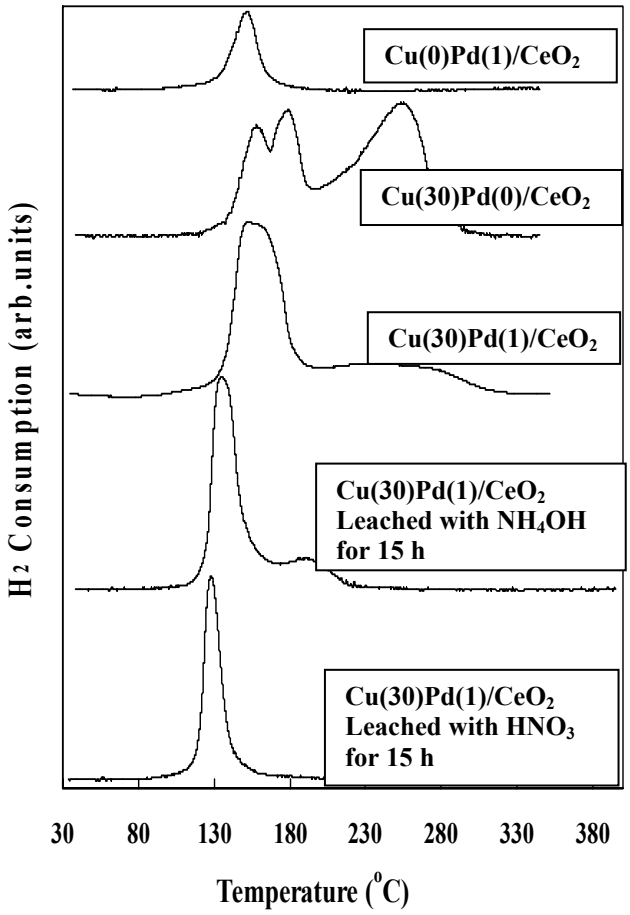

Figure 2.TPR profiles of leached and unleached $CuPd/CeO_2$ catalysts.

The sharp peak centering at 130°C in the HNO_3 treated sample can be attributed to the reduction of CuO clusters, highly dispersed on the CeO_2 and interacting closely with PdO. The sharpening of the peak and the absence of the high temperature shoulder clearly indicates that significant amounts of bulk-like CuO species are removed by the HNO_3 treatment. Since the CO conversion remains above 99 % even after removing significant amount of bulk-like CuO (see Fig. 1), it is tentatively concluded that small CuO clusters dispersed on CeO_2 surface and interacting closely with PdO

species contribute significantly to the conversion of CO in the OWGS reactions. The existence of a broad shoulder around 200°C in the NH_4OH treated sample suggests that NH_4OH treatment retains some amount of bulk-like CuO. In addition, a dramatic decease in the CO conversion over this sample (see Fig. 1) reveals that there is a significant loss in the active species upon NH_4OH treatment. It is likely that the NH_4OH treatment removes in addition to the bulk-like CuO, significant amount of highly dispersed CuO that are responsible for the catalytic activity.

Further characterization of the leached samples by using XRD, XPS and SEM to understand the changes in the structural features, surface chemical compositions and morphology upon leaching treatments are currently in progress and the detailed results will be reported.

Conclusion

Leaching experiments on a highly active $Cu(30)Pd(1)/CeO_2$ catalyst under H_2-rich conditions indicated that the catalyst retains the CO conversion well above 99 % CO even after leaching with HNO_3 for 15 h in the oxygen-assisted water-gas shift reaction. On the other hand, the catalyst leached with NH_4OH looses about 40 % of the catalytic activity. It is tentatively concluded that in the $Cu(30)Pd(1)/CeO_2$ catalyst, CuO clusters dispersed on CeO_2 and interacting closely with PdO contribute significantly to the catalytic activity.

References

(1) Song, C. *Catalysis Today* **2002**, *77*, 17.
(2) Sekizawa, K.; Yano, S.-i.; Eguchi, K.; Arai, H. *Appl. Catal. A-Gen.* **1998**, *169*, 291.
(3) Fu, Q.; Saltsburg, H.; Flytzani-Stephanopoulos, M. *Science* **2003**, *301*, 935.
(4) Bickford, E.S.; Velu, S.; Song, C. *Prepr. Pap.-Am.Chem.Soc., Div. Pet. Chem.* **2003**, 48, 810.
(5) Bickford, E.S.; Velu, S.; Song, C. Catal.Today **2004** (Submitted).
(6) Liu, W.; Flytzani-Stephanopoulos, M. *J.Catal*. **1995**, 153, 304.
(7) Burkin, A. R. *The Chemistry of Hydrometallurgical Processes*; D. Van Nostrand Inc.: Princeton, NJ, 1966.
(8) Li, K.; Fu, Q.; Flytzani-Slephanopoulos, M. *Appl. Catal. B-Environ.* **2000**, *27*, 179-191.
(9) Hungria, A. B.; Iglesias-Juez, A.; Martinez-Arias, A.; Fernandez-Garcia, M.; Anderson, J. A.; Conesca, J. C.; Soria, J. *J. Catalysis* **2002**, *206*, 281-294.

,.

DEVELOPMENT OF SYNTHESIS GAS PRODUCTION CATALYST AND PROCESS

Fuyuki Yagi[*1], *Shuhei Wakamatsu*[1], *Ryuichi Kanai*[1], *Ryuichirou Kajiyama*[1], *Yoshifumi Suehiro*[2], *Mitsunori Shimura*[1]

[1] R&D Center,
Chiyoda Corporation,
Kawasaki, Kanagawa, 210-0855, Japan

[2] Oil&Gas Technology Research & Development,
Japan Oil, Gas and Metals National Corporation,
Mihama, Chiba, 261-0025, Japan

Introduction

Gas To Liquid(GTL) processes have recently been praised as effective technologies for the utilization of natural gas fields on medium or small scales which are not available for LNG. The capital cost of synthesis gas production section in GTL processes has been accounted for around 60% of the total capital cost[1), 2)]. Therefore the development of more compact synthesis gas production processes with high energy efficiency is desired.

We have been developing new CO_2/H_2O reforming catalyst and process through Japan Oil, Gas and Metals National Corporation (JOGMEC) GTL National project since 1999. The new process by using a tubular reformer which does not need an expensive oxygen plant can directly generate the stoichiometrically balanced synthesis gases which have no excess of H_2 and CO as suitable feed gases for Fisher-Tropsch(FT) synthesis, methanol and dimethyl ether and so forth. This proprietary catalyst with a high resistance to carbon deposition can produce synthesis gases by lower CO_2/Carbon and H_2O/Carbon molar ratio in the feed gas composition with low energy consumption. For elucidation and blush up of catalyst performance, several characterizations (for example: XPS, TPD, TPR and TEM etc.) have been carried out.

The simulator to predict the temperature profile and gas compositions in the catalyst bed has also been developed for the design of the tubular reformer.

The pilot plant tests of this process were successfully carried out at Yufutsu gas field in Japan, and high economics were shown on the feasibility study.

Experimental

Catalyst. The commercial size ring catalysts of 16mm outer diameter, 8mm inner diameter and 16mm length were prepared by loading of novel metals (Rh, Ru and Pt etc.) on basic metal oxide supports. An average side crashing strength of the catalysts was 500N/piece. Catalyst surface property, Lewis acidity and basicity, was designed precisely to exhibit high activity and decoking nature.

Pilot test. For the pilot plant operations, about 120L of commercial size catalysts were charged in mono-tube reformer which has 12.0m length and 11.0cm inner diameter, and were reduced at around 800□ under atmospheric pressure before starting the reaction tests. Synthesis gas with $H_2/CO=2$ was generated directly by CO_2 and H_2O reforming of natural gas. Feed H_2O/CO_2/Carbon ratio was 1.15-1.64/0.40-0.60/1, and reaction conditions were at 865-890, 1.5-1.9MPaG and GHSV=3000 1/HR. The total content of higher hydrocarbons in natural gas, for example ethane and propane, was around 13% and total sulfur content was around 1ppm.

Characterization. The XP spectra were measured with a apparatus use a JEOL JPS-9010MC spectrometer equipped with a single-channel detector, employing Al K_α radiation (1486.6eV, anode operated at 10kV x 30mA). O(1s) spectra were recorded with the analyzer in constant pass-energy mode (pass energy at 50eV). Measurement samples were calcined with pure O_2 at 400□ followed by reduction with 1% H_2/He gas at 300, 500 and 900□, respectively.

Simulator. The concept of the simulator is shown in Fig. 1.

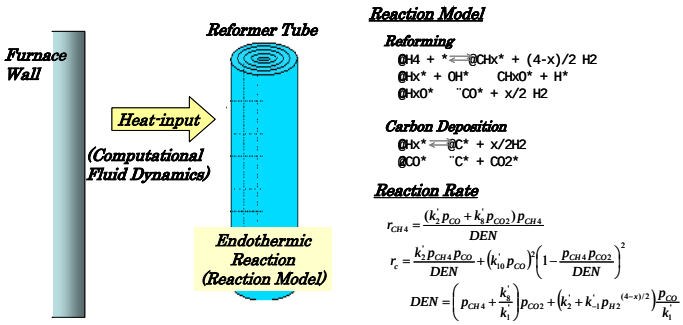

Figure 1. Concept of CO_2 reforming Simulator

The heat–input of the reformer tube from the burners is calculated by computational fluid dynamics, and the endothermic heat-flux is calculated by the simulator. The modeling of reactions for reforming and carbon formation on the catalyst surface is conducted with consideration from the laboratory experimental results and information on literatures[3)]. Catalysts life under optional operation conditions can be estimated because the carbon formation rate is taken into the consideration. Representative elementary reactions are shown. The reaction rate of CH_4 and the carbon formation reaction rate are expressed by the rate constant on elementary reactions and the partial gas pressures.

Results and Discussion

Fig.2 shows the relation between volume of feed gases and compositions of those to obtain constant amount of synthesis gases with H_2/CO molar ratio of 2.0.

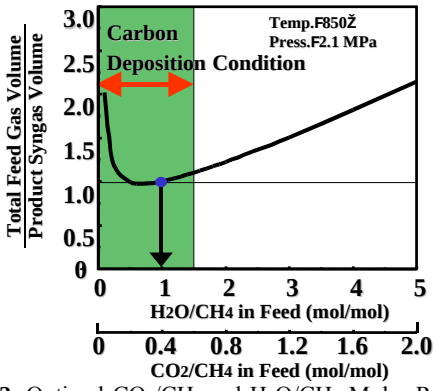

Figure 2. Optimal CO_2/CH_4 and H_2O/CH_4 Molar Ratio in Feed Gas to Produce Syngas ($H_2/CO=2.0$) for FT Synthesis

The volume of synthesis gases was estimated by the equilibrium calculation of steam reforming and water-gas shift reactions at 850°C and 2.1MPa. At the point of nearby feed molar ratio of $CH_4:CO_2:H_2O=1.0:0.4:1.0$, volume of feed gas is minimized and it is predicted that preferable operations with lower energy consumption can be accomplished. But on CO_2/H_2O reforming with ordinary reforming catalysts, the selection of these operating conditions is prohibited by higher potential for carbon formation, and particular technologies for decoking will be required [4),5)].

The results of the pilot plant operation are shown in Fig. 3. In this figure, the conversions of natural gas are presented by comparison with the percentage of the equilibrium values at the same reaction conditions.

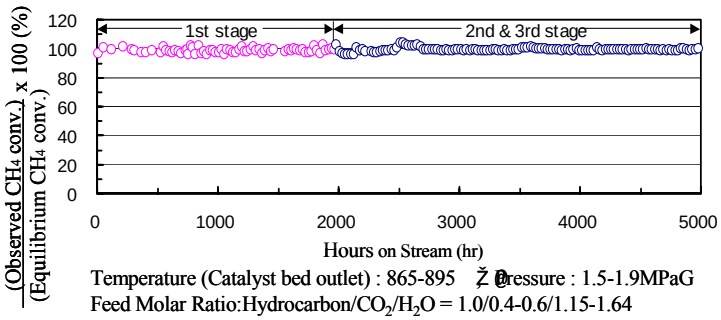

Figure 3. Results of Pilot Plant Tests for CO_2 Reforming

Although catalyst reloading was done after 1st stage operation, some parts of discharged catalysts were recharged at the same position which had been loaded before. So we could investigate total experience of the catalysts. As shown in Fig. 3, the stable operation for more than 5,000 hours has been attained under the target reaction condition. During the operation, little change of the temperature and pressure drop of the catalyst bed was observed. After the total tests, the catalyst was discharged from the reformer and the carbon content of the catalysts was analyzed. The amounts of the carbon deposition on the catalysts which have been loaded during the total test were less than 0.1wt%. From the results, the carbon-free operation has been demonstrated.

The result of the characterization (XPS(O1s)) is shown in Fig. 4.

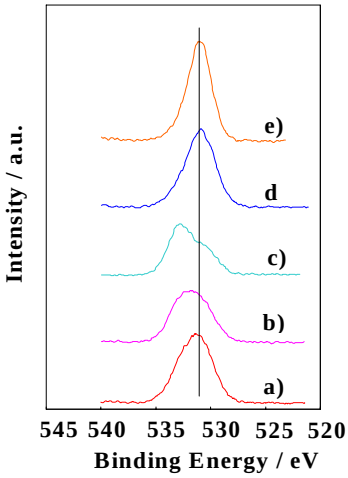

Figure 4. Results of X-ray photoelectron spectroscopy(O1s); a)Before reduction, b), c), d)300, 500, 900□ reduction, e)Support

This catalyst was the same as the one that had been installed in pilot test, and it had exhibited high decoking property. The shapes of O (1s) spectra were changed by H_2 reduction at various temperatures. Especially, O (1s) spectrum on the one reduced at 500□ showed two major peaks. The peak observed at higher binding energy of 532.9eV is originated from the oxygen with lower electron density. Katzer et al. assigned these two peaks to the oxygen of the support (531.9eV) and hydroxyl group terminating the support (532.9eV) [6]. Hydroxyl group could be generated with hydration of support because H_2O would be originated by the reduction of loaded metal oxide. These results suggest that the interaction between loading metal and support is strong and/or the metal-support interfaces are active for hydration. Such properties are considered to be some of the reasons on the decoking nature of the reforming catalysts[4),5)]. By using other characterization methods (TPD, TPR and TEM etc.), we confirmed that it was effective method to control the acidity and basicity of the support for the suppression of carbon deposition.

Typical fitting results to determine kinetics parameters are shown in Fig. 5. This figure stands each gas compositions with the reaction times. The plots represent the observed value, and corresponding curves present the calculation results. As shown in this figure, calculation results fitted with observed value well, and kinetics parameters in reaction model could be obtained.

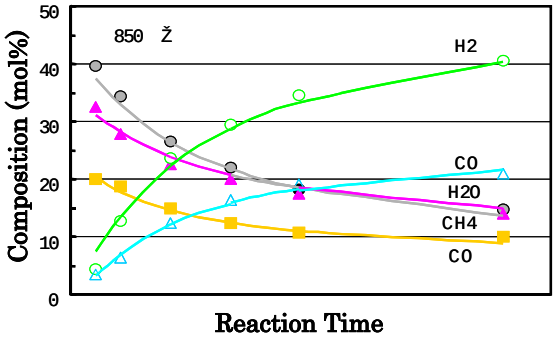

Figure 5. Results of parameter fitting

Through the analysis of the pilot plant test results by the simulator incorporated that reaction model, it was confirmed that it could be effectively used for the CO_2 reformer design.

The feasibility studies of the new GTL process for the utilization of those gas fields have been done. In the Southeast Asia, a lot of gas fields of those sizes containing a certain amount of CO_2 are found. In those natural gas fields, the CO_2 reforming process will be successfully applied to the synthesis gas production as feed for FT synthesis. The basic assumptions of the feasibility studies are as follows, Gas Field Size ; 1.75TCF, Plant Capacity; 15000BPSD (Stand Alone/Grass Roots), Natural Gas Composition; $CH_4/C_2H_6/C_3H_8/C_4^+/N_2/CO_2$ = 77.5/1.0/0.3/0.3/0.8/20.1 (vol%). It is estimated that the plant cost is 560 million US$, and the product oil price COE (Crude Oil Equivalent price) is around 18 US$/bbl.

Acknowledgements

Grateful acknowledgements for the financial support is made to Japan Oil, Gas and Metals National Corporation.

References

1. P. J. Lakhapate, V. K. Prabhu, *Chemical Engineering World,* **2000,** *35,* 77.
2. *Oil & Gas Journal.* June 15 (1998) 34.
3. M. C. J. Bradford and M. A. Vannice, *Appl. Catal.*, **1996,** *142,* 97.
4. I. Alstrup, B.S. Clausen, C. Olsen, R. H. H. Smith and J. R. Rostrup Nielsen, Studies in Surface Science and Catalysis(Natural Gas Conversion V), **1992,** *119,* 5
5. Y-G. Chen, K. Tomishige, K. Yokoyama, K. Fujimoto, *Appl. Catal. A*, **1997,** *165,* 335.
6. M. A. Baltanas, J. H. Onuferko, S. T. Mcmillan and J. R. Katzer, *J. Phys. Chem.*, **1987,** *3772,* 91.

OXYGENATE SYNTHESIS VIA HYDROFORMYLATION ON SOLID CATALYSTS

Yi Zhang, Youhei Shiki, Yoshiharu Yoneyama,, Noritatsu Tsubaki

Department of Applied Chemistry, School of Engineering, Toyama University, Gofuku 3190, Toyama 930-8555, Japan

Introduction

Hydroformylation, the addition of synthesis gas (CO and H_2) to alkenes, is one of the most important syngas-related reactions. The hydroformylation reaction was first discovered on a heterogeneous Fischer-Tropsch (F-T) catalyst.[1] It recognized that cobalt carbonyls generated from the heterogeneous cobalt metal during the reaction were responsible for the catalysis. All current commercial processes are based on homogeneous catalysts, mostly using rhodium. The successful development of a heterogeneous catalyst for hydroformylation would avoid the drawbacks of homogeneous catalysis, such as, very high pressure, the catalyst separation and recovery steps. A great number of papers and patents concerning olefin hydroformylation catalyzed by rhodium complexes or other noble metals supported on inorganic carriers have been published.[2] Whereas rhodium is the most active hydroformylation catalytic component; efforts have been made to study and exploit cheaper metals, thus replacing rhodium in catalysis for economic reasons.

Cobalt is extensively applied in homogeneous process of this reaction due to its high activity and low cost. Supported cobalt catalysts were known to be highly active for Fischer-Tropsch synthesis (FTS). Nevertheless, supported cobalt catalysts usually show low catalytic activity and selectivity for olefin hydroformylation because of high catalytic activity for olefin hydrogenation proceeding at same time.[3] Thus far, only a limited number of papers relating to supported cobalt catalyzed hydroformylation have appeared. However, it was reported that the activity and selectivity of supported cobalt catalysts for hydroformylation could be promoted by various promoters. Qiu et al.[4] reported that the Pd promoted Co/SiO_2 catalyst was very active and selective for the hydroformylation of 1-hexene. The promoting effect of iridium was also founded for the gas-phase hydroformylation of ethane over Co/SiO_2 catalyst.[5] In the present work, the promotional effect of noble metals, such as Pt, Pd and Ru, was studied for active carbon-supported cobalt catalyzed hydroformylation of 1-hexene.

Experimental

Catalyst Preparation. The active carbon-supported cobalt catalyst was prepared by impregnation of cobalt nitrate aqueous solution onto active carbon (Kanto Chemical Co., specific surface: 1071.7 m^2/g, pore volume: 0.43m^3/g, pellet size: 20-40 mesh). The noble metals promoted Co/A.C. catalysts were prepared by co-impregnation of cobalt nitrate and noble metal salts aqueous solution with different noble metal loading. The cobalt loading of all of catalysts was 10wt%. After impregnation, the catalyst precursors were dried at 393 K for 12 h, and then calcined at 673 K for 6 h under the nitrogen flow. At last, the catalysts were reduced by hydrogen at 673 K for 6 h and passivated by 1% oxygen.

Hydroformylation Reaction. Hydroformylation reaction was carried out at in a magnetically-stirred autoclave with inner volume of 85 ml. The catalyst of 20-40 mesh and 1-hexene were loaded into the reactor with a stirrer. The reaction conditions were 403K, 5.0MPa, CO/H_2=1. The weight of catalyst was 1.0g, and that of 1-Hexene was 40mmol. The reaction time was 2h. After the reaction, the reactor was cooled to 273K and depressurized. After filtration to remove the solid catalyst, the liquid products were analyzed quantitatively by gas chromatograph (Shimadzu GC 14A) with a capillary column and a flame ionization detector (FID).

Results and discussion

The main products of 1-hexene hydroformylation were normal and iso-heptanal with Co/A.C. catalysts. Meanwhile, small amounts of heptanol and condensation products (C_{13}+C_{14}) were also produced.

3-1) The effects of noble metals addition to Co/A.C. catalyst

For silica-based catalyst, it was reported that the noble metals, such as Pt, Ru and Pd, were not active for hydroformylation. However, the hydroformylation activity would be increased by addition of small amount of noble metals to cobalt silica catalysts.[4] Based on this, the promotional effect of addition of various metals to cobalt active-carbon catalysts was studied. **Table 1** showed the reaction performance of cobalt active carbon catalysts promoted by various metals. For the supported cobalt catalyst, conversion of 1-hexene gave 37.8%, and oxygenates, including aldehydes (C_7-al) and alcohols (C_7-ol), predominated the product, as 60.8% nal and nol selectivity. The additions of only 1wt% of Pt, Pd and Ru promoters improved the catalyst performance significantly, as increasing the conversion of 1-hexene and selectivity of oxygenate, while ruthenium exhibited the best promoting effect. 97.04% 1-hexene conversion and 79.13% selectivity of oxygenate products were obtained on Co/A.C. catalyst promoted by 1wt% Ru. The 1wt% Pt promoted Co/A.C. catalyst also presented higher activity for hydroformylation of 1-hexene as 96.35% 1-hexene conversion and 66.68% oxygenate selectivity. For the Co/A.C. catalyst promoted by Pd, the activity and selectivity were lower than those of Co/A.C. catalysts promoted by Pt or Ru in this study, even though, Pd showed significantly promotional effect than Pt and Ru for Co/SiO_2 catalyst in hydroformylation of 1-hexene.[4] The additions of alkaline earth oxide, such as Mg, Sr and Ca, did not present promotional effect for hydroformylation of 1-hexene in this study. For Mg promoted Co/A.C.catalyst, the conversion slightly increased than Co/A.C. catalyst, but isomerization and hydrogenation of 1-hexene were significantly promoted by Mg, leading to the decreased selectivity of oxygenate. The catalysts added by Sr or Ca showed lower activity and selectivity than cobalt active carbon catalyst.

3-2) The contribution of Ru loading for cobalt active carbon catalyst.

Although supported ruthenium and supported cobalt were much less active than supported rhodium in olefin hydroformylation, the combination of these two metals has been demonstrated to exert a striking influence on the rate enhancement of oxygenate formation in F-T synthesis and olefin hydroformylation. In this study, the promotional effect of Ru for hydroformylation of 1-hexene was carried out with different Ru loading. Different amounts of Ru, such as 0.05wt%, 0.10wt%, 0.5wt% and 1.00wt%, were added to 10wt% Co/A.C. catalyst, respectively. Hydroformylation reaction was carried out at 403K for 2h. The reaction performance of various Ru-promoted Co/A.C. catalysts was shown in **Table 2.** The conversion of 1-hexene increased with increased Ru loading. The conversion of 0.5wt% Ru promoted Co/A.C. catalyst was almost 100%. As blank test, the Ru/A.C. catalysts was prepared and tested in hydorformylation of 1-hexene. This kind of catalyst showed a negligible activity for 1-hexene hydroformylation, as no oxygenate was produced and 1-hexene was only converted to hydrogenation and isomersization products. It was proved that Ru supported active carbon catalyst had no catalytic activity of 1-hexene hydroformylation to form oxygenates.

The observed rate enhancement of 1-hexene hydorformylation with Ru promoted Co/A.C. catalyst accounted for a synergy of ruthenium and cobalt, which might be explained

in terms of catalysis by bimetallic particles or by ruthenium and cobalt monometallic particles in intimate contact. On the other hand, it was considered that the increased noble metal loading would increase the active site number on the surface of catalysts, contributing to the improved the reaction rate. It was reported that the addition of ruthenium to cobalt base catalyst could significantly improve the reduction degree.[6] The higher reduction degree of catalyst can provide more cobalt metal centers for the reaction and lead to higher catalytic activity. Base on this, it was considered that the active cobalt site remarkably increased due to the addition of ruthenium.

On the other hand, the atoms at the corners and edges of metal particles are thought to be advantageous for hydroformylation reation.[5] Therefore, the high dispersion or small particle size of metal on the catalyst, where the number of atoms at the corners and edges of metal particles is more, is also important for the improvement of catalytic performance. It is considered for Ru promoted Co/A.C. catalyst, the reduction degree was significantly improved, while the dispersion of supported cobalt was also very well. The small particle size of supported cobalt was advantageous for CO insert reaction, contributing to form the oxygenate products.

The hydrogenation and isomerization of 1-hexene decreased with the increased ruthenium loading. It is considered that with the increased active site number on the surface of catalyst, the CO adsorption was improved, contributing to CO insert reaction and inhibiting the isomerization of 1-hexene. The formation of oxygenate was advantageous with increasing Ru loading.

Conclusion

The addition of small amount of Pt, Pd and Ru exhibited significant effect on the Co/A.C. catalyst. The Ru promoted Co/A.C. catalyst was very active and selective for the hydroformylation of 1-hexene.

References

1. Cornils, B., in: Falbe, J. (Ed.), New Synthesis with Carbon Momoxide, Springer, New York, 1980.
2. Lenarda, M.; Storaro, L.; Ganzerla, R., *J. Mol. Catal*. A **1996**, 111, 203-211.
3. Arakawa, H.; Takahashi, N.; Hnaoka, T.; Takeuchi, K.; Matsuzaki, T.; Sugi, Y., *Chem. Lett*. **1988,** 1917-1918.
4. Qiu, X.; Tsubaki, N.; Fujimoto, K.; *Catal. Comm*. **2001**, 2, 75-80.
5. Takahashi, N.; Tobise, T.; Mogi, I.; Sasaki, M.; Mijin, A.; Fujimoto, T.; Ichikawa, M., *Bull. Chem. Soc. Jpn*. **1992,** 65 2565-2572.
6. Tsubaki, N.; Sun, S.; Fujimoto, K., *J. Catal.,* **2001**, 199, 236-246.

Table.1 The effect of noble metals on Hydroformylation of 1-Hexene over 10 wt% Co/A.C.

Catalyst	Conv.(%)	Sel. (%)						Yield (%)	
	1-Hexene	Hexane	Isomer	*iso*-Heptanal	1-Heptanal	C7-nol	nal and nol	Oxygenate	n/iso
10wt%Co	37.80	9.38	18.82	33.37	26.84	0.60	60.80	25.13	0.80
+1wt%Ru	97.04	5.57	10.06	42.11	32.64	4.38	79.13	81.58	0.78
+1wt%Pt	96.35	20.74	6.50	36.40	28.37	1.90	66.68	68.88	0.78
+1wt%Pd	84.01	19.51	6.08	36.08	33.78	1.26	71.12	60.84	0.94
+1wt%Mg	56.78	31.02	13.66	26.71	17.52	0.65	44.88	29.79	0.66
+1wt%Sr	38.23	9.53	22.07	31.62	28.14	0.58	60.34	24.22	0.89
+1wt%Ca	28.45	11.46	22.52	31.91	26.74	0.40	59.05	17.73	0.84

Reaction conditions: catalyst: 20-40 mesh, 0.10 g; 1-Hexene: 40.0 mmol; reaction temperature: 403K; reaction time: 2h

Table.2 The effect of content on Hydroformylation of 1-Hexene over 10 wt% Co/A.C.

Catalyst	Conv.(%)	Sel. (%)						Yield (%)	n/iso
	1-Hexene	Hexane	Isomer	*iso*-Heptanal	1-Heptanal	C7-nol	nal and nol	Oxygenate	
10wt%Co	37.80	9.38	18.82	33.37	26.84	0.60	60.80	25.13	0.80
+0.05wt%Ru	26.25	14.17	28.45	29.22	19.57	0.42	49.21	14.49	0.67
+0.10wt%Ru	44.20	0.00	37.40	30.13	20.56	0.59	51.29	26.29	0.68
+0.50wt%Ru	97.81	0.00	24.56	36.26	30.67	2.69	69.61	72.26	0.85
+1.00wt%Ru	97.04	5.57	10.06	42.11	32.64	4.38	79.13	81.58	0.78

Reaction conditions: catalyst: 20-40 mesh, 0.10 g; 1-Hexene: 40.0 mmol; reaction temperature: 403K; reaction time: 2h

THERMOGRAPHICAL STUDIES ON NOBLE METAL CATALYSTS DURING REFORMING AND COMBUSTION OF METHANE

Baitao Li, Kenji Maruyama, Mohammad Nurunnabi, Kimio Kunimori, and Keiichi Tomishige

Institute of Materials Science
University of Tsukuba
1-1-1, Tennodai, Tsukuba
Ibaraki 305-8573
Japan

Introduction

In the presence of oxygen, the hot spot is always a serious problem concerning to the autothermal reaction and/or partial oxidation, because the combustion reaction is much faster than the reforming reaction, it usually proceeds on the catalyst near the bed inlet, while the reforming reaction takes place over the catalyst bed after oxygen is consumed [1, 2]. Generally, the combustion zone does not overlap the reforming zone. Therefore, the temperature of the catalyst in combustion zone is expected to be very high. As a result, a large temperature gradient will appear in the catalyst bed during the catalytic partial oxidation of methane [3-5]. In addition, the hot spot, in which the temperature expectedly becomes much higher than other places in the reactor, is one of the main difficulties in operating the partial oxidation [6-8].

The purpose of this study is to evaluate the possibility of hot spot formation over granule Al_2O_3 supported Rh, Pt and Pd catalysts in autothermal reforming of methane by means of IR thermographical observation. From the fundamental viewpoint, the investigation on the temperature profiles in autothermal reforming of methane is quite attractive to develop a catalytic process in which the exothermic combustion and endothermic reforming zones can overlap so as to exert a heat transfer with high efficiency.

Experimental

Catalyst preparation. Preparation of alumina supported noble metal (Rh, Pt, Pd) catalysts were performed by an impregnation method. Alumina was prepared by the calcination of JRC-ALO-1 in air at 1473 K for 3 h. The JRC-ALO-1 support material has a spherical shape (diameter of 2-3 mm and surface area of 143 m^2/g). However, after the calcination at 1473 K, the micro structure of JRC-ALO-1 was changed to α-Al_2O_3 from γ-Al_2O_3, although the spherical shape was maintained. BET analysis showed that the surface area of the calcined alumina was 6 m^2/g. Loading of Rh, Pt and Pd on this alumina was carried out by impregnating the support material with aqueous solution containing precursor salts. The precursor of Rh, Pt and Pd was $RhCl_3 \cdot 3H_2O$, $H_2PtCl_6 \cdot 6H_2O$ and $PdCl_2$, respectively. After evaporation and dry, the catalyst was calcined in air at 773 K. The loading amount of the noble metal was 3.0×10^{-5} mol/g-catalyst.

Performance testing. Activity test of methane reforming was carried out in a fixed bed flow reactor under atmospheric pressure. Schematic diagram of the fixed bed reactor is illustrated in Figure 1. A quartz tube of 1.5 mm i.d used as a thermowell was inserted from the bottom of the reactor and the tip was located near the outlet of the catalyst bed. Reaction temperature was controlled by a thermo-controller with this thermocouple for monitoring. An electronic furnace was connected with the thermo-controller, and it had a window (15 mm x 15 mm) for the observation of the temperature profile of catalyst granules. The temperature profile was measured with IR thermography equipment (TH31 from NEC San-ei Instruments Ltd.). The concentration of CO, CO_2 and CH_4 in the effluent gas was determined by FID-GC equipped with a methanator using a stainless steel column packed with Porapak N. The concentration of H_2 was determined by TCD-GC using a stainless steel column packed with a molecular sieve 13 X.

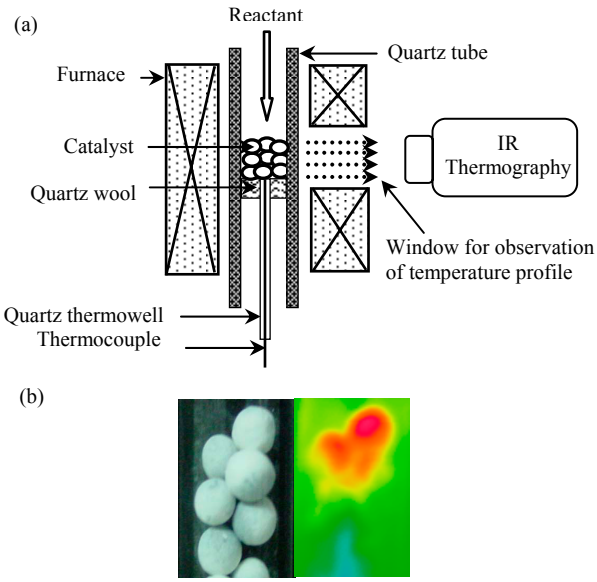

Figure 1. (a) Schematic diagram of the reactor unit in the reforming of methane, (b) Temperature profile observation before reaction (left) and during reaction (right).

Results and Discussion

The combustion activity was measured under the partial pressure of $CH_4/H_2O/O_2/Ar$=10/0/20/70, which corresponded to the complete combustion of methane. The temperature profiles in the combustion reaction over Rh/Al_2O_3, Pt/Al_2O_3 and Pd/Al_2O_3 catalysts are shown in Figure 2(a). Under this condition, only the methane combustion occurred, and the formation of CO and H_2 were not observed. In this case, the methane conversion over three catalysts was almost 100%. In the temperature profiles of the catalyst bed, high temperature section was observed clearly over all three catalysts. In addition, a high temperature region at a rather small size was detected near the catalyst bed inlet. These indicate that the combustion reaction proceeded in the small region and this was related to high reaction rate of combustion. The highest temperature in this methane combustion was 1256 K, 1322 K and 1323 K over Rh/Al_2O_3, Pt/Al_2O_3 and Pd/Al_2O_3, respectively. Since it is thought that high temperature could be caused by high combustion activity, the order of combustion activity is as follows: Pt≈Pd>Rh.

Figure 2(b) depicts the results of temperature profiles in the methane reforming with steam and CO_2 over Rh/Al_2O_3, Pt/Al_2O_3 and Pd/Al_2O_3 catalysts. The reaction was performed under $CH_4/CO_2/H_2O/Ar$=30/10/50/10, which corresponds to the gas composition when methane combustion only proceeded under $CH_4/H_2O/O_2/Ar$=40/30/20/10. In this case, only endothermic reaction (steam and CO_2 reforming of methane) proceeded, and the endothermic profiles were observed by IR thermography. At W/F=0.4 gh mol^{-1}, the lowest temperature in the catalyst bed over Rh/Al_2O_3 was detected as 1023 K; however, it was 1073 K over Pt/Al_2O_3 and increased to 1085 K over Pd/Al_2O_3. It can be concluded that Rh/Al_2O_3 exhibited higher reforming activity than Pt/Al_2O_3, and Pd/Al_2O_3 exhibited much lower activity than Rh/Al_2O_3 and Pt/Al_2O_3.

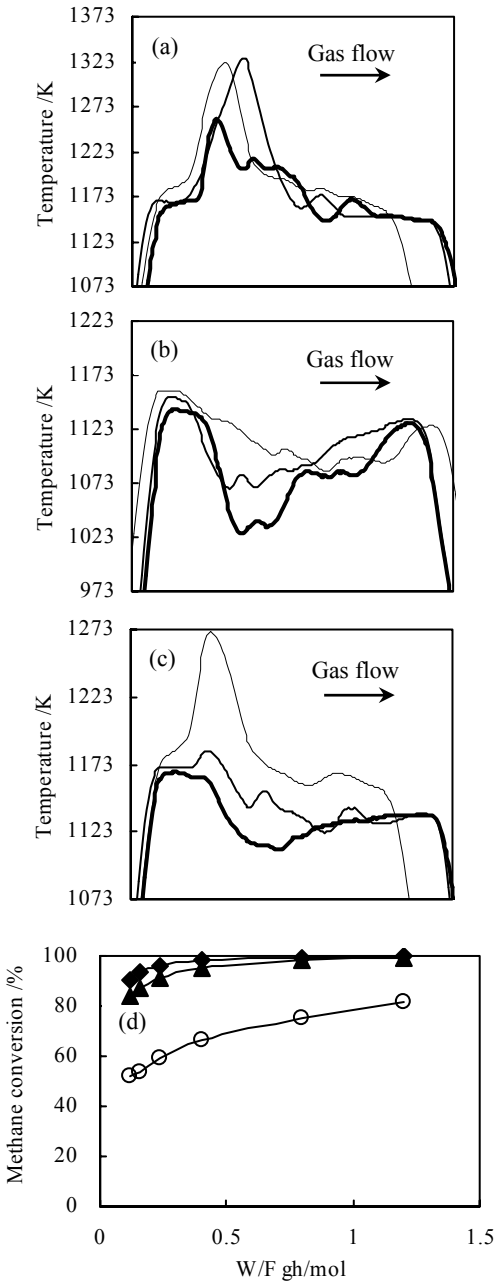

Figure 2. Temperature profiles under different partial pressure of $CH_4/CO_2/H_2O/O_2/Ar$ (a)-(c). {(a) 10/0/0/20/70 (combustion reaction), (b) 30/10/50/0/10 (reforming with H_2O and CO_2), (c) 40/0/30/20/10 (autothermal reforming). Rh/Al_2O_3 (bold solid line), Pt/Al_2O_3 (solid line), Pd/Al_2O_3 (thin solid line).} and methane conversion in the autothermal reforming of methane (d). {Rh/Al_2O_3 (◆), Pt/Al_2O_3 (▲), Pd/Al_2O_3 (○).}
Reaction conditions: temperature 1123 K, W/F=0.4 gh/mol (except in (d)), total pressure 0.1 MPa, catalyst weight 0.14 g, H_2 pretreatment 1123 K 0.5 h.

Figure 2 (c) displays the feeding gas at the partial pressure of $CH_4/H_2O/O_2/Ar$=40/30/20/10 containing the combustion gas (CH_4/O_2=10/20) and the steam reforming gas (CH_4/H_2O=30/30), and whose composition was close to the autothermal condition. At the reaction temperature of 1123 K, the inlet temperature was 1173 K and 1183 K over Rh/Al_2O_3 and Pt/Al_2O_3, respectively, where the exothermic profiles were not observed. However, the bed temperature jumped to 1273 K over Pd/Al_2O_3, so that a large exothermic peak was clearly detected at the catalyst inlet. The reason for this high temperature is due to the very small overlap of combustion zone with reforming zone, and combustion activity of Pd/Al_2O_3 was as high as that of Pt/Al_2O_3, as shown from the temperature profiles of combustion (Figure 2(a)). In addition, the effect of W/F on catalytic properties was also performed, the results is presented in Figure 2 (d). Methane conversion over Rh/Al_2O_3 and Pt/Al_2O_3 catalysts was dramatically lower than that over Pd/Al_2O_3. The results strongly reveal that Rh catalyst exhibited high methane conversion and low inlet temperature in the autothermal reforming of methane. Based on the findings, it is suggested that this behavior can contribute to the effective inhibition of the hot spot formation.

Conclusions

From the temperature profiles in the combustion reaction, the order of the combustion activity was as follows: Pd≈Pt>Rh. In the activity test of methane reforming with H_2O and CO_2, the order of the reforming activity was as follows: Rh>Pt>Pd. It was found that Rh is the most effective catalyst for autothermal reforming in terms of high reforming activity, low combustion activity, and the overlap between two reaction zones.

Acknowledgement. A part of research was supported by Chiyoda Corporation and Japan Oil, Gas and Metals National Corporation.

References

(1) Mallens, E. P. J.; Hoebink, J. H. B. J.; and Marin, G. B. *Catal. Lett.* **1995**, 33, 291.
(2) Dissanayaki, D; Rosynek, M. P.; and Lunsford, J. H. *J. Phys. Chem.* **1993**, 97, 3644.
(3) Heitnes, K.; Lingberg, S.; Rokstad, O. A.; and Holmen, A. *Catal. Today* **1995**, 24, 211.
(4) De Groote, A. M.; and Froment, G. F. *Appl. Catal. A* **1996**, 138, 245.
(5) Basile, F.; Fornasari, G.; Trifiro, F.; and Vaccari, A. *Catal. Today* **2001**, 64, 21.
(6) Tomishige, K.; Kanazawa, S.; Sato, M.; Ikushima, K.; and Kunimori, K. *Catal. Lett.* **2002**, 84, 69.
(7) Tomishige, K.; Kanazawa, S.; Suzuki, K.; Asadullah, M.; Sato, M.; Ikushima, K.; and Kunimori, K. *Appl. Catal. A* **2002**, 233, 35.
(8) Tomishige, K.; Kanazawa, S.; Ito, S.; and Kunimori, K. *Appl. Catal. A* **2003**, 244, 71.

ENHANCED FORMATION OF MIDDLE ISOPARAFFINS THROUGH TWO-STAGE FISHER-TROPSCH REACTION

*Tian-Sheng Zhao, Yoshiharu Yoneyama and Noritatsu Tsubaki**

Department of Material System and Life Science,
School of Engineering, Toyama University,
Gofuku 3190, Toyama 930-8555, Japan
Tel/Fax : (81)-76-445-6846 Email: tsubaki@eng.toyama-u.ac.jp

Introduction

Fischer-Tropsch synthesis (FTS) has found increasing applications as the world economical development. Selectivity control of the products is of significant for this purpose. FTS using supported metal catalysts yields a wide range of hydrocarbons, which are mainly normal paraffins. Both catalysts renovate as well as reactor design have been conducted for desired product distribution. For instance, zeolite supported various metals were employed as catalysts for syngas conversion to limit product chain growth.[1, 2] Improved product distribution can also be realized using the hybrid of FT catalysts with zeolites.[3-6]

In this work, enhanced synthesis of middle isoparaffins from syngas was reported through two-stage Fisher-Tropsch reaction. Isoparaffins can be used as gasoline component with high-octane number.

In the first stage reactor, a hybrid catalyst by Co/SiO_2 FTS catalyst and H-ZSM-5 zeolite was used for limiting the formation of long chain hydrocarbons by the cracking of primary FTS products. Meanwhile the activity and lifetime of Co/SiO_2 was sustained due to the removal of wax accumulation. In the second stage reactor, H-zeolites alone or their hybrid with Pd/SiO_2 catalysts were employed to enhance the formation of C_4-C_6 isoparaffins by further cracking and isomerizing the first stage reaction products in the presence of hydrogen, with the lowest amount of olefinic hydrocarbons. Pd/SiO_2 addition was expected to extend the lifetime of the H-zeolites by means of hydrogen spillover.

In addition, having Fisher-Tropsch reaction conducted in two-stage reactor was based on the consideration of reaction temperatures. The desired temperatures for FTS catalyst and zeolite in the present work were 513-523K and 553-593K, respectively.

Experimental

Catalyst preparation. Co/SiO_2 (20 wt%) as the FTS catalyst was prepared by the incipient wetness impregnation method with commercially available silica gel (Fuji Silysia Chem, ID, BET surface area: 120 m^2/g, pore volume: 1.2 ml/g) and an aqueous solution of $Co(NO_3)_2$. Pd/SiO_2 (2.5 wt%) catalyst was prepared by the similar method to that of Co/SiO_2 with the precursor of $Pd(NH_3)_2(NO_2)_2$ acidic solution (Tanaka Co.). H-ZSM-5(23), H-Beta(27), H-USY(6.3) and H-Mordenite (19) were commercially available zeolite powder (Tosoh, data in parenthesis stand for the SiO_2/Al_2O_3). The desired H-zeolites were physically mixed well with the above two catalysts in certain weight ratio without binder, respectively. All the catalysts including the mixed ones were pressed to 20-40 mesh pellets at 60.0 MPa. The first stage catalyst was reduced in flowing hydrogen at 673 K for 10 h. The second stage catalyst was activated in hydrogen gas flow at 673 K for 1 h under atmospheric pressure.

Reaction procedure. Both the first reactor and the second reactor were the flow-type fixed-bed pressurized ones with the dimension of 8 mm i.d.× 300mm. Reaction conditions were as follows unless otherwise noted: first stage reaction: Co/SiO_2 + H-ZSM-5, 1:1(wt.), total weight, 1.0 g; $H_2/CO=2$, contact time $W(Co/SiO_2)/F$, 5.0 g h/mol; temperature, 513-523K; pressure, 1.0 MPa; second stage reaction: Pd/SiO_2 + H-Zeolite, 1:4(wt.), total weight, 1.25 g (Pd/SiO_2 0.25g + H-Zeolite 1.0g), in the case of no Pd/SiO_2 addition, H-Zeolite weight, 1.0g; $H_2/CO=3$; contact time W(H-zeolite)/F, 7.5 g h/mol; temperature, 553-593K; pressure, 1.0 MPa. H_2 flow rate in the inlet of the second stage reactor was additionally adjusted to $H_2/CO=3$, assuming that $H_2/CO=2$ syngas in the first stage reactor has no reaction. The effluent hydrocarbon products were analyzed on-line by FID gas chromatograph (GL Science GC390B), with a capillary column (Neutrabond-1) coupled with V Station software. CO, CH_4 and CO_2 were analyzed by TCD gas chromatograph, with an activated carbon column. All the products were assigned on a GC-MS (Shimadzu GCMS 5050A) with the same column and temperature program.

Results and Discussion

In order to understand the hydrocracking and isomerization of hydrocarbons on acidic catalysts, four kinds of H-zeolites were used in the second stage reactor. The reaction conditions and the hydrocarbon distributions are showed in Figure 1. In this case, the CO conversions were between 74% and 75.3%, which is attributable to the same first stage reaction at 513K. The CO_2 selectivity was below 3.2%. The selectivity of C_4–C_6 isoparaffins changed from 26.5% to 58.4%. C_7^+ hydrocarbons were not produced when using H-Beta and H-USY as the second stage catalysts, while the selectivity of C_7^+ hydrocarbons was 9.4% and 15.8% in the cases of H-ZSM-5 and H-Mordenite, respectively. Furthermore, no C_4-C_6 olefins were found except for using H-Mordenite. The activity in terms of C_4-C_6 isoparaffin selectivity increased in the order: Co/SiO_2 + H-ZSM-5 ‖ H-Mordenite < Co/SiO_2 + H-ZSM-5 | | H-ZSM-5 < Co/SiO_2 + H-ZSM-5 | | H-Beta < Co/SiO_2 + H-ZSM-5 | | H-USY.

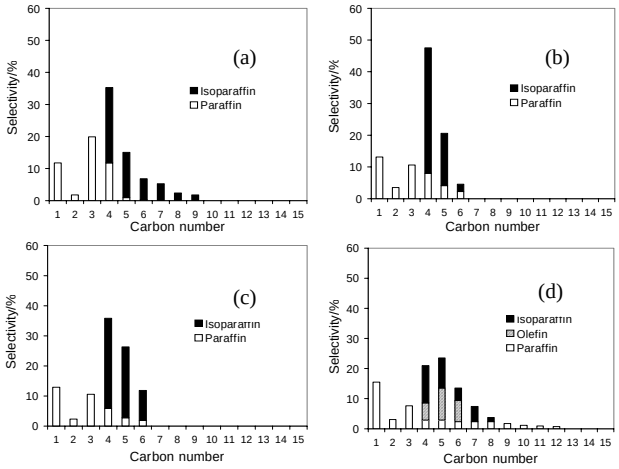

Figure 1. Hydrocarbon distributions for two-stage FTS reaction 1st stage temp., 513K, 2nd stage temp., 573K. 2nd stage cat. : (a) H-ZSM-5; (b) H-Beta; (c) H-USY; (d) H-Mordenite.

These results indicate that the products from the first stage reaction were further conversed to isoparaffins as the main product components. The distinct changes in hydrocarbon distributions can be explained in terms of the secondary reactions following conventional FTS reaction, such as hydrocarbon cracking, skeletal isomerization and hydrogen transfer, as the longer chain hydrocarbons were easily hydrocracked. The products from the first

stage catalysts diffused to the surfaces of the second stage catalysts and were further hydrocracked or isomerized to the lighter isoparaffins and the C_7^+ hydrocarbons were therefore eliminated. In addition, the activity sequence can be attributable to the disparity in the instinct acidity and microporous structure of the H-zeolites. The second stage reactions were simultaneously effected by the acidity and microporous structure of the H-zeolites.

The results and the product distributions for using the hybrid of H-zeolites with Pd/SiO_2 as the second stage catalysts are shown in Figure 2. The CO conversions retained unchanged compared with the above results and the CO_2 selectivity and methane selectivity were below 3.2 % and 12.9 %, respectively. The C_7^+ fraction in the products did not appear and the carbon number of the products terminated at 6, while the selectivity of C_2-C_6 normal paraffins changed to a certain extent. The selectivity of C_4-C_6 isoparaffins increased slightly, compared to that without Pd/SiO_2 addition. H-Beta + Pd/SiO_2 in the second stage exhibited as high C_4-C_6 isoparaffins selectivity as 64.4%. Similarly, it is clear that the olefin formation was completely suppressed. The olefins from FTS reaction were mainly 1-olefins and 1-olefins were effectively hydrogenated on the added Pd/SiO_2. The hydrocracking of n-octane used as a model compound of FTS reaction over hybrid catalyst composed of Pd/SiO_2 + H-ZSM-5 has shown high activity, giving more isoparaffin-rich hydrocarbons than on those without Pd/SiO_2 catalyst. [6] The activity in terms of C_4-C_6 isoparaffins increased in the order: Co/SiO_2 + H-ZSM-5 | |H-ZSM-5 + Pd/SiO_2 < Co/SiO_2 + H-ZSM-5 | | H-Beta + Pd/SiO_2.

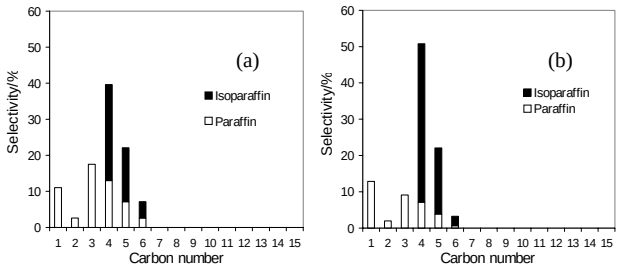

Figure 2. Hydrocarbon distributions for two-stage FTS reaction 1st stage temp., 513K, 2nd stage temp., 573K. 2nd stage cat. : (a) H-ZSM-5 + Pd/SiO_2; (b) H-Beta+ Pd/SiO_2.

The time-on-stream change in CO conversion and hydrocarbon selectivity of the two-stage reaction is shown in Figure 3. It can be seen that within 30 h, the CO conversion was stabilized at 83%. The selectivity of C_4-C_6 isoparaffins was around 50%, while there were no olefins to be found. These results showed that the catalysts for the present two-stage reaction were very stable. H-ZSM-5 zeolite in the first stage catalysts cracked timely the formed waxy components; the disappearance of wax layer on the FTS catalyst could accelerate diffusion of syngas and produce hydrocarbons. The coexisting of Pd in the second stage catalysts activated hydrogen from gaseous H_2 to stabilize or strengthen the acidic sites of zeolite via spillover effect. [7] Because the H-zeolite coexistence in the first stage catalyst released the reaction from diffusion-controlled regime and the hydrogen spillover effect of Pd/SiO_2 on H-zeolite in the second stage catalysts, the lifetime of hybrid catalyst was therefore extended remarkably.

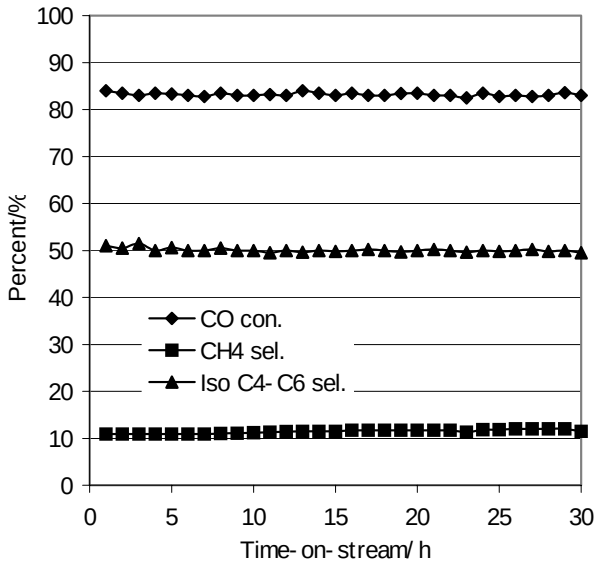

Figure 3. CO conversion and product distributions as time-on-stream for two-stage FTS reaction. 1st stage cat.: Co/SiO_2 + H-ZSM-5; T: 523K; 2nd stage catalyst: H-Beta + Pd/SiO_2; T: 553K.

By this modified two-stage FTS, high selectivity of C_4-C_6 branched hydrocarbons was achieved directly from syngas using hybrid catalysts with different functions. High selectivity of C_4-C_6 isoparaffins resulted from the secondary cracking of heavy hydrocarbons in the first stage reaction to some extent, and mainly from further hydrocracking, isomerization of the first stage reaction products to more desired products in the second stage reaction. Furthermore, conducting the FTS in this reactor can avoid the mismatch of most suitable temperature for Co/SiO_2 and H-zeolites. In the case of using Co/SiO_2 + H-ZSM-5 for the first stage catalyst and H-Beta + Pd/SiO_2 for the second stage catalyst, the highest selectivity for C_4-C_6 isoparaffins was obtained and the products terminated in C_6 hydrocarbon with the CO conversion of 74.8%. With H-ZSM-5 hybrid in the first stage catalyst, wax deposition was restrained and with Pd/SiO_2 hybrid in the second stage catalyst the acid sites of H-zeolites could be maintained by hydrogen spillover effect. The catalytic performance of the total hybrid catalysts was therefore remarkably improved.

Acknowledgement. The grant from NEDO, Japan is greatly appreciated.

References

1. Nijs, H. H., Jacobs, P. A., Uytterhoeven, J. B., *J. Chem. Soc. Chem. Commun.*, **1979**, 180.
2. Tatsumi, T., Shul, Y. G., Sugiura T., Tominaga, H., *Applied Catalysis.*, **1986**, *21*, 119.
3. Udaya, V., Rao, S., Gormley, R. J., *Catalysis Today*, **1990**, *6*, 207.
4. Fujimoto, K., Adachi, M., Tominaga, H., *Chem. Lett.*, **1985**, 783.
5. Tsubaki, N., Yoneyama, Y., Michiki, K., Fujimoto, K., *Catalysis Communications.*, **2003**, *4*, 108.
6. Li, X., Asami, K., Luo, M., Michiki K., Tsubaki, N., Fujimoto, K., *Catalysis Today*, **2003**, *84*, 59.
7. Zhang, A., Nakamura, I., Aimoto, K. and Fujimoto, K., *Ind. Eng. Chem. Res.*, **1995**,*34*, 1074.

IMPACT OF PROMOTERS ON THE PERFORMANCE OF THE SKELETON IRON CATALYST IN THE APPLICATION TO FISCHER-TROPSCH SYNTHESIS PROCESS

Yijun Lu, Peizheng Zhou

R & D Center
Hydrocarbon Technologies, Inc.
1501 New York Ave.
Lawrenceville, NJ 08648

Introduction

As all we realized, this painful gasoline price fly will occur inevitably and frequently in the coming future. Natural gas and remote coal resources have been consistently considered as the alternative fuel by most of the big energy consuming countries. However, Gas-To-Liquid conversion processes was traditionally defined being competitive only when the crude oil price is over US$35/bbl, although it yields ultra-clean hydrocarbon based fuels. As one key part of the increased worldwide interest of GTL technology, HTI has developed a series of proprietary Raney Fe catalyst and the related Integrated Hydrocarbon/Ammonia Production process. As detailed in other places, Raney Fe catalyst, patented as ZIP catalyst, possesses most advantages that the current used precipitated and supported iron catalysts do not have[1,2,3]. Along with the scaling-up of Raney Fe catalyst application, it brought up many interesting points for both research and commercialization purpose. This presentation is to discuss the effect of principle FTS iron catalyst promoters on this novel iron catalyst and its performance of said reaction. The major promoters (elements) addressed here are K, Cu and Mn.

Experimental

Catalyst Samples. The Raney Fe catalysts used in this study are the basis HTI patent ZIP catalyst, and the modified one. All samples are prepared form an amorphous alloy precursor by a way of caustic solution leaching and impregnation process.

The preparation procedure has been provided in the related US patents and other literatures. The distinct skills for controlling the alloy and catalyst chemical formula and physics properties include screening proper additive substance, operating optimum melting procedure, immediate organic-inorganic exchange and discreet transfer under vacuum condition. All catalyst samples before test were stored in ethanol alcohol or slurry phase medium, Durasyn 164.

Characterization & Analysis. The typical measurement data in terms of catalyst chemical, morphological properties have been published in other documents. The techniques contain BET surface area, N2-adsorption for pore size distribution, X-ray diffraction for chemical phase and crystallization extent, scanning electron microscope and surface element probe analysis.

Catalyst Evaluation. Fischer-Tropsch synthesis was conducted in a 1 liter CSTR and operated under commercial conditions (270°C, 2.5MPa, 2.0Nl/gcat/h, 15wt% catalyst loading). Most of the test lasted over 300 hours. All promoters in this study were primarily added in the parent precursor of Raney Fe catalyst, except that K was impregnated onto the skeleton bulk iron particle.

Results and Discussion

Before any test data investigation, it is necessary to clarify one experimental observation that the Raney Fe catalyst does not need any activation or induction period. **Figure 1** indicates the reaction conversion of CO with TOS from zero and there is insignificant induction stage after dramatic temperature increasing to 270°C. The no activation can be simply attributed to the metallic phase (XRD) of Raney Fe catalyst, nevertheless the no induction phenomenon is strongly against the popular point that active Fe catalyst requires to be carbonized to some extent but not reduced to α-Fe phase.

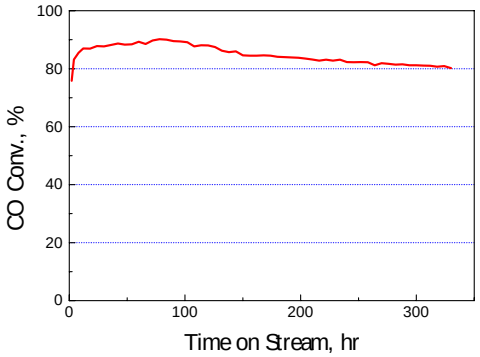

Figure 1. The CO hydrogenation reaction activity as a function of time.

Based on the characterization (XRD & Mossbaur spectra) of Raney Fe catalyst samples after reaction, and the experiment data that FTS product selectivity and activity slightly changed after 1000hours evaluation, Raney Fe catalyst can be concluded as one physical/chemical stable iron cell. The magnetite phase Fe_3O_4 was discovered as the dominant component mixed with trace FeC_x and α-Fe. A recent study reported that using nano-iron unsupported catalyst to undergo CO activation (reduction) and 120hours Fischer-Tropsch synthesis test, the catalyst sample was not converted to most carbide (12wt%) yet. While the micro size iron catalyst showed higher percentage of FeC_x (40wt%). The conclusion was that nano-iron (α-Fe_2O_3) is subject to be stable in Fe_3O_4 phase, i.e., with the iron particle size increasing, the tendency to be carbonized is enhanced. However, for the novel Raney Fe case, amorphous physics property helped greatly to harness the carbonization of Fe. One fact we have to realize that, the composition relationship with catalytic properties of Fe-based FTS catalysts during reaction and identity of active phase still remain controversial.

Potassium Promotion. K as the most important alkali promoter, has been extensively utilized in fused, supported, precipitated FTS iron catalyst[4,5,6,7]. Different authors gradually come to the same conclusion about the K role (or experiment observation) in these different iron catalysts. It was believed that there is an optimum of K/Fe ratio, and among this range the yield of CH_4 and higher paraffins decreased and olefins increased as K amount increased. Besides, the ratio CO_2/H_2O in products increased with increasing K/Fe, and the carburization of Fe in synthesis gas proceeded more rapidly on K promoted catalysts.

For the well-known precipitated-Fe catalyst preparation, originally, potassium was added by mixing an aqueous solution of ferric nitrate, potassium nitrate/carbonate and with other nitrate compound if necessary (like copper nitrate). After high temperature calcinations and complete reduction, the K promoter was thought rich on the surface of catalyst and interacting with Fe atoms strongly. Since the recent application of precipitated Fe catalyst has involved in the spray-dried step (which is purposing on the K_2O and SiO_2 promoters addition) in the preparation process, K promoter was assumed to mostly bind with SiO_2 rather than Fe atoms. This poor K-Fe interaction obviously led people to increase K concentration in the catalyst (1~4% comparing with the optimum range 0~0.4 conclude from the co-precipitated Fe catalysts)[6,7,8].

Before starting the K promoter impregnation onto Raney Fe particles, the difficulty that metallic Fe catalyst is air sensitive and water sensitive when the temperature is over room temperature had to be resolved. The methnolic solution of potassium and vacuum rotate evaporizer were chosen to accomplish the loading object. Impregnating temperature was controlled below 70°C and after 3 hours loading/drying the inert paraffins was introduced to protect active catalyst exposing to air. Catalyst was subsequently transferred into the CSTR and heat treated at 300°C and 0.7 MPa under N_2 or H_2 for 20hours in order to purge and vaporize out all possible oxidant substance that may contacting with the active catalyst particles. The reactant gas was fed in a ratio of H_2/CO=1, and the Fischer-Tropsch synthesis occurred instantly as confirmed from the first 1 hour vent gas analysis.

Table 1. Comparison of the FTS performance on Raney Fe catalyst containing different K loading

Run No.	224-77	224-88	224-101	224-89
Raney Catalyst	Fe/Al/Mn Base			
K/Fe, wt%	0	0.3	0.6	1.1
Conv., mol%				
CO	84.4	89.3	85.1	89.7
H_2	44.0	64.1	54.3	71.0
CH_4 sel., %	12.0	10.1	8.3	7.1
Deactivation rate, %/d	1.45	0.88	0.83	0.30

(CH4 selectivity here is represented as the percentage to whole HC product).

Table 1 demonstrated that K promoter played an incredible role in the Raney Fe catalyst. It was apparent that methane selectivity was decreased and deactivation rate was minimized as well as the hydrogenation activity enhanced by increasing the K/Fe ratio. However the impregnated K amount was relatively lower comparing with those over precipitated Fe catalysts which have obtained much nearly catalytic performance.

Copper Promotion. Copper is another extensively researched promoter to Fe-based FTS catalysts. Especially for the precipitated iron catalyst, copper (CuO) was proved by sufficient studies to play great role in reducing the iron oxide reduction temperature, and believed contributive to the initial carburization, extent of carburization and the stability of higher FTS rate. It was clearly recommended by many authors to use copper and potassium both at the same time, so as to possibly increase the activation sites and subsequently form multiple and smaller carbide crystallites[9]. Nevertheless, the Raney Fe catalyst in this presentation showed very slight requirement of copper as structural promoter. After a series FTS tests over different copper promoter percent and different copper chemical phase (Cu and CuO), it was found the copper in Raney Fe catalyst system had little effect on the activity or stability, except led slight increase in oxygenates yield.

Manganese Promotion. In fact the manganese was traditionally defined as active element for the FTS reaction, and some literatures have used manganese content over 40wt% iron catalyst. The mostly agreed effect of manganese on the iron based catalyst was the enhancement of olefin selectivity especially the low molecular olefins. The catalyzing/promoting mechanism was thought to form bi-metallic catalyst surface sites, so as to reduce hydrogenation probability and increase thermal stability as well as the carburization inhabitation or carbide deposition. X. Li et al have suggested to adjust the manganese amount during the co-precipitation process could obtain unique Fe/Mn oxides in the form of spinel compound ($MnFe_2O_4$) after relative high temperature calcinations (1100°C)[10].

Three different manganese type catalysts were studied in this work, $MnCO_3$, Mn_2O_3, Mn were all separately added to the parent alloy of Raney Fe catalyst, the ratio to Fe was controlled as < 5wt%. The steady state test data demonstrated that manganese addition to the Raney Fe catalyst greatly enhanced the activity and stability comparing with the one has no manganese promoter. But the proper reaction temperature to reach satisfying performance was found increased by 10-30°C. One possible explanation about this temperature difference was that the reduction tendency of iron surface oxide species was inhabited when manganese added, the characterization results of the proof of spinel compound somewhat supported the observation. Once $FeMnO_x$ crystallite is formed, surface active sites were smaller than the iron clusters. **Table 2** lists the manganese promoted Raney Fe catalyst and their FTS catalytic properties.

Table 2. Comparison of FTS performance over Raney catalyst with manganese promoters

Run No.	224-68	224-83	224-104	224-89
Raney Catalyst	Fe/Al Base			
Manganese, wt%	0	*Mn_2O_3 4	*Mn 2	$MnCO_3$ 5
Potassium, wt%	0	0	0	1.1
Conv., mol%				
CO	67.7	69.3	86.2	89.7
H_2	30.0	45.7	53.1	71.0
CH_4 sel., %	8.56	6.8	7.3	7.1
Deactivation rate, %/d	3.60	4.01	0.75	0.30

- Reaction temperatures were 290°C.

Conclusions

From the above discussion, it can simply be concluded that Cu had little influence on the CO hydrogenation activity comparing with the significant K contribution. Mn promoter was proved playing positive role in the CO hydrogenation and olefin selectivity but turned out negative effect on the reaction stability when both Mn and K were present in the Ranbey Fe catalyst. The reason was thought to be the high selectivity in wax that inevitably enhanced the viscosity and primary product transfer resistance, particularly the oxidizing by-products. Further characterization by morphological, species analysis and H_2/CO adsorption in-situ could provide better explanation of these observations.

Acknowledgment. Catalyst characterization was provided by the Material Science & Engineering Center of New Jersey, Institute of Technology.

References

1. Lu, Y.J., et al., ACS Preprints, Fuel Chemistry Division, 2001, 46(2), 500
2. Zhou, J.L., et al., US Pat. No. 6265451
3. Zhou, P. Z., et al., US Pat. No. 6277895
4. Davis, B.H., Catalysis Today 84(2003)83-98
5. Bukur, D.B., et al., Ind. Eng. Chem. Res., 1990,29,1588-1599
6. Bukur, D.B., et al., Applied Catalysis A; General 186(1999)255-275
7. Mahajan, D., et al., Catalysis Communications 4(2003) 101-107
8. Anderson, R.B., The Fischer-Tropsch Synthesis, Academic Press, Inc. 1984
9. Li. Senzi, et al., J. Phys. Chem. B 2001,105,5743-5750
10. Li. X. G., et al., Hyperfine Interactions, 1991,69(1-4), 867

CATALYSTS FOR DIRECT ETHANOL FUEL CELLS

Jonathan Mann, M. Scott Daubin, and Andrew B. Bocarsly

Chemistry Department
Princeton University
Princeton, NJ 08544

Background

Of the two existing pre-market proton exchange membrane fuel cells: hydrogen-oxygen and direct methanol, H_2/O_2 is suggested for applications involving high energy density, while direct methanol holds pragmatic promise for small low power application where ease of fuel handling is critical. Of equal importance, is the energy per unit volume when matching an application to a fuel, since available volume for a mobile application is often a limiting consideration.

A simple review of the thermochemical parameters (provided in Table 1) indicates that ethanol has fuel characteristics similar to methanol. However, it substantially exceeds methanol with respect to volumetric energy density providing 68% of the volumetric energy density of gasoline. Thus, from an energy storage point of view, ethanol appears to be a preferred fuel over methanol.

Table 1. Energy Content of Fuel Cell Fuels Assuming Complete Combustion

Thermochemical Parameter	Ethanol	Methanol	Gasoline
ΔH^o, kJ/mol	-1406	-658	
ΔG^o, kJ/mol	-1324	-702	
Specific Energy, MJ/kg	26.8	19.9	44.4
Energy Density, MJ/L	21.2	15.8	31.1

Likewise, a strong environmental argument can be made for ethanol over methanol. Methanol is water soluble and rather toxic. As recently seen with the withdrawal of MBTE as a gasoline additive this combination of properties represents an environmental threat. Ethanol though water soluble, is much less toxic than methanol, thus the environmental threat is dramatically attenuated.

Introduction

Ethanol oxidation at the anode of a fuel cell requires the development of a catalyst. The complete anode reaction (1) involves the breaking of C-H bonds and C-C bonds as well as the formation of C=O bonds. New alloys for this catalysis were investigated.

$$CH_3CH_2OH + 3\ H_2O \rightarrow 2\ O_2 + 12\ H^+ + 12\ e^- \qquad (1)$$

Preliminary fuel cell studies at elevated temperature have shown that ethanol can be oxidized to CO_2 with a yield of 96% above 140˚C.[1] It has also been reported that the concentration of ethanol at the electrode surface has a significant effect, with ethanol concentrations much higher than 1 M resulting in catalytic poisoning by adsorbed, partially oxidized ethanol species. This is easily explained by understanding that a high ethanol concentration also means a lower water concentration. It is easy to see from reaction (1) that a decrease in water concentration at the electrode interface will result in incomplete oxidation.[2]

In addition, studies[3] have shown that a variety of bimetallic catalysts containing platinum and a second post-transition metal may be catalytically superior to a pure platinum electrocatalyst. Three different types of broad-based systems have been suggested: bulk alloys, surface ad-atom composites and (quite recently) intermetallic phases.[4]

To date, alloy base systems have received the most attention. Though similar, different trends are noticed for methanol and hydrogen oxidation than for ethanol. Specifically, Pt/Sn alloy systems have been shown to demonstrate higher activity than Pt/Ru, the preferred alloy for methanol and reformed hydrogen oxidation. This finding has been correlated with the need for a large quantity of adsorbed oxygen in the case of ethanol oxidation. Tin adopts an oxidized state while platinum and ruthenium remain in more reduced states. This added oxygen promotes the ethanol oxidation on the Pt/Sn surface over others. It is well established from electrochemical studies that bulk ethanol is oxidized only partially, while surface adsorbed ethanol undergoes complete oxidation to CO_2. As might be expected, the complete oxidation of ethanol requires a higher potential than does the partial oxidation to acetaldehyde or acetic acid; surface adsorbed species do not diffuse away from the electrode before the higher potential is reached. This conclusion not only suggests a strategy for the development of new catalysts, but also indicates that electrochemical studies (which typically utilize low surface area electrodes in contact with an aqueous electrolyte) may not faithfully model the fuel cell environment that incorporates a supported nanoparticulate catalyst bed in contact with a polymer electrolyte.

Experimental

Electrodes. Anodes were prepared from a commercial carbon cloth with a single gas diffusion layer (ETEK). Catalysts (ETEK) were Pt binary and ternary alloys on carbon. They were suspended in a solution of iso-propanol and sprayed onto the diffusion layer of the electrode. The catalytic loading was aimed at 0.4 mg/cm^2, and the exact loading was calculated by mass difference. The same procedure was used to impregnate Nafion into the newly deposited active layer of the anode electrodes. Loadings of 0.6 mg/cm^2 were the aim for the Nafion.

Cathodes were prepared from commercial carbon cloths with a pre-applied active layer of 0.4 mg/cm^2 of Pt (ETEK). Nafion was impregnated into the active layer of the catalysts at a loading of 0.6 mg/cm^2.

Membranes. Nafion 115 membranes were uses after a boiling in successive bathes of 0.5 M H_2SO_4, H_2O, 3% H_2O_2, and H_2O twice. Membranes made from dissolved Nafion (Ion Power) combined with metal oxide particles and cast into membranes were also used. This second type of membrane underwent the same kind of treatment before being assembled into the cell.

Cell Testing. The membrane and electrodes were assembled according to existing procedures.[5] The membrane electrode assembly (MEA) was then inserted into a GlobeTech single cell test station where the potential on each electrode was independently cycled from 0.1 to 1.0 volts at 100 mV/s under nitrogen.

The cell was then moved to a modified GlobeTech single cell test station equipped to deliver liquids to the anode. The liquid at the anode was 1.0 M ethanol flowing at 0.2 mL/min. The cathode was pure oxygen with a flow rate of 150 mL/min. Both sides of the cell were pressurized above 60 psig.

Polarization curves were used to evaluate cell performance as a function of temperature and anode catalyst material. The dependence on flow rate, membrane, and pressure was also considered.

Preliminary Results

Polarization curves for the tested cells confirmed that the Pt:Sn, alloy (3:1 atomic ratio) is the preferred catalyst among Pt:Ru (1:1) and Pt (not shown). Both open circuit voltages and activation over potentials are more favorable for the Sn alloy. (Fig. 1.)

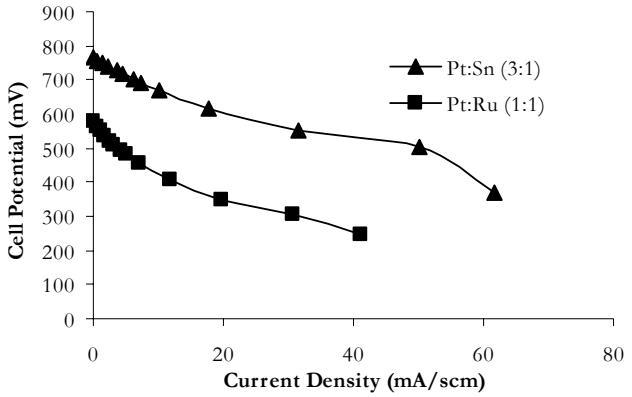

Figure 1. Reproducible comparison of performance of Pt:Sn catalyzed cell with Pt:Ru catalyzed cell.

The standard cell potential for the ethanol reaction is 1.14 V, about 90 mV less then the H_2/O_2 cell, while the open circuit of the ethanol cell, measured as high as 808 mV, is less than 200 mV below that of the common H_2/O_2 cell. This reasonably high open circuit potential is a promising number considering the relatively unresearched array of possible catalytic particles available. However, the extraordinarily low current densities demonstrate that the presently employed catalysis is insufficient at extracting power from the fuel.

Summary

The study of ethanol as a fuel in fuel cells is a relatively new exploration in the field. The motivation to use it over hydrogen or methanol is several-fold, while its demonstrated abilities leave something to be desired. Continued exploration into the vast array of catalytic particles will reveal the most ideal catalytic system which then can be combined with the most successful *in situ* conditions to produce a power source capable of competing with existing electrochemical cells.

References

1 (a) Arico, A.S., Creti, P., Antonucci, P.L. and Antonucci V., *Electrochemical and Solid-State Letters*, **1998**, *1*, 66, (b) S. Srinivasan and C. Yang, Private Communication, Princeton University **2000**.

2 Wang, J., Wasmus, S., and Savinell, R.F., *Journal of the Electrochemical Soceity* **1995,** *142*, 4218.

3 Zhou, W.J, et al. *Journal of Power Sources*, **2004,** *126*, 16.

4 Casado-Rivera, E., *et al. Journal of the American Chemical Society*, **2004,** *126*(12) 4043.

5 Adjemian, K.T., *et al. Journal of The Electrochemical Society* **2002**, *149*, A256.

WHAT MATTERS AFTER FIRST ELECTRON TRANSFER IN OXYGEN REDUCTION: A KINETIC STUDY OF Pt(111) AND Pt/C THIN LAYER CATALYSTS ON ROTATING DISK ELECTRODES

Jia X. Wang, Junliang Zhang, and Radoslav R. Adzic

Materials Science Department, Building 555
Brookhaven National Laboratory
Upton, NY 11973

Introduction

Oxygen reduction is one of widely studied reactions because it is the cathodic reaction in fuel cells, corrosion, and several other important processes. From the catalytic point of view, the reaction mechanism on a Pt electrode has attracted most attention because Pt and Pt-alloys are still the most active cathode catalysts for low temperature fuel cells. In electrocatalytic reduction of oxygen, the first electron transfer appears to occur simultaneously with the adsorption of oxygen molecules since there is no evidence for oxygen adsorption at potentials higher than the onset of oxygen reduction reaction (ORR). Although this step may have the highest activation energy and is hence considered to be the rate-determining step, many experimental observations show that the Pt-OH formation and other anion adsorption played an important role in determining catalytic performance.

In this study, we carried out a kinetic analysis of the rotating disk electrode (RDE) polarization curves obtained for Pt(111) in $HClO_4$ and H_2SO_4 solutions using the adsorption isotherms measured from the voltammetry curves. A negative electronic effect on ORR kinetics was found for both OH and bisulfate adsorbates in addition to site blocking[1]. To further study the role of OH adsorption on nanoparticle catalysts, RDE measures of thin-layer catalysts were carried out. The surface oxidation of Pt, was found more irreversible and occurs over wider potential region on nanoparticles than on bulk Pt. The time dependent polarization curves in $HClO_4$ were measured and the roles of the reaction intermediates and the dynamic equilibrium coverage of Pt-OH in determining the quasi-stable kinetic current of ORR will be demonstrated.

Experimental

The carbon-supported Pt catalyst (20%Pt/C HP, E-TEK) was deposited on a glassy carbon electrode by placing 15 μl catalyst suspension over 0.168 cm^2 electrode area with Pt loading between 30 and 60 nmol/cm^2. The 0.1 M $HClO_4$ solution was prepared from ultrapure perchloric acid and MilliQ UV-plus water (Millipore). An Ag/AgCl/(3M KCl) reference electrode was used with a double-junction reference chamber and all potentials are quoted with respect to reversible hydrogen electrode (RHE).

Results and Discussion

Intrinsic kinetic parameters and anion adsorption effects on the Pt(111) electrode. In analysis of the RDE polarization curves for Pt(111) in $HClO_4$ and H_2SO_4 solutions, the Tafel slope and the exchange current on an adsorbate-free surface were defined as the intrinsic kinetic parameters. The site blocking and electronic effects of adsorbed anions were evaluated with the adsorption isotherms incorporated in the model. As shown in Fig. 1, a reversible OH (in $HClO_4$) adsorption occurs at potentials positive of 450 mV and (bi)sulfate ions adsorb above 370 mV, which blocks the OH adsorption up to 900 mV. The anion adsorption isotherms were obtained by integrating the corresponding current curves above these potentials.

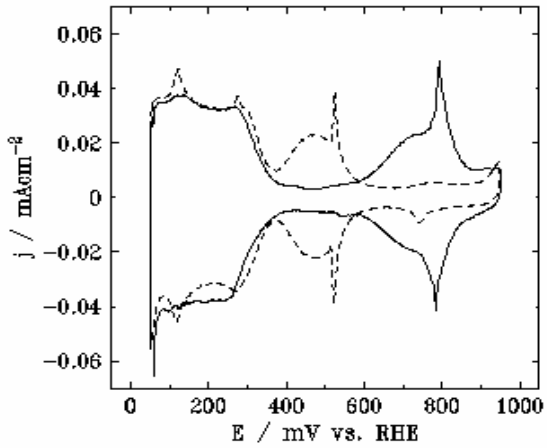

Figure 1. Linear sweep voltammetry curves for Pt(111) in Ar-saturated 0.1 M $HClO_4$ (solid line) and 0.05 M H_2SO_4 (dashed line) solutions. Sweep rate 50 mV/s.

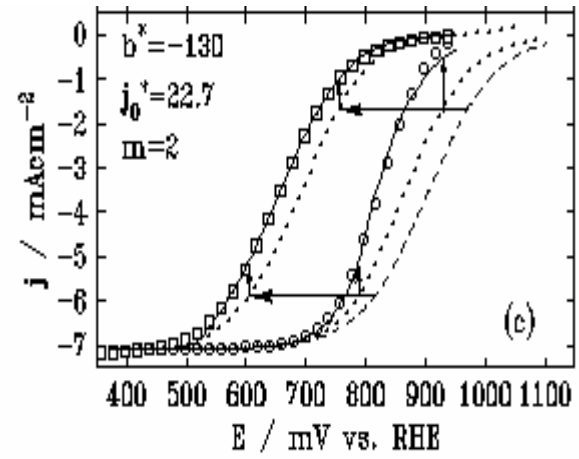

Figure 2. Polarization curves for Pt(111) in 0.1 M $HClO_4$ (circles) and 0.05 M H_2SO_4 (squares) solutions with calculated curves discussed in the text.

With the intrinsic kinetic parameters kept to the same values for the RDE polarization curves in both solutions, the anion adsorption effects were quantitatively evaluate using the following equation for the kinetic current:

$$j_k(E) = -j_0^*(1-\gamma_A\theta_A(E))^m \exp(2.303(E-E^0-\varepsilon_A\theta_A(E))/b^*)$$

where γ and ε are the site-blocking and energy coefficients for either OH or bisulfate anion, and *m* is the number of Pt sites involved in the rate determining step. The best fits, shown by the solid lines in Fig. 2, yielded the intrinsic Tafel slope in the range from –118 to –130 mV/dec, supporting single electron transfer in the rate-determining step with the corresponding transfer coefficients equal to 0.50 and 0.45, respectively.

To illustrate the effect of anion adsorption on the ORR kinetics, additional lines were provided in Fig. 2. The dashed line is obtained with the intrinsic kinetic parameters without any adsorption effects and the dotted lines are calculated with the electronic effect included. The differences between the dashed and dotted lines show the

electronic effect of adsorbed anions on the activation energy causing a potential shift indicated by the horizontal arrows. Since the solid lines include both the site-blocking and electronic effects while the dotted lines excludes the site-blocking effect, the differences between the two curves show the site blocking effects as marked by the vertical arrows. For $HClO_4$ solutions, both effects increase at higher potentials, which cause the slope of the ORR polarization curve, or the apparent Tafel slope, deviates from the intrinsic value. Since bisulfate adsorption saturates at a low potential, both site-blocking and electronic effects are nearly constant over the mixed kinetic-diffusion controlled region in H_2SO_4 solutions, and thus the apparent Tafel slope remains close to the intrinsic value.

These analyses also show that the catalytic performance of Pt for ORR is largely constrained by the OH adsorption and surface oxidation in the absence of other specifically adsorbed anions. Further studies of these effects were carried out on Pt nanoparticle catalyst as discussed below.

OH adsorption and surface oxide formation on Pt nanoparticles. Recently, we demonstrated that a thin-layer of a carbon-supported Pt nanoparticle catalyst can be deposited onto a glassy carbon rotating-disk electrode without using Nafion to stabilize it, and that to extract useful kinetic information from rotating-disk electrode's measurements, it is important to have a small enough loading so that full utilization is reached[2]. For the oxygen-reduction, we found that the suitable Pt loading is 30-50 nmol/cm^2.

Fig. 3a shows several voltammetry curves with different positive potential limits. When the potential was swept to more positive limits, the current in the reversed sweep increases below 100 mV, which indicates that OH adsorption on nanoparticles occurs over a wide potential region and the corresponding reduction requires a very low potential. This behavior is reflected on the dependence of the ORR polarization curve on the sweep rate. As shown in Fig. 3b, the curve taken at 50 mV/s exhibits higher activity than that measured at 10 mV/s.

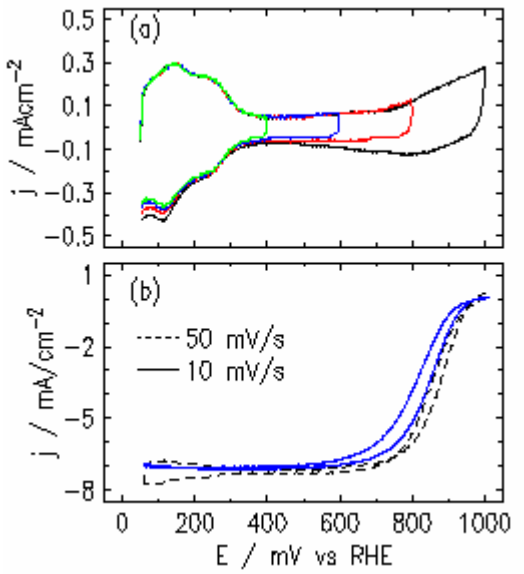

Figure 3. (a) Linear sweep voltammetry curves for Pt/C (20%wt, E-TEK, 30 nmol Pt/cm^2) in Ar- saturated 0.1 M $HClO_4$. Sweep rate 50 mV/s. (b) Polarization curves in oxygen saturated 0.1 M $HClO_4$.

To obtain time-dependent polarization curve, we measured current at 2500 rpm as a function of time after stepping the potential from 50 mV to a given value as shown in Fig. 4. For all measured potentials, the maximum ORR current was reached within 1 sec and a gradual decay of activity follows. The maximum currents near 1 sec, and the currents at 1 and 5 min are plotted as a function of potential in Fig. 5.

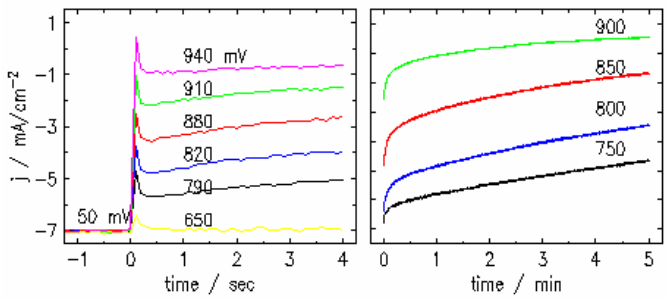

Figure 4. ORR currents at 2500 rpm as a function of potential after stepping the potential from 50 mV to the given potentials in 0.1 M $HClO_4$ solution.

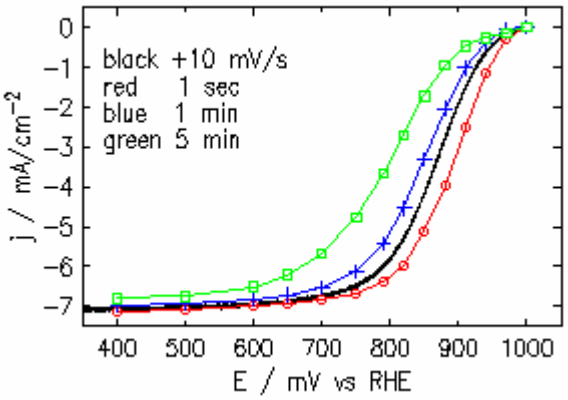

Figure 5. Time-dependent polarization curves for ORR at 2500 rpm in 0.1 M $HClO_4$ solution.

More data will be provided to identify the cause of the activity decay, which has also been studied by Uribe et. al in polymer electrolyte fuel cells[3]. The implications of the findings will be discussed.

Acknowledgement. This work is supported by U.S. Department of Energy, Divisions of Chemical and Material Sciences, under the Contract No. DE-AC02-98CH10886.

References

1. Wang, J.X.;, Markovic, N.M.; Adzic, R.R., *J. Phys. Chem. B* **2004**, *108*, 4127.
2. Wang, J.X.; Brankovic, S.R.; Zhu, Y.; Hanson, J.C.; Adzic, R.R., *J. Electrochem. Soc.*, **2003,** *150*, A1108.
3. Uribe, F. A.; Zawodzinski Jr., T. A., Electrochimica Acta **2002**, *47*, 3799.

FUNCTIONALIZED NANOSTRUCTURED CARBONS FOR FUEL CELL ELECTRODES

*Mark W. Perpall, Ibrahim Shaban, Hua Mei, Stephen E. Creager, Darryl D. Desmarteau, Dennis W. Smith, Jr.**

Department of Chemistry, Clemson University, Clemson, SC 29678

Introduction

Bis-*ortho*-diynyl arene or BODA monomers[1] have been used to fabricate nanostructured carbon materials[2] through their unique combination of excellent processability and high carbon yield. The enediyne functionality of the monomers undergo a thermal Bergman cycloaromatization reaction that yields reactive naphthalene diradicals which polymerize to form polynapthalene. (**Figure 1**) The tetrafunctionality of the monomers allows for both a higher processing window due to extensive branching and ultimately the formation of network polymers. The high carbon yield results in less shrinkage of the polymer upon pyrolysis to the glassy carbon state. This allows for the faithful templating of carbon structures from a polymeric precursor.

Hydrogen fuel cell electrodes require several properties for optimum performance. An ideal electrode would have as high a surface area as possible with an uniform dispersion of nano-scale catalyst particles attached to the surface. The electrode must be electrically conductive and have good mass transport for products and reactants. Carbon supported platinum is the best known catalyst for the oxidation of hydrogen at the anode and the reduction of oxygen at the cathode of a proton exchange membrane fuel cell (PEMFC)[3]. The material also must have good compatibility with the material used for the proton exchange membrane in the membrane electrode assembly (MEA), usually a sulfonated fluoropolymer such as Nafion.

We have undertaken a study to prepare a high surface area carbon material through a BODA templating method which can then be functionalized with both well dispersed platinum nanoparticles to act as catalysts and fluorophilic groups to facilitate the compatibility of the membrane and electrodes in the MEA.

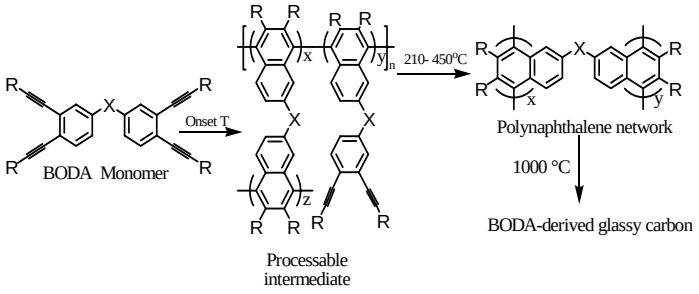

Figure 1. Polymerization of BODA monomers

Experimental

Materials. All BODA monomers were synthesized as previously reported.[1,2b] H_2PtCl_6 was purchased from Strem Chemicals. Karstedt's catalyst was purchased for GFS Chemicals. 4-acetylamino-phenol was purchased from Avocado Research Chemicals. All chemicals were used as received, unless otherwise noted.

Fabrication. BODA derived carbon materials were templated with a disordered monolith composed of nanoparticles of silica synthesized from a sol-gel and sintered together at 900 °C. The BODA monomer was melted into the free space in the monoliths to replicate the disordered porosity of the template into the polymer. The polymer was fully cured by heating under nitrogen. Further heating leads to pyrolysis of the polymer network and glassy carbon formation. The template was then removed with HF.

Platinum Functionalization. Platinum functionalization was attempted by several different methods. The platinum particles can be preliminarily synthesized and adsorbed onto the carbon surface, or the particles can be formed from an adsorbed platinum precursor with in situ reduction methods. Further attempts have included the adsorption of Pt(0) species which theoretically would lose the organic ligands and coalesce into Pt(0) particles. Method 1. Platinum sol formed from H_2PtCl_6 reduced with sodium citrate, then adsorbed onto carbon.[4] Method 2. H_2PtCl_6 adsorbed onto carbon then reduced with formaldehyde.[4] Method 3. H_2PtCl_6 adsorbed onto carbon then reduced with sodium borohydride.[3] Method 4. H_2PtCl_6 adsorbed onto carbon then reduced under H_2 flow in tube furnace.[5] Method 5. Karstedts's Catalyst $[Pt_2(((CH_3)_2C_2H_3Si)_2O)_3]$ (1 mL 10 % in xylene) was adsorbed onto 0.029 g carbon, dried and heated under N_2 at 300 °C in a tube furnace for 1h.

Fluorine Functionalization. Incorporation of fluorine containing groups onto the surface of the carbon materials was attempted in several different ways. Direct fluorination of aromatic groups is possible using certain classes of electrophilic fluorine reagents. Alternatively, incorporation of fluorine containing groups can be achieved through reaction of carbon or functional groups on carbon A few methods have already been attempted. N-fluorobenzene sulfonimide (NFSi) reacted with carbon samples from Aerogel and templated BODA samples.[6] Diethylamino Sulfur trifluoride (DAST) was reacted with oxidized carbon aerogel sample (refluxed in HNO_3, 13h) at –78 °C to room temperature.[7] Carbon reacted with diazonium salt[8]. Diazonium salts were all synthesized from their corresponding amines.[9] The Trifluorovinylether aniline was first synthesized by Harris et al.[10]

Surface Area Measurements. BET surface area measurements were performed using N_2 gas adsorption on a Micromeritics instrument.

Results and Discussion

BODA-Derived Carbon Foams. The carbon used in a fuel cell electrode must have high specific surface area for maximum efficiency in facilitating the redox reactions at the catalyst. BODA monomers were therefore templated with colloidal silica nanoparticles and thermally polymerized and carbonized in situ to yield an a open shell three dimensional carbon foam with very high specific surface area (**Figure 3**). The templating fidelity of the monomers is dependent on its wettability with the template material. This can be controlled through the variability of the terminal group R on the monomer (**Figure 2**). Templated carbon materials were prepared using the same process from several different monomers. The BET surface area was then measured using N_2 gas adsorption. The results are summarized in **Table 1**. The carbon templated using monomer **1** yielded the highest specific surface area of 275 m^2/g.

Monomer	X =	R =
1	C $(CF_3)_2$	Ph
2	C $(CF_3)_2$	$C(CH_3)_2OH$

3 =

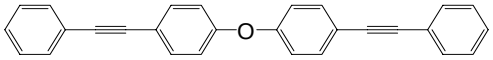

Figure 2. BODA monomers **1**, **2** and Bisacetylene **3**.

Table 1 Composition of Precursor BODA Polymer Network and BET Specific Surface Area of Templated Carbon Foams

Monomer composition	BET Surface Area, (m^2/g)
100 % **1**	275
100 % **2**	135
80% **1**, 20% **3**	51
100 % **3**	95

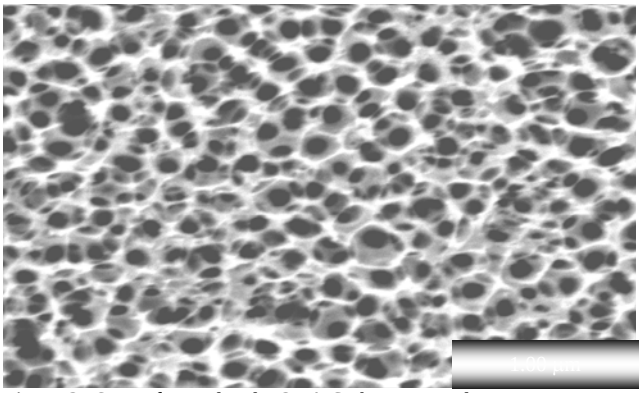

Figure 3. SEM of Templated BODA Carbon Material.

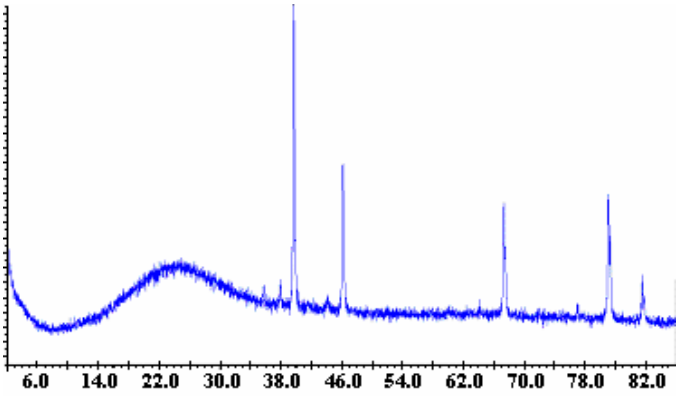

Figure 4. X-ray diffraction of Pt particles on BODA derived carbon

Platinum Incorporation. The platinum nanocatalyst syntheses can be divided into two basic paradigms: 1) pre-synthesis/ adsorption and 2) in situ reduction. Methods 1 and 5 represent the pre-synthesis/ adsorption route, where a Pt (0) species is adsorbed directly onto the surface of the carbon. This technique ensures that all of the platinum incorporated into the material will be surface bound and accessible for reaction in the fuel cell. Particle size is also better controlled and more monodisperse. Methods 2, 3, and 4 are all variations of the in situ reduction of a platinum salt method. This method involves immersing the carbon in a solution of a platinum salt and then using a chemical reducing agent to form the Pt (0) species within the framework of the carbon. This approach leads to a good dispersion of platinum particles over the entire surface of the carbon material.

Each method was attempted using enough platinum or platinum precursor to yield a final Pt loading of 20 % by weight with a carbon aerogel material. The samples were then analyzed using scanning electron microscopy (SEM) to determine catalyst size and dispersity and energy dispersive x-ray spectroscopy (EDX) for elemental analysis. The nanoparticles of platinum were not observed in any of the samples due ether to too small of size for the resolution of the microscope or due to coalescence of the particles together on the surface. The EDX data, as summarized in **Table 2** support the conclusion that the loading of platinum was too high for the surface area of the carbon and the size of particle formed. There is a greater that expected loading of platinum observed on the surface of the carbon for three of the methods. Method 1 seems to suffer from a poor adsorption of the platinum sol onto the carbon surface. The lack of control over loading is a major drawback for this method. Method 4 showed a platinum content very close to the expected platinum loading value. This indicates either good dispersity throughout the sample or a low yield of Pt (0) species from the precursor salt. In future experiments, the loading of the platinum should be related to the available surface area of the carbon support to prevent coalescence of the platinum nanoparticles on the limited surface.

The platinum nanoparticles may also be analyzed using wide angle x-ray scattering (WAXS) techniques, such as the pattern shown in **Figure 4**, which shows the platinum particles remaining after thermal oxidative removal of the carbon support. The large broad reflection indicates the presence of some carbon that was not fully removed. The sharp lines indicate the platinum that is left after the oxidation step. It is uncertain exactly what species is indicated. The peak width may be exploited to determine particle size. Unfortunately the particles are not visible in WAXS unless the carbon is removed, in a step which may also effect either the platinum species that exists or the particle size

Table 2. EDX-Derived Elemental Analyses for Surfaces of Platinum Incorporated Carbon Samples.

Platinum incorporation method	C content (%)	Pt content (%)
1	86.5	2.7
2	16.2	80.9
3	15.1	83.1
4	72.3	16.8
5	27.5	53.7

Fluorine Incorporation. The incorporation of fluorine onto the carbon electrode material to aid in compatibilizing the electrode with the proton exchange membrane for close contact can be achieved by either the direct fluorination of the carbon material or incorporation of another fluorine containing functionality. Attempts at analyzing carbon materials with diamond ATR-IR have had only moderate success due partially to the inherent absorption of light by carbon. New peaks are detected around 1100 cm^{-1} that may be attributable to new aromatic C-F bonds formed by the direct fluorination of carbon using DAST. No such peaks are visible for the other direct fluorination methods. The incorporation of fluorine may also be possible by including it with another group that can readily be attached to carbon such as a diazonium salt. Diazonium salts add to carbon materials, by dediazoniation to form a reactive phenyl cation which then adds to the carbon.[11] Several diazonium salts have been prepared as shown in **Figure 5** with R = CF_3 and $OCFCF_2$. The latter species is a reactive species from which high molecular weight fluoropolymers may be grown from the surface of the carbon. This allows for high fluorine content to be achieved from even moderate carbon functionalization yields.

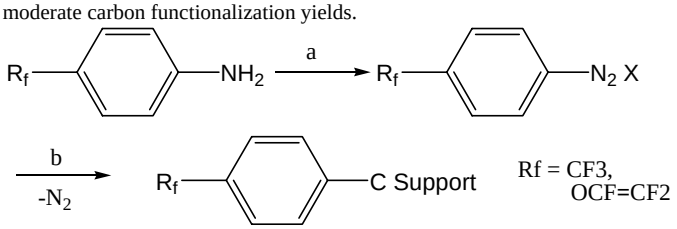

Figure 5. Synthesis of Diazonium Salts and functionalization of carbon. support. a) $NaNO_2$, HCl, H_20 b) Carbon powder, H_3PO_2, 5 °C, 40 min.

Conclusions

Through the right combination of a suitable platinum nanoparticle formation technique, a suitable surface fluorine incorporation technique and the templated BODA carbon fabrication method, a very attractive approach for fabricating hydrogen PEM fuel cell electrodes should show promise for reducing some of the efficiency depriving faults in today's fuel cells technology.

Acknowledgement. The authors would like to recognize the financial support of NSF/ NER for funding the project. We would also like to recognize the assistance of Dr. K. Prasanna Perera, Dr. Suresh Iyer, Dr. Sibylle Glaser, and Dr. Chris Topping.

References

(1) Smith, Jr., D.W.; Babb, D.A.; Snelgrove, R.V.; Townsend, III, P.H.; Martin, S.J. *J. Am. Chem. Soc.* **1998**, *120*, 9078-9079.
(2) a) Perpall, M.W.; Zengin, H.; Perera, K.P.U.; Zhou, W.; Shah, H. Wu, X.; Creager, S.E.; Smith, Jr., D.W; Foulger, S.H.; Ballato, J. *Proc. of SPIE*, **2003**, *4979*, 307-316. b) Perpall, M.W.; Perera, K.P.U.; Dimaio, J.; Ballato, J.; Foulger, S.H.; Smith, Jr., D.W. *Langmuir* **2003**, *19*, 7153-7156.
(3) Ye, S.; Vijh, A.K.; Dao, L H. *J. Electrochem. Soc.* **1996**, *143*, L7-L9.
(4) Frelink, T.; Visscher, W.; van Veen, J.A.R. *J. Electroanal. Chem.* **1995**, *382*, 65-72.
(5) Joo, S.H.; Choi, S.J.; Oh, I.; Kwak, J.; Liu, Z.; Terasaki, O. Ryoo, R. *Nature* **2001**, *412*, 169-172.
(6) Singh, S.; Desmarteau, D.D.; Zuberi, S.S.; Witz, M.; Huang, H.-N. *J. Am. Chem. Soc*. **1987**, *109*, 7194-7196.
(7) Middleton, W.J. *J. Org. Chem.* **1975**, *40*, 574-578.
(8) Pandurangappa, M.; Lawrence, N.S.; Compton, R.G. *Analyst* **2002**, *127*, 1568-1571.
(9) Finger, G.C.; Oesterling, R.E. *J. Am. Chem. Soc.* **1956**, *78*, 2593-2596.
(10) Choi, W.-S.; Harris, F.W. *Polymer* **2000**, *41*, 6213-6221.
(11) Zollinger, H. *Diazo Chemistry I;* VCH: New York , NY, 1994; Vol. 1, pp 161-212.

DEVELOPMENT OF AIR-BREATHING DIRECT ETHANOL FUEL CELLS WITH PtSn AS ANODE

Luhua Jiang[a], Zhenhua Zhou[b], Suli Wang[a], Jianguo Liu[a], Xinsheng Zhao[a] Gongquan Sun[a], Qin Xin[ac], Bing Zhou[b]*

[a]Direct Athanol Fuel Cells Laboratory, Dalian Institute of Chemical Physics, CAS, P.O. Box 110, Dalian 116023, China
[b]Headwaters Nanokinetix, 1501 New York Avenue, Lawrenceville, NJ 08648, USA
[c]State Key Laboratory of Catalysis, Dalian Institute of Chemical Physics, CAS, P.O. Box 110, Dalian 116023, China

Introduction

In the past decades direct methanol fuel cells (DMFCs) have been studied extensively as promising power sources for portable devices, electric vehicles due to their high power density, simplified system and the ease of fuel transportation and storage. Although great progress has been made in this field [1-7], the commercialization process of the direct methanol fuel cell is postponed due to the sluggish methanol oxidation kinetics, methanol crossover and the toxicity of methanol. Compared to methanol, ethanol with reduced crossover is cleaner, safer and available from fermentation of sugar-containing raw materials. These features make ethanol more attractive than methanol for direct alcohol fuel cells operating at lower temperatures [8,9]. Great efforts have been made so far [10-13]. However, difficulties and challenges for crack of C-C bond via optimal PtRu based electrocatalysts are great [14-16]. In this paper, with PtSn as anode, the performance of DEFCs with two different electrode structures was measured using pure oxygen and air as oxidant, respectively. More importantly, a comparable performance of air-breathing DEFC to DMFC is supplied for the first time [17].

Experimental

PtSn/C (with different Pt/Sn atomic ratios of 2:1, 3:1, 4:1, denoted as Pt_2Sn/C, Pt_3Sn/C, Pt_4Sn/C, respectively) and Pt/C employed in the present paper were all homemade according to literature [18]. Electroactivities of the homemade PtSn/C catalysts were measured first by cyclic voltammetry using an EG&G model 273 potentiostat/galvanostat and a three-electrode test cell at room temperature. The conventional membrane electrode assemblies (MEAs) were fabricated according to the method described in the literature [19]. The improved CCM MEAs were prepared by spraying the catalyst on the Nafion membrane. MEAs were made by hot-pressing the diffusion layer on either side of Nafion membranes with catalyst layers at 140 ^oC for 90 s. Nafion 115 (DuPont) was used as the electrolyte membrane for all the MEAs reported here. MEAs were tested using a homemade 4 cm^2 single cell with reservoir. The ethanol was injected into the fuel reservoir using a micro syringe. The cathode was opened to air. The load was varied using a rheostat when voltage (*V*)-current density (*I*) curves were collected. The MEAs had been activated by 1 M ethanol for 2 hours before all the data were collected.

Results and Discussion

The TEM images of homemade 20 wt.% Pt/C, 50 wt. % Pt/C and 20 wt.% Pt_3Sn/C catalysts are shown in Fig. 1.

Fig. 2 shows the cyclic voltammogram of ethanol electrooxidation with PtSn/C as electrode. It can be seen clearly that the ethanol oxidation current peaks with different PtSn/C catalysts all started at around 500 mV, but the Pt_3Sn/C catalyst brought the highest oxidation current in contrast to the Pt_4Sn/C with the lowest oxidation current. This result indicated that Pt_3Sn/C might be a better catalyst for ethanol oxidation.

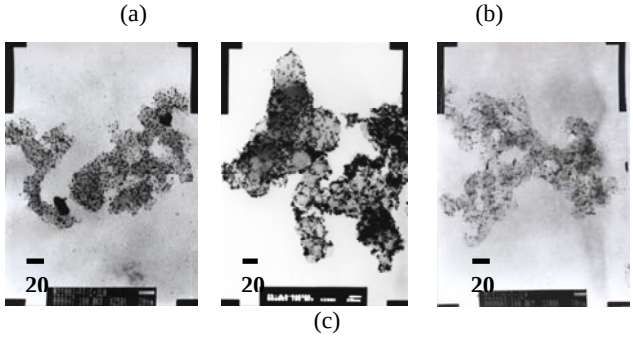

Figure 1. TEM images of (a) 20 wt.% Pt/C (b) 50 wt.% Pt/C (c) 20 wt.% PtSn/C

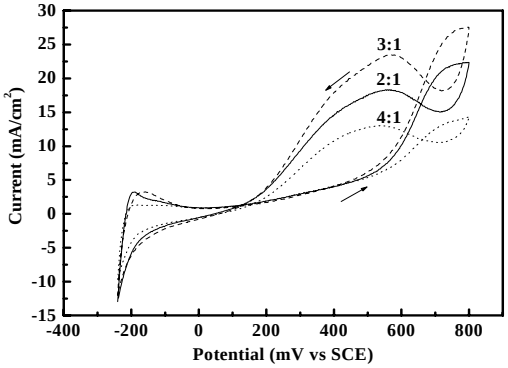

Figure 2. The CV results of PtSn/C catalysts with different atomic ratio for ethanol electro-oxidation. Operation Temperature: 25 ^oC. Scan rate: 50 mV/s. Electrolyte: 0.5 M EtOH + 0.5 M H_2SO_4

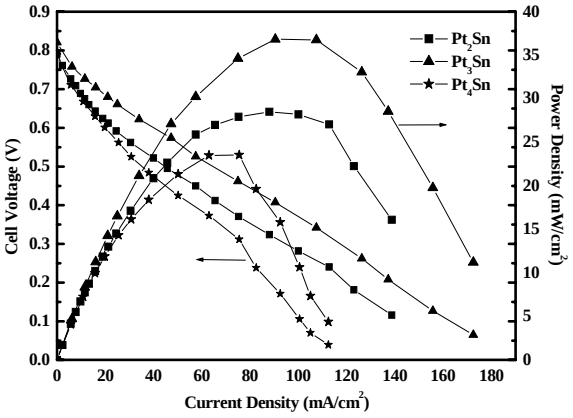

Figure 3. Performance of the active direct ethanol fuel cell with conventional electrode structure operated at 90 ^oC. Anode catalyst and metal loading: PtSn/C, 1.5 mg Pt/cm^2, cathode catalyst and metal loading: 1.0 mg Pt/cm^2 (20 wt. % Pt/C), ethanol concentration and flow rate: 1 M & 1.0 ml/min, oxidant: O_2

Fig. 3 shows the performance for electrodes with conventional electrode structure. It can be seen that the Pt_3Sn/C electrode shows the best performance and the maximum output power density is about 38 mW/cm^2. The next is Pt_2Sn/C, which shows a maximum power density of 27 mW/cm^2. Pt_4Sn/C electrode presents the worst performance. This result is in good agreement with the above CV screening results. Another interesting phenomenon could be observed in Fig. 3. As are known, the cell voltage of DMFCs decreases sharply at high current density, which might be due to the mass transport limitation rising from anode or cathode. However, unlike the *V-I* curves of DMFCs, the *I-V* curves of DEFCs decrease linearly with current density increasing. This might suggest that for DEFCs, mass transport limitation whether from anode or from cathode might be not the rate- determining step (RDS). It is not surprising that the mass transport is not the RDS for the slow dynamics of ethanol oxidation at such temperature.

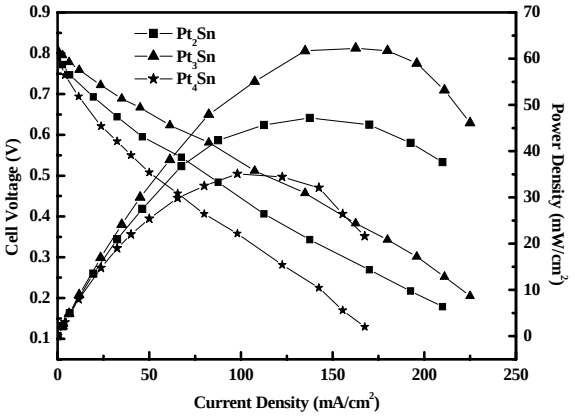

Figure 4. Performance of the active direct ethanol fuel cell with CCM electrode structure operated at 90 ^oC. Anode catalyst and metal loading: PtSn/C, 2.0 mg Pt/cm^2, cathode catalyst and metal loading: 1.0 mg Pt/cm^2 (50 wt.% Pt/C), ethanol concentration and flow rate: 1 M & 1.0 ml/min, oxidant: O_2

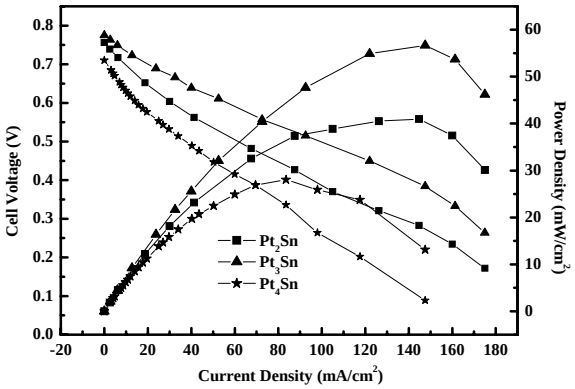

Figure 5. Performance of the active direct ethanol fuel cell with CCM electrode structure operated at 90 ^oC. Anode catalyst and metal loading: PtSn/C, 2.0 mg Pt/cm^2, cathode catalyst and metal loading: 1.0 mg Pt/cm^2 (50 wt.% Pt/C), ethanol concentration and flow rate: 1 M & 1.0 ml/min, oxidant: air

Fig. 4 shows the performance of DEFCs with CCM electrode structure. It can be observed that the performance of DEFCs with CCM electrode structure was enhanced greatly in comparison with the performance of DEFCs with the conventional one. The best performance is still presented by Pt_3Sn/C, which brought the maximum power density of 62 mW/cm^2. Even the worst catalyst Pt_4Sn with CCM electrode structure in this research shows a comparable performance (the maximum output power density is 35 mW/cm^2) with the best catalyst Pt_3Sn/C with conventional one. While even with the CCM electrode structure, mass transport limitation phenomenon is not observed yet. This might indicate that the ethanol oxidation is still the RDS at the operation temperature, although the CCM electrode structure enhances the DEFCs performance.

Fig. 5 is the performance of DEFCs with CCM electrode structure operated with air as oxidant. It can be observed that the change of oxidant from O_2 to air brought a little decrease of the performance. The maximum output power density is 57 mW/cm^2 (Pt_3Sn/C), 41 mW/cm^2 (Pt_2Sn/C) and 28 mW/cm^2 (Pt_4Sn/C), respectively. It is understandable that there is only a little drop of cell performance with the oxidant changing from O_2 to air on the premise of ethanol oxidation being the RDS as the above discussion. Based on this premise, the oxygen in air is enough to meet the reaction requirement. So it is extremely suitable for ethanol to act as air-breathing fuel considering the insensibility of ethanol oxidation to the concentration of oxygen.

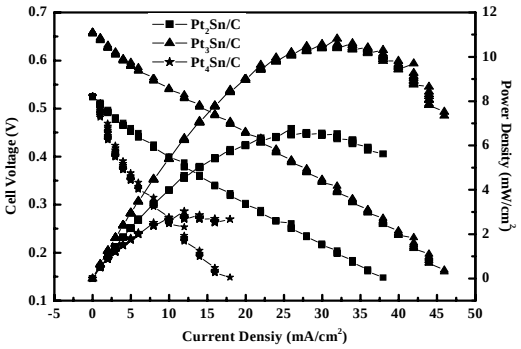

Figure 6. Performance of the passive air-breathing direct ethanol fuel cell operated at 30 ^oC. Anode catalyst and metal loading: PtSn/C, 2.0 mg Pt/cm^2, cathode catalyst and metal loading: 1.0 mg Pt/cm^2 (50 wt.% Pt/C). The ambient air was used as oxidant.

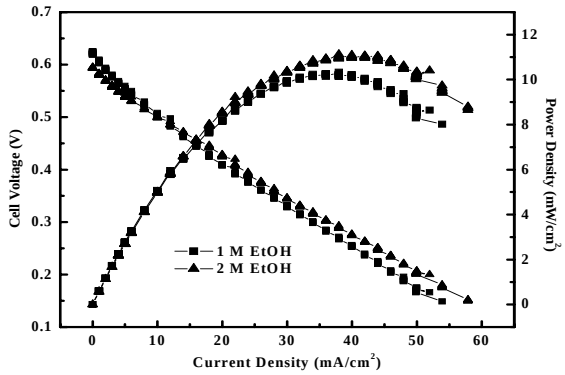

Figure 7. The effect of ethanol concentration on the performance of the passive air-breathing DEFCs operated at 30 ^oC. Anode catalyst and metal loading: Pt_3Sn/C, 2.0 mg Pt/cm^2, cathode catalyst and metal loading: 1.0 mg Pt/cm^2 (50 wt.% Pt/C). The ambient air was used as oxidant.

The air-breathing performance tests were conducted at room temperature under static feed conditions: air was fed only through natural convection and the methanol solution was stored in the reservoir that contacted the MEA on the anode side. Different ethanol concentrations were employed to test the cell performance. The results were shown in Fig. 6. It can be seen that the cell performance with Pt_3Sn/C as the anode catalyst showed the best performance. The maximum output power density with Pt_3Sn/C, Pt_2Sn/C and Pt_4Sn/C as the anode catalyst are 10 mW/cm^2, 6 mW/cm^2 and 2.5 mW/cm^2, respectively.

Fig. 7 shows the influence of ethanol concentration on the performance of DEFCs with CCM electrode structure. It can be seen that the concentration increase of ethanol from 1 M to 2 M only brought a little performance improvement of 1 mW/cm^2. It can be seen that the cell performance is insensitive to the ethanol concentration in the studied range. This suggests that the anode mass transport has little influence on the performance of DEFCs. But usually, it is believed that the performance of DMFCs with the CCM electrode structure is enhanced via improving the mass transport in MEAs. It was observed that the delamination of the catalyst layer and the electrolyte membrane in DEFCs with CCM electrode structure is not so serious as those with conventional one after performance tests. In order to quantify the effect of cell internal impedance on the improvement of DEFCs performance, the impedance of the DEFCs with different electrode structures was measured. The results showed that all the DEFCs with CCM electrode structure present much smaller internal impedance than those with conventional one. The improvement of the DEFCs performance might be mainly derived from the decreased internal impedance of the former.

Highly active PtSn/C electrocatalyst was employed to the anode of DEFCs with a CCM electrode structure. This electrodes exhibited excellent performance. Using homemade 20 wt.% PtSn/C and 50 wt.% Pt/C yielded the best performance. With the CCM electrode structure, power density as high as 62 mW/cm^2 and 57 mW/cm^2 were achieved with pure O_2 and air as oxidant at cell temperature of 90 ^{o}C, respectively, for a cathode with a Pt loading of 1 mg Pt/cm^2 and anode with 2 mg Pt/cm^2. With the same anode and cathode noble metal loadings, power density of air-breathing DEFCs is about 10 mW/cm^2 at 30 ^{o}C. The improvement of the DEFCs performance might be mainly derived from the decreased internal impedance in the DEFCs with the CCM electrode structure. Further research on the optimal electrode structure for DEFCs and the reaction mechanism of ethanol on PtSn catalysts is being carried out.

Acknowledgment. The present work was partly supported by National Natural Science Foundation of China (Grant No 29976006, Grant No 29876040) and Innovation Foundation of Dalian Institute of Chemical Physics (K2003D2). The authors are grateful to Engineer Fengliang Zhao and Likang Chen for kindly offering the air-breathing test device. We are also grateful to Professor Shaohua Yang for discussion and revision.

References

1. Ren, X.; Zelenay, P.; Thomas, S.; Davey, J.; Gottesfeld, S., J. Power Sources, **2000**, 86, 111.
2. Lamy, C.; Lima, A.; LeRhun, V.; Delime, F.; Cutanceau, C.; Leger, J-M., J. Power Sources, **2002,**105,283.
3. Ren, X.; Wilson, M.; Gottesfeld, S., J. Electrochem. Soc., **1996,** 143, 12.
4. Wasmus, S.; Kuver, A., J. Electroanal. Chem., **1999,** 461, 14.
5. Wei, Z.B.; Wang, S.L.; Yi, B.L.; Liu, J.G.; Chen, L.K.; Zhou, W.J.; Li, W.Z.; Xin, Q., J. Power Sources, **2002**, 106, 364.
6. Surampudi, S.; Narayanan, SR.; Vamos, E.; Frank, H.; Halpert, G.; Laconti, A.; Kosek, J.; Prakash, G.; Olah, G., J. Power Sources, **1994**, 47,377.
7. Liu, J.G.; Sun, G.Q.; Zhao, F.L.; Wang, G.X.; Zhao, G.; Chen, L.K.; Yi, B.L.; Xin, Q., J. Power Sources, **2004**, in press.
8. Ianniello, R.; Schmidt, V.M.; Rodriguez, J.L.; Pastor, E.; J.Electroanal. Chem., **1999**, 471, 167.
9. Chen, G.L.; Chen, S.P.; Zhou, Z.Y.; Zhen, C.H.; Sun, S.G., J. Electrochem.(Chinese), **2001**, 7, 96.
10. Arico, A.S.; Creti, P.; Antonucci, P.L.; Antonucci.V., Elecrochem. Solid-State Lett., **1998,** 1, 66.
11. Tremiliosi-Filho, G.; Gonzalez, E.R.; Motheo, A.J.; Belgsir, E.M.; Leger, J.-M.; Lamy. C., J. electroanal. Chem., **1998**, 444, 31.
12. Lamy, C.; Belgsir, E.M.; Leger, J-M., J. Appl. Electrochem., **2001**, 31, 799.
13. Ha, S.; Adams, B.; Masel, R.I., J. Power Sources, **2004**, in press.
14. Zhou, W.J.; Zhou, Z.H.; Song, S.Q.; Li, W.Z.; Sun, G.Q.; Tsiakaras, P.; Xin, Q., Appl. Catal., **2003**, 46, 273.
15. Zhou, W.J.; Zhou, B.; Li, W.Z.; Zhou, Z.H.; Song, S.Q.; Sun, G.Q.; Xin, Q.; Douvartzides, S.; Goula, M.; Tsiakaras, P., J. Power Sources, **2004**, 126, 16.
16. Zhou, W.J.; Li, W.Z.; Song, S.Q.; Zhou, Z.H.; Jiang, L.H.; Sun, G.Q.; Xin, Q.; Poulianitis, K.; Kontou, S.; Tsiakaras, P., J. Power Sources, **2004**, in press.
17. Dillon, R.; Srinivasan, S.; Arico, A.S.; Antonucci, V., J. Power Sources, **2004,** in press
18. Zhou, Z.H.; Wang, S.L.; Zhou, W.J.; Wang, G.X.; Jiang, L.H.; Li, W.Z.; Song, S.Q.; Liu, J.G.; Sun, G.Q.; Xin, Q., Chem. Comm., **2003**, 3, 394.
19. Zhou, Z.H.; Wang, S.L. Zhou, W.J.; Jiang, L.H.; Wang, G.X.; Sun, G.Q.; Zhou, B.; Xin, Q., Phys. Chem. Chem. Phys., **2003**, 5 , 5485.

ELECTROCATALYST MATERIALS FOR PEM FUEL CELLS BASED ON HETEROPOLY ACIDS

Andrew M. Herring,[1] Mei-Chen Kuo,[1] Ronald J.Stanis,[1] Brad R.Limoges[1], John A. Turner.

Department of Chemical Engineering[1]
Colorado School of Mines
Golden, CO 80401-1887

Hydrogen and Electricity, Systems and Infrastructure Group[2]
National Renewable Energy Laboratory
Golden, CO 80401-3393

Introduction

One of the major barriers to the commercialization of proton exchange membrane, PEM, fuel cells is the expense of the platinum needed to catalyze the electrodes. In addition the kinetics of oxygen reduction is slower than desirable and the platinum anode is easily poisoned by carbon monoxide a by-product of hydrogen production from hydrocarbon reforming. The ideal electrode materials for a commercially viable fuel cell would be inexpensive, have fast kinetics and not be poisoned by small molecules.

The Heteropoly acids (HPA) a large and diverse class of polyoxometallates that can act as redox catalysts when substituted by a transition metal, are proton conductors, and can be reduced to form electronically conducting materials [1]. This makes the HPA ideal candidates for an electrode material in a PEM fuel cell as the catalyst would ideally enable fast transfer of protons and electrons as well as be a selective catalyst. Some heteropolyoxometalates have been explored as possible electrocatalysts for PEM fuel cell applications [2]. Functionalized heteropoly acids, HPA, based on iron and vanadium have the potential to act as cost effective catalysts for fuel cell oxidations as well as facilitate both proton and electron conduction. The goal of this research is to develop a non-platinum electrocatalyst based on an HPA or to enhance the catalytic activity of a conventional platinum catalyst in a co-catalyst system and so reduce the amount of precious metals.

Experimental

The HPA and lacunary HPA and iron and vanadium substituted HPA were prepared by literature methods. The materials were characterized by IR, NMR, TGA, Mössbauer, and ICP-AA elemental analysis. Cyclic voltammetey was measured using a polished glassy carbon disk electrode in 1M H2SO4.

The Nafion® membrane (Ion Power) was cleaned and converted into the acid form by successively boiling the membranes for at least one hour in each of the following solution: 3% H_2O_2, deionized (DI) water, 0.5 M H_2SO_4, and DI water again. The acid form Nafion® 117 was stored in DI water in the dark prior to use. Approximately 1 g of the catalyst was dissolved in 40 mL of DI water and heated at about 60 °C with stirring. A 5 cm^2 piece of uncatalyzed thick gas diffusion electrode (GDE) (the DGE was developmental gas diffusion electrodes-Type V 2.33-very thick standard ELAT-all hydrophilic, E-tek) was floated in the catalyst solution overnight. The GDE was removed from the solution, washed with DI Water, and dried in the oven. HPA loading was about 0.08 mg/cm^2. The catalyzed GDE layer and a 5 cm^2 piece of GDE which is hand fabricated single side coating standard 0.5 mg/cm^2 TM loading using 20 % Pt on Vulcan XC-72 were hand painted with Nafion® solution and allowed to dry in the air. The maximum Nafion® loading is 1.9 mg/cm^2 when pure oxygen was imployed as the oxidant. [3]. These two electrodes were pressed into Nafion® 117 with heated plates at 115 °C and 75 psi for 90 seconds. The MEAs were conditioned to achieve constant polarization curve prior to use. Polarization curves in H2/O2 were measured at 80°C with humidified gasses using standard 5 cm2 active area fuel cell hardware.

Results and Discussion

The loadings of HPA on the XC-72 carbon based ELAT GDEs are very low, typically 0.1 mg/cm^2. After conditioning the MEA current densities are typically on the order of 100 mA/cm^2 at 0.1 V using H_2/O_2, but the OCV of 0.75 V is somewhat low presumably due to the poor activation of the iron catalyst compared to platinum. When the MEA is turned over and the iron-substituted HPA is run as the anode an electrochemical wave is observed. After exposure to H_2 as the anode the catalyst improves to give close to 150 mA/cm^2 under the same conditions on the cathode, **Figure 1**. This activity appears to be stable, multiple polarization curves can be run after the reduction step.

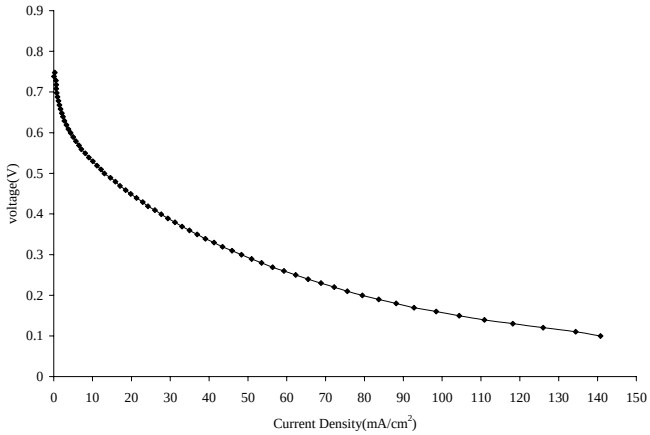

Figure 1. Polarization curve for a iron substituted HPA aftere reduction on the cathode and Pt on the anode on ELAT GDE at 80 °C, using H_2/O_2 humidified at 90 °C.

We speculate that the mechanism involves fast protonation of an oxygen atom bonded to an iron center, followed by a slow chemical re-oxidation of the iron:

$$Fe\text{-}O + 2H^+ \rightarrow Fe + H_2O$$

$$Fe + \tfrac{1}{2} O_2 \rightarrow Fe\text{-}O$$

When O_2 is switched for N_2 on the cathode and successive polarization curves are run the limiting current density falls, initially rapidly and then more slowly, **Figure 2**. As there is no oxygen to regenerate the catalyst the activity is diminished with each successive sweep. The rapid fall of current density is due to the reversible depletion of the oxygen from the iron centers. The slow fall in activity at longer times/lower current densities is due to the irreversible depletion of skeletal tungsten bound oxygen. This is borne out in experiments in which the catalyst is run under N_2 to exhaustion, on exposure to O_2, the catalyst does not recover all of its activity. When the catalyst is depleted under N_2 only to the end of the rapid reversible current density loss we would expect it to recover all its activity on re-exposure to O_2. Interestingly the catalyst performs better and better on each successive cycle of experiments. From these results we speculate that electrochemical or chemical reduction of these iron substituted HPA results in the formation of iron/tungsten oxide nanoparticles that may be the true catalyst.

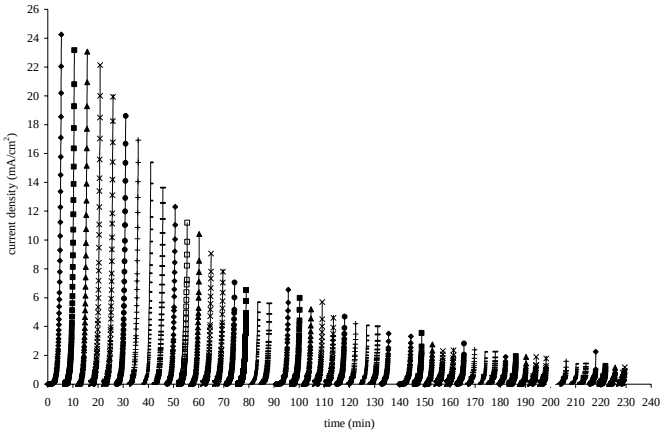

Figure 2. Successive polarization curves for an iron substituted HPA after O_2 exposure on the cathode and Pt on the anode on ELAT GDE at 80 °C, using H_2/N_2 humidified at 90 °C.

We have also investigated vanadium substituted HPA [5]. These materials exhibit very similar behavior to the iron-substituted HPA, but limiting current densities achieved on the cathode are only 24 mA cm^{-2} at 80 °C. The temperature dependence of the catalytic activity improves dramatically with temperature leading us to believe that these may be very interesting catalysts for higher temperature PEM fuel cells.

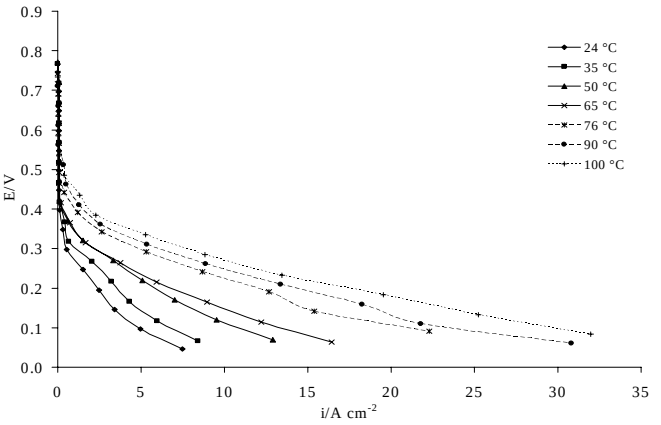

Figure 3. Temperature dependence of a vanadium substituted HPA as a cathode catalyst.

These vanadium substituted HPA materials are much more interesting when used as a co-catalyst on the fuel cell anode, **Figure 4**. A 30% improvement in current density and power is seen with the vanadium HPA/Pt versus the Pt catalyst. Control experiments with and without Nafion® in the electrodes indicate that at least some of this activity is due to the proton conducting ability of the HPA. Additional controls with unsubstituted HPA and V_2O_5 indicate that the catalytic activity only originates from the vanadium substituted HPA and in addition the catalyst must contain more than two vanadium atoms.

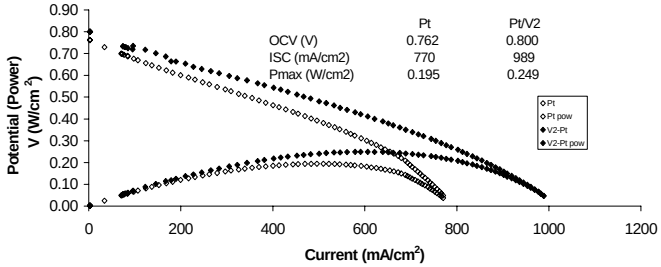

Figure 4. Polarization and power curves for Pt on ELAT electrodes as both anode and cathode catalysts and for a vanadium substituted HPA/Pt co-catalyst system as anode with a Pt cathode.

Conclusions

Heteropoly acids may be immobilized on carbon supports and used in PEM fuel cells as catalysts. Iron substituted HPA exhibit catalytic activity comparable to the best non-platinum catalysts so far discovered. Vanadium substituted materials may be useful as co-catalysts for Pt systems. Co tolerance of the co-catalyst anodes will be investigated in the future and further characterization will be performed on the iron cathodic catalyst to determine then exact nature of the catalyst.

Acknowledgement. This work was supported by the Xcel Energy renewable development fund, project No. CB07.

References

(1) Mizuno, N.; Misono, M. *Chem. Rev.*, **1998,** *98,* 199-217.
(2) Savadogo, O.; Bartolacci, G. *Int. J. Hydrogen Energy* **1992,** *17,* 109-114.
(3) Ren, X.; Wilson, M. S.; Gottesfeld, S. In "Proton Conducting Membrane Fuel Cells I", Gottesfeld, S.; Halpert, G.; Landgrebe, A. Editors, *95* (23), p. 252, The Electrochemical Society Proceedings Series, Pennington, NJ (**1995**).
(4) Litster, S.; McLean, G. *J. Power Sources*, **2004,** 109, 61-76.
(5) Limoges, B. R.; Herring, A. M.; Turner, J. A. *Electrochimica Acta,* Submitted.

FLUORINATED SULFONIMIDE ELECTROLYTES GRAFTED ONTO CARBON: A POTENTIAL ROUTE TO HIGH-PERFORMANCE PEM FUEL CELL ELECTRODES

Stephen E. Creager, Hua Mei, Bing Liu, Mark W.Perpall, Ibrahim Shaban, Dennis W. Smith, Jr, Darryl D. Desmarteau

Department of Chemistry, Clemson University, Clemson, SC 29634-0973

Introduction

Proton-conducting polymer electrolytes based on fluorinated sulfonimide superacids (1-4) are being developed as alternatives to fluorinated sulfonic acid-based polymer electrolytes such as Nafion™ that are commonly used in PEM fuel cell technology. The sulfonimide group can be incorporated into a rich variety of functional derivatives which provides opportunities for making crosslinked ionomers and ionomers with greater TFE character to provide dimensional stability at high ionic content, as is desired to achieve high conductivity and usefulness in PEM fuel cells.

An important issue in PEM fuel cell technology is the integration of electrolyte with electrode. Present technology involves simple mixing to achieve good contact between ionomer and electrode. Improvements are needed to provide for greater integration and contact with electrocatalyst, and also longer life by preventing phase segregation between the carbon electrode support and the electrolyte.

This contribution concerns one such derivative in which a sulfonimide functional group is attached at the para-position of an aryl diazonium inner salt. The resulting compound has structure $^{+}N_2$-C_6H_4-SO_2N-SO_2CF_3, and we show that the aryl diazonium portion of the molecule may be used to graft a sulfonimide anion onto the surface of carbon electrodes by formation of a covalent carbon-carbon bond. In this contribution we consider the formation of grafted electrolytes on carbon formed by electroreduction of the diazonium inner salt at glassy carbon electrodes, and also by thermal treatment of porous carbon aerogels with solutions of the diazonium salt in organic solvents.

Experimental

Synthesis of the target compound will be described in detail separately. (5) Cyclic voltammetry was accomplished using a CH Instruments model 660 Electrochemical Workstation. Conditions were as follows: 3-electrode cell: carbon plate working electrode, Ag/AgCl reference electrode, Pt auxiliary electrode. Diazonium salt was present at 10^{-3} M in acetonitrile solution containing 0.10M $TEABF_4$. Scans were from 0 to −0.9 V, 20−30 cycles.

Results and Discussion

Figure 1 presents a crystal structure of the fluorosulfonamide diazonium salt studied in this work. The presence of the diazonium functionality on one side and the fluorosulfonamide on the other are clearly evident.

Figure 2 presents a series of cyclic voltammgrams of the compound from Figure 1 at a glassy carbon plate electrode. The diminishing current with continues scanning indicates coating of the electrode with a grafted, covalently bonded coating of the target molecule. XPS analysis of the carbon plate confirms that coating has occurred; the survey XPS scan indicates the coated surface composition is approximately 73.5% C, 14.7% O, 3.2% N, 4.2% F, 2.8% S. In contrast, the uncoated surface composition by XPS is 92.7% C and 7.2% O, with no other elements present.

It is of interest to extend the approach above to nanoporous carbon aerogels being developed at Clmeson and elsewhere for use as electrodes in PEM fuel cells. Figure 3 presents an SEM micrograph of a carbon aerogel sample, showing the pore structure on submicrometer length scales. TO modify the interior pore surfaces of this aerogel with fuorsulfonimide electrolyte, we impregnated dry ground-up particles of carbon aerogel (40-200 micrometers particle size) with the solution and allowed them to react for 2 hours at ambient temperature or 55 ^{o}C). EDX analysis of the resulting particles showed the binding had occurred, e.g., for an aerogel sample modified at 55 ^{o}C the EDX analysis indicated an aerogel bulk composition of 84.6% C, 3.2% N, 7.2% O, 2.0% F, and 2.9% S.

Conclusions

We have synthesized a fluorosulfonimide aryl diazonium salt and used it to modify the flat surface of a glassy carbon plate electrode and the surface of the interior pores of a carbon aerogel sample. XPS and EDX analysis confirm immobilization of F, N, and S, which indicates grafting of the fluorosulfonimde electrolyte.

Acknowledgement: Financial support of this work by the National Science Foundation, DMI-0303645, is gratefully acknowledged.

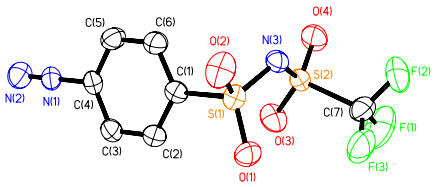

Figure 1. X-ray crystal structure of structure $^{+}N_2$-C_6H_4-SO_2N-SO_2CF_3, that was used in this work to chemicall modify carbon surfaces.

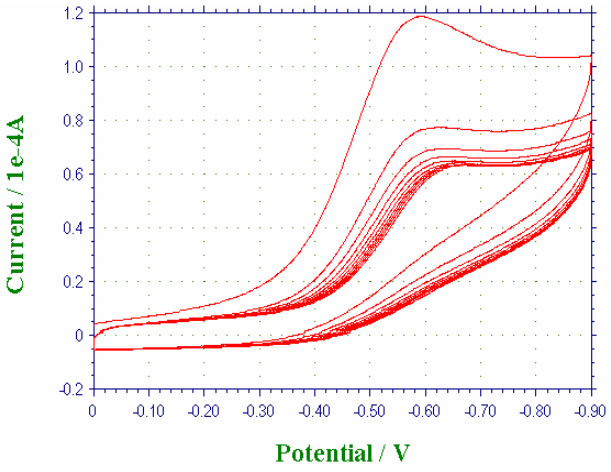

Figure 2. Cyclic voltammgrams of a solution of fluoroslufonamide aryl diazonium salt at a glassy carbon plate electrode.

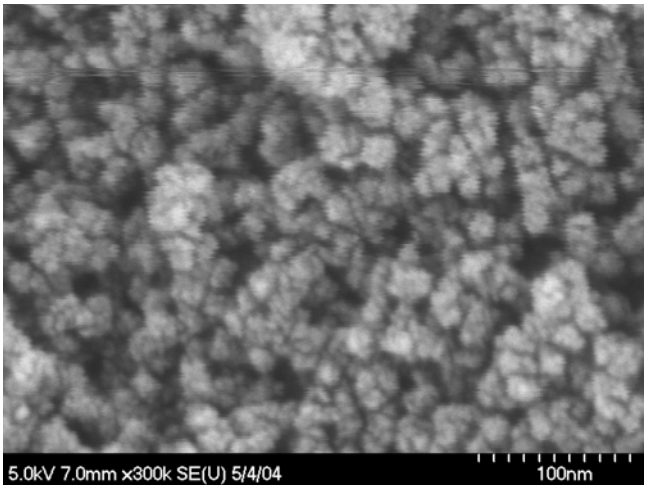

Figure 3. Field-emission SEM micrograph of an RF carbon aerogel prepared using literature methods.(6)

References

1. Atkins, J.R., C.R. Sides, S.E. Creager, J.L. Harris, W.T. Pennington, B.H. Thomas, and D.D. DesMarteau, Effects of Equivalent Weight on Ionic Conductivity in Bis[(perfluoroalkyl)sulfonyl]imide Perfluorinated Ionomers. Journal of New Materials for Electrochemical Systems, 2003. 6: p. 9-16.
2. Savett, S.C., J.R. Atkins, C.R. Sides, J.L. Harris, B.H. Thomas, S.E. Creager, W.T. Pennington, and D.D. DesMarteau, A Comparison of bis[(perfloroalkyl)sulfonyl]imide Ionomers with Perfluorosulfonic Acid Ionomers for Applications in PEM Fuel Cell Technology. Journal of the Electrochemical Society, 2002. 149(12): p. A1527-1532.
3. Creager, S.E., J.J. Sumner, R.D. Bailey, J.J. Ma, W.T. Pennington, and D.D. Desmarteau, Effects of water uptake and iononmer crystallinity on proton conductivity in bis[(perfluoroalkyl)sulfonyl]imide-based perfluorinated ionomers. Electrochemical and Solid-State Letters, 1999. 2: p. 434-436.
4. Sumner, J.J., S.E. Creager, J.J. Ma, and D.D. DesMarteau, Proton conductivity in Nafion 117 and in a novel bis[(perfluoroalkyl)sulfonyl]imide ionomer membrane. Journal of the Electrochemical Society, 1998. 145(1): p. 107-110.
5. Hua Mei, Bing Liu, Stephen E. Creager, Mark W.Perpall, Dennis W. Smith, Jr, Darryl D. Desmarteau. " Novel Diazonium Salts for Grafting Fluorinated Polyelectrolytes to Fuel Cell Electrodes", preprint, Fuel Division, ACS National Meeting, Fall 2004.
6. Saliger, R., V. Bock, R. Petricevic, T. Tillotson, S. Geis, and J. Fricke, Carbon aerogels from dilute catalysis of resorcinol with formaldehyde. Journal of Non-Crystalline Solids, 1997. 221: p. 144-150.

Multifunctional Composites Containing Molybdenum Carbides as Potential Electrocatalysts

Erich C. Weigert[a], *Joseph South*[b], *Jingguang G. Chen*[c]

[a] Center for Catalytic Science and Technology, Department of Materials Science and Engineering, University of Delaware, Newark, DE 19716

[b] Army Research Laboratory, Building 4600, Aberdeen Proving Ground, MD 21005

[c] Center for Catalytic Science and Technology, Department of Chemical Engineering, University of Delaware, Newark, DE 19716

Introduction

Currently, the most widely used electrocatalysts for Proton Exchange Membrane (PEM) and Direct Methanol Fuel Cells (DMFC) are platinum (Pt) containing alloys such as Pt-Ru [1-3] and Pt-Sn [1-5]. The primary disadvantages of these Pt alloys are their relative scarcity and high cost. In the case of functionalized RVC carbon foam, it is not economically feasible to simply coat the foam surfaces with Pt. Furthermore, because Pt does not bond strongly with carbon foam, Pt would most likely be in the form of clusters instead of being highly dispersed on the foam surfaces. Solutions to these problems are to either produce cost-effective electrocatalysts using less expensive components, or to reduce the Pt loading by improving its dispersion on the carbon foam.

Early transition metal carbides have been shown in previous studies [6,7] to behave similarly to the Pt group metals (Pt, Pd, Ir, Rh, Ru). For example, research done by our group has shown that carbide modified W(111) and W(110) surfaces showed high activity toward the dissociation of methanol, although about 14% of the adsorbed methanol decomposed to produce methane [8,9], an undesirable process for the application in DMFC. An additional study from our research group on the carbide modified Mo(110) surface showed that the methane formation pathway was not present on C/Mo(110) [10]. In addition, this study indicated that the C/Mo(110) surface was more active toward the dissociation of water than the C/W(111) or C/W(110) surfaces. Overall, these surface science studies suggest the possibility of using molybdenum carbides as an alternative electrocatalyst for DMFC.

In the present study we have investigated using molybdenum carbides, and platinum modified molybdenum carbides as potential electrocatalysts for DMFC's. In particular, we are interested in determining the feasibility of the integration of the electrocatalytic functionality on the surfaces of carbon foam. If successful, the multifunctional composite materials would provide the fuel cell functionality into the structural components in many military and domestic applications.

Experimental

Deposition. Sample preparation was performed in a stainless steel vacuum system with a typical base pressure of 3×10^{-8} Torr. The system was equipped with Mo and Pt metal sources for physical vapor deposition (PVD). The PVD deposition was conducted on reticulated vitreous carbon (RVC) foam. Samples were introduced into the vacuum chamber individually and coated with Mo and/or Pt by PVD to produce samples of Mo-C/foam, Pt/foam and Pt/Mo-C/foam. For all samples to be tested in the electrochemical cell, exposure time and metal source current were adjusted such that the surface ratio of Mo/C was approximately 0.17, based on standard XPS sensitivity factors [11]. Molybdenum carbides were formed on the surface by resistive heating of the Mo/carbon samples in vacuum to temperatures between 823 and 973 K. Pt modified surfaces were prepared by PVD of Pt on either foam or Mo-C/foam surfaces. The Pt PVD deposition current and time were controlled to achieve a surface atomic ratio of 0.17 Pt/C.

Techniques. The PVD system was equipped with an Al/Mg dual anode X-ray source and a concentric hemispherical analyzer (CHA) for in-situ XPS. Studies using XPS enabled us to control the surface concentrations of Mo and Pt as well as to verify carbide formation. Other characterization techniques used to examine the synthesized samples were Near Edge X-ray Absorption Fine Structure (NEXAFS) at Brookhaven National Laboratory and SEM. These two techniques provided additional and complementary information about the Mo-C thin films. The Pt/foam and Pt/Mo-C/foam samples were also evaluated using Cyclic Voltammetry (CV). The CV measurements were performed in an electrochemical half-cell. The half-cell was a glass vessel containing 1 Liter of 0.05M H_2SO_4 electrolyte, equipped with a Saturated Calomel Electrode (SCE) and a Pt counter electrode.

Results and Discussion

Deposition on RVC foam. Following metal deposition on the RVC foam samples, the annealing was allowed to continue for an extended period of time at 973 K to ensure uniform heating of the sample. The results from XPS show no clear evidence of carbide formation on the Mo modified RVC surface, as suggested by the observation that the C 1s signal does not shift significantly after sample heating.

It was unclear whether the lack of a characteristic carbide peak at 284.0 eV was the result of insufficient sample heating, insufficient surface coverage of Mo, or a dominance of the graphitic C 1s signal from the channels in the carbon foam. As described in a review, NEXAFS is much more sensitive than XPS in detecting the carbidic carbon in transition metal carbides [12]. Newly prepared samples of RVC foam were analyzed with NEXAFS, shown in Figure 1. The presence of the carbon K-edge feature at 285.5 eV in spectrum b is indicative of carbidic carbon, confirming the formation of Mo-C on the foam surface.

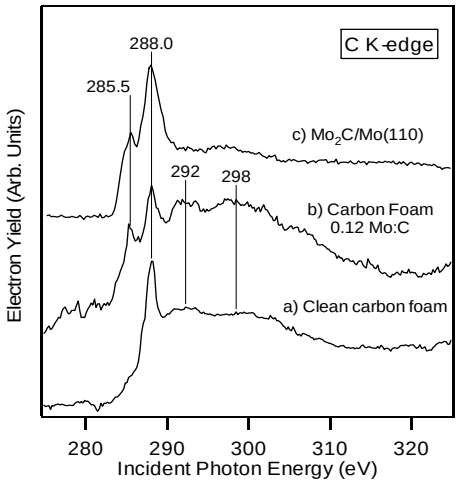

Figure 1. NEXAFS spectrum of clean and carbide modified carbon and Molybdenum substrates.

Cyclic Voltammetry (CV) Characterization of Electrochemical Stability. Figure 2 shows results of a preliminary study conducted on Pt/foam and Pt/Mo-C/foam samples to determine their electrochemical stability. Each sample, partially immersed in a dilute H_2SO_4 environment purged with either N_2 or H_2 gas, was subjected to a voltage sweep between -0.05 and 0.8 V. All CV data were collected with the assumption that the sample surface was uniform.

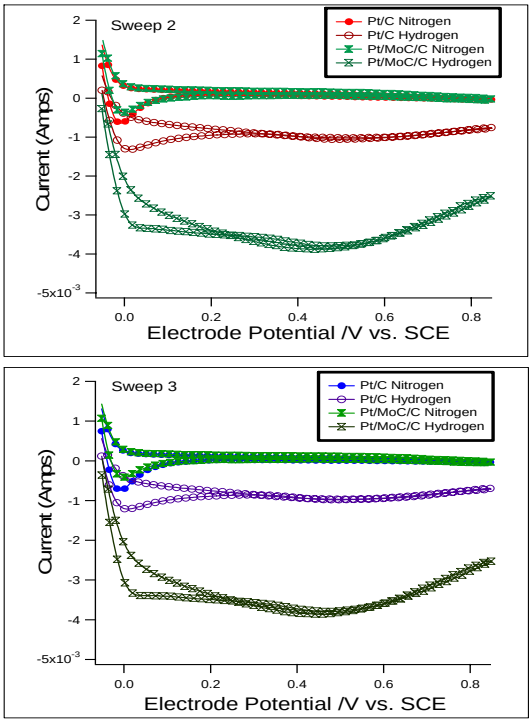

Figure 2. Cyclic Voltammograms of Pt/foam and Pt/Mo-C/foam partially immersed in a 0.05M H_2SO_4 solution.

The dissimilarity of these CV curves to those obtained from other studies on Pt modified carbon surfaces [13, 14] is not well understood at this time. Overall, the initial electrochemical study suggests that the Pt/foam and Pt/Mo-C/foam samples have significantly distinguishable performances, and that they possess some level of electrochemical stability in the sulfuric acid electrolyte solution.

Conclusions

From the results described above, the following conclusions can be made regarding the functionalization of carbon foams by Mo carbides:

(1) The formation of molybdenum carbides on the surface of RVC substrates has been found using XPS and NEXAFS.

(2) Preliminary CV measurements on the Pt/foam and Pt/Mo-C/foam samples indicate that there is an increase in the electrocatalytic activity when the carbon foam surface is functionalized with Pt and Pt/Mo-C. Multiple sweeps of the CV experiments show identical CV curves, indicating the electrochemical stability of the PVD films.

References

(1) M.M.P. Janssen, J. Moolhysen, Electrochim. Acta 21 (1976) 869.
(2) M.M.P. Janssen, J. Moolhysen, Electrochim. Acta 21 (1976) 861; J. Catal. 46 (1977) 289.
(3) K. Wang, H.A. Gasteiger, N.M. Markovic, P.N. Ross Jr., Electrochim. Acta 41 (1996) 2587.
(4) C. Panja, N. Saliba, B.E. Koel, Surf. Sci. 395 (1998) 248.
(5) A.N. Haner, P.N. Ross, J. Phys. Chem. 95 (1991) 3740.
(6) J.G. Chen, Chem. Rev. 96 (1996) 1477, and references therein.
(7) S.T. Oyama, The Chemistry of Transition Metal Carbides and Nitrides, Blackie, Glasgow, 1996.
(8) N. Liu, K. Kourtakis, J.C. Figueroa, J.G. Chen, J. Catal. 215 (2003) 254.
(9) H. Hwu, J.G. Chen, J. Phys. Chem. B 105 (2001), 10037.
(10) H. Hwu, J.G. Chen, Surf. Sci. 536 (2003) 75.
(11) Moulder J.F., Stickle W.F., Sobol P.E., Bomben K.D. Handbook of X-ray Photoelectron Spectroscopy. Physical Electronics, Eden Prairie MN. 1995.
(12) J.G. Chen, Surf. Sci. Reports, 30 (1997) 1.
(13) L.M. Roen, C.H. Paik, T.D. Jarvi, Electrochem. and Solid-State Lett. 7 (2004) A19-A22.
(14) H. Tang, J. Chen, L. Nie, D. Liu, W. Deng, Y. Kuang, S. Yao, J. of Colloid and Interface Sci. 269 (2004) 26-31.

Pt-BASED CATALYSTS FOR DIRECT ETHANOL FUEL CELLS

S. Song[1], Q. Xin[1,2], G. Sun[1], P. Tsiakaras[3*]*

[1]Direct Alcohol Fuel Cell Lab, [2]State Key Lab of Catalysis, Dalian Institute of Chemical Physics, CAS P. O. Box 110, Dalian 116023, China

[3]Department of Mechanical and Industrial Engineering, School of Engineering, University of Thessaly Pedion Areos, 383 34, Greece

Introduction

Direct ethanol fuel cells (DEFCs) have spurred more and more interest in recent years due to ethanol intrinsic advantages such as its low toxicity, renewability, and its easy production in great quantity by the fermentation from sugar-containing raw materials. The main challenge for DEFC is to break the C-C bond, which is difficult to occur at low temperatures. Sn has been found to be a good modifier to enhance the electrocatalytic activity of Pt to ethanol oxidation [1]. Sn's valence state [2] and Sn content [3] play an important role in ethanol electrooxidation and consequently in the single DEFC performance. From the practical point of view, the development of DEFC depends on the progress in the electrocatalytic materials for ethanol electrooxidation to a great extent. Ethanol adsorption, dissociation and oxidation are mainly affected by the composition and structure of electrocatalysts and the catalyst preparation procedure plays a crucial role in electrocatalysts' composition and structure, especially in the interaction between different components. In the present work, a PtSn/C catalyst synthesized by the direct decoration of commercial Pt/C with Sn as anode electrocatalyst in direct ethanol fuel cell. The techniques of cyclic Voltammetry, anode polarization curve and single DEFC tests were applied to compare the electrocatalytic activity of the prepared PtSn/C and the commercial PtRu/CPt to ethanol oxidation.

Experimental

PtSn/C catalyst with a Pt to Sn atomic ratio of 2 was prepared by using 20 wt.% Pt/C (Johnson Matthey Corp.) as support and $SnCl_2$ as tin precursor by a modified poly method [4]. The catalysts were characterized by XRD on a Rigaku X-3000 X-ray powder diffractometer using Cu Kα radiation with a Ni filter. Cyclic voltammetry of as prepared PtSn/C and commercial PtRu/C was performed in a conventional three-electrode cell with saturated calomel electrode and Pt wire as the reference electrode and counter electrode respectively in 1.0 M C_2H_5OH+1.0 M H_2SO_4 aqueous solutions at room temperature. The anode polarization curves of ethanol oxidation on PtSn/C and PtRu/C were obtained by supplying the cathode of the DEFC with humidified H_2 instead of O_2, which was used both as a *dynamic hydrogen reference electrode* (DHE) and as the counter electrode. The anode potential was controlled with a potentiostat/galvanostat (EG&G Model 273A) at a scan rate of 2.0 mV/s. The DHE was made by feeding 40 mL/min of H_2 humidified at 90°C at atmospheric pressure. The anode compartment was pumped by the preheated 1.0 mol/L ethanol aqueous solution at a flow rate of 1.0 ml/min, acting as the working electrode for the electrochemical measurements. Single DEFC tests were carried out with MEAs prepared according to the method described in literature [5] by pumping 1.0 mol/L ethanol aqueous solution at 1.0 ml/min to the anode and at the same time feeding 2 atm oxygen to the cathode at 90 °C. The polarization curves were obtained by an Arbin fuel cell test station in a galvanodynamic state.

Results and Discussion

XRD characterization results showed that after the modification by Sn, there is no change in Pt (fcc) characteristic and Sn exists in oxidative state. Fig. 1 shows cyclic voltammograms for ethanol electrooxidation over PtSn/C and PtRu/C catalysts. It can be clearly seen from Fig. 2 that in the investigated potential range, there are two oxidation peaks during the forward sweep in both cases of PtSn/C and PtRu/C and these two oxidation peaks of ethanol over PtSn/C are higher than those over PtRu/C. This means from the current density point of view, PtSn/C presents higher catalytic activity to ethanol electrooxidation in comparison with PtRu/C. The oxidation peak during the backward sweep could be attributed to the further oxidation of the adsorbed intermediate species of ethanol. From Fig. 2, it can also be seen that, in the case of PtSn/C, this backward oxidation peak is higher with respect to PtRu/C. This could be attributed to the more promoting role of Sn in the oxidative removal of the adsorbed intermediate species of ethanol oxidation over platinum. On the other hand, the shift of the oxidation peak potential for PtSn/C to more negative with respective to that of PtRu/C indicates that in the case of PtSn/C, the energy necessary for ethanol electrooxdation is lower, which could be attributable to both the synergetic role of tin in platinum catalytic activity to ethanol electrooxidation and the structural modification of Sn toPt. CV results show that PtSn/C is more suitable electrocatalyst for ethanol oxidation in comparison with PtRu/C.

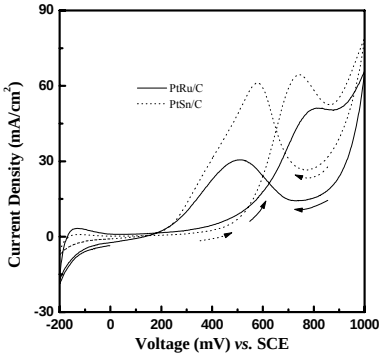

Figure 1. Cyclic voltammetry spectra of PtSn/C and PtRu/C in 1.0 mol/L CH_3CH_2OH/ 1.0 mol/L $HClO_4$ aqueous solution at room temperature. The potential sweep rate was 50 mV/s.

Anode polarization curves can eliminate the other factors except the electrochemical activity of Pt-based catalysts to ethanol electrooxidation and the results are illustrated in Figure 2. It can be clearly seen that the onset potential of ethanol electro-oxidation over PtSn/C is shifted by about 100 mV negatively in comparison with that over PtRu/C. The negative potential shift of the beginning of ethanol oxidation on PtSn/C could be attributable to the oxidation of the adsorbed residues formed during its dissociative adsorption by adsorbed OH species present on Sn sites in oxidized states [6]. Figure 2 also shows that when the potential is less than about 80 mV (vs. DHE), PtSn/C presents a lower activity while it exhibits steeply increment in current density from about 80 mV (*vs.* DHE) until about 300 mV (*vs.* DHE) with a maximum *i*(PtSn/C)/ *i*(PtRu/C) ratio of about 5 at about 200 mV (*vs.* DHE). And then the increment of the polarization current on PtSn/C slows down while the corresponding value on PtRu/C becomes obvious. Along with the potential increment, PtSn/C shows inferior activity for ethanol oxidation to PtRu/C again.

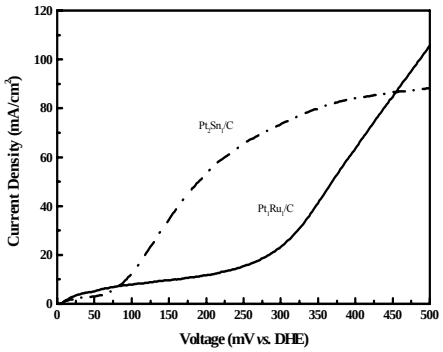

Figure 2. Anode polarization curves of ethanol electro-oxidation over in-house PtSn/C and commercial PtRu/C at 90°C. Anode: PtSn/C or PtRu/C wit a a loading of 1.3 mg/cm^2, $C_{ethanol}$ = 1.0 mol/L, flow rate: 1.0 ml/min. Cathode: Pt/C (20 wt.%, Johnson Matthey Corp.), the metal loading: 1.0 mg Pt/cm^2, P_{H2} = 1 atm, flow rate: 40 mL/min $T_{H2\text{-}humidified}$=90°C. Electrolyte: Nafion®-115 membrane.

Figure 3 compares the cell performances of direct ethanol fuel cells with PtSn/C and PtRu/C as anode catalysts. Obviously, the single cell performance with the PtSn/C is better than that of PtRu/C.

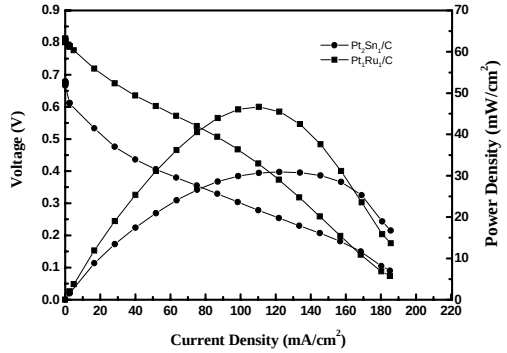

Figure 3. Performance comparison of DEFCs adopting in-house PtSn/C and commercial PtRu/C as anode respectively at 90°C. Anode: PtSn/C or PtRu/C wit a a loading of 1.3 mg/cm^2, $C_{ethanol}$ = 1.0 mol/L, flow rate: 1.0 ml/min. Cathode: Pt/C (20 wt.%, Johnson Matthey Corp.), the metal loading: 1.0 mg Pt/cm^2, P_{O2} = 2 atm. Electrolyte: Nafion®-115 membrane.

The voltages are about 0.81 V and 0.68 V at open circuit condition, and 0.46 V and 0.31 V at 100 mA/cm^2 for PtSn/C and PtRu/C, respectively. The maximum power densities are about 46 mW/cm^2 for PtSn/C and 30 mW/cm^2 for PtRu/C respectively. It can also be seen from Figure 3 that there is a rapid initial fall in voltage with PtRu/C as anode catalyst but the voltage falls less with PtSn/C as anode catalyst in the low current density. The rapid initial fall in voltage is caused by the slow reaction of ethanol oxidation taking place on the surface of the electrode. A proportion of the voltage generated is lost in driving the electrochemical reaction that transfers the electrons to or from the electrode. Activation overvoltage is the most important cause of voltage drop. As for DEFC, with the same conditions except for different anode catalysts, the slower initial voltage drop can be attributed to the more effective and active catalytic ability of PtSn/C than PtRu/C to ethanol electrooxidation. However, above about 160 mA/cm^2, the cell performance with PtSn/C as anode catalyst is slightly less than that obtained with PtRu/C, which may be due to the higher internal resistance of fuel cell with PtSn/C as anode catalyst. This can also be observed from Figure 3, the voltage drops more significantly with PtSn/C than with PtRu/C in the ohmic control region. In this region, the voltage drop is simply proportional to current. Therefore, the more significant the voltage drops, the bigger the area specific resistance is in the ohmic control region of I-V characteristics of fuel cells. The higher internal resistance of fuel cell with PtSn/C as anode catalyst may be attributed to that tin is in the oxidized state is less conductive. Accordingly, the electrical resistance of the anodic electrode increases.

Conclusions

Pt/C catalyst modified by Sn shows superior electrocatalytic activity to ethanol oxidation than commercial PtRu/C. Even if considered as the most active electrocatalyst for methanol electrooxidation, PtRu/C is not considered as a suitable one for ethanol electrooxidation. The results of cyclic voltammetry and anode polarization are coordinated with those of single DEFC tests. PtSn/C can exhibit a more negative ethanol oxidation onset potential and a higher oxidation current density.

Acknowledgement. The authors would like to thank the *"Greece-China Joint Research and Technology Programme 2003-2005"* and the National Natural Science Foundation of China (Grant No.: 20173060) for funding.

References

(1) Zhou, W., Zhou, Z., Song S., Li, W., Sun, G., Tsiakaras, P., Xin, Q. *Appl. Catal. B: Environmental*, **2003**, *46*, 273.
(2) Jiang, L., Zhou, Z., Li, W., Zhou, W., Song, S., Li, H., Sun, G., Xin, Q. *Fuel & Energy*, **2004**, accepted for publication.
(3) Zhou, W., Song, S., Li, W., Zhou, Z., Sun, G., Xin, Q., Douvartzides, S., Tsiakaras, P. *J. Power Sources*, **2004**, submitted.
(4) Wang, Y., Ren, J., Deng, K, Gui, L., Tang, Y., *Chem. Mater.* **2000**, *12*, 1622.
(5) Li, W., Liang, C., Zhou, W., Qiu, J., Li, H., Sun, G., Xin, Q. *Carbon*, **2002**, *42(2)*, 436.
(6) Delime, F., Léger, J-M., Lamy, C. *J. Appl. Electrochem.*, **1999**, *29*, 1249.

Novel high performance platinum and alloy catalysts for PEMFC & DMFC

*Yu-Min Tsou *, Lixin Cao, and Emory De Castro*

E-TEK, a Division of De Nora North America, Somerset, NJ, USA; Tel (732)545-5100; Fax (732)545-5170; yu.min.tsou.dnna@denora.com

ABSTRACT

In the past two years, E-TEK has advanced the technologies in manufacturing Pt-based catalysts to meet the increasing demand for catalysts in the fuel cell industry. The application of the new method leads to enhanced catalyst performance as the results of dramatic decrease in Pt crystalline size and poisoning impurities as well as uniform spatial distribution on supports. Supported platinum catalysts (10-80 wt% Pt) on various carbon blacks as well as pure platinum black with a controlled size of 5.3 nm have been readily prepared for proton exchange membrane fuel cells (PEMFC) and direct methanol fuel cells (DMFC). By combining novel platinum and ruthenium chemistry, we have succeeded in developing a new process for making thoroughly mixed Pt:Ru alloy at all loadings as evidenced by XRD analysis. Electrochemical experiments indicated that the newly developed Pt:Ru catalysts exhibited the best performances among all commercial products for CO tolerance and methanol oxidation.

INTRODUCTION

The first commercial Pt catalyst on Vulcan XC-72 for phosphoric acid fuel cells was supplied by E-TEK scientists in the 1980's. The traditional E-TEK method for Pt and Pt:Ru catalyst preparation was based on platinum and ruthenium sulfite compounds that undergo redox chemistry to form absorbable fine particles on carbon supports [1]. Other published methods include formation of surfactant-shell stabilized Pt colloidal particles in an organic solvent [2] and reduction of metal chlorides with $LiBH_4$ in THF [3]. The disadvantages of these published methods include toxic solvents, tedious procedures, contaminants, poor size control, and Pt/Ru phase separation.

In this presentation we will describe the characterization of supported and unsupported platinum catalysts prepared from a novel chemistry and process. The new method resulted in excellent catalyst particle size control, electrochemical activity, and low contaminants. Also included in the discussion is the characterization of supported and unsupported platinum ruthenium alloy catalysts prepared from a novel chemistry and process. Besides the advantage described above for the new Pt catalysts, the Pt:Ru alloy catalysts exhibit good mixing on atomic scale which is crucial for methanol oxidation activity.

RESULTS

The goal of developing the unique platinum chemistry in this work is to ensure the formation and deposition of catalyst particles on the support with uniform size and exhibit minimum growth in subsequent treatments. These catalysts (HP, high performance) were shown to have smaller XRD crystalline sizes and larger surface areas than the previous E-TEK catalysts (Table 1). At a loading higher than 40% on Vulcan XC-72, the XRD size of the previous catalysts increases dramatically but that of the new catalyst increases very slightly with the loading. Besides having controllable crystalline size, the new catalysts also have more uniform size distribution and spatial distribution over the support. These features give rise to enhanced current distribution and performance in comparison with other commercial products, and essentially no poisoning contaminants. Pt black and 60-80% Pt/C are good candidates for cathode catalysts in DMFC cells. The new Pt chemistry affords Pt black with smaller XRD size (5.3 nm) and higher surface area than other commercial products (Table 2). Figure 1 compares the polarization curve of a gas diffusion electrode with the E-TEK new HP 30% catalyst and that of a commercial 30% Pt/C catalyst.

Synthesis of PtRu methanol catalysts usually follows similar procedures as those for Pt catalysts. Fundamental studies in our lab as well as others indicate that the following factors are crucial for catalystic activity: (i) Pt/Ru alloying degree; (ii) minimum separate Ru phase in XRD spectra, which is ineffective for methanol oxidation. XRD peaks were found to probe alloying degree in Pt:Ru catalysts. The closeness of XRD derived Pt:Ru ratios and bulk Pt:Ru ratio indicates good alloying. E-TEK's new HP Pt/Ru chemistry leads to thorough alloying of the two elements in the catalysts without Ru phase separation; whereas other commercial products give significant deviations (Table 3) and some have single Ru phase. Rotating disk electrode (RDE) experiments (Figure 2) show that the electrochemical activities of E-TEK HP PtRu catalysts for methanol oxidation are better than other commercial products. These new HP PtRu catalysts have replaced the previous versions on the market. These new PtRu catalysts are also excellent for CO tolerance. Crystalline and morphological factors which might affect the performance of catalysts along with electrochemical diagnosis tool to predict performance will be discussed.

Table 1. Crystalline Size (XRD, nm) of E-TEK Pt Catalysts on Vulcan XC-72

Pt loading(%)	Previous catalyst	New catalyst
10	2.2	1.8
20	2.5	2.4
30	3.2	2.7
40	6.4	3.3
60	8.8	4.1
80	25.0	4.9
100	--	5.3

Table 2. Crystalline Size (XRD, nm) and BET Surface Area of Pt Blacks

	XRD size(nm)	BET surface area (m^2/g)
New E-tek	5.3	34
Company 1	10.0	20
Company 2	6.4	27

Table 3. Pt:Ru Alloying Degree and XRD Size (mn), Bulk Pt:Ru ratio: 50:50 Except Company 2, 40:60.

Pt:Ru loading(%)	E-TEK HP Pt:Ru catalyst		Company 1 Pt:Ru catalyst		Company 2 Pt:Ru catalyst	
	ratio	size	ratio	size	ratio	size
30	52:48	2.6	47:54	2.4	25:75	3.7
60	46:54	2.8	39:61	2.7	20:80	3.8
100	48:52	2.7	38:62	2.7	--	--

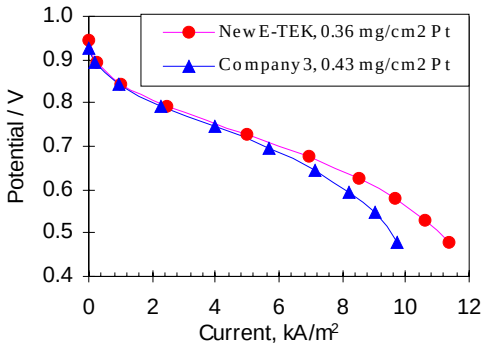

Figure 1. Comparison of 30% cathode catalysts, 70 °C.

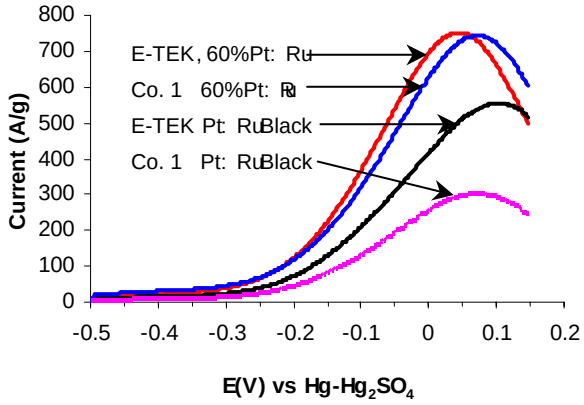

Figure 2. RDE results of methanol oxidation on Pt:Ru (1:1) catalysts, 1M CH_3OH, 50 °C, 1600 rpm.

REFERENCES

1. Petrow, H.G.; Allen, R. J. *US Patent 4,044,193*, August 23, **1977**.
2. Bonnemann, H.; Brijoux, W. in "*Advanced Catalysis and Nano-structured Materials*", Ed., W. Moser, Academic Press, **1996**, p. 165.
3. Lee, A.S.; Park, C. Y.; Choi, J.H.; Kwon, B. K.; Sung, E. Y. *J. Electrochem. Soc*., **2002**, 149 (*10*), A1299.

Novel, Size-controlled Pt Cluster Electrocatalysts for H_2 Fuel Cells

Eric N. Coker, William A. Steen, Michael J. Kelly, Ion C. Abraham, and James E. Miller

Sandia National Laboratories
PO Box 5800, Albuquerque NM 87185-1349

Introduction

One of the biggest hurdles to market acceptance of fuel cell-powered vehicles is the precious metal (PM) requirement; a commercially viable fuel cell electrocatalyst will require almost an order-of-magnitude reduction in PM usage compared to current state of the art to meet both cost and PM availability issues. Therefore, reducing or eliminating the need for Pt as an electrocatalyst is paramount. Another important attribute for a versatile fuel cell catalyst is its durability to poisons such as CO and S, which may be real concerns when reformate is considered as a H_2-source. Alloys of platinum with, *e.g.*, ruthenium, have received considerable attention, due to their higher CO-tolerance.

Studies of cluster chemistry have shown that the physics and chemistry of nanoparticles is extremely sensitive to the number of atoms comprising the cluster, especially when they contain less than a few dozen atoms. For example, the rate of adsorption of H_2 onto a cluster of ten iron atoms is almost three orders of magnitude greater than that of a 17 atom cluster[1]. We are developing a Fourier Transform Ion Cyclotron Resonance Mass Spectrometer (FT-ICR-MS), similar to others in the literature,[2] in an effort to identify electrocatalyst cluster sizes with increased H_2 adsorption (and ideally lowered CO adsorption). Initial efforts have focused on Pt but Pt alloys and other alternatives are being considered. Concurrent with the cluster chemistry studies, we are synthesizing catalysts containing Pt or Pt-alloy clusters of precisely controlled size and narrow size-distribution. Once ideal cluster sizes have been identified by FT-ICR-MS, we will be able to prepare the appropriate catalyst materials for evaluation.

The electrocatalyst synthesis protocol we have adopted utilizes a microporous zeolite as a sacrificial host for the PM clusters. This approach was chosen for a number of reasons: a) to introduce good spatial distribution of the PM-cluster precursors (*i.e.*, $(NH_3)_4Pt^{2+}$); the precursor complex is molecularly dispersed at ion exchange sites which are homogeneously distributed throughout the zeolite structure; b) to restrict cluster growth due to the volume limitation of the zeolite cavities (in the case of zeolite X, the largest cavities are 1.3 nm in diameter), and; c) to impose restriction of cluster-migration during thermal processing due to the constraints of the zeolite porosity (*i.e.*, reduction of sintering). It is known that the rate of heating a $(NH_3)_4Pt^{2+}$-exchanged zeolite can influence the size of the resulting Pt clusters, and clusters as small as *ca.* 1nm have been reported.[3]

Experimental

To prepare a platinum-on-carbon electrocatalyst with the desired control over cluster size, the following general protocol was adopted: 1) tetra-ammine platinum(II) nitrate (50.29 wt.-% Pt, Alfa Aesar) was ion exchanged from 0.05M solution into zeolite X (Molecular Sieve 13X powder, Aldrich) to the desired loading (typically between 1 and 20 weight percent); 2) the $(NH_3)_4Pt^{2+}$-exchanged zeolite was then heated in air to 350-400°C to decompose the Pt complex to a mixture of Pt(0) and Pt(II)/Pt(IV) oxides, depending on the cluster size. These materials are referred to as PtX(n), where n is the heating rate in °C min^{-1}; 3) the PtX(n) material was degassed to remove adsorbates and water from the pore volume, and was then impregnated with furfuryl alcohol (99%, Aldrich or Acros); 4) after evacuation to ensure complete infiltration of the monomer into the zeolite pores, the sample was heated in air to 80 – 120°C to induce polymerization; 5) the PtX(n)/polymer composite was then carbonized at between 400°C and 1200°C under an inert and/or reducing atmosphere to convert the polymer to conductive carbon and ensure the platinum was fully reduced; 6) the insulating zeolite template was removed by acid or base digestion, leaving a conductive platinum-on-carbon (Pt/C) electrocatalyst.

The above procedure is currently being adapted for the preparation of Pt-alloys, as well as clusters of other PMs.

Characterization Techniques. The PtX(n), Pt/C, and intermediate materials have been characterized using a variety of techniques, including Transmission Electron Microscopy (TEM), X-ray diffraction (XRD), EXAFS and ^{13}C MAS-NMR. Electrocatalyst evaluation has been performed using standard voltammetric techniques.

Results and Discussion

Figure 1 shows TEM micrographs of two different PtX(n) samples, prepared from the same $(NH_3)_4Pt^{2+}$-X precursor (containing 20 wt.-% Pt), but heated in air to 400°C at different rates. The sample heated at 2°C min^{-1} (PtX(2), Fig. 1A) possesses Pt clusters ~3-6nm in diameter, while the sample heated at 0.1°C min^{-1} (PtX(0.1), Fig. 1B) contains almost exclusively sub-nm clusters with a very narrow size distribution (most clusters are between 0.6 and 0.9nm). By heating the precursor at intermediate rates, Pt clusters of intermediate size were synthesized. XRD analysis indicated that PtX(2) contained Pt metal and amorphous silica-alumina; clearly the growth of Pt particles beyond the size of the zeolite cavities had contributed to the amorphization of the host. The XRD pattern of PtX(0.1), however, revealed the zeolite to have retained its crystallinity, while the Pt clusters were too small to diffract X-rays coherently. Preliminary EXAFS data corroborate those from TEM and XRD and indicate that the Pt clusters are fully oxidized in air, but readily reduce to Pt^0 under H_2 at 250°C. Thus, by heating the $(NH_3)_4Pt^{2+}$-X precursor at a specified rate, control over Pt cluster size is garnered. Further control is realized by adjusting the platinum loading; a slight decrease in Pt-Pt coordination number (hence cluster size) was observed by EXAFS on identical heat-treatment of precursors with decreasing Pt-loading in the range 20 wt.-% down to 5 wt.-% Pt.

After impregnation, polymerization and carbonization to 600°C, the Pt clusters in PtX(0.1) were observed by TEM to have increased slightly in size to *ca.* 0.7 to 1.2nm. For comparison, identical heat treatment of PtX(0.1) without introducing the polymer resulted in a doubling of the cluster diameter. The carbon matrix resulting from the 600°C carbonization was identified by ^{13}C MAS-NMR to be mostly sp^2 carbon (*i.e.*., graphene sheets), however, measurements of electrical conductivity after carbonizing at temperatures between 400 and 1200°C indicated that carbonization temperatures in excess of 700°C were required for optimal electron transport.

Figure 2 shows representative cyclic voltammograms of one of our Pt/C materials derived from PtX(0.1) compared with a Pt Black standard. Approximately 10µg Pt-equivalent of each catalyst was deposited onto a glassy carbon electrode and cycled at 50mV s^{-1} in 0.5M H_2SO_4. Features characteristic of H_2 adsorption and desorption can be seen at *ca.* -200$mV_{Ag/AgCl}$ for each electrode and have comparable charge (*i.e.*, comparable electroactive surface area). Fundamental kinetic studies are also being conducted as the cluster chemistry studies reveal how to optimize the nanostructure of the Pt/C catalyst allowing performance beyond that of standard fuel cell electrocatalysts.

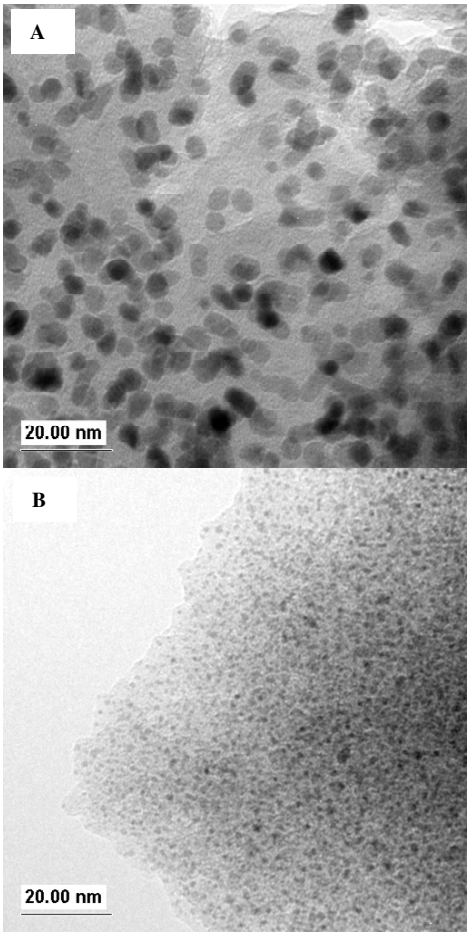

Figure 1. TEM images of PtX samples after heating $(NH_3)_4Pt^{2+}$-zeolite X (20 wt-% Pt) to 400°C in air at (A) 2°C min^{-1}, and (B) 0.1°C min^{-1}.

Conclusions

Controlled heat-treatment of $(NH_3)_4Pt^{2+}$-exchanged zeolite X, followed by reduction under reducing atmosphere, produces small Pt clusters, which can be tuned in size from < 1 nm to > 3 nm depending on the heating rate and Pt loading. Electro-active H_2 oxidation and O_2 reduction catalysts have been prepared from these Pt zeolites through impregnation of a carbonaceous material into the pores of the zeolite, followed by polymerization and carbonization. The zeolite host may be removed by acid or base digestion to yield a Pt/C catalyst with unprecedented control over the size and uniformity of Pt clusters. Electrochemical tests have verified the activity of these catalysts, which compare favorably with state of the art commercial materials.

Acknowledgement. Sandia is a multiprogram laboratory operated by Sandia Corporation, a Lockheed Martin Company, for the United States Department of Energy's National Nuclear Security Administration under contract DE-AC04-94AL85000. EXAFS measurements were conducted at sector 10 (MRCAT) of the Advanced Photon Source (APS), Argonne, IL. Use of the APS was supported by the U.S. Department of Energy Basic Energy Science, under Contract No. W-31-109-Eng-38. Work performed at MRCAT is supported, in part, by funding from the Department of Energy under grant number DEFG0200ER45811.

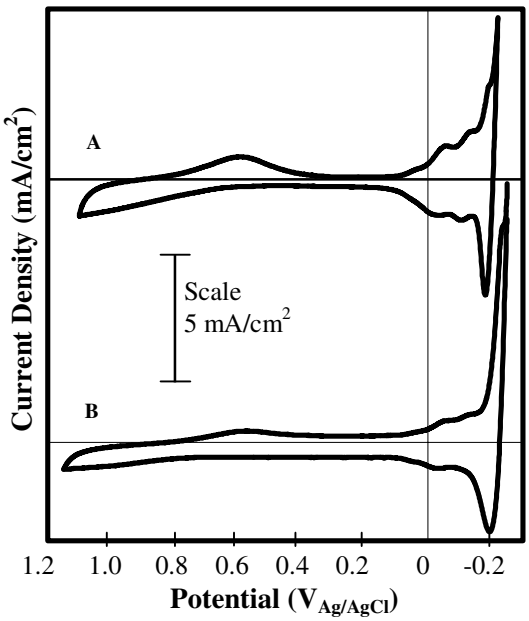

Figure 2. Cyclic voltammograms of a Pt Black standard (A), and of Pt/C prepared from PtX(0.1) (B). Scan rate in 0.5M H_2SO_4 is 50mV/s. Current density is per surface area of substrate, a glassy carbon electrode. Pt loading is *ca.* 10μg for each electrode.

References

1 Riley, S.J. In *Clusters of Atoms and Molecules II*, Haberland, H. Ed.; Springer Verlag, Berlin, 1994; p.226.

2 Maruyama, S.; Anderson, L.R. and Smalley, R.E., *Rev. Sci. Instrum*. **1990**, *61(12)*, 3686; Vakhtin, A.B. and Sugawara, K., *Chem. Phys. Lett*. **1999**, *299*, 553; Jarek, R.L. and Thornberg, S.M., *IEEE Trans. Semiconductor Manuf*., **2001**, *14(1)*, 20; Jeong, S.; Fisher, K.J.; Howe, R.F. and Willett, G.D., *Microp. Mesop. Materials* **1998**, *22*, 369.

3 de Graaf, J; van Dillen, A.J.; de Jong, K.P. and Koningsberger, D.C., *J. Catal*., **2001**, *203*, 307.

In-situ pH measurement in a Nafion® based Polymer electrolyte fuel cell by fluorescence spectroscopy

Yatin P. Patil[1], Thomas A. P. Seery[1,3], Montgomery T. Shaw1[,2] and Richard S. Parnas[1,2]

[1]Polymer Program, Institute of Materials Science, [2] Department of Chemical Engineering and [3]Department of Chemistry
University of Connecticut
Storrs, CT 06269-3136

Introduction

Proton conductivity of the most often used polymer electrolyte membrane, Nafion®, manufactured by du Pont de Nemours & co., depends on its water content. The ionic domains swell with water adsorption and form interconnected proton-conducting channels above a critical water content. The membrane water content depends on the humidity of the gases and the interplay between electro-osmotic drag and back diffusion. Also, uneven gas distribution and uneven electrochemical reactions can lead to uneven water distribution in the membrane. Water management is therefore very important for the optimum functioning of fuel cells. With change in the membrane water content, the pH inside the membrane will change. We have incorporated a pH sensitive fluorescent molecule inside the membrane, which responds to the change in the pH and hence the water content inside the membrane. By introducing a bare fiber optic we are able to measure the fluorescence response and hence the pH inside the membrane.

Experimental

A commercially available 20 wt% Nafion® solution in water-Isopropanol was obtained from Solution Technology Inc. (equivalent weight 1100 g/mol sulfonic acid groups). Rhodamine-6G was obtained from Sigma-Aldrich and was used without further purification. A very dilute dye solution in Nafion® was made by mixing the 20 wt % Nafion® solution with a 4.12×10^{-4} mol/L ethanol solution of Rhodamine-6G. The membrane was cast by pouring the 20 wt% Nafion® solution on a 4-cm × 4-cm glass plate with a 350-µm bare optical fiber (OZ Optics) in it. The end of the fiber was positioned at the center of the membrane. Before embedding the bare optical fiber, its tip was coated with the Nafion® dye solution. The final concentration of the dye in the dry membrane at the tip of the fiber was calculated to be 5.75×10^{-7} mol/g. The thickness of the cast membrane was 400-µm. The membrane was coated with the catalyst obtained form Tanaka Kikinzoku Kogyo K. K., Japan by the decal transfer process. The catalysts, 46.5 wt.% Pt/C on the cathode and 30.1% Pt-23.4% Ru/C on the anode were impregnated with Nafion® solution. The electrodes were first screen printed on a Teflon sheet and then hot pressed with the membrane between two rubber sheets at 150 °C for 10 min. under 207×10^3 Pa (30 psig). The membrane electrode assembly was assembled in a 5 cm^2 fuel cell with series sweep flowfields (Electrochem Inc.; model no. FC05-01SP). The cell was closed by applying a uniform torque of 3.5 N m to each of the eight bolts. High purity hydrogen and oxygen, passed through water-filled sparger bottles, were used. The humidity of the gases was controlled by controlling the temperature of the sparger. The cell temperature was maintained at 80 °C for all the experiments.

Fluorescence spectra were recorded using an Ocean Optics fiber optic fluorescence spectrometer (HR 2000) equipped with an attachment to connect bare optical fiber. UV-Vis spectra were recorded with a Perkin-Elmer Lambda 6 UV-Vis spectrometer.

Results and Discussion

To study the effect of Nafion® membrane water content on the fluorescence behavior of Rhodamine-6G, a membrane was cast from the Nafion® dye solution at 60°C in an oven. A piece of the membrane was vacuum dried and weighed at room temperature. It was soaked in deionised water and patted dry to remove excess water. The water soaked sample was placed on a balance to monitor the water weight loss with simultaneous fluorescence measurements. The fiber optic was oriented at an angle of 60° with respect to the membrane. The fluorescence behavior of the wet Nafion® membrane containing Rhodamine-6G with loss of water and the experimental geometry is shown in the figure 1. At high water content the fluorescence exhibited a maximum at 552 nm, whose intensity initially increases and then decreases with loss of water. This behavior was observed in two different fluorescence spectrometers.

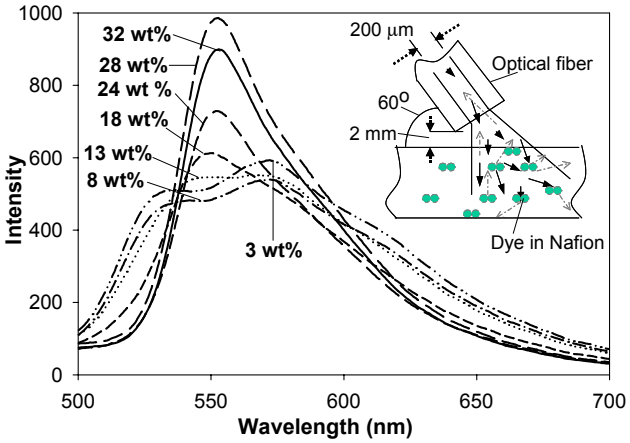

Figure 1. Fluorescence spectra of rhodamine-6G in Nafion® with loss of water and the geometry for fluorescence measurement.

Not only does the intensity of the peak at 552 nm decrease with loss of water, but also it disappears and new peaks appear with further loss of water. Similar behavior of Rhodamine-6G in Nafion® membranes has been reported in the literature[1-3]. Zhu et al.[1] has proposed that Rhodamine-6G forms a complex with water that has higher absorbance compared to an uncomplexed form, and hence the fluorescence intensity increases with the water content. Mohan et. al. reported similar behavior of rhodamine-6G in Nafion®. When the wet membrane containing the dye dried out in air the intensity at 550 nm decreased and new peaks appeared[2,3].

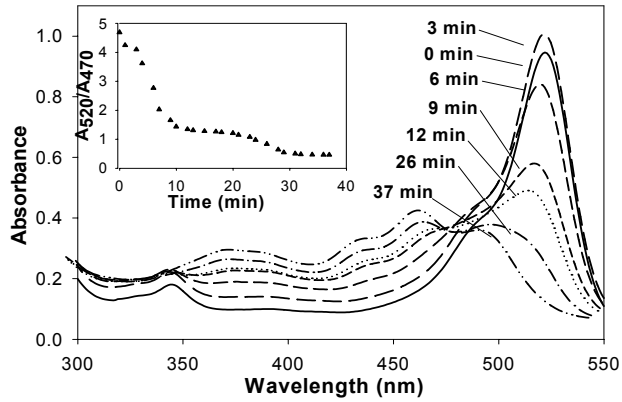

Figure 2. Absorption spectra of Nafion® containing Rhodamine-6G with loss of water.

They proposed that Rhodamine-6G in Nafion® exists in two equilibrium forms, protonated and non-protonated. The protonated form absorbs at 470 nm and has low absorbance whereas the non-protonated form absorbs at 525 nm and has high absorbance. The relative fraction depends on the concentration of H^+ ions i.e. pH. At high pH the non-protonated form dominates whereas at low pH the protonated form dominates. They have verified this by monitoring the absorbance ratio A525/A470 of a membrane immersed in aqueous acidic solutions; the absorbance ratio decreased with increasing concentration of the H^+ ions. They reported a similar trend during the drying of the Nafion® membrane. In Nafion®, the number of sulfonic acid groups does not change unless the membrane undergoes degradation. However, with change in its water content the pH changes and hence the absorbance and fluorescence behavior will change. The absorbance trend of the dye-containing membrane during drying is shown in figure 2. As reported we found that the intensity ratio decreased with loss of water. The absorbance below 480 nm increased with the loss of water.

The absorbance shows a drastic change at 520 nm but to avoid excitation and emission overlap we chose an excitation band from 400-460 nm as the dye emits in the 500-700 nm range. The fluorescence intensity decreases with decreasing pH but we chose to follow intensity ratio as the fluorescence intensity depends on the source intensity and orientation of the fiber with respect to the sample. The fluorescence intensities at 552 and 620 nm were used. The intensity ratio as a function of membrane water content is shown in figure 3. Based on the membrane weight and its water content one can approximate the concentration of H^+ ions inside it. The intensity ratio shows a sigmoidal trend as a function of membrane water content.

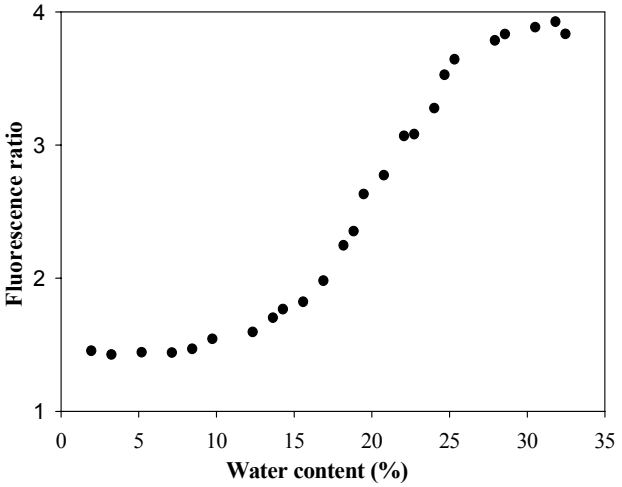

Figure 3; Fluorescence intensity ratio as a function of Nafion® water content

For in-situ fluorescence measurements, the cell temperature was raised from room temperature to 80 ^oC and was fed with 100% humidified hydrogen and oxygen gases. For proper humidification of the membrane, the cell was operated at steady state for 12 h. The current, drawn at a constant voltage of 0.2 volts, was measured until it reached a steady state. Figure 4 shows the fluorescence ratio and the current response of the cell from its start until it reached a steady state. As the cell temperature increased the membrane lost water, which reduced its conductivity and the current. The fluorescence ratio decreased as the pH fell down. The membrane subsequently adsorbed water from the humidified gases and its conductivity increased, which increased current. The fluorescence ratio increased as a result of increase in pH inside the membrane. Increased current corresponds to increased amount of proton transfer; however, protons are transported as hydronium ions, where each proton is accompanied by at least one water molecule[4]. Thus, increased current does not lower the pH as water content also goes up due to membrane water uptake and electro-osmotic drag. The fluorescence response is very fast and sensitive towards the change in the pH of the membrane as the peaks in the current match well with the peaks in the fluorescence.

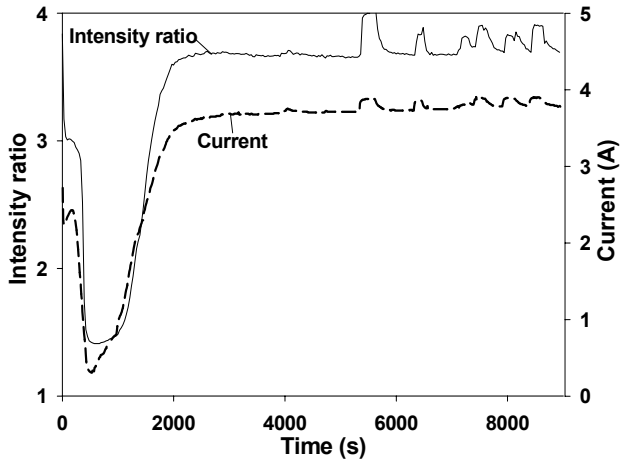

Figure 4; Fluorescence ratio and current as a function of time.

Similar experiments were performed by changing the relative humidities of the hydrogen and oxygen gas. The fluorescence response and current decreased with the decrease in the humidities of the gases. Also at different relative humidities we found a step change in the fluorescence signal corresponding to a step change in the current drawn. To quantify the pH corresponding to the in-situ measured fluorescence signal, we need to establish a correlation curve similar to figure 3 at the cell operating temperature.

The fluorescence technique outlined above may be useful for understanding fuel crossover, membrane degradation, and membrane phase specific behavior. Since there are many fluorescent dye molecules, a variety of physical and chemical phenomena can now be accessed during fuel cell operation using embedded optical fiber fluorescence spectroscopy. In particular, current work is focused on integrating the probe with porous nanoparticles with a localized fluorescence molecule on it.

Acknowledgement This work was supported by the Army Research Office and through the Connecticut Global Fuel Cell Center. We would like to thank Prof. James Fenton and Vijay Ramani for letting us use their fuel cell set.

References

(1) Zhu, C.; Bright, F. V.; Wyatt, W. A.; Hieftje, G. M. *Proceedings - Electrochemical Society* **1987**, *87-9*, 476-483.

(2) Mohan, H.; Iyer, R. M. *Journal of the Chemical Society, Faraday Transactions* **1992**, *88*, 41-45.

(3) Mohan, H.; Iyer, R. M. *Analyst (Cambridge, United Kingdom)* **1993**, *118*, 929-932.

(4) Zawodzinski, T. A.; Davey, J.; Valerio, J.; Gottesfeld, S. *Electrochimica Acta* **1995**, *40*, 297-302.

COMPARISON OF TWO DIFFERENT APPROACHES FOR ENHANCEMENT OF CO_2 REMOVAL BY ADSORPTION ON CARBONS

C.E. Snape, K. M. Smith, A. Arenillas,, and T.C. Drage

Nottingham Fuel and Energy Centre, School of Chemical, Environmental and Mining Engineering, University of Nottingham, NG7 2RD, UK. colin.snape@nottingham.ac.uk

Introduction

It is widely believed that emissions from the combustion of fossil fuels are contributing to a rise in the concentration of CO_2 in the atmosphere, which in turn has raised concerns that these CO_2 emissions may be causing global warming. Consequently, CO_2 capture has recently received much attention as a potential means of mitigating fossil fuel CO_2 emissions with adsorption in particular considered to be one of the most promising methods. Activated carbons are well known as adsorbents of gases and vapors. Although the textural properties of the adsorbent plays a key role in the adsorbate/adsorbent interactions, other features such as surface chemistry should also be taken into consideration[(1)].

The surface chemistry of activated carbon is governed by the presence of heteroatoms such as oxygen, nitrogen, etc. Sometimes the original chemistry of the activated carbon surface is not potent enough to enhance the specific adsorbate-adsorbent interactions or catalytic processes. In such cases the surface chemistry can be modified by the impregnation of an appropriate reagent. Alternatively, modifications can be engendered by the alteration of the surface chemistry of the carbon matrix via the incorporation of heteroatoms.

In this study, two different approaches of developing CO_2 adsorbents are compared. Firstly, the modification of the surface chemistry of carbon concentrates from fly ash (PFA) with a series of nitrogen-containing reagents. Secondly, a range of high nitrogen content carbon matrix adsorbents have been developed by the carbonisation and subsequent activation of a series of sugar and N-compound mixtures. The results of both approaches for developing CO_2 adsorbents will be discussed comparing both the adsorption capacity versus temperature and the ease of regeneration of the different adsorbents.

Experimental

Materials. For the first approach the substrates comprise a high surface area (HS1) and two low surface area (LS1 and LS2) activated PFA-derived unburned carbon concentrates (PFA_ ACC). The PFA_ ACCswere steam activated in a vertical tube fixed bed furnace. This involved heating these in a stream of nitrogen to 800-850^{o}C, whereupon steam was introduced for a set time interval while the furnace temperature was kept constant. For the impregnation of the substrates, three amines were used, namely poly-ethylenimine (PEI), di-ethanolamine (DEA) and tetra-ethylene-penta-amine-acrylonitrile (TEPAN). DEA and PEI were obtained from chemical suppliers, with both a low molecular mass (mm) and a high mm form of PEI being used, their mms being 600 and 1800 respectively. TEPAN was produced in the laboratory in accordance with a method devised by Birbara, *et al.* [(2)]. The amine impregnation method was based on that used by Xu, *et al.* [(3)], and the amine loadings are expressed as a percentage of the sum total of the amine and substrate mass.

For the second approach used in this work, common sugar was used as the carbon matrix source for the adsorbents obtained. The nitrogen source comprised a series of nitrogen compounds with different nitrogen functionalities (i.e., acridine, proline, carbazole and urea), which were supplied by Fisher. In order to increase the char yield, prior to the carbonisation process the mixtures at 50 wt% were pre-treated with sulphuric acid. The carbonisation step was performed by heating the samples in a closed reactor at 10°C min^{-1} up to 400°C under an inert atmosphere. The products of carbonisation were then activated with CO_2 (100 mL min^{-1}) for 0.5 hours at 900^{o}C. The final adsorbents obtained after the activation step were denoted as MTA, MTC, MTP and MTU, corresponding to the pre-treated mixtures of sugar with acridine, carbazole, proline and urea, respectively.

Characterisation. The surface area, meso- and micro- pore volumes and average pore diameter of the substrates were calculated from N_2 adsorption and desorption isotherms obtained at -196^{o}C using a Micromeritics ASAP 2010 unit. The carbon and nitrogen content of the substrates and sorbents were determined using a using a Carlo Erba NA1500 elemental Analyzer. The thermal stability of the substrates was measured by heating them at a rate of 15^{o}C/min in a Perkin-Elmer thermogravimetric analyzer (tga) from room temperature to 800^{o}C in a stream of nitrogen.

The CO_2 adsorption capacity of the prepared sorbents, which is expressed as the percentage of CO_2 adsorbed by mass of the sorbent (on a dry basis), was measured using the tga. For the isothermal (75^{o}C) tests, approximately 10 mg of the sample were placed into an alumina crucible and dried at 100^{o}C for 30 minutes under a flow of N_2 gas. The temperature was then decreased to 75^{o}C and the gas flow, whilst being kept at a steady flow rate of 20 ml min^{-1}, was shifted from N_2 to CO_2. After 40 minutes, the gas flow reverted to N_2 while the temperature was maintained at 75^{o}C. The temperature-programmed CO_2 adsorption test differed from the isothermal CO_2 adsorption test in that subsequent to the drying stage, the temperature was decreased to 25^{o}C, following which the N_2 gas flow was switched to CO_2. These operating conditions were maintained for 2 h, after which time the temperature was increased at 0.25^{o}C min^{-1} up to 100^{o}C. Once the sample reached the final temperature (100^{o}C), the gas flow was reverted to to N_2 while the temperature was maintained at 100^{o}C.

Results and Discussion

CO_2 adsorption at 75^{o}C: Influence of amine and substrate. Table 1 lists the activation conditions and pore structure properties of the substrates. Figure 1 below displays the adsorption capacity at 75^{o}C of the amine-impregnated forms of LS1 and LS2.

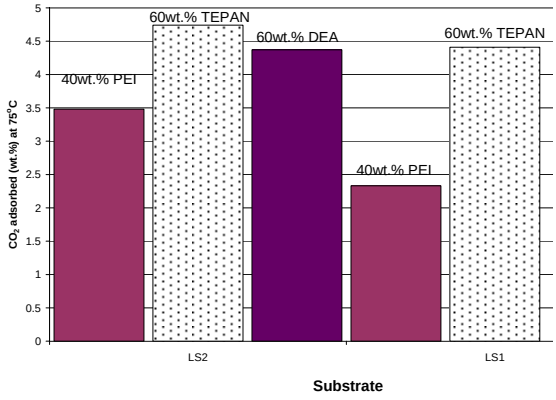

Figure 1. CO_2 uptake of impregnated substrates at 75^{o}C

Of the three amines studied, TEPAN yielded the highest CO_2 uptake. The optimum loading of PEI upon the PFA_ ACCs, which was 40 wt.%, at a temperature of 75^{o}C, yielded a CO_2 uptake of approximately 3.5 wt.% whereas the highest CO_2 uptake achieved with the same PFA_ ACC (LS2) loaded with the optimum loading of TEPAN (60wt.%) was 4.7wt.%. The CO_2 uptakes reported here

compare to those of ca. 10-12 wt.% with PEI impregnated on MCM-41[3] and on a series of mesoporous silicas which will be reported elsewhere.

Table 1. Textural characteristics and activation conditions of substrates

Sample name	Substrate name	Activation temp (°C)	Activation time (hrs)	Burnout of carbon (wt.%)	BET surface area (m^2/g)	Average pore diameter (nm)	BJH ave pore diameter (nm)	Cumulative BJH Pore Volume of mesopores (cm^3/g)	Cumulative BJH mesopore surface area (m^2/g)
Columbian PFA_ACC	HS1	800	7	55	472.1	2.9	4.7	0.160	136.3
High Marnham PFA_ACC	LS2	850	2	43.8	127.0	3.9	5.4	0.102	75.0
	LS1	800	7	53.92	166.46	4.3	5.4	0.160	118.6

Generally, the highest uptake of CO_2 by mass of amine would be expected to be achieved by PEI, owing to its greater ratio of CO_2-attracting amine groups to carbons; for TEPAN and DEA the amine to carbon ratio is ca. 1:4, whereas for PEI it is 1:2. However, whereas a PEI loading of 40 wt.% produced the optimum CO_2 uptake upon the PFA_ ACCs, the same PFA_ ACCs dosed with TEPAN yielded the optimum CO_2 uptake at a loading of 60 wt.%. This tallies with TEPAN's low mm – 311[4], as opposed to 1800 for PEI. The lower mm of the TEPAN molecule should enable it to achieve better penetration of the substrate and hence the substrate should be able to accommodate more TEPAN than PEI. The hypothesis that TEPAN's lower mm causes it to have better penetration properties than PEI is corroborated by the fact that the highest CO_2 uptake attained at 75°C using the PFA_ ACCs (4.7wt.%), was achieved with TEPAN.

Influence of PEI mm. Investigations were conducted to ascertain whether a lower molecular mass PEI might prove more effective in elevating the CO_2 adsorption capacity of PFA_ ACCs. The results of this work are displayed in Figure 2.

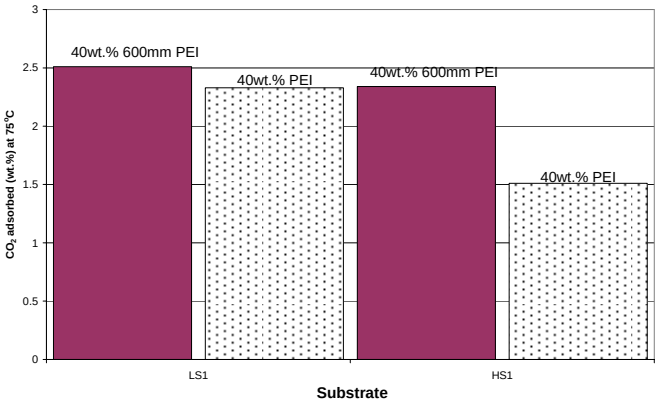

Figure 2. Comparison of CO_2 uptake of substrates impregnated with PEI of mm 600 and 1800 respectively at 75°C

Figure 2 shows that overall PEI 600mm only produces a significant improvement in the performance of HS1. However, it is worth noting that the 600mm PEI molecule has a mm that is nearly double that of TEPAN, therefore its mm might still prove prohibitive in facilitating high penetration of low mesoporosity substrates. What is also interesting to note from Figures 1 and 2 is that PFA_ ACC LS2, despite, as shown in Table 1, having a considerably lower mesopore volume and surface area and than either LS1 or HS1, has a far higher uptake of CO_2 when impregnated with a PEI (1800mm) loading of 40wt.% (3.5wt.%, as opposed to 2.3wt.% and 1.5wt.% for LS1 and HS1 respectively). Potential explanations for this behaviour include its lower burnout of carbon and hence its higher ratio of unburned carbon to ash and additionally its higher activation temperature and the attendant alterations in its pore structure that this might engender.

Thermal stability. The thermal stability of PEI (1800mm), DEA and TEPAN was analyzed. A broad correlation between the temperatures at which the amines began to exhibit a high rate of evolution and their mms was found. These temperatures were ca. 320°C, 225°C and 185°C for PEI, TEPAN and DEA respectively. The thermal stability of these amines was found to drop when they were impregnated in substrates. The diminished temperature evolution is attributable to the fact that the amines are present as a film on the substrates, rather than being in a bulk form, thus increasing their surface area and hence susceptibility to evolution on heating.

CO_2 adsorption of sugar-derived nitrogen enriched carbons. According to the results presented in Table 2 it can be said that carbazole is the N-compound that incorporates the least amount of nitrogen into the carbon, while urea yields the highest nitrogen-containing adsorbent.

Table 2. Chemical Characteristics of the Adsorbents Studied

Sample	N (wt%)	C (wt%)	C/N ratio
MTA	3.9	76.0	0.04
MTC	2.3	81.0	0.02
MTP	3.4	74.9	0.04
MTU	6.3	76.8	0.07

The adsorption capacities of the adsorbents studied are plotted against temperature in Figure 3. In Figure 3a the CO_2 adsorption capacity is expressed as the percentage of CO_2 adsorbed by mass of the sorbent. For these N-enriched carbons the highest adsorption capacity (i.e., highest weight uptake) occurs at room temperature, and a clear decrease is observed as the temperature increases. Furthermore, the process seems to be totally reversible, as the adsorbents reach the initial weight after switching the reactive gas (i.e., CO_2) to N_2 at 100ºC. In order to get a clearer picture of the N content effect, the adsorption capacities of these N-enriched carbons were normalised with respect to the BET surface area, taking into account the great influence of this parameter on the CO_2 capture performance of the sorbents. Thus, the weight uptake during the temperature-programmed CO_2 adsorption tests was normalised by the surface area of the adsorbent and the initial mass of the sample, giving a new parameter denoted as W_S. The W_S.profiles versus temperature are shown in Figure 3b. It is worth noting that in terms of W_S, the sample with the highest content of nitrogen (i.e., MTU) has the lowest adsorption capacity and the sample obtained by co-pyrolysis with carbazole, MTC, although possessing a comparatively low nitrogen content (see Table 2), has the highest CO_2 adsorption capacity. This indicates that it is not just the amount of nitrogen in the adsorbent, but also the nitrogen functionality that has a strong influence upon the performance of the carbons.

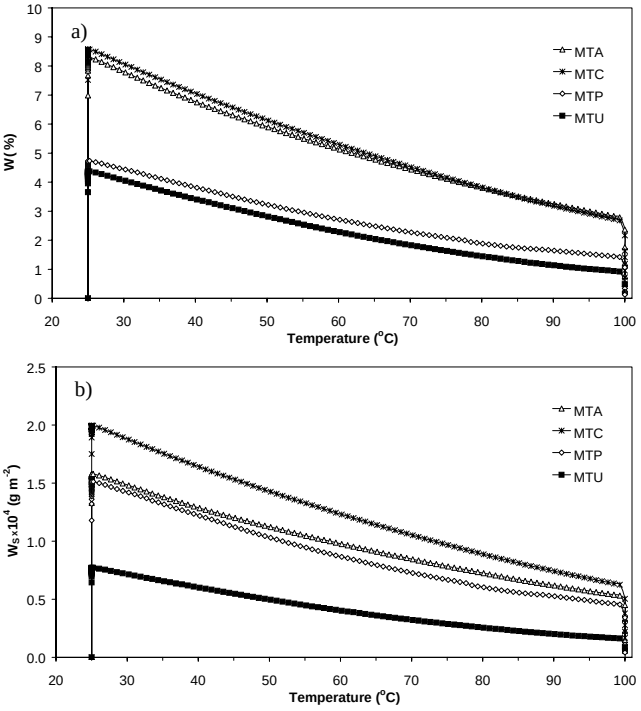

Figure 3. CO_2 adsorption capacities measured during temperature-programmed adsorption/desorption tests of the N-enriched carbons studied

In comparison to the amine-loaded substrates, the N-enriched carbons perform better than the PFA_ ACCs. Further work is intended in order to see how the performance of these adsorbents may be improved and furthermore how the substrates perform over a period of multiple adsorption/regeneration cycles.

Conclusions

CO_2 adsorptions have been successfully prepared by impregnating amines upon PFA_ ACCsand through the carbonization and subsequent activation of mixtures of sugar and nitrogen containing compounds. For the PFA_ ACCs, TEPAN was a stronger CO_2 adsorption enhancing amine than DEA or PEI. Of the N-compounds mixed with the sugars, urea yielded the highest nitrogen content in the resulting carbons but carbazole, despite yielding the lowest nitrogen content, engendered the highest adsorption capacity both in terms of the overall amount of CO_2 adsorbed by the sorbents and also the mass of CO_2 adsorbed per m^2 of their surface area. This indicates that it is not just the amount of nitrogen in the adsorbent, but also the nitrogen functionality that has a strong influence upon the performance of the carbons.

Acknowledgements. AA thanks *Secretaria de Estado de Educación y Universidades* and *Fondo Social Europeo* for financial support. The authors thank The Carbon Trust, BCURA and the Research Fund for Coal & Steel (RFCS) for financial support.

References

(1) Leon y Leon, C.A., Radovic, L.R., In *Chemistry and Physics of Carbon*, Thrower, P.A., Ed.; M. Dekker, New York, **1992**; Vol. 24, pp. 213.
(2) Birbara, P.J., Filburn, T.P., Michels, H.H. and Nalette, T.A. Hamilton Sundstrand Corporation, Sorbent system and method for absorbing carbon dioxide (CO_2) from the atmosphere of a closed habitable environment, U.S. **2002**, 6, 364, 938.
(3) Xu, X., Song, C., Andresen, J.M., Miller, B.G., Scaroni, A.W. *Microporous and Mesoporous Materials* **2003**, 62 (1-2), 29.
(4) Filburn, T., Weiss, R. A., Helbe, J., Huang, S. and Papale, W. Prepr. Pap. - *Am. Chem. Soc., Div. Fuel Chem.*, **2002,** 47 (1)**,** 61-61.

COMPARISON OF AIR AND CARBON DIOXIDE ACTIVATION OF MULTI-WALLED CARBON NANOTUBES FOR HYDROGEN STORAGE

John M. Andrésen and Eric K. Chastain

The Energy Institute, The Pennsylvania State University
407 Academic Activities Bldg., University Park, PA 16802

Introduction

As energy demand increases throughout the world, the need for clean energy sources, that do not impact the urban air quality as well as the global climate, increases accordingly (1). Hydrogen has been touted as the fuel to satisfy this future energy need due to its very benign combustion product, namely water. However, several questions remain as to how this will be accomplished. Storage of this energy gas is a vital element of the proposed "hydrogen economy." There are several options for hydrogen storage under research, including alloys and intermetallics, sodium and lithium alanates, nanocubes, and carbon nanotubes (2). In particular, carbon nanotubes may provide the highly anticipated answers to the challenging hydrogen storage quest due to its potential to form a light-weight storage material that can satisfy the 6-7 wt% benchmark storage target set by Department of Energy (3). Although unaltered carbon nanotubes are capable of adsorbing some H_2, activating nanotubes can substantially increase the potential for adsorption (4). Accordingly, this paper focuses on the activation of multi-walled carbon nanotubes with physical agents such as carbon dioxide gas and oxygen.

Experimental

The multi-walled nanotube sample was obtained from Nanostructured & Amorphous Materials, Inc. The activation was conducted at 550°C under a flow of carbon dioxide or air. The surface area was measured using a Micromeritics ASAP 2000 under N_2 at 77K. A thermogravimetric analyzer, Cahn TGA-151, was used to conduct pressure-composition isotherm measurement studies of the hydrogen absorbed where the pressure and time related uptake of hydrogen and the associated kinetics was followed as a function of the modified composition of the activated carbon nanotubes. During a typical hydrogen adsorption test about 200 to 400 mg of sample is placed into the analyzer and degassed using helium or nitrogen gas. Following degasification the system is pressurized to the desired pressure using dry H_2 gas. While reaching the desired pressure the sample is held isothermal at room temperature and the weight change of the sample is monitored. Any increase in weight is attributed to an uptake of H_2 into the sample.

Results and Discussion

Figure 1 shows the changes in surface area after activation in air at 550°C for a multi-walled carbon nanotube sample. As the MWNT sample is activated with air up to 10 minutes there is a 50% increase in the surface area of the resultant activated sample compared with the original MWNT. Beyond 10 minutes activation there is a significant decrease in overall surface area from about 140 m^2/g at 10 minutes down to about 10 m^2/g at 20 minutes. The results indicate that air attacks the MWNT selectively leaving behind metallic catalyst and amorphous carbon that yield very little surface area compared to the carbon nanotubes. From TEM analysis on the pristine MWNT it was estimated that the sample was about 20 to 30% pure MWNT with the reminder being mainly amorphous carbon. The weight loss for the 10 minutes activated sample was about 10% indicating that about 1/3 to 1/2 of the carbon nanotube structure has been oxidized at this point. After 20 minutes close to 20 wt% was lost corresponding to the low surface area of the resulting sample. The results suggest that MWNT can easily be activated using air or oxygen.

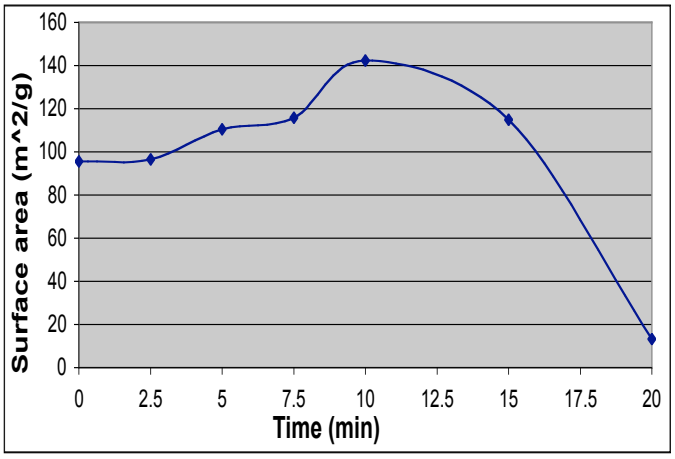

Figure 1. Activation of multi-walled nano-tubes in air at 550°C.

Figure 2 shows the MWNT activated in carbon dioxide at 550°C up to 960 minutes. After the first 100 minutes very little change in the surface area has occurred although about 10 wt% of the sample has been lost. This indicates that oxidation using carbon dioxide may preferentially attack the amorphous carbon at shorter activation times. Extending the activation time to 250 minutes resulted in an 18 wt% loss and a 35% increase in the surface area suggesting that the MWNT are being activated. The difference in activation for air (Figure 1) and CO_2 (Figure 2) indicates that there is a great potential for physical activation of MWNT to generate activated samples for hydrogen storage with various adsorption sites.

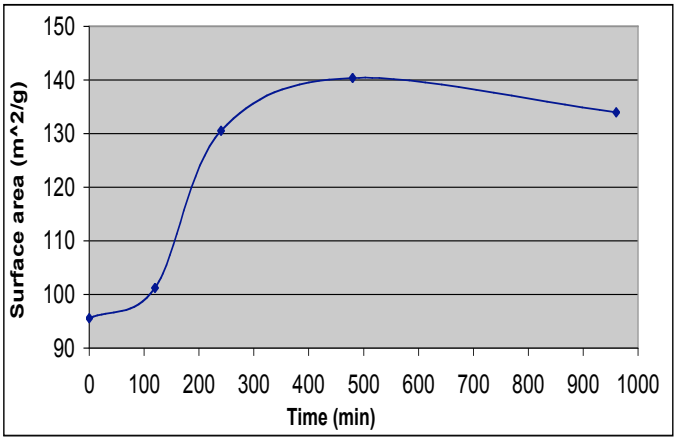

Figure 2. Activated multi-walled nano-tubes in CO_2 at 550°C up to 960 min.

Conclusions

Figure 1 indicates that the MWNT structure is made accessible for hydrogen storage using air activation at relatively low temperatures. Typical MWNT structures are several nanometer thick with about 20-30 layers of carbon. Hence, most

of the carbon is therefore not accessible for hydrogen adsorption due to encapsulation by the outer layer. Further, the extreme length of the multi-walled carbon nanotubes compared to their diameter is limiting the storage of hydrogen within the MWNT themselves. Hence, liberating the structure through partial oxidation as shown above can significantly introduce hydrogen adsorption sites in MWNT.

References

[1] Schultz, M.G., Diehl, T., Brasseur, G.P., Zittel, W., Science, 302 (5645), 624-627, 2003

[2] Dillon, A.C., Heben, M.J., Applied Physics A-Materials Science & Processing, 72 (2), 133-142, 2001

[3] Hynek, S., Fuller, W., Bentley, J., Int. J. Hydrogen Energy, 22, 601, 1997.

[4] Smith, M.R., Bittner, E.W., Shi W., Johnson J.K., Bockrath B.C., J. Physical Chemistry B, 107 (16), 3752-3760, 2003

DEVELOPMENT OF ACTIVATED CARBONS FROM COAL AND BIOMASS COMBUSTION AND GASIFICATION CHARS

M. Mercedes Maroto-Valer, Yinzhi Zhang and Bruce Miller

The Energy Institute and Department of Energy and Geo-Environmental Engineering, The Pennsylvania State Universtiy, 405 Academic Activities, University Park, PA 16802

Introduction

High carbon content chars, which are a byproduct stream from gasifiers and some coal-fired combustors are currently disposed as a waste. During 2002, around 900 million metric tons (Mt) of coal were burned, and about 107 Mt of coal combustion by-products were generated, including around 57 Mt of fly ash, that contain various levels of uncombusted coal or chars [1]. However, due to the increasingly restricted landfill use, the utility industry needs to find uses for high carbon chars [2, 3]. Following this demand, the authors have previously developed a one-step activation protocol to produce activated carbons from coal combustion chars [3]. Compared to the conventional two-step process that includes a devolatilization of the raw materials, followed by an activation step, chars only require a one-step activation process, since they have already gone through a devolatilization process while in the combustor. The authors' previous work has focused on coal-derived chars[2, 3]. This paper compares the physical and chemical properties of coal and biomass chars derived from combustion and gasification processes, as well as their potential use as feedstock for activated carbons.

Experimental

Fly ash samples. Two char samples, FA1 and GT, were collected and characterized. FA1 was collected from the Penn State University pulverized coal-fired research boiler (2 MM Btu/hour) that uses a high volatile bituminous coal from the Middle Kittanning seam. GT-Woodchar was a wood-based sample obtained form a gasifier. In addition, two lignite-based commercial activated carbon samples, Darco FGD and FGL, were provided by Norit Americas Inc.

Characterization of the samples. The loss–on-ignition (LOI) contents of the samples were determined according to the ASTM C311 procedure. The porosity of the samples was characterized by conducting N_2 adsorption isotherms at 77K using a Quantachrome adsorption apparatus, Autosorb-1 Model ASIT. The pore volume was calculated from the volume measured in the nitrogen adsorption isotherm at a relative pressure of 0.95 (V_t). The total specific surface area, S_t, was calculated using the multi-point BET equation in the relative pressure range 0.05-0.35, as described previously[2,3]. From the adsorption isotherm, the micropore (<2nm) volume, V_{mi}, and external surface area, S_{mi}, were calculated using the α_S-method, where non-graphitized non-porous carbon black Cabot BP 280 (S_{BET}=40.2m^2/g) was used as a reference adsorbent[4]. The mesopore (2-50nm) volume (V_{me}) was calculated by subtracting the volume of V_{mi} from V_t. The pore size distribution was calculated using the BJH method.

One-step activation. The activation of the samples was performed in a horizontal activation reactor. The sample was heated under nitrogen flow to the desired temperature, and then steam was introduced into the reactor for 30 minutes, while the reactor was kept under isothermal conditions.

Results and Discussion

LOI of the char samples. Table 1 shows the LOI of the study samples The coal char sample, FA1, and the wood char sample, GT-Woodchar, have very high LOI values (63 and 85%, respectively). FGD is a lignite-based commercial activated carbon, with very small particle size (less than 45 μm), and is claimed as a free flowing powdered carbon. Its LOI value is 65% as listed in Table 1 (i.e., it contains 35% ash). FGL is also a commercial lignite-based activated carbon and its LOI is 68%.

Table 1. Summary of the study samples.

Sample	Coal Used	System	LOI, wt%	Ash,%
FA1	Subbit.	Boiler	63	37
GT-Woodchar	Wood	Gasifier	85	15
FGD	Lignite	AC	64	36
FGL	Lignite	AC	68	32

Thermogravimetric analysis of the coal and wood char samples. The TGA profiles of the char samples are shown in Figure 1. The coal-char sample, FA-1, began to loss weight at around 450°C and continued to lose weight at a constant rate until 650°C with one step change. Compared to the coal char sample, the wood char sample has a lower starting point for the initiation of weight loss (180-300°C), and has more than one weight loss step during a broader temperature range. For example, the wood char sample lost around 80% of its weight in the temperature range 180 to 350°C, then lost another 2% weight at 550 to 700°C.

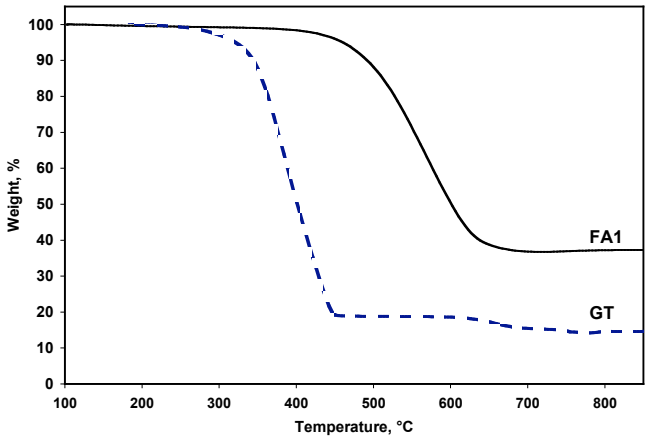

Figure 1. TGA profiles of the char samples.

Isotherms of activated chars. The char samples, FA1 and GT, were activated with steam at 850°C for 30 minutes. The isotherms of the resultant activated carbons, FA1-30 and GT-30, are shown in Figure 2. For comparison, the isotherms of the activated chars shown in Figure 2 are on a carbon basis. The isotherms of the commercial activated carbons, FGD and FGL are also shown in Figure 2. It is obvious that the activated GT char has a similar isotherm as the commercial activated carbon. All isotherms contain a hysteresis loop, which is usually associated with the filling and emptying of mesopores by capillary condensation. Besides the steep rise at the low relative pressure, which corresponds to micropore filling, the isotherm keeps increasing with the relative pressure, even near saturation pressure, which suggests there are mesopores and macropores in the sample. In

contrast, activated coal-based char, FA1-30, has a near type 1 isotherm, which features a steep increase at low relative pressure and levels off at higher relative pressure. However, compared to the raw char, both activated char samples (FA1-30 and GT-30) have much more developed porosity after the 30 minutes one-step activation process.

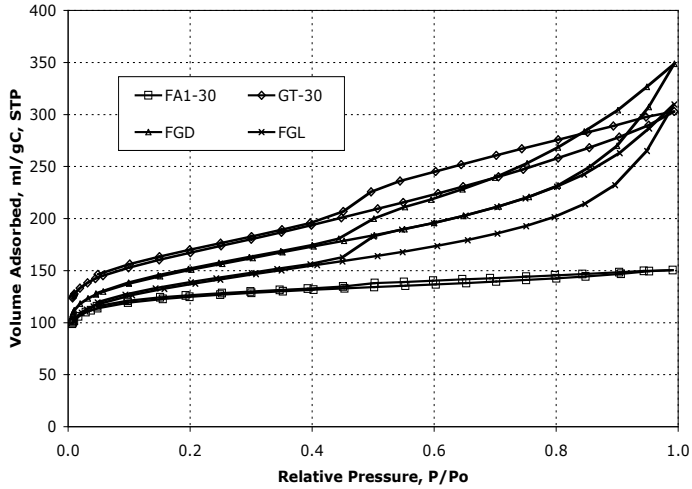

Figure 2. Isotherms of activated chars (FA1-30 and GT-30) and commercial activated carbons (FGD and FGL)

Pore surface area and volume distribution of activated chars. The surface area and pore volume distribution of the samples were calculated from the isotherms presented in Figure 2 using the alpha-s method and the results are presented in Figures 3 and 4.

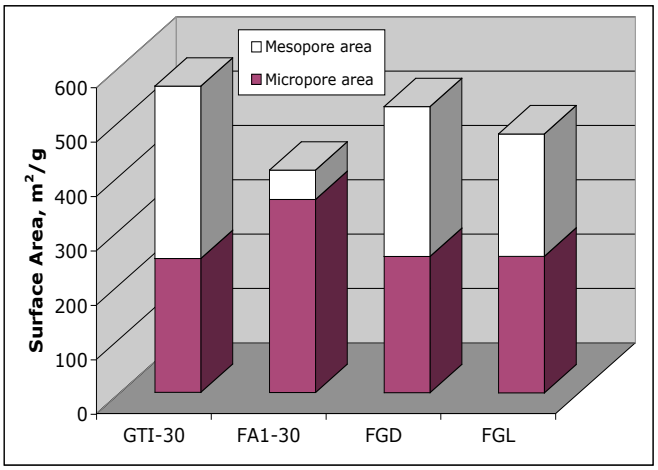

Figure 3. The surface area distribution of the activated chars (GT-30 and FA-30) and commercial activated carbons (FGD and FGL)

The activated GT sample has the greatest surface area ($564m^2/g$) on a carbon basis, of which $317m^2/g$ is contributed from mesopores, which account for ≈56% of the total. The commercial activated carbon FGD has a surface area of $526m^2/g$, and ≈53% ($275m^2/g$) is from mesopores. Corresponding to its different isotherm shape, activated FA1 has only 13% surface area that is contributed from mesopores (54 vs. $409m^2/g$).

FGD has a total pore volume of 0.473 ml/g and 77% of the pore volume is from mesopores. GT-30 has a similar pore volume distribution, with a total pore volume of 0.447ml/g of which ≈73% is from mesopores. Activated FA1 has more micropores and a larger mesopore volume, but the mesopores only account for 25% of the total pore volume.

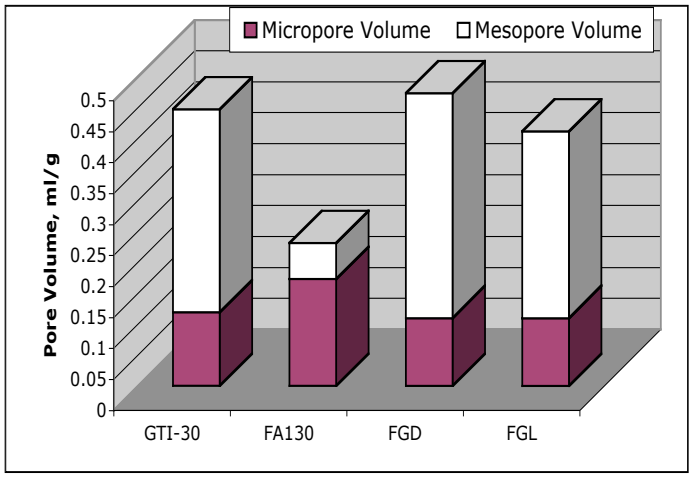

Figure 4. The pore volume distribution of the activated chars (GT-30 and FA-30) and commercial activated carbons (FGD and FGL)

Conclusions

Of the samples collected, the wood-based sample has higher LOI than the coal-based samples. The lignite-based commercial activated carbon, Darco FGD, contains 35% ash. The wood-based sample has a lower starting point for weight loss (180-300°C vs. 200-400°C) than the coal based char, and its thermal reaction is more complex. Compared to the raw char (FA1 and GT), both activated char samples (FA1-30 and GTI-30) have much more developed porosity after the 30 minutes one-step activation process. The activated GT sample has surface area as high as $564m^2/g$ on a carbon basis, which is comparable to the commercial activated carbon FGD of $526m^2/g$. The mesoporosity of activated GT char is 56% on a surface basis or 73% on a volume basis. This is comparable to the commercial activated carbon FGD, which is 53% is on a surface basis or 77% on a volume basis. Both samples have a porous structure containing a large amount of mesopores, suggesting that they will have good mass transfer properties.

Acknowledgements. The authors would like to acknowledge the Consortium for Premium Carbon Products from Coal (DOE Award number: DE-FC26-98FT40350; Internal Agreement Number: 2482-TPSU-DOE-0350) for financial support.

References

(1) Kalyoncu RS. Coal Combustion Products, U.S. Geological Survey Minerals Yearbook, 2000

(2) Maroto-Valer MM, Schobert HH. Carbonaceous combustion waste as precursor for activated carbons, 24th Biennial Conf. on Carbon, 1999, Charleston, 1, 588-589

(3) Zhang YZ, Lu Z, Maroto-Valer MM, Andresen JM, Schobert HH. Comparison of High-Unburned-Carbon Fly Ashes from Different Combustor Types and Their Steam Activated Products, Energy & Fuels, 2003:17, 369-377

(4) Kruk, M.; Jaroniec, M.; Gadkaree, K.P., J. Colloid Interface Sci., 1997, 192, 250

EFFECT OF γ-IRRADIATION OF ACTIVATED CARBONS ON THE GENERATION OF NEW FREE RADICALS AND POROSITY

Demet Erçin[1], Mahmut Eken[1], Zeki Aktas[2], Sevil Çetinkaya[3], Billur Sakintuna[4] and Yuda Yürüm[4]

[1]Materials Research Department, Ankara Nuclear Research and Training Center, Besevler, 06100 Ankara, Turkey
[2]Department of Chemical Engineering, Ankara University, Besevler, 06100 Ankara, Turkey
[3]Department of Chemistry, Hacettepe University, Beytepe, 06532 Ankara, Turkey
[4]Faculty of Engineering and Natural Sciences, Sabanci University, Tuzla, 34956 Istanbul, Turkey

Introduction

Ion beam irradiation is one approach that has been utilized to modify macromolecular materials primarily by alteration of the macromolecular structure or chemical composition of the carbon materials[1]. The erosion of polymer surfaces by high energy ions or particles is of interest for polymers used in space vehicles[2,3]. It is reported that little is known about the radiolysis of condensed organic materials with heavy ions[4]. The radiolysis of active carbons with γ-rays is not an extensively studied topic. Products of such an interaction should be a complex mixture of ions, free radicals and simple molecules and a solid restructured carbonaceous material.

Originally present and/or newly created organic free radicals in carbonaceous solids have been shown to interact with paramagnetic gases such as oxygen[5]. The interactions between a paramagnetic gas and organic free radicals occur over short distances, typically on the order of a few nanometers and often result in measurable broadening of ESR spectral lines[6]. Because of this short interaction distance, free radicals accessible to oxygen are expected to be located on or just beneath the external and internal surfaces of carbonaceous solids. Such interactions thus are expected to form new structures on the surface of carbon materials

In this paper the results of the surface treatment of activated carbons prepared from Turkish Elbistan lignite with γ-irradiation from a ^{60}Co source are presented and associated modification of the structure of the activated carbon is discussed in terms of changes in surface area and free radical concentration.

Experimental

Materials. Elbistan lignite was used in the study. Analysis of the Elbistan lignite is presented in **Table 1**. The lignite sample was ground under a nitrogen atmosphere to 100 μm size and stored under nitrogen.

Table 1. Proximate and Elemental Analysis of Elbistan Lignite

Proximate Analysis	**%, dry**
Volatiles	*44.8*
Fixed Carbon	*20.9*
Ash	*34.3*
Elemental Analysis	**%, dmmf**
C	*53.0*
H	*5.8*
N	*1.8*
S	*3.6*
O (by difference)	*35.8*

Pyrolysis experiments. Coal samples were dried at 100°C an inert atmosphere. 8.00 g sample was placed into a porcelain crucible and then placed into a furnace purged with ultra high-purity nitrogen. Coal samples were heated to four different temperatures 500, 700, 800, 900 and 1000°C with a heating rate of 10°C/min, under a nitrogen flow of 100 ml/min for 120 minutes. After the pyrolysis experiments, chars were cooled to room temperature under the nitrogen flow.

Activation experiments. Chars were activated under a carbon dioxide flow of 100 ml/min at the final pyrolysis temperature for an additional two hours. System was cooled to room temperature under the nitrogen flow.

Irradiation experiments. A PX-γ-30 ^{60}Co gamma cell having a dose rate of 1.85 kGyh^{-1} at room temperature was used for γ-radiolysis. The dose rate profile of the gamma source was determined by Fricke dosimetry.

Surface analysis. Surface areas of activated carbons were measured by ASAP2000 Accelerated Surface Area and Porosimetry system manufactured by Micromeritics Co., USA. Surface area of the samples was determined by using BET equation in the relative pressure range of between 0.05 to 0.25, over five adsorption points.

FTIR spectrometry. FT-IR spectra of activated carbon samples were measured with a Bruker EQUINOX 55 FT-IR spectrometer. Activated carbon samples were dried under a nitrogen atmosphere at 110°C for 24 hours. KBr pellets were prepared by grinding 2.5 mg of dry sample with 200 mg of dried KBr. Spectra were obtained with 200 scans at a resolution 2 cm^{-1}.

ESR spectroscopy. ESR spectra of the activated carbon samples, 20 mg, transferred into tubes of 4 mm i.d. were recorded using a Bruker EMX ESR spectrometer operating at 9.6 GHz, with a single cavity resonator, 3300 field set, 100 kHz field modulation, 0.50 G peak to peak modulation amplitude and 0.6 mW microwave power to determine the radical concentrations, signal intensities, linewidths and g values. All spin concentration measurements were performed using a standard DPPH sample in the cavity of the resonator. The intensity of the ESR signal is proportional to the number of free radicals in the sample and is, therefore, an indication of the spin density. Relative spin density $N_{s\text{-}rel}$ is calculated from the ratio of the relative intensities of the samples to that of the raw lignite[7].

Results and Discussion

BET areas of irradiated samples are measured to be greater than those of non-irradiated samples, shown in **Figure 1**. This might be considered as an indication to surface erosion by high energy ions and particles as it was observed by Young and Slemp[2], on polymer surfaces. BET areas of both irradiated and non-irradiated samples of activated carbons increased up to 800°C. The BET areas of the samples produced at 900°C and 1000°C decreased to lower values than those of measured for samples obtained at 800°C. The reason for the decrease of BET areas in samples obtained at temperatures higher than 800°C might be the melting of the minerals originally present in the raw lignite samples and clogging of the porosity in the carbons by the glassy structures formed at these temperatures during pyrolysis and activation experiments.

Percent increase in BET areas of the irradiated samples relative to non-irradiated samples is presented in **Figure 2**. Surface erosion by high energy ions and particles seemed to increase as the temperature of activation was increased. A steady increase in the BET areas was observed in samples obtained in the range of 500-900°C. The effect was amplified in the irradiated sample obtained at 1000°C. While the percent difference was in the range of 5-22 for the samples obtained between 500°C and 900°C, the percent difference sharply increased to 372 between the non-irradiated and irradiated samples obtained at 1000°C.

ESR peak widths, (ΔH_{pp}), g values and relative intensities of activated carbons were given in **Table 2 and 3**. ESR peak intensities increased between 700°C and 900°C.

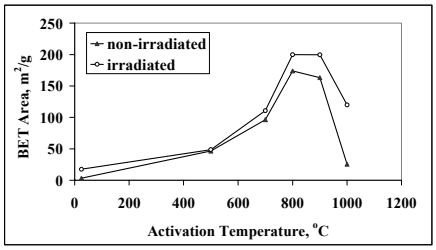

Figure 1. Change of BET area with temperature of activation for non-irradiated and irradiated samples.

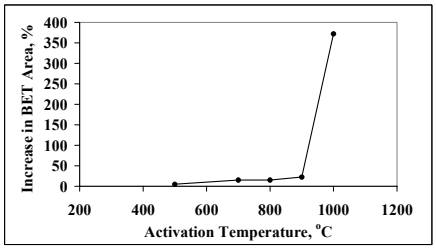

Figure 2. Change of percent BET area increase between non-irradiated and irradiated samples with activation temperature.

Table 2. ESR Peak Width and G Values Before and After Irradiation of the Activated Carbons.

Activation Temp., °C	Peak width before irradiation (ΔH_{pp}), Gauss	Peak width after irradiation (ΔH_{pp}), Gauss	g values before irradiation	g values after irradiation
Raw lignite	*6.3*	*5.4*	*2.0041*	*2.0030*
500	*6.5*	*6.9*	*2.0035*	*2.0018*
700	*78.2*	*78.2*	*1.9869*	*2.1080*
800	*850.4*	*855.3*	*2.0481*	*2.0455*
900	*830.9*	*821.1*	*2.0560*	*2.0590*
1000	*909.1*	*1026.4*	*2.1330*	*2.1804*

Table 3. ESR Relative Intensity Before and After Irradiation of the Activated Carbons.

Activation Temp., °C	Relative intensity before irradiation	Relative intensity after irradiation
Raw lignite	*1*	*1*
500	*5*	*5*
700	*27*	*19*
800	*39055*	*38403*
900	*47870*	*45903*
1000	*35943*	*44764*

Radical concentration was decreased in the temperatures higher than 600°C. The g value of activated carbons was increased at 600°C, similar to recombination reactions. Decreasing peak intensity and increasing g value at 1000°C was due to disappearing radical concentration. ESR peak widths were increased with increasing temperature. It is known that paramagnetic groups is increasing up to 550°C[8]. At high temperatures peak widths were increased. g values were increased with increasing temperature. ESR peak width (ΔH_{pp}) and peak intensities of original Elbistan Lignite and activated carbons did not change after irradiated.

^{13}C NMR spectra of raw Elbistan lignite and irradiated activated carbons at different temperatures were shown in **Figure 3** and **Figure 4** respectively. According to **Figure 4**, peak intensities of C-H bonds in the NMR spectra, decreased with increasing temperature. sp, sp^2 and sp^3 hybridized carbons were observed in these spectra .

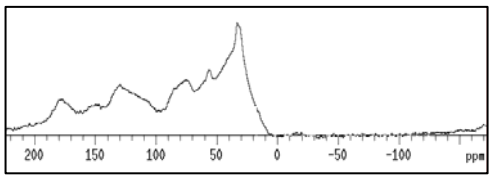

Figure 3. ^{13}C NMR of Non-Irradiated, Original Elbistan Lignite

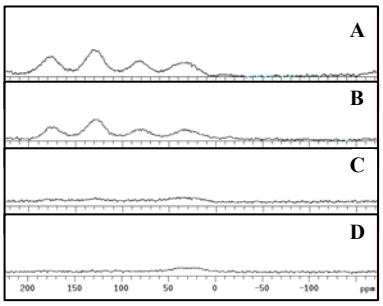

Figure 4. A. ^{13}C NMR of irradiated activated carbon at 500°C, **B.** at 700°C, **C.** at 800°C, **D.** at 900°C.

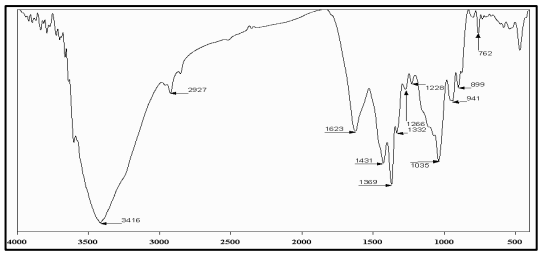

Figure 5. FTIR spectra of Raw Elbistan Lignite.

FTIR spectra of raw Elbistan Lignite was shown in **Figure 5**. Both in irradiated and non-irradiated activated carbons, functional groups were increased with increasing temperature. With irradiation, peak intensities in FTIR spectrums were also increased**.** Porous carbon material have characteristic bands near 3500 cm^{-1}, 1600 cm^{-1} and 1430 cm^{-1} are due to OH stretching, aromatic C-H absorption due to the aromatic structure of resultant carbon and C-O, C-C groups.

References

1. M.Celina; H. Kudoh; T.J. Renk; K.T. Gillen; R.L. Clough *Radiat.Phys.Chem.* **1998**, *51*, 191.
2. Young P.R.; Slemp W.S. *Polymer Preparation* **1990**, *31*, 353.
3. Young P.R.; Siochi E.J.; Slemp W.S. *Polymer Preparation* **1994**, *35*, 916.
4. LaVerne; J.A. Chang Z.; Araos M.S. *Radiat.Phys.Chem.* **2001**, *60*, 253.
5. Van Krevelen D.W.; Elsevier: Amsterdam, 1993.
6. Subczynski W.K.; Hyde J.S. *Biophys. J.* **1984**, *45*, 743.
7. Erçin D.; Tanyolaç A.; Korkmaz M.; Yurum, Y. *Fuel Processing Technology* **2001**, *69*, 95-106.
8. Pilawa B.; Wieckkowski A.B.; Lewandowski M.; Reson M. *Chem.* **1999**, *37*, 871-877..

Investigation of The Structural Changes in Freeze-dried Low-rank Turkish Coals and in Their Supercritical Extracts

Serkan Bas, Billur Sakintuna, Burak Birkan, Yusuf Menceloglu, Alpay Taralp, and Yuda Yürüm

Faculty of Engineering and Natural Sciences, Sabanci University, Tuzla, Istanbul 34956, Turkey

Introduction

Coal structure consists of asset of clusters attached by groups containing bonds potentially capable of undergoing free rotation[1]. The clusters contain aromatic and hydroaromatic systems. Most of the clusters are divalent, that is covalently bonded to only two other clusters. Some portion of the clusters are tri- or higher valent so that tridimensional macromolecules exist in the coal structures. Their presence in the coal causes the whole system to be linked into one large molecule, one in which a chain of covalent bonds attaches any atom to all other atoms. In addition to the covalent branch points, many branch points exist because of hydrogen bonding. Strongly basic solvents can break coal-coal hydrogen bonds. The results of solvent swelling in strongly basic solvents would be quite different from those obtained with the solvents which do not break hydrogen bonds. Swelling experiments are useful in terms of investigation and modification of the coal structure[1,2].

Lyophilizing is used to eliminate solvents in the interest of solute without destroying the structure reached after freezing. It is based on sublimation of freezed solvent under vacuum.

Turkish Beypazari and Elbistan lignite samples were swolen in ethylene diamine and dimethyl sulfoxide, in the present work. The change of surface area and morphology of the coal particles after swelling and lyophilization experiments were compared with those of untreated samples.

Experimental

Beypazari and Elbistan lignite samples were used in the present work. Elemental analyses[3] of these are given in the **Table 1**.

Table 1. Elemental Analysis of the Lignites Used, dmmf

Elements	Beypazari	Elbistan
C	65.2	62.7
H	5.4	4.7
N	2.1	0.8
S (total)	5.4	4.0
O (by diff.)	21.9	27.8

The lignite samples were ground to –100 mesh size before using. The swelling behavior of the lignite samples was studied by Liotta's method[4]. Approximately 100 mg of a sample was placed in a 6 mm o.d. tube and centrifuged for 10 minutes at 5000 rev/min. The height of the sample was measured as h_1. Excess ethylenediamine or dimethylsulfoxide (~1 ml) was added into the tube and the contents of the tube were mixed and the tube was centrifuged after 24 hours and the height of the sample in the tube (h_2) was measured. Swelling kinetics of dried coals were determined until equilibrium.

The swollen Elbistan and Beypazari lignite samples were frozen in two different ways before lyophilization. The first method was to freeze samples directly in liquid N_2 . In the other method pre-cooled samples at -20^{o}C were then frozen in liquid N_2 as it was in the first method. The samples were lyophilized at room temperature and a pressure of 0.120 mbar by using a Christ ALPHA 1-2 LD lyophilizer. The lyophilized and raw samples were examined with a Gemini scanning electron microscope. All samples were coated with gold before taking any image because of insufficient conducting of the lignite samples. The change in the structure after lyophilization was compared with those of the raw samples.

Lyophilized samples were treated with supercritical carbon dioxide in a Thermo Haake C35P supercritical system at 50 bar and 80^{o}C. Raw samples and supercritically treated samples were extracted in tetrahydrofuran digestively, for 24h at 20^{o}C and in 130 rpm. Extracts obtained were analyzed using a Shimadzu GC-17A GC-MS system. The surface area of the raw and treated samples were measured using an ASAP 2000 Accelerated Surface Area and Porosimetry system manufactured by Micromeritics Co., USA.

Results and Discussion

Swelling ratios of Beypazari and Elbistan lignites in dimethylsulfoxide and ethylenediamine were measured until equilibrium values were attained. The swelling ratio of Beypazari lignite sample in dimethylsulfoxide and of Elbistan lignite sample in ethylenediamine were measured as 1.42 and 1.46, respectively.

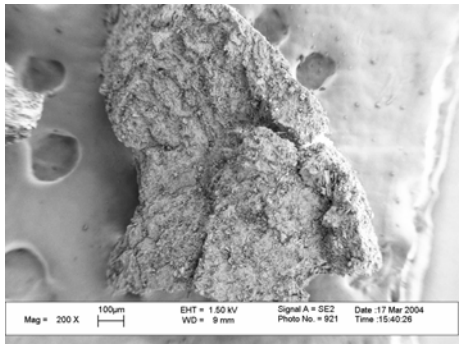

Figure 1. Micrograph of raw Elbistan lignite sample.

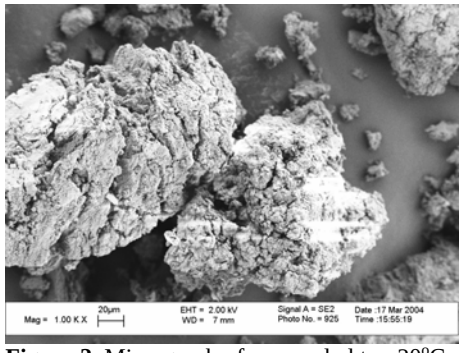

Figure 2. Micrograph of pre-cooled to –20^{o}C and then cooled in liquid nitrogen and lyophilized Elbistan lignite sample.

Micrographs of raw and treated lignite samples (**Figures 1-6**) indicated the presence of disintegrated particles in the solvent swollen and lyophilized samples. Particles seemed to develop new porosity on the surface. Surface areas of the treated samples increased compared to those of the raw samples.

GC-MS analyses revealed differences in the composition of THF extracts obtained after supercritical carbon dioxide treated lyophilized lignite samples. The components present in the total ion chromatograms (TIC) of the raw lignite (**Figure 7**) seemed to contain fewer number of peaks compared to those of TIC's of the extracts of treated lignite samples (**Figure 8 and 9**). Mass spectra of the components identified in the TIC's indicated the presence of complex structures in the extracts.

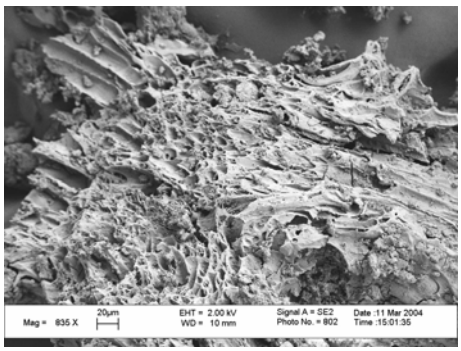

Figure 3. Micrograph of cooled in liquid nitrogen and lyophilized Elbistan lignite sample.

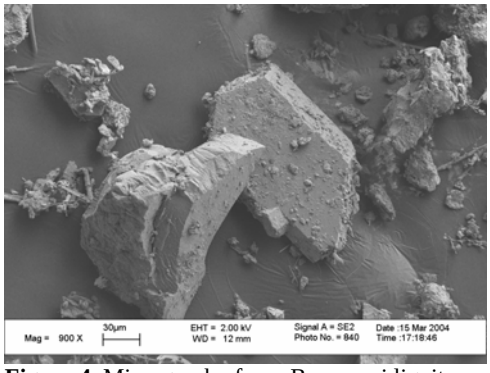

Figure 4. Micrograph of raw Beypazari lignite sample.

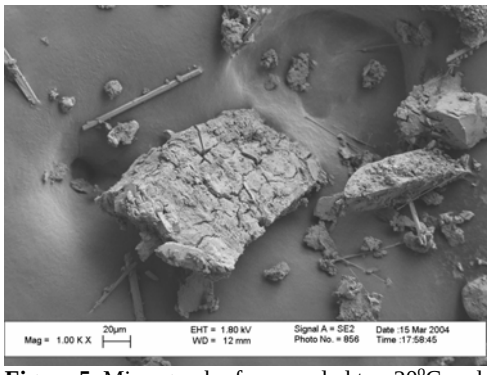

Figure 5. Micrograph of pre-cooled to –20^{o}C and then cooled in liquid nitrogen and lyophilized Beypazari lignite sample.

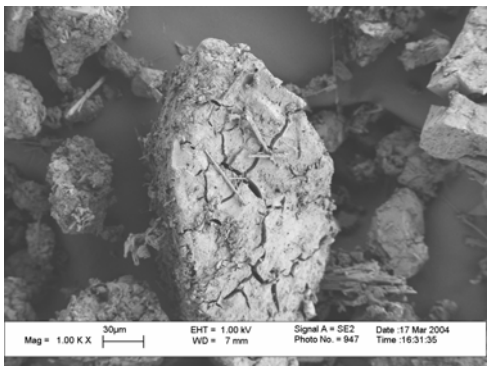

Figure 6. Micrograph of cooled in liquid nitrogen and lyophilized Beypazari lignite sample.

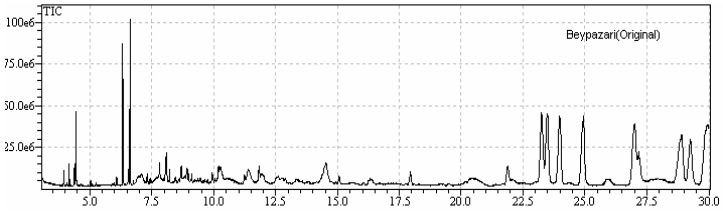

Figure 7. Total ion chromatogram of the extract obtained from raw Beypazari lignite.

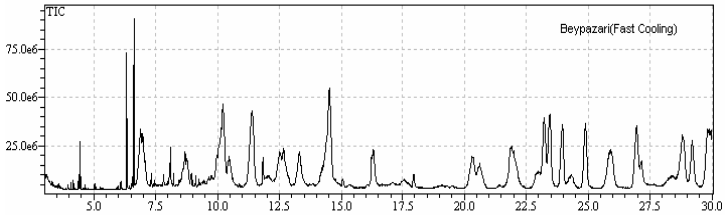

Figure 8. Total ion chromatogram of extracts obtained from Beypazari lignite sample which was first cooled in liquid nitrogen and then lyophilized.

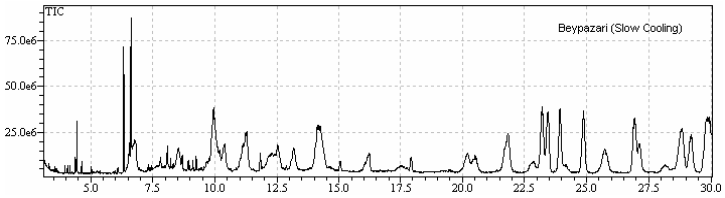

Figure 9. Total ion chromatogram of extracts obtained from Beypazari lignite sample which was first pre-cooled to –20^{o}C and then cooled in liquid nitrogen and lyophilized.

The work is in progress and it is expected that the complete set of analysis of the material present in the extracts and the effect of lyophilization on the morphology of particles will be determined in the future studies.

References

1. Larsen, J.W., Macromolecular structure of coals, status and opportunities, In "New Trends in Coal Science" Yürüm, Y. (Editor), NATO ASI Series, Series C, Vol. 244, 1988, pp. 73-116

2. Larsen, J.W., The physical and macromolecular structure of coals, In "Clean Utilization of Coal – Coal Structure and Reactivity, Cleaning and Environmental Aspects" Yürüm, Y. (Editor), NATO ASI Series, Series C, Vol. 370, 1992, pp.1-14

3. Basaran, Y.; Denizli, A.; Sakintuna, B; Taralp, A.; Yürüm, Y., Energy and Fuels, **2003**, 17, 1068.

4. Liotta, R., Brons, G and Isaacs, J., Fuel, **1983**, 62, 781.

TEMPLATED SYNTHESIS OF POROUS CARBONS AND FLOWER-LIKE CARBON FLUORIDES USING NATURAL ZEOLITE

Billur Sakintuna[1], Zeki Aktaş[2] and Yuda Yürüm[1]

[1]Faculty of Engineering and Natural Sciences
Sabanci University, Tuzla, 34956 Istanbul, Turkey
[2]Department of Chemical Engineering,
Ankara University, Tandogan, 06100 Ankara, Turkey

Introduction

In recent years, there has been growing interest porous carbons. They are widely used as industrial adsorbents because of the hydrophobic nature of their surfaces, high surface area, large pore volumes, chemical inertness, good mechanical stability and good thermal stability. Application areas are wide including gas separation, water purification, catalyst support, chromatography columns, storage of natural gas, and use as electrodes of an electric double-layer capacitor[1-3].

Porous carbons are usually obtained via carbonization of precursors of natural or synthetic origin, followed by activation. To meet the requirement, novel approach, the template carbonization method, has been proposed. Replication, the process of filling the external and / or internal pores of a solid with a different material, physically or chemically separating the resulting material from the template, is a technique that is widely used in microporosity and printing. Replica polymers[4], metals[5] and semiconductors[6] have been prepared from solids with pores on the length scale of nanometers to microns. Knox *et.al.* was synthesized rigid mesoporous and some microporous carbon, with Brunauer-Emmett-Teller (BET)[7] surface area 500 m^2/g, by carbonization of polymerized precursors in the silica gel[8]. The resultant carbon is now commercially available as a column packing material for liquid chromatography.

Because of the presence of the three-dimensional channels, zeolites have molecular-sieve property used in adsorption and catalytic purposes. The advantage to use zeolite templates that the zeolite-templated carbons had large surface areas and micropore volumes, without activation that is required to open new accessible microporous structure[9,10].

We have synthesized new porous carbon materials by using the natural domestic zeolite template and silica sol. The structure and morphology of zeolite-carbon composite and resulted carbon materials were characterized by several means.

Experimental

Natural Zeolite Sample. A natural domestic zeolite clinoptilolite from Manisa Gördes Turkey, with - 30 μm size was used in this study. SEM image of zeolite was given in **Figure 1**. Their BET surface area of zeolite is 59.44 m^2/g, BJH method[11] cumulative desorption pore volume is 0.1323 cc/g and BJH method desorption pore diameter is 39.39 Å.

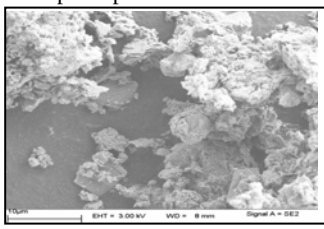

Element	Atom (%)
Oxygen	*79.22*
Silicon	*15.50*
Aluminum	*3.69*
Potassium	*0.81*
Calcium	*0.65*
Sodium	*0.14*

Figure 1. SEM image and EDX results of the natural domestic zeolite template.

Synthesis Procedure. The zeolite templates were impregnated with aqueous solution of Furfuryl Alcohol, FA, (ratio of 10 ml of FA per g of zeolite) at room temperature for 5 days. Filtered FA impregnated zeolite was polymerized and carbonized under 110 cm^3/min flowing argon (99.9% pure). In order to polymerize the impregnated zeolite was heated at 80°C for 24 h and 150°C for 8 h. The samples were carbonized at 700°C - 1000°C for 3 h. The FA impregnated zeolite samples were washed with concentrated HF, HCl, 5 N NaOH solutions and the combination of them.

For comparison, a blank experiment was done on FA mixed with oxalic acid (5 mg/ml FA), as the catalyst. In addition, a silica sol was prepared by stirring a mixture of TEOS, ethyl alcohol, water and zeolite in a mole ratio of 1;4;2;0.1 at 80°C for 3 h. after the mixture was cooled, FA was added to silica sol with a mole ratio of FA/TEOS was 0.5. The mixtures were carbonized at 700°C under the same conditions to that of the FA impregnated templates.

Characterization Methods. Surface areas of carbons were determined by a Quantachrome NOVA 2200 Series volumetric gas adsorption instrument by using BET equation in the relative pressure range of 0.05 to 0.30, over five adsorption points. X-ray diffractograms of carbons were measured with a Bruker axs advance powder diffractometer fitted with a Siemens X-ray gun, using CuK_α radiation and equipped with Bruker axs Diffrac PLUS software. The sample was rotated (10 rpm) and swept from 2q = 10º through to 90º. The X-ray generator was set to 40kV at 40 mA. Samples were probed further by ^{13}C CPMAS, ^{29}Si CPMAS, ^{19}F MAS and ^{27}Al MAS NMR using an Inova 500MHz NMR Varian system.^{13}C CPMAS, ^{29}Si CPMAS, ^{27}Al MAS NMR and ^{19}F MAS spectra were acquired at 125 MHz, 100 MHz, 130 MHz and 8-15 kHz fields respectively, using Si_3N_4 rotors set to 6 Hz. In the ^{19}F MAS spectra, spinning at different speeds is necessary to ensure no spectral overlap of spinning sidebands with the signals. Pulses were separated by a 1s delay in the case of carbon, 2s delay in the case of silicon and 0.25s delay in the case of aluminium. Leo Supra 35VP Field emission scanning electron microscope, Leo 32 and EDX software was used for images and analysis.

Results and Discussion

The percentage of elements of framed areas of samples, estimated by EDX, was given in **Table 1**. The samples which carbonized at 700°C and washed with HCl, NaOH and HF-NaOH, have maximum carbon contents 69%., 89% and 82% respectively. According to SEM images and EDX results in **Figure 2-5,** after demineralization step, the residue of demineralization solution was remained on the samples. In the case of HCl and NaOH washed samples, silicon from the zeolite templates were still remained. The maximum carbon content of 91% was obtained with HF washed samples although they contain high percentage of fluorine in some parts of samples. According to SEM images, a flower- like pattern was observed that composed of carbon and fluorine shown in **Figure 5A**.

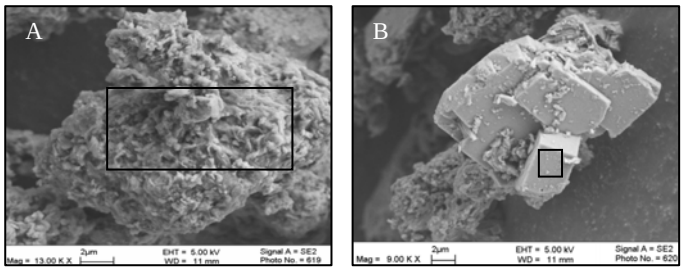

Figure 2A-2B. SEM images of HCl washed carbon (700°C).

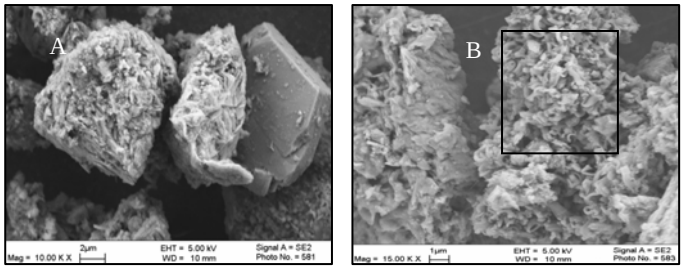

Figure 3A-3B. SEM images of NaOH washed carbon (700°C).

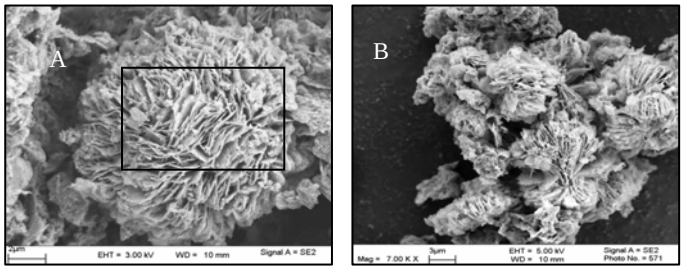

Figure 4A-4B. SEM images of HF washed carbon (700°C).

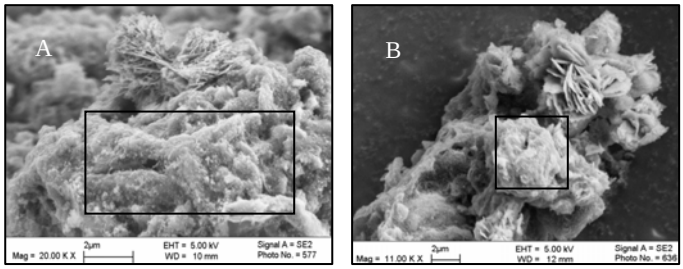

Figure 5A. SEM image of HF washed carbon (700°C).**5B.** SEM image of HF washed carbon (900°C).

Carbon contents of HF washed samples were 95%, 98% and 92% respectively at temperatures 800°C, 900°C (**Figure 5B**) and 1000°C. With increasing temperature the abundance of flower-like carbon fluoride compounds observed in SEM was decreased.

Table 1. Atomic Percentages Of Elements Analysed by EDX.

Element	HCl **Fig. 2A**	HCl **Fig. 2B**	NaOH **Fig. 3B**	HF- **Fig.4A**	HF- **Fig.5A**
Carbon	69.85	6.48	89.38	22.92	91.14
Oxygen	22.25	77.14	6.72	19.63	3.24
Silicon	5.94	13.05	1.58	-	-
Aluminium	1.96	3.33	0.34	3.38	0.14
Sodium	-	-	0.89	-	-
Magnesium	-	-	0.15	0.61	3.24
Fluorine	-	-	0.93	53.47	5.39

According to **Figure 6**, after elimination of spinning sidebands in ^{19}F MAS NMR, the peak positions were at 102, 140, 149, 165 and 182 ppm at the spinning speed 14 kHz. From the comparison with the MAS spectra's at different spinning rates, the overlap of a spinning sideband can be seen between 190 and 250 ppm. In ^{13}C NMR shown in **Figure 7**, sp, sp^2 and sp^3 hybridized carbons were observed in the 80, 120 and 30 ppm respectively. With increasing carbonization temperature, C-H bonds, so the peak intensities in ^{13}C NMR were decreased.

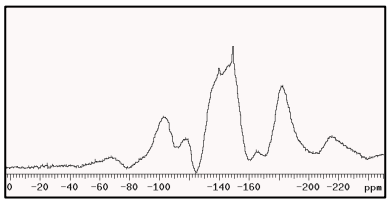

Figure 6. Solid state ^{19}F MAS spectrum of carbon at 14 kHz spinning rate that carbonized at 700°C and washed with HF.

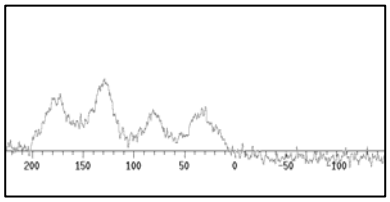

Figure 7. Solid state ^{13}C MAS spectrum of carbon at 125 MHz spinning rate that carbonized at 700°C and washed with HF.

After removing the silica template by washing with different demineralization solutions, carbon structures were examined in the XRD. Broad diffraction features were observed at 25 ° and 41° 2θ which was represented of (002) and (10) reflections of graphitized carbon, corresponding to the stacking of carbon sheets, that found in turbostratic structure of carbon. The d_{002} values is traditionally used to estimate a graphitisation degree of the carbon and, growing disorder in the materials is reflected in increased values of d_{002}. d_{002} value of carbon, carbonized at 700°C and washed with HF, was *3.59 Å* for the templated carbon which carbonized at 700°C, is larger than that of ideal graphite (d_{002} = *3.35 Å*), indicating that the carbon was formed with some degree of disorder[12].

References

(1) Ryong Ryoo; Sang Hoon Joo; Michal Kruk; Jaroniec, M. *Advance Materials,* **2001**, *13*, 677-681.
(2) Shoushan Fan; Micheal G. Chapline; Nathan R. Franklin; Thomas W. Tombler; Alan M. Cassell; Dai, H. *Science* **1999**, *283*, 512-514.
(3) Subramoney, S. *Advanced Materials* **1998**, *10*, 1157-1171.
(4) Parthasarathy RV; Martin, C. *Nature* **1994**, *369*, 298-301.
(5) CR. Martin *Advanced Materials* **1991**, *3*, 457-459.
(6) Klein JD; Herrick RDI; Palmer D; Sailor MJ; Brumlik CJ; CR, M. *Chem. Mater* **1993**, *5*, 902-904.
(7) Brunauer S.; Emmett PH.; Teller E *Journal of American Chemical Society* **1938**, *60*, 309.
(8) J.H. Knox; B. Kaur; Millward, G. R. *Journal of Chromatography* **1986**, *352*, 3.
(9) Takashi Kyotani; Takayuki Nagai; Sanjuro Inoue; Tomita, A. *Chem. Mater* **1997**, *9*, 609-615.
(10) Stacky A. Johnson; Elaine S. Brigham; Patricia J. Ollivier; Mallouk, T. E. *Chem. Mater* **1997**, *9*, 2448-2458.
(11) Barrett, E. P.; Joyner, L. G.; Halenda, P. H. *Journal of American Chemical Society* **1951**, *73*, 373-380.
(12) P.M. Barata-Rodrigues; T.J. Mays; Moggridge, G. D. *Carbon* **2003**, *41*, 2231-2246.

Plane of Zero Concentration in a Catalyst Slab with a Reacting Interface

Dr. Kal Renganathan Sharma PE

Formerly Principal, Sakthi Engineering College
Anna University Affilaited, (opp. MGR Gardens), Rampuram
Chennai Tamil Nadu, India
Email: jyoti_kalpika@yahoo.com

Abstract

The Cattaneo-Vernotte non-Fick diffusion and relaxation hyperbolic damped wave equation was solved for by transformation to the wave coordinates. The resulting equation was transformed using Laplace transform and the solution of composite Bessel function of the fist kind and zeroth order was found. An exponential decay in time for the concentration at the boundary of a semi-infinite medium was considered. The solution is damped oscillatory;

$u = \exp(-\tau/2)\, J_0 (½ \text{ sqrt}(X\tau - X^2))$

The plane of zero concentration occurs when $2.49 = X\tau - X^2$. This is much before the wave front.

Introduction

Morse & Feshbach (1) hypothesized and Cattaneo (2) and Vernotte (3) argued for a more physically reasonable wave speed equation to do better than the instantaneous propagation of thermal signals. Their expression for heat conduction as equation which when combined with the energy balance results in hyperbolic damped wave partial differential equation. By analogy the law for mass diffusion and relaxation may be generalized to a modified Fick's law to;

$$J = -D\partial C/\partial x - \tau_r\, \partial J/\partial t \qquad (1)$$

Only few studies have been reported to evaluate the feasibility of this equation to a variety of transient processes such as fixed bed adsorption, chromatography, fluidized bed to surface heat transfer, simultaneous fast reaction and diffusion, nuclear runaway fission reactions, reversible polymerization reactions, CPU overheating, chemisorption and hydrogen storage, membrane separations, biotransport etc. Reviews have been provided by Osizik and Tzou (4), Joseph and Preziosi (5,6). Experimental evidence for hyperbolic wave propagative and relaxation heat equation was provided by Peshkov who measured a velocity of heat of 19 m/s in liquid helium at 1.4 K (7). Churchill and Brown (8) measured a second sound along with Chester (9). Mitra, Kumar, Vedavarz and Moellami (10) report relaxation time of the order of 20-30 seconds. Combined with the mass balance equation (6) was solved for the semi-infinite case by the method of Laplace transforms by Bausemeister and Hamill (11, 12) for the heat transfer at CWT. Their expression needs further integration prior to use. Taitel (13) had considered the problem in finite slab, in the framework of hyperbolic heat conduction. He obtained the transient temperature and pointed out that the absolute value of the temperature change may exceed the difference with the wall temperature. This was later analyzed by Barletta and Zanchini (14) using an entropic balance and the determination of conditions were the Clausius inequality is violated. Sharma (15) used the FINAL condition at steady state as the fourth condition to give a bounded solution in obeyance of Clausius inequality. The wave speed C was shown by Chester (9) as $\text{sqrt}(\alpha/\tau_r)$ and by analogy for mass diffusion and relaxation as $\text{sqrt}(D/\tau_r)$. In this study an attempt is made to obtain an exact solution for the semi-infinite body problem subject to an exponential decay in time at the boundary using the method of transformation to the wave coordinates after removal of the damping term.

Theory

Consider a semi-infinite slab with an initial concentration at C_0. It is assumed that at the interface of one of the faces of the slab a first order simple reaction is considered. An example is the combustion of volatiles evolved on coal gasification and reacting at the interface. The initial condition is given as follows

$$t = 0,\ Vx,\ C = C_0 \qquad (2)$$

Boundary Conditions in Space

$$t > 0,\ x = 0,\ C = C_0 + (C_s - C_0) \exp(-t/2\tau_r) \qquad (3)$$

$$t > 0,\ x = \infty,\ C = C_0 \qquad (4)$$

The fourth and final condition in time,

$$t = \infty,\ Vx,\ C = C_0 \qquad (5)$$

The governing equation can be obtained by a 1 dimensional mass balance (in – out + reaction = accumulation). This is achieved by by eliminating J_x between equations (1) and the equation from mass balance ($-\partial J/\partial x = \partial C/\partial t$). This is achieved by differentiating equation (1) with respect to x and the mass balance equation with respect to t and eliminating the second cross derivative of J with respect to r and time. Thus,

$$\tau_r\, \partial^2 C/\partial t^2 + \partial C/\partial t = D\, \partial^2 C/\partial x^2 \qquad (6)$$

Obtaining the dimensionless variables;

$$u = (C - C_0)/(C_s - C_0) \qquad (7)$$

$$\tau = t/\tau_r \qquad (8)$$

$$X = x/\text{sqrt}(D\tau_r) \qquad (9)$$

The governing equation in the dimensionless form is then;

$$\partial u/\partial\tau + \partial^2 u/\partial\tau^2 = \partial^2 u/\partial X^2 \qquad (10)$$

The solution is obtained by the method of transformation to relativistic variables. Initially the damping term is eliminated using

$$u = W \exp(-n\tau) \qquad (11)$$

Substitution, Equation (10) then becomes

$$W_{xx} = W(-n + n^2) + W_\tau (1 - 2n) + W_{\tau\tau} \qquad (12)$$

At $n = ½$

$$W_{xx} = -W/4 + W_{\tau\tau} \qquad (13)$$

Equation (13) can be solved by the following transformations to the wave coordinates or canonical form; Let the transformation be as follows;

$$\eta = \tau + X \qquad (14)$$

$$\xi = \tau - X$$

Then equation (13) becomes;

$$\partial^2 W/\partial\tau^2 = \partial^2 W/\partial\eta^2 + \partial^2 W/\partial\xi^2 + 2\partial^2 W/\partial\xi\partial\eta \quad (15)$$

$$\partial^2 W/\partial X^2 = \partial^2 W/\partial\eta^2 + \partial^2 W/\partial\xi^2 - 2\partial^2 W/\partial\xi\partial\eta \quad (16)$$

$$4\,\partial^2 W/\partial\xi\partial\eta = W/4 \quad (17)$$

At this stage Laplace transforms is obtained in the ξ domain;

$$d\underline{W}/d\eta = \underline{W}/16/s \text{ or the solution is } \underline{W} = C' \exp \eta/16s \quad (18)$$

At, $\xi = 0$, $\tau = X$. This is at the wave front. The time taken at a point x in the medium to see the disturbance at the boundary traveling with a speed of sqrt(D/ τ_r). Only for times greater than this the problem exists. For times equal to and less than this time, the initial concentration remain and thus W = u = 0. Using the boundary condition given by equation (3) $W = \exp(-\tau/2)\exp(\tau/2) = 1$ at $\eta = \tau$.

$$1/s = C' \exp(\tau/16s) \text{ or } C' = 1/s \exp(-(\tau/16s) \quad (19)$$

$$\text{Thus, } \underline{W} = 1/s \exp(\eta - \tau)/16s = 1/s \exp(X)/16s \quad (20)$$

The inversion of equation (20) is within the tables available (16). So,

$$u = \exp(-\tau/2)\, J_0 (\tfrac{1}{2} \text{ sqrt}(X\tau - X^2)) \quad (21)$$

It can be seen that at infinite time the expression becomes zero as specified. The expression is valid only for times greater than the penetration time $t > x/\text{sqrt}(D/\tau_r)$. For X = 0, the imposed boundary condition $u = \exp(-\tau/2)$. The Bessel composite function of the first kind and zeroth order has many zeros and can be seen to be damped oscillatory. In order to amplify the wavy nature of the solution the exponential decay boundary condition was considered in this study.

The plane of zero concentration is when,

$$X\tau - X^2 = 2.49 \quad (22)$$

$$\text{Thus } X = (\tau \pm \text{sqrt}(\tau^2 - 9.96))/2$$

Thus for example for $\tau = 10$, X = 7.24 is a valid root of the quadratic equation and indicates the plane of zero concentration. This is before the wave front at X = 10.

References

1. P. M. Morse, H. Feshbach, 1953, Methods of Theoretical Physics, 1, McGraw Hill, New York, NY, USA.
2. C. Cattaneo, C., 1958, Comptes Rendus, 247, 431.
3. P. Vernotte, 1958, Les paradoxes de la theorie continue de l'equation de la chaleur, C. R. Hebd. Seanc. Acad. Sci. Paris, 246, 22, 3154.
4. M. N. Ozisik, D. Y. Tzou, 1994, ASME Journal of Heat Transfer, 116, 526-535.
5. D. D. Joseph, L. Preziosi, 1989, Reviews of Modern Physics, 61, 41-73.
6. D. D. Joseph, L. Preziosi, 1990, Reviews of Modern Physics, 62, 375 – 391.
7. V. Peshkov, 1944, Journal of Physics, USSR, 8, 381.
8. Brown, S. W. Churchill, 1989, AIChE Annual Meeting, San Francisco, CA, USA.
9. M. Chester, 1963, Physical Review, 131, 5, 2013-2015.
10. K. Mitra, S. Kumar, A. Vedavarz, A, M. K. Moallemi, Journal Of Heat Transfer-Transactions Of The ASME, 1995, l 117, 1, 6.
11. K. J. Baumeister, T. D. Hamill, 1969, 91, ASME Journal of Heat Transfer, 543 –548.
12. K. J. Baumeister, T. D. Hamill, 1971, 93, ASME Journal of Heat Transfer, 126 –128.
13. Y. Taitel, 1972, International Journal of of Heat and Mass Transfer, 15, 369 – 371.
14. A. Barletta, E. Zanchini, 1997, International Journal of Heat and Mass Transfer, 40, 5, 1007 -1016.
15. K. R. Sharma, 2003, Critical Radii of Zirconium Nuclear Fuel Rod Neither Greater than the Shape Limit Nor Less than Cycling Limit, AIChE Spring National Meeting, Presentation Record, New Orleans, LA, USA.
16. H. S. Mickley, T. S. Sherwood, C. E. Reed, 1975, Applied Mathematics in Chemical Engineering, Tata McGraw Hill, New Delhi, India.

Synthetic Fuels from Synthesis Gas Activities in Japan

Kaoru FUJIMOTO

Faculty of Environmental Engineering
The University of Kitakyushu
Hibikino 1-1, Wakamatsu-ku, Kitakyushu,
Fukuoka 808-0135, Japan

Introduction

Production of liquid fuels from raw materials other than petroleum is exclusively important for Japan, which consumes huge amount of petroleum, coal, and natural gas, while their domestic production is negligibly small. The production of sulfur free liquid fuel from natural gas or coal from outside of Japan and its transportation to Japan is one of effective method of importing petroleum substitute and clean fuels.

Synthetic fuel is not limited to liquid hydrocarbons. Dimethyl ether (DME), fuel methanol, and liquid petroleum gas (LPG) are also promising synthetic fuels in Japan. Among many methods of synthetic fuel production (Fig. 1), the route which passes through synthesis gas is most promising and well studied.

Japan has long history for developing sciences and technologies of synthetic fuel production and some of them are now on the way of commercialization.

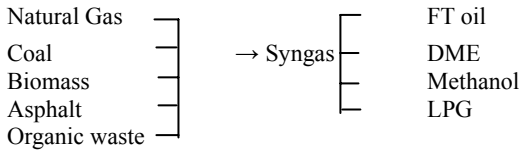

Figure 1. Synthetic Fuel Production Scheme

Dimethyl Ether (DME)

The direct synthesis of DME from synthesis gas has bean published by the present authors in 1982, where the catalyst was composed of the methanol synthesis catalyst and methanol dehydration catalyst[1,2]. The essential of this study is that the quick conversion of methanol, whose unfavorable synthesis equilibrium from synthesis gas can be overcome, giving a much higher one-pass yield than that of methanol synthesis. This technique can be applied

$$CO + 2H_2 \rightleftarrows CH_3OH$$
$$2CH_3OH \rightleftarrows CH_3OCH_3 + H_2O$$
$$CO + H_2O \longrightarrow CO_2 + H_2$$

to the effective syngas to gasoline (STG) process. The DME synthesis technology was converted to the liquid slurry process which utilizes the modified catalyst. The slurry process has run on the path for commercialization which pass through small bench plant (50 kg/d), pilot plant (5t/d), and demonstration plant (100 t/d, running since 2003) promoted by JFE group[3].

Indirect process, which passes through the methanol synthesis, has been also developed by Mitsubishi Gas Chemical and Tokyo Engineering.

DME utilization is now on the road in many directions.

Fischer-Tropsch Synthesis (FTS)

The basic research of FTS after so-called "oil crisis" has started in1975, which clarified the behaviors of adsorbed CO on various supported noble metals by TPR and IR method, concluding that the active species for CO hydrogenation is formed by the dissociation of carbon-oxygen bonding on the metal surface[4]. Since then numerous studies have been made by many groups mainly on cobalt and ruthenium catalysts from the stand point of developing catalyst with higher activity and a higher carbon chain growth. The present authors have developed the FTS process under super-critical (SC) conditions, which make it possible to extract heavy hydrocarbons from the catalyst surface and quick transfer of the product[5]. The FTS in the SCphase results in the extraordinary high concentration of olefins in the product and high yield of wax[6,7].

The kinetic and catalytic analysis of slurry phase FTS with supported cobalt catalyst clarified the effect of pore structure and additives on the rate and the product selectivity[8]. Also, it was proved that the small amount of added noble metal promoted the degree of cobalt under reaction conditions to promote the catalytic reaction[9]. This analysis made it possible the development of high performance of cobalt catalyst (1 kg-oil/kg-cat·h and $\alpha = 0.9$) proven in the pilot plant operation.

Iso-paraffin Synthesis

Conventional FTS gives straight chain aliphatic hydrocarbons as the main product. Linear olefins can be utilized as chemicals while liner paraffins with suitable boiling range is excellent diesel fuel. However, the straight chain hydrocarbons are unsuitable for Otto-cycle engine because of their low octane number. The present authors has been developing reaction systems which makes iso-paraffin rich hydrocarbons whose catalyst is composed of cobalt-base FTS catalyst and modified zeolite in either one stage or two stages the products are mostly distributed over C_3-C_6 hydrocarbons which are rich in iso-paraffins[10].

Methanol Synthesis

Methanol synthesis with Cu-Zn catalyst is the well established process and is thought to have little room to be developed. It has been tried to develop technologies by utilizing the liquid phase carbonylation of alcohol with methoxide catalysts to formic acid ester, and its hydrocracking to methanol and alcohol. However,

$$ROH + CO \rightarrow ROCOH$$
$$ROCOH + 2H_2 \rightarrow ROH + CH_3OH$$

This process (especially the carbonylation step) is strongly poisoned by either water or CO_2, which make it difficult to commercialize. The present authors have developed two types of low temperature liquid phase methanol synthesis. One is the utilization of carbonates or formates of alkali for the carbonylation step and the utilization of special hydrogenation catalyst[11]. Another system is the utilization of new concept of methanol formation[12,13].

$$CO_2 + H_2 + ROH \rightarrow ROCOH + H_2O$$
$$ROCOH + H_2 \rightarrow ROH + CH_3OH$$
$$CO + H_2O \rightarrow CO_2 + H_2$$

Both systems are operated at around 150-160 □ under pressurized conditions, giving 60-70% one-pass yield of methanol from synthesis gas even in the presence of H_2O or CO_2.

Liquid Petroleum Gas (LPG)

LPG is one of the most important home fuel and transportation fuel in Asian countries. LPG is the by product of crude oil production or natural gas production and the mixture of C_3 and C_4 paraffins. Selective production of LPG from synthesis gas by FTS catalyst is difficult because of the limitation of ASF distribution and the formation of large amount of CH_4. The present authors have shown that the synthesis gas conversion on the hybrid catalyst composed of methanol synthesis catalyst and zeolite gives the mixture of hydrocarbon composed of C_2 □ C_5 paraffins with high selectivity and with very low CH_4 selectivity[14,15]. The high

LPG selectivity is attributed to the quick carbon-carbon bond formation from methanol (or DME) on zeolite to olefins and their quick hydrogenation to paraffins.

The combination of the heat tolerant methanol synthesis catalyst and suitable zeolite shows excellent catalyst stability and product selectivity. This technology is going to start its industrial application.

Conclusion

Synthetic fuel production technologies including FTS reaction, which can produce sulfur-free fuel, are now becoming the stage of industrial development depending on the local conditions and technology level.

References

1. K. Fujimoto, K. Asamai, T. Shikada, H. Tominaga, Chem. Lett., **1984**, P2051
2. Fujimoto, K., Asamai, K., Saima, H., Shikada, T., and Tominaka, H., Ind & Eng. Chem., Prod. Res. Dev. **1986**, **25**, P262.
3. Y. Adachi, M. Komoto, I. Wantabe, Y. Ohno, K, Fujimoto, Fuel **2000 79**, (4), P229-234.
4. Fujimoto, K., Kameyama, I. Abe, T. Kunugi, J. Japan Petrol. Inst., **1981**, **24**, P233.
5. Yokota, K., and Fujimoto, K., Fuel, **1989**, **68**, P225.
6. K. Yokota and K. Fujimto, Ind and Eng. Chem. Res.., **1991**, **45**, P95.
7. K. Fujimoto, L. Fan and K. yoshii, Topics in Catalysis, **1995**, **2**, P259-266.
8. L. Fan, K. Yokota, and K. Fujimoto Topics in Catalysis, **1995**, **2**, P267-283.
9. S. Sun, K. Fujimoto, Y. Yoneyama, N. Tsubaki , Fuel, **2002**, **81**, P1583-1591.
10. Xiaohong Li, Kenji Asami, Mengfei Luo, Keisuke Michiki, NOritatsu Tshbaki, and Kaoru Fujimoto, Catalysis Today, **2003**, **84**, P59-65.
11. Yoshitada S., Fan, Li., Kaoru F., Sekiyu Gakkaishi **1998**, **41**, (5), P354-375 Jianqing Zeng, Kaoru Fujimoto, and Noritatsu Tsubaki, Energy & Fuels, **2002**, **16**, P83-86.
12. Jian-Qing Zeng, Noritatsu Tsubaki, Kaoru Fujimoto, Fuel, **2002**, **81**, P125-127
14. Saima, H., Fujimoto, K., and Tominaga, H., J. Catalysis, **1985**, **94**, P16.
15. Fujimoto, K., Saima, H., and Tominaga, H., I & EC Research, **1998**, **27**, P920.

CATALYSTS FOR HYDROGEN PRODUCTION FROM METHANE

Huifang Shao, Edwin L. Kugler and Dady B. Dadyburjor

Department of Chemical Engineering
West Virginia University, Morgantown WV 26506-6102

Abstract

Bimetallic carbides such as Co_6W_6C have been synthesized and used for the reforming of methane to synthesis gas. These catalysts are active, selective and stable when they have been pretreated above 750°C. Reactivity experiments, coupled with characterization by XRD, show the effect of preparation procedure.

Introduction

Three processes exist for the production of hydrogen from methane: steam reforming, partial oxidation and dry reforming. The three main reactions are indicated below.

$CH_4 + H_2O \rightarrow CO + 3\ H_2$ (Steam Reforming) [1]

$CH_4 + \frac{1}{2}\ O_2 \rightarrow CO + 2\ H_2$ (Partial Oxidation) [2]

$CH_4 + CO_2 \rightarrow 2\ CO + 2\ H_2$ (Dry Reforming) [3]

Side reactions of importance include:

$H_2O + CO \leftrightarrow H_2 + CO_2$ (Water-Gas Shift) [4]

Dry reforming produces a product (synthesis gas, or syngas) of a lower H_2/CO ratio than the other two processes. However, there are advantages to this process, including the use of the greenhouse gas CO_2 as a reactant.

Traditionally, a supported nickel catalyst has been used for dry reforming (1). However, this material deactivates rapidly, due to coke formation. Addition of alkali or alkaline-earth metals or passivation of the catalyst with, e.g., sulfur has been shown (2,3) to be effective. Noble-metal catalysts, e.g., Pt, have also been used. They are active and stable, but may be prohibitively expensive. Metal carbides are reasonably active and reasonably priced. (4).

Our work has concentrated on the use of bimetallic carbides as a way to modify the behavior if the carbides. Early work (5,6) used commercial material from Nanodyne. We have now started preparing the material in-house. In the current work, we report on a series of preparation and pretreatment techniques and show how they influence the reactivity behavior of these materials as well as their bulk characteristics.

Experimental

Catalyst Preparation. The procedure is similar to that of Polizzoti *et al.* (7,8) In brief, precursor solutions of ammonium triethylenediamine tungstate and cobalt chloride are mixed at room temperature. The tungstate solution is prepared by dissolving 14.5 g tungstic acid in 400 ml of a 1:1 aqueous ammonium chloride solution and 300ml of ethylenediamine, followed by heating and stirring until the solution is clear. The cobalt solution is prepared by dissolving 13.8 g of the hexahydrate in 50 ml of distilled water. After mixing the two precursor solutions, the volume is reduced by 50% by evaporation.. Pure cobalt triethylenediamine tungstate $(Co(en)_3WO_4)$ is obtained by filtering, washing with acetone, and drying the filter cake in the hood for 24 h.

The bimetallic carbide is obtained by a temperature-programmed reaction (TPRx) of this material, using a mixture of CO and CO_2 of specified ratio. The process is carried out at 1 atm in a fixed-bed reactor. In the TPRx procedure, the temperature is first ramped up to 650°C during the flow of 130 sccm of an equimolar mixture of Ar and H_2, and the temperature held for 3 h. Then the mixture is flushed with Ar at 190 sccm for 0.5 h while the temperature is increased to 850°C. Last, the CO_2-CO mixture flows through for 24 h with a total flow rate of 60(1+x) sccm, where x is the ratio CO_2 / CO. The reactor is then purged by flowing Ar at 190 sccm, and cooled down to room temperature.

Catalyst Characterization. The material was characterized by N_2 BET and by x-ray diffraction. XRD measurements were carried out both before and after reaction.

Reactor Setup. Reactions were performed in a stainless-steel reactor (SS 304L) with an outer diameter of 0.5 in and a length of 25 in, which was placed in an 18-in single zone furnace from Applied Test Systems. A stainless-steel sheathed thermocouple was inserted into the center of the catalyst bed to monitor and control the reaction range. The products were sampled immediately downstream at preset intervals using a Valco six-port gas-sampling valve. To prevent the outlet from heating up the valve beyond its operating range, a cooling system was added between the reactor outlet and the sampling valve, using circulating silicone oil at 90°C. The composition of the outlet gas was analyzed using an on-line Hewlett-Packard 5890 gas chromatograph (GC) equipped with a thermal-conductivity detector (TCD), which provided quantitative analysis for H_2, CO, CH_4, CO_2, and H_2O.

Typically 0.3 g of the catalyst sample was used for each test. The catalyst was pretreated by reducing with flowing hydrogen at 60 sccm for 1 h, followed by another hour of flushing with argon at 400°C. The reaction started once the pretreatment finished. The reactor was operated at 3.4 atm and 850°C with equal amounts of methane and carbon dioxide in the feed stream. The gas-hourly space velocity was kept constant at 9000 scc/hr/g cat. The conversions of the feed gases, the yields of the products, and the carbon balance, given by

Carbon Balance = (carbon out – carbon in) / (carbon in) [5]

could then be calculated..

Results and Discussion

Characterization and reactivity data are discussed below for values of x equal to 0.1, 0.2, 0.5 and 0.75.

Catalyst Characterization. BET results indicate that the surface area of the fresh catalyst does not depend on the value of x. Typical surface area values were found to be 2-3 m^2/g. This is approximately equal to the values for the Nanodyne materials, approximately 5 m^2/g.

XRD patterns are shown in Figures 1-4 for the different catalyst materials. The major components present in the bulk are summarized in Table 1. Here Co_3W_3C represents an interstitial carbide with twice the amount of C present than in the bimetallic carbide Co_6W_6C.

Table 1. Bulk Components of Catalyst Materials as a Function of Pretreatment Conditions

x = CO_2 / CO	Bulk Components
0.1	Co_3W_3C, Co, WC
0.2	Co_3W_3C
0.5	Co_6W_6C
0.75	Co_6W_6C

.

Clearly the bulk components are dependent upon the ratio x (= CO_2 / CO), at least for values less than or equal to 0.5. Table 1 indicates that the relative amount of carbon present in the bulk compounds decreases, in general, as x increases, at least up to x = 0.5.This is consistent with the decreasing chemical activity of carbon, a_C, as the CO_2/CO ratio decreases.

More importantly, Table 1 indicates that the bulk compounds present for the material made with x = 0.1 are those found in the Nanodyne catalyst after it reached its steady-state catalytic performance (6). This would seem to imply that the catalytically active material could be made directly by using in-house techniques.

Catalyst Reactivity and Stability. The catalytic performance of the bimetallic carbides prepared and characterized as described above is shown in Figures 5-7. While the individual behaviors are different, note that all three catalysts are characterized by an unsteady-state period of approximately 20 h, after which the catalyst is stable for at least the next 80 h. Clearly, the catalyst is still undergoing a solid-state reaction to

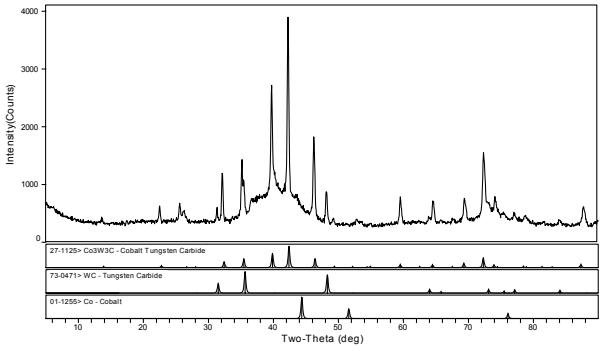

Figure 1. XRD spectrum from material made with x (= CO_2 / CO) = 0.1

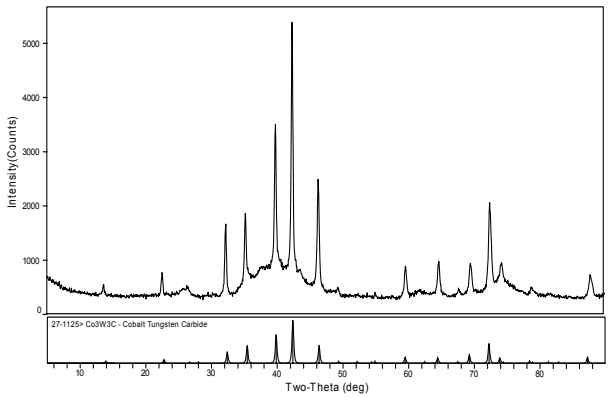

Figure 2. XRD spectrum from material made with x (= CO_2 / CO) = 0.2

.

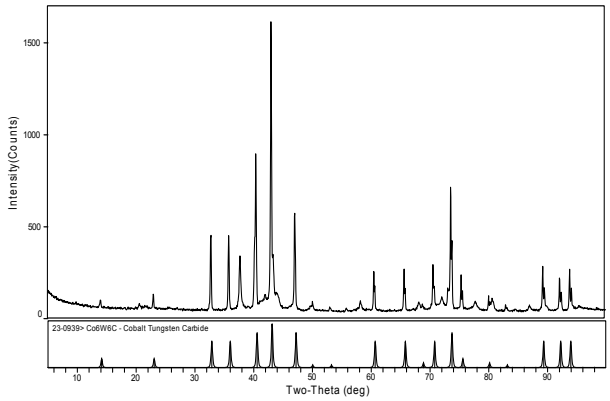

Figure 3. XRD spectrum from material made with x (= CO_2 / CO) = 0.5.

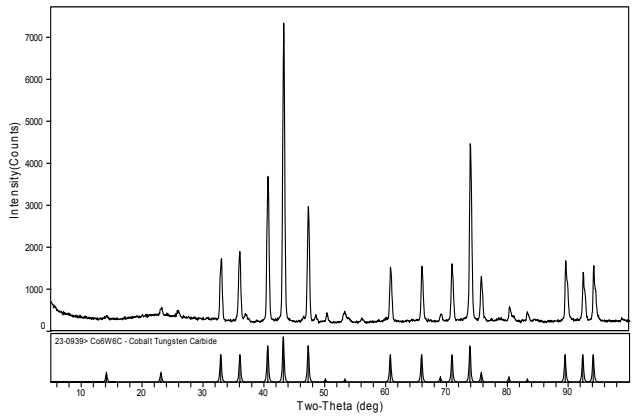

Figure 4. XRD spectrum from material made with x (= CO_2 / CO) = 0.75.

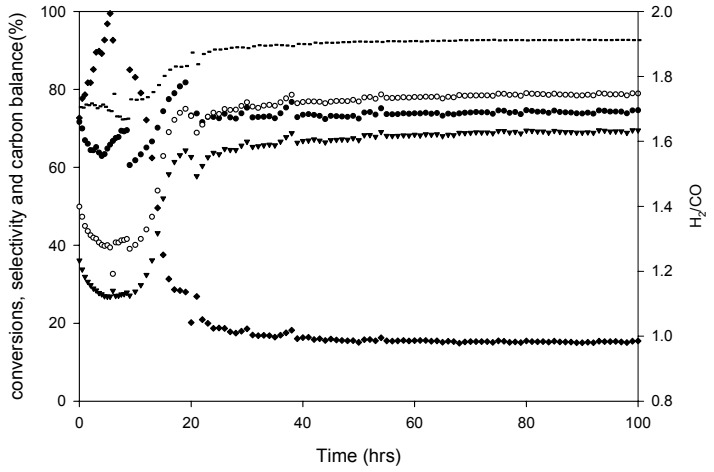

Figure 5. Catalytic performance of material made with x (= CO_2 / CO) = 0.1. Closed circles = CH_4 conversion, open circles = CO_2 conversion, triangles = CO yield, diamonds = H_2/CO, dashed lines = carbon balance.

a more-stable phase, which is also the more catalytically active phase. The unsteady-state period is characterized by H_2/CO ratios much higher than the expected (stoichiometric) value of 1 and a relatively low carbon balance of 70-80%. These observations are consistent with a laydown of carbon on the catalyst surface. Hence, in all cases, it would appear that carbon deposition leads to a more-stable, more-active phase on the catalyst surface.

From Table 1, the material prepared using x = 0.75 has the same bulk structure as the Nanodyne material. Hence it is worthwhile comparing the catalytic performance of these two materials. The Nanodyne material reaches its steady-state

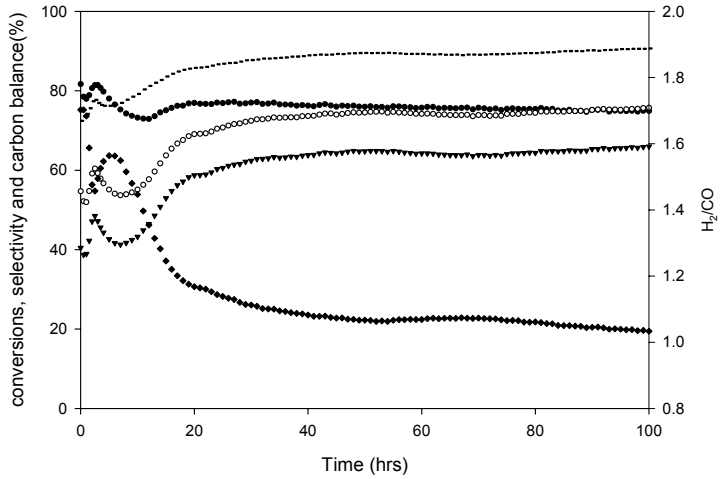

Figure 6. Catalytic performance of material made with x (= CO_2 / CO) = 0.2. Symbols have the same meaning as in Fig. 5.

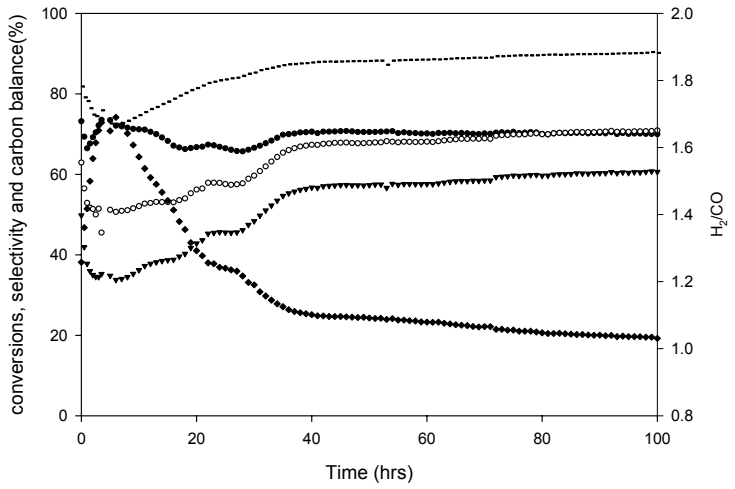

Figure 7. Catalytic performance of material made with x (= CO_2 / CO) = 0.75. Symbols have the same meaning as in Fig 5.

value in well under 20h (6), whereas the in-house material takes longer to approach steady state. The CH_4 conversion is greater than the CO_2 conversion in Figure 7, at least initially, whereas the reverse is observed (6) for the Nanodyne material, and at all times on stream. The ratio of H_2/CO is significantly greater than the stoichiometric value (1.0) for the in-house material, especially during the unsteady-state period. All these observations imply that the in-house material results in greater carbon deposition and more water-gas shift products. The in-house material is also further from its final, catalytically active state than is the Nanodyne material.

As mentioned earlier, Table 1 indicates that the material prepared using x = 0.1 has the same bulk constituents found in the Nanodyne material (or the material prepared with x = 0.75) after it had reached its final, active state. Hence, one would expect the catalytic performance of the former material to require little or no time on stream to reach steady-state behavior, and for this behavior to be comparable to the steady-state behavior of the x = 0.75 (or Nanodyne) material. However, Figure 5 shows that steady-state behavior still requires 20 h on stream to be achieved, even though this amount is less than the comparable period for Figure 7. Clearly, even the catalyst that contains WC and Co in the bulk phase at the start needs pretreatment. Further, the H_2/CO at unsteady state is much higher than the corresponding value in Figure 7. The CO_2 conversion at steady state is somewhat greater than the CH_4 conversion, implying less water-gas shift than for the x = 0.75 (or Nanodyne) material.

Finally, we consider the catalytic performance of the x = 0.2 material (Figure 6). The time to reach steady state in Figure 6 lies in between those in Figures 5 and 7. The catalytic performance in Figure 6 is more closely related to that in Figure 7 than that in Figure 5. This would appear to be counter-intuitive, given the values of x used in these three procedures and the bulk materials obtained from XRD. Again,

the nature of the catalytically active surface needs to be determined.

Figures 8 and 9 represent XRD patterns for materials after the reactions. For the x = 0.75 material (Figure 8), the bulk species after reaction are those obtained with the Nanodyne material, *viz.*, WC, Co and C. For the x = 0.1 material (Figure 9), the bulk materials observed after reaction, in addition to C, are similar to those observed before, *viz.*, Co_3W_3C, WC and Co, but in different relative amounts than before.

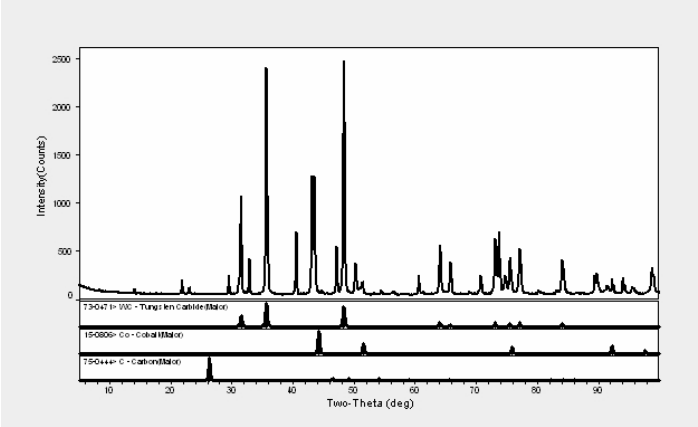

Figure 8. XRD after reaction for material prepared with x = 0.75.

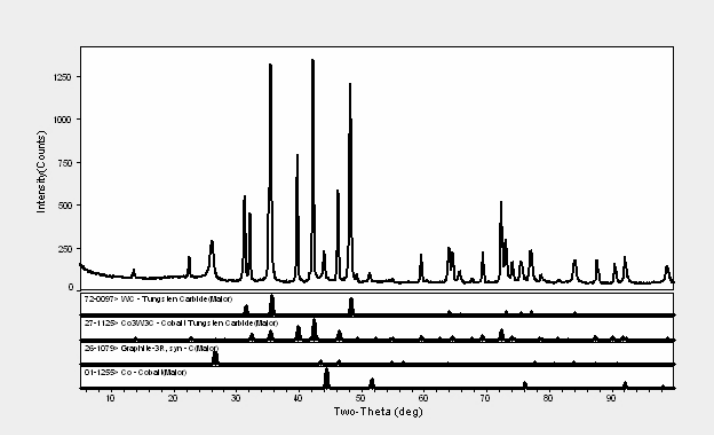

Figure 9. XRD after reaction for material prepared with x = 0.1

Conclusions

Bimetallic carbides such as Co_6W_6C have been synthesized and used for the reforming of methane to synthesis gas. These catalysts are active, selective and stable when they have been pretreated at 850°C. Reactivity experiments, coupled with characterization by XRD, relate the activity data to the formation of various chemical species in bulk. In all cases, there is an initial unsteady-state period characterized by carbon deposition and solid-state transformation of the material to a more catalytically active phase. However, it would appear that the connection between bulk structure and reactivity is ambiguous. Clearly, the surface nature of the catalyst needs to be obtained.

Acknowledgement. Financial support from the U.S. Department of Energy under Cooperative Agreement DE-AC22-99FT40540 with the Consortium for Fossil Fuel Science is gratefully acknowledged. The assistance of Professor M.S. Seehra, Department of Physics, in obtaining the XRD patterns is appreciated.

References

(1) Bradford, M. C. J.; Vannice, M. A. *Applied Catalysis A: General* **1996**, *142*, 73-96.
(2) Osaki, T.; Mori, T. *J. Catal.* **2001**, *20*, 89-97.
(3) Rostrup-Nielsen, J. R. *J. Catal.* **1984**, *85*, 31-43.
(4) Babilius, A. *Materials Science* 2003, *7*, 183-186.
(5) Iyer, M.V.; Norcio, L.P.; Kugler, E.L.; Dadyburjor, D.B. *Ind. Eng. Chem. Res* **2003**, *442(12)*, 2712-2721.
(6) Iyer M.V.; Norcio, L.P.; Punnoose, A.; Kugler, E.L.; Seehra, M.S.,; Dadyburjor, D.B. *Topics in Catalysis*, in press.
(7) Kugler, E.L.; McCandlish, L.E.; Jacobson, A.J.; Chianelli, R.R. *U.S. Patent 5,138,111*; **August 11, 1992**.
(8) Polizzoti, R.S.; McCandlish, L.E.; Kugler, E.L *U.S. Patent 5,338,330*; **August 16 1994**.

HYBRID CATALYSTS WITH MICROCRYSTALLINE ZEOLITE AND SILICA-ALUMINA FOR WAX HYDROCRACKING

Nobuo Aoki, Hiroyuki Seki, Masahiro Higashi, Toshio Waku, and Masakazu Ikeda

Central Technical Research Laboratory
Nippon Oil Corporation
8 Chidori-cho, Naka-ku,
Yokohama, 231-0815 JAPAN

Introduction

The demand for heavy residues such as asphalt is decreasing while that for clean fuels is increasing in order to reduce particulate matter and others in automobile exhaust. One possible solution to this situation is the development of asphalt-to-liquid (ATL) process. ATL process consists of three steps: gasification of asphalt, wax production by F-T synthesis, and production of clean fuels by wax hydrocracking. This paper focuses on the development of catalyst for wax hydrocracking.

There are two major requirements for wax hydrocracking catalysts, high activity and high selectivity of middle distillates (MD). As is well known, it is quite challenging to meet the both requirements. For instance, silica-alumina shows high MD selectivity,[1] but its activity is insufficient. On the contrary zeolites show high activity, but their MD selectivity is generally lower than silica-alumina since their high activity causes overcracking of MD.

We have clarified in our last report, however, that both requirements are satisfied at a fairly high level with the catalysts which contain microcrystalline USY zeolite (MC-USY).[2] The higher MD selectivity of MC-USY based catalysts is assumed to be achieved by shorter pore lengths of MC-USY which has a particle size of less than 0.5 μm, with less overcracking of .

In order to enhance the performance of MC-USY based catalysts further we are trying to hybridize this key material with various amorphous solid acids. This paper reports the performance of the hybrid catalyst with MC-USY and silica-alumina. The mechanism of collaboration of the two components is also discussed.

Experimental

Catalysts. MC-USY was prepared by crystallizing smaller seeds than usual, followed by steaming and acid treatment. Its SiO_2/Al_2O_3 ratio was adjusted to 30, according to the method in our previous report.[2] Commercially available amorphous silica-alumina (alumina 14 mass %) powders were used in combination with MC-USY. Extrudates with a composition of 3 mass% MC-USY, 57 mass% silica-alumina and the rest alumina binder were prepared using a usual method. On these extrudates a given amount of platinum was loaded with an aqueous solution of nitric acid (1N) containing hexachloroplatinum acid by the incipient wetness method. The Pt-loaded extrudates were calcined at 500 °C for 1 h.

Catalysts containing single acid component, MC-USY or silica-alumina, were also prepared.

Performance Tests. Tests were carried out with a flow reactor. The catalysts (100 ml) were first reduced at 340 °C for 1 h before the reaction started. Feed wax was treated under the condition below:

pressure: 3 MPa, H_2/oil: 3500 scf/b, LHSV: 2 h^{-1}.

The product oil was fractionated into naphtha (<145 °C), kerosene (145-260 °C), gas oil (260-360 °C), and wax (>360 °C). The term of middle distillates (MD) means the total of kerosene and gas oil.

Results and Discussion

The performance of the hybrid catalyst loaded with 0.8 mass % Pt is shown in **Figure 1** and **Figure 2** with those of catalysts containing single acid component

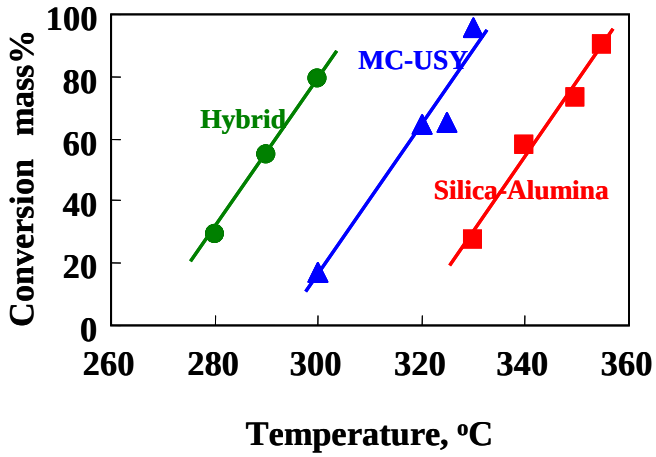

Figure 1. Cracking activity of tested catalysts. Pt: 0.8 mass %

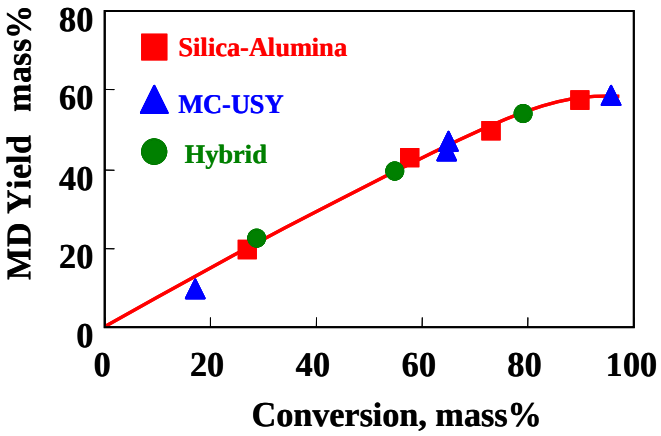

Figure 2. Middle distillates (MD) selectivity of tested catalysts. Pt: 0.8 mass %

Figure 1 shows that cracking activity increases in the order of silica-alumina, MC-USY, and Hybrid. This indicates the hybrid catalyst can hydrocrack wax at lower temperature range where the catalysts containing single acid component cannot.

It is clear from **Figure 2** that despite the high activity of the hybrid catalyst it maintains the same level of high MD selectivity as the catalyst containing only silica-alumina as acid component.

There has already been a widely accepted reaction mechanism for wax hydrocracking by USY zeolite based catalysts with Pt, as is shown in **Figure 3**. This mechanism consists of four steps below.

(1) olefin formation by dehydrogenation of wax on P
(2) isomerization on acid sites of USY zeolite
(3) cracking of the isomers on acid sites of USY zeolite
(4) stabilization of cracked products through hydrogenation on Pt

In this mechanism, step (2) is considered to be rate determining.[3] Silica-alumina in the hybrid catalyst is assumed to accelerate step (2) and consequently enhance the overall reaction rate.

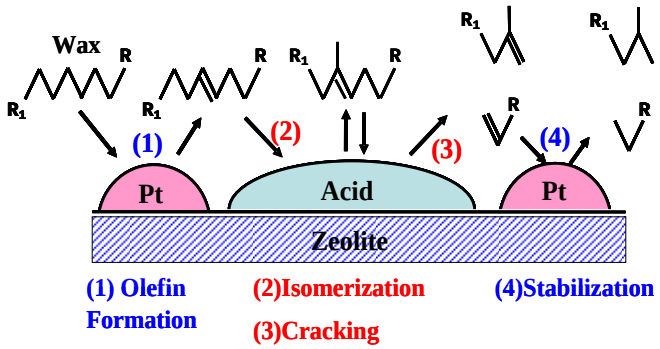

Figure 3. Reaction mechanism for wax hydrocracking by USY zeolite based catalysts with Pt.

The type of silica-alumina affects the performance of the hybrid catalyst. For instance, the high MD selectivity of the hybrid catalyst is not obtained when another silica-alumina is used which contains 5 mass % of alumina and has higher acid strength than silica-alumina of this report.

The ratio of silica-alumina to MC-USY can also affect the performance and we have started to optimize the ratio. The result will be reported in near future.

Because Pt plays an important role in wax hydrocracking, the effect of the amount of Pt on the catalytic performance was studied. The results are presented in **Figure 4** and **Figure 5**.

Figure 4 shows that the hybrid catalyst exhibits constant cracking activity even with Pt less than 0.8 mass %. This indicates that the rate determining step of this hybrid catalyst is still step (3) in **Figure 3**. However it can be seen from **Figure 5** that MD selectivity of the hybrid catalyst decreases gradually, depending on the amount of Pt, in the range less than 0.8 mass %. This tendency is not observed in the case of the catalysts containing single acid component except for the range less 0.2 mass %. This means that the stabilization ability in step (4) in **Figure 3** is insufficient in the hybrid catalyst with Pt less than mass 0.8 % and that the hybrid catalyst requires more Pt than the catalyst containing single acid component to gain the same level of MD selectivity.

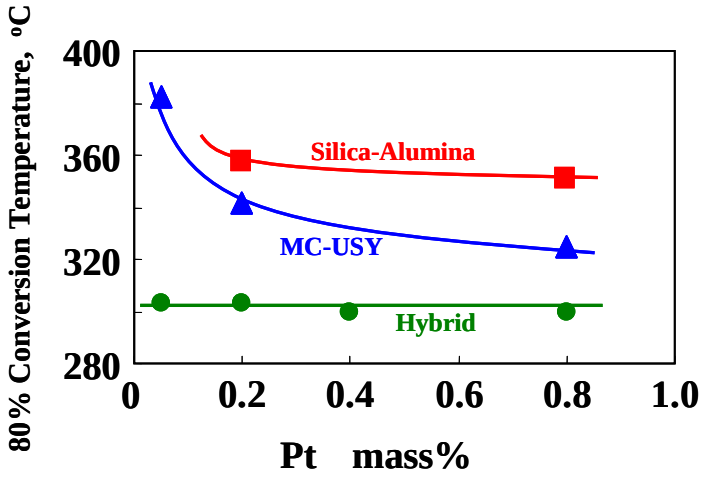

Figure 4. Effect of the amount of Pt on cracking activity.
Vertical axis shows the temperature at which 80% of conversion is gained and relates to cracking activity.

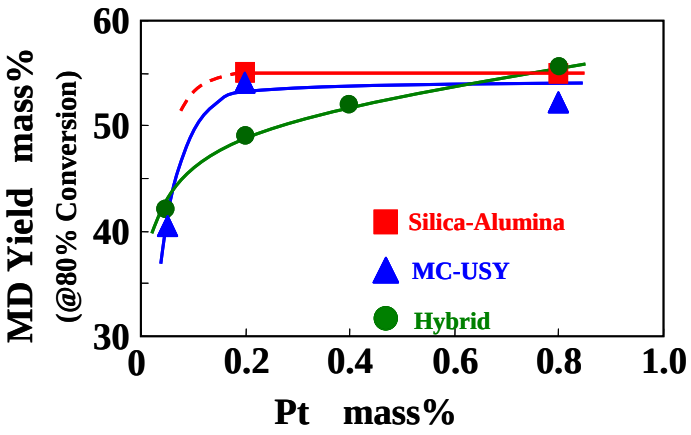

Figure 5. Effect of the amount of Pt on MD selectivity.

Table 1 presents the properties of the gas oil obtained with the hybrid catalyst (Pt 0.8 mass %) along with that of the catalyst containing only MC-USY. By hybridization more preferable gas oil with lower pour point is obtained.

Table 1. Properties of Gas Oil

	Density, @ 15° C	Cetane Index	Pour point °C
MC-USY	0.7876	94	-17.5
Hybrid	0.7876	94	-22.5

Conclusions

(a) The hybrid catalyst with both MC-USY and silica-alumina exhibits higher activity than that containing only MC-USY and has the same level of high selectivity as that containing only silica-alumina.

(b) Silica-alumina in the hybrid catalyst is assumed to accelerate the isomerization step that is considered to be rate determining in an accepted reaction mechanism.

(c) While cracking activity of the hybrid catalyst is independent of the amount of Pt, MD selectivity is sensitive to it

Acknowledgement. This work was done as a part of the Asphalt-to-Liquid (ATL) research project of the New Energy and Industrial Technology Development Organization (NEDO) of Japan with a subsidy from the Ministry of Economy, Trade and Industry

References

(1) Calemma, V.; Peratello, S.; Pavoni, S.; Clerici, G.; and Perego, C., *Stud. Sur. Sci. Catal.*, **2001**, *136*, 307.

(2) Seki, H.; Aoki, N.; and Ikeda, M. , Prepr. Pap. –*Am.Chem.Soc., Div. Pet. Chem.*, **2003**, *48* (3), 139.

(3) Weitkamp, J. and Ernst, S., *Catalysis. Today*, **1994**, ***19,*** 107.

A NEW LOW-TEMPERATURE METHANOL SYNTHESIS FROM LOW-GRADE SYNGAS

*Prasert Reubroycharoen [a], Yamagami Tetsuji [a], Yoshiharu Yoneyama [a], Tharapong Vitidsant [b], Noritatsu Tsubaki [a]**

[a]Dept. of Material System & Life Science, School of Engineering, Toyama University, Gofuku, Toyama, 930-8555, Japan

[b]Dept. of Chemical Technology, Faculty of Science, Chulalongkorn University, Bangkok, 10330, Thailand

* Tel/Fax: (81)-76-445-6846; E-mail: tsubaki@eng.toyama-u.ac.jp

Introduction

Methanol, which is an alternative fuel, is being produced by 30-40 million ton per year around the world from $CO/CO_2/H_2$. It is now commercially produced by ICI process under high temperature and high pressure (523-573 K, 50-100 bar), using Cu/ZnO catalyst developed by ICI Co.. However, the efficiency of methanol synthesis is severely limited by thermodynamics,[1,2] theoretic CO conversion is around 20% at 573 K and 50 bar.[3] Therefore, developing a low-temperature process for methanol synthesis will greatly reduce the production cost by utilizing the intrinsic thermodynamic advantage at low temperature.[4]

Brookhaven National Laboratory of USA (BNL) realized this synthesis at 373-403 K and 10-50 bar, using very strong base catalyst (mixture of NaH, alcohol and acetate) and pure syngas ($CO + H_2$). However, a remarkable drawback of this process is that trace amount of carbon dioxide and water in the feed gas ($CO + H_2$) or reaction system will deactivate the strongly basic catalyst soon,[5,6] which implies high cost from the complete purification of the syngas from the methane reformer or the gasification plant, as well as the re-activation process of the deactivated catalyst.

The present authors proposed a new method of low-temperature synthesis of methanol from CO/H_2 containing CO_2.[7, 8] It consists of the following fundamental steps:

$$CO + H_2O = CO_2 + H_2 \quad (1)$$
$$CO_2 + H_2 + ROH = HCOOR + H_2O \quad (2)$$
$$HCOOR + 2H_2 = CH_3OH + ROH \quad (3)$$
$$CO + 2H_2 = CH_3OH \quad (4)$$

In this study, the influence of chemical composition of Cu/ZnO catalyst was studied in a batch reactor. The effects of reaction condition on the synthesis of methanol from $CO/CO_2/H_2$ on Cu/ZnO catalyst were investigated. A flow-type semi-batch reactor was employed, where catalyst lifetime change could be observed.

Experimental

Catalyst Preparation. The catalyst was prepared by the conventional co-precipitation method of an aqueous solution containing copper, zinc nitrates and an aqueous solution of sodium carbonate at 338 K and pH of 8.3-8.5. The molar ratio of Cu/Zn was varied.

Low-temperature Methanol Synthesis. The reaction apparatus was a flow-type semi-batch autoclave reactor with an inner volume of 85 ml. The configuration of the reactor is shown in Figure 1. 3.0 g (Cu:Zn = 1:1 and 100-200 mesh) of passivated catalyst and 20 ml of alcohol (purity > 99.5 %) were used. The temperature of reactor exit and cold trap was controlled. After purging the system with feed gas at room temperature, increasing the pressure of reactor to 50 bar, the temperature was enhanced to 443 K in 20 min. The composition of feed gas was $CO/CO_2/H_2/Ar$ = 32.6/5.2/59.2/3.0, in which argon was employed as an internal standard. The effluent gas was introduced to TCD. The liquid products in the cold trap and those remaining in the reactor were collected together and then analyzed by FID with methanator after the reaction. All liquid products were confirmed on GC-MS (Shimadzu GCMS 1600).

The reaction of activity test of home-made Cu/ZnO catalyst with different Cu/Zn ratio was conducted in a closed batch reactor with the inner volume of 85ml.

Total carbon conv. = CO conv.×a/(a+b) + CO_2 conv.×b/(a+b)
(a, b were the contents of CO, CO_2 in the feed gas)

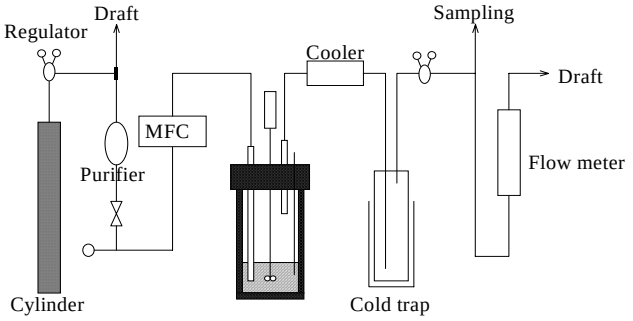

Figure 1. The semi-batch continuous apparatus for methanol synthesis reaction.

Results and Discussion

In Figure 2, the reaction activity and its relationship with the chemical composition of Cu/ZnO in a closed reactor were displayed. It is clear that too much Cu or Zn percentage was not favorable to the catalyst activity. Cu/ZnO with the molar ratio of 1 exhibited the best reaction activity. More interestingly, while the total conversion was lower, the selectivity of ethyl formate was high. With the enhanced conversion, the selectivity of methanol increased, indicating that methanol was the final product and formate was intermediate in this consecutive reaction series.

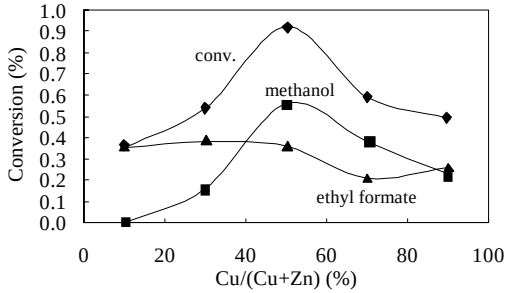

Figure 2. The reaction performances of Cu/ZnO catalysts with different Cu/(Cu + Zn) molar ratio in a batch reactor. Temperature = 443 K; initial pressure = 30 bar; reaction time = 2 h; Cu/ZnO = 0.20 g; ethanol 10 ml; stirring speed = 1260 rpm.

In Figure 3, the conversion and yield of methanol increased with increasing in time of reaction. Methanol yield gradually increased with the decreased ethyl formate yield, while the latter correspondingly decreased and became equilibrium at about 2 h, indicating that ethyl formate was an intermediate of methanol synthesis.

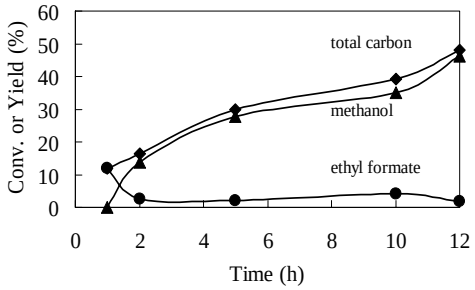

Figure 3. The effect of reaction time in batch reactor. Temperature = 443 K; initial pressure = 30 bar; Cu/ZnO = 1.00 g; ethanol = 20 ml; stirring speed = 1260 rpm.

In Figure 4, it is shown the time-on-stream and conversion on Cu/ZnO during 20 h. The conversions were very low at initial stage due to the dead volume of the reactor and trap filled by the feed gas. The total carbon conversion was about 47%. Furthermore, at the initial 10 h, the CO_2 conversion dropped to minimum –42% and then increased again to about 3%.

According to the time-on-stream of the conversions above, that CO was converted to CO_2, and then CO_2 converted to methanol through the designed routes, step (1) - (3). It should be noted that if no alcohol was used as solvent, for example, in the case where hexane was used instead as an inert solvent, no activity was observed.

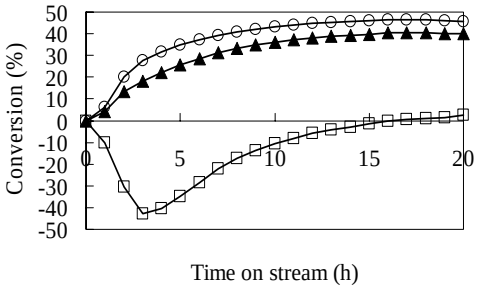

Figure 4. Variations of conversions with time on stream for the methanol synthesis from $CO/CO_2/H_2$. Temperature = 443 K; pressure = 50 bar; Cu/ZnO = 3.00 g; 2-butanol 20 ml; stirring speed = 1260 rpm; 20 ml/min; (○) CO%; (□) CO_2%; (□) total carbon%.

In Figure 5, the relationship between conversion and reaction pressure is shown. It was found that the total carbon conversion increased gradually with increasing reaction pressure.

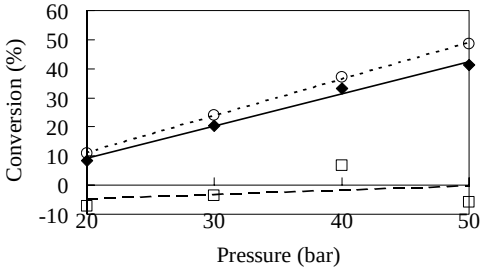

Figure 5. Variations of conversions with for the methanol synthesis from $CO/CO_2/H_2$. Temperature = 443 K; Cu/ZnO = 3.00 g; 2-butanol 20 ml; stirring speed = 2000 rpm; 20 ml/min; (○) CO%; (□) CO_2%; (□) total carbon%.

In Figure 6, it is shown the conversion and reaction temperature. It is interesting that the conversion continuously increased with increasing in temperature of reaction without changing in the methanol selectivity (>98%). In contrary with high temperature methanol synthesis, high reaction temperature lowers the methanol selectivity.

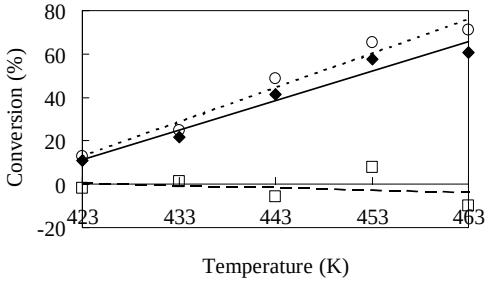

Figure 6. Variations of conversions with temperature for the methanol synthesis from $CO/CO_2/H_2$. Pressure = 50 bar; Cu/ZnO = 3.00 g; 2-butanol 20 ml; stirring speed = 2000 rpm; 20 ml/min; (○) CO%; (□) CO_2%; (□) total carbon%.

In Table 1, the results on catalyst weight showed the conversion can be improved by increasing the catalyst weight, in contrary to high-temperature gas phase reaction, the increased catalyst weight indeed improved the conversion due to relief of thermodynamic limitation.

Table 1 Methanol synthesis with various weight of catalyst

Cat. (g)	Conversion (%)			CH_3OH selectivity (%)
	CO	CO_2	Total C	
3.0	48.5	-5.8	41.4	98.5
6.0	63.8	-11.5	53.9	99.2

Temperature = 443K Pressure = 50 bar; 2-butanol 20 ml; stirring speed = 2000 rpm; 20 ml/min.

Conclusions

The low-temperature methanol synthesis from $CO/CO_2/H_2$ using 2-butanol as solvent has exhibited very high activity and selectivity for methanol formation at temperature as low as 443 K and 50 bar. Since the reaction employed conventional solid catalyst, very mild reaction conditions and syngas containing CO_2 and H_2O, it might be a promising practical method for methanol synthesis at low temperature. The total carbon conversion increased with the increasing of reaction temperature, pressure, and catalyst weight. The high conversion of methanol synthesis at low-temperature was produced from CO and H_2 containing small amount of CO_2.

References

(1) Herman, R. G.; Simmons, G. W.; Klier, K. *Studies in Surf. Sci. Catal.* **1981**, *7*, 475.
(2) Graaf, G. H.; Sijtsema, P.; Stamhuis, E. J.; Oosten, G. *Chem. Eng. Sci.* **1986**, *41*,2883.
(3) Marchionna, M.; Lami, M.; Galleti, A. *CHEMTECH*, 1997, April, 27.
(4) Zheng, J.; Tsubaki, N.; Fujimoto, K. *Fuel* **2002**, *81*, 125.
(5) Haggin, J. *Chem. & Eng. News* **1986**, Aug. 4, 21.
(6) Brookhaven National Laboratory, U.S.Patent, 4,614,749, 4,619,946, 4,623,634, 4,613,623 (1986), 4,935,395 (1990).
(7) Tsubaki, N.; Sakaiya, Y.; Fujimoto, K. *Appl. Catal.* **1999**, *180*, **L**11.
(8) Tsubaki, N.; Ito, M.; Fujimoto, K. *J. Catal.* **2001**, *197*, 224.

Development of high-performance F-T synthesis catalyst and demonstrative operation of a pilot plant with the catalyst by JOGMEC-GTL project in Japan

Ken-ichiro Fujimoto[1], Kimihito Suzuki[1], Masato Kageyama[1], Yasuhiro Ohnishi[2], Noriyuki Yamane[1], Ikuo Jitsuhara[1], Yoshifumi Suehiro[3]

[1] Technical Development Bureau
Nippon Steel Corporation
20-1 Shintomi, Futtsu-city, Chiba 293-8511, Japan

[2] Energy Facilities, Civil Engineering & Marine Construction Div.
Nippon Steel Corporation
5-9-1 Nishihashimoto, Sagamihara-city, Kanagawa 229-1131, Japan

[3] Oil & Gas Technology Research & Development
Japan Oil, Gas and Metals National Corporation
1-2-2 Hamada, Mihama-ku, Chiba-city, Chiba 261-0025, Japan

Introduction

Natural gas is now reconsidered as a promising energy source, because of its environmental friendliness and abundances in reserves. While its demand will be thought to increase, there are many stranded gas fields untapped in South East Asia and Oceania regions that were found in marginal location. These have been left un-commercialized by the conventional means of LNG form or through pipeline as their reserves are not large enough to invest in such infrastructures. GTL technology seems to be one of the attractive ways to develop these gas fields. By GTL technology, natural gas can be transformed to liquid hydrocarbon that is easy to be handled and transported.

Japan Oil, Gas and Metals National Corporation (JOGMEC) and five private companies (Japan Petroleum Exploration Co., Ltd., Chiyoda Corporation, Cosmo Oil Co., Ltd., Nippon Steel Corporation, and INPEX Corporation) have been making collaboration in the development of new GTL technology as JOGMEC-GTL project. Authors joined to this project and have been developing non-precious metal based F-T synthesis catalysts, and doing some research of simulation for F-T synthesis process. And we made a demonstrative operation of pilot plant last year with using our developed catalyst at Yufutsu in Hokkaido, Japan.

In this paper, we would like to report the obtained results introduced above.

Development of catalysts for F-T synthesis in laboratory scale

Nippon Steel Corporation joined to this project in 2001, and has been developing cobalt-based catalysts using modified silica support. In this project, some target values for the catalyst performance shown in **Table 1** are set, and the catalyst also should have very high attrition resistance since the slurry phase reactor (slurry bubble column reactor: SBCR) is employed as a F-T reactor, and it is operated at very high superficial gas velocity (0.16m/s).

Experimental. Autoclaves (capacity: 100ml, 300ml) were used for F-T synthesis, and desired amount of catalyst and n-hexadecane as a solvent were put in the autoclave. After the autoclave was purged with nitrogen, syngas (H_2/CO=2.0) containing Ar as an internal standard was introduced to the autoclave and pressurized to desired pressure. Then temperature was raised to desired temperature stirring the slurry at 800 rpm, and F-T synthesis reaction was started in this CSTR system. The effluent gas that contained unreacted syngas and light hydrocarbons was introduced to gas chromatography (TCD, FID) after getting through the trap that was kept at 273 K, and CO conversion, CH_4 selectivity, and CO_2 selectivity were calculated. Standard reaction conditions were as follows;

Temperature: 503 K
Pressure: 2.2 MPaG
W/F(H_2+CO): 5 g.h/mol

Results and discussion. Optimizing the properties of silica-based support and the preparation method of catalyst, the catalyst that shows splendid properties has been developed. This catalyst cleared all the target values shown in **Table 1** and was tested in 800-hour long run of F-T synthesis. The result is shown in **Figure 1**. Induction period is observed for the first 100 hours. It seems that this phenomenon is due to solvent replacement from n-hexadecane to heavy hydrocarbons produced by F-T synthesis. After this period, the catalyst activity is fairly stable. Re-designing the silica-based support, we could increase the physical strength and the attrition resistance of the catalyst. The particle size distribution of the catalyst was measured not only before and after 500-hour long run of F-T synthesis but also before and after ultrasonic attrition test [(1)]. By this series of tests, destruction and pulverization of the catalyst particle was not observed, and high attrition resistance of the catalyst was confirmed, so that applicable catalyst to SBCR was obtained. We also analyzed the by-product water. Although it showed weak acidity (pH=3.3 @ 298 K) as organic acids were formed a little, concentrations of other oxygenated organic compounds were low as expected, so it could not be problems for the operation of F-T synthesis reaction.

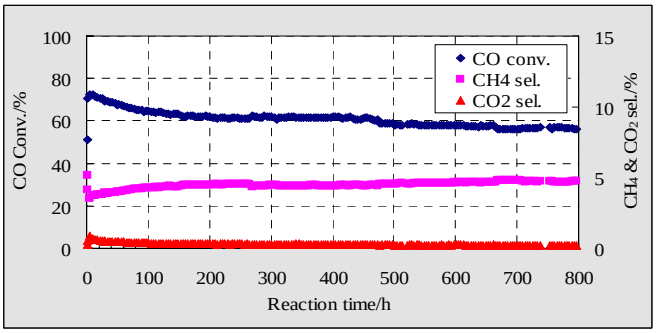

Figure 1. The result of long term F-T synthesis test.
503 K, 2.2MPaG, H_2/CO=2.0, W/F=1.5 g.h/mol

Figure 2. GTL pilot plant at Yufutsu in Hokkaido, Japan.

Table 1. Catalyst Performance Demonstrated at Yufutsu Pilot Plant.

	Temperature K	W/F g.h/mol	CO conv. %	C_5^+ sel. %	α –	C_5^+ Productivity g/kg-cat.h	Production bbl/d
Target	–	–	> 60	> 85	> 0.9	–	–
	513	1.8	62.3	85.2	0.91	1325	5.0
	503	4.5	75.3	88.7	0.91	689	2.6

2.2MPaG, H_2/CO=2.0

Demonstrative operation of pilot plant with developed catalyst

As shown above, the high-performance catalyst that is applicable for the pilot plant has been developed. So, the demonstrative operation was carried out last year at Yufutsu pilot plant (**Figure 2**). The results are shown in **Table 1**. All target values were cleared by this series of operation, and full load operation was attained at 7.3 bbl/d, which was beyond designed capacity of 7 bbl/d. And remarkably, very high C_5^+ productivity of over 1300 g/kg-cat.h was also recorded.

Development of scale-up technology for F-T synthesis reactor

As scale-up technology for a slurry phase reactor, techniques based on mathematical models like a axial dispersion model and tank-in-series model are mainly adopted [(2)]. But, these techniques need experimental parameters that describe the hydrodynamics in a gas-liquid system, and these parameters are usually obtained in a completely different system in dimension and physical properties from those of real plant like water-air system with using small-scale apparatus. Therefore, when these parameters are used for designing the real plant, an inaccuracy due to extrapolation should be taken into account. Then, in this research, we decided to develop the simulation technology of gas-liquid fluid aided with CFD (Computational Fluid Dynamics) technique that has made remarkable progress in the area of scale-up technology.

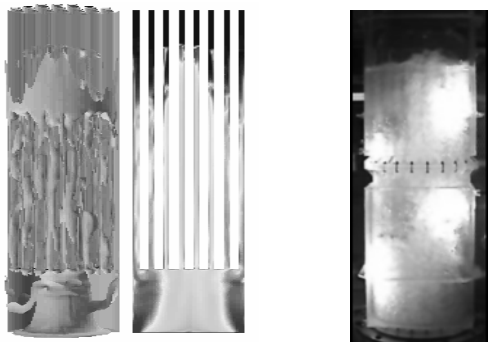

Figure 3. Visualization of the hydrodynamics.

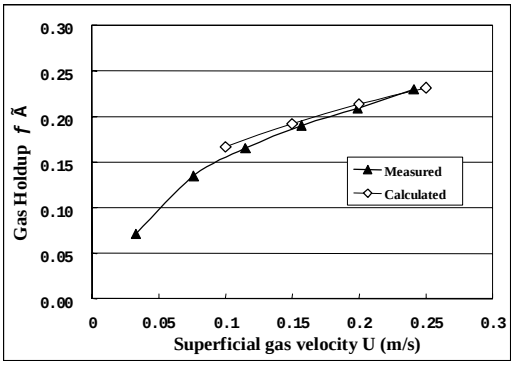

Figure 4. Comparison of calculated and measured gas holdup.

CFD technique for gas-liquid fluid. Though there are some methods for a gas-liquid fluid simulation technique by CFD like averaging method, bubble-tracking method, and VOF method [(3)], averaging method was employed as designing method in this research, because of the realistic calculation load for simulation industrially.

Cold model experiment. For the accuracy verification of this simulation method, cold model experiment was conducted with using water and air in our laboratory. In this research, fairly large apparatus (ID: 0.58 m, L: 3 m) made of acrylic resin that was easy to be observed inside was used. 34 tubes were set inside the apparatus as mock cooling tubes, and then air was introduced from its bottom (0.04-0.32 m/s).

Calculation results. The simulated results that visualize gas volumetric fraction is shown in a) of **Figure 3**. Iso-surface of gas volumetric fraction is shown in left side, and gas volumetric fraction contours in vertical centerline plane of the column is shown in right side. White linear parts in figures indicate cooling tubes. A photo of cold model experiment is shown in b) of **Figure 3** for a reference. Calculation results are depicting the waves of top surface and the hydrodynamics very well.

Calculated relation between gas holdup and superficial gas velocity is shown in **Figure 4** with experimental data obtained from cold model experiment. Calculated results are in accordance with the results obtained by experiment.

Considering the results mentioned above, this simulation method is well describing the hydrodynamics in the reactor with accuracy. Authors will make fluid analysis of the commercial size reactor with this method, and design the commercial scale plant.

Summary

With the high-performance F-T synthesis catalyst developed in this project, the first stable operation of GTL pilot plant in Japan at full load ended in success, and the outstanding properties of the catalyst could be demonstrated at the plant. Authors will continue the pilot plant operation and establish the scale-up technology with applying the simulation.

Acknowledgment. Authors acknowledge collaborators of this project (JAPEX, Chiyoda Corp, Cosmo Oil, and INPEX), and thank Yufutsu GTL for dedicated operation of the pilot plant and ChAS for computer calculations and Professor Akio Tomiyama for helpful discussions and suggestions.

References

(1) Zhao, R.,; Goodwin Jr., J. G.; Oukaci, R. *Appl. Catal. A.*, **1999**, *189*, 99.
(2) Deckwer, W.-D., *Bubble Column Reactors*, John Wiley & Sons, **1992**.
(3) Tomiyama, A., "The state of the art and perspective of computational bubble dynamics.", Trans. JSME, B, **2000**, *66*, 1618.

Aldehyde-Water Shift Catalysis: H_2 Production from Water and Aldehydes via a Homogenous Dirhodium Tetraphosphine Catalyst

George G. Stanley, David A. Aubry, Novella Bridges, Bobby Barker and Brandy Courtney*

Department of Chemistry, Louisiana State University, Baton Rouge, LA 70803-1804, USA

Introduction

A new catalytic reaction to produce H_2 from aldehydes and water has been discovered (eq. 1).

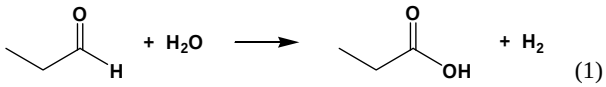

(1)

This is called aldehyde-water shift catalysis in analogy with the water-gas shift reaction: $CO + H_2O \rightleftharpoons CO_2 + H_2$. The aldehyde-water shift reaction is thermodynamically downhill with ΔG^o (363K) = –28.4 kJ/mol, ΔH^o = –9.6 kJ/mol, and ΔS^o = 51.9 J/molK. The proposed catalyst for this reaction is [*rac*-$Rh_2(\mu\text{-}CO)_2(CO)_2$(et,ph-P4)]$(BF_4)_2$, **1**, shown below.

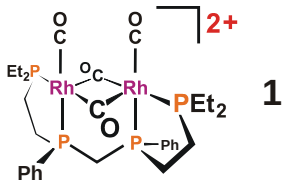

1

The potential of this catalysis for fuel cell applications comes from the possibility of using formaldehyde to make formic acid and H_2, followed by decomposition of the formic acid to make another H_2 and CO_2 (eq. 2):

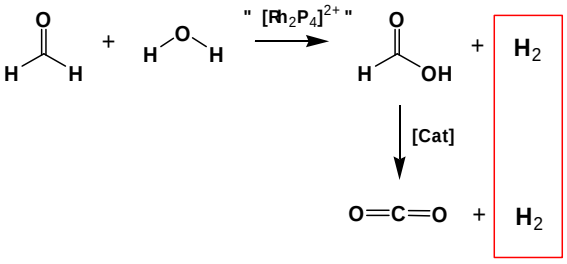

(2)

A formaldehyde-water mixture has one of the highest H_2 energy storage capacities on a per weight basis for fuel cell applications.

Experimental

The catalyst precursor used was [*rac*-$Rh_2(nbd)_2$(et,ph-P4)]$(BF_4)_2$ (nbd = norbornadiene) prepared according to literature methods,[1] or [*rac*-$Rh_2(CO)_4$(et,ph-P4)]$(BF_4)_2$ prepared and isolated from the carbonylation of the norbornadiene complex (details available from the principle author). 1-hexene, heptaldehyde, acetaldehyde, and acetone were all obtained from Aldrich and degassed with N_2 prior to use. 1-hexene was further purified by passing it through a short alumina column under N_2 prior to use. This removes any peroxide impurities that can deactivate the dirhodium catalyst. Water was normal distilled water from our in-house system and also degassed with N_2 prior to use.

Catalytic reactions were performed in 150 mL Parr 4560 mini-reactors equipped with standard thermocouples, pressure transducers and Parr packless magnetic stirrers. Data was collected and partially analyzed on Parr 4850 or 4870 process controllers. The autoclave is configured to run under constant pressure with gas being supplied from a 1 L high pressure reservoir equipped with a pressure transducer and dual stage regulator. The autoclave set-up is shown in Figure 1. Products were analyzed on HP 5890 GC using a DB-1 30m capillary column or on a HP GC-MS system.

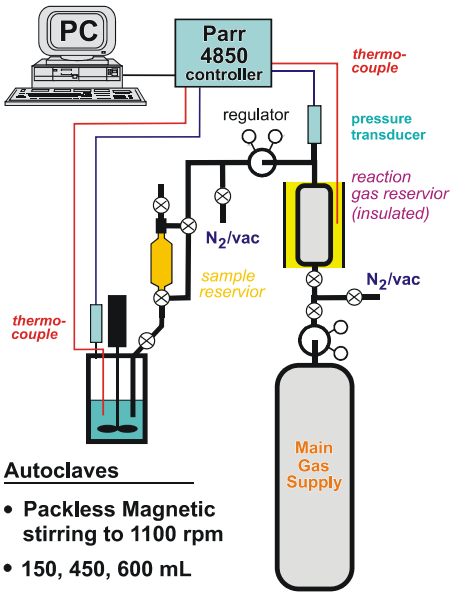

Figure 1. Schematic of autoclave setup.

Tandem Hydroformylation and Aldehyde-Water Shift Catalysis. With our current batch autoclave setup the most consistent results are obtained by first starting the catalysis under hydroformylation conditions using 1-hexene as the starting substrate and a 1:1 mixture of H_2/CO gas. The autoclave was loaded under an inert atmosphere with 1.0 mM [*rac*-$Rh_2(nbd)_2$(et,ph-P4)]$(BF_4)_2$ and 80 mL of 30% water (by volume) in acetone. The autoclave was then purged three times with H_2/CO, and the catalyst solution stirred at 1000 rpm stirring for 15-20 min under 45 psig 1:1 H_2/CO as the temperature was increased to 90ºC. After the temperature has stabilized at 90ºC the pressure of the reaction vessel was decreased to ~45 psig and 1000 equivalents of 1-hexene (99+% and passed through a neutral alumina column under inert atmosphere immediately prior to use, 8.9×10^{-2} mol, 11 mL) was pushed into the autoclave with 90 psig of H_2/CO. The progress of the reaction was monitored by gas uptake from a higher pressure gas storage reservoir connected to a two-stage regulator delivering synthesis gas at a constant pressure of 90 psig to the reaction vessel.

After 10 min of hydroformylation (representing approximately 80% conversion of the 1-hexene to heptaldehyde) the gas supply to the autoclave is turned off and the H_2/CO gas in the high pressure reservoir is replaced with pure CO. This takes about 5 mins. The autoclave is then opened to the pure CO reservoir. Aldehyde-water shift catalysis occurs during this period converting the heptaldehyde to heptanoic acid and H_2. The rapid build-up of H_2 in the autoclave typically stops the aldehyde-water shift catalysis at about 75-80% conversion of the aldehyde to carboxylic acid.

Simple Flow-Reactor Studies. Aldehyde can be directly reacted with water to make carboxylic acid and H_2 using a simple flow setup in our autoclaves. After the initial catalyst precursor ([*rac*-$Rh_2(nbd)_2$(et,ph-P4)]$(BF_4)_2$) soaks under 1:1 H_2/CO at 90 ºC to generate the active catalyst, the feed gas is switched to 90 psig of pure CO and a needle valve is employed to constantly purge the

reaction vessel. 1000 equivalents of heptaldehyde are pressure added to the catalyst solution and a CO purge rate of 4-5 psig/min (based on the pressure drop in the high pressure reservoir cylinder) provided good conditions for aldehyde-water shift catalysis. A maximum of about 75% conversion to carboxylic acid was achieved, with an approximate turnover frequency of 1000 TO/hr (from GC analysis) and with undetectable side products. The aldehyde-water shift catalysis is quite sensitive to reaction conditions and both timing and proper purge rates are critical to achieve good conversion. These are still being optimized.

Results and Discussion

The most consistent results for the aldehyde-water shift catalysis have been obtained by first performing hydroformylation catalysis on 1000 equivalents (1M concentration) of 1-hexene (smaller 1-alkenes are expected to work fine for this as well) under our standard reaction conditions: 90ºC, 90 psig 1:1 H_2/CO, and 30% water (by volume) and acetone as the solvent.[2] Water-acetone solvent dramatically stabilizes our highly active and selective dirhodium catalyst system by inhibiting fragmentation to unreactive species.[2] After 10 mins of rapid hydroformylation, approximately 80% of the 1-hexene has been converted to heptaldehyde. At this point the H_2/CO gas feed to the autoclave is turned off and then switched over to pure CO. The continuing hydroformylation rapidly generates H_2-deficient conditions in the autoclave that shifts the dirhodium catalyst equilibrium away from the hydroformylation dihydride catalyst,[1b] [*rac*-$Rh_2H_2(\mu\text{-}CO)_2$(et,ph-P4)]$^{2+}$, to simple dirhodium carbonyl complexes that we believe are important for the aldehyde-water shift catalysis.

It is at this point under hydrogen depleted conditions that the aldehyde-water shift catalysis initiates. Average turnover frequencies (based on GC analysis) range from 1700 hr^{-1} up to 2100 hr^{-1}. A representative reactant-product consumption-production plot is shown in Figure 2. We have not directly measured the H_2 being produced, but the stoichiometry of the reaction, number of turnovers, and high selectivity of the reaction leaves little doubt that H_2 is one of the products.

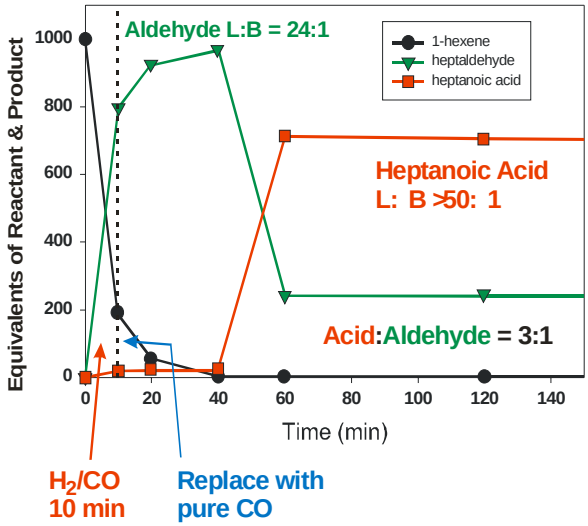

Figure 2. GC analysis of a tandem hydroformylation and aldehyde-water shift catalysis experiment.

The rapid production of H_2 leads to rapid inhibition of the aldehyde-water shift catalysis as seen after the 60 min mark in Figure 2. We typically get conversions of about 75% (750 turnovers), although we have seen one of our early runs with over 90% conversion that had a relatively rapid accidental leak that purged hydrogen gas out of the autoclave.

We propose that the active catalyst species for the aldehyde-water shift catalysis is the dirhodium complex [*rac*-$Rh_2(\mu\text{-}CO)_2(CO)_2$(et,ph-P4)]$(BF_4)_2$, **1** (see introduction for structural drawing). Under normal hydroformylation conditions with a 1:1 ratio of H_2/CO no aldehyde-water shift catalysis is observed. We have established that the aldehyde-water shift catalysis is inhibited by the presence of too much H_2, although we have not established the precise amount. Interestingly, some hydrogen is necessary to form the CO-bridged species, **1**. We believe that hydrogen addition to the "open-mode" (non-CO bridged) isomer [*rac*-$Rh_2(CO)_4$(et,ph-P4)]$^{2+}$ makes a Rh dihydride complex that can far more readily close up to make the bridged CO hydroformylation catalyst complex [*rac*-$Rh_2H_2(\mu\text{-}CO)_2$(et,ph-P4)]$^{2+}$. Reductive elimination of H_2 from this species produces the bridged CO complex **1** critical for the aldehyde-water shift catalysis. **1** only exists in very low concentrations during hydroformylation catalysis when there is considerable H_2 present.

DFT quantum calculations on **1** indicate that the bridging CO ligands link and stabilize the lowest unoccupied molecular orbital (LUMO) making it a far better acceptor for activating the aldehyde for nucelophillic attack by water. The π^* systems of both the terminal and bridging CO ligands form bonding interactions with the Rh p_z orbitals. This lowers the energy of the LUMO of **1** by 0.8 eV relative to the open-mode, non-CO bridged isomer of **1**.

The direct conversion of aldehyde and water is more difficult because our autoclave systems are not designed as flow reactors. Nevertheless, we have successfully performed aldehyde-water shift catalysis by activating the catalyst precursor under H_2/CO, then using a constant purge of pure CO to react heptaldehyde and water (using 30% water in acetone as the solvent) to make heptanoic acid and H_2. The generality of the reaction was partially demonstrated by converting acetaldehyde and water to acetic acid and H_2. The volatility of the acetaldehyde, however, made this a considerably more difficult experiment and a slower purge rate had to be used to reduce the loss of acetaldehyde. Due to these experimental difficulties only 100 equivalents of acetaldehyde were converted. The ability to convert both heptaldehyde and acetaldehyde indicates that this reaction may work for aldehydes in general.

We are currently upgrading one of our autoclaves with a mass flow controller, condenser, and automated back-pressure regulator to setup a more sophisticated flow reactor system to study more volatile reactants such as acetaldehyde and especially formaldehyde.

Conclusions

Aldehyde-water shift catalysis is a new reaction for producing H_2 from water and aldehyde. The use of water both as an oxidizing agent and a source of the H_2 being produced is remarkable. We believe that bimetallic cooperativity in the proposed dirhodium catalyst [*rac*-$Rh_2(\mu\text{-}CO)_2(CO)_2$(et,ph-P4)]$(BF_4)_2$, **1**, is playing an important role in helping to activate the aldehyde and to provide a low energy route for hydrogen production.

Acknowledgement. We thank the NSF for funding (CHE-0111117).

References

(1) Broussard, M. E.; Juma, B.; Train, S. G.; Peng, W. J.; Laneman, S. A.; Stanley, G. G. *Science* **1993**, *260*, 1784. (b) Matthews, R. C.; Howell, D. K.; Peng, W.-J.; Train, S. G.; Treleaven, W. D.; Stanley, G. G. *Angew. Chem., Int. Ed. Engl.* **1996**, *35*, 2253.

(2) Aubry, D. A.; Bridges, N. N.; Ezell, K.; Stanley, G. G. *J. Am. Chem. Soc.*, **2003**, *125*, 11180.

COMBUSTION CHARACTERIZATION OF GTL DIESEL FUEL

André L. Boehman, James P. Szybist, Juhun Song, Vince Zello and Mahabubul Alam

The Energy Institute
The Pennsylvania State University
405 Academic Activities Building
University Park, PA 16802

Kirk Miller

ConocoPhillips
600 N. Dairy Ashford
Houston, TX 77252

Introduction

Synthetic diesel fuel production from natural gas offers the potential of both monetizing stranded natural gas resources and providing a supply of ultra clean transportation fuels. Gas-to-liquids (GTL) diesel fuels produced by the Fischer-Tropsch process typically have very high cetane number and zero sulfur content and can provide reductions in particulate and NOx emissions [1]. ConocoPhillips is developing a demonstration scale plant in Ponca City, OK to produce GTL diesel. The present study is part of an Ultra Clean Fuels project entitled "Ultra Clean Fuels from Natural Gas," sponsored by U.S. Department of Energy under Cooperative Agreement No. DE-FC26-01NT41098.

In this paper, we present results from in-cylinder imaging in a Cummins 5.9L, turbocharged, six-cylinder, 4-stroke direct injection (DI) diesel engine using an engine videoscope system. The imaging studies provide a comparison of the fuel injection timing, ignition timing, spray formation and flame luminosity between different fuels. Results are presented for an ultra low sulfur diesel fuel with 15 ppm sulfur content ("BP15") and for a GTL diesel fuel produced by ConocoPhillips. Also, we present experimental results on combustion and emissions with this ConocoPhillips Fischer-Tropsch diesel fuel (COP F-T diesel), in comparison with an ultra low sulfur diesel fuel. Together, these results show the potential impact of GTL diesel fuel on injection, combustion, and emissions formation in diesel engines.

Experimental

Two different experimental systems were used in the work described here: a highly instrumented 6-cylinder DI turbodiesel engine equipped with an in-cylinder visualization capability and a highly instrumented, single-cylinder DI diesel engine equipped with in-cylinder and fuel injector sensors.

In-Cylinder Imaging. Tests were performed with a Cummins ISB 5.9L turbodiesel engine (MY2000, 235 HP max output) connected to a 250 HP capacity, eddy current absorbing dynamometer. The engine has been heavily instrumented, with a 0.1 crank angle resolution crank shaft encoder, a cylinder pressure sensor, a needle lift sensor and in-cylinder visualization using an AVL 513D Engine Videoscope. The engine and dynamometer are operated through an automated control system. Results are presented at an engine setting of 1800 rpm and 10% load.

Injection Timing and Heat Release Analysis. The single-cylinder engine tests were performed in a Yanmar L70 EE air-cooled, 4-stroke, single cylinder, DI diesel engine with a maximum power output of 7 hp was operated at 25% and 75% load and 3600 RPM (two operating modes from the G2 test from the ISO 8178-4.2 [2]). Cylinder pressure and fuel-line pressures were measured using Kistler piezoelectric pressure transducer models 6052B1 and 601B1, respectively. A Hall-effect proximity sensor, installed by Wolff Controls Corporation, was used to measure needle-lift in the injector. An AVL 364 shaft encoder installed on the engine crankshaft, along with a Keithley DAS 1800 data acquisition board enabled 0.1 CA degree resolutions of these signals. NOx emissions were measured using an Eco-Physics NOx analyzer integral in an AVL GEM 110 emissions bench.

Results and Discussion

In-Cylinder Imaging. Results from the in-cylinder imaging are shown in Figures 1 and 2. The figures compare the structure of the spray and flame for the BP15 and COP F-T diesel fuels at the same point in time after the start of injection (SOI), shown in terms of crank angle degrees after SOI. In the Cummins ISB engine it was observed that the BP15 fuel was injected at 0.2 crank angle degrees earlier than the COP F-T diesel, so comparisons are made relative to SOI. Also, each figure shows two views of each spray or flame. The viewing angle and orientation of the videoscope camera probe can provide different perspectives on the injection and combustion processes. In both Figures 1 and 2, a close-up view of the spray provides a clear view of the spreading angle and both the start and end of injection, while a view from a greater distance can provide an image of the entire length of the spray showing differences in penetration into the combustion chamber. Figure 1 shows images at 4 crank angle degrees after SOI (ASOI). Figure 2 shows images at 10 crank angle degrees ASOI. In both sets of images, Figure 1 showing the spray prior to ignition and Figure 2 showing flame structure well after ignition, there are no significant differences in the general structure of the spray or flame that are visible in this qualitative comparison, despite the significant differences in fuel properties.

Injection Timing and Heat Release Analysis. With the engine set at 25% load, Figures 3 and 4 compare injection timing and heat release results at two injection timing settings, set using shims between the fuel injection pump and the cylinder block. For the ultra low sulfur diesel fuel, BP15, combustion is delayed as injection is delayed leading to degraded combustion, which is particularly evident at the retarded injection timing. The higher cetane number of the COP F-T diesel causes the F-T diesel blend to perform well despite retarded injection timing, as seen for the late injection timing in Figure 4. As Figure 5 shows for the "late" static fuel injection timing, the differences in the heat release rate are not as significant at higher load where the ultra low sulfur fuel does not display degraded combustion as it does at the light load. Nonetheless substantial differences in emissions and fuel consumption are observed between the test fuels as injection timing and load are varied. Figure 6 presents brake specific fuel consumption, NOx emissions and CO emissions at 25% load for the "early" and "late" fuel injection timings. At the late injection timing, CO emissions increase and fuel consumption increases for the ultra low sulfur diesel fuel relative to the COP F-T diesel. NOx emissions are observed to have a more complex trend with fuel type. NOx decreases with retardation of injection timing, as expected. But, at light load NOx emissions are slightly lower for the ultra low sulfur diesel fuel than for the F-T diesel. However, the lower NOx with the ultra low sulfur diesel fuel at light load and retarded injection timing is at the substantial expense of CO and fuel consumption. At the higher load setting, NOx, CO and fuel consumption are always lower for the COP F-T diesel fuel.

Angles	BP15	FT100
Endo-scope 60 / Illumi-nation 70		
Endo-scope 30 / Illumi-nation 30		

Figure 1. Videoscope images of injection of BP15 and COP F-T diesel within Cummins ISB 5.9L turbodiesel engine at 4 degrees ASOI.

Angles	BP15	FT100
Endo-scope 60 / Illumi-nation 70	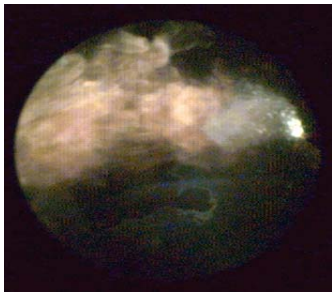	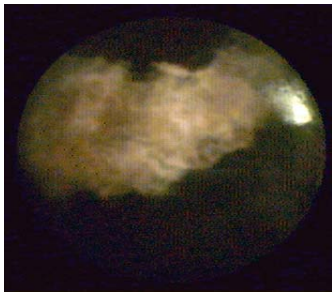
Endo-scope 30 / Illumi-nation 30	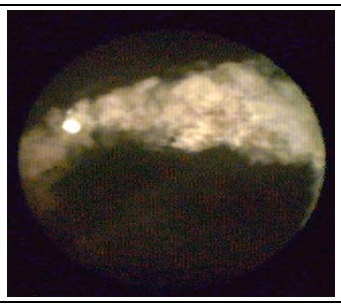	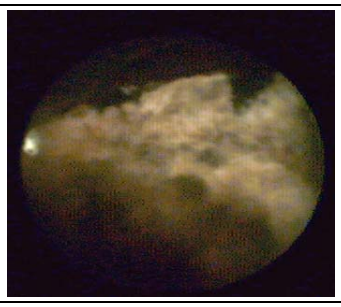

Figure 2. Videoscope images of injection of BP15 and COP F-T diesel within Cummins ISB 5.9L turbodiesel engine at 10 degrees ASOI.

Conclusions

While in-cylinder imaging comparisons of ultra low sulfur diesel fuel and synthetic diesel fuel show no significant differences in spray or flame structure, injection timing and heat release analysis show that the high cetane number and low bulk modulus of compressibility of the F-T diesel fuel lead to significant differences in heat release and pollutant formation.

Acknowledgement. The authors wish to thank ConocoPhillips, Cummins Engine Company, the U.S. Department of Energy and the Pennsylvania Department of Environmental Protection for their support of this work. The authors especially wish to thank Etop Esen, Doug Smith, Keith Lawson, Ed Casey, Raphael Espinoza and Jim Rockwell of ConocoPhillips, and John Wright and Edward Lyford-Pike of Cummins Engine Company for their support of this work.

This paper was written with support of the U.S. Department of Energy under Cooperative Agreement No. DE-FC26-01NT41098. The Government reserves for itself and others acting on its behalf a royalty-free, nonexclusive, irrevocable, worldwide license for Governmental purposes to publish, distribute, translate, duplicate, exhibit, and perform this copyrighted paper.

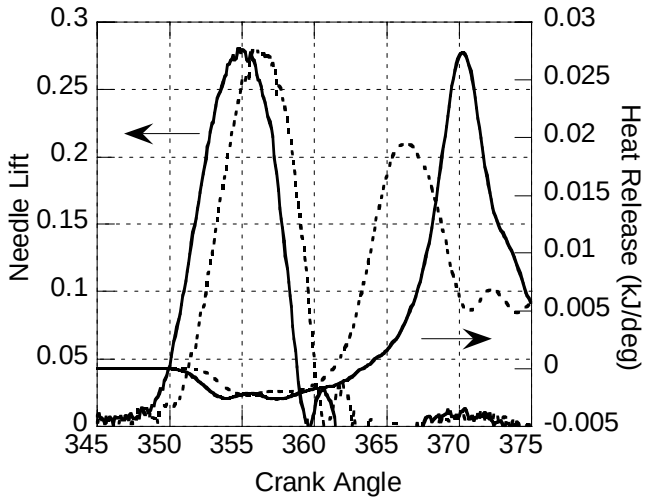

Figure 3. Needle lift and heat release versus crank angle for the "early" static injection timing at 25% load and 3600 rpm, in a Yanmar L70 DI diesel engine. (—) BP15 ultra low sulfur diesel fuel and (- - -) COP Fischer-Tropsch diesel fuel.

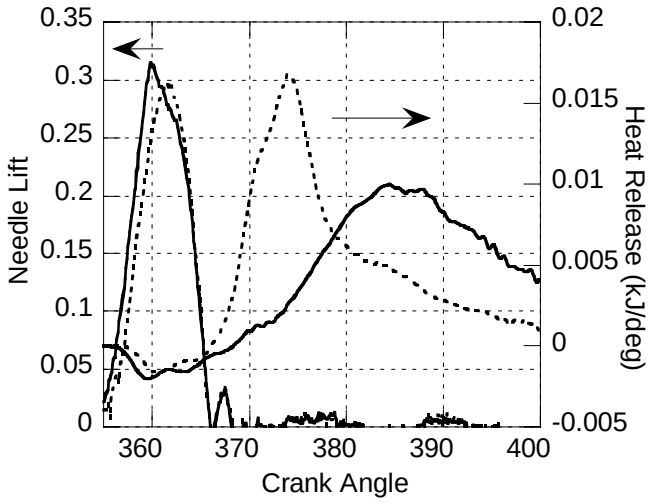

Figure 4. Needle lift and heat release versus crank angle for the "late" static injection timing at 25% load and 3600 rpm, in a Yanmar L70 DI diesel engine. (—) BP15 ultra low sulfur diesel fuel and (- - -) COP Fischer-Tropsch diesel fuel.

This material was prepared with the support of the Pennsylvania Department of Environmental Protection. Any opinions, findings, conclusions, or recommendations expressed herein are those of the author(s) and do not necessarily reflect the views of the DEP.

References

(1) Lloyd, A.C. and Cackette, T.A., *J. Air & Waste Manage. Assoc.*, **2001**, *51*, 809-847.

(2) International Organization for Standardization, ISO 8178: Reciprocating internal combustion engines - Exhaust emissions measurement - Part 4. Test Cycles for different engine applications. 1995.

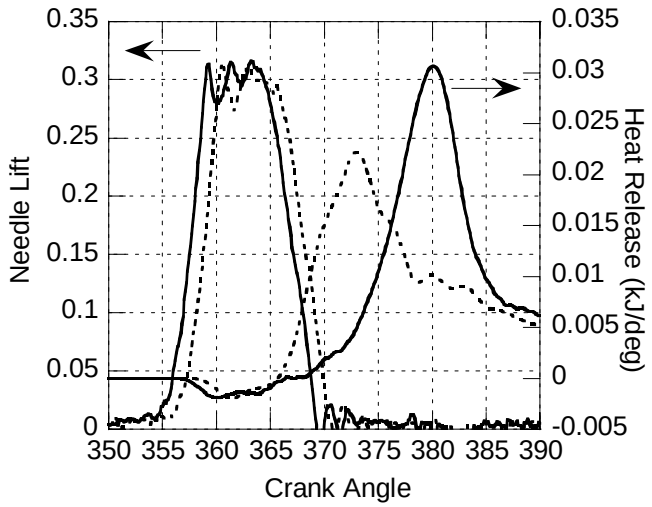

Figure 5. Needle lift and heat release versus crank angle for the "late" static injection timing at 75% load and 3600 rpm, in a Yanmar L70 DI diesel engine. (—) BP15 ultra low sulfur diesel fuel and (- - -) COP Fischer-Tropsch diesel fuel.

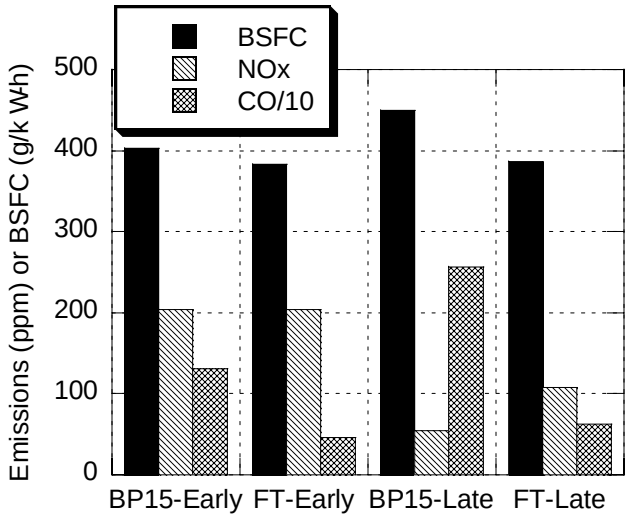

Figure 6. Brake specific fuel consumption, NOx emissions and CO emissions for BP-15 and COP F-T diesel fuels at 25% load and 3600 rpm, at the "early" and "late" injection timing settings.

SELECTIVE PRODUCTION OF GASOLINE-RANGED ISOPARAFFINS OVER Co/SiO_2 AND METAL/β CATALYSTS FROM SYNGAS

Zhong-Wen Liu[†, ††], Xiaohong Li[,†], Kenji Asami[†], Kaoru Fujimoto[†]*

[†]Department of Chemical Processes and Environments, Faculty of Environmental Engineering, The University of Kitakyushu, Kitakyushu, Fukuoka 808-0135, Japan

[††]College of Chemistry and Chemical Engineering, Nanjing University of Technology, Nanjing 210009, P. R. China

Introduction

The Fischer-Tropsch (FT) synthesis is an effective route to convert coal or natural gas derived synthesis gas (syngas, $CO + H_2$) to liquid fuels and high-value added fine chemicals. [1] However, the FT products which are composed mainly of mixture of normal paraffins are nonselective and the product distribution is controlled by the so-called Anderson-Schulz-Flory (ASF) polymerization kinetics. [1] To selectively synthesize desired products such as diesel or high-octane gasoline, it is essential to circumvent the ASF distribution. Several groups have tried to selectively produce isoparaffins by utilizing FT active components supported on acidic zeolites. [2,3] However, acidic zeolites are not a stable support under FT reaction conditions, and typical results show low activity and high methane selectivity. In our previous investigations, [4,5] a fundamental concept on direct production of isoparaffins over physical mixture of a FT catalyst to synthesize long-chain hydrocarbons and a Pd-supported zeolite catalyst to hydroconvert the FT products was proposed and preliminary experiments were carried out both in one reactor and a consecutive dual reactor system. Results showed that high selectivity to isoparaffins of C4 ~ C8 can be more efficiently and easily achieved in a dual reactor system by loading Pd/β catalyst in the downstream reactor. [5] In this investigation, Pt- and Pd-supported zeolite β catalysts were comparatively studied at different time on stream (TOS) for selective production of isoparaffin from syngas in a consecutive dual reactor system, i.e., Fischer-Tropsch (FT) synthesis over Co/SiO_2 catalyst in the up-stream reactor and hydrocracking & hydroisomerization of FT hydrocarbons over the metal-supported zeolite β catalyst in the down-stream reactor.

Experimental

The Co/SiO_2 catalyst (20 wt% Co) was prepared by the incipient wetness impregnation of aqueous solution of cobalt nitrate on the silica gel (Fujisilicia Q-15). The zeolite β (Sud Chemie, SiO_2/Al_2O_3=25) was ion-exchanged at 353 K for 6 h in the solution of $Pt(NH_3)_4Cl_2$ and $Pd(NH_3)_4(NO_3)_2$, respectively, for the preparation of Pd/β and Pt/β catalysts (0.5 wt% loading). The final catalysts were dried overnight at 393 K and then calcined at 723 K for 2 h.

The reaction was carried out in consecutive dual fixed-bed reactors (SUS tube, 8mm I.D.), in which 0.4 g Co/SiO_2 mixed with 0.1 g β and diluted with 0.5 g quartz sands was loaded in the upper reactor and 0.5 g metal/β catalyst diluted with the same amount of quartz sands was in the lower reactor. Before reaction, the catalysts were pretreated at 673 K for 3 h in a flow of hydrogen. The operating conditions were P (system)=1.0MPa, H_2/CO=2.0, W/F(syngas)=4.97 $g \cdot h \cdot mol^{-1}$. The effluent hydrocarbons, which were cooled at 453 K, were analyzed by an on-line GC equipped with a NB-1 capillary column and a FI detector. The CO, CH_4, and CO_2 in the effluent after cooling in an ice-water trap were on-line analyzed by a GC with a packed active carbon column and TC detector. The selectivity of hydrocarbons in this study was calculated on the basis of carbon number.

Results and Discussion

To comparatively study the effect of catalyst loaded in the lower reactor on the isoparaffin selectivity, the catalyst in the upper reactor and its operating conditions were kept the same for all the experiments. For simple expression, only the metal/β catalyst loaded in lower reactor will be mentioned. The product distribution over Pd/β catalyst in the dual reactor system was given in Figure 1. It is clear that the ASF distribution of the FT products was significantly changed, i.e., long-chain hydrocarbons produced in FT synthesis was dominantly hydrocracked and high selectivities toward C4 to C7 hydrocarbons were observed. It is a common fact that very less isoparaffins was produced from FT synthesis over Co/SiO_2 catalyst. However, in the present case, very high selectivities of isoparaffins with carbon numbers from 4 to 7 were observed as shown in Figure 1. At the present operating conditions, CO conversion was about 55%, indicating that an appreciable amount of unreacted hydrogen from the upper reactor was available in the lower reactor. Therefore, it is reasonable to propose that the main reactions occurred over Pd/β catalyst were hydrocracking and hydroisomerization. Comparing the carbon number distribution at different TOS, a slight decrease of the isoparaffin selectivity was observed. This can be reflected clearly from the molar ratio of total isoparaffins to C4+ hydrocarbons (I/C4+). The I/C4+ decreased from 62.1 at TOS of 2.5 h to 58.5 at TOS of 7 h.

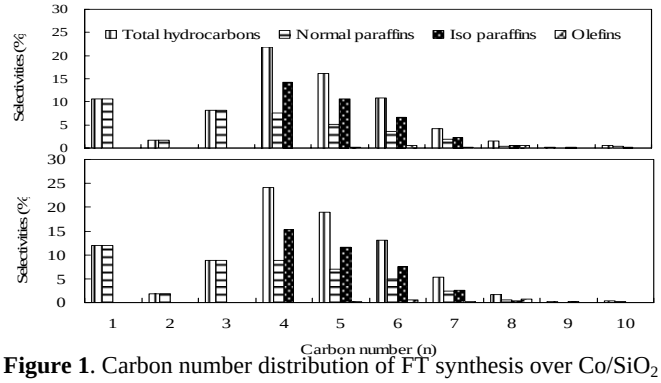

Figure 1. Carbon number distribution of FT synthesis over Co/SiO_2 and Pd/β catalysts in a dual reactor system (T=508 K (upper reactor), T=573 K (lower reactor)) at time on stream of 2.5 h (upper) and 7 h (lower).

From Figure 2, which was the carbon number distribution over Pt/β catalyst, it was clear that the ASF distribution of FT products was also significantly altered. But, in comparison with the results over Pd/β, an appreciable amount of hydrocarbons with carbon number larger than 11 was still observed, suggesting that heavy hydrocarbons produced on Co/SiO_2 was less hydrocracked over Pt/β than that over Pd/β. Furthermore, obvious higher olefin selectivities were found over Pt/β catalyst than that over Pd/β catalyst, especially at the later stage of the reaction. These results suggest that hydrocracking of FT products over Pt/β catalyst is less efficient than that over Pd/β catalyst. It should be pointed out that a significant decrease of isoparaffin selectivity occurred by comparing the carbon number distribution at TOS of 2 h and 10 h. This was more clearly reflected from the sharp decrease of calculated I/C4+ ratios, i.e., from 67.3 at TOS of 2 h to 36.7 at TOS of 10 h. It is worthy to note that the sharp decrease of isoparaffins with TOS was accompanied with significant increase of olefin selectivity as shown in Figure 2.

To compare the selectivities of individual isoparaffin with the corresponding normal paraffin at different TOS, C4, C5 and C6 were chosen and calculated respectively, and the results were given in

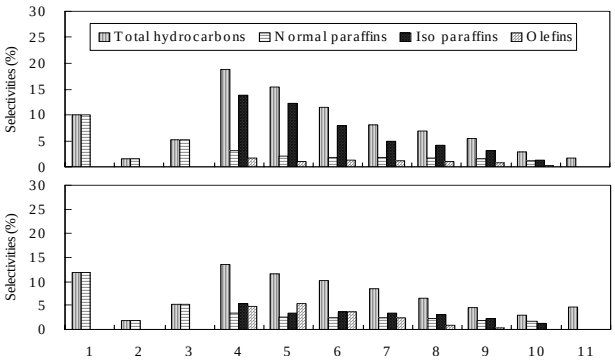

Figure 2. Carbon number distribution of FT synthesis over Co/SiO_2 and Pt/β catalysts in a dual reactor system (T=505 K (upper reactor), T=573 K (lower reactor)) at time on stream of 2 h (upper) and 10 h (lower).

Figures 3 and 4. Over Pd/β catalyst, the ratio of isobutane to n-butane was low even at TOS of 2.5 h (1.9) and decreased slightly to 1.7 at TOS of 7 h. When pentane and hexane were considered, almost same values and changing trends with TOS were observed. In the case of Pt/β catalyst, a quite different pattern appeared. A very high molar ratio of isoparaffin to the corresponding normal paraffin was produced at TOS of 2 h, and then decreased sharply with TOS and reached 1.66, 1.65, and 1.55 for butane, pentane and hexane, respectively.

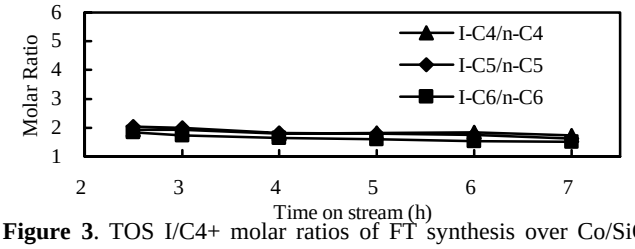

Figure 3. TOS I/C4+ molar ratios of FT synthesis over Co/SiO_2 and Pd/β catalysts in a dual reactor system (T=508 K (upper reactor), T=573 K (lower reactor)).

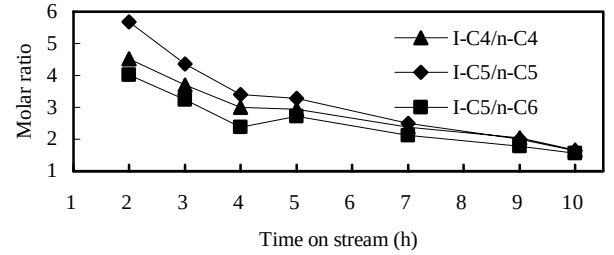

Figure 4. TOS I/C4+ molar ratios of FT synthesis over Co/SiO_2 and Pt/β catalysts in a dual reactor system (T=505 K (upper reactor), T=573 K (lower reactor)).

Blank tests showed that CO conversion was less than 2% at the present operating conditions when only either Pt/β or Pd/β was loaded. As mentioned above, the catalyst and operating conditions in the upper reactor were kept the same for each experiment, almost the same CO conversion and CH_4 selectivity were obtained irrespective the catalyst used in the lower reactor. Therefore, the above phenomena must only be related to the hydroconversion function of the metal/β catalysts loaded in the lower reactor.

For the hydroconversion of normal paraffins over metal/solid acid catalysts, it is generally accepted that acid sites are responsible for the cracking or isomerization reactions although the action mechanism of metal is still controversial. [6] However, zeolite β used in this study is the same for both Pd/β and Pt/β catalysts. Thus, the possible explanation on the different performance of Pd/β and Pt/β in the titled reaction may be from the interaction of metal and β zeolite. It is believed that Pt has high activity for hydrogenation/dehydrogenation of hydrocarbons and Pd doesn't have while both metals show high activity for the dissociation of hydrogen. Therefore, it is reasonable to propose that hydroconversion reactions of the FT hydrocarbons may be preceded in different mechanisms over the two catalysts.

Because water was produced in FT synthesis and the activity of water-gas shift reaction over Co was low, steam was always present in the lower reactor. Furthermore, it is a common fact that steam has a negative effect on solid acids. Therefore, the slight decrease isoparaffin selectivity over Pd/β catalyst may be caused by the deteriorative effect of steam on the acid sites over zeolite β. Another reason may be from the accumulation of coke on the catalyst as coke formation always accompanied with the hydroconversion of hydrocarbons over solid acid. Presently, anyone of the above reasons cannot be ruled out.

It is surprising that the Pt/β catalyst deactivated sharply for the titled reaction, additional reasons must be there. To the best of our knowledge, there is no report on the application of Pt/β catalyst for hydroconversion reactions in the FT conditions although Pt-supported solid acid catalysts were intensively investigated for hydroconversion of pure normal alkanes. In the present conditions, besides paraffins with a wide range of carbon number, olefins, steam and unreacted CO were also fed to the lower reactor. The fast deactivation of Pt/β catalyst may be arisen from these factors. Deteriorative effect of CO on the hdyroconverion of n-butane over Pt/sulfated ZrO_2 was observed.[7] Moreover, the hydrocracking ability of Pt supported sulfated zirconia was severely reduced when n-C16 was co-fed with a C16 olefin.[8] In another work for the hydroconversion of n-C24 in a batch reactor [9], the same authors found that Pt supported on WO_3/ZrO_2 showed much lower hydrocracking ability. These findings support our present explanation. However, to clearly answer why Pt/β catalyst showed a fast deactivation in comparison with Pd/β catalyst, purposefully designed experiments and characterization works are in progress.

Acknowledgment. The authors acknowledge the financial support by Japan Oil, Gas and Metals National Corporation (JOGMEC).

References

(1) Vannice, M. E. *Cat. Rev. Sci. Eng.* **1976**, *14 (2)*, 153–191.
(2) Jothimurugesan, K.; Gangwal, S. K. *Ind. Eng. Chem. Res.*, **1998**, *37*, 1181.
(3) Koh, D.J.; Chung, J.S.; Kim, Y.G. *Ind. Eng. Chem. Res.*, **1995**, *34*, 1969.
(4) Li, X.; Luo, M.; Asami, K. *Catal. Today*, 2004, in press.
(5) Li, X.; Asami, K.; Luo, M.; Michiki, K.; Tsubaki, N.; Fujimoto, K. *Catal. Today*, **2003**, *84* , 59.
(6) Fujimoto, K. In *Hydrotreatment and Hydrocracking of Oil Fractions;* B. Delmon, B.; Froment, G.F.; Grange, P.; Ed.; Elsevier Science B. V.: Amsterdam, 1999, Vol.127, p37.
(7) Song, X.; Sayari, A. *Energy Fuels*, **1996**, *10*, *561*.
(8) Venkatesh, K.R.; Hu, J.; Wang, W.; Holder, G.D.; Tierney, J.W.; Wender I. *Energy Fuels*, **1996**, *10*, *1163*.
(9) Zhou, Z.; Zhang, Y.; Tierney, J.W.; Wender I. *Fuel Proc. Tech.*, **2003**, *83*, 67.

HUBBERT'S PEAK : THE IMPENDING WORLD OIL SHORTAGE

Kenneth S. Deffeyes

Geosciences Department
Princeton University
Princeton NJ 08544

Invited Presidential Event Presentation

World oil production will peak on Thanksgiving Day, 2005, with an uncertainty of only a month or two. In 1956, M. King Hubbert predicted that U.S. oil production would peak in the early 1970's. Although Hubbert was widely criticized by some oil experts and economists, 1970 was the largest year of U.S. oil production. Hubbert's methods applied to world oil production, show that growth in production has ceased and a decline will follow. The present chaos in energy prices may, in fact, be the leading edge of a major crisis. This means that we must turn to long-term solutions to our future energy problems.

OUR ENERGY CHALLENGE

Richard E. Smalley

Center for Nanoscale Science and Technology
Rice University
6100 Main Street, MS100
Houston TX 77005

Invited Presidential Event Presentation

Somehow within the next few decades we must find a new energy source that can provide at least 10 terawatts (TW) of clean power on sustainable basis, and do this cheaply. To do this with nuclear fission would require 10,000 breeder reactors. In order for the billions of people in the developing world to achieve and sustain a modern lifestyle, we really need 50 TW. Assuming we don't get it all from "clean coal" or nuclear fission, where is that 10-50 TW of new power going to come from? How will we transport this energy, store it, and transform it? Who will make the necessary scientific and engineering breakthroughs? Can it be cheap enough to bring 10 billion people to a reasonable standard of living? Can it be done soon enough to avoid the hard economic times, terrorism, war and human suffering that will otherwise occur as we fight over the dwindling oil and gas reserves on the planet? Energy may very well be the single most critical challenge facing humanity in this century.

THE ROLE OF CHEMISTRY IN PROVIDING FUELS FOR THE FUTURE

Stanley Bull

National Renewable Energy Laboratory
1617 Cole Boulevard, MS 1731
Golden, CO 80401-3393

Invited Presidential Event Presentation

This presentation will focus on the role that chemistry will play in meeting the challenges for developing fuels for the future. While humankind has tapped into solar, wind, biomass, and geothermal energy sources for millennia, science and technology are the keys for making these sources a significant part of the rapidly growing energy needs of the world in the 21st century. Through the application of chemistry, in concert with physics, biology, biotechnology, nanoscience, engineering, and other disciplines, come clean transportation fuels from biomass, new ways to produce electricity from sun, wind, and the heat of the earth, and hydrogen as a means to provide fuel for transportation, distributed electricity generation, and heating buildings. The presentation will focus on fuels for the future and will address the following questions. What current chemical sciences will initiate the shift to our future fuels? What are some examples of how chemistry today is helping to mold the fuels of the future? Are there gaps in our knowledge of chemistry that need to be filled? What will chemical fuelsciences look like in the future?

FUELS FOR THE FUTURE: THE GLOBAL PERSPECTIVE

Shirley Neff

Goldwyn International Strategies, LLC
1225 19th Street, NW
Suite 300
Washington, DC 20036

Abstract for Invited Presidential Event Presentation

Clearly there are significant differences among the worlds regions and nations regarding needs and issues surrounding development of fuels for the future. For example, technologically advanced nations will strive to secure their supply of fuels to ensure continued prosperity, while developing countries will struggle to develop fuel supplies and infrastructure in order to simply improve their economies and the quality of life of their citizens. This paper will present the global perspective on fuels for the future and address the following global energy issues. How will other nations and regions of the world handle issues such as balancing fuel resource development with environmental stewardship and economic issues? What technologies are other nations considering for future fuel supplies? What role will America play in the world context?

Meeting the Fuels and Energy Policy Challenge

Drew Kodjak

National Commission on Energy Policy
1616 H Street, NW 6th Floor
Washington, DC 20006

Invited Presidential Event Presentation

The attacks of September 11th, the California energy crisis, growing concern over global climate change, and the tremendous progress in new clean energy technologies all suggest a rapidly changing landscape of energy needs, vulnerabilities, and opportunities. The National Commission on Energy Policy intends to propose a series of near-term measures that are necessary to improve our nation's long-range energy position. These recommendations will be contained in the final report of the Commission scheduled for release in late 2004 / early 2005. This presentation will touch on a number of issues under active consideration by the Commission, such as how to harness market forces towards multiple social ends, what key energy technologies deserve greater public and private investment, and how to ensure adequate future supplies of clean energy given current difficulties in siting new generating facilities, waste storage sites, pipelines and transmission lines.

FOSSIL AND RENEWABLE FUELS CHALLENGES FOR THE 21st CENTURY

André L. Boehman, Mercedes Maroto-Valer, Alan W. Scaroni and Harold H. Schobert

The Energy Institute
The Pennsylvania State University
University Park, PA 16802

Introduction

In a 1981 issue of *Physics Today*, U-C Berkeley anthropology professor Laura Nader wrote that "The energy problem is not a techonological problem. It is a social problem. We must build technologies that recognize human frailty." (1) This sentiment summarizes quite clearly the multi-faceted problem of planning and building an energy infrastructure that is sustainable in the long term and that accommodates societal, economic and political realities. Our hunger for cost-effective and environmentally friendly energy continues to grow into the 21st century [2]. The U.S. Energy Information Administration has forecast that in the first two decades of the 21st century, energy demand will increase by 60% over the level at the end of the 20th century [3]. Fossil fuels (coal, petroleum and natural gas) have been the major primary energy sources, providing over 85% of the total energy demand, and their role is expected to continue growing due to their inherent cost competitiveness compared to non-fossil energy sources. In Pennsylvania, fossil fuels provide about 76% of total energy needs, with coal accounting for over 50% of the electricity generated [4]. Under this energy scenario, where the elimination of fossil fuels from our energy portfolio would irrefutably lead to an energy famine, the 2001 National Energy Policy (NEP) has reported a fundamental imbalance between energy supply and demand, where, if energy production increases at the same rate as during the last decade, the projected energy needs will be 40% higher than the expected levels of energy production [5]. Accordingly, the NEP proposes to advance new, environmentally friendly technologies to increase energy supplies and encourage cleaner, more efficient energy use. To achieve this goal we need (i) to educate and train a workforce of scientists and engineers at the interface of energy and the environment; (ii) to advance fundamental and practical research to develop the required technologies; and (iii) to create public awareness of energy development and use, including information on energy and a clean environment.

While there is much discussion about transitioning the United States and the world to a "hydrogen economy," the world will undoubtedly rely on the use of fossil fuels for much of its energy needs for some time to come. What remains for engineers and scientists, particularly fuel chemists, is to envision and design the means of maintaining a portfolio of fuels choices so that fuel flexibility, economic growth and environmental protection can be achieved simultaneously.

In this paper, we review some of the remaining technical challenges regarding fuels for mobile and stationary power sources. We also offer suggestions for research and development strategies to overcome these challenges so that we have sufficient and satisfactory fuels for the future.

Fuel Related R&D Challenges

This section is organized by energy sector, highlighting specific challenges faced within each sector.

Transportation Fuels – Spark Ignition Fuels. The EPA-mandated shift in 2006 to ultra-low-sulfur fuels for on-road vehicles will enable significant enhancements in pollution control technologies for passenger cars and trucks of all classes [6]. For gasoline-fueled vehicles, whether hybrid electric or conventional, the pressure will be to move beyond the ultra-low emissions vehicle (ULEV) category to the super-ultra-low emissions vehicle (SULEV) and equivalent zero emissions vehicle (EZEV) categories [7]. Spark-ignition direct-injection (SIDI) engine development will continue the push toward maximizing SI engine efficiency and will be made more viable by the potential for sulfur-sensitive NOx control strategies that will be enabled by ultra-low-sulfur fuels. A key challenge in this area is overcoming the coking tendencies of the fuel which can lead to clogged fuel injectors and engine deposits. This is a more critical barrier to SIDI engines than conventional SI engines, due to the need to precisely prepare an ignitable but stratified charge to prevent misfiring and excessive hydrocarbon emissions (8).

To achieve the proposed renewable fuels standard, which may require an average renewable fuels content of 5%, the apparent trend is to ramp up production of fuel-grade ethanol [9]. While this is politically attractive and will provide additional markets for farm products, the yield of renewable energy from ethanol production is poor compared to other renewable fuels. Ethanol provides roughly 1.3 units of renewable energy content for each fossil energy unit consumed in its production [10]. This ratio must be improved to obtain a higher renewable energy content.

Transportation Fuels – Compression Ignition Fuels. The shift in 2006 to ultra-low-sulfur diesel fuel for on-road vehicles [6], combined with the phased requirements to reduce diesel particulate matter (DPM) by more than 90% in 2007 and NOx emissions by more than 90% in 2010 [6], will permit greater dieselization of the vehicle fleet without sacrificing air quality. This trend will permit fuel economy improvements that can enhance energy security and can help cut or stabilize CO_2 emissions. To achieve these stringent emissions regulations, advances in both in-cylinder pollutant control and exhaust aftertreatment will be necessary. The trend toward higher fuel injection pressures, common rail fuel injection, injection rate shaping and exhaust gas recirculation will enhance particulate control, but will make fuel systems more sensitive to injector coking. The enhanced coking witnessed with ultra-low-sulfur diesel will require additive or formulation strategies to mitigate this coking tendency to maintain fuel system performance [11]. So- called "low temperature combustion modes," wherein combustion takes place under rich conditions or through homogeneous charge compression ignition (HCCI) operation, may also provide combined efficiency enhancements and substantially reduced emissions over traditional compression ignition direct injection (CIDI) [12]. In particular, HCCI engine operation may require an entirely new type of fuel and fuel rating approach. A "good" HCCI fuel is not presently well defined by either the standard octane rating or cetane rating specifications [12,13]. Moreover, there are potentially significant impacts on refinery operations if a unique fuel product stream suited to HCCI engine operation is required to achieve the necessary injection and ignition characteristics, which themselves remain a topic of research. Implementation of diesel particulate filters (DPF) on diesel vehicles can reduce DPM emissions by more than 90%, but may require fuel-borne additives or active control techniques to burn off collected particulates (referred to as trap regeneration) [14]. Control strategies for NOx may be based on adsorber catalysts, which require a brief swing to locally fuel-rich conditions to reduce adsorbed NOx. This may be achieved by fuel injection into the exhaust or mild fuel reforming with a catalytic fuel reformer or by in-cylinder "reforming" from a late fuel injection pulse [15]. In both the DPM and NOx control strategies, there are unresolved issues regarding the interaction of fuel formulation and the effectiveness of the catalytic control technologies.

A nationwide trend in municipal transit has been to convert from diesel to natural gas-fueled buses. While this trend yields immediate benefits for total particulate matter (PM) emissions, there is evidence that PM emissions from natural gas engines without oxidation catalysts are higher and more of a health hazard than those from a diesel engine equipped with a DPF [16]. In addition, natural gas-fueled engines operate at lower efficiency than conventional diesel engines and typically emit high levels of total hydrocarbons, due to unburned methane emissions. Hydrogen enrichment of natural gas has been shown to provide the potential for substantial enhancements in efficiency, reduction in emissions and a practical means of incorporating hydrogen into the existing fuel infrastructure [17]. However, the impacts on durability, operability, safety (particularly with regard to the effectiveness of odorants for leak detection) require further study. In addition, there is a potential for onboard hydrogen generation through incorporation of solid oxide fuel cells as auxiliary power units on transportation vehicles. The uses of this source of hydrogen for enabling low temperature combustion, HCCI and reduced emissions during conventional CIDI operation represent a substantial opportunity for emissions reduction [18].

With regard to renewable fuels for CIDI engines, there has been a recent surge in interest in biodiesel and coordinated efforts by producers, distributors and regulators to achieve viable fuels standards and specifications so that customers and original equipment manufacturers [OEMs] can be confident of the performance and quality of biodiesel. The challenges with biodiesel are many, however, since users may be interested in neat biodiesel ("B100"), the widely used 20 volume % blend ("B20") that the Energy Policy Act of 1992 [EPAct] regulations specifically identify as necessary to obtain renewable fuel credits, or a low-level blend for the purpose of providing a lubricity enhancement to the base diesel fuel (e.g., a 2 vol.% blend, "B2"). Fuel system operating parameters such as fuel injection timing, duration and rate may be affected by the changes in fuel density and calorific value at these various biodiesel usage levels [19]. Also, as with the production and distribution of petroleum-derived fuels, there are needs for each stage of the supply chain to adhere to proper fuel processing, handling, and storage practices to ensure reliable performance for the end user. In the case of biodiesel, remaining critical issues involve the widely observed increase in NOx emissions and the need for robust measures to assess and certify the oxidative stability of the fuel [20]. Also, since there are resource limitations on biodiesel production, a challenge is to find ways to maximize the yield and quality of biodiesel produced from the available agricultural resources [21].

Synthetic diesel fuels, produced from, or containing, components from natural gas, biomass, oil sands and coal, can provide a means of extending and replacing petroleum supplies [22]. For instance, stranded natural gas resources can be converted to high ignition quality, zero-sulfur Fischer-Tropsch [F-T] diesel fuel. However, F-T diesel is widely known to have low lubricity and very high cetane number, greater than 70. The lubricity problem can be overcome with additives, but the cetane number poses a challenge for the refiner. There is no currently realizable benefit from using a neat fuel with a cetane number above 55. However, such fuel streams may provide a cost-effective means of upgrading lower quality middle distillate streams in the refinery to an acceptable cetane number. Biomass-derived F-T diesel, produced from biomass gasification, has the potential to supply substantial high-quality diesel fuel with very high renewable energy to fossil energy ratio, but faces challenges associated with biomass gasification and producing a synthesis gas of sufficient quality for the F-T process [10]. When derived from coal co-processing rather than from indirect liquefaction or from the hydroprocessing of oil sands, synthetic fuel stocks may have adverse impacts on diesel fuel quality, such as enhanced sooting tendency and reduced ignition quality [23].

Stationary Power Generation – Carbon Dioxide Emissions. The current fossil energy scenario is undergoing significant transformations, especially to accommodate increasingly stringent environmental challenges of contaminants such as sulfur dioxide, nitrogen oxides and mercury, while remaining affordable. Furthermore, fossil fuel utilization is inherently associated with greenhouse gas emissions, especially carbon dioxide. Pennsylvania is the tenth largest producer of carbon dioxide in the U.S. from electric utilities, with over 2,700 thousand short tons/square mile [24]. Should worldwide government policies dictate a reduction in greenhouse gas emissions or the imposition of carbon taxes, fossil fuels would lose much of their competitive appeal to nuclear and renewable energy sources. However, the current non-fossil fuel energy share of the worldwide energy market is below 15% (and below 2.5% in Pennsylvania), and therefore it is more likely that fossil fuel energy producers would adapt to the new requirements by developing and implementing emission control and trading strategies.

Research Recommendations for Fuels for the Future

This section is organized by energy sector, highlighting specific recommendations for research to address the challenges that have been identified. With regard to carbon sequestration, a series of carbon sequestration research programs is presented, including carbon storage by mineral carbonates, geological sequestration and capture systems

Transportation Fuels. *1.Fuel Stability* Research is needed in the areas of oxidative and pyrolytic stability of automotive fuels, particularly in: the coking tendency of gasolines for SIDI engines and ultra-low-sulfur diesel fuels; and the oxidative stability of biodiesel.

2.Fuel for Advanced Combustion Regimes Additional research is needed in fuels for HCCI applications, since both the fuels and the engines themselves are under development, particularly to assess the impacts of producing HCCI fuels on refinery operations.

3.Synthetic and Renewable Fuels Research is needed on engine configuration and operating strategies for capitalizing on the extremely high cetane number available in F-T diesel fuels. Further study is needed on the impacts of using fuels produced from the co-processing of coal and hydroprocessing of oil sands on the combustion and ignition quality of diesel fuels. For renewable fuels, research is needed to maximize the renewable content achieved per unit of fossil energy input, where presently for ethanol the ratio is 1.3 and for biodiesel it is 3. For biodiesel fuels, research is needed to overcome the NOx emissions increase associated with biodiesel use.

Stationary Power Generation – Carbon Sequestration. *1.Mineral carbonation*, which includes the reaction of magnesium-rich minerals with CO_2 to form stable mineral carbonates, is a novel and promising approach to carbon sequestration. Suitable feedstocks include olivine (Mg_2SiO_4) and serpentine ($Mg_3Si_2O_5(OH)_4$) minerals, although serpentine exists in far greater quantities. The mineral carbonation approach offers several inherent advantages: long term stability of benign mineral carbonates; the vast capacity of natural mineral deposits; and the overall process being exothermic, and therefore potentially economically viable (25). However, the reaction kinetics are a substantial drawback. Previous studies have required extensive comminution of the raw minerals (<37 μm), heat treatment (600-650°C), high temperatures (>155°C), high partial pressures (>125 atm), and long reaction times (>6 hours) to overcome the kinetic barriers.

The primary research objective should be to investigate the effectiveness of various pretreatment methods aimed at promoting and accelerating carbonation reaction rates and efficiencies through surface activation and moisture removal. Previous studies have

shown that mineral dissolution rates are surface controlled, and the carbonation reaction stops when the magnesium at the mineral's surface becomes depleted and/or blocked due to mass transfer resistance. It has also been demonstrated that the inherent water content of serpentine is detrimental to the carbonation process. Therefore, it can be envisioned that an increase in surface area and decrease in moisture would result in higher reaction rates and efficiencies. This would allow the integration of various synergistic features for the development of a cost-effective sequestration technology, including accelerating the carbonation efficiency without extensive mineral particle comminution or heat treatment and lowering the temperature and pressure conditions of the carbonation reactions.

The most promising results have been with chemically activated serpentines. A carbonation efficiency of nearly 53% was observed at 20°C, and relatively low pressure, 45 atm. These reaction conditions are a significant improvement over previous studies involving thermal activation and grinding that have required temperatures over 155°C and pressures of at least 125 atm (26). Furthermore, high-temperature heat treatment was avoided and a coarser particle size, 75 μm, was used in this work, compared to <37μm in previous studies. Current work is focused on the development of a continuous CO_2 sequestration module.

2.*Geologic Sequestration.* The existence of large volumes of accessible subsurface brine provides a potential high capacity route for the conversion of CO_2 into geologically stable mineral carbonates, such as calcium carbonate and magnesium carbonate (27). Under the appropriate conditions, CO_2 dissolves in brine to initiate a series of reactions that ultimately leads to the bonding of carbonate anions to various metal cations inherent in brine to precipitate carbonates. Subsurface saline aquifers may sequester CO_2 in various forms. However, any ex-situ sequestration process will have to rely on an efficient conversion to mineral carbonates. An investigation into the parameters, most importantly pH, that affect this conversion rate is required, since the evolution of brine pH following adjustment and during reaction with CO_2 at various temperatures and pressures is highly variable.

The rate of the mineral trapping process is slow and serves as the major disadvantage of this technology. It has been suggested that pH has a significant effect on both conversion rate and the specific species that are precipitated (28). The conversion to carbonates can thus be promoted by increasing brine pH through the addition of a strong base. This research qualitatively identifies the effects of various parameters on carbonate precipitation. However, pH evolution throughout the reaction is not well documented. It is necessary to further understand the effects of temperature, pressure, and most importantly pH on the formation of mineral carbonates during the reaction of CO_2 with various natural gas well brines (29). Additionally, the evolution of brine pH following a pH adjustment, but prior to reaction with CO_2, should be studied. This analysis would help determine a relationship between brine composition and a brine's ability to maintain an elevated pH over time.

Preliminary results have revealed large differences in the metal concentrations of brines from various depths and locations. These compositional differences are related to the brine's ability to maintain an elevated pH after treatment with a strong base to address the natural acidity of brine (29).

3.Capture. The costs of current CO_2 separation and capture technologies are estimated to be about 75% of the total cost of ocean or geological sequestration, including the costs for compression to the required pressure for subsequent sequestration (30). New solid-based sorbents should be investigated, where amine groups would bond to a solid surface, resulting in an easier regeneration than with conventional liquid-phase amine absorbents (31). The supports used thus far, including commercial molecular sieves, are generally expensive and hinder the economical viability of the process. Accordingly, there is a need to find low-cost precursors that can compete with expensive commercial supports, and to develop effective solid sorbents that can be easily regenerated, and therefore, which would have an overall lower cost over their lifetime.

Activated carbons are sorbents used in a wide range of household, medical, industrial, military and scientific applications, including gas-phase and liquid-phase processes. The activation process, together with the intrinsic nature of the precursors, strongly determines the characteristics of the resulting activated carbons. Many precursors have the inherent chemical properties, fine structure and relatively low price that make them excellent raw materials for the production of activated carbons. It is anticipated that high-surface-area carbon materials that have been amine impregnated would satisfy this need and provide a superior low-cost CO_2 sorbent (32).

Conclusions

Energy security and development of a sustainable energy infrastructure require advancements in our understanding of the production and utilization of energy resources and of mitigation of their environmental impacts. Such understanding can only come from targeted, fundamental research. It is incumbent on government, industry and academia to invest in frank discussion and insightful planning to ensure that we develop this understanding. Further, it is important to recognize that the nation needs a balanced energy portfolio, rather than relying so heavily (≥99%) on petroleum for our transportation fuels. All energy resources have inherent technological advantages and disadvantages; all have economic incentives and disincentives; and all have associated environmental issues. Our challenge is to strike the appropriate balance among all these factors.

References

(1) Nader, L., abridged version appearing in *The Industrial Physicist,* Aug/Sep **2002**, pp. 24-27.

(2) M.M. Maroto-Valer (Editor), C. Song, and Y. Soong, Environmental Challenges and Greenhouse Gas Control for Fossil Fuel Utilization in the 21st Century, Kluwer Academic / Plenum Publishers, New York, 2002, 447pp. [ISBN 0-306-47336-4].

(3) International Energy Outlook 2002, Energy Information Administration, DOE/EIA-0484 (2002).

(4) Energy Consumption Estimates by Source 1960-2000, Energy Information Administration, http://www.eia.doe.gov (Accessed March, 2004).

(5) National Energy Policy, Report of the National Energy Policy Development Group, May 2002, ISBN 0-16-050814-2.

(6) Control of Air Pollution From New Motor Vehicles: Proposed Heavy-Duty Engine and Vehicle Standards and Highway Diesel Fuel Sulfur Control Requirements, U.S. Environmental Protection Agency, Federal Register, Vol. 65, No. 107, Friday, June 2, 2000.

(7) Green Vehicle Guide, U.S. Environmental Protection Agency, http://www.epa.gov/greenvehicles/about.htm (Accessed May 2004).

(8) Aradi, A.A., Avery, N.A., Wells, P.P., and Grosser, R.W., Society of Automotive Engineers, **1999**, Technical Paper No. 1999-01-3690.

(9) U.S. House of Representatives, H.R.6, Energy Policy Act of 2003.

(10) McCormick, R.L., 8th Diesel Engine Emissions Reduction Conference, August 25-29, 2003, Coronado, CA, http://www.orau.gov/deer/DEER2002/Session4/McCormick.pdf, (Accessed May 2004).

(11) Wain, K., Ph.D. Thesis, **2004**, Dept. of Chem. Engr., Penn State University.

(12) Zhao, F., T.W. Asmus, D.N. Assanis, J.E. Dec, J.A. Eng and P.M. Najt (Eds.), Homogeneous Charge Compression Ignition (HCCI) Engines:

Key Research and Development Issues, Society of Automotive Engineers, Warrendale, PA, 2003.
(13) Sjoberg, M and Dec, J., 9th Diesel Engine Emissions Reduction Conference, August 25-28, 2003, Newport, RI http://www.orau.gov/deer/DEER2003/presentations.htm, (Accessed May 2004).
(14) Allansson, R., Blakeman, P.G., Cooper, B.J., Hess, H., Silcock, P.J. and Walker, A.P., Society of Automotive Engineers, **2002**, Technical Paper No. 2002-01-0428.
(15) West, B., Thomas, J., Kass, M., Storey, J., Lewis, S., Gui, X., Ren, S., Price, K., Dou, D., 9th Diesel Engine Emissions Reduction Conference, August 25-28, 2003, Newport, RI http://www.orau.gov/deer/DEER2003/presentations.htm, (Accessed May 2004).
(16) Ullman, T.L., Smith, L., Anthony, J.W., Slodowske, W.J., Trestrail, W.M., Bunn, W., Lapin, C.A. and Wright, K.J., Society of Automotive Engineers, **2003**, Technical Paper No. 2003-01-1381.
(17) Collier, K., Hoekstra, R.L., Mulligan, N., Jones, C. and Hahn, D., Society of Automotive Engineers, **1996**, Technical Paper No. 960858.
(18) Mauss, M., 9th Diesel Engine Emissions Reduction Conference, August 25-28, 2003, Newport, RI http://www.orau.gov/deer/DEER2003/presentations.htm, (Accessed May 2004).
(19) Tat, M.E, and Van Gerpen, J.H., NREL/SR-510-31462. 2003, p.114.
(20) Graboski, M.S. and McCormick, R.L., *Prog. Energy Comb. Sci.*, **1998**. 24(2):125-164.
(21) U.S. Department of Agriculture, Agricultural Research Service, **2002**, http://www.ars.usda.gov/is/AR/archive/apr02/biofuel0402.pdf (Accessed May, 2004).
(22) Eberhardt, J.J., 9th Diesel Engine Emissions Reduction Conference, August 25-28, 2003, Newport, RI http://www.orau.gov/deer/DEER2003/presentations.htm, (Accessed May 2004).
(23) Yang, Y., Boehman, A.L., and Santoro, R.J.,, **2003**, Proc. 2003 Tech. Mtg. of the Eastern States Section of the Combustion Institute, October 26-29, 2003, University Park, PA, pp. 277-280.
(24) State Electricity Profiles, Energy Information Administration, **2002**, http://www.eia.doe.gov (Accessed March, 2004).
25 Lackner, K.S.; Wendt, C.H.; Butt, D.P.; Joyce, E.L.; Sharp, D.H. Carbon Dioxide Disposal in Carbonate Minerals. *Energy* **1995**, *20* (11), 1153-1170.
26 Maroto-Valer, M.M. Kuchta, M.E. Zhang, Y. Andrésen, J.M. and Fauth, D.J. Prepr. Am. Chem. Soc. Div. Fuel Chem., **2004**, 49(1), 373-375.
27 Energy Information Administration, International Energy Annual 2001 Edition. http://www.eia.doe.gov/emeu/iea/carbon.html (accessed March 18, **2003**).
28 Soong, Y.; Jones, J. R.; Hedges, S. W.; Harrison, D. K.; Knoer, J. P.; Baltrus, J. P.; and Thompson, R. L. Prepr. Pap. - *Am. Chem. Soc., Div. Fuel Chem.*, **2002**, *47 (1)*, 43.
29 Druckenmiller, M.L. and Maroto-Valer, M.M. Prepr. Am. Chem. Soc. Div. Fuel Chem., **2004**, 49(1), 418-419.
30 Herzog, H.J. **1998** Proc. Stakeholders' Workshop on Carbon Sequestration, MIT EL 98-002, Massachusetts Institute of Technology.
31 Siriwardane, R.V.. Shen, M.S.. Fisher, E.P. Poston. J.A. **2001** Energy Fuels. *15*, 279.
32 Tang, Z. Maroto-Valer, M.M. Zhang, Y. Prepr. Am. Chem. Soc. Div. Fuel Chem., **2004**, 49(1), 298-299.

COAL-DERIVED LIQUID FUELS: AN OPTION TO HELP MEET A GROWING DEMAND

John C. Winslow

National Energy Technology Laboratory
U.S. Department of Energy
P.O. Box 10940
Pittsburgh, PA 15236-0940

Introduction

The events of September 11, 2001 have heightened U.S. awareness of the need for greater national security in all aspects of our daily lives. Energy is the key component for the continued operation of a modern society and security of supply is crucial for our continued economic and social prosperity. Every day the U.S. imports a substantial quantity of petroleum (53 percent in 2002) and a substantial quantity of this comes from politically unstable areas of the world. For example, the U.S. imports about 2.5 million barrels per day of petroleum crude and refined products from the Middle East.

Energy security will require not only political, but technological approaches to insure a continued secure supply of affordable transportation fuels. Transportation is the focus because almost all of our transportation energy is derived from petroleum. Although diversity of petroleum supply is important, only energy produced from our domestic resources will truly be secure. These domestic resources include renewables, petroleum, natural gas and our vast coal resources that can provide electricity, hydrogen and liquid fuels to meet our stationary and mobile energy demands. Thus, there are many choices that can be made regarding energy source and fuel to reduce our dependence on imported oil. This paper addresses one combination – the conversion of coal to zero sulfur, high performance Fischer-Tropsch fuel that is compatible with our present liquid fuel infrastructure and can be used directly or reformed at distributed locations to produce hydrogen.

The Polygeneration Concept

It is envisioned that production of these F-T fuels will follow a progression based on Integrated Gasification Combined-Cycle (IGCC) technologies. After successful demonstration, "polygeneration" plants that produce liquid fuels and electric power are likely to be deployed. The plants would be designed to incorporate carbon capture with appropriate storage in oil reservoirs for enhanced oil recovery or in saline aquifers.

In its simplest form the polygeneration concept consists of diverting clean coal-derived synthesis gas from the combined-cycle-power block of an Integrated Coal Gasification Combined Cycle (IGCC) unit to a synthesis reactor. This plant could also be designed to divert some of the hydrogen produced for use in fuel cell applications.(Figure 1). The tail gas from the synthesis reactor consisting of unreacted synthesis gas, carbon dioxide, water, and light hydrocarbons is then combusted in the combined-cycle power generation unit. Combining processes in this manner has certain technical and economic advantages. Coal cannot be combusted directly in gas turbines; it must first be converted into clean synthesis gas. Once the coal is in gaseous form, the high efficiencies associated with gas turbine combined cycle performance now become accessible to coal. However, once the clean synthesis gas has been produced from the coal, the plant can be made even more efficient by co-producing liquid transportation fuels through Fischer-Tropsch (F-T) or other synthesis technology. Compared to a stand-alone F-T facility, using a once through synthesis process in this configuration avoids the significant inefficiencies of synthesis gas recycle and light hydrocarbon reforming that would be necessary in configurations that produce only an all-liquid product

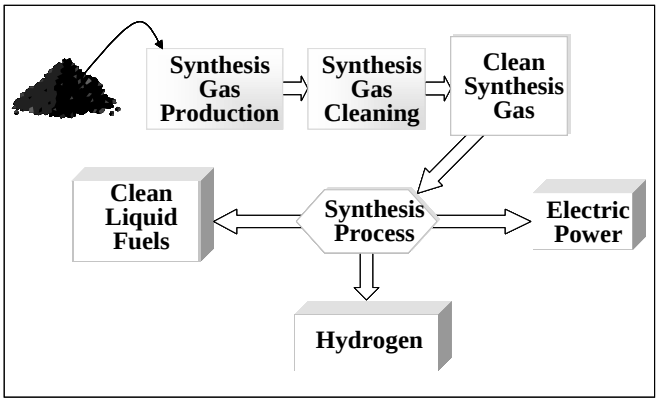

Figure 1. The Overall Technology Concept

The basic IGCC plant needs to be modified to reconfigure it as a polygeneration facility. The additional equipment required includes synthesis, product recovery and refining, water-gas shift, hydrogen recovery, sulfur polishing for synthesis gas cleaning, and product tankage and shipping facilities. In addition to this equipment, it is necessary to modify the steam system of the combined cycle section since the synthesis and shift reactors produce steam that is used to supplement the steam cycle of the combined cycle electric power generation system.

Technology Status

The chemistry is proven, essentially two major exothermic reactions are involved – the reaction of carbon monoxide with hydrogen, followed by carbon monoxide and water reacting through the water-gas shift. At end of WWII, F-T was being studied by most industrial nations, but the low cost and high availability of oil led to decline in interest. The only commercial plants using this technology today are in South Africa (Sasol) and Malaysia (Shell). At the present time, no coal-based facilities based on modern entrained gasification have been constructed that can produce both liquid transportation fuels and electric power., although a project team led by Waste Management Processors, Inc. has been selected by the Department of Energy to build a pre-commercial scale plant in the eastern Pennsylvania anthracite region. This plant would polygenerate 5,000 barrels/day F-T fuel, 50 MWe net electricity and some low pressure steam for industrial heating.

In order to improve the current technology and achieve the increases in performance and reduction in costs, enabling R&D is necessary in the following broad areas:

- Synthesis gas generation (Gasification)
- Gas cleaning
- Synthesis gas conversion reactors, catalysts, catalyst/wax separation
- Integration of power production with synthesis gas conversion
- Carbon capture and sequestration
- Hydrogen separation
- Systems analyses to optimize the plant efficiency, operability, safety and economics

COAL AS RESOURCE FOR FUELS OF THE FUTURE

David Gray and Glen Tomlinson

Mitretek Systems
3150 Fairview Park Drive South
Falls Church
Virginia 22042

Introduction

Oil is a finite resource and there is credible and increasing evidence to suggest that world oil production could peak and start to irreversibly decline within a decade or two. Some analysts even expect peak oil production to occur as soon as 2007. Abundant, low cost liquid hydrocarbon fuels that power automobiles, trucks, aircraft, trains, ships, and the military are the lifeblood of modern economic societies. There are no obvious alternatives to these liquid fuels envisioned for several decades. The peaking of world oil production, resulting in an irreversible decline in petroleum production and an imbalance between supply and demand, will dramatically increase oil prices and have severe long-term economic impacts both nationally and internationally unless decisive actions are taken.

The key question is how can the U.S. be prepared for this inevitable peak and decline in future world oil production? The long-term solution is to move completely away from a petroleum-based transportation system towards development of a more sustainable energy structure. Several options have been proposed for future clean transportation energy systems. The "Hydrogen Economy" and "electrification" are two of the most prominent suggestions. In both of these systems, primary energy sources are required to produce the energy carrier, be it hydrogen or electricity. These primary energy sources could be renewables, nuclear or fossil fuels. If fossil fuels were to be used, carbon dioxide capture and sequestration technologies might be necessary to limit greenhouse gas emissions.

Utilization of these future energy carriers in our transportation sector will require moderate to complete changes in the current transportation fuels infrastructure. Electric transportation will require significant breakthroughs in low cost, high power density electric storage battery technology and even when battery technology has improved, changing from the current petroleum based transportation infrastructure to an electric based system could take several decades. Transitioning from liquid petroleum to gaseous hydrogen will require a complete change in the current liquid fuels production, distribution, and end-use infrastructure. A change of this magnitude is likely to take many decades and billions of dollars to accomplish. The transition, of course, will be gradual and the actual time required to accomplish it is uncertain. Much depends on success in overcoming the major hurdles that this transition poses. These include obtaining breakthroughs in reliable and economically competitive fuel cell vehicle technology and hydrogen on-board storage. Also, large numbers of new central and distributed hydrogen production facilities will need to be constructed together with an extensive new pipeline delivery network and new dispensing facilities. The current Bush administration has already endorsed the concept of a future hydrogen economy and has proposed several government/industry programs including the FreedomCar and FutureGen initiatives. The goal of the Department of Energy is to speed the transition to a hydrogen economy and the hope is that the necessary technologies and infrastructure will be in place for major implementation of hydrogen by 2035. The National Academies in their study "The Hydrogen Economy: Opportunities, Costs Barriers and R&D Needs" supports the movement toward a hydrogen economy but also cautions that this fast tracking requires major breakthroughs and cost reductions that may delay a complete infrastructure change until 2050 or later. The Academy states, "Widespread success is not certain", and further recommends that DOE should "keep a balanced portfolio of R&D efforts and continue to explore supply-and-demand alternatives that do not depend upon hydrogen."

It is clear, therefore, that the sustainable hydrogen energy solution is a long-term option where hydrogen, produced eventually from sustainable energy sources such as renewables and nuclear, is used in many energy sectors including transportation. Hydrogen has many potential advantages. It would eventually replace petroleum, which will be necessary once oil production has peaked and is in decline. It could essentially eliminate carbon dioxide emissions, reduce urban and regional pollution, and may provide a sustainable and affordable energy source for the future. As the National Academy cautions, if we embarked on this hydrogen transition today, as a high national priority, it is unlikely that a complete infrastructure change could be accomplished much before 2040. But with the threat of world oil peaking looming, 2040 may be too late to complete the transition to a hydrogen energy system and avoid an economic crisis.

If proactive action is taken to address future energy supply and demand, there are three approaches and all three must be addressed simultaneously: increase end use efficiency, diversify liquid fuels supply, and prepare for a long term non-petroleum-based economy like hydrogen or electricity. Reducing petroleum consumption can be accomplished by demand side management. This means implementing more stringent CAFÉ standards to improve fleet efficiency and encouraging deployment of hybrid electric vehicles. However, conservation alone is not a quick fix. It will take almost two decades before the benefits of improved end-use efficiency have major national impact. The supply side preparedness options are to supplement declining petroleum fuels with liquid hydrocarbon fuels from our non-petroleum domestic resources in the mid term and, in the long term, to eventually replace liquid fuels with hydrogen or electric power obtained from renewable resources.

If liquid hydrocarbon fuels are to be produced from our non-petroleum domestic energy resources then the choices are biomass, natural gas, shale oil, or coal. Although several domestic resources will be required in a balanced energy portfolio, there are limits to each potential resource. Biomass fuels can make a contribution but will be limited because of huge land use requirements. Domestic natural gas production is in decline and the gas would have to be imported as LNG. There is no commercial technology yet to exploit methane hydrates, although they could be important in the future. Shale oil, while a large domestic resource, lacks commercially viable technology. The most practical supply option is to produce liquids from the nation's coal reserves. Coal, our most abundant domestic fossil resource, with over 250 years supply, could therefore be a practical and major source of clean liquid fuels. This paper discusses the concept of using our vast coal resources to provide liquid hydrocarbon fuels in the mid term and hydrogen in the long term.

Using Coal to Produce Clean Liquid Hydrocarbon Fuels

At the present time ***no*** coal-based facilities based on modern entrained gasification have been constructed that can produce both liquid transportation fuels and electric power. In the US there are two operational IGCC plants producing only electric power. These are the Polk plant near Tampa, Florida and the Wabash facility in Indiana. The Tampa plant uses the Texaco coal gasification process and the Wabash plant uses the E-Gas process. Both Texaco and E-Gas are modern entrained flow gasifiers.

At Mitretek Systems conceptual commercial plants have been simulated using computer models to estimate the technical performance and economics of coproduction plants. If current technology were used, the required selling price (RSP) of the clean liquid fuels produced would be about $37/barrel, advanced technology with no carbon sequestration would reduce this cost to about $31/barrel, and advanced technology with carbon sequestration would require a RSP of about $40/barrel. On a crude oil equivalent basis these RSPs should be reduced by at least $5/barrel because these high quality Fischer-Tropsch fuels will have a premium over crude oil of at least $5/barrel. Therefore the crude oil equivalent RSP for the advanced sequestered plant will be $35/barrel if the value of the coproduced power were $36/MWH. If the power value were $50/MWH, the RSP of the liquid fuels would be reduced to $30/barrel on an equivalent crude oil basis.

Using Coal to Produce Hydrogen

At Mitretek Systems conceptual commercial plants have also been simulated using computer models to estimate the technical performance and economics of producing hydrogen and electric power from coal. The performance and economics of these technologies are analyzed including configurations for carbon sequestration. For comparison, the economics of producing hydrogen from natural gas has been included.

Hydrogen can be produced from coal with current gasification technology at about 64 percent efficiency (HHV basis) for a cost of production in the range $6.50 to $7.00 per MMBtu. The need to sequester carbon dioxide from such a facility would raise this production cost to just over $8.00/MMBtu and decrease efficiency to about 59 percent. Advanced gasification technology and membrane separation has the potential to reduce the cost of production of hydrogen with carbon sequestration to less than $6.00/MMBtu and increase the efficiency of production to about 75 percent. However, considerable additional R&D and performance demonstration is necessary to verify this.

If hydrogen is produced in an advanced gasification coproduction facility that also generates electric power the production costs of the coproduced hydrogen can be reduced depending on the value of the power. If the coproduced electric power is valued at $35.6/MWH (the cost of producing power from a natural gas combined cycle plant (NGCC)) hydrogen can be produced for about $5.50/MMBtu. If the carbon dioxide is sequestered in this coproduction facility, the cost of hydrogen is only slightly increased if it is assumed that the coproduced power is valued at $53.6/MWH (the cost of producing power from a sequestered NGCC plant). Utilization of advanced membrane separation technology has the potential to reduce hydrogen production costs to about $4.00/MMBtu.

The greatest potential for reducing the production cost of hydrogen from coal is in configurations that include solid oxide fuel cells (SOFC). Coproduction facilities that use SOFC topping cycles to produce electric power and hydrogen have the potential to reduce the production cost of hydrogen to below $4.00 per MMBtu. Clearly such potential warrants continuing RD&D in such integrated facilities that include advanced coal gasification, SOFC topping cycles, and advanced membrane separation technologies. However, it must be cautioned that many of these advanced systems are only in the research phase and significant progress in demonstration and scale up must be made before these systems become a commercial reality.

Costs of producing hydrogen from traditional steam methane reforming of natural gas are of course dependent on fuel costs. If natural gas is $3.15/MMSCF then the resulting cost of hydrogen is about $5.50/MMBtu. Eventually sustainable production of hydrogen from renewable sources like sunlight using photovoltaic (PV) water electrolysis could be a future goal. Continuing RD&D to significantly reduce the costs of PV systems is necessary for hydrogen production costs to be in the same range as production from coal.

Carbon Dioxide Emissions Implications of Using Coal to Produce Clean Fuels and Hydrogen

The carbon dioxide implications of using coal to produce both hydrogen and clean liquid fuels have been analyzed. Plant configurations that capture and sequester the carbon dioxide have been simulated along with plants that do not capture the carbon dioxide and the resulting tailpipe carbon dioxide emissions have been estimated and compared to those from conventional petroleum-based transportation systems. For clean liquid fuels systems, a future sequestered coproduction plant producing transportation fuels used in diesel/hybrid vehicles and electric power will produce only about 0.16 pounds of net carbon dioxide per mile compared to 0.79 pounds of carbon dioxide per mile for a current conventional petroleum-based vehicle.

For coal to hydrogen systems, if the hydrogen produced is used in fuel cell vehicles that obtain 62.5 miles per gallon, even with no carbon capture and sequestration the resulting carbon dioxide emissions would only be about one percent higher than conventional current petroleum based systems.

Acknowledgement. This work was supported by the United States Department of Energy's National Energy Technology Laboratory (NETL) under a subcontract with Concurrent Technologies Corporation under contract DE-AM26-99FT40465.

CATALYTIC DEHYDROGENATION OF HYDROCARBONS: ALTERNATIVE, ONE STEP PROCESS TO PRODUCE PURE HYDROGEN AND CARBON NANOTUBE BYPRODUCTS

Gerald P. Huffman, Naresh Shah, Yuguo Wang, Frank E. Huggins

Consortium for Fossil Fuel Science (CFFS), University of Kentucky, 533 South Limestone Street, Lexington, KY 40508-4005

Introduction

Traditionally, hydrogen has been produced by reforming of natural gas to produce synthesis gas, followed by the water-gas shift reaction to convert CO to CO_2 and produce more hydrogen, followed by separation and purification procedures. In the "FutureGen" concept[1] advocated by the U.S. Department of Energy, the syngas would be produced by coal gasification.

Non-oxidative, catalytic decomposition of hydrocarbons is an alternative, one-step process to produce pure hydrogen. Nanoscale, binary Fe-based alloy catalysts supported on high surface area alumina [(0.5%M-4.5%Fe)/Al_2O_3, M=Mo, Ni or Pd] have been shown to have high activity for the catalytic decomposition of undiluted methane, ethane, or propane into pure hydrogen and multiwalled carbon nanotubes[2,3,4]. One of the problems with non-oxidative dehydrogenation is coking of the catalyst and reactor due to carbon build up. Under proper reaction conditions, however, these binary catalysts promote the growth of carbon nanotubes that transport carbon away from the catalyst surfaces, thereby preventing catalyst deactivation by coking as well as producing a potentially valuable by-product.

For utilization of fuel cells in vehicles, it is desirable to have a simple process for producing hydrogen from liquid fuels on-board. Therefore, we have also developed catalysts that are very effective for one-step production of pure hydrogen from cyclohexane and methyl cyclohexane[5].

Experimental Procedures

Detailed descriptions of the experimental procedures have been given elsewhere[2,4,5,6]. Briefly, the catalysts are prepared by deposition of the metal precursors onto the alumina or stacked-cone CNT by either coprecipitation or incipient wetness procedures using aqueous solutions of the appropriate metal salts. The resulting paste is extruded into pellets that are vacuum-dried and calcined for 5 hours at 500°C. Normally, one gram of catalysts is loaded in the continuous flow reactor and reacted in situ in flowing hydrogen at 700°C for 2 hours prior to reaction. The undiluted hydrocarbons are then fed to the reactor in precisely controlled amounts using mass flow controllers for gaseous alkanes and a syringe pump for liquid hydrocarbons. The products are measured by on-line gas chromatography.

Results and Discussion

Gaseous alkanes. Nanoscale, binary, Fe-M catalysts supported on alumina (0.5%M-4.5%Fe/γ-Al2O3, M = Ni, Mo, or Pd) have been shown to decrease the decomposition temperature of methane, ethane, and propane by 400-500 ºC. For methane (Figure 1), the only decomposition products are hydrogen and carbon in the form of multi-walled carbon nanotubes (CNT), while ethane and propane decompose to hydrogen, methane, and CNT. The most active temperature range for all three feed gases is 650-800 ºC, where 70–90 % of the product gas is pure hydrogen and the remainder is unreacted methane. In Figure 1, the hydrogen production from methane is shown as a function of temperature for the three binary catalysts, a 5% Fe/Al_2O_3 catalyst and the alumina support (non-catalytic).

Characterization of the catalysts by XAFS and Mössbauer spectroscopy, TEM, and XRD indicates that the active phase is an Fe–M–C austenitic metal alloy and that the catalyst particles are anchored to the alumina support by an Fe-aluminate, hercynite[6]. The catalysts exhibit good time on stream behavior because the Fe-M-C phases are very effective in stabilizing carbon in the form of CNT, which efficiently carry the carbon away from the active alloy particle surfaces.

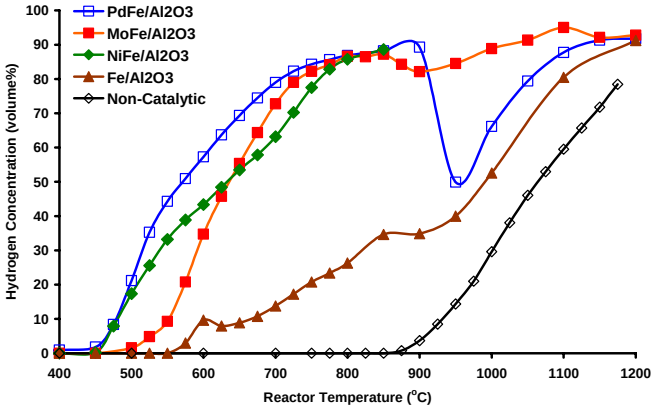

Figure 1. Catalytic decomposition of methane: hydrogen concentration vs. temperature

High resolution TEM has been used to investigate the structures of the CNT. Multi-walled CNT with parallel, concentric, graphene walls are produced at high temperatures (650-700 ºC). At low temperatures (450-500 ºC), a stacked–cone CNT (SCCNT) structure is produced in which the graphene sheets lie at an angle to the tube axis, which results in extensive graphene sheet edge openings at the circumference of the CNT (Figure 2). Consequently, most of the graphene sheet surface, both exterior and interior, is accessible from the outer periphery of the SC-CNT. Additionally, the outer surface of the SC-CNT has a high density of active carbene sites[7]. Because of this structure, the SC-CNT appear promising as hydrogen storage materials, catalyst supports, and sorbents. Preliminary measurements on hydrogen storage have been conducted by Bockrath and co-workers at the National Energy Technology Laboratory[8]. We have explored the use of SC-CNT as catalyst supports, as discussed further below.

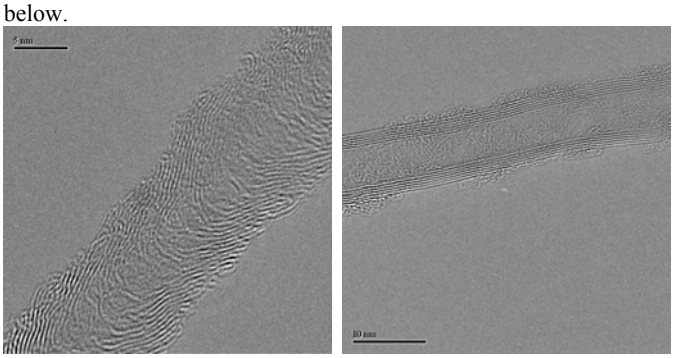

Figure 2. Catalytic decomposition of propane produced stacked-cone CNT at 475 ºC and multi-walled CNT with concentric parallel graphene sheets at 625 ºC.

Liquid hydrocarbons. In our initial studies of catalytic dehydrogenation of liquid hydrocarbons, we are investigating dehydrogenation of the model compounds cyclohexane and methyl cyclohexane. Cyclohexane is completely converted to benzene and hydrogen at 315 ºC using a catalyst consisting of only 0.25 wt.% Pt supported on stacked-cone CNT (Figure 3). Similar results were obtained for the catalytic dehydrogenation of methyl cyclohexane to toluene and hydrogen. Additional studies are planned using several alloy catalysts and other hydrocarbon liquids, including Fischer-Tropsch fuels.

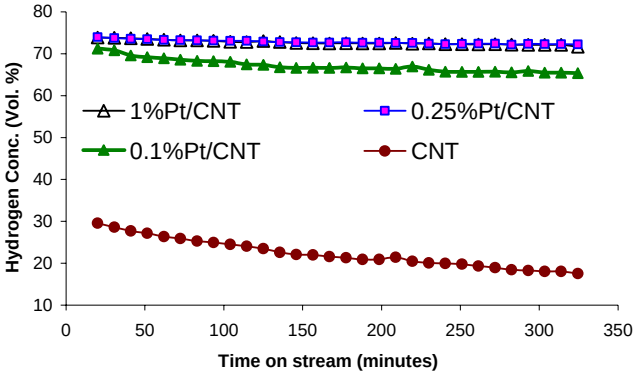

Figure 3. Hydrogen production by catalytic dehydrogenation of cyclohexane using Pt on SC-CNT catalysts. The results obtained using the SC-CNT alone are also shown.

Future work

Topics to be investigated in future research are briefly summarized below.

1. Development of a fluid bed process for continuous production of hydrogen and carbon nanotubes by catalytic dehydrogenation of gaseous alkanes.
2. Further investigation of applications for stacked-cone CNT, including gas storage, catalyst supports, and as environmental sorbents.
3. Development of more economical alloy catalysts for dehydrogenation of hydrocarbon liquids.
4. Catalytic dehydrogenation of additional hydrocarbon liquids, including Fischer-Tropsch fuels.
5. Carry out an economic and energy balance analysis of catalytic dehydrogenation of gaseous and liquid hydrocarbon fuels.

Acknowledgement. This research was supported by the U.S. Department of Energy, Office of Fossil Energy, under the management of the National Energy Technology Laboratory, U.S. DOE Contract No. DE-FC26-02NT41594.

References

1. http://www.fe.doe.gov/programs/powersystems/futuregen/
2. Shah, N.; Panjala, D.; Huffman, G.P. *Energy & Fuels,* **2001,** *15(6)*, 1528-34.
3. Makkuni, A.; Panjala, D.; Shah, N.; and Huffman, G.P. *ACS Fuel Chemistry Div. Preprints*, **2002**, *47(2)*, 782-783.
4. Shah, N.; Wang, Y.; Panjala, D.; Huffman, G.P. "Production of hydrogen and carbon nanostructures by non-oxidative catalytic dehydrogenation of ethane and propane", *Energy & Fuels* **2004**, *18(3)* in press.
5. Wang, Y.; Shah, N.; Huffman, G.P. "Pure hydrogen production by partial dehydrogenation of cyclohexane and methyl cyclohexane over nanotube supported Pt and Pd catalysts", submitted to *Energy & Fuels.*
6. Shah, N.; Pattanaik, S.; Huggins, F.E.; Panjala, D.; Huffman, G.P., *Fuel Processing Technology*, **2003**, *83*, 173-183.
7. Radovic, L.R.; and Bockrath, B. *ACS Fuel Chemistry Div. Preprints*, **2002, *47(2),*** 428.
8. Bradley Bockrath et al. (2003) unpublished research.

TRANSPORTATION FUELS AND DOE'S VISION OF THE FUTURE

Kevin Stork and Stephen Goguen

U.S. Department of Energy
Office of FreedomCAR and Vehicle Technologies
EE-2G/Forrestal Building
1000 Independence Avenue, S.W.
Washington, DC 20585

Introduction

The Department of Energy's end-use transportation fuels research is coordinated by the Fuels Technologies Sub-Program within the FreedomCAR and Vehicle Technologies Program in the Office of Energy Efficiency and Renewable Energy, and is designed to support the major R&D programs in transportation research including the Freedom CAR Initiative and the 21st century Truck Partnership (1). The Fuels Technologies sub-program has three component activities as shown in Figure 1:

- Advanced Petroleum-Based Fuels (APBF)
- Non-Petroleum-Based Fuels (NPBF)
- New Technology Impacts

APBF and NPBF activities are undertaken to enable current and emerging advanced combustion engines and emission control systems to be as efficient as possible while meeting future emission standards and to reduce reliance on petroleum-based fuels. To differentiate these two activities, an advanced petroleum based fuel consists of a petroleum base fuel derived from crude oil, possibly blended with performance-enhancing non-petroleum components. In contrast, a non-petroleum based fuel is envisioned as consisting of a fuel or fuel-blending component derived primarily from non-crude-oil sources such as agricultural products, biomass, natural gas, or coal.

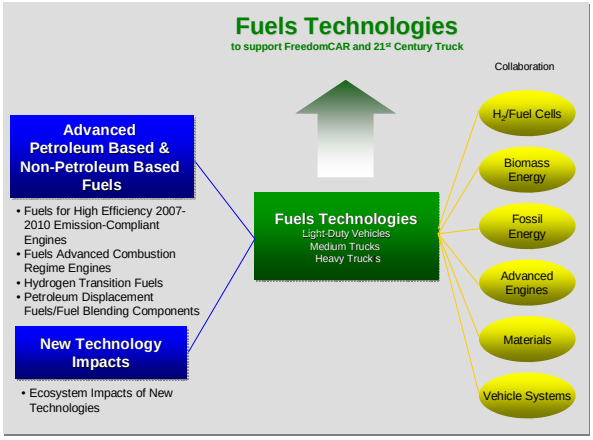

Figure 1. Activities, Collaborations, and Outputs of the Fuels Technologies Sub-Program

A major focus of both the APBF and NPBF activities is to determine the impacts of fuel properties on the efficiency, performance, and emissions of advanced internal combustion engines. For the long term, the Fuels Technologies sub-program is focused on fuels optimized for advanced combustion regimes, a general term intended to include a variety of in-cylinder strategies that have the potential to provide diesel-like or greater efficiency with extremely low engine-out emissions. Homogeneous charge compression ignition (HCCI) and low-temperature combustion (LTC) are examples of such combustion regimes. Research will be conducted to identify fuel-related factors which can foster the expansion of HCCI and LTC operability. Co-development of fuels and engines is likely to be a necessary step in the post-2010 timeframe due to increasingly strict emissions regulations. This strategic approach of co-development necessitates a much-improved state of fundamental knowledge about fuel composition and properties, and their impact on engine combustion phenomena. Additionally, the NPBF activity (Figure 2) has the goal of identifying practical, economic fuels and fuel-blending components which have the potential to directly displace significant amounts of petroleum. These fuels and fuel components are anticipated to be derived from non-fossil sources such as biomass, vegetable oils, and waste animal fats, as well as from fossil sources other than light, sweet crude oil such as natural gas, heavy crude, oil sands, oil shale, and coal. The production of diesel fuel from these sources is technically feasible and some are coming into limited use in the US. The NPBF activity focuses on the properties and quality of the finished fuels derived from these sources and not primarily on their production.

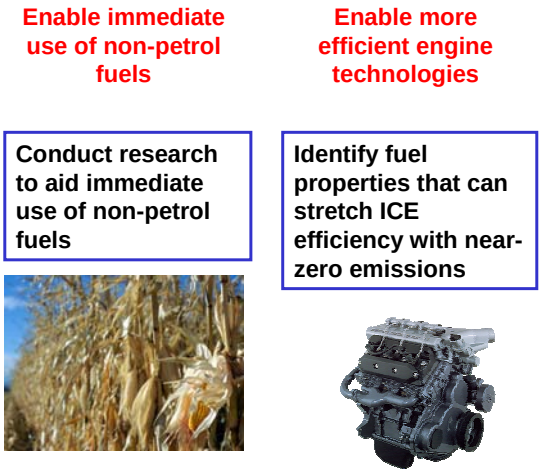

Figure 2. NPBF aims to replace petroleum-based fuels and enable more efficient engine technologies

Specific Program Goals of the Fuels Technology activity relative to reducing the US dependence on petroleum include:

- By 2007, identify fuel formulations optimized for use in 2007-2010 technology diesel engines that incorporate use of non-petroleum-based blending components with the potential to achieve at least a 5 percent replacement of petroleum fuels.
- By 2010, identify fuel formulations optimized for use in advanced combustion engines (2010-2020) providing high efficiency and very low emissions, and validate that at least 5 percent replacement of petroleum fuels could be achieved in the following decade.

Current Status

World crude oil is becoming heavier (lower API gravity) and more sour (including greater amounts of sulfur) over time. This trend is well-established and not expected to change. Moreover, much domestic crude is heavy, such as California crude from the San Joaquin Valley. Many potential future sources of energy are heavier still, including bituminous coal and oil sands. These sources may present different refining issues than light crude and the fuels

produced from these feedstocks may differ from those for which our domestic refining industry is optimized. On the positive side, Venezuelan and domestic heavy crude use in US refineries is well-established and refining of synthetic crude derived from oil sands is growing in Canada and entering US petroleum pools. Fischer-Tropsch diesel fuels, synthesized from natural gas or coal, have been studied in numerous engine tests to determine their impact on emissions and have been used as a blending material in California diesel fuels since 1993. Use of fuels derived from biomass appears to be increasing in Europe. Exploiting some of these developments presents a significant opportunity for displacement of foreign petroleum in the US and is an important element of the NPBF activity.

More detail of the chemistries of these new fuel sources is needed and will require cooperation between DOE, national laboratories, private industry, and universities. The APBF and NPBF activities can play an important role to in the pre-competitive development of these fuel sources in partnership with the energy, engine and automotive industries, and universities.

A recent workshop (2) gathered representatives of these groups and made many recommendations including:

- Research is needed to determine optimal fuel properties for advanced combustion engines
- Renewable fuels and blending components need to be analyzed on a "well-to-wheels" basis for cost effectiveness and carbon reduction
- New fuels need to be compatible with existing vehicles and fuel infrastructure

Barriers to Program Implementation

The primary goal of the APBF and NPBF activities is to identify fuel formulations with increasingly significant non-petroleum components that could replace petroleum fuels and that will enable engines and vehicles to be more energy-efficient while meeting future emissions standards. Specific barriers include:

- Inadequate data and predictive tools for fuel property effects on combustion and engine optimization
- Inadequate data and predictive tools for fuel effects on emissions and emissions control system impacts
- Long-term impact of fuel and lubricants on emission control systems
- Infrastructure and cost

The Fuels Technology Program is addressing these barriers with guidance and assistance from representatives of energy, automotive, and engine companies, industry associations, national laboratories, and universities.

Task-Based Approach to NPBF Research and Development

The program plan is being implemented with three major tasks and associated sub-tasks designed to address the barriers and specific recommendations from partner and advisor groups.

Task 1. Fuels and Lubricants to Enable High Efficiency Engine Operation while Meeting 2007–2010 Standards

- Evaluate long-term degradation and loss of effectiveness of light- and heavy-duty engines equipped with 2007–2010 technology emission control devices and using 15-ppm-sulfur diesel fuel
- Improve fundamental understanding of the effect of fuel and lubricant composition on aftertreatment systems by applying experimental and modeling approaches
- Identify fuel properties other than sulfur that are critical to improving the efficiency, performance, and emissions of light-duty diesel engines and aftertreatment systems
- Develop measurement techniques and characterize unregulated emissions from 2007–2010 engines and aftertreatment system
- Study fuels-based in-cylinder strategies to achieve high-efficiency, low-emissions operation at high power density and to improve understanding of hydrocarbon molecular structure effects on the soot generation by diesel fuel constituents

Task 2. Fuel Properties Effects on Advanced Combustion Engines

- Develop fundamental understanding of fuel effects on in-cylinder combustion and emissions formation processes in advanced combustion regimes through experimental and modeling approaches
- Develop predictive tools that relate molecular structure to ignition behavior and heat release for fuels used in advanced combustion engines
- Evaluate new fuels and fuel blends for efficiency, emissions, and operating stability with advanced combustion regimes
- Evaluate the potential of reforming small amounts of fuel to generate additives that can be used to achieve fast control in low-temperature combustion modes
- Evaluate the performance of traditional lubricant formulations in engines using advanced combustion regimes and identify any performance deficiencies

Task 3. Petroleum Displacement Fuels/ Blending Components

- Study combustion and emissions formation processes of NPBFs and blending components using experimental and modeling approaches
- Identify renewable and synthetic fuel blending components that provide enhanced efficiency, performance, and emissions characteristics
- Quantify the potential for improving engine and/or vehicle fuel economy through the use of renewable bio-lubricants
- Enhance the use of petroleum displacement fuels and NPBF infrastructure development through technical forums and by providing specialized technical support to early adaptors of advanced NPBF vehicle technologies
- Review and revise appropriate codes and standards to increase the availability of petroleum displacement fuels

Summary

The Fuels Technologies program emphasizes the linkage between fuel properties and performance in advanced combustion regimes and emissions control technology, as well as petroleum displacement. Research in the program focuses on developing an understanding of fuel chemistry effects and predictive, data-based tools for fuel performance.

References

1) Fuels Technologies Sub-Program, Chapter 4.7, FCVT Multi-Year Program Plan, U.S. Department of Energy, draft form, 2004.
2) Invitational Workshop on Advanced Combustion and Fuels, Summary Report, U.S. Department of Energy, FreedomCAR and Vehicle Technologies Program, June 16-17, 2003.

FUEL EFFECTS ON SPARK ASSISTED HCCI COMBUSTION IN A GASOLINE ENGINE

Bruce G. Bunting

Engineering Science and Technology Division
Fuels, Engines, and Emissions Research Center
Oak Ridge National Laboratory
2360 Cherahala Blvd.
Knoxville, TN 37932

Introduction

Homogeneous charge compression ignition combustion offers the potential for reduced nitrogen oxides (NOX) emissions and improved fuel economy in internal combustion engines. In this form of combustion, the fuel and air are premixed and brought to reaction conditions during the compression stroke of an engine. If conditions are just right, the fuel rapidly ignites at the right time (near top dead center) and produces work during the expansion stroke. Controlling the process generally requires a large dilution of the charge with excess air or high levels of exhaust gas recirculation to limit burn rate. This dilution also reduces peak flame temperature which results in lower NOX generation. Some form of additional energy input is also used to control reaction kinetics, often taking the form of intake temperature control. Heat release is faster than conventional IC engine combustion and can result in improved fuel efficiency. Since the fuel ignition process is kinetically driven, fuel properties also play a large role in the process. In various forms, this technology can be applied to gasoline, diesel, or natural gas fueled engines. The main barriers to the implementation of this combustion technology are stability and control and operation at low and high engine speeds and loads. There is a large amount of research being conducted in these areas.

The work described in this presentation was conducted in a single cylinder, port fuel injected, spark ignited research engine equipped with hydraulically actuated variable valve timing. HCCI combustion was initiated by early closing of the exhaust valve to retain exhaust in the cylinder, adding both increased temperature and pressure to the subsequent compression and combustion processes. Four gasoline range fuels were investigated which varied primarily in their motor octane number (MON). Trends were found that higher MON resulted is slower combustion, lower peak pressures, improved fuel efficiency, and lower NOX emissions. These trends may also show some fuel chemistry or property effects which could not be sorted out with the number of fuels tested. Other work was done relative to spark assist of HCCI combustion to improve operating range, stability, and control.

Experimental Work

A photo of the engine and main attributes are shown in Figure 1. Data was taken at a variety of speed, load, and timing conditions, but only data from 1600 rpm and 3.0 bar indicated mean effective pressure (IMEP) will be presented here. This condition represents a part load condition typical of US passenger car engine operation. All tests were run at stoichiometric fuel / air ratio (lambda = 1). This engine is located at AVL Powertrain Engineering, Inc. in Plymouth, MI and was operated under sub-contract to ORNL.

The test rig was equipped with a complete emissions bench, combustion pressure analysis, and the normal compliment of engine instrumentation. Intake and exhaust valve timing and lift, spark timing, and fuel injection quantity were controlled with test cell automation and could be varied with the engine in operation.

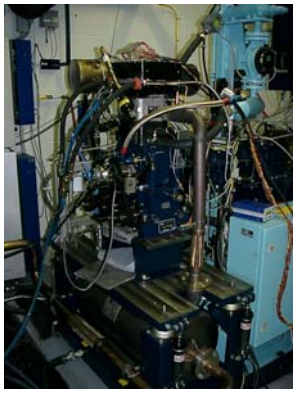

- **Capable of HCCI, mixed mode, and conventional operation**
- **500 cc, 11.34 C/R**
- **2 valves, naturally aspirated**
- **Gasoline port fuel injection**
- **Spark ignition**
- **Fully variable valve actuation**
- **HCCI initiated by early exhaust valve closing**
  - **Retains heat in cylinder**
  - **Internal EGR**
  - **Typically operates at > 50% EGR**

Figure 1. Single cylinder research engine with list of main attributes.

Analysis of this engine is somewhat complex because exhaust is retained in the cylinder rather than externally recirculated, so that it is difficult to measure. There are also confounding effects between total mass, heat, pressure, and residual gas composition. The engine was operated in conventional combustion mode as well in order to document performance improvements from HCCI operation. Figure 2 presents a comparison of engine operation in conventional and HCCI modes, and this figure also helps explain the operation of the engine in HCCI mode. In addition to varying the exhaust valve closing to trigger HCCI, intake valve opening is also varied in a symmetric way.

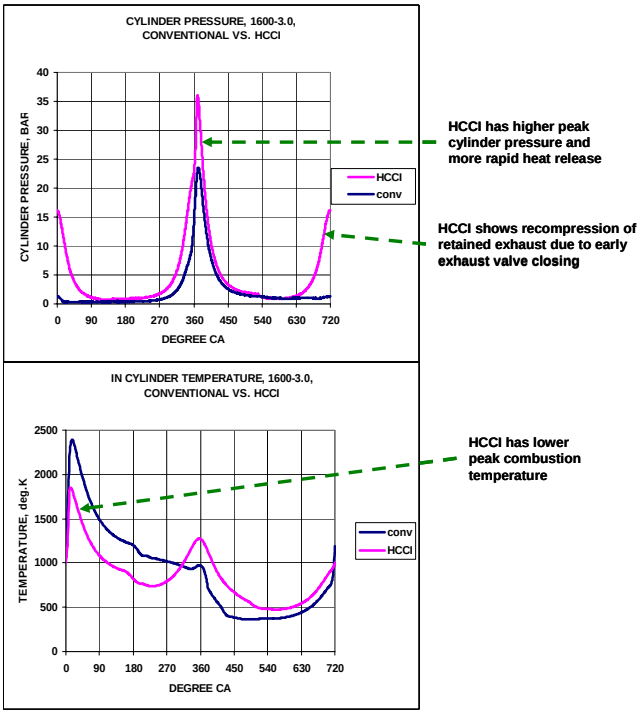

Figure 2. Comparison of engine operation and performance in conventional and HCCI modes.

Although not a subject of this presentation, over the speed and load range tested, the engine averaged 12% more fuel efficient and produced 95% less NOX in HCCI mode compared to conventional operation. Spark assist was found to extend the range of operation

and to assist in the transition from conventional to HCCI combustion. All data presented here is with spark assist active.

Four fuels were evaluated for their effect on HCCI engine operation. These fuels included an indolene base fuel and three fuels blended from pure hydrocarbon compounds. Fuels varied primarily in their MON values, but there were also differences in fuel chemistry and other properties. Fuel properties for the four fuels are shown in Table 1. The blended fuels were obtained from a major oil company who is assisting with this research.

Table 1. Properties of Fuels Tested

FUEL	RON	MON	DENSITY, 60F	RVP, PSI	GROSS HEATING VALUE, BTU/LB	IBP, C	FBP, C	FUEL BLEND
indolene	96.5	88	0.745	8.3	19550	31	198	full boiling range
fuel 1	97.4	80.9	0.822	3.8	18867	62	110	4 pure HC
fuel 2	99.5	86.8	0.76	3.2	19647	72	117	5 pure HC, 50% # 1and # 3
fuel 3	96.3	94.5	0.695	1.9	20487	98	104	2 pure HC - PRF

Results and Discussion

The combustion characteristics of the engine in conventional and HCCI combustion is best understood by running a series of test points with varying exhaust timing to transition the engine from conventional to HCCI mode. As more exhaust is retained in the cylinder (earlier exhaust valve closing), NOX output drops due to the resulting lower peak cylinder temperature. Compression pressures and temperatures increase until the engine transitions to HCCI combustion. At this point, duration of heat release (10 to 90% burn) drops from 20 to 30 deg. CA to less than 10 deg. CA, ISFC improves, and peak cylinder pressure and rate of pressure rise increase. In HCCI mode, the spark has only a small effect and the engine will continue to run if the spark is turned off. Combustion is initiated kinetically and 1% heat release takes place at 22.1 ± 0.2 bar cylinder pressure and 995 ± 20 deg.K cylinder temperature for indolene at 1600 rpm, 3.0 bar IMEP. This can be considered to represent the combustion conditions required for this fuel. Some of this verbal engine operation description can be visualized by examining Figure 2.

The four fuels were compared by running a group of test points in HCCI mode and comparing results obtained. The data presented represents an average of four sets of 160 engine cycles. The fuels were compared for both combustion characteristics and engine performance. Data is shown in Figure 3. General trends show that with higher MON, NOX and ISFC improve and combustion pressures and heat release rates are lower. Interestingly, all fuels show the same cylinder pressure at 1% heat release indicating similar ignition temperature characteristics. The trends with MON are not monolithic, and the two center fuels are reversed in their behaviors. This may be due to some other fuel property or fuel chemistry effects since indolene is a fully range fuel, while fuel 2 is blended from only 5 pure hydrocarbons. More fuels would be necessary to test this hypothesis.

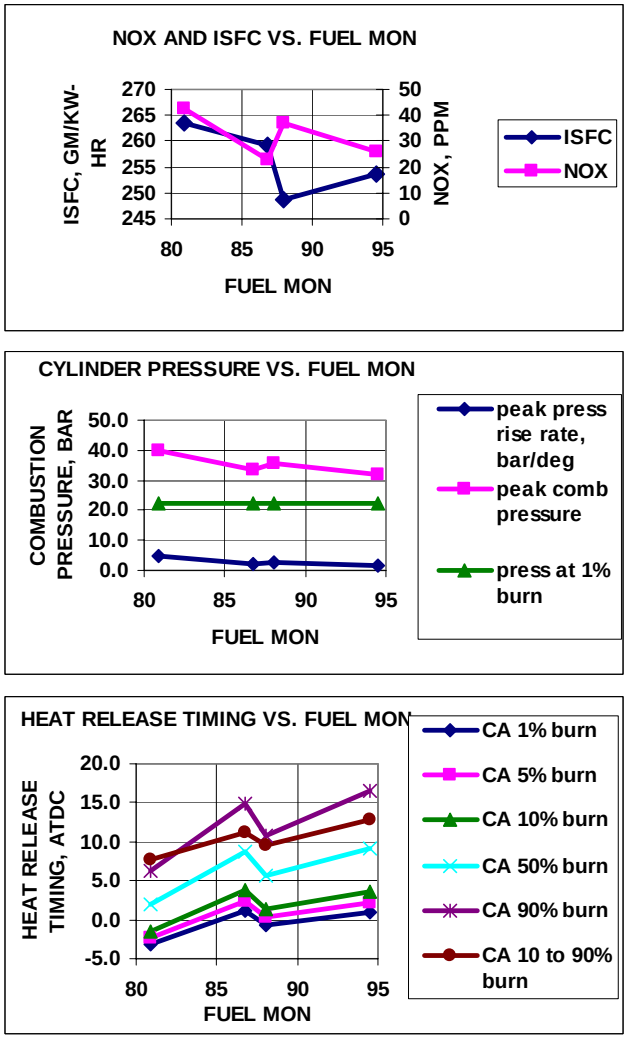

Figure 3. Combustion and Performance Results for Four Fuels.

Conclusions

An evaluation of four gasoline range fuels in a spark assisted HCCI engine showed combustion and performance characteristics trending with fuel MON. General trends show that with higher MON, NOX and ISFC improve and combustion pressures and heat release rates are lower. All fuels started heat release under similar cylinder conditions. The engine was also run in conventional mode and HCCI was found to have improved fuel efficiency and reduced NOX.

Acknowledgement. This work was supported by U.S. Department of Energy, Energy Efficiency and Renewable Energy Division, Steve Goguen and Kevin Stork program managers. The engine work and combustion analysis were performed by AVL Powertrain Engineering, Inc. in Plymouth, MI under subcontract to Oak Ridge National Laboratory. We would also like to acknowledge assistance obtained from a major U.S oil company in fuel blending, advice, and assistance with data interpretation.

THE HIGHLY EFFICIENT INTEGRATED PLASMA FUEL CELL (IPFC) ENERGY CYCLE FOR CONVERSION OF FOSSIL AND BIOMASS FUELS TO ELECTRIC POWER GENERATION AND HYDROGEN AND LIQUID TRANSPORTATION FUEL PRODUCTION WITH REDUCED OR ZERO CO_2 EMISSION

Meyer Steinberg

HCE LLC, Melville, NY 11747
mrsteinb@optonline.net

Introduction

In an earlier paper [1] the IPFC is principally applied to electrical power production. In this paper the IPFC is applied as a co-producer of electricity and hydrogen and/or transportation fuel (i.e., gasoline and diesel). The basic concept is the integration of the Hydrogen Plasma Black Reactor (HPBR) [2-3] with the Direct Carbon Fuel Cell (DCFC).[4-6]

The HPBR decomposes any dry carbonaceous fuel to elemental carbon and gaseous H_2 and CO. Since no oxygen or steam is used in this gasification reactor, CO gas is only formed when oxygen is present in the feedstock, as in coal and biomass fuel. Since the temperature in the thermal hydrogen arc is very high (~1500^{o}C) the conversion to elemental carbon and gaseous products is near 100%. Because the thermodynamic energy of decomposition of the feedstock fuel is small compared to the heating value of the feedstock, the thermal efficiency is found to be over 90%.[2-3] This means that the electrical energy requirement for the HPBR is very small. Based on the thermodynamic energy (enthalpy) of decomposition of natural gas and petroleum, the electrical energy efficiency (process energy efficiency) was determined to be 60% for an industrial unit.[3] Although, the specific energy requirement for decomposition of solid fuel (coal and biomass) is yet to be determined, this process efficiency was applied to the thermodynamics of decomposition of these feedstocks. It should also be noted that the thermodynamic energy (enthalpy) of decomposition is less for petroleum than for natural gas and coal is less than for petroleum. Other plasma reactors have been operated for steam gasification of solid fuels, however, these required higher power inputs because the steam gasification reactions are highly endothermic, requiring higher electrical energy inputs.[10] Due to the much lower endothermicity of the thermal decomposition reaction and operation in a dry hydrogen atmosphere the HPBR requires much less energy than the plasma steam gasifier.

The elemental particulate carbon is separated from the gas stream cyclonically or by asbestos bag filters or by absorption directly into a molten carbonate salt stream. The latter is preferred since the Direct Carbon Fuel Cell (DCFC) operates with a molten carbonate electrolyte. The ash should form molten agglomerates, which can be separated from the carbon particulates cyclonically or gravimetrically in a fluidized bed. The carbon/molten salt slurry is sent to the anode compartment of the DCFC and air is fed to the cathode. The mixed molten carbonate salt (Na, K salts) acts as the electrolyte operating at 700-800^{o}C. The carbonate ion carries the electrons from the cathode to the anode compartment through a membrane, which then reacts with the carbon at the anode releasing undiluted CO_2 gas thus completing the electrical fuel cell circuit. Voltage efficiencies of 80 to 90% have been obtained with amorphous carbon at reasonable current densities (0.2-0.8 Kw/M^2).[4-6] The overall reaction in the DCFC is the oxidation of carbon to CO_2, the theoretical thermodynamic efficiency of which is 100% since the entropy change for the reaction is zero.

The combination of HPBR with DCFC is unique in that no outside source of electricity is necessary to drive the process. The DCFC supplies the HPBR with electrical power and the HPBR supplies the carbon for operation of the DCFC. The high efficiency of the DCFC and the relatively low power requirements for the HPBR produces a highly efficient integrated system for electrical power generation. The gases from the HPBR after cleaning can be used to produce either H_2 or syngas depending on the type of feedstock used.

The flowsheet for hydrogen production is completed by adding a water gas shift (WGS) reactor to convert the CO to hydrogen and CO_2 with the addition of steam (water). The CO_2 is separated by membrane or absorption/stripping and a clean pure H_2 stream is produced for sale.

Alternatively the syngas can be water gas shifted either forward or reverse (depending on the feedstock) to produce a stream in which the ratio of H_2/CO is 2.0 for feed to a Fischer-Tropsch catalytic converter to produce either gasoline (C_8-C_{11} average C_8H_{18}) or diesel (C_{11}-C_{21} average $C_{16}H_{34}$) [7,8,9] transportation fuel. Figure 1 shows the IPFC-FT flowsheet.

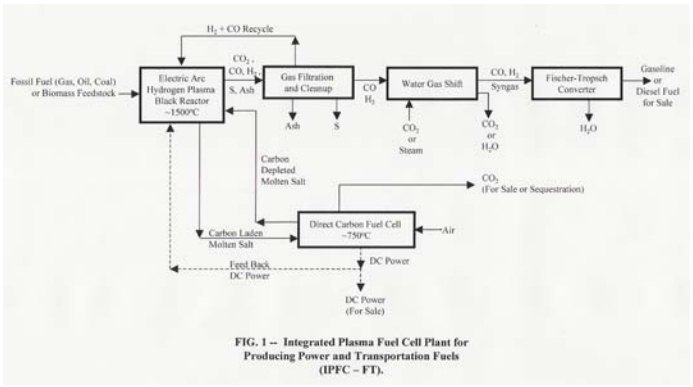

FIG. 1 -- Integrated Plasma Fuel Cell Plant for Producing Power and Transportation Fuels (IPFC – FT).

For reverse shift the CO_2 can be obtained from the DCFC. Note that using the higher heating value, the water gas shift reactions are essentially energy neutral ($\Delta H \cong O$). The exothermic reactions in the Fischer-Tropsch catalytic reactor are represented by the following typical reaction with the unit CH_2 representing the unit hydrocarbon fuel molecule: $2H_2 + CO = CH_2 + H_2O$. Typically, the enthalpy of reaction is ΔH = -49.5 Kcal/gmol of unit CH_2, exothermic

Energy Efficiency of IPFC

Using thermodynamic data for each of the feedstocks, the thermal efficiency of the IPFC is defined as follows: The Output Electrical Energy + Higher Heating Value of the Transportation Fuel (H_2 or CH_2) divided by the HHV of the feedstock for 5 fuel feedstocks. Integrated together with the assumed reactor efficiencies, the calculated thermal efficiencies for electricity and hydrogen production range around the 90% value.

Table 1 gives the mass and energy balances and the thermal efficiencies for electricity and transportation fuel production using the IPFC-FT cycle. The efficiencies range from 70% to 83% for the 5 feedstocks studied in this paper. The liquid hydrocarbon transportation fuel can be used in current internal combustion engine vehicles and in the recent gas-electric hybrids as well as in other automotive vehicles that will be developed in the future to increase miles/gal (mpg) efficiency. The benefit of liquid fuels is that the current infrastructure for distribution, storage and engines are in place, which is not the case for hydrogen as an automotive fuel in fuel cell vehicles.

Table 1
Integrated Plasma Fuel Cell (IPFC) Cycle
Electrical Power and Transportation Fuel Production
Mass and Energy Balances and Thermal Efficiency
Basis – 1 gmol of Feedstock Fuel

Fuel Feedstock	Natural Gas	Petroleum	N. Dakota Lignite Coal	Kentucky Bit. Coal	Biomass (wood)
Molar Composition (MAF)	CH_4	$CH_{1.7}$	$CH_{0.77}O_{0.24}$	$CH_{0.81}O_{0.08}$	$CH_{1.38}O_{0.81}$
(MW)	16.00	13.70	16.61	14.09	22.82
Plasma Decomp. Products Mole/Mole Fuel					
C	1.0	1.0	0.76	0.92	0.41
CO	0	0	0.24	0.08	0.59
H_2	2.0	0.85	0.385	0.41	0.69
Ash, S, N (wt%)	-	~1.0	9.8	12.6	1.1
Enthalpy of Decomp. Kcal/gmol feestock	18.0	3.0	3.6	4.8	12.7
Water gas shift, (WGS) gmol CO, and H_2 per mol feed to obtain $H_2/CO = 2.0$	0.667	0.283	0.032	0.083	0.163
Transportation Fuel Production Gasoline or Diesel gmol CH_2/mol feed	0.667	0.283	0.208	0.163	0.427

Electric Power and Transportation Fuel Production Enthalpy Energy Values in Kcal/gmol Fuel

Unit	Eff%					
DCFC	90	84.6	84.6	64.3	77.8	34.7
WGS	100	-	-	-	-	-
HPBR	60 consumed	-30.0	-5.0	-6.0	-8.0	-21.2
Net Electricity Prod.		54.6	79.6	58.3	69.8	13.5
F-T Gas. Diesel Fuel*		103.5	43.7	32.1	25.2	66.0
Total Energy Output		158.1	123.3	90.4	95.0	79.5
HHV of Fuel Feedstock		212.0	149.0	110.3	119.0	112.8
Thermal Efficiency %		74.5	82.8	82.0	79.8	70.4

*HHV of gasoline and diesel fuel = 154.5 Kcal/gmol

The CO_2 emissions from IPFC are compared to that of an equivalent IGCC plant providing the same quantity and ratio of product electricity and hydrogen output. Estimates of the efficiency of the IGCC vary from 54 to 72% while the IPFC efficiencies range from 87 to 92%. As a result, the CO_2 emission reduction for IPFC is from 20 to 40% less per unit energy in the products than the IGCC. Furthermore, CO_2 emitted from the IPFC is undiluted ready for sequestration. Whereas for IGCC, the CO_2 is diluted with nitrogen and steam.

The CO_2 emission reduction for IPFC at 82% efficiency compared to IGCC at 60% efficiency when electricity and transportation fuel (gasoline or diesel) are produced in the same relative amounts, when using a lignite coal is 26% lower than for IGCC. Compared to a coal burning steam plant generating power at 38% efficiency, the IPFC plant shows a 76.4% reduction in emission of CO_2 per unit of electricity. There is a 36.4% reduction in CO_2 for IPFC producing gasoline compared to a gasification synfuel plant producing gasoline alone.

Preliminary economic estimates (11) indicate that IPFC plants can produce electricity and hydrogen or transportation fuels at a significantly lower cost than conventional steam and combined cycle plants (NGCC and IGCC). Furthermore, production of two co-products permits adjusting the sale price of electricity upwards to meet current market price, which allows adjusting the price downward of the co-product IPFC synthetic transportation fuel to allow direct competition with current oil refinery production prices.

References

(1) Steinberg, M. *An Innovative Highly Efficient Combined Cycle Fossil and Biomass Fuel Power Generation and Hydrogen Production with Zero CO_2 Emission,* Second International Conference on Carbon Sequestration, US DOE, Alexandria, VA (May 6-8, 2003).

(2) Gaudernack, B. and Lynum, S. 11th World Hydrogen Energy Conference, Cocoa Beach, Florida, pp. 511-23 (June 1996).

(3) Seguin, L. The Karbomont Production Plant, Montreal Canada, Private Communication (2002).

(4) Cooper, J.F., et al., Turning Carbon Directly into Electricity, Science and Technology Review pp. 4-12, Lawrence Livermore National Laboratory, Livermore, CA (June 2001).

(5) Cooper, J.F., et al., Direct Electrochemical Conversion of Carbon" Report UCRL-JC-138900 DOERD-059, Lawrence Livermore National Laboratory, Livermore, CA (2000).

(6) Cooper, J.F. *Direct Conversion of Coal and Coal Derived Carbon in Fuel Cells*, 2nd International Conference on Fuel Cell Science, Engineering and Technology ASME, Rochester, NY (June 14-19, 2004).

(7) Probstein, R.F. and Hicks, R.E. *Synthetic Fuels,* pH Press, Cambridge, MA, **1990**; *271-276*.

(8) Xu, L. et al., Don't Rule Out Iron Catalysts for Fischer-Tropsch Synthesis, *Chemtec*, **1998**, *47-53*.

(9) Sasol Synfuels International Fischer-Tropsch Conversion, Johannesburg, South Africa (1997).

(10) Do, R.T. An Integrated Plasma Gasification Combined Cycle IPGCC) System for Many Domestic Fuels, Solena Group, Inc., Washington, DC (2002).

(11) To be presented in a subsequent HCE LLC report (2004).

FINDING FUELS FROM THE LAND – THE POTENTIAL FOR A LARGE SCALE CONTRIBUTION OF BIOMASS

Ralph P. Overend, Robert Perlack, Robin Graham, and Tom Foust

National Bioenergy Center
National Renewable Energy Laboratory
1617 Cole Blvd.
Golden, CO 80401

Introduction

The estimation of future biomass supplies for large scale fuels, chemicals and electricity production is confounded by the many ways in which biomass is generated and used. Today the biomass for energy stream is composed of residues from primarily industrial and societal activities. In the absence of major technological breakthroughs, future large scale use will require that land be allocated to feedstock production, and possibly will call for significant changes in the food, feed and fiber production systems through the introduction of multi-functional cropping systems that simultaneously meet demands for traditional uses as well as energy. Thus, the production of biomass feedstocks, and bioenergy use is today very dependent on the functioning of some other components of the economy -- the three major areas being forestry, agriculture, and the urban environment. As time goes on this dependency will become more strongly integrated with these sectors.

Source of Bioenergy

To simplify the discussion of biomass, it is necessary to provide some definitions and characterization of where in the economy biomass is generated or utilized as bioenergy. One methodology is to identify the stage of processing/utilization since the creation of the biomass by photosynthesis. Energy crops are a primary supply and involve the production and growth of biomass specifically for biomass to energy and fuels applications. Primary production is widespread in developing countries for fuelwood, as well as examples of Eucalypt forestry for charcoal production in iron production in Brazil [1]. Also in Brazil a significant fraction of the sugar cane crop is dedicated to ethanol production [2], while 9% of the corn harvest in the United States is used in the production of ethanol from starch [3]. Research and development in Europe and the United States is developing the use of woody or straw materials (lignocellulosics) as high yielding non-food energy crops. Primary residues are produced as a by-product of a primary harvest for another material or food use of grown biomass. A representative of this is the use of tops and limbs as well as salvage wood from forestry operations cutting saw-logs or pulpwood. This material along with forest thinning is a developing biomass supply system in Finland, for example [4].

Secondary and Tertiary Residues

The majority of biomass used today in the energy system is generated as secondary and tertiary residues. Secondary residues arise during the primary processing of biomass into other material and food products. Sugarcane bagasse is widely used to fuel combined heat and power plants (CHP) providing the heat and electricity needs of sugar processing as well as export of electricity to the grid. In the forest industries black liquor from kraft pulping is a major fuel for CHP and the recovery of process chemicals. The meat, dairy and egg production in concentrated animal feed operations (CAFO) is a rapidly growing area in which bioenergy production is part of the solution to environmental issues created by this landless food production system.

Tertiary residues, urban or post consumer wastes, are a major component of today's bioenergy system. In fact the official statistics of the IEA, for example, describes biomass as combustible renewables and waste, and in many countries the tertiary sector is captured under the title of municipal solid waste or MSW. The tertiary sector generates energy in combustion facilities as well as from the generation of methane as land fill gas (LFG) from properly managed burial of mixed wastes from cities. Methane is also produced in sewage treatment facilities. Individual rates of residue generation are currently about 22 MJ person^{-1} d^{-1} in the United States. This, combined with the high population densities of metropolitan areas, results in very high bioenergy potentials in this sector [5]. Currently, MSW and landfill gas contribute about 0.5 EJ of primary energy in the United States [6].

U.S. Projection

There is a consensus biomass resource potential estimate for 2020 in the U.S. that captures most of the sources described above, other than the CAFO potential [6]. This is described in the form of a supply curve and indicates that there are about 7 - 8 EJ of primary energy at less than 4.0 $ GJ^{-1}. This represents about 450 Mt of dry lignocellulosic biomass potential, which can be compared with today's utilization of about 190 Mt. The ultimate technical potential for biomass in the United States is not yet established, however, work is underway on what is called the Gigatonne scenario, which would investigate the effect of seeking double the 2020 projection for say the 2040 - 2050 period.

References

1. Rossillo-Calle, F.; Bezzon, G., *Production and use of industrial charcoal*, in *Industrial Uses of Biomass Energy: The example of Brazil*, F. Rossillo-Calle, S.V. Bajay, and H. Rothman, Editors. Taylor and Francis: London, 2000, pp. 183 -199.
2. Goldemberg, J., et al., *Ethanol learning curve--the Brazilian experience.* Biomass and Bioenergy, 2004, **26**(3): pp. 301-304.
3. NCGA, *World of Corn Consumption 2002*. 2003, http://www.ncga.com/03world/main/consumption.htm, National Corn Growers Association.
4. Eriksson, H.M.H. J.P.; Helynen, Satu, *Rationale for forest energy production*, in *Forestry Sciences*, J.B. Richardson, R.; Hakkila, P.; Lowe, A.T. and C.T. & Smith, Editors, Kluver Academic Publishers: Dordrecht, NL, 2002, pp. 1 - 17.
5. Chum, H.L.; Overend, R.P., *Biomass and Bioenergy in the United States*, in *Advances in Solar Energy: an Annual Review*, Y. Goswami, Editor, American Solar Energy Society: Boulder, CO. USA, pp. 83-148.
6. Haq, Z., *Biomass for Electricity Generation*. 2002, http://www.eia.doe.gov/analysis/2001anal08.html , Energy Information Administration.
7. Energy Information Administration, U.S. Department of Energy, Renewable Energy Annual 2002, November 2003, DOE/EIA-0603 (2002), Washington, D.C.

Technology Advances in Biobased Fuels

Kelly N. Ibsen

National Bioenergy Center
National Renewable Energy Laboratory
1617 Cole Blvd.
Golden, CO 80401

Introduction

In 2001 consumption of biodiesel (diesel from soybeans and other oil feedstocks) reached 20 million gallons and in 2003, ethanol production from starch topped 2.8 billion gallons. Both biobased fuels have had a long road to the limited percentage they have now in the fuel pool. Ethanol is roughly 2% of the gasoline pool and biodiesel is less than 0.5% of the diesel pool, and both are primarily used as additives. But new governmental and corporate policies are indicating that this is not just the beginning of biobased fuels but also biobased chemicals and materials. The demand for green but sustainable and profitable biobased products must lead to new feedstocks that are cheaper and more abundant, and the technologies to utilize them efficiently and economically. This paper discusses some of the recent advances in biochemical technology to convert biomass, specifically lignocellulosic biomass (i.e. non-starch biomass), to ethanol. This is a portion of the work being done under the Office of the Biomass Program (OBP) in the US Department of Energy and also in the private sector. Not discussed here, but equally important, are advances in syngas catalyst development and modular, distributed gasification systems that are components of OBP's thermochemical program.

The Advantages of Biobased Fuels

Fuels from lignocellulosic biomass reduce oil consumption and greenhouse gas emissions. A comprehensive study by NREL and a consortia of feed and soil experts found that "for each kilometer fueled by the ethanol portion of E85, the vehicle uses 95% less petroleum compared to a kilometer driven in the same vehicle as gasoline."[1] E85 is a blend of 85% ethanol and 15% gasoline. It is currently available in limited supply in the US for use in a FFV, or flexible-fuel vehicle, like the Ford Taurus. The energy balance (energy used to produce the fuel vs. energy in the fuel) from a life cycle assessment is positive for both starch[2] and lignocellulosic ethanol. Life cycle assessment results depend heavily on the data and boundaries used, and conflicting numbers have and will continue to be reported, but the value of these analyses is an increased understanding that practices in growing, collecting and processing the biomass can be optimized to reduce the fossil energy use and maintain the soil health.

Overcoming the Challenges of Biomass Conversion

Variability of biomass composition, recalcitrance to depolymerization and metabolism, and solids handling are a few of the key challenges to making biomass conversion technically and economically feasible.

Biomass Composition. Lignocellulosic biomass is a complex and non-standard feedstock. It contains a mix of long chain compounds, the fractions of which vary as a result of genetics, growing conditions, and collection methods. **Table 1** summarizes the primary constituents in biomass, such as agricultural residues (corn stover or straw), forest and mill residues, energy crops such as switchgrass and urban waste. Understanding and predicting the effect this variability has on processing needs is key to efficiently converting biomass via biochemical or thermochemical routes. Near infrared analysis (NIR) methods are being developed to infer the biomass composition quickly and cheaply. This will enable a "carbohydrate" or "carbon" biomass economy in which feedstocks are valued on these fractions, and processes can be optimized with feed-forward control.

Table 1. Major Components of Lignocellulosic Biomass

Component	Amount	Description
Lignin	15-25%	-Complex aromatic structure -Resists biochemical conversion -Requires high temperatures to convert
Hemicellulose	23-32%	-Polymer of 5 and 6 carbon sugars -Easily depolymerized -5 carbon sugars difficult to metabolize
Cellulose	38-50%	-Polymer of glucose -Semi-crystalline structure -Susceptible to enzymatic attack -Glucose easy to metabolize

In **Figure 1**, the measurement of several corn stover (the stalks, leaves and cobs) components via both NIR and wet chemical methods shows good correlation between the two.

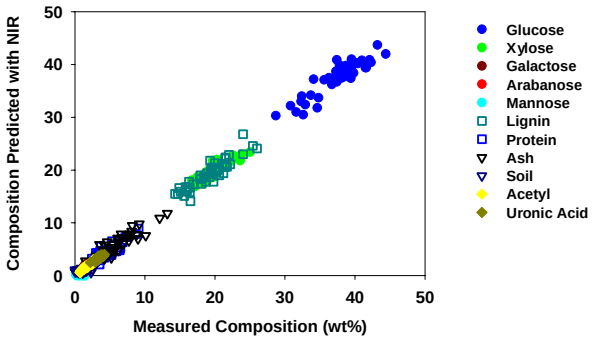

Figure 1. Correlation of NIR with wet chemistry methods for stover.

Recalcitrance to depolymerization. The highly linked structures of biomass make it resistant to depolymerization. Advances in both the thermochemical and biochemical methods of depolymerizing biomass include continued development of a host of various pretreatment methods that could suit certain feedstocks better than acid methods or create a new and different process intermediate. Through multi-year partnerships with Genencor and Novozymes Biotech, leading enzyme companies, the cost of cellulase, the catalyst for depolymerizing cellulose, has been reduced over 10 fold. The significance of the cost reduction in terms of its contribution to ethanol production cost is seen in **Figure 2**.

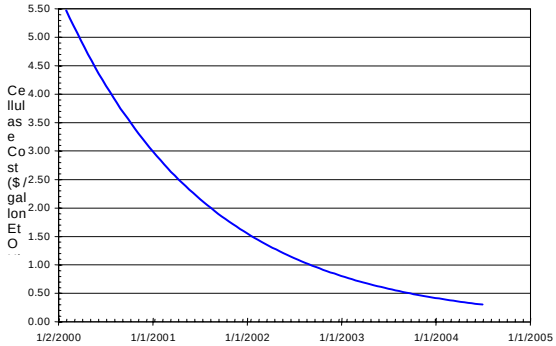

Figure 2. Cellulase enzyme cost reductions.

Solids handling. Maintaining a high solids loading throughout any process decreases the size of equipment and can reduce the capital cost of the plant. High solids pretreatments have been performed in the NREL pilot plant up to 35% solids, which reduces the cost of downstream equipment by as much as $0.18 per gallon ethanol from a 20% solids loading.

The Cost of Producing Ethanol from Biomass

Process configurations, mass and energy balances, and cost estimates provide quantified snapshots of the state of different biomass conversion technologies. NREL routinely develops process information like that shown in **Figure 3** to illustrate what portions of the process contribute the most to the production cost – this particular example is for an ethanol process using dilute acid.

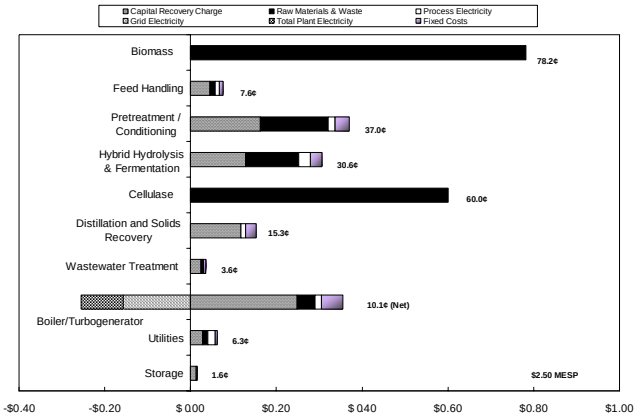

Figure 3. Estimate of current state of dilute acid technology

The other necessary picture to have is the target – where the R&D program is headed and what constitutes success. **Figure 4** shows the costs by process area of ethanol production from a dilute acid/enzymatic hydrolysis process for a production target of less than $1.10 per gallon ethanol, sufficient to compete in the corn ethanol market. Although there are many ways to get to a cost target, having at least one baseline pathway shows that the process is technically and economically feasible with appropriate R&D in the key areas. This target case was published in 2002 by NREL.[3]

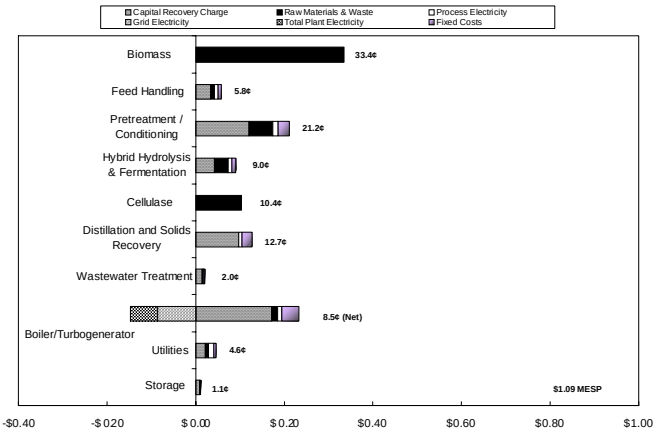

Figure 4. Target for entry into ethanol market.

Biorefineries

The biorefinery concept is considered by many to be the best way to boost the economic viability of biobased fuels. Its premise is that by adding high value chemicals from biomass (either starch or lignocellulose) to the product slate from an ethanol plant, one can buy-down the cost of producing the ethanol. Added to this is the benefit of producing biobased chemicals, which is becoming increasingly popular in both governmental and industry arenas for a variety of reasons including reducing the environmental footprint of chemical production. **Figure 5** shows one possible configuration for a biorefinery utilizing both biochemical and thermochemical conversion. Several companies including Dupont, Cargill, Cargill Dow and Dow have projects underway, some co-funded by DOE's OBP to develop these emerging biorefineries. Other companies that currently produce corn ethanol like Aventine Renewable Energy, Broin Companies and Abengoa Bioenergy, are developing value-added products from the solids stream resulting from corn ethanol production. These plants represent the current generation of biomass biorefineries that could also include the forest products industry.

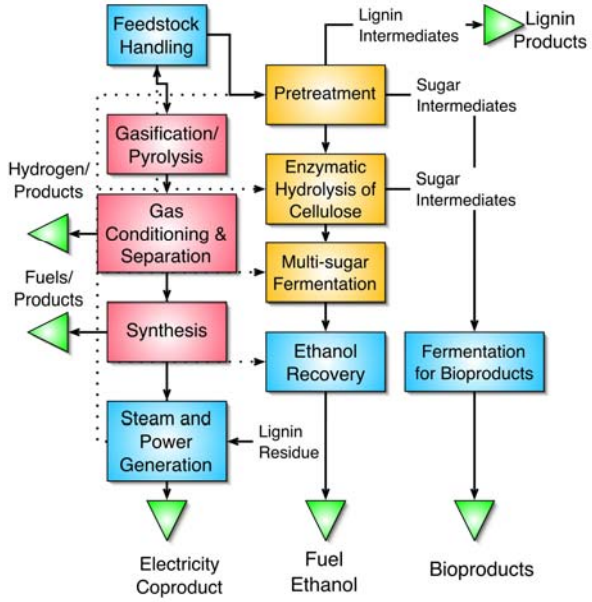

Figure 5. One biorefinery concept for lignocellulosic feedstocks

Conclusions

Affordable cellulases, varied pretreatment options, a fundamental understanding of biomass feedstocks, and capital cost reductions are all areas where significant advances are being made to make biomass conversion technology more technically and economically viable. Biorefinery concepts may enable integration into existing dry mills and eventually lead to stand alone facilities that produce fuels and other products from biomass. Thermochemical processes like gasification and pyrolysis provide diversity in processing and as such, enable a larger set of industries to utilize biomass.

Acknowledgement. The Office of the Biomass Program of the U.S. Department of Energy funded this work.

References

[1] Sheehan, J.; Aden, A.; Paustian, K.; Kendrick, K.; Brenner, J.; Walsh, M.; and Nelson, R. "Energy and Environmental Aspects of Using Corn Stover for Fuel Ethanol". In a special edition of *Journal of Industrial Ecology*, **2004**, *vol. 7, no 3-4*.

[2] Shapouri, H.; Duffield, J.; Wang, M. "The Energy Balance of Corn Ethanol: An Update", in *Agricultural Economic Report No. 813*. **2002**.

[3] Aden et al. "Lignocellulosic Biomass to Ethanol Process Design and Economics Utilizing Co-Current Dilute Acid Prehydrolysis and Enzymatic Hydrolysis For Corn Stover", NREL report TP-510-32438 **2002**.

RUNNING ON EMPTY REVISITED: LESSONS OF THE PAST FOR FUELS OF THE FUTURE

Howard P. Stephens, Virginia A. Stephens and James D. Cochran

Vision Trust, Inc.
P.O. Box 10423
Albuquerque, NM 87184

Introduction

Why hasn't more been accomplished in the last quarter of a century to solve America's energy problems? How long does it take to deploy fuel and energy alternatives? And, why does America, the most technologically advanced nation in the world, continue to have serious problems with fuel and energy supplies? To address these questions, the authors draw upon the extensive research that was the basis of the public radio documentary Running on Empty: America's Energy Crisis. The documentary traced history through the twentieth century to the roots of America's current energy crisis; surveyed current resources, consumption patterns and energy infrastructure; examined energy policy; and then looked ahead to see how conservation, new technology and untapped resources could help solve the U.S. energy crisis. In researching and producing the program, we found many lessons of the past that may aid in dealing with today's energy issues.

If development of technology were the only factor required to bring new fuels to the marketplace, America would have no shortage of fuel and energy supplies today. Obviously, this is not the case. Technology resulting from research and development (R&D) is just the first step of many processes involved in the deployment of new fuels and energy supplies. The issues involved in bringing fuel and energy technology to the marketplace are complex and integrated with our culture, economy, government, environment, and political system. In this short paper, we review a few significant lessons of the past to see how these may guide today's approaches for developing policy and deploying new technology for transportation fuels.

Running on Empty – the Documentary's Context and Content

We produced the public radio documentary *Running on Empty: America's Energy Crisis*, underwritten by the American Chemical Society's Fuel Chemistry Division, in response to a re-emerging energy crisis at the turn of the twenty-first century. After nearly two decades of a seemingly plentiful energy supply, Americans were again concerned about energy issues. Californians, especially, faced a major energy crisis. Attendees of the 2001 Spring National ACS Meeting in San Diego, California may recall the high level of public anxiety at the time. Californians were worried sick about the rolling electricity blackouts and the cost of natural gas and gasoline. Public apathy regarding energy issues had suddenly ended, at least in California.

While at the San Diego ACS meeting, there were daily news reports of business and school closings, and car crashes caused by traffic signal lights failing due to rolling electricity blackouts. ACS meeting attendees found flashlights on conference room tables with notes reminding them that blackouts could prevent speakers' presentations. Californians were deeply concerned about losing their jobs and the impact of a looming recession. They were experiencing in very real and personal economic terms just what fuel and energy shortages meant. Yet, news broadcasts reported only the effects of the crisis. They contained little information about the causes that would help the public to understand the developing energy crisis.

We asked ourselves: Why does America, the most technologically advanced nation in the world, continue to have serious energy problems? Why haven't Americans insisted on a long-term commitment to deal with the nation's energy woes?

We felt that America's complacency toward energy was, in part, due to a lack of public understanding of energy issues and the technological developments that could provide options to help solve current energy problems. We decided to try to fill a portion of that information void with a documentary on energy.

Production of *Running on Empty* required months of research, thirty hour-long recorded interviews with experts ranging from scientists to politicians resulting in over four hundred pages of transcripts. After completing script writing, audio production, and editing, and compact disc mastering, the program made its debut in May of 2001 on public radio station KUNM FM 89.9 in Albuquerque, New Mexico.

During 2001 to 2003, *Running on Empty* aired on over 100 public radio stations nationwide representing a service area population of 100 million. The documentary received national awards for excellence in broadcast journalism. And, the nation's largest non-religious organization, the American Automobile Association, endorsed *Running on Empty* as "Energy 101 for motorists." The following is a synopsis of the content of the documentary.

- The first segment - *Why Are We Running on Empty*? – - weaves audio from archived newscasts with interviews and the thoughts of the person-on-the-street, to trace history through the twentieth century to the roots of America's current energy crisis.
- Through extensive interviews of energy experts, the second segment - *Where Are We Now*? - paints a picture of the current American energy landscape--our resources, consumption patterns, infrastructure, and the factors that shape costs.
- *Who's at the Wheel?* - the third segment - examines energy policy through the eyes of politicians, political scientists, economists and stakeholders, to see how public and national interests, environmental concerns, and market forces are balanced.
- In the last segment - *Driving the Future* - scientists, engineers, and strategists give their views on how conservation, new technology and untapped resources can solve our energy crisis.

We found that the research forming the basis for the content of the documentary was equal to the public outreach value. Contained in the documentary and the four hundred pages of transcripts were many lessons of the past regarding the social, political, technological, economic and environmental responses to America's voracious energy appetite.

Running on Empty Revisited—Lessons of the Past

"Our decision about energy will test the character of the American people and the ability of the President and the Congress to govern this nation. This difficult effort will be the 'moral equivalent of war'. . .." Some may remember those words spoken by President Jimmy Carter as he declared war on the nation's energy crisis in 1977. However, after a quarter of a century, we are still facing our energy woes, as spotlighted by President Bush in his first State of the Union address, January, 2001: *"We have a serious energy problem that demands a national energy policy."*

Perhaps the most serious energy problem America has faced over the past quarter of a century is dependence on foreign petroleum for our transportation fuels. At the time of the fuel crisis of 1973, triggered by the OPEC oil embargo, U.S. imports [1] amounted to 37% of our total supply (17 million barrel/day). Today America

imports 56% of its supply (20 million barrel/day) [2]. The vulnerability to fuel supply shortages and price spikes is obvious.

As Philosopher George Santayana wrote: "Those who cannot remember the past are condemned to repeat it." If we'd remembered the energy lessons of the past, perhaps we would be much farther ahead in solving our transportation fuel problems. With continued rumblings of major energy problems, it is appropriate to revisit *Running on Empty*, the documentary, to examine the past and some of its lessons.

1. R&D provides options, not solutions. During the decades following the energy crisis of the 1970s, thousands of scientists and engineers contributed to U.S. Department of Energy and private industrial programs to augment U.S. energy supplies. They played the crucial role of providing a portfolio of new technology options through their R&D efforts. However, until energy technology is deployed and begins to make a significant contribution to energy supply problems, it remains an option, not a solution.

After proven to be technically feasible by scientists and engineers, new technology faces many challenges. To be successful, new technology, must pass tests of cost effectiveness, environmental and social acceptability, and compatibility with current energy infrastructure.

The following are two examples of new fuel technology options that scientists and engineers have added to the U.S. fuel portfolio since the 1970s. These are demonstrated to be either economically feasible or nearly so. A brief status of each is given with respect to deployment.

Liquid fuels from coal. Over the past three decades, $1.7 billion of government R&D has been invested in developing processes to convert coal, America's most abundant fossil energy resource, to liquid transportation fuels. The latest process concepts, called co-production, combine coal gasification with slurry phase Fischer Tropsch synthesis and electric power generation to achieve high efficiencies. Cost analyses of conceptual processes, based on the operation of commercially available components, show that liquid fuels (diesel and naptha) from coal can be produced for about $35 dollars a barrel [3]. Compare this to the current price of petroleum of $41/barrel as of May, 2004. Additionally co-production processes are much cleaner and much more efficient than previously developed coal liquefaction technology.

Two DOE demonstration projects are planned. No commercial plants have been built, largely because of the fluctuating price of oil and the large capital investment required. An investment of about one billion dollars is required to construct a plant that produces 30,000 barrel/day of diesel and naptha, AND generates 700 MW of electricity. Coal co-production, as with the use of all fossil fuels, including petroleum and natural gas, faces environmental compatibility challenges, including the issues related to reducing greenhouse gas emission of CO_2.

Biofuels. Two biofuels ethanol (grain alcohol) for spark ignited engines and biodiesel for compression ignited engines have entered the fuels market.

Ethanol is extensively used as a gasoline oxygenate additive (a mixture of 10% ethanol in gasoline, called E10) to reduce tailpipe emissions. By the end of 2004 U.S. fuel ethanol production capacity will be 3.4 billion gallons—most of this used for E10. This may be compared to U.S. annual gasoline consumption of 132 billion gallons [1]. In 1996 a new fuel called E85 (85% ethanol, 15% unleaded regular gasoline) was introduced as were cars called flexible fuel vehicles (FFVs) that can run on E85, gasoline or any mixture of the two. For 2004 the "big three" and other automakers are marketing twelve models. There are 3.5 million FFVs on the road today. Even though E85 is the fastest growing fuel market in the U.S., annual consumption amounts to only 22 million gallons. With tax incentives, E85 is cost competitive with regular gasoline. Currently ethanol is produced primarily from crops that yield starches or sugars. R&D efforts are now focusing on producing ethanol from biomass sources such as such as wood and animal wastes.

Biodiesel consists of fatty acid alkyl esters produced from soybeans and other vegetable oil feedstocks. Annual production capacity is about 70 million gallons, compared to U.S. annual total petroleum distillate consumption of 38 billion gallons [1]. Biodiesel operates in compression-ignition engines, just like petroleum diesel. Blends of up to 20% biodiesel (mixed with petroleum diesel fuels) can be used in nearly all diesel engines and are compatible with most storage and distribution equipment. Biodiesel offers advantages of improving low sulfur petroleum fuel lubricity and lowering tailpipe emissions.

It is clear from these examples that the scientists and engineers have done their jobs. Their R&D efforts since the energy crises of the 1970s have provided a portfolio of new alternatives to petroleum-based fuels. It is now time for the political, governmental, commercial and public sectors to bring these fuel technologies to the marketplace.

2. Change occurs incrementally. One of the most important lessons of the past three decades was pointed out in our interview of Professor Don E. Kash, author of the definitive book, "U.S. Energy Policy – Crisis and Complacency" [4]. Professor Kash stated [5]: "It seems to me that if there's any message of the last 30 years, in connection with energy, is that the energy system is big, complex, and adaptation has to occur incrementally."

Energy system inertia. Why does change in our energy system occur incrementally? To answer this we apply the term "inertia"—the tendency of a system to remain at rest, if at rest; or if moving to keep moving in the same direction unless affected by an outside force. The enormous size of America's energy infrastructure, mostly a fossil-fueled energy system, represents a huge amount of inertia.

For example, the world's capital investment in energy represents a replacement cost of ten trillion dollars, with an average lifetime of facilities of 30 to 40 years. From a business perspective, the energy industry is represented by large powerful commercial interests vested mainly in oil, gas, electricity, coal, and nuclear energy. Three of the top seven Fortune Five Hundred companies are fuel and petrochemical producers representing annual revenues of $424 billion. From a political perspective, Representatives and Senators from energy producing states dominate key congressional committees that develop energy legislation and policy. For example, 15 of the 23 members of the Senate Energy and Natural Resources Committee represent fossil energy producing states. And there are myriad energy policies on the books that literally take acts of Congress to change.

Historical timescales for deployment of new fuels. With respect to large-scale deployment of new energy infrastructure, examination of historical patterns of deployment of a new fuel provides a temporal measure of the inertia in America's fuel system. This can be taken as a guide to what may be expected for future rates of change in our energy system. Let's take as this guide the time it takes for a new fuel to increase its share of the total U.S. energy supply from 10% (the point at which the fuel resource and fueling infrastructure has penetrated the supply market) to 50% (the point at which the fuel and infrastructure is the major portion of the total supply).

For coal (replacing wood as America's first fuel resource) this period was 35 years (1850 to 1885); for petroleum and natural gas, also 35 years (1910 to 1945). These fuel resource substitution periods [6] are also consistent with the above estimates of 30 to 40 years for average energy facility lifetimes.

For a completely new fuel concept, the additional time required for up-front R&D could add decades, extending the period for widespread implementation of new energy technology to 50 years or more. For our energy supply and infrastructure, the implications of change occurring incrementally over a period of decades are profound:

- New technologies cannot provide immediate solutions for a serious fuel or energy crisis.
- It takes decades to respond to environmental concerns such global climate change with new technology. Even if we respond immediately to an identified environmental threat such as climate change, deployment of technology will take decades to have an impact.
- The concept of a non-carbon based hydrogen energy economy is a laudable goal that we should vigorously pursue. However, many hydrogen technologies are in early stages of development [7], and compared to fossil fuels that supply 85% of U.S. energy needs [1], there is little infrastructure for hydrogen. Hydrogen will not be a major contributor (say 50% of supply) to the U.S. energy system for nearly half a century.
- To be effective, development of energy policy must take into account that change in the energy system must occur incrementally over decades.

It is clear that because of the long time scales involved in incrementally changing our energy system, implementation of new technologies must be vigorously pursued and supported or they will not begin to make significant contribution to energy supply for many decades.

3. Stable long-term energy policies are needed. Policy is what is done through government to solve public problems or resolve public issues. Since the energy crisis of the 1970s, there have been myriad energy policies enacted by Congress. The difficulty with current and past energy policy is that it hasn't provided stable long-term solutions to U.S. energy problems. Development of energy policy must recognize and be consistent with the time scale and incremental evolution of the U.S. energy system, as noted above. To be effective, energy policy must continuously evolve over decades in response to changing U.S. energy requirements and new technology.

The instability of U.S. energy policy development is evident from examination of the intense period of U.S. energy policy development that followed the OPEC oil embargo of 1973. Three administrations--Nixon, Ford, and Carter--several Congresses, and a multitude of energy and environmental interest groups struggled to develop energy policies that would solve the problem created by the paradigm shift of energy abundance to energy scarcity. By 1980 basic long-range energy policies had been hammered out. America had the beginnings of a national consensus on energy issues.

The policy system started working. The policies created incentives for energy conservation and efficiency, for producing more oil and gas, and for producing clean coal technologies. Policies also gave emphasis to environmental concerns and placed a moratorium on new nuclear power plants. And, R&D programs were initiated to develop and provide alternative energy options. The conservation and efficiency policy efforts, especially the mandated improved mileage for automobiles (CAFE standards), caused a drop in demand for oil in the 1980s, helping to create the seemingly abundant, low-cost energy we've enjoyed for nearly two decades.

So what happened? Why are we facing many of the same 1970s energy problems today? One reason is that the energy policy pendulum swung in the opposite direction—away from policy-guided to market-guided decisions. In 1981 President Reagan's administration, espousing a "free market" philosophy, with broad political and public support, began a process of dismantling the policy system that had evolved over a decade. The Reagan administration also drastically reduced R&D budgets for new energy technology. The feeling during the 1980s and 90s was that energy is plentiful and cheap, so why do we need energy policy? Let the market deal with the supply and demand issues. Today America is experiencing some of the consequences of the dismantling of the energy policy system of the 1970s, and will have to revisit many of the same issues to develop new policies to deal with them.

But what's the status of U.S. energy policy today? In an interview for Running on Empty, Senator Jeff Bingaman, Ranking Member of the Senate Energy and Natural Resources Committee, summarized the policy situation as Congress wrestled with energy policy in 2001 [8]:

"The truth is we've got lots of energy policies sitting around Washington and, you know, you could look at virtually any two-year period for the last 20 years and find at least one energy policy that has been developed and put out there for everyone to consider.

"The problem is we haven't had a set of policies that we could pursue with any kind of consistency and commitment over a long enough period of time to make any difference. And so that's what we really are challenged with doing this year [2001], is to come up with a set of policies that we will actually commit the country to pursuing for a period of time and that, of course, are enlightened enough to move us in the right direction."

The energy policy efforts of the 1970s has taught us that policy must be made incrementally, especially for something as big and complex as our energy system. We have to approach energy policy by recognizing our strengths. We have to understand the institutional and political landscape as it is, then consistently move in small steps toward broadly defined goals.

4. Continuous public involvement and support is essential. Politicians are sensitive to the views of the public. After all, they owe their jobs to the electorate. Public concerns become political concerns addressed by policy. In our interview of James Schlesinger [9], the first U.S. Secretary of Energy, he noted connection between public support and policy:

"There is a strong degree of public support for cleaning up the environment. In the environmental area we are prepared to spend more on automobiles, we are prepared to force utilities to clean up their emissions and you have a willingness to clean up the air from pollutants. In the energy area dedication comes and goes."

"This is a democratic country and the public wants low energy prices, and if you want to move in the direction of diminishing dependency on foreign sources of supply, or move in the direction of government support for additional infrastructure, that tends to add to energy prices. The public has wanted to keep energy prices [low] and in a democracy the politicians are very sensitive to that. In the abstract, people like myself may say that energy policy should have been far more ambitious in this respite that we've had since the early 1980s but it has not been because there's been no public demand, and those who have worried about the problem have tended not to earn support at the election booth."

Clearly public interest waxes when there are energy shortages or energy and fuel prices rise, and wanes when supplies are plentiful and prices low. How can public interest be maintained through the ups and downs of energy prices, and how can the public be brought more directly into the policy making process? Here are a couple of thoughts.

Public outreach. For all our dependency on energy, the public has little understanding of the technology and systems that deliver power to our fingertips, and little knowledge of technological developments that can provide solutions to current energy problems and associated environmental concerns. The nation's political,

educational, and media systems must redouble efforts to provide the knowledge and skills necessary for Americans to think critically about the costs and benefits of energy technology development and use. And, scientists and engineers must share their knowledge with the public, in terms that can be understood. This needs to be done continuously, not just in times of energy crisis.

Energy town hall meetings. Public participation in planning and developing recommendations for long-term national energy policy could be implemented through a consensus-driven town hall approach, such as the Twenty-ninth Town Hall on New Mexico's Energy, Economics and Environment [10] conducted in 2002 by New Mexico First, a non-profit, non-partisan public policy organization. The New Mexico First Town Hall process reflects the vision of New Mexico First's founders, United States Senators Pete V. Domenici (R-NM) and Jeff Bingaman (D-NM), who wanted a vehicle for policy makers to hear from the citizens of New Mexico regarding policy recommendations.

Recommendations resulting from the town halls carry weight with New Mexico's legislators, cabinet secretaries, and the executive branch for two reasons. Town hall participants represent New Mexico's diverse cultural, geographic, economic and political population, and the recommendations result from a consensus-driven process. The recommendations of the Twenty-ninth Town Hall on New Mexico's Energy, Economics and Environment have found their way into recent New Mexico energy legislation. A similar process, with a series of nationwide town halls, could be used to bring the public into the national energy policymaking process.

A Road to Fuels of the Future.

Why a road is needed. Today, America has a challenging opportunity to build a road to fuels of the future that will supply the needs of our transportation system and avert an imminent fuel crisis. The opportunity results from U.S. dependence on imported petroleum and a gap that will soon form between the supply and demand curves for petroleum as global petroleum demand increases by 50% over the next two decades, and worldwide petroleum production peaks within this decade [11]. Our interview [12] of Dexter Sutterfield, Division Director of Petroleum Technology Management for the DOE's National Petroleum Technology Office underscores the urgency of the petroleum situation:

"Our [worldwide] consumption of crude oil right now [2001], is about 77 million barrels a day. By 2020 we expect that consumption to be about 117 million barrels a day. And the biggest increase is in that use worldwide will be in developing countries like China, Africa, South America, places that are developing and also that have a lot of the resource, and as such, we will be hard-pressed in the United States because we will need to be more efficient because they're going to use their own resources and so running on empty is a real term here. When there's a demand for us and demand for the country where the crude oil's being produced, I have an idea that we will be the ones that wind up on empty."

Policy enables filling the fuel supply/demand gap. How can America fill the gap between supply and demand for transportation fuels as this gap forms, then widens? Technology options compatible with our current fuel supply infrastructure are available. What will it take to deploy these options? The lessons of the past tell us that we will need to:

- Deploy the options incrementally over a period of decades.
- Have stable long-term policy to support deployment of the options.
- Have continuous public involvement and support.

To fill the gap U.S. energy policies will have to tackle both the supply and demand curves to bring them into alignment to eliminate the gap. And the public will have to encourage and be supportive of development of those policies.

As the supply-demand gap forms, U.S. transportation fuel supply can be incrementally augmented by liquid fuels produced from coal and biomass. With respect to demand, the fuel efficiency of vehicles must be dramatically improved with technology such as hybrid electric vehicles. Policy in the areas of augmenting supply (for example an alternative fuel standard similar to the renewable electricity standard considered by Congress) and decreasing demand (a return to improved CAFE standards) will be needed to insure that once we start down the road to fuels of the future, we stay on course to complete the journey—that in the long term, we protect the technologies we deploy.

In our interview of James Schlesinger [9], he underscored the need to protect investment in new technology: "…we must recognize that even when we have vast technological improvements that those technologies require long lived, costly investments and those who we wish to induce to make those investments must feel that they have some protection against what is still a very powerful set of oligopolists in OPEC. That is something that we have learned with regard to new technologies. That new technologies must be protected if they are to be introduced en masse."

A modest investment with large returns. Let's make a simple estimate of the investment that would be required for one scenario, that of filling the supply-demand gap with coal-derived transportation fuels. (An equivalent investment must also be made in biofuel alternatives, but for lack of cost data will not be examined here.) Suppose the U.S. government makes an investment equal to just 2% of the $500 billion annually invested worldwide for energy supply systems, and commits $10 billion/year for ten years to develop alternative fuel infrastructure. Further, suppose government shares half the cost of constructing the new infrastructure with American companies, making the combined investment of $20 billion/year. Assumptions are: a construction cost of $1 billion to build a plant producing 30,000 barrel/day of gasoline and diesel and 700 Mw of electricity, and a plant construction time of about five years. Within fifteen years, the investment could add an additional six million barrels a day of gasoline and diesel from coal (or 60% of current imports), and 140,000 megawatts of electricity (20% of current supply).

Compared to the other government programs, the cost is modest. The annual cost of $20 billion/year would amount to only 0.17% of U.S. gross domestic product ($11.4 trillion for 2004 [13]). The total government and private investment for coal co-production energy infrastructure over ten years would be $200 billion. When compared to the estimated ten-year defense budget of $3.7 trillion, it's a real bargain.

Investment in our energy infrastructure will yield payoffs equal to one of the best long-term government investments America ever made--the Interstate Highway System. That program involved every state, hired millions of Americans, positioned the U.S. for improved international competitiveness, enriched the life of virtually every American, and returned six dollars for every dollar of the $400 billion it cost. Investment in our energy infrastructure will surely do the same.

References

1. U.S. Department of Energy, Energy Information Agency, Annual Energy Review 2002, October 24, 2003.
2. U.S. Department of Energy, Energy Information Agency, Monthly Energy Review, April 28,2004.

3. Gray, D. and Tomlinson, G., Coal as a Resource for Fuels of the Future, Prepr. Pap.-Am. Chem. Soc., Div. Fuel Chem. ***2004***, 49 (2), xxxx.
4. Kash, D. E., U.S. Energy Policy: Crisis and Complacency, University of Oklahoma Press, 1984.
5. Kash, D. E., Interview for Running on Empty, March 1, 2001.
6. Kash, D. E., U.S. Energy Policy: Crisis and Complacency, University of Oklahoma Press, 1984, page 47.
7. The Hydrogen Economy: Opportunities, Costs, Barriers, and R&D Needs, The National Academies Press, 2003.
8. Senator Jeff Bingaman, Interview for Running on Empty, March 12, 2001.
9. James Schlesinger, Interview for Running on Empty, April 12, 2001.
10. New Mexico's Energy, Economics and Environment – Report of the Twenty-Ninth New Mexico First Town Hall, November 14 – 17, 2002, New Mexico First, 320 Gold Avenue, SW, Suite 300, Albuquerque, NM 87102.
11. Deffeyes, K. S., Hubbert's Peak: The Impending World Oil Shortage, Princeton University Press, 2001, p. 158.
12. Dexter Sutterfield, Interview for *Running on Empty*, March 22, 2001.
13. U.S. Department of Commerce, Bureau of Economic Analysis, National Income and Accounts Table, April 29, 2004.

DOE FE DISTRIBUTED GENERATION PROGRAM

Mark C. Williams and Bruce Utz

US Department of Energy, National Energy Technology Laboratory, PO Box 880, 3610 Collins Ferry Road, Morgantown, WV 26507-0880

Abstract

The U.S. Department of Energy's (DOE) Office of Fossil Energy's (FE) National Energy Technology Laboratory (NETL), in partnership with private industries, is leading the development and demonstration of high efficiency solid oxide fuel cells (SOFCs) and fuel cell turbine hybrid power generation systems for near term distributed generation (DG) market with emphasis on premium power and high reliability. NETL is partnering with Pacific Northwest National Laboratory (PNNL) in developing new directions in research under the Solid-State Energy Conversion Alliance (SECA) initiative for the development and commercialization of modular, low cost, and fuel flexible SOFC systems. The SECA initiative, through advanced materials, processing and system integration research and development will bring the fuel cell cost to $400/kilowatt (kW) for stationary and auxiliary power unit (APU) markets. The use of fuel cells is expected to bring about the hydrogen economy. FutureGen is a major new Presidential initiative to produce hydrogen from coal.

Solid State Energy Conversion Alliance

The SECA Program is the main thrust of the DOE FE DG Fuel Cell Program. SECA is also recognized as part of the Hydrogen Program. Achieving the SECA goals should result in the wide deployment of the SOFC technology in large high volume markets. This means benefits to the nation are large and cost is low, which is the SECA goal. Less expensive materials, simple stack and system design, and high volume markets are the three criteria that must be met by a fuel cell system to compete in today's energy market. Near zero emissions, fuel flexibility, modularity, high efficiency, simple CO_2 capture will provide a national payoff that gets bigger as these markets get larger.

The SECA program is dedicated to developing innovative, effective, low-cost ways to commercialize SOFCs. The program is designed to move fuel cells out of limited niche markets into widespread market applications by making them available at a cost of $400 per kilowatt or less through the mass customization of common modules. SECA fuel cells will operate on today's conventional fuels such as natural gas, diesel, as well as coal, gas, and hydrogen, the fuel of tomorrow. The program will provide a bridge to the hydrogen economy beginning with the introduction of SECA fuel cells for stationary (both central generation and distributed energy) and auxiliary power applications.

The SECA program is currently structured to include competing industry teams supported by a crosscutting core technology program. SECA has six industry teams working on designs that can be mass-produced at costs that are ten-fold less than current costs. The SECA core technology program is made up of researchers from industry suppliers and manufacturers as well as from universities and national laboratories all working towards addressing key science and technology gaps to provide breakthrough solutions to critical issues facing SECA. Delphi, in partnership with Battelle, is developing a 5 kW, planar, 700 °C – 800 °C, anode supported SOFC compact unit for the DG and APU markets. Delphi is expert at system integration and high volume manufacturing and cost reduction. They are focused on making a very compact and light weight system suitable for auxiliary power in transportation applications. General Electric is initially developing a natural gas 5 kW, planar, 700 °C – 800 °C, anode supported SOFC compact unit for residential power markets. GE is evaluating several stack designs and is especially interested in extending planar SOFCs to large hybrid systems. They also have a radial design that can simplify packaging by minimizing the need for seals. GE has made good progress in achieving high fuel utilization with improved anode performance using standard materials by optimizing microstructure. SWPC is developing 5-10 kW products to satisfy multiple markets. SWPC has developed a new tube design for their 5 kW units that use flat, high power density tubes. This allows for a shorter tube length and twice the power output compared to their current cylindrical tube. Cummins and SOFCo-EFS are developing a 10 kW product initially for recreational vehicles that would run on propane using a catalytic partial oxidation reformer. The team has produced a conceptual design for a multilayer SOFC stack assembled from low cost "building blocks." The basic cell, a thin electrolyte layer (50 75 micron), is fabricated by tape casting. Anode ink is screen printed onto one side of the electrolyte tape, and cathode ink onto the other. The printed cell is sandwiched between layers of dense ceramic that will accommodate reactant gas flow and electrical conduction. The assembly is then co fired to form a single repeat unit. FuelCell Energy and Acumentrics represent additional industry design alternatives that will enhance the prospects of success of SECA fuel cells for a broader market.

SECA Core Research Issues

Developing the solid oxide fuel cell which meets both performance and cost targets is a matter of complex trade-offs. Within each sub-system and its components there exist research needs. The needs may be different for the various system alternatives and their design – anode supported, cathode supported, and electrolyte supported; planar, radial tubular. While progress has been made in power density and utilization, the cathode remains an important area of research if low temperatures are to be achieved. To achieve low overpotentials at reduced temperature requires optimization over composition and structure. Mixed ionic and electronic conducting cathodes with sufficient catalytic activity are being considered. Seals are a long-standing issue in some SOFC designs. The requirements on the seal are demanding to ensure thermal cyclability and gas tightness. The use of low-cost metallic interconnects is highly desirable for some designs.

SOFC's and Hydrogen

One of the ways in the U.S. to produce hydrogen may be with coal. Coal is a very abundant resource in the U.S. and for energy independence should be used as the primary fuel in the U.S. Coal must be in our future for energy independence. Over 50 percent of the electricity in the U.S. comes from coal, and coal use is increasing. The President recently announced the FutureGen project to produce hydrogen from coal. From the perspective of fuel cells, the goal is to aggregate SECA fuel cells into larger systems and to produce a very high-efficiency fuel cell-turbine hybrid module. The SOFC hybrid is a key part of the FutureGen plants. The highly efficient SOFC hybrid plant will produce electric power and other parts could produce hydrogen and sequester CO_2. The hydrogen produced can be used in fuel cell cars and for large SOFC DG applications. The fuel cell or hybrid could operate on syngas or hydrogen and segregation/isolation of CO_2 if operating on syngas is possible with some fuel cell designs.

References

(1) Fuel Cells--A Handbook (Revision 4, November 1998), Report Number DOE/FETC-99/1076 (CD).
(2) M. Williams, "Status of SOFC Development and Commercialization in the US", 6th International SOFC Symposium, in Proceedings, pp. 3-9 (1999).
(3) M. C. Williams, "Fuel Cells - Realizing the Potential", Fuel Cell Seminar, Portland, November 1, 2000, in Proceedings Fuel Cell Seminar, pp. (2000).
(4) M. Williams, "Energy Decision Magazine Roundtable on DG", during Electric Power 2000, Cincinnati, Ohio, in Energy Decision, June pp. 26-32, 2000.
(5) M. Williams, "Energy Futures: Advanced Fuel cell Power Systems," Brookings Institute Seminar, "Science and Technology Policy: Current and Emerging Issues," June 14, 2000.
(6) "SECA Workshop Proceedings," June 1-2, 2000, Baltimore, MD.
(7) N. Minh, et. al., in Solid Oxide Fuel Cells VI, S. C. Singhal and M Dokiya, Editors, PV 99-19. p.68, The Electrochemical Society Proceedings Series, Pennington, NJ (1999).
(8) J. Thijssen, et.al., Conceptual Design of POX SOFC 5 kW net System, Arthur D. Little, Inc. Report # 71316 (to be published), Cambridge MA (2000).
(9) M. Williams and S. Singhal, "Mass-produced ceramic fuel cells for low-cost power," in Fuel Cell Bulletin, no. 24, pp. 8-11 (September 2000).
(10) M. Williams, "Fuel Cells: Realizing the Potential for Natural Gas," Key Note Address in Proceedings Fuel Cells 2000, Philadelphia, PA, September 27, 2000.
(11) M. C. Williams, "Fuel Cells - Realizing the Potential", Fuel Cell Seminar, Portland, Oregon, November 1-3, 2000, in Proceedings Fuel Cell Seminar, pp. .
(12) M. Williams, "Status of SOFC Development and Commercialization in the US", 7th International SOFC Symposium, Japan, in Proceedings, (2000).
(13) M. C. Williams, "Distributed generation fuel cells and power reliability," #1605, Energy 2001, Baltimore, Md., 2001.
(14) M. Williams, "Fuel Cells and the World Energy Future," in Proceedings PowerGen, Orlando, FL, 2001.
(15) David A. Berry, Wayne A. Surdoval, and Mark C. Williams, "The solid state energy conversion alliance - program to produce mass manufactured ceramic fuel cells," in Proceedings ACS Fuel Cell Symposium, Chicago August 2001.
(16) M. C. Williams, "New Direction in the US Fuel Cell Program," in Proceedings 7th Grove Fuel Cell Symposium, September 11, 2001.
(17) Catherine Greenman, "Fuel Cells: Clean, Reliable (and Pricey) Electricity," The New York Times, May 10, 2001, p. D8.
(18) "SECA Workshop Proceedings," March 29-30, 2001, Arlington, VA.
(19) "SECA Workshop Proceedings," March 21-22, 2002, Washington, DC.
(20) "SECA Workshop Proceedings," April 15-16, 2003, Seattle, WA.

Defect chemistry of p-type perovskite conductor used in solid oxide fuel cells

Xiao-Dong Zhou and Harlan U. Anderson

Department of Ceramic Engineering, Electronic Materials Applied Research Center, University of Missouri-Rolla, Rolla, MO 65409

Introduction

The development of solid oxide fuel cells (SOFCs) has been driven by both industry and academy for the purpose of searching for the alternative energy sources. Over last several years, operation of SOFCs in the intermediate temperature regime (500 – 700ºC) is of particular interest, which seems mandatory for SOFC commercialization. Strict materials requirements are of great importance for the electrode of SOFCs operated over the intermediate temperature region. Therefore, it is necessary to study the electrode materials by understanding the mechanisms for the conductive and catalytic behavior and developing reliable and stable experimental methods to measure defect density and catalytic ability. Perovskite type oxides are of great interest for use as the electrodes in SOFCs because (1) site occupancy is determined mainly by ionic radius so lattice site location of a particular cation is fairly certain; (2) electronic conductivity (σ) is determined by B site ion; and (3) ionic conductivity results from the presence of oxygen vacancies. Thus, this family of oxides was tailored to use as mixed ionic and electronic conductors, superionic conductors, and superconductors. Defect chemistry is a particularly powerful technique in understanding the mass and charge transfer properties by determining defect type, density, association and mobility. In this article, it is our intent to report the global solutions to defect chemistry models, with an emphasis on the p-type perovskite conductors which are being considered as the electrodes of SOFCs. The global defect chemistry models allow us to better understand and predict the electrochemical properties of perovskite type p-type conductors.

Defect Chemistry Modeling

The procedure is to write the defect formation reactions: 1) list the basic defect types and reactions which can occur: intrinsic, stoichiometric, oxygen excess and oxygen deficient; 2) write the overall neutrality relation and 3) combine the resulting equations to yield a relationship which can be solved for particular temperature and oxygen activity regimes. Considering a general type perovskite type oxide (ABO_3), the occupants at A site can be (Kroger-Vink notation is used) $A_A^{\times}$, $V_A^{'''}$ and $Sr_A^{'}$ (for simplicity, assume Sr is the low valence element substituting at the A site). The occupants at the B site are $B_B^{\times}$, $B_B^{'}$, $B_B^{\bullet}$ and $V_B^{'''}$, where $B_B^{\times}$ indicates a majority of B cations which are in valence of 3+, $B_B^{'}$ represents that some B site cations are in 2+ state and $B_B^{\bullet}$ shows some B site cations are in 4+ valence state. The oxygen site can have two type of occupants, $V_O^{\bullet\bullet}$ and $O_O^{\times}$.

Since there exist nine variables, nine equations are needed to obtain these values. Two methods can be used to solve the resulting equations: 1) divide into regions of particular neutrality conditions and solve for that particular region or 2) do not use limiting conditions, but allow a computer to make a numerical solution to the overall equation using the total neutrality condition. More detailed equations and solutions can be found elsewhere. [1] A global solution will be discussed in this article, in which the overall electron neutrality expression is used results in a term named as the ability for oxygen vacancy generation (AOG). This method is considered as a model based on delocalized electron holes.

The total electrical conductivity, σ, is given by

$$\sigma = N\mu q \tag{1}$$

where μ is the mobility, q is the carrier charge and N is the carrier concentration. Because of the mobility of either the electrons or holes is much higher than that of oxygen ions, the total conductivity in ferrites is dominated by hole conduction. The carrier concentration, N is:

$$N = [Sr_{La}^{'}] - 2[V_O^{\bullet\bullet}] \tag{2}$$

where $[Sr_{La}^{'}]$ is the acceptor level and $[V_O^{\bullet\bullet}]$ is the oxygen vacancy concentration. For simple analysis, it is assumed that all doping centers are dissociated. Generation of oxygen vacancy, $V_O^{\bullet\bullet}$, follows:

$$O_O^{\times} \rightarrow V_O^{\circ\circ} + \frac{1}{2}O_2 + 2e^{'} \cdot \tag{3}$$

The reaction constant (K_1) of reaction in Eq. (3) is:

$$K_{V_O^{\bullet\bullet}} = [V_O^{\bullet\bullet}]\, pO_2^{1/2}\, n^2 \tag{4}$$

where, pO_2 is the oxygen partial pressure and n is the electron concentration. Assuming this reaction follows the Ahrennius law:

$$K_{V_O^{\bullet\bullet}} = K_{V_O^{\bullet\bullet},0} \exp(-\frac{E_{V_O^{\bullet\bullet}}}{kT}), \tag{5}$$

where $E_{V_O^{\bullet\bullet}}$ is the activation energy for oxygen vacancy generation and k is Planck's constant. Considering $np = K_i$, then the expression can be rearranged to yield

$$\ln(\frac{[V_O^{\bullet\bullet}]}{([Sr_{La}^{'}] - 2[V_O^{\bullet\bullet}])^2}) = \ln(\frac{K_{V_O^{\bullet\bullet},0}}{K_i^2}) - \frac{1}{2}\ln(pO_2) - \frac{E_{V_O^{\bullet\bullet}}}{kT} \cdot \tag{6}$$

From this expression the oxygen vacancy concentration can be derived as a function of substitution level ($[Sr_A^{'}]$), temperature, and materials properties:

$$[V_O^{**}] = \frac{(4MN+1) - \sqrt{1+8MN}}{8A} \text{ where} \tag{7}$$

$$M = \frac{K_{V_O^{\bullet\bullet},0}}{K_i^2} \cdot \exp(-\frac{E_{V_O}}{kT}) \cdot P_{O_2}^{-1/2} \text{ and } N = [Sr_{La}^{'}] \cdot$$

The term M can be expressed as $AOG*pO_2^{-1/2}$, where AOG stands for the ability for oxygen vacancy generation, which is a function of temperature and intrinsic materials properties. Fig. 1 shows a plot of carrier concentration calculated from Eqs. (2), (6) and (7). The ability for oxygen vacancy generation as a function of temperature and oxygen activity can be determined by simulating experimental conductivity data with the current defect chemistry. Fig. 2 shows a plot of the experimental and simulated conductivity of LSM, LSF and LSCF. Table 1 lists the AOG values of these compounds. It is worthwhile to note again that the B site cation can be easily driven from 4+ to 3+ for the perovskites which possess high values of AOG, such as $(La,Sr)FeO_{3-\delta}$. For instance, $\delta \sim 0.2$ takes place at ~1500ºC for $La_{0.60}Sr_{0.40}FeO_{3-\delta}$ in air, which indicates that all of the Fe ions are in the 3+ valence state. If the temperature is lowered to 1000ºC, the oxygen activity has to be lowered to $\sim 10^{-14}$ atm to observe this state. Activation energy values for AOG of manganites and chromites are larger than those of ferrites, hence, it is expected that Cr and Mn cations can be reduced to 3+ in air only if the temperature is sufficiently high.

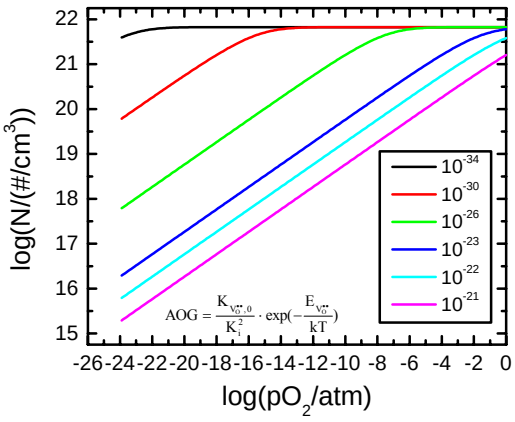

Figure 1. A plot of carrier concentration as a function of oxygen activity with various AOG values

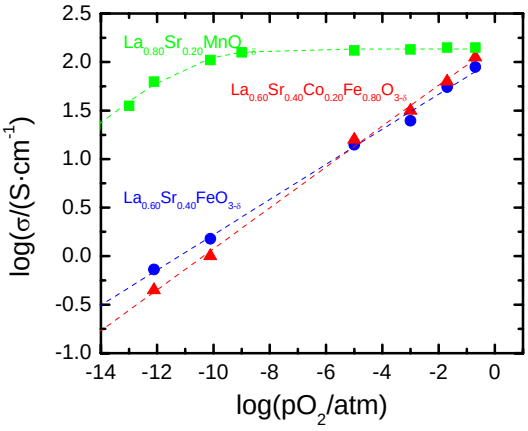

Figure 2. Plot of log(σ) vs. log(pO_2) for LSM, LSF and LSCF. The solid points are experimental data. The dash lines are fitting results from the global defect chemistry model. [2-4]

The knowledge of the values for the AOG terms can enable us to understand the maximum conductivity of many p type conductors. For example, from the previous results, we know that at temperatures < 600ºC in air LSF possesses nearly stoichiometric oxygen occupancy. Thus it can be expected that the oxygen vacancy concentration is extremely low at relatively low temperature (~ room temperature), therefore conductivity should increase with increasing temperature because of the increasing mobility. At elevated temperature, more oxygen vacancies are generated which will decrease the total carrier numbers because of the increasing oxygen vacancy concentration. The mobility, however, continuously increases with increasing temperature. Hence, a maximum conductivity at a specific temperature is expected due to an increasing mobility and decreasing carrier concentration. A shift of the temperature corresponding to the maximum conductivity is observed as shown in Table 1. As discussed previously this maximum in conductivity represents the temperature at which the oxygen vacancy concentration starts to influence the carrier concentration. It does not mean that the oxygen vacancy concentration is negligible at this temperature, but on the other hand, the influence of oxygen vacancy concentration on total carrier concentration is negligible below this temperature and the concentration of oxygen vacancies is so small that their contribution to transport processes becomes minimal.

The values of AOG and understanding of the maximum conductivity are of particular importance in the search for materials for energy conversion devices. Since oxygen vacancies are required for lower cathodic overpotentials, this temperature also represents the temperature below which a cathode can be expected to have high overpotentials. Therefore, when pure LSM is used as the cathode, it will be expect to work well when the operation temperature is ~ 1000°C because the oxygen vacancy concentrations are sufficiently high to support the required transport processes of the cathode. Below this temperature range, overpotential problems are commonly encountered. It has been found that the addition of a second ionic conducting phase to the cathode enhances the ionic transport processes, which allows lower temperature operation. Thus the use of cathodes consisting of mixtures of LSM and YSZ or LSM and CGO has become common practice in the SOFC industry, but these mixtures will not extend the temperature much below 750-800°C before cathodic overpotentials become too large because the concentration of oxygen vacancies is insufficient to support the transport processes which are required for oxygen reduction and transport of the oxygen ions to the electrolyte.

Conclusions

The understanding of the defect chemistry in the perovskite family p type conductors allows us to search for the novel materials for use in fossil energy conversion system, which requires a sufficient vacancy density, a mixed ionic and electronic conductance, high catalytic ability and stability. Examples include the electrodes used in SOFCs where the cathode component which requires high oxygen vacancy density and electronic conductance and the anode requires stability in a very reducing atmosphere, electronic conductance, and oxygen vacancy density.

Acknowledgement. This work was supported by contracts DE-FC26-02NT41563 and DE – FC36 – 01G011084.

References

(1) Zhou X D and Anderson H U. unpublished.

(2) Kuo J H, Anderson H U, Sparlin D M, "Oxidation-reduction behavior of undoped and strontium-doped lanthanum manganese oxide ($LaMnO_3$): defect structure, electrical conductivity, and thermoelectric power," *J. Solid State Chem.* (1990) **87**, 55-63.

(3) Tai L W, Nasrallah M M, Anderson H U, Sparlin D M, Sehlin S R, "Structure and electrical properties of $La_{1-x}Sr_xCo_{1-y}Fe_yO_3$, part 2. The system of $La_{1-x}Sr_xCo_{0.2}Fe_{0.8}O_3$," *Solid State Ionics* (1995), **76**(3,4), 273-83.

(4) Kaus I, Anderson H U, "Electrical and thermal properties of $La_{0.2}Sr_{0.8}Cu_{0.1}Fe_{0.9}O_{3-d}$ and $La_{0.2}Sr_{0.8}Cu_{0.2}Fe_{0.8}O_{3-\delta}$," *Solid State Ionics* (2000), **129**(1-4), 189-200.

Table 1 AOG and T_{max} for four p type conductors

	LSM	LSF	LSCF	LSFCu
AOG	2.9×10^{-27}	3×10^{-21}	3×10^{-20}	
T_{max} (ºC)	900	600	550	400

Peculiar Properties of Novel Self-stabilized NiO-YSZ Nanocomposite Materials for Solid Oxide Fuel Cell Anode

Ming-Yao Cheng and Bing-Joe Hwang

Dept. Chemical Engineering
National Taiwan University of Science and Technology
106, Taipei, Taiwan,
ROC

Introduction

In electrochemical systems, for example, an electrochemical sensor, the length of three-phase-boundary at electrode/electrolyte interface governs its sensitivity and selectivity. Although it is difficult to estimate the length of three-phase-boundary, smaller particles, proper ratio and well dispersion of electrode and electrolyte materials would create larger three-phase-boundary length. Similarly, it would be helpful to improve the power density of solid oxide fuel cell (SOFC) by increasing three-phase-boundary length. Meanwhile, utilization of fuel would be more efficient as well.

Liu et al. have fabricated nanostructured electrode materials by combustion chemical vapor deposition technique and shown excellent performance at low temperatures 1 . Structure stabilities of the nanostructured electrode materials were not shown in this work. Mamak et al. have synthesized mesoporous electrode materials for SOFC applications, indicating the three-phase-boundary length of the synthesized materials can be improved 2-5 . However, collapse nature of mesoporous materials should be considered during its preparation process. Nevertheless, the sintering of nanostructured materials in SOFC applications might be extremely serious and result in losing great quantity of three-phase-boundary length. Therefore, it is of great importance to stabilize the structure of nanostructured materials in SOFC applications. In this work, self-stabilized NiO-YSZ nanocomposite materials were synthesized for SOFC applications. The grain growth of the synthesized NiO-YSZ SOFC anode materials is significantly inhibited during high-temperature treatment. The properties of the self-stabilized NiO-YSZ nanocomposite anode materials are also characterized and discussed here.

Experimental

Synthesis. Nickel hydroxide was chosen as the precursor for self-stabilized NiO-YSZ nanocomposite (referred as S.S. NiO-YSZ) powders. Proper amounts of nickel hydroxide (Acros, USA) were added into 100ml 1-propanol solution with stirring. 70wt% zirconium propoxide dissolved in 1-propanol solution Aldrich, USA was then added into the above solution. The molar ratio of nickel hydroxide to zirconium propoxide was fixed to 10 3 to make the volume ratio of Ni to YSZ as 1 1. Yttrium nitrate Acros, USA was dissolved into 1-propanol first followed by adding into the above solution. The molar ratio of zirconium to yttrium was fixed to 92 8. The solution was sealed and kept at room temperature with stirring. Reaction of zirconium propoxide with nickel hydroxide took place until totally evaporation of 1-propanol in the solution. The reaction was processed for several days. After reaction, the precursors were transferred into furnace immediately for preventing hydrolysis of the precursors. The furnace was operated with a heating rate of 5 /min to 600 and held for 1 hour and the said S.S. NiO-YSZ powders were synthesized. For comparison, NiO-YSZ powders by a traditional route 6 were synthesized from $NiCO_3$-$Ni(OH)_2$ Showa, Japan and 8YSZ powders TOSOH, Japan as precursors. The mixed precursors were ball-milled for 12 hours followed by heat treatment at 600 for 1 hour and denoted as t-NiO-YSZ later.

Characterization. For characterizing the synthesized materials, XRD was performed with Rigaku diffractometer and Cu K_α was taken as radiation source. The sweeping rate was 10 degree/min in the 2θ range of 20~90°. In order to investigate the behavior of grain growth, S.S. NiO-YSZ powders were further heated to higher temperature step by step up to 1000 and held for 1 hour for each step.

To understand the morphologies of the synthesized materials, electron microscope was performed with JEOL-2010 field emission SEM with 40-second Pt coating on the surfaces of the samples.

Results and Discussion

XRD patterns of S.S. NiO-YSZ and t-NiO-YSZ powders were shown in figure 1(a) and (b), respectively. From 1(a), it exhibited that cubic-fluorite YSZ materials were obtained and the doping process of yttrium ions into zirconia crystalline structures was confirmed. In addition, the cubic NiO peaks are still broad in the S.S. NiO-YSZ materials even after 1000 calcination, indicating their grains are still very fine.

(a)

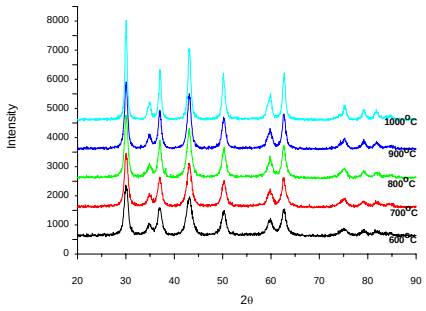

(b)

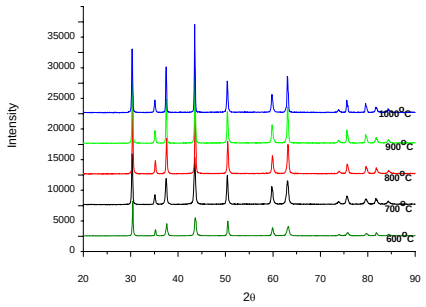

Figure 1. XRD patterns of (a) self-stabilized and (b) traditional NiO-YSZ materials of various calcination temperatures

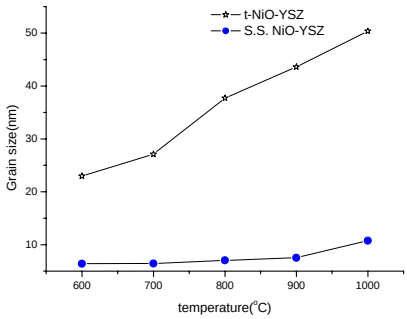

Figure 2. Calculated grain sizes of NiO in S.S. NiO-YSZ -ψ- and t-NiO-YSZ -,- to various calcinations temperatures

(a) (b)

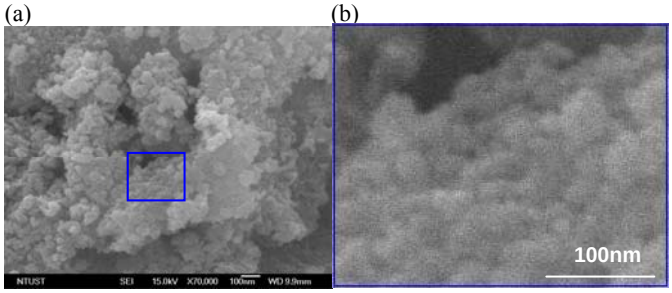

Figure 3. SEM morphologies of S.S. NiO-YSZ material (a) 70,000× (b) Enlarging part of blue-line area in (a)

Scherrer equation was used to further analyze the grain growth behaviors of NiO in the S.S. NiO-YSZ materials according to the FWHM of NiO (200) peak in figure 1. The calculated grain sizes of NiO in the S.S. NiO-YSZ and t-NiO-YSZ were shown in figure 2. The grain size of NiO in the S.S. NiO-YSZ was found to be 6.4 nm at 600 and 10.7 nm at 1000 . It is interesting that the grain size of NiO in S.S. NiO-YSZ almost no changes until 1000 . For the t-NiO-YSZ, however, the grain size of NiO was around 22.3 nm at 600 and 50.4 nm at 1000 . It was found that the synthesized S.S. NiO-YSZ materials showed better structural stability than the t-NiO-YSZ materials even though sintering effect of nanostructured materials should be more serious in general. Undoubtedly, the length of three-phase-boundary of SOFC anode would be much larger in the S.S. NiO-YSZ materials.

From morphology observation by FESEM shown in figure 3, nanocrystalline nature of the S.S. NiO-YSZ materials was revealed. Even though it was hard to resolve NiO and YSZ grains individually from FESEM, other techniques were still underway for resolution of NiO distribution in the microstructure.

Acknowledgment. The authors would like to thank National Science Council (NSC 92-2214-E-011-010) for financial support and National Taiwan University of Science and Technology for XRD and FESEM assistances.

References

1. Mamak, M., Coombs, N. and Ozin, G. A., *Chem. Mater.* **2001,** *13,* 3564-3570.
2. Mamak, M., Coombs, N. and Ozin, G. A., *J. Am. Chem. Soc.* **2000,** *122,* 8932-8939.
3. Mamak, M., Métraux, G. S., Petrov, S., Coombs, N., Ozin, G. A., and Green, M. A., *J. Am. Chem. Soc.* **2003**, *125*, 5161-5175.
4. Mamak, M., Coombs, N. and Ozin, G. A., *Adv. Mater.* **2000**, *12*, 198-202.
5. Liu, Y., Zha, S., and Liu, M., *Adv. Mater.* **2004**, 16, 256-260.
6. Negishi, H., Sakai, N., Yamaji, K., Horita, T. and Yokokawa, H., *J. Electrochem. Soc.* **2000**, 147, 1682-1687.

Solid Oxide Fuel Cell Exhaust Studies of Simple and Complex Fuels with FTIR Spectroscopy

Michael B. Pomfret[a], Oktay Demircan[a], Mary Sukeshini[a], Robert A. Walker[a,b]

[a]Department of Chemistry and Biochemistry, University of Maryland, College Park, MD 20742
[b]Chemical Physics Program, University of Maryland, College Park, MD 20742

Introduction

Solid oxide fuel cells (SOFC) have long been viewed as a potential source of clean, reliable, efficient electrical power. While progress has been made in fuel cell development and fabrication numerous questions exist about the actual mechanism(s) by which fuel is oxidized in SOFCs. Most studies have focused on engineering and electrochemical issues to improve the overall efficiency.[1-3] Considerably less attention has focused on the way in which complex fuels (i.e. butane and toluene) are oxidixed to CO_2 and H_2O.

Standard SOFC designs use a nickel or Ni/YSZ (yttria stabilized zirconia) anode to oxidize fuel.[4] Oxidation occurs as O^{2-} ions are created at the cathode and transported through the electrolyte –most commonly YSZ – to the anode. Most models of fuel cell operation postulate that the fuel is oxidized at the three-phase boundary. The anode then carries the resulting electrons out of the cell to an exterior circuit. Recently, hydrocarbon fuels have taken on increased importance as C_4H_{10} has been shown to increase cell productivity if used as a fuel. Specifically, power densities for H_2 operation increase greatly after C_4H_{10} has been used as a fuel.[5]

SOFC efficiencies that depend on fuel type raise concerns about both anode poisoning and enhanced conductivity. To fully understand the effect hydrocarbon fuels have on fuel cell performance detailed, molecular mechanisms of the chemistry occurring at the anode surface during oxidation must be developed. One means of building this understanding is by monitoring the products of oxidation in SOFCs. This strategy can be pursued by analyzing the exhaust, as well as any deposits that remain in the cell, using Fourier-transform infrared (FTIR) spectroscopy.

The present work employs FTIR to study samples of SOFCs using hydrogen, methane and butane as fuels. The resulting spectra demonstrate the important role that spectroscopy can play in identifying chemistry that occurs in SOFCs.

Experimental

Fuel Cell Operation. Experiments described in this work use two types of fuel cells. Both cells have 0.8 mm thick, 8% polycrystalline YSZ electrolytes and lanthanum strontium manganate (LSM) cathodes. One cell has a Ni/YSZ cermet anode to be used for H_2 and CH_4 fuels, while the other has a Cu/CeO2 cermet anode to be used for H_2 and C_4H_{10} fuels. The fuel cell rig is comprised of Hastelloy-X Ni alloy and the electrolyte operational temperature is 800°C.

The three fuels are diluted with argon to regulate the number of H_2 atoms in the reaction zone at a single time for all fuels. The H_2 flow is 139 sccm H_2 and 275 sccm Ar. The CH_4 flow is 69.79 sccm CH_4 and 137.46 sccm Ar. The C_4H_{10} flow is 13.4 sccm C_4H_{10} and 26.8 sccm Ar. This results in residence times of 0.800 s for H_2, 0.662 s for CH_4 and 3.52 s for C_4H_{10}. Open circuit voltages are -1.03 V for H_2, -0.89 V for CH_4, and -0.79 V for C_4H_{10}. Typical currents drawn were on the order of 10 mA.

Both cells are first operated with the H_2 mixture and allowed to equilibrate for 30 min. After stable operation has been achieved the fuel is switched to the hydrocarbon mixtures and again allowed to equilibrate for 30 min.

Exhaust Collection and IR Characterization. A custom-built glass collection manifold with auxiliary exhaust outlets is attached to the anode exhaust outlet. An IR gas cell with a volume of 35.0 cm^3 and NaCl crystal windows is evacuated and then attached to the collection chamber and the auxiliary outlets closed. The valves on the IR cell are then opened and the exhaust flow of the fuel cell is flowed through the collection system for 10 min. After this time the IR cell's valves are closed, the cell detached, and the spectrum taken.

Spectra are obtained using a ThermoNicolet Nexus 670 FTIR Spectrometer with a tungsten source. Each spectrum consists of 64 scans. All reported spectra have been corrected for any background features arising from the evacuated cell.

Results and Discussion

Figure 1 shows exhaust spectra of all three fuels. They all exhibit well resolved bands that can be readily assigned to stable, low molecular weight species. The H_2 exhaust spectrum (**a**) shows only water stretching and bending bands, as expected. The CH_4 exhaust (**b**) also shows water peaks. In addition, the spectrum shows carbon dioxide bands (2360 and 2341 cm^{-1}) from the full oxidation of the hydrocarbon. The other bands (CH_4 at 3015 and 1303 cm^{-1}, and carbon monoxide at 2170 and 2119 cm^{-1}) indicate incomplete oxidation of the fuel and intermediate species. This observation is illustrated even more dramatically by the C_4H_{10} exhaust spectrum (**c**).

Complete oxidation would lead to only water and carbon dioxide peaks in the IR spectra of the exhaust. In the C_4H_{10} case many other species are present, most notably CH_4. There also appear to be other small hydrocarbons ($\leq$ 4 carbons) as well as larger, polyaromatic hydrocarbons – in agreement with previous studies.[6,7]

The 2500-3500 cm^{-1} region of the spectra is expanded in **Figure 2**. Both the CH_4 (**a**) and C_4H_{10} (**b**) exhausts contain a significant amount of CH_4 in the exhaust, with easily distinguishable, identical P, Q, and R branches. Additional lines in the C_4H_{10} spectrum reflect the presence of both aromatic and aliphatic C-H stretching from other hydrocarbon species. The most important aspect of Figures 1 and 2 is that incomplete oxidation of C_4H_{10} results in the formation of overwhelming amounts of CH_4. An outstanding question is whether CH_4 is formed on the metal electrolyte anode assembly itself or through a gas phase reforming reactions.[8] The answer to this question carries important consequences for evaluating SOFC operation. If CH_4 is being created due to incomplete oxidation at the anode, then the chemical composition of the anode assembly surface is likely to be substantially different from the original material.[9] However, should the reforming happen in the gas phase starting fuel identity should not matter as complex hydrocarbons will simply decompose to create CH_4 before reaching the anode.

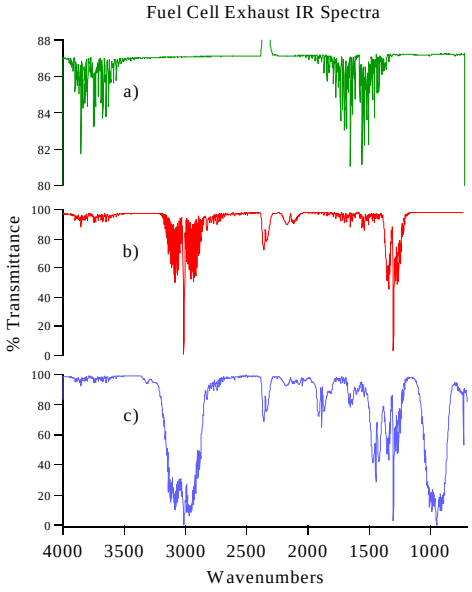

Figure 1. The IR spectra of the exhaust of the three SOFC fuels; a) H_2, b) CH_4, c) C_4H_{10}. Note the different % transmittance scales.

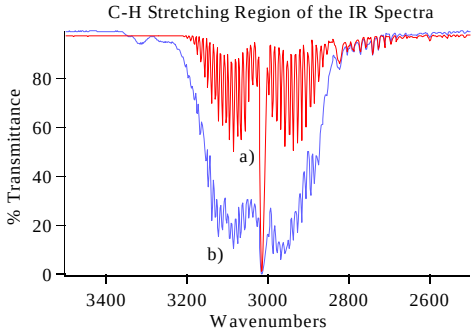

Figure 2. The 3500 – 2500 cm^{-1} region of the IR spectra of the hydrocarbon fuels; a) CH_4, b) C_4H_{10}.

Figure 3 displays the 1900-2500 cm^{-1} region in the IR spectra of the CH_4 (**a**) and C_4H_{10} (**b**) exhausts. This part of the IR shows an interesting detail. The CH_4 spectrum has a CO/CO_2 peak area ratio of 0.58, while the C_4H_{10} spectrum's ratio is 0.30. This result suggests that although both fuels experience incomplete oxidation, C_4H_{10} is at least slightly more efficient in the SOFC in terms of its ability to react to completion implying that C_4H_{10} does not pyrolyze to form CH_4 quantitatively.

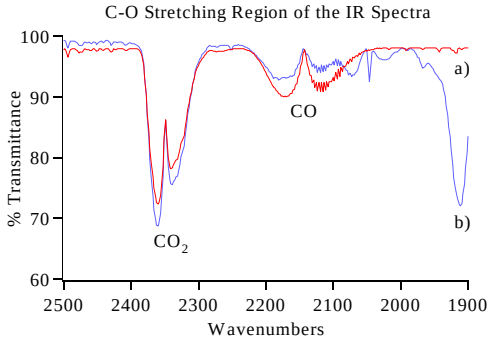

Figure 3. The 1900 – 2500 cm^{-1} region of the IR spectra of the hydrocarbon fuels; a) CH_4, b) C_4H_{10}.

Conclusion

The present experiment clearly demonstrates the utility and importance of optical spectroscopy in the study of solid oxide fuel cells. This work clearly shows how infrared spectroscopy can aid in the determination of the products of the fuel cell process and the evaluation of the efficiency of oxidation of various fuels. Isotopically labeled fuels as well as GC/MS analysis of effluent gases will greatly assist in interpreting oxidation chemistry in SOFCs.

Acknowledgements. This work is supported by the Office of Naval Research through the Multiple University Research Initiative Grant # 0110138816, in association with the Colorado School of Mines and the California Institute of Technology.

References

(1) Weber, A.;Ivers-Tiffee, E. *J. Power Sources* **2004**, *127*, 273-283.
(2) Srikar, V.T.; Turner, K.T.; Ie, T.Y.A.; Spearing, S.M. *J. Power Sources* **2004**, *125*, 62-69.
(3) Ormerod, M.R. *Chem. Soc. Rev.* **2003**, *32*, 17-28.
(4) Zhu, W.Z.; Deevi, S.C. *Mat. Sci. Eng. A-Struct.* **2003**, *362*, 228-239.
(5) McIntosh, S.; Vohs, J.M.; Gorte, R.J. *J. Electrochem. Soc.* **2003**, *150*, A470-A476.
(6) McIntosh, S.; He, H.P.; Lee, S.I.; Costa-Nunez, O.; Krishnan, V.V.; Vohs, J.M.; Gorte, R.J. *J. Electrochem. Soc.* **2004**, *87*, 331-336.
(7) Demrican, O.; Sukeshini, M.; Pomfret, M.; Jackson, G.; Walker, R.; Eichhorn, B. *J. Electrchem. Soc.* **2004**, submitted.
(8) Naik, C.; Cartensen, H.-H.; Dean, A.M. *Proceedings of the 3rd Joint Meeting of the U.S. Sections of the Combustion Institute* **2003**.
(9) Pomfret, M.; Sukeshini, M.; Stoltz, C.; Eichhorn, B.; Walker, R. *J. Electrochem. Soc.* **2004**, submitted.

SOLID OXIDE FUEL CELLS FOR DIRECT UTILIZATION OF HYDROCARBONS PREPARED BY LAMINATION METHODS

Kipyung Ahn, Shung-Ik Lee, Yingyi Huang, John M. Vohs, and Raymond J. Gorte

Department of Chemical and Biomolecular Engineering
University of Pennsylvania, Philadelphia, PA 19104 USA

Introduction

Solid oxide fuel cells (SOFCs) show great promise for power generation in a wide range of applications. Because they are based on a ceramic, oxygen ion-conducting membrane, a SOFC can theoretically operate on any combustible fuel, including CO [1,2] and hydrocarbons [3-5], allowing them to be used with fuels that are readily available today. However, in order to operate on hydrocarbon fuels, it is necessary to choose the materials that are used in the anode with great care. For example, Ni, which is commonly used in anodes on fuel cells that utilize H_2, tends to form carbon fibers in the presence of hydrocarbons.

In general, the first step in fabricating SOFC electrodes involves high-temperature sintering of mixed oxides including electrolyte materials. This approach limits the choice of materials that can be used for the electrode since the oxides may decompose or undergo unwanted solid-state reactions at high temperatures. Therefore, alternative methods are required for preparation of electrode composites in order to incorporate a wide range of materials that may have superior catalytic or current collection properties.

Recent work in our laboratory has demonstrated that it is possible to prepare SOFC electrodes from a wide range of materials by using low-temperature methods in which the electronically conductive component is added by impregnation with soluble salts to a porous matrix of the electrolyte material [6,7]. The primary advantage of producing electrodes in this manner is that the porous matrix can be sintered together with the electrolyte to very high temperatures before the active component is added, allowing the processing temperatures for the two components to be decoupled.

In this paper, we describe the fabrication of SOFCs with high-performance electrodes, having controlled structures and capable of producing electrons directly from hydrocarbon fuels, without reforming. These SOFCs were produced using a single, high-temperature sintering step in which the initial structure consists of a dense layer of YSZ separating two porous layers and is produced by lamination of green ceramic tapes. An additional layer with holes was laminated on top of one of the porous layers to provide mechanical strength and rigidity.

Experimental

The YSZ components of the fuel cells were fabricated using YSZ green tapes prepared by tape casting. The YSZ powder (8 mol% Y_2O_3, TZ-8Y, Tosoh) used in the tapes was initially ball milled for 20 h with water and a dispersant (Darvan C, R.T. Vanderbilt Company, Inc.) to break up agglomerates. Emulsion-type binder solutions (Duramax HA-12 and B-1000, Rohm and Haas) were added to the slurry and mixed by stirring for 24 h before casting. Pyrolyzable pore formers such as graphite (325 mesh, Alfa Aesea) and polystyrene-divinylbenzene (200-400 mesh, Alfa Aeser) were added together with the YSZ powder to the tapes used in the electrodes in order to introduce porosity.

An SOFC was prepared by lamination of various green tapes using a uniaxial hydraulic press equipped with heating platens (Carver Inc.). To improve the mechanical strength of the cell a relatively thick YSZ support layer was used. This support layer was in turn laminated together with the layers that would make up the cathode, electrolyte, and anode, as shown schematically in Fig. 1. The thicknesses of the anode, cathode, and electrolyte layers after firing were 100 μm, 60 μm, and 25 μm, respectively. The anode layers contained a mixture of graphite and polystyrene-divinylbenze pore formers, while the cathode layer contained only graphite. After lamination, the tapes were fired at 1823 K for 4 h. The anode and cathode composites were fabricated using impregnation of the porous YSZ matrices with aqueous solutions. The final composition of the tested cell was 15 wt% CeO_2, 21 wt% Cu, 9 wt% Co for the anode and 40 wt% $La_{0.6}Sr_{0.4}CoO_3$ for the cathode.

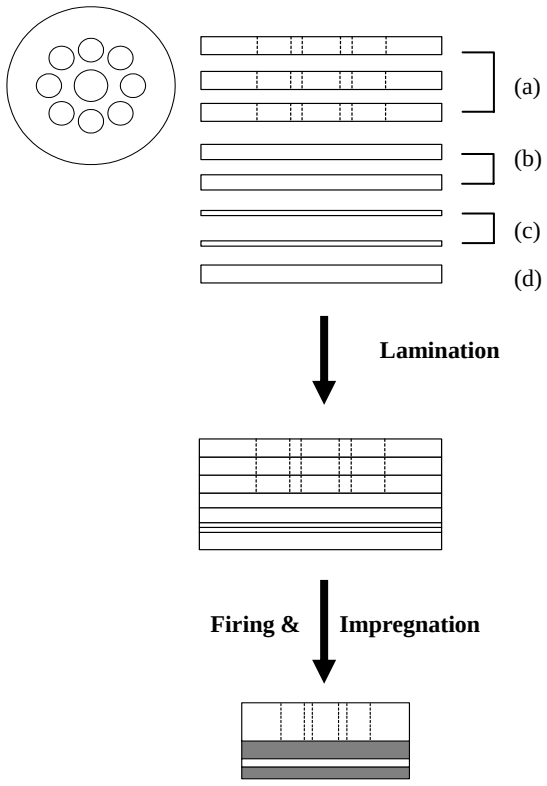

Figure 1. Schematic of the fabrication procedure for the laminated cells. (a) support layer, (b) YSZ + graphite + polystyrene divinylbenzene, (c) dense YSZ, (d) YSZ + graphite

Results and Discussion

Figure 2 shows an SEM image of a cross section near the electrolyte interface of the cell that was prepared by the lamination process shown in Figure 1, prior to the impregnation of the anode and cathode materials. Only small pores in the range of 1 to 2 μm in diameter were present in the cathode layer, while the anode layer had large pores with a size of about 20 μm in addition to the small pores. The small and large pores in the electrodes were introduced by graphite and polystyrene-divinylbenzene pore formers, respectively. The porosities of the anode and cathode porous layers were 65 % and 70%, respectively. The cell consists of three support layers, two anode layers, two electrolyte layers and a cathode layer. The micrograph demonstrates that there was good contact between the electrolyte layer and the porous YSZ electrode layers, with no evidence for cavities between layers. This result shows the microstructure of the electrodes can be engineered by laminating several layers having different microstructures. Furthermore, the dense support layer was found to provide mechanical strength to the cell so that thin electrolytes and electrodes can be used. This indicates some of the issues encountered in electrolyte or electrode supported cells can be avoided by using support layers [8].

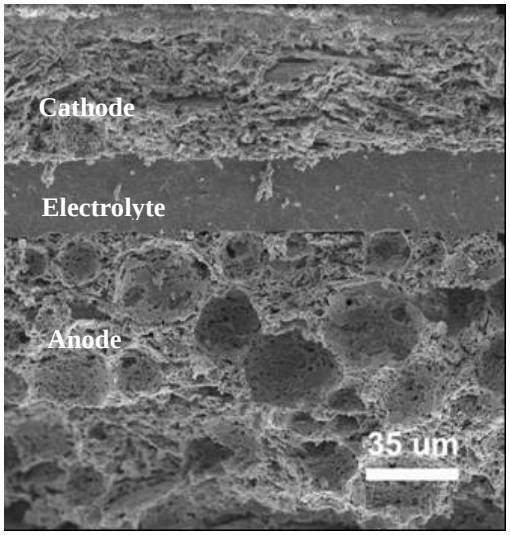

Figure 2. SEM image of the YSZ structure used for making the cell in this study

In previous work, it was shown that $Cu_{0.7}Co_{0.3}$ bimetallic mixtures are stable towards carbon fiber formation in the presence of hydrocarbon fuels, even though Cu and Co do not form an alloy [9]. It appears that Cu coats the surface of the Co crystallites, suppressing carbon formation. However, the presence of the Co within the anode still enhances the electrochemical performance. The performance of the $Cu_{0.7}Co_{0.3}$-CeO_2-YSZ| YSZ |Co-YSZ cell in H_2 and n-butane at 1023 K is shown in Figure 3. For operation using H_2 with 3 vol% H_2O, the open-circuit voltages (OCV) were close to the theoretical, Nernst potential of 1.1 V. A maximum power density of 770 mW/cm^2 was achieved at 1023 K. For n-butane, the OCV was slightly lower than predicted by the Nernst potentials, ~1.12 V. The maximum power density was 490 mW/cm^2 at 1023 K, lower than that with H_2, showing that the chemical oxidation reaction must partially limit performance.

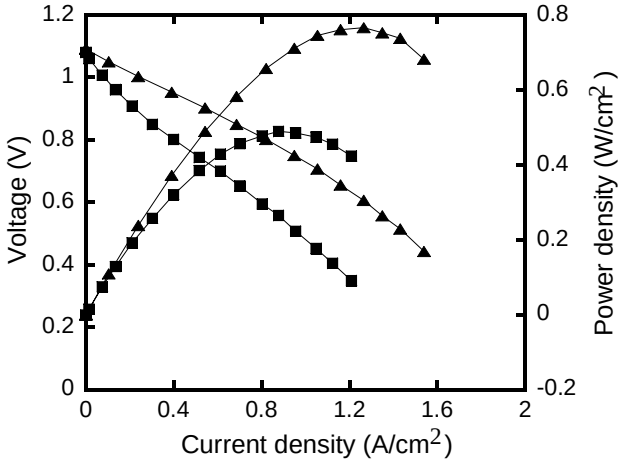

Figure 3. Cell performance curves at 1023 K in (▲) H_2 and (■) n-butane

Conclusions

We have demonstrated a new fabrication method for SOFCs for direct utilization of hydrocarbon fuels. The method involved lamination of ceramic tapes prepared by tape casting with or without pore formers and a single step firing, followed by impregnation of nitrate solutions. Utilization of perforated support layers allowed SOFCs consisting of thin electrolytes and thin electrodes to be fabricated, providing flexibility in designing cell structure.

Acknowledgements. This work was funded by DARPA, through the Palm Power Program.

References

1. W. Galvita, V. D. Belyaev, A. V. Frumin, A. K. Demin, P. E. Tsiakaras, and V. A. Sobyanin, *Solid State Ionics*, **2002**, 152, 551
2. X. Zhang, S. Ohara, T. Chen, and T. Fukui, *Fuel*, **2002**, 81(8), 989
3. S. Park, J. M. Vohs, and R. J. Gorte, *Nature*, **2000**, 404, 265.
4. E. P. Murray, T. sai, and S. A. Barnett, *Nature*, **1999**, 400, 649.
5. B. C. H. Steele, I. Kelly, H. Middleton, and R. Rudkin, *Solid State Ionics*, **1988**, 28, 1547.
6. R. J. Gorte, S. Park, J. M. Vohs, and C. Wang, *Adv. Mater*., **2000**, 12, 1465.
7. H. He, Y. Huang, J. Regal, M. Boaro, J. M. Vohs, and R. J. Gorte, *J. Am. Ceram. Soc.*, **2004**, 87, 331.
8. EG&G Technical Services Inc. and Science Apllications International Corporation, *Fuel Cell Handbook*, 6th Edition, Ch.8, pp. 11-23, US Department of Energy, Morgantown, WV (**2002**).
9. S.-I. Lee, J. M. Vohs, and R. J. Gorte, *J. Electrochem. Soc*., In press.

ANALYTICAL AND EXPERIMENTAL STUDY OF OXYGEN REDUCTION MECHANISM ON OXYGEN ELECTRODES OF SOFCs: Case study on $La_{(1-x)}Sr_xMnO_3$

Bilge Yildiz, Gerardo Jose la O', Yang Shao-Horn

Electrochemical Energy Laboratory
Massachusetts Institute of Technology,
77 Massachusetts Ave., Cambridge, MA02139

Introduction

The power of a solid oxide fuel cell (SOFC) is limited by the current associated with oxygen reduction at the cathode under a given operating voltage. The current can in general be treated as the combination of charge transfer in the cathode from two pathways, as shown in Figure 1. The first is the adsorption and reduction of oxygen at the cathode surface followed by bulk diffusion of the ions that yield the charge transfer at electrode/electrolyte interface at the 2PB (Figure 1a). The second is the surface- adsorption and transport of oxygen that leads to the reduction of oxygen and charge transfer at the 3PB region (Figure 1b). A theoretical model that takes into account the defined combined current behavior to simulate physically the cell I-V characteristics is necessary to understand the electrochemical behavior of the SOFC cathode under different operating conditions and for optimizing the properties of cathode materials.

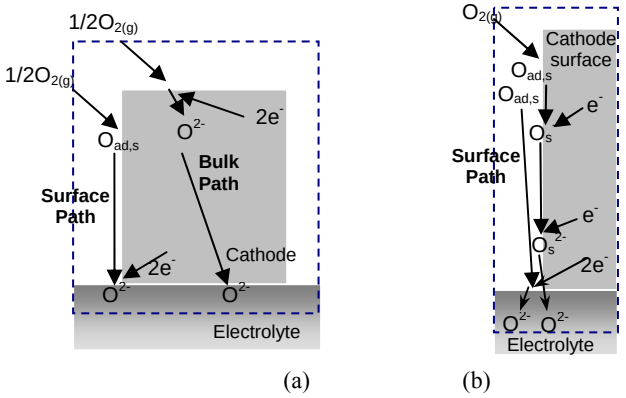

Figure 1. (a) Bulk and surface as the main charge transfer pathways on an SOFC cathode. (b) Parallel charge transfer schemes for the surface pathway of an SOFC cathode.

Although this two-pathway charge transfer behavior and modeling of SOFC cathodes has been studied in literature, a comprehensive physical model that takes into account the effect of both pathways has not been developed. A theoretical model for understanding the I-V characteristic of SOFC electrodes has initially been developed by Adler et al. [1] and this work provides important insights for charge transfer characteristics in SOFC electrodes. However, the model considers only the bulk process followed by 2PB vacancy exchange and it is limited to mixed ionic and electronic conducting electrodes with bulk ionic transfer much faster than surface charge transfer. Although there have been few recent studies that model both bulk and surface pathways[1-4], both pathways are not treated in a single coupled consistent model. For example, the overpotential have been treated as an independent variable rather than being coupled to the oxygen reaction on cathode[2,3].

To further complicate our understanding of oxygen reduction at the cathode, there is lack of consistent experimental evidence to explain the surface reaction characteristics, even for the most commonly used cathode $La_{(1-x)}Sr_xMnO_{3+\delta}$ (LSM) system[5,6]. While the surface path typically dominates the cell current for porous LSM electronic conductor electrode, the oxygen ion diffusion along the bulk path of LSM is shown to control the current in dense thin film LSM electrodes. In addition, under high cathodic polarization (typically <-200mV) the LSM system becomes a mixed electronic and ionic conductor [7] and allows the bulk path of charge transfer in LSM to be a major contributor to cell current. Therefore, it is essential to develop a physical model to analyze the charge transfer characteristics of SOFC cathodes from both surface and bulk pathways under different operating conditions and electrode configurations.

In our study, we plan to develop a two dimensional continuum model that handles the surface and bulk charge transfer pathways in a coupled and consistent way for SOFC cathodes. We first model the surface charge transfer characteristics - the rate determining pathway and the rate determining steps (rds), of LSM cathode as our initial case study. This paper presents the analytical and experimental study of oxygen reduction on LSM under different temperature and voltage conditions. The reaction pathway on the surface and rate limiting step revealed in this study will be used to determine the oxygen reduction rate along the surface path required in the coupled continuum model.

Theoretical Analysis

The overall oxygen reduction reaction can be represented as

$$O_{2(g)} + 4e^- + 2V_O^Y \Leftrightarrow 2O_0^Y \qquad [1]$$

where V_O^Y and O_0^Y refer to vacancies and oxygen ions in the electrolyte YSZ lattice, respectively. This reaction consists of multiple consecutive steps, one or more of which may be rate determining. Two surface dominated schemes for oxygen reduction on LSM are first considered in this work, as presented in Table 1. Both pathways can occur in parallel to contribute to the cathode current. Other surface models that include 2 electron charge transfer at one step or the transport of totally reduced oxygen ($O^{=}$) on the LSM surface away from the 3PB are not considered in this preliminary study.

The rate equations of the proposed reaction steps in each model are written as a function of rate constants and concentrations of species for each step. We assume that the steps that are not rds occur much faster than the rds and thus the net rate of these steps is taken as zero provided that they are in equilibrium. This approach allows the determination of the overall rate of oxygen reduction, *r*, without computing intermediate species concentrations, and the final rate expression consists of the following parameters: P_{O2}, temperature, overpotential, and a combination of rate constants that can be correlated with the exchange current density for the cathode.

Table 1. Selected Reaction Models for Oxygen Reduction on LSM

STEPS Model 1	EQUATION	PROCESS / LOCATION
1	$O_{2(g)} \Leftrightarrow 2O_{ad,s}$	Dissociative adsorption on LSM surface
2	$O_{ad,s} + e^- \Leftrightarrow O_s^-$	Partial reduction of $O_{ad,s}$ on the surface or the extended 3PB
3	$O_s^- \Leftrightarrow O_{3PB}^-$	Diffusion of intermediate oxygen species O_s^- along the surface to 3PB
4	$O_{3PB}^- + e^- \Leftrightarrow O_{3PB}^{2-}$	Complete reduction of intermediate oxygen species at 3PB
5	$O_{3PB}^{-2} + V_O^Y \Leftrightarrow O_0^Y$	Transfer of O^{2-} at 3PB into YSZ lattice
Model 2		
1	$O_{2(g)} \Leftrightarrow 2O_{ad,s}$	Dissociative adsorption on LSM surface
2	$O_{ad,s} \Leftrightarrow O_{3PB}$	Diffusion of $O_{ad,s}$ to 3PB along the surface
3	$O_{3PB} + e^- \Leftrightarrow O_{3PB}^-$	Partial reduction of O_{3PB} at 3PB or extended 3PB
4	$O_{3PB}^- + e^- \Leftrightarrow O_{3PB}^{2-}$	Complete reduction of intermediate oxygen species O_{3PB}^- at 3PB
5	$O_{3PB}^{2-} + V_O^Y \Leftrightarrow O_0^Y$	Transfer of O^{2-} at 3PB into YSZ lattice

The current from each pathway is then expressed as follows:

$$i_m = -n_e F r_m \qquad [2]$$

and $i_m = i_{m,a} - i_{m,c}$ [3]

where

$$i_{m-a} = 1 \Big/ \sum_j \left(1/i_{m-a,j}\right) \quad \text{and} \quad i_{m-c} = 1 \Big/ \sum_j \left(1/i_{m-c,j}\right) \qquad [4]$$

Total current from each possible scheme: $i = \sum_m i_m$ [5] In Eq.'s 2-5, the subscripts *a* and *c* represent anodic and cathodic reactions as shown in Table 1, respectively. The parameters *m* and *j* stand for each model and for each of the rds in the model, respectively. In this work, *m* stands for Model 1 and Model 2 in Table 1. Surface diffusion and oxygen ion transfer to YSZ are considered as the rate limiting steps in both models.

As the cathode current is expressed a function of overpotential or cell voltage, one can derive the impedance Z for the oxygen reduction process from:

$$Z(\omega) = \frac{FFT\left(\eta(\omega,t)\right)}{FFT\left(I(\omega,t)\right)} \qquad [6]$$

where η, *I, FFT,* ω *and t* represent overpotential, cell current, fast Fourier transform, frequency and time respectively.

The exchange current density expressions for the surface transport of oxygen and the vacancy transfer at LSM/electrolyte interface were obtained from Chen et al [8]. Figure 2 shows the cell resistance calculated from Eq. 6 plotted against the reciprocal of temperature. The slope of the plot is then used to calculate the activation energy, E_a, of the rds, which is 1.55 eV in this case. This value suggests the rate determining [10-12] mechanisms of dissociative adsorption or surface diffusion on LSM.

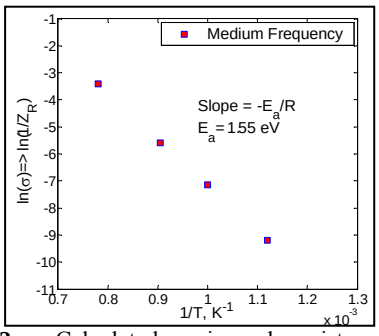

Figure 2. Calculated reciprocal resistances as a function of temperature at 1 atm based on theoretical evaluation (0.1 – 500 Hz)

Experimental Analysis

The $La_{(1-x)}Sr_xMnO_{3+\delta}$ with x=0.2 cathode and 8YSZ electrolyte samples were prepared by RF sputtering on a single crystal silicon wafer. AC impedance measurements were performed at 0V DC (OCV) with 20mV of amplitude using a Solartron 1260 frequency response analyzer in the frequency range of 0.01 to 10^7Hz in the temperature range from 450°C to 550°C and at atmospheric pressure. Preliminary AC impedance data showed two semicircles, which became more distinct at lower temperatures, in Figure 3. The resistances in the AC impedance spectra at different temperatures were calculated and the dependence of the reciprocal of resistance was used to find the activation energy of the rate determining process(es), as shown in Figure 4.

The activation energy of 1.1eV was found for the high frequency arc, which is close to values reported for the transfer of oxide ions from LSM to YSZ lattice as 1eV[11].

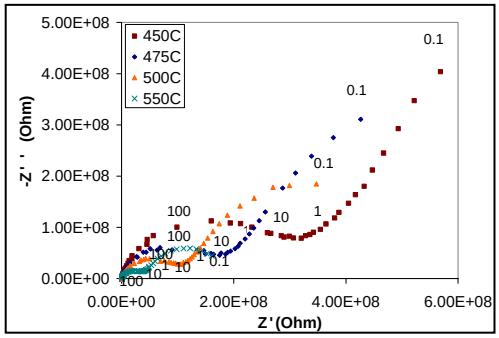

Figure 3. Impedance data obtained for LSM/YSZ at OCV

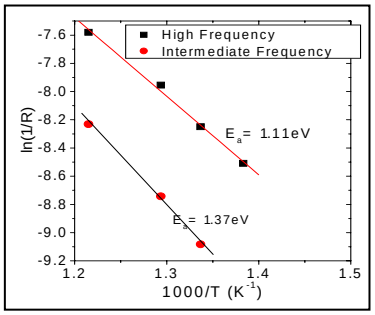

Figure 4. Calculated reciprocal resistances as a function of temperature at 1 atm based on impedance measurements.

The activation energy of 1.37eV was found for the intermediate frequency arc, which could be associated with the dissociative adsorption or the surface diffusion of oxygen species on LSM. The range of activation energy for these processes, although widely studied, greatly varies in the literature - the overall range of E_a for these processes reported falls from 1.5 to 2 eV [10-11]. It should be noted that, the 1.55 eV value for E_a obtained from theoretical impedance analysis having surface diffusion as one of the rds is similar to the E_a found experimentally for the intermediate frequency arc. This preliminary result suggests that the surface diffusion, not the dissociative adsorption, is one of the rds for the oxygen reduction in our experiments.

Additional experiments under changing P_{O2} and temperature conditions and modeling work are underway to probe surface reaction mechanisms for LSM, which is essential to develop continuum models of the SOFC cathodes in two-dimensional geometry.

References

(1) Adler, S.B., Lane, J.A., Steele, B.C.H., *J. Electrochem. Soc.* **1996** 143 (11): 3554-3564
(2) Svensson, A.M., Sunde, S., Nisancioglu, K., *J. Electrochem. Soc.* **1998** 145 (4): 1390-1400
(3) Coffey, G. *J. Electrochem. Soc.* **2003** 150 (8): A1139-A1151
(4) Tanner, C.W., Fung, K.Z., Virkar, A.V., *J. Electrochem. Soc.* **1997** 144 (1): 21-30
(5) Jorgensen, M.J., Mogensen, M., *J. Electrochem. Soc.* **2001** 148 (5): A433-A442
(6) McIntosh, S., Adler, S.B., *Electrochem. Solid St.* **2004** 7(5): A:111-A114
(7) Hammouche, A., Siebert, E., *J. Electrochem. Soc.* **1991** 138 (5): 1212-1216
(8) Chen, X.J., Khon, K.A., Chan, S.H., *J. Power Sources* **2003** 123(1): 17-25
(9) Juhl M., Primdahl, S., Manon C., Mogensen M., *J. Power Sources* **1996** 61 (1-2): 173-181
(10) Murray, E.P., Barnett, S.A., *Solid State Ionics* **2001** 143: 265-273
(11) Siebert, E., Hammouche, A., Kleitz, M., *Electrochim Acta* **1995** 40 (11): 1741-1753

Cerium L_{III}-edge EXAFS Investigation of the Structure of Crystalline and Amorphous Cerium Oxides

Ahmed M. Shahin[1] and Thomas P. Schuman[1], Fernande Grandjean[1,2], and Gary J. Long[1]

1-Department of Chemistry, University of Missouri-Rolla, Rolla-MO 65409-0010, USA.
2-Department of Physics, B5, University of Liège, B-4000 Sart, Belgium

Introduction

As a consequence of changing properties, e.g., mechanical, magnetic, or electrical, the nanocrystalline phase of rare earth metal oxides has become of immense interest.[1] Of these, cerium oxides have attracted considerable research interest due to a diversity of applications. For instance, the basicity function of cerium oxide when combined with the hydrogenation property of a metal such as Pt or Pd denotes cerium oxide as a promising conversion catalyst. Thus, cerium oxide can lead to selective hydrogenation catalysis of unsaturated compounds.[2] Of interest is the ability of the cerium oxide to store oxygen. The phenomenon is associated with a fast valence change in the solid, i.e., $Ce^{IV} \leftrightarrow Ce^{III}$, and also with anionic vacancies $CeO_2 \rightarrow CeO_{2-x} + (x/2)O_2$.[3] In this study, we report the synthesis of cerium oxide using different precipitation conditions. We also investigated the valence state of cerium ions and covalence with oxide ligands by varying the reaction conditions.

Experimental section

A dilute aqueous ammonia solution (0.01M) was added dropwise to a mixture of 0.05 mol of an aqueous solution of cerium nitrate hexahydrate, $Ce(NO_3)_3 \cdot 6H_2O$, and hydrogen peroxide. Because the oxidation with H_2O_2 is slow in an acidic media, a few drops (10-20) of aqueous ammonia were added to accelerate the oxidation of Ce^{III} to Ce^{IV}. Cerium oxide was precipitated at two different hydrogen peroxide concentrations. The molar ratios of cerium to hydrogen peroxide were 1:0.8 (sample **I**) and 1:1.2 (sample **II**).

X-Ray Absorption Measurements. X-ray absorption measurements were carried out at the unfocused 4-3 beamline of Stanford Synchrotron Radiation Laboratory. The measurements were carried out in both transmission and fluorescence modes at room temperature.

Results and Discussion

XANES Spectral Results. X-ray diffraction (XRD) patterns of both hydrous CeO_2 and **I** revealed a fluorite structure with a particle size of ~6 nm derived from the line broadening.[4] The particle size of anhydrous CeO_2 was larger than that of hydrous CeO_2 and sample **I**, whereas **II** was amorphous.[4] The XANES spectra for anhydrous CeO_2, hydrous CeO_2, **I**, and **II** are depicted in Figure 1. Four peaks were fit in the XANES spectra, a high energy peak A, main peak B, low energy peak C, and pre-edge peak D. Peaks A and B were assigned as due to a mixture of the multielectron configurations $L4f^{0}5d^{1}$ and $L4f^{1}5d^{1}$, respectively, where L denotes the hole in the $2p$ shell, and $5d^1$ refers to the excited electron in the previously unoccupied $5d$ state.[5] Integration of peak C at ~5723 eV displayed a different area for each of the samples. Based on this and other[4] observations, the electronic transition that occurred at ~5723 eV was interpreted as arising from a combination of crystal field splitting and excitation of different amounts of a Ce^{III} contaminant present in all the samples. Unfortunately, the characteristic white line of a typical Ce^{III} compound, $Ce(NO_3)_3 \cdot 6H_2O$, is observed at the same energy as peak C.[6] No significant change in the white line areas, as determined from the many-body configuration theory for a core transition to localized electronic states, was observed in all of the samples under study. Furthermore, changing the hydrogen peroxide concentration during the precipitation of cerium oxide did not result in a significant change in the electronic cerium mixed-valence state.

Modeling of the XANES spectra, in terms of the one-electron band structure of the crystal for a core transition to delocalized electronic states, is a useful approach to determine the cerium valence state and to support the results obtained from the many-body configuration theory for a core transition to localized electronic states. The XANES features have been calculated using FEFF8.20 code, figure 2.[7] The calculated valences obtained from the XANES spectra simulation using FEFF8.20 are in agreement with those obtained from the many-body configuration theory, Table 1.

EXAFS Spectral Results and Discussion. Results of the fitting of the EXAFS spectra are summarized in Table 2. The extracted k^3-weighted EXAFS oscillations, the corresponding Fourier filtered data, and modeled EXAFS results for anhydrous CeO_2, hydrous CeO_2, **I**, and **II** are shown in Figure 3. The EXAFS spectrum of the amorphous precipitate (sample **II**) exhibited a different structure than that of either anhydrous CeO_2, hydrous CeO_2, or **I**. Above the spurious low-R feature, the major oxygen Fourier transformed peak appeared dampened and had practically non-existent outer-shell, Ce-Ce or Ce-O2, features. The increase of Ce-O1 distance in **II** reflects a high-σ^2 value and the necessity of allowing an additional anharmonic correction term for the O1 path. Visual inspection of the hydrous CeO_2 and **I** spectra showed that the samples' near-neighbor structure deviated significantly from either anhydrous CeO_2 or **II**. The Ce-O1, the Ce-Ce, and the Ce-O2 neighbor coordinations in hydrous CeO_2 appeared more ordered with smaller σ^2 as compared with **I**, or **II**, but less ordered than the crystalline anhydrous CeO_2. Analysis of EXAFS spectrum of **I** indicated comparable oscillation amplitudes to those of hydrous CeO_2. The distance between cerium centers and oxygen neighbors in the first coordination shell are of similar magnitude, 2.360 and 2.364 Å for hydrous CeO_2 and **I**, respectively. However, larger deviations were observed in Ce-Ce and Ce-O2 distances between hydrous CeO_2 and **I** samples. Hydrogen peroxide thus induced changes in the coordination spheres around cerium, longer bond distances and fewer coordinated atoms. The parameters in the EXAFS analysis yielded higher N_{O1} values, higher σ^2, and longer Ce-O bond distances for both hydrous CeO_2, **I**, and especially **II** compared to anhydrous CeO_2. Increasing the coordination number, N1, was attributed to incorporating H_2O molecules that resulted in decreasing the crystalline order. The evaluation of each parameter in going from anhydrous CeO_2 to **II** indicates a decrease in crystalline order. The Fourier transformed peak representing the Ce-Ce interaction of hydrous and **I** were more pronounced than in amorphous **II**, and less pronounced than in crystalline anhydrous CeO_2. The enhanced Ce-Ce distance, and the decreased coordination number, N2, in both hydrous CeO_2 and **I** compared with anhydrous CeO_2 were attributed to a higher degree of defect sites in these nanocrystalline materials.

Conclusions

Different hydrogen peroxide concentrations were employed during the precipitations of cerium oxide. XANES analysis clearly showed a significant change in the intensity of the white line peaks of precipitated cerium oxide revealing a smaller particle size as compared to anhydrous CeO_2. However, no significant change in cerium spectroscopic valence for precipitated cerium oxides was observed, regardless of peroxide concentration, in comparison to the anhydrous CeO_2. Precipitation of cerium oxide utilizing H_2O_2 resulted in an increased bond distance, $R_{Ce\text{-}O}$, as well as coordination number of the first coordination shell Ce-O. A decrease in the coordination numbers of the second shell, Ce-Ce, and the third shell, Ce-O, were observed from the radial distribution function. Furthermore, the Debye-Waller factor for the three shells exhibited a

consistent trend as the value of the three coordination shells increased going from anhydrous CeO_2, hydrous CeO_2, sample **I**, to sample **II**. Based on these observations, the degree of disorder increased with increasing H2O2 concentration during precipitation of cerium oxide, consequently increasing the potential for cerium oxide precipitate to function as oxygen traps. Decreasing the particle size of cerium oxide precipitates, with probable increase in oxygen trapping capability offers additional insight into the enhancement of the fuel cells performance using cerium oxide precipitates.

Table 1. Cerium L_{III}-edge XANES Fits of the Two Characteristic Peaks.

Sample	Anhydrous CeO2	Hydrous CeO2	**I**	**II**
Peak (A) position	5735.1	5735.2	5734.3	5734.7
Peak (A) width	3.5	3.2	3.6	3.8
Peak (B) position	5727.6	5727.1	5726.5	5726.5
Peak (B) width	2.8	2.9	3.0	3.2
Valence-Least square fitting	3.45	3.51	3.47	3.48
FEFF-calculated valence	3.48	3.49	3.51	3.52

Table 2. Parameters Extracted from Least-Squares Fitting of the EXAFS Spectra

Sample	Crystallo-graphic data	Anhydrous CeO2	Hydrous CeO2	**I**	**II**
Ce-O1 R(Å)	2.343	2.343*	2.360 (2)	2.364 (3)	2.420 (1)
Ce-O1 N1	8	8*	9.5 (1)	10 (1.5)	11.5(1.3)
Ce-O1 σ^2 (10^{-3} Å^2)	-	3.20(4)	6.45(5)	9.43(2)	10.22 (6)
Ce-Ce R(Å)	3.826	3.826*	3.847 (3)	4.122 (2)	3.814 (4)
Ce-Ce N1	12	12*	7.4 (1.1)	6.6 (1.6)	3.6 (1)
Ce-Ce σ^2 (10^{-3} Å^2)	-	1.50(2)	3.30(6)	4.20(1)	9.60(2)
Ce-O2 R(Å	4.487	4.487*	4.210 (5)	4.127 (17)	-
Ce-O2 N1	24	24*	18.0 (1.6)	16.1 (1)	-
Ce-O2 σ^2 (10^{-3} Å^2)	-	2.40(1)	3.20(5)	4.80(5)	-

* Fixed parameters

Acknowledgement. Support for this project was provided through the Air Force Research Laboratory Materials and Manufacturing Directorate, project manager Steve Szaruga. Portions of this research were carried out at the Stanford Synchrotron Radiation Laboratory, a national user facility operated by Stanford University on behalf of the U.S. Department of Energy, Office of Basic Energy Sciences.

References

(1) Winterer, M.; Nitsche, R.; Hahn, H., *J. Phys. IV France* **1997**, 7, C2-1211.
(2) Fierro, J. L. G.; Soria, J.; Sanz, J.; Rojo, M. J., *J. Solid State Chem.* **1987**, 66, 154.
(3) Sun, Y.; Sermon, P. A., *J. Mater. Chem.* **1996**, 6, 1025.
(4) Schuman, T., "Cerium oxide pigments for anti-corrosion primer coatings," submitted.
(5) Bianconi, A.; Marcelli, A.; Dexpert, H.; Karnatak, R.; Kotani, A.; Jo, T.; Petiau, J., *Phys. Rev. B* **1987**, 35, 806.
(6) Wu, Z.; Benfield, R. E.; Guo, L.; Li, H.; Yang, q.; Grandjean, D.; Li, q.; Zhu, H., *J. Phys.: Condens. Matter* **1994**, 6, 8429.
(7) Ankudinov , A. L; Bouldin, C.; Rehr, J. J.; Sims, J.; Hung, H., *Phys. Rev. B* **2002**, 65, 104107.

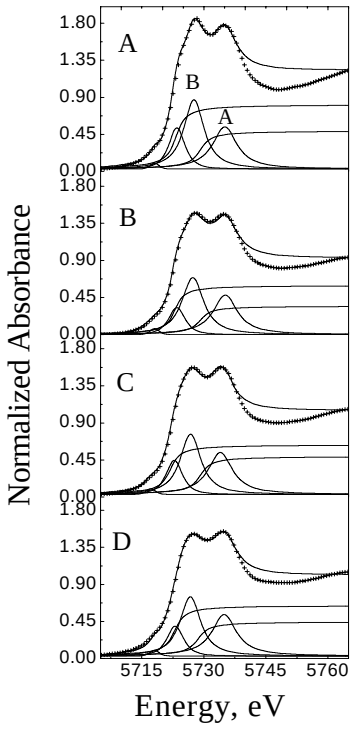

Figure 1. Ce L_{III}-edge XANES spectra with fits of (A) anhydrous CeO_2, (B) hydrous CeO_2, (C) Sample **I**, and (D) Sample **II.**

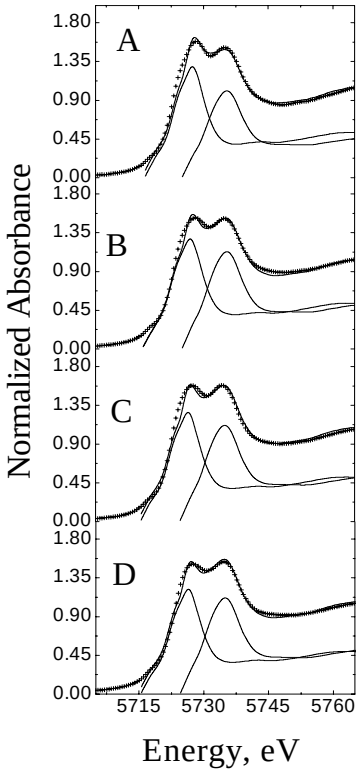

Figure 2. Ce L_{III}-edge XANES spectra with the calculated XANES spectra of (A) anhydrous CeO_2, (B) hydrous CeO_2, (C) Sample **I**, and (D) Sample **II**.

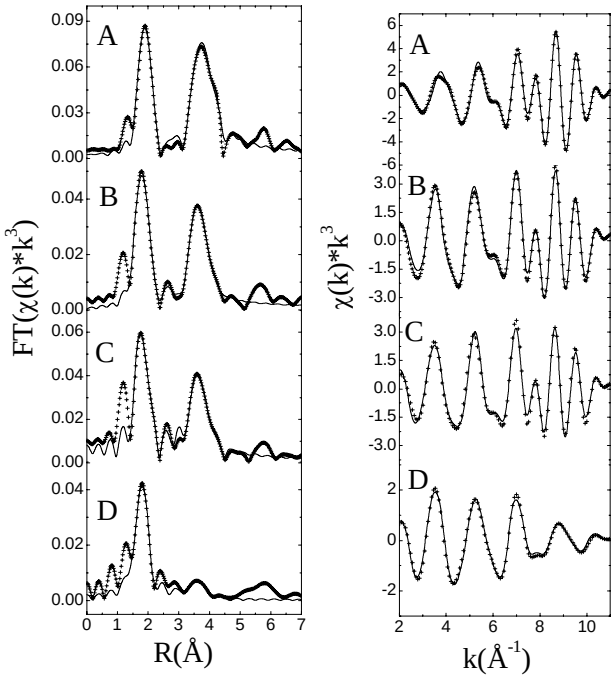

Figure 3. R-space fit result for (A) anhydrous CeO_2, (B) hydrous CeO_2, (C) Sample **I**, and (D) Sample **II**. Right Panel: Corresponding Fourier-filtered data back-transformed fit.

Deposit Formation within a Solid Oxide Fuel Cell (SOFC) Operating on Butane

Katie O'Gara, Chad Sheng and Anthony M. Dean

Chemical Engineering Department
Colorado School of Mines
Golden, CO 80401

Introduction

Fuel cell technology presents the possibility of increased energy efficiency with decreased detrimental environmental impact over conventional combustion. Solid-oxide fuel cells (SOFC), in particular, offer a very promising method for direct production of electrical energy from currently available fossil fuels, thus postponing the need to build a hydrogen delivery infrastructure. Hybrid SOFCs, coupled with a heat recovery system such as a gas turbine generator, have the potential for fuel-to-electricity efficiencies approaching 75–80%. However, the use of hydrocarbon fuels opens the possibility of deposit formation. The high operating temperatures of a SOFC can lead to fuel degradation and formation of carbonaceous deposits within the fuel channels and porous anode structures. SOFCs that run on H_2 as a fuel source often utilize nickel as the electrical conductor. However, nickel is known to react with hydrocarbons to form deposits. Several studies have reported on the use of different materials to minimize deposit formation, e.g. [1], as well as upstream conversion of hydrocarbon fuels to syngas (CO and H_2) as a way to avoid deposit formation, e.g. [2].

An important feature of SOFC operation is the electrochemical formation of H_2O and CO_2 on the anode side. These species form at the three-phase (fuel, anode, electrolyte) boundary and diffuse through the porous anode to the anode channel, thus diluting the fuel stream. While still in the anode, these species can participate in "internal reforming" reactions, performing the same function of converting hydrocarbon fuel to CO and H_2 that might be accomplished by the upstream reforming discussed earlier. Under these conditions it is likely that the water-gas shift reaction would also take place, converting CO + H_2O to H_2 + CO_2. These reactions can further complicate the identity of the "fuel" that will participate in the electrochemical reactions. In addition, steam gasification, to remove any deposits already formed, might be catalyzed by the metal in the anode cermet.

A complete SOFC model is very complex, requiring descriptions of kinetics in multiple phases and coupling the kinetics to multiple transport processes. Chemical reactions within the SOFC occur in three regions: in the anode channel (gas-phase kinetics), on the surface of the porous anode (heterogeneous catalysis) and at the three-phase boundary (electrochemical catalysis). Thus the homogeneous and heterogeneous kinetics have the potential to substantially change the nature of the species that ultimately undergo electrochemical oxidation. It is essential to account for such kinetic modifications to properly characterize SOFC operation and predict the overall efficiency.

As a first step toward characterizing the complex kinetics, we need to make sure that we properly understand the gas-phase hydrocarbon chemistry. The effect of gas phase reactions of methane in SOFCs has been reported [3]. We have recently extended this approach to butane, which is significantly more reactive than methane and thus more representative of a range of hydrocarbon fuels [4]. We showed that we could capture the effect of temperature on both conversion and major product selectivity using a detailed chemical mechanism. In this work, we focus on the effects of the electrochemical production of H_2O and CO_2 on the gas-phase production rate of deposits. Earlier it was shown that the electrochemical production of H_2O and CO_2 did indeed significantly impact the predictions regarding deposit formation from methane [3]. Here we discuss the effects of H_2O and CO_2 on deposits from butane, and we also explore the effects of upstream reforming and partial oxidation on deposit formation.

Reaction Mechanism. The reaction mechanism that was utilized in this study consists of 291 species and 2498 elementary reactions [4]. The mechanism includes pyrolysis and oxidation kinetics for C_6 and smaller species. It includes molecular weight growth chemistry to allow formation of PAH species up to C_{24}. Beyond formation of naphthalene, PAH growth is modeled using the approach proposed by Frenklach and Warnatz [5].

Deposit Formation from Butane Pyrolysis. In our experiments, qualitative observations of deposit formation were made by examining the quartz reactor after running a specific mixture containing butane through the reactor for 4 hours. We observed no apparent deposit formation within the reactor for any of the mixtures at 650ºC or lower temperatures. As the reactor temperature was increased to 700°C, an obvious deposit film was observed on the inner walls of the quartz reactor with the neat butane (100% nC_4) mixture. The deposit film was noticeably less dense for a 50/50 (by mole) nC4/N2 mixture, and barely evident for a 50/50 nC4/H2O mixture. The first inference from these qualitative observations is that dilution does play a role in minimizing deposit formation. This is to be expected, since the lower concentration of reactive species would be expected to decrease the rate of molecular weight growth leading to deposits. The marked difference in the nitrogen and steam mixtures suggests that the steam is either actively participating in inhibition of molecular weight growth or that it is participating in some type of gasification of the deposit. All three mixtures show significant deposit formation at 800ºC.

To compare to the kinetic model, we considered all species in the model predictions above C_4 (denoted as C_5^+) as potential deposit precursors. The predicted C_5^+ mole fraction is a very strong function of temperature as illustrated in Fig. 1.

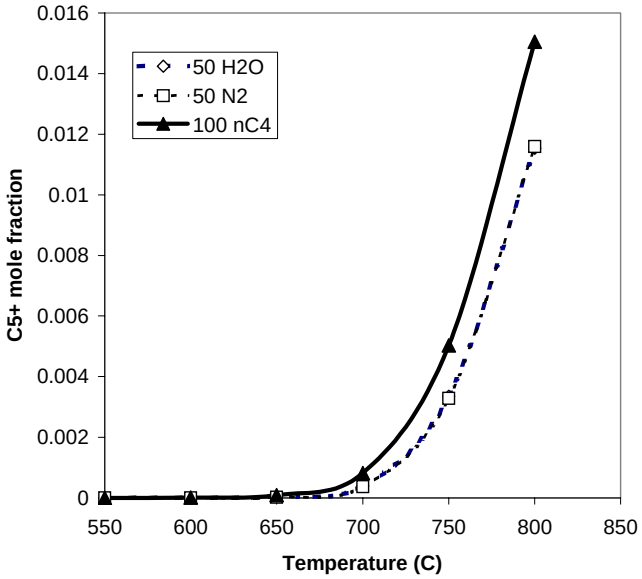

Figure 1. Predicted effect of temperature on the mole fraction of C5+ species.

It is encouraging to note that the predicted rapid increase in deposit precursors near 700ºC is consistent with the experimental observations. The predicted C_5+ values for the steam and nitrogen dilution cases are virtually identical. This is consistent with our

observation that any gas-phase reactions of steam are very slow under these conditions, and thus steam is simply acting as a diluent, just like nitrogen. This is in contrast to the experimental observations that steam diminished deposit formation. This effect is probably due to heterogeneous reactions. The ratio of C_{5+} predicted for the neat butane case to that of the diluted mixtures decreases from approximately five at 550ºC to only slightly greater than unity at 800ºC. Thus at the higher temperatures, the predictions suggest that the inhibition of deposit formation by dilution is much less effective.

Effects of Electrochemistry on Deposit Formation. To account for electrochemical production of steam and carbon dioxide, we assume a current density of 0.5 amp/cm^2 and use the overall stoichiometry to determine the number of moles formed:

$$C_4H_{10} + 13O^{2-} \rightarrow 4\,CO_2 + 5\,H_2O + 26\,e^-$$

We then allow this electrochemical flux to enter uniformily along the anode channel as pictured below.

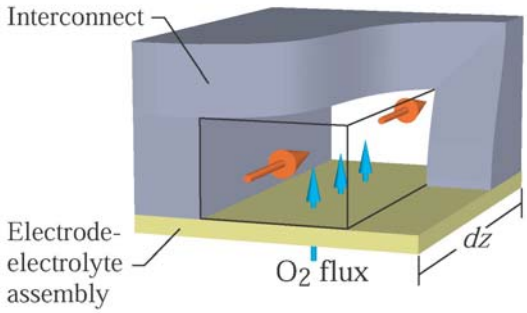

Fig. 2 illustrates the effect of this electrochemical flux on the temperature dependence of formation of C_5^+. The predictions show that added dilution from the CO_2 and H_2O production allows operation at higher temperatures. By comparing to Fig. 1, note that the effect of the electrochemical production is larger than that due to 50/50 dilution by N_2.

Effects of Partial Oxidation or Steam Reforming on Deposits. We also looked at the effect of pretreating the fuel by partial oxidation or steam reforming on the amount of C_5^+ species produced at various temperatures. The results of the fuel stream being split, 50% treated and 50% sent directly to the fuel cell, for both pretreatment options are also shown in Fig. 2. The fuel composition used in the model came from equilibrium **calculations based on of the following stoichiometries:**

$$C_4H_{10} + 2H_2O \rightarrow CO + H_2 + \ldots \text{(Steam reforming)}$$
$$C_4H_{10} + 3.76N_2 + O_2 \rightarrow CO + H_2 + \ldots \text{(Partial oxidation)}$$

As expected, upstream partial oxidation and reforming of the fuel further reduces the propensity to form deposits because it dilutes the stream and breaks the fuel down into lighter species that are less likely to form deposits. When the entire fuel stream was pretreated, we observed no signs of molecular weight growth at temperatures below 1000ºC.

Conclusion

The kinetic model predicts a significant decrease in the amount of C_5^+ species formed when electrochemistry is accounted for and even less when there is upstream steam reforming or partial oxidation of the fuel, possibly allowing for a higher operation temperature of the SOFC. Because heterogeneous chemistry at the anode surface was not included in these predictions, the actual amount of deposit formation cannot be predicted from this model. Nevertheless, the fact that certain metals can be added to the anode to promote internal reforming suggests this is an additional mechanism to avoid deposit formation.

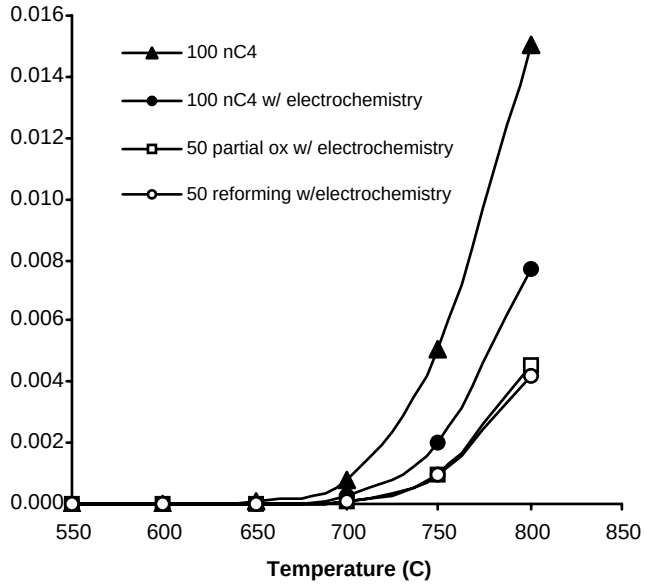

Figure 2. Predicted effect electrochemistry and pretreating the fuel on the mole fraction of C_{5+} species produced vs temperature.

Acknowledgements. This work was funded under DARPA Contract Number MDA972-01-C-0068 and a DoD Multidisciplinary University Research Initiative (MURI) program administered by the Office of Naval Research under Grant N00014-02-1-0665. The authors would like to thank ITN Energy Systems, Inc. for the use of their facilities where the experimental work was conducted. We also would like to thank Hans-Heinrich Carstensen and Chitral Naik for providing some of the elementary reaction rates used in the current model and Gaurav Gupta for performing some of the modeling calculations.

References

1. Lu, C., et al., *SOFCs for Direct Oxidation of Hydrocarbon Fuels with Samaria-Doped Ceria Electrolyte.* Journal of The Electrochemical Society, 2003. **150**(3): p. A354-A358.
2. Krummenacher, J.J., K.N. West, and L.D. Schmidt, *Catalytic partial oxidation of higher hydrocarbons at millisecond contact times: decane, hexadecane, and diesel fuel.* Journal of Catalysis, 2003. **215**: p. 332-343.
3. Walters, K.M., et al., *Homogeneous kinetics and equilibrium predictions of coking propensity in the anode channels of direct oxidation solid-oxide fuel cells using dry natural gas.* Journal of Power Sources, 2003. **123**(2): p. 182-189.
4. Sheng, C.Y. and A.M. Dean, *The importance of gas-phase kinetics within the anode channel of a solid-oxide fuel cell.* J. Phys. Chem A, asap.
5. Frenklach, M. and J. Warnatz, *Detailed Modeling of PAH Profiles in a Sooting Low-Pressure Acetylene Flame.* Combustion Science and Technology, 1987. **51**: p. 265-283.

CARBON DEPOSIT FORMATION FROM THERMAL STRESSING OF PETROLEUM FUELS

Orhan Altin and Semih Eser

Department of Energy and Geo-Environmental Engineering and The Energy Institute
101 Hosler Building
The Pennsylvania State University
University Park, PA, 16802

Introduction

The thermal stability of fuels is of concern for the maintenance of all types of combustion engines. Thermal stability is measured in terms of the fuel's tendency to form deposits on fuel lines and nozzles of jet engines as well as on intake valves, fuel injectors, and combustion chamber surfaces in gasoline and diesel engines. Fuel degradation can cause engine failure, engine malfunction, and affects engine performance. Poor stability of fuel can lead to increased maintenance costs, and maintenance problems, such as equipment vulnerability and decreased reliability which may result in profit losses.

This article covers thermal decomposition of diesel fuel, gasoline, and jet fuel, and their respective reactions on metal surfaces leading to the deposition of carbonaceous solids.

Petroleum Fuels

Petroleum fuels, such as gasoline, diesel, and jet fuel contain a complex mixture of hundreds of hydrocarbons. The hydrocarbons vary by class—paraffins, olefins, and aromatics, depending on the nature of chemical bonding between the carbon atoms in hydrocarbon molecules. These fuels also contain additives designed for specific purposes. The molecular composition of fuels determines their physical properties, engine performance, and thermal stability characteristics. In general, fuels are produced to meet the property limits dictated by the industrial specifications and regulations, not to achieve a specific distribution of hydrocarbons by class, or size. Figure 1 shows a carbon number distribution of typical gasoline, which is in the range of C_4 to C_{12} with the average carbon number of $C_{6.8}$. Gasoline also contains small amounts – less than 0.1 volume % – of heteroatom compounds with sulfur, nitrogen, or oxygen atoms (excluding added oxygenates) in their structures. Compared to gasoline, typical diesel fuel consists of a more complex mixture of thousands of individual compounds, most with carbon numbers between 10 and 22. Most of these compounds are members of the paraffins group (normal-, iso-, or cyclo-paraffins), or aromatic hydrocarbons boiling between approximately 150˚C and 400˚C. Originally diesel fuels were straight-run products obtained from crude distillation in a refinery. Today, where the demand for high-octane number gasolines and distillate fuels are high, diesel fuels may also contain distillates from cracking processes, such as light cycle oils (LCO) from Fluid Catalytic Cracking (FCC) unit.

Jet fuels (military and civilian turbine fuels, JP-5, JPTS, JP-7, JP-8, JP8+100, Jet-A, and Jet A-1) are mainly kerosene type having a carbon number distribution between about 8 and 16 carbon numbers, as seen in Figure 1. Kerosene fuels like JP-8 (military) or Jet A (civil) also contain a mixture of literally thousands of hydrocarbons. For JP-8, these hydrocarbons can be divided into three broad classes—aromatics (about 20%), n-paraffins and isoparaffins (60%), and cycloparaffins (naphthenes, 20%). Typically, normal paraffins have the highest concentration among the hydrocarbons and cycloparaffins and aromatics consist mostly of methyl-substituted single-ring molecules. The concentration of various components can vary significantly from one batch to another, depending on the crude oil used and the process history of the fuels.

Problem of Thermal Stability

Thermal stability is typically described in terms of the fuel's tendency to form deposits on fuel lines, valves, injectors, and combustion chamber surfaces in engines. These fuel system deposits can be created by two distinct free radical pathways: low temperature autoxidation--usually called fouling--and higher temperature pyrolysis, called coking or carbon deposition.

Autoxidation or oxidative stability differs from thermal stability by referring to the rate at which oxygen is consumed and oxidative products are formed. Autoxidation reactions occur during fuel storage and exposure to high temperature in fuel lines which results in a series of liquid oxidation reactions of alkyl radicals generating hydroperoxides and other oxidized products which are believed to be responsible for solid deposit formation (1-4).

At elevated temperatures (>350°C), carbon deposits usually form via two different routes: Decomposition of hydrocarbons to elemental carbon and hydrogen; or polymerization/condensation of hydrocarbon species to larger polynuclear aromatic hydrocarbons (PAHs) which then nucleate and grow to become carbonaceous deposit. Metal catalysis of carbon deposition often follows the decomposition route, whereas non-catalytic (or thermal) carbon deposition usually proceeds via the polymerization route.

The formation of catalytic or non-catalytic carbon deposit depends on the characteristics of the substrate surface. A non-catalytic surface may affect the heat/mass transfer in the system and act as an inert substrate to collect the carbon deposit the formation of which is thermally initiated in the fluid phase. In contrast, a catalytic surface could, in addition, interact with the reactive species and accelerate the deposit formation.

Carbon Deposit Formation on Metal Surfaces During Thermal Stressing

Gasoline Fuel. Almost all types of gasolines produce carbon deposits on engine components over time. The rate of deposit formation depends on the nature of metal surfaces in the fuel systems and gasoline additives used to inhibit solid deposition. Carbon deposits mainly build up on fuel injectors, intake valves and ports, and in the combustion chamber. Fuel injectors are designed accurately meter fuel to the engine and deliver it in a precise pattern of fine droplets. Since the fuel passages are small, injectors are highly sensitive to small amounts of deposits in the critical regions where the fuel is metered and atomized. These deposits can reduce the fuel flow and alter the spray pattern, degrading driveability, decreasing power and fuel economy and increasing emissions. Deposit formation can cause similar problems in carbureted engines because carburetors also use a number of small channels and orifices to meter the fuel.

Problems with solid deposition in the combustion chamber and or in the intake system can sometimes be underestimated during initial engine development. Often, these problems become apparent after long duration of engine running time. Deposit precursors in the fuel delivery, or combustion units are formed by thermal cracking, oxidation, and polymerization of the fuel, and these processes may be catalyzed by metal surfaces.

Numerous investigations have suggested some possibilities for reducing these problems in the future. For example, Aradi et al. (5) investigated the role of surface catalytic activity in injector deposit formation and observed that in the presence of stainless steel walls greater amount of insoluble materials formed on the surface than that on a glass insert. Guthrie (6), on the other hand, found that the surface temperature was the most important factor in the formation of

deposits. Similarly, Kinoshita et al. (7) suggested that the best solution for deposit control was to use an insulating material on the areas of the injector exposed to the combustion chamber so as to raise the surface temperature to levels high enough to prevent deposit formation, i.e., 350˚C, through oxidation/gasification of deposits, or deposit precursors

Deposit formation in gasoline engines appears to depend strongly on the chemical composition of high-boiling components of gasoline that have high deposition tendencies. Charlisle et al. (8) studied the effect of fuel composition on air-assisted direct injection spark ignition research engine and concluded that the aromatic hydrocarbon content of the fuel has a significant effect on deposit formation, higher the aromatics content more extensive was the deposit formation. The fuel olefin content, however, showed a less significant effect on deposit formation.

Intake valves and ports are subject to more deposit build up than fuel injectors because they operate at higher temperatures. Heavy valve and port deposits reduce maximum engine power because they restrict air flow. Intake valve deposits have also been shown to affect exhaust emissions, particularly VOCs and NOx. The engine deposits could cause substantial increase in exhaust gas temperatures, and therefore the octane number requirement because of preheating of the charge drawn into the cylinder. The increased octane number requirement prevents the use of optimum compression ratio and ignition timing, and consequently limits the engine efficiency well below the maximum possible with a fuel of a given octane number used in a clean engine.

Diesel Fuel. Diesel fuels can form deposits in the nozzle area of injectors that is exposed to high cylinder temperatures. The extent of deposit formation varies with engine design, fuel composition, lubricant composition, and operating conditions. Excessive deposit accumulation affects the injector flow patterns which ,in turn, hinders the fuel-air mixing process that results in decreased fuel economy and increased emissions of soot and unburned fuel. To avoid the deposit formation problems on fuel injectors, detergent type additives are added to the fuel to keep the injectors clean. These additives are composed of a polar group that bonds to deposits and deposit precursors, and a non-polar group that dissolves in the fuel. Thus, the additive can redissolve deposits that already have formed and reduce the formation of deposits by stabilizing the deposit precursors.

Carbon deposit formation from diesel fuels mainly involves the chemical conversion of precursors to species of higher molecular weight with limited fuel instability. The precursors include nitrogen and sulfur containing compounds, organic acids, and reactive olefins. Pedley et al. (1) established a mechanism by which insolubles are formed in the acid-catalyzed conversion of phenalenones and indoles to complex indolylphenalene salts. Phenalenones are formed by oxidation of certain reactive olefins; indoles occur naturally in certain blend components of diesel fuel. Certain dissolved metals, especially copper, contribute by catalyzing oxidation reactions.

Thermal stability of diesel fuels is important because of their function as heat transfer fluid. More stringent thermal stability requirements may be necessary for future injector designs that employ higher pressures to achieve better combustion and lower emissions. Spilners and Hedenburg (9) who studied carbon deposit formation in single cylinder test engine observed that the olefin content of the fuel had the greatest effect on the deposit formation tendency.

Fuel injectors in diesel engines are precision instruments. Their function is to measure exactly the right amount of fuel into the combustion chamber on each compression stroke, to control engine combustion, fuel economy, and engine noise. Injector carbon deposits cause operational problems, such as excessive smoke emission, loss of power, poor fuel economy, degraded emission, excessive engine noise, rough engine operation, and poor drivability. Injector carbon deposits, that usually appear as a lacquer on the piston that squirts the fuel through the injector nozzle, are believed to result from the reactions of the oxidation products of unstable diesel fuel (10).

Jet Fuel. Recent advances in jet aircraft and engine technology have placed an ever-increasing heat load on the aircraft. Currently, jet fuels play two important roles in advanced aircraft, propellant and coolant. The need to cool hot parts of the engine had been evident ever since the invention of the internal combustion engine. As engine performance goals and flight speeds have increased, the need for more effective cooling has also increased. For example, the thermal stability limit of JP-8 fuel was established at a bulk temperature of 163˚C and a wetted wall temperature of 204˚C. Exposure to higher temperatures accelerates the fuels reactions that lead to gum and carbon deposit accumulation in: i) fuel filters, increasing the pressure drop across the filter and reducing fuel flow, ii) fuel injector nozzles, disrupting the spray pattern, which may lead to hot spots in the combustion chamber, iii) the main engine control, interfering with fuel flow and engine system control, and iv) heat exchangers, reducing heat transfer efficiency and fuel flow. These deposits may lead to increased maintenance and in extreme cases, to disastrous accidents. To resolve the problem, an Aircraft Thermal management Working Group of Wright Research and Development Center (WRDC) recommended the development of high thermally stability fuels, such as: (i) a high temperature thermally stable JP-8+100 fuel which provides a 50% improvement in the heat sink capability over conventional JP-8 fuel, and (ii) a new fuel JP-900 that has a 482˚C thermal stability and could eliminate the need to recirculate fuel onboard an aircraft. To meet the evolving challenge of improving the cooling potential of jet fuel, while maintaining the current availability at minimal cost a joint government/industry/academia program developed an additive package for JP-8 fuel named as JP8+100 fuel. Hundreds of additives have been tested and a package has been formulated that contains a detergent/dispersant in addition to the standard antioxidant and metal deactivator additives. The additive package allows the bulk fuel temperature to increase from 163˚C to 218˚C without generating fuel system deposits (11).

Marteney and Spadaccini (12) suggested two basic coking processes: 1) A homogeneous oxidation reaction occurring in the fuel free stream forming coke particles which adhere to the fuel passage surface. 2) A heterogeneous catalytic reaction occurring at the fuel passage metal surface. If mechanism #1 dominates, a polished surface may prevent carbon from adhering. If, on the other hand, mechanism #2 dominates, an inert surface should reduce the coking rate.

Metal surfaces could act as catalysts for dehydrogenation reactions that lead to the formation of carbon deposits. At elevated temperatures, stainless steel surfaces deposit large amounts of carbonaceous deposits from jet fuel decomposition. Carbon deposit precursors such as radicals and unsaturated hydrocarbons are formed in the gas phase and react with active centers on metal surfaces (13,14) An effective way of preventing deposition from pyrolysis of fuels was found to be the use of inert coatings such as Zirconia (15) and Silcosteel® (Restek Corp, State College, PA) (14). Coating of metal alloy surfaces prevents interaction between deposit precursors and active metal surfaces that lead eventually to deposition of solid carbon.

Trace amounts of some sulfur compounds may also affect the rate of deposit formation and metal surface degradation. The sulphidation of metals at high temperatures has become a matter of increasing concern in industrial applications, particularly in energy conversion systems using fossil fuel. Because of high diffusivity and formation of eutectic melts with metals, sulfur reacts with metals to

form metal sulfides at relatively low temperatures, causing severe localized corrosion on heat-resistant alloys and superalloys. Taylor (16) examined the role of sulfur compounds in deposit formation from a JP-5 fuel. Addition of 300 ppm diphenyl sulfide and phenyl benzyl sulfide to JP-5 fuel enhanced the carbon deposit formation significantly. On the other hand, addition of benzothiophene and dibenzothiophene did not contribute to the formation of deposits. Figure 2 summarizes the carbon deposit formation mechanism on metal surfaces by combining hydrocarbon degradation on catalytic metal surface with sulfur–metal reaction resulting in amorphous and filamentous carbon deposition.

Conclusions

The long-term automotive and aircraft related technological benefits can be derived from fundamental understanding of fuel thermal stability issues such as, free radical autoxidation mechanism, establishing a global chemistry model, understanding of fuel-metal surface interactions, and developing additive packages to increase the thermal stability of gasoline, diesel, and jet fuels. Research and development efforts in these areas will help eliminate the operational problems associated with carbon deposit accumulation on various components of fuel delivery and combustion systems in internal combustion engines.

References

(1) Pedley, J. F.; Hiley, R. W.; Solly R. K., *Fuel*, 1989**,** *68*, 27-31.

(2) Zabarnick, S., *Chem. Ind. Eng. Chem. Res*. **1993**, *32*, 1012-1017.

(3) Haneghan, P. S.; Zabarnick, S., *Fuel*, **1994**, *73*, 35-43.

(4) Edwards, T.; Zabarnick, S., *Ind. Eng. Chem. Res.* **1993**, *32*, 3117-3122.

(5) Aradi, A. A.; Imoehl, B.; N. L. Avery, N. L.; Wells, P. P.; R. W. Grosser, R. W., SAE Paper, 1999-01-3690.

(6) Guthrie, P. W., SAE Paper, 2001-01-1202.

(7) Kinoshita, M.; Narasimhan, S.; Shibata H.; Niwa Y., European Patent EP0828075, 1998.

(8) Charlisle, H. W.; Frew, R. W.; Mills, J. R.; Aradi, A. A.; Avery, N. L., SAE Paper 2001-01-2030.

(9) Spilners, I. J.; Hedenburg J. F., In *Chemistry of Engine Combustion Deposits*; Ebert, L. B., Ed.; Plenum Press, New York, 1985; 289.

(10) Sapienza, R. S.; Butcher, T.; Krushna, C. R.; Gaffney, J., In *Chemistry of Engine Combustion Deposits*; Ebert, L. B., Ed.; Plenum Press: New York, 1985; 263-272.

(11) Haneghan, S. P.; Zabarnick, S.; Ballal, D. R.; Harrison, W. E., 34th Aerospace Sciences Meeting and Exhibit , Reno, NV, Jan 15-18, 1996; AIAA 96-0403.

(12) Marteney , P. J.; Spadaccini, L. J., J. Eng. Gas Turb. Pow. (ASME Transactions). **1986**, *108*, 648-654.

(13) Altin, O.; Eser, S., *Ind. Eng. Chem. Res.* **2001**, *40*, 596-603

(14) Altin, O.; Eser, S., *Ind. Eng. Chem. Res.* **2001**, *40*, 589-595.

(15) Sticles, R. W.; Dodds W. J.; Koblish T. R.; Sager J.; Clouser S., *J. Eng. Gas Turb. Pow. (ASME Transactions).* **1993**, *115*, 439-447.

(16) Taylor, W. F., *Ind. Eng. Chem. Prod. Res. Dev.* **1976**, *15*, 64-68.

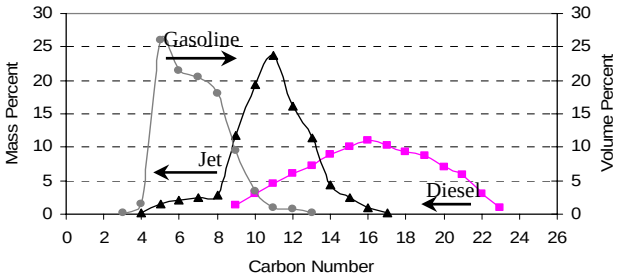

Figure 1. Carbon number distribution of petroleum fuels.

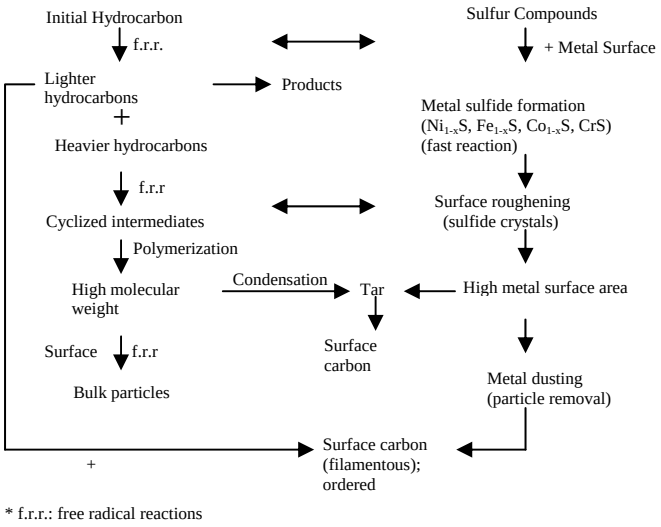

Figure 2. Carbon deposition mechanism including sulfur-metal surface involvement.

CHARACTERIZATION OF DIESEL AND BIODIESEL SOOT

Juhun Song, Mahabubul Alam and André L. Boehman

The Energy Institute
The Pennsylvania State University
405 Academic Activities Building
University Park, PA 16802

Kirk Miller

ConocoPhillips
600 N. Dairy Ashford
Houston, TX 77252

Introduction

Diesel fuel production from renewable sources such as vegetable oils and animal fats offers the potential of both reducing fossil carbon emissions and producing alternative ultra clean transportation fuels. It is well known that biodiesel, neat or in blends, can provide reductions in PM mass emission through either oxygen content or enhanced air entrainment due to the higher boiling range of biodiesel [1]. However, recent observations have indicated that biodiesel may provide other benefits with regard to particulate emissions. These observations have shown an oxidation reactivity variation with soots derived from different fuels. Identifying the dominant mechanism during oxidation, if any, may have practical implications for reducing the temperature required to regenerate catalyzed diesel particulate filter (DPF) [2-3]. There exists evidence of correlation between reactivity and structure in the case of carbon blacks or coal chars that are synthesized from different hydrocarbons and at different temperature conditions [4-5]. However, the manner in which crystallinity or pore structure affects soot oxidation rates has not been clarified for diesel soot whether that soot is derived from conventional or alternative fuel sources.

In this paper, we present comparison of soot nanostructures of particulates produced from two different fuels (an ultra low sulfur diesel fuel and its B20 blend) on commercial direct injection (DI) diesel engine by means of high resolution electron microscopy imaging. This crystalline information such as the graphene layer size and orientation is used to interpret the quantitative reactivity difference measured in an idealized TGA/DSC oxidation experiment. Together, these results show the potential impact of biodiesel blending on the low temperature oxidation characteristics of soot.

Experimental

PM Production and Sampling. A highly instrumented 6-cylinder Cummins ISB 5.9L DI turbodiesel engine, connected to a 250 HP eddy current dynamometer, was used to produce different particulate samples at a fixed engine operating condition (2700 rpm and 25% load of peak). The engine has been heavily instrumented with a 0.1 crank angle resolution crank shaft encoder, a cylinder pressure sensor and a needle lift sensor. The engine and dynamometer are operated through an automated control system. To isolate any effect of cylinder temperature history from possible changes in soot nanostructure due to differences in the fuels, the time evolution of in-cylinder mean temperature was obtained through cylinder pressure trace analysis, along with consideration of injection timing and cylinder geometry. Two test fuels were considered, an ultra low sulfur diesel with 15 ppm sulfur content, BP15, and a B20 blend (e.g., a blend of 20 wt.% methyl esters in BP15 fuel). Some fuel properties are provided in Table 1. For TPO test, bulk samples were collected in quartz filters from diluted exhaust gas via a mini-dilution tunnel (Sierra Instruments BG-1). Then, the filter was crushed into a powder and 10 mg of the powder was evenly deposited into the sample pan in the furnace. For HRTEM imaging, thermophoretic sampling was used to capture PM from the raw exhaust. For imaging of the partially oxidized samples, an acoustic suspension in ethanol was used to disperse the sample onto a TEM carbon grid.

Table 1. Properties for Ultra Low Sulfur Diesel and its B20 blend

Fuels	Sulfur Content, ppm	Oxygen Content, wt.%	Cetane Number
BP-15 ULSD	15	0	50.5
B20 Blend	13	2	52.5

Particulate Reactivity. The temperature programmed oxidation (TPO) is examined in two different laboratory reactors as a means of evaluating the differences in reactivity of the soot samples. All particulate samples were treated by 30 minutes heating at 500 ^{o}C under inert gas (i.e. argon) in the TGA to eliminate the soluble organic fraction (SOF). Then, samples were subjected to slow heating to obtain the burning rate of each sample on both DSC (TA2920) and TGA (PE-TGA7). This pretreatment for SOF removal has been reported to yield the same effect as post extraction with dichloromethane (CH_2Cl_2) [6]. Ignition temperature was used to determine the oxidation reactivity of the samples. From the mass loss curve from the TGA, ignition temperature is determined as the temperature at which soot starts oxidizing at an appreciable rate. A detection of heat release by DSC was used as a supplement to gauge the ignition temperature of different particulate samples [7]. In this DSC configuration, the ignition temperature is determined by thermal runaway that is controlled by competition between heat of combustion and heat loss to gas flow.

Soot Nanostructure Imaging. Structural properties of the diesel particulates were obtained by electron beam probes. Among several characterization techniques to detect the degree of crystallinity of graphene layer, a bright field image method by high-resolution transmission electron microscopy (HRTEM) was employed on field emission JOEL 2010F operated on 200 kV, with a point to point resolution of 0.23 nm. In bright field image mode, graphene layer segments are observed as the dark lines blocking/scattering the incident electron beam, thereby creating a dark image on the screen. A thin isolated particle deposited a perforated carbon film is used to obtain the sharp phase contrast while minimizing the interference with the condensable fraction and the grid substrate, since the existence of adsorbed hydrocarbon may block the high contrast imaging of the carbon-rich dry soot.

Results and Discussion

Particulate Reactivity. Figure. 1(a) compares from mass loss curve of TGA while Figure 1 (b) compares heat release curve of DSC, both of which indicate the differences in the ignition temperature of the soot samples. Compared to BP15 diesel soot, the B20 soot exhibits a lower ignition temperature by 40~50 ^{o}C in both the burning rate curve by DSC and mass reduction by TGA.

Soot Nanostructure. Results from HRTEM imaging are shown in Figures 2a-d. The figures compare the soot nanostructure for the BP15 and B20 soot at two different oxidation stages, shown in terms of burn off time. From the comparison between BP15 soot and B20 soot at the initial stage (no burn-off), a more amorphous and disordered arrangement of short-range graphene segments is apparent for the B20 soot as shown in Figures 2a and 2b.

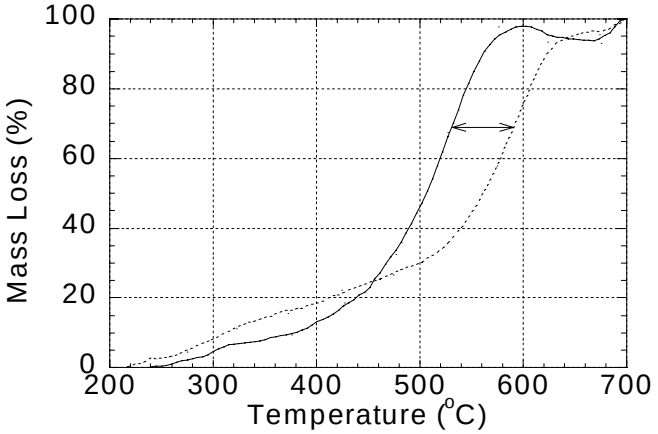

(a)

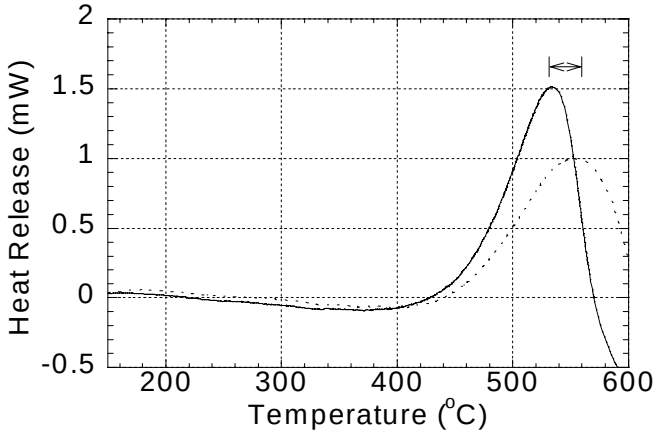

(b)

Figure 1. (a) Mass reduction TGA curve of pretreated samples under 21% oxygen; (b) DSC burning rate of pretreated samples under 21% oxygen. Treated sample is prepared by 30 minutes heating at 500 °C under inert argon. (- - -) BP15 soot and (—) B20 soot.

Within this primary particle from the B20 soot, wrinkled or curved crystallites with many misalignments relative to each other and structural defects are more pronounced. In contrast, BP15 diesel soot possesses typical the shell-core structure in which graphene layers are oriented parallel to external outer surface, but are randomly oriented in a central core. The more reactive edge site carbon, which is more prevalent with short-range amorphous arrangement of the crystallites, is known to be more vulnerable to oxidative attack due to greater accessibility and electronic affinity for O_2 chemisorption [4,5]. Consistent with this understanding of the relationship between structure and oxidative activity, B20 soot indeed leads to higher reactivity compared to the BP15 soot partly due to differences in soot nanostructure.

The partially oxidized samples shown in Figures 2c and 2d display nanostructural changes after exposure to 500°C for 30 minutes. The BP15 soot, that has initially a shell-core structure, remains untouched or slightly graphitized, indicating slow surface burning progression during the course of oxidation. On the contrary, for the B20 soot, porous and ragged layers have developed, indicating a faster burning through either internal burning or stripping of the outer crystallite structure. Although few if any studies have compared the microstructural variations during oxidation for soots derived from different fuels, the observations in this work are consistent with the reported progression of soot oxidation wherein more surface area was developed through opening of micropores by removal of adsorbed hydrocarbon, followed by pre-graphitization before the outer crystallite is stripped away at greater extent of burn-off [8-9]. Consistent with the quantitative measures in Figure 1, this qualitative comparison of nanostructure between the partially oxidized samples supports a significant difference in reactivity.

Although identifying the dependence of soot nanostructure on the conditions during soot formation is not the main objective of the present work, a preliminary hypothesis can be offered to explain the amorphous soot structure observed with biodiesel addition, related to effects of Biodiesel on the combustion process and affecting soot formation. Due to the effect of temperature and its time variation on the extent of carbonization of soot, variation in soot nanostructure and soot oxidation rate is known to exist between mature soot and soot precursor particles that are not yet fully carbonized [10]. As seen in Figure 3, comparison of temperature-time history (regarding the length of time that soot precursor particles experience various temperatures after soot inception and through the carbonization period) shows that there is no significant difference between the two fuels in terms of temperature-time history during ignition and the premixed burn period, during which time changes in temperature could have altered soot inception and growth.

Therefore, other factors, most likely related to fuel composition and its decomposition chemistry, are likely to be responsible for the more amorphous structure in the B20 soot. Based upon calculations of the evolution of equilibrium soot structures [11], when insufficient PAH is available during the soot inception period to attain the threshold mass requirement, a soot particle will not transition into the ordered morphology of the typical shell-core structure. Differences in the soot growth mechanism, caused by different soot growth species formed during the fuel decomposition period may also lead to differences in structure, as hypothesized and verified in recent work by Vander Wal and Tomasek. [12]. While formation of heavy PAH species leads to an amorphous structure through the coalescence growth mechanism, light acetylene (C_2H_2) addition on the radical sites of PAH species leads to formation of graphitic structures through the HACA (Hydrogen Abstraction Carbon Addition) mechanism. The coalescence growth mechanism may be more pronounced for combustion and soot growth conditions with the B20 fuel, leading to a more amorphous soot nanostructure.

Conclusions

With B20 fuel, soot exhibits higher oxidative reactivity in DSC/TGA tests. A more short-range, amorphous structure in the B20 soot is partly responsible for its enhanced reactivity. However, other effects arising from internal pore structure or surface functional group on soot oxidation remain to be investigated.

Acknowledgement. The authors wish to thank Etop Esen, Doug Smith, Keith Lawson, Ed Casey, Rafael Espinoza and Jim Rockwell of ConocoPhillips, and John Wright and Edward Lyford-Pike of Cummins Engine Company for their support of this work. This work is a part of ongoing Ultra Clean Fuels project entitled "Ultra Clean Fuels from Natural Gas," sponsored by U.S. Department of Energy under Cooperative Agreement No. DE-FC26-01NT41098.

The Government reserves for itself and others acting on its behalf a royalty-free, nonexclusive, irrevocable, worldwide license for Governmental purposes to publish, distribute, translate, duplicate, exhibit, and perform this copyrighted paper. High Resolution Transmission electron microscopy was performed using the facilities of the Materials Research Institute at The Pennsylvania State University and the authors are grateful for access to these facilities.

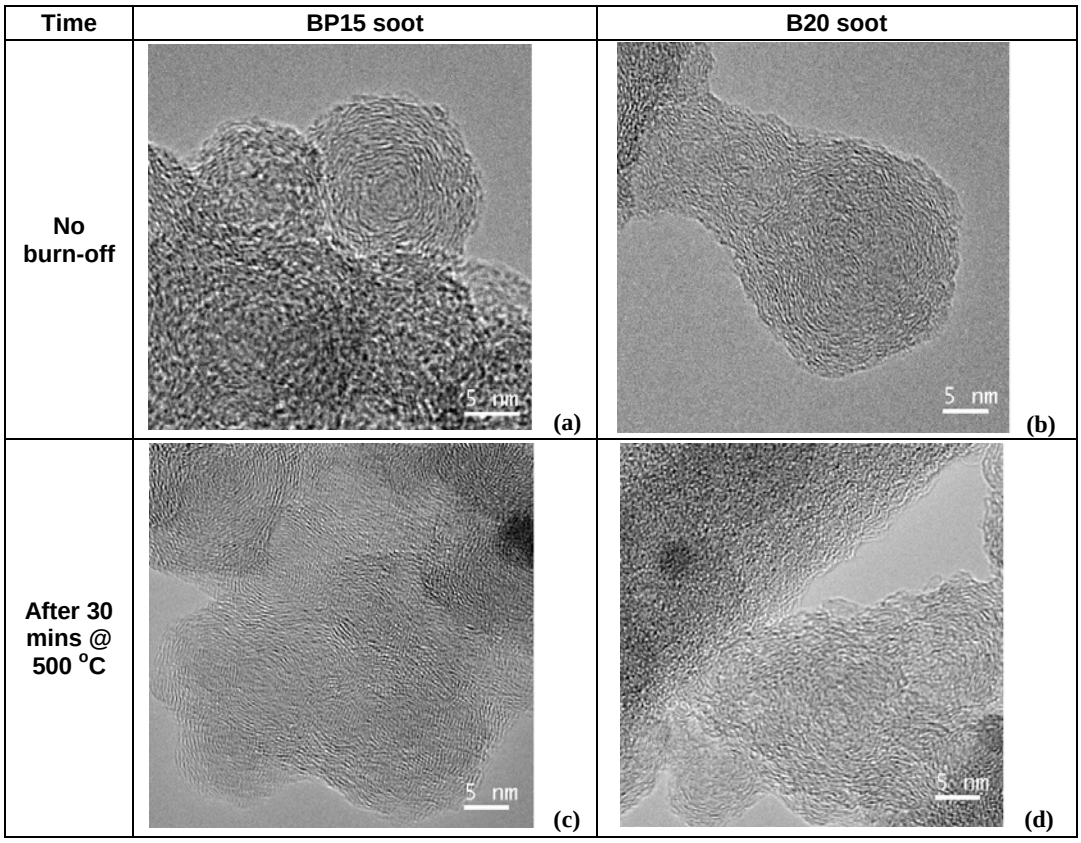

Figure 2. HRTEM images of BP15 diesel and its B20 soot at two different stages of oxidation

This material was also prepared with the support of the Pennsylvania Department of Environmental Protection. Any opinions, findings, conclusions, or recommendations expressed herein are those of the author(s) and do not necessarily reflect the views of the DEP.

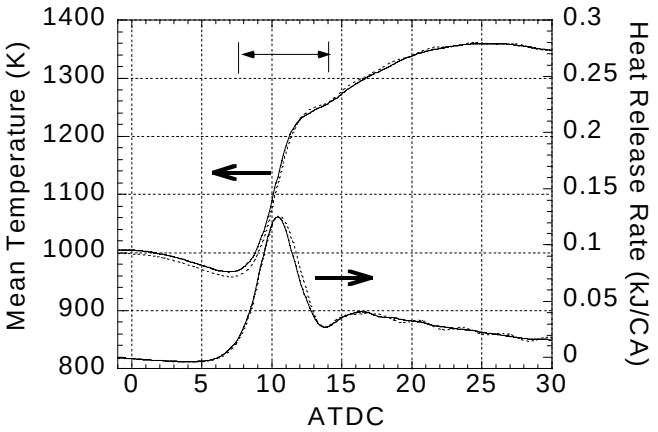

Figure 3. Time evolution of in cylinder mean gas temperature during ignition and premixed burn period of diesel combustion process leading to soot inception and growth. (- - -) BP15 fuel and (—) B20 fuel.

References

[1] Graboski, M.S. and McCormick, R.L., "Combustion of Fat and Vegetable Oil Derived Fuels in Diesel Engines", Prog. in Energy and Comb. Sci., Vol.24, p.125-164, 1998.

[2] Allanson, R., Blakeman P.G., Cooper, B.J., Howard, H., Silcock, P.J. and Walker, A.P., "Optimizing the Low Temperature Performance and Regeneration Efficiency of the Continuously Regenerating Diesel Particulate Filter(CR-DPF) System", SAE 2002-01-0428, 2002.

[3] Stanmore, B.R., Brilhac, J.F. and Gilot, P., "The Oxidation of Soot: A Review of Experiments, Mechanisms and Models", Carbon, Vol. 39, p.2247-2268, 2001.

[4] Vander Wal, R.L. and Tomasek, A.J., "Soot Oxidation: Dependence upon initial nanostructure", Comb. and Flame, Vol. 132, 2003.

[5] Marsh, H., "Kinetics and catalysis of carbon gasification", in: Introduction to Carbon Science, p.107-152, Butterworths, London, 1989.

[6] Stratakis, G.A. and Stamatelos, A.M., "Thermogravimetirc Analysis of Soot Emitted by a Modern Diesel Engine Run on Catalyst-Doped Fuel", Comb. and Flame, Vol. 132, p.157-169, 2003.

[7] Neeft, J.P.A., Nijhuis, X., Smakman, E., Makkee, M. and Moulijn, J.A., "Kinetics of the Oxidation of Diesel Soot", Fuel, Vol. 76, p.1129-1136, 1997.

[8] Ishiguro, T., Suzuki, N., Fujitani, Y. and Morimoto, H., "Microstructural Changes of Diesel Soot During Oxidation", Comb. and Flame, Vol.85, p 1-6, 1991.

[9] Palotas, A.B., Rainey, L.C., Sarofim, A.F., Sande, J.B.V., Ciambelli, P., "Effect of Oxidation on the Microstructure of Carbon Blacks", Energy & Fuels, Vol. 10, p.254-259, 1996.

[10] Chen, H.X. and Dobbins, R.A.,"Crystallogenesis of Particles Formed in Hydrocarbon Combustion", Comb. Sci. and Tech., Vol.159, p.109-128, 2000.

[11] Hurt, R.H., Crawford, G.P. and Shim, H.S., "Equilibrium Nanostructure of Primary Soot Particles", Proc. of the Combustion Institute, Vol. 28, p.2539-2546, 2000.

[12] Vander Wal, R.L. and Tomasek, A.J., "Soot Nanostructure: Dependence upon Synthesis Conditions", Comb. and Flame, Vol. 136, , p. 129-140, 2004

THE EFFECT OF CHEMICAL COMPOSITION OF COAL-DERIVED JET FUELS ON CARBON DEPOSITS

Leslie R. Rudnick, Ömer Gül, Harold H. Schobert

The Energy Institute,
C205 Coal Utilization Laboratory
The Pennsylvania State University,
University Park, Pennsylvania 16802

Introduction

Thermal stability of aviation jet fuel refers to its resistance to decomposition at elevated temperatures to form deleterious solid deposits.

The carbonaceous deposits formation on metallic surfaces from thermal decomposition of jet fuels is a major concern in the development of high-speed aircraft in which the fuel is presently used as a coolant, in addition to its primary use as a propellant. It is used to cool the lubrication system, avionics, electrical systems and environmental control systems, and is also used as a hydraulic fluid (1). The jet fuel instability has been studied for almost five decades (2-5). Solid deposits from fuel degradation can attach to the surface of the flow lines or plug filters and create problems with the fuel system operation. The carbonaceous deposit formation appears to depend on a combination of different conditions, such as the reactivity of the starting fuel, the temperature, the pressure, the concentration, and the nature of the substrate surface. Various metallic alloy candidates were examined at Penn State to observe their catalytic activity in carbon deposit formation from jet fuel decomposition and found that Inconel X and Inconel 718 collected significantly less amount of deposit at 500 and 600°C during jet fuel stressing experiments (6-7).

Temperature is one of the most important parameters that affect the rate and reaction mechanisms of fuel degradation. Autooxidation of fuels takes place at temperatures less than 260°C, decomposition of oxygenated products at intermediate temperatures between 290 and 350°C, and pyrolysis at temperature greater than 350°C (8).

The composition of jet fuels is very complex. Many studies have been carried out with light hydrocarbons (9-13) to understand the mechanism of carbon formation on metals. One distinguishing property of carbon deposits is their oxidation reactivity, which depends on the chemical composition and the structure of the deposits. Differences in oxidation reactivity of the deposits are manifested in the evolution of CO_2 peaks at different temperatures during temperature-programmed oxidation (TPO) experiments (14,15). The TPO analysis is, therefore, useful to help understand the role of the metal surface in carbon deposit formation.

This study examines the thermal stability behavior of different severity hydrotreated of 1:1, 2:1 and 3:1 blends of refined chemical oil (RCO) with light cycle oil (LCO), and JP-8 on Inconel 718 surface at 470°C of fuel temperature in terms of carbon deposit amount.

Experimental

Thermal Stressing Experiments. The fuels tested in the thermal stressing experiments on Inconel 718 are coal-based blends HDT- (1:1 vol) RCO/LCO), HDT- (2:1 vol) RCO/LCO), HDT- (3:1 vol) RCO/LCO), and petroleum-based JP-8. The nominal composition of Inconel 718 alloy is (wt%) Ni:52.5, Fe:18.5, Cr:19, Mo:3.05, Al:0.5, Ti:0.9, Nb+Ta:5.13, Cu:0.15, Mn:0.18, Si:0.18, C:0.04, S:0.0008. The alloy foils, 15 cm x 3 mm x 0.6 mm, were cut and rinsed in acetone. Thermal stressing of fuels was carried out at 470°C fuel temperature (500°C wall temperature) and 250 psig (17 atm) in the presence of Inconel 718 foil. The fuel was subjected to stressing for 5 hr at a 4 ml/min flow rate. The alloy foil was placed in the 26.5 cm and 1/4 in OD glass lined stainless steel tube reactor. The fuel was preheated to 200°C before entering the reactor. Throughout the experiments, the reactor outlet temperature, wall temperature, fuel pressure, and liquid fuel flow rate were kept at 470°C, 500°C, 17 atm., and 4 mL/min, respectively. The stainless steel preheating section is 2 mm in i.d. (1/8-in. o.d.) and 61 cm in length. The fuel residence time in this preheating zone is 22 sec. at a liquid fuel flow rate of 4 mL/min. The fuel residence time in the reactor (4 mm. i.d., 0.25 in. o.d. and 31.75 cm length) is 59 sec. at the same fuel flow rate. At the end of the reaction period (5 h.), the foils were cooled under an argon flow in the reactor. Details about the flow reactor system are reported (16).

Chemical composition of jet fuels before and after thermal stressing was determined by using GC/MS analysis. The total amount of carbon deposition on metal strips was determined using a LECO Multiphase Carbon Analyzer. The deposits formed on Inconel 718 surface were characterized by temperature-programmed oxidation (TPO).

Materials. Inconel 718 was obtained from Goodfellow Metals Ltd (Cambridge, U.K.)

Jet fuels used in thermal stressing were obtained from PARC. They were hydrotreated in different severity. To verify the reproducibility of the experimental results, duplicate experiments of jet fuel stressing were carried out with different jet fuel blends in the presence of Inconel 718. The results of duplicate experiments showed that the TPO profiles were reproducible with respect to individual peak positions and relative peak intensities. The total amount of deposition measured for different jet fuel blends were reproducible ±10% of the deposit mass.

Results and Discussion

In this study, relationships between carbon deposition and chemical composition of the jet fuel were sought, chemical compositions of original sample and thermally stressed fuel samples were determined with GC-MS.

The JP-8 fuel used in this study consists mainly of long-chain paraffins, with lower concentrations of alkyl cyclohexanes, alkyl benzenes, and alkyl naphthalenes (9). The coal derived-blends contained mostly tetralin, naphthalene, decalin and their alkyl substitutes, with lower concentration of paraffins, saturated cyclics, alkyl benzenes and indanes. Neither indene or its derivatives were observed.

Exposure of jet fuel to high temperatures in aircraft fuel lines triggers pyrolysis reactions that eventually lead to deposition of carbonaceous solids on metal surfaces. This is particularly important problem for advanced future aircraft which may expose fuel to very high temperatures.

A wide range of variation was observed in the amount of carbon deposits obtained from different blends. Table 1 shows the compositions of coal-derived jet fuel components: naphthalenes, tetralins, decalins in %, sulfur (ppm) and nitrogen (ppm), and carbon deposits produced from thermally stressing of fuels, reported in terms of micrograms of carbon deposit per square centimeter foil. The lowest and the highest carbon depositions were obtained with EI-082 and EI-103, respectively, among the 12 coal derived-blends and JP-8. The lowest carbon deposition amount was 4.08 $\mu g/cm^2$ with EI-082, and the highest carbon deposition amount was 33.62 $\mu g/cm^2$ with EI-103. This large difference in deposition tendency under the same stressing conditions can be attributed to

the differences in the chemical composition of fuels, and their S and N concentrations. EI-103 has the highest sulfur concentration and also it has the highest naphthalenes concentration among the tested fuels. EI-103 also has the lowest tetralins and decalins concentration as a result of lower severity hydrotreating conditions.

When all of the thermally stressed samples were taken in to consideration, no relationship was found between alkyl benzenes or indanes and carbon deposition.

All of the coal derived-blends contain 40% or higher amount of tetralins but the observed carbon deposit varied from blend to blend. One can conclude that, carbon deposition is independent of tetralins concentration when the tetralins concentration is 40% or higher. For example, if the first two 1:1 blends are compared, the carbon deposits are almost same but tetralins concentrations are different.

To assess the effect of chemical composition on carbon deposition relationships between chemical group concentration and deposits were plotted. A plot of saturated cyclics versus deposit for each blend ratio separately shows that carbon deposition increases as the saturated cyclic concentrations decreases. Saturated cyclics don't contain decalin or its derivatives and decalins were evaluated separately.

If decalin concentrations are plotted relative to carbon deposit, similar trends to that found for saturated cyclics is observed, e.g. as decalins concentrations decreases carbon deposit increases.

All of the blended jet fuels contain different amounts of tricylic compounds (4.20 to 9.63%), Some of these have been identified as dibenzofuran, octahydro phenanthrene, octahydro anthracene, hexahydro fluorene, acenaphthene, and hexahydro acenaphthylene. Carbon deposition on metal coupon increased with increasing tricyclic compounds concentration in the blend. Due to their larger structure, and if they are exposed to severe conditions, they can form radical and further react to form larger molecule which can become carbonaceous materials which are not desired.

It can be seen from the GC-MS analysis of before and after thermal stressing samples that the component that decreased the greatest was naphthalene or its derivatives, while the tricyclic compounds concentration was increased. These molecules (naphthalenes, alkyl naphthalenes) thermally form radicals and further reaction of these molecules may produce higher molecular weight compounds leading to deposits.

Relatively high carbon deposition was obtained from thermal stressing of JP-8 (17.48 μg C/cm^2). This may also be explained by JP-8's chemical composition. JP-8 contains some alkene+alkyne (Table 1) which may also form radicals and result as initiators for the formation of carbonaceous materials. GC-MS analysis results on the JP-8 sample obtained after the thermal stressing experiment showed that there was about 25% decrease in their concentration.

Figure 1 shows the TPO profiles for the deposits of three fuels on the Inconel 718. This figure compares samples having the highest and lowest carbon deposits obtained from coal derived-blends and JP-8. The low temperature peaks around 150 and 350°C can be attributed to adsorbed liquids on the deposits and hydrogen-rich amorphous deposits, respectively. While the JP-8 and EI-082 had given broad and low-intensity relative-carbon signal band, EI-103 gave a sharp and narrow band in the TPO profile because of the significantly higher deposit. The most intense peak evolved at approximately 450°C for JP-8.

Conclusion

In this work it was found that jet fuels containing low sulfur and nitrogen and higher amount of decalins and saturated cyclics gave low carbon deposition at 470°C. Carbon deposition was found to be independent of RCO-LCO blend ratio.

Acknowledgement. Financial support for this work was provided by the U.S. Air Force Office of Scientific Research.

References

(1) Zabarnick, S.: Ind. Eng. Chem. Res. **1994**, 33, 1348
Bol'shakov, G. F.; Technical Report; Wright-Paterson Air Force Base, Dayton, OH, **1972**
(2) Schimdt, J. E.: Kirklin, P. W., David, P., Eds.; ASTM STP 1138; ASTM:
Philadelphia, PA, **1992**
(3) Heneghan, S. P. ; Martel, C.R.; Williams, T.F.; Ballal, D. R. Trans. ASME J. Eng. Gas Turbines Power **1993**, 115, 480
(4) Edwards, T.; Zabarnick, S. Ind. Eng. Chem. Res. **1993**, 32, 3117
(5) Hunt, J. E.; Winans, R. E.; Ahrens, M.; and Xu, L. Prepr. Pap. – *Am.Chem. Soc., Div. Fuel Chem.*, **1999**, *44* (3), 610.
(6) Altin, O.; Eser, S.; Ind. Eng. Chem. Res., **2001**, 40, 589.
(7) Elliot, P.; Hampton, A.F.; Oxid. Met., **1980**, 14, 449.
(8) Song, C,; Eser, S.; Schobert, H.H.; Hatcher, P.G. Energy Fuels. **1993,** 7(2), 234
(9) Trimm, L.D. Catal. Rev.-Sci. Eng. **1977,** 16, 155
(10) Trimm D.L. :Albright, L.F., Crynes, B.L., Corcoran, W.H., Eds.; Academic Press: New York, **1983**.
(11) Baker, R.T.K.; Harris, P.S. : Walker P.L., Jr., Thrower, P.A., Eds.; Marcel Dekker Inc.: New York, **1978**.
(12) Albright, L.F.; Tsai, C.-H.T. : Albright, L.F., Crynes, B.L., Corcoran, W.H., Eds.; Academic Press: New York, **1983**.
(13) Froment, G.F. Rev. Chem. Eng. **1990**, 16(4), 293.
(14) McCarty, J.G.; Wise, H. J. Catal. **1979**, 57, 406.
(15) Marecot, P.; Akhachane, A.; Micheaud, C.; Barbier, J. Deactivation by Coking of Supported Palladium Catalysts. Effect of Time and Temperature. Appl. Catal. A: Gen. **1998**, 169, 189.
(16) Altin, O.; Eser, S., Ind. Eng. Chem. Res. **2001**, 40, 596-603.

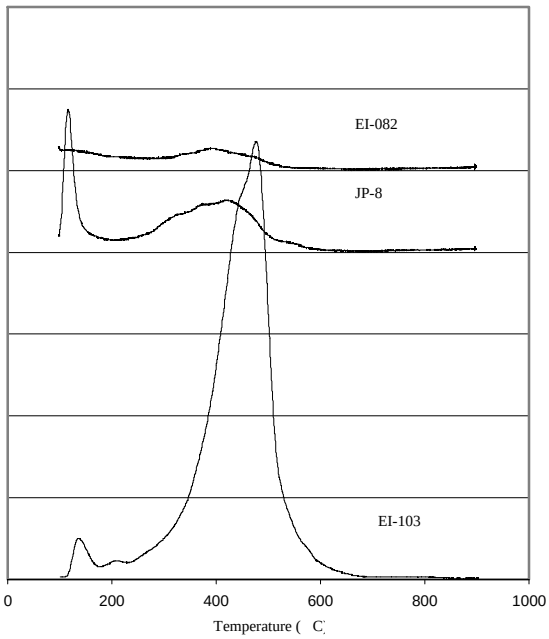

Figure 1. Selected TPO profiles of carbon deposits from thermal stressing of coal derived-blended fuels and JP-8 on Inconel 718 at 470 °C fuel temperature for 5h with 4 mL/min flow rate.

Table 1. Total Carbon Deposit and Compositions of HDT Coal-Derived Jet Fuels (JP-900 prototypes): Thermal Decomposition on Inconel 718 at 470 °C /17 atm (250 psig) / 5 h / 4 mL/min Flow Rate.

Sample Code	Fuel Type	Paraffins %	Sat. Cyclics %	Alkyl Benzenes %	Indanes %	Naphthalenes %	Tetralins %	Decalins %	Tricyclic Comp.s %	Alkene+ Alkyne	Alkyl alcohols	S, ppm	N, ppm	C Deposit (ug C/cm^2)
	JP-8	73.50	7.31	9.27	-	2.70	0.25	0.05	-	4.20	2.72	na	Na	17.48
EI-072	1:1 RCO/LCO	1.1	0.51	4.08	3.25	19.97	62.34	0.57	8.19	-	-	160	967	15.06
EI-073	1:1 RCO/LCO	0.94	0.49	7.77	5.04	31.02	47.08	0.55	7.13	-	-	68	1500	15.78
EI-076	1:1 RCO/LCO	0.96	0.60	6.17	5.17	31.75	48.2	0.39	6.75	-	-	23	205	7.21
EI-079	1:1 RCO/LCO	1.47	2.78	7.65	4.56	4.19	66.58	5.59	7.19	-	-	61	16	11.52
EI-082	1:1 RCO/LCO	0.79	7.73	7.22	3.39	4.52	50.54	21.61	4.20	-	-	1	1	4.08
EI-085	2:1 RCO/LCO	0.70	3.96	2.65	3.89	9.05	63.78	8.02	7.96	-	-	3.4	3.6	7.56
EI-088	2:1 RCO/LCO	0.76	0.29	3.10	4.42	40.02	42.5	0.11	8.81	-	-	38.6	1000	15.67
EI-091	2:1 RCO/LCO	1.22	2.77	3.44	4.61	20.42	52.11	8.31	7.11	-	-	101	18.6	9.64
EI-094	2:1 RCO/LCO	0.99	5.06	2.89	3.29	9.00	58.64	13.16	6.98	-	-	3.4	9	6.28
EI-097	3:1 RCO/LCO	0.49	3.14	1.43	3.07	10.36	64.86	7.01	9.63	-	-	18.5	18.2	10.52
EI-100	3:1 RCO/LCO	0.84	0.69	1.17	4.53	27.32	54.86	1.91	8.68	-	-	9	162	11.26
EI-103	3:1 RCO/LCO	0.79	0.33	1.71	5.69	42.23	39.84	0.15	9.27	-	-	1100	64	33.62

MORPHOLOGY OF CARBON DEPOSITS AS A FUNCTION OF COAL-DERIVED JET FUEL CHEMICAL COMPOSITION

Ömer Gül, Leslie R. Rudnick, Harold H. Schobert

The Energy Institute,
The Pennsylvania State University,
University Park, Pennsylvania 16802

Introduction

Because of high thermal loads in future advanced aircraft, jet fuel will be exposed to much higher temperatures, reaching as high as 540°C, before combustion (1-3). At such high temperatures, both homogenous and heterogeneous reactions of jet fuel can lead to solid deposition on metal surfaces (4,5). The formation of carbonaceous deposits on metal surfaces in the fuel system is, therefore, a major concern for the development of advanced aircraft. Thermal stability of aviation jet fuel refers to its resistance to decomposition at elevated temperatures to form deleterious solid deposits.

Solid deposits from fuel degradation can attach to the surface of the flow lines or plug filters and create problems with the fuel system operation. The carbonaceous deposit formation appears to depend on a combination of different conditions, such as the reactivity of the starting fuel, the temperature, the pressure, the concentration, and the nature of the substrate surface.

Temperature is one of the most important parameters that affect the rate and reaction mechanisms of fuel degradation. Autooxidation of fuels takes place at temperatures less than 260°C, decomposition of oxygenated products at intermediate temperatures between 290 and 350°C, and pyrolysis at temperature greater than 350°C(6).

The composition of jet fuels is very complex. Many studies have been carried out with light hydrocarbons (7-11) to understand the mechanism of carbon formation on metals. One distinguishing property of carbon deposits is their oxidation reactivity, which depends on the chemical composition and the structure of the deposits. Differences in oxidation reactivity of the deposits are manifested in the evolution of CO_2 peaks at different temperatures during temperature-programmed oxidation (TPO) experiments (12,13). The TPO analysis is, therefore, useful to help understand the role of the metal surface in carbon deposit formation.

McCarty et al.(14) used temperature-programmed surface reaction with hydrogen to characterize carbon deposits produced on an alumina-supported nickel methanation catalyst upon exposure to carbon monoxide at 277°C. Based on the relative reactivity of the deposits toward hydrogen, the deposited carbon species were classified as chemisorbed carbon atoms (α) evolving around 190°C, bulk nickel carbide, amorphous carbon (β) around 385°C, filamentous carbon at 600°C, encapsulating carbon at 690°C, and crystalline graphite platelets at temperatures above 800°C.

This study examines the morphology of carbon deposits of thermally stressed hydrotreated 1:1, 2:1 and 3:1 blends of refined chemical oil (RCO) and light cycle oil (LCO), and JP-8 on Inconel 718 surface at 470°C fuel temperature.

Experimental

Thermal Stressing Experiments. The fuels tested in the thermal stressing experiments on Inconel 718 are coal-based blends HDT-(1:1 vol) RCO/LCO), HDT-(2:1 vol)RCO/LCO), HDT-(3:1 vol)RCO/LCO), and petroleum-based JP-8. The composition of Inconel 718 alloy and experimental procedure has been reported (15). Throughout all reported experiments, the reactor outlet temperature, wall temperature, fuel pressure, and liquid fuel flow rate were kept at 470°C, 500°C, 17 atm., and 4 mL/min, respectively. The stainless steel preheating section is 2 mm in i.d. (1/8-in. o.d.) and 61 cm in length. The fuel residence time in this preheating zone is 22 sec. at a liquid fuel flow rate of 4 mL/min. The fuel residence time in the reactor (4 mm. i.d., 0.25 in. o.d. and 31.75 cm length) is 59 sec. at the same fuel flow rate. At the end of the reaction period (5 h.), the foils were cooled under an argon flow in the reactor. The details about the flow reactor system can be found in elsewhere paper (16).

Materials. Inconel 718 was obtained from Goodfellow Metals Ltd (Cambridge, U.K.)

Jet fuels hydrotreated to different severity used in thermal stressing tests were obtained from PARC. To verify the reproducibility of the experimental results, duplicate experiments of jet fuel stressing were carried out with different jet fuel blends in the presence of Inconel 718. The results of duplicate experiments showed that the TPO profiles were reproducible with respect to individual peak positions and relative peak intensities. The total amount of deposit measured on several different jet fuel blends were reproducible ±10(wt)% of the deposit.

Instrumental Analysis. Chemical composition of jet fuels was determined by GC/MS analysis.

Carbon Deposit Analysis; The deposited foils were analyzed using a LECO RC-412 multiphase carbon analyzer to determine the total carbon content and TPO profiles of the deposits on the foils. The surface morphology of the deposits was examined with an ISI-DS130 dual-stage scanning electron microscope (SEM). To examine the morphology of the carbon deposits on the strips, 1 cm long pieces were cut from the center of the strip.

Results and Discussion

In this study, morphology of carbon deposits and chemical composition were correlated. Chemical compositions of jet fuel samples were determined with GC-MS.

JP-8 fuel consists mainly of long-chain paraffins, with lower concentrations of alkyl cyclohexanes, alkyl benzenes, and alkyl naphthalenes. The coal derived-fuels consist of mostly tetralin, naphthalene, decalin and their alkyl substitutes, with lower concentrations of paraffins, saturated cyclics, alkyl benzenes and indanes. No indene or its derivatives were observed.

Exposure of jet fuel to high temperatures in aircraft fuel lines triggers pyrolysis reactions which eventually lead to deposition of carbonaceous solids on metal surfaces. This is particularly important problem for advanced future aircraft which may expose fuel to very high temperatures.

The chemical compositions of jet fuels have been reported recently (15). All of the coal derived-blends contain 40% or higher amount of tetralins, and also contain tricyclic compounds in the changing amount from 4.20 to 9.63%. The amount of other grouped compounds were varied according to hydrotreating severity.

The substrate temperature is a significant parameter having a major influence not only on the rate, but also on the type of carbonaceous deposition (8,17,18). In this study, different kinds of solid carbon deposits were observed with different coal derived-blends regarding to their chemical composition on Inconel 718 under the same conditions.

TPO profiles show peaks as a function of temperature. The different peaks observed in these plots can be evaluated as different natures of deposits. Observations from the TPO and SEM images of the deposits were discussed below.

Figure 1 shows the TPO profiles of the carbon deposits from thermal stressing of HDT-(1:1)RCO/LCO at 470°C and 250 psig

for 5h. Each fuel gave different TPO profiles. The major peak for 1:1 blends were observed at ~400°C.

The 1:1 blends (low saturated cyclics (<1%), decalins (<1%), and higher amount of naphthalenes (>19%)) gave the dominant peak at 400°C and also gave relatively high carbon signal. These peaks can be attributed to amorphous carbon and fine filaments as shown by the SEM image of EI-073 (Figure 2). These blends also gave lower temperature peaks (~150°C) which probably represent hydrogen-rich chemisorbed carbonaceous substance (16). Reactive deposits burn off at the lower temperatures, while less reactive deposits burn off at higher temperatures.

On the other hand, jet fuel blends, containing less aromaticity as naphthalenes (<5%) and higher amounts of saturated compounds, gave higher temperature peaks with lower carbon signal, i.e., TPO of EI-079.

Chemical compositions of EI-073 and EI-076 were very similar to each other, but their TPO profiles and SEM images (Figure2 and Figure3) were very different. One can conclude that, this difference might be related to their sulfur and nitrogen contents.

High temperature peaks (600°C) in the TPO profiles indicate the presence of relatively low reactive carbon deposits. Highly ordered structures in the deposits, having pre-graphitic or graphitic order would reduce the oxidation reactivity compared to that amorphous carbon with no apparent structural order (16). No deposits of this type were observed with 1:1 blended jet fuels based on TPO profiles.

TPO profiles in Figure 1 were obtained from thermal stressing of HDT- (1:1 vol.) RCO/LCO blends. The blends each gave different TPO profiles which could imply that carbon was deposited at different rates and perhaps by a different mechanism under the same conditions.

HDT-(2:1 vol.) RCO/LCO blends gave broader bands than those of HDT-(1:1 vol.) RCO/LCO blends (Figure 4). TPO profiles of 2:1 blended fuels showed a similar trend but changing relative carbon signal, except EI-088. This can be concluded that they may undergo similar deposition mechanisms during thermal stressing of fuels as a result of their similar chemical compositions. EI-088 has the lowest saturated cyclics, decalins and tetralins among four 2:1 blends.

SEM image of EI-085 (Figure 5) shows that strip surface covered more orderly form than that of EI-088. SEM image of EI-088 has been given in Figure 6 and it shows that there was an agglomeration instead of covering the surface completely.

Figure 7 shows the TPO profiles of carbon deposits from thermal stressing of HDT-(3:1 vol.) RCO/LCO and JP-8 at 470°C and 250 psig for 5h. The chemical compositions of these blends (3:1) change, i.e., while the amount of saturated cyclics, decalins, tetralins decrease from EI-097 to EI-103, the amount of indanes, naphthalenes increased. Carbon deposition TPO profiles showed some change as a result of the chemical composition. For example, the peak intensity at ~150°C increased from EI-097 to EI-103. This could imply that increasing aromaticity and decreasing saturated compounds in fuels could result in more chemisorbed and more amorphous carbon formed on Inconel 718.

The SEM image of EI-088 showed agglomerated carbon deposits, whereas EI-103 showed deposits of a more uniform structure, evenly spread over the surface of the Inconel 718. Chemical compositions of these two fuels were similar, i.e., naphthalenes (~40%), tetralins (~40%), decalins (~0.11%), saturated cyclics (~0.30%). However the sulfur concentrations of EI-103 was significantly higher than for EI-088. Sulfur has been previously implicated with carbon deposition mechanism (19). This difference could be the reason for that deposition and surface covering with different mechanism.

It was also seen from the SEM images of EI-097 and EI-100 that deposits obtained from these fuels has covered the surface completely.

TPO of JP-8 shows a major peak at 500°C and a minor peak at 150°C. These peaks could be attributed as pre-graphatic and chemisorbed peaks, respectively. It was seen from the SEM image of JP-8 that there was filamentous-like deposit and that the surface of metal coupon was almost fully covered with carbonaceous materials.

Conclusion

In this work it was seen that increasing the RCO/LCO ratio in the blend changed the deposit nature and increased the surface coverage. It was also observed that if two fuels having similar chemical compositions but different sulfur and nitrogen concentrations, the carbon deposit morphology or coverage was different.

Acknowledgement. Financial support for this work was provided by the U.S. Air Force Office of Scientific Research.

References

(1) Edwards, T.; Zabarnick, S. Ind. Eng. Chem. Res. **1993**, 32, 3117.
(2) Heneghan, S.P.; Martel, C.R.; Williams, T.F.; Ballal, D.R. Trans. ASME J. Eng. Gas Turb. Power. **1993**, 115, 480.
(3) Hazlett, R.N.: Kirklin, P.W., Daiv, P., Eds.; ASTM STP 1138; ASTM:Philadelphia, PA, **1992**.
(4) Heneghan, S.P.; Zabarnick, S.; Ballal, D.R.; Harrison III, W.E. Trans. ASME J. Eng. Gas Turbines Power. **1996**, 118. 170.
(5) Jone, E.G.; Balster, W.J. Energy Fuels. **1995**, 9, 610.
(6) Song, C,; Eser, S.; Schobert, H.H.; Hatcher, P.G. Energy Fuels. **1993,** 7(2), 234.
(7) Trimm, L.D. Catal. Rev.-Sci. Eng. **1977,** 16, 155.
(8) Trimm D.L.: Albright, L.F., Crynes, B.L., Corcoran, W.H., Eds.; Academic Press: New York, **1983**.
(9) Baker, R.T.K.; Harris, P.S.: Walker P.L., Jr., Thrower, P.A., Eds.; Marcel Dekker Inc.: New York, **1978**.
(10) Albright, L.F.; Tsai, C.-H.T.: Albright, L.F., Crynes, B.L., Corcoran, W.H., Eds.; Academic Press: New York, **1983**.
(11) Froment, G.F. Rev. Chem. Eng. **1990**, 16(4), 293.
(12) McCarty, J.G.; Wise, H. J. Catal. **1979**, 57, 406.
(13) Marecot, P.; Akhachane, A.; Micheaud, C.; Barbier, J. Appl. Catal. A: Gen. **1998**, 169, 189.
(14) McCarty, J.G.; Hou, P.Y.; Sheridan, D.; Wise, H.: Albright, L.F., Baker, R.T.K., Eds.; ACS Symposium Series 202; American Chemical Society: Washington D.C., **1982**; Chapter 13, p 253.
(15) Rudnick, L. R.; Gül, Ö.; Schobert, H. H. ,Prepr. Pap.- Am. Chem. Soc., Div. Fuel Chem., **2004**, Phila., to be presented.
(16) Altin, O.; Eser, S., Ind. Eng. Chem. Res. **2001**, 40, 596.
(17) Albright, L.F.; Marek, J.C. Ind. Eng. Chem. Res. **1988**, 27, 755.
(18) Baker, R.T.K.; Yates, D.J.C.; Dumenic, J.A.: Albright, L.F., Baker, R.T.K., Eds.; ACS Symposium Series 202; American Chemical Society: Washington, D.C., **1983**; Chapter 1, pp 1-22.
(19) Altin, O.; Bock, G.; Eser, S. Prepr. Pap.- Am. Chem. Soc., Div. Petroleum Chem., **2002**, 47(3), 208

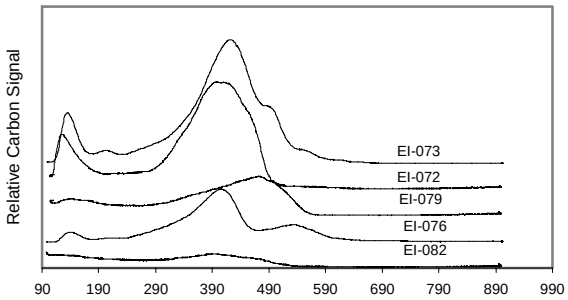

Figure 1. TPO profiles of carbon deposits from thermal stressing of 1:1 coal derived-jet fuels on Inconel 718

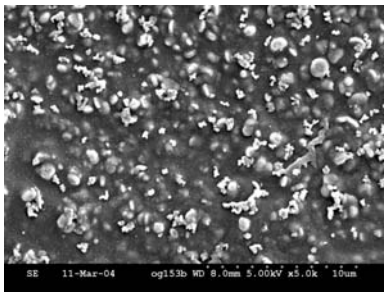

Figure 2. SEM image of carbon deposit from EI-073 at 470°C

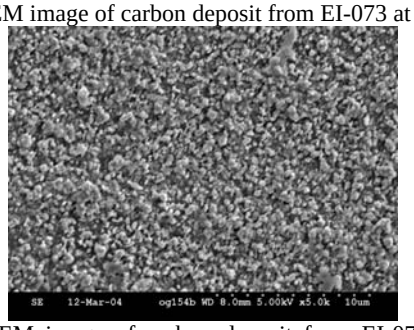

Figure 3. SEM image of carbon deposit from EI-076 at 470°C

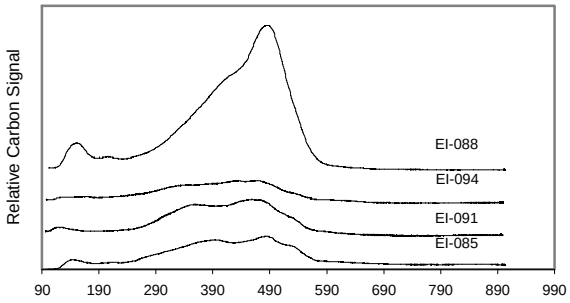

Figure 4. TPO profiles of carbon deposits from thermal stressing of 2:1 coal derived-jet fuels on Inconel 718 at 470°C

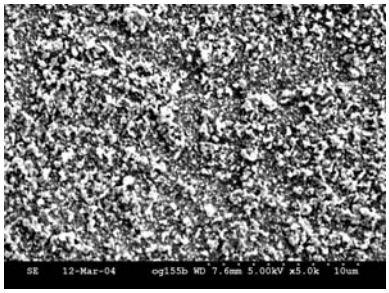

Figure 5. SEM image of carbon deposit from EI-085 at 470°C

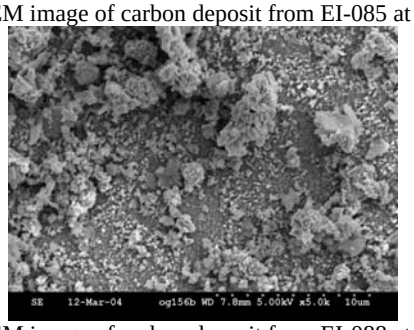

Figure 6. SEM image of carbon deposit from EI-088 at 470°C

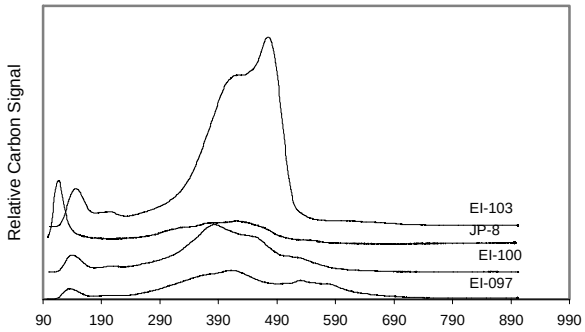

Figure 7. TPO profiles of carbon deposits from thermal stressing of 3:1 coal derived-jet fuels on Inconel 718 at 470°C

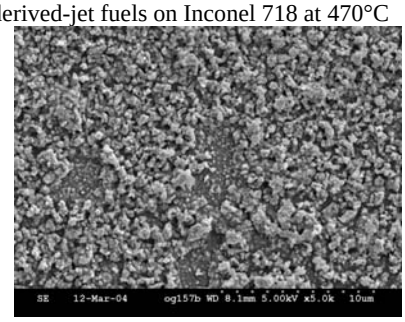

Figure 8. SEM image of carbon deposit from EI-103 at 470°C

FUTURE COILS FOR ETHYLENE FURNACES: REDUCED OR NO COKING AND INCREAED COIL LONGEVITY

Marvin G. McKimpson[a] *and Lyle F. Albright*[b]

[a]Institute of Materials Processing
Michigan Technological Institute
Houghton, MI 49931-1295

[b]School of Chemical Engineering
Purdue University
West Lafayette, IN 47907-2100

Introduction

Significant improvements have occurred in reducing undesired coke production in ethylene furnaces and in increased longevity of the coils during the last 40 years and especially in the recent past. Filamentous coke which is catalyzed with nickel or iron is an excellent collection site for the coke formed by two distinctly different mechanisms (1). Inner surfaces of coils used in ethylene furnaces that are essentially free of nickel and iron do not produce these filaments. Baker and Chludzinski (2) have found that certain surfaces result in much lower levels of coke formation. Albright and Marek (3) found that the surface of metal had a large effect on the morphology of the coke; three distinct coking mechanisms produce coke deposits of very different character. The ability to collect coke or coke precursors is obviously an important factor relative to the amount of coke that eventually collects.

Coated Coils

In the last 5-10 years, several companies have publicized coils with inner surfaces that result in much reduced levels of coke formation. The following companies claim reduced coke deposits by factors of perhaps two to three: Alon Surface Technologies, Inc.; Westaim Surface Engineering Products; and Daido Steel (in cooperation with Royal Dutch/Shell Group). In all cases, rather thin coatings have been formed on the inner surfaces of high-alloy steels. These coatings have low concentrations of nickel, iron, and other metals that produce filamentous coke. It must be emphasized that at the high temperatures experienced in the coils that considerable diffusion of metal atoms occur in the walls of the coils and metal oxides form in the inner surfaces (4). In regular (non-coated) coils of high-alloy steels, the inner surfaces often become much enriched in oxides of chromium, manganese, aluminum, silicon, and titanium. Simultaneously, a sublayer enriched in iron and nickel forms. Claims have been made for these coils that the coatings are regenerated as the coil is used and as metal (or metal oxides, sulfides or carbides) are lost from the surface.

Additives

For many years, numerous additives have been mixed in relatively small amounts with the feedstocks to ethylene furnaces to reduce coke formation. Apparently in all cases, the additive changes the composition of the inner surfaces of the coil.

Compounds containing sulfur are widely used when ethane and propane are feedstocks. When naphthas and gas oils are feedstock, such additives are generally not needed since the feedstocks already contain adequate sulfur. Additives employed include hydrogen sulfide, dimethyl sulfide, dimethyl disulfide, mercaptans, etc. Although details are not known, these compounds decompose at the high temperatures releasing elemental sulfur. This sulfur plus other sulfur-containing intermediates react in part at least converting metal oxides on the surface to metal sulfides (5). Tests have shown that hydrogen sulfide treatment of a coil that had just been decoked reduces coke formation immediately following decoking (6).

The following questions relative to sulfur compounds apparently have not been answered. (1) Which portions of the coil should be sulfided? Presumably the exit potion of the coil should be since here coking is most pronounced. (2) Can the method of introducing the compound be improved? In current methods, most sulfur is possibly freed and reacted before it reaches the exit end. Sulfide formation often contributes to reduced coil life.

Other additives have been reported, but explanations for the improvements are still needed. Several additives include:

1) Tin-silicon additive marketed by Chevron-Phillips. Presumably the surface of the coil is enriched with tin and silicon (probably as oxides).
2) An organo-phosphorus compound marketed by Nalco-Exxon is used in numerous furnaces plus at least two transferline exchangers (TLE's).
3) Technip Benelux have suggested a pretreatment that produces a silica layer on top of sulfur-treated metallic sublayer. Further dimethyldisulfide is continuously added.
4) SK Corp. provides an additive that forms an inner film containing silicon, chromium, and aluminum oxides plus alkali or alkali-earth metals. Alkali and alkali-earth metals have been reported to act as catalysts to promote the oxidation of coke (via carbon-steam reactions at high temperature).

A key question with all additives is can improved methods be developed to introduce the additive to the coil? The answer likely is yes.

Pretreated Coils

Nova Chemical Co. (7, 8) has reported that their pretreated coils often experience coke reductions by factors of 14-16 times. In one case, the time before decoking of a furnace using ethane-propane feedstock was extended to 520 days. One patent claims that chromium-manganese spinels are produced on the inner surfaces. Similar pretreatments were earlier investigated (9) and the data since analyzed (10). The stainless steels were pretreated with hydrogen-steam mixtures at 800-1000^{o}C for extended periods of time. Nova's preferred conditions overlap those reported earlier.

The question, as yet unanswered, is why has coke formation been so greatly reduced as compared to other technologies just discussed. Two possible explanations are as follows: First, the coke and/or coke precursors fail to adhere to the pretreated surface. Examples were found earlier (9) of poor adherence. Second the pretreated surface act as a catalyst to promote gasification of the coke.

Longevity of Coils

The longevity of ethylene furnace coils is influenced by numerous factors, including furnace operating conditions, decoking practices and alloy selection. In many cases, coil service life is limited by carburization and localized tube wall thinning. Frequent and/or aggressive decoking practices appear to accelerate this carburization. An improved understanding of the inter-relationships between carburization and decoking is likely to be very useful for further extending coil life.

Alloy composition also has a substantial influence on coking characteristics and the coil longevity. Ethylene furnaces present some of the most severe operating conditions encountered anywhere in the chemical process industries. Coil materials experience coking, carburization, oxidation, creep and thermal cycling during service, and must be able to be welded for field installation. Over the last several decades, furnace temperatures have tended to rise, placing increasingly-stringent requirements on these coils.

Increasing coil longevity will require materials increasingly resistant to all of these phenomena but still exhibiting adequate fabricability. Most current coils are cast, fully austenitic modified HP alloys containing nominally 25 Cr and 35 Ni with "micro-alloying" additions of elements such as Nb, W, Ti, and Mo. This family of austenitic alloys, however, may be approaching its useful operating limits. Alloys with increased Cr and Ni contents show limited improvements in creep resistance and decreased melting points. Equally important, these alloys rely primarily on Cr coupled with low levels of Mn and Si to provide oxidation and carburization resistance. At higher temperatures, both increased rates of coking and the volatility of chromium oxides become a major concern.

Several groups, including Oak Ridge National Laboratory and Special Metals Corporation, are exploring alloys with higher aluminum contents. These materials have potential for higher melting temperatures, improved oxidation resistance, improved carburization resistance and reduced coking compared to current alloys. Ferritic oxide dispersion strengthened alloys such as Special Metal's Incoloy® MA956 (Fe-20Cr-4.5 Al-0.5Ti-0.5Y_2O_3) also exhibit substantially higher creep resistance (11). Novel approaches such as clad tubes with a ferritic core and austenitic sheath are being considered to address concerns about material ductility and weldability. The current status of this work will be reviewed.

References

(1) Albright, L.F.; Marek, J.C., *Ind. Eng. Chem. Res*., **1988**, *27*, 755.
(2) Baker, R.T.K.; Chludzinski, J.J., *J. Catalysis*, **1980**, *64*, 464.
(3) Albright, L.F.; Marek, J.C., *Ind. Eng. Chem. Research*, **1988**, *27*, 751.
(4) Luan, T.C.; Eckert, R.E.; Albright, L.F., *Ind. Eng. Chem. Research* **2003**, *42*, 4741.
(5) Tsai, C.H.; Albright, L.F., *Industrial and Laboratory Pyrolysis*, ACS Symposium Series 32, L.F. Albright and B.L. Crynes, Eds., pp. 274-295, Amer. Chem. Soc., Washington, D.C., 1976.
(6) Crynes, B.L.; Albright, L.F.; *Ind. Eng. Chem. Processes Design Develop*. **1969**, *8*, 25.
(7) Benum, L., Achieving Longer Furnace Runs at Nova Chemicals, Spring Meeting, AIChE, New Orleans, 2002.
(8) Benum, L.C.; Oballa, M.C.; Petrone, S.S.A.; Chao, W., Canadian Patent Applic. 2, 355, 436, March 27, 2002.
(9) Szechy, G.; Luan, T.C.; Albright, L.F., Novel Production Methods for Ethylene, L.F. Albright and B.L. Crynes, Eds., Chapt. 18, Marcel Dekker, Inc., New York, 1992.
(10) Luan, T.C.; Eckert, R.E.; Albright, L.F., *Ind. Eng. Chem. Research* **2003**, *42*, 4741.
(11) Hosoya, K., et. al., Application of New Ethylene Furnace Tube—OxideDispersion Strengthened (ODS) Alloy, 13th Ethylene Forum, Baton Rouge, LA, 2001.

Ti AND Al OXIDE COATINGS ON INCONEL 718 AGAINST METAL SULFIDE FORMATION AND CARBON DEPOSITION FROM HEATED JP-8 FUEL

Orhan Altin[a], Semih Eser[a], Ajit R. James[b], and Xiaoxing Xi[b]

[a]The Energy Institute
[b]Department of Physics, 303 Davey Laboratory
The Pennsylvania State University
University Park, PA, 16802

Introduction

The trend of advanced aircraft toward increasing performance results in higher thermal loads and higher fuel temperatures and eventually the formation of carbon deposits on metal cooling line surfaces (1). The buildup of deposits in aircraft fuel systems is a major concern because it may lead to fuel system failure. Exposure of metal surfaces to jet fuel at temperatures higher than 400˚C leads to the accumulation of carbonaceous deposits (2,3). Previous experimental results clearly showed that certain elements such as Ni, Co, Fe, and Mo in the fuel system dramatically increase fuel coking by catalyzing carbon deposit formation. On the contrary, the elements Ti, Al, Si, Cr, Ta, and Nb do not show much chemical, or catalytic activity upon heating with jet fuels to 500˚C.

Thus, two inert surface coatings, Ti and Al oxides, were evaluated to investigate the potential for carbon deposit reduction. Among others, Marteney and Spadacini (4) suggested that two basic carbonaceous deposit formation processes occur: 1) A homogeneous oxidation reaction occurring in the fuel feedstream forming carbon particles which adhere to the fuel passage surface, 2) A heterogeneous catalytic reaction occurring at the fuel passage surface. Particularly for thermal stressing of jet fuels above 400˚C, Mechanism 2 dominates leading to surface catalytic reaction between the reactive alloy elements and carbon deposit precursors. In addition to carbon deposit formation, sulfur compounds present in the fuel may react with transition metal elements on the alloy surfaces.

The effect of the trace amount of some sulfur compounds appears to be significant on the rate of deposit formation and metal surface degradation. The sulfidation of metals at high temperatures has become a matter of increasing concern in industrial applications, particularly in energy conversion systems using fossil fuel systems. Because of the high diffusivity and formation of eutectic melts with metals, sulfur reacts with metals at relatively low temperatures forming severe localized corrosion on heat-resistant alloys and superalloys (5-7).

Protective coatings on metal alloy surfaces may prevent contact between reactive fuel species and active metal surfaces to inhibit surface reactions and carbon deposition through heterogeneous reactions. Pulsed laser deposition is a relatively new method for the production of thin films. PLD provides a mechanism to deposit highly adherent thin films of a variety of tribological (friction, lubrication and wear properties) coatings. Donley and Zabinski (8) suggested that PLD films often exhibit superior performance as compared to those obtained by conventional coating techniques. Also, PLD offers the possibility of tailoring film properties by the appropriate choice of substrate materials, deposition parameters and after deposition treatments (9-10).

The objectives of this study were to coat Inconel 718 coupons with titanium and aluminum oxides by Pulse Laser Deposition and to investigate the effectiveness of these coatings in inhibiting carbon deposition and metal sulfide formation from heated JP-8 fuel.

Experimental

Mechanically polished Inconel 718 coupons were coated with Ti and Al oxides using Pulsed Laser Deposition (PLD). An eximer laser (Lambda Physik, LEXTRA 300C) was used as energy source to provide KrF laser irradiation (wavelength=248 nm, pulse duration=34ns) which was focused by a silica lens on the target through a quartz window. The laser at a repetition rate of 5Hz was applied for 10 min on the TiO_2 target (i.e., 5x10x60 = 3000 shots were used) and for Al_2O_3,10 Hz was applied for 15 min., (i.e. 10x15x60 = 9000 shots). The high purity O_2 (99.995%) was introduced into the chamber through a fine control valve. The substrate temperature was kept at 500˚C throughout the coating processes. The oxygen pressure was 10^{-4} torr. Prior to coating, the Inconel 718 substrate surfaces were ground by using 320, 600, and 1200 grade SiC abrasive disks and polished by 0.5μ diamond suspension on red felt.

Thermal stressing Experiments. The thermal stressing of JP-8 fuel in the presence of Ti and Al oxides coated Inconel 718 superalloy foil (Goodfellow Co.) was performed in 1/4" (OD) glass-lined flow-through reactor. The elemental composition of Inconel 718 (wt %) is as follows: Ni:52.5, Fe:18.5, Cr:19, Mo:3.05, Al:0.5, Ti:0.9, Nb+Ta:5.13, Cu:0.15, Mn:0.18, Si:0.18, C:0.04, S:0.0008. The foils, 15x0.3 cm, were placed at the bottom of 20 cm long reactor. The reactor was preheated to 515°C for 2 hours in flowing argon at 34 atm before introducing the fuel. The fuel was preheated to 250°C in a valve oven before entering the reactor. The fuel flow rate was kept at 4mL/min.

The morphology of the substrate, Ti and Al oxide deposited films, and carbon deposits was examined by using field emission scanning electron microscopy (FESEM, JEOL JSM-6300F), transmission electron microscopy (TEM, Philips EM420ST) scanning electron microscopy (Hitachi S-3400N), and tapping mode atomic force microscope (AFM, Digital Instruments- Dimension 3100). The structure of the thin films was examined by glancing incidence X-ray diffraction (XRD, Philips) where incident angle was fixed at a value of 1˚.

Results and Discussion

Surface morphology and structure characterization. The thickness of the TiO_2 and Al_2O_3 coatings obtained on alloy substrates was approximately 1 μm. FESEM images showed that the polished Inconel 718 surface prior to coating is very smooth. The SEM images showed that the smooth substrate surface resulted in the formation of smooth coatings through uniform nucleation of the precursor and smooth growth of the oxide crystals. It was observed that polycrystalline morphology of the Ti oxide coating on Inconel 718 with average crystallite diameter of 0.2 μ. In contrast, Al oxide coating appears to be featureless. The thickness of Ti and Al oxide coatings was 1.1 μm and 1.0μm, respectively, as measured by SEM cross-section examination.

Tapping mode AFM topographic images in Figure 1 show that coatings of Ti and Al oxides on polished Inconel 718 surface are quite smooth because of the smooth substrate surface. While the average roughness value of Inconel 718 is approximately 10 nm, the coated surface roughness values for Ti and Al are 23.7 and 12.9 nm, respectively.

Grazing Incident X-ray diffraction analysis was applied for the identification of TiO_2 and Al_2O_3 thin film phases deposited on Inconel 718 surfaces. The angle between the incident X-ray and coated surface was 1˚. GIXRD patterns showed that the TiO_2 deposition was in the form of anatase and Al oxides were mostly in the amorphous form on Inconel 718 surface after 10 min PLD deposition. The TiO_2 coating on Inconel 718 surface produced mainly anatase phases without leading any outward cation diffusion

from the substrate. Since the substrate temperature was 500˚C, anatase, rather than brookite, or rutile, formed. GIXRD results indicate that at 500˚C substrate temperature, the crystalline Al oxide phase does not form. Stable Θ-Al_2O_3 and α-Al_2O_3 phases form at 900-1000˚C and 1000-1100˚C in oxygen atmosphere. Hirschauer et al. (11) studied different substrate temperatures to obtain crystalline α-Al_2O_3 on Si (111) wafers by using PLD and obtained highly crystalline α-Al_2O_3 structures at 850˚C substrate temperature. They reported that below 850˚C metallic Al was observed because of the higher desorption rate of oxygen than aluminum from the surface. However, for our case higher substrate temperature would result in creation of oxide layers which will affect the coating mechanism and adhesion. At 500˚C substrate temperature surface diffusion length is smaller than the adsorbed species diameter, Ti and Al, which did not lead to significant void or dome formations.

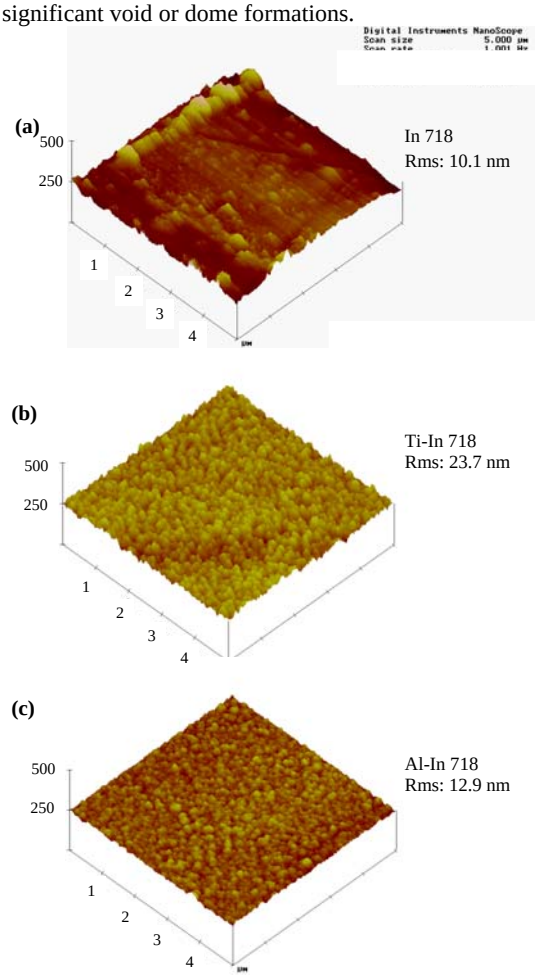

Figure 1. AFM images of polished Inconel 718 substrate (a), Ti oxide coated (b), and Al oxide coated (c) Inconel 718 surfaces.

Thermal Stressing of JP-8 Fuel on Alloy Substrate and Coated Surfaces. The JP-8 thermal stressing experiments were carried out on both bare substrate and Ti and Al oxides coated Inconel 718 surfaces at 470˚C fuel temperature and 34 atm for 24h with a 4 mL/min flow rate.

Bare Inconel 718 substrate surface collected significant amount of carbon and sulfur deposits from JP-8 decomposition at 470˚C and 34 atm after 24h as shown in Figure 2. Figure 2 shows SEM and TEM images of the stressed Inconel 718 surface indicating the presence of faceted crystalline metal sulfides, carbon filaments and amorphous carbon structures. The X-ray diffraction and EDS analysis results indicated that the metal sulfides consist of Ni_3S_2, $Ni_{1-x}S$, and $Fe_{1-x}S$. These observations show that the bare Inconel 718 surface was significantly corroded by the formation of sulfide crystallites that are approximately 0.5 µm or smaller in diameter. As seen in Figure 2a, the formation of sulfides reconstructs the metal surfaces to produce very fine faceted structures which are especially important in catalytic reactions that lead to structured carbon deposits.

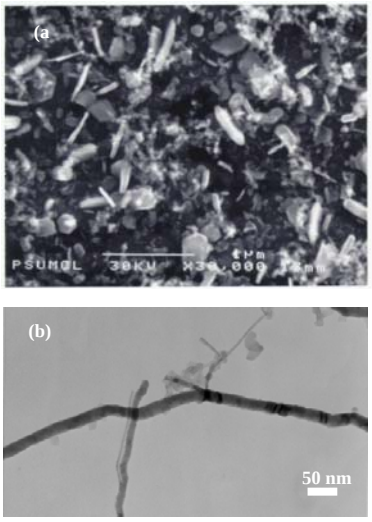

Figure 2. SEM (a) and TEM (b) images of carbon and sulfur deposits from JP-8 decomposition at 470˚C fuel temperature and 34 atm for 24h on bare Inconel 718 surface.

Figure 2b shows a TEM image of filamentous carbon and nanotubes produced on Inconel 718 at 470˚C fuel temperature. The filaments are 10 to 15 nm in diameter and 2-5 µm in length. The micrograph also shows carbon nanotubes (4-6 nm in diamater) as well as spherical carbon deposits growing on the surface of the filaments containing metal particles which are presumably Ni and Fe. Thermal decomposition of jet fuels produces reactive gas species which are chemisorbed on metal surfaces. The Ni, Co, and Fe rich alloy surfaces catalyze decomposition of chemisorbed hydrocarbons to produce carbon and hydrogen. Carbon then diffuses through any dislocations on the metal surface and finally precipitates in these locations as solid deposit (12,13). The increased concentration of precipitated carbon creates a stress at dislocations, and after a certain tensile strength of the metal is reached, the metal crystallite is removed from the surface producing a filament with a metal particle at the tip.

From our baseline experiments, and previous work in this laboratory, it becomes clear that the chemical composition of metal alloy surfaces, in particular, the activity for producing filamentous carbon plays a critical role in initiating the deposition process. Roughness of the substrate surface could also play an important role for the accessibility of the active sites and the chemisorption of deposit precursors.

The coated substrates were stressed with JP-8 under the same conditions that the bare Inconel 718 was stressed (at 470°C for 24 h.), and the stressed samples were examined by FESEM/EDS. As shown in Figure 3, both coatings appeared to be effective in inhibiting the catalytic activity of the bare metal surfaces. On both Ti and Al oxide surfaces, the deposit amount was significantly low compared to bare substrate surface because of the higher thermodynamic stability of TiO_2 and Al_2O_3 films. Lesser degree of

carbon deposit formation was observed on Ti oxide coated surface than on Al oxide coated surface. The morphology of deposits is almost similar for both coated surfaces. They consist of apparently amorphous solids. Thus, Ti and Al oxide coatings appear to collect only amorphous deposit. No filamentous carbon was observed on the TiO_2 and Al_2O_3 coated surfaces.

The amount of carbon deposit on the TiO_2 coated surface is lower than that on the Al_2O_3 coated surface as seen in Figures 3a and 3b. Agglomerated amorphous deposits observed on the Al_2O_3 coated surfaces (Figure 3b) can be attributed to the presence of some metallic Al on the surface that tends to react with sulfur and carbon. It is well known that aluminum plays a significant role as an alloying addition, determining the scaling resistance of materials in oxygen, sulfur and carbon containing environments. Addition of aluminum content of about 5% in the alloys based on Fe-Cr, Co-Cr, and Ni-Cr greatly improve the sulfur corrosion resistance of the alloy if good protective α-Al_2O_3 scale formed.

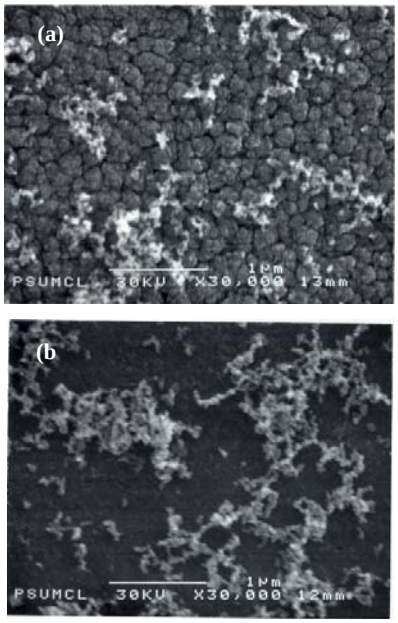

Figure 3. FESEM images of carbon deposits from JP-8 decomposition on Ti (a) and Al (b) oxide coated Inconel 718 surface at 470˚C fuel temperature and 34 atm for 24h at a 4 mL/min flow rate.

Conclusions

Approximately 1 µm coatings of Al and Ti oxides were obtained on Inconel 718 coupons using pulsed laser deposition. JP-8 fuel stressing at 470˚C and 34 atm in the presence of bare and coated Inconel 718 coupons indicated that both coatings reduced carbon deposition by eliminating the catalytic activity of the metal alloy surface. In addition, no metal sulfide formation was observed on the Ti and Al oxide coated surfaces after thermal stressing with the JP-8 fuel. The Al oxide coated surface collected a larger amount of carbon deposit than the Ti oxide coated surface presumably because of the presence of metallic Al in the former. For better and efficient coating of stable α-Al_2O_3 oxide, the substrate temperature can be increased to 850˚C to reduce the metallic Al formation. This may totally eliminate sulfur corrosion and subsequent surface roughening upon stressing with the jet fuel.

Acknowledgement. This work is part of a project funded by the Air Force Office of Scientific Research.

References

(1) Zabarnick, S.; Zelesnik, P.; and Grinstead, R. R. *J. Eng. Gas Turb. Pow*. **1996**, *118* 271.
(2) Maurice, L. Q.; Lander, H.; Edwards, T.; and Harrison III, W. E. *Fuel*, **2001**, *80*, 747.
(3) Diane, L. L.; Meyer, M. L.; Edwards, T.; and Eitman, D. A, *33rd Joint Propulsion Conference and Exhibit*, AIAA-97-3041, Seattle, Washington, July 6-9, 1997.
(4) Marteney, P. J.; and Spadicini, L. J., *ASME Paper* 91-GT-36, June 1991
(5) Altin, O.; and Eser, S., *Ind. Eng. Chem. Res.* **2001**, *40* 589.
(6) Altin, O.; and Eser, S., *Ind. Eng. Chem. Res.*, **2001**, *40*, 595.
(7) Narita, T.; and Ishikawa, T., *Mat. Sci. Eng.* **1987**, *87* , 51.
(8) Donley, M. S.; and Zabinski**,** J. S., *Tribological Coatings***,** In *Pulsed Laser Deposition of Thin Films*, D. B. Chrisey, G. H. Hubler (Eds.), Wiley, NY, Chp.18, 1997**.**
(9) Sturm, K.; Fahler, S.; and Krebs, H.U., *Appl. Surf. Sci.,* **2000,** *154,* 462.
(10) Yin, X.; Miura, R.; Endou, A.; Gunji, I.; Yamauchi, R. ; Kubo, M.; Stirling, A.; Fahmi, A.; and Miyamoto, A., *Appl. Surf. Sci*. **1997**, *119,* 199.
(11) Hirschauer, B.; Soderholm, S.; Chiaia, G.; and Karlsson, U. O., *Thin Solid Films*, **1997,** *305*, 243.
(12) Bianchini, E. C. **;** and C. R. F. Lund, *J. Catal*., **1989**, *117* 455.
(13) J. –W. Snoeck, G. F. Froment, and M. Fowles, J. Catal. 169 (1997) 240.

MODELING ELEMENTARY REACTIONS IN COKE FORMATION FROM FIRST PRINCIPLES

Veronique Van Speybroeck, Marie-Françoise Reyniers[#], Guy B. Marin[#] and Michel Waroquier

Laboratory of Theoretical Physics, Center for Molecular Modeling, Ghent University, Proeftuinstraat 86, B-9000 Gent, Belgium and [#]Laboratorium voor Petrochemische Techniek, Universiteit Gent, Krijgslaan 281-S5, B-9000 Gent, Belgium

Introduction

Thermal cracking of hydrocarbons is the simplest and oldest method for petroleum refinery processes and is considered as the main process for the production of light olefins such as ethene. The thermal cracking of hydrocarbons is known to proceed through a free radical chain mechanism. Radicals are mainly formed via C-C bond breaking and propagation occurs through abstraction and addition reactions. Decomposition of radicals by β-scission results in the desired gas-phase olefins. During this process, highly undesirable carbon-rich products are formed on the inner walls of the reactor giving rise to the formation of a coke layer. This coke layer has a negative influence on the efficiency of the cracking unit.

The process of coke formation is a complex phenomenon[1,2]. Initially coke is formed by a heterogeneous catalytic mechanism in which the properties of the inner tube skin play an important role. Once the metal surface is covered with coke the catalytic activity of the metal particles diminishes and a heterogeneous non-catalytic mechanism becomes important. The coke layer thus formed has a polynuclear aromatic character. Usually one focuses on the second process since the period of catalytic coke formation is very small with respect to the total run length.

In today's operation of a plant simulation models play a very important role. Recently a coking model based on elementary reactions was developed at the Laboratorium voor Petrochemische Techniek[3,4]. In view of the fundamental nature of the elementary steps considered such a model is of general applicability . One of the main challenges in the development of an accurate and broadly applicable model is the assignment of values for rate coefficients of the individual reactions occurring in the reaction network. The fundamental nature of the elementary steps considered allows the use of theoretical calculations to provide kinetic and thermodynamic data and to obtain microscopic insight in the basic reaction steps of the coke formation model. The elementary reaction steps that lead to incorporation of carbon atoms and growth of the coke surface can be divided in five classes of reversible reactions (cf. Fig. 1) :

- **(i)** Hydrogen abstraction reactions by gas phase radicals and reverse reactions
- **(ii)** Substitution reactions by radicals at the coke surface and reverse reactions
- **(iii)** Addition reactions of radical surface species to gas phase olefins and the inverse ß-scission of a radical surface species in smaller surface species and gas phase olefins
- **(iv)** Addition reactions of gas phase radicals to olefinic bonds in a surface species and the inverse decomposition of radical surface species to gas phase radicals and olefinic surface species
- **(v)** Cyclization of radical surface species and decyclization

Due to the increasing capabilities of computing power and optimization of numerical models it is now possible to perform high level ab initio calculations on systems of industrial importance. Kinetic parameters, such as the preexponential factor and activation energy, can be obtained by means of Transition State Theory (TST). The microscopic quantities are obtained by means of ab initio calculations In this work preference has been given to Density Functional Theory calculations, since this approach is computationally attractive for the larger structures that are involved in this work. This approach has been successfully applied to a variety of important chemical reactions.

In the first part of this paper, microscopic routes starting from benzene leading to the formation of naphthalene are investigated with the aim to identify important coke precursors and to obtain insight into the elementary reaction classes that determine the rate of coke formation. In the second part of the paper, larger polyaromatic clusters are considered in order to determine the influence of the coke matrix on the kinetics of the elementary reactions.

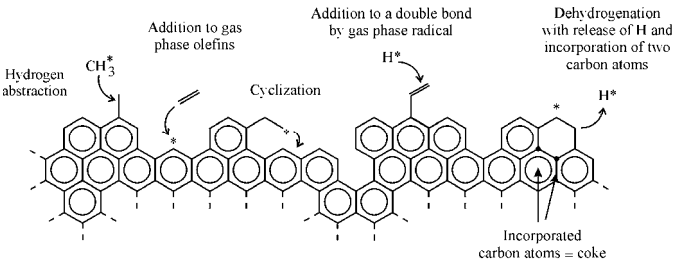

Figure 1. Radical elementary reaction steps leading to coke growth.

Microscopic pathways for the formation of naphthalene from benzene. In order to obtain microscopic insight into the elementary reactions leading to cokes, various pathways are studied starting from benzene that lead to the formation of naphthalene. For this study the coke layer is approximated by only one benzene ring. The composition of the process gas is an important factor in the coke formation A lot of work in this research field has been done by Kopinke et al., who performed tracer experiments with ^{14}C-labeled hydrocarbons added to straight run naphtha to establish structure-reactivity relations and relative coking rates for various types of hydrocarbons[5]. The most important coke precursors were found to be olefins and aromatics. Ethene has the lowest coking tendency of the olefinic hydrocarbons but its high concentrations in the gas phase, explains its large contribution to the coke formation in a thermal cracking unit. Propene shows similar properties. Ethyne is more reactive than ethene but appears in much smaller concentrations, limiting its contribution to coke formation. To investigate these earlier experimental findings all reaction routes with ethyne and ethene as typical coke precursors are taken into consideration (cfr. Fig. 2).

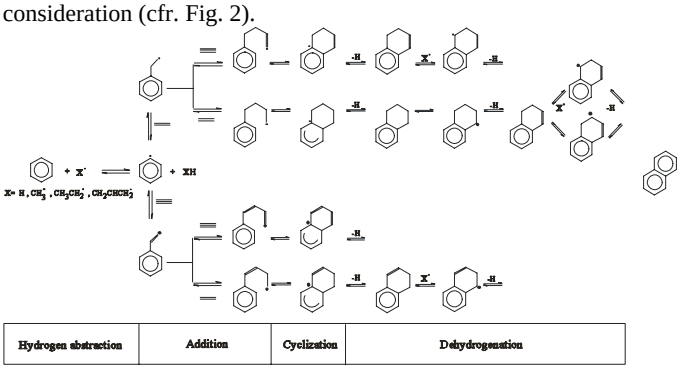

Figure 2. Radical elementary reaction steps leading to coke growth

The reaction sequence is initiated by hydrogen abstractions from benzene with gas phase radicals creating radical surface species. In turn these radicals react further with unsaturated gas phase components. Earlier experimental work indicated that hydrogen, methyl, ethyl and allyl radicals are very reactive in the coke

formation during thermal cracking[6]. Therefore all hydrogen abstractions in which the latter radicals are involved are taken into consideration. Based on the proposed reaction scheme. several conclusions concerning the coking tendency of gas phase components and the relative importance of the various reaction types can be drawn.

Influence of gas phase precursors on the coking rate. For all studied addition reactions with ethyne and ethene, both gas phase unsaturated components yield activation energies which are in the same order of magnitude, with respect to each other. The preexponential factor for reactions with ethyne is higher than for the corresponding additions with ethene, resulting in relative rate constants for additions to ethyne that are approximately twice as high as the ones for additions to ethene.

To estimate however the relative importance of both gas phase components as a coke precursor, their concentration has to be taken into account also. Gas phase concentration profiles were obtained from a simulation program, which is based on a detailed network of elementary reactions, developed at the Laboratorium voor Petrochemische Techniek[7,8]. The reactor geometry and the operating conditions are taken for a typical ethane cracking unit. The process gas temperature profile as a function of the axial reactor coördinate is shown schematically shown in fig. 3 and varies between 800 K at the reactor inlet to reach a coil outlet temperature of 1100 K.

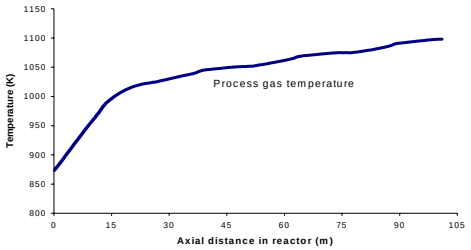

Figure 3. Temperature profile of the process gas along the reactor coil for typical ethane cracking conditions.

Typical concentrations of ethene and ethyne were obtained at the reactor inlet, in the middle of the reactor length and at the outlet the reactor. These values are presented in Table 1.

Table 1. Concentrations of ethyne and ethene at various axial reactor distances during ethane cracking .

Axial distance (m)	Ethene (mol/dm3)	Ethyne (mol/dm3)
1,09	$2.52\ 10^{-7}$	$1.51\ 10^{-15}$
44.02	$3.14\ 10^{-3}$	$3.90\ 10^{-6}$
100.96	$5.88\ 10^{-3}$	$5.35\ 10^{-5}$

Taking these concentrations into account, ethene shows the highest coking tendency despite its lower reaction rates. This result is in accordance with earlier reported experimental data[5]. However, at the higher temperatures prevailing in the last passes of the reactor, the coking tendency of ethyne becomes more important due to the smaller difference in concentrations between the two unsaturated hydrocarbons.

Relative importance to coke formation of the various reaction types. At second instance it is interesting to search for rate determining reaction steps along the reaction sequence going from benzene to naphthalene. Since the reaction network contains both bimolecular and unimolecular reactions, it is not possible to compare directly the rate constants of the elementary reaction steps. Again concentration profiles have to be taken into account to compare absolute rates of the various reaction steps. It is found that the initial hydrogen abstraction are relatively slow, due to the low concentration of the gas phase radicals. The individual rate constants however were found to be one of the highest in the total reaction network. The initially created radical surface species can further grow by means of various subsequent additions. The first addition of ethene or ethyne to the phenyl radical is characterized by a high rate constant. This can be explained by the reactivity of the phenyl radical. The subsequent additions are much slower and determine the coking efficiency. After the second addition all further reaction steps, i.e. the cyclizations and dehydrogenation, proceed very fast. Previous discussion reveals that the initial creation of surface species and the subsequent additions determine the coking efficiency of the reaction network.

Influence of the coke matrix on the kinetic parameters

The reaction network discussed in the previous section was based on the assumption that the coke surface could be approximated by only one benzene ring. It is however important to investigate the validity of this approximation. Therefore calculations were performed on larger polyaromatic compounds to establish the importance of the local environment of the active surface site in the coke formation.

Classification of PAHs based on Bond Dissociation Energies. A measure of the chemical reactivity of a site at an aromatic cluster is the bond dissociation energy (BDE) of the corresponding C-H bond. BDEs of all C-H bonds were calculated for the series of PAHs shown in fig. 4.

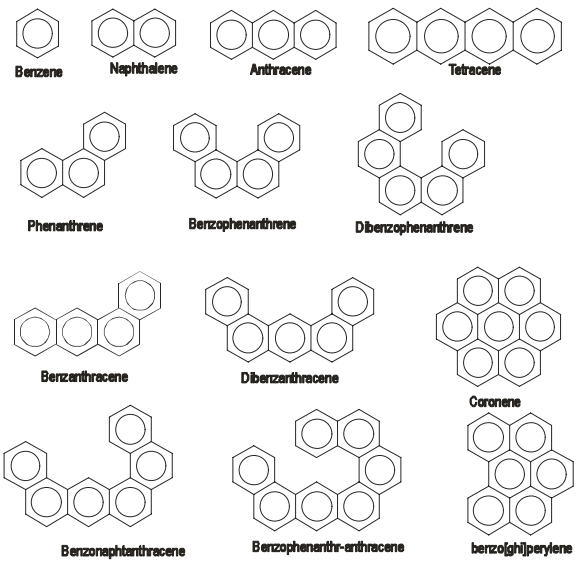

Figure 4. PAHs considered in this study

Based on the BDEs the C-H bonds in aromatic structures can be divided into four types with different reactivity, which can be related to the local structure around the site (Fig. 5). Similar conclusions were made by various other authors [9].

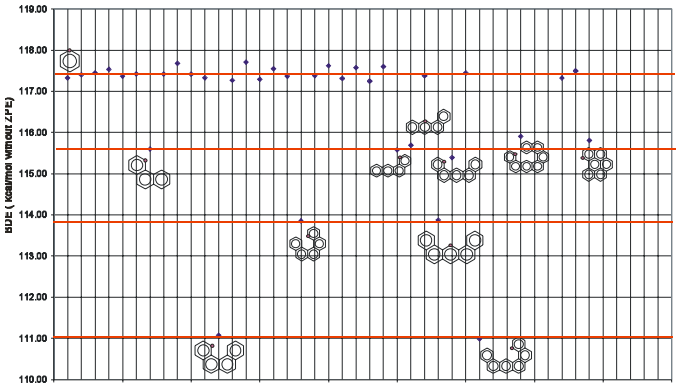

Figure 5. BDEs for a series of PAHs

The types of sites at the coke surface are defined based on their reactivity as well as on the structure of the local surroundings. Although benzene, naphthalene and anthracene have similar reactivities, they are retained as separate surface sites for further kinetic calculations due to their structural differences. This results in six different sites which are based on differences in local structure and/or on differences in chemical reactivity. The six different sites are named according to the smallest aromatic compound that exhibits the same local structure i.e. a benzene-like, naphthalene-like, anthracene-like, phenanthrene-like, benzophenanthrene-like and dibenzo(c,g)-phenanthrene-like site.

Kinetics of hydrogen abstraction reactions on PAHs. Attention is focussed on the influence of the local polyaromatic structure on the kinetic parameters of hydrogen abstractions reactions with a methyl radical. The latter reactions are known to determine the global coking rate. The kinetic parameters are determined for six different sites as introduced in the previous section. A conformational and vibrational analysis was performed for each of the reactants, products and transition states at the B3LYP/6-311G** level of theory. The resulting kinetic parameters, calculated in the temperature interval from 700 to 1100 K which is characteristic for thermal cracking, are given in table 2.

Table 2. Kinetic parameters (700-1100K) for hydrogen abstractions at PAHs

Hydrogen abstraction	Ea (kJ/mol)	A (m^3/mol.s)
at benzene-like site	79.68	$1.7\ 10^9$
at naphthalene-like site	81.82	$8.2\ 10^7$
at anthracene-like site	84.63	$2.4\ 10^8$
at phenanthrene-like site	85.94	$1.7\ 10^7$
at benzophenanthrene-like site	85.42	$4.8\ 10^6$
at dibenzo(c,g)-phenanthrene-like site	85.81	$4.5\ 10^6$

The microscopic calculations give insight into the factors that determine the kinetic parameters. The activation energy varies only slightly in terms of the local PAH structure. The small differences must be traced back to the steric hindrance between the attacking methyl radical and the polyaromatic structure. The frequency factor however varies largely with the number of aromatic rings involved in the polyaromatic structure. These variations must be traced back to the occurrence of skeletal vibrations in the larger PAH structures. For larger PAH structures more skeletal vibrations are present in the reactant structures and thus the PAH obtains a larger degree of conformational flexibility and a larger partition function. This results in smaller rates for hydrogen abstractions at larger polyaromatics. This is further illustrated by comparing absolute rates in the temperature interval which is typically encountered in an industrial cracking unit. The relative rates for hydrogen abstractions with a methyl radical at site X (X=naphthalene, anthracene, phenanthrene, benzophenanthrene) with respect to a benzene-like site are presented in fig. 6.

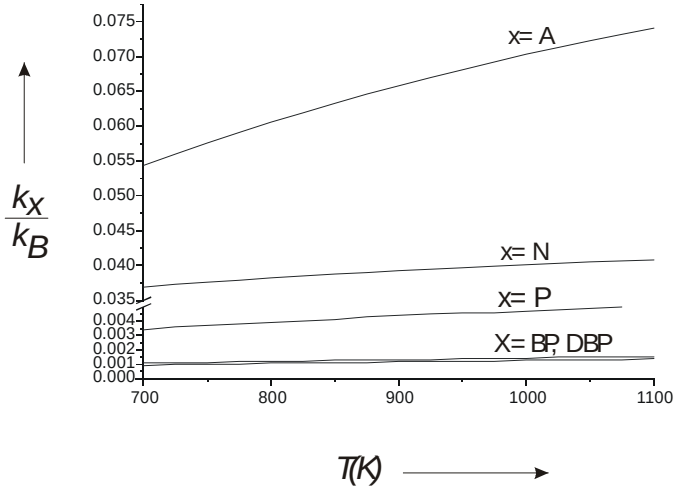

Figure 6. Rate constant for hydrogen abstractions with a methyl radical at site X, relative to the rate constant at the B site, as a function of temperature.

The initial creation of radical surface species predominantly occurs at the smaller clusters and preferentially at a benzene-like site.
For other elementary classes of the coke formation network, also a strong correlation was observed between the size of the PAH and the rate constants [10,11].

Conclusions

In this paper, various elementary reaction steps important for coke formation during thermal cracking of hydrocarbons are studied. In a first instance all elementary reaction steps of a reaction network starting from benzene and leading to naphthalene were studied. The importance of various gas phase components as coke precursors was evaluated by considering all reaction routes in which ethene and ethyne are involved. It was shown that, despite its lower reactivity in the various elementary steps, ethene is an efficient coke precursor due to its high concentration.. Although ethyne is more reactive, it contributes only significantly to coke formation at higher axial distances in the reactor. The theoretical calculations of the rate constants also reveal that the initial hydrogen abstractions and the subsequent addition occur at lower rates than cyclization and dehydrogenation reactions.

In a second instance, the kinetic calculations were extended to larger polyaromatics, to investigate the influence of the local environment of the coke surface on the kinetic parameters. A classification for the reactivity of PAH's based on BDE's was proposed. Four different classes of C-H bonds could be identified. Based on reactivity and local structural difference six types of active sites for coke growth were identified. The influence of the local environment of the active site on the kinetics was investigated by studying a series of hydrogen abstraction reactions. The latter reaction class was derived to determine the global coking rate of the reaction network. It was found that the rate constants can vary largely depending on the local structure of the polyaromatic surface.

Moreover at typical temperatures encountered during cracking, hydrogen abstractions preferentially occur at the smaller PAHs, such as benzene, naphthalene and anthracene.

Acknowledgement. This work is supported by the Fund for Scientific Research-Flanders (FWO) and the Research Board of Ghent University

References

(1) Wauters,S; and Marin, G.B., *Ind.Eng.Chem.Res*, **2002**, *41*(10), 2379.
(2) Wauters,S; and Marin, G.B. , *Chem.Eng.J.*, **2001**, *82*(1-3), 267.
(3) Wauters,S, PhD Thesis. *Kinetics of coke formation during thermal cracking of hydrocarbons based on elementary reactions*, **2001**, Ghent University
(4) Van Geem,K.M.; Heynderickx, G.J.; Marin,G.B.; *AICHE Journal*, **2004**, *50*, 173-183.
(5) (a) Kopinke,F.D.; Zimmerman,G.; Nowak,S., *Carbon*, **1988**, *26*(2), 117-124. (b) Kopinke,F.D.; Zimmerman,G.; Reyniers,G.C.; Froment, G.F., *Ind.Eng.Chem.Res.*, **1993**, *32*, 56-61. (c) Kopinke,F.D.; Zimmerman, G.; Reyniers,G.C.; Froment, G.F., *Ind.Eng.Chem.Res.*, **1993**, *32*, 2620-2625.
(6) Froment, G.F. *Fouling of heat transfer surfaces by coke formation in petrochemical reactors*, in E. Summerscales, J.G. Knudson (Eds.), *Fouling of Heat Transfer Equipment*, Hemisphere Publ. Corp., **1981**.
(7) Clymans, P.J.; Froment,G.F., *Comput.Chem.Eng.*, **1984**, *8*, 137-142.
(8) (a) Reyniers, G.C.; Froment,G.F.; Kopinke,F.D.; Zimmerman,G., *Ind. Eng.Chem.Res.*, **1994,** *33*(11), 2584-2590. (b) Plehiers,P.M.; Reyniers,G.C.; Froment,G.F., *Ind. Eng.Chem.Res.*, **1990**, *29*, 636-641.
(9) (a) Aihara,J.; Fujiwara,K.; Harada,A.; Ichikawa,H.; Fukushima,K.; Hirota,F.; Ishida,T.; *J.Mol. Struct. (Theochem)*, **1996**, *366*, 219-226. (b) Chen, R.H.; Kafafi,S.A.; Stein,S.E.; *J.Am.Chem.Soc.*, **1989**, *111*, 1418-1423. (c) Cioslowski,J.; Liu,G.; Martinov,M.; Piskorz,P.; Moncrieff, D.; *J.Am.Chem.Soc.*, **1996**, *118*, 5261-5264. (d) Stein,S.E.; Brown,R.L., *J.Am.Chem.Soc.*, **1991**, *113*, 787-793. (e) Wang,H.; Frenklach,M.; *J.Phys.Chem.*, **1993**, *97*, 3867-3874.
(10) Van Speybroeck, V.; Reyniers,M.F., Marin,G.B.; Waroquier, M.; *ChemPhysChem*,**2002**, *3*, 863-870.
(11) Van Speybroeck,V.; Hemelsoet,K.; Waroquier,M.; Marin,G.B.; *Int. J.Quant.Chem.*, **2004**, *96*, 568-576.

AUTOMATED MODELING OF GAS-PHASE CHEMISTRY FOR PYROCARBON-FORMING HIGH-CONVERSION ETHANE PYROLYSIS

David M. Matheu[a], *Jeffrey M. Grenda*[b]

[a]National Institute of Standards and Technology
Physical and Chemical Properties Division
100 Bureau Dr. Stop 8380
Gaithersburg, MD 20899-8380

[b]ExxonMobil Research and Engineering Company
1545 Rt. 22 East
Annandale, NJ, 08801

Introduction

Pyrolytic carbon deposition remains a key problem for the industrial cracking of light alkanes, and the deposition rate depends in part on the chemistry of the gas phase. The deposits degrade heat transfer efficiency, and must be periodically removed from pyrolysis reactors, necessitating expensive shutdowns. Furthermore, in the intentional deposition of pyrolytic carbon material from small hydrocarbons, the gas-phase chemistry has important effects on the quality of the carbon deposited [1]. But the processes leading to pyrolytic carbon deposition are still seriously debated in the literature.

Glasier and Pacey recently performed a series of neat ethane pyrolysis experiments focused on the gas-phase products and pyrocarbon deposition rates at very high conversion (900-1200 K, 0.4 atm, conversion > 98%) [2]. The large "soup" of species and reactions at such high conversion, however, makes developing an appropriate detailed chemical kinetic model extremely difficult; to our knowledge, no published model exists which is appropriate to the experimenters' conditions. That is unfortunate, since a reliable model for the Glasier and Pacey experiments could be useful, as an intermediate step, toward the ultimate understanding of how the higher aromatic species are formed and deposited in pyrolysis systems.

In this work we apply a new, automated mechanism generation tool, called "XMG-PDep" [3;4], to rigorously construct an elementary-step-based chemical kinetic model for the conditions of the Glasier and Pacey experiments. We then apply reaction pathway analysis, sensitivity analysis, and equilibrium analysis to understand those chemical pathways that control the formation and destruction of the minor products measured by the experimenters. The results suggest that rarely considered pathways may play key roles in minor product chemistry, and proper, systematic treatment of the pressure-dependence is important for all the minor products.

Computational Method: The XMG-PDep Algorithm

XMG-PDep is based upon XMG [5], which developed from NetGen [6]. It employs flux-based termination of the otherwise combinatorial growth in species and reactions. To do this, the code periodically constructs and integrates the set of differential equations that represent the evolution of the reacting system in time. It evaluates a characteristic mechanism flux $R_{char}(t)$, which is similar to a root-mean-square average of chemical fluxes in the mechanism [7]. XMG-PDep then compares this flux with those to candidate species that have been discovered, but not yet included, in the mechanism. Those species whose fluxes exceed the cutoff flux (equal to a user-specified fraction of $R_{char}(t)$) are included in the mechanism and their reactions are explored, to generate new candidates. Eventually, all fluxes to candidate species are below the threshold $R_{char}(t)$ and generation is terminated.

XMG-PDep can systematically discover and include arbitrary pressure-dependent reactions using the algorithm of ref. [8]. To allow the most flexibility, XMG-PDep considers any elementary step of the form A + B $\rightarrow$ C, B $\rightarrow$ C or B $\rightarrow$ C + D to initiate a partial pressure-dependent network. For each partial network, XMG-PDep uses the QRRK/MSC code CHEMDIS [9] to estimate the value of the pressure-dependent rate constant $k(T,P)$ for every net pressure-dependent reaction. It also examines the maximum flux to all non-included portions of the partial pressure-dependent network. If this flux is greater than the cutoff flux, the partial network is "grown" by one isomer, with all its high-pressure-limit elementary steps, and the $k(T,P)$ calculation is repeated. Growth of each partial pressure-dependent network is halted when the flux to non-included portions is less than the cutoff flux. In this way pressure-dependent reactions can be included systematically and rationally. A full description of the integrated algorithm for generating mechanisms is presented in ref. [3].

XMG-PDep includes a number of other features designed to make it accurate and useful. It employs literature-based libraries of rate constants and thermochemical parameters whenever possible. Its rate rules are subdivided as much as is reasonable to provide the best estimates for high-pressure-limit rates when these are not available from the library. Thermochemical data (when not available from the data library) are taken from a group contribution method [9] and used to ensure thermodynamic reversibility. The code will produce a CHEMKIN-style mechanism when finished with generation. Finally, we have recently added to XMG-PDep two new capabilities essential for treating the Glasier and Pacey system: an internal plug-flow reactor model to overcome the batch reactor restriction, and an ability to construct mechanisms spanning a temperature range.

Application to High-Conversion Ethane Pyrolysis

Figures 1-3 present selected predictions of our generated model along with experimental results. Agreement with the data is quite good, considering that no parameters were adjusted to fit the experiments, thermodynamic consistency is enforced, and all steps in the mechanism are generated "a priori".

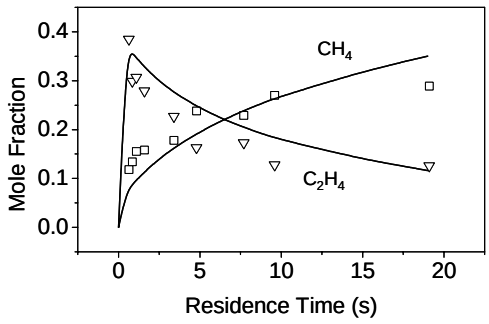

Figure 1. CH_4 and C_2H_4 concentrations with residence time in the Glasier and Pacey flow reactor. Symbols are experimental data points; lines are auto-generated model predictions.

Reaction pathway analysis, shown in simplified form in Figures 4 and 5, of the very large mechanism generated for this system suggests that the fates of the minor products, and some major ones, are governed in part by a large and complex set of interconnected reactions. Conventional kinetic models for ethane or ethylene pyrolysis do not capture many of these pathways.

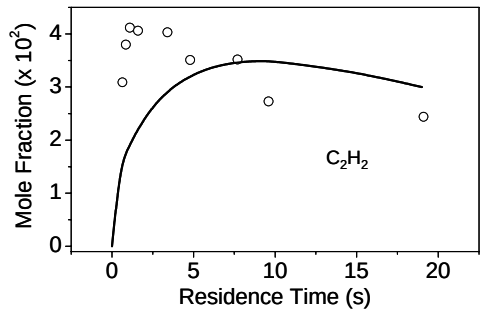

Figure 2. Experimental and predicted acetylene concentration with residence time.

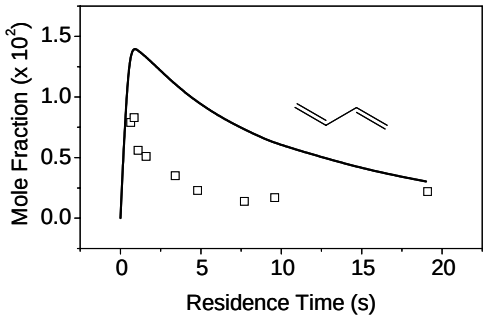

Figure 3. Experimental and predicted 1,3-butadiene concentration with residence time.

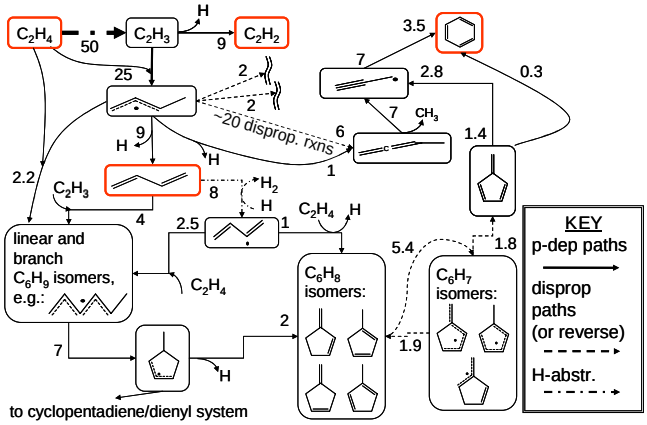

Figure 4. Partial pathway diagram for the production and consumption of minor products within the reactor "hot zone" (from 7.5 to 30 cm). Each arrow represents a collection of parallel, reversible reaction pathways of the same general type: solid lines are net pressure-dependent pathways; dotted lines are radical disproportionation reactions; dash-dotted lines are radical abstraction reactions. Numbers represent integrated, net molar flux relative to C2H4 consumption (= 100).

A key feature in Figures 4 and 5 is the presence of multiple, interconnected routes to the important minor products. There are at least three routes to benzene, four routes for the formation of propylene, and two alternatives to the well-known vinyl radical beta scission route for acetylene formation. Many of these pathways are pressure-dependent at the experimental conditions. Sensitivity analyses confirm the overall view that vinyl radical addition to ethylene to form the resonantly-stabilized allylic butenyl radical is a key rate limiting step for both 1,3-butadiene and benzene formation, as has been alluded by Roscoe et al [10].

Another unusual feature of the model is the set of radical disproportionation reactions which generate 1,2-butadiene – the 1,2-butadiene yields propargyl radicals which combine to form benzene (Figure 4). No single reaction in this set of 20 is important enough, by itself, to be noticeable during sensitivity analysis. Our a priori effort suggests, however, that the aggregate affect of the pathways could be quite important.

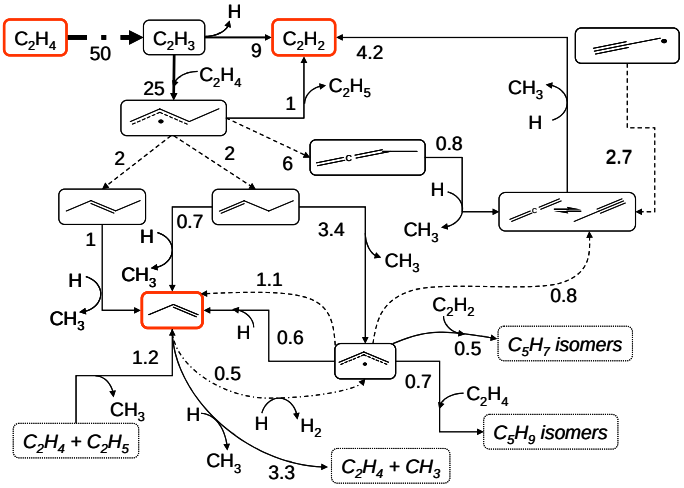

Figure 5. Continuation of Figure 4.

Conclusions

Application of the XMG-PDep algorithm to the experimental system of Glasier and Pacey yields a systematic kinetic model which appears to describe the gas-phase chemistry. This a priori model may prove useful as a base for advancing the mechanistic understanding of aromatics and pyrocarbon formation. Although complex, the generated model affords an understanding of the rate-limiting steps and pathways to the measured minor products in this system, such that changes in their behavior with temperature and pressure can be predicted (as is planned for future work). XMG-PDep explores many pathways not usually considered in other pyrolysis systems, and finds certain sets of reaction pathways, such as radical disproportionations, which might elude by-hand model construction.

References

(1) Oberlin, A. *Carbon* **2002**, *40*, 7-24.
(2) Glasier, G. F.; Pacey, P. D. *Carbon* **2001**, *39*, 15-23.
(3) Matheu, D. M. *Integrated Pressure-Dependence in Automated Mechanism Generation: A New Tool for Building Gas-Phase Kinetic Models*, Ph.D. Thesis, Massachusetts Institute of Technology, **2002**.
(4) Matheu, D. M. , Dean, A. M., Grenda, J. M., and Green, W. H. Jr. *J. Phys. Chem.*, submitted for publication.
(5) Grenda, J. M. ; Androulakis, I. P.; Dean, A. M.; Green, W. H. Jr. *Ind. Eng. Chem. Res.* **2003**, *42*, 1000-1010.
(6) Susnow, R. G.; Dean, A. M.; Green, W. H.; Peczak, P.; Broadbelt, L. J. *J. Phys. Chem. A* **1997**, *101*, 3731-40.
(7) Song, J.; Stephanopoulos, G.; Green, W. H. *Chem. Eng. Sci.* **2002**, *57*, 4475-4491.
(8) Matheu, D. M.; Lada, T. A.; Green, W. H.; Grenda, J. M.; Dean, A. M. *Comp. Phys. Comm.* **2001**, *138*, 237-249.
(9) Chang, A. Y.; Bozzelli, J. W.; Dean, A. M. *Z. Phys. Chem.* **2000**, *214*, 1533-1568.
(10) Roscoe, J. M.; Bossard, A. R.; Back, M. H. *Can. J. Chem.* **2000**, *78*, 16-25.

A SIMULINK MODEL FOR CALCULATION OF FUEL CELL STACK PERFORMANCE

Jeremy A. Schaeffer[1], Lea-Der Chen[1] and James P. Seaba[2]

[1]Department of Mechanical and Industrial Engineering
National Advanced Driving Simulator
The University of Iowa
Iowa City, IA 52242

[2]Emerging Technology
420 S. Keeler Avenue
ConocoPhillips
Bartlesville, OK 74004

Introduction

A fuel cell is an electrochemical device that converts the chemical energy stored in the fuel into electrical work. To generate the necessary cell voltage, fuel cells are often connected in series to form a fuel cell stack. If the electrolyte used in the fuel cell is liquid, for example, as that in phosphoric acid [1] and alkaline fuel cells, the electrolyte of different cells is shared through a common manifold, which might result in the presence of shunt current. Similarly, shunt current may also be present when water is used as the coolant in polymer electrolyte fuel cell stacks. An electrical circuit model is used to simulate the electrical processes of liquid electrolyte fuel cell stacks. The calculation is compared with experimental data of an electrolyzer stack [2].

Electrical Circuit

The shunt current can be modeled using the electrical circuit shown in Fig. 1 [2], in which 20 represents the manifold, 24, 26, 28, 30, 32, and 34 represent the channels, and 4, 6, 8, 10, 12, and 14 represent the individual cells; Re represents the cell (or electrolyte) resistance, R_c the channel resistance, and R_m the manifold resistance, and V_0 is the cell potential, I the current flowing through the stack. The i's represent the current that flows through the cell after the shunt current (j's) has been accounted for. The k's represent the current that flows through the manifold segments [2]. Most of the current will flow through the cell (R_e) because this resistance is generally the smallest as compared to R_m and R_c. A small amount of current, or shunt current, will flow through the channel and manifold. To reduce the shunt current, a protective current, k_0 (shown on the far left of the manifold), is applied in [2].

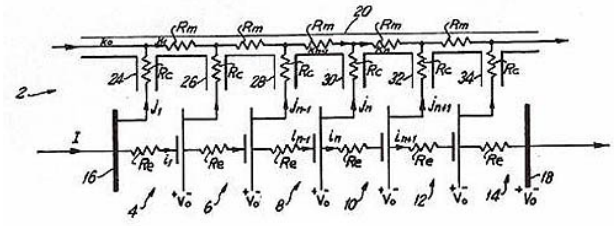

Figure 1. Electrical circuit used to model fuel cell stack [2].

An electrical circuit is created in Simulink© environment to model the electrical current and voltage of the circuit given in Fig. 1. The Simulink© model is given in Fig. 2, which calculates the current flowing through the cells (EC), channels (CC), and manifold (MC) by using a Matlab© function.

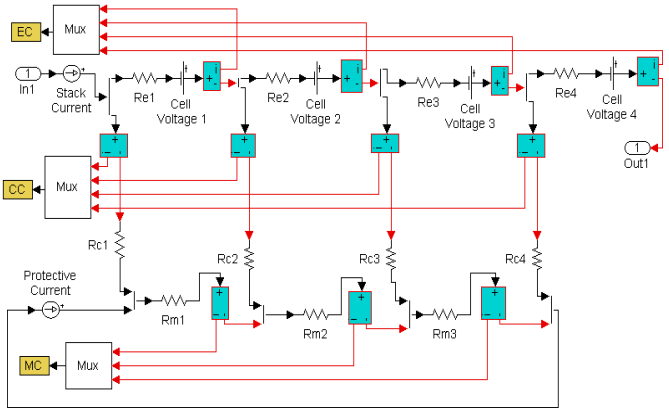

Figure 2. Illustration of a Simulink© model for 4-cell stack, protective current applied to the manifold.

Results and Discussion

Due to limited availability of fuel cell stack data, results of the Simulink© stack model were compared with experimental data of a 10-cell electrolyzer stack [3]. The applied current (420 mA), protective current (17.5 mA) and electrode area (968 mm^2 or 1.5 in^2) were given in [3]. The distance between the electrodes was estimated to be 31.75 mm (1.25 in) [3]. The resistance of the channel, manifold segment, and electrolyte (based on an estimated electrolyte conductance of 0.15 Ω^{-1} cm^{-1}) is estimated to be 1000 Ω, 150 Ω, and 2.187 Ω, respectively. The cell voltage is set to 2.54 V. The experimental results had a precision error of either ± 0.39 mA or ± 1 mA, depending on whether the range selector for the current meter was set to 10 mA or 30 mA full scale [3]. The Simulink© results, along with experimental data of no protective current, are shown in Fig. 3 in which error bars denote experimental precision error of ± 1 mA. The Simulink© results are in reasonable agreement with experimental data. The calculation underestimates the shunt currents in channels 1 and 10 by 31% and overestimates the shunt currents in 3 through 9. The maximum difference in channels 3 through 9 is 1.4209 mA. It is noted that the calculation results in a positive current for channel 5, while the experiment registered a small negative current was within the experimental uncertainty of 10 and 30 mA.

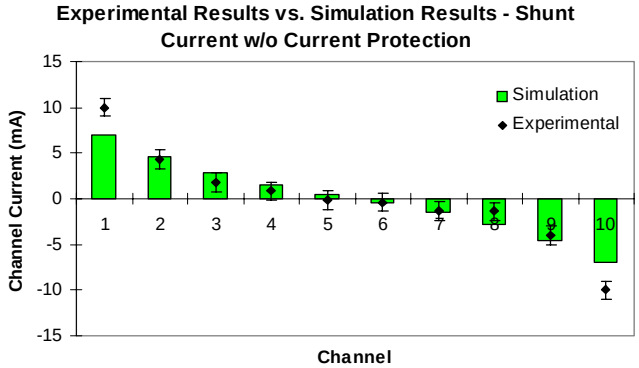

Figure 3. Comparison of simulation and experimental shunt current without protective current: R_e = 2.187 Ω, R_m = 150 Ω, R_c = 1000 Ω, V = 2.54 V, I = 0.42 A; Error bars ± 1 mA.

A protective current of 17.5 mA was applied to the manifold in the Simulink© model, similar to the condition given in [2]. The channel current results are summarized in Fig. 4. The calculation shows a symmetric decreasing trend, with current leaving the stack through the first 5 channels and entering the stack through the last 5 channels and maximum magnitudes at the end channels. The experimental results, however, do not show a clear trend in channel currents. The experimental data show that current was leaving channels 6, 8, and 9 while the calculation shows that current was entering the stack at these channels. It is noted that the measured channel currents are within the precision error; cf., Fig. 4; thus, it is difficult to make a definitive assessment on the results with protective current.

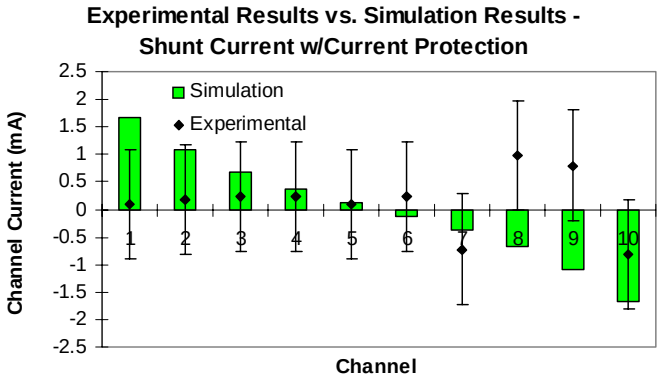

Figure 4. Comparison of simulation and experimental shunt current with protective current; R_e = 2.187 Ω, R_m = 150 Ω, R_c = 1000 Ω, V = 2.54 V, I = 0.42 A, I_p = 0.0175 A.

To estimate the uncertainty in stack parameters, a Monte Carlo simulation was performed with a sample size of 15,000, which was shown to be sufficient for present study [4]. A standard deviation of 5% of the mean value is applied to channel and manifold resistance and cell voltage, with and without protective currents. Detailed results are reported in [4]. This variation in the manifold resistance causes the resulting channel currents to vary approximately ± 0.2 mA. It can also be seen that this variation results in zero probability of the channel current flow reversing directions (it does not result in any probability of current that normally leaves the stack to enter the stack, or vice versa).

The results of varying the manifold resistance with standard deviation of 5% of the mean value are shown in Fig. 5. This variation in the manifold resistance causes the channel currents to vary approximately ± 0.3 to ± 0.4 mA. The variation of 5% standard deviation results in a non-zero finite probability of channel current flow reversing directions in channels 5 and 6. There is also a small non-zero finite probability of channel current flow reversing directions in channels 4 and 7. Similar results are obtained when varying channel resistance, cell resistance, and voltage with a standard deviation of 5% of the mean value with protective current applied. The Monte Carlo simulation shows a maximum difference of 0.391% of the shunt current magnitude when the channel resistance values are varied and a maximum power loss of 0.184% when the manifold resistance is varied.

A Simulink© model is built for a 100-cell stack with a common manifold. The Simulink model calculation of a four-node circuit was validated by the calculation using second software, PSpice©. Agreement to the seventh decimal point or better was obtained [4]. The resistance in each manifold segment is 75 Ω, the resistance in each channel is 500 Ω, and the resistance in each cell is 0.25 Ω. The cell voltage is set at 0.65 V and the current flowing through the stack is 1 A. The calculated shunt currents are shown in Fig. 6 when protective current is not applied. The overall amount of current flowing in the channels is 23.9 mA and the power lost due to shunt current is 1.13%. When a protective current of 12.0 mA is applied, the shunt currents are reduced to 10^{-15}A, shown by the insert in Fig. 6. Calculation of the protective current is given in [4].

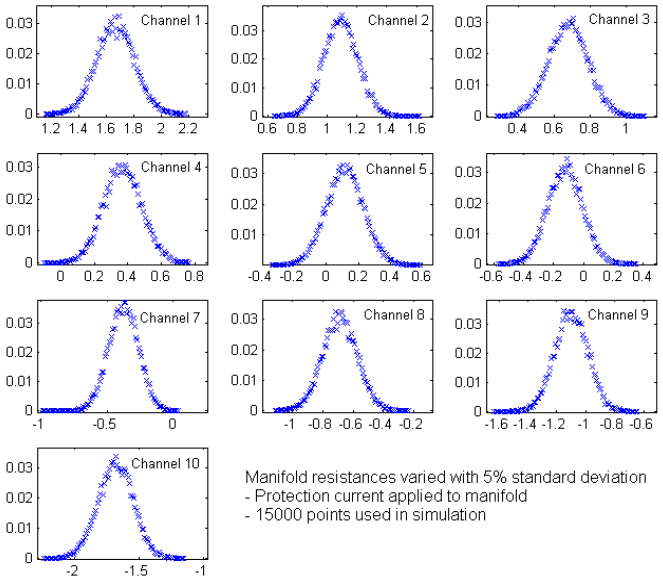

Figure 5. Histogram of Monte Carlo simulation of channel currents with standard deviation of the manifold resistance set by 5% and with protective current applied.

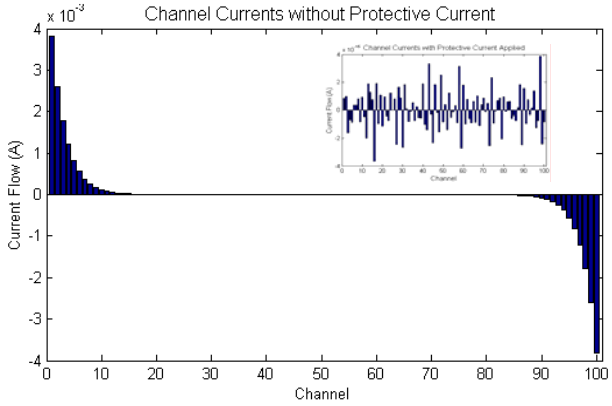

Figure 6. Channel currents of 100-cell fuel cell stack..

Acknowledgment

This work was supported, in part, by ConocoPhillips..

References

1. Katz, M., *J. Electrochemical Soc.*, **1978,** 125 (4): 515-520.
2. Zahn, M.; Grimes, P.G.; Bellows, R.J., U.S. Pat. No. 4,197,169, **1980**.
3. Bellows, R.J, Private Communication, **2004**.
4. Schaeffer, J., *Electrical Circuit Modeling of Fuel Cells*, MS Thesis, Dept. Mech. and Ind. Eng., The University of Iowa, Iowa City, IA, **2004**.

A UNIQUE SUB 5KW SOLID OXIDE FUEL CELL/HEAT ENGINE HYBRID GENERATOR

Andy C. Foley

School Of Mechanical Engineering
Ohio University
Athens , OH.

Nomenclature

E : Ideal Voltage (V)
ΔG : Change in Gibbs free energy (kJ/kmol)
n : Number of electrons released per molecule fuel.
T : Temperature (K)
F : Faraday's constant (96485 C)
i : Current density. (mA/cm^2) i_l : leakage current
i_o : Exchange current
ΔV : Change in voltage.
r : Area specific resistance (Ωcm^2)

Introduction

With ever increasing demands for more efficient power generation and distribution the goal of providing an efficient 5 kW generator suitable for domestic use is the focus of this research. This paper therefore describes an analytical model of a hybrid fuel cell/heat engine generator. The model generator quantifies the benefits of the significant symbiosis to be had from two existing and well established technologies. The first technology utilized is that of the Stirling engine. These have been around since 1826 and as external combustion engines probably represent one of the most robust and simple types of heat engine available. Despite these obvious advantages Stirling engines have not achieved widespread use as they have been unable to compete successfully with internal combustion engines. Primarily because of their low specific power ratings and the significant cost reductions brought about by the existing mass manufacture of the internal combustion engine.

The second technology is that of Solid oxide fuel cells (SOFC). As with most fuel cell technologies these are currently experiencing a fervor of interest and after the low temperature Polymer Electrolyte Membrane (PEM) these cells appear to be the most promising for short term commercialization. Indeed it is already possible to purchase a 200 KW hybrid SOFC gas turbine generator from Siemens Westinghouse. Initial capital costs however still mean that these generators are catering for the fairly small niche market that can afford to bear the high initial expense.

Primary benefits of using the SOFC relate to its relatively inexpensive solid electrolyte compared to other cell electrolytes consisting of molten salts, caustic alkaloids or expensive fragile membrane. This offers a simple and potentially robust fuel cell that also has the benefit of not requiring expensive catalysts at its operating temperature of 900 ^{o}C + . This high operating temperature also brings the added advantage that waste product gases are of a temperature compatable with a downstream heat engine. Finally the nature of theis particular electrolyte is such that oxygen ions (O^{--}) carry charge from the cathode to the fuel anode, unlike most other types of fuel cell that rely on Hydrogen ions (H^+) to carry charge from the anode to the cathode. This subtle difference means that the SOFC is able to use various hydrocarbon fuels apart from pure Hydrogen. Indeed fuels such as Carbon monoxide would actually poison other types of fuel cell.

Finally the reforming required to make this multi fuel capability possible is also conveniently possible within the fuel cell itself. The quantity and temperature of heat required being provided by the SOFC's own 'losses' and the reformer design therefore being the relatively straightforward process of heat exchange and re-cycling of the anode's waste water product.

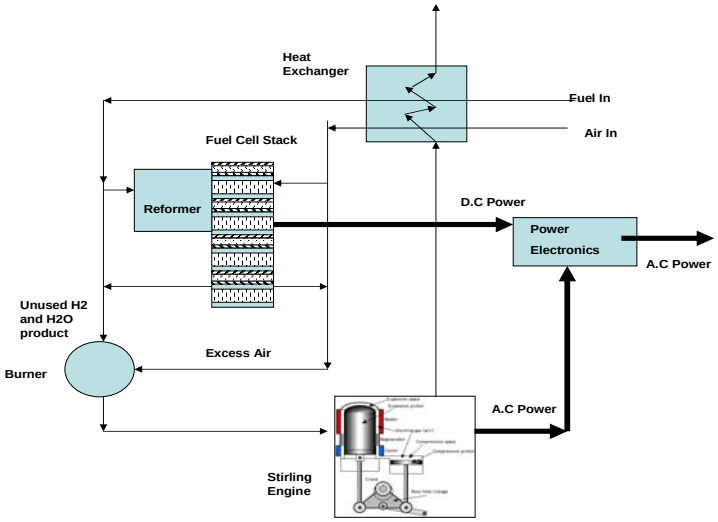

Figure 1. Schematic of SOFC / Stirling Hybrid

Numerical Modeling

Once design of a fuel cell system commences it is not long before one realizes that there are a myriad of parameters that need to be considered. Fortunately once the application has been decided a number of these are easily fixed. For our application we were interested in a domestic power generation system that will produce D.C power that can be relatively easily inverted to 110V A.C. As such a Voltage setting of 48 V D.C was selected to allow efficient Voltage conversion and reduced D.C currents but also low enough so as to not pose a significant human safety risk.

To undertake the detailed and somewhat iterative modeling of this hybrid system, Microsoft Excel with its application Visual Basic was found convenient for the Fuel Cell stack modeling. For the Stirling Engine analysis the use of the 'Simple Analysis' code (ref. Israeli (1984)) for the modeling of the Stirling cycle was found more than comprehensive.

Figure 1 shows a schematic of the system.

Method Of Solution

Modified Nernst Equation. Based on a desired operating temperature and pressure decided by the user (1000^{o}C and 1.1 bar) the Fuel Cell spreadsheet and associated visual basic code calculates the ideal operating voltage of the fuel cell can be calculated from the Nernst equation :-

$$E = \frac{\Delta G}{nF} + \frac{RT}{nF}\log_e\left[\frac{a_{H2}\left(a_{O2}\right)^{\frac{1}{2}}}{a_{H2O}}\right] \quad \text{.....(1)}$$

where a_x is the activity of the reactant/product.

For SOFC's at high temperature this is the ratio of the partial pressure of the species to atmospheric pressure.

Once operating voltage, pressure and temperature have been set the user has a number of parameters to input. The primary parameter is a fuel flow rate (liters/hour). For the model presented in this paper the

fuel used is Hydrogen, however Methane or other suitable Hydrocarbons could easily be used .

After the fuel flow rate has been fixed the user has the option of deciding on a fuel utilization rate. Typically this is about 90% as some flow rate of Hydrogen is required to take the water product away from the anode and also keep concentration losses to a minimum at the cell exit.

With a fuel flow rate input the current passing through an individual cell is calculated based on the number of electrons freed in the oxidation of the fuel. (i.e. 2 electrons for each Diatomic hydrogen molecule.)

Losses. Knowing the current available for a given flow rate it is now possible to calculate the voltage losses within the fuel cell itself. These comprise activation losses, leakage losses, ohmic losses and concentration losses.

Activation losses are calculated using the Tafel equation with constants taken from Davies (1967).

Data for leakage losses are calculated measuring fuel use during open circuit operation or alternately can be derived from published Voltage/ Current performance graphs if the electrolyte thickness is known. (Pham (2001)). For the relatively thick electrolyte used in the current design, leakage is significantly reduced to just under 1% of total fuel flow. Calculation of the resulting voltage loss is achieved by including the leakage with the useful current flow in the Tafel equation: i.e.

$$\Delta V_{act+leak} = \frac{RT}{2\alpha F}\log_e\left(\frac{i+i_l}{i_0}\right)$$

The next loss considered is the Ohmic loss. The area specific resistance is a function of the electrolyte thickness and conductivity which are in turn functions of temperature. Correlations for this parameter where taken from Laraminie & Dicks (2003). And the voltage loss computed simply from :-

$$\Delta V_{ohm} = i \times r$$

Finally concentration losses were computed by applying the Nernst equation at the exit to the fuel cell where Hydrogen and Oxygen concentrations where at their lowest and computing the resulting Nernst voltage. The difference between the voltage so computed at inlet and that at the outlet was halved and to a first, and reasonable approximation, this equated to documented empirical concentration losses.

Once all the losses were accounted for the operational fuel cell voltage was computed and hence the number of cells required in the stack could be found.

The final part of the design involved optimizing the individual fuel cell size such that the current density was high enough to provide a useful specific power and hence a compact stack whilst at the same time producing only moderate ohmic and concentration losses. By examination of figure 2. it can be seen that useful operational range was achieved between 550mA/cm^2 and 800 mA/cm^2. The efficiency is kept above 45% and specific power has not dropped significantly from its peak.

Stack Geometry. Once the actual cell operating voltage and optimum current density have been determined it is relatively straightforward to dimension an appropriate stack. For the design arrived at in this study 80 cells each of 7cm diameter were required. Each cell had a standard yttrium stabilized zirconia electrolyte $(ZrO_2)_{0.92}(Y_2O_3)_{0.08}$, Nickel zirconia anode and strontium doped lanthanum manganite $(La_{0.84}\,Sr_{0.16})\,MnO_3$ cathode. The electrolyte was a relatively robust 200µm thick which makes fabrication easier and prolongs fuel cell life. Between each cell a bipolar plate is inserted to allow gas distribution and enhance stack structural stability. Material for these plates is an inconel alloy although work is being undertaken with the possible use of stainless steel and various thermal barrier coatings.

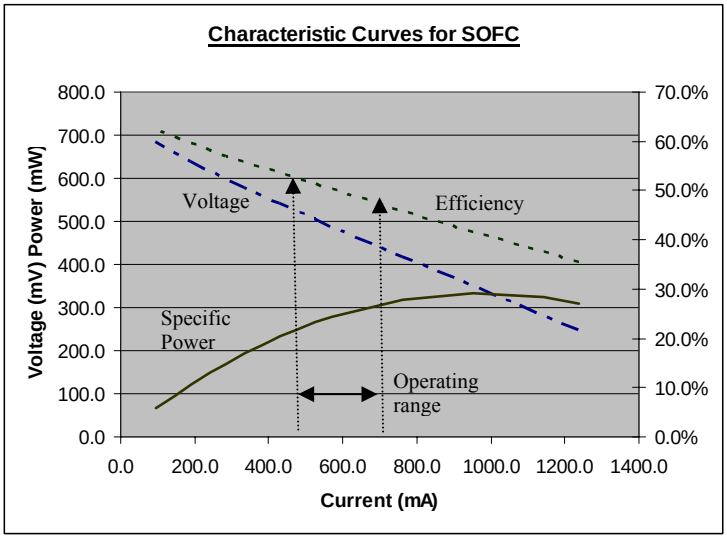

Figure 2. Model Performance Characteristics for SOFC design.

Stirling Engine. For the initial product design initial capital costs were a key factor and hence a simple Alpha type Stirling engine was selected as the downstream heat engine.(Figure 3.) This engine would take the hot excess air (Stoichiometry of cell was set at 5) and the unused Hydrogen/Water products and use these to heat the engines hot space. (Combustion of the excess hydrogen further enhances the heating capability of the waste products). Using appropriate heat transfer coefficients for a scaled Stirling engine available to the author a very conservative 20% efficiency of this engine was predicted. With some refinement to the design it is conceivable that this value will ultimately be improved to around 30%.

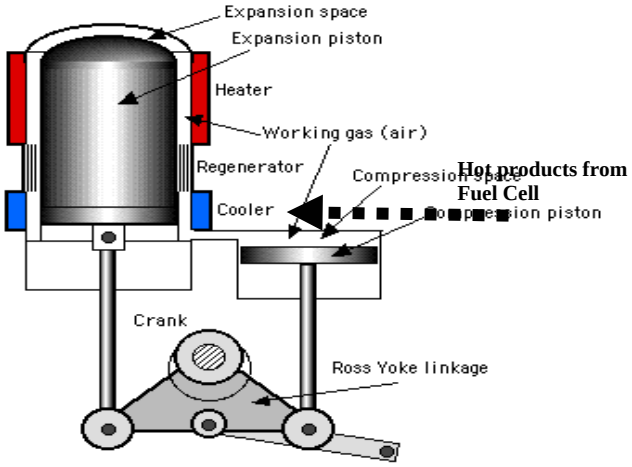

Figure 3. Alpha Type Stirling Engine with Ross Yoke Linkage.

Table 1. Model performance for three operating points around nominal 5KW output.

Fuel Flow liters/hour	*Cell current density (mA)*	*Cell Operating Voltage (mV)*	*Stack Power (W)*	*Stirling Power (W)*	*Total Hybrid Power Output (W)*	*System Efficiency based on LHV of Hydrogen*	
30.0	421.6	550.1	2855.7	768.4	3624.2	54.1%	
40.0	**562.2**	**497.2**	**3807.7**	**1214.7**	**5022.3**	**50.8%**	← Operating point.
50.0	702.7	445.7	4759.6	1803.9	6563.5	47.6%	

Overall Performance Of Hybrid Generator. The cell operating point consumed 40 liters per hour of hydrogen or reformed equivalent. At this point just over 5KW combined power was produced at an efficiency of almost 51%. 25% of this total power was produced by the Stirling Engine. It is also interesting to note that by increasing the fuel flow 25% a predicted increase in power of 30% can be achieved with only a 3.2% reduction in efficiency.

Conclusions

The preliminary analytical design of a simple Stirling/ Solid Oxide fuel cell generator has been undertaken. Using 'off the shelf' materials and well established technologies it has been conservatively predicted that a 5KW generator with an efficiency of 51% can be fabricated. For a system of this size, this is almost double what a comparable internal combustion distributed power generator is capable of. As none of the materials are unique and the envisaged fabrication techniques are standard it is hoped that final bulk manufacturing costs can reach the prized $400 / KW mark although a detailed cost analysis has yet to be completed.

Currently fabrication of an initial 500W prototype is underway and trials are planned in the coming months. Analytical investigations into moderate pressurization of the system using the Stirling engine are also commencing as are investigations into bi-polar plate design and materials.

References

(1) Urieli, I. (1984);. *Stirling Cycle Engine Analysis.* : A.Hilger , *ASIN 0852744358*.

(2) Davies C.W (1967); *Electrochemistry*, Newnes, London. p.188

(3) Pham A,Brandon W et al (2001) pap *Demonstration of High Power Density Planar Solid Oxide Fuel Cell Stacks*, Proceedings of Electrochemical Society Vol 2001-16 p.148-154.

(4) Laraminie, J. Dicks, A (2003) ; Fuel Cell Systems Explained 2nd Ed, p 211; Wiley 2003 ISBN 0-470-84857-X

PERFORMANCE OF PBI-BASED MEAs AND STACKS IN ELEVATED TEMPERATURE FUEL CELLS FOR PORTABLE ELECTRONIC APPLICATIONS

Allison M. Fisher, Stephen R. Samms, Jerry Hallmark, Ramesh Koripella, Stephen Roger, and Billy Mylan

Energy Technologies-Motorola Labs
2100 E. Elliot Rd.
Tempe, AZ 8584

Introduction

Low temperature polymer electrolyte membrane fuel cells (PEMFCs) are of three main types: direct liquid methanol, direct hydrogen, and reformate, although reforming of hydrocarbons or chemical hydrides is also being considered.[1] Direct methanol fuel cells currently require high loadings of precious metal catalyst, and tend to be limited in power density. Low temperature direct hydrogen fuel cells have relatively high power densities and require a minimum of precious metal catalyst, but require very pure H_2 fuel in order to operate properly. Carrying the fuel for these cells as pure H_2 gas is not practical because of the low energy densities of current H_2 storage technologies. Methanol reformate fuel cells are based on the generation of H_2 on-board by reformation of methanol fuel. Methanol is a convenient fuel for portable applications because it has a relatively high energy density (4780 $W_e$hr/l or 6090 $W_e$hr/kg at 100% theoretical electrochemical efficiency) while being able to be steam-reformed at temperatures as low as 200ºC. However, at lower temperatures methanol reformate PEMFCs will lower a system's energy density dramatically because it requires either an additional series of bulky and often inefficient reactors, or an expensive and higher pressure palladium-based membrane separator in order to clean the H_2 product sufficiently to avoid CO poisoning of the catalyst (<<100ppm CO at 80°C).

Interest in elevated temperature (>100°C) PEMFCs has been growing steadily since the demonstration in the mid 1990s that polybenzimidazole doped with strong oxo-acids are capable of good proton conductivity, low gas permeability, and do not require humidification, among other benefits.[2] These benefits, along with the relatively high power densities possible using them, provide a solution to the issues associated with low-temperature PEMFCs. Operation at temperatures near 200°C significantly increases carbon monoxide tolerance of the electrocatalysts, allowing operation with H_2 fuel containing up to ~100-300x the CO limits for low temperature direct hydrogen cells.[3] The benefit of high CO tolerance is that the production of the H_2 feed by reformation of a liquid hydrocarbon, such as methanol, can be done in a single, relatively small reactor and with no Pd membrane separator, significantly reducing the penalty paid for on-board fuel processing. Additional benefits include: enhanced kinetics for both electrode reactions, and simplified water management , as only gas-phase water is present.

While other materials are actively under investigation as candidates for elevated temperature PEMFC applications,[1,4,5] PBI-based MEAs are currently the only commercially available materials for elevated temperature PEMFCs. We have built linear compact elevated-temperature stacks using Celtec® MEAs for integration with our methanol-steam reformation based miniature fuel processor. This paper describes the performance of these stacks under H_2-Air and simulated reformate at temperatures of 160°C.

Experimental

Materials. Celtec® MEAs were obtained from PEMEAs, Inc, our development partner for micro applications. Simulated reformated gases (75%H_2-24%CO_2-1%CO; 74%H_2-24%CO_2-2%CO) were purchased from Scott Specialty Gases. A variety of cell hardware material candidates were investigated, as the fuel cell environment is extremely corrosive. An accelerated corrosion test for stack plate materials was developed as a way to estimate the effect of the PBI MEA and operating conditions on cell hardware. Briefly, in this test two plate materials and controls were heated in phosphoric acid (200C) with a potential of 0.65V between plates for 100hr as illustrated in Figure 1. The weight of the sample was measured before and after exposure in order to determine mass loss.

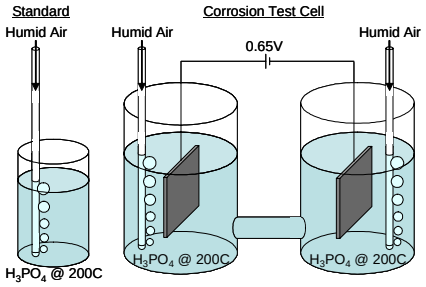

Figure 1. The accelerated corrosion test of material candidates for cell hardware..

Cell/Stack Assembly and Testing. Single cells and stacks were assembled by sandwiching the MEAs between graphite endplates, bipolar plates, gaskets, and backing plates. The assembly was tightened until leak-tight at 5psi. Cells and stacks were tested using test stations purchased from Fuel Cell Technologies, Inc. Breakin was carried out using H_2-Air at a constant current of approximately 200mA/cm^2 at 160°C for 72hr.

Results and Discussion

One critical issue when building elevated temperature stacks is finding chemically and thermally robust cell hardware and sealing materials. The hot phosphoric acid environment of an elevated-temperature PEMFC so harsh that few materials may be capable of holding up over thousands of hours of operation. Like the MEAs used for low-temperature fuel cells, PBI MEAs are susceptible to poisoning by metals, resulting in permanent performance degradation. Our initial work building PBI-based elevated temperature stacks focused on planar 4-cell stacks housed in low-temperature cofired ceramic substrates.[6] Not surprisingly, some performance degradation was observed during long-term testing in these materials. As a result, we developed a corrosion testing procedure as a way to evaluate the potential long-term stability of cell hardware materials. A variety of ceramic and graphite materials were subjected to this test, and a lightweight graphite composite was found to be stable to this corrosion test. Endplates and bipolar plates were fabricated using this material based on a simple flow field design for benchmarking elevated temperature stacks capable of generating up to 30W for powering a net 20W-25W fuel cell system prototype.

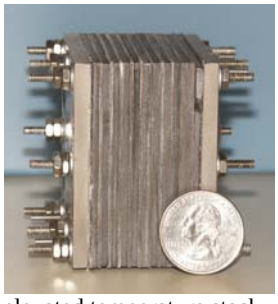

Figure 2. A 10-cell elevated temperature stack..

Figure 2 shows a 10-cell stack made recently using these graphite materials and Celtec® MEAs. Overall dimensions are 2.32in X 2.32in X 1.60in. Fuel cell testing using the graphite hardware was begun recently using single cells. For thermal and efficiency reasons, the stacks incorporated into portable fuel cell systems will be operated at current densities near 200mA/cm^2. Cell polarization and power density curves in this region are shown in Figure 3. Performance is observed to be somewhat lower than obtained in poco graphite cell hardware, probably because of the higher resistance using this form of graphite (~0.25Ωcm^2 *vs.* ~0.10Ωcm^2).

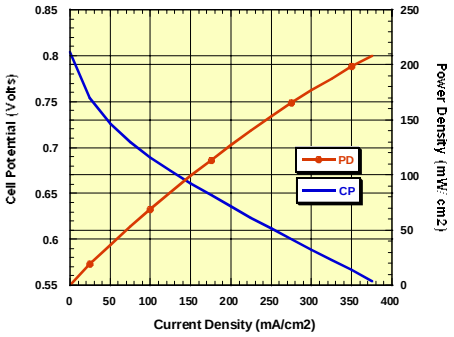

Figure 3. Single cell performance of Celtec® MEA in stack hardware under H_2-Air at 160°C.

The lifetime of PBI-based MEAs like Celtec® under fuel cell conditions have been demonstrated to be more than 6000hr at 160°C with minimal performance degradation.[1] Figure 4 shows the performance of a single cell under H_2-Air over 200hrs at constant current of 200mA/cm^2.

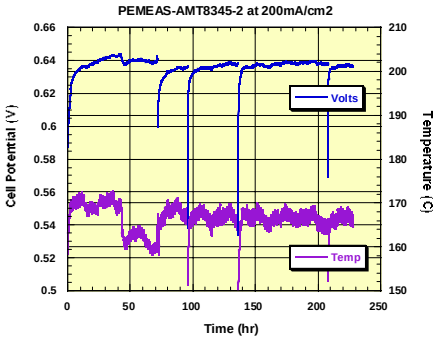

Figure 4. Constant current performance of Celtec® MEA in stack hardware under H_2-Air at ~165°C.

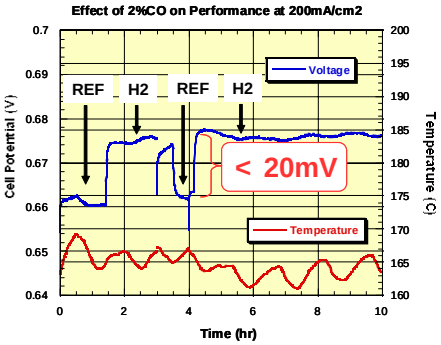

Figure 5. Effect of CO on cell voltage at 200mA/cm^2 and 165°C.

Using simulated reformate instead of H_2, a performance loss of <20mV at ~165°C was observed. Figure 5 shows the effect of 2%CO on the performance of a Celtec® MEA in poco graphite hardware. As cell temperature is increased up to 200°C, the effect of CO diminishes.

Our initial stack results are shown in Figure 6 under H_2-Air. Subcells were within 30mV and stable at 198mA/cm^2 and 160°C. Total stack voltage was 3.29V, corresponding to a power output of 8W. Assuming a voltage loss of 15mV/cell when running under simulated reformate, this stack would produce in excess of 7.5W.

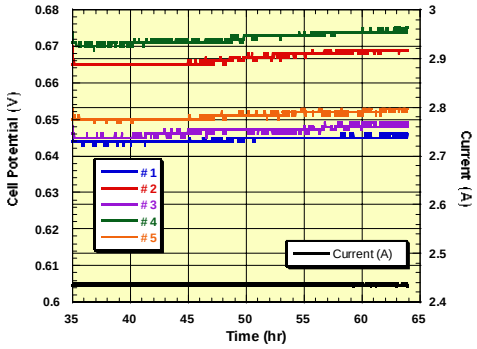

Figure 6. Constant current performance of 5-cell Celtec® stack at 160°C.

Conclusions

Portable energy is one of the key arenas for PEM fuel cells to enter into the power source market. It is expected that miniature fuel cells will one day provide power for a wide range of consumer/portable products such cellular phones, 2-way radios, laptop computers, PDAs, portable cameras and electronic games. We have successfully built elevated-temperature stacks using Celtec® MEAs and lightweight, compact graphite cell hardware. The performance of a 5-cell stack using a simple flow field design was shown to be capable of generating an average of 0.658V/cell, for a total output of 8W under H_2-Air, and estimated to produce 7.8W under simulated reformate-Air.

Acknowledgement. This work was supported through collaborative participation in the Power and Energy Consortium sponsored by the U.S. Army Research Laboratory under the Collaborative Technology Alliance Program, Cooperative Agreement DAAD19-01-2-0010.

References

(1) Li, Q.; He, R.; Jensen, J.O.; Bjerrum, N.J. *Chem. Mater.*, **2003**, *15* (26), 4896.
(2) Ma, Y.-L.; Wainright, J.S.; Litt, M.H.; Savinell, R.F. *J. Electrochem. Soc.*, **2004**, *151*(1), A8.
(3) Li, Q.; He, R.; Gao, J.-A.; Jensen, J.O.; Bjerrum, N.J. *J. Electrochem. Soc.*, **2003**, *150*(12), A1608.
(4) Jannasch, P. *Curr. Opin. Coll. Interface Sci.*, **2003**, *8*, 96.
(5) Savadogo, O. *J.Power Sources*, **2004**, *127*(1-2), 135.
(6) Rogers, S.; Gervasio, D.; Koripella, R.; Samms, S.; Tasic, S. *Proceedings of the Power Sources Conference*, **2002**, *40*, 269.

REACTION ENGINEERING PERSPECTIVE OF PEM FUEL CELLS: THE STIRRED TANK REACTOR AS A BUILDING BLOCK

Ee-Sunn J. Chia, Jay B. Benziger, and Ioannis G. Kevrekidis

Department of Chemical Engineering
Princeton University
Princeton, NJ 08544

Introduction

There has been widespread research on polymer electrolyte membrane (PEM) fuel cells since they have been touted as the next alternative power source. The PEM fuel cell consists of two reactors separated by an ion-conducting barrier (membrane). Protons produced at the anode are transported across the membrane to the cathode where water is produced. The two sequential chemical reactions in a PEM fuel cell are thus coupled to the transport of the intermediate products between the reactors. Before PEM fuel cells become commercially viable for mobile applications, predictive models of fuel cell performance that correctly incorporate the transient interplay of reaction and transport processes are critical.

PEM fuel cells are often constructed and modeled as two- and three- dimensional integral reactors.[1-4] These integral reactors may be modeled as differential (stirred tank) reactors in series. A differential fuel cell reactor has uniform compositions at the anode and cathode; the only spatial gradients are transverse through the membrane. This circumvents the complexities of the existing integral reactors since there are no spatial variations involved in the stirred tank reactor. From a differential PEM fuel cell, we are able to extract valuable information pertaining to the kinetics and the convective transport. We have shown that a stirred tank PEM fuel cell reactor exhibits ignition/extinction phenomena and have reproducibly demonstrated steady state multiplicity.[5-7]

We present here a summary of the stirred tank PEM fuel cell reactor findings, the remarkable analogy to the autocatalycity in an exothermic stirred tank reactor, and an extension of the stirred tank PEM fuel cell to approximate the conventional integral reactor.

PEM Fuel Cell Reactor

Differential Reactor. The differential PEM fuel cell shown in **Figure 1** consists of two stirred tank reactors separated by the membrane electrode assembly (MEA) with a membrane area of 1 cm^2. The current collecting graphite plates contained gas plenums with volumes of 0.2 cm^3. Pillars were machined onto the graphite plates to ensure a uniform sealing pressure on the MEA. The fuel cell was designed to ensure uniform gas compositions above the membrane.

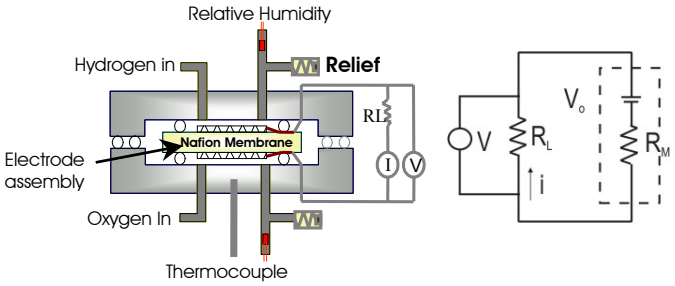

Figure 1. Schematic depiction of the stirred tank PEM fuel cell reactor and its equivalent circuit. The membrane electrode assembly separates the anode and cathode chambers.

The fuel cell is connected in series to an external load resistance R_L. The voltage and current are measured across R_L. The fuel cell was constructed such that the residence times of the reactant gases (*Volume*/*Flow rate*) are larger than the characteristic diffusion time ($Volume^{2/3}/D$). Flow rates of the reactant gases (1-10 mL/min) were controlled with mass flow controllers. As the reaction progresses, the amount of water in the membrane changes and this alters the membrane resistance, R_M (a dryer membrane indicates a higher value of R_M). We study the fuel cell behavior under the influence of four operating parameters: temperature (T), external load resistance (R_L), flow rates of reactants into the anode and cathode, and relative humidity of the inlet reactant streams.

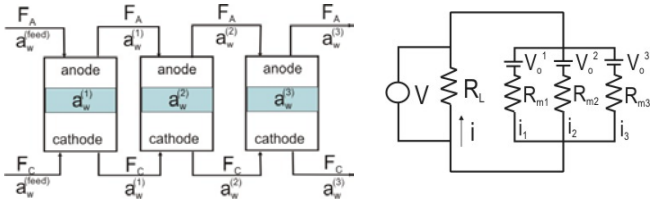

Figure 2. Stirred tank reactors in series approximate an integral reactor. The reactors are parallel electrically.

Integral Reactor. The other extreme of a well-mixed reactor is the plug flow (integral) reactor where the reactants flow downstream without dispersion. The stirred tank PEM fuel cell can be thought of as a differential element in an integral reactor. Therefore, we may approximate the standard serpentine flow PEM fuel cell integral reactor by placing many stirred tank PEM fuel cells in series as shown in **Figure 2**. The membrane hydration in each tank will vary downstream. Thus each tank is associated with a different R_M. Although several reactors are placed in series, they are electrically in parallel as depicted in **Figure 2**.

Results and Discussion

Multiple steady states. Water plays an important role in the fuel cell because it eases proton transport from the anode to the cathode. In fact, Yang et al. has shown that the membrane conductivity is exponentially dependent on the water activity in the membrane but only weakly dependent on temperature.[8] It is the water balance in the fuel cell that leads to the multiple steady states shown in **Figure 3**. The steady state current achieved in a stirred tank reactor fuel cell depends on the initial water content in the membrane.[5] Moreover, the water balance in the stirred tank reactor fuel cell is analogous to the energy balance in the classical chemical engineering exothermic stirred tank reactor.

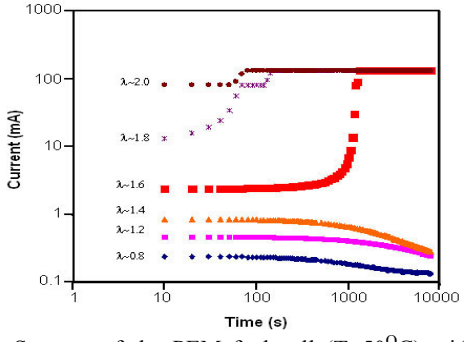

Figure 3. Start-up of the PEM fuel cell (T=50^{O}C) with different initial membrane water contents ($\lambda = H_2O/SO_3$) and dry feeds.

The product water in the PEM fuel cell hydrates the membrane, enhances proton transport, and thereby autocatalytically accelerates the reaction rate. In an exothermic reaction, the produced heat accelerates the reaction via an Arrhenius temperature dependence in the reaction rate constant. Based on this analogy, we have shown that the classical analysis of heat autocatalycity can be implemented to our stirred tank PEM fuel cell as well.[7]

Dynamics. We have also observed the fuel cell response to changes in the operating parameters. As depicted in **Figure 4** a decrease in R_L is followed by a sharp jump in current before a relatively slower equilibration to the new steady state current. We have observed similar types of responses to changes in other parameters. We believe that the membrane acts as a *reservoir* for water and any change in operating conditions will alter the water balance inside the membrane. The membrane requires about 10^2 s to equilibrate to the new operating conditions.

In addition to these responses, we have recorded the occurrence of autonomous oscillations in the stirred tank reactor PEM fuel cell. Despite maintaining fixed operating conditions, the fuel cell oscillates regularly between two currents as shown in **Figure 5**. We believe that the oscillations are attributed to a coupling between the transport processes and the mechanical relaxation of the membrane.[9]

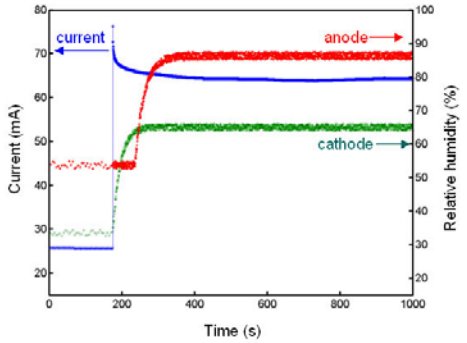

Figure 4. Response to a decrease in R_L from 20Ω to 7Ω. The fuel cell current increases sharply but eventually equilibrates at a lower current.

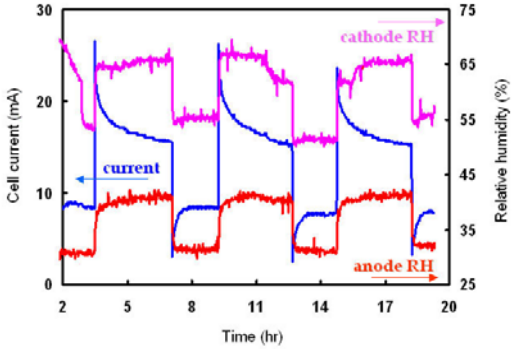

Figure 5. Autonomous oscillations observed under fixed conditions of T=80^{O}C, R_L=20Ω, F_{anode}=5 mL/min, $F_{cathode}$=10 mL/min.

Tanks in series. We have placed several stirred tanks in series to approximate the behavior of an integral PEM fuel cell. The product water or unused reactant exiting an earlier tank will be fed directly into the subsequent tank. Tracking how the current evolves in each tank over time is equivalent to tracking the current down an integral reactor over time. This method allows us to observe regions where the fuel cell will ignite. Hydrogen may flow co-current or counter-current to the oxygen flow. **Figure 6** shows that in counter-current flow, a large current is attainable in the middle tanks but only the last tank in a co-current flow scheme will generate a large current at long times. When the flows are co-current, the initial tanks remain dryer while more water is brought into the last tank, creating suitable ignition conditions in the final tank. However, in a counter-current scheme, water from the first and last tanks are flowing in opposite directions, making it easier for ignition in the middle. The flow rate of hydrogen is twice that of oxygen in **Figure 6**.

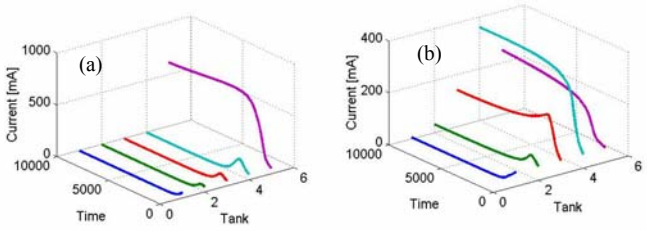

Figure 6. Current profiles for 5 tanks in series with flow of reactants in (a) co-current and (b) counter-current.

Conclusions

Our results have indicated that the interplay of proton transport with water activity in the PEM membrane underpins the observed dynamical phenomena. Water ionizes and shields stationary anions in the membrane, enhancing proton transport by orders of magnitude. Existing fuel cell literature contains extensive reports that PEM fuel cells only operate when sufficient water is present in the membrane. We have demonstrated that it is possible to operate the PEM fuel cell with dry feeds of hydrogen and oxygen. We have elucidated the role of a *critical initial* membrane water content for ignition.

We have established that the product water catalyzes the reaction in an autocatalytic manner analogous to the autocatalytic rate acceleration in the exothermic stirred tank reactor. The water balance in the membrane leads to multiple steady states in the fuel cell. In addition, the membrane functions like a reservoir for water and needs time to equilibrate to changes in the operating conditions. Although the model reactors are not optimal for reactant conversion, they are specifically designed to measure system parameters, including effective kinetic and transport properties.

Acknowledgement. This work is supported under NSF grant CT50354279.

References

(1) Springer, T. E.; Zawodzinski, T. A.; Gottesfeld, G., *J. Electrochem. Soc.* **1991**, *138*, 2334.
(2) Bernardi, D. M.; Verbrugge M. W., *J. Electrochem. Soc.* **1992**, *139*, 2477.
(3) Fuller, T. F.; Newman, J., *J. Electrochem. Soc.* **1993**, *140*, 1218.
(4) Janssen, G. J. M., *J. Electrochem. Soc.* **2001**, *148*, A1313.
(5) Moxley, J. M.; Tulyani, S.; Benziger, J. B., *Chem. Eng. Sci.* **2003**, *58*, 4705.
(6) Benziger, J. B.; Chia, E.; Karnas, E.; Moxley, J.; Teuscher, C.; Kevrekidis, I. G., *AIChE J* **(in press)**.
(7) Chia, E.; Benziger, J. B.; Kevrekidis, I.G., *AIChE J* **(in press)**.
(8) Yang, C. R.; Srinivasan, S.; Bocarsly, A. B.; Tulyani, S.; Benziger, J. B., *J. Membrane Science* **(in press)**.
(9) Benziger, J. B.; Chia, E.; Moxley, J.; Kevrekidis, I. G. *Chem. Eng. Sci* **(submitted)**.

DYNAMIC SIMULATION OF FUEL CELL SYSTEMS

Rory A. Roberts, Jack Brouwer, and Scott Samuelsen

National Fuel Cell Research Center
University of California, Irvine

Abstract

The development of dynamic simulation tools for fuel cell systems and fuel cell/gas turbine (FC/GT) systems is required to understand the response of fuel cell systems to both scheduled and unscheduled perturbations. These tools supply the foundation on which control strategies can be developed and tested before they are actually implemented in a physical system. For high temperature fuel cell systems that generally incorporate reformation of hydrocarbon fuels externally and/or internally, knowing how the system can potentially respond to a load perturbation or a fuel flow composition perturbation is extremely important to system performance and reliability.

In addition, when developing control strategies for high temperature fuel cell systems, it is important to identify of the hazardous conditions that may lead to degradation in performance or the destruction of the fuel cell and other components of the system. Being able to identify these conditions with a detailed and robust dynamic model can lead to safer and more responsive operation for fuel cell systems. This work provides a dynamic simulation of a load perturbation that could produce undesirable conditions if proper control strategies are not designed for the fuel cell system. In addition, the dynamic simulations provide insights into both component and system dynamic performance parameters that illuminate some less than obvious dynamic responses within representative integrated high temperature FC/GT hybrid systems.

Approach

Dynamic models for molten carbonate fuel cells (MCFC), heat exchangers, gas turbines (GT) and catalytic oxidizers have been developed in a Simulink™ platform. The dynamic models are based on first principles. Descriptions of the models are found in previous papers [1, 2]. All the models incorporate the conservation equations for energy, mass, and momentum. The MCFC model incorporates the electrochemistry and internal reformation chemistry reactions as well. The catalytic oxidizer model assumes complete combustion. The gas turbine uses general performance maps. These components are integrated to simulate a complete molten carbonate fuel cell/gas turbine (MCFC/GT) system.

In each of the significant component models (e.g., fuel cell, heat exchanger) some degree of geometric resolution is captured, albeit in a simplified (usually one-dimensional) manner. The dynamic equations that govern the concurrent processes of heat, mass, and momentum transfer, chemical reaction and electrochemical reaction are solved, for example along one dimension of the component representing that which varies most significantly and including geometrical features such as actual fuel cell size and shape. This approach to dynamic simulation is significantly more computationally intensive than the traditional bulk component model approach, but it provides significant added value. First, insights into the performance parameters of each component are provided (e.g., temperature profiles) so that one can determine whether or not significant component stress or other conditions of concern may be reached during responses to perturbations. Only if this insight is provided can one determine what needs to be controlled and how to control it. Secondly, accurate predictions of component performance cannot be achieved without this dimensional and geometric resolution. This is certainly the case for reactors such as catalytic oxidizers or fuel cells which rates of chemical reaction are exponentially dependent upon local temperature. This is also true for systems as simple as heat exchangers whose dynamic performance cannot be captured through a bulk effectiveness heat transfer model. As a result, these more complex and computationally intensive, yet simply resolved component models both contribute to increased insight and more accurate predictions of fuel cell system performance.

Results

A complete dynamic MCFC/GT system model was constructed to simulate a 1MW MCFC/GT system similar to the sub-MW Direct Fuel Cell/Gas Turbine (DFC/GT) hybrid system developed by FuelCell Energy. A diagram of the system configuration is presented in Figure 1. The model was developed by integrating individual robust simulation modules of the type described above, each simulating the dynamic performance of a component shown in Figure 1. The integration is accomplished using the graphical user interface and toolbox utilities of Simulink™.

To demonstrate the dynamics of this type of hybrid fuel cell system, a load perturbation was simulated on an open loop system of the type presented in Figure 1. For the load perturbation investigated, the MCFC underwent a 3% load drop. The power drop was achieved by changing the external load resistance applied to the MCFC. Figure 2 presents the results for the MCFC, GT and total plant power as the integrated system responds to the load perturbation. The MCFC power initially drops, undershooting by approximately 12% (90 kW)of the final steady state power. This effect is due to the temporary deficit of fuel in the anode gas (at the end of the anode compartment of the fuel cell). The MCFC power quickly recovers to a lower steady state value of power output. The total plant power reflects the dynamics of the MCFC power response. The GT power begins to rise after 5 seconds due to a rise in the turbine inlet temperature (TIT). It takes approximately two minutes for the GT to reach steady state. There is a slight recovery in total power because of the rise in GT power.

When the MCFC drops to a lower power level, there is more unspent fuel in the anode stream. This increase in unspent fuel causes the catalytic oxidizer temperature to rise. The rise in catalytic oxidizer temperature is illustrated in Figure 3. The rise in catalytic oxidizer temperature increases the GT TIT, which results in higher GT power. The increase in catalytic oxidizer temperature also increases the cathode inlet temperature, which is presented in Figure 3 as well.

Decreasing the MCFC power by 3% caused an 11% increase in GT power and an overall 2% decrease in total plant power. The cathode inlet temperature experienced a 14ºC temperature rise, which could potentially overheat the MCFC.

Conclusions

Open loop results were presented to demonstrate the dynamics of the MCFC/GT system. From the dynamic results it can be seen that great care must be taken to control the MCFC/GT hybrid system. Safe operating temperatures need to be maintained throughout the system to improve the performance and life cycle of the system. To design FC/GT systems with load following capabilities one must include intelligent control strategies that can meet changing load demands while maintaining high performance and safe operation. The integration of various component technologies (e.g., fuel cell, GT, heat exchangers) results in a complex system with dynamic response characteristics that are not easy to elucidate without robust and geometrically resolved models.

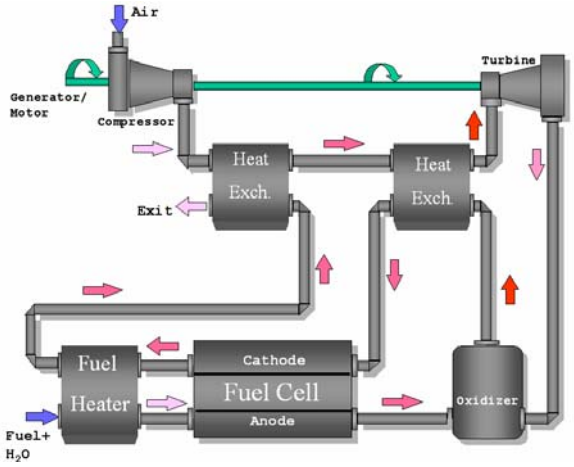

Figure 1. DFC/GT hybrid system diagram

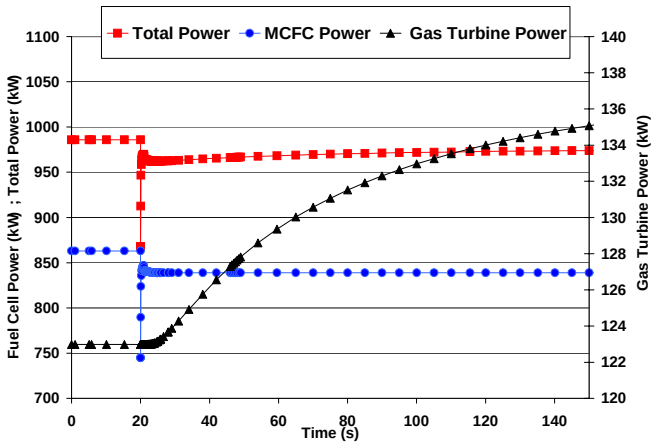

Figure 2. Total plant power, MCFC, and gas turbine power due to a load drop on the MCFC

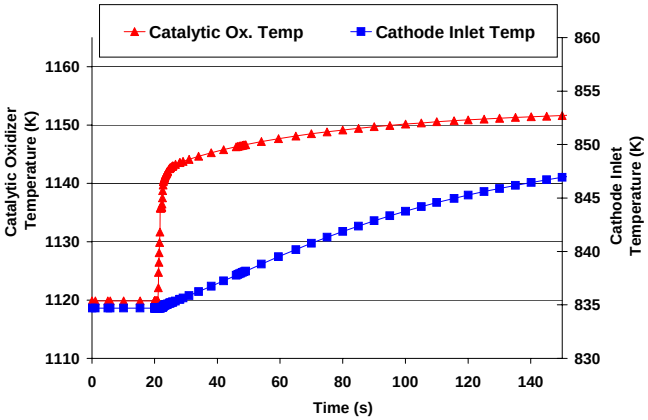

Figure 3. Catalytic oxidizer temperature and cathode inlet temperature

Acknowledgements. This project was made possible by support received from the California Energy Commission, and the U.S. Department of Defense Fuel Cell Program.

Legal Notice

This paper was prepared in part as a result of work sponsored by the California Energy Commission (Commission). It does not necessarily represent the views of the Commission, its employees, or the State of California. The Commission, The State of California, its employees, Contractors and Subcontractors make no warranty, expressed or implied, and assume no legal liability for the information in this paper; nor does any party represent that the use of this information will not infringe upon privately owned rights. This paper has not been approved or disapproved by the Commission nor has the Commission passed upon the accuracy or adequacy of the information in this paper.

References

1. Roberts, R.A., Brouwer, Jack, Gemmen, Randall, Liese, Eric, *Dynamic Simulation of Carbonate Fuel Cell-Gas Turbine Hybrid Systems.* ASME Turbo Expo, Vienna, Austria, 2004. **GT2004-53653**.
2. Roberts, R.A., Brouwer, Jack, Gemmen, Randall, Liese, Eric, *Inter-Laboratory Dynamic Modeling of a Carbonate Fuel Cell for Hybrid Application.* 2003 ASME Turbo Expo, Atlanta, Georgia, 2003. **GT2003-38774**.

BIOMASS CONVERSION TO FUELS AND CHEMICALS

Helena L. Chum and Ralph P. Overend

National Bioenergy Center
National Renewable Energy Laboratory
1617 Cole Boulevard, Golden, Colorado, USA

Introduction

Biomass has a significant potential to provide liquid, solid and gaseous fuels in conjunction with the co-production of food, feed, fiber and new bioproducts. The selection of a conversion technology will be a function of both the supply of locally available feedstock and the markets for products and will determine the degree to which various biological and chemical routes are deployed. This paper reviews the major technical principles and challenges in the evaluation of feedstocks and conversion systems for the energy markets of the future. The challenges of energy supply, reliability, environmental performance and lifecycle impacts will also be discussed for thermochemical biomass conversion via gasification.

Biomass Supply

The growing acceptance of biomass as the only renewable source of carbon for the future requires that a realistic appraisal of its potential be undertaken. While solar energy captured by wind, PV or high temperature concentrating solar systems, have very high energy supply potentials—far exceeding today's total primary energy supply of approximately 417 EJ (IEA,TPES data for 2000)—it will be delivered in the form of electricity and potentially hydrogen. However, before a purely hydrogen and electrical economy can arrive, during the 21st century the world has to undergo a carbon usage transition from directly emitting fossil carbon dioxide into the atmosphere to one in which fossil carbon is captured and sequestered, and biomass becomes the sole form of the earth's carbon resource that can be emitted directly to the atmosphere due to its short term photosynthetic cycle in the biosphere.

Unlike fossil fuels for which exploration, discovery and assessment of resources and reserves is a well known science, renewable energy accounting introduces a flow concept to describe the size and availability of the resource. Biomass is rather unusual; it exists somewhere between the intermittent, flux–only resources such as solar and wind, and the traditional fossil fuel stock perspective. This is because of its annual and perennial storage capability, allowing dispersed and captured solar energy to be concentrated and converted into useful, energy and products on a continuous basis at centralized facilities according to normal demand patterns. Thus, the photosynthesis process of solar collection, crop harvest, and transport of biomass fuels will define the availability of biomass for energy and materials purposes.

As with fossil resources, the energy conversion technologies play a huge role in enabling the solar resources by dictating the efficiency, and the utility of renewables with respect to society and the environment—in sum, their sustainability. However, this presentation will concentrate on the biomass system only up to the conversion plant gate.

Biomass resources in the USA

The renewable energy cycle for biomass starts with photosynthesis, which captures the fraction of light between 400 nm and 700 nm in the solar spectrum to provide the energy to fix carbon dioxide and split water molecules, producing raw photosynthate according to the equation:

$$CO_2 + H_2O + \text{sunlight} \rightarrow CH_2O + O_2$$

The photosynthate formula, CH_2O, is essentially the same as sugar, starch, or cellulose, the latter being the most common natural polymer on earth. Energy is obtained from biomass by means of combustion with oxygen as in a fire, or through metabolic processes, e.g., respiration to provide chemical energy for muscles and other processes:

$$CH_2O\ (\text{Biomass}) + O_2 \rightarrow CO_2 + H_2O$$

Either way, the net result is a closed cycle in which carbon dioxide and water vapor are returned to the atmosphere. This solar-energy powered closed-loop supports all life on earth, providing food for humanity, feed for animals, fibers for clothing, and materials for buildings and consumer products, in addition to fuel.

A theoretical estimate of the efficiency of photosynthesis is about 5.5%. The energy received from the sun at any given location varies with latitude and season; and the annual photosynthetic capture is a function of the water and nutrient availability and the seasonal climate variations. As a result actual crops achieve much less than this. The variation is very large ranging from the annual accumulation of less than 1 t ha^{-1} y^{-1} of dry biomass in a mature boreal forest, to approximately 50 t ha^{-1} y^{-1} of total biomass for a record corn yield (in Iowa, in 1999) of 408.2 bushels of corn per acre. This is calculated by accounting for the stalk and other above ground biomass components by means of the harvest index, which has a value of 0.5 applied to the 25.6 t ha^{-1} y^{-1} of corn kernels.

Sources of bioenergy

The primary biomass sources are natural forests, planted trees and shrubs, and agricultural crops. However, much of today's bioenergy is derived from secondary, tertiary, and post-consumer residues derived from these primary resources. Secondary residues are mainly harvesting residues and include: forest slash; crop residues such as straw and stover from cereal production; as well as minor sources such as orchard, rights of way, and vineyard prunings. Tertiary sources are usually process residues and include: black liquor produced in kraft pulping; sawdust and bark from solid wood processing; and sugar cane bagasse. Food processing tertiary residues include: orange and potato peelings; and large quantities of water containing various amounts of proteins, starches, and sugars. Animal operations that produce dairy products, eggs, and meat generate a large stream of residues (at ever increasing scales) from large feedlot operations. These are becoming regulated as concentrated animal feed operations (CAFO)s. These tertiary residues are usually high moisture and most often are treated by a process of anaerobic digestion to produce biogas, a mixture of methane and carbon dioxide, as fuel.

Much of the post consumer residues are in fact biomass: paper, packaging, crates, pallets, demolition lumber, food scraps, and sewage treatment residues. These are more and more often entering the bioenergy, biofuels, and bioproducts stream as society practices resource conservation and use. The Environmental Protection Agency's (EPA) preferred method is source reduction, which includes reuse, followed by recycling and composting, and, lastly, disposal in combustion facilities and landfills.

These primary, secondary, tertiary, and post consumer pathways are significant when compared with the US TPES of about 100 EJ. The total forest harvest is on the order of 203 M tonnes of air–dried

round wood equivalents per year, which corresponds to > 3.5 EJ of primary energy equivalent. In recent years the annual corn harvest of almost 10 billion bushels (254 Mt) corresponds to over 4 EJ of primary energy equivalent produced on 3,000 km^2 (about 75 million acres, or about half of the arable crop area of the USA). Though corn stover is partly required to remain on the land to maintain fertility and reduce soil erosion, the quantity available is similar to the amount of crop and represents the largest agricultural residue potential.

Effect of Transportation on Cost

The key determinant of the feasibility of biomass is the cost of the biomass that contains the stored "free" solar energy. As the cost varies with the transportation distance from the process plant to the field or forest, as well as the opportunity cost of the feedstock, the cost is usually obtained from a supply curve. There are many factors that go into deriving the supply curve for the resource. Due to the bulk of biomass, its transportation over long distances by road is not economical, though with low cost transportation by rail, the distance can be increased. While an 80 km collection is often cited, this is only an order of magnitude. In each case, the actual collection radius will be a function of the biomass density per unit area, the nature of the terrain, road network density, and the condition and type of transportation available.

Density Relationship

One of the highest biomass densities is, in fact, the post consumer residue production of the urban areas. Cities draw upon the resources of vast areas and concentrate them in a small area resulting in a "footprint" that is much greater than the physical urban area. A useful number is a *per capita* urban residue energy generation rate of about 22 MJ *caput*$^{-1}$ d^{-1} (1.86 kg d^{-1} of residue with 11.6 MJ kg^{-1} heat of combustion, 1990). Major metropolitan areas have population densities of greater than 2000 person km^{-2}. For this population density, the thermal energy equivalent in their residues is about 4.4 GWh km^{-2}. If a short rotation woody crop was grown at yields of 15 tonne ha^{-1} y^{-1}, it would produce about 7.8 GWh km^{-2}.

Conclusion

The predicted 2020 potential of biomass costing less than 4 $ GJ^{-1} is about 8 EJ. The sources and constraints on the biomass resources contributing to this total will be discussed.

BIO-OIL FROM RICE STRAW BY PYROLYSIS USING FLUIDIZED BED AND CHAR REMOVAL SYSTEM

Young-Kwon Park[1], Jong-Ki Jeon[2], Seungdo Kim[3], Joo-Sik Kim[1]*

(1) Faculty of Environ. Eng. Univ. of Seoul, Seoul, Korea
(2) Dept. of Chem. Eng., Dongyang Univ., Youngjou, Korea
(3) Dept. of Environ. System Eng., Hallym Univ. Chuncheon, Korea
* Corresponding author: joosik@uos.ac.kr

Introduction

Rice straw is one of abundant biomass whose production sums up to about 7 milion ton annually in Korea. It is usually utilized as a compost or forage in Korea. Nowadays intensive attention has been paid to rice straw from the viewpoint of a potential renewable energy source, due to high price of petroleum. Thermochemical conversion of biomass is one of the most common routes for conversion into energy. Among thermochemical conversion processes, pyrolysis of biomass is a promising tool to provide bio-oil which can be used as an alternative fuel oil or chemical feedstocks. In the last two decades, extensive researches have been carried out to understand the complexity of pyrolysis, to obtain optimal conditions for producing bio-oil, and to analyze the composition of bio-oil quantitatively and qualitatively. A great portion of past researches have focused on the pyrolysis of wood or wood wastes. Pyrolysis of rice straw, however, has been conducted not so intensively and once it is performed, only in small laboratory scale plants. This paper reports the results of pyrolysis of rice straw in a bench scale plant equipped mainly with a fluidized bed, a char separating system and a quench system. We investigated the influence of reaction temperature on the production of bio-oil, the efficiency of a char-separating system and some physical and chemical analyses of bio-oil, product gas and char.

Experimental

Rice straw. Rice straw obtained from a province in Korea was cut into rectangular form with a size of about 5 mm. Including elemental analysis, some analyses were performed. Table 1 shows characteristics of rice straw fed. The amount of cellulose, hemicellulose and lignin is based on volatile portion of rice straw.

Table 1. Analysis of rice straw.

Composition	wt%
cellulose	54.67
hemicellulose	32.53
lignin	12.83
Water, ash, volatile	wt%
water	6.48
volatile	82.30
ash	11.22
Elemental analysis	wt%
C	39.2
H	4.84
N	1.60
S	0.67
O	53.69
Alkali metal	Concentration (ppm)
Na	250
Mg	930
Ca	2100
K	12000

Bench scale pyrolysis plant. Experiments were carried out using a bench scale plant with a capacity of up to 3 kg/h. The fluidized bed reactor made of sus-304 has a free diameter of 154mm and a length of 616 mm. It is heated indirectly by electric power. Rice straw enters the reactor through two screw conveyors and then is pyrolyzed. A cyclone and a hot filter serve as char separator. These separators are heated up to 400 ^{o}C to prevent from the condensation of product gas. A series of quenching system is applied to cool product gas efficiently and quickly. Product gas is circulated into the fluidized bed using a compressor.

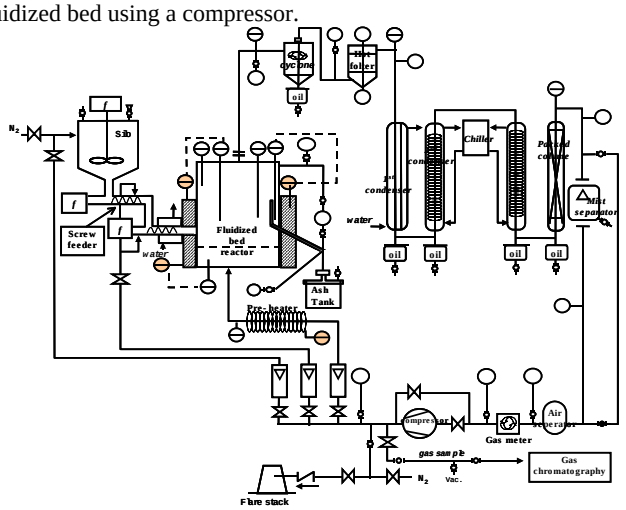

Figure 1. Fluidized bed reactor system.

Reaction conditions. Reaction conditions are shown in Table 2. In every experiment, particle size of feed was about 5 mm and product gas was served as a fluidizing medium. The residence time of product gas in the reactor lay ca. 2 or 3 seconds in each experiment and this makes it possible to compare the influence of reaction temperature on the product spectrum relatively clearly. Particle size of the sand used in the fluidized bed was ca. 0.4 mm.

Table 2. Parameters of experiments.

	Run1	Run2	Run3	Run4	Run5
Temperature (^{o}C)	412	443	516	545	598
Amount of input (g)	1700	1500	1560	1500	1500
Duration (min)	118	87	67	80	80
Feed rate (g/h)	864	1034	1397	1125	1125

Analysis. Qualitative and quantitative analysis of pyrolysis gas and oil has been performed by GC and GC-MS system. Using ICP the content of alkali metals in products was also analyzed. Solid content in bio-oil was measured using acetone as a solvent. In addition to chemical analysis, physical characteristics of bio-oil was also examined, such as density, viscosity etc.

Results and Discussion

Mass balance The behavior of biomass pyrolysis is dependent on many parameters, such as reaction temperature, residence time of gas in reactor, particle size of feed material and feed rate. This paper focuses on the influence of reaction temperature. Mass balance of each experiment is shown in Figure 2. As reaction temperature rises, the amount of gas increases. It is also shown that there is an optimum temperature to produce more bio-oil. In the reaction temperature range between 412 and 516 ^{o}C, the yield of oil was relative constant to give a maximum yield of 50 wt% and then decreases distinctly with increasing temperature.

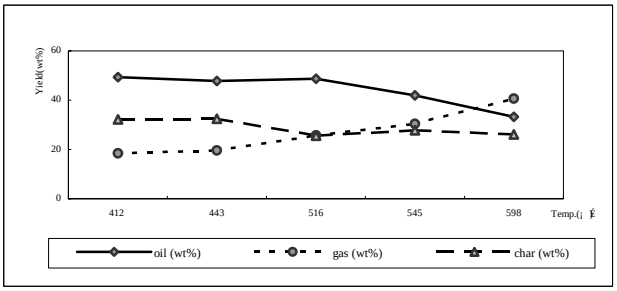

Figure 2. Product distribution with temperature.

This tendency is typical for the pyrolysis of biomass, which results from the secondary reaction of volatiles[1]. The yield of bio-oil is lower than in the case of pyrolysis of wood, which is largely due to lower content of organic portion in rice straw than in wood and a larger content of ash in rice straw, some metallic components in which lower the yield of bio-oil by catalytic decomposition of oil portion. The use of hot filter can reduce the yield of bio-oil in which thermal cracking of pyrolysis vapor takes place. In the experiments, we used rice straw particle whose diameter lies about 5 mm for easy transporting it into the reactor. This relative larger size in comparison with typical pyrolysis of biomass can have an influence on the reduction of bio-oil yield [2].

Product gas. Figure 3 shows the development of main components in product gas with temperature. Methane, CO and CO_2 consist mainly of product gas. Ethene and ethane was other important components in the product gas. Hydrogen content was under 1 wt% in every experiment. It is shown in the Figure 3 that higher temperature leads to high yield of methane and CO, which results mainly from the secondary cracking of volatiles[3]. This tendency including higher content of other hydrocarbon gases at elevated reaction temperature gives high heating value to product gas.

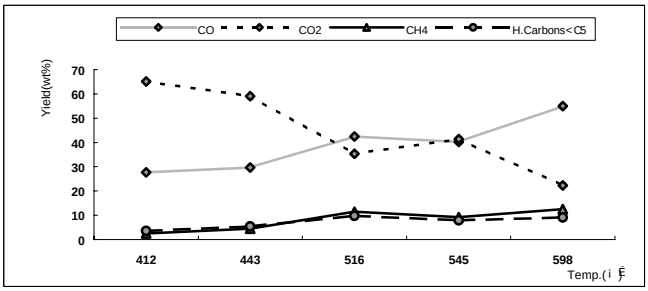

Figure 3. Gas composition with temperature

Bio-oil. Obtained bio-oil shows a phase separation. Large portion of tar was deposited in bio-oil containers. Therefore, it was very difficult to sample it accurately. We conducted sampling according to the procedure at VTT and various chemical and physical characterizations of bio-oil were carried out [4]. Some distinct features of bio-oil are listed in Table 3. Water content in bio-oil was very variable according to samples but lay in the range of 50-60wt%. Product oil showed nearly metal-free character, which simplifies the treatment of bio-oil during up-grading and reduces catalytic reactions during storge. Reduction of density and increase of pH value in comparison with typical bio-oil from wood is caused mainly by high content of water in bio-oil. Solid content in bio-oil lay around 0.03 wt%. The value is somewhat high in comparison with mineral oil whose value is about 0.01 wt%. Applying of a hot filter, however, reduced solid content distinctly, compared with other processes without it. Solid seems to consist of hydrocarbons implied by the ash content in bio-oil (0.007 wt%).

Table 3. Characteristics of bio-oil.

Analysis		Run5 (598 ^{o}C)
Alkali Metals (g/L)	Na	not detected
	Ca	4
	Mg	under 1
	K	3
Solid content (wt%)		0.03
pH		4.07
Ash (wt%)		0.007
Density (15 ^{o}C, g/cm^{3})		1.0089
Flash point (^{o}C)		69
Pour point (^{o}C)		-10
Viscosity (50 ^{o}C, cSt)		71

Bio-oil was analyzed by GC and GC-MS system. Using acetone as a solvent, qualitative analysis was conducted. Some typical components, such as acetic acid, phenol and alkylated phenols, furan derivatives, furfural and anhydrosugers were identified.

Char. Char formed during pyrolysis serves as vapor cracking catalysts to reduce the yield of bio-oil. It can also raise bio-oil viscosity through catalytic reaction during storage, and is likely to be detrimental to most applications. Therefore efficient removal of char is necessary for the production of bio-oil of high quality. We used a hot filter and a cyclone for removal of char. In cyclone, particles with sizes of 10-100 μm were captured. In contrast, the hot filter could catch particle size around 0.1μm. Most of alkali metals in feed was found in char and the C/H ratio of char was in the range of 4 and 5. Figure 4 shows particle distributions of char obtained in hot filter.

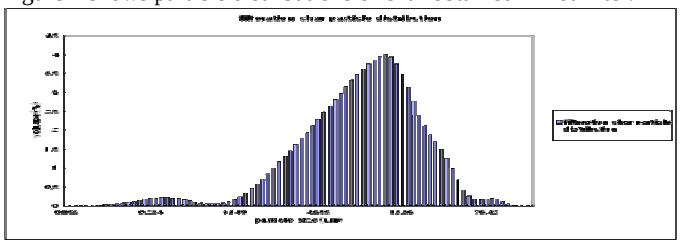

Figure 4. Particle size distribution of char from hot filter.

Conclusion

High quality bio-oil was obtained from rice straw using a fluidized reactor and a char removal system. Optimum reaction temperature for the high yield of bio-oil lay between 410 and 510 ˚C. Bio-oils obtained in experiments showed very low content of alkali metals, and solid content in bio-oil was about 0.03wt%. In the future, some more works are needed for more yield of bio-oil with smaller size of particle to feed and less water content in feed by drying.

Acknowledgment. This subject is supported by the Ministry of Environment in Korea as "The Eco-technopia 21 project".

References

1. Bradbury, A.G.W., Sakai, Y. and Shafizadeh, F., J. Appl. Polym. Sci., 1979, Vol. 23, pp. 3271.
2. Dobele, G. in Bridgwater, et al., Fast Pyrolysis of Biomass: Handbook Vol. 2, pp150, CPL Presss: Newbury, 2002.
3. Radlein, D., in Bridgwater et al., Fast Pyrolysis of Biomass: A Handbook, pp165, CPL Press: Newbury, 1999.
4. Oasmaa, A., et al, Physical charaterisation of biomass-based pyrolysis liquids, VTT Publication 306, pp12, Espoo, 1997

VALUABLE AND STABLE CARBON CO-PRODUCT FROM FOSSIL FUEL EXHAUST SCRUBBING

*Danny Day *[1], Robert J. Evans[2], James W. Lee[3], Don Reicosky[4]*

[1]Eprida, Inc., 6300 Powers Ferry Road, Suite 307, Atlanta, GA 30339
danny.day@eprida.com

[2]National Renewable Energy Laboratory, 1617 Cole Blvd, Golden, CO, 80401, bob_evans@nrel.gov

[3]Oak Ridge National Laboratory, 4500N, A16, MS-6194, Oak Ridge, TN 37831, leejw@ornl.gov

[4]USDA-Agricultural Research Service, 803 Iowa Avenue, Morris, MN 56267 reicosky@morris.ars.usda.gov

Introduction

A Sustainable Carbon Sink With Hydrogen Production. The increasing anthropogenic CO_2 emissions and possible global warming have challenged the United States and other countries to find new and better ways to meet the world's increasing needs for energy while reducing greenhouse gas emissions. The need for sustainable energy with little greenhouse gas emissions has lead to demonstration work in the production of hydrogen from biomass through steam reforming of pyrolysis gas and pyrolysis liquids. Our research to date has demonstrated the ability to produce hydrogen from biomass under stable conditions.[1] Future large-scale renewable hydrogen production using non-oxidative technologies will generate co-products in the form of a solid sequestered carbon. This char and carbon ("C") material represent a form of sequestered C that decomposes extremely slow[2] and retains the bio-capture CO_2 for centuries.

The limitation of the use of this form of carbon is a profit centric use. It was apparent that additional value needed to be added to this material that would justify large-scale handling and usage. In 1990s, C in the form of CO_2, accumulated at rates ranging from 1.9 to 6.0 Pg C/yr and increasing CO_2 levels by 0.9 to 2.8 ppm/yr. [3]. The volume of waste and unused biomass economically available in the United States is over 314 gigatons per year [4]. Sequestering a small percentage as valued added carbon could significantly reduce the atmospheric loading of CO_2 while simultaneously producing hydrogen. Normally hydrogen is referred to as a zero emissions fuel, however from life cycle perspective it can be viewed as a negative emissions fuel. In order to accomplish this economically, the sequestered C must have a very large and beneficial application such as a soil amendment and/or fertilizer.

The concept of utilizing charcoal as a soil amendment is not new. Man-made sites of charcoal rich soils intermingled with pottery shards and human artifacts have been identified covering 50,000 hectares of the Central Amazon rainforest each averaging 20ha and the largest at 350ha. [5] The radiocarbon dating of the sites have shown ages dating back 740–2,460 years BP[6] and 30% of the soil organic matter is made up of pyrolytic black carbon which is 35 times higher than the adjacent poorer quality soils (Oxisols) [7]. Most terra preta sites are identified by their thick black layers of soil (40-80cm) and some have been found in layers up to 2 meters thick[8]. These soils are so rich and fertile that they are dug up and sold as potting soil[9]. The current agricultural methods of the Kayapó (an ancient people with little European contact until the 19th century) has changed little and give evidence to the man-made techniques (slow burning fieldsand biomass) for creation of this fertile and sustainable method of agriculture which can be farmed intensively for up to 11 years . [10] This ability to farm soils without fertilization for many years is an anomaly in the rainforest. Despite the abundance of rainforest growth, their red and yellow soils are notoriously poor: weathered, highly acidic, and low in organic matter and essential nutrients.

Experimental Project Description

The approach [11] in our research applies a pyrolysis process that has been developed to produce charcoal like by-product and synthetic gas (containing mainly H_2, and CO_2) from biomass, which could come from both farm and forestry sources. In this novel system [12], a portion of the hydrogen is used to create ammonia where economical, or ammonia is purchased leaving hydrogen for fuel utilization. The ammonia is then combined with the char, H_20 and CO_2, at atmospheric pressure and ambient temperature to form a nitrogen enriched char. The char materials produced in this process contains a significant amount of non-decomposable carbons such as the elementary carbons that can be stored in soil as sequestered C. Furthermore, the carbon in the char is in a partially activated state and is highly absorbent. Recent research has shown that lower temperature charcoal produced at 500°C adsorbed 95% of ammonia versus charcoal produced at 700°C and 1000°C which had higher surface areas but only adsorbed 40%[13]. Matsui noted that acidic functional groups such as carboxyl were formed from lignin and cellulose at 400°C -500°C. [14,15]. Charcoals, regardless of biological source, were found to form acidic functional groups at these temperatures which will preferentially adsorb base compounds such as ammonia and that the chemical adsorption plays the primary role over surface area. This research points to the carbonization conditions as a key ingredient in optimizing a charcoal as a nutrient carrier and binding compound for ammonia. Thus when used as a carrier for nitrogen compounds (such as NH_4^+, urea or ammonium bicarbonate) and other plant nutrients, the char binding forms a slow-release fertilizer that is ideal for green plant growth. A combined NH_4HCO_3-char fertilizer is probably the best product that could maximally enhance sequestration of C into soils while providing slow-release nutrients for plant growth.

A flue gas scrubbing process [16,17] utilizing hydrated ammonia was tested in combination with a low temperature char. This approach utilized a chemical process, to directly capture greenhouse gas emissions at the smokestacks by converting CO_2, NO_x, and SO_x emissions into valued added fertilizers (mainly NH_4HCO_3, ~98% and $(NH_4)2SO_4$ and NH_4NO_3, <2%). These fertilizers can potentially enhance crop growth for sequestration of CO_2 and reduce NO_3^- contamination of groundwater. As discussed above, the low temperature charcoal forms surface acid groups, which adsorbs and binds ammonia to the porous media for nucleation of CO_2. When used as a scrubbing agent with fossil fuel exhaust, a mechanically fluidized cyclone creates a fertilizer-matrix with a commercially acceptable amount of nitrogen and a high percentage of very stable C. In addition, the inorganic carbon component (HCO_3) of the NH_4HCO_3 fertilizer is non-digestible to soil bacteria and thus can potentially be stored in certain soil (ph > 7.9) and subsoil terrains as even more sequestered C. This community-based solution operates as a closed loop process, integrating C sequestration, pollutant removal, fertilizer production, increased crop productivity and restoration of topsoil through the return of carbon and trace minerals. The benefits of producing a value added sequestering co-product from coal fired power plants and other fossil energy producing operations, can help bridge the transitions to clean energy systems that are in harmony with the earth's ecosystem. [18] An important benefit of this approach to the power industry is that it does not require compressors or prior separation of the CO_2. The use of biomass in combination with fossil energy production, can allow agriculture, and the agrochemical industry infrastructure to assume a more holistic relationship of mutual support in helping each meet Kyoto greenhouse gas reduction targets.

The char component of the material acts to provide the same benefits as in terra preta sites reducing the leaching of soluble nutrients.[19] This increases plant growth, nutrient uptake and reduces nitrogen runoff. One experimental goal of the project was to identify process parameters that would produce a carbon material optimized for agricultural use. Since it has been shown that the that charcoal addition from 2000 years ago is still providing significant soil fertility benefits [20] and farmers report up to three times crop yields over immediately adjacent non-terra preta soils. Recent research, conducted by Steiner, on the addition of charcoal to non terra preta soils [21] showed significant crop yield increases.

Charcoal has been found to support microbial communities [22] even greater than activated carbon (which is charcoal processed at higher temperatures with steam). Prior researchers assumed that the porous structure provided safe haven but we propose that it may be the availability of microbial nutrients. The processes of pyrolysis create an intrapore deposition of organic polycondensates[23].The deposition of these materials may increase microbial activity. [24]

Experimental Set-up and Results

SEM Investigation of a Low Temperature Char. The low temperature char particles are hydrophobic in nature and grind easily. The internal gases that escape from the material during the charring help develop charcoals natural porosity. The evolution of this adsorbent material provides a porous internal structure as well. We selected 400 ^{o}C as the target temperature for the char before being discharged from the pyrolysis reactor. The resulting char was cooled for 24 hours then fed through a two-roll crusher and then sieved with a mechanized screen through 30 mesh and 45 mesh screens. The resulting fraction remaining above the smaller screen was chosen as our starting material.

SEM Investigation of an Enriched Carbon, Organic Slow-release Sequestering (ECOSS) Fertilizer. Bench scale demonstrations by Oak Ridge National Laboratory recently demonstrated the removal of flue-gas CO_2 via formation of solid NH_4HCO_3 through ammonia carbonation in the gas phase. [25] The results indicated that it is possible to use NH_3+ H_2O+CO_2 solidifying process in gas phase to remove greenhouse-gas emissions from industrial facilities such as a coal-fired power plant. A study of agriculturally optimized charcoal produced by Eprida were combined with the above process created via the sequestration of a CO2 stream. It was proposed that the char could act as a catalyst (providing more effective nucleation sites) to speed up the formation of solid NH_4HCO_3 particles and enhance the efficiency of the gas phase process. A pilot demonstration was constructed to evaluate production and material characteristics of the NH_4HCO_3-char product. The process also showed promise that it could remove SOx and NOx, enhance sequestration of carbon into soils; providing an ideal "Enriched Carbon, Organic Slow-release Sequestering" ("ECOSS") fertilizer and nutrient carrier for plant growth. The value would be enhanced if the production of NH_4HCO_3 could be developed inside the porous carbon media.

To test the production of a charcoal- NH_4HCO_3 fertilizer, we used a mechanical fluidized cyclone, easily adaptable to any gas stream and injected CO_2, and hydrated ammonia. A 250g charge of 30-45 mesh 400 ^{o}C char was fed in at regular intervals varying from 15-30 minutes. A higher rotor speed increased the fluidization and suspended the particles until they became too heavy from the deposition of $NH_4HCO_3$to be supported by fluidized gas flows.

SEM Investigation of the Interior of an ECOSS-15 Char Particle. The material produced was evaluated by scanning electron microscopy. The examinations revealed The very small molecules of NH3.H2O (hydrated ammonia) are adsorbed into the char fractures and internal cavities. As CO_2 enters, it converts the NH3.H2O into the solid NH_4HCO_3, trapping it inside the microporous material. The SEM's of the original char and the resulting product clearly evidenced the intra-pore development of the fibrous NH_4HCO_3 inside the carbon-charcoal framework. The material accumulated as internal flat-top volcano like structures. This demonstration of the process showed that we can deposit nutrients inside the porous media using a low cost gas phase application. We analyzed the required amounts of hydrogen, reformed from biomass, which would be required as ammonia and calculated that 31.6% of the H_2 would be necessary for ECOSS production leaving (using all charcoal available from the process) leaving 68.4% of the hydrogen for use as a fuel.

The amount of C, directly converted from exhaust CO_2 is equal to 15.2% of the total sequestered carbon as a ammonium bicarbonate and for each 100kg of biomass, we will produce a total of 28.3kg of utilized carbon. In acid soils, this part of the carbon will convert to CO_2 but in alkaline soils, (pH>8) it will mineralize and remain stable. According to USDA reports, 60-70% of worldwide farmland is alkaline, so conservatively allowing for 50% of the bicarbonate to convert to CO_2, this will leave us with approximately 25 kg of stable carbon in our soils for each 100kg of biomass processed. This carbon represents 91.5 kg of CO_2 of which 88% is stored as a very beneficial and stable charcoal. A different way to look at this is to compare the amount of energy produced and the resulting CO_2 impact. With 6.78 kg hydrogen extra produced per 100 kg of biomass, then 25/6.78 = 3.69 kg C/ kg H or 3.66x3.69=13.5 kg CO_2 / kg of hydrogen produced and used for energy. From a power perspective, that is 13.5kg CO_2 / 120,000 KJ of hydrogen consumed as a renewable energy or 112 kg/GJ of utilized and stored CO_2.

Global Potential

The large majority of increases in CO_2 will come from developing countries and a sustainable technology needs to be able to scale to meet the growing population needs. The second point is that The energy from a total systems point of view could create a viable pathway to carbon negative energy as detailed in the IIASA focus on Bioenergy Utilization with CO_2 Capture and Sequestration (BECS) [26]. The effects) (i.e. providing 112kg of CO_2 removal for each GJ of energy used) could allow major manufacturers to offset their carbon costs. For a quick test of reasonableness, if we take the atmospheric rise of 6.1GT and divide by 112kg/Gj = 54.5EJ. This number falls amazingly along the 55EJ estimate of the current amount of biomass that is used for energy in the world today. [27] While the potential reaches many times this for the future utilization of biomass, this shows that there is a chance that we can be proactive in our approach. Economic projections of a study based on the ORNL process were compared to this process. Equivalent 20% CO_2 reductions and credits needed to return a 33% ROI was estimated to cost $46 million for a 700MW facility utilizing purchased ammonia. However, if the market for nitrogen were an upper limit, and renewable hydrogen were used for producing the worlds ammonia, and all the world's N fertilizer requirements were met from NH_4HCO_3 scrubbed from power plant exhaust, then the total carbon capture at (1999 N levels) then coal combustion CO_2 could be reduced by ~39.9%. The factors of increased biomass growth with the addition of charcoal as found by Mann[28], Hoshi[29], Glaser[30], Nishio[31], and Ogawa[32] show increase biomass growth from 17% to as 280% with non-optimized char. The direct utilization of an optimized char plus slow release nitrogen/nutrients may allow the increase biomass growth targets worldwide. A portion of this increased biomass growth will be converted to soil organic matter, further increasing C capture (especially if no-till management practices are adopted).

The ability to slow down the release of ammonia in the soil will allow plants to increase their uptake of nitrogen. This will lead to a reduction in NO_2 atmospheric release. For each ton of nitrogen produced, 0.32 tons of C are released, and the 80.95 million tons of nitrogen utilized would represent 26 million tons of C. This is a small a small number in relative terms to the amounts released by combustion of coal (2427 million tons) [33], however if we assume [34] 1.25% of our nitrogen fertilizer escapes into the atmosphere as N_2O, then 1.923 million tons of N_2O are released, with an CO_2 equivalence of 595.9 million tons or 162.5 million tons of C equivalent.

The economics of hydrogen from biomass has been addressed in the 2001 report by Spath[35]. Our analysis shows that inside plant use of renewable hydrogen would no longer be 2.4-2.8 times the costs from methane, but is approaching 1.6-1.9 times with the increase in natural gas prices. Since market price of nitrogen increases with natural gas prices and this process shows intra plant usage of renewable hydrogen (i.e. no storage or transport expense) becomes significantly more competitive at our current natural gas prices. A review of traditional ammonia processing, shows that due to unfavorable equilibrium conditions inherent in NH_3 conversion, only 20-30% of the hydrogen is converted in a single pass. We determined that the ECOSS process could only utilize 31.6% of the hydrogen as we were limited by the total amount of char produced and the target 10% nitrogen loading. This means that a single pass NH_3 converter could be used and the expense of separating and recycling unconverted hydrogen is eliminated. The 68.4% hydrogen is then available for sale or use by the power company/fertilizer partnership. This last bracket shows that the ECOSS process thus favors the inefficiencies of ammonia production and reduces costs inherent in trying to achieve high conversion rates of hydrogen.

Conclusions

This concept of biomass energy production with agricultural charcoal utilization may open the door to millions of tons of CO_2 being removed from industrial emissions while utilizing captured C to restore valuable soil carbon content. This process simultaneously produces a zero emissions fuel that can be used to operate farm machinery and provide electricity for rural users, agricultural irrigation pumps, and rural industrial parks. The use of value added carbon while producing hydrogen (or energy) from biomass can lead to energy with an associated carbon credit (ie negative carbon energy). With this development non-renewable of carbon dioxide producers

can work with agricultural communities to play a significant part in reducing greenhouse gas emissions while building sustainable economic development programs for agricultural areas in the industrialized and economically developing societies.

Acknowledgements. Kim Magrini, Stefan Czernik, Bob Evans and Calvin Fiek and Don Reicosky and James Lee who have been seeking solutions to our CO2 buildup. Thanks to Nigel Smith, Bruno Glaser, Christoph Steiner, Johannes Lehman, Bill Woods, Bill Denevan and Susanna Hecht who has taught us with the history of terra preta and finally Michael Obersteiner for his encouragement.

Literature Cited

[1] Day, D., Activities web report of a 100 hour production run of hydrogen from biomass in Blakely, GA, USA; 2002 http://www.eprida.com/hydro/
[2] Gavin, D.G., Brubaker, L.B., and Lertzman, K.P. Holocene fire history of a coastal temperate rain forest based on soil charcoal radiocarbon dates. In press for Ecology: 2003
[3] IPCC, "Climate change 2001: the scientific basis", Intergovernmental Panel on Climate Change, 2001 (see also at http://www.grida.no/climate/ipcc_tar/wg1/index.htm.)
[4] Walsh, Marie et al., Biomass Feedstock Availability in the United States: 1999 State Level Analysis, 1999 http://bioenergy.ornl.gov/resourcedata/index.html
[5] Glaser et.al, The 'Terra Preta' phenomenon: a model for sustainable agriculture in the humid tropics, Naturwissenschaften **2001**, 88: 37–41
[6] Saldarriaga JG, West DC, Holocene fires in the northern Amazon basin. Quat Res **1986**, 26: 358–366
[7] Glaser, et. al., Black Carbon in the Terra Preta Soils of the Brazilian Amazon Region, Proceedings 9th Annual V.M.Goldschmidt Conference, Cambridge, MA 1999, #7391
[8] Smith NJH, Anthrosols and human carrying capacity in Amazonia. Ann Assoc Am Geogr **1980**, 70: 553–566
[9] Mann, C., The Real Dirt on Rainforest Fertility, Science **2002**; 297:920-923
[10] Hecht, S and D. Posey. "Preliminary Results on Soil Management Techniques of the Kayapó Indians." Advances in Economic Botany **1989**, 7: 174-188.
[11] Y. Yeboah,et al., Hydrogen from Biomass for Urban Transportation, Proceedings of the 2002 US DOE Hydrogen Program Review
[12] Day, Danny; Robert Evans, James Lee U.S. Patent Application, 2002
[13] Asada, T. et al, Science of Bamboo Charcoal: Study on Carbonizing Temperature of Bamboo Charcoal and Removal Capability of Harmful Gases, Journal of Health Science **2002**, 48(6) 473-479
[14] Matsui, T. et al, Preparation and Analysis of Carbonization Products from Sgi, Cryptomra japonica D. Don) Wood. Nippon Kagakukaishi **2000**; 1:53-61 (Japanese)
[15] Nishimaya, K. et al., Analysis of Chemical Structure of Wood Cjrcoal by X-ray photoelectron spectroscopy **1998**, Journal of Wood Science,44, 56-61
[16] Lee, J. W.; Li, R., A Novel Strategy for CO2 Sequestration and Clean Air Protection, Proceedings of First National Conference on Carbon Sequestration, Washington, DC, May 1417, **2001**. http://www.netl.doe.gov/publications/proceedings/01/carbon_seq/p12.pdf
[17] Lee, J. W.; Li, R, Method for Reducing CO2, CO, NOx, and SOx Emissions, 1998 Oak Ridge National Laboratory Invention Disclosure, ERID 0631; 2002 U.S. Patent No. US 6,447,437 B1.
[18] Lee, J. W., and R. Li, Integration of Coal-Fired Energy Systems with CO2 Sequestration through NH4HCO3 Production, Energy Conversion Management **2003**; 44: 1535-1546.
[19] Schleppi P., Bucher-Wallin I., Siegwolf R., Saurer M., Muller N. & Bucher J.B., Simulation of increased nitrogen deposition to a montane forest ecosystem: partitioning of the added N; Water Air Soil Pollution **1999**; 116: 129-134
[20] Glaser B., Lehmann J., Zech W. Ameliorating physical and chemical properties of highly weathered soils in the tropics with charcoal – a review. Biology and Fertility of Soils **2002**; 35: 219-230.
[21] Wardle, D. A. et al., The charcoal effect in Boreal forests: mechanisms and ecological consequences**,** Oecologia **1998**; Volume 115 Issue 3: 419-426
[22] Pietikäinen, Janna, Soil microbes in boreal forest humus after fire (thesis 1999) http://ethesis.helsinki.fi/julkaisut/maa/mekol/vk/pietikainen/soilmicr.html
[23] Runkel, R.O.H and Wilke, K, Chemical composition and properties of wood heated at 140C to 200C in a closed system without free space. Part II Holz als Roh und Werkstoff 1951; 9: 260-270 (Ger.)
[24] Godsy, E. Michael, Impact of Human Activity on Groundwater Dynamics (Proceedings of a symposium held during the Sixth IAHS Scientific Assembly at Maastricht, The Netherlands, July 2001). IAHS Publication no. 269, 2001, pp. 303–309.
[25] Li, E. Hagaman, et al., "Removal of carbon dioxide from flue gas by ammonia carbonation in the gas phase," Energy & Fuels **2003**; 17: 69-74.
[26] Oberstiener, et al., Biomass Energy, Carbon Removal and Permanent Sequestration - A 'Real Option' for Managing Climate Risk, Report no. IR-02-042, Laxenburg, Austria: International Institute for Applied Systems Analysis, 2002.
[27] Hall, D.O., F. Rossillo-Calle, R.H. Williams and J. Woods,: Biomass for energy: Supply prospects. In: Renewable Energy: Sources for Fuel and Electricity [Johansson, T.B., H. Kelly, A.K.N. Reddy, and R.H. Williams (eds.)]. Island Press, Washington, D.C., 1993:593-652
[28] Mann, C., The Real Dirt on Rainforest Fertility, Science **2002**; 297:920-923
[29] Hoshi, T. (web report of growth studies with charcoal amendments on green tea yields) **2002** http://www.fb.u-tokai.ac.jp/WWW/hoshi/cha
[30] Glaser, et.al, Potential of Pyrolyzed Organic Matter in Soil Amelioration, 12th ISCO Conference, China, **2002**; 3:421
[31] Nishio, M., Microbial Fertilizers in Japan, Bulletin by National Institute of Agro-Environmental Sciences, Japan, **1999**
[32] Ogawa, M., Effect of charcoal on the root nodule and VA mycorrhizal formation of soybean, Proceedings of the Third Inter-national Mycology Congress, Tokyo, Ja-pan, **1983**: 578
[33] World Carbon Dioxide Emissions from the Consumption of Coal, 1992-2001 http://www.eia.doe.gov/emeu/iea/tableh4.html
[34] Mosier, et.al, Closing the Global N2O budget: Nitrous Oxide Emissions through the Agricultural Nitrogen Cycle, Nutrient Cycling and in Agro Ecosystems **1998**, 52: 223-245
[35] Spath, et al, Update of Hydrogen from Biomass -Determination of the Delivered Cost of Hydrogen, National Renewable Energy Laboratory, Milestone Report for the U.S. Department of Energy's Hydrogen Program 2001, United States

PRODUCTION OF HYDROGEN FROM VEGETABLE OIL

Ross A.B., Dupont V., Hanley I., Jones J.M., Twigg M.V.

Energy and Resources Research Institute, The University of Leeds
Leeds, LS2 9JT, UK.

Introduction

The production of hydrogen from biomass and bio-oils represents a realistic renewable source. The development of the bio-diesel infrastructure could enable hydrogen to be produced from vegetable oil derived materials by either decentralised stationary reformers or on-board fuel processors.

Unmixed steam reforming first proposed by Kumar, Lyon and Cole [1], is an emerging concept for enhancing the steam reforming process. It encompasses the concepts of unmixed combustion, regenerative sorption assisted steam reforming, and is potentially autothermal. It can be operated on a smaller scale to conventional steam reforming at lower pressures. The process operates in two steps forming a cycle. Firstly, an oxygen mass transfer catalyst is oxidised under air flow. In this study, the catalyst is Ni-based and its oxidation results in the formation of NiO compounds. The reaction is exothermic and heats up evenly the reactor bed. During this step, the reactor also contains a carbonate, here a Spanish dolomite (50/50% $CaCO_3/MgCO_3$). Some of the heat evolved during the Ni oxidation is used to decompose the carbonate, releasing the CO_2. Secondly, the air feed is discontinued and is switched to the fuel/steam mix. Upon contact with the hot catalyst bed, the steam reforming reaction progresses, and CH_4, CO, CO_2, and H_2 are evolved. Under this step, the NiO reduces back to Ni while there is CO_2 capture on the adsorbent. The latter shifts the equilibrium of the water gas reaction toward increased hydrogen production. Hydrogen production is therefore intermittent, and for a continuous hydrogen yield, at least two identical reactor beds would need to run in parallel, each operating out of step. The cycle of reactions involved in the unmixed reforming process of an oxygenated hydrocarbon fuel such as vegetable oil is postulated below:

- Under air feed *:*

$Ni + 0.5\ O_2 \Rightarrow NiO$ ($\Delta H<0$)

$MCO_3 \Rightarrow MO + CO_2$ ($\Delta H>0$) where M is either Mg or Ca.

The gas product from this half cycle is an O_2-depleted, CO_2-rich air stream.

-Under fuel/steam feed:

$(MO+NiO) + fuel_{(v)} + H_2O_{(v)} \Rightarrow (MCO_3+Ni)$ + little (CO, CO_2) + ca.80% H_2 + H_2O ($\Delta H>0$)

For sunflower oil fuel, the elemental composition is taken to be $C_{18}H_{34.4}O_{2.1}$.

The benefits of this process include an evenly heated reactor bed across its whole cross section, two product streams being either H_2 or CO_2 rich, low sensitivity to coking, low sensitivity to sulphur poisoning, autothermal behaviour, and, when running on a renewable fuel, no net-CO_2 emissions.

Experimental

Following a period of catalyst and CO_2-adsorbent screening using a micro-reactor [2], the bench scale demonstration unit of unmixed reforming described in **Figure 1** was designed to run on either methane or vegetable oil. The unit operates at pressures between 1-2 bar. The reactor temperature is maintained within the region of 600-800^{o}C, initially by means of an external heating coil, which can be phased out in the event of autothermal operation setting-in.

The liquid flow rates of oil or water are maintained within the range 0-3.2 ml/min depending on conditions. The two feed flows are preheated at 400^{o}C, the temperature at which vegetable oil is completely vapourised. For a more detailed description of the reactor and its operation we refer the reader to [3]

During the fuel step a flow of either nitrogen diluted methane or nitrogen and vapourised vegetable oil mixture pass through the reactor together, this is then switched to air during the oxidative step. When using CH_4 and N_2 as the fuel feed, the inlet flows are 200 and 600 sccm respectively. When using sunflower oil, the liquid flow is 0.57 ml/min. Various steam to carbon ratios were studied.

The product gases are cooled using a water cooled condenser before entering a water trap followed by a chemical water trap (silica gel). The dry gaseous products are fed through a series of analysers. The gas volume concentrations of CO, CO_2, CH_4, H_2 and O_2 were monitored online using analysers from ABB. The gas reaching the analysers was dry and at room temperature.

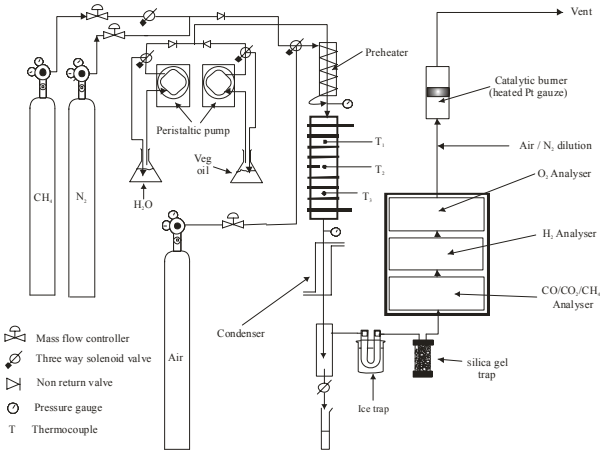

Figure 1. Schematic diagram of bench scale unmixed reforming reactor.

Results and Discussion

H_2 production under fuel feed

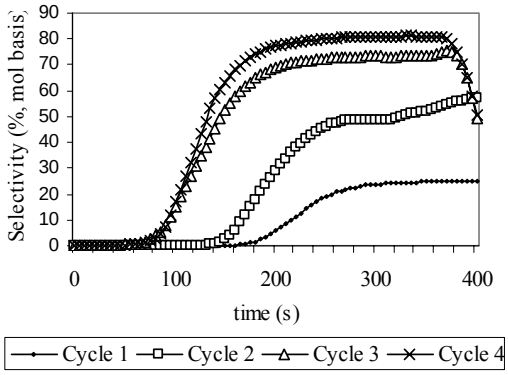

Figure 2. Selectivity to H_2 (%) with varying steam/carbon ratio during the methane feed step experiments when there is no CO_2 adsorbent in the reactor. Cycle 1 has no steam, cycles 2, 3, and 4 have steam/C of 1.65, 3.3 and 4.95 respectively. Water produced in the reactor makes for the balance to 100 %.

Because the peak dry H_2 concentrations corresponding to **Figure 2** were quite low (10%, 16%, 25%, 27% respectively), due to the presence of the diluent N_2, we choose to show how the selectivity to H_2 improved with the presence of steam in the feed. In **Figure 3**, the effect of reactor temperature for the non-diluted methane feed in the reactor containing the CO_2 adsorbent can be seen on the dry H_2 concentration.

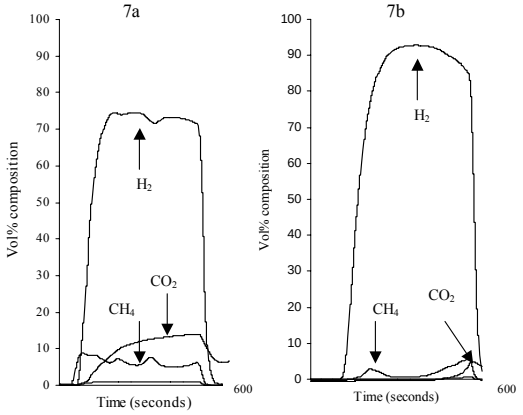

Figure 3. Typical dry gas composition of gaseous products during the fuel step for:-
7a. methane at 650°C, Steam/C of 4.
7b. methane at 600°C, Steam/C of 4.

Figure 3 a-b show that CO_2 and CH_4 dry gas concentrations are significantly reduced to the benefit of that of H_2 when the average reactor temperature of the fuel step is lowered from 650°C to 600°C. This indicates increased adsorption of CO_2 and the expected effect of shift in the water gas reaction. The extent to which CO_2 adsorption is maintained on a continuous basis is dependent upon the extent of regeneration of the adsorbent achieved during the previous oxidation cycle.

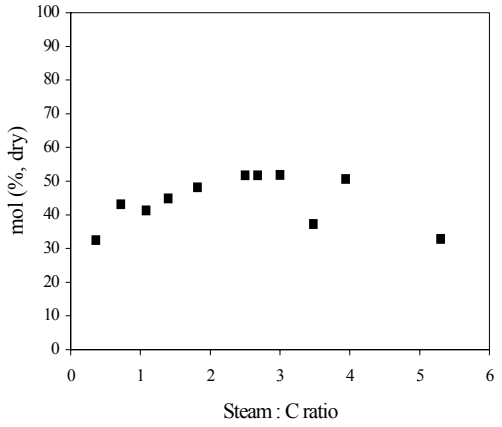

Figure 4. shows the effect of steam carbon ratio on the peak dry H_2 concentration when using a nitrogen (558 sccm) and sunflower oil (0.57 ml/min) mix in a reactor containing just the Ni catalyst, in the absence of CO_2 adsorbent.

The points shown in **Figure 4** are the results of experiments carried out on three different days on the same catalyst. In spite of this, a clear trend can be picked up whereby the maximum dry H_2 concentration is obtained for steam carbon ratios between 2 and 4, as was found for methane fuel. However, the selectivity to H_2 when using sunflower oil was of the order of few percent, hardly comparable to the methane experiments. This was concurrent with a production of water which was of the same order as the amount as the water reactant.

Catalyst redox cycles under air and fuel feed. Before we could attempt to operate the process autothermally, a major hurdle had to be overcome, namely the ability of the catalyst to reduce under the fuel feed and oxidize at similar rates under the air feed. Our first experiments with methane fuel indicated a rate of reduction two orders of magnitude slower than the oxidation rate, hence the subsequent experiments with sunflower oil were operated with an equivalent fuel molar rate two orders of magnitude larger than the methane. This had several effects. The reduction and oxidation rates were now both of the order of 10^{-4} mol/s, but for a small adjustment. In counterpart, using a much larger fuel flow without changing the air feed had the effect of increased carbon formation by two orders of magnitude as well (order 10^{-4} mol/s). This increased carbon formation was an additional oxygen sink to the nickel catalyst during the air feed which tended to produce CO and CO_2 in similar concentrations while it burned at a rate ca. 10^{-3} mol/s. Under the previous lower methane flow, hardly any CO had evolved during the air feed, while all products of oxidation were NiO and CO_2. Clearly, further optimization of the flows need to be carried out before the timing of the flows can be adjusted for autothermal operation.

Conclusions

During the methane feed step, the main dry gas product was hydrogen. However, solid carbon is the main carbon product throughout the whole fuel feed step, while water is the principal hydrogen containing product during an initial phase. A much improved selectivity to H_2 product (up to 80%) is achieved when introducing steam in the feed. During the air feed step, the oxidation of Ni to NiO is slowed down by the carbon deposited during the previous fuel step. When operating with an adsorbent, the production of hydrogen is increased although the adsorption of CO_2 is sensitive to the bed temperature.

When using vegetable oil at a rate two orders of magnitude larger than in the methane experiments, chosen in order to achieve the desired NiO reduction rate, carbon formation is increased in proportion. The dry gas H_2 concentration is larger than with methane but the selectivity to H_2 much lower. The NiO reduction rate under fuel feed and the Ni oxidation rate under air feed are of similar magnitude, suggesting both feeds need little adjustment in the next optimisation phase of the process. Future work will focus on achieving autothermal operation in the reactor while maximizing the H_2 yield and the separation of the CO_2 from the H_2 product stream.

Acknowledgement. The work presented here was financially supported by the Engineering and Physical Science Research Council (EPSRC). The authors are also grateful to Mr Gavin Rickett and Dr Phil Ingram at Johnson Matthey.

References

(1) Kumar R. V.; Cole J. A.; Lyon R. K.; *Preprints of Symposia, J. Am. Chem. Soc*. 1999, 44, (4)
(2) Ross A.B.; Dupont V.; Hanley I.; Ahmad O.S.; Jones J.M.; Twigg MV. Proceedings of the 7th International Conference on Energy for a Clean Environment, 7-10 July 2003, Lisbon, Portugal.
(3) Ross A.B.; Hanley I.; Dupont V.; Jones J.M.; Twigg M.V. Sixth International Conference in Science in Thermal and Chemical Biomass Conversion (STCBC), 30 Aug-2 Sept.2004, Victoria, B.C., Canada.

SUSTAINABLE HYDROGEN FROM BIO-OIL - CATALYTIC STEAM REFORMING OF ACETIC ACID AS A MODEL OXYGENATE

Kazuhiro Takanabe, Ken-ichi Aika
Tokyo Institute of Technology, Interdisciplinary Graduate School of Science and Engineering, 4259 Nagatsuta, Midori-ku, Yokohama, 226-8502, Japan.

K. Seshan, and Leon Lefferts
University of Twente, Institute of Mechanics, Processes and Control Twente (IMPACT), Faculty of Science and Technology, P.O. Box 217, 7500AE, Enschede, The Netherlands.

Introduction

Hydrogen as a fuel has recently been an important issue due to developments in fuel cell technology. Hydrogen production from sustainable sources, e.g. biomass, is gaining attention for a CO_2 neutral energy supply. Recent developments in flash pyrolysis technologies make it possible to convert lignocellulosic biomass efficiently to a bio-oil, which is easier for handling and transport.[1] The bio-oil so generated contains a variety of aliphatic and aromatic oxygenates (aldehydes, ketones, acids, alcohols).

Combination of catalytic steam reforming and water gas shift reaction is the most promising option to generate hydrogen since these reaction steps maximize hydrogen yield. During steam reforming of bio-oil, deactivation due to coke/oligomer deposition on the catalysts is a severe problem. It has been reported[2] that deactivation is unavoidable even in the presence of excess steam ($H_2O/C > 5$). Economically, lower steam/carbon (S/C) ratio (< 2) is preferable. In this study, Pt/ZrO_2 has been investigated since earlier work [3] has shown excellent activity and stability for Pt/ZrO_2 under conditions favorable for coke formation, for e.g., even in the absence of steam, during CO_2 reforming of natural gas.

Bio-oil is a mixture of oxygenates. In order to provide a knowledge base for the design of active and stable catalysts for steam reforming of bio-oil, studies have been initiated with model oxygenates. Acetic acid (HAc) has been chosen as a model compound in this study because it is a major component of bio-oil (up to 32 wt%).[1] It is known that steam reforming and water gas shift reaction ($CO + H_2O \rightleftharpoons CO_2 + H_2$) occur simultaneously and the overall stoichiometry is represented (Equation 1),

$$CH_3COOH + 2H_2O \rightarrow 2CO_2 + 4H_2 \quad \ldots(1)$$

This study describes attempts to understand the reaction and deactivation mechanisms in order to establish guidelines for the design of efficient catalysts for steam reforming of bio-oil.

Experimental

Catalyst preparation. Pt/ZrO_2 was prepared by wet impregnation technique[3]. Pt loading was set to 0.5 wt%. The catalyst was calcined at 925 K for 15 h.

Catalytic measurements. The amounts of 50 mg of catalysts were loaded in a fixed bed reactor and held by quartz wool plugs. The catalyst was first reduced in 5% H_2 in N_2 at 925 K fir 1 hr. An aqueous solution of HAc giving a steam to carbon molar ratio (S/C) of 5 was introduced by using a microfeeder (KD Scientific) and a syringe (Hamilton co.). Gas mixture, $HAc/H_2O/N_2/Ar$, was fed to give a ratio of 3/30/5/82 ml min^{-1} (N_2 as an internal standard). For analysis, a flame ionization detector (FID) and a Hayesep Q column were used for HAc, acetone, ketene, and hydrocarbons; a thermal conductivity detector (TCD) and a Carbosieve column were used for H_2, N_2, CO, CH_4, and CO_2.

Pulse experiments were performed with 20 mg of Pt/ZrO_2. After reduction at 925 K, the system was purged in Ar at a flow rate of 37.5 ml min^{-1}. Pulses of HAc aqueous solution (S/C = 5, 3.5 μmol of HAc) at 293 K were introduced.

The hydrogen yields were calculated based on Equation 1. For carbon containing compounds, the yields were calculated based on C1 equivalent values.

Catalyst characterization. Thermogravimetry (TG) (Mettler Toledo TGA/SDTA 851E) was used to determine the amount of deposits in the catalysts.

IR spectra were recorded *in situ* under vacuum in transmission mode (Bruker, Vector 22, MCT detector). The catalyst reduced *ex situ* at 925 K was mounted in the IR cell and firstly reduced *in situ* by introducing 0.1 mbar of H_2 at 725 K. After evacuation, oxygenates and steam were introduced into the system with an S/C molar ratio of 5 at a total pressure of 0.1 mbar at 725 K. Each spectrum consists of 32 scans taken at 4 cm^{-1} resolution.

Results and Discussions

Figure 1 shows HAc conversion and yields of products during HAc/H_2O reaction over Pt/ZrO_2. Conversion was close to 100% and constant for 3 h, however, yields of products changed with time. In the beginning (5 min), H_2 and CO_2 were the main products, CH_4 and CO were observed in small quantities. H_2 yield (47%) was close to equilibrium value (56%). The product yields and pattern indicates that the catalyst was active for steam reforming However, after 25 minutes time on stream, H_2 and CO_2 yields decreased drastically, and an increase in acetone was observed.

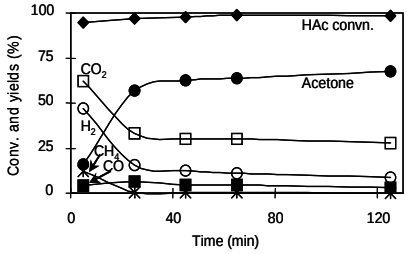

Figure 1. Conversion and yields for steam reforming of HAc over Pt/ZrO_2 catalyst. (725 K, S/C = 5, GHSV = 160000 h^{-1}).

Figure 2 shows HAc conversion and yields of products during HAc/H_2O reaction over ZrO_2 (without Pt). HAc conversion was close to 90%. The conversion of HAc and yields of the products were constant for 3 h. However, no steam reforming activity (H_2 and CO) was observed, and only acetone and CO_2 were observed as products. HAc is known to convert to acetone easily and the reaction is catalyzed by a variety of oxides.[4] ZrO_2 is also known as such an oxide. The stoichiometry of the products observed (acetone and CO_2, 1:1) correspond to the ketonization reaction (Equation 2).

$$2CH_3COOH \rightarrow CH_3COCH_3 + CO_2 + H_2O \quad \ldots(2)$$

Both Pt/ZrO_2 and ZrO_2 were very active for HAc conversion. However, H_2 and CO, i.e., steam reforming products were produced only over Pt/ZrO_2 and not over ZrO_2. This implies that presence of Pt is essential for steam reforming. ZrO_2 shows acetone yields similar to those observed over Pt/ZrO_2 after 25 minutes time on stream (Figure 1), indicating that even after the active sites for steam reforming were deactivated, the accessible ZrO_2 sites still provided the activity to form acetone and CO_2.

For Pt/ZrO_2 and ZrO_2, TG experiments showed approximately 1.2 and 0.8 wt% deposits, respectively, after 3 hour test. Regeneration in air restored catalytic activity, indicating that blocking active sites by deposits caused deactivation of the Pt/ZrO_2 catalyst for the steam reforming.

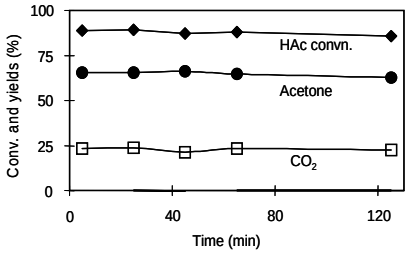

Figure 2. Conversion and yields for steam reforming of HAc over ZrO_2 catalyst. (725 K, S/C = 5, GHSV = 160000 h^{-1}).

Presence of acetone in the product mixture and formation of deposits on ZrO_2 indicates a role for acetone in catalyst deactivation. Acetone is known to undergo aldol type condensation and give products such as diacetone alcohol, mesityl oxide (MO) and MO is known to form oligomers easily ($CH_3COCH_3 \rightarrow (CH_3)_2C(OH)CH_2COCH_3 \rightarrow (CH_3)_2C{=}CHCOCH_3 \rightarrow$ oligomers).[5] In order to check if these oligomers play a role in deactivation, kinetic and *in situ* IR measurements were carried out with Pt/ZrO_2 pre-exposed to MO.

Table 1 shows comparison between HAc conversion and H_2 yield with or without MO treatment during pulse experiment. It is seen that Pt/ZrO_2 catalyst deactivated for H_2 formation (steam reforming) more rapidly when contacted with MO in comparison to HAc.

Table 1. Comparison of HAc Conversion and H_2 Yield between Fresh and MO Treated Pt/ZrO_2

Catalyst (Pt/ZrO_2)	HAc convn. (%)	H_2 yield (%)
Fresh	98.2	60.0
MO treated[a]	82.4	29.1

[a]MO/H_2O pulse (0.32 µmol-MO, S/C = 5) was introduced before a HAc/H_2O pulse.

In situ IR spectra recorded over Pt/ZrO_2 are shown in **Figure 3**. In the presence of HAc/H_2O (**Figure 3a**) characteristic peaks for linear CO adsorbed on Pt at 2060 cm^{-1} were observed. This confirms the production of CO in the *in situ* experiment. Additionally bands due to oxygenates (acetate, carbonate) derived from HAc (1541, 1426 and 1405 cm^{-1}) were also seen. Exposure-evacuation cycles with HAc/H_2O were repeated three times (not shown) and no significant difference in IR spectra were observed.

After pre-exposure to MO, *in situ* IR spectra were recorded with HAc/H_2O (**Figure 3b**). The spectra showed similar oxygenate peaks on the support but the CO peak was very weak. This implies the activity towards CO formation (steam reforming) was deactivated as expected from kinetic experiments. However, when CO was introduced in the gas phase, the intensity of the peak for CO significantly increased (**Figure 3c**). This indicates that the Pt surface was not blocked completely even though the activity for steam reforming was lost. This further implies that only part of the surface Pt atoms are responsible for steam reforming. Since oligomerization reactions of MO occur on the support, and the fact that Pt sites were deactivated with MO, we conclude that the Pt sites active for steam reforming are at the close vicinity of the support. This is in agreement with a bi-functional mechanism proposed by us for the steam or CO_2 reforming of methane, where methane is activated on the metal and steam or CO_2 on the support, the reaction occurring at the metal support boundary.[3,6] Thus, ZrO_2 may have a key role in the mechanism for steam reforming in the activation of water. Once MO, or the oligomers derived from it, is formed on the support even in small amounts, they could block the boundary sites and deactivate the Pt/ZrO_2 catalyst.

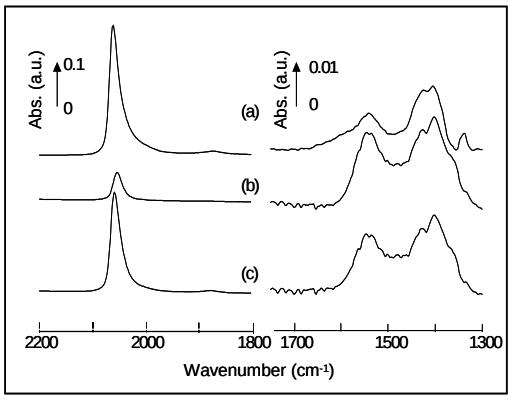

Figure 3. *In situ* IR spectra over Pt/ZrO_2 at 725 K (Steam/Carbon = 5, 0.1 mbar). (a) HAc/H_2O, (b) HAc/H_2O after MO/H_2O treatment and evacuation, (c) CO treatment after (b) without evacuation

The acid-base properties of the support oxides play a key role in catalyzing the condensation reactions.[5] ZrO_2 has an important role in steam reforming *via* steam activation. However, condensation reaction could also happen over ZrO_2. Thus, design of a stable catalyst should be aimed at improvement of the support, minimizing the condensation reactions as well as enhancing the steam activation capacity.

Conclusions

The Pt/ZrO_2 catalysts showed high activities at initial time on stream, but lost its activity for steam reforming (H_2 production) rapidly.

Results obtained in the study point to a bifunctional mechanism for steam reforming of HAc on Pt/ZrO_2, i.e., HAc activation takes place on Pt and steam activation on ZrO_2. The reaction occurs at the Pt periphery in close proximity of ZrO_2. The catalysts deactivate due to blocking of active sites by oligomers derived from HAc/acetone on ZrO_2. In order to develop a durable catalyst, the oligomerization/condensation reactions which take place on the support need to be minimized.

Acknowledgement. One of us (K. Takanabe) thanks the Huygens exchange program (Nuffic, the Netherlands) for financial support. This work was performed under the auspices of NIOK, The Netherlands Institute for Catalysis.

References

(1) Milne, T.; Agblevor, F.; Davis, M.; Deutch, S.; Johnson, D. In Developments in Thermochemical Biomass Conversion; Bridgwater, A.V.; Boocock, D.G.B, Ed.; Blackie, 1997, pp. 409-424.
(2) Wang, D., Montané, D., Chornet, E., *Appl. Catal. A*, **1996**, 143, 245-270.
(3) Bitter, J.H., Seshan, K., Lercher, J.A., *J. Catal.* 1998, 176, 93-101.
(4) Rajadurai, S., *Catal. Rev. -Sci. Eng.*, **1994**, 36, 385-403.
(5) Iglesia, E., Barton, D.G., Biscardi, J.A., Gines, M.J.L., Soled, S.L., *Catal. Today*, **1997**, 38, 339-360.
(6) Nagaoka, K., Seshan, K., Aika, K., Lercher, J.A., *J. Catal.*, **2001**, 197, 34-42.

DETERMINATION OF THE OXIDATION CHARACTERISTICS OF FIR (*Abies bornmulleriana*) WOOD

Ahu Gümrah Dumanlı, Billur Sakintuna, and Yuda Yürüm

Faculty of Engineering and Natural Sciences, Sabanci University, Tuzla, Istanbul 34956, Turkey

Introduction

About 90% of the energy used by humankind is based on combustion – mainly combustion of fossil fuels (oil, coal, and natural gas), with a relatively small contribution from the combustion of biomass (wood). The main exceptions to combustion are nuclear fission and hydro for the generation of electricity. Energy conversion by combustion has a significant impact on the planet's atmosphere by means of ground-level air pollution (photochemical smog,, acid rain, global climate change, and stratosphere particulate matter, SO2, CO, toxic organic gases and vapors and toxic metals), acid rain, global climate change, and stratosphere ozone depletion.

Although energy production from biomass residues is limited due to availability and high cost compared to fossil fuels[1,2], biomass provides a renewable source of energy on a scale sufficient to play a significant role in the development of sustainable energy programmes, so vital if we are to create a greener, more ecologically sensitive society[3,4].

By optimal utilization of biomass resources and development of new technical advances, biomass will become more efficient and competitive as an energy source. In order to consider the optimum conditions for biomass utilization one should start investigating the combustion characteristics of the biomass. In this study we aimed to find the combustion characteristics of wood samples as the starting point for the evaluation of to use as an energy source.

Experimental

The wood sample used in this work was a bark-free fir (*Abies bornmulleriana*) sawdust sample obtained from Bolu forests (northwest Anatolia) in Turkey. The proximate and elemental analyses of the wood sample were done at the Instrumental Analysis Laboratory of the Scientific and Technical Research Council of Turkey, Ankara, is given in Table 1. The sawdust was ground and sieved to below 175 μm (–80 mesh) size.

Table 1. Proximate and Elemental Analyses of the Fir Wood Sample

Proximate analysis, % (as received)	
Volatile matter	85.5
Fixed carbon	10.5
Moisture	3.7
Ash	0.3
Elemental analysis, % (daf)	
C	47.2
H	6.1
N	0.3
O (by difference)	46.7

Characterization Techniques. Combustion and decomposition characteristics of the wood sample were analyzed by using a Netsch 449C thermogravimetric analyzer (TGA). TGA analysis was done in the following manner; the wood samples were heated up to a temperature range between 500°C and 1000°C with different heating rates of 5K/min, 10K/min, 20 K/min and 30 K/min. In addition to this, TGA analysis was combined with an Bruker Equinox 55 FTIR in order to monitor the released gases during combustion and decomposition. The ashes obtained from TGA analysis were examined with a Leo G34-Supra 35VP scanning electron microscope (SEM) and SEM images were compared with the images obtained from unburnt wood sample. Additionally the wood sample was objected to heat treatment at different temperatures between 100°C and 400°C. The mass loss according to the heat treatment was recorded and these samples were analyzed with an IKA-Calorimeter System-C4000-Adiabatic calorimeter, again included the comparison with the untreated sample.

Results and Discussion

The heating rate seemed to be very effective on the oxidation of the samples and different mass losses were observed. There were two main temperatures for mass losses; as the heating rate was increased the greatest mass loss was detected at higher temperatures.

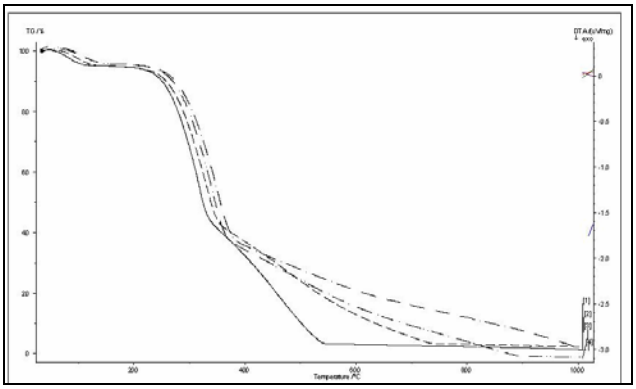

Figure 1. TGA traces of the wood samples.

Table 2. Percent Mass Loss and Change of Calorific Values

Heat Treatment Temperature, °C	Mass Loss, %	Calorific Value, kJ/kg
Unheated	-	18746
100°C	5.9	19135
200°C	11.0	19521
300°C	32.0	3149
400°C	99.3	-

While heat treatment of the wood sample up to 200°C increased the calorific value of the wood due the removal of the low volatile compounds. As the heat treatment temperature was increased to 300oC and higher temperatures due to the pyrolytic losses of carbonaceous material from the structure of the wood the calorific values decreased sharply.

The FTIR spectra of the volatiles obtained during TGA measurements are presented in **Figures 2-4**. The peaks due to CO_2 and H_2O can be seen near 2335 cm^{-1} and 3240 cm^{-1}, respectively and a complex peak near between 1500- and 1700 cm^{-1} is due to H_2O.

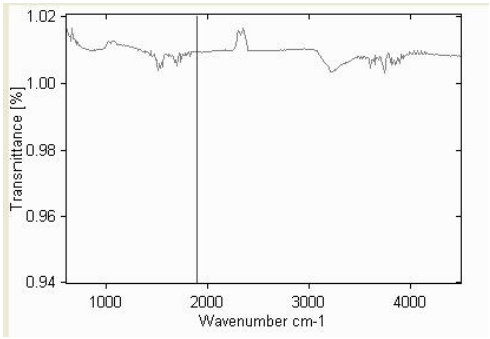

Figure 2. FTIR spectrum of the volatiles evolved at the 14th second during TGA measurement.

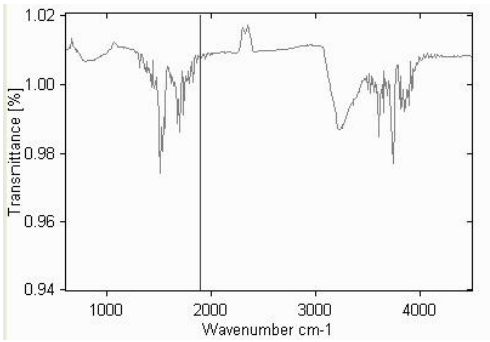

Figure 3. FTIR spectrum of the volatiles evolved at the 1506th second during TGA measurement.

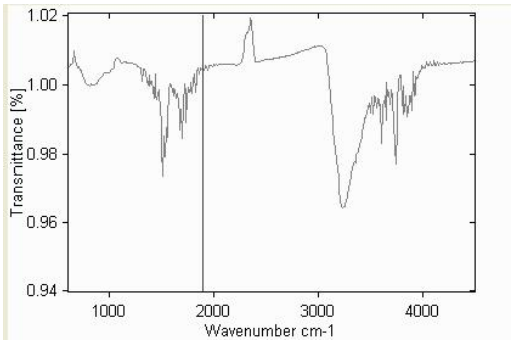

Figure 4. FTIR spectrum of the volatiles evolved at the 2041st second during TGA measurement.

SEM micrographs of the wood dust before and after oxidation are presented in the **Figure 5** and **6**. Fibrous structure of the wood was destroyed and a structure with a relatively greater porosity seemed to form after the oxidation experiments.

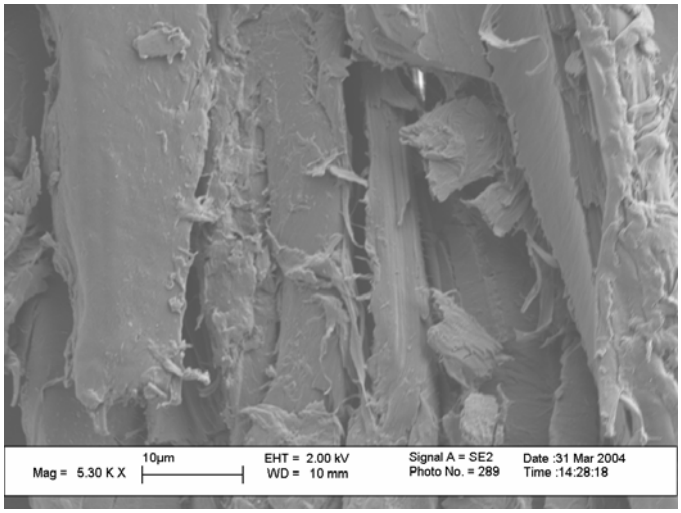

Figure 5. SEM micrograph of the wood dust before oxidation.

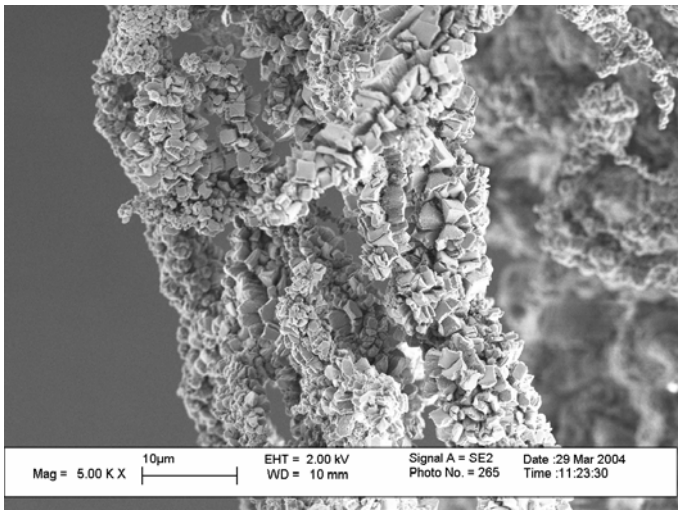

Figure 6. SEM micrograph of the wood dust after oxidation.

Conclusions

The effect of heat treatment on the calorific values and structural changes of a wood sample before its oxidation was investigated by using a TGA system and scanning electron microscope. Heat treatment up to 200°C increased the calorific value of the wood. Structural changes during oxidation reactions observed indicated the loss of volatiles and production of pporosity on the surface of the residue. The work is in progress and it is expected that the complete set of analysis of the material evolving during oxidation and changes in the morphology of the residual material of wood are being investigated in detail.

References

1. Dornburg, V.; Faaij, A. P. C. *Biomass and Bioenergy* **2001**, *21*, 91-108.
2. Mc Gowin, C. R.; G.A., W. *Biomass and Bioenergy* **1997**, *10*, 167-175.
3. Holliday, L. *Ionic Polymers*; John Wileys & Sons: New York - Toronto, 1975.
4. Wahlund, B.; Yan, J.; Westermark, M. *Biomass and Bioenergy* **2003**, *26*, 531-544.

KINETICS OF PULVERIZED COAL COMBUSTION AT HIGH PRESSURES

Donlad. J. Eckstrom, Albert S. Hirschon*, Ripudaman Malhotra*, Stephen Niksa[#]*

*SRI International, 333 Ravenswood Avenue
Menlo Park, CA 94025
[#]Niksa Energy Associates, 1745 Terrace Dr., Belmont, CA 94022

Introduction

As part of the U.S. Department of Energy's project called "High Pressure Coal Combustion Kinetics," SRI has performed a series of experiments on pulverized coal that are characteristic of the near burner flame zone (NBFZ). The objectives of these experiments are (a) to provide new data for pressurized coal combustion that benchmark kinetic models for pyrolysis, gaseous and solid product production and burnout, and pollutant formation, and (b) to generate samples of solid combustion products for analyses to fill crucial gaps in knowledge of char morphology, formation of inorganic fumes and fly ash, and fly ash utilization potential for combustion at high pressure. In pursuit of these objectives, we determine all solid, aerosol, and gaseous product formation during the transition from secondary pyrolysis, through vapor phase and soot burnout, to partial char burnout. In another phase of this project, the data from these experiments are being used to develop chemistry submodels that could be plugged into full-scale CFD simulators.

Tests in the NBFZ test configuration simulate near-burner p.f. flame conditions without the complications of turbulent, rotational, swirling flow fields. For tests with a particular fuel-type, particle size, and pressure, the furnace temperature, suspension loading, and nominal residence time are fixed while the inlet O_2 concentration is varied from 0 to 50 %, to progressively increase the S. R. values. A case without O_2 determines the total volatiles yield and distributions of so-called secondary volatiles pyrolysis products, which are the volatiles and soot remaining after the primary volatiles from the coal are pyrolyzed further in hot gases. They consist of soot, oils, CH_4, C_2H_2, CO, CO_2, H_2O, H_2, H_2S and N-species. As the inlet O_2 level is progressively increased in succeeding tests, the process chemistry moves through oxidative pyrolysis, volatiles combustion, soot oxidation, and char oxidation. Of course, these stages exhibit considerable overlap, depending on the relative burning rates of the various fuels in the reaction system. They are resolved by depletion of the available O_2; i.e., flows with higher inlet O_2 levels progress deeper into the sequence of chemical reaction stages before the flames are extinguished by the consumption of O_2.

Experimental

The Experimental Facility. The experiments were performed in a slightly modified version of our pressurized-radiant coal flow reactor shown schematically in **Figure 1**.[1] The pulverized coal path begins in the pressure vessel on the left, in which a positive displacement feeder releases coal into the drop tube where it is entrained by gases fed into the pressure vessel from below. The entrained coal passes through a U-tube and is fed into the central tube of the injector. A sheath flow of the same gas composition is fed into an annulus that surrounds the core flow; the areas, and therefore the flow rates of the entrainment and sheath flows are equal. The sheath flow was designed to keep coal particles from impinging on the flowtube walls in the hot zone, but modeling studies show that at the high pressures of these experiments turbulence rapidly mixes the particles throughout the tube cross section, and, in fact, tends to concentrate them near the walls (Liu and Niksa 2003).

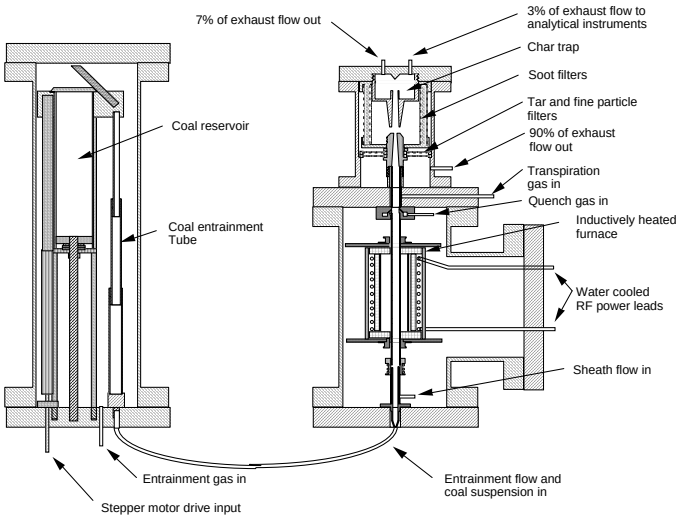

Figure 1. SRI's short-residence-time radiant-coal-flow reactor (SRT-RCFR).

The flow tube in these experiments was made of mullite, and was 16 mm OD x 12 mm ID. This tube passes through a furnace consisting of an RF-induction heated graphite sleeve of 10 cm diameter and 15 cm length. The graphite temperature is maintained in the range of 1560 – 1620 °C during the experiments, resulting in a radiant flux on the mullite tube of approximately 60 W/cm^2. The mullite tube is in near radiative equilibrium with the graphite, leading to a comparable mullite wall temperature as well as a comparable radiative flux on the particles within the tube.

The entrainment gas was argon with a varying percentage of oxygen. Because these gases are transparent to infrared radiation, the gas within the furnace is heated by a combination of conduction from the walls and convection from the radiatively superheated particles. In the absence of combustion, the gas temperature at the end of the furnace is calculated to be approximately 450 K while particle temperatures are approximately 1050 K.

At 5 cm downstream of the furnace, cold N_2 gas is injected into the flow stream at a rate of approximately 75% of the combined entrainment and sheath flow rate in order to drop the gas temperature to below 1,000 °C and thus to "freeze" the chemistry. The mixed flow is then transported through a sintered wall "transpiration" tube where another 25% of N_2 flow is added to reduce deposition on the tube walls. The flow is finally accelerated through a slightly converging nozzle into a virtual impactor called a centripeter. Particles with sufficient mass and momentum penetrate the quasi-stagnation flow at the tip of the char trap and are collected as "char." Lighter particles, characterized as tar and soot, follow the gas streamlines and are trapped on a series of quartz paper filters. Calculations indicate that the division between "heavy" and "light" particles occurs at around 15 – 20 μm. Since partially burned char particles are always larger than this and tar or soot particles are much smaller, the division between types of solid products is well defined.

After passing through the fine particle filters, the majority of the exhaust stream passes through a throttling valve that drops the pressure to atmospheric. A small fraction of gases is bled off through the char trap to assist in char capture, and additional gas is drawn from the same area for product analysis by a battery of instruments as shown in **Table 1**. Major products (CO, CO_2, H_2O) as well as O_2 are characterized to the 0.01% level, while hydrocarbons and nitrogen-containing species are measured to the ppm level. The analytical gas line is heated to minimize condensation of H_2O and oils.

Table 1. Analytical Equipment for Determining Various Gases

Analytical Equipment	Gases
Gas Chromatograph	CH_4, C_2H_x, C_3H_x, oils, H_2
FTIR	CO*, CO_2*, HCN*, NH_3, NO
Non-dispersive IR	CO, CO_2, H_2O
Paramagnetic Resonance	O_2
Wet Chemistry	HCN, NH_3

* Redundant determination

Solid product yields are determined gravimetrically. Tar samples are extracted from the filters by solution in THF followed by evaporative drying, and char, tar, and soot samples are submitted to an outside laboratory for elemental analysis. The coal feed rate is determined by calibration, and consistency of the measurements is confirmed by determining that the mass balance between coal fed and solid + gaseous products produced closes to within 5%. Furthermore, the elemental balance on C, H, and O typically also closes to 5%, with some excursions to 10%. Elemental nitrogen does not balance because we do not measure N_2 production, although at low oxygen levels N_2 is not a major product, and other species then close the N balance to about 20%.

Test Conditions. Three coals were tested, including two high volatile bituminous (Pittsburgh No. 8 and Illinois No. 6) and one western sub-bituminous (Powder River Basin). The coal samples were obtained from the Penn State coal bank; their specific identifications and properties are given in **Table 2**. Pitt #8 coal was tested at 1, 2, and 3 MPa (10, 20, and 30 bar), Illinois #6 was tested at 1 and 2 MPa, and PRB was tested at 1 MPa. The coal was ground, pre-classified by aerodynamic vortexing, and sieved to the double cut range of –140 + 200 (75 – 105 μm). Test samples were dried at 90°C overnight to moisture levels < 1% before being placed in the coal feeder reservoir.

Table 2. Composition of Coals Studied

Coal Name	Proximate Analysis, ad wt.%				Ultimate Analysis, daf wt.%				
	M	Ash	VM	FC	C	H	O	N	S
Pit. #8 DECS 23	0.7	12.3	37.9	49.1	80.8	5.4	5.8	1.7	6.3
Ill. #6 DECS 24	0.2	17.3	35.8	46.7	74.1	5.5	8.2	1.4	10.8
PRB DECS 26	0.1	5.0	39.4	55.5	73.7	5.6	19.0	1.1	0.6

The entrainment and sheath flow rates were adjusted to give an average velocity at the inlet to the furnace of 30 cm/s at all pressures. The nominal residence time in the furnace was then 500 ms, while actual residence times were substantially less because of expansion of the gas due to heating. The nominal coal feed rate was 1.5 g/min, resulting in suspension loadings of approximately 0.05 g_{coal}/g_{gas} at 1 MPa, 0.025 g_{coal}/g_{gas} at 2 MPa, and 0.017 g_{coal}/g_{gas} at 3 MPa. Higher coal feed rates led to problems of clogging or of overheating the flow tube. Oxygen concentrations in the entrainment and sheath flows ranged from zero to approximately stoichiometric. Absence of feed oxygen gave secondary pyrolysis conditions, while stoichiometric levels of oxygen were sufficient to convert tars and aerosols to soot within the available residence time. Seven to ten ratios of oxygen/coal were tested for each coal and pressure condition in order to map the transition from secondary pyrolysis through tar

Results and Discussion

Figures. 2-6 give an example of the results of measurements for Pittsburgh #8 coal at 1 MPa. **Figure 2** shows that secondary pyrolysis gives a char yield of 53% (char product/coal fed = 0.53 on a DAF basis), while the tar + soot yield was 23% (all product yields are given on a DAF basis). For this coal, an O_2/coal ratio of 2.1 corresponds to a stoichiometric ratio (S.R.) of 1. At S.R. = 1, 60% of the char and 90% of the soot have been consumed. Hydrogen is 95% consumed (**Figure 6**), while the volatile hydrocarbon products are essentially totally consumed at oxygen levels well below stoichiometric (**Figure 4**). The volatile nitrogen species HCN and NH_3 decrease by >99% and 90%, respectively, as the oxygen level increases, while NO increases (**Figure 5**). These opposing trends result in a minimum in the nitrogen pollutants at an S.R. = 0.75. Note that the experiments are conducted in Ar/O_2 mixtures rather than N_2/O_2 mixtures, so that the thermal NOx mechanism is not operative. Analogous sets of data were collected at other pressures and for the other coals to study the effect of pressure and coal type on the combustion.

The effects of pressure on pyrolysis and combustion of Pittsburgh #8 coal are summarized in **Figures 7-9**. In these figures, the burnout histories of char, soot, and hydrocarbons with increasing oxygen are presented in the form of percent burnout of the initial quantity of each species produced by secondary pyrolysis. The increasing thermal capacity of the entrainment gas with increasing pressure results in lower gas temperatures, and thus delayed flame ignition, and it is this effect that dominates the reduced char burnout with increasing pressure seen in **Figure 7**. However, the same effect is not apparent in the soot and hydrocarbon burnout histories.

The effect of coal type at a pressure of 1 MPa is summarized in **Figures 10-12**. **Figure 10** shows that char burnout is much more extensive for the sub-bituminous PRB coal than for the bituminous Illinois #6 or Pittsburgh #8 coals, consistent with expectations based on coal rank. Similar trends hold for soot burnout shown in **Figure 11**, although this may be a thermal effect (i.e., somewhat higher flame temperatures and more extensive flames because of enhanced char burnout) since the soot compositions were found to be nearly independent of coal type.

Conclusions

In spite of the challenges of measuring complete gaseous and solid product yields at elevated pressures and temperatures, we were able to cover the entire NBFZ operating domain by running the SRT-RCFR facility at a fixed coal feedrate with variable inlet O_2 concentrations to impose the same range of S.R. at all test pressures. This strategy yielded datasets for three coals at 1.0, 2.0 and 3.0 MPa. These data represent a major advance in the fundamental characterization of near-burner p.f. combustion at elevated pressures.

The measurements are of such quality that only relatively small adjustments to the raw data were needed to close the balances on mass and C/H/N within ± 5 % in individual runs. The adjusted datasets show the expected tendency in the burnout of gaseous and solid fuels to increase steadily for progressively more oxidizing conditions. They also show that formation of NOx increases rapidly at S.R. values above 0.5. These data are well suited to serve as benchmarks for development of kinetic models for pyrolysis, gaseous and solid product production and burnout, and pollutant formation, as well as for characterizing char and ash properties. The data are also being used to tune chemical submodels that describe evolution of the different species in a manner that can be incorporated into full-scale CFD process simulators.[2]

Acknowledgement. This research was sponsored by the National Energy Technology Laboratory, U. S. Department of Energy, under subcontract Agreement No. FY00012SRI from Prime Contract DE-FC26-01NT40777 to Fluent Incorporated.

References

(1) Cor, J., Manton, N., Mul, G., Eckstrom, D., Olson, W., and Malhotra, R., *An Experimental Facility for the Study of Coal Pyrolysis at 10 Atmospheres*, Energy and Fuels, **14**, 692-700, 2000.

(2) Liu, G. and Niksa, S., *DoE High Pressure Coal Combustion Kinetics, Task 1.3. P-RCFR Simulations for NBFZ Tests*, Third Interim Report, March 26, 2003 (unpublished).

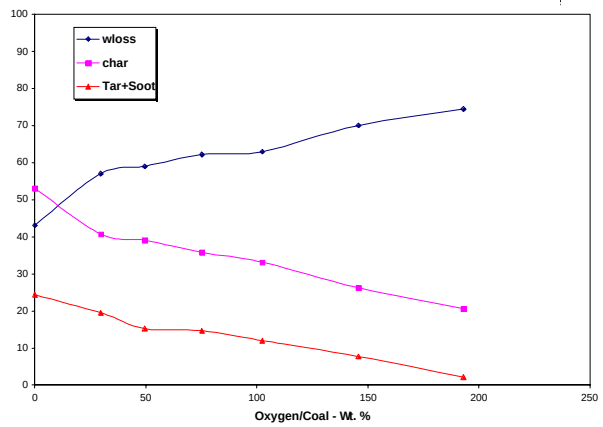

Figure 2. Yield of major products during combustion of Pitt coal at 1.0 MPa.

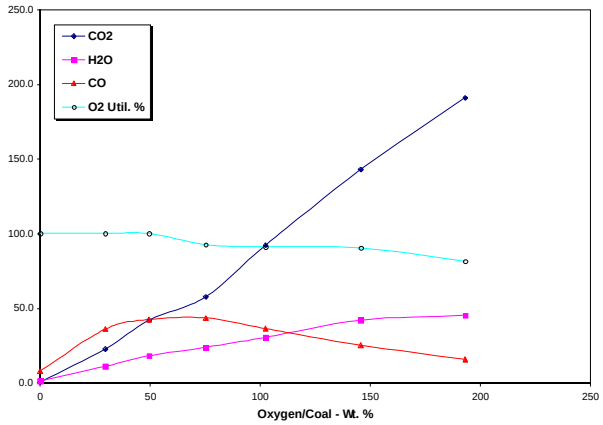

Figure 3. Yield of oxygenated gases during combustion of Pitt coal at 1.0 MPa.

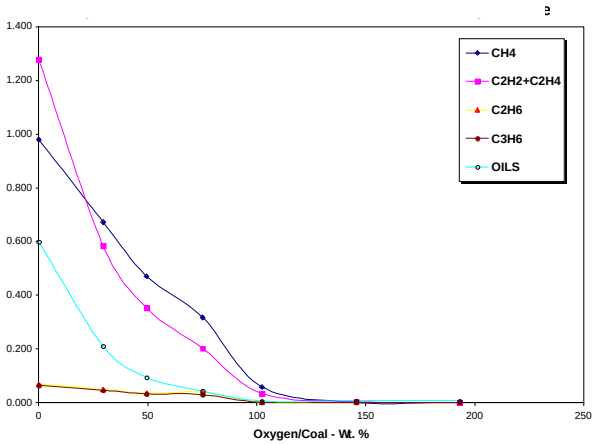

Figure 4. Yield of hydrocarbon gases during combustion of Pitt coal at 1.0 MPa.

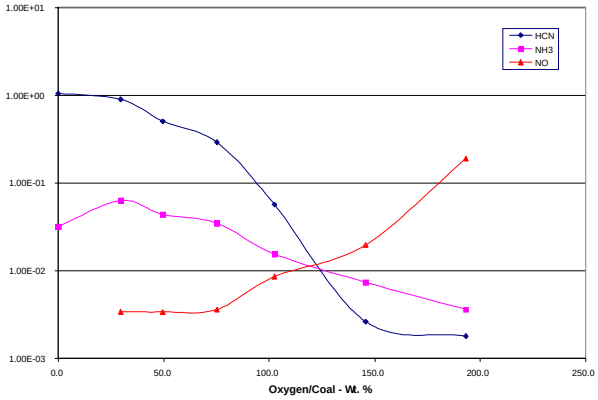

Figure 5. Yield of nitrogen gases during combustion of Pitt coal at 1.0 MPa.

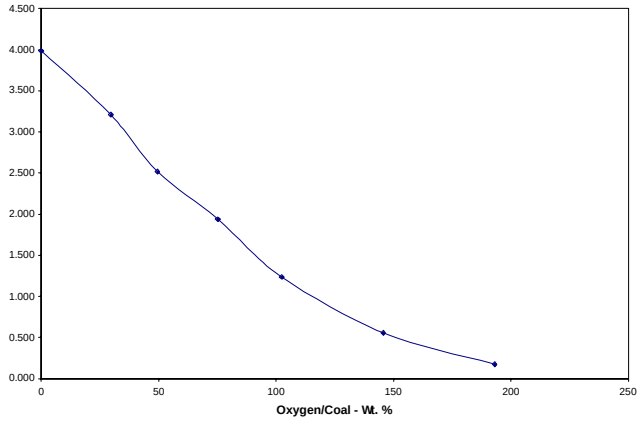

Figure 6. Yield of Hydrogen during combustion of Pitt coal at 1.0 MPa.

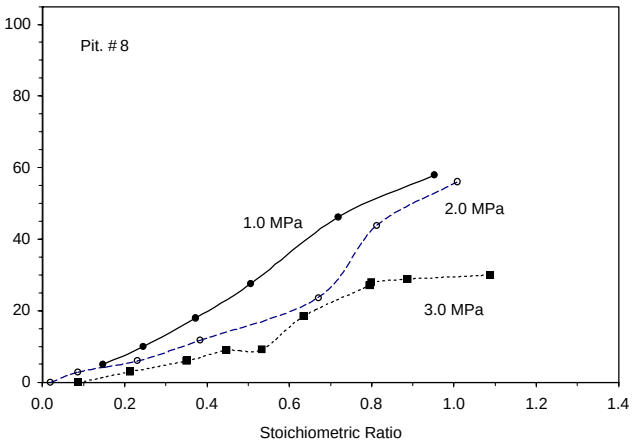

Figure 7. Char burnout at various pressures for Pitt coal.

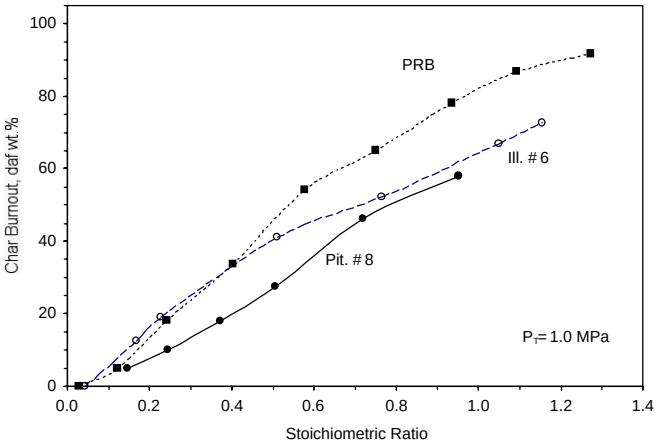

Figure 10. Char burnout for PRB, Pitt, and Ill coals at 1.0 MPa..

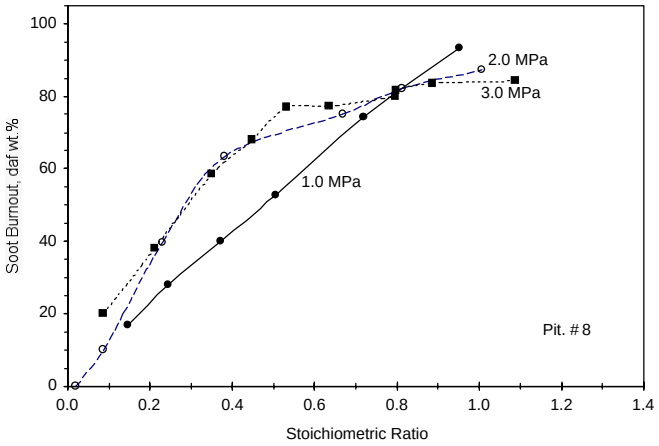

Figure 8. Soot burnout at various pressures for Pitt coal.

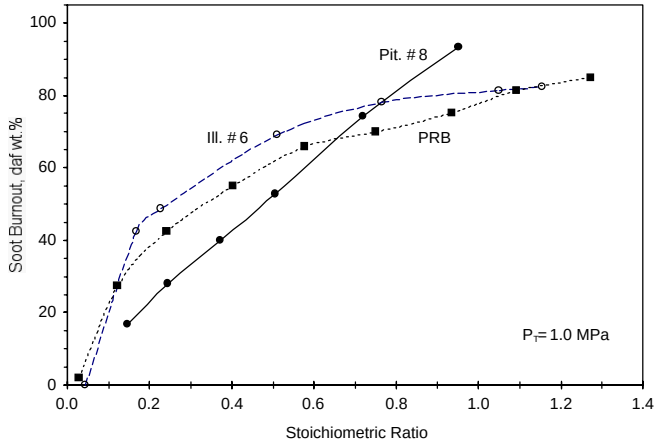

Figure 11. Soot burnout for PRB, Pitt, and Ill coals at 1.0 MPa..

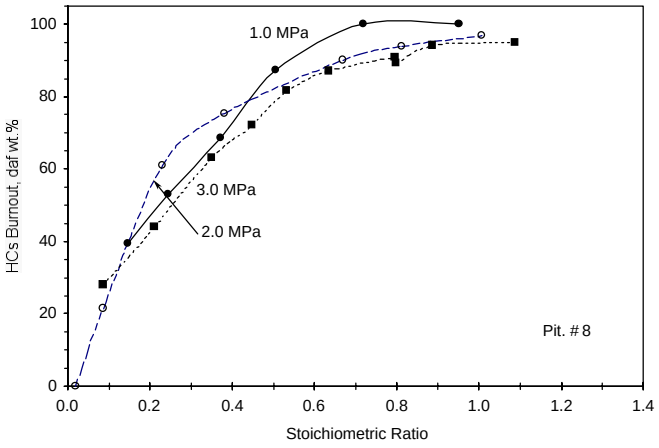

Figure 9. Hydrocarbon burnout at various pressures for Pitt coal.

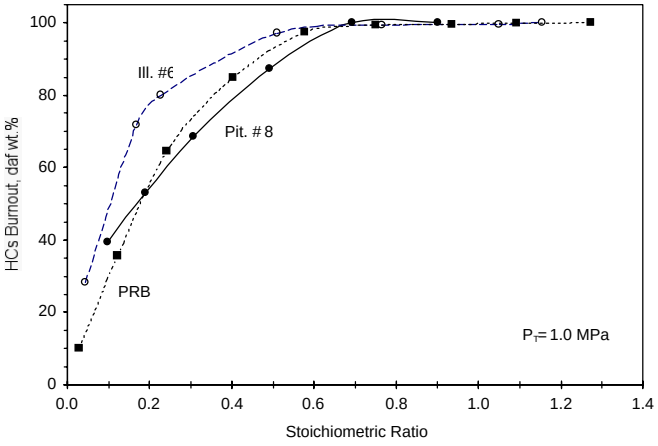

Figure 12. Hydrocarbon burnout for PRB, Pitt, and Ill coals at 1.0 MPa..

Application of a Circulating Fluidized Bed Process for the Chemical Looping Combustion of Solid Fuels

Yan Cao, Kunlei Liu, John T. Riley and Wei-Ping Pan

Institute for Combustion Science and Environmental Technology (ICSET)
Western Kentucky University, Bowling Green, KY 42101
Email: yan.cao@wku.edu

Introduction

In recent years more concerns have arisen about CO_2 emission due to global warming. Among available or proposed technologies, chemical looping combustion[1] (CLC) is the most promising technology to combine fuel combustion and CO_2 purification. It uses a solid oxygen carrier to transfer the oxygen from the air to fuel in a reducer and oxidizer. Thus, air is never mixed with the fuel, and the CO_2 does not become diluted by the nitrogen of the flue gas. NO_x formation can be largely eliminated. A number of metals have been discussed in the literature,[2] such as oxides of Fe, Ni, Co, Cu, Mn.

Solid fuels such as coal and biomass have been ignored in CLC process due to technical problems, including the separation of oxygen carrier from fuel and ash, the possible interaction between the fuel ash and oxygen carriers and the combustion of unburned carbon particles in the oxidizer due to the circulation of solid fuel particles. The adaptation of the CLC to the combustion of solid fuels presents many challenges.

In this paper, an innovative concept – application of a CFB combined with a moving bed on the chemical looping combustion of solid fuels is introduced.

Technical Approach

Is it possible to add solid fuel into a reducer directly? There exist several technical difficulties. The reaction rate between solid fuel and the oxygen carrier is slow for a solid fuel due to low solid-solid contact efficiency and reactivity. The solid fuel gasification rate is always 1000 times slower compared to combustion at the same evaluated temperature.

In order to overcome the technical difficulties mentioned, it is proposed that a CFB coupled with a moving bed be used for the chemical looping combustion of solid fuels. In this approach, the facility will consist of three major components – a high-velocity riser acting as an oxidizer, a down-flow moving bed acting as a gasifier and a low-velocity bubbling bed acting as a deep reduction reactor and separation device for the oxygen carrier from fuel ash as well as unburned carbon. The whole system uses two loop seals for oxygen carrier circulation.

Kinetic Analysis. The CLC process is governed by the prevailing chemical thermodynamics and kinetics. The gasification rate could be fast enough to match the rate of oxygen carrier reduction in the down-flow moving bed.

All reactions related to the pyrolysis and gasification of fossil fuel are endothermic, as illustrated by Equations (1), (2) and (3). In the proposed CLC system, the gasification process for solid fuel is combined with a reduction process for the oxygen carrier in the reducer where no oxygen exists. The only way to supply heat for the fossil fuel gasification process is the reduction reaction of oxygen carrier with the syngas produced.

$C_nH_mO_p \rightarrow (p\text{-}n)CO_2 + (2n\text{-}p)CO + (2/m)H_2$, 5 Kcal/mol (1)
$C + H_2O \rightarrow CO + H_2$, 28.3 Kcal/mol (2)
$C + CO_2 \rightarrow 2CO$, 38.4 Kcal/mol (3)

Just a few metal oxides that have been developed as oxygen carriers for the CLC process show exothermic properties when reacted with carbon. The possible reactions related to oxygen carrier candidates and carbon in the reducer are shown in Table 1. Thus, the enthalpy of solid fuel combustion in the chemical looping process is equal to the sum of the enthalpies of the two steps. Copper oxide shows an exothermic property due to the smaller enthalpy of its oxidizing step than those of solid fuel direct combustion.

Table 1. Reaction Enthalpies at 1000°C and 1 atm [3]

$C + O_2 \rightarrow CO_2$, -392.75 KJ/mol
Endothermic
$2\ NiO + C \rightarrow 2\ Ni + CO_2$, 75.21KJ/mol
$2\ MnO + C \rightarrow 2\ Mn + CO_2$, 378.98 KJ/mol,
$2\ Mn_3O_4 + C \rightarrow 6\ MnO + CO_2$, 56.7 KJ/mol
$2/3\ Fe_2O_3 + C \rightarrow 4/3\ Fe + CO_2$, 146.37 KJ/mol
$2\ PbO + C \rightarrow Pb + CO_2$, 32.82 KJ/mol
Exothermic
$2\ CuO + C \rightarrow Cu + CO_2$, -96.51 KJ/mol
$2\ Cu_2O + C \rightarrow 4\ Cu + CO_2$, -61.04
$2\ Mn_2O_3 + C \rightarrow 4\ MnO + CO_2$, -33KJ/mol

Lead is a hazardous element and not used. Manganese oxides could produce non-reactive compounds. Also, there is a thermodynamic limitation in the reduction reaction of manganese. Most of oxygen in copper oxide is active for reaction with methane, and the highest efficiency could be achieved. Thus, it is selected as the preliminary candidates for oxygen carriers for the CLC for solid fuel combustion.

Thermodynamics Analysis. Chemical reaction thermodynamics phase diagram for the reduction reactions by CO produced in solid fuel gasification process are shown in Figures 1.

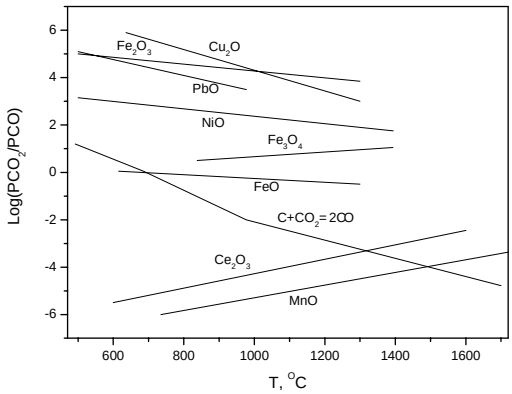

Figure 1. Variation of the thermodynamics equilibrium factor for MeO-CO as a function of temperature[3]

Figure 1 shows that the ratio varies from approximately 10^5 for the reduction of Cu_2O to values on the order of 10^{-5} or less for the reduction of MnO to Mn. For the reduction of a metal oxide with CO in the absence of solid carbon, the oxides of copper, lead and nickel will be reduced to elemental form at gas ratios between 10^5 and 10^2. Therefore, the completeness of the reaction could be

achieved and a concentrated CO_2 stream will be obtained in the proposed CLC system. The reduction of manganese requires a CO_2-free environment, which is practically impossible for the CLC of solid fuel to achieve. Because carbon is also present in the reaction mixture in the proposed reducer, the reduction of metal oxide and carbon gasification to CO_2 occurs simultaneously. As shown in Figure 1, above the simultaneous equilibrium temperature where two curves for the reduction of metal oxides and the Boudouard reaction intersect, MnO needs to be above 1600^{o}C, which is impossible in the CLC due to high temperature. In contrast, the curves for NiO, Cu_2O, PbO and Fe_2O_3 do not have intersection with the carbon curve even at low temperatures. The simultaneous reactions are not limited by thermodynamics, they are determined entirely by kinetics, which typically are fast in the CLC. Thus, using NiO, Cu_2O, CuO and PbO as oxygen carriers could result in higher ratios of $P_{CO2}/P_{CO.}$

Similarly, analysis of the reduction of metal oxides with H_2 shows that it is less exothermic than its corresponding reaction with CO. Moreover, equilibrium of the water-gas reaction will occur and shift to the right at lower temperatures. This shows H_2 at high temperature is a better reducing agent than CO for oxygen carriers.

Process Analysis. The volume of the gas flow in the air reactor is much larger than that in a reducing reactor because a large amount of nitrogen in the air is carried in. Moreover, the oxidizing rate of the oxygen carrier is much faster than the rate of the reducing reaction. Thus, a high gas velocity is chosen in the oxidizing reactor to keep a reasonable size reactor and to reduce the capital cost. In the reducer, long residence times, on the order of minutes, is needed for solid fuel gasification and oxygen carrier reduction due to slow reaction rates. Meanwhile, only a small amount of gas is needed for fossil fuel gasification, so a down-flow moving bed was selected. In accordance with the huge density and size differences between ash and the oxygen carrier, a low-velocity bubbling bed was chosen to separate the oxygen carrier from fuel ash as well as unburned carbon. The whole system uses two loop seals for oxygen carrier circulation.

Conclusions

Purifying CO_2 in an efficient and energy-saving way is the first and most important step for its sequestration. Chemical looping combustion could achieve this goal when it is applied to solid fuel in a highly practical way. An innovative concept was proposed to apply a CFB combined with a moving bed in the CLC of solid fuels. A coal gasification process which occurs in the moving bed in a loop seal, will be combined with a reduction process of metal oxide to achieve direct utilization of solid fuel. Thermodynamics Analysis showed that using Cu_2O, CuO as oxygen carriers could result in higher ratios of P_{CO2}/P_{CO} in solid fuel CLC process.

References

1. Marion, J.; Naskala, Y.N.; Griffin, T. "Controlling Power Plant CO_2 Emissions: a Long Range Approach," *Proceedings* of the First National Conference on Carbon Sequestration, **2001**, Washington, DC, DOE/NETL-2001/1114. (on CD-ROM).
2. Mattisson, T.; Jarders, A.; Lyngfelt, A. "Reactivity of some Metal Oxide Support on Alumina with Alternating Methane and Oxygen-application for Chemical-looping Combustion," *Energy & Fuels*, **2003,** *17*, 643-651.
3. P.W. Atkins. *Physical Chemistry*, fifth edition, W.H. Freeman and Company, New York.

CARBONACEOUS MATERIALS FOR GAS PHASE DESULFURIZATION: ROLE OF SURFACE HETEROGENEITY

Andrey Bagreev, Teresa Bandosz

Department of Chemistry, The City College of New York
New York, N Y 10031

Introduction

Removal of sulfur containing species becomes nowadays a strategic issue [1, 2]. It is due to strict environmental regulations combined with searching for new clean sources of energy such as fuel cell. For fuel cell application gaseous fuel has to be almost free of sulfides or mercaptans. Those species poison the reforming catalysts thus causing shortening of the life-time of a cell and an increase in the costs of energy. Since sulfur containing gases are toxic and they have very low odor threshold all efforts are made to filter air form facilities where anaerobic digestion can occur such as, for instance form municipal waste water treatment plants [3-6].

Among various methods used to remove hydrogen sulfide, adsorption on activated carbons is considered as a very efficient and cost effective approach. This is the result of unique surface properties of carbonaceous adsorbents [7-10] such as high surface area, and pore volume, along with surface chemistry, which promotes catalytic oxidation of H_2S in the presence of even small amounts of air and moisture [11-23]. As a result of surface reaction, hydrogen sulfide is oxidized either to sulfur or sulfur dioxide. The latter process, in order to retain a significant amount of sulfur species on the surface, has to proceed further and SO_2 is oxidized to sulfuric acid. Due to the reactions mentioned occur at room temperature and under atmospheric pressure the physical adsorption of hydrogen sulfide is negligible at these conditions [15].

To enhance the catalytic properties of activated carbon various methods have been used [2] from which the most common is impregnation of activated carbon with sodium or potassium hydroxide or salts containing potassium such as potassium carbonate [3, 5, 23-27]. Doing this only slightly increases the cost of materials leading to the much better performance [6]. But since an ideal solution never exists the application of caustic impregnated carbons carries certain drawbacks. The most significant is a low ignition temperature. In the presence of caustic a strong exothermic reaction occurs and a carbon bed can easily self-ignite resulting in enormous cost of extinguishing and a widely spread environmental damage. Another issue is related to safety of working with hazardous materials, as is a caustic solution present on the surface of carbons.

All of these resulted in a search for better adsorbents that, with sustained efficiency, would be much safer to work with. The window of opportunity opened in surface chemistry of carbons. This is an important factor governing their catalytic properties [10, 28, 29]. One method of modification, usually applied during production of adsorbent, is introduction of nitrogen containing groups [30-32]. Like in the case of caustic materials, such carbons are basic and the high dispersion of catalytic sites in the pore system provides efficient oxidation. The catalytic action is so pronounced that a surface of such carbons not only converts hydrogen sulfide to sulfur as in the case of caustic impregnated materials, but oxidation proceeds even further to sulfuric acid. The presence of sulfuric acid was seen as another "plus" in application of nitrogen enriched adsorbents. They can be washed out with water and thus they regeneration is inexpensive. The Calgon patent describing the performance of Centaur® claims that after loosing 20% the initial capacity as a result of the first run, the carbons maintain their performance on 80% level practically forever [31]. Taking into account that the capacity of such carbon is about half of the capacity of the caustic impregnated materials the situation looked almost ideal. But, as mentioned above an ideal solution does not exit. Additional step in the preparation of carbon (impregnation with urea of low temperature chars) increases the cost of materials. Although the smaller capacity than that of caustic impregnated carbon can be compensated by many steps of inexpensive regeneration, once again the practical and safety reasons limit the applications of such carbons. Concentrated sulfuric acid present on the surface can lead to health hazard (skin burning) and many facilities do not feel comfortable with regeneration system where strong acid is generated.

The mentioned above factors directed the attention of scientists and engineers to virgin materials. During the last few years the performance and suitability for hydrogen sulfide removal of many types of unmodified carbon have been described in the literature [6, 13-16, 33]. When the concentration of hydrogen sulfide in air is less then 100 ppb virgin carbons can provide the sufficient protection for few years [6]. It was shown that the capacity and the degree of hydrogen sulfide oxidation depend on the porosity and the surface chemistry [13-16]. Moreover, the content of inorganic matter in ash has proven to be important [34]. This concept led to the development of new, sewage sludge adsorbents [35-38]. Although their content of carbon is only about 20 %, their capacity is much better than that of virgin, coconut shell based activated carbon. An important advantage of those materials is conversion of hydrogen sulfide to sulfur and low costs of production.

An objective of this paper is to demonstrate the importance of surface heterogeneity and its effect on the amount of hydrogen sulfide adsorbed on carbonaceous materials and on the products of surface reactions. Very often the choice of adsorbent is governed not only by its cost and removal capacity but also by the other factors such as, for instance, the possibility of regeneration or the level of toxicity of the spent materials. The results presented here summarize the effects of surfaced features on the capacity and chemistry of the processes occurring during adsorption of H_2S on carbonaceous materials.

Experimental

Materials. Five carbonaceous materials were investigated in this research. They are as follows: STIX (cautic impregnated bituminous cola based- Watrelink Barnabey and Sutcliffe) Midas OCM^{TM} (US Filters) [39], Centaur® (Calgon), S-208 (coconut shell based- Waterlink Barnabey and Sutcliffe), and laboratory made sewage sludge derived adsorbent, referred here as SC carbon. After exhaustion in H_2S breakthrough capacity test the letter E is added to the name of the samples.

Methods

H_2S breakthrough capacity. The standard dynamic test (ASTM D 6646-01) [40] was used to evaluate the performance of carbons for H_2S adsorption. Humidified air (relative humidity 80% at 293K) containing 1% (10,000ppm) of H_2S was passed through a column of carbon (diameter 1", bed height 9"). The test was stopped at breakthrough concentrations of 50 ppm. Then the breakthrough capacity for H_2S adsorption was calculated using concentration of adsorbat, flow rate, breakthrough time and volume of carbon.

pH of carbon surface. A pH of the carbon surface was evaluated according to ASTM D 3838 standard procedure. Briefly, 10 g of activated carbon was placed in 100 mL of hot water and boiled gently for 900 s. Then the flask content was filtered, filtrate was cooled, and pH was measured.

Sorption of nitrogen. Nitrogen isotherms were measured using a ASAP 2010 (Micromeritics) at –196 ^{o}C. Before the experiment the samples were heated at 120 ^{o}C and then outgassed at this temperature under a vacuum of 10^{-5} Torr to constant pressure. The isotherms were used to calculate the specific surface area, micropore volume (DR method), V_{mic}, mesopore volume, V_{mes}, total pore volume, V_t,, and pore size distributions [41-42].

Thermal analysis. Thermal analysis was carried out using TA Instruments Thermal Analyzer. The instrument settings were: heating rate 10 deg/min and either air or nitrogen atmosphere with 100 mL/min flow rate. The residues after heating in nitrogen and air (ash content) at 1000^{o}C are reported. From the experiments run in air the ignition temperature was determined [6]. Experiment carried out in nitrogen provided information about the speciation of surface oxidation products.

Apparent density. Apparent density of carbons was evaluated using ASTM Method D 2854 [43]. It is determined on a granular sample be measuring the volume packed by a free fall from a vibrating feeder into an approximately sized graduated cylinder and determining the mass of the known volume.

Moisture. Content of moisture was evaluated using ASTM Method D 2867 [43]. A sample of carbon is put into a dry, closed weighting dish and weighted accurately. Then the dish is opened and placed with the lid in a preheated oven. The sample is dried to constant weight and cooled in dessicator. The weight loss is expressed as a percentage of the weight of the original sample.

Results and Discussion

From the measurement of the hydrogen sulfide breakthrough curves, taking into account the density of materials, the breakthrough capacity was calculated. The results are summarized in Table 1 along with the pH values of the carbon surfaces. Analyzing the data it is seen that Midas® outperforms other materials. Its capacity per unit volume bed is twice higher than that of Centaur® whereas the capacity the sewage sludge derived material is twice higher than that of STIX. The carbons also behave differently when water adsorption is considered. As shown previously [34], presence of water is a crucial factor enhancing hydrogen sulfide adsorption. It enables dissociation of to HS^- ions [13], when the pH allows it. It is well known that activated carbon surface is considered as hydrophobic. Adsorption of water usually occurs as a result of the presence of oxygen or nitrogen containing functional groups and inorganic matter [44]. High adsorption of water on Midas® and Centaur® is the result of long exposure to humidified air (longest breakthrough time) and also affinity of surfaces to retain water. In the case of Centaur® this is linked to the nitrogen containing groups whereas in the case of Midas® hydration of inorganic matter likely plays a role.

In order to discuss the performance of materials as removal media in the process where catalytic action is expected to enhance their performance, the structural and chemical features of surfaces have to be described. The simplest estimation of carbon surface chemistry is the measurement of the pH of its water suspension [13]. As listed in Table 1 all materials are basic and the pH of Midas and SC is over 10. That pH is the result of the presence of inorganic matter (basic oxides). In the case of Centaur® the closest to neutral pH value is caused by protonation of the nitrogen containing groups [45]. High pH of STIX is caused by the presence of potassium hydroxide.

Table 1. H_2S Breakthough Capacity, Amount of Water Adsorbed and pH Values of the Carbon Surfaces.

Sample	H_2S breakthrough capacity [g/g of carbon]	H_2S breakthrough capacity [g/cm^3 of carbon]	Water adsorbed [mg/g]	pH initial	pH exhausted
S208	0.036	0.02	0.04	9.8	8.82
Centaur®	0.130	0.060	0.41	8.30	1.47
Midas®	0.608	0.251	0.12	10.85	10.38
STIX	0.230	0.140	0.06	10.2	7.2
SC	0.079	0.052	0.03	10.58	9.63

The amount of ash in each material may indicate the importance of the presence of catalytic inorganic phase (Table 2). In the case of SC and Midas® the ash content is the highest. In SC it comes as a natural component of the sewage sludge precursor [35-38] whereas, in the case of Midas it was added as a part of the material preparation procedure [39]. It is important to mention that the ash content of Midas® twice exceeds the content of basic metals oxides described in the patent [39]. Relatively high amount of ash in Centaur® is linked to its bituminous coal origin. In the case of STIX about 13% of ash has its main origin in potassium hydroxide used for impregnation along with ash coming from a bituminous coal precursor.

Table 2. Density, Ash Content, Ignition Temperature and the Initial Moisture Content.

Sample	Bulk density [g/cm^3]	Ash content [%]	Moisture [%]	T_{ign} [^{o}C]
S208	0.55	1.9	5.2	425
Centaur®	0.48	5.5	6.6	510
Midas®	0.41	26.8	12.2	524
STIX	0.60	12.9	8	320
SC	0.66	76.9	2.5	426

From the nitrogen adsorption isotherms the structural parameters were calculated. They are collected in Table 3. The data clearly shows that Midas® has the highest surface area and pore volume whereas SC- the lowest. Also, either for the latter carbon or Midas® a significant contribution of mesoporosity is found. On the other had, S-208, Centaur®, and STIX, are very homogenously microporous. The highest nitrogen uptake noticed for Midas®, the lowest for SC, which is related to the differences in the chemical composition of materials. Midas® contains 70% of carbonaceous phase, SC- only 20.

Not only porosity but also the density of materials is liked to their content of inorganic matter. The densest is SC, then Midas, Centaur and S-208. This has an effect on the capacity calculated per gram (Table 1) and thus affects the cost of materials in real life operations.

The evaluation of the materials' performance is more valid when the products of surface reaction are discussed. The pH values of exhausted carbons listed in Table 1 clearly indicate the differences in the surface reaction products. Highly acidic pH of Centaur® and a noticeable decrease in the pH for S-208 and STIX suggest a significant degree of sulfuric acid formation. For SC and Midas® the pH, however slightly decreases, is still on a very high level. Such a

decrease can be caused by formation of sulfides and sulfates from oxides. Those species and sulfur, should not cause dramatic decrease in the pH value.

Table 3. Structural Parameters Calculated from Sorption of Nitrogen.

Sample	S_{N2} [m^2/g]	V_{mic} [cm^3/g]	V_t [cm^3/g]	V_{mic}/V_t
S208	877	0.43	0.46	0.96
S208E	800	0.40	0.42	0.95
Centaur®	987	0.44	0.56	0.79
Centaur®E	443	0.18	0.26	0.69
Midas®	1110	0.43	0.81	0.53
Midas®E	95	0.03	0.14	0.21
STIX	620	0.30	0.35	0.85
STIXE	340	0.18	0.26	0.69
SC	98	0.04	0.16	0.25
SCE	28	0.01	0.10	0.10

Comparison of the DTG results obtained on exhausted samples (the low temperature peak, < 250 ^oC for pure carbon materials represents removal of SO_2 from reduction of sulfuric acid [13-16] and the peaks between 300- 500 ^oC are linked to removal of sulfur from various pore sizes (from larger to smaller) [13-16]) revealed that indeed in the case of Centaur® almost only SO_2 is released, for -S208 and STIX there is a mixture of SO_2 and elemental sulfur . In the case of Midas® a huge peak representing removal of sulfur from pores of various sizes was found. For sewage sludge derived adsorbent a broad peak present between 200-400 ^oC represents sulfur [36-38]. Although its position is close to that for sulfuric acid ion S208 that shift is caused by removal of sulfur from large pores, which are present in this material. This process requires much less energy (lower temperature) than evaporation of sulfur polymers from the microporous structure as that in S-208.

Those significant amounts of sulfur adsorbed on the materials studied are stored in their pore system. As shown from Table 1 for all carbons the volumes of pores, micropores in particular, significantly decreases. This is of course linked to the decrease in the surface areas. An exact location of oxidation products is seen from the analysis of pore size distributions for carbons after exhaustion. Whereas for S-208 and Centaur® mainly volumes in pores smaller than 20 Å are affected for SC and Midas® sulfur is deposited in all pore sizes and smaller micropores are completely filled. It looks like the capacity lasts until that volume is exhausted and more pore volume would provide more capacity as expected when the catalytic actions is involved.

Another important factor which should be evaluated here is the ignition temperature of adsorbents (Table 3). The evaluation of temperature of self-ignition based shows high ignition temperature of catalytic carbons. The ignition temperatures of S-208 and SC are almost identical and about 100 ^oC lower that that for Centaur® and Midas®. Since manufacturing of those carbons requires additional steps some additive may work as fire retardants. Low ignition of caustic impregnated carbon is the result of the presence of highly reactive potassium hydroxide.

Based on the comparison presented above, and the results published elsewhere where the mechanisms of adsorption/oxidation are discussed [13, 26, 33, 36-38], the materials containing a catalytically active inorganic phase mixed with the activated carbon seem to be the best performing adsorbents. On their surface, thanks to the presence of catalytic oxides, hydrogen sulfide is oxidized to sulfur. The catalytic action is complex and consists of two different mechanisms: one on pure activated carbon surface and one on the catalytic phase. It is likley that the reaction of H_2S oxidation occurs on the carbon and oxides surfaces simultaneously with formation of elemental sulfur, metal sulfides and sulfuric acid which later reacts with carbonates.

As indicated above, the presence of water on activated carbons contributes to the dissociation of hydrogen sulfide and facilitates to its oxidation to sulfur and sulfur dioxide [33] The proposed mechanism involves 1) H_2S adsorption on the carbon surface, 2) its dissolution in a water film, 3) dissociation of H_2S in an adsorbed state in the water film , 4) surface reaction with adsorbed oxygen with formation of elemental sulfur 4a) or sulfur dioxide 4b), and 5) further oxidation of SO_2 to H_2SO_4 in the presence of water :

$$H_2S_{gas} \xrightarrow{K_H} H_2S_{ads} \quad (1)$$

$$H_2S_{ads} \xrightarrow{K_S} H_2S_{ads\text{-}liq} \quad (2)$$

$$H_2S_{ads\text{-}liq} \xrightarrow{K_a} HS^-_{ads} + H^+ \quad (3)$$

$$HS^-_{ads} + O^*_{ads} \xrightarrow{K_{R1}} S_{ads} + OH^- \quad (4a)$$

$$HS^-_{ads} + 3\,O^*_{ads} \xrightarrow{K_{R2}} SO_{2\,ads} + OH^- \quad (4b)$$

$$SO_{2ads} + O^*_{ads} + H_2O_{ads} \xrightarrow{K_{R3}} H_2SO_{4\,ads} \quad (5)$$

$$H^+ + OH^- \longrightarrow H_2O \quad (6)$$

where H_2S_{gas}, $H_2S_{ads\text{-}liq}$, and H_2S_{ads} correspond to H_2S in gas, liquid and adsorbed phases, respectively; K_H, K_S, K_a and K_{R1} , K_{R2} , K_{R3} are equilibrium constants for related processes (adsorption, gas solubility, dissociation, and surface reaction constants); O^*_{ads} is dissociatively adsorbed oxygen, S_{ads} , SO_{2ads} , $H_2SO_{4\,ads}$ represent sulfur, SO_2 and H_2SO_4 as the end products of the surface oxidation reactions.

It is known that oxides of iron, zinc and copper are used in industry as absorbents and /or catalysts of H_2S removal from different gaseous media at low (20-200^oC) and high (300-800^oC) temperatures [2]. The H_2S removal at low temperatures mainly occurs due to gas-solid reactions in a thin hydrated lattice of metal oxides. This process leads to sulfides formation:

$$ZnO + H_2S \longrightarrow ZnS + H_2O \quad (7)$$

$$CuO + H_2S \longrightarrow CuS + H_2O \quad (8)$$

$$Fe_2O_3 + 3H_2S \longrightarrow FeS + FeS_2 + 3H_2O \quad (9)$$

$$Fe_2O_3 + 3H_2S \longrightarrow Fe_2S_3 + 3H_2O \quad (10)$$

$$2Fe_2S_3 + 3O_2 \longrightarrow 2Fe_2O_3 + 6S \quad (11)$$

Carbonates of calcium and magnesium are also supposed to have high affinity for H_2S adsoption in wet condition due to neutralization reactions ([7]

$$CaCO_3 + H_2S \longrightarrow Ca(HCO_3)_2 + Ca(HS)_2 \quad (12)$$

Moreover, transition metal ions can catalyze the H_2S oxidation in aqueous solutions by molecular oxygen due to the redox process

[2]. For example, in the case of iron the following reactions may occure:

$2Fe^{3+} + HS^- \text{ ----> } 2Fe^{2+} + S + H^+$ (13)

$4Fe^{2+} + O_2 + 2H^+ \text{ ----> } 4Fe^{3+} + 2OH^-$ (14)

On the surface of caustic impregnated carbon the following reaction path have been proposed in addition to those occurring on the surface of pure carbon [21]s:

$NaOH + H_2S \text{ ---->} NaHS + H_2O$ (15)

$2NaOH + H_2S \text{ ---->} Na_2S + H_2O$ (16)

$NaHS + 0.5O_2 \text{ ---->} S + NaOH$ (17)

$Na_2S + 0.5O_2 + H_2O \text{ ---->} S + 2\ NaOH$ (18)

$2\ NaOH + H_2SO_4 \text{ ---->} Na_2SO_4 + 2H_2O$ (19)

And side reactions:

$NaOH + CO_2 \text{ ---->} NaHCO_3$ (20)

$2NaOH + CO_2 + H_2O \text{ ---->} Na_2CO_3 + 2\ H_2O$ (21)

$Na_2CO_3 + H_2S \text{ ---->} NaHCO_3 + NaHS$ (22)

The presence of NaOH and strongly basic environment enhances the dissociation of hydrogen sulfide. Moreover, according to the reactions 17-18, NaOH and basic environment is regenerated in the system enabling more H_2S to be dissociated and, as a final product, oxidized to elemental sulfur following reaction 17. The results published elsewhere [28] showed that on one mole of NaOH 3 to 4 moles of H_2S are adsorbed which clearly indicates the catalytic effect of the carbon surface. A question raises what causes that the reaction stops and it stops when almost the same capacities are reached on all materials. The possible reason for this is "inactivation" of sodium hydroxide. This may happen as a result of reactions 19-20 where carbonates and sulfates are formed on the surface. Although the pH remains basic in most cases, this can be due to the presence of carbonates not hydroxide. It makes the formation of sodium sulfides, sodium hydrogen sulfides, sodium sulfates, and sulfuric acid the most important reactions in this system. When all NaOH is used sulfuric acid is formed which was observed as very low pH of exhausted samples used in sewage treatment plants [6]. On the other hand, following reactions 1-11, and 17, sulfur must be formed in the system and it does not affect the surface pH.

Slightly different pattern than that on the virgin carbon surface is proposed to occur on the surface of catalytic carbon , Centaur®. This is a very microporous carbon enriched with nitrogen [32]. That nitrogen is likely in the form of pyridinic-like groups. As in the case of sodium, their basicity enhances the dissociation of hydrogen sulfide to HS- ions. Owing to high microprosity of this carbon, that process occurs in the confined space where big sulfur polymers cannot be formed following reaction 4. Thus small sulfur radicals are readily oxidized to sulfur dioxide and further to sulfuric acid. Reaction likely proceeds from small pores to larger until low pH of sulfuric acid suppresses the dissociation of H_2S, which results in the observed breakthrough.

Conclusion

The results presented here show the differences in the performance of various materials as hydrogen sulfide adsorbents. For comparison, only the best commercial materials are used. As demonstrated, the variety of the oxidation products can be found on the surface and the speciation depends on textural and chemical heterogeneity of their surfaces. However, the desired speciation depends on the final application and options of disposal, a good carbonaceous material for H_2S removal should be basic in its nature and have available pore space to store oxidation products.

Acknowledgement. This research was supported by NYC Department of Environmental Protection.

References

(1) http://www.epa.gov/air/caaac/dieselreview.pdf
(2) Stirling, D. *The Sulfur Problem: Cl;eaning up Industrial Feedstocks*, RCS, Cambridge, 2000.
(3) Turk, A.,;Sakalis, S.; Lessuck, J.,; Karamitsos, H.; and Rago, O. *Environ. Sci. Technol.* 1989, **33**, 1242
(4) Stuetz, R. M.,;Fenner, R. M; Engin, G; *Wat. Res.* **1999**, *33*, 453.
(5) Turk, A.,; Sakalis, E.; Rago, O.; Karamitsos, H. *Annals New York. Academy of Sciences* **1992**, *661*, 221
(6) Bandosz, T. J.; Bagreev, A.; Adib, F.; Turk, A. *Environ. Sci. Technol*. **2000**, *34*, 1069.
(7) Bansal, R. C.; Donnet, J. B.; Stoeckli, F. *Active Carbon*: Marcel Dekker: New York, 1988.
(8) Avgul, N.N.; Kiselev, A. V. in *Chemistry and Physics of Carbon*; Walker, P. L., Jr., Ed.; Marcel Dekker: New York, 1970; Vol.6.
(9) Puri, B. R., In *Chemistry and Physics of Carbon*; P.J. Walker, Jr. Ed.; M. Dekker: New York, 1970; Vol. 6, p. 191.
(10) Leon y Leon, C. A., and Radovic, L. R. In *Chemistry and Physics of Carbon*; P.A. Thrower, Ed.; M. Dekker: New York, 1992; Vol. 24., pp. 213-310.
(11) Kaliva, A. N.; Smith, J. W. *Can. J. Chem. Eng.* **1983**, *61*, 208 .
(12) Bandosz, T. J., In *Fundamental of Adsorption 6*, Munier, F., Ed.: Elsevier: Paris 1998; p. 635.
(13) Adib, F.; Bagreev, A.; Bandosz, T. J. *Environ. Sci. Technol***. 2000,** *34*, 686.
(14) Adib, F.; Bagreev, A.; Bandosz, T. J. *J. Coll. Interface Sci*. **1999**, *214*, 407
(15) Adib, F.,; Bagreev, A.; Bandosz, T. J. *J. Coll. Interface Sci.* **1999,** *216*, 360.
(16) Adib, F.; Bagreev, A.; Bandosz, T. J. *Ind.Eng.Chem.Res*. **2000**, *39*, 2439.
(17) Klein, J.; Henning, K-D. *Fuel* **1984**, *63*, 1064.
(18) Hedden, K.,; Humber, L.; Rao, B. R. *VDI-Bericht* **1976**, *37/42*, 253.
(19) Meeyoo, V.; Lee, J. H.; Trimm, D. L.; Cant, N. W. *Catalysis Today* **1998**, *44*, 67.
(20) Meeyoo, V.; Trimm, D. L.; Cant, N. W. *J. Chem. Tech. Biotechnol*. **1997**, *68*, 411.
(21) Coskun, I; Tollefson, E. L..*Can. J. Chem. Eng.* **1986,** *58*, 72.
(22) Ghosh, T. K.; Tollefson, E. L. *Can. J. Chem. Eng.* **1986**, *64*, 960.
(23) Bagreev, A.,Adib, F.; Bandosz, T.J. Carbon, **2001**, 39, 21987.
(24) Choi, J. J.; Hirai, M.; Shoda, M., *App. Catal. A*, **1991**, *79*, 241.
(25) Li, C. T., U. S. *Patent No. 4,196,183*, (1980).
(26) Bagreev, A.; Bandosz, T.J. *Ind. Eng. Chem. Res*. **2002**, *41*, 672.
(27) Przepiorski J.; Oya A. *J Mat Sci Lett* **1998**, *17*, 679-82
(28) Radovic, L.R.; Rodriguez-Reinoso F. In *Chemistry and Physics of Carbon*; Thrower PA, Ed.: M. Dekker; New York, 1997; Vol.25, pp. 243-358.
(29) Salame, I.I.; Bandosz, T.J. *Langmuir* **2000**, *16*, 5435.
(30) Matviya, T. M., Hayden, R. A., *U.S. Patent 5,356,849* (1994).
(31) Hayden, R.A. *U.S. Patent 5,444,081* (1995).
(32) Adib, F.; Bagreev, A.; Bandosz, T. J. *Langmuir* **2000**, *16*, 1980.
(33) Bandosz, T.J. J. *Colloid Interface Sci.* **2002**, *246*, 1.
(34) Bagreev, A., Bandosz, T.J. Carbon, **2001**, *39*, 2303.
(35) Bagreev A.; Bandosz T.J.; Locke DC. *Carbon* **2001**, *39*, 1971.
(36) Bagreev, A.; Bashkova, S.; Locke, D.C.; Bandosz T.J. *Environ. Sci. Technol.* **2001**, *35*, 1537.

(37) Bashkova, S.; Bagreev, A.; Locke, D.C; Bandosz, T.J. Fundamentals of Adsorption -7, Kaneko K, Kanoh H, Hanzawa Y. Eds., IK International, Chiba, Japan, 239-246, 2002
(38) Bagreev, A.; Bandosz, T.J. *Environ. Sc.i Technol* **2004**, *38*, 345.
(39) Graham, J. US Patent No. 60.254,9000 (2004)
(40) ASTM D6646-01.
(41) Lastoskie, Ch. M.; Gubbins, K. E.; Quirke, N., *J. Phys. Chem.* **1993**, 97**,** 4786 ;
(42) Olivier ,J. P.; Conklin, W. B. *Presented at 7th International Conference on Surface and Colloid Science*, Compiegne, France, 1991
(43) ASTM Standards (1998). Vol.15.01. Refractories; Carbon and Graphite Products; Activated Carbon; Advanced Ceramics.
(44) Brennan, J.K.; Bandosz, T.J.; Thomson, K.T.; Gubbins, K.E. *Colloids and Surface A,* **2001**, *187-188*, 539.
(45) Kortum, G.; Vogel, W.; Andrussow, K. In *Dissociation Constants of Organic Acids in Aqueous Solutions*. Butterworth, London, 1961.

DENSITY FUNCTIONAL THEORY STUDY OF CARBON-H_2O REACTIONS DURING GASIFICATION WITH STEAM

Juan F. Espinal,[1] Fanor Mondragón,[1] and Thanh N. Truong[2]

[1] Institute of Chemistry, University of Antioquia
Medellin, Colombia A.A. 1226
[2] Department of Chemistry, University of Utah
Salt Lake City, Utah, USA 84112

Introduction

Carbon gasification is an alternative process to the combustion of coal since it produces less pollution and is more efficient. Basically, carbon gasification is the reaction of carbon with an oxidant agent such as oxygen, steam and/or carbon dioxide. Steam gasification is a process that has been widely studied by experimental techniques. Several mechanisms have been proposed for this reaction.[1-9] However, it is still not clear which of the proposed mechanisms is correct. Furthermore, these mechanisms do not provide any molecular-level details due to the complexity of the system.

In a recent theoretical study of the carbon-H_2O reaction a novel mechanism for the formation of molecular hydrogen was proposed which does not imply dissociation of the water molecule on the surface rather than a rearrangement of the hydrogen atoms.[10] This shows that molecular modeling is a powerful tool for improving our understanding of the gasification process.

The goal of this study is to carry out a Density Functional Theory study of thermodynamics of selected reactions that can take place during the steam gasification process. Particularly, we studied the interaction of the H_2O molecule with the active sites of clean carbonaceous models and possible pathways for the evolution of molecular hydrogen during the carbon-H_2O reaction.

Computational Details

Carbonaceous materials are macrostructures formed mainly by aromatic clusters. For char, it is known from solid-state ^{13}C-NMR experiments that it has structures of randomly connected graphene clusters consisting of 12-25 aromatic carbon atoms (3-7 benzene rings).[11] Since the gasification reactions take place at high temperatures, the active sites are simulated as edge carbon atoms of a graphene layer that have lost a hydrogen atom. In the carbonaceous model used for the calculations the other edge carbon atoms are terminated with hydrogen atoms. It has been reported previously that the use of H to terminate the boundaries of finite graphite models is a good choice.[12] The models shown as the reactants in Figures 1 and 2 are reasonable representations of the active sites environment in zigzag and armchair edges, respectively. Note that the π-bond network is implied in these figures. It is important to note that although the char has a highly condensed aromatic ring structure where the graphene units may have different sizes and orientations, the size of the carbonaceous models used in this study correspond to those suggested from NMR experimental data. In previous investigations it was also shown that the reactivity of a carbon material depends more strongly on the local structure of the active site rather than on the size of the graphene layer.[13,14]

In order to investigate the reaction of steam with the carbonaceous models we fully optimized each structure and some of the complexes that can be formed. All calculations (energies, optimizations, and frequencies) were done at B3LYP Density Functional Theory level (DFT), using the 6-31G(d) basis set for all atoms except for the hydrogen atoms in the water molecule where the 6-31G(d,p) basis set was used. In a previous study it was shown that spin contamination in unrestricted wave function at B3LYP level of theory is small for carbonaceous models.[15] Each model was optimized in its electronic ground state. Question on the roles of the excited states in these reactions is deferred to a separate study. This was done by performing single-point energy calculations at the same level of theory for several electronic states using geometries that were optimized at the AM1 semiempircal method for a given species, the ground state was taken as the one with the lowest energy. Furthermore, frequency calculations were done in order to confirm the stability of the optimized structures. All calculations were done using the Gaussian 98 program.[16]

Results and Discussion

Reaction of Steam with Clean Surfaces. The reaction of steam with the active sites of the carbonaceous models is a highly exothermic reaction either on zigzag or armchair configuration as can be seen in Figures 1 and 2. These reactions involve the production of a hydroxyl group after the dissociative chemisorption of the water molecule. If there is an active site next to the hydroxyl group, the hydrogen atom of this group would potentially further react with that active site to form a semiquinone group, in a reaction that is exothermic on both zigzag and armchair configurations.

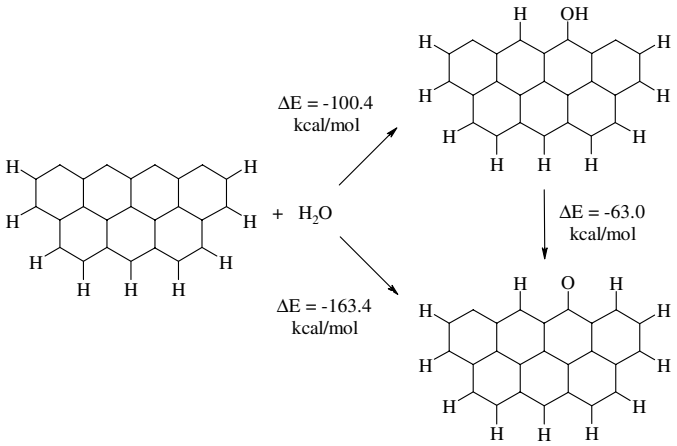

Figure 1. Reaction of the H_2O molecule on the active sites of the clean zigzag model and thermodynamic data.

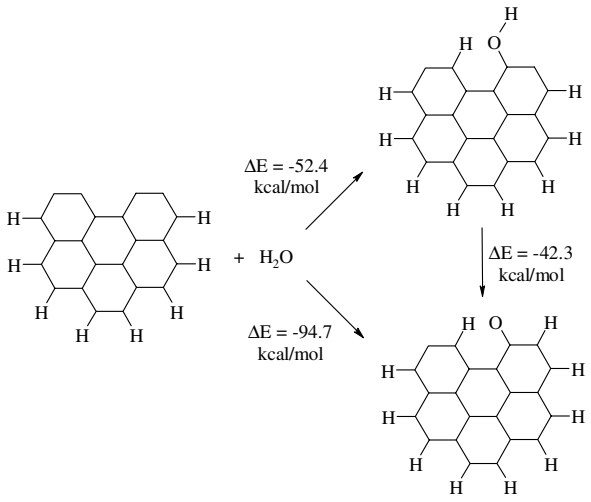

Figure 2. Reaction of the H_2O molecule on the active sites of the clean armchair model and thermodynamic data.

The reactions shown in Figures 1 and 2 are in agreement with the published experimental results where it was reported that after adsorption of water on graphite at low temperatures (25°C) the water molecule is chemisorbed and phenol and carbonyl (semiquinone) groups would be formed.[17] From the data shown, the dissociation of the water molecule at the active sites of carbonaceous materials is a thermodynamically favorable process.

Hydrogen Evolution. We studied several possibilities for the production of molecular hydrogen during the carbon-H_2O reaction on zigzag and armchair configurations. One possible pathway for the evolution of hydrogen is shown in Figure 3.

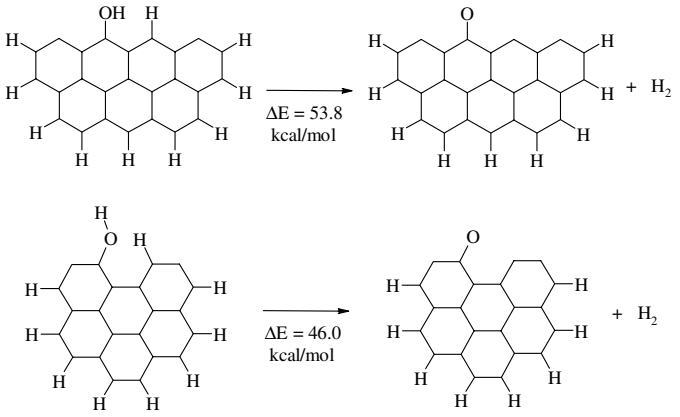

Figure 3. Possible pathways for molecular hydrogen evolution after chemisorption of one water molecule on the carbon surface.

Another route for the evolution of molecular hydrogen is found when two water molecules react on consecutive active sites as shown in Figure 4. From a thermodynamic point of view, the reactions shown in Figure 4 are more favorable ways to produce hydrogen from zigzag and armchair edges.

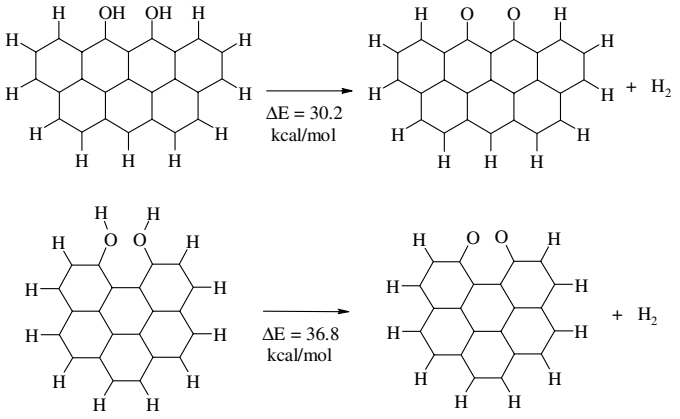

Figure 4. Molecular hydrogen evolution after carbon reaction with two water molecules and thermodynamic data.

The reactions shown in Figure 4 involve the dissociative chemisorption of two water molecules in such a way that two neighbor hydroxyl groups are obtained. These groups are precursors for subsequent hydrogen evolution leaving two semiquinone groups on the surface that could desorb as carbon monoxide or carbon dioxide as the gasification reaction proceeds.[18,19]

Conclusions

The reaction of steam with the active sites of the carbonaceous models is a highly exothermic reaction either on zigzag or armchair configuration. This reaction produces a hydroxyl group after the dissociative chemisorption of the water molecule. We propose an alternative pathway for hydrogen evolution that involves two neighbor hydroxyl groups that are precursors for molecular hydrogen production leaving two semiquinone groups.

Acknowledgements. The authors wish to thank the University of Antioquia for the financial support of the "Sostenibildad 2003" program. JFE acknowledges Colciencias and the University of Antioquia for the PhD. scholarship. We also thank the Center for High Performance Computing at the University of Utah for computer support.

References

(1) Pierce, C.; Smith, R. N.; Wiley, J. W.; Cordes, H. *Journal of the American Chemical Society* **1951**, *73*, 4551.
(2) Johnstone, H. F.; Chen, C. Y.; Scott, D. S. *Industrial and Engineering Chemistry* **1952**, *44*, 1564.
(3) Smith, R. N.; Pierce, C.; Joel, C. D. *Journal of Physical Chemistry* **1954**, *58*, 298.
(4) Giberson, R. C.; Walker, J. P. *Carbon* **1966**, *3*, 521.
(5) Yang, R. T.; Duan, R. Z. *Carbon* **1985**, *23*, 325.
(6) Yang, R. T.; Yang, K. L. *Carbon* **1985**, *23*, 537.
(7) Hermann, G.; Hüttinger, K. J. *Carbon* **1986**, *24*, 705.
(8) Hüttinger, K. J. *Carbon* **1988**, *26*, 79.
(9) Hüttinger, K. J.; Merdes, W. F. *Carbon* **1992**, *30*, 883.
(10) Zhu, Z. H.; Finnerty, J.; Lu, G. Q.; Wilson, M. A.; Yang, R. T. *Energy & Fuels* **2002**, *16*, 847.
(11) Perry, S. T.; Hambly, E. M.; Fletcher, T. H.; Solum, M. S.; Pugmire, R. J. *Proceedings of the Combustion Institute* **2000**, *28*, 2313.
(12) Chen, N.; Yang, R. T. *Carbon* **1998**, *36*, 1061.
(13) Montoya, A.; Truong, T.-T. T.; Mondragón, F.; Truong, T. N. *Journal of Physical Chemistry A* **2001**, *105*, 6757.
(14) Montoya, A.; Mondragón, F.; Truong, T. N. *Carbon* **2002**, *40*, 1863.
(15) Montoya, A.; Truong, T. N.; Sarofim, A. F. *Journal of Physical Chemistry A* **2000**, *104*, 6108.
(16) Frisch, M. J.; Trucks, G. W.; Schlegel, H. B.; Scuseria, G. E.; Robb, M. A.; Cheeseman, J. R.; Zakrzewski, V. G.; J. A. Montgomery, J.; Stratmann, R. E.; Burant, J. C.; Dapprich, S.; Millam, J. M.; Daniels, A. D.; Kudin, K. N.; Strain, M. C.; Farkas, O.; Tomasi, J.; Barone, V.; Cossi, M.; Cammi, R.; Mennucci, B.; Pomelli, C.; Adamo, C.; Clifford, S.; Ochterski, J.; Petersson, G. A.; Ayala, P. Y.; Cui, Q.; Morokuma, K.; Malick, D. K.; Rabuck, A. D.; Raghavachari, K.; Foresman, J. B.; Cioslowski, J.; Ortiz, J. V.; Baboul, A. G.; Stefanov, B. B.; Liu, G.; Liashenko, A.; Piskorz, P.; Komaromi, I.; Gomperts, R.; Martin, R. L.; Fox, D. J.; Keith, T.; Al-Laham, M. A.; Peng, C. Y.; Nanayakkara, A.; Gonzalez, C.; Challacombe, M.; Gill, P. M. W.; Johnson, B.; Chen, W.; Wong, M. W.; Andres, J. L.; Gonzalez, C.; Head-Gordon, M.; Replogle, E. S.; Pople., J. A. Gaussian 98, Revision A.8; Gaussian, Inc.: Pittsburg, PA, 1998.
(17) Miura, K.; Morimoto, T. *Langmuir* **1988**, *4*, 1283.
(18) Espinal, J. F.; Montoya, A.; Mondragón, F.; Truong, T. N. *Journal of Physical Chemistry B* **2004**, *108*, 1003.
(19) Montoya, A.; Mondragón, F.; Truong, T. N. *Journal of Physical Chemistry A* **2002**, *106*, 4236.

SIMULATION & NO_x CORRELATION FOR COAL-FIRED BOILER

Mel Fox and André L. Boehman

The Energy Institute
The Pennsylvania State University
405 Academic Activities Building
University Park, PA 16802

Introduction

Oxides of nitrogen (NO_x) are a major pollutant evolving from combustion processes. Federal emissions regulations are become increasingly stringent, in order to abate harmful NO_x emissions. Some of the proposed NO_x reduction strategies for stationary combustion systems are:

- Combustion modifications
- Reduction technologies (both catalytic and non-catalytic)
- Fuel additives and alternative fuels
- Reburning technologies
- Low-NO_x burners
- Feedback control & monitoring technologies.

Computational Fluid Dynamics (CFD) has been used to simulate combustion for decades. Simulations have been employed to assist in the design of improved burner geometries, the analysis of alternative fuels and reburning conditions, and various other applications. While studies have shown simulated results for NO_x emissions, temperature profiles and flow fields, for given planes within the boiler, no numerical relationships between such data have been determined.

The desire to implement a temperature measurement-based monitoring and feedback control system for improved NO_x control necessitates the discovery of a functional correlation between boiler temperature distributions, boiler operating parameters, and NO_x formation. This numerical simulation effort has the objective of determining how best to implement the temperature profile information that can be obtained with a new fiber optic temperature sensor under development at Penn State University, which can provide a measurement of the temperature distribution along a line-of-site across the interior of a boiler.

The work herein is focused on modeling the "demonstration boiler" at the Energy Institute at PSU. The grid was generated in Gambit 2.1, and a commercial CFD code, FLUENT 6.1, was used for simulation. Tests were designed and data was collected for typical and low-NO_x conditions. Data was collected at several planes within the boiler.

Numerical Modeling Approach

Two different cases were modeled based upon the configuration of the demonstration boiler: a normal case, where primary, secondary and tertiary air flow rates were set at conventional operating conditions; and a low-NOx case, where the secondary air flow rate is decreased and that air flow is redirected to become a tertiary air flow.

Demonstration Boiler. The demonstration boiler, located at Penn State's Energy Institute, is a D-type design watertube boiler, manufactured by Tampella Power Corporation [1].The boiler has approximate dimensions (in meters) of 2.65x1.83x2.59. It is rated for 15,000 lb/h steam (@300 psig), and was initially designed for fuel oil-firing, but has since been modified for coal-based fuels.

The three-dimensional, nonuniform grid of the demonstration boiler is shown in Figure 1. The grid was meshed at a spacing of 3, and comprises nearly 273,000 nodes.

Numerical Model. The solutions were obtained using an implicit, segregated solver, for non-premixed, steady state combustion. The *k*-ε model was employed as the turbulence model for this work, which is widely used combustion modeling [2].

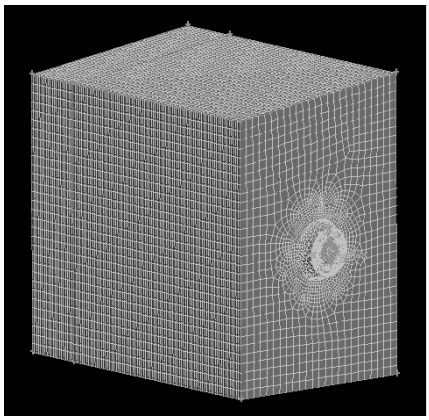

Figure 1. Three-dimensional demonstration boiler grid

The turbulent intensity is a function of the upstream flow conditions. The mixture fraction/PDF formulation, which was developed specifically to model turbulent diffusion flames [3], was used to model the combusting flow, along with the P-1 radiation model and NO_x postprocessor. Chemical equilibrium relates instantaneous mass fractions and temperature with the mixture fraction. The P-1 radiation model is advantageous due to its simple diffusion equation, which allows particulate scattering [4] and requires low CPU demand. The mixture fraction method permits intermediates, dissociation effects, and coupling between turbulence and chemistry to be accurately accounted for. A probability density function (PDF) accounts for the interaction of turbulence and chemistry [3], simulating realistic finite chemistry in turbulent flames. The density-weighted time-averaged Navier Stokes equations are solved for temperature, velocity, species concentrations and variance, from which the time-averaged NO formation rate is computed at each point, using the averaged flow-field information [3, 5]. Since the rate of NO_x formation is sensitive to temperature, the combustion solution must be highly accurate to attain reasonable results.

A Rosin-Rammler distribution was assumed for the coal particle size distribution. The particles were injected at four positions, for a total mass flow rate of coal of 0.37 kg/s. The air was injected according to Table 1.

Solutions are calculated based on the conservation equations. The continuity equation is:

$$\frac{\partial \rho}{\partial t} + \frac{\partial}{\partial x_j}(\rho u_j) = 0 \qquad (1)$$

The turbulent flow conservation equations for momentum and energy are as follows, respectively:

$$\frac{\partial}{\partial t}(\rho u_i) + \frac{\partial}{\partial x_j}(\rho u_i u_j) = -\frac{\partial p}{\partial x_i} + \frac{\partial \tau_{ij}}{\partial x_j} \qquad (2)$$

$$\frac{\partial}{\partial t}(\rho h_t) + \frac{\partial}{\partial x_j}(\rho u_j h_t) = \frac{\partial p}{\partial t} + \frac{\partial}{\partial x_j}(u_i \tau_{ij} - q_i) \quad (3)$$

Table 1. Inlet and Outlet Conditions for Both Cases

	Normal	Low-NO_x
Inlet Conditions		
Primary Air Flow Rate (k g/s)	0.2	0.20
Secondary Air Flow Rate (k g/s)	0.53	0.76
Tertiary Air Flow Rate (k g/s)	1.23	1.00
Fuel Flow Rate (kg/s)	0.37	0.37
Outlet Conditions		
Area Weighted Ave. T (K)	1712.72	1456.16
Area weighted Ave. NOx (ppm)	397.31	283.81

Results & Discussion

Calculations were performed for the conventional and low-NOx cases, from which temperature and NOx distributions were generated.

Figure 2 and **Figure 3** portray various temperature gradients over the specified surfaces. At conventional operating conditions, the elevated temperatures are indicative of coal particles trapped in recirculating flow regions, depleting available oxygen, and hence yielding significant NOx formation with adequate residence time. In the low-NOx case with air-staging, high temperature zones are fuel-rich and therefore lead to higher CO production. Though the temperature and residence time may be conducive to NOx formation, the depleted oxygen reduces net NOx formation. Successful air staging provides significant stratification of the combustion process, and thermal non-uniformity, as shown in the low-NOx case temperature profile, which indicates the extent of stratification.

Statistical Analysis. Data, in the form of 1D "lines" of information (simulating the data to be collected from the fiber-optic sensor, spanning the boiler), resulting from CFD calculations will be analyzed statistically in order to determine a correlation.

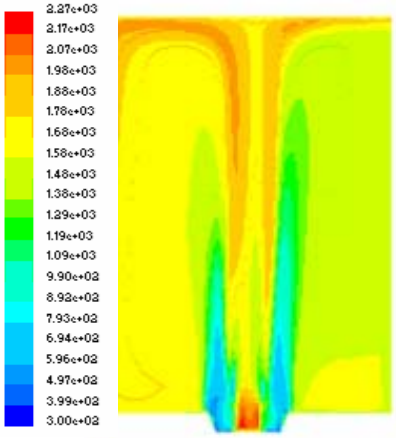

Figure 2. Low-NOx case temperature profile (axial surface)

Regression studies will be employed for the conventional and low-NOx cases. A series of regressions will be performed for each scenario, with NOx concentration held as the response variable, while predictor variables comprise T, velocities and other stoichiometric parameters in various combinations. The combination providing the best (highest) R-squared value for each case will be accepted and used in a regression study comparing the two cases.

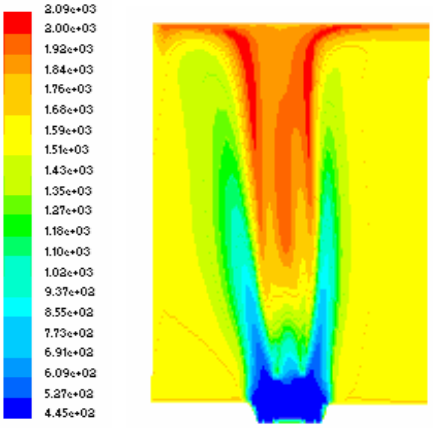

Figure 3. Conventional case temperature profile (axial surface)

Conclusions

Two separate calculations were performed with secondary and tertiary air flow rates as the only variables. The temperature profiles presented for each case provide evidence that data from a one dimensional sensor spanning a boiler in strategic locations may provide pertinent information to allow real-time NOx control.

Temperature, NOx concentrations and velocity profiles were collected for specified planes within the boiler. These parameters will be compared against one another via statistical analysis, in order to determine an algorithm for implementation in a NOx control system, in conjunction with a fiberoptic, in-situ temperature sensor.

Acknowledgements. This paper was written with support of the University Coal Research program of the U.S. Department of Energy, National Energy Technology Laboratory under contract no. DE-FG26-02NT41532. The Government reserves for itself and others acting on its behalf a royalty-free, nonexclusive, irrevocable, worldwide license for Governmental purposes to publish, distribute, translate, duplicate, exhibit, and perform this copyrighted paper.

References

1. The Energy Institute., *Demonstration Boiler Fact Sheet*, www.energy.psu.edu.
2. Launder, B.E et al, *The Numerical Computation of Turbulent Flows.* Computer Methods in Applied Mechanics and Engineering, 1974. **3**: p. 269-289.
3. Fluent Inc., *User's Guide*. 1996, Fluent Incorporated: Lebanon. p. 19-43.
4. S.S. Sazhin et al., *Modelling of the Gas to Fuel Droplets.* Fuel, 2000. **79**(14): p. 1843-1852.
5. Fluent Inc., *Fluent 6.1 Documentation*. 2003, Fluent Incorporated: Lebanon.

DIMETHYL ETHER OXIDATION AT ELEVATED TEMPERATURES

Claudette M. Rosado-Reyes, and Joseph S. Francisco

Department of Chemistry and
Department of Earth and Atmospheric Sciences
Purdue University
West Lafayette, IN 47907

Joseph J. Szente, and M. Matti Maricq

Research Laboratory
Ford Motor Company, P.O. Box 2053, Drop 3083
Dearborn, MI 48121

Introduction

The fact that current diesel engine emissions will not meet future standards, has spurred research into alternative fuels in order to reduce emissions without compromising fuel economy. Oxygenated hydrocarbons such as ethers have been proposed for use as alternative fuels or as additives in diesel engines[1]. The chemical and thermodynamic properties of dimethyl ether (DME) make it ideal for this purpose: higher cetane number of 55-60[2], lower self ignition temperatures, NO_x emissions and engine noise[3], and no soot formation. The determination of alternative fuels emissions under operating conditions (high pressure and temperature) is required to assess the impact of these materials on the atmospheric reactivity of tailpipe emissions[4].

The use of DME as a fuel for solid oxide fuel cells (SOFCs) has also been under consideration[5]. There are potential applications for its use in vehicle based fuel cells. Direct oxidation of hydrocarbons eliminates the need for fuel reformers and can reduce the cost and weight of SOFC systems. The temperature dependence of DME thermal decomposition is important in determining the power output of SOFCs and their contamination by coking.

Under laboratory conditions, chlorine atoms - produced by the photolysis of Cl_2 - initiate the chemistry. Methoxymethyl radicals (CH_3OCH_2) are produced as a result of the abstraction of a methyl hydrogen from DME. Under high O_2 concentrations, methoxymethyl radicals combine with oxygen to produce methoxymethyl peroxy radicals ($CH_3OCH_2O_2$). Previous product studies of chlorine initiated chemistry at low temperature showed a dependence on total pressure, where production of formaldehyde and methyl formate compete against each other[6]. This pressure dependence was explained by proposing and showing that the oxidation of dimethyl ether proceeds via two different competitive pathways: a pressure dependent and a pressure independent pathway.

In the pressure dependent pathway, the energetically excited peroxy (RO_2*) is collisionally deactivated into a stabilized peroxy radical that can continue reacting by usual peroxy radical reactions. From these methoxymethyl peroxy radical reactions, methyl formate ($CH_3OC(O)H$) is formed as a main by-product. Also a significant yield of formic acid (HC(O)OH) has been previously reported[7], although it is not clear how the proposed mechanism can account for it. The pressure independent pathway takes place via the intramolecular rearrangement of peroxy radical followed by dissociation into two molecules of formaldehyde and one molecule of hydroxyl radicals (2 HC(O)H + OH). This pressure independent pathway is of particular interest with respect to combustion because OH radicals are an important reactive intermediate in combustion processes. The production of hydroxyl radicals can initiate and sustain a chain reaction between DME and OH. The original study of the dimethyl ether photoinitiated chemistry intended to determine the branching ratio of $CH_3OCH_2 + O_2$ reaction with respect to pressure[6]. Time-resolved UV/IR spectroscopy was utilized to perform real time kinetic measurements of this reaction at temperatures between 230 and 350 K, pressures between 10 and 200 Torr, and a time regime of up to 60 microseconds. At room temperature, the peroxy radical stabilization becomes more significant as pressure increases, but the dissociation pathway becomes insignificant to sustain combustion chain reactions. As the temperature increases the reaction shifts to the formaldehyde production, but this change is not as significant as the one dependent on pressure. The investigation of the kinetics of the photo-initiated $CH_3OCH_2 + O_2$ chemistry at elevated temperatures above 295 K revealed thermally induced reactions taking place independent of photolysis. Also these results raised the possibility that at even higher temperatures >350K, the dissociation channel might become significant enough to sustain DME + OH chain reaction, and be even more significant near or at combustion temperatures. This study intends to determine the branching for the $CH_3OCH_2 + O_2$ reaction pathways at pressures of 20-200 Torr and temperatures of 295-700 K, and the importance of dimethyl ether degradation in the presence of O_2 over the temperature range of 295-700 K.

Experimental

To investigate the temperature dependence on the degradation of dimethyl ether and consequently on the $CH_3OCH_2 + O_2$ branching ratio, the kinetics of the reaction of $CH_3OCH_3 + Cl_2$ in the presence of O_2 is being studied at elevated temperatures. Flash Photolysis/Transient Infrared Spectroscopy is used to evaluate the yield and kinetics of Formaldehyde, Methyl Formate, and Formic Acid, at the 1709 cm^{-1}, 1742 cm^{-1}, 1791 cm^{-1} vibrational lines respectively. The measurements include the direct probing of product concentration for the first 900 μsec after Cl_2 photolysis, and in the absence of Cl, at three different dimethyl ether concentrations (6, 12, 20 × 10^{16} molecules/cm^3). These experiments were carried out at three different total pressures (60, 250, 600 × 10^{16} molecules/cm^3) and eight different temperatures between 295 and 700 K (increments of 50K).

The Flash Photolysis/Time-Resolved IR Spectroscopy experimental apparatus is described as follows. A reagent gas mixture is inserted into a quartz cylindrical reaction cell. The gas mixtures for these experiments consisted of dimethyl ether (1-7 Torr), 4.8% chlorine/N_2 (2-11 Torr), O_2 (11-38 Torr), and N_2 to make up the balance. The reaction cell is wrapped with electrical heaters and insulated for thermal stability. Temperature is monitored and controlled by thermocouples positioned along the outside of the cell. The gases are pre-heated prior to entering the cell. Photo-dissociation of Cl_2 is initiated by 351 nm light from a Lambda Physik model LPX 301 excimer laser. Two dichroic beam-steering mirrors, placed at opposite ends of the reaction cell, reflect the UV laser light into the reaction cell while allowing the transmission of IR light. Conditions were such that the reaction cell was well evacuated and the gas mixture replenished between laser pulses. A high-resolution, cryogenically cooled, Pb-salt diode laser is used as the infrared light source to probe the ro-vibrational carbonyl stretch mode of by-products at frequencies between 1700 and 1800 cm^{-1}. After passing though a mode selecting monochromator, it is directed through the reaction cell where it counterpropagates relative to the excimer laser. The IR light is focused to a LN_2 cooled HgCdTe detector with a response time of 0.3 μsec. Frequency drift is prevented by frequency locking the laser radiation to the ro-vibrational absorption line being monitored. The IR light intensity is measured for several milliseconds following the laser photolysis pulse to obtain time

dependent absorbances. In order to quantify the concentrations of the by-products, their IR absorption cross sections (σ) at the respective IR absorbance lines are determined by introducing a known amount of by-product into the reaction cell of pathlength l. The concentration is then calculated by Beer's Law via,

$$c(t) = \left(\frac{1}{l\sigma}\right)\ln\left(\frac{I_0}{I}\right)$$

The initial halogen radical concentration from photolysis is calculated indirectly by substituting methanol for DME and measuring the formaldehyde yield from the photoinitiated oxidation reaction.

Results and Discussion

For the thermally induced chemistry measurements, the gas mixture of $DME/O_2/N_2$ was allowed to equilibrate to the selected temperature while flowing through the cell. Residence time in the cell was between 2 and 4 seconds. Figure 1 shows the formaldehyde yield, in the absence of chlorine, relative to dimethyl ether initial concentrations at temperatures between 295K and 700K. At temperatures between 450K and 500K, dimethyl ether thermally-induced oxidation is starting to take place. Above these temperatures, main by-products are being produced reaching maximum concentrations between 600K and 650K, starting then to decline. At low pressure conditions, formaldehyde yield is lower compared to medium and high pressure conditions. The change in formaldehyde yield is not significant going from 250×10^{16}/cm^3 to 650×10^{16}/cm^3 total pressure. Methyl formate and formic acid yields follow a similar trend, although formaldehyde yield is greater by a factor of 2 and 10 respectively. Figure 1 clearly shows a total pressure dependency as a function of temperature in the methoxymethyl peroxy radical chemistry, but also shows that the formaldehyde yield is independent of DME initial concentration.

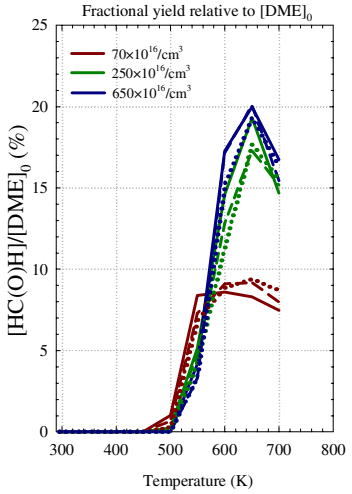

Figure 1. Formaldehyde yield relative to dimethyl ether initial concentration in the temperature regime of 295-700K at three different total pressure conditions.

Figures 2 and 3 show the pressure dependent yields of the three main by-products from photo-initiated DME oxidation experiments at 295K and 500K respectively. Due to the high initial radical concentrations, > 10^{14}/cm^3, for these measurements, the products are monitored for only a few milliseconds after the chemistry is initiated by chlorine atoms. At a given temperature, the formation of formaldehyde shows pressure dependence due to the change in the fraction of peroxy radicals that undergo dissociation. In contrast, methyl formate yield remains essentially the same over this pressure range. No detectable levels of formic acid are measured during the first few milliseconds of the reaction.

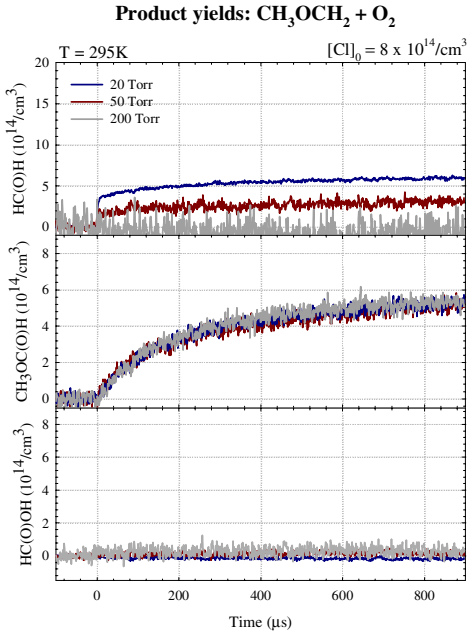

Figure 2. Formaldehyde, methyl formate, and formic acid concentration vs time profile from Cl_2-initiated DME degradation at room temperature as a function of pressure.

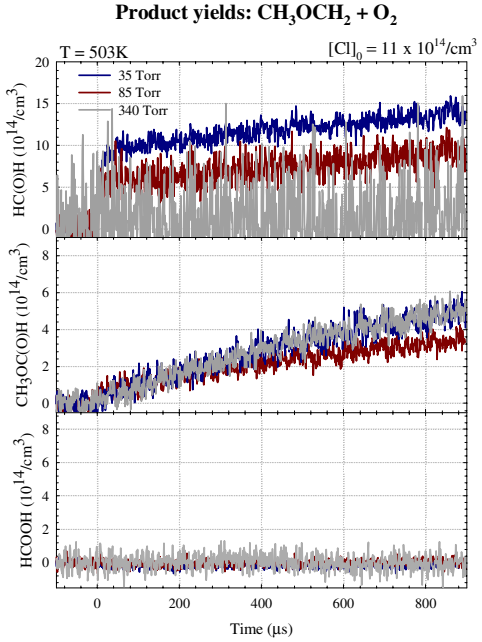

Figure 3. Formaldehyde, methyl formate, and formic acid concentration vs time profile from Cl_2-initiated DME degradation at 503K as a function of pressure.

As the temperature is raised from 295K to 503K, the formaldehyde yield increases, by as much as a factor of 3, with the

greatest increase occuring at low pressures, and becoming less at the higher pressure. As total pressure is increased, IR detection of the products becomes increasingly difficult due to both the smaller product concentrations and the pressure broadening effect on absorbance cross section. While the methyl formate yield reaches similar levels at both temperatures, the rate of formation is slower as temperature increases.

A reaction mechanism for the oxidation of DME is being used to predict the temperature and pressure dependence of the methoxymethyl peroxy stabilization vs. dissociation branching ratio as well as the peroxy radical self reaction rate constant. The methoxymethyl peroxy radical chemistry will be further described by Lindemann and Arrhenius analysis of these parameters.

References

1. Leppard, W. R.; *SAE Trans*., **1991**, 912313.
2. Kapus, P. E.; Cartellieri, W. P.; *SAE Trans*., 1995, 952754.
3. Roubi, M. A,; *Chem. Eng. News*, **1995**, 44, 37.
4. Japar, S. M.; Wallington, T.J.; Richert, J. F. O.; Ball, J. C.; *Int. J. Chem. Kinet*., 1990, 22, 1257.
5. Murray, E. P.; Harris, S. J.; Jen, H; *J. Electrochem. Soc.*, **2002**, 149, A1127.
6. Maricq, M. M.; Szente, J. J.; Hybl, J. D.; *J. Phys. Chem. A*. **1997**, 101, 5155.
7. Liu, I.; Cant, N. W.; Bromly, J. H.; Barnes, F. J.; Nelson, P. F.; Haynes, B. S.; Chemosphere, **2001**, 42, 583.

Simulation Study of CO2 Separation Process by Using Hollow Fiber Membrane

Dae-Hwan Lee, Hyung-Taek Kim

Dept. of Energy Studies, Ajou University
Wonchon-dong Yeongtong-gu
Suwon, Korea 443-749

Introduction

In accordance with the Kyoto Protocol and consecutive several international agreements, Korea must prepare for the duty of the reduction of CO_2 emission. Most of the CO_2 absorption/separation processes are energy–consuming so that optimum arrangement of CO_2 absorption system should be acquired through the simulation. In the present investigation, membrane separation process with hollow fiber is simulated to find an optimum design/operation parameter for low energy-consuming one.

The membrane separation of CO_2 requires relative low energy consumption comparing to absorption or distillation type. It can be operated easily and inexpensively since its physical separation mechanism. Also it is suitable to apply in a small-to-medium scale of CO_2 separation process. Therefore, system models for the CO_2 separation process is set up by using the membrane separator then the CO_2 separation process is simulated with changing the parameter of operation condition, separation characteristics by changing the shape of mixed membrane, and etc. The optimum conditions for the CO_2 separation process are obtained by analyzing the design and operation parameters when energy requirement is the lowest.

Methods

Simulation of 1 membrane module is initially made by using the FORTRAN program. After that using these results, 4 bundles of membrane module connected with cascade type is also simulated. During the simulation, operation/design parameters are calculated such as required membrane area, number of modules, permeated CO_2 concentration and the amount of permeated gas with no recycle streams. Finally, recycle mode of membrane simulation is proceeded by using the FORTRAN.

Simulation for 1 module. Simulation of 1 membrane module is conducted with the overall material balance equation is below:

$$(\alpha-1)y_i^2+\left(1-\alpha-\frac{1}{R}-\frac{x(\alpha-1)}{R}\right)y_i+\frac{\alpha x}{R}=0 \qquad \cdots(1)$$

$$A=\frac{(Vy)_{out}}{(J_A)_{out}}=\frac{(Vy)_{out}}{Q_A(P_1x-P_2y_i)_{ave}}$$

$$=\frac{(Vy)_{out}}{Permeate\ flux\times(x-Ry_i)_{ave}} \qquad \cdots(2)$$

α : selectivity

x : Feed composition

y_i: Permeate composition

P_1: Feed Pressure

P_2: Permeate Pressure

R : Pressure ratio(P_2/P_1)

V : Permeate rate

Flow diagram of 1 membrane module simulation is illustrated in **Figure.1**. Several parameters such as operating pressure are varied during the simulation as in **Table. 1**. Different methods of simulation are utilized in the current study. One method is fixing x_t for 0.01, in which x_t represents the retentate composition of CO_2. Then it is calculated that required membrane area, number of required modules, flow rate, and CO_2 concentration of permeate. Another method is fixing number of total modules as 50, then flow rate, CO_2 concentration of permeate, and x_t are calculated.

Table 1. Input Parameters

parameter	amount	parameter	amount
P_1	6 atm	No of HF per module	5000
P_2	0.1 atm	Feed rate	1000 m^3/day
Selectivity	20	Length of HF	50 cm
Permeability	20	Pressure ratio	P_2/P_1

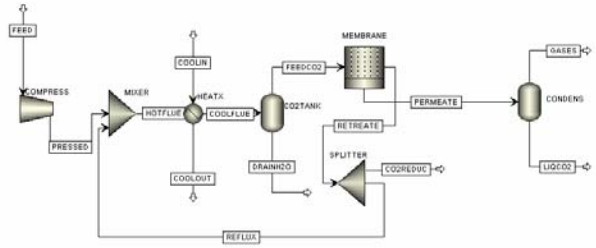

Figure 1. Overall Flow diagram

Simulation for 4 bundles of membrane without recycles. Flow diagram of 4 bundles of membrane module is composed like a cascade in **Figure. 2**. From the simulation, calculated results are illustrated as required membrane area, number of required modules for each bundles, total required membrane area, flow rate and CO_2 concentration of permeate with no recycle streams.

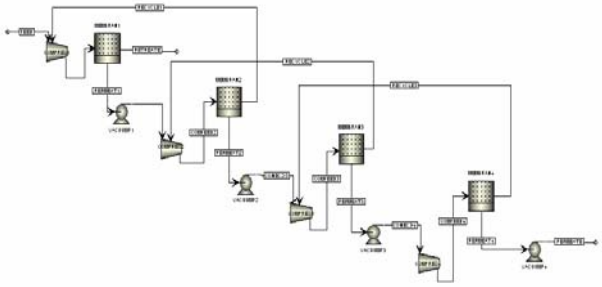

Figure 2. 4 bundles of membrane

Simulation for 4 bundles of membrane with recycles. Simulation with recycle streams is conducted as below. Since the simulation is 4 bundles of membrane module with recycles, calculation is iterated 10 times. It is calculated that required membrane area, number of required modules for each bundle, total required membrane area, number of total required module, flow rate, and CO_2 concentration of permeate.

Results and Discussion

Simulation for 1 module

1. Fixing x_t for 0.01

The result is below in **Table. 2**:

Table 2. Result at fixing x_t for 0.01

parameter	amount
Required membrane area	241.016 m^2
No of required modules	76.72 77
Flow rate of permeate	10.144 m^3/hr
CO_2 concentration of permeate	37.967 %

It is simulated during changing the pressure.

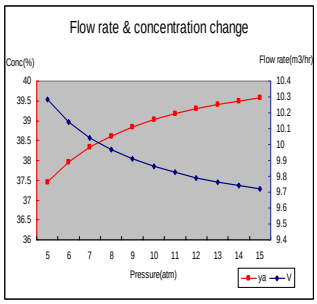

Figure 3. Flow rate & CO_2 concentration change

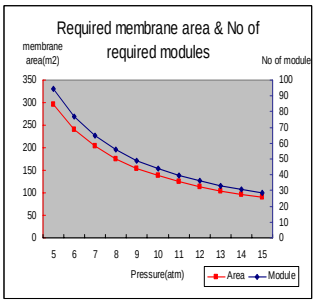

Figure 4. Required membrane area & No of required modules

2. Fixing No of modules for 50
The result is below in **Table. 3**:

Table 3. Result at fixing No of modules for 50

parameter	amount
Flow rate of permeate	6.202 m^3/hr
CO_2 concentration of permeate	48.467 %
x_t	0.0327

It is simulated during changing the No of modules.

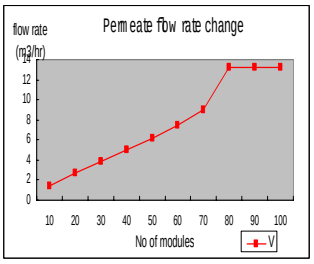

Figure 5. Permeate flow rate change

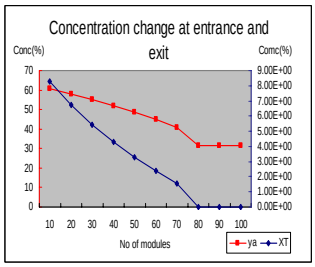

Figure 6. Concentration change at entrance & exit

Simulation for 4 bundles of membrane without recycles. It is calculated that required membrane area & No required of modules for each bundle, total required membrane area & No of required module and flow rate & CO_2 concentration of permeate with no recycles.

Table 3. Result of 4 bundles of membrane without recycles

Parameter	amount
Required membrane area(1stage)	237.016 m^2
No of required modules(1stage)	75.49 76
Required membrane area(2stage)	53.795 m^2
No of required modules(2stage)	17.12 18
Required membrane area(3stage)	22.884 m^2
No of required modules(3stage)	7.28 8
Required membrane area(4stage)	16.018 m^2
No of required modules(4stage)	5.10 6
Required membrane area(total)	329.857 m^2
No of required modules(total)	108
No of required HF(total)	540000
Feed flow rate	41.667 m^3/hr
Flow rate of permeate	2.4718 m^3/hr
CO_2 concentration of permeate	93.329 %

Simulation for 4 bundles of membrane with recycles. It is calculated that required membrane area & No required of modules for each bundle, total required membrane area & No of required module and flow rate & CO_2 concentration of permeate with recycles.

Parameter	amount
Required membrane area(1stage)	275.448 m^2
No of required modules(1stage)	87.68 88
Required membrane area(2stage)	50.111 m^2
No of required modules(2stage)	15.95 16
Required membrane area(3stage)	17.660 m^2
No of required modules(3stage)	5.62 6
Required membrane area(4stage)	10.107 m^2
No of required modules(4stage)	3.22 4
Required membrane area(total)	353.326 m^2
No of required modules(total)	114
No of required HF(total)	570000
Feed flow rate	41.667 m^3/hr
Flow rate of permeate	2.8708 m^3/hr
CO_2 concentration of permeate	93.866 %

Table 4. Result of 4 bundles of membrane with recycles

Calculation is iterated 10 times. The result is below in **Figure. 7** & **Figure. 8**.

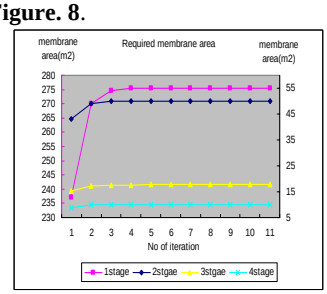

Figure 7. Required membrane area

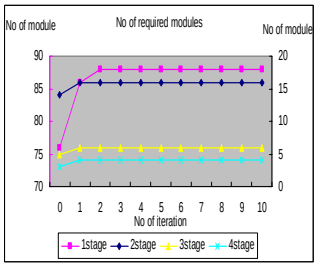

Figure 8. No of modules

Conclusions

When there are recycles, flow rate & CO_2 concentration of permeate are increased about 0.4m^3/hr and 0.53%. Required membrane area & No of required modules at 1st stage are increased. But, required membrane area & No of required modules at other stage are decreased. Total required membrane area & total No of required modules is increased. Total No of required modules is increased about 6 modules.

These results indicate that we can remove more CO_2 and get the high CO_2 concentration. If more bundles are attached, the separation units by using the hollow fiber membrane remove more CO_2 and get the high CO_2 concentration. Therefore, it is very useful that CO_2 separation process by using the hollow fiber membrane.

References

(1) James Marriott; Eva Sorensen; *Chemical Engineering Science 58*, **2003**, 4975-4990.
(2) R. Wang; S. L. Liu; T. T. Lin; T. S. Chung; *Chemical Engineering Science 57*, **2002**, 967-976.
(3) Li Xu; Lin Zhang; Huanlin Chen; *Desalination 148*, **2002**, 309-313.
(4) G. C. Kapantaidakis; G. H. Koops; *Journal of Membrane Science 204*, **2002**, 153-171.

NUMERICAL SIMULATION OF VOLATILES RELEASE FOR MICRONIZED COAL REBURNINIG

Manyin Hu[1], Hezhong Tian[2], Zhong Liu[1], Xiaomin Wang[1]

1. School of Environmental Science and Engineering, North China Electric Power University, Baoding 071003, China
2. Department of Environmental Science and Engineering, Tsinghua University, Beijing 100084, China

1. Introduction

Micronized coal reburning is an effective and promising technology in NO_X emission control of coal-fired utility boilers. NO_X is reduced in two routes with coal reburning: one is the homogenous reaction between NO_X and volatiles under fuel-rich conditions, and the other is the heterogenous reaction between NO_X and char which formed after coal pyrolysis. More NO_X can be reduced if more volatiles release from coal pyrolysis[1-3], and the corresponding char has higher reactivity also[4, 5].

Coal is composed of various functional groups. In the heating process, with the increase of temperature, various bonds between coal molecules destroy and produce volatiles through complex reactions, the volatiles release into gas phase through char pores[6]. Volatiles mainly include CH_4, C_2H_4, C_3H_6, H_2, CO, CO_2 and tar, in which C_nH_m, HCN, NH_3, H_2 and CO can react with NO. Heating rate has important influence on volatiles release during coal pyrolysis, and volatiles especially hydrocarbons release and the release rate directly affect NO reduction. Further, heating rate have effects on char structures and inner face activity points, as well as various reactions rates.

Mathematical simulation is one of the important ways to study coal pyrolysis. Volatiles release under reburning conditions in an entrained flow reactor (EFR) was mathematically simulated, in which coal less than 100 mesh and 320 mesh were used as reburning fuels, respectively. The total volatiles release and various volatiles release rates were calculated, also the effects on NO reduction were analyzed.

2. Mathematical models

2.1 Energy conversation equations

The flow in EFR is laminar. In this study, heterogenous energy transfer is determined by heat exchange and radiate heat transfer, while energy transfer between reaction system and furnace wall is determined by convective and radiate heat transfer. Pulverized coals flux is relatively smaller (about 20% of total fuel) under reburning conditions, excess air coefficient is less than 1, coal particles can not combust completely in reburning zone, the dispatch between heat absorbed and emitted--total reactive caloric is far less than other heat transfers. Therefore, reactive caloric, as well as the gas productions is omitted.

Gas phase energy conversation equation is expressed as follows:

$$\frac{d(Q_g C_{pg} T_g)}{dL} = N_v A[\frac{\lambda_g}{r_{ps}}(T_s - T_g) + \varepsilon_g \sigma(T_s^4 - T_g^4)]4\pi r_{ps}^2 + [\varepsilon_g \sigma(T_w^4 - T_g^4) + h_c(T_w - T_g)]\pi D \quad (1)$$

While, solids phase energy conversation equation is:

$$\frac{d(W_s C_{ps} T_s)}{dL} = N_v A[\frac{\lambda_g}{r_{ps}}(T_g - T_s) + \varepsilon_s \sigma(T_g^4 - T_s^4) + \varepsilon_s \sigma(T_w^4 - T_s^4)]4\pi r_{ps}^2 \quad (2)$$

For using time differential equation, the following equation:

$$dt = \frac{A}{Q_V} dL \quad (3)$$

can be used to convert energy conversation equations to time differential format. Therefore, with the above energy conversation equations, temperature fields in furnace as well as volatiles release can be calculated.

2.2 Volatiles release chemical mechanism models

According to chemical kinetic theory, in the reaction chains of one species, reactions with lower activation energies have higher reaction rate; while reactions with higher activation energies have lower reaction rate. Elementary reactions that have higher activation energy are controlling steps on the whole chain. In this study, coal pyrolysis models developed by Suubergand Solomon is simplified, and N pyrolysis models are complemented, then coal rapid pyrolysis models under reburning conditions is deduced(detail omitted for length limitation).

2.3 Volatiles release kinetics models

Coal pyrolysis productions mainly include CH_4, C_2H_4, C_2H_6, H_2, CO, CO_2, tar, HCN, and NH_i. In order to simplify the models, it is supposed secondary devolatilization take place after tar formed, and part of the species converts to gas volatiles, the remain is char. Volatiles release models of David Merrick[7] are adopted in calculations. Hydrocarbons higher than ethane are dealt with 'ethane equivalent', while gaseous nitrogen is dealt with 'ammonia equivalent'. Double-C hydrocarbons consist of C_2H_4 and C_2H_6, and ammonia equivalent are consist of NH_3 and HCN. According to the experiential data, C_2H_4: C_2H_6 is 1:7, and NH_3: HCN is 1:1.

The approach adopted to predict the final yields of the volatile matters is to establish a set of 9 simultaneous linear equations with the final masses of tar and eight volatiles as variables. These equations can be expressed as followings:

$$\sum_{j=0}^{9} A_{ij}\overline{m}_j = b_i \qquad i = 1,\cdots 9 \quad (4)$$

Where: A_{ij} is a matrix of constants; $\overline{m}_j$ are the final yields (as mass fractions of coal $_{daf}$) of CH_4, C_2H_6, CO, CO_2, H_2, H_2O, NH_3, HCN and tar; b_i is a vector of constants. Therefore, the final yields of volatiles can be figured out with these equations.

Volatiles release rates can be figured with the following equation:

$$\frac{dV_j}{dt} = K_j(V_j^* - V_j) \quad (5)$$

Where: V_j is the final yield of species j at time t (as mass fractions of coal $_{daf}$); V_j^* is the V_j at the time of $t\to\infty$, and these have been figured out through the above matrix; K_j is the reaction rate constant and comply with Arrhenius law.

$$K_j = A_j \exp(-E_j / RT) \quad (6)$$

A_j and E_j of different reactions for creating CH_4, C_2H_6, CO, CO_2, H_2, H_2O and NH_3 are showed in Table 2. With equation (6), volatiles release rates and volatiles yields at different times can be calculated.

3. Calculating parameters

Mathematical models are developed on the basis of an experimental EFR with standard 1600×φ60mm. Flue gas temperature in furnace is 1300℃. Inlet flue gas temperature is 20℃, and flux is 1.83m^3/h. pulverized coal flux is 1.457g/min□the relative reburning fuel fraction is 25%.

Table 1 Physical parameters adopted in calculation

Physical parameters	Formulations	References
Gas phase specific heat, C_{pg}	(0.9986+9.3*E*-5*(T_g-273))*29	[8]
Solid phase specific heat, C_{ps}	$0.222+2.18\times10^{-4}\times T_s$ $9741.666/T_s^2$	[9]
Solid darkness, Gas darkness	0.9□0.149	[10]
Gas heat transfer coefficient ($kWm^{-1}K^{-1}$)	$57\times10^{-6}\times[(T_s+T_g)/1600]\times0.75$	[11]
Temperature of inlet flue gas and coal	20℃	Measured
Tube wall temperature□flue gas flux	1300℃, 10.1736m^3/h	Measured

The entrained flow is divided into some time differential segments with 0.001s. Physical parameters used in calculation are showed in Table 1 and Table 2, respectively.

Table 2 Results of coal and char analysis

Items		Coal less than 100 mesh	Coal less than 320 mesh	Char less than 100 mesh	Char less than 320 mesh
Ultimate analysis (%)	C_{ad}	66.01	65.11	76.76	75.53
	H_{ad}	4.361	4.056	0.618	0.223
	O_{ad}	17.3	17.44	8.701	8.137
	N_{ad}	0.824	0.71	0.796	0.745
	S_{ad}	0.552	0.59	0.964	0.717
Proximate analysis (%)	A_{ad}	12.7	13.9	19.33	21.36
	W_{ad}	5.2	5.3	1.76	0.5
	V_{ad}	29.2	27.8	3.53	0.72

4. Results and discussion

Using the above models and parameters, the heating rate and volatiles release of coal particles that less than 100 mesh and 320 mesh, are calculated under the conditions of NO reduction with 25% reburning fuel fraction in 1300℃ EFR.

4.1 Simulation of coal particles heating rate

Fig.1 shows the simulation results of the heating rate of two sizes of coal particles during coal reburning.

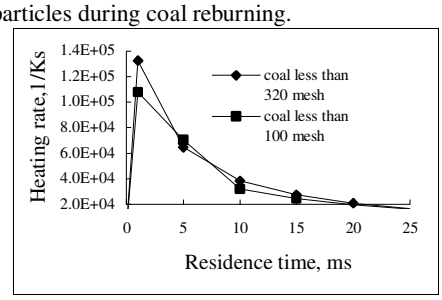

Fig.1 Simulation results of coal particles heating rate

As can be seen from Fig.1, the heating rates of two sizes of coal are all higher than 105K/s, and the heating rate of coal less than 320 mesh is obviously higher than that of coal less than 100 mesh. This implies that finer coals has higher heating rate under the same conditions, and finer coal can attain higher temperature in shorter time. At the same time, finer coal has better burning and burnout capability, which is in favor of boiler economically operation.

4.2 Simulation results of volatiles final yields

Total various volatiles final yields are showed in Fig. 2.

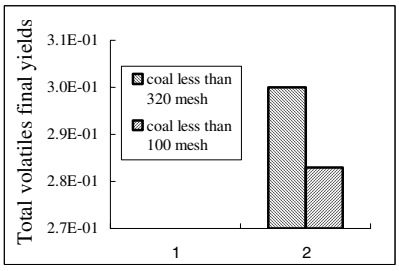

Fig. 2 Total volatiles yields of two sizes of micronized coals

It can be seen that the total volatiles final yields of coals less than 320 mesh is higher than that of coals less than 100 mesh.

Simulation results of coals heating rate show that finer coal has higher heating rate, and coal pyrolysis is more completely, also more volatiles are released. On one hand, C_mH_n, HCN and NH_3 are the main species to realize NO homogeneous reduction. More volatiles can reduce more NO. On the other hand, because finer coal achieves higher temperature in the same time, the corresponding char can also attain higher temperature and higher reaction rate to reduce NO.

4.3 Simulation results of volatiles release

Nine volatiles yields at different time are calculated. As an example, volatiles yields of C_iH_j and HCN at different time are showed in Fig. 3 and 4, respectively.

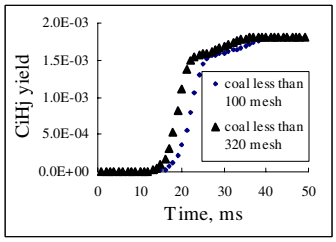

Fig.3 C_iH_j yield at different time

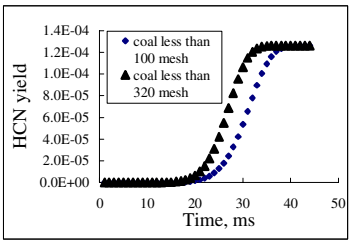

Fig. 4 HCN yield at different time

Fig.3 and Fig.4 show that volatiles release earlier from finer coal, and Fig.1 show that finer coal has higher heating rate. Finer coal attained higher temperature in the same time, so finer coal starts to devolatilize earlier, and coal devolatilize more acutely and completely.

Various volatiles almost release completely in 50ms. CO_2 has the highest release rate, and almost release completely in 18ms, then CH_4 in 28ms, and C_2H_4, CO, HCN, H, NH_3 in 40ms, C_2H_6 has the lowest release rate, and almost release completely in 47ms. This is because that the destruction of bonds that produce CO_2 needs less activation energy than that produce C_2H_6.

5. Conclusions

1-demension mathematical models based on an EFR laminar flow are developed. Then, the heating rate and volatiles release for different size of coals during NO reduction with coal reburning in an EFR are simulated and analyzed in detail. It is demonstrated that finer coal has higher heating rate and begin to devolatilize earlier, coal pyrolysis is more completely, and more volatiles are released.

With finer coal as reburning fuel, NO emission can be reduced and coal particles burning and burnout capabilities are improved. This benefits boilers economically operation. Therefore, micronized coal is better as reburning fuel than conventional pulverized coal.

References

1. Smart J P, Morgan D J. Fuel, **1994**, 73(9):1437-1442
2. Kicherer A, et al. Fuel, **1994**, 73(9):1443-1446
3. Zhong B.J., et al. J. of Eng. Thermo. **2000**, 21(3):383-387
4. Liu Z., et al. Proceedings of the CSEE, **2003**, 23(10):204-208
5. Zhong B.J., et al. J. of Combust. Sci. & Tech., **2001**, 7(2):116-119
6. Juntgen H. Fuel, **1987**, 63: 731-737
7. Merrick D. Fuel, **1983**, 62: 534-539
8. Shen W.D., et al. Engineering Thermodynamics. Beijing: higher education press, 1988
9. Perry R. H. and Gree W. D. 'Perry' s Chemical Engineers 'Handbook', 6th Ed. McGraw-Hill, New York, 1984
10. Vamvuka D., et al. Fuel, **1995**, 74: 1452-1460
11. Gururajan V. S., et al. Combust. Flame, **1988**, 72: 1-12

ACHIEVING SEPARATIONS AND DISTRIBUTED PRODUCTION TECHNICAL TARGETS OF THE PRESIDENT'S HYDROGEN FUEL INITIATIVE

Steven Chalk, Program Manager
Arlene Anderson, Technology Development Manager

Hydrogen, Fuel Cells, and Infrastructure Technologies Program
Office of Energy Efficiency and Renewable *Energy*
U.S Department of Energy

EE-2H, 1000 Independence Avenue, SW Washington, D.C. 20585

The President's Hydrogen Fuel Initiative

Announced on January 28, 2003 by the President in his State of the Union Address, the Hydrogen Fuel Initiative envisions a hydrogen economy that could have fundamental and dramatic benefits regarding energy security and the environment.

A transition to hydrogen as a major fuel in the next 50 years could fundamentally transform the U.S. energy system, creating opportunities to increase energy security through the use of a variety of domestic energy sources for hydrogen production while reducing environmental impacts, including atmospheric CO_2 emissions and criteria pollutants.

New Hydrogen Separations and Purification Research

With funding from the President's Hydrogen Fuel Initiative, next year DOE's Office of Energy Efficiency and Renewable Energy will cost-share 80% of total R&D expenditures for several new hydrogen separations and purification projects. The total funding for these projects is expected to be up to $10 million (including 20% cost share) and, the DOE Office of Fossil Energy is providing a portion of the DOE funding for hydrogen to coal related separations research. As a result of this research, within three to four years DOE will verify advanced pilot scale membranes that meet or exceed the membrane separations targets listed in Table 1.

As part of integrated decentralized hydrogen production systems and potentially as part of many possible technologies to be utilized for hydrogen production, DOE received many highly qualified research applications for new hydrogen membrane separation and purification technologies based on membrane systems that cost-effectively optimize different types of membrane characteristics while maintaining key attributes for producing high purity hydrogen.

Desirable membrane system characteristics include: 1) a high flux rate; 2) low cost; 3) improved durability; 4) low parasitic power requirements; and 5) low membrane fabrication costs. This new research will lend itself to membrane systems that integrate the hydrogen separation and purification steps with a shift reactor as a one step operation.

Another key theme of the research includes the development of membranes suitable for use with a wide range of fuels especially in reforming renewable biomass based liquid fuels (e.g. ethanol, methanol, biomass pyrolysis oils, etc.) and in a robust syngas environment, as from natural gas or coal-based applications. The targets shown in Table 1 are based on a palladium membrane that is fuel neutral and that can be used for hydrogen separation and purification from a variety of fuels. Sulfur tolerance and lower cost fabrication techniques are also desirable membrane system characteristics.

Table 1. Membrane Separations Targets

Characteristics	Units	Target
Flux Rate	scfh/ft^2	200
Cost	\$/ft^2	<100
Durability	Hrs	100,000
Operating Temp	^{o}C	300-600
Parasitic Power	kWh/ 1,000 scfh	2.8

New Distributed Reforming Hydrogen Production Research

Also with funding from the President's Hydrogen Fuel Initiative, DOE will cost-share 65% of total R&D expenditures for several new distributed reforming projects. The total funding for these projects will be about $8 million (including the 35% DOE cost share). As a result of this research, within three to four years DOE will verify pilot scale systems that can meet or exceed the targets specified in Table 2.

Small-scale distributed reforming production (i.e., 1,500 kg/day or less) of hydrogen from natural gas and/or liquid fuels at refueling stations, with an emphasis on fuels produced from renewable biomass resources (e.g. ethanol, methanol, biomass pyrolysis oils, etc.), is a viable approach to hydrogen production, but current small-scale distributed technologies are too expensive to compete with gasoline. Renewable biomass based liquid fuels have the added advantage of near-zero green house gases emissions. DOE is funding this new research to develop low cost, highly efficient distributed hydrogen production technologies from natural gas, other liquid fuels and renewable biomass based liquid fuels aimed at distributed production for refueling stations at capacities of 100-1,500 kg/day of hydrogen.

The hydrogen purity for use in Polymer Electrolyte Membrane fuel cells is critical. Hydrogen purity requirements are:

Hydrogen Purity: 98% minimum on a dry basis;
Carbon Monoxide <1 ppm;
Carbon Dioxide <100 ppm;
Sulfur <10 ppb;
Ammonia <1 ppm;
Non-methane hydrocarbons <100ppm;
Oxygen, Nitrogen, and Argon <2% in total.

Opportunities for cost reductions in distributed hydrogen production systems include better heat integration, improvements in reforming catalysts and purification technology, development of a single-stage shift reactor, and other unit operation integration.

Delivery of hydrogen at 5,000 psi on a cost effective, synergistic approach, integrated with the production step with capacities of up to 1,500 kg/day of hydrogen is also important to this research.

Costs used to develop the targets in Table 2 are based on a hydrogen refueling station serving 138 vehicles per day (690 kg per day) with on-site production assuming a high (90%) utilization factor and relatively low capital recovery factor (11%). Much lower utilization factors would be expected during the early years of fuel cell vehicle introduction. Capital equipment cost targets assume mature production volumes of 100 units per year. Energy costs assume a natural gas price of $4.40/MMBtu (LHV) and a power

price of $0.07/kWh. Primary energy efficiency of each step is defined as Hydrogen Output LHV / Energy Input LHV of that process step. Input energy associated with on-site power use assumes a 35% production and transmission efficiency penalty – a typical US grid mix. The total primary energy efficiency is defined as the net Hydrogen Output LHV / Total Energy Input LHV into the process.

Table 2. Distributed Production Targets

Characteristics		Units	Target
Reforming	Natural Gas Cost	$/kg H_2	0.58
	Cost	$/kg H_2	0.24
	Primary Energy Efficiency	%(LHV)	75
Purification	Cost	$/kg H_2	0.03
	Hydrogen Efficiency	%(LHV)	90
Compression	Cost	$/kg H_2	0.24
	Primary Energy Efficiency	%(LHV)	88
Storage & Dispensing	Cost	$/kg H_2	0.11
	Primary Energy Efficiency	%(LHV)	100
Other	Cost	$/kg H_2	0.30
	Primary Energy Efficiency	%(LHV)	100
Total	Cost	$/kg H_2	1.50
	Primary Energy Efficiency	%(LHV)	75

New Advanced Electrolysis Systems Research

DOE is also funding new technologies suited for power park and utility size systems including alkaline and solid oxide electrolysis. Key research areas include system cost reduction and efficiency improvement including power conversion, storage, and other components through renewable system integration, and steam electrolysis materials and systems development.

Regarding renewable energy/electrolysis system engineering, new technologies are targeting low-cost electrolysis systems capable of efficient, reliable integration with renewable electricity that may include the use of reversible solid oxide fuel cells. For example, systems are being designed to match utility scale wind turbines in the 500-1,500kW range and that have the modular capability to allow scaling to multi-Megawatt utility applications. These new systems will also have the potential for direct integration with other renewable energy sources. Projects include electrolyzer system design, renewable electric system interface, and grid interface with the focus on lowering capital costs and improving efficiency of system components including storage, power electronics, and other components.

As a result of this research, within three to four years DOE will verify pilot scale 500-1,500kWe electrolysis systems that can be modularly integrated with a utility sized renewable electricity system to verify the potential of producing 10,000 kg per day hydrogen at $2.00 per kg at the plant gate.

High temperature steam electrolysis research activities will explore solid-oxide technology for low cost hydrogen production and opportunities for co-generation of hydrogen and electricity. This research includes development of electrodes and system designs for reversible electrolysis/fuel cell systems or development of system designs for low cost production of hydrogen using solid oxide technology.

Renewable power park applications and distributed production of hydrogen and electricity are key focus areas where DOE will verify low-cost, reversible electrolysis/fuel cell electrode materials and pilot scale system designs to achieve 70% energy efficiency and hydrogen production cost of $2.00 per kg at the plant gate when scaled to a 500kW system.

References

(1) U.S. Department of Energy, Energy Efficiency and Renewable Energy*, Hydrogen, Fuel Cells & Infrastructure Technologies Program, Multi-Year Research Development and Demonstration Plan*, **2003**

FUELING OUR FUTURE: FOUR STEPS TO A NEW RELIABLE, CLEANER, DECENTRALISED ENERGY SUPPLY BASED ON HYDROGEN & FUEL CELLS

Arno A. Evers

Arno A. Evers FAIR-PR
Achheimstr. 3
82319 Starnberg, Germany

Abstract

This presentation demonstrates the possible driving factors and necessary elements needed to move Hydrogen and Fuel Cells (H2/FC) to worldwide commercialisation. Focusing not only on the technology itself, this presentation looks at the "bigger picture" explaining how certain trends have impacted the progress of new technologies developments in the past. The presentation demonstrates how these models can be applied to our present day situation. Examining different Distributed Generation scenarios, the catalyst to the Hydrogen Economy may be found through distributed generation via fuel cells. One possible step could be the use of Personal Power Cars equipped with Fuel Cells which not only drive on Hydrogen, but also supply (while standing) electricity /heat to residential and commercial buildings. This scenario, as well as, the inter-dependability between supply and consumer-driven demand (or better, demand and supply) will be further explained.

FUEL CELL APPLICATIONS

(STATIONARY/MOBILE/PORTABLE). More than 100 international Fuel Cell companies are supplying their equipment to a number of Utility companies around the globe. Car manufacturers worldwide are working on vehicles with Fuel Cells and electrical motor drives or ICE's, powered by Hydrogen. All computer manufacturers are working on portable fuel cells. A Toshiba H2/FC notebook powered by Hydrogen will come on the market in 2004 as announced at CeBIT '03, March 2003.

ON PROBATION OR READY FOR TAKE-OFF? Fuel Cell technology has been on worldwide probation for the last 30 years. Billions of US $ – both from Private finance and Governmental funds - have already been invested. Adoption was announced several times, but often postponed. There are two critical issues to bear in mind. First, how long will it take for H2/FC to become commercial? Second, will H2/FC be on probation for another 30 years?

IMPLEMENTATION TIME OF NEW PRODUCTS.

Figure 1. Chart illustrating implementation time of new products. According to Siemens AG, over the years, new appliances have taken different time spans to reach 100 million U.S. customers. The radio, for example, took 90 years to reach 100 million U.S. customers; telephone, 70 years; television, 50 years; cable TV Network, 25 years; computer, 20 years; mobile phones, 15 years; Internet less than 5 years. The speed of implementation continues to grow faster and faster with every new product invented. I am convinced that the introduction of Hydrogen and Fuel Cells applications, products and services will take even less time; maybe just a few years.

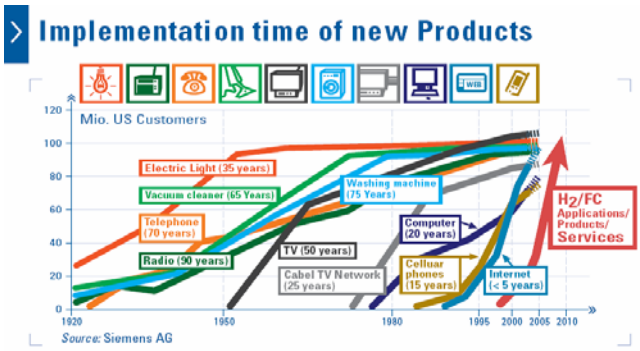

Figure 1. Chart illustrating implementation time of new products

Home appliance ownership in every 100 Shanghai, P.R. China, families. As the Chinese economy grew fast in recent years, the income of Chinese people had increased largely. As China's overall economy is expected to continue its growth over the next years, the income level of Chinese residents will also continue to grow. The reasonable rise of the income will ensure the purchasing power needed for unexpected expansion of daily-use electrical appliance market. This is demonstrated in **Figure 2** by the demand for highly efficient new products bought by the average Shanghai family.

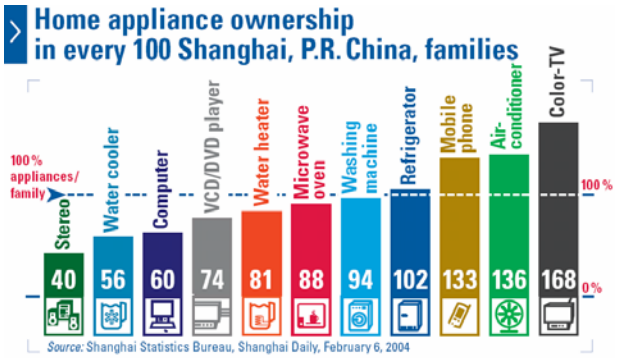

Figure 2. Home appliance ownership in P.R. China

Evolution of Cellular Phone 1983-2004. Figure 3. Evolution of the Cellular Phone 1983-2004. The progression of the telecommunications industry is immense; for example, a 3,000 USD Dynetek cellular phone from 1983 with a weight of 3 lbs without display has less performance than a 299 USD Samsung cellular phone from 2004 with a weight of 3,6 oz. with color LCD. Worldwide, this progress is not driven by any governmental subsidy; it is only driven by the demand of the consumer who is looking for added value. The increase of quantities per time of the units leads to a sharp decrease in the price per unit.

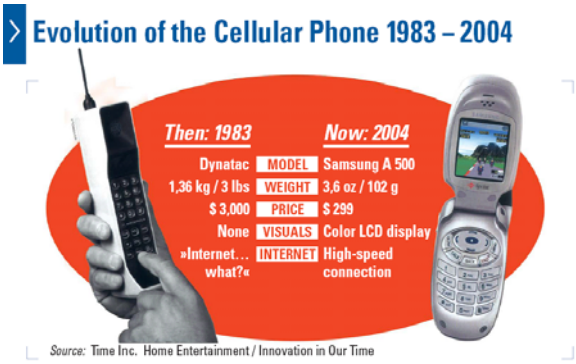

Figure 3. Evolution of the Cellular Phone 1983-2004

Evolution of the Aircraft Industry 1903-2005. Figure 4. Evolution of the Aircraft Industry comparing Wright's Flyer with today's Airbus A380 over the past 102 years. When Orville and Wilbur Wright left their plane after the first powered flight (lasting 57 seconds) in Kitty Hawk, North Carolina, December 17th, 1903, they would never imagine that only 100 years later there would be an aircraft built with a range of more than 8000 miles carrying 550 passengers in peace and comfort. Today's Hydrogen and Fuel Cell industry status compares with the time of the Wright Brothers. There are more dramatic developments coming than anyone can imagine, hopefully, in less than 100 years.

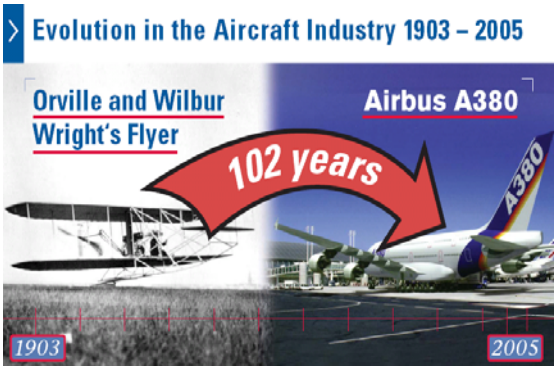

Figure 4. Evolution of the Aircraft Industry comparing Wright's Flyer with today's Airbus A380 over the past 102 years

FOUR STEPS TO AN ENERGY SUPPLY BASED ON HYDROGEN AND FUEL CELLS. Figure 5: Illustration of steps towards a cleaner, reliable, decentralised energy supply. In my opinion, cars could be the key for a new Energy Supply based on H2/FC. All it takes is four steps. Step 1 – Renewable energies (like wind, solar, hydroelectric and/or biomass energy) produce Hydrogen. Step 2 – The cars drive on Hydrogen using Fuel Cells and electrical motors. (The first two steps are readily available worldwide. However, at this time, there's no public demand for use of these options. To get the repeatedly promised Hydrogen economy on its wheels, two more steps must follow.) Step 3 – While parked, these vehicles drive idle and supply electricity to the buildings where they are parked. Step 4 – Car owners earn money based on the electricity/heat supplied by their cars.

The incentive for car owners driving and using vehicles equipped with Hydrogen and Fuel Cells systems is twofold. They can either save or earn money while their cars are parked and plugged into buildings via a smart docking station. For example, your car parked at home in your garage will supply electricity to your home and additionally, replace the function of your existing boiler and even all air conditioning units, thus saving you money. You can earn money by selling the electricity generated, but not used at home at that time, to the utilities and feed it into the existing electricity grid.

Figure 5. Illustration of steps towards a cleaner, reliable, decentralised energy supply

REVOLUTION IN THE GARAGE. Figure 6. Illustration of Personal Power Car taking over the role of the boiler & delivering electricity to house & electrical grid whereby creates a "revolution in the garage". Looking at today's so-called "western" countries, if all registered cars would be equipped with a Fuel Cell system, they could (all together) easily take over the function of today's existing stationary power plants. This is due to the fact that the total power installed in the cars' engines exceed the capacity of existing stationary power plants by 20-35 times.

In the first stage, the Hydrogen needed to power this system will come from natural gas which is presently and widely available. The individually produced Hydrogen will be stored in a personal tank inside the garage or the cellar. The Fuel Cell in the cars produces DC, which will be converted in the house into AC. DC can also be used directly with nearly all advanced appliances like computers, plasma screens, mobile phones. The heat generated by the fuel cell in the car will warm your home in winter, and in summer, the heat will be converted by means of special heat exchangers to eventually replace all residential air-conditioning units. This idea has many "fathers", Amory B. Lovins to mention one, and is just one example of where we could apply this technology.

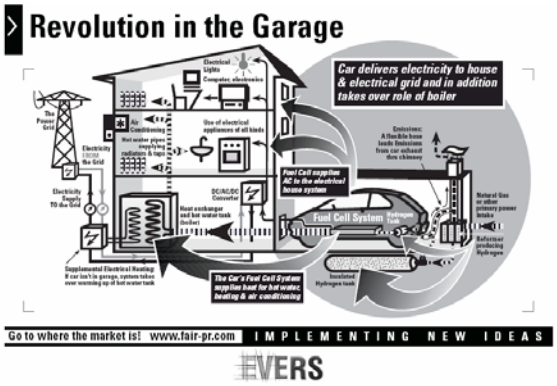

Figure 6. Illustration of Personal Power Car taking over the role of the boiler & delivering electricity to house & electrical grid whereby creates a "revolution in the garage".

NECESSARY CONDITIONS TO REACH THE FINAL GOAL: MASS DEMAND WILL DRIVE MASS PRODUCTION. **Figure 7**. Illustration of Strategic Alliances and relationship to Mass Production. To achieve early market entry, it is first necessary to make the consumer excited and eager to use the new services provided by the H2/FC technology. Nobody will ever buy a Fuel Cell just to have one. What the public will buy (and pay a lot of money for) are new services unknown today. All new inventions began as "luxury" goods. The consumer must be motivated and be given certain incentives: personal advantages, product reliability and usefulness. Only when these factors are guaranteed, will the price, at least in the beginning, play a less important role. This means the more expensive the product/service is, the more chances the early adopters will buy this "luxury". In addition, entrepreneurs involved in R&D, production & marketing of H2/FC services must also be motivated and stand firmly behind their vision. Commitment and belief in their technology will play a critical role in the early stages of fuel cell commercialisation. Strong efforts are needed in convincing the politicians, the media, and the involved companies that H2/FC is a viable solution for the growing energy demand. Raising energy security concerns and the impact of global pollution will additionally support the implementation. These general conditions will lead to worldwide mass-production and make H2/FC's appearance in the marketplace, sooner rather than later**.**

Figure 7. Illustration of Strategic Alliances and relationship to Mass Production

MARKET OUTLOOK: EUROPE AND CHINA

Europe.

Figure 8. Map of European Fuel Cell stationary units and buses including percentage share of Euro industry by country. In Europe, there are currently 81 Stationary H2/FC units (power plants) in operation with a total capacity of 12 MW power. There are 27 H2/FC buses planned by the EU-sponsored CUTE programme. Germany leads with a share of the European industry of 31% followed by UK with 19%, Italy with 7% and France, Spain with 6%.

Some recent EU policy actions: Action plans on energy efficiency include improving energy efficiency by +18% from 1995 to 2010 and increasing the share of co-generation to 12% of EU-15 (member countries) electricity by 2010. A white paper on renewable energies recommends doubling the share of renewable energies from now 6% to future 12% of final energy. There are active committees who analyse the communication on alternative fuels. They propose Hydrogen with a share of 5% of road transport fuel by 2020.

China.

The National Natural Scientific Foundation (NSFC) is responsible for Fundamental Research. Projects include: The "863 High Technology Research and Development" project deals with commercially potential ventures. Key projects include: Fuel Cell cars and buses with a allocated budget of 33 million EURO; Fuel Cell Key Material Project concentrating on membrane and bi-polar development; Future Energy Project focusing on DMFC, MCFC, SOFC.

The "973 Project" is dedicated to high technology fundamental research on Hydrogen Energy (including Fuel Cells). The NSFC is looking at new material possibilities and new Fuel Cell concepts. The Chinese Academy of Sciences, Ministry of Education works on fundamental and applied fundamental research in Fuel Cell engines and Hydrogen Technology. The up-and-coming Chinese H2/FC industry deals with applied fundamental research such as advances in Hydrogen production from Natural Gas, Methanol and Gasoline.

CONCLUSION

This industry overview shows that the demand of the consumer will play the critical role in the mass-market evolution of H2/FC products and services. At first, H2/FC powered products/services will be considered luxury items with only a handful of the population being able to afford to buy them. However, over time and as the technological awareness and knowledge about the advantages grows, the consumer will become better educated as to the many benefits offered by services powered by H2/FC technologies. Increased convenience and awareness rather than the price of the merchandise, will have an enormous impact on the consumer and will compel them to buy H2/FC powered goods, and furthermore, lead to the development of completely new H2/FC products and services which are unobtainable today. The Personal Power Car as described is just one example. However, the current activities in Europe and China as presented are sure to further accelerate the trend towards the coming Hydrogen Economy. **Figure 10**: Diagram of growth and development - Hydrogen + Fuel Cells Group Exhibit

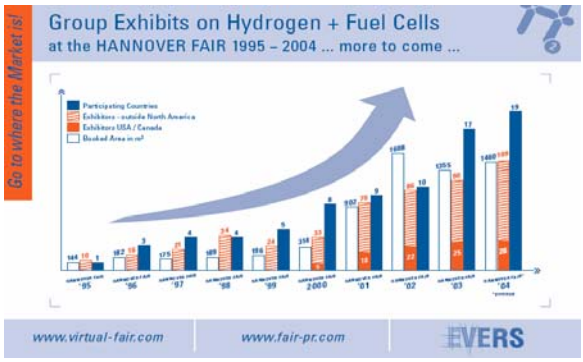

Figure 10. Diagram of growth and development - Hydrogen + Fuel Cells Group Exhibit

Seven Drivers to the Hydrogen Economy

Rahul Iyer

Intelligent Energy, Inc, 2955 Redondo Avenue, Long Beach, CA 90806.

The global demand for electric power is growing at an aggressive pace. An additional capacity of 183GW will be required from years 2000 and 2030. There are **seven** key distinctions between this growth and the previous 30 years of capacity growth. These distinctions will drive a dramatic paradigm shift from the homogenous and centralized energy systems of developed economies, to diversified and H2 based micro-grid systems established first in developing economies. Contrary to the notion that environmental concern is the only driver to the hydrogen economy, the forces pushing us towards H2 are diverse and numerous. The promise of the H2 economy rests largely on the concept of hydrogen's use as an "energy-currency."

In this new energy economy, diverse primary energy sources compete to provide an appropriate cost effective blend of energy. Fuel cells provide highly efficient energy conversion near the point of use for any number of applications. With H2 as the energy carrier, the delicate balance between scale, capital expenditure, and profitable plant operation becomes more robust. The rising marginal utility of increases in power/hydrogen generation capacity promotes more sustainable growth in infrastructure. Distributed H2 generation will become a viable industry.

Renewable energy sources are currently plagued with availability issues. Renewable sources of any scale geared to produce hydrogen fuel whenever the primary renewable source is available increases the value of all renewable energy. Renewables and non-renewables compete to supply the demand of hydrogen fuel for vehicles, stationary, and other applications. Markets with a larger number and higher diversity of suppliers create a more stable and economical energy supply. As with all majoreconomic change, early stages are fraught with technological missteps. A fresh approach based on appropriate energy solutions will meet and exceed the world's demands not only for power, but quality of life.

1. Emerging Markets

The most dramatic growth in the energy industry will come from emerging markets and entirely new groups and types of customers. These new markets have demands and priorities which have not, and will not, be met by traditional energy market approaches. As developed economies are characterized as post industrial revolution economies, these emerging economies will be characterized as post information revolution economies. As such, these economies will rely heavily on high quality and high availability power, a requirement for high technology economies.

2. Sustainable Development

Focus on Sustainable Development and environmental concerns will take on new importance, driving certain technologies forward. New market vectors around these concepts will evolve and play a major role in future energy economics.

3. Deregulation

General global drift towards deregulation, and the fall of fully funded state and para-state energy regimes help foster entirely new types of organizations and businesses to meet energy needs of emerging markets.

4. Financial Markets

The financial world has evolved to embracing shorter time horizons, generally supporting smaller investments, and tolerating less risk. These market forces primarily impact the way energy programs and markets around the world will be structured, and secondarily impact technology choice.

5. Cognizant Consumption

The socioeconomic weight of the global energy market is undeniable. The geopolitical implications of installing low wattage lighting, and choosing to drive a hybrid vehicle, are fast becoming factors in consumptions patterns.

6. Market Convergence

As communications technology and use have converged by way of the internet, so too will energy technology and use converge by way of the hydrogen economy. Domestic power and motive power markets will experiences a convergence, resulting in new technologies and business constructs. These new concepts will be as numerous and diverse as were spawned by the recent and ongoing information economy transformation.

7. Flexibility

Flexibility and dynamism will become an important aspect of energy technologies, as infrastructure growth is increasingly required to be as dynamic as the populations which they serve. As populations, communities, families, and individuals have become more dynamic and diverse, the energy infrastructures (including transportation) will be called on to exhibit the same level of flexibility.

THE NATIONAL HYDROGEN STORAGE PROJECT

Antonio Bouza, John Petrovic[1], Carole Read, Sunita Satyapal, and JoAnn Milliken

U.S. Department of Energy
Office of Hydrogen, Fuel Cells and Infrastructure Technologies
1000 Independence Ave. SW
Washington DC 20585

Introduction

The transition to a hydrogen economy with fuel cell-powered vehicles over the next few decades is crucial to energy security and environmental quality in the United States and around the world. This energy vision was put forward by President Bush in his January 2003 State of the Union address.

A critical enabling technology for the development of hydrogen fuel cell-powered vehicles is the capability to have sufficient on-board hydrogen storage to enable greater than 300-mile driving range under the weight, volume, and cost constraints posed by customer expectations. Current vehicular hydrogen storage systems cannot meet this ultimate requirement. New materials and approaches are needed and that is why the U.S. Department of Energy (DOE) is proceeding with the implementation of a National Hydrogen Storage Project.

Requirements for On-Board Hydrogen Storage

Storing sufficient hydrogen on a vehicle to achieve a greater than 300-mile driving range is difficult. On a weight basis, hydrogen has nearly three times the energy content of gasoline (120 MJ/kg for hydrogen versus 44 MJ/kg for gasoline). However, on a volume basis the situation is reversed (8 MJ/L for liquid hydrogen versus 32 MJ/L for gasoline).

On-board hydrogen storage system performance targets have been developed through the FreedomCAR Partnership between DOE and the U.S. Council for Automotive Research (USCAR). These targets are system-driven and are based on achieving similar performance and cost levels as current gasoline fuel storage systems.

Current Status of On-Board Hydrogen Storage

Current on-board hydrogen storage approaches involve compressed hydrogen gas tanks, liquid hydrogen tanks, complex metal hydrides, chemical hydrogen materials such as chemical hydrides, and carbon-based materials. Carbon fiber-reinforced 5000-psi and 10,000-psi compressed hydrogen gas tanks are under development, as are liquid hydrogen tanks. Issues with compressed gas tanks include high pressure, volume and cost. Liquid hydrogen tanks have boil-off and liquefaction energy penalties and cost issues. Complex metal hydrides have low hydrogen capacity, unacceptable uptake and release kinetics and cost issues. Chemical hydrogen materials include key issues associated with regeneration energy requirements and cost. Carbon-based materials, which are at an earlier stage of development, are encountering hydrogen storage capacity, performance reproducibility issues and high cost.

The current status of on-board hydrogen storage systems are shown in Table 1 based upon estimates provided to DOE by program participants and available in the open literature.

Table 1. Current Status of On-Board Hydrogen Storage Systems

Storage Approach	Gravimetric Energy Density (kWh/kg)	Volumetric Energy Density (kWh/liter)	Storage System Cost ($/kWh)
5000-psi gas tanks	2.1	0.8	$12
10,000-psi gas tanks	1.9	1.3	$16
Liquid H_2 tanks	2.0	1.6	$6
Metal hydrides	0.8	0.6	$16
Chemical hydrides	1.6	1.4	$8
2010 System Target	**2.0**	**1.5**	**$4**
2015 System Target	**3.0**	**2.7**	**$2**

At the present time, there is no on-board hydrogen storage technology that can meet the combined requirements of weight, volume, and cost that are necessary for implementation of hydrogen fuel on the full spectrum of light-duty vehicle platforms by the target year of 2020 put forward by President Bush. For example, the volumetric energy capacity required for full implementation in all light-duty vehicle platforms is greater than that of liquid hydrogen. The most promising technologies require using solid-state materials or liquids as storage media, but very little scientific work exists on these approaches. This is the main driver for DOE proceeding with the implementation of a National Hydrogen Storage Project.

The National Hydrogen Storage Project

The DOE in July 2003 issued a "Grand Challenge" for Basic and Applied Research in Hydrogen Storage. This Grand Challenge called for the establishment of hydrogen storage Centers of Excellence: Metal Hydrides, Chemical Hydrogen Storage, and Carbon-Based Materials, led by a DOE national laboratory and having a number of university, industry, and federal laboratory partners. In addition, independent projects are established with respect to new materials and concepts, off-board hydrogen storage systems, and analysis. The new Centers and independent projects, together with existing DOE hydrogen storage efforts, constitute the framework of the National Hydrogen Storage Project.

The structure of the National Hydrogen Storage Project is shown in Figure 1. On April 27, 2004 the Secretary of Energy Spencer Abraham announced the selections for the Hydrogen Storage Grand Challenge.

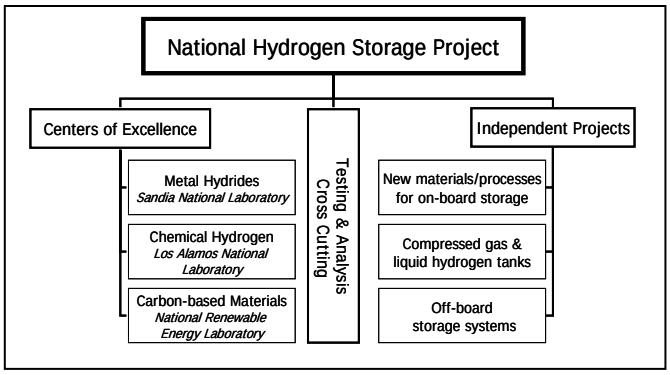

Figure 1. Structure of the National Hydrogen Storage Project

[1] Laboratory Fellow, Los Alamos National Laboratory, on assignment to DOE Headquarters.

The Metal Hydride Center is led by Sandia National Laboratories in Livermore, California. The Sandia Center will focus on the development of advanced metal hydride materials. The Metal Hydride Center includes 7 university partners, 3 industrial partners, and 5 federal laboratories.

The Chemical Hydrogen Storage Center is led by the Los Alamos National Laboratory in Los Alamos, New Mexico in partnership with Pacific Northwest National Laboratory in Richland, Washington. The Los Alamos Center will focus on three "tiers" of R&D for chemical hydrogen storage: borohydride-water, novel boron chemistry, and innovation beyond boron. The Chemical Hydrogen Storage Center includes 6 university partners, 3 industrial partners, and 2 federal laboratories.

The Carbon-Based Materials Center is led by the National Renewable Energy Laboratory (NREL) in Golden, Colorado. The NREL Center will focus on breakthrough concepts for storing hydrogen in carbon-based materials such as hybrid nanotubes, aerogels, and nanofibers, as well as novel materials such as metal-organic frameworks and conducting polymers. The Carbon Center includes 7 university partners, 1 industrial partner, and 4 federal laboratories.

The National Hydrogen Storage Project also involves independent projects that explore promising new hydrogen storage materials and concepts, off-board hydrogen storage needed for a hydrogen delivery infrastructure, standardized testing of hydrogen storage capacities, and analyses of life-cycle cost, energy efficiency, and environmental impact for materials-based hydrogen storage systems. Some of the new materials/concepts being studied include nanostructured materials, amine borane complexes, metal perhydrides, clathrates, lithium nitride, glass microspheres, and irradiation activation of materials.

A down-select process has been incorporated into all of the Grand Challenge projects, so that the most promising hydrogen storage approaches can be identified and focused on as quickly as possible. Starting in Fiscal Year 2005, the DOE will provide funding at a level of $150 million over a five year period (subject to congressional appropriations) for the National Hydrogen Storage Project. The result of this R&D effort will be the development of hydrogen storage systems capable of meeting the 2015 DOE targets.

HIGH-TEMPERATURE OXYGEN SEPARATION MEMBRANES FOR USE IN THE SULFUR-IODIDE THERMOCHEMICAL CYCLE FOR HYDROGEN PRODUCTION

Andrea Ambrosini,[1] Terry Garino[2] and Tina Nenoff[1]

[1] Chemical and Bio Technologies, Sandia National Laboratories, PO Box 5800, MS 0734, Albuquerque, NM 87185-0734
[2] Ceramic Materials, Sandia National Laboratories, PO Box 5800, MS 1411, Albuquerque, NM 87185-1411

Introduction

Efficient and environmentally sound methods of producing hydrogen are of great importance to the US as we progress toward the H_2 Economy. Current studies are investigating the use of high temperature systems driven by nuclear and/or solar energy to drive thermochemical cycles for H_2 production. These processes are advantageous since they do not produce greenhouse gas emissions that are a result of hydrogen production from electrolysis or hydrocarbon reformation. Earlier studies have identified over 100 possible reaction cycles that produce H_2 at high temperatures.[1] Of the cycles identified as the most promising, many require the removal of O_2 or H_2 to push reaction equilibriums in favorable directions. Based on a previous extensive survey of over 100 thermochemical cycles, which took into account such metrics as efficiency, cost, number of steps, number and phases of reactants, among others, the Sulfur-Iodide (SI) cycle was deemed to be one of the most promising. As shown in Figure 1, the first step of the SI cycle involves the decomposition of H_2SO_4 into O_2, SO_2, and H_2O at temperatures around 850 ºC. Removal of O_2 from this reaction pushes the equilibrium towards dissociation, thus increasing the overall efficiency. The membrane required for this step must withstand the high temperatures and corrosive conditions inherent in this process. Perovskites are promising materials for such membranes due to their robustness and mixed ionic/electronic conductivities. A mixed ionic-electronic conductor would benefit the process by alleviating the need for an applied electrode across the membrane to balance the oxygen ion flux. To this end, dense ceramic membranes based on the double-substituted perovskite, $A_xSr_{1-x}B_yCo_{1-y}O_{3-\delta}$ (A=La, Y; B=Cr, Mn, Fe, Ni) were synthesized by solid state methods and structurally characterized using powder x-ray diffraction. TGA vs. temperature and oxygen partial pressure was performed to test the oxygen absorption and desorption properties of the material, while conductivity and permeability measurements are in process.

Experimental

Synthesis. Perovskite oxides were synthesized by the nitrate-citrate method.[2] Metal nitrates were dissolved into 100 mL of deionized H_2O. Citric acid was added in a 1:1 citric acid:metal cation molar ratio and the solution was heated to 90 ºC with stirring until water evaporated and then dried overnight in drying oven. Resulting powder was ignited at 350 ºC to burn off nitrates and citrates, ground with a mortar and pestle, and sintered at 1250 ºC for 24 hours.

Structural characterization. The materials were structurally characterized by powder x-ray diffraction (PXRD) on a Siemens D500 diffractometer (Cu K_α radiation, Bragg-Brentano geometry) and refined using the Jade 6.5+ [3] and FullProf [4] Rietveld refinement software.

Thermal studies. Thermal studies on samples determined to be single-phase were performed using a TA Instruments STD 2960 DTA-TGA in order to obtain information on oxygen stability and oxygen adsorption/desorption. To estimate oxygen stoichiometry, samples were reduced under 5% H_2/N_2 at 1000°C until weight loss stabilized, usually at about 14%. For absorption/desorption, multiple-cycle thermogravimetric analysis (TGA) was run on the single-phase samples. First the temperature was cycled three times between 50 - 850°C under an O_2 atmosphere. This was followed by cycling between O_2 (high pO_2) and Ar or He (low pO_2) atmospheres at a constant temperature of 850°C. PXRD studies were run before and after thermal study samples to confirm retention of the structure.

Results and Discussion

The double-substituted perovskites were indexed in the cubic Pm-3m (221) space group. Table 1 shows the compositions of the synthesized materials that were determined to be single phase, their lattice parameters, weight loss after reduction, and their average weight loss versus temperature and oxygen partial pressure. Yttria-stabilized zirconia (YSZ), a well-known ion conductor, is included in Table 1 for comparison purposes.

Figure 1 illustrates an example of a multiple-cycle TGA analysis. The first part of the graph shows the weight change as the temperature is cycled between 50-850 °C, under a constant flow of O_2 gas. This describes an easily reversible temperature-swing adsorption/desorption of oxygen. The second part of the graph illustrates the reversible weight change as a function of oxygen partial pressure, by cycling the gas between O_2 and Ar or He at a constant temperature of 850 °C. This implies that the material can transport oxygen across a membrane with an oxygen partial pressure differential. Post-TGA powder diffraction patterns reveal no structural changes after the temperature and gas treatments, demonstrating the robustness of the material. (Figure 2)

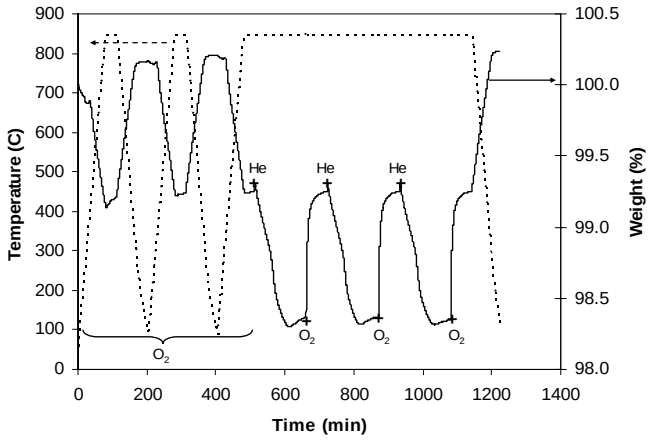

Figure 1. TGA of $La_{0.1}Sr_{0.9}Co_{0.7}Mn_{0.3}O_{3-\delta}$. The crosses mark where the atmosphere was changed between O_2 and He.

The most promising material thus far is the $La_{0.1}Sr_{0.9}Co_{1-x}Mn_xO_{3-\delta}$ perovskite. As shown in Table 1, the oxygen sorption properties increase with increasing Mn doping. Studies are currently underway to determine the extent of this solid solution and the composition of greatest oxygen conductivity.

Ongoing work involves the determination of the conductivity and permeation of these materials. For conductivity purposes, a four-point conductivity test instrument has been designed and built. Measurements have begun on samples of synthesized materials as well as on standard materials (YSZ), for comparison. Pressed and heat-treated powder samples are machined into bars nominally 2mm x 2 mm x 20 mm. Platinum wires are then wrapped around the bars at four places, both ends and just inside each end. Conducting paint

Table 1. Composition, desorption properties, and lattice parameters of single-phase perovskites.

Nominal Composition	Avg.Weight Loss vs. T	Avg. Weight Loss vs. Atm	Weight loss upon reduction	Lattice Parameter (Å)
YSZ (3%)	0.470%	0.0955%	N/A	N/A
$Y_{0.1}Sr_{0.9}Co_{0.9}Fe_{0.1}O_{3-\delta}$ (YSCF1991)	1.38%	0.892%	13.66%	3.840
$La_{0.1}Sr_{0.9}Co_{0.9}Ni_{0.1}O_{3-\delta}$ (LSCN1991)	1.21%	0.624%	13.98%	3.847
$La_{0.1}Sr_{0.9}Co_{0.8}Ni_{0.2}O_{3-\delta}$ (LSCN1982)	1.37%	0.730%	14.16%	3.847
$La_{0.1}Sr_{0.9}Co_{0.9}Mn_{0.1}O_{3-\delta}$ (LSCM1991)	1.36%	0.707%	14.00	3.845
$La_{0.1}Sr_{0.9}Co_{0.8}Mn_{0.2}O_{3-\delta}$ (LSCM1982)	1.13%	0.780%	12.99%	3.844
$La_{0.1}Sr_{0.9}Co_{0.7}Mn_{0.3}O_{3-\delta}$ (LSCM1973)	0.949%	0.910%	10.40%	3.841
$La_{0.1}Sr_{0.9}Co_{0.9}Cr_{0.1}O_{3-\delta}$ (LSCCr1991)	1.15%	0.699%	12.99%	3.868
$La_{0.1}Sr_{0.9}Co_{0.9}Fe_{0.1}O_{3-\delta}$ (LSCF1991)	1.45%	0.624%	13.51%	3.852

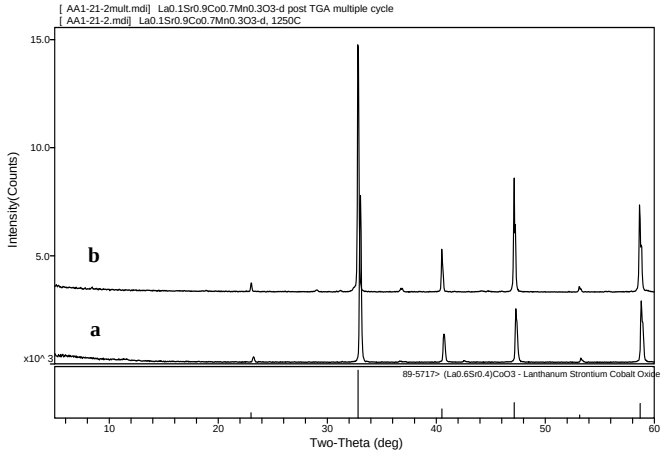

Figure 2. Powder x-ray diffraction pattern of $La_{0.1}Sr_{0.9}Co_{0.7}Mn_{0.3}O_{3-\delta}$ (a) after sintering at 1250 ºC and (b) after multiple-cycle TGA. The bottom pattern is a reference of a perovskite with the space group Pm-3m.

(silver-palladium) is used to ensure good electrical contact between the wires and the sample. The samples are placed in a tube furnace under controlled temperature and atmosphere. Measurements are being made in the 400º to 800 ºC range. A DC current source is connected to the wires at the ends of the sample and voltage drop across the other two wires is measured with a voltmeter. The conductivity is then simply determined from the current, voltage and the geometry. The initial measurements for each sample are done in air. Materials with high conductivity (comparable to that of the YSZ reference material) are measured in other pO_2 atmospheres (e.g., UHP Ar and 3% hydrogen in Ar) to determine whether the conductivity is ionic or electronic: ionic conductivity will be independent of the oxygen pressure while electronic conductivity will scale with it. For materials of interest, AC measurements (impedance spectroscopy) will also be performed to learn more details about the mechanism of conductivity. In addition, a high temperature permeation unit is under construction to test the oxygen permeation properties of these materials at 850 ºC under an oxygen partial pressure differential. The unit will be connected to a residual gas analyzer (RGA) to monitor the permeate.

Conclusions

Double-substituted perovskites, $A_{1-x}Sr_xCo_{1-y}B_yO_{3-\delta}$ (A=Y, La; B=Fe, Ni, Cr, Mn) were synthesized for use as ceramic high-temperature oxygen separation membranes. Preliminary results show the materials have promising oxygen sorption properties and are structurally robust under varying temperatures and atmospheres. Continuing work will focus on conductivity and permeation measurements, as well as stability under reaction conditions of H_2SO_4, SO_2, and H_2O at high temperatures.

Acknowledgement. Sandia is a multiprogram laboratory operated by Sandia Corporation, a Lockheed Martin Company, for the US DOE's NNSA, contract DE-AC04-94-Al85000. The authors would like to thank John Heald for the acquisition of the x-ray data and Dr. Fred Gelbard and Dr. Terry Guilinger for their helpful discussions.

References

(1)Brown, L.; Besenbruch, G.; Lentsch, R.; Schultz, K.; Funk, J.; Pickard, P.; Marshall, A.; Showalter, S. *High Efficiency Generation Of Hydrogen Fuels Using Nuclear Power*; Grant No. DE-FG03-99SF21888; Technical Report prepared for the Nuclear Energy Research Initiative (NERI) Program: December 2003.

(2)Yang, Z.; Lin, Y.; Zeng, Y., High-temperature sorption process for air separation and oxygen removal. Ind. Eng. Chem. Res. **2002,** 41, (11), 2775.

(3)*Jade 6.5+*, 6.5+; Materials Data Inc.: Livermore, CA, 2002.

(4)Rodriguez-Carvajal, J. *FullProf.2k*, 2.60; ILL: 2004.

INDUCED DEFECTS IN CARBONACEOUS MATERIALS FOR HYDROGEN STORAGE

Angela D. Lueking, Caroline E. Burgess Clifford, Deepa L. Narayanan

Department of Energy & Geo-Environmental Engineering
The Energy Institute
The Pennsylvania State University
University Park, PA 16802

Introduction

The use of hydrogen as an energy carrier will require a means to transport and store hydrogen, yet no existing technology meets the performance requirements established by the U.S. Department of Energy. Carbon nanomaterials (SWNT, MWNT, GNF) have several properties favorable for adsorption—surface area, pore size, and electrical conductivity—and these properties can be tuned by judicious selection of the conditions by which the carbons are prepared. However, hydrogen storage claims in these carbon nanomaterials have been highly scattered, ranging from 0.4%-67%. The discrepancies in these reports are thought to be due to experimental artifacts, impurities, carbon properties, and assessment techniques.

There has been a recent resurgence in hydrogen storage claims for graphite nanofibers (GNF) and multi-wall nanotubes (MWNT), and the results have been reported by a number of research groups: 3.8% at 69 bar,[1] 6.5% at 120 bar for GNF[2]; and 1.97% at 40 bar[3] to 6.3% at 148 bar[4] for MWNT. These recent claims discuss how: (a) the nanotube structure and defects relate to hydrogen uptake,[1] (b) these defects can be formed during synthesis or subsequent pretreatment[1]; (c) terminal carbon groups act to dissociate hydrogen,[1, 2]; and (d) the carbon structure may become expanded after exposing the carbon to hydrogen.[5] The ball-milling of graphite has been used to obtain a total hydrogen capacity of 7.4% with neutron diffraction evidence of chemisorbed hydrogen.[6] Ball-milling of carbon nanotubes has also shown promise, as long as the graphitic nature of the nanotubes is partially retained.[7] Additionally, graphitic carbon has shown a synergistic effect when ball-milled with magnesium.[8] These reports suggest that defects within the graphitic structure lead to enhanced hydrogen storage and that this effect can be magnified through synthesis, pretreatment, and processing.

The goal of this project was to induce defects in carbonaceous materials through both ball-milling and/or carbon exfoliation; here, we report initial exfoliation results. This study serves to test the emerging hypothesis in the literature: carbon defects chemisorb hydrogen, with possible expansion of the graphite lattice. If the advantageous effect of carbon defects is confirmed and better understood, controlled introduction of defect may increase hydrogen storage by introducing new hydrogen storage sites.

Methods

Materials. Ultra-high purity hydrogen (99.999%) was used in adsorption experiments, and ultra high purity helium (99.999%) was used to determine the bulk density of the adsorbents for buoyancy corrections, both gases were pretreated with an in-line 3A molecular sieve zeolite column to eliminate possible moisture contamination. Graphite nanofibers were purchased from Catalytic Materials, Ltd. A powdered graphite sample was obtained from Carbone and used as received.

Introduction of Defects. Carbon exfoliation served as one means to impart defects and increase interlayer spacing between graphene sheets. Methods to exfoliate graphite are well known and were extended here to other graphitic carbons. The primary exfoliation method used in this study was a mixture of nitric and sulfuric acids followed by thermal shocking at 700 °C.[9]

Materials were treated *in situ* on the IGA prior to adsorption measurements. The thermal treatments were chosen based on previous studies[1] and the thermal stability of the fibers.

Characterization. Standard physisorption methods, including surface area and pore size distribution, were determined in situ on the Hiden IGA-003 after thermal degassing and prior to adsorption measurements. Electron microscopy, including TEM and SEM (Philips XL20), was used to determine the morphology and diameter of the material, before and after treatments. The bulk density of the carbon materials was determined by helium isotherms on the IGA. Carbon materials were thermally decomposed on the IGA in 100 ml/min helium with a ramp rate of 4 °C/min. These thermal decomposition studies were used to determine applicable degas temperatures and to give an indication of the thermal stability of the fibers after the treatments.

Hydrogen Uptake. A high-pressure TGA (Hiden Isochema IGA-003) was used to evaluate hydrogen uptake at pressures up to 20 bar. The IGA provided a high sensitive measurement with precise temperature and pressure control for automated measurements of adsorption and desorption isotherms. In addition, the IGA enabled *in situ* treatment and characterization prior to hydrogen measurements; typical pretreatments consisted of inert thermal treatments with or without partial thermal degradation. All hydrogen uptake measurements are normalized to sample mass after pretreatment, with buoyancy corrections determined from bulk density measurements with helium.

Results and Discussion

Introduction of Defects and Exfoliation of Graphite Lattice. The relatively mild sulfuric/nitric acid treatment successfully exfoliated graphite (Figure 1), in agreement with previous results.[9] Preliminary results of GNF exfoliation with the same method illustrate definite differences in SEM micrographs (Figure 2): exfoliated GNF had ragged edges when compared to the untreated GNF. TEM analysis is underway to better analyze the effect of exfoliation and quantify the GNF diameter before and after exfoliation. There was some indication that a milder exfoliation method may be needed for GNF, as SEM indicated that some regions of the sample lost the fiber structure after exfoliation (data not shown). The bulk density of the GNF, as measured by helium buoyancy on the IGA, changed from 1.86 g/cc to 1.31 g/cc upon exfoliation.

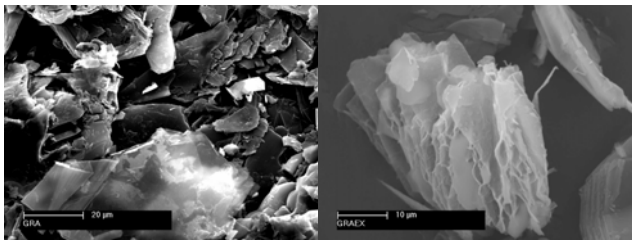

Figure 1. Exfoliation of powdered graphite in a mixture of nitric/sulfuric acid with thermal shocking at 700 °C (a) before exfoliation; (b) after exfoliation.

Thermal decomposition of the GNF before and after sulfuric/nitric acid exfoliation indicated a clear loss of thermal stability. Prior to exfoliation, the GNF showed no significant degradation in helium at temperatures up to 1000 °C; however, the onset of thermal degradation of the sulfuric/nitric acid exfoliated

GNF was at 100 °C with a maximum rate of mass loss at 120 °C (Figure 3). This thermal reactivity is an initial indication of both the increased reactivity and the decreased graphicity of the GNF samples upon exfoliation. Comparison of the 70% mass loss to SEM visualization suggests that the increased reactivity occurs in both amorphitized GNF and exfoliated GNF, however further quantification of this is clearly needed.

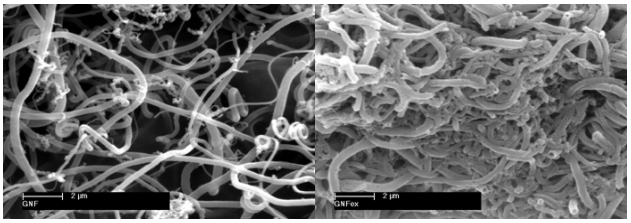

Figure 2. Exfoliation of GNF in a mixture of nitric/sulfuric acid with thermal shocking at 700 °C (a) before exfoliation; (b) after exfoliation.

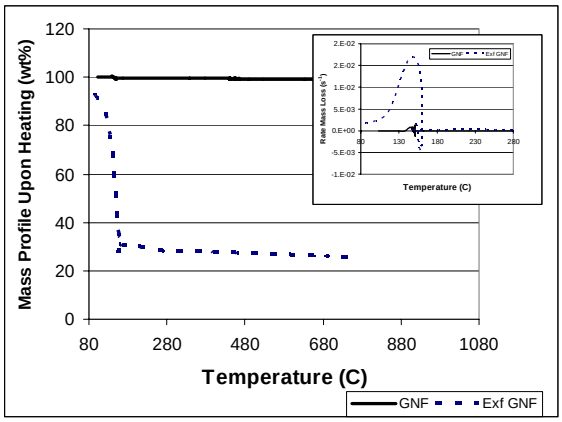

Figure 3. Exfoliation of the GNF in a mixture of nitric/sulfuric acid resulted in a loss of thermal stability of the materials, indicating a higher overall reactivity of the fibers caused by loss of graphitic structure and/or chemical defects. The inset shows the rate of mass loss for the fibers; the rate of thermal degradation was greatest at 120 °C.

Hydrogen Uptake. Prior to exfoliation, the GNF had 0.02% hydrogen uptake, with apparent saturation at 10 bar (Figure 4). Exfoliation of the GNF led to a slight increase in hydrogen uptake: 0.046 % after outgassing at 80 °C and 0.099% after outgassing at 100 °C. The two temperatures were chosen based on the thermal degradation discussion, with mass loss at 80 °C corresponding outgasing but little or no thermal degradation and 100 °C corresponding to partial gasification of the exfoliated GNF (Figure 3). It is expected that the amorphous carbon is more reactive than GNF, and decomposes before the GNF. Thus, the higher pretreatment temperature is intended to preferentially remove amorphous carbon leaving a higher purity of exfoliated GNF. Future studies will include characterization of the materials to quantify the GNF content.

Conclusions

GNF exfoliation enhanced the hydrogen uptake by a factor of five compared to the untreated GNF. Further studies will explore additional exfoliation methods and further characterize the sample to better quantify the degree of exfoliation. The nitric/sulfuric exfoliation method may have been too severe for GNF as evidenced by the high thermal reactivity; our next attempt will be the milder nitric/formic acid exfoliation method, as described previously.[10, 11] However, the overall degree of hydrogen uptake was low; we will explore additional carbon samples and verify the extent of exfoliation before addressing the expanded graphite lattice and/or defect hypothesis.

Acknowledgement. This work was funded through start-up funds proved by Pennsylvania State's Institute for the Environment, The Energy Institute, and The College of Earth & Mineral Sciences. Funding for exfoliation of carbon for hydrogen storage was provided, in part, by the H_2E Center at Penn State University.

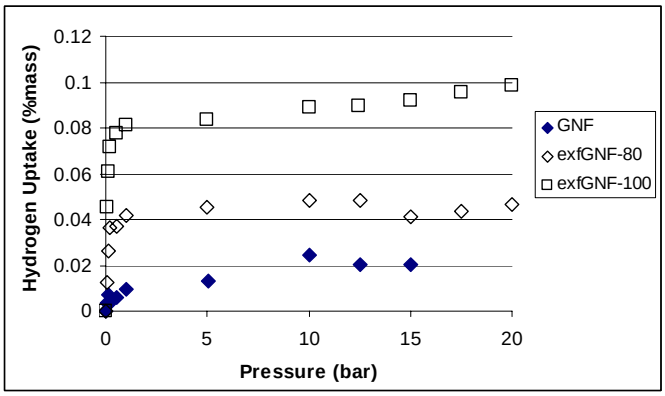

Figure 4. Hydrogen uptake of the GNF before (a) and after (b) exfoliation, followed by different degrees of thermal degradation. Hydrogen uptake is normalized per mass of carbon remaining after each pretreatment.

References

1. Lueking, A. D.; Yang, R. T.; Rodriguez, N. M.; Baker, R. T. K., Hydrogen Storage in Graphite Nanofibers: Effect of Synthesis Catalyst and Pretreatment Conditions. *Langmuir* **2004,** 20, 714-721.
2. Browning, D. J.; Gerrard, M. L.; Lakeman, J. B.; Mellor, I. M.; Mortimer, R. J.; Turpin, M. C., Studies into the storage of hydrogen in carbon nanofibers: Proposal of a possible reaction mechanism. *Nano Letters* **2002,** 2, (3), 201-205.
3. Lee, S. M.; Park, K. S.; Choi, Y. C.; Park, Y. S.; Bok, J. M.; Bae, D. J.; Nahm, K. S.; Choi, Y. G.; Yu, S. C.; Kim, N. G.; Frauenheim, T.; Lee, Y. H., Hydrogen adsorption and storage in carbon nanotubes. *Synthetic Metals* **2000,** 113, (3), 209-216.
4. Hou, P. X.; Yang, Q. H.; Bai, S.; Xu, S. T.; Liu, M.; Cheng, H. M., Bulk storage capacity of hydrogen in purified multiwalled carbon nanotubes. *Journal of Physical Chemistry B* **2002,** 106, (5), 963-966.
5. Gupta, B. K.; Srivastava, O. N., Further studies on microstructural characterization and hydrogenation behaviour of graphitic nanofibres. *International Journal of Hydrogen Energy* **2001,** 26, (8), 857-862.
6. Orimo, S. I.; Matsushima, T.; Fujii, H.; Fukunaga, T.; Majer, G.; Zuttel, A.; Schlapbach, L., Nanostructured graphite-hydrogen systems prepared by mechanical milling method. *Molecular Crystals and Liquid Crystals* **2002,** 386, 173-178.
7. Hirscher, M.; Becher, M.; Haluska, M.; Quintel, A.; Skakalova, V.; Choi, Y. M.; Dettlaff-Weglikowska, U.; Roth, S.; Stepanek, I.; Bernier, P.; Leonhardt, A.; Fink, J., Hydrogen storage in carbon nanostructures. *Journal of Alloys and Compounds* **2002,** 330, 654-658.
8. Imamura, H.; Tabata, S.; Shigetomi, N.; Takesue, Y.; Sakata, Y., Composites for hydrogen storage by mechanical grinding of graphite carbon and magnesium. *Journal of Alloys and Compounds* **2002,** 330, 579-583.
9. Chung, D. D. L., Exfoliation of Graphite. *Journal of Materials Science* **1987,** 22, (12), 4190-4198.
10. Toyoda, M.; Katoh, H.; Inagaki, M., Intercalation of nitric acid into carbon fibers. *Carbon* **2001,** 39, (14), 2231-2234.
11. Toyoda, M.; Sedlacik, J.; Inagaki, M., *Synthetic Metals* **2002,** 130, 39-43.

PURE HYDROGEN FROM MULTIPLE FUELS IN MEMBRANE REFORMERS

A.S. Chellappa, T. R. Vencill, D. C. LaMont

MesoFuel, Inc. 1001 Menaul Boulevard NE, Albuquerque, NM 87107

Introduction

The ability to produce hydrogen from multiple fuels using the same hydrogen generator is desirable for a wide range of applications. Of greater impact for compact PEM fuel cell power systems, is the ability to produce pure hydrogen using membrane reformers. We have recently demonstrated "hot-swapping" of fuels with uninterrupted production of pure hydrogen. This paper will discuss performance metrics and challenges associated with using membrane steam reformers in fuel cell power systems.

MesoChannel™ Membrane Reformers

A schematic representation of a MesoChannel™ membrane reformer is shown in Figure 1. The system consists of 3 main components, namely: (1) a reactor, (2) a combustor, and (3) a hydrogen separation membrane. This membrane-based system therefore produces pure hydrogen for PEM fuel.

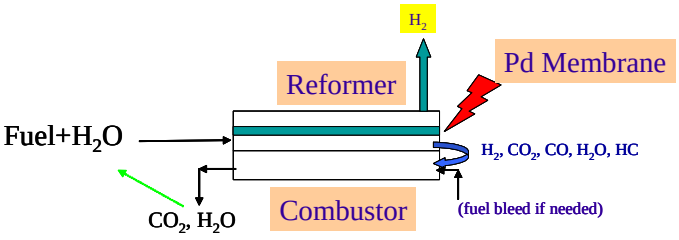

Figure 1. Membrane Reformer (Fuel = methane, propane, butane, ethanol etc).

cell applications in a single unit. These three components are integrated in an intimate fashion with each other to facilitate high heat and mass transfer rates, which in turn translate to higher processing rates per unit volume and subsequently to a compact and efficient fuel processor.

The fuel is mixed with water (steam) and is fed into the reactor where hydrogen is produced in the presence of a catalyst. In the absence of a hydrogen separation membrane, the product gas stream can consist of up to a maximum of 70% hydrogen on a dry basis, with the remaining constituents being CO, CO_2, and un-reacted hydrocarbons. The integration of a separation membrane module with the reactor greatly facilitates the selective removal of the desired hydrogen from the reactor, as it is produced, to yield a very pure hydrogen stream (> 99.9%) which is then routed to the PEM fuel cell. The availability of this pure H_2 fuel leads to increased operating efficiencies of the PEM fuel cell. The reject gas is routed into the combustion chamber where it is combusted to supply the heat required for reforming.

Another advantage of a membrane reformer is that the *in-situ* removal of hydrogen allows higher hydrocarbon conversions at temperatures as low as 600°C to 650°C, relative to competing processes that use no hydrogen separation membrane. Operating at these lower temperatures permits the use of conventional materials of construction and machining/manufacturing practices that lead to lower costs per unit. (In contrast, industrial reactors are operated at temperatures greater than 750°C, and require the use of specialty alloys and refractory materials).

This approach also obviates the conventional process train that contains water gas shift units, and CO polishing units such as preferential oxidation and /or pressure swing adsorption units that are both capital intensive and unsuitable for compact applications such as portable power systems, battery chargers, back-up power supplies and transportation applications.

Pure Hydrogen Production

Pure hydrogen was produced by steam reforming of several fuels while operating at 575 to 650 °C, 6 to 7 bar and S/C ratio of 2 to 4. The targeted hydrogen production rates were in the 300 to 500 sccm range - sufficient to power a 20 to 40 W PEM fuel cell suitable for compact power applications.

Figure 2 shows pure hydrogen production rates from a synthetic kerosene (C_{12}) fuel. As can be seen, about 300 sccm of hydrogen was produced in a stable manner for 1000 h confirming reliability of the reformer. The purity of hydrogen was assessed using helium ionization detectors and an FID was found to be > 99.96%.

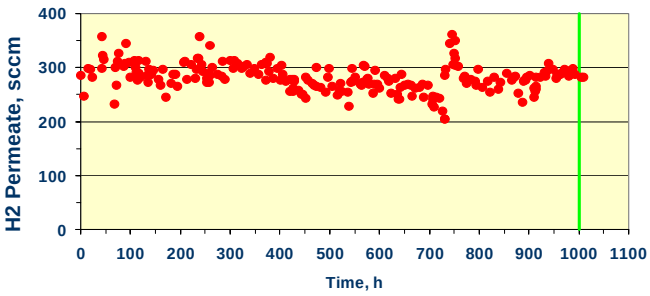

Figure 2. Pure hydrogen (> 99.96% purity) from kerosene: reliability test.

In a subsequent test, after establishing steady state operation under kerosene reforming, the kerosene fuel was replaced with propane (LPG) while the unit was at temperature. That is, the fuels were "hot swapped". The propane (or LPG) fuel was desulfurized prior to feeding into the reformer. The hydrogen production rates during this test are shown in Figure 3.

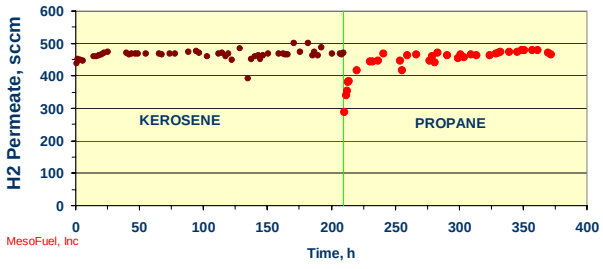

Figure 3. "Hot -swap" of fuels: hydrogen from kerosene and propane.

After demonstrating pure hydrogen production from kerosene for about 210 h, kerosene was cut-off and replaced with propane (LPG). Note that the targeted hydrogen production rate of about 450 sccm was maintained even after the fuel swap. This test demonstrates the robustness of our membrane reformers; a desired characteristic for portable power applications. Purity levels of the hydrogen product at three different run times are shown in Table 1.

Table 1. Purity levels of hydrogen during the hot-swapping from kerosene to propane.

Sample	Fuel	TOS (h)	CH4 (ppm)	CO_2 (ppm)	CO (ppm)	H_2 (purity, %)
1	Kerosene	43	3.58	9.98	2.71	99.998
2	Kerosene	113	5.99	22.31	3.06	99.997
3	Propane	279	15.05	30.23	5.72	99.995

At > 99.99% purity and with CO levels < 10 ppm, the hydrogen product is suitable for powering PEM fuel cells without any subsequent polishing steps. We have successfully powered PEM FCs of several vendors using the hydrogen that was produced, and have demonstrated that pure hydrogen (as opposed to a CO free reformate stream) affords 'Plug 'N Play' interaction between the hydrogen generator and the PEM FC.

Pure hydrogen production from renewable fuels such as ethanol has also been demonstrated. A reformer unit similar to that used for the hydrocarbon fuels was used for the ethanol reforming tests. The ethanol/water fuel feed was formulated using absolute ethanol (99.5% purity, Aldrich) and distilled water. The fuel was then routed into the membrane reformer. Hydrogen production was assessed while operating at 500°C to 650°C, and 6 bar while changing the space velocity and S/C ratio.

Figure 4 shows purity levels of the hydrogen product at 625 °C, 6 bar and at S/C ratios of 3 to 4. The hydrogen production rates were in the 350 to 400 sccm range. As can be seen, hydrogen at > 99.98% purity levels was produced during this test. The hydrogen product was also collected twice during the course of the test, and analyzed by a third party for validation of purity.

The hydrogen purity was unaffected by a change in operating parameters (Figure 4), but as expected, hydrogen production rates decreased while increasing the S/C ratio from 3.2 to 4.2 (dilution effects).

Carbon balance closures were within 10% and ethanol conversion was 100%. We did not observe any coke formation, nor did we detect any intermediate products such as ethylene and acetaldehyde.

During the course of the ethanol reforming test, ethanol was replaced by methanol – a "hot swap" of fuels. Uninterrupted hydrogen production was once again demonstrated using the hot swap of these oxygenated fuels. More details will be provided during the presentation.

Conclusions

Pure hydrogen (> 99.96% purity) was produced by steam reforming of multiple fuels using our MesoChannel™ membrane reformers while operating at 4 to 6 bar and 575 to 625 °C. Stable hydrogen production at rates of 300 to 500 sccm was achieved. The CO levels in the hydrogen product are below 10 ppm, and generally below 5 ppm. As a result, the hydrogen product can be used to power PEM fuel cells without any polishing. "Hot swapping" of fuels has been demonstrated. Packaging of the reformers to yield a compact hydrogen generator is in progress. These hydrogen generators are potentially robust and can be used for a wide range of commercial and military applications.

Acknowledgments. This work was funded in part by the DARPA Palm Power program.

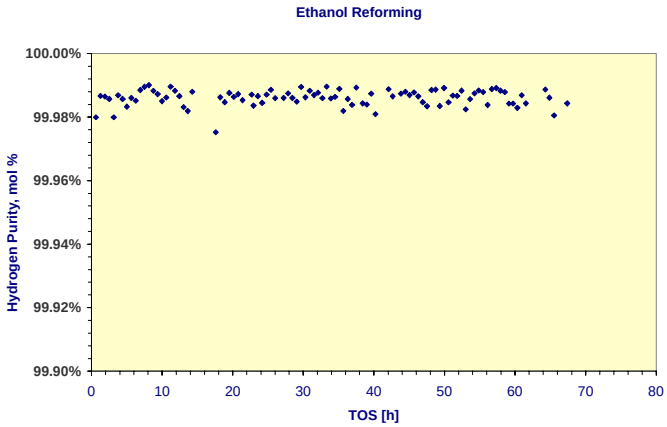

Figure 4. Purity of hydrogen produced by steam reforming of ethanol in a MesoChannel membrane reformer. P = 6 bar, T = 625 °C.

Hydrogen storage in chemical hydrides

Michael, A. Matthews, Thomas A. Davis, and Eyma Y. Marrero-Alfonso

University of South Carolina
Department of Chemical Engineering
301 Main, Swearingen Engineering center
Columbia, SC 29208

Introduction

This is an investigation of a gas/solid chemical reaction between steam and chemical hydrides that liberates pure hydrogen gas. The aim is to obtain fundamental kinetic, chemical, catalytic, and thermodynamic data on the reaction so that sufficient information is known to evaluate this technology rigorously for its potential as a means of delivering hydrogen for fuel cells and internal combustion engines.

It is known that simple chemical hydrides (e.g. LiH, CaH_2) as well as complex hydrides ($NaBH_4$, $LiBH_4$, and others) react with liquid water to produce H_2. For example, $NaBH_4$ has been extensively studied:

$$NaBH_4 + (2+x)\ H_2O \rightarrow 4H2 + NaBO_2 \cdot xH_2O + \text{heat} \quad (1)$$

In equation 1, x is the "escess hydration factor", representing the fact that the solid byproduct can exist in varying degrees of hydration. This liquid reaction has some disadvantages. For example, in the case of $NaBH_4$, an acid catalyst is required to liberate 100% of the hydrogen, because dissolved $NaBH_4$ is stable in basic solution, and the byproducts (sodium borate and similar compounds) are basic in solution. In this reaction, the ideal case is where $x = 0$, in which case the mass yield is 10.3 kg H_2 per 100 kg of reactants. In practice, excess water is required (x=2 is more realistic) so that the $NaBH_4$ and byproducts remain completely dissolved. Excess water rapidly reduces the mass efficiency of the system.

A recent discovery shows that by vaporizing water prior to contact with the hydride, hydrogen yields in excess of 90% may be obtained without the need for a catalyst. Thermodynamic considerations show that, in principle, the heat liberated by the reaction is more than sufficient to vaporize the stoichiometric water required for the steam. Thus, there is the possibility of developing a hydrogen reactor/delivery system that is autothermal at steady state, that produces pure hydrogen in 100% yield, that requires no catalyst, that does not involve strongly caustic solutions, and that uses a minimum of water. Furthermore, the solid reaction products should be nearly free of water, which in the long term will facilitate recycling and regeneration to the hydride.

Experimental

Figure 1 shows a schematic representation of the $NaBH_4$ steam hydrolysis reactor system. The reactor itself is a cylindrical quartz reactor tube placed inside a Thermolyne Model 21100 tube furnace that controls the temperature. One thermocouple placed in the center of the reactor vessel monitors the reaction temperature.

The reaction temperature is also affected by the temperature of the incoming steam. Steam temperature is controlled by a three-stage heater. The first stage of the heater system preheats the steam to approximately 100°C. This preheated liquid/vapor mixture then enters the second and third stage, which superheats the water vapor to the desired reaction temperature. A KD Scientific Model 200 Programmable Syringe Pump is used to pump the desired water flow to the evaporator.

Figure 1. Schematic of the steam hydrolysis reactor system

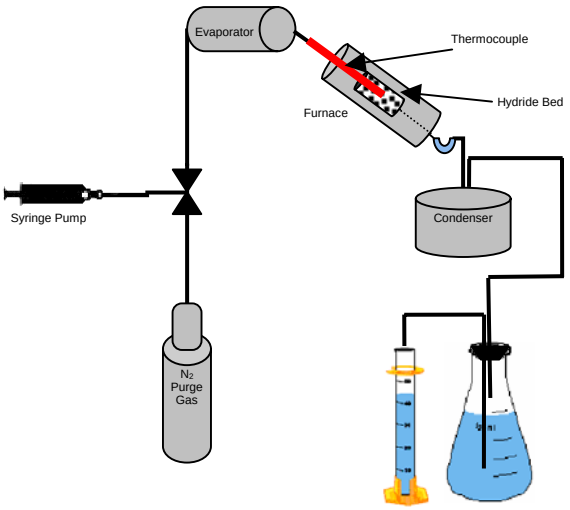

The volumetric flow rate and cumulative volume of hydrogen are measured as the volume of water displaced from the Erlenmeyer flasks to the graduated cylinder. Condensable water is removed in a cold trap, leaving a stream of hydrogen with a trace amount of water. The gas product stream has a septum port (not shown) before the condenser for sampling the product gases. A gas-tight syringe is used to withdraw a small sample from the system for analysis.

All experiments were conducted with one gram of $NaBH_4$ mixed with glass beads packed into the reactor between glass-wool plugs in a glass reaction tube. After installation, the reactor is purged with a steady stream of nitrogen to ensure that the reactants are continuously under a blanket of inert gas until the hydrolysis begins.

Results and Discussion

Figure 2 shows the volume of hydrogen collected over the course of the experiments. The horizontal line labeled "Theoretical Yield" shows that theoretically 2,550 mL (0.106mol) of H_2 can be produced from 1 g of $NaBH_4$. The three lines labeled "Theoretical rates" were calculated based on the Equation (1), assuming that water is the limiting reactant and that the reaction is instantaneous. Calculations were done for x=0, 4 and 6. For example, if no excess water is added (x=0) and the water flow rate is 0.1 mL/min (0.0055 mol/min), the theoretical rate of hydrogen production is 0.011 mol/min, which is the slope of the line shown in the graph.

Figure 2. Experimental H_2 yield for1 gram of $NaBH_4$.

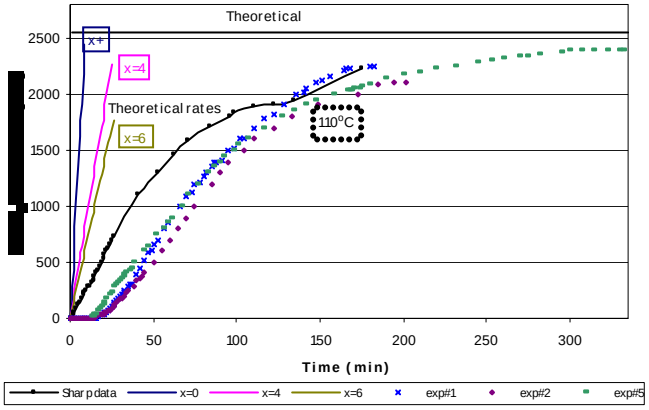

Figure 2 shows the experiments done with pure steam at 110°C. Experimental conditions are listed in Table 1. The data show good reproducibility and are in agreement with work done in the past.[1] Hydrogen yields from 82% to 94% of the maximum were obtained without the need of an additive. The curve labeled "Sharp data" is from past work with a different experimental apparatus. The Sharp data show a greater initial rate than the new experiments, but similar H_2 yield.[1] All the experimental rates are lower than the theoretical rates, because the excess water required moves the slope to the right decreasing the reaction rate. The 15-min. induction period seen in some of the curves was an artifact of the apparatus used at that time, and it disappeared when the design was modified (see Figure 3).

The initial rate of the reaction, expressed as moles of H_2 produced per minute per gram of $NaBH_4$, was determined for each experiment by measuring the slope of the curve after the induction period and is shown in Table 1. Additives, methanol and acetic acid, did not increase the initial rate, and raising the temperature to 140C decreased the reaction rate. Experimental results of the past work [1] show that for the different hydrides used, higher yields of hydrogen were obtained at the lowest temperature (110°C).

Table 1. Initial Rates

Exp#	Description	T (°C)	Initial Slope (mol/g_{NaBH4}* min)	% of Theo. H_2 Yield	Time (min)
1	Old $NaBH_4$	110	8.12E-04	88.2%	128
2	Old $NaBH_4$	110	7.17E-04	82.7%	202
3	1% acetic acid	110	5.82E-04	101.4 %	228
4	1% methanol	110	7.15E-04	92.7%	250
5	New $NaBH_4$	110	7.17E-04	94.0%	323
6	New $NaBH_4$	140	3.49E-04	67.1%	296
7	New $NaBH_4$	140	2.69E-04	40.8%	154
8	6.5% methanol	110	5.45E-04	68.5%	365
9	15% methanol	110	5.89E-04	82.0%	450
Sharp data	$NaBH_4$	110	1.10E-03	87.4%	175
Theoretical Rates		x=0	1.11E-02	100%	-
		x=4	3.70E-03	100%	-
		x=6	2.78E-03	100%	-

Figure 3 shows hydrogen yield from the experiments done at 140°C and the experiments done at 110°C. Both the initial rates and the yields were lower at 140°C, consistent with earlier work. [1]

Figure 3. Experimental H_2 yield for1 gram of $NaBH_4$ at 110°C & 140°C

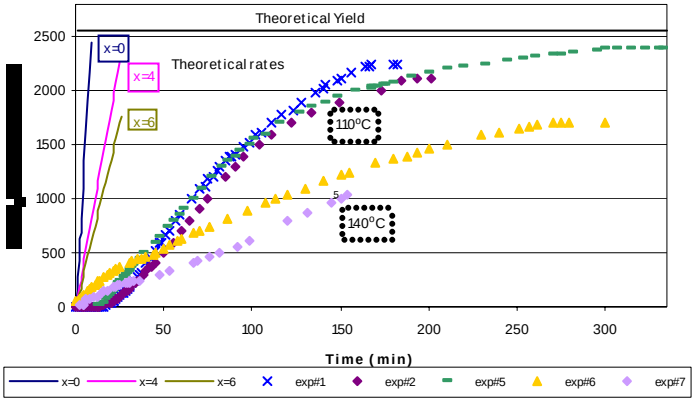

The lower rates and yields at higher temperature are counterintuitive, but they might be attributable to mass transfer limitations in the particle. Observation of the reactor contents after the experiments indicates that the solid particles remain intact but agglomerated. The agglomerated material was soft and wet after the 110ºC experiment and hard and dry after the 140ºC experiment. Presumably the $NaBH_4$ on the surface of the particle reacts first and forms a layer of sodium borate ($NaBO_2$), which grows in thickness as the reaction proceeds. That $NaBO_2$ would be hydrated at lower temperatures but not at higher temperatures. The lower reaction rates at higher temperatures would be explained if the dehydration makes the $NaBO_2$ less permeable to water vapor. This theory remains to be proven.

Figure 4 shows the hydrogen yields for the experiments with additives. Separate aqueous solutions of 1mol%, 6.5mol% and 15 mol% of methanol and 1mol% of acetic acid were injected by the syringe with the same procedures used for the other experiments. The initial rate of the reaction was about the same regardless of the type or concentration of the additive, but different yields were obtained. Yields of 68% to 93% of the maximum were obtained with methanol, but no explanation is offered for the fact that the best yield occurred with the lowest concentration of methanol. The best yield with methanol is no better than yields with just steam (82% to 94%) as shown in Table 1. The use of acetic acid gave a yield of 100%. For safety reasons and to avoid any undesired byproduct the use of additives must be considered carefully.

Figure 4. Experimental H_2 yield for1 gram of $NaBH_4$ using additives

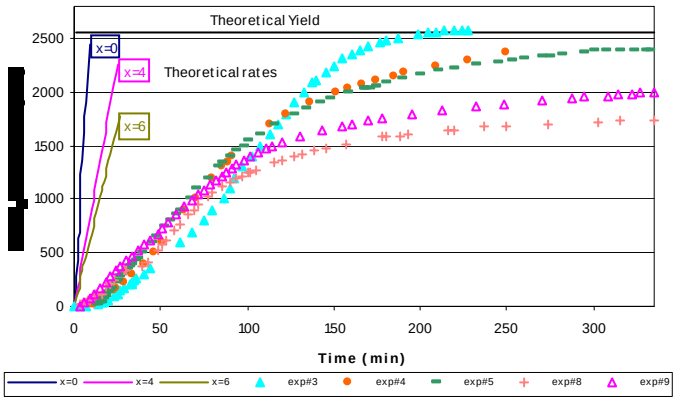

The Department of Energy (DOE) designs the FreedomCAR Technical Targets to promote scientific research in the area of hydrogen storage.[2] New technologies should meet these targets. One of the targets is the usable specific energy from hydrogen (net useful energy/max system mass) and is shown in Table 3. Values of kWh per mass of the reactants were calculated for each experiment to provide an indication of the mass available for a reactor to meet the target. Figure 6 shows the calculations of the energy as function of time. It was observed that the usable specific energy reaches a maximum. Subsequently, the specific energy decreases due to the excess water required.

Table 3. FreedomCAR Targets for Specific Energy [2]

Usable specific energy from Hydrogen			
Year	2005	2010	2015
Target (kWh/kg system)	1.5	2	3
Target (kg H2/kg system)	0.045	0.060	0.090

Figure 6. Usable Specific Energy from H_2.

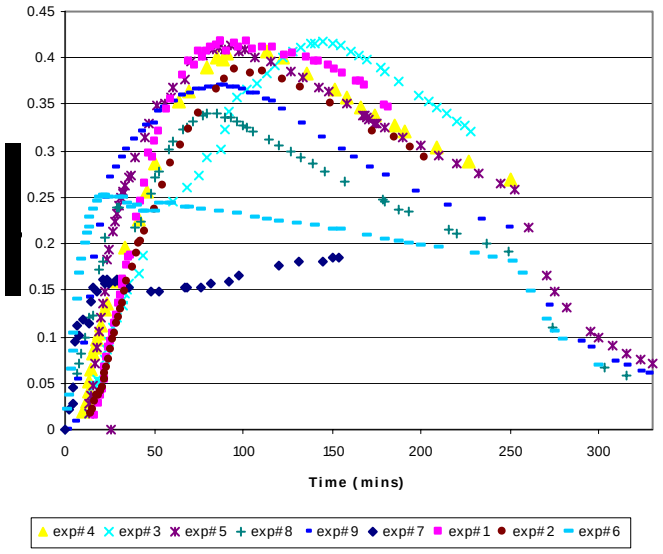

Conclusions

With the data collected it is shown that more that 80% yields of H_2 can be obtained without the need of any additive. The intrinsic reaction kinetics may be obscured because of impermeable byproducts. More knowledge in that area will help to approach an improvement in the rate of the reaction without the need of excess water. Using less water to obtain a high yield will make this technology viable as a medium for hydrogen storage.

Acknowledgement.

This work was carried out under Agreement No. DAAB07-03-3-K416 with the US Army Communications-Electronics Command (CECOM) for Hybrid Advanced Power Sources with guidance from the RDECOM / CERDEC Fuel Cell Technology Team at Fort Belvoir, VA.

References

(1) Aiello R.; Sharp J.; Matthews M. *International Journal of Hydrogen Energy;* **1999**, 1123-1130.
(2) www.eere.energy.gov/hydrogenandfuelcells/pdfs/freedomcar_targets_explanations.pdf-

Water Gas Shift Catalysts for H_2 Production in Membrane Reactors

Thomas Henry Vanderspurt, Rhonda R. Willigan, Rakesh Radhakrishnan, Caroline A. Newman, Susanne M. Opalka, Zissis Dardas, Mallika Gummalla, Fabienne Wijzen, Xia Tang, Harry Cordatos, Ying She and Fangxia Feng*

United Technologies Research Center, 411 Silver Lane, East Hartford, CT 06108 USA

Polymer electrolyte fuel cells perform best on pure H_2. Low sulfur hydrocarbon fuels can be converted to PEM fuel grade H_2 using a compact membrane reactor architecture[1]. Consequently United Technologies Research Center (UTRC) is developing integrated Pd Membrane reactors for H_2 production through reforming of fossil fuels and the subsequent conversion of the CO in the reformate to hydrogen through the Water Gas Shift (WGS) Reaction. This not only allows the shifting of the WGS equilibrium through H_2 removal but it greatly simplifies the system design by eliminating all the other reactors, as well as a major part of the multiple heat exchangers and the air mixers down steam of the reactor that they are integrated with in the traditional fuel processing system for H_2 generation.

Metal supported tubular Pd membranes have high modularity and thus can be easily scaled up to any system capacity while they do not employ components with low reliability like frequently actuated rotating valves. This approach results in significant system cost savings and controls simplicity (thus higher system reliability) due to system and system controls simplification through component elimination. These are significant advantages over the currently applied and more mature technology for H_2 production, the Pressure Swing Adsorption. However this approach requires cost effective, air tolerant catalysts with high volumetric activity and high stability for prolonged operation at ~ 400 °C. On the basis of Gorte's[2] studies noble metal on nano-crystalline ceria-mixed metal oxide catalysts were explored to provide such a catalyst. Eventually a high temperature metal alloy on ceria based mixed metal oxide catalyst was found that gave excellent performance during an 880 hr test with synthetic reformate. This test included 560 hrs at ~420 °C. Although projecting life and stability has to be done cautiously the projected activity of this catalyst after 10,000 hrs at 420 °C was 73% of its 100 hr lined out activity or a turn over frequency TOF of >2.4 CO/Pt-sec.

This catalyst was a member of a family of catalysts designed from the outset to have both high surface area and a network of pores sized to eliminate internal mass transfer. To this end a synthesis route to 2.5 to 3.5 nm doped ceria-zirconia or ceria hafnia oxide crystallites was devised. This route and its variants can accommodate a wide variety of both Ce/Zr or Ce/Hf ratios and dopants. The careful processing allows the recovery of a fractal structured material wherein the fundamental crystallites link through their high energy faces to form high porous ~100 nm particles. These particles link together forming even larger pores inside micro-sized aggregates. A typical $Ce_{(1-x)}Zr_xO_2$ with skeletal density of ~6 and a crystallite size of 3 nm by PXRD can be obtained with 270 m^2/gm surface area. To put this in perspective this is about 70% of the theoretical surface area for the crystallite size. If the oxide had the same skeletal density as γ-Al_2O_3 then these catalysts would have a surface area of about 425 m^2/gm. Surface area of ~ 200m^2/gm are typical of oxides designed for long term ~ 310 °C operation.

Significantly, the nano-crystallites are primarily cubic (Fm3m) in structure as determined by a combination of PXRD and Raman spectroscopy even at oxide compositions that in larger crystallites are tetragonal ($P4_2$/nmc) according to Kaspar[3]. Raman is critical for determining the structure of these nano-crystalline materials as broader peaks caused by the small crystallite size tends to preclude definitive PXRD determination. $Ce_{0.50}Zr_{0.50}O_2$ crystallites with an average size of 3.45 nm by PXRD exhibits a major, broad Raman peak at ~465 cm^{-1} with a low shoulder extending beyond 650 cm^{-1} ascribed to oxygen vacancies. This shoulder appears even at 10% Zr and grows with Zr concentration. The Raman spectra of the nano-crystalline $Ce_{0.25}Zr_{0.75}O_2$ is dominated by a broad 465 cm^{-1} peak though with a weaker ~640 cm^{-1} peak. $Ce_{0.17}Zr_{0.83}O_2$ on the other hand is tetragonal by PXRD and had Raman spectra indicative of a tetragonal structure.

These oxides were converted to WGS catalysts by loading with noble metals either alone, in combination or with transition metal promoters. Gorte[4] has demonstrated the major impact that Fe can have on Pd/CeO_2 activity. For the $Ce_{(1-x)}Zr_xO_2$ and $Ce_{(1-x+y)}Zr_xDp_yO_2$ prepared by our techniques Pt seems superior to the other metals. As prepared these supported Pt catalysts have 100% dispersion by CO chemisorption. High resolution TEM investigation is consistent with the majority of the Pt forming small, ~1nm rafts. After loading with Pt these oxides are reducible at low temperatures by TPR. This is not a function of either Pt or oxide crystallite size. A $Pt/ Ce_{(1-x)}Zr_xO_2$ catalyst was calcined at 1000 °C in air and had a major reduction peak at ~130°C despite very large Pt crystallites and nil surface area.

These high surface area catalysts were first explored for their low temperature water gas shift activity. Besides automated micro-reactor screening and kinetics studies, VASP atomistic modeling of the $Ce_{(1-x+y)}Zr_xDp_yO_2$ system along with in-situ CIR-FTIR studies were initiated. A range of compositions were examined as 80-120 mesh granules diluted with 40 mesh α-alumina run at high space velocity. Typically between 210 and 240 C the kinetic expression $r = Aexp(-Ea/RT)[CO]^0[H_2O]^{0.6}[CO_2]^{-0.2}[H_2]^{1-0.6}$ would fit the data with E_a values ranging from 66 to 73 kJ/mole. These results are consistent with a rate limiting step involving water. The modeling work predicted domination of the oxide surface by a formate like species, but that this domination could be lessened by doping the Ce-Zr oxide with any of several species, Mo among them. The in-situ FTIR spectra taken at low space velocity indeed indicated domination of the surface by a formate like species as well as carbonate for $Pt/Ce_{0.65}Zr_{0.35}O_2$. Doping with La apparently increased and changed the nature of the adsorbed CO while also enhancing peaks attributable to CO on Pt. Mo doping on the other hand decreased the apparent intensity of peaks attributed to CO and carbonate adsorbed on the oxide. These results were consistent with reactor studies where a Mo doped catalyst exhibited a lower apparent activation energy that the undoped material.

While Mo exhibited some low temperature promoting ability it did not increase high temperature activity. The catalysts suitable for long term <320 ºC deactivated when exposed to high temperatures for hundreds of hours. Catalysts deactivated even with UHP feed gases passed through activated carbon, mole sieve and Oxisorb^{tm} traps as well as a heated ZnO bed. Analysis of these deactivated catalysts revealed only slight oxide crystallite growth or loss of surface area. Their PXRD patterns showed no evidence of severe Pt agglomeration and there were no drastic changes in their Raman spectra. Notably however the low temperature reduction peak so evident in the TPR of fresh catalysts was absent.

A promoter M was found for $Pt / Ce_{(1-x)}Zr_xO_2$. Kinetic studies were carried out and Athena software used to fit the data to $Aexp(-E_a/RT)[CO]^{\alpha}[H2O]^{b}[CO2]^{\gamma}[H2O]^{\delta}$ $(1-\beta)$ where β is the approach to equilibrium. At low temperatures, below 250 ºC, E_a

was 71 kJ/mole and α = -0.2, b = 0.8, γ = -0.12, δ = -0.4, while at high temperatures the activation dropped to 46 kJ/mole and α = 0.2, b = 0.4, γ = -0.2, δ = -0.4. This promoted catalyst still lacked the requisite high temperature stability. A Pt-M/$Ce_{[1-(x+y)]}Hf_xDp_yO_2$ catalyst with a skeletal density >8.0 and a surface area of 146 m^2/gm and a crystallite size of 3.3 nm was synthesized. On a skeletal density adjusted basis its surface area was equivalent to about 190 m^2/gram for a 60% cerium, 40% zirconium oxide. This catalyst was tested for 880 hrs at 740,000 hr^{-1} space velocity under a variety of conditions. Its activity retention was excellent. Under 7.5% CO, 5.5% CO_2, 27.6% H_2O, 28.9% H_2, bal. N_2 at 740,000 hr^{-1} after ~560 hours at 420 °C this catalyst's TOF was 3.0 CO/Pt-sec.

On the basis of an activity versus log of time plot its projected activity at 10,000 hrs was > 2.4 CO/Pt-sec suggesting that it might retain 73% of its 100 hr activity at 10,000 hrs. United Technologies Research Center is working with HydrogenSource LLC and their suppliers to commercialise this catalyst technology for hydrogen production. Extended monolith tests are planned.

References

1. Gummalla, M.; Olsommer, B.; Dardas, Z.; She, Y.; Vanderspurt, T.H. "On-Board Cost Effective Hydrogen Enhancement Technology for Transportation PEM Fuel Cells" DOE Merit Review, Berkeley CA May 19, 2003

2. Bunluesin,T.; Gorte, R.J.; Graham, G.W. Applied Catalysis B:Environ. **1998**, *15* (1-2), 107-114.

3. Kaspar, J. and Fornasiero, P. in *Catalysis by Ceria and Related Materials*; Trovarelli, A. Ed. Imperial College Press, London 2002 pp. 217-241.

4. Wang, X.; Gorte, R.J. Applied Catalysis, A: General **2003**, *247* (1), 157-162.

THE EFFECT OF ANTIOXIDANT ADDITION ON NO_x EMISSIONS FROM BIODIESEL

Melissa A. Hess, Michael J. Haas, Thomas A .Foglia, and William N. Marmer

United States Department of Agriculture, Agricultural Research Service, Eastern Regional Research Center
600 E. Mermaid Lane
Wyndmoor, Pennsylvania, 19038

Introduction

Although the use of biodiesel offers many environmental advantages over petrodiesel, an increase in NO_x emissions from biodiesel combustion, relative to levels observed from petrodiesel combustion, has been reported by several researchers. (1-3) This increase is of concern in areas that are subject to strict environmental regulations. For universal acceptance of biodiesel, it is desirable to reduce these NO_x emissions at least to levels observed with petrodiesel combustion.

NO_x can be formed by two major pathways during diesel fuel combustion: the Zeldovich (thermal) mechanism and the Fenimore ("prompt") mechanism. The rate of the Zeldovich reactions is flame temperature-dependent, whereas the Fenimore pathway is more complex. In the Fenimore mechanism, free radicals formed from the fuel react with N_2 to eventually form NO_x. This takes place very early in the combustion process and is partly dependent upon the fuel radical concentration and how it is established. (4)

Some data have indicated that the chemical makeup of biodiesel can influence the amount of NO_x formed during its combustion. McCormick *et al.* (5) published data that correlated the properties of various biodiesels to NO_x emissions. One notable result was a strong positive correlation between the iodine value of the fuel (a function of the number of double bonds) and NO_x: as iodine value increased, so did the NO_x emissions. These data suggest a role of double bonds in elevating NO_x output. Sites of unsaturation are known to have a greater propensity for radical formation than do carbon-carbon single bonds. It is conceivable that this increase in free radical generation is at the heart of the increase in NO_x output by some biodiesels. If so, a quenching of free radicals during combustion may reduce or eliminate this NO_x elevation. Antioxidants are known to be free radical quenching agents.

Acting on this postulate, McCormick *et al.* (6) added a common antioxidant, *tert*-butyl hydroquinone (TBHQ), to biodiesel as a possible method of NO_x reduction. They observed a slight reduction in NO_x and suggested that the use of antioxidants as a NO_x mitigation strategy deserved more study. Moreover, the addition of antioxidants to biodiesel is being investigated to increase its storage stability and it is important to understand the impact that such addition may have on NO_x formation.

Experimental

Materials. Certified diesel fuel was obtained from Chevron Phillips Chemical Company (Houston, Texas). The fuel used was low sulfur (365 ppm), with a cetane number of 46.8. The biodiesel used was Soygold, a methyl soyate biodiesel purchased from Ag Environmental Products (Omaha, Nebraska) in one-gallon units to protect the fuel from extensive oxidation. 2-Ethylhexyl nitrate (2-EHN), 2,2'-methylenebis(6-*tert*-butyl-4-methylphenol), vitamin E, *tert*-butylhydroquinone, propyl gallate, diphenylamine, and butylated hydroxyanisole were purchased from Sigma-Aldrich Chemical Co. (St. Louis, Missouri). Structures of the antioxidants are shown in Figure 1.

The fuel used had a blend composition of 80% petrodiesel and 20% biodiesel (B20). Additives were tested at a level of 1000 ppm.

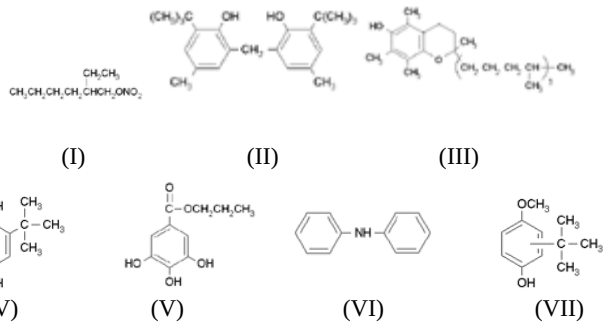

Figure 1. Structures of selected additives. (I) 2-ethylhexyl nitrate. (II) 2,2'-methylenebis(6-*tert*-butyl-4-methylphenol) (III) Vitamin E (IV) TBHQ (V) Propyl gallate (VI) Diphenylamine (VII) BHA

Method. A Yanmar L100 single cylinder, four stroke, naturally aspirated, direct injection diesel engine from Bowers Power Systems (Kent, Washington) was installed and instrumented for NO_x measurements. The engine had a compression ratio of 20:1, a displacement of 0.418 L, and a fuel injection timing of 17±0.5 degrees before top dead center (bTDC). The engine was connected to an electrical generator. Load was added to the engine by using the generator to power work lights. The results discussed here are obtained at a load of 5 kW (82% maximum load) and an engine speed of 3200 rpm. These conditions were chosen to generate NO_x levels high enough to allow small changes in NO_x emission levels to be detected.

NO and NO_2 were measured using single gas monitors (model CA-CALC) manufactured by TSI Instruments (Shoreview, Minnesota). These monitors have electrochemical sensors as opposed to the chemiluminescence methods normally employed for NO_x detection. The monitors were chosen for simplicity and affordability, and were calibrated frequently using calibration gases. Exhaust temperature was monitored using a thermocouple from Omega Instruments (Stamford, Connecticut) inserted into the exhaust gas stream.

Since the engine was minimally instrumented with no provisions for the control of such variables as inlet air temperature and humidity, the baseline numbers were generally not repeatable on a daily basis. Therefore, for each test, NO_x emission levels from petrodiesel, B20, and B20 with the additive were measured against those fuels without the additive. An experiment began by bringing the engine to steady state using certified diesel fuel. The speed of the engine was monitored using a tachometer. The engine was held at a constant speed and load for the duration of the test and the NO_x emissions of the petrodiesel were measured. A minimum of triplicate measurements were made to ensure an accurate NO_x measurement. The fuel was then switched to B20 without disrupting the operation of the engine. The engine was run at steady state for a time sufficient to ensure that the petrodiesel was flushed from the system and that steady state had been achieved. The NO_x emissions from B20 were then measured. The fuel was then switched to B20 containing 1000 ppm of the antioxidant additive again without disrupting engine operation. The engine was allowed to come to steady state and the NO_x levels were measured again. Experiments were performed to ensure that when the fuel was switched back to B20, the same results as prior to running the additized blend were achieved. The NO_x emission levels for the additized fuel were compared to the NO_x

levels measured for B20 in that experiment only. The percent changes in NO_x emissions from experiment to experiment were compared.

Results and Discussion

The engine system employed here proved effective and reliable as a screening method to determine if antioxidant fuel additives have an effect on NO_x levels. Candidate additives that show promise with such a system will be tested at a rigorous engine test facility in the future.

It was necessary to confirm that the reported difference in NO_x emissions between biodiesel and petrodiesel could be observed. As shown in Table 1, a 6.2% increase in NO_x emissions was observed when B20 was used as opposed to petrodiesel. The increase observed here was fairly consistent throughout the tests and is in agreement with results reported in the literature. (1-3)

It was also of interest to establish that reduction in NO_x by the use of accepted NO_x-lowering treatments could be attained. To accomplish this 2-EHN was added to the fuel at a 1000 ppm level. 2-EHN is known to be an effective additive for reducing NO_x emissions at this level in a variety of diesel engines. (7,8) This additive increases the cetane number of the fuel, which leads to shorter ignition times that result in decreased NO_x emissions. Again, the results observed here corroborate those seen by others; the addition of 2-EHN at 1000 ppm reduced NO_x by 4.5%. This observation suggests that this engine system responds typically to a known NO_x reducing agent.

The antioxidants were chosen based on several considerations. Several are readily available and inexpensive since they are used in the food industry to prevent lipid oxidation. Additionally, Mittelbach and Schober (9) performed a study in which antioxidants were rated for their effectiveness in terms of fuel stability. Antioxidants that they found to be effective (such as *n*-propyl gallate and TBHQ) were tested in hopes that these additives would serve two functions, namely increasing storage stability and reducing NO_x.

Table 1 lists the effect of the addition of each of six antioxidants on NO_x emissions during B20 combustion. The antioxidants used had minimal effect on NO_x emissions, but the results from three antioxidants were notable.

Table 1. Effect of Additive Addition on NO_x Emissions

Fuel	Change in NO_x from B20 Levels
Diesel Fuel (B0)	-6.2%
B20 + 2-EHN	-4.5%
B20 + 2,2'-methylenebis(6-*tert*-butyl-4-methylphenol)	+0.2%
B20 + Vitamin E	+0.3%
B20 + TBHQ	-0.9%
B20 + Propyl Gallate	-0.4%
B20 + diphenylamine	+0.7%
B20 + BHA	-4.4%

TBHQ induced a 0.9% reduction in NO_x emissions when added to B20 at 1000 ppm, but the data from this particular additive had a great deal of scatter. Reductions as high as 8.7% were observed, but other tests showed an increase as great as 5.3%. TBHQ was the only additive that exhibited such erratic behavior.

One possible explanation for this behavior may lie in the storage stability of the antioxidants. Although the antioxidants were stored in a cool, dry place and out of light, they were not stored under inert gas and may have reacted with oxygen, thus reducing their effectiveness. The possibility of pre-oxidation must be investigated further.

Diphenylamine was notable in that it consistently increased NO_x emissions, though the increase was small (+0.7%). It is likely that this increase might have been due to the nitrogen present in the additive. Although this increase may not appear significant, it should be considered when selecting an antioxidant for fuel storage stability purposes.

Butylated hydroxyanisole (BHA) was the most effective of the antioxidants studied, giving a 4.4% decrease in measured NO_x emissions. This decrease is approximately the same as was observed with an identical amount of 2-ethylhexyl nitrate. We conclude that the addition of BHA to the B20 does work to combat the "prompt" NO_x that is formed during the combustion process.

BHA and TBHQ have similar structures, as shown in Figure 1. Decreases in NO_x levels observed with TBHQ addition, however, were not repeatable. The similarity in structure of BHA and TBHQ suggests that structure may play a role in determining antioxidant activity and effectiveness in reducing NO_x emissions.

Conclusions

The system described in this work was designed for screening additives that may potentially reduce NO_x emissions from biodiesel. Despite minimal instrumentation, it was possible to observe changes in NO_x levels with changes in fuel formulations. While more thorough engine testing will be required to confirm the results reported here, the system we used represents a relatively inexpensive approach to examining the effect of fuel additives on NO_x production by biodiesel fuels.

The use of butylated hydroxyanisole (BHA) should be investigated further as this additive did produce a small but significant decrease in NO_x emissions. TBHQ also should be investigated. Blends of additives should be investigated to look for synergistic effects.

References

(1) Grabowski, M.S.; and McCormick, R.L. *Prog. Energy. Comb. Sci.* **1998**, *24*, 125.
(2) Choi, C.Y.; and Reitz, R.D. *Fuel*, **1999**, *78*, 1303.
(3) Song, J.; Cheenkachorn, K.; Want, J.; Perez, J, Boehman, A.L.; Young, P.J., and Waller, F.J. *Energy and Fuels*, **2002**, *16*, 294.
(4) Miller, J.A.; and Bowman, C.T. *Prog. Energy Combust. Sci.* **1989**, *15*, 287.
(5) McCormick, R.L.; Grabowski, M.S.; Alleman, T.L.; Herring, A.M.; and Tyson, K.S. *Environ. Sci. Technol.* **2001**, *35*, 1742
(6) McCormick, R.L.; Alvarez, J.R.; and Grabowski, M.S. Report NREL/SR-510-31465, **2003**.
(7) Suppes,G.J.; Goff, M.; Burkhart, M.L.; Bockwinkel, K.; Mason, M.H.; Botts, J.B.; and Heppert, J.A. *Energy and Fuels*, **2001,** *15*, 151.
(8) Liotta, F.J. *SAE Paper 932767*, **1993**.
(9) Mittelbach, M.; and Schober, S. *J. Am. Oil Chem. Soc.* **2003**, *80*, 817.

Functionalization of nickel on 4-aminothiophenol modified glassy carbon electrodes and the enhanced electrochemical activity towards the oxidation of ethanol

Jan Marwan, Ouassim Ghodbane, Eric Lascombe, Gwenaël Chamoulaud, Daniel Bélanger and Mohamed Touaibia

Département de Chimie, Université du Québec à Montréal, Case Postale 8888, succursale Centre-Ville, Montréal (Québec) Canada H3C 3P8

Introduction

Organized self-assembled monolayers (SAMs) on various solid supports have attracted much attention in recent years and are commonly used to impart desired chemical or physical properties to surfaces. SAM's offer the possibility to control the film structure at the molecular and supramolecular level and therefore to realize the tailoring of the surface properties. Monolayers of organic thiols, especially those formed of alkanethiols, are the most studied self-assembled monolayer system since they offer stability and high degree of organization[1]. Monolayers formed from aromatic thiols, although not that intensively studied, are of considerable interest since they offer together with the properties given by aliphatic thiols the additional advantage of having a high electrical conductivity[2]. Their use as surface modification agents opens up new possibilities to arrange metal particles on modified electrode surfaces with supposedly enhanced electrochemical activity.

It is well-known from the literature that the thiol-containing group of any aliphatic and aromatic compound can be adsorbed onto Pt, Cu and Ag[3]. This might be an interesting approach to the formation and arrangement of metal particles on aryl modified electrode surfaces. Nickel, showing a high affinity to the amine group in nickel amine complexes, is then expected to be functionalized onto the 4-aminothiophenol modified electrode. Nickel has been reported to be a good catalyst for the oxidation of various organic compounds[4]. We have chosen in our studies ethanol as compound with the aim to investigate the electrochemical activity of nickel in this oxidation process.

Experimental

Glassy carbon electrodes (AIMCOR, Pittsburgh, grade GC-10) were prepared from 3 mm diameter rods embodied into epoxy resin (Hysol, 56C) and were used as working electrodes. Platinum gauze and a Ag/AgCl (saturated KCl) electrode were used as counter and reference electrodes, respectively. All potentials were reported versus the Ag/AgCl reference electrode. The glassy carbon electrode surface was cleaned by polishing with 1 µm and 0.05 µm alumina slurry. After polishing, the electrode was washed with water and ultrasonicated for 5 min in acetonitrile. Electrochemical modification of the glassy carbon electrode was carried out in acetonitrile containing 1 mM aminothiophenol and 0.1 M NBu_4BF_4. The applied potential was 2.0 V for the deposition of 4-aminothiophenol. After the modification, the electrode was thoroughly washed by rinsing in acetonitrile and then in deionized water. A solution containing 97.6 wt% methanol, 2 wt% acetic acid and 0.4 wt% nickel(II)chloride hexahydrate (reduced to Ni zero state by 0.4 M sodium borohydride) has been prepared in which the modified electrode has been soaked for 20 minutes at 45-50 °C to functionalize nickel. After rinsing with deionized water again, electrochemical measurements of the nickel prepared modified electrode were carried out at room temperature (18-23°C) in 1 M NaOH and in further experiments with the addition of ethanol using various concentrations. Before each experiment the solution was sparged for 10-15 minutes with a stream of highly purified nitrogen to displace dissolved oxygen. Electrochemical measurements were performed in a one-compartment cell using the three-electrode configuration. Cyclic voltammetry was performed using either a potentiostat/galvanostat model M263A (EG&G Princeton Applied Research) or an electrochemical interface SI1287 (Solartron Instruments) interfaced with a PC and the electrochemical set-ups were both controlled with the model DC Corrware (Scribner Associates, version 1.2) software.

Results and Discussion

Figure 1 shows the typical cyclic voltammetry in 1 M NaOH at 50 mV/s of nickel loaded onto 4-aminothiophenol corresponding to 1.8×10^{-9} mol/cm^2. Initially the GC electrode surface (0.07 cm^2 electrode area) was modified with 4-aminothiophenol at 2.0 V vs Ag/AgCl for 240s. The voltammetry of nickel is characterized by reasonably well-understood surface reactions corresponding to the formation and stripping of hydroxide films at the metal surface. Starting on the anodic scan we can clearly note in figure 1 the presence of a well-established peak at 0.43 V attributable to the formation of NiOOH, and on the reverse scan the corresponding peak due to the reduction of the anodically formed NiOOH occurs at 0.34 V. More anodically the oxygen evolution arises at the onset potential of 0.55 V. The voltammetric features shown in this figure are comparable to those reported in the literature for ordinary nickel electrodes and dispersed nickel on modified electrode surfaces in basic solution[5]. With the characteristics outlined in this figure we can clearly confirm the presence of nickel functionalized on the modified GC electrode. One could argue that the deposition of nickel might occur onto the glassy carbon surface and this may then be responsible for the voltammetric features given in figure 1. This assumption is rather unlikely since recent studies showed complete blocking of the electrochemistry on the modified electrode when using redoxactive species so that any deposition of nickel onto GC in the presence of 4-aminothiophenol grafted onto the electrode is more to be doubted. This should therefore give strong indication that the presence of nickel in our voltammetry is only due to the surface reactions on the nickel film functionalized on the modified electrode surface.

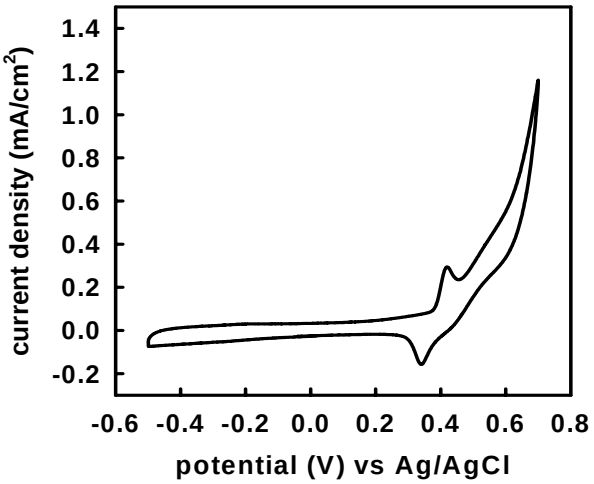

Figure 1. Cyclic voltammetry in 1 M NaOH at 50 mV/s of nickel functionalized onto the 4-aminothiophenol modified GC electrode surface (0.07 cm^2 electrode area). 4-Aminothiophenol as surface modification agent was grafted at 2.0 V vs Ag/AgCl for 240s onto the glassy carbon (GC) electrode.

To give further evidence that nickel is present on the modified GC electrode and to make these studies conclusive, **figure 2** shows the XPS core level spectrum of Ni2p obtained after the functionalization of nickel onto aminothiophenol. We restrict our studies to the $Ni2p_{3/2}$ region since this will provide us with sufficient information. Curve fitting of the $Ni2p_{3/2}$ gives different Ni species with binding energies of 855.9±0.1 and 857.2±0.1 eV. On the basis of their binding energies these peak values were assigned to $Ni(OH)_2$ and NiOOH, respectively, with the ratio in area underneath the peak of 0.92. The $Ni2p_{3/2}$ spectrum shows at higher binding energies (862±0.2 eV) an intense satellite signal which may be attributed to a multielectron excitation (shake-up peaks). It is relevant to point out that at lower binding energies below 854 eV the XP signal for nickel metal and NiO does not appear in this spectrum. This fact might indicate that Ni is fully covered by an hydroxide layer after its functionalization onto the modified electrode. Further support for this was given by the O1s spectrum. The fact that nickel was shown to be functionalized onto the 4-aminothiophenol electrode surface opens up new possibilities for further investigations in which we were particularly interested in the oxidation of ethanol on nickel.

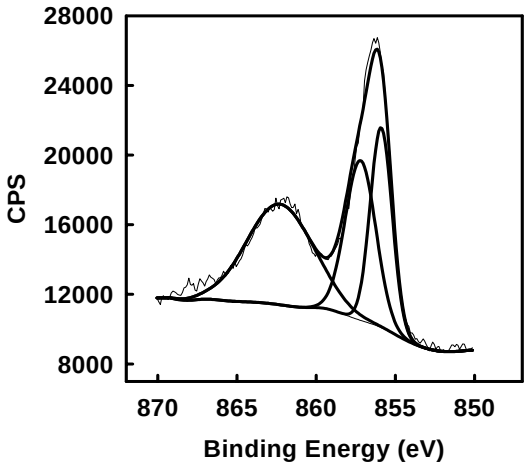

Figure 2. X-ray photoelectron Ni2p core level spectrum for nickel functionalised onto the 4-aminothiophenol modified electrode surface.

Directing our attention towards **figure 3** we notice on following the anodic scan in voltammogram a) a peak at 0.53 V with its corresponding peak on the reverse scan at the same potential. This experimental finding is consistent to that reported in the literature about the ethanol oxidation process on nickel electrodes[6] so that we found our experimental results attributable to this electrochemical process. On continuing the anodic scan we see the start of the oxygen evolution with the onset potential of 0.68 V. Comparing these voltammetric features to those shown in voltammetry b) and c) we hardly note any difference except the fact that higher current densities were obtained with increasing ethanol concentration. This issue is essential, and we certainly want to stress this fact that with increasing the ethanol concentration in figure 3 fast kinetic processes and negligible shift of about a few mV in peak potential for the ethanol oxidation process occur when comparing the voltammetries and thus a clear separation between this process and the oxygen evolutionis can still be seen even at high ethanol concentrations (5M). These are remarkable features and are clearly in contrast to the results shown in published material on ordinary nickel electrodes[6] and nickel based alloys dispersed on a modified electrode[7]. Here the electrochemical surface reactions are accompanied by an increase in solution resistance near the electrode surface leading then at high ethanol concentrations to an ohmic drop. Kim and Park[7] showed this behaviour in their work when using Ru-Ni alloys describing that the peak for the ethanol oxidation at higher concentrations (>0.5 M) is rather indistinguishable from the oxygen evolution in the voltammetry. In addition, we want to emphasize the fact that we obtained reasonable current densities for the ethanol oxidation process with a low amount of nickel loaded onto the modified electrode. Comparable electrochemical activity was obtained when using almost 300 fold less quantity of nickel as catalyst material. Running the ethanol oxidation constantly at 0.5 V vs Ag/AgCl in 1 M NaOH using the 4-aminothiophenol modified electrode on which nickel was loaded revealed appreciable current densities (>5mA/cm^2). With the focus on further improvement we might therefore consider this electrode as one alternative to the Pt based alloy electrodes for the anodic oxidation of ethanol in fuel cells.

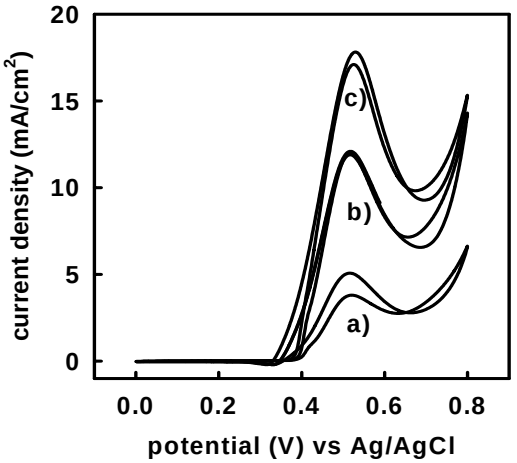

Figure 3. Set of cyclic voltammograms at 50 mV/s in 1 M NaOH with increasing concentration of ethanol from 0.5 M a), 2 M b) to 5 M c) of nickel functionalised onto the 4-aminothiophenol modified GC electrode surface. 4-Aminothiophenol as surface modification agent was grafted at 2.0 V vs Ag/AgCl for 240s onto the GC electrode. In this voltammetry the same nickel prepared electrode was used as in figure 1

Acknowledgment. We gratefully thank the financial support of the Natural Science and Engineering Research Council of Canada (NSERC).

References

1) Qu, D.; Morin, M., *J. Electroanal. Chem.* **2002,** 524, 77.
2) Hayes, W. A.; Shannon, C.,. *Langmuir* **1996,** 12, 3688.
3) Hubbard, A. T., *Chem. Rev.* **1988,** 88, 633.
4) Manandhar, K.; Pletcher, D., *J. Appl. Electrochem.* **1979,** 9, 707.
5) Nelson, P. A.; Elliott, J. M.; Attard, G. S.; Owen, J. R., *Chem. Mater.* **2002,** 14, 524.
6) Motheo, A. J.; Machado, S. A. S.; Rabelo, F. J. B.; Santos Jr., J. R., *J. Bras. Chem. Soc.* **1994,** 5, 161.
7) Kim, J.-W.; Park, S.-M., *J. Electrochem. Soc.* **2003,** 150, E560.

Kinetics, Characterization and Mechanism for the Selective Dehydration of Ethanol to Diethyl Ether over Solid Acid Catalysts

T. Kito- Borsa and S.W. Cowley

Department of Chemistry and Geochemistry
Colorado School of Mines
Golden, CO 90401

Introduction

Ethanol is a clean burning alternative automotive fuel to gasoline[1-2]. However, one serious disadvantage of ethanol is that it has a lower vapor pressure (-3 psia at 38 °C) than winter grade gasoline (~11 psia at 38 °F)[3]. A time-honored standard in the fuel industry mandates that fuels have sufficient vapor pressure to cold-start an automobile at temperatures as low as –30 °C. This is not possible with ethanol. One promising way to solve this problem is to convert a portion of the ethanol into a more volatile compound, such as diethyl ether, on board the vehicle prior to or during the cold-start operation.

The main objective of this study is to develop a catalyst material that exhibits acceptable activity and selectivity for the dehydration of ethanol to diethyl ether (DEE) under the severe operating conditions that exist on board an automobile. Aliphatic alcohols, with exception of methanol, have two modes of dehydration, bimolecular dehydration to produce ethers and intra molecular dehydration to olefins, see equations (1) and (2).

$$2CH_3CH_2OH \rightarrow CH_3CH_2OCH_2CH_3 + H_2O \quad (1)$$
$$CH_3CH_2OH \rightarrow CH_2{=}CH_2 + H_2O \quad (2)$$

Both dehydration reactions are known to proceed over solid acid catalysts[5]. However, ethylene is undesirable, since it contributes to automotive pollution and catalyst fouling. Diethyl ether formation is thermodynamically favorable over a wide range of tempertures, including the 50-500 ºC range commonly employed in catalytic processes. However, the formation of ethylene is also thermodynamically favored and predominates at temperatures above 100 ºC. Operating a solid acid catalyst at temperatures below 100 ºC results in the selective formation of diethyl ether, but the reaction is kinetically limited and gives rates too slow for an automotive application. In order to overcome this dilemma, a catalyst is needed that can selectively produce diethyl ether at temperatures in excess of 100 °C. In this study, such a catalyst is reported and a possible mechanism for its observed selectivity for diethyl ether production is discussed.

In order to design an on board catalytic dehydration reactor, it is necessary to determine the required fuel properties of a ternary mixture of ethanol, water, and diethyl ether for cold-starting a vehicle. This information is needed in order to determine the % ethanol conversion that is required from an on-board catalytic reactor. This also plays an important role in selecting the appropriate catalyst material and the optimum reaction conditions in our laboratory studies. A significant amount of information has been published regarding ethanol as a fuel[2-3], but the literature is nearly void of information regarding the diethyl ether assisted cold-starting of a vehicle[5]. Vapor-liquid equilibrium phase diagrams, for ternary mixtures of ethanol, diethyl ether, and water, at various temperatures, have been reported by Kito-Borsa and Cowley[6] using ASPEN Plus software. Their results suggest that ethanol conversions between 40 and 85% at 100 % diethyl ether selectivity is required to produce an acceptable fuel mixture that can cold-start a vehicle at temperatures down to –30 °C without forming two immiscible liquid phases.

Highly acidic ion exchange resins catalyze the dehydration of ethanol almost exclusively to diethyl ether over a temperature range of 80-120 °C[7-8]. Although these materials are highly selective, the narrow temperature range and low reaction rates severely limit their viability for any cold-start application. At temperatures above 120 °C, the particles begin to fuse together causing a dramatic increase in pressure drop through the catalyst bed or a complete blockage of flow[9]. Karpuk and Cowley[10] reported the dehydration of methanol to dimethyl ether (DME) and water occurs readily over fluorinated γ-alumina. Amorphous silica-alumina, γ-alumina, and alumina-phosphoaluminate (APA) also gave good yields. In a review of hydrocarbon formation, Chang[11] discusses the possible mechanisms for DME formation. Depending on the catalyst type, Lewis acid sites, Bronsted acid sites, or both appear to be involved in the methanol dehydration reaction through a complex set of surface reactions. Since all of these catalysts are highly active for methanol dehydration, they may also be suitable for ethanol dehydration as well. The selectivity of these materials for ether versus ethylene production has not been investigated.

Experimental

The following experimental procedures were used in the evaluation of the catalyst composition and the catalyst performance.

Catalyst Preparation. The aluminophosphate-alumina (APA) catalysts were prepared using a conventional coprecipation method. In general, the APA catalysts were prepared by combining an aqueous solution of aluminum nitrate and orthophosphoric acid with an ammonium hydroxide solution to form a solid hydrogel. The gel was washed with ammonium hydroxide solution, dried at 120 °C for 24 hours, and calcined at 500 °C for 16 hours. The calcined materials were sized to 20/40 mesh. An attempt was made to prepare P/Al ratios of 0.0, 0.1, 0.5, 0.8 and 1.0 by varying the amount of orthophosphoric acid added. The actual P/Al ratios were determined by ICP analysis. The PS-1, PS-2 and PS-3 cataysts were prepared by impregnating 20/40 mesh sized silica gel (Davison Chemical grade 57) with a solution of phosphoric acid. The PA-1, PA-2 and PA3 catalyst was prepared by impregnating 20/40 meshed sized γ-alumina (Norton SA-6273) with a solution of phosphoric acid. The silica-alumina was provided by Davison Chemical (Grade 980-13).

Catalyst Evaluation. The catalyst evaluations were carried out under a variety of temperatures in a continuous-flow, fixed bed catalytic reactor, using 1.27 cm o.d. stainless steel tube. Ethanol was injected via syringe pump, then vaporized at 120 °C and mixed with a He (99.9999%) carrier gas. The partial pressure of ethanol in the feed was 0.48, and the space velocity was 2080 cm^3/g-cat-hr. Approximately, 0.5 g of catalyst was mixed with 1.5 g of quartz chips to insure uniform flow and minimize temperature gradients in the catalyst bed. Each catalyst was tested at 200, 250, and 300 °C for 3 hours at each temperature. The product gas was analyzed by an on-line gas chromatograph (SRI 8610B) using a TC detector and fitted with a 1.5 mm column packed with Porapak Q.

Catalyst Characterization. The XRD patterns of the catalysts were collected with a LINT 2000 diffractometer by Rigaku using a Cu K_α source at an applied voltage of 40 kV and a current of 150 mA. The radial distribution functions (RDF) of the amorphous APA catalysts were obtained by collecting the x-ray scattering data in the same instrument using a Mo K_α source with an applied voltage of 40 kV and a current of 200 mA.

The ^{27}Al MAS NMR spectra were measured at 130 MHz with a CMX Infinity 500 NMR spectrometer. The sample spin speed was

14 kHz. The spectra were recorded with π/4 excitation with a pulse width of 1.0 μsec, and a pulse delay of 0.1 second. All of the ^{27}Al chemical shifts were referenced to a 1 M aqueous solution of aluminum nitrate.

The XPS studies were performed on a Kratos HSi instrument using Al K_α radiation and a band pass of 20 eV.

Temperature programmed desorption (TPD) results were obtained by placing approximately 0.3 g of the catalyst sample in a quartz cell. The sample was pretreated by heating it to 525 °C for 3 hours in a helium flow of 20 cm^3/min. Ammonia was adsorbed onto the catalyst sample at 175 °C by flowing a 1:1 volume mixture of anhydrous ammonia and helium through the cell for 30 min. After adsorption was complete, the sample was heated at a rate of 20 °C/min. in flowing helium until a final temperature of 500 °C was reached. The desorbed ammonia was passed through an scrubber containing 20.0 mL of standardized 0.05 N sulfuric acid solution. The total amount of ammonia desorbed was determined by titrating the acid solution with a 0.05 N standard solution of sodium hydroxide. Pyridine was introduced into the helium flow using a saturator maintained at 0 °C. The adsorption period for pyridine was 1 hour.

Results and Discussion

The catalysts used in this study were selected because they have varying surface densities of Lewis and Brönsted acid sites. Gamma-alumina (GA) has predominantly Lewis acidity, silica-alumina (SA) has both Lewis and strong Brönsted acidity, aluminophosphate-alumuina (APA) has both Lewis and weak Brönsted acidity, phosphoric acid on silica (PS) has only Brönsted acidity, and phosphoric acid on γ-alumina (PA) has both Lewis and weak Brönsted acidity. The catalyst compositions are reported in Table 1.

Table 1. Bulk Composition of Catalysts

Catalyst	Wt. % SiO_2	Wt % Al_2O_3	Wt. % P_2O_5*	P/Al Mole Ratio**
GA	0	100		
SA	86.5	13.0		
APA 0.0				0.0
APA 0.1				0.090
APA 0.5				0.488
APA 0.8				0.657
APA 1.0				0.746
PS-1	96.6		3.36	
PS-2	93.9		6.14	
PS-3	86.1		13.9	
PA-1	97.9		2.07	
PA-2	95.5		4.50	
PA-3	90.8		9.20	

* All of the P_2O_5 is present on the surface of the catalyst, and is not distributed throughout the bulk of the sample.

** As determined by ICP analysis.

Catalyst Evaluation. The activity and selectivity were calculated using the following equations. Where X_E^o, X_E, X_D, and X_N represent the mole fractions of ethanol in the feed, and ethanol,

$$\% \text{ Activity} = (X_E^o - X_E) \times 100 \quad (3)$$

$$\% \text{ Selectivity} = X_D/(X_D + X_N) \times 100 \quad (4)$$

dimethyl ether, and ethylene in the product. The catalyst test results are presented in Table 2. A blank run was made using only quartz chips in the catalyst tube. The absence of any ethanol conversion showed that catalytic wall or thermal effects were absent. The conversions for all catalysts were typically less than 10% activity at 200 °C. At temperatures of 250 and 300 °C, only the APA catalysts (0.5-1.0) give activity and selectivity sufficient to cold start a vehicle. A kinetic study was made using the APA 0.5 catalyst. The following rate expression gave the best fit to the data.

$$Rate = \frac{k'P_E}{(1 + K_E P_E + K_W P_W)} \quad (5)$$

The adsorption constant for water is 436 and that for ethanol is 26.7, which implies that a strong product inhibition by water exists. In summary, the APA catalysts exhibit the desired activity and selectivity for the ethanol dehydration reaction. In order to gain a better understanding of the surface chemistry responsible for this desired result, selected catalysts were analyzed in more detail in order to understand the possible cause of this selectivity.

Table 2. Catalyst Activity and Selectivity

Catalyst	250 °		300 °	
	Act.	Sel.	Act.	Sel.
GA	52.5	93.0	83.6	31.4
SA	79.3	71.0	99.2	0
APA 0.0	61.6	93.5	88.1	23.2
APA 0.1	23.3	96.2	73.2	89.3
APA 0.5	54.8	98.0	78.8	87.0
APA 0.8	55.3	98.1	79.5	86.9
APA 1.0	51.5	97.7	78.8	88.5
PS-1	0	-	2.9	54.6
PS-2	2.0	100	4.9	55.4
PS-3	2.4	100	2.8	45.9
PA-1	70.1	92.7	88.6	18.2
PA-2	61.9	94.9	85.4	39.0
PA-3	51.4	97.1	80.9	76.3

Catalyst Characterization. Selected catalysts were analyzed by XRD, RDF, NMR, and TPD. Figure 1 shows the XRD patterns for the APA catalysts. The APA 0.0 catalyst contains no aluminophosphate and gives a diffraction pattern similar to the commercial γ-alumina sample (GA). This was the expected result. The addition of even a small amount of phosphate to the structure inhibits the crystallization of the γ-alumina phase. See the XRD pattern for the APA 0.1 catalyst. The addition of more phosphate results in a pattern similar to that of amorphous silica at around 23 degrees 2θ.

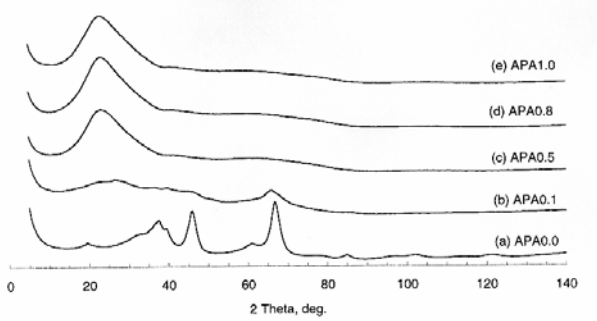

Figure 1. XRD patterns for APA 0.0, 0.1, 0.5, 0.8, and 1.0 catalyst samples.

Radial distribution function (RDF) analysis can be used to investigate amorphous materials. A comparison of silica glass, APA 0.1 and APA 1.0 are shown in figure 2. The Al-O (1.74 Å) and P-O (1.74 Å) bond distances are consistent with a tetrahedral configuration, similar to that observed for Si-O (1.61Å). The variation in the Al-O and P-O bonds is likely responsible for the broader peak observed for the APA 1.0 sample. The APA 0.1 sample gives an Al-O (1.88 Å) bond distance. This value is essentially identical to the Al-O (1.9 Å) bond length reported for an aluminum octahedron[12]. This result suggests that the addition of phosphate forces more aluminum atoms to adopt a tetrahedral configuration.

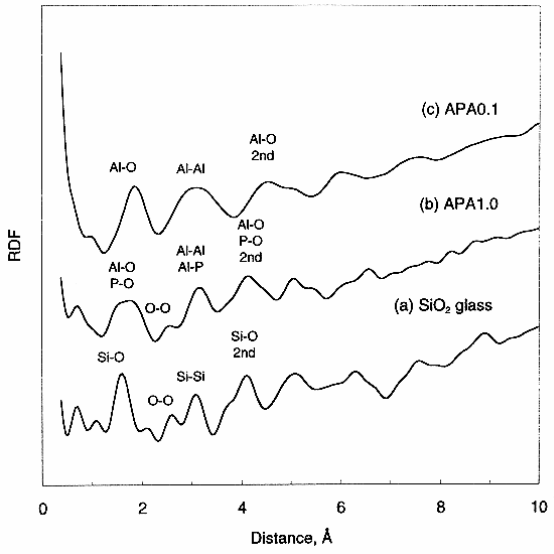

Figure 2. RDFs of Silica, APA 0.1 and APA 1.0.

The chemical shifts for the MAS NMR spectra for the ^{27}Al atoms in samples of GA, APA 0.1, APA 1.0, PA-1, and PA-3 are given in table 3. For the GA sample, the ^{27}Al atoms are present in 4-coordinate (tetrahedral) sites at 67. 4 ppm and 6-coordinate (octahedral) sites at 9.1 ppm, see figure 3. The observed octahedral to tetrahedral ratio of 2.0 : 0.9 is typical for γ-alumina[13]. As phosphate is added to the structure, a new 5-coordinate site appears at 34.0 ppm, apparently at the expense of tetrahedral sites. The

Table 3. Chemical Shifts for NMR Spectra of ^{27}Al.

	^{27}Al MAS NMR Chemical Shift (ppm)		
Catalyst	**4-coord.**	**5-coord.**	**6-coord.**
GA	67.4	0	9.1
APA 0.1	71.3	34.0	5.2
APA 1.0	44.1	17.6	-9.6
PA-1	67.4	0	8.3
PA-3	69.0	0	9.9

APA 1.0 sample shows a dramatic change in the NMR spectra, with all three ^{27}Al peaks being shifted to the right, and a significant increase in the 4-coordinate species. This is in agreement with the RDF data. It is likely that this new species plays a role in making the APA catalysts more selective for diethyl ether production. The PA-1 and PA-3 samples gave NMR spectra very similar in peak area and chemical shifts to that for γ-alumina. This is expected since the phosphate is only located at the surface and the preponderance of the NMR signal comes from the γ-alumina support.

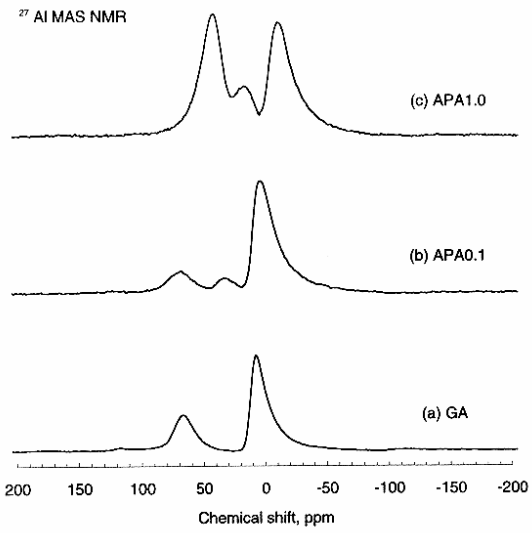

Figure 3. ^{27}Al MAS NMR Spectra of GA, APA 0.1, and APA 1.0 catalyst samples.

XPS analysis of the APA samples was done to determine if there was a direct correlation between the surface and bulk phosphorus to aluminum (P:Al) mole ratio. No enrichment of phosphorus on the surface of the APA samples was observed.

Ammonia and pyridine TPD studies provide information about the relative amounts of Lewis and Brönsted acid sites on the catalyst surfaces. Ammonia is known to adsorb onto both Lewis and Brönsted acid sites, while pyridine absorbs only onto Lewis acid sites. Since Brönsted sites of γ-alumina, Al-OH, are too week to protonate pyridine, Lewis acidity is thought to be exclusively responsible for the observed acidity for γ-alumina[14]. Silica is known to have very little acidity. Table 4 gives the TPD results for the desorption of ammonia and pyridine from our catalyst samples.

Table 4. Relative amounts of ammonia and pyridine desorption from catalyst samples.

Catalyst Sample	**Ammonia Desorbed**	**Pyridine Desorbed**	**Pyridine to Ammonia Des. Ratio**
GA	0.89	1.69	1.91
SA	0.55	0.48	0.86
APA 0.0	0.76	1.27	1.67
APA 0.1	0.55	0.74	1.36
APA 0.5	2.12	1.10	0.52
APA 0.8	2.59	0.86	0.33
APA 1.0	3.04	0.74	0.24
Silica	0.04	0.03	0.57
PS-1	0.34	0.29	0.86
PS-3	2.04	0.74	0.36
PA-1	0.91	1.60	1.77
PA-2	0.88	1.52	1.73
PA-3	0.99	1.46	1.47

A decrease in the ratio of pyridine to ammonia desorption suggests a decrease in the population of Lewis acid sites. The pyridine to ammonia ratio decreases for the APA catalysts as the phosphate

content increases. Considering these observations, it is apparent that the addition of phosphate decreases the surface concentration of Lewis acid sites. This has important implications with respect to the surface dehydration mechanism. It is proposed that the dehydration of ethanol to ethylene requires two adjacent Lewis acid sites or strong Brönsted acid sites. The APA catalysts dilute the surface concentration of Lewis acid sites without adding strong Brönsted acid sites. The dehydration of ethanol to diethyl ether requires only a single Lewis acid site.

Conclusions

The unique acidic properties of the aluminophosphate-alumina catalysts make them highly selective for the dehydration of ethanol to diethyl ether at elevated temperatures (200-300 °C).

Acknowledgement. This work was funded by DOE and NREL. Catalyst support samples were provided gratis of Grace (Davison Division) and Norton Chemical Companies.

References

(1) Cook, G. "A Question of Balance",, *NREL in Review: Science and Technology*, **1994**, 16 (2, summer), pp. 2-5.
(2) Egebäck, K. E., Petersson, L. J., and Westerholm, R., XI International Symposium on Alcohol Fuels proceedings Vol. 1, 1996, pp. 750-761, Sun City, South Africa.
(3) Barber, E., Quissek, F., and Hulak, K., IX International Symposium on Alcohol Fuels proceedings Vol. 2, 1991, pp. 566-573, Florence, Italy.
(4) De Boer, J. H., Fahim, R. B., Linsen, B. G., Visseren, W. J., De Vleesschauwer, W. F. N. M. *J. Catal*. **1967**, 7, 163-172.
(5) Nagai, Y. and Ishii, N. *J. Soc. Chem. Ind. Japan*, **1935**, 38, 8-12.
(6) Kito-Borsa, T., Pacas, D. A., Salim, S. and Cowley, S. W. *Ind. & Eng. Chem. Res.*, **1998**, 37(8), 3366-3374.
(7) Apecetche, M. A., and Cunningham, R.E., *Lat. Am. J. Chem. Eng. Appl. Chem.* **1976**, 6, 91-103.
(8) Gates, B. C., and Johanson, L. N. *J. Catal.* **1969**, 14, 69-76.
(9) Kito, T., Wittayakun, J., Pacus, D., Selim, S., and Cowley, S. W., XI International Symposium on Alcohol Fuels proceedings Vol. 1, 1996, pp. 166-177, Sun City, South Africa.
(10) Karpuk, M. and Cowley, S. W. International Fuels and Lubricants Meeting and Exposition, Portland, Oregon, 1988, October 10-13, *SAE Technical Paper Series*, 881678.
(11) Chang, C. D., Catal. Rev. Sci. Eng., **1983**, 25, 36-48.
(12) Shannon, R. D. and Prewitt, C. T., *Acta Cryst.* **1969**, B25, 925-946.
(13) Müller, D., Gessener, W., Behrens, H. J., and Scheler, G. *Chem. Phys. Lett.***1981**, 79, 59-62.
(14) Peri, J. B. *Discuss. Faraday Soc.* **1971**, 52, 55-65.

EFFECTS OF NITROGEN CHEMISTRY ON CHAR FORMATION FROM BIOMASS

Robert J. Evans, Mark R. Nimlos, Luc Moens

National Bioenergy Center
National Renewable Energy Laboratory
Golden, Colorado 80401

Introduction

The fate of nitrogen during pyrolysis or combustion is an important consideration in the utilization of biomass. Nitrogen oxide emissions from biomass combustion are thought to arise primarily from fuel-bound nitrogen[1] and an understanding of the chemical transformations involving nitrogen may lead to improvements in these emissions. An important source of nitrogen in biomass is proteins and amino acids, which can react catalytically with the carbohydrates by reactions generally characterized as Maillard chemistry[2]. This chemistry produces complex mixtures of products and has been the subject of numerous studies. However, less is known about the role that this chemistry plays in the formation of char. The partitioning of nitrogen into char or gas phase products will be critical towards determining the routes for converting nitrogen from biopolymers into NO_x emissions.

We have studied reactions of amino acids with carbohydrates and how these reactions affect the composition of the resulting char. We have used Molecular Beam Mass Spectrometry (MBMS) to characterize the gaseous emissions from the pyrolysis of model mixtures of amino acids with carbohydrates. The remaining char has been characterized using elemental analysis and reflectance FTIR spectroscopy.

Of particular interest in the char formation are effects due to the Maillard chemistry involving proline. We have shown that proline is more reactive in Maillard chemistry than other amino acids[3], which is consistent with literature reports of proline as a catalyst for asymmetric aldol condensations[4-6]. In particular, we would like to investigate how proline affects the maturation of char.

Experimental Techniques

Experiments were conducted by sequentially heating samples of model compounds or biopolymers in flowing helium. Gas phase products were measured directly using an MBMS, and the remaining solid materials were retained for further analysis. Samples (100 mg to 400 mg) were placed in a quartz boat and slid into a heated tubular reactor. The furnace was set so that sliding the sample further into the reactor produces higher temperatures. Sequential heating experiments were conducted by sliding the sample into a fixed temperature region (as determined by a thermocouple attached to the boat) and holding for five minutes. A subsequent heating was conducted by sliding the material further into the reactor and holding it at that higher temperature for five minutes.

Results and Discussion

Figure 1 shows integrated mass spectra for staged heating experiments using proline mixed with a carbohydrate matrix composed of glucose, cellulose and pectin (Pro:Glu:Cell:Pect = 1:1:2:2). This mixture was used because the glucose will react vigorously with the glucose and the cellulose/pectin mixture produces a significant amount of char. In these experiments, the samples are heated to 550 °C directly (bottom spectrum) or sequentially (top two spectra). In the spectrum on the top, the sample was heated to 170 °C for 5 min. then to 350 °C for 5 min. before being heated to 550 °C. In the middle spectrum the sample was heated to 350 °C before being heated to 550 °C. The mass spectra in this figure are obtained by integrating over the pulse that occurs during the last temperature of each given sequence.

The intensity of the high m/z peaks are shown in the insets and the scales for these are on the right side of the plots. As can be seen, there are characteristic clusters of peaks in the high m/z portion of these spectra. For instance, there are clusters around m/z = 200, 214, 227 and 242. These spectral clusters are also observed for other amino acids but are not as prominent as for proline. Furthermore, the location of these clusters seems to be dependent upon the amino acid but not the type of carbohydrate used. These peaks appear to be associated with Maillard reactions between proline and the carbohydrates and probably result from secondary reactions. As can be seen from these spectra, the formation of these high m/z clusters of peaks is enhanced when the sample is not thermally pretreated. They are more intense in the bottom spectrum than in the middle spectrum and more intense in the middle spectrum than in the top spectrum. This suggests that low temperature reactions of the proline with the carbohydrates tend to decrease the formation of these secondary Maillard products.

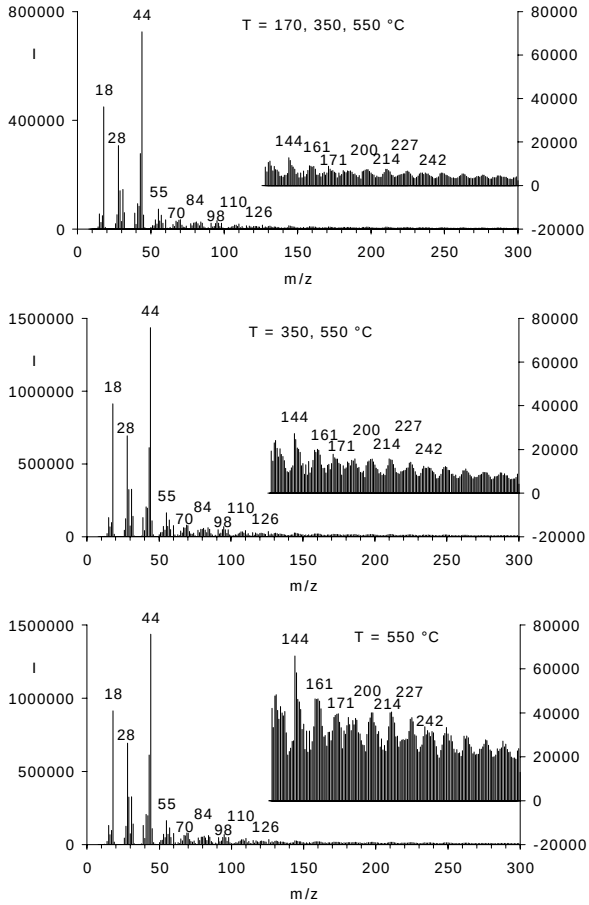

Figure 1. Mass spectra from the staged heating of proline mixed with a matrix of glucose, cellulose and pectin. These spectra have been averaged over triplicate experiments.

The infrared spectra of the char also shows interesting changes in the solid that result from Maillard reactions. Fig. 2 shows a plot of

the FTIR spectra of the char from the pyrolysis of our carbohydrate matrix without proline. The lower spectrum is of the unheated matrix. The peaks at 3300 cm^{-1} (O-H stretch), 2890 cm^{-1} (C-H stretch), 1330 cm^{-1} (C-H bend) and 1050 cm^{-1} (C-O stretch) are characteristic of carbohydrates. At moderate pyrolysis temperatures (170 ^{o}C and 350 ^{o}C) carbonyl peaks are formed (1750 cm^{-1} and 1630 cm^{-1}, C=O stretch). At 550 ^{o}C peaks arising from aromatic groups are seen at 3040 cm^{-1} (C-H stretch), 1590 and 1436 cm^{-1} (C-C stretch), 1230 cm^{-1} (C-H in-plane bend) and 815 cm^{-1} (C-H out-of-plane bend).

Similar peaks are seen in the char FTIR spectra shown for proline (Fig. 3) mixed with the carbohydrate matrix. However, the presence of the proline leads to maturation of the char at lower temperatures. For neat matrix experiments there is still significant intensity for the carbohydrate peaks at 350 °C, while in the presence of proline, these peaks are essentially gone at 350 °C. For the mixture including proline the carbonyl peaks form at 170 °C but disappear at 350 °C, where they are replaced by aromatic peaks. This again shows the ability of proline to accelerate the char maturation process. Other amino acid can also accelerate the formation of aromatic groups in char but not to the extent that occurs with proline.

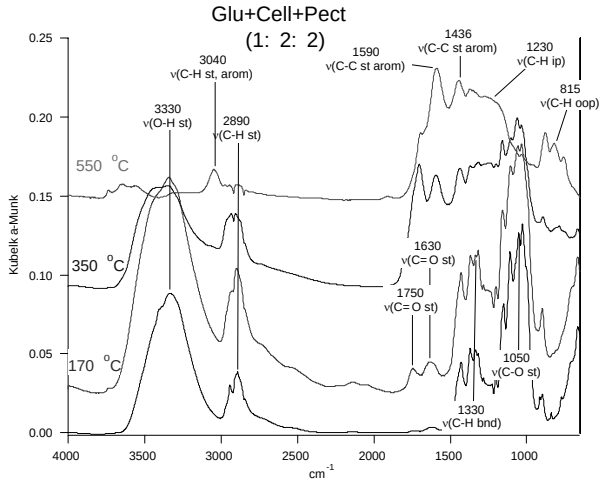

Figure 2. Reflectance FTIR spectra of carbohydrate matrix heated to different temps.

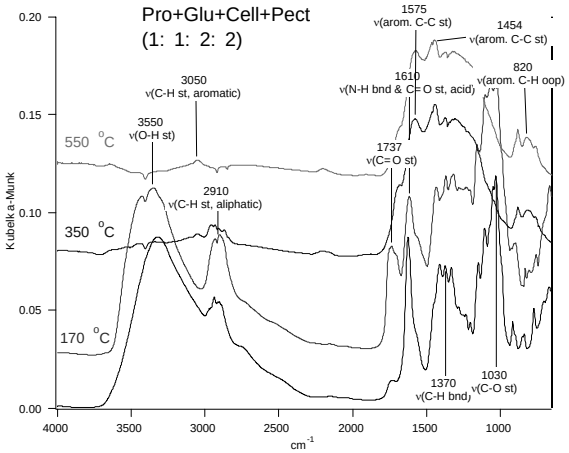

Figure 3. Reflectance FTIR spectra of char from pyrolysis of proline + matrix**.**

Measurement of char yields from the sequential pyrolysis experiments and elemental analysis of the remaining solid material allow a determination of the partitioning of nitrogen between the solid and gas phase. The plot in Fig. 4 shows this partitioning for sequentially heating a mixture of proline and the carbohydrate matrix to 170°C, 350 °C and 550°C. This plot shows that the nitrogen has a tendency to stay in the char.

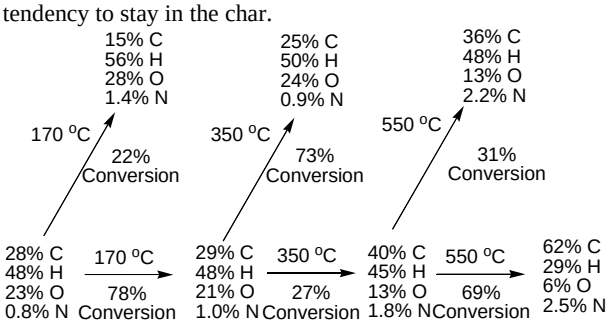

Figure 4. Partitioning of elements during sequential heating of proline mixed with the carbohydrate matrix (Glu+Cell+Pect). The composition in the lower left is for the starting material and the values along the bottom are for the char after heating. The values at the top are for the gas phase after heating.

Conclusions

The conclusions of this work are that proline can drastically change the rate of formation of mature char (highly aromatized) through its vigorous reaction with carbohydrates. Further, this Maillard chemistry appears to leave significant amounts of the nitrogen in the char.

Acknowledgment. We would like to acknowledge the support of Philip Morris USA, and stimulating discussions with Geoffrey Chan and Mohammad R. Hajaligol.

References

1. Brink, A., P. Kilpinen, and M. Hupa, Energy Fuels, 2001. 15(5): 1094.
2. T. P. Labuza, G.A.R., V. M. Monnier, J. O'Brien, J. W. Baynes, ed. *Maillard Reactions in Chemistry, Food and Health.* 1994, Royal Society of Chemistry: Cambridge.
3. Moens, L; Evans, R. J; Looker, M. J.; Nimlos, M. R. *Fuel*, In Press.
4. Movassaghi, M. and E.N. Jacobsen, Science, 2002. 298(5600): 1904.
5. Sakthivel, K., W. Notz, T. Bui, and C.F. Barbas, J. Am. Chem. Soc., 2001. 123(22):5260.
6. List, B., R.A. Lerner, and C.F. Barbas, J. Am. Chem. Soc., 2000. 122(10): 2395.

NMR STUDY OF THE TRANSFORMATIONS IN PECTIN AND CELLULOSE (WITH 10% N-15 PROLINE) DURING PYROLYSIS

*R. J. Pugmire, M. S. Solum, Z. Ma, Y. J. Jiang, J. B. Wooten**

Department of Chemical and Fuels Engineering, University of Utah, Salt Lake City, Utah 84112 and Philip Morris USA Research Center,* P.O. Box 26583, Richmond, Virginia 23261

Introduction

In preparation for the analysis of tars made from a tobacco plant grown from N-15 enriched nutrients several chars made from pectin and cellulose (with 10% by weight of N-15 enriched proline added) have been studied by C-13 and N-15 NMR and ESR methods. The carbon skeletal structure was analyzed in terms of the previously described structural and lattice parameters.[1,2] Only a few of the highest temperature chars (550 and 600 ˚C) start to show a small amount of graphite like structures.[3] The spin lattice relaxation time in both the laboratory and rotating frame were measured for all samples and showed correlation with the carbonization of the samples.

Experimental

All C-13 NMR spectra were run on a Chemagnetics CMX-100 spectrometer operating at a carbon frequency of 25.152 MHz and using a 7.5 mm probe with a ceramic housing for reduced carbon background. The proton decoupling power was 62.5 kHz. The spinning speed was locked to 4.1 kHz. Chemical shift ranges used in references 1 and 2 were modified to somewhat account for the overlap of the aromatic region with the anomeric carbon in carbohydrates in some of the samples. The contact time chosen for the dipolar dephasing experiments was five times the longest T_{CH} as measured in variable contact time experiments.

Nitrogen-15 spectra were run on a Chemagnetics CMX-200 spectrometer also with a 7.5 mm probe. This field was chosen, instead of the higher S/N spectrometer operating at 400 MHz, so that the formation of pyridinic type nitrogens with large chemical shift anisotropies could be more accurately followed.[3]

All chars were prepared at Philip Morris and heated to temperatures of 150 to 600 ˚C.

Results and Discussion

Carbon-13 CPMAS spectra of some pectin chars are shown in Figure 1. The pectin resonances are the larger broader resonances at about: 171 ppm for the carboxyl carbon, 101 ppm for the anomeric carbon, 70 ppm for carbons next to one oxygen and 54 ppm for the methoxy group. The five resonances from proline are the smaller sharper lines. As can be seen in the spectrum from the sample heated to 150 ˚C proline is the first to react. A small amount of aromatic and carbonyl carbons have been produced where there were none in the original mixture. Also the aliphatic part of the spectrum has become broad in the region where the sharp proline resonances were before. At 250 ˚C most of the pectin has also reacted and the spectrum looks like a lignite coal. A large amount of aromatic carbons have been formed but the sample still retains a wide range of oxygen functional groups: carbonyls, carboxyls, phenolics and oxygenated aliphatic carbons. There may still be a small amount of anomeric carbons under the aromatic band at about 105 ppm. These may be able to be separated from the aromatic carbon by a csa type filtering experiment.[5] At 350 ˚C the original material has mostly reacted and the oxygen functional groups have greatly decreased along with some aliphatic material. As the temperature is increased further the samples become more and more aromatic. At 550 ˚C the aromaticity is 0.95. The average aromatic cluster size is estimated to be about 9 in the 150 ˚C sample where the aromatic material first starts to appear and progressively increases to about 19 carbons in the 550 ˚C sample.

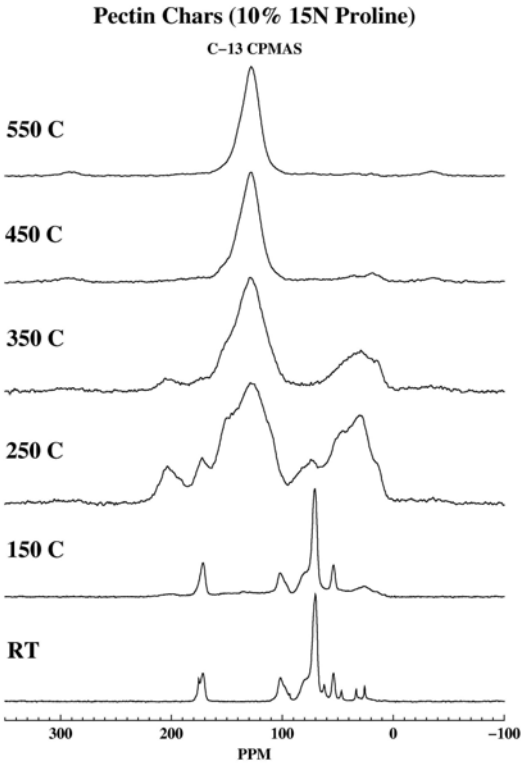

Figure 1. C-13 CPMAS spectra of the pectin and proline mixture heated to the listed temperatures.

Some important NMR relaxation parameters for the pectin/proline samples are presented in Table 1. One can see that after some scatter in the starting sample and the 150 ˚C sample that the T_1^H values decrease as the temperature that the sample was heated increased. Others have seen this relaxation time go through a minimum and then increase when the electron spin exchange rate changes and the relaxation is not proportional to the number of static unpaired electrons.[6] The spin-lattice relaxation in the rotating frame, $T_{1\rho}^H$, also decreases as the temperature is increased, reaches a minimum at 450 ˚C, and then starts to increase for the 550 ˚C sample. This is a common occurrence that has been seen in other pyrolysis series.[2,6]

Table 1. NMR Parameters from Pectin Chars.

Sample	T_1^H (s)	$T_{1\rho}^H$ (ms)	T_L (ms)
RT	0.188(76%) 4.97(24%)	3.8 (line 2)	--
150 ˚C	0.729(94%) 10.9(6%)	6.0(whole spectrum)	0.38
250 ˚C	0.271	5.4	0.67
350 ˚C	0.131	2.7	0.79
450 ˚C	0.027	2.1	1.3
550 ˚C	0.017	8.4	1.7

The last column in Table 1 is the Lorentzian (exponential) time constant from a dipolar dephasing experiment. This time constant represents dephasing from protons that are not directly attached to aromatic carbons. The dipolar dephasing[7] experiment used here was sequence C from reference 7 that does not include dephasing from chemical shift anisotropy. As one can see as the temperature increases the time constant T_L gets larger as there are fewer protons or the protons are farther away from the nonprotonated aromatic carbons.

Conclusions

This preprint shows that NMR can be used to quantify the changes in the structure in a pectin/proline mixture heated to various temperatures. Additional work is currently under way to study the nitrogen incorporation in the various chars and to measure the unpaired electron spin concentration and see how it correlates to the various NMR relaxation time constants. Additional samples heated between 150 ˚C and 250 ˚C are currently being examined because this is the temperature range where the largest amount of structural modification seems to occur.

Acknowledgement. This work was supported by Phillip Morris, USA.

References

1. Solum, M. S., Pugmire, R. J., Grant, D. M., *Energy & Fuels*, **1989**, 3, 187.
2. Solum, M. S., Sarofim, A. F., Pugmire, R. J., Fletcher, T. H., Zhang, H., *Energy & Fuels*, **2001**, 15, 961.
3. Jiang, Y. J., Solum, M. S., Pugmire, R. J., Grant, D. M., *Energy & Fuels*, **2002**, 16, 1296.
4. Kelemen, S. R., Afeworki, M., Gorbaty, M.,, Kwiatek, P. J., Solum, M. S., Hu, J. Z., Pugmire, R. J., *Energy & Fuels*, **2002**, 16, 1507.
5. Mao, J.-D., Schmidt-Rohr, K., *Solid State NMR*, **2004**, in press.
6. Wind, R. A., Li, L., Maciel, G. E., Wooten, J. B., *Appl. Magn. Reson.*, **1993**, 5, 161.
7. Newman, R. H., *J. Magn.Reson.*, **1992**, 96, 370.

PROBING THE PYROLYSIS OF METAL DOPED CELLULOSE CHARS AT DIFFERENT POINTS ALONG THE REACTION COORDINATE

Andrew M. Herring, J. Thomas McKinnon, Joshua G. Lee, Bryan D. McCloskey, Ryan A. Pavelka, Matthew S. Kirchner, and Dimitri R. Dounas-Frazer.

Department of Chemical Engineering
Colorado School of Mines
Golden, CO 80401-1887

Introduction

Cellulose is a major component of biomass, along with hemi-cellulose and lignin, and is a useful model for thermo-chemical conversion of biomass. The conversion of biomass via pyrolysis has important applications in the development of new renewable chemicals and bio-carbons, as well as combustion processes leading to combined heat and power, forest fires and cigarette smoking. The process of cellulose and cellulose char pyrolysis of is still not fully understood despite rapid progress in the last couple of decades.[1-3] The influence of metal salts on charring and subsequent pyrolysis has long been known to alter the chemistry of these processes.[1,4] Metal cations occur naturally in biomass particularly in the hemi-cellulose, they may also be added to the growing plant in the form of fertilizer. In general inorganic materials in the form of ash are considered a problem that must be mitigated against in the pyrolysis and combustion of biomass.[5] However, metal cations may be deliberately added to the biomass to alter its pyrolysis chemistry in a favorable way to reduce the formation of polycyclic hydrocarbons, PAH, or in the synthesis of new bio-carbons.[6]

In order to more fully understand the effect of metal doping on cellulose pyrolysis chemistry we have doped Avicel cellulose with a series of mono- and di-valent cations. Both main group and transition metals were chosen in order to probe both the effects of promoting ionic pathways and possible catalytic pathways in the charring and pyrolysis chemistry. We chose to dope cellulose with metal acetates as not only is the acetate anion relatively inert but all of these metal acetates decompose below the charring temperature of 375 °C. The chars were characterized primarily by DRIFTS and NMR. The char structure and pyrolysis chemistry at very short times, several ms was studied by laser pyrolysis molecular beam mass spectroscopy, LP-MBMS.[7,8] We also sampled the product gases and trapped the free radicals produced using cold and chemical trapping at slightly longer times, several 100 ms.

Experimental

Avicel cellulose (5 g) was doped at 1mol% with sodium, potassium, magnesium, calcium, palladium, copper and zinc acetates by the incipient wetness technique using aqueous solutions of the as received metal acetates. The doped cellulose samples were dried in an oven at 115 ºC overnight pressed into a 1" diameter pellet at 10,000 psi in a Carver press and charred under $Ar_{(g)}$ at 375 ºC for ½ h.

For the DRIFTS experiments the chars were ground in air and placed in a Harrick Scientific, heatable variable atmosphere chamber in a Harrick Scientific Praying Mantis Diffuse Reflectance attachment. The chars were heated under dry $He_{(g)}$ for 10 mins at 400 °C and then cooled to room temperature at which point the DRIFTS was recorded using a Thermo-Nicolet Nexus 670 FT-IR spectrometer equipped with a $N_{2(l)}$ cooled MCT detector. The data was treated with a Kubelka-Munk transformation to enable its quantitative interpretation.

The details of the LP-MBMS experiment have been described previously.[8] After cooling, the metal doped cellulose chars samples were transferred under inert gas to a $He_{(g)}$ filled chamber. LP-MBMS experiment performed at 6.5 W for 2 s. The first 0.25 s data corresponding to a temperature between 900 and 1000 ºC is reported here.

For the cold-trapping experiments the charred pellet was mounted in the center of a $N_{2(l)}$ cooled brass collection cup, ca. 2 mm from the cold surface. The brass collection cup had been previously coated with Diphenyldisulfide to which a known quantity of chlorobenzene had been added as an internal standard. The charred pellet was irradiated with the CO_2 at 13 W whilst being spun through one revolution. After the experiment, the cold trap is washed with methylene chloride. The methylene chloride extract is filtered and concentrated by evaporation. The concentrated extract is then injected onto a capillary GC column and the species identified using a MSD. We cannot currently observe species smaller than toluene or benzothiophene, because of the elution of the large solvent peak

Results and Discussion

The DRIFTS of the reheated and dried samples are shown in Figure 1. All of the samples show the same basic spectral features at the following approximate locations, a broad υ(OH) reaching a maximum at. 3400 cm^{-1}, sharper aliphatic and aromatic υ(CH) at 2900 cm^{-1}, a υ(C=O) at 1750 cm^{-1}, an aromatic υ(C=C) at 1650 cm^{-1}, a complex fingerprint region and two weaker aromatic γ(CH) bands at 850 cm^{-1}. Clearly metal doping as a profound effect on the residual char especially in terms of the ratio of OH and carbonyl groups to hydrocarbon. The palladium doped char has by far the most OH remaining in the structure whereas sodium and potassium have the least. The copper doped char has the highest ratio of carbonyl to aromatic hydrocarbon.

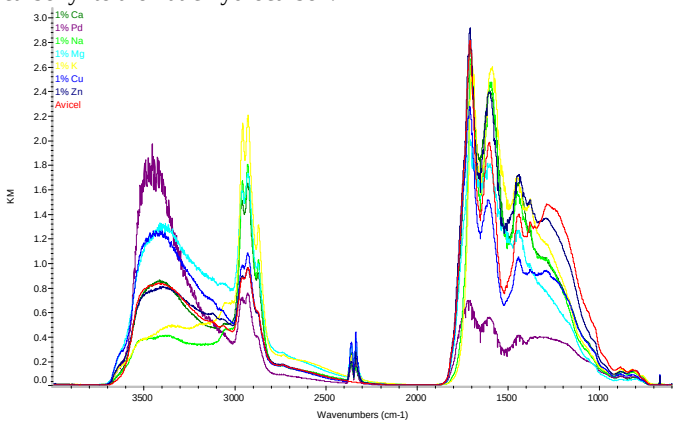

Figure 1. DRIFTS of cellulose and 1 wt% doped cellulose ½ h 375 °C chars after heating to 400 °C under $He_{(g)}$.

Solid state MAS ^{13}C NMR, not shown, also shows similar profound differences between the doped char samples. The zinc doped char appears similar to the undoped char, whereas most of the other chars appear very different or appear to have charred less.

The LP-MBMS experiment may be regarded as a snapshot of the initial reactive cloud of molecules evolved from the pyrolyzing char surface. The primary radical that we have proposed to evolve with these species is propargyl.[7,8] When Avicel cellulose is doped by wt% of metal acetate and charred the amount of CO_2 produced during pyrolysis is proportional to the molar amount of metal originally doped. This implies that one of the basic reactions of the metal in the char is to stoichiometrically oxidize the adjacent char. All metal doped chars produce slightly more toluene than the

undoped cellulose but palladium doped char produces a much larger quantity of this species than any other char during pyrolysis. The relative intensities of PAH species relative to m/z 202, pyrene are shown in Figure 2. It can be seen that whilst the initial ratios of the species produced are altered no distinct pattern emerges. All the chars produce more m/z 215, potassium doped more so. Universal suppression of PAH is only seen for the larger m/z 263 and 304. Most of the metals actually increase the initial amount of m/z 252, benzo-*a*-pyrene.

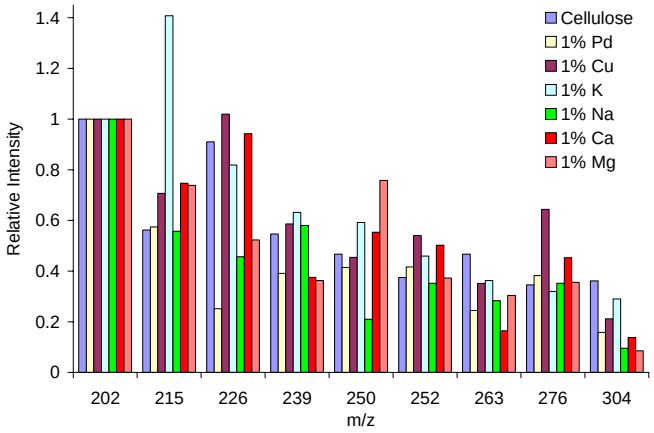

Figure 2. Relative intensities vs. m/z 202, pyrene, of selective masses of cellulose and 1 wt% doped cellulose.

In the chemical/cold trap experiment radicals are trapped as their phenylsulfide adducts, Figure 3. No propargyl radical is observed in the cold trap experiment as presumably the reaction is being sampled further along the reaction coordinate. The dominant reactive species observed from cellulose char is the hydrogen radical, together with methyl, phenyl, and phenylacetylene (trapped as benzothiophene) radicals. Only calcium doping cause the amount of these trapped radicals to increase. Palladium and calcium create the observance of methyl naphthalene radical. All the other metals in general suppress the formation of radicals consistent with a more ionic char decomposition pathway during pyrolysis.

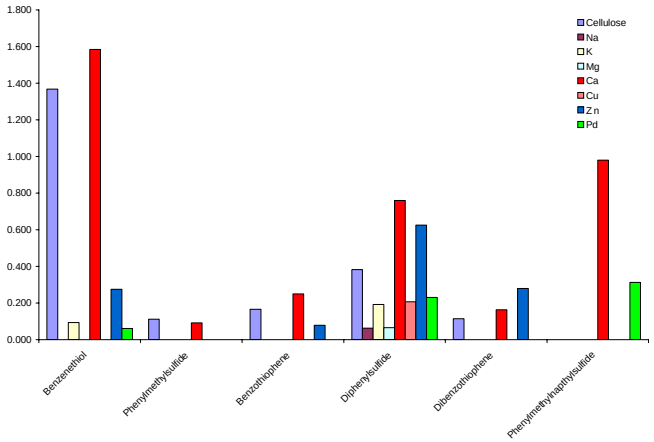

Figure 3. Relative abundances of PhS trapped reactive intermediates from the 13 W laser pyrolysis of ½ h 375 °C Avicel cellulose char and 1 mol% metal acetate doped Avicel cellulose char.

In addition to the chemically trapped radicals we also observe the PAH formed at this point of the reaction. The slate of aromatic and PAH species observed for the undoped cellulose char are shown in Figure 4. Toluene, naphthalene and acenapthalene are the dominant products. In addition to the hydrocarbon species we also observe a number of *O*-aromatic molecules. PAH as big as benzofluoranthene are easily observed. The ratio of these products changes with metal doping and further analysis of this data should provide insight in to some interesting tends.

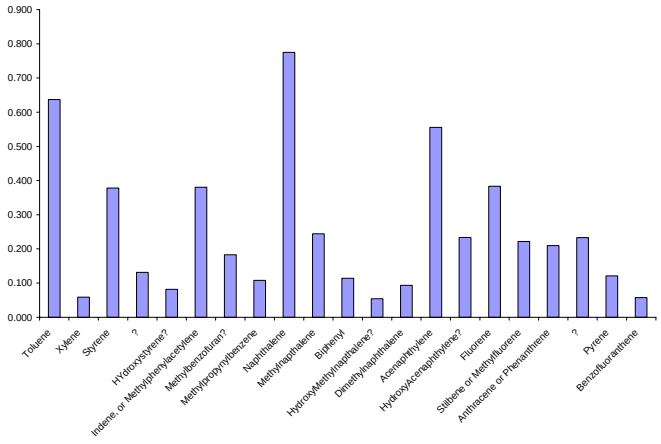

Figure 4. PAH observed from the 13 W laser pyrolysis of ½ h 375 °C Avicel cellulose char.

Conclusions

Obviously the fact that the PAH are still in existence with radicals in the LP-MBMS and cold trap experiment suggest that we are not yet observing the final slate of reaction products. We hope to be able to correlate the LP-MBMS data with the cold trapped data with conventional tube furnace data in order to build a complete picture of the reaction pathways involved in the pyrolysis evolved reacting volatile plume.

Acknowledgement. We would like to tank Philip Morris, USA, for support.

References

(1) Evans, R. J.; Milne, T. A. *Energy & Fuels* **1987**, *1*, 123.
(2) Antal Jr., M. J.; Grnli, M. *Ind. Eng. Chem. Res.* **2003**, *42*, 1619
(3) Shafizadeh, F. *Journal of Analytical and Applied Pyrolysis* **1982**, *3*, 283.
(4) Sekiguchi, Y.; Shafizadeh, F. *Combustion and Flame* **1984**, *29*, 1267.
(5) Davidsson, K. O.; Stojkova, B. J.; Pettersson, J. B. C. *Energy Fuels* **2002**, *16*, 1033
(6) Herring, A. M.; McKinnon, J. T.; McCloskey, B. D.; Filley, J.; Gneshin, K. W.; Pavelka, R. A.; Kleebe, H.-J.; Aldrich, D. J. *Journal of the American Chemical Society* **2003**, *125*, 9916
(7) Herring, A. M.; Thomas McKinnon, J.; Gneshin, K. W.; Pavelka, R.; Petrick, D. E.; McCloskey, B. D.; Filley, J. *Fuel* **2004**, *In Press, Corrected Proof.*
(8) Herring, A. M.; McKinnon, J. T.; Petrick, D. E.; Gneshin, K. W.; Filley, J.; McCloskey, B. D. *Journal of Analytical and Applied Pyrolysis* **2003**, *66*, 165.

QUANTUM MECHANICAL MODELING OF THE DECOMPOSITION OF SUGARS DURING ACID HYDROLYSIS OF BIOMASS

Mark R. Nimlos, Xianghong Qian, David K. Johnson, Michael E. Himmel

[1]National Bioenergy Center
National Renewable Energy Laboratory
Golden, Colorado 80401

Introduction

The treatment of biomass with hot acid is an intriguing option for preparing cellulose for enzymatic hydrolysis or for directly hydrolyzing cellulose. The goal of these two procedures is to convert the cellulose in biomass into sugars that can either be used as a fermentation substrate for ethanol, a transportation fuel, or as a feedstock for chemical production. A key issue during hydrolysis is the yield of the sugars. Ideally one would like to convert all of the hemicellulose and cellulose to monosaccharides. However, it is known that some of the sugars formed by hydrolysis are decomposed under acidic conditions[1]. Further, it has been demonstrated that furanyl compounds are formed by this decomposition and these furanyl compounds can polymerize[2] and may restrict access to unreacted polysaccharides.

In spite of the importance of sugar decomposition in hot acid, there is uncertainty concerning the mechanisms of these processes. Reaction (1) shows a proposed mechanism[2] for conversion of xylose (**1**) to furfural (**7**) that involves a ring opening. Since xylan is an important constituent of corn stover, this process may be important in the full utilization of corn.

Ring Opening Mechanism:

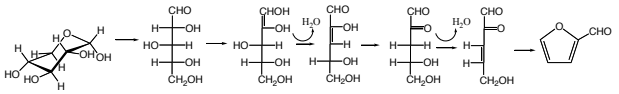

(1)

1 **2** **3** **4** **5** **6** **7**

In this mechanism, the sugar in the pyran form opens to the aldehyde (**2**), which then tautomerizes to an enol (**3**). Dehydration of this enol by a six centered transition state to form **4**. Another tautomerization produces **5**, which dehydrates again to form **6**. This compound can cyclyze and dehydrate to form furfural, **7**.

An alternative mechanism for forming furfural from xylose involves direct formation of the furan after protonation of the pyran[3] form (**1**). Xylose protonated at the 2 hydroxyl group can lose a water molecule and the resulting carbo cation is susceptible to attack by the ring ether forming a dihydroxy furan (**9**). This compound can then dehydrate to form furfural, **7**,

Direct Mechanism:

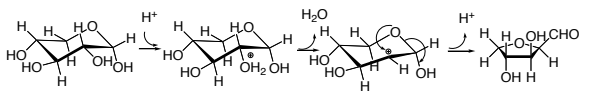

(2)

1 **8** **9**

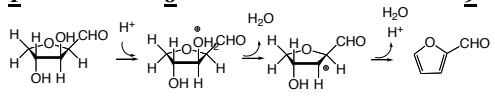

(3)

9 **10** **11** **7**

We have studied the mechanisms of sugar decomposition shown in Rxns. (1) – (3) with quantum mechanical molecular modeling in an attempt to determine which mechanism is prevalent. Small molecular systems are used to model the reaction steps shown in this mechanism. This allows the use of accurate computational techniques to capture the essential chemistry of these mechanisms.

Computational Techniques

The calculations in this study were carried out using the Gaussian 03 suite of programs. Local minima and transitions states were found using Berny optimizations. Starting geometries for the transition state optimizations were often located using a potential energy scan, where one internal coordinate was systematically changed while all other coordinates where allowed to relax. The geometry at the calculated maximum of this scan was used as a starting geometry for a transition state (TS) optimization. Stable structures had only positive vibrational frequencies while transition states had one imaginary frequency. The transition states were confirmed by visual inspection of the imaginary frequency using the Molden visualization package.

Results and Discussion

Ring Opening Mechanism

The first step in this mechanism is the opening of the pyran ring, **1**, to form the aldehyde, **2**. This step involves a four-centered transition state as is shown for the simplified structure in Rxn. (4).

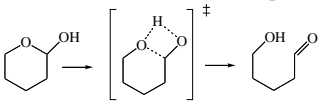

(4)

We have calculated the barrier for this reaction for several C5 and C4 sugars as well as hydroxymethyl methyl ether using density functional theory, B3LYP/6-31G(d). Values of 35 to 40 kcal mol^{-1} were obtained. Figure 1 shows a plot of the calculated results for hydroxymethyl methyl ether. The barriers for these reactions are greatly reduced with the addition of proton. For instance, with hydroxymethyl methyl ether the barrier is lowered from 40.4 kcal mol^{-1} to 14.3 kcal mol^{-1} with the addition of a proton. This suggests that protic solvents or added acid should accelerate this rate. This lower barrier is also consistent with kinetic measurements made in water[4].

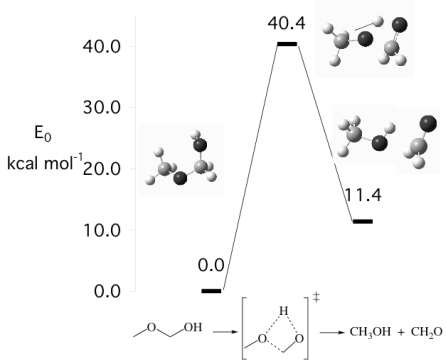

Figure 1. A potential energy plot of the calculated relative energies for the unimolecular decomposition of hydroxymethyl methyl ether.

The second step in the ring opening mechanism as show in Rxn. (1) is a keto-enol tautomerization. Unfortunately, the barriers for these reactions are typically high. Our calculations show that the tautomerization of acetaldehyde to vinyl alcohol has a barrier of 67.8 kcal mol^{-1}. We find that protonation does not significantly lower this barrier. Since the mechanism in Rxn. (1) contains two tautomerization steps, this pathway appears unlikely at practical temperatures.

We propose an alternative mechanism for furfural formation whereby the opened sugar undergoes a double dehydration as shown in reaction (5). In this mechanism, a proton catalyzes the ring opening step. Protonation of the C3 hydroxyl group on the resulting sugar, **2**, can lead to a double dehydration, forming **14**. This compound can then cyclize and further dehydrate to give furfural, **7**.

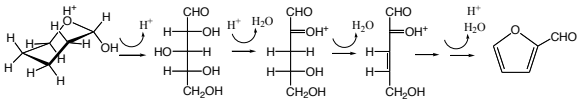

(5)

12 **2** **13** **14** **7**

We have modeled this double dehydration using protonated glycerol as a model system. Figure 2 shows a plot of the calculated potential energy for this reaction. The barrier to loss of the first water molecule from protonated glycerol is 22.4 kcal mol^{-1}. The barrier to the loss of a second water is calculated to be 36.5 kcal mol^{-1}. This second barrier is high because a primary carbocation is formed. In double dehydration of xylose, Rxn. (5), a secondary carbocation is formed. We calculated the second barrier when a methyl group is attached to glycerol to better simulate dehydration in xylose. In this case the barrier is 21.7 kcal mol^{-1} as shown in the figure. Thus the barriers for this double dehydration (22.4 and 21.7 kcal mol^{-1}) are low enough that this reaction could be fast at moderate temperatures.

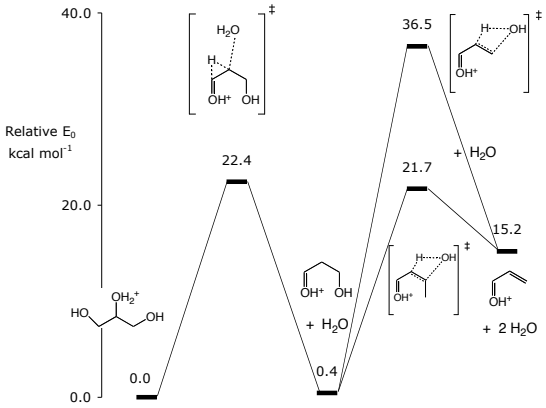

Figure 2. A potential energy plot of the calculated energies for the double dehydration of glycerol (CBS-QB3).

Direct Mechanism

We have calculated the barrier for a model reaction similar to reaction (2). The potential energy for the reaction of a protonated dihydroxy pyran is shown in Figure 3. We find that there is a concerted reaction for loss of water and rearrangement to the furan. The calculated barrier for this reaction is 13 kcal mol^{-1}.

Calculated Rate Constants

The geometries and vibrational frequencies from these calculations can be used to estimate rate constants for the xylose decomposition reactions. These calculated values are used to estimate the entropy change in going from a reactant to a transition state (DS^{+}), which is used to calculate the pre-exponential Arrhenius factor using Transition State Theory (TST).

$$A_{TST} = \left(\frac{kt}{h}\right)\left(\frac{1}{RT}\right)^{(\Delta n)} e^{(1-\Delta n)} \exp(\Delta S^{+}/RT) \qquad (6)$$

Rate constants calculated using Eqn. 6 are collected in Table 1. As can be seen, the rate constants are high at typical pretreatment conditions. The activation energies, $A_{TST,}$ for these mechanisms are consistent with measure global activation energies for xylose decomposition[5]. The table is divided into rate constants for the ring opening mechanism, left, and the direct mechanism, right.

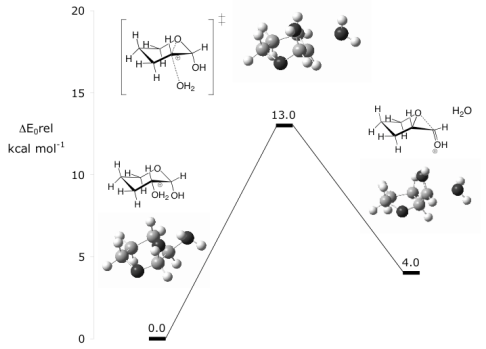

Figure 3. Plot of the potential energy for the direct conversion of a protonated pyran to a furan.

Table 1 Calculated rate constants using TST

	Ring Opening Mech.			Direct
	Ring Opening	1st Dehyd.	2nd Dehyd	Rxn 2
Ea (kcal mol^{-1})	14.3	20.9	21.7	13.0
A_{TST} (s^{-1})	8.2 x 10^{13}	6.3 x 10^{14}	6.3 x 10^{14}	6.3 x 10^{14}
Temp. (^{0}C)	**Calculated TST Rate Constants**			
100	3.4 x 10^{5}	9.1 x 10^{3}	4.6 x 10^{2}	1.5 x 10^{7}
150	3.3 x 10^{6}	2.5 x 10^{5}	1.5 x 10^{2}	1.2 x 10^{8}
200	2.0 x 10^{7}	3.5 x 10^{6}	2.2 x 10^{5}	6.2 x 10^{8}

Conclusions

The rate constants that we obtain for the ring opening mechanism appear to be lower than for the direct mechanism. However, this does not include the dehydration steps such as are shown in Rxn. (3). These reactions should have barriers of about 20 kcal mol^{-1}, which should make the two mechanisms more comparable.

Acknowledgment

We would like to acknowledge The Office of the Biomass Program of the U.S. Department of Energy, who funded portions of this work and the National Center for Supercomputer Applications (NCSA Grant # CHE-980028n) for computer time.

References

1. van Dam, H. E.; Kieboom, A. P. G.; van Bekkum, H. *Starch* **1986**, *38*, 95.
2. Kuster, B. F. M. *Starch*, **1990** *42*, 314
3. Antal, M. J., Jr. ; Leesomboon, T., Mok, W. S.; Richards, G. N. *Carbohydrate Res.* **1991**, *217*, 71.
4. Serianni, A. S.; Pierce, J.; Huang, S-G.; Barker, R. *J. Am. Chem. Soc.* **1982**, *104*, 4037.
5. McKibbins, S. W.; Harris, J. F.; Saeman, J. F. *Forest Prod. J.* **1962**, 17.; van Dam, H. E.; Kieboom, A. P. G.; van Bekkum, H. *Starch*, **1986**, *38*, 95

MECHANISTIC INVESTIGATION INTO THE FORMATION OF POLYCYCLIC AROMATIC HYDROCARBONS FROM THE PYROLYSIS OF TERPENES

Phillip F. Britt, A. C. Buchanan, III, and Clyde V. Owens, Jr.

Chemical Sciences Division
Oak Ridge National Laboratory
P.O. Box 2008, Oak Ridge, TN 37831-6197

Introduction

Currently, there is interest in utilizing renewable energy resources, such as wood and agriculture waste, for power generation, production of liquid fuels, and specialty chemicals as a consequence of the environmental benefits.[1] However, pyrolysis, gasification, and combustion of biomass produces polycyclic aromatic hydrocarbons (PAHs), which are environmental pollutants and soot precursors.[2,3,4,5,6,7] In pyrolysis, PAHs are proposed to be formed by pyrosynthesis, in which radicals undergo a series of bimolecular reactions with alkenes, alkynes, and aromatics to form larger ring structures. The yield of PAHs are found to increase with temperature and gas phase residence times.[8,9] In gasification and combustion, it has been postulated that PAHs arise from pyrolysis reactions in oxygen-deficient regions.[-10] A better fundamental understanding of the initial pyrolysis reactions that occur in the thermochemical processing of biomass, and subsequent reactions of the vapor phase products could provide insight into reducing PAH emissions from biomass combustion, reducing tar formation from gasification, and enhancing production of specialty chemicals from the fast pyrolysis of biomass.

As a consequence of the chemical complexity of biomass and its pyrolysis products, it has been difficult to gain detailed information on the formation pathways of specific products.[11,12] Thus, to gain fundamental kinetic and mechanistic information on product formation in biomass pyrolysis, efforts have focused on the pyrolysis of key chemical constituents found in biomass. In our previous investigations, we have focused on the pyrolysis of plant steroids as potential precursors to PAHs.[13,14] It was shown that the native ring structure of the steroid was maintained to form PAHs, such as phenanthrene and chrysene, and the yield of PAHs was dependent on the steroid structure. PAH yield and ring size were also shown to increase with residence time, temperature, and concentration. In this investigation, the pyrolysis of plant terpenes was investigated at 600-800 °C and at short residence times (≤1 s). This study focused on the pyrolysis of solanesol, squalene, phytol, and β–carotene. These terpenes are

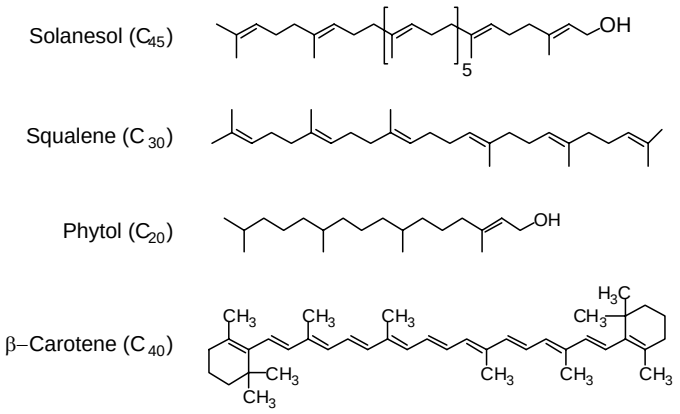

predominately found in the foliage. The yield of PAHs from the pyrolysis of terpenes will be compared to those found from steroids to determine if the alkenes produced from the pyrolysis of terpenes, such as isoprene, enhance the formation of PAHs.

Experimental

The flow pyrolysis reactor used in this study has been previously described.[ ] After the pyrolysis, both cold traps were washed with CS_2, and the washings were combined (total volume 10-20 mL). Solutions of hexatriacontane, phenanthrene-d_{10}, and 1,2-benzanthracene-d_{12} were added as standards, and the reaction mixtures were analyzed by GC-MS and quantitated by GC-FID as previously described. Typical shot to shot reproducibility was ±2% with the exception of the smaller products (<0.1 mol%) in the presence of a large background in which the shot to shot reproducibility wastypically ±5-10%. Products were quantitated by averaging the GC-FID output relative to the internal standards. Response factors were measured with authentic samples or estimated from measured response factors for structurally related compounds and based on carbon number relative to the internal standards (hexatriacontane, phenanthrene-d_{10} or 1,2-benzanthracene-d_{12}). The limits of detection (LOD) for the PAHs depended upon the complexity of the reaction mixture, but the LOD was typically 5-20 $\mu g\ g^{-1}$.

The residence time in the reaction chamber was calculated from the volume of the reactor (1.06 mL or 11.7 mL) in the hot zone, the helium flow rate at room temperature, and a correction for the gas flow rate at the reaction temperature. The reactor was also calibrated by the pyrolysis of phenethyl acetate, whose well-defined first order kinetics allows verification of the reactor temperature and residence time.

Results and Discussion

The flow pyrolysis of solanesol was investigated at high concentration at 700 and 800 °C with residence times of 0.13 and 1.0 s. The yields of selected PAHs are shown in Table 1. One surprising observation was the lack of substantial quantities of 3-ringed or larger PAHs at temperatures less than 800 °C. On the basis of Severson's study,[15] it was expected that solanesol would produce significant quantities of PAHs, since it was concluded that solanesol contributed as much as 40% of the benzopyrenes produced from the pyrolysis of the petroleum ether extract of tobacco. Duplicate pyrolysis runs at 800 °C produced product yields that were ±20-30% of those reported in Table 1 confirming the low yields of PAHs from the pyrolysis of solanesol.

At 600 °C and 0.13 s residence time, dipentene (limonene, *m/z* 136) and isoprene (*m/z* 68) were the dominant products. Small amounts of toluene, *m*-xylene and isomeric products with *m/z* 136 (4 isomers) and 138 (1-methyl-4-(1-methylethyl)cyclohexene and isomer) were also found. At 700 °C with 0.13 s residence time, *m*-xylene, toluene, and isoprene were the dominant products, and only small amounts of dipentene and isomers were found. Small amounts of aromatic products, such as trimethylbenzene, methylisopropenylbenzene, methylindene, and methylnaphthalene, were also formed. A similar product distribution was found in the low concentration (68 mg h^{-1}, $3x10^{-6}$ M), short residence time (0.15 s), flow pyrolysis of solanesol at 700 °C, but the product yields were lower. As the temperature and residence times increased, larger PAHs, such as phenanthrene, were detected. However, four ringed aromatic compounds, such as pyrene and chyrsene, were only found at 800 °C. Increasing the residence time from 1.0 s to 9.0 s at 700 °C significantly increased the yield of PAHs. It appears that solanesol only forms significant quantities of 3-5 ringed aromatics at high temperatures (800 °C) or at long residence times (≥1 sec).

Table 1. Product Yields From the Flow Pyrolysis of Solanesol at High Concentration.

Temperature (°C)	700	700	700	700	800
Contact Time (s)	0.13	0.15	1.0	9.0	1.0
Concentration (μM) [a]	130	3.0	83	130	72
Products (mg/g)					
Benzene	8.50	4.6	23.1	ND	67.6
Toluene	30.2	22.7	47.8	ND	61.3
Styrene	6.70	5.4	12.6	ND	21.5
Indene	2.03	0.16	5.45	ND	12.6
Naphthalene	0.91	0.53	3.67	ND	23.2
2-Methylnaphthalene	1.72	0.91	4.40	ND	13.4
1-Methylnaphthalene	1.07	0.55	2.94	10.8	8.28
Acenaphthylene	0.51	0.00	1.28	2.2	6.47
Fluorene	0.00	0.00	0.77	ND	2.97
Phenanthrene (Phen)	0.00	0.00	0.37	2.7	4.10
Anthracene (An)	0.00	0.00	0.26	0.88	1.90
MethylPhen/An	0.00	0.00	1.30	5.4	6.71
Fluoranthene	0.00	0.00	0.00	0.89	0.71
Pyrene	0.00	0.00	0.00	1.5	1.15
Methylpyrenes	0.00	0.00	0.00	3.5	3.84
Benz[*a*]anthracene	0.00	0.00	0.00	0.42	0.67
Chrysene	0.00	0.00	0.00	0.38	0.61
Benzo[*a*]pyrene	0.00	0.00	0.00	0.42	0.39

[a] Concentration determined by sublimation rate/gas flow rate at the reaction temperature. ND = Not Determined.

It had been previously proposed that the terpene components of tobacco form PAHs by decomposing into isoprene and pyrosynthesis into larger PAHs.[16] Isoprene is the major component of the unsaturated gaseous hydrocarbons present in tobacco smoke[17] and pyrolysis of isoprene at 600–800 °C forms PAHs, including benzo[a]pyrene (2-3 s residence time).[18] Larger PAHs can form from isoprene pyrolysis by concerted Diels–Alder or free radical reactions. Dimerization of isoprene, via Diels–Alder reaction, yields dipentene (also called *p*-mentha-1,8-diene or limonene) and mixtures of dimethylvinylcyclohexenes (see below), but tobacco smoke contains only dipentene and 2,4-dimethyl-4-vinylcyclohexene.[19]

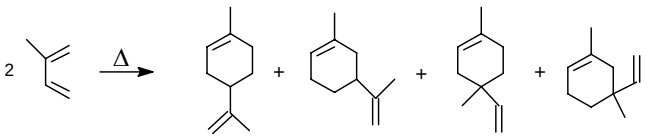

This suggests that free radical pathways form the products in tobacco. The pyrolysis of solanesol has been studied previously (residence time unknown), and it was found that at temperatures up to 550 °C, the hydrocarbon fraction was mainly composed of monoterpenoids with only traces of aromatic hydrocarbons.[20] For example, pyrolysis of solanesol at 500 °C under nitrogen produced pyronenes, dimethyloctadiene, dimethylvinylcyclohexenes,Δ^1-menthene, and dipentene. The major gas phase products were isoprene (64 parts), 2-methyl-2-butene (8 parts), and one part each of 2-methyl-1-butene and 3-methyl-1-butene. Running the pyrolysis in hydrogen altered the product yields confirming that the products were formed by free radical rather than a concerted pathway. At 600 °C, the monocyclic fraction (93 % by weight of the total sample) contained benzene (5 wt%), toluene (30 wt%), xylenes (38 wt%) and C_9 alkylbenzenes (21 wt%). Similar results were found in our study at 600 °C. At temperatures above 650 °C, only aromatic compounds were formed and no terpenes were found.

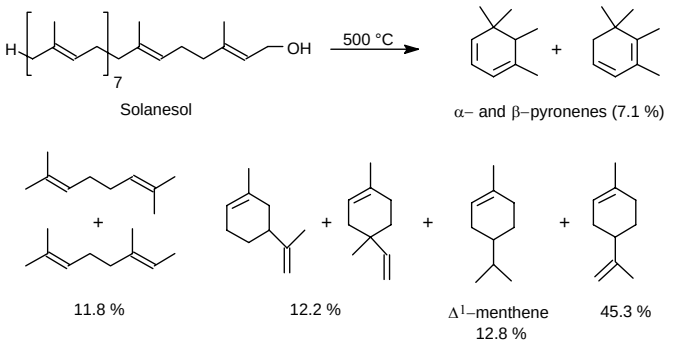

The pyrolysis of dipentene (limonene) has been studied at 450 °C over copper pellets (residence time unknown).[21] The dominant products were pyronenes, other alkylcyclohexadienes, and a small amount (9%) of aromatic hydrocarbons. It was proposed that limonene decomposed by a biradical mechanism in which radicals from C–C homolysis of the bisallylic bond underwent disproportionation to form a triene that can isomerize (1,5-hydrogen shift) and undergo electrocyclic ring closure to form the pyronenes and 1,3-dimethyl-1-ethyl-3,5-cyclohexadiene (not shown). Independent pyrolysis of the pyronenes at 450 °C gave a similar distribution of aromatic hydrocarbons.

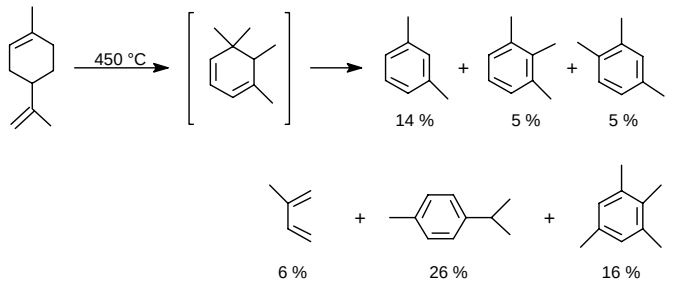

Thus, on the basis of the literature evidence, it is proposed that solanesol decomposes directly to isoprene and dipentene, as the major products, and alkylcyclohexenes by a free radical pathway. Depending on the reaction severity (residence time and temperature), these initial products can undergo additional free radical reactions to form alkyl-substituted monocyclic aromatic hydrocarbons, and larger PAHs. A potential mechanism for dipentene formation by a free radical pathway is shown in Figure 1a. The TG-MS of solanesol showed a significant loss of water at relatively low temperatures (i.e., 360 °C). Therefore, water can be eliminated by a concerted 1,4-elimination to form a terminal diene. Homolysis of the bisallylic C–C bond forms an isopropenyl radical (C_5H_7•) that can hydrogen abstract from solanesol to give isoprene. The allylic radical can undergo an intramolecular 1,6-cyclization reaction competitively with β–scission. As previously reported, the ratio of intramolecular radical addition to β–scission for 1-hex-5-enyl radical is 124 at650 °C and 39 at 750 °C, which indicates that cyclization should dominate.[22] After cyclization, β–scission of the tertiary radical forms dipentene and a radical that can continue the

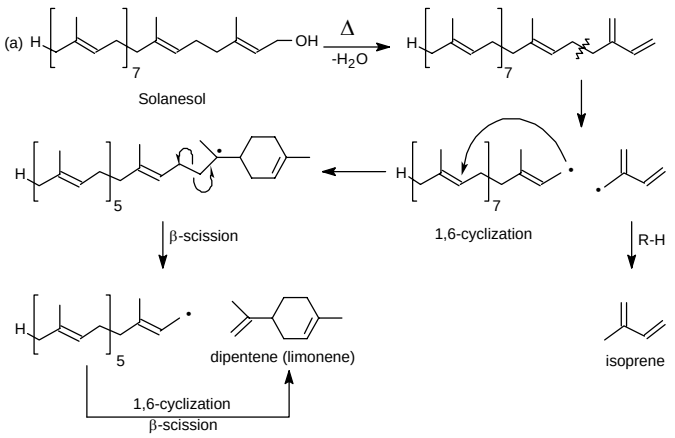

Figure 1a. Mechanism for the formation of dipentene and isoprene from solanesol.

unzipping process. Hydrogen abstraction from solanesol at the allylic site between the double bonds also forms an intermediate that can undergo 1,6-cyclization to form dipentene. Hydrogen abstraction from the methyl group (Figure 1b) followed by 1,6-cyclizations and β–scission forms 2,4-dimethyl-4-vinylcyclohexene (which is found in tobacco smoke).

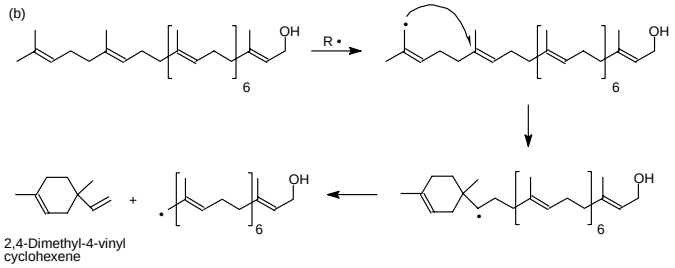

Figure 1b. Formation of 2,4-dimethyl-4-vinylcyclohexene from the decomposition of solanesol.

Larger PAHs must arise from reaction of the monocyclic aromatic hydrocarbons with the low molecular weight unsaturated products, such as isoprene. In the combustion of 1,3-butadiene in a sooting flame (i.e., fuel rich flame), it was concluded that monocyclic PAHs were made by free radical pathways involving C_4H_5• as the dominant species. The Diels–Alder reaction of butadiene was too slow and concentration of the reagents too low, to account for the PAHs formed in the flame.[23] In the pyrolysis of solanesol, larger PAHs are most likely formed by a similar pathway with aromatic and benzylic radicals adding to unsaturated products, such as isoprene, in the hot zone of the furnace (i.e., pyrosynthesis). However, the specific reaction pathway from the primary products (i.e., isoprene and dipentene) to the large PAHs are only implied and are not specifically known. Solanesol and other terpenes could also enhance PAH yields from pyrolysis of other substrates by providing hydrocarbons (i.e., isoprene) for pyrosynthesis. For example, in the pyrolysis of cellulose, replacing the nitrogen carrier gas with propene increased the yield of benzo[a]pyrene 1.9 fold at 350-450 °C and 6.9 fold at 450-550 °C even though the propene did not produce benzo[a]pyrene at temperatures >550 °C.[24]

Preliminary results on the yield of PAHs produced from the pyrolysis of solanesol, β–carotene, squalene, and stigmasterol (a plant steroid) at 800 °C with a residence time of 1.0 s is shown in Figure 2. In general, the steroid produces more PAHs than the terrpenes, especially phenanthrene, anthracene, benz[a]anthracene, and chrysene which can be derived from dehydrogenation, dealkylation, and rearrangement of the steroid. Surprisingly, squalene produces fewer PAHs than solanesol. The prolysis of β–carotene and squalene is currently being investigated at 700 and 600 °C with a residence time of 1.0 s and 0.13 s. These results will be discussed in the oral presentation.

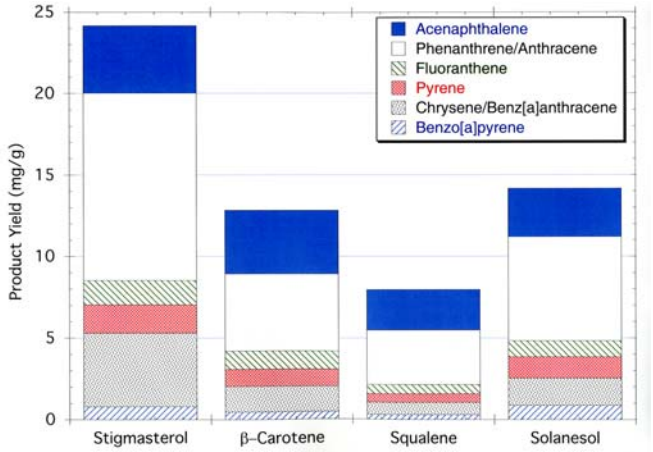

Figure 2. PAH yields from the pyrolysis of terpenes at 800 °C in helium with a residence time of 1.0 s.

Conclusions

In this investigation, terpenes were found to produce three, four, and fived-ringed aromatic hydrocarbons at high temperatures and at short residence times. At long residence times, the yield of larger PAHs, such as benz[a]anthracene and benzo[a]pyrene, increase more than the yield of smaller PAHs, such as phenanthrene and fluoranthene. Although terpenes produce fewer PAHs than steroids (stigmasterol), terpenes produce large yields of low molecular weight products such as isoprene, toluene and xylenes. Under short residence time conditions, it does not appear that the low molecular hydrocarbons enhance the pyrosynthesis of PAHs.

Acknowledgement. This research was supported by Philip Morris USA. Additional support was provided by the Division of Chemical Sciences, Geosciences and Biosciences, Office of Basic Energy Sciences, U.S. Department of Energy, under contract DE-AC05-00OR22725 with Oak Ridge National Laboratory, managed and operated by UT-Battelle, LLC. CVO was supported by an appointment to ORNL Postdoctoral Research Program administered jointly by Oak Ridge Institute for Science and Education and ORNL.

References

(1) *Developments in Thermochemical Biomass Conversion*; Bridgwater, A. V., Boocock, D. G. B., Eds.; London: Blackie Academic, 1997 and references therein.
(2) Mastral, A. M.; Callén, M. S. *Environ. Sci. Technol.* **2000**, *34,* 3051.
(3) Elliott, D. C. In *Pyrolysis Oils From Biomass*; Doltes, E. J., Milne, T. A., Eds.; ACS Symposium Series 376, Washington, DC: American Chemical Society, 1988, pp 55.
(4) *Fundamentals of Thermochemical Biomass Conversion*; Overend, R. P.; Milne, T. A.; Mudge, L. K., Eds.; London: Elsevier Applied Science, 1985 and references therein.
(5) Khalfi, A.; Trouvé, G.; Delobel, R.; Delfosse, L. *J. Anal. Appl. Pyrolysis* **2000**, *56,* 243.
(6) Brage, C.; Yu, Q.; Sjöström, K. *Fuel* **1996**, *75,* 213.
(7) Homann, K. -H. *Angew. Chem. Int. Ed.* **1998**, *37,* 2434.

(8) Richter, H.; Howard, J. B. *Prog. Energy Combust. Sci.* **2000**, *26,* 565 and references therein.
(9) Marinov, N. M.; Pitz, W. J.; Westbrook, C. K.; Vincitore, A. M.; Castaldi, M. J.; Senkan, S. M.; Melius, C. F. *Combust. Flame* **1998**, *114*, 192.
(10) Marsh, N. D.; Zhu, D.; Wornat, M. J. *Proceedings of the Combustion Institute* **1998**, *27,* 1897.
(11) Antal, M. J., Jr. In *Biomass Pyrolysis: A Review of the Literature Part II-Lignocellulose Pyrolysis.;* Beor, K. W.; Duffie, J. A., Eds.; Advances in Solar Energy, New York; ASES Publications; 1982, p. 61 and references therein.
(12) Antal, M. J., Jr. In *Biomass Pyrolysis: A Review of the Literature Part I-Carbohydrate Pyrolysis*; Beor, K. W., Duffie, J. A., Eds.; Advances in Solar Energy, New York; ASES Publications; 1985; p. 175 and references therein.
(13) Britt, P. F.; Buchanan, A. C., III, Kidder, M. K.; Owens, C.; Ammann, J. R.; Skeen, J. T.; Luo, L. *Fuel* **2001**, *80*, 1727.
(14) Britt, P. F.; Buchanan, A. C., III; Kidder, M. K.; Owens, C. V., Jr. *J. Anal. Appl. Pyrolysis* **2003**, *66*, 71.
(15) Severson R. F.; Schlotzhauer, W. S.; Chortyk, O. T.; Arrendale, R. F.; Snook, M. E. In *Polynuclear Aromatic Hydrocarbons*; Jones, P. W., Leber P. Eds.; Ann Arbor, MI Ann Arbor Science, 1979, p 277.
(16) Gil-Av E.; Shabtai, J. *Nature* **1963**, *197*, 1065.
(17) Vilcins, G. *Beitr. Tabakforschung* **1975**, *8*, 181.
(18) Oró, J.; Han, J.; Zlatkis, A. *Anal. Chem.* **1967**, *39*, 27.
(19) Stedman R. L. *Chem. Rev.* **1968**, *68*,153.
(20) Grossman, J. D.; Ikeda, R. M.; Deszyck, E. J.; Bavley, A. *Nature* **1963**, *199*, 661.
(21) Pines, H.; Ryer, J. *J. Am. Chem. Soc.* **1955**, *77*, 4370.
(22) (a) Handford-Styring, S. M.; Walker, R. W. *J. Chem. Soc., Faraday Trans.* **1995**, *91*, 1431. The rate expression for β–scission to form ethylene and 1-but-3-enyl radical is log $k(s^{-1})$ = 13.0 – 29.9/θ, while intramolecular cyclization has a rate expression of log$k(s^{-1})$ = 10.0 – 8.4/θ. (b) For a cyclic system, the rate expression for the intramolecular cyclization of the 2-allylbenzyl radical is log$k$ (s^{-1}) = 11.14 –16.28/θ. Franz J. A.; Alnajjar, M. S.; Barrows, R. D.; Kaisaki D. L.; Camaioni, D. M.; Suleman, N. K. *J. Org. Chem.* **1986**, *51*, 1446.
(23) Cole, J. A.; Bittner, J. D.; Longwell, J. P.; Howard, J. B. *Combust. Flame* **1984**, *56,* 51.
(24) Robb, E. W.; Johnson, W. R.; Westbrook, J. J.; Seligman, R. B. *Beitr. Tabakforschung* **1966**, *3*, 597.

NOVEL CARBON NANOFORMS FROM DISCOTIC LIQUID CRYSTALS

[1] *Kengqing Jian,* [1]*Christopher Chan,* [1]*Matthew Sousa,* [1] *Yuming Gao,* [2] *Nancy Yang,* [3]*Michael Paukshto,* [1]*Gregory Crawford,* [1] *Robert Hurt*

[1] Brown University, Providence, RI
[2] Sandia National Laboratories, Livermore CA
[3] Optiva, Inc., South San Francisco

Introduction

Much of the excitement surrounding new carbon nanomaterials can be traced to their *directional* properties, which arise through precise orientation of the graphene layers [1-3]. A long term goal in nanocarbon synthesis is to develop techniques for systematic control of graphene layer arrangement in order to produce nanomaterials with crystal structures tailored for specific applications. A new and general method has been developed for achieving molecular control in carbon materials based on non-covalent assembly of polyaromatics [4-7]. Some polyaromatic liquids form liquid crystalline phases that adopt defined molecular order modes near surfaces (surface anchoring states [5] and in confined nanospaces [6]. Discotic liquid crystals were employed in combination with various inorganic templates to produce "orthogonal-symmetry" nanofibers [6] (see Fig. 1) and nanoporous carbons with graphene edge-rich inner surfaces [7] by this principle. These carbon materials exhibit crystal structures that reflect the original supramolecular assemblies, which can be covalently captured by heating.

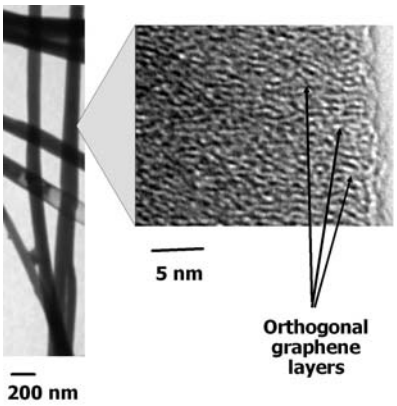

Figure 1. Orthogonal carbon nanofibers from discotic naphthalene polymer (AR mesophase).

In this paper we demonstrate the extension of this technique for producing novel hollow forms through solvent processing. Infiltration of polyaromatic solutions into nanochannel alumina followed by solvent evaporation coats thin organic films on the inner wall surfaces that can be covalently captured in the form of sp^2-hybridized carbon structures. Here our goal is to use nanochannels not only to dictate overall nanomaterial shape by the negative replica concept, but also to direct the molecular structure of the material through polyaromatic/alumina surface interactions.

Experimental

Two carbon precursors, (a) the solutions of naphthalene polymer (AR mesophase, HP grade from Mitsubishi Gas Chemical) in strong aromatic solvents, pyrindene and quinoline, and (b) indanthrone disulfonate (ammonium salt) aqueous solutions, were utilized in the experiment. In indanthrone disulfonate solutions, face-to-face stacking of the amphiphilic discotic molecules is extensive, leading to rod-like aggregates of ~ 1.5 nm in diameter and about 300 nm in length [8]. At high concentrations these solutions form lyotropic liquid crystalline phases in which the rod-like aggregates align by self exclusion and electrostatic repulsion [8].

Carbon nanoforms were produced by capillary infiltration of precursor solutions into nanochannel alumina followed by overnight drying and slow heating (4 °C/min) to 700 °C for 4 hours. The 700 °C treatment converts the organic nanotubes into monodisperse carbon tubes of 100 nm radius and 60 μm length, which form free standing ordered arrays upon removal of the alumina template by NaOH etching (see Fig. 2A). The resulting nanomaterials were then washed thoroughly and dried. SEM (scanning electron microscopy), TEM (transmission electron microscopy), and HRTEM (high-resolution TEM) were applied for morphology and structural analysis.

Results and discussion

Figures 2 shows the SEM images of carbon nanotubes and ribbons produced from indanthrone disulfonate. Using 12 wt-% indanthrone disulfonate solutions, the tubes show a cellular structure with hollow cavities separated by internal membranes (see Fig. 2A). This "bamboo" structure can be suppressed almost entirely by reducing solvent concentration from 12% to 2% to produce primarily hollow tubes with corresponding thinner walls (see Fig 3A).

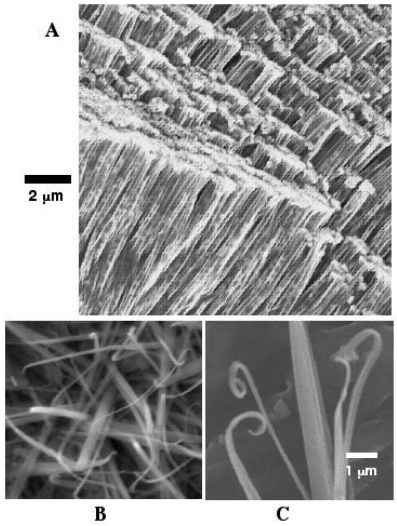

Figure 2. Carbon nanotube array (A) and dispersed nanoribbons (B, C) formed by capillary infiltration of indanthrone disulfonate solutions.

Dipping the filled nanochannel membrane in 10 wt% $BaCl_2$ solutions prior to drying and carbonization leads not to tubes but to nanoribbons — continuous carbon strips of 60 μm in length, 200 nm in width with rectangular cross section (Fig. 2 B,C). The divalent barium ion cross-links the negatively charged aggregates and reduces the solubility of the rod-like aggregates leading to

early precipitation *within* the nanochannels rather than deposition on wall surfaces.

High resolution fringe images (see Fig. 3) reveal a unique crystallography in these thin-walled carbon nanotubes, in which the graphene layers orient *perpendicular* to the tube axis. These meandering graphene layers are typical for a low-temperature carbon derived from a liquid crystal precursor [3, 6], and reflect the structure of the liquid crystalline phase at the point of solidification. The key feature in Fig. 3 is the uniform perpendicular alignment, which establishes the unique crystal orientation of this nanomaterial. Heat treatment of these phases can coalesce the layers and produce longer and straighter fringes, but does not alter the basic crystal symmetry set in the low-temperature carbon material [3].

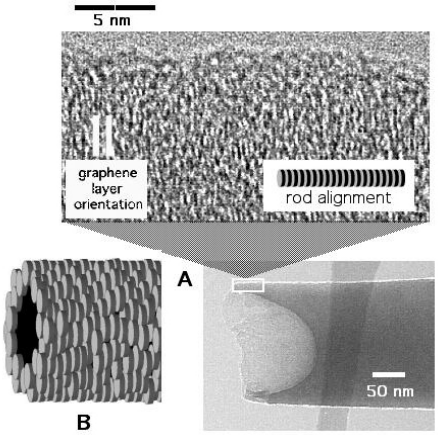

Figure 3. High-resolution TEM image of carbon nanotubes made from indanthrone-disulfonate. (Molecular disk size is B exaggerated for visibility).

We believe this unique crystal structure is formed by orientational ordering of the rod-like supramolecule aggregates driven by configurational entropy as the rods concentrate in the curved thin liquid films that coat the inner nanochannel walls. The dried solid film is then covalently captured by thermal polymerization with accurate translation of the molecular order into an arrangement of linked graphene layers.

Figure 4 shows the results for the other polyaromatic precursor---naphthalene polymer. The cylindrical carbon nanofoams have a similar graphene layer arrangement to the indanthrone-derived tubes, which shows a strong preferential alignment *perpendicular* to the tube axis. It is remarkable that both precursors give this unusual structure, which suggests some general principle in polyaromatic assembly. In fact the same basic perpendicular symmetry is observed when AR naphthalene polymer is melt processed in nanochannel alumina into fully dense fibers [6]. We believe that the driving force for assembly of these structures is the preservation of internal π-bonds, which are the strongest non-covalent interactions among large polyaromatics [3]. The molecular structure shown in Fig. 4 (massive axial π-stacked columns) achieves the maximum extent of internal π-bonding by exposing only graphene edges at the outer and inner wall surfaces. Further, the axial orientation of the columns avoids nanoscale curvature in the tangential direction. By this mechanism, large planar polyaromatic precursors provide a natural route to new carbon forms with edge-rich surfaces, provided that the supramolecular order can be captured upon heating.

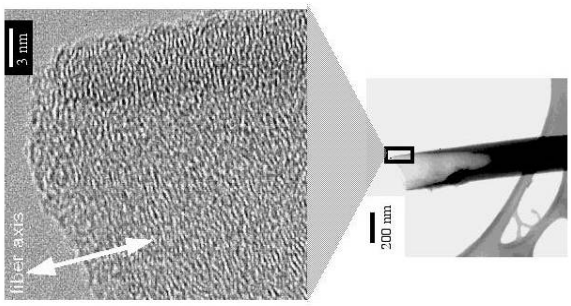

Figure 4. Perpendicular graphene layer arrangement in carbon nanotubes made from high-concentration solutions of naphthalene polymer in pyridine.

Conclusions

Polyaromatic solution processing can produce a unique set of cylindrical carbon nanoforms (tubes, ribbons) depending on synthesis conditions. The tubes and foams are crystallographically inverted and thus quite distinct from "conventional" carbon nanotube structures [1,9,10]. They exhibit graphene edge planes at both inner and outer surfaces and are interesting for a variety of applications where high-activity surfaces or access to interlayer spaces are advantageous.

Acknowledgements. This work was supported by the National Science Foundation through a Nanoscale Interdisciplinary Research Team (NIRT) Grant, CMS-0304246.

References

(1) Harris, P.J.F. Carbon Nanotubes and Related Structures, Cambridge University Press: Cambridge, **2001**.
(2) Ajayan, P.M. Ch. 8 in *Handbook of Nanostructured Materials and Nanotechnology, Vol 5: Organics, Polymers, and Biological Materials* (H.S. Nalwa Ed.) Academic Press, N.Y. **2000**.
(3) Hurt, R.H.; Chen, Z-Y. *Physics Today*, **2000**, 53(3), 39.
(4) Hurt, R.H.; Krammer, G.; Crawford, G.; Jian, K.; Rulison, C.; *Chem. Mater*, **2002**, 14, 4558.
(5) Jian, K.; Shim, H.S.; Tuhus-Dubrov, D.; Woodward, C.; Bernstein, S.; Pfeffer, M.; Steingart, D.; Sachsmann, S.; Gournay, T.; Crawford, G.P.; Hurt, R.H. *Carbon*, **2003**, 41 (11), 2073.
(6) Jian, K., Shim, H.-S., Schwartzman, A., Crawford, G.P., Hurt, R.H., *Adv. Mater.*, **2003**, 15 (2), 164-167.
(7) Yang, N.Y.C.; Jian, K.; Kulaots, I.; Crawford, G.P.; Hurt, R.H; *J. Nanosci. Nanotech* **2003**, 3 (5), 386.
(8) Dembo A. *Mol. Mater.*, **2001,** 14, 275.
(9) Iijima, S. *Nature*, **1991,** 354, 56.
(10) Kyotani, T.; Tsai, L.; Tomita, A. *Chem. Mater.*, **1995**, 7, 1427.

LARGE-SCALE SYNTHESIS OF HIGH-QUALITY DOUBLE-WALLED CARBON NANOTUBES FROM COAL-BASED CARBON RODS IN VACUUM BY ARC DISCHARGE

Jieshan Qiu[a],Yongfeng Li[a], Yunpeng Wang[a], Fayu Wu[b], Huiming Cheng[b], Guobin Zheng[c] and Yasuo Uchiyama[c]*

[a] Carbon Research Laboratory, School of Chemical Engineering, Center for Nano Materials and Science, Dalian University of Technology, 158 Zhongshan Road, P.O .Box 49, Dalian 116012, China. E-mail: **jqiu@dlut.edu.cn**; Fax: +86-411-8363-3080

[b] Shenyang National Labratory for Materials Science, Institute of Metal Research, CAS, Shenyang 110016, China.

[c] Department of Materials Science and Engineering, Nagasaki University, 1-14 Bunkyo-machi, Nagasaki 852-8521, Japan

Introduction

Since the first report about the preparation of double-walled carbon nanotubes (DWNTs) [1], great efforts have been made to their synthesis. The driving force behind this is because DWNTs consist of two concentric cylindrical graphene layers, which endows the DWNTs with some novel physical properties that are not found in other types of carbon nanotubes. For example, DWNTs can offer excellent field emission properties, which have low threshold voltage for electron emission like SWNTs and high durability similar to MWNTs. Up to now, several methods have been developed to synthesize DWNTs, which includes stable arc discharge,[2-4] pulsed arc discharge,[5] coalescence of C_{60} and catalytic chemical vapor deposition (CCVD).[6-11] Though some progresses have been made in the synthesis of DWNTs, it is still difficult to obtain pure DWNTs (without other forms of carbon materials such as the presence of SWNTs), and the production of cheap DWNTs in large quantity is still a challenge. Of those available techniques, the arc discharge is simple, cheap and easy to operate, and has some advanctages in production of DWNTs with high purity.

Here we report that it is possible to synthesize high-quality DWNTs in large quantity from coal-based carbon rods with Fe as catalyst by arc discharge in vacuum. Unlike the reported conventional arc techniques for synthesis of DWNTs, [2-4] our approach does not need buffer gas that is indispensable in conventional arc discharge.

Experimental

Carbon rods prepared from coal and iron powders was used as the anode in the arcing experiments. To make the carbon rods, the coal powder (*ca.* 150 μm) was first finely mixed with binder (coal tar) and iron powder (*ca.* 120 μm) in a weight ratio of 30% and 5%, respectively. The mixed paste was subsequently pressed at about 10-20 MPa to form composite coal rods. The coal rods were then put into an electric furnace and carbonized in flowing Argon to make composite carbon rods with a diameter of *ca.* 10 mm. The composite carbon rods were used as the anode in arc discharge, while a high purity graphite rod with a diameter of 16mm was made as the cathode. Before arcing, a wire cage was put inside the reactor for direct collecting the as-formed DWNTs, of which the detailed information can be found elesewhere.[12] The arc-discharge was conducted with a DC of 60-70 A and a voltage of 40-50V in low vacuum (only 0.001~0.01Pa of air). The typical arcing experiment normally lasted for about 5~7 min. After arc discharge, the wire cage was taken out, of which the surface was covered with web-like deposits that were directly peeled off and examined by scanning electron microscopy (SEM, JSM-5600LV), transmission electron microscopy (TEM, JEOL 2010) and Raman spectroscopy (Jobin Yvon LabRam HR 800, excited by 623.8 nm laser).

Results and Discussion

Figure 1 shows macroscopic web-like DWNTs deposited on the wire cage. The repeated experiments show that for the vacuum approach with iron-containing coal-based carbon rods as starting carbon source, the production rate of DWNTs varies in arange of 20~25 mg/min.

Figure 1. Macroscopic image of web-like DWNTs, formed on the wire cage by vacuum arc discharge.

Typical SEM images of DWNTs peeled off from the wire cage are shown in Figure 2. The SEM results indicate that most of products appear in a uniform film-like morphology, as can be seen in Figure 2a, or in well-aligned thread-like morphology, as shown in Figure 2b, which is quite similar to the morphology of film-like SWNTs.[12] But the DWNTs film is less sticky compared with the SWNTs films.

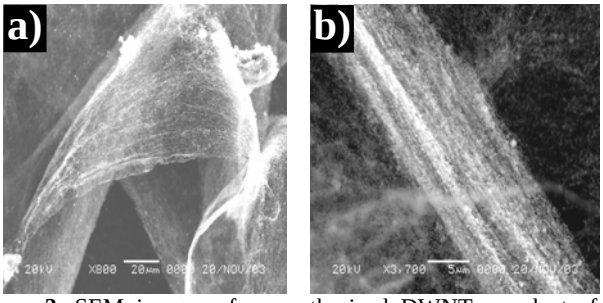

Figure 2. SEM images of as-synthesized DWNTs products from coal-based carbon rods under vacuum arcing conditions, (a) film-like DWNTs, (b) aligned thread-like DWNTs.

The as-synthesized DWNTs samples were further examined by TEM, which confirms that DWNTs dominate in the products with the content being over 95%, and only a few SWNTs are present, no MWNTs is found. This significantly differs from the DWNTs prepared by traditional arc discharge or CCVD methods, of which only about 90% are DWNTs even under the optimum preparation conditions. Figure 3a shows some isolated DWNTs and most of them have a smooth surface and average outer diameter of 4-5 nm. A typical DWNTs bundle usually consists of 4 to 10 individual nanotubes, as can be seen in Figure 3b. Figure 3c is a high-magnification TEM image, showing two double-walled nanotubes with the interlayer spacing being *ca.* 0.40nm in the section as the arrows indicates. Figure 3d shows a DWNTs bundle consisting of 4 DWNTs, of which the average outer diameter is *ca.* 4.2 nm. It should be noted that the DWNTs in bundles seem to have a smaller diameter than those isolated DWNTs.

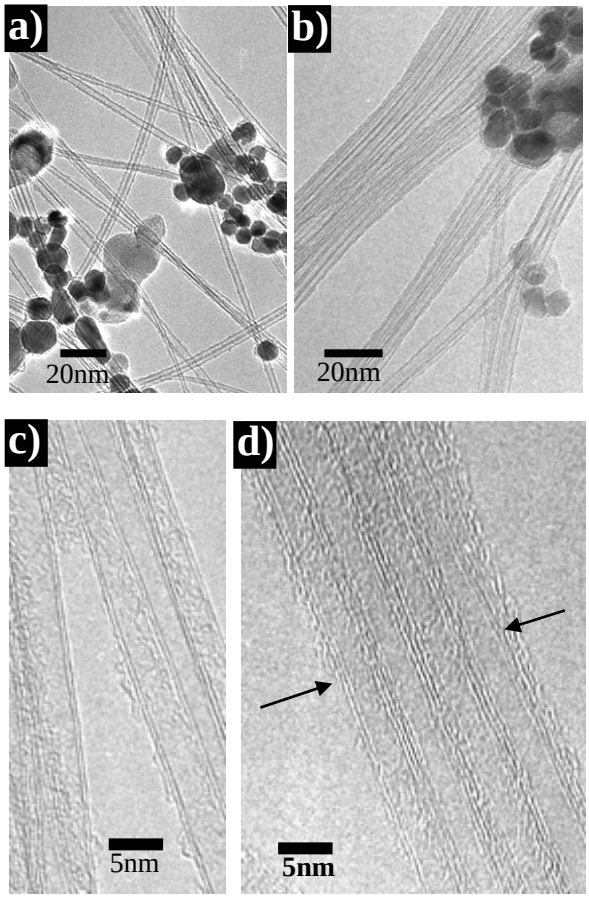

Figure 3. TEM images of DWNTs obtained from coal-based carbon rods with Fe as catalyst under vacuum arcing conditions, (a) and (b), low magnified images, showing some isolated and bundle-like DWNTs, (c) two isolated DWNTs and (d) four DWNTs joining together to form a bundle.

Raman spectroscopy was also used to characterize the obtained DWNTs, which yields some information about the diameter of as-prepared DWNTs. It is necessary to mention that carbon nanotubes with a diameter over 3 nm exhibit a weak Raman signal, and their radial breathing mode (RMB) band is difficult to detect.[2,8] The HRTEM studies discussed above reveal that most of the DWNTs have an average diameter around 4.0-5.0nm, here the diameter distribution calculated according to Raman shift only represents those DWNTs with a diameter less than 3 nm. A typical DWNTs Raman spectrum in the range of 0-2000 cm^{-1} is shown in Figure 4, and the inset is the RMB in the low frequency range of 50-300cm^{-1}. In the Raman spectroscopy, a weak D-band at 1325.6 cm^{-1} and a strong G-band at 1584.5cm^{-1} can be seen. The weak D-band means that the DWNTs products is high-purity nanotube material, while the high value of G/D imply that the content of the disordered or defective graphitic structure in the DWNTs nanotubes is low, which is consistent with the SEM and TEM observation. The diameter of DWNTs is calculated by the well-known expression $\omega_r = 238/d^{0.93}$, where d is diameter of tubes in nm and ω_r is the frequency of RMB in cm^{-1}. [13] The peak positions between 101.8 and 219.6cm^{-1} correspond to the presence of carbon nanotubes with diameter between 2.49 and 1.09 nm. The two pair peaks at position of 131.9 and 219.6cm^{-1} reveal that some DWNTs have outer diameter of 1.89nm and inner diameter of 1.09nm.

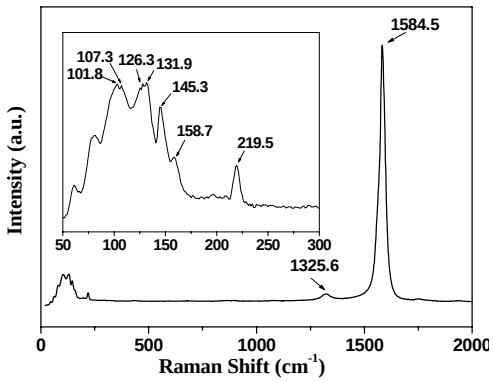

Figure 4. Raman spectra of DWNTs synthesized from coal-based carbon rods under vacuum arcing conditions, the inset showing RMB band of DWNTs below 300 cm^{-1}

In summary, a large amount of DWNTs with high quality have been successfully synthesized from coal-based carbon rods by arc discharge under vacuum conditions. Most of DWNTs have an outer diameter of 4-5 nm and a small amount of them have a diameter less than 2 nm. Our results demonstrate for the first time that it is possible to prepare high quality DWNTs with a diameter of 4.0-5.0 nm from coal-based carbon rods without any inert buffer gas, this approach may become an favorable option for making high quality DWNTs with bigger diameters.

Acknowledgment. This work was partly supported by the National Science Foundation of China (No. 29976006, 20376011), the Natural Science Foundation of Liaoning Province (No. 9810300701, 2001101003), the National Basic Research Program of China (Grant No. G2003CB615806) and the Ministry of Education of China.

References

(1) Hutchison J.L.; Kiselev N.A.; Krinichnaya E.P.; et al. *Carbon*, 2001, 39, 761.
(2) Saito Y.; Nakahira T; and Uemura S. *J. Phys. Chem. B*, 2003, 107, 931.
(3) Huang H.; Kajiura H.; Tsutsui S.; et al. *J. Phys. Chem. B*, 2003, 107, 8794.
(4) Sugai T.; Yoshida H.; Shimada T.; Okazaki T.; Shinohara H.; *Nano Lett.,* 2003, 3, 769.
(5) Colomer J.F.; Henrard L.; Flahaut E.; Tendeloo G.Van; Lucas A.A.; Lambin Ph.; *Nano Lett.,* 2003, 3, 685.
(6) S. Bandow, M. Takizawa, K.Hirahara, M.Yudasaka and S. Iijima, *Chem. Phys. Lett.*, 2001, 337, 48.
(7) Ren W.; Li F.; Bai S.; Cheng H.M.; *Chem. Phys. Lett.*, 2002, 359, 196.
(8) Ci L.; Rao Z.; Zhou Z.; Tang D.; Yan X.; Liang Y.; Liu D.; et al. *Chem. Phys. Lett.*, 2002, 359, 63.
(9) Lyu S.C.; Lee T.J.; Yang C.Y.; Lee C.J.; *Chem. Comm*, 2003, 1404.
(10) Flahaut E.; Bacsa R.; Peigney A.; Laurent Ch.; *Chem. Comm*, 2003, 1442.
(11) Qiu J.S.; Li Y.F.; Wang Y.P.; Wang T.H.; Zhao Z.B.; Zhou Y.; Li F.; Cheng H.M.; *Carbon*, 2003, 41, 2159.
(12) Ci L.; Zhou Z.; Yan X.; Liu D.; Yuan H.; et al. *J. Phys. Chem. B*, 2003, 107, 8760.

COAL-DERIVED HOLLOW CARBON CAPSULES WITH INNER DIAMETER OVER 40 NANOMETERS: GIANT MULTISHELL FULLERENES?

Jieshan Qiu, Yongfeng Li, Xiuna Wang, Zongbin Zhao

Carbon Research Laboratory, Center for Nano Materials and Science, State Key Laboratory of Fine Chemicals, Dalian University of Technology, 158 Zhongshan Road, P.O .Box 49, Dalian 116012, China. E-mail: jqiu@dlut.edu.cn

Introduction

After the macroscopic preparation of fullerenes (C_{60}) in 1990,[1] a number of nano-sized novel carbon materials including nanotubes(CNTs), carbon onions, carbon horns, multishell fullerenes, graphite polyhedral crystals, tubular graphite cones and other nano-sized carbon particles [2-10] have been found. The morphology and properties of these novel carbon nanomaterials are closely related to the techniques and the carbon precursors used. One of the techniques widely used is the arc discharge method, in which high purity graphite or composite graphite electrodes are normally used as carbon precursor. However, when coal, one of the cheapest carbon sources in nature, is used instead of expensive graphite, various forms of carbon nanomaterials such as fullerenes, multi-walled CNTs and single-walled CNTs can also be prepared. [11-18] It is believed that the unique chemical structure of coal and coal-based carbons plays a key role in the formation of various novel carbon nanomaterials. Here we report the synthesis of a novel form of carbon capsules with a nano-sized hollow central cavity by arc discharging coal-based iron-containing carbons. The size distribution of these hollow carbon capsules (thereafter called HCCs) is quite uniform with outer diameters around 50-70nm and inner diameters around 40nm.

Experimental

The conventional DC arc-discharge method was used to prepare giant hollow carbon capsules (HCCs) with the coal-derived carbon rods as the anode. The coal sample used is an anthracite coal, and its proximate and ultimate analyses can be found elsewhere.[17] The coal-derived carbon rods were prepared according to the following procedure. The coal powder (less than 150μm) was mixed with coal tar in a weight ratio of 20% and then pressed in a mold to form coal tubes (10 mm o.d., 5mm i.d. and 120mm in length). Then, the coal tubes were put into an electric furnace and heated at a heating rate of 10 ^{o}C/min till 900 ^{o}C in flowing N_2. The tubes were kept at 900^{o}C for 4 h before being cooled back to room temperature to get carbon tubes. Some tubes were crushed to make char powders (less than 150μm) which were mixed with iron powders (less than 150μm) in a weight ratio of 50:50. The mixture was packed into the carbon tubes, of which both ends were sealed with graphite plugs. The coal-based carbon rods were subjected to electrical arcing, which was conducted in He with an initial pressure of 0.065MPa. The arc was generated between the coal-derived anode and a graphite cathode (16 mm in diameter) with a current of 50-70A and a voltage of 30-50V. The arcing experiments normally lasted about 20 min. After the arc-discharge was finished, three types of products were collected in different parts inside the arc-reactor chamber: fullerenes-containing soot deposited on the inner walls; hard and gray deposits on the tip of cathode and fiber-like black deposit on the periphery of the end of coal-based anode. All these three types of the products were examined by TEM (JEM-2000EX, operated at 100kV). The samples were sonicated in ethanol for 5 min before being dropped onto a copper grid for TEM examination. It is in the fiber-like black deposits on the periphery of the end of coal-based anode that the HCCs was found.

Results and Discussion

The typical TEM images of HCCs are shown in Figure 1, from which bamboo-shaped CNTs (as shown in Fig. 1a) and normal multi-walled CNTs (as shown in Fig. 1b) can also be seen occasionally. This means that the HCCs are formed spontaneously with CNTs, and this leads one to believe that they might be an intermediate product between small carbon molecules (fullerenes) and giant carbon molecules such as the bamboo-shaped CNTs shown in Fig. 1a. Some of the HCCs have a perfect ball-like shape or core–shell morphology as shown in Fig. 1c and some have, to some degree, a distorted or elongated ring-like shape, which may be due to the fluctuations of the concentrations of the active carbon particles that were released from coal-based carbon rods by arcing discharge and directly incorporated into the HCCs. It is interesting to note that there is a similarity between the conical caps of the hollow compartments in the bamboo-shaped nanotube and the hollow carbon capsules (HCCs), which can be easily visualized that if one of the HCCs were cut into two halves, one half would make a rather perfect cone-shaped cap of the hollow compartment in the bamboo-shaped nanotube, as shown by arrows in Fig. 1a. This analogy leads one to believe that both the HCCs and the bamboo-shaped carbon tubes start to grow from the same precursors. It is known that small fullerenes molecules can coalesce to form larger ones. For example, Mochida et al[19] has shown that heat treatment of C_{60} at high temperature (up to 2400 ^{o}C) resulted in the formation of fullerene-like nanoparticles with diameters in a range 5~15nm. With these in mind, the observations discussed above could also lead one to speculate that at the high temperature (~3000^{o}C) of the arc plasma, the HCCs might be the intermediate species in the growth process of the bamboo-shaped nanotubes.

On average, these novel HCCs have an outer diameter around 50-70nm and an inner diameter around 40-50nm. It is estimated that for these HCCs, the volume ratio of the inner space to the whole particle is about 30-52%, which is far greater than 1% for the conventional polyhedral carbon particles described in literature. [4] It is interesting to note that similar to C_{60}-type fullerenes, the central cavity of these HCCs are totally empty and none of them is filled with metal particles or metal carbides.

The purity of HCCs is very high, as shown in Fig. 1c-1e. From the TEM images, it has been estimated that the content of the giant HCCs in the deposits at the end of anode may reach up to 80-90%. It is known that polyhedral carbon nanoparticles with large central cavity are not stable under electron bombardment. [3,7] This is also the case for HCCs. During the TEM examination, some HCCs would collapse and lose part of their inner empty space, as indicated by the arrows in Fig. 1d. This happened frequently when we were trying to focus the microscopy to get a clear image of the HCCs in spite of the low operation voltage of 100kV.

An analogy can be made between the nano-sized hollow carbon capsules reported here and multishell fullerenes with a cage-inside-cage concentric structure that were foreseen by Kroto et al [20] shortly after the discovery of the fullerene C_{60}, and several multishell fullerenes such as double-shell $C_{60}@C_{240}$, $C_{240}@C_{560}$ and triple-shell $C_{60}@C_{240}@C_{560}$, $C_{80}@C_{240}@C_{560}$ were successfully prepared by laser vaporization of composite carbon-metal targets.[8] For the HCCs reported here that are structurally related to large and multishell fullerenes, pentagons and heptagons may have played a primordial role in their formation, which is similar to the formation of single-shell and multishell fullerenes as well as carbon nanotubes. [6,7]

Up to now, hollow carbon nanoparticles with much smaller inner central cavity are usually obtained by arc discharge of pure

graphite electrodes.[4,7] The graphite-derived nanoparticles usually display a polyhedral morphology with an inner empty space (3-10nm in diameter)[3,7] that is at least 4 times smaller than the inner diameter of the HCCs reported here. Those nanoparticles with large central cores tend to be more faceted than those with small inner shells and are frequently irregularly shaped with more than six sides.[7] In contrast to the traditional carbon nanoparticles, the HCCs obtained from coal-based carbon by arc discharge with iron as catalyst have two peculiar characteristics: a nearly perfect spherical shape and the inner diameter around 40-50nm that is much larger than that of the common polyhedral nanoparticles.

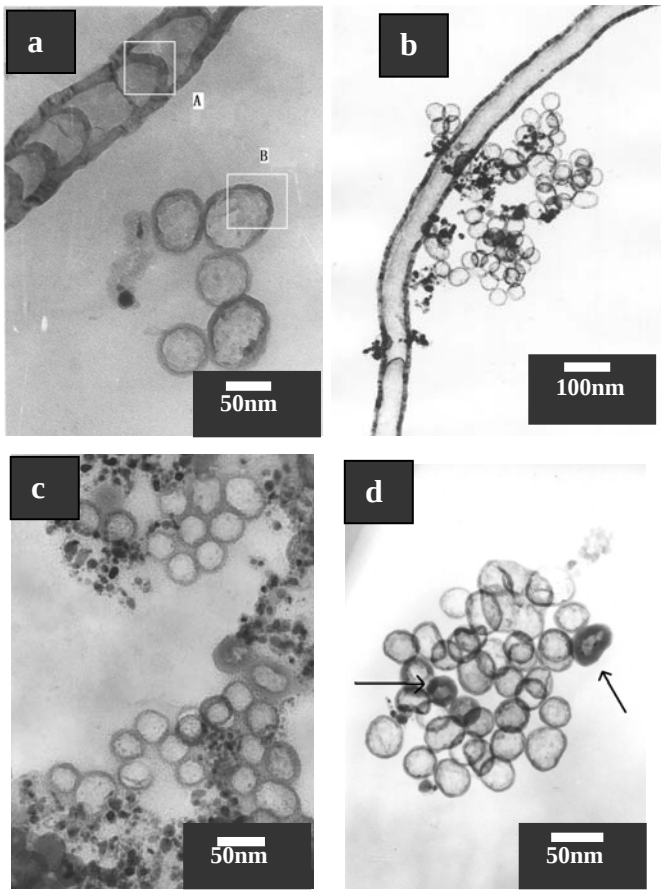

Figure 1. TEM images of hollow carbon capsules (HCCs) prepared from coal with Fe as catalyst, on the average, these HCCs have a quite uniform particle size, with outer diameters around 50-70nm and inner diameters around 40-50nm; (a) five HCCs accompanied with a bamboo-shaped carbon nanotube; (b) many HCCs accompanied with a long multiwall carbon nanotube; (c) and (d) TEM image showing most of the HCCs with almost perfect sphere-like shape.

The formation mechanism of these HCCs is not clear at the moment, nevertheless it must be related to the chemical structure of coal-based carbon and the presence of Fe metal. It is well known that the chemical structure of coal-based carbons is very complex and resembles graphite crystalline in the domain of 1-10 nm in which the basic units are small graphitic crystallites containing a few layer planes. These small graphitic crystallites are joined together by relatively weak crosslinks that would break first under arcing conditions to release some of the small graphitic crystallites (termed as SGCs thereafter) as free particles, and some of them might be directly incorporated into HCCs without going atomization as in the case of graphite process in which the graphite sheets need to be first decomposed into C_1 or C_2 species,[6,7,12] but it should be noted that the SGCs might go further decomposition to result in a large amount of aromatic specie such as polycyclic aromatic hydrocarbons (PAHs) and C_1 or C_2 species, which then take part in the formation reaction of HCCs as the basic building blocks in the presence of Fe metal particles. It is known that iron group metals are good catalysts for carbon graphitization reactions and for CNTs preparation, thus Fe metal particles or atoms might be responsible for catalyzing the formation of the HCCs.

For comparison, the arc-evaporation of iron-filled graphite anode was also conducted under the same arcing conditions, with a hope to get some indirect evidence that will help us to understand how these HCCs are formed. The high purity graphite electrode was first drilled to make a hole for filling the same iron particles as in the case of coal-based carbon tubes, but no HCCs were found. This indicates, indirectly and clearly, that the formation of HCCs is due to the peculiar chemical structure of coal-based carbon, though the detailed mechanism involved in the formation process is not known.

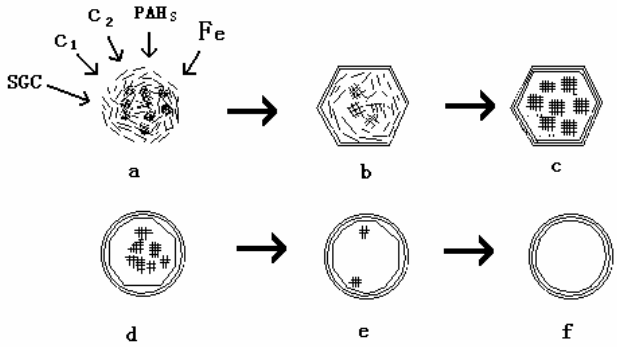

Figure 2. Schematic illustration of the growth stages of HCCs; (a) the initial stage in which a mixture consisting of molten Fe metal particles and various carbon species such as small graphitic crystallites (SGCs) and polycyclic aromatic hydrocarbon (PAHs) as well as C_1/C_2 species is formed. The mixture may be in liquid phase or quasi-liquid phase; (b) graphitization begins from the surface of the particles induced by Fe catalyst. (c-e) Fe metal particles are driven out of the shells leaving the empty capsule behind, at the same time, the polyhedral shape is gradually transformed into a quasi-spherical one because of the high-energy electron irradiation and high temperature in the arc plasma. (f) well-developed hollow carbon capsules are formed.

To understand the nature of how the HCCs are formed, a model is proposed to explain the growth process of the HCCs, in which the roles played by SGCs, PAHs, C_1 or C_2 species and Fe metal particles are all taken into account, which is schematically shown in Fig. 2. The first step for the growth of HCCs is the formation of clusters consisting of the molten Fe metal particles and the aromatic carbon species such as SGCs and PAHs as well as the C_1 or C_2 species. The carbon species are released from the coal-based carbon rod that is vaporized in arc plasma of high temperature (*ca.* 3000°C). In the initial stage (Fig. 2a), the mixture consisting of various carbon species and Fe metal particles may be in liquid phase or quasi-liquid phase. Then, the formation of graphitic carbon layers starts due to the catalytic effect of Fe metal and the high temperature, as shown in Fig. 2b and 2c. Since the outer periphery of the particles will likely consist of larger, more favorably oriented layers [20] that possess fewer

energetic and structural barriers to realignment and growth than those in the inner interior, the growth of graphitic layers is supposed to start on the outer surface and progress toward the center [3]. It is known that the melting point of carbon is much higher than Fe, thus, the initial density of carbon in the particle or cluster should be lower than pure carbons. In other words, the vapor pressure of Fe is much higher than carbon, which causes Fe atoms evaporate through the defects of the outer graphitic carbon layers, in the stage (c) to (e), as shown in Fig. 2c-2e. At the same time, the transformation of polyhedral shape into a quasi-spherical one also takes place due to the high-energy electron irradiation and high temperature in the arc plasma zone, which leads to the HCCs with perfect sphere shape, as shown in Fig. 2f. It is worth noting that none of the HCCs obtained in this way is filled with Fe particles or other elements. This might be due to the fact that the starting building blocks of the HCCs mainly consist of the large aromatic species such as the SGCs and PAHs species rather than the small units such as C_1 and C_2 species as in the case of arc-evaporation of graphite. This may account for why the formed HCCs have a big inner diameter. For some unknown reasons, the coalescence of large aromatic carbon species would lead to relatively more defects in cage shells during the growth from stage (b) to stage (e), as shown in Fig. 2, which makes the Fe being easily driven out of many shells and leaving the empty capsules behind, as shown in Fig. 2f.

Conclusions

In summary, a novel form of hollow carbon capsules (HCCs) have been prepared from coal-based carbon by arc discharge with iron as catalyst. These HCCs have a uniform size distribution with outer diameters around 50-70nm and inner diameters around 40-50nm. The growth mechanism of this novel HCCs has been discussed in terms of the chemical structure of coal-based carbon and the arcing discharge conditions.

Acknowledgment. This work was partly supported by the National Science Foundation of China (No. 29976006, 20376011), the Natural Science Foundation of Liaoning Province (No. 9810300701, 2001101003), the National Basic Research Program of China (Grant No. G2003CB615806) and the Ministry of Education of China.

References

(1) Kratschmer, W.; Lamb, L.D.; Fostiropoulos, K.; Huffman, D.R.; *Nature.* **1990,** 347, 54.
(2) S. Iijima, *Nature* **1991**, 354, 56.
(3) Ugarte, D.; *Carbon.* **1995**, 33, 989.
(4) Saito, Y.; *Carbon.* **1995**, 33, 979.
(5) Saito, Y.; Nishikubo, K.; Kawabata, K.; Matsumoto, T.; *J. Appl. Phys.* **1996**, 80, 3062.
(6) Dresselhaus, M.S.; Dresselhaus, G.; Eklund, P.C.; *Science of Fullerenes and Carbon Nanotubes*, Academic Press, London, **1996**.
(7) Harris, P.J.F.; *Carbon Nanotubes and Related Structures*, Cambridge University Press, **1999**.
(8) Mordkovich, V.Z.; Takeuchi, Y.; *Chem. Phys. Lett.* **2002**, 355, 133.
(9) Gogotsi, Y.; Libera, J.A.; Kalashnikov, N.; Yoshimura, M.; *Science*. **2000**, 290, 317.
(10) Zhang, G.Y.; Jiang, X.; Wang, E.G.; *Science.* **2003**, 300, 472.
(11) Pang, L.S.K.; Vasslalo, A.M.; Wilson, M.A.; *Nature.* **1991**, 352, 480.
(12) Wilson, M.A.; Patney, H.K.; Kalman, J.; *Fuel.* **2002**, 81, 5.
(13) Qiu, J.S.; Zhou, Y.; Wang, L.N.; Tang, S.C.; *Carbon.* **1998**, 36, 465.
(14) Qiu, J.S.; Zhou, Y.; Yang, Z.G.; Wang, L.N.; Zhang, F.; Tsang, S.C.; Harris, P.J.F.; *Molecular Materials.* **2000**, 13, 377.
(15) Qiu, J.S.; Zhou, Y.; Yang, Z.G.; Wang, D.K.; Guo, S.C.; Tsang, S.C.; Harris, P.J.F.; *Fuel.* **2000**, 79, 1303.
(16) Williams, K.A.; Tachibana, M.; Allen, J.L.; Grigorian, L.; Cheng, S.C.; Fang, S.L.; Sumansekera, G.U.; Loper, A.L.; Williams, J.H.; Eklund, P.C.; *Chem. Phys. Lett.* **1999**, 310, 31.
(17) Qiu, J.S.; Zhang, F.; Zhou, Y.; Han, H.M.; Hu, D.S.; Tsang, S.C.; Harris, P.J.F.; *Fuel.* **2002**, 81, 1509.
(18) Li, Y.F.; Qiu, J.S.; Zhao, Z.B.; Wang, T.H.; Wang, Y.P.; Li, W.; *Chem. Phys. Lett.* **2002**, 366, 544.
(19) Mochida, I.; Egashira, M.; Korai, Y.; Yokogawa, K.; *Carbon* **1997**, 35, 1707.
(20) Kroto H.W.; MaKay, K.; *Nature.* **1988**, 331, 328.
(21) Saito, Y.; Yoshikawa, T.; Okuda, M.; *Chem. Phys. Lett.* **1993**, 209, 72.

FLAME SYNTHESIS OF CARBON NANOTUBES USING CATALYST PARTICLES PREPARED BY LASER ABLATION

*Randy L. Vander Wal, Gordon M. Berger and Thomas M. Ticich**

The National Center for Microgravity Research (NCMR)
c/o The NASA-Glenn Research Center
M.S. 110-3
21000 Brookpark Rd.
Cleveland, OH 44135

* Centenary College of Louisiana
Dept. Of Chemistry
2911 Centenary Blvd.
Shreveport, LA 71134

Introduction

Carbon nanotubes and nanofibers are sought for many applications reflecting their novel mechanical, thermal and electrical properties including reinforcing, catalyst support, gas storage and electrochemical energy storage [1]. These applications will require bulk synthesis methods, producing ton quantities. Towards this goal, flame synthesis has demonstrated potential for producing nanoscale materials such as TiO_2, SiO_2 and carbon black on an industrial scale. Thus, we are pursuing flame synthesis for nanotubes and nanofibers.

Our previous work has shown a strong reactivity difference between Fe and Ni nanoparticles [2-4]. The metals manifest a high selectivity towards either CO or C_2H_2. Ni reacts with CO/C_2H_2 gas mixtures to produce nanofibers; whereas, Fe reacts with CO to produce SWNTs. The catalyst to product correlation is very high. Fe has not been observed to catalyze MWNTs nor nanofibers, and Ni has not been observed to catalyze SWNTs.

Moreover, these metals also demonstrate a different onset of catalytic activity. Previous studies used in situ catalyst particle formation using nebulized metal salt solutions. To avoid the complex chemistries involved in this process and directly study the highly selective reactivities of these different metals, the onset of catalytic activity and the potential associated particle size effects, laser ablation was used to generate the metal nanoparticles [5].

Experimental

Laser ablation was used to create the catalyst nanoparticles of Fe or Ni. As aerosols, the nanoparticles were entrained within a gas flow and introduced into the central tube within a custom, McKenna premixed burner. Apart from the premixed flame, whose composition could be varied but was maintained constant for these experiments, gas mixtures through the central tube of the burner consisted of CO/H_2/He/C_2H_2 mixtures, with each gas controlled independently and regulated by mass flow controllers or rotameters. Further details of the burner, operating conditions and TEM microscopy have been reported previously [2-4].

The water-cooled burner was operated using a rich premix of acetylene and air. Fuel-air equivalence ratios were 1.5 to 1.55, produced using an acetylene flow rate of 1.5 slpm and an air flow rate ranging from 11.3 to 11.5 slpm. A 3 inch long, 1 inch OD quartz chimney served to stabilize the post-combustion flame gases against buoyancy-induced flicker and guided the metal aerosol and associated reaction gases as a laminar flow. Samples of the metal-catalyzed products were collected by thermophoretic sampling directly upon lacey TEM grids above the chimney for analysis.

Results and Discussion

Onset of catalytic reactivity and selectivity based on gas identity. Fe reacted in both the CO and CO/C_2H_2-based gas mixtures, producing SWNTs. Fig. 1 shows TEM images of these products at various magnifications. In contrast, Ni was unreactive towards the CO gas mixture. It only reacted with the CO/C_2H_2 gas mixture, producing nanofibers. This is shown in the TEM images of Fig. 2.

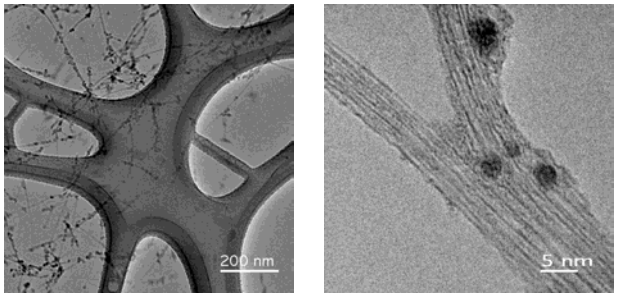

Figure 1. TEM images of SWNTs, shown as sampled from the flame, using Fe as the catalyst.

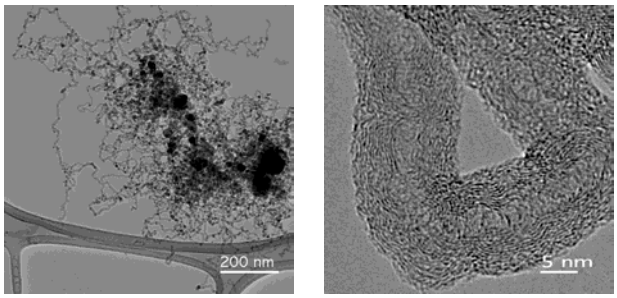

Figure 2. TEM images of nanofibers, shown as sampled from the flame, using Ni as the catalyst.

Ni. A greater yield of nanofibers of greater length were produced with the the CO/C_2H_2 based gas mixture than with C_2H_2 alone. Moreover, the reactivity of Ni towards C_2H_2 (at the same concentration) in the absence of CO appears to be increased, where fewer nanofibers, of shorter lengths were produced (along with encapsulated particles). Not only do these results suggest that C_2H_2 serves as the main carbon supply for Ni-catalyzed nanofibers, but that CO plays an inhibitory role in that its adsorption and associated slower reactivity restricts the rate of C_2H_2 adsorption (by site blockage), and hence, slows the rate of carbon supply. Our results also suggest that ultrasmall Ni particles (< 4 nm) may not be particularly active towards catalyzing C_2H_2 dissociation. Finally, there is an absence of SWNTs catalyzed by Ni with either C_2H_2 or CO/C_2H_2 gas mixtures. Ultrasmall Ni nanoparticles may not be sufficiently reactive. Therein, it appears that the onset of catalytic activity of Ni for nanotube synthesis is attained only by larger particles, beyond a minimum size of roughly 4 nm. Upon reaching this size range, the catalyst particles are too large for SWNT synthesis. Instead, they catalyze nanotubes or nanofibers.

Fe. On the basis of bulk crystal studies, Fe is considered to be more reactive than Ni [6]. Clearly, it achieves an earlier onset of reactivity, as only the very smallest Fe particles catalyze nanotubes, in this case SWNTs. Therein, Fe might be expected to readily react with C_2H_2, particularly since it reacts with CO. One might even predict that CO, as a less reactive carbon source could yet play a similar role in restricting the rate of carbon supply through C_2H_2 dissociative adsorption, as it does with Ni. The difference here is that it would also contribute to the carbon supply. Yet further tests show that Fe exhibits selective reactivity towards CO. Moreover, the absence of nanofibers of MWNTs suggests a decline in reactivity with increasing particle size for Fe nanoparticles, in contrast to Ni.

Metal Nanoparticles. For each molecule, dissociative adsorption involves both electron donation and withdrawal [7, 8]. Additionally, in a metal nanoparticle, the density of electronic states is finite and the traditional conduction and valence bands are absent due to the small number of constituent atoms [9, 10]. With > 75% of the atoms residing at the surface for a 1 nm particle, the particle properties will largely be determined by the surface atoms. This will be particularly true for those atomic orbitals not participating (contributing electron density) in the free conduction band of the metal, such as the 3d orbitals of the transition metals [6, 7]. If the electronic properties of a metal nanoparticle resembles those of the individual element, given the finite size and high surface area, then based on energetics associated with its outer electron configuration, $[Ar]5s^23d^6$, Fe atoms can achieve a stable half filled d-shell by loss of electron density such as by donation of electron density to an adsorbate, e.g. CO. In contrast, acceptance of electron density might be expected to be energetically unfavorable, given the increase in energy associated with pairing electron density within the d-shell orbitals. Therein, Fe would be expected to be unreactive towards C_2H_2.

The situation for Ni is exactly opposite. Adopting the premise that the individual elemental identity still (largely) governs the electronic properties of the surface atoms and hence, their reactivities, it would be energetically favorable for Ni to accept electron density to achieve a more stable, filled d-shell, namely $[Ar]5s^23d^{10}$. Therein, Ni would be expected to be highly reactive towards adsorbates which donate electron density, e.g. C_2H_2. Correspondingly, Ni would be unreactive towards adsorbates that accepted (withdrew) electron density from the metal nanoparticle, e.g. CO.

This exceedingly simple explanation certainly neglects several factors. First, it ignores the possible contribution of other adsorbates to the nanoparticle-adsorbate system. For example, bulk single crystal studies show that H_2 upon dissociative adsorption can donate electronic charge density to Fe [6, 11]. The preferential reactivity of Fe and Ni towards particular gases may also be related to steric effects which make a somewhat larger nanoparticle more accessible to species which adsorb in a sideways configuration (parallel to the nanoparticle surface like C_2H_2) rather than in an end-on configuration (such as CO) [11]. Undoubtedly, other factors such as thermal restructuring, adsorbate-enhanced restructuring and electronic interactions between adsorbates mediated by the catalyst particle are integral to these results.

Acknowledgements. This work was supported by a NASA NRA 97-HEDs-01 combustion award (RVW) administered through NASA cooperative agreement NCC3-975 with The National Center for Microgravity Research on Fluids and Combustion (NCMR) at The NASA-Glenn Research Center. The authors gratefully acknowledge Dr. Y. L. Chen and David R. Hull for the TEM imaging.

References

(1) *Carbon Filaments and Nanotubes: Common Origins, Differing Applications?* (Biro, L. P.; Bernardo, C. A.; Tibbetts, G. G.; and Lambin, Ph., Eds.), Nato Science Series, Kluwer Academic Publishers, Dordrecht, The Netherlands, **2001**, Vol. 372.
(2) Vander Wal, R. L., *Carbon*, **2002**, 40, 2101.
(3) Vander Wal, R. L., *Combust. and Flame*, **2002**, 130, 37.
(4) Vander Wal, R. L.; L. J. Hall, *Chem. Phys. Lett.*, **2001**, 178, 349.
(5) Gnedovets, A. G.; Kul'batskii, E. B.; Smurov, I; Flamant, G., *Appl. Surf. Sci*., **1996**, 96-98, 272.
(6) Somorjai, G. A.; Kim, C. M.; Knight, C., in "Surface science of catalysis: In situ probes and reaction kinetics", (Dwyer, D. J.; and Hoffman, F. M., Eds.) American Chemical Society, Washington DC, **1992**.
(7) Chemical Kinetics and Catalysis, (Van Santen, R. A.; and Niemantsverdriet, J. W., Eds.) Plenum Press Inc. New York, **1995**, Chp. 6
(8) Campbell, I. M., *Catalysis at Surfaces*, Chapman and Hall Inc., New York, **1988**, Chp. 5
(9) Zhang, J. Z., *Acc. Chem. Res.*, **1997**, 30, 423.
(10) El-Sayed, M. A., *Acc. Chem. Res.*, **2000**, 34, 257.
(11) Dry, M. E.; Shingles, T.; Boschof, L. J.; Van Botha, H. C. S., *J. of Catalysis*, **1970**, 17, 347.

IMMOBILIZATION OF CARBON NANOFIBERS (CNFs); A NEW STRUCTURED CATALYST SUPPORT

Nabeel A. Jarrah, Jan G. van Ommen and Leon Lefferts

Faculty of Science and Technology, IMPACT, University of Twente, P. O. Box 217, 7500 AE, Enschede, The Netherlands

Introduction

One of the main problems in reactions performed in liquid phase over solid catalyst is to avoid mass transfer limitation. Slow diffusion as well as frequent occurrence of low reactant concentrations (e.g. dissolved H_2 or O_2) are responsible for this, resulting in concentration gradients around and in catalyst particles. Variation of the local concentrations of reactants and products over the active sites affects both activity and selectivity and thereby frustrates optimization of the operation of such reactors.

The concentration gradient in a catalyst particle strongly depends on the size of the catalyst particle. Downsizing of catalyst particles is limited due to hydrodynamic constraints in trickle bed reactors and filtration problem in suspension reactors.

CNF are graphite materials, which can be catalytically produced by decomposition of a carbon containing gas over small metal particles like nickel. In many cases the fibers are strongly entangled, forming aggregates. These aggregates are potentially attractive alternative catalyst supports because of their high surface area, combined with high macro-porosity (up to 2 cc/g) and low tortousity[1]. The main problem is encountered when such a fluffy materials is used in conventional catalytic reactors. The goal of this work is to investigate how CNFs can be immobilized to macro-structured materials. Two macro-structured materials is used as examples in this work, i.e. ceramic monolith and metal foam. From the perspective of the use of monoliths as structured materials to support catalysts, this work aims on the preparation of improved washcoats based on CNFs, competing the well known relatively dense inorganic washcoats. Metal foams are much less explored as structured catalyst supports and in this case the preparation of stable and uniform washcoats is still a challenge[2].

Experimental

Materials. Ceramic cordierite monolith samples (600 cells per square inch, obtained from Degussa), bare (without washcoat), and with 17 μm average thickness of γ-alumina washcoat, were used. Nickel was deposited on the monolith from a pH-neutral nickel solution (0.1 M).

Ni foam (obtained from RECEMAT) is a three dimensional network of connected strands. Each strand is shaped like a prism. The average characteristic strand width was 80 ± 5 μm and the pore diameter was 0.4 mm.

CNFs formation. The samples were reduced. Then, CNFs were formed catalytically by decomposition of CH_4 or C_2H_4 in the case of monolith, while only C_2H_4 was used to synthesize CNFs on the Ni foams. The conversion of the hydrocarbon used to synthesize the CNFs was determined by on-line chromatographic analysis (Varian GC model 3700 equipped with a 15 m Q-Plot column).

Characterization. The BET surface area, pore volume and pore size distribution were measured by N_2 adsorption-desorption at 77 K using ASAP 2400 (Micromeritics) instrument. The morphology of both CNF and the support structure were studied with Scanning Electron Microscopy (SEM) (LEO 1550 FEG SEM) equipped with EDX analysis. The stability of the CNFs formed on Ni foam towards shear forces, which would be necessary when applied as catalyst support in liquid phase, was tested by flowing water through the foam at room temperature with a linear velocity of 1 m/s. The extent of loss of CNFs was calculated from the difference between the initial and final weight of the foam.

Results and Discussion

Detailed microscopic evaluation of the **monolith** revealed that at the outer surface of the washcoat a hairy layer is formed with a typical thickness of 1 μm containing CNFs exclusively (**micrograph 1.A**). The structure of this layer is similar to the inverse structure of a traditional alumina washcoat, although much thinner. The hairy layer is supported on a composite layer containing both CNF and fragments of the alumina washcoat. The influence of the Ni particle size and synthesis conditions on the properties of the resulting material will be presented. It turns out that the thickness of the CNF layer at the outermost surface as well as the diameter of the fibers increases with mean Ni-particle size.

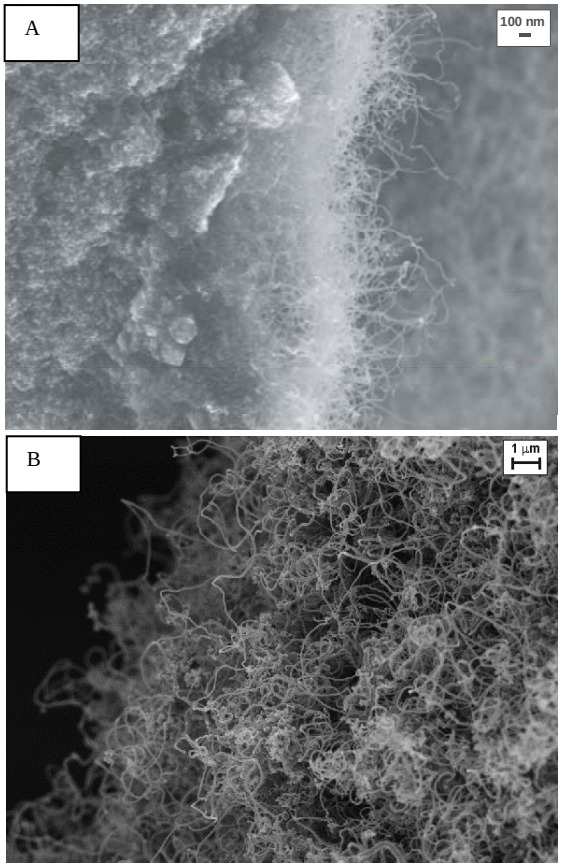

Figure 1. Scanning Electron Micrographs of the CNF layer at the outer surface of (a) monolith loaded with 1.2 wt% Ni. Formation conditions: 200ml/min 50 % CH_4, 10 % H_2 in N_2 at 843 K for 3 hrs (b) Ni foam. Formation conditions: 107ml/min 25 % C_2H_4 in N_2 at 623 K for 3 hrs.

Growing CNFs on the monolith using methane leads to immediate fragmentation and doubling of the thickness of the washcoat independent on the amount of CNFs, forming a macro-porous composite layer of entangled alumina particles and CNF with a typical diameter of 10-30 nm. Immediate fragmentation is due to the fact that some of the fibers are too thick for the pores in the washcoat. The total porosity decreases with the amount of CNF whereas the surface area per gram monolith increases[3].

Large Ni particles are able to grow CNF for longer times, resulting in detachment of the washcoat from the cordierite, which is

caused by extensive growth of CNF out of the washcoat. Furthermore, extended growth of CNF inside the cordierite body causes disintegration of the monolith body when macro-pores are locally overfilled with CNF. Methane is preferred over ethene for growing CNF because ethene grows CNF rapidly even on relatively large Ni particles, resulting in thick fibers up to 70 nm in the macro-porous cordierite, destroying the monolith.

A rough and hairy layer of entangled CNFs (**micrograph 1.b**) was formed on the surface of the **nickel foam**. The surface area of the Ni foam increased from less than 1 m^2/g to about 30 m^2/g. The pore volume of the synthesized CNFs layer is 1 cm^3/g. Moreover, the voids between the CNFs are macropores and thus significantly larger than the typical mesopores in conventional inorganic catalyst supports.

The initial morphology of the surface of the Ni foam was typical for polycrystalline Ni, with grains in the size range between 1 and 10 μm. A rough surface with small Ni particles, sized in the range of 10-100 nm, formed when the polycrystalline Ni surface was exposed to ethene at 450°C for 0.5 hour. Some of the Ni particles started to synthesize CNFs with diameters between 10 and 70 nm. The size of the Ni particles is significantly smaller than the size of the grains in the Ni foam. Thus, fragmentation of the Ni grains into small Ni particles occurs before CNFs start to form. Fragmentation of polycrystalline Ni into small Ni particles is well known in corrosion literature as metal dusting[3].

Figure 2 shows that the formation rate of CNFs on pre-shaped small Ni particles supported on monolith takes off with a high rate followed by deactivation exclusively. In contrast, formation rate of CNFs on polycrystalline Ni foam at constant temperature initially increased, reached a maximum value and then decreased. The initial increase in the formation rate of CNFs on polycrystalline Ni is caused by the necessity of fragmentation of Ni grains into small Ni particles.

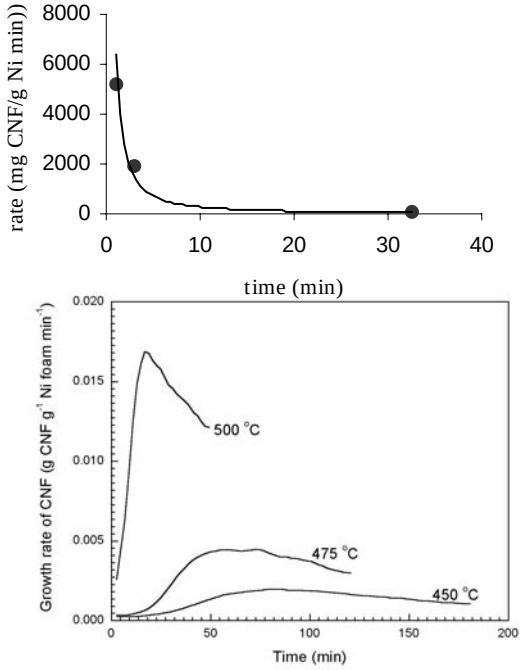

Figure 2. CNFs formation rate on (a) monolith loaded with 3.0 wt% Ni. Formation conditions: 200ml/min 50 % C_2H_4, 10 % H_2 in N_2 at 843 K (b) Ni foam. Formation conditions: 107ml/min 25 % C_2H_4 in N_2.

The integrity of the samples and strong attachment of the CNFs to the Ni surface or to monolith are necessary for application of the final composite materials as structured catalyst supports.

The monoliths can easily disintegrate when CNF formation is excessive, either in the cordierite or on the interface between the cordierite and the washcoat. However, CNFs are always observed in the macro-porous cordierite and it is concluded that the interweaved fiber layer, extending from the cordierite *via* the composite layer to the hairy top layer, is essential to generate mechanical stability of the structure.

The integrity of the Ni foam was lost after synthesizing 138 wt% CNFs at 500°C in 3 hours. On the other hand, the foams were stable after synthesizing 50 wt% CNFs at 450°C in 6 hours. The Ni foam collapsed at high temperature because of the increase in the rate of corrosive metal dusting with temperature[3]**.** The CNF layer on Ni foam can withstand shear forces caused by flowing water (1 m/s) through the foam.

The optimum conditions for generating a macro-porous CNF layer with a high surface area will be presented for both examples, circumventing disintegration of the macro structured materials.

Conclusions

A thin highly porous washcoat based on CNFs on ceramic structures can be synthesized without disintegrating the final composite materials.

Stable Ni-CNFs-foam composite structures can be obtained under the conditions that the extent of corrosive metal dusting of Ni is limited, via decreasing the temperature and/or the formation time. Metal dusting is needed to form small Ni particles that allow formation of CNFs.

Acknowledgement. This work was performed under the auspices of NIOK, the Netherlands Institute of Catalysis Research. The authors gratefully acknowledge Degussa for supplying monolith samples and RECEMAT for supplying Ni foams.

References

(1) De Jong, K., Geus, J., *Catal. Rev. – Sci. Eng.*, **2000**, 42(4), 481
(2) Matatov-Meytal, Y., Sheintuch, M., Applied Catalysis A: General, **2002**, 231,1.
(3) Jarrah, N. A. , van Ommen, J. G., Lefferts, L., J. Mat. Chem.,
(4) Pippel, E., Woltersdorf, J., Schneider, R., Materials and Corrosion, **1998**, 49, 309.

Chemical Processing of bundled Carbon Nanotubes into Macromolecules in Solution

[1]U.J.Kim, [3]C.A.Furtado, [1]X.Liu, [4]R.Saito, [5,6]M.Dresselhaus, [1,2]P.C.Eklund

The Pennsylvania State University, University Park, PA, 16802
[1]Department of Physics,
[2]Department of Materials Science and Engineering,
[3]Centro de Desenvolvimento da Tecnologia Nuclear – CDTN/CNEN, Belo Horizonte, MG, Brazil
[4]Department of Physics, Tohoku University and CREST JST, Sendai 980-8578, Japan
Massachusetts Institute of Technology, Cambridge, Massachusetts 02139-4307, USA
[5]Department of Physics
[6]Department of Electrical Engineering and Computer Science,

Introduction

An effective chemical process to obtain clean, individual single-walled carbon nanotubes (SWNTs) in a stable solution is an important step needed for developing many large scale applications for these molecular filaments, e.g., as electrostatic shielding additives, field emission flat panel displays, radar paints, conductive inks, or in nanotube-polymer composites. Of particular interest, is the potential for chemical change, or damages to the SWNTs during purification. Raman and IR have been found very useful in studying these changes. However, to our knowledge, nobody has used these 2 tools together to chart the outcome of the processing and, in particular, the impact of the processing on the eventual dispersion of individual nanotubes in amide solutions. During the course of this research, we have been able to identify, for the first time, the IR-active modes for small diameter 1.2 -1.6 nm nanotubes.

Experimental

Arc discharge nanotube soot (Carbolex, Inc.; USA) produced using ~4 atomic % Ni-Y loaded carbon electrodes was studied here. To primarily remove amorphous carbon, we either used dry oxidation (DO) or hydrogen peroxide (H_2O_2) reflux. DO involves a thermal soak at 355ºC for 20 minutes in flowing dry air (100sccm). This achieves selective oxidation of the amorphous carbon, and also minimizes nanotube mass loss. Amorphous carbon was also removed by a reflux in 30 vol.% of H_2O_2 in H_2O for 18hrs. The Ni-Y was dissolved by reflux in either 3N HNO_3(16h), or in weakly oxidizing 6N HCl (24h).

The tubes were then "debundled" in N-methyl pyrrolidone (NMP) or N, N-dimethylformamide (DMF) using ultrasound for 4hrs. Centrifugation (14000rpm, 90min) was carried out to remove remaining large bundles or particles. A drop of this solution was placed on a mica substrate and the solvent was evaporated in air and then AFM (Digital Instruments Nanoscope (Model IIIA)) measurements were made to determine the fraction of tubes appearing as single isolated tubes on the substrate.

FTIR and Raman spectra of the raw and processed SWNT samples were collected using a BOMEM DA3+ FT spectrometer that is equipped with. Nd:YAG laser (1064nm).

Results and Discussion

Fig.1 shows Raman spectra collected at various stages of the chemical processing indicated. Above 1000cm^{-1}, two Raman bands are observable; (1) a relatively broad, disorder-induced or "D-band" at ~1350 cm^{-1}, and (2) a first-order-allowed band with substructure appears at1590cm^{-1} (SWNT-G-band). D band intensity and G band width are considered as probes of SWNT wall integrity that may be compromised by chemical processing leading to defect sites or functionalization. The G band has 5 Lorentzian components. We find that only the H_2O_2 and HNO_3 treated samples exhibit broadening of the G band. A small upshift of the peaks is also seen. This sample processing leads to exhibit D band enhancement as well. We also have considered dry oxidation (DO) to remove amorphous carbon and a subsequent HCl reflux to remove catalyst residue. This processing produces no broadening of the G band components. After annealing the DO/HNO_3 sample at 1100ºC for 24h hours in vacuum (Fig.1(g)), the broadened and distorted Raman band returns to that of raw soot, which means the wall damage or functionalization is largely removed. After high T vac annealing the DO/HCl processed soot, no change in the Raman bands was observed.

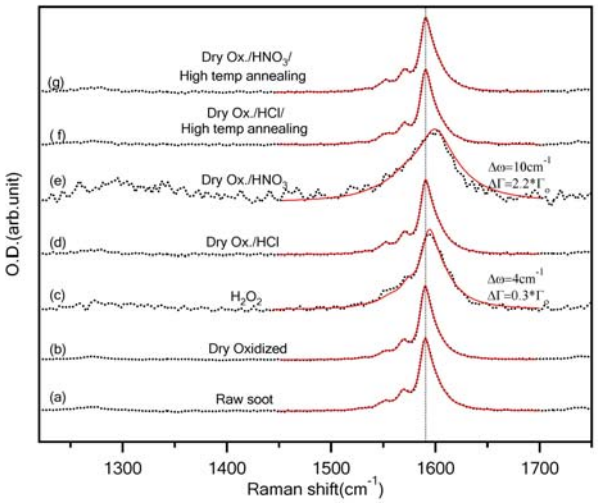

Figure 1. Raman spectra of raw soot (a), DO at 355ºC for 20nm (b), H_2O_2 reflux for 18h (c), DO/HCl (24h) (d), DO/HNO_3(16h) (e), DO/HCl(24h)/annealing at 1100ºC for 24h (f), and DO/HNO_3(16h)/ annealing at 1100ºC for 24h(g).

We have also carried out an FTIR study of the chemically processed SWNT samples. This probe is more sensitive than Raman to functional groups on the tubes. The IR spectra for tubes processed in various ways is shown in Fig.2. The shaded bands in the figure indicate the range where the indicated functional group would appear. As can be seen in Fig.2(a),(b),(d), the IR spectra of DO/HCl is similar to that of the raw soot ,except for an enhancement of the ~1100cm^{-1} band. As seen in Fig.2(c),(e), the band at ~1740cm^{-1}(in the region of C=O stretching vibration) is enhanced in the H_2O_2 and HNO_3 refluxed samples. Note that a very broad band appears in the ~3230-3500cm^{-1} range, (–OH stretching mode) that is consistent with carboxylic acid or hydroxyl functional groups. A new broad band at ~1230cm^{-1} appears which can be assigned as the -OH bending mode. Fig.2(f),(g) show the IR spectra of annealed DO/HCl and DO/HNO_3 at 1100ºC for 24h. By annealing DO/ HNO_3 sample, the broad bands at ~3230cm^{-1} and ~1230cm^{-1} are removed. They appear to be due to –OH. According to Kinoshita, oxygen containing surface groups will be completely eliminated, and –CH groups should be removed, or at least decreased drastically at our annealing conditions[2]. The 3 sharp bands near ~2900cm^{-1} and the bands at ~1380cm^{-1} and 1460cm^{-1} have been assigned previously to –CH asymmetric and symmetric stretching modes and bending modes, respectively by other groups[3]. But as seen in Fig.4, these bands do not decrease in intensity upon annealing. This suggests that they are SWNT phonons. Via connection with theoretical calculations, we can identify most of the sharp vibrational features in the FTIR spectra of high-T annealed samples with SWNT vibrational modes.

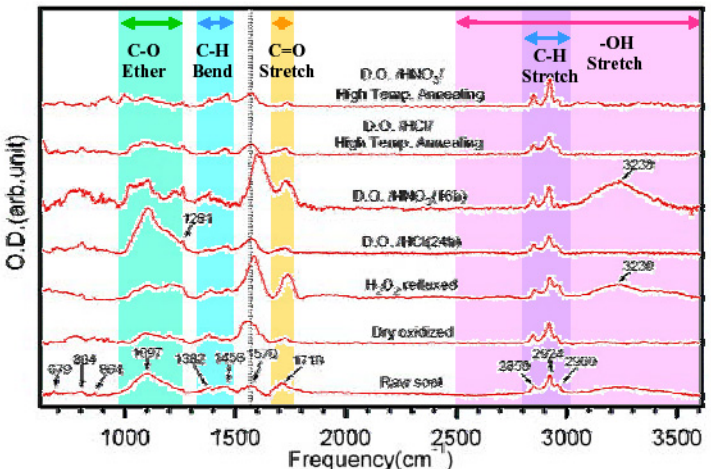

Figure 2. IR spectra of raw soot (a), DO at 355°C for 20nm (b), H_2O_2 reflux for 18h (c), DO/HCl (24h) (d), DO/HNO_3(16h) (e), DO/HCl(24h)/annealing at 1100°C for 24h (f), DO/HNO_3(16h)/ annealing at 1100°C for 24h(g). A smoothly varying electronic background has been subtracted from the data.

Fig. 3(a) is a typical topographic AFM image of ultrasonically processed carbon nanotubes deposited from DMF or NMP solution onto cleaved mica substrates, Fig. 3(b) shows Z scan analysis of the lines labeled as (1), (2), (3), (4) in Fig. 3(a). In Fig. 3(b), the data for lines. (1), (2), (3) all refer to the same tube. The average filament diameter in this case is $\bar{d}$ =1.45nm ± 0.07nm. The line labeled as (4) in Fig. 3(a) cuts across 7 tubes and 2 small particles and the Z scan is also shown in Fig. 3 (b); examples of isolated tubes and very small bundles (2~3 tubes/ one bundle) can be seen.

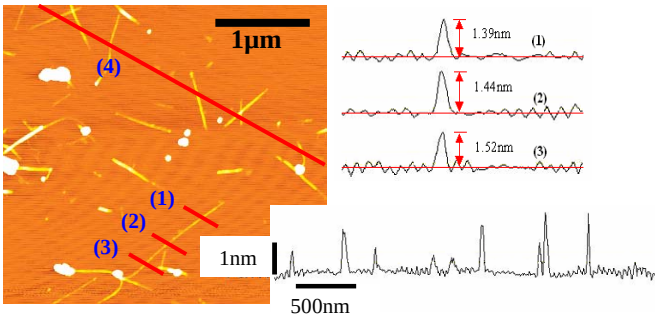

Figure 3. (A) Typical AFM images showing the dispersion of SWNTs in DMFor NMP, (b) shows Z scan analysis of the lines labeled (1),(2),(3),(4) in (a).

To see the real effects of various chemical process schemes on the nanotube dispersion, we show (Fig.4) AFM result for filament height (left) and filament length (right) distributions for several purification/de-bundling processes. For the diameter, DO/HCl/NMP(Fig.4(a)) and H_2O_2/HCl/NMP processing (Fig.4(c)) exhibit a peak in the bin (1.4-2.0nm), consistent with the average diameter (~1.4nm) reported for Carbolex tubes. Interestingly, the AFM data in Fig.4(b) indicates that small diameter tubes are more commonly found after the HNO_3/DMF process than after the HCl/DMF, HCl/NMP or H_2O_2/HCl/NMP processes. The reason for this is not clear; it may be that an HNO_3-reflux preferentially functionalizes smaller diameter SWNTs, causing bundles containing them to be preferentially exfoliated. As observed in Fig,2(e), HNO_3 refluxed sample were functionalized by carboxylic acid and hydroxyl group.

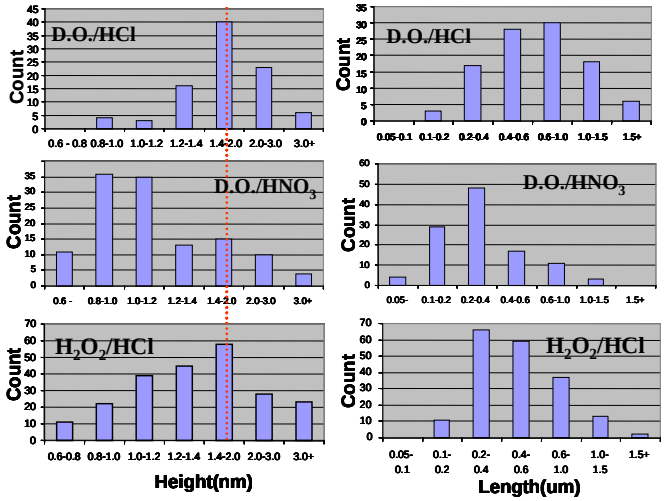

Figure 4. AFM Diameter (left) and length (right) distributions for arc-derived SWNTs after various purification and de-bundling processes.

We can define a quantitative measure of the success in debundling or dispersion by a "dispersion yield"(Y_D), defined as the fraction of the nanotubes found in the final solution as individual nanotubes. From data in Fig's 4(a)-(c) we find Y_D~50% for HCl/(DMF or NMP), Y_D~90% for HNO_3/DMF and Y_D~70% for H_2O_2/HCl/NMP. It is interesting that functionalized tubes by HNO_3 reflux or H_2O_2 reflux produce better dispersion yield in amid solvents. In one experiment, to investigate the effects of HNO_3 reflux on debundling, we then tried to disperse the bundled SWNT material in amides (DMF and NMP) after annealing HNO_3 refluxed SWNTs at 1100°C under vacuum (10^{-7} Torr). We found that the purified and high-T annealed material dispersed much less efficiently. This may be evidence that functional groups aid the debundling process in amid solvents. In Fig.4((d)-(f)) we exhibit the length distributions for the debundled tubes obtained from AFM z-scan analysis whose diameter distributions appear in Fig.4((a)-(c)). HNO_3-and HCl reflux were found to reduce the average tube length to ~300nm and ~800nm, respectively, whereas the H_2O_2/HCl/NMP(Fig.4(f)) exhibits shorter tube length(~500nm) than DO/HCl/NMP; H_2O_2 may cut the tubes, as proposed earlier.

Acknowledgement. This work was supported by NSF-DMR-0103585, and NSF-DMR-0304178 and the PSU MRSEC-DMR-0213623. C. A. Furtado thanks CNPq-Brazil for financial support.

References

[1] C. A. Furtado, U. J. Kim, H. R. Gutierrez, Ling Pan, E.C. Dickey, and Peter C. Eklund, accepted in J.Am.Chem.Soc in March,2004

[2] Kinoshita, K. In Carbon - Electrochemical and Pysicochemical Properties; John Wiley & Sons, Inc., Ed.; New York, 1988;Chapter 3.

[3] Bishun N. Khare, M. Meyyappan, Alan M. Cassell, Cattien V. Nguyen, and Jie Han, Nano Lett., V2, 2002, 73

CARBON NANOTUBES AS A CHEMICAL SENSOR

G. U. Sumanasekera[1], B. K. Pradhan[2], C. K. W. Adu[3], R. E. Romero[3], P. C. Eklund[3].

[1]Department of Physics, University of Louisville, KY 40292
[2]Columbian Chemicals Company, Marietta, GA 30062
[3]Department of Physics, Penn State University, University Park, PA 16802

Introduction

Carbon nanotubes have extremely interesting and unique chemical and physical properties. These properties are being investigated for vital applications such as field emission devices, actuators, nano-electronics, gas storage, etc.[1]. These application can involve individual nanotubes, individual bundle of nanotubes, or mats of entangled bundles of nanotubes. Recent reports show the capability of carbon nanotubes as chemical sensors. It has been demonstrated experimentally that very small concentrations of gas molecules (NO_2 and NH_3) can substantially change the electrical transconductance of individual field-effect transistors based on *semiconducting* nanotubes, and this property can be used for the design of high sensitivity chemical sensors[2]. In these cases, charge transfer is suspected to amplify the effect of adsorption. Other experimental investigations have shown that O_2 adsorption has a significant effect on the electrical transport of carbon nanotubes and induces a change in sign of the TEP [3–4]. Charge transfer [5] and the presence of defects [6,7] have been identified as important to the O_2–SWNT system. Interestingly, small systematic changes in the resistivity and the TEP of SWNTs were also observed due to collisions with non-reactive gases[8] and small molecules (He, Ne, Ar, Ne, Kr, Xe, N_2, CH_4, and H_2). In such cases, the changes in *S* and *R* upon gas exposure were identified as resulting from weak interactions between the gas and the metallic nanotubes that induce changes in the electron and hole free carrier lifetimes. These results also suggested that even gas collisions with the nanotube walls at a few hundred degrees celsius and 1 atm affect the transport properties of SWNTs]. In this paper, we present the results of a systematic study of the changes in the TEP and four-probe resistance of vacuum-degassed thin films of nanotube bundles induced by the adsorption of (a) polar alcohols ($C_nH_{2n+1}OH$; n = 1–4) and water (b) six-membered ring molecules (C_6H_{2n}; n = 3–6)]. Someya *et al* [9] have reported on the influence of alcohols on the characteristics of field-effect transistors (FET) fabricated from individual carbon nanotubes. They observed significant, reversible changes in the FET drain current when the device is exposed to various kinds of alcoholic vapors.

Experimental

The SWNT material studied here was obtained from CarboLex, Inc., and consisted of ~50-70 vol% carbon as SWNTs produced by the arc discharge method using a Ni–Y catalyst. Chemical purification of the arc-derived material was carried out in a two-step process: (1) oxidation in dry air for 30 min at 350 ^{0}C followed by (2) refluxing in 4 M HCl at
120 ^{0}C for 4 h. The purified SWNT material was then finally subjected to a ~10^{-7} Torr vacuum-degassing process at 1000 ^{0}C for 24 h. SWNT samples were in the form of thin films
of tangled ropes deposited from an ethanol suspension onto a glass substrate. Two chromel–Au/7 at.% Fe thermocouples and two additional Cu leads were attached with small amounts of silver epoxy to four corners of the 2 mm× 2 mm sample to measure the TEP and the DC four-probe electrical resistance simultaneously. The TEP (i.e., Seebeck coefficient) data were collected using a heat pulse technique[9]. The nanotube sample was also vacuum-degassed *in situ* in the TEP apparatus at 500 K before water or various $C_nH_{2n+1}OH$ molecular vapors were introduced. A glass bulb containing the water or alcohol or hydrocarbon liquids was connected via a valve to the TEP apparatus. All the chemicals were spectral grade (Sigma-Aldrich, Co.) and had been previously vacuum-degassed. After the thermoelectric and resistive responses to a particular molecular vapor were recorded, the sample was then degassed *in situ* at 500 K again until the TEP and four-probe resistance of the sample returned to the original 'degassed' values. Then the same film was exposed to the next molecular vapor and so on.

Results and Discussion

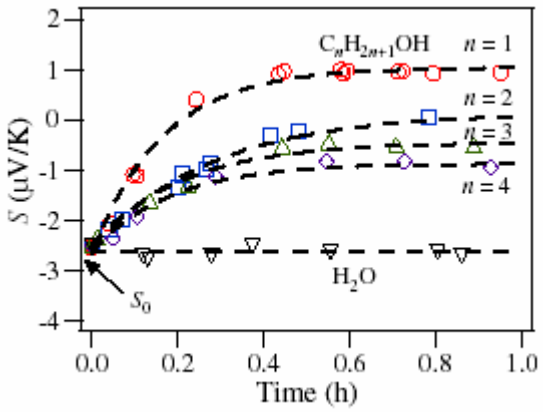

Figure 1. The time dependence of the TEP response of a SWNT thin film to successive exposure to vapours of water and alcohol molecules ($C_nH_{2n+1}OH$; n = 1–4) at 40 ^{0}C. Dashed curves are fits to *S(t)* data using an exponential function.

In Fig. 1 we show the *in situ* thermopower response to the vapors of alcohols and water. It is seen that for methanol, ethanol, isopropanol and butanol the TEP also rises exponentially with time from the degassed value S_0 ~ -2.7 μV/K to a higher plateau after ~1 h. For methanol and ethanol, *S* is even driven positive, saturating at S_{max} ~ +1.1 and +0.1 μV/K, respectively. Exposure to larger alcohol molecules, i.e., isopropanol and butanol, is found to lead to smaller changes in *S* and saturation at S_{max} ~ -0.5 and -1.0 μV/K, respectively. Interestingly, exposure to water vapour (another small, but very polar molecule) induces virtually no change in the TEP. Bradley *et al* [8] have also found very weak or no response of the TEP of mats of bundled SWNTs to water vapour. Concomitantly, exposure to methanol shows the largest change in the four-probe resistance *R*, with an increase of ~8.2%. The exposure to methanol, ethanol, isopropanol, butanol and water induce an increase in R, with $\Delta R/R$ saturating at ~8.2%, 7.5%, 6.8%, 5.4% and 4.4%, respectively. Both *R(t)* and *S(t)* exhibit simple exponential behavior.

Figure 2 displays the evolution of the thermopower versus the fractional change in the four-probe resistance ($\Delta R/R_0$) at fixed temperature (40 ^{0}C). As the coverage of the molecules on the SWNTs increases with increasing time of exposure to the respective molecular vapour, both *S* and $\Delta R/R_0$ increase. It is very important to note that the data for all the alcohols show linear behaviour for *S* versus $\Delta R/R_0$, consistent with physisorption and not for a chemisorption process involving significant charge transfer. Thus, the linearity of *S* versus $\Delta R/R_0$ implies that little or no charge transfer is taking place between the adsorbedmolecules and the SWNTs; i.e.,

H_2O and the alcohols that are physisorbed onto high *T* annealed films do not chemically dope the SWNTs.

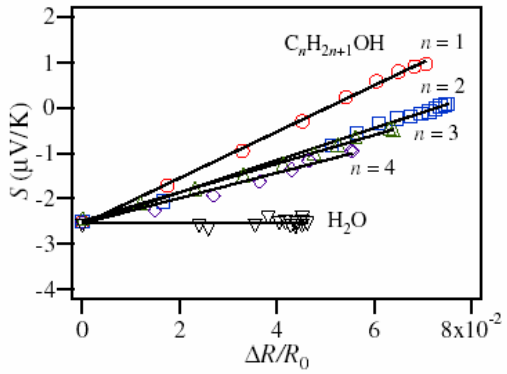

Figure 2. *S* versus $\Delta R/R_0$ plots during exposure of degassed SWNT bundles to water and $C_nH_{2n+1}OH$; *n* = 1–4. The solid lines are linear fits to the data until saturation is established.

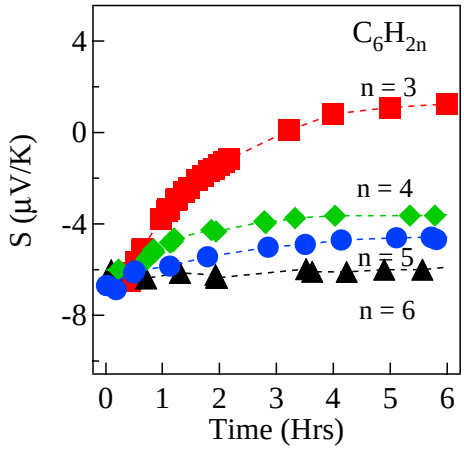

Figure 3. In situ 40 ^{0}C thermoelectric power (S) vs time (t) during successive exposure of a degassed SWNT film to vapors of six-membered ring molecules C_6H_{2n}; n = 3–6. The dashed lines are guides to the eye.

In Fig. 3 we show the *in situ* thermopower response with time to the vapors of benzene (C_6H_6), 1,3-cyclohexadiene (C_6H_8), cyclohexene (C_6H_{10}), cyclohexane (C_6H_{12}). For C_6H_6 (benzene), with increasing exposure time, the thermopower is seen to increase with time from its initial (degassed) value *S* = -6.4 μV/K, eventually saturating after ~6 h at a positive value *S* = +13 μV/K. Subsequent exposure to 1,3- cyclohexadiene leads to a similar time dependence of the thermopower and a saturation at ~3.6 μV/K. Cyclohexene was studied and found to induce a smaller change in thermopower, saturating at *S*= 46 μV/K. Interestingly, cyclohexane, which has no π electrons, was found to exhibit no detectable change in the thermopower. Concomitantly, exposure to benzene shows the largest change in resistance with an increase of 13% at saturation. 1,3-Cyclohexadiene and cyclohexene induce increases in resistance saturating at 10% and 7%, respectively. Consistent with the thermopower results, exposure to cyclohexane shows essentially no change in four-probe resistance. Fig. 4 shows the S vs $\Delta R/R_0$ for each C_6H_{2n}; n = 3–6. As shown in Fig. 4, a universal behavior (i.e., independent of *n*) is observed for the dependence of the thermopower on the change in resistance $\Delta R/R_0$. This non-linear character in the C_6H_{2n}/SWNT system is not well understood, and we have tentatively identified it with a multiple-electron-scattering process].

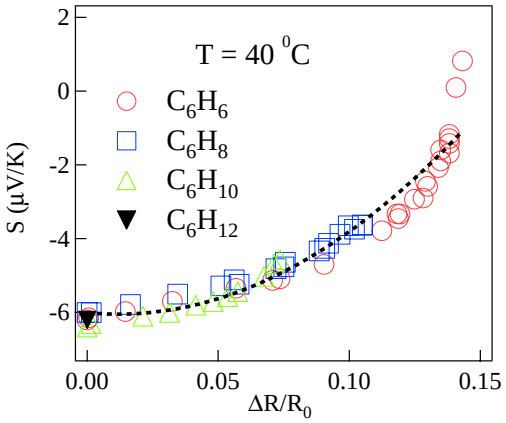

Figure 4. *S* vs $\Delta R/R_0$ during exposure to C_6H_{2n}; n = 3–6. The dashed curve is a fit of a quadratic function

Conclusions

We have utilized *in situ* measurements of TEP and resistivity to investigate the adsorption of various hydrocarbons with varying number of π electrons, polar molecules (alcohols and water) in bundled SWNTs. We observe a strong effect on both the TEP and resistivity for methanol, ethanol, isopropanol and utanol.Surprisingly, water vapour does not have any effect on the TEP. We have also observed that *S* exhibits a linear relationship with $\Delta R/R_0$, consistent with the creation of a new impurity scattering channel via physisorption. We observe strong, systematic effects on the resistance and thermopower for six-membered ring hydrocarbons and a universal behavior is observed for *S* vs $\Delta R/R_0$.

References

(1) Dresselhaus, M. S; Dresselhaus, G; Eklund; P. C., 1996 *Science of Fullerenes and Carbon Nanotubes* (San Diego, CA: Academic)

(2) Kong; J., Franklin; N. R., Zhou; C., Chapline; M. G., Peng; S., Cho; K ., Dai; H., **2000** *Science, 287* 622

(3) Collins, P. G.; Bradley, K.; Ishigami, M.; Zettl, A., *Science*, **2000**, *287*, 1801

(4) Sumanasekera, G. U.; Adu, C. K. W.; Fang, S. L.; Eklund, P. C., *Phys. Rev. Lett.*, **2000**, *85*, 1096

(5) Jhi, S-H; Louie, S. G.; Cohen, M. L., *Phys. Rev. Lett*, **2000**, *85*, 1710

(6) Ulbricht H.; Moos, G.; and Hertelet al, *Phys. Rev. B*, **2002**, *66*, 075404 (2002)

(7) Goldoni; A., Larciprete; R., Petaccia; L., Lizzit; S., **2003** *J. Am. Chem. Soc. 125* 11329

(8) Adu, C. K. W.; Sumanasekera, G. U.; Pradhan, B. K.; Romero, H. E.; Eklund, P. C., *Chem. Phys. Lett.*, **2001**, *337*, 31

(9) Someya; T., Small; J., Kim; P., Nuckoll; C., Yardley; J. C., **2003** *Nano Lett. 3* 877

(10) Sumanasekera, G. U.; Grigorian, L.; Eklund, P.C., Meas. Sci. Technol., **2000**, *11*, 273

CARBON NANOTUBE NANOELECTRONIC DEVICES FOR CHEMICAL DETECTION IN LIQUID HYDROCARBONS

Alexander Star, Keith Bradley, Jean-Christophe P. Gabriel and George Grüner

Nanomix Inc.
5980 Horton Street, Suite 600.
Emeryville, CA 94608

Introduction

Hydrocarbon fuels are complex mixtures of 150-260+ aliphatic and aromatic hydrocarbon compounds containing varying concentrations of benzene, n-hexane, toluene, xylenes, naphthalene, and certain n-C9-C12 fractions.[1] Due to their natural petroleum base, the chemical composition of different hydrocarbon fuels is not defined, and the fuels are classified according to broad performance criteria such as flash and boiling points, complicating chemical comparisons. The recent emergence of nano-scale electronic devices offers the opportunity for extremely sensitive detection of chemicals by monitoring the device characteristic when the devices or their components are exposed to an environment where the chemicals are present.

In this work, we have used field-effect transistors fabricated using semiconducting carbon nanotubes (NTFETs).[2] Such devices have been recently explored as chemical sensors.[3,4] The response of the device characteristics to chemical analytes in the gas phase occurs through charge transfer between the nanotube conducting channel and the analytes, as evidenced by experiments involving electron donating (NH_3) and electron withdrawing (NO_2) molecules.[4]

Experimental

NTFET Devices. NTFET and NTNFET devices were prepared according to published procedures,[5] using standard photolithography techniques on 100 mm wafers. NTFET devices were fabricated using SWNTs grown by chemical vapor deposition (CVD) at 900°C using dispersed iron nanoparticles as growth promoter and a methane/hydrogen gas mixture. Electrical leads were patterned on top of the nanotubes from titanium films 30 nm thick capped with a gold layer 120 nm thick. A fair proportion of the tens of thousands of devices made on each wafer are p-type NTFET with a modulation of 1 (tested using an autoprober), indicative that for those devices only semiconducting nanotubes are present. The devices used in this study were selected among those.

Electronic Measurements. Electronic measurements of NTFET devices, such as current flow between S/D electrodes as a function of applied gate voltage, were conducted using a semiconductor parameter analyzer (Keithley 4200). Devices in air were contacted with pin probes. A glass pipette was used to position a drop of liquid on the device. Chemicals were purchased from Aldrich and used as received.

Results and Discussion

Figure 1 depicts the schematic layout of the NTFET device architecture. SWNTs on silicon substrates contacted with metal (Ti / Au) contacts, together with a doped Si back gate, form the basic elements of the NTFET. In the actual devices, multiple nanotubes were connecting the source and drain electrodes. We have monitored the change of the source-drain current (I) as a function of the gate voltage (Vg) both with increasing and decreasing gate voltages. In devices that have a multitude of nanotubes, both metallic and semiconducting nanotubes contribute to the source-drain current. For the experiments reported here, devices dominated by semiconducting nanotube transistor channels were selected using a wafer autoprober.

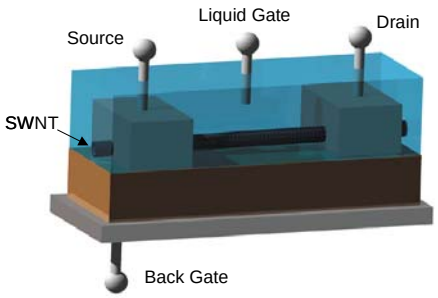

Figure 1. Detection in liquids with NTFET devices by using either back gate or liquid gate configurations.

As expected, the conductivity of the liquids plays an important role in NTFET device operation using a silicon back gate. With conductive liquids, such as water, (i) the screening of the gate voltage prevents gating of the device, (ii) the liquid provides an additional conduction channel, and (iii) mobile ions associated with the conducting liquid lead to a large hysteresis. On the other hand, in liquids with low conductivity such as cyclohexane and toluene, the device conductance is dominated by the nanotube channel and the operation of NTFET changes little as compared to air.

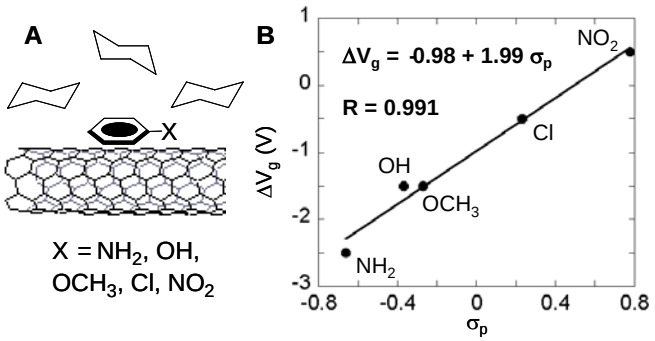

Figure 2. Detection of aromatic compounds with NTFET devices. (A) Schematic of a single wall carbon nanotube conducting channel with a monosubstituted benzene molecule adsorbed on the side-wall of the nanotube in a cyclohexane solution. (B) Linear regression analysis of the gate voltage shift (ΔV_g) of devices in 0.1M cyclohexane solutions of the selected aromatic compounds.

We have explored[6] the effects of monosubstituted benzene compounds, such as aniline, phenol, anisole, toluene, chlorobenzene, and nitrobenzene, on the NTFET device characteristic (**Figure 2**). The compounds all have similar geometry in their non-covalent binding to the carbon nanotube conducting channel, but substituent groups on the benzene ring provide different inductive and resonance effects upon binding. Consequently their relative electron donating effects (NH_2>OH>OCH_3>Cl>NO_2) are well known. The charge transfer to the nanotube channel can be estimated from the empirical Hammett constants (σ_p) of the substituents on these aromatic compounds. A clear linear relation with a positive slope (ρ value) of +1.99 is found between the gate voltage shift and the Hammett values (**Figure 2B**).[6]

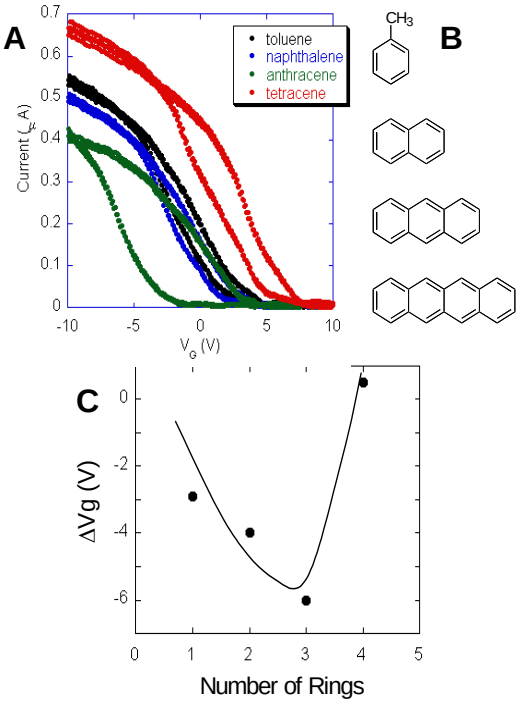

Figure 3. Comparison of number of aromatic rings with the NTFET response, i.e. I-Vg dependence. (A) The response to 0.5 mM solutions of naphthalene, anthracene, and tetracene in toluene, as compared to pure toluene solvent. (B) Chemical structures of the aromatic compounds. (C) Threshold gate voltage shift as a function of the number of aromatic rings in the studied compounds. Threshold shift (ΔVg) is calculated as a shift of the device characteristics in air.

We have also explored the effect of a number of aromatic rings on the NTFET device characteristics. Source-drain current dependence on the gate voltage, I-Vg, shows significant shift in threshold values when larger aromatic compounds, such as naphthalene, anthracene, and tetracene were added to toluene. (**Figure 3A)** The value and the direction of the threshold shift is characteristic for each aromatic compound. While the binding energy of aromatic compounds increases with the number of rings, the charge transfer to nanotube transistor channel is expected to remain the same per aromatic ring unit. The exposure to toluene solvent (one ring) results in ~3 V threshold shift to more negative gate voltage values, as compare to air. The addition of larger aromatic compounds with two and three rings in toluene results in progressive negative shift. However, the addition of tetracene (four rings) introduce an unexpected positive shifts (**Figure 3C**). The observed change in the response is probably due to curvature of carbon nanotubes. These results imply that NTFET can be potentially used for characterization of aromatic hydrocarbons, not only by their charge transfer to carbon nanotube transistor channel, but also by their geometrical parameters.

In addition to aliphatic and aromatic hydrocarbons, hydrocarbon fuels may contain certain additives, such as amines, alcohols and ethers (MTBE). NTFET devices have been already shown to be sensitive to different alcohols[7] and amines.[8] Here, we have investigated the selectivity of the response to amino compounds of the NTFET device characteristics. The addition of amino compounds into cyclohexane solution result in a significant threshold shift (**Figure 4A**). This threshold shift is analogous to the concentration-dependent shift observed when NTFET devices with liquid gate were exposed to aqueous ammonia.[9] The response to amines is selective as evident from the control experiment, where oleic acid, an organic acid with approximately same number of carbons, was dissolved in cyclohexane (**Figure 4B**).

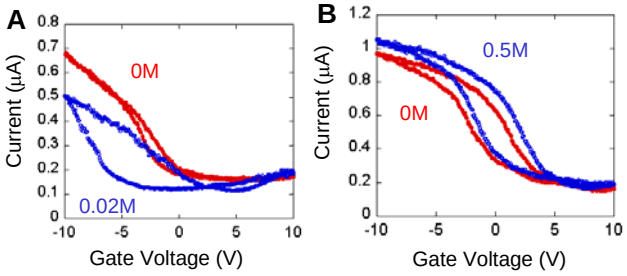

Figure 4. Detection of amino compounds by NTFET. The device characteristics, I-Vg in the presence and absence of the chemical. (A) Response to 0.02 M of 1-hexyldecylamine in cyclohexane. (B) Control experiment with 0.5 M of oleic acid in cyclohexane.

Conclusions

We have shown that NTFETs can be used for selective detection of aromatic hydrocarbons and amino compounds in the presence of aliphatic / aromatic hydrocarbons. Potentially, NTFET devices can be used as small low power electronic probes to monitor hydrocarbon fuel composition, including amine and ethanol fuel additives both in vapor and liquid phases.

Acknowledgment. We acknowledge the Nanomix technical staff for their assistance with device fabrication and measurements. This work was supported partially by Environmental Protection Agency, under contract EP-D04-045.

References

1. Ritchie, G. D., Still, K. R., Alexander, W. K., Nordholm, A. F., Wilson, C. L., Rossi, J., Mattie, D. R., *J. Toxicol. Env. Health*, **2001**, *4*, 223-312.
2. Tans S., Verschueren A., Dekker C., *Nature* **1998**, *393*, 49–52.
3. Collins P. G., Bradley K., Ishigami M., Zettl A., *Science* **2000**, *287*, 1801–1804.
4. Kong J., Franklin N. R., Zhou C., Chapline M. G., Peng S., Cho K., Dai H., *Science* **2000**, *287*, 622–625.
5. Gabriel, J.-C. P., *Mat. Res. Soc. Symp. Proc.* **2003,** *762*, Q.12.7.1-7.
6. Star, A., Han, T.-R., Gabriel, J.-C. P., Bradley, K., Grüner, G., *Nano Lett.* **2003**, *3*, 1421-1423.
7. Someya, T., Small, J., Kim, P., Nuckolls, C., Yardley, J. T., *Nano Lett.*, **2003**, 3, 877-881.
8. Kong, J., Dai, H., *J. Phys. Chem. B* **2001**, *105*, 2890-2893.
9. Bradley, K., Gabriel, J.-C. P., Briman, M., Star, A., Grüner, G., *Phys. Rev. Lett.* **2003**, *91*, 218301.

H_2 SEPARATION THROUGH ZEOLITE THIN FILM MEMBRANES

Margaret E. Welk, Tina M. Nenoff

Sandia National Laboratories, PO Box 5800, MS 0734, Albuquerque, NM 87185-0734
mewelk@sandia.gov

Introduction

The synthesis and testing of inorganic zeolite membranes has been intensely studied because of their potential applications in the domains of gas separation, pervaporation, reverse osmosis and in the development of chemical sensors and catalytic membranes.[1,2,3,4,5] Specifically, development of new technologies, such as zeolite membranes, for H_2 separation and purification has a high priority for the future of H_2 as a fuel source. H_2 is commonly produced by the reformation of hydrocarbons, creating CO_2, CO, CH_4 and H_2O as by-products. A successful membrane for the separation of H_2 from other reformate gases must have both high flux and high selectivity for H_2 in the presence of these other gas species. Inorganic membranes, which have good thermal stability and chemical inertness, are highly attractive. Distinctively, zeolite membranes combine pore size and shape tunability with the inherent mechanical, thermal, and chemical stability necessary for long term separations. The effective pore size distribution, and hence the separation performance, of a defect free zeolite membrane is intrinsically governed by the choice of the zeolitic phase.[6,7,8,9]

Numerous pure gas permeation studies have been performed on MFI-type zeolite membranes that allow ideal selectivities to be calculated.[10,11,12,13,14,15,16,17,18,19,20,21] Typical literature selectivity values of H_2 from CO_2, CH_4 and CO range from 2 to 8, below the values necessary for successful industry integration. It is well recognized that gas mixtures flowing through separation membranes will behave differently than pure gases owing to adsorption effects and other phenomena. We report here the study of the permeance and selectivity of both ZSM-5 and silicalite-1 zeolite membranes under the flow of three gas mixtures, two chosen as benchmarks (50/50 mol% H_2/CH_4 and 50/50 mol% H_2/CO_2) and one chosen to emulate an industrial methane reformate stream. The H_2 selectivities for both membranes outstrip the calculated ideal selectivity values from pure gas data by eight times or more.

Experimental

Gases. Reagent grade pure gases were purchased from Matheson Trigas. H_2, CO_2, O_2, CH_4, N_2, CO were used to test the permeability of the membranes. SF_6 was used to asses membrane quality, He was used to clean and purge the unit, shown in Figure 1. Three reagent grade gas mixtures pre-mixed by Matheson Trigas were also tested: 50/50 mol% H_2/CH_4, 50/50 mol% H_2/CO_2 , and a four gas component mixture that approximates a methane steam reformate stream, excluding the water vapor (will be referred to as the reformate mixture) : 76.2% H_2, 13.6% CO_2, 6.8%CO, and 3.4% CH_4.

Membrane Synthesis. A thorough description of the silicalite membrane growth has been published elsewhere.[22] The support cleaning, seed synthesis,[12,22] and seeding methodology for the ZSM-5 membranes are identical to the steps for silicalite also can be found in the same reference. A description of the ZSM-5 gel and hydrothermal synthesis of the ZSM-5 membranes is presented here.

In the gel used for the hydrothermal synthesis, the silicon source for the membrane synthesis was colloidal silica Ludox SM-30; the source of aluminum was $Al_2(SO_4)_3{\cdot}18H_2O$, and NaOH is the alkalinity source. Ludox SM-30 was filtered prior to use to remove any SiO_2 flakes; all other reagents were used as received. 2.14 g of NaOH, and 0.832 g of $Al_2(SO_4)_3{\cdot}18H_2O$ were added to 68.4 g of H_2O, and stirred until dissolved. 20 g of Ludox SM-30 was added drop-wise to the mixture while stirring. Each gel was then aged for 24 hours while being stirred at room temperature. Gels that were not aged under agitation did not result in selective membranes. The aged gels in this work were homogeneous and no precipitate had formed prior to the reactions.

The alpha-alumina substrates supplied by Inocermic Gmbh have a 1.8 μm average pore size, a diameter of 13 mm and a thickness of 1 mm. Their high density ensures good mechanical properties and robustness. MFI zeolite seeds were rubbed onto both sides of the cleaned substrates; the seed synthesis and application has been described elsewhere.[23] The seeded substrates were held vertically in the Teflon lined Parr reactor using Teflon holders to prevent sedimentation on top of the membrane. The homogenous gel was then poured in the reactor until the membrane was fully immersed. The hydrothermal syntheses were carried out in Parr reactors with a 23 ml Teflon liner at 170°C for 12 hours under autogenous pressure.

After the hydrothermal synthesis, the two-sided membrane was removed from autoclave, washed with DI water and dried in air at 50°C for few hours. A permeation test on the as-synthesized, uncalcined membrane allows the rapid assessment of its quality before the time-consuming calcination step. At this stage, a good quality membrane should be impermeable for SF_6. The SF_6 kinetic diameter of 5.5 Å is similar to the pore dimensions of the calcined ZSM-5 zeolite (diameter range 5.1 – 5.6 Å). Substantial SF_6 diffusion through the uncalcined membrane indicates the presence of detrimental membrane defects larger than the zeolite pores which will be opened during calcination.[23] Any existing large defects (partial coverage of the substrate and micro-cracks) may be repaired by a second hydrothermal synthesis step, using a shorter reaction time and more diluted starting gel.

Once the quality of the membrane was established, the water was removed from the membrane pores by calcination in air. A calcination temperature of 600°C led to cracks in the membrane and drastic reduction in permeation performance unless a slow temperature ramp rate was used. The stress at the interface between the zeolitic layer and the alumina substrate due to thermal expansion mismatch has to be minimized by using slow heating rates,[24] below 1°C/min. A typical successful temperature profile for the calcination is a heating and cooling rate of 0.5°C/min with a maximum temperature of 600°C maintained for 6 hours. This ensures the removal of water from the pores without creating detrimental defects within the membranes.

Characterization Techniques. The zeolite membranes were characterized by X-ray diffraction (Siemens D500 diffractometer, Cu Kα radiation, Bragg-Brentano geometry) and by Scanning Electron Microscopy (JEOL–6300V equipped with a Link Gem Oxford 6699 EDAX attachment).

Permeation Measurements. The membrane permeations were measured at room temperature using pure and mixed gases and a constant trans-membrane pressure of 16 PSI controlled by a backpressure regulator (see Figure 1). The membrane was sealed in a Swagelok fitting using Viton O-rings. The gas flow through the membrane was measured using an acoustic displacement flowmeter (ADM 2000 from J&W) and a digital bubble flowmeter (HP-9301). Between permeation measurements with different pure (SF_6, H_2, CO_2, O_2, CH_4, N_2, CO) and mixed (50/50 H_2/CO_2, 50/50 H_2/CH_4, and the reformate mixture) gases, the whole system was purged, flushed with He and evacuated several times. For the pure gases, the ideal gas selectivity was calculated as the ratio of the permeances in the steady regime.

Residual Gas Analyzer. For the mixed gas studies, an RGA (Stanford Research Systems QMS 200 Residual Gas Analyzer) in Pressure vs. Time graphing mode was attached to the permeate side of the membrane. The RGA tracks the partial pressure of each gas species over time using an internal mass spectrometer. Data points are taken once per second. Before each run, both sides of the membrane were evacuated and flushed with He three times. The permeate side of the membrane was then filled with He to atmospheric pressure, and the retentate side was evacuated just prior to the initiation of mixed gas flow. A constant trans-membrane pressure of 16 PSI was controlled by the back pressure regulator. Selectivities were calculated as the ratio of the partial pressures of the gas species of interest.

Results and Discussion

The mixed gas permeance and selectivity results have been presented elsewhere.[25] Table 1 below includes the selectivity data, where selectivity = $[y_i/(1-y_i)]_{permeate}/[y_i/(1-y_i)]_{inlet}$. Please see reference 25 for graphs and additional details.

Table 1. H_2 Selectivity Through ZSM-5 and Silicalite Membranes Using Gas Mixtures

	Reformate Mix	50/50 H_2/CO_2	50/50 H_2/CH_4
ZSM-5 H_2 Selectivity	58.8	60.1	39.4
Silicalite-1 H_2 Selectivity	21.5	22.9	16.9

According to the pure gas data, the ZSM-5 membrane was calculated to have an ideal selectivity for H_2 from the other reformate gases around 4 to 10, depending on the gas species.[25] In both 50/50 gas mixtures, the actual selectivities jumped almost 8-fold to 39.4 and 60.1. The selectivity for H_2 in the reformate mixture jumped to 58.8, a value more than six times that of the pure gas approximation.

Both ZSM-5 and Silicalite-1 are MFI type zeolites. Although they have identical structures, the pore chemistry differs owing to the presence of even a small amount of aluminum replacement of the silicon atoms in the ZSM-5 compound. The pore chemistry directly impacts adsorption and therefore, the permeation characteristics of the membranes, particularly the pure gas permeation results. Silicalite-1 membranes have a higher permeance for pure CO_2 than for pure H_2 because of the adsorption of CO_2 to the all-silica pore surfaces, while the ZSM-5 membranes show a strong preference for H_2, even though the percentage of aluminum substituting for silicon is very small – 0.25%. With gas mixtures, the silicalite membranes are selective for H_2, having lower H_2/CO_2 selectivities as compared with the ZSM-5 membranes for the 50/50 H_2/CO_2, the 50/50 H_2/CH_4 and the reformate gas mixtures.

Conclusions

The testing of the permeation of mixed gases through both ZSM-5 and Silicalite-1 zeolite membranes has revealed the extraordinary selectivities of these membranes for H_2. The ZSM-5 membrane had the following H_2 selectivities for the 50/50 H_2/CH_4 mixture, the 50/50 H_2/CO_2 mixture and the reformate mixture respectively: 39.4, 60.1, and 58.8, respectively. The silicalite membrane had lower H_2 selectivities for the same gas mixtures, 16.95, 22.9 and 21.73. The high permeances and extremely high selectivities of these membranes make them viable choices for H_2 gas separation applications.

Further studies on these MFI-type membranes continue, and include elevated temperatures, increased lifetime studies, pressure variations, and additional gas mixtures. We will also investigate different microporous materials as well as b-axis oriented MFI type zeolite membranes. The effects of different support materials on membrane performance are also under investigation.

Acknowledgement. Sandia is a multiprogram laboratory operated by Sandia Corporation, a Lockheed Martin Company, for the United Stated Department of Energy under contract DE-AC04-94-AL85000. We thank the DOE/Hydrogen, Fuel Cells, and Infrastructure Technologies Program for continued funding. We also wish to acknowledge MesoFuel, Inc. for constructive discussions, collaborations, and industrial perspective.

References

[1] Armor, J. N. *J. Membr. Sci.* **1998**, *147*, 217.
[2] Caro, J.; Noack, M.; Kolsch, P.; Schafer, R. *Microp. Mesop. Mat.* **2000**, *38*, 3.
[3] Chiang, A. S. T.; Chao, K-J. *J. Phys. Chem. Solids* **2001**, *62*, 1899.
[4] Noack, M.; Kolsch, P.; Schafer, R.; Toussaint, P.; Caro, *J. Chem. Eng. Technol.* **2002**, *25*. 221.
[5] Thoma, S. G.; Trudell, D. E.; Bonhomme, F.; Nenoff, T. M. *Microp. Mesop. Mat.* **2001**, *50*, 33.
[6] Vroon, Z. A. E. P.; Keizer, K.; Gilde, M. J.; Verweij, H. Burggraaf, A. J. *J. Membr. Sci.* **1996,** *113*, 293.
[7] Geus, E. R.; DenExter, M. J.; van Bekkum, H. *J. Chem. Soc. Faraday Trans.* **1992,** *88*, 3101.
[8] Bakker, W. J. W.; Kapteijn, F.; Poppe, J.; Moulijn, J. A. *J. Membr. Sci.* **1996**, *117*, 57.
[9] Bai, C.; Jia, M-D.; Falconer, J. L.; Noble, R. D. *J. Membr. Sci.* **1995,** *105*, 79.
[10] Lai, R. ; Gavalas, G. R. *Ind. Eng. Chem. Res.* **1998**, *37*, 4275.
[11] Hedlund, J.; Noack, M.; Kolsch, P.; Creaser, D.; Caro, J.; Sterte, J. *J. Membr. Sci.***1999,** *159*, 263.
[12] Tuan, V. A.; Falconer, J. L.; Noble, R. D. *Ind. Eng. Chem. Res.* **1999,** *38*, 3635.
[13] Lai, R.; Gavalas, R. *Microp. Mesop. Mat.* **2002,** *38*, 239.
[14] Xomeritakis, G.; Nair, S.; Tsapatsis, M. *Microp. Mesop. Mat.* **2000,** *38*, 61.
[15] Hedlund, J.; Sterte, J.; Anthonis. M.; Bons, A. J.; Carstensen, B.; Corcoran, N.; Cox, D.; Deckman, H.; De Gijnst, W.; de Moor, P-P.; Lai, F.;McHenry, J.; Mortier, W.; Reinoso, J.; Peters, J. *Microp. Mesop. Mat.* **2002,** *52*, 179.
[16] Noack, M.; Kolsch, P.; Schafer, R.; Toussaint, P.; Sieber, I.; Caro, J. *Microp. Mesop. Mat.* **2002,** *49*, 25.
[17] Lai, Z. P.; Bonilla, G.; Diaz, I.; Nery, J. G.; Sujaoti, K.; Amat, M. A.; Kokkoli, E.; Terasaki, O.; Thompson, R. W.; Tsapatsis, M.; Vlachos, D. G. ***Science***, **2003,** *300*, 456.
[18] Xomeritakis, G.; Lai, Z.P.; Tsapatsis, M. *Ind. Eng. Chem. Res.* **2001,** *40*, 544.
[19] Lovallo, M. C.; Tsapatsis, M *AICHE Journal* **1996,** *42*, 3020.
[20] Lovallo, M. C.; Gouzinis, A.; Tsapatsis, M. *AICHE Journal* **1998,** *44*, 1903.
[21] Poshusta, J. C.; Noble, R. D.; Falconer, J. L. *J. Membr. Sci.* **1999,** *160*, 115.
[22] Bonhomme, F; Welk, M. E.; Nenoff, T. M.; *Microp. Mesop. Mat.* **2003,** *66*, 181.
[23] Breck, D.W. Zeolite Molecular Sieves, (John Wiley and Sons, New York 1997).
[24] Dong, J.; Lin, Y. S.; Hu, M. Z. C.; Peascoe, R. A.; Payzant, E. A. *Microp. Mesop. Mat.* **2000,** *34*, 241.
[25] Welk, M. E.; Nenoff, T. M. *J. Membr. Sci.* **2004** submitted.

HYDROGEN GAS SEPARATIONS USING A HIGHLY MICROPOROUS POLYMER

Chad L. Staiger, Chris J. Cornelius & David R. Wheeler

Chem & Biotechnologies/Micro Analytical Systems Departments
Sandia National Laboratories, PO Box 5800, MS 0888
Albuquerque, NM 87185-0888 e-mail: clstaig@sandia.gov

Introduction

Increasing interest by governmental entities to realize a future in which hydrogen is a dominating fuel source has spurred great interest in all aspects of hydrogen production, storage and utilization. Currently, hydrogen is produced by reforming fossil fuels (natural gas, oil, and coal). The capital and energy intensive reforming step does not produce pure hydrogen, but a mixture of light gases (syngas). Current methods for hydrogen purification/separation include pressure swing adsorption or cryogenic technologies. While these technologies work well, membranes for hydrogen separation represent an attractive alternative to further lower the costs of hydrogen production. Recently, McKeown *et al* reported a series of highly porous polymers (**1**) which have good thermal and mechanical stability.[1-3] The bisspiroindane ring system induces an extreme amount of contortion into the polymer backbone. Rotational freedom in the polymer backbone is limited because of the ladder structure. The contortion and rigidity allow a high degree of void volume to exist. High polymer void volumes typically lead to increased gas throughput (permeability), however selectivity can be negatively affected.[4,5] We have prepared one of these microporous polymers and evaluated its permeability and selectivity for use in hydrogen and other light gas separations.

Scheme 1. Preparation of spiro polymer **1**.

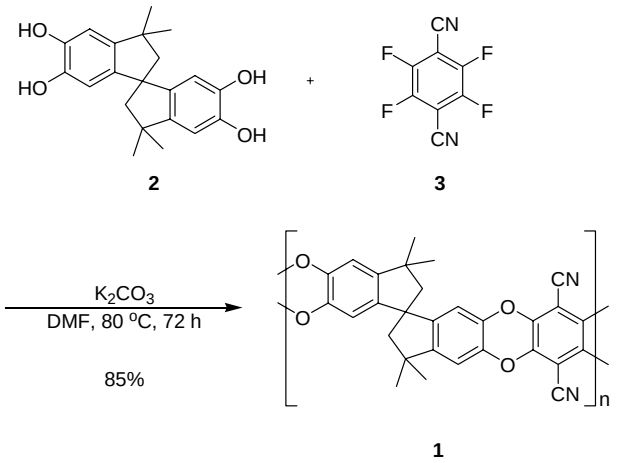

Experimental

All solution NMR spectra were recorded on a Bruker Avance DRX spectrometer. Proton spectra were obtained at an operating frequency of 400 MHz. Infrared spectra (FTIR) were obtained using a Perkin Elmer Model 1600 FTIR spectrometer. Thermal analyses were performed on a Perkin Elmer TGA 7 and a TA 2010 DSC. Size exclusion chromatography was performed using a Polymer Labs PL-GPC210 operating at 40 °C equipped with RI detection. The mobile phase was THF at a flow rate of 1.00 mL/min. Separation was affected using two 300 × 7.5 mm PLgel 5 μm mixed-C columns. Calibration curves were generated using polystyrene standards. Surface area and pore analysis obtained by N_2 adsorption at 77 K using a Quantachrome Autosorb 6B. Membrane permeabilities were obtained using a home made permeation apparatus described elsewhere.[6] Reagents and anhydrous grade solvents (Aldrich or Acros) were used as received unless otherwise stated.

Poly(3,3,3',3'-tetramethyl-1,1'-spirobisindane-5,5',6,6'-tetrol-*co*-2,3,5,6-tetraflourophthalonitrile) (1). A mixture of K_2CO_3 (6.91 g, 50.0 mmol), 3,3,3',3'-tetramethyl-1,1'-spirobisindane-5,5'6,6'-tetrol (3.40 g, 10.0 mmol) and 2,3,5,6-tetraflourophthalonitrile (2.00 g, 10.0 mmol) were stirred in DMF (50 mL) at 80 °C for 72 h. The heterogeneous solution was cooled to room temperature and then poured into rapidly stirred H_2O (300 mL). The solid was collected by vacuum filtration and washed with MeOH (2 × 100 mL). The bright yellow solid was taken up in a minimum amount of THF (~25 mL) and precipitated into rapidly stirring MeOH (400 mL). The polymer was collected by vacuum filtration and dried under vacuum (0.1 mm Hg @ 50 °C) to give 4.07 g (88%) of a bright yellow solid. ^{1}H NMR (400 MHz, $CDCl_3$) δ6.90-6.70 (br s, 2H), 6.60-6.30 (br s, 2H), 2.70-1.90 (br m, 4H), 1.70-0.80 (br m, 12H). IR (KBr) ν 2959, 2235, 1452, 1314, 1011 cm^{-1}. GPC: M_w=90,010; M_n=30,800; PDI = 2.92. BET surface area = 818 m^2/g.

Film preparation of spiro polymer 1. Spiro polymer **1** (550 mg) was dissolved in CH_2Cl_2 (15 mL) and filtered (2 μm glass microfiber). The filtered solution was pouring into a flat Petri dish (12 cm dia.) and then placed in a vacuum dessicator with the gas inlet open to the atmosphere. The solution was allowed to evaporate for 4 days. The dish was removed and the clear yellow film released from the glass using H_2O.

Results and Discussion

A prototypical microporous polymer **1** was prepared by heating a DMF solution of 3,3,3',3'-tetramethyl-1,1'-spirobisindane-5,5'6,6'-tetrol and 2,3,5,6-tetraflourophthalonitrile at 80 °C for 72 h in the presence of K_2CO_3 (Scheme 1). After cooling the solution, polymer **3** was precipitated by pouring into water. The bright yellow polymer was further purified by dissolving in THF and reprecipitated by pouring into methanol. Yields of the polymer **1** after drying under vacuum were generally in excess of 85%. Size exclusion chromatography revealed a molecular weights typically greater than 100,000 (M_w) with a PDI's of 3 to 3.5.

The thermal stability of polymer **1** was investigated using DSC and TGA under an atmosphere of nitrogen. The DSC was unremarkable with the exception of a decomposition event with an onset of 395 °C. There was no discernable glass transition (T_g) present. The TGA showed the onset of weight loss at 484 °C and by 800 °C had only lost 55% of the original mass. The high thermal stability of spiro polymer **1** can be attributed to its ladder structure, since two bonds must be broken to cleave the polymer backbone.

Surface area analysis of spiro polymer **1** by N_2 adsorption/desorption revealed a highly porous structure. The surface area, calculated from BET, was 818 m^2/g. The pore volume at 0.99 relative pressure (P/P_o) was 1.06 cc/g. The pore size distribution (BJH Desorption) suggested a significant number of pores between 20 and 30 Å. The microporosity of the material (pore size < 20 Å) is currently being evaluated.

Spiro polymer **1** films were cast into free standing films (~60 μm thick) from CH_2Cl_2 and then subjected to gas permeability

measurements. Single gas permeabilities were measured for helium, hydrogen, carbon dioxide, oxygen, nitrogen and methane at 35 ^{o}C using the time lag method (Table 1). Spiro polymer **1** showed high permeability for each gas, with H_2 having the highest permeability of 1763 Barrers. In addition, permselectivities were particularly good for O_2/N_2, H_2/CH_4 and CO_2/CH_4 with respect to there permeabilities.[7]

Table 1. Single gas permeabilities and ideal permselectivities of spiro polymer 1. Permeabilities are the average of two different films.

Permeability at 35 ^{o}C (Barrers)

He	H_2	CO_2	O_2	N_2	CH_4
877	1763	1590	496	135	157

Ideal Permselectivity

He/H_2	0.5	H_2/CO_2	1.1	CO_2/O_2	3.2	O_2/N_2	3.7
He/CO_2	0.6	H_2/O_2	3.6	CO_2/N_2	11.8	O_2/CH_4	3.2
He/O_2	1.8	H_2/N_2	13.1	CO_2/CH_4	10.1		
He/N_2	6.5	H_2/CH_4	11.2			N_2/CH_4	0.9
He/CH_4	5.6						

Conclusion

A highly contorted ladder polymer was prepared and evaluated for gas transport. The membrane permeabilities were consistent with those of a polymer containing large amount of free volume. While permeabilities were high, permselectivities were also good, particularly for O_2/N_2, H_2/CH_4 and CO_2/CH_4 separations. Manipulating polymer functionality or structure in this class of polymers may allow for increased permeabilities and permselectivities.

Acknowledgement. Sandia is a multiprogam laboratory operated by Sandia Corporation, a Lockheed Martin Company, for the United States Department of Energy's National Nuclear Security Administration under contract DE-AC04-94AL85000. We would like to thank Margaret Welk for her assistance with some of the gas permeability measurements.

References

(1) Budd, P. M.; Elabas, E. S.; Ghanem, B. S.; Makhseed, S.; McKeown, N. B.; Msayib, K. J.; Tattershall, C. E.; Wang, D. *Adv. Matls.* **2004**, *16*, 456-459.
(2) Budd, P. M.; Ghanem, B. S.; Makhseed, S.; McKeown, N. B.; Msayib, K. J.; Tattershall, C. E. *Chem. Commun.* **2004**, 230-231.
(3) Budd, P. M.; Makhseed, S.; Elabas, E. S.; Ghanem, B. S.; Msayib, K. J.; Tattershall, C. E.; McKeown, N. B. *Mater. Today* **2004**, *7*, 40-46.
(4) Masuda, T.; Isobe, E.; Higashimura, T. *Macromolecules* **1985**, *18*, 841-5.
(5) Merkel, T. C.; Bondar, V.; Nagai, K.; Freeman, B. D. *J. Polym. Sci., Part B: Polym. Phys.* **2000**, *38*, 273-296.
(6) Cornelius, C. J. PhD Thesis, Virginia Polytechnic Institute and State University, 2000.
(7) Robeson, L. M. *J. Membr. Sci.* **1991**, *62*, 165-185.

REMOVING HYDROGEN SULFIDE FROM HYDROGEN-RICH GAS STREAMS BY SELECTIVE CATALYTIC OXIDATION

Xianxian Wu, Andrew K. Kercher, Viviane Schwartz, Steven H. Overbury and Timothy R. Armstrong

Oak Ridge National Laboratory (ORNL)
Oak Ridge, TN 37831

Introduction

As the ideal fuel for proton-exchange membrane (PEM) fuel cells, hydrogen will mainly be generated from fossil fuels by steam reforming or partial oxidation before a long term energy solution is developed. One main problem associated with hydrogen production from fossil fuels is sulfur which is commonly in the form of hydrogen sulfide (or is chemically combined with hydrocarbons and can be converted into hydrogen sulfide during fuel processing). Hydrogen sulfide (H_2S) is a strong poison for fuel processing catalysts and PEM fuel cells, thus it must be removed at the early stages.

Among the available techniques for sulfur removal, direct oxidation of H_2S to elemental sulfur by the use of a special, highly selective oxidation catalyst and moderate temperatures is the preferred approach for dilute H_2S-containing gas streams.[1] The selective oxidation of H_2S has the thermodynamic potential to remove H_2S to the parts-per-billion level at low temperature.[2] This technology can be easily integrated into the current fuel processing plants,[3] it can be used with diverse gas streams, and it does not consume H_2 or other useful gas components.[4] As for the catalysts, activated carbons have been shown to be the most suitable candidates.[5] Their use in partial oxidation of H_2S has been identified as a highly promising approach for removing sulfur content in fuel cell feedstocks.[3] Experimental investigations showed that the by-products like SO_2 and COS are a potential problem associated with the use of commercial activated carbons.[3] There is, then, a need to develop optimized catalysts. In this study, we report the test results of an activated carbon made at ORNL, and compare them with those of selected commercial carbons using reformate as the model gas stream.

Experimental

Three commercial activated carbons were used for this study: Centaur (Calgon Carbon, bituminous coal-based, physical activation), WV-B (Westvaco, wood-based, chemical activation), VA-507 (PICA, coconut shell-based, physical activation). The laboratory-made activated carbon (ORNLB) used cellulosic material as the precursor. Carbonization was conducted in a Kiln furnace at 850°C (6 h dwell) in the presence of 9.4 L/min N_2 flow. The activation was carried out in a Lindberg tube furnace (model 59754-A) at 875-975°C with a CO_2 flow of 0.5 L/min. Inert gas was used during heating to the designed temperature and cooling down to room temperature.

The nitrogen adsorption/desorption isotherms of these samples were determined at 77 K using an AUTOSORB-1 (Quantichrome Corporation). The outgas temperature was 300°C. Characteristic data derived from the isotherms are listed in Table 1.

Table 1. Properties of Activated Carbon Samples

Sample	BET surface area (m^2/g)	V_t (cm^3/g)	D-R micropore volume (cm^3/g)	D-A avg. pore diameter (Å)
Centaur	817	0.465	0.344	15.6
WV-B	1840	1.49	0.957	19.2
VA-507	1022	0.545	0.414	15.6
ORNLB	579	0.341	0.245	13.6

Catalytic experiments were conducted in a laboratory-scale, fix-bed reactor system. The gas flow rates were controlled by a mass flow controller system (Omega, Model FMA-700 series controllers coupled with FMA-78P4 readout/power supply). The glass reactor tube used was 49.5 cm long with an I.D. of 1.25 cm. It is vertically positioned in an ATS single zone split tube furnace (Series 3210) in the down flow mode. Approximately 7.8 cm carbon sample is loaded in its center region. The reaction temperature is controlled by a K-type thermocouple in the furnace and monitored by another K-type thermocouple axially centered in the reactor tube. The concentrations of the exhaust gases from the reactor are monitored by a Gas Chromatography (GC) and a FTIR Spectrometer (MIDAC). The GC (Model 910, Buck Scientific, Inc.) has a 30 meter metal column (Q-Plot, Restek Corporation) and a FPD detector which can detect sulfur compounds down to about 200 ppb.

Results and discussion

The ORNL laboratory-made activated carbons have showed excellent activity (complete conversion of H_2S) and selectivity (100% to elemental sulfur) in H_2 stream.[6] Generally, the processing gases in H_2 production processes are only hydrogen-rich streams which contain a large amount of H_2O, CO, CO_2 and other components. When selective oxidation is used for sulfur removal from these streams, COS and SO_2 formation becomes a problem.[3] In this study, the catalytic behaviors of activated carbons were tested in a model reformate: 50% H_2, 15% CO_2, 9% CO, 1% N_2, ~24% balance H_2O with 1000 ppm input H_2S. Air was introduced at the inlet according to an O_2:H_2S ratio of 2:1. The experiments were conducted at 150°C at atmospheric pressure with a space velocity of 3100 h^{-1} (GHSV).

The measured catalytic activities for the four activated carbons are shown in Figure 1. The Centaur sample, WV-B sample and ORNLB-1 Sample showed 100% conversion of H_2S over an almost 9 h test, while the VA-507 sample showed a breakthrough of H_2S after being on stream for about 4 h and only about 70% H_2S conversion afterwards. The catalytic selectivity (to elemental S, calculated from the equation: $sulfur\ yield = \frac{C_{H_2S,in} - C_{H_2S,out} - C_{SO_2,out} - C_{COS,out}}{C_{H_2S,in} - C_{H_2S,out}}$) of the samples is shown in Figure 2. It is seen that only the laboratory-made sample (ORNLB) showed 100% selectivity in the whole test. Neither COS nor SO_2 was detected for this sample. The measured COS concentrations at the reactor exit for different catalysts are shown in Figure 3. The emission of COS was detected right after the introduction of H_2S and air when the Centaur sample or the WV-B sample was used, while COS was measured after about 3 h and SO_2 was measured after about 5 h (as shown in Figure 3) when the VA-507 sample was used. The VA-507 sample displays the worst selectivity after being on stream for about 5 h.

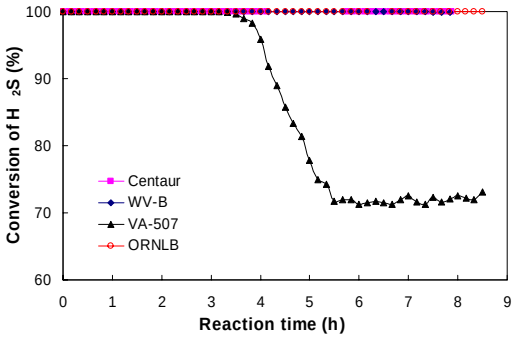

Figure 1. Conversion of H_2S versus time on stream.

The Centaur sample had relatively low specific surface area, pore volume and contained about 5% ash. According to the manufacturer, although it is not impregnated with metals or alkali, it displays the catalytic function of these materials. Our test showed this activated carbon is a strong catalyst which intends to over-oxidize the sulfur to undesired by-products. A better selectivity was observed for the WV-B sample than for the Centaur sample, but the immediate emission of a small amount of COS also is a problem for this sample. In the first 3 h, the VA-507 sample converted all H_2S to elemental sulfur, but both activity and selectivity became progressively worse afterwards. The observed diverse behaviors emphasize the importance of determining the factors responsible for the catalytic effects of activated carbons. On-going analysis and testing are aimed at understanding these factors and determining why the laboratory-made sample behaviors better than commercial samples.

Conclusions

The formation of COS is a problem for the use of commercial activated carbons as the oxidation catalysts of H_2S in reformate. The activated carbon synthesized at ORNL has the ability to selectively oxidize H_2S down to ppb level without detectable occurrence of unwanted side-reactions.

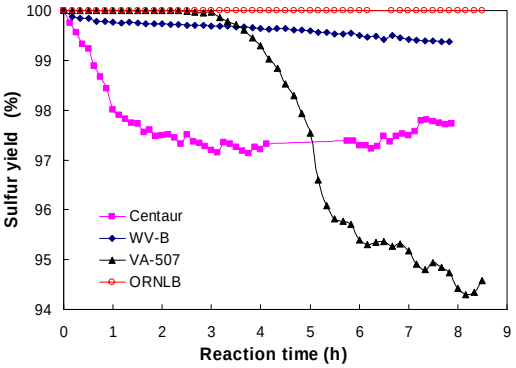

Figure 2. Selectivity (to S) versus time on stream.

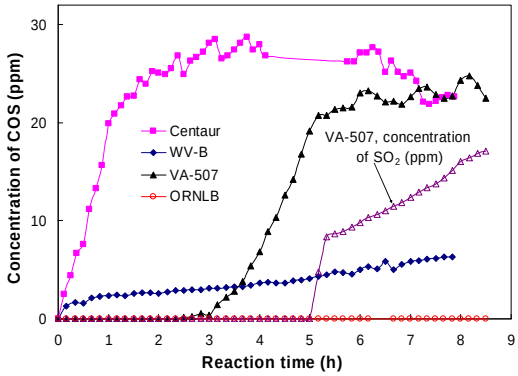

Figure 3. Exit concentration of COS versus time on stream.

Acknowledgements. This research was sponsored by the U.S. Department of Energy, Office of Hydrogen, Fuel Cells and Infrastructure Technologies under contract DE-AC05-00OR22725 with UT–Battelle, LLC, at Oak Ridge National Laboratory. The research was supported in part by an appointment to the Oak Ridge National Laboratory Postdoctoral Research Associates Program administered jointly by the Oak Ridge Institute for Science and Education and Oak Ridge National Laboratory.

References

(1) Kohl, A. L.; Nielsen, R. *Gas Purification*, 5th ed.; Gulf Professional Publishing Company: Houston, 1997.
(2) Gamson, B. W.; Elkins, R. H. *Chemical Engineering Progress* **1953**, *49*, 203.
(3) Gardner, T. H.; Berry, D. A.; Lyons, K. D.; Beer, S. K.; Freed, A. D. *Fuel* **2002**, *81*, 2157.
(4) Lagas, J. A.; Borsboom, J.; Berben, P. H. *Oil & Gas Journal* **1988**, *86*, 68.
(5) Steijns, M.; Mars, P. *Industrial and Engineering Chemistry Product Research and Development* **1977**, *16*, 35.
(6) Wu, X. X.; Kercher, A. K.; Schwartz, V.; Gallego, N. C.; Overbury, S. H.; Armstrong, T. R. "Activated carbons as catalyst for selective partial oxidation of hydrogen sulfide"; Carbon2004, July 11-16, 2004, Providence, RI.

KINETICS AND MICROSTRUCTURE OF Cu DEPOSITS FROM ELECTOLESS PLATING BATHS

Federico Guazzone, Erik E. Engwall, Ivan P. Mardilovich and Yi Hua Ma

Center for Inorganic Membrane Studies
Department of Chemical Engineering
Worcester Polytechnic Institute
100 Institute Road
Worcester, Massachusetts 01609 USA

Introduction

One method for hydrogen production is to use metal supported Pd or Pd-alloy membranes in steam reforming reactors. The resistance to sulfur poisoning of the $Pd_{60}Cu_{40}$ alloy may make it suitable for the reforming of hydrocarbons with high sulfur content[1]. Pd-Cu membranes have already been prepared by Ma et al[2], yet they showed low hydrogen permeability mainly due to a Cu wt% far from the optimum 40wt%. A better understanding of Cu plating baths is actually needed to reach the optimal Cu content. The objective of this work was to investigate the effects of pH and Cu concentration on the Cu deposition kinetics and the structure, including microstructure, of Cu deposits by electroless deposition. Non porous stainless steel plates were used as the surrogate for the porous support for the investigation.

Experimental

Non-porous stainless steel (316L) plates, $1cm^2$, were cleaned with high alkaline solution for grease removal, oxidized at 400ºC and activated following the procedure described Ma et al.[3]. Copper was deposited using the electroless deposition method. Table 1 shows the typical bath chemistry for Cu deposition and includes: $Cu_2SO_4{\cdot}5H_2O$ as copper ion source, HCHO as reducing agent and EDTA (or Rochelle salt) as complexing agent. The pH was adjusted with 10M NaOH and varied between 10 and 13.5. The temperature was set at 60ºC

Table 1. Copper bath chemistry used for copper electroless deposition on non-porous stainless steel plates

$CuSO_4{\cdot}5H2O$ (g/l)	3-20
$Na_2EDTA\ 2H_2O$ (g/l)	30
HCHO (37 %) (ml/l)	14
pH	10-13.5
Temperature (°C)	60

The thickness of Copper deposits was determined by gravimetric methods. The microstructure was characterized by Scanning Electron Microscope (SEM) (Amray 1600 Turbo) and X-Ray Diffraction (XRD) (Rigaku Geigerflex, Cu Kα (λ=1.5418Å) radiation source and monochromator) for grain size measurements.

Results and Discussion

The behavior of an EDTA based copper plating bath has been studied and the copper deposition rate are listed in Table 2 as a function of pH and $Cu_2SO_4{\cdot}5H_2O$ concentration. EDTA concentration was 30g/l and the formaldehyde concentration was 14ml/l. The deposition rate was measured within an accuracy of 0.5μm/hour.

Three important observations can be made from Table 2. The first one is that copper deposited very slowly when pH was below 12. The second important result is that the Cu deposition rate increased when the concentration of Cu(II) ions was increased at a given pH. The copper deposition rate should have increased if the pH was increased according to the results reported by Ohno et al.[4]. However, for $Cu_2SO_4{\cdot}5H_2O$ concentrations of 6 and 9g/l listed in Table 2, the copper deposition rate appeared to decrease when the pH was increased. This might be due to an increase in the viscosity of the solution.

Table 2. Copper deposition rate (μm/hour) as a function of pH and $Cu_2SO_4{\cdot}5H_2O$ (g/l)concentration

	pH			
	10	12	≈13	≈13.5
3	≈0	≈0	1.7, 1.8	2.3, 2.4
6	-	-	8.0, 8.5	7.2, 7.9
9	≈0	≈0	10.4	8.2, 9.9
12	≈0	≈0	-	-
20	≈0	≈0	13.6	-

The deposited Cu was dull and lacked brightness when its deposition rate was fast. Using 3g/l $Cu_2SO_4{\cdot}5H_2O$ concentration led to better deposits, which appeared brighter. The same experiment was carried out for that specific $Cu_2SO_4{\cdot}5H_2O$ concentration (3g/l) but changing the complexing agent to Rochelle salt ($NaKC_4H_4O_6$). Again, no Cu could be deposited at pH below 12. On the other hand, the depostion rate at a pH of 12.5 was measured to be 1.5μm/hour. Since $NaKC_4H_4O_6$ is a weaker complexing agent than EDTA the deposition rate of EDTA based baths should be lower than the deposition rate of $NaKC_4H_4O_6$ based bath. However, the value of 1.5μm/hour at pH 12.5 of the $NaKC_4H_4O_6$ based bath is very closed to the deposition rate that an EDTA based bath at pH 12.5 would have, see Table 2.

The XRD pattern of a 1.5μm Cu deposit from the Rochelle salt based bath is shown in Figure 1. Cu peaks appear as shoulders since reflections of Cu and substrate (316L) are very close. The overlapping of the two patterns is due to the thinness of the Cu layer.

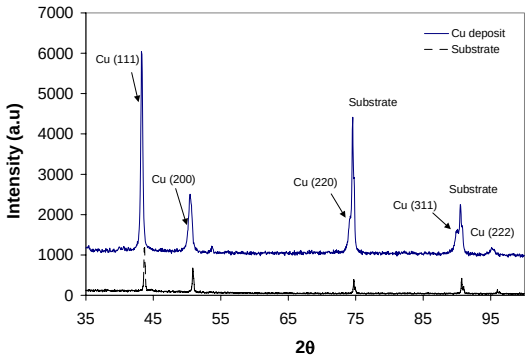

Figure 1. XRD pattern of a thin (1.5μm) Cu layer on stainless steel. Reflections from Cu are so close to stainless-steel peaks that Cu peaks appear as shoulders on the left side of the substrate peaks

In order to measure Cu grain size, thicker Cu substrates were needed in order to avoid peak broadening from the overlapping of the patterns. Figure 2 shows the XRD pattern of a 9μm thick copper deposit obtained from a high Cu(II) ion concentration (9g/l) and high pH (13). The patterns from the substrate and from the thin Cu layer

of Figure 1 are also included for comparison purposes. It is clearly seen in Figure 2 that all diffracted rays come from the copper layer since the intensity ratios of all peaks are equivalent to the intensity ratio of a Cu polycrystalline sample. For example, the intensity of peak (220) is similar to the intensity of peak (311) which is not the case in Figure 1 due to the presence of the substrate peak.

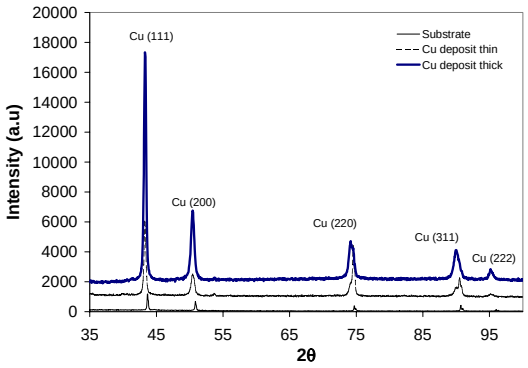

Figure 2. XRD pattern of a thick (9μm) Cu deposit obtained from a 9g/l Cu(II) bath at pH 13. Patterns from Figure 1 are also shown for intensity comparison

Copper crystallites using Scherrer equation after machine broadening correction ranged between 5-15 nm. This result is in good agreement with the results reported by Lin et al.[5] and Xu et al.[6]

SEM micrographs of Cu deposits from Rochelle salt based bath showed uniform layers composed of 0.3-1μm clusters in diameter. In fact, such clusters, seen in Figure 3, are agglomerates of Cu grains with dimensions smaller than 20nm as stated above.

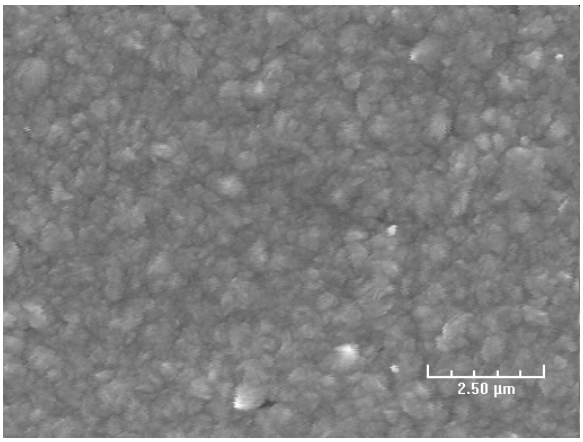

Figure 3. Copper deposit on oxidized stainless steel plates. Cu deposits as spherical clusters including nano-crystallites.

Conclusion

Copper deposited very slowly when pH was below 12. The Cu deposition rate increased when the concentration of Cu(II) ions was increased. At high Cu concentrations The Cu deposition rate decreased when pH was increased which might have been due to an increase in viscosity. The Cu was dull in appearance when the deposition rate was fast (above 10μm/hour). Cu deposited very uniformly on oxidized non-porous stainless steel. The deposits were characterized by clusters as large as 1μm including crystallites smaller than 20 nm.

Acknowledgement. The authors gratefully acknowledge the financial support provided by Shell Hydrogen and Shell International Exploration and Production, Inc.

References

1 McKinley, D.L. & W. Va. Nitro. 1969. U.S. Patent 3,350,845

2 Ma, Y. H.; Mardilivich, I. P.;Engwall E. E. Advanced Mambrane Technology 984 (**2003**) 346-360

3 Mardilovich, P. P.; She, Y.; Ma, Y. H. and Rei M. H. *AIChe journal*, Vol. 44, No. 2, (**1998**) 310-322

4 Ohno I., Wakabayashih O. and Haruyama S. *J. Electrochem. Soc.*: ELECTROCHEMICAL SCIENCE AND TECHNOLOGY, Vol. 132, No. 10, (**1985**) pp 2323-2330

5 Lin, W. H. and Chang, H. F. *Surface and coatings Technology* 107 (**1998**) 47-54

6 Xu L., Zhou K., Xu H., Zhang H., Huang L., Liao J., Xu A., Gu N., Shen H, Liu J. *Applied surface science*, 183 **(2001**) 58-61

A NOVEL LOW-COST HEATED Pd MEMBRANE SEPARATOR FOR HYDROGEN RECOVERY FROM REFORMATES

P. Bossard, J. Mettes

Power & Energy, 106 Railroad Dr., Ivyland, PA 18974 USA

Abstract

Thinner membranes not only reduce the amount of costly palladium needed but also produce higher hydrogen throughput per surface area. These two effects combine to reduce the amount of palladium needed by the square of the reduction ratio of the Pd membrane thickness which is the motivation behind a number of current state of the art studies. Thinner membranes need to be supported by a rigid hydrogen permeable substrate which can be made either from porous metal or from ceramic material. Power and Energy, Inc. has identified the main technical bottlenecks associated with the first approach and has generated corresponding novel solutions. A mathematical model of the physics involved in a practical separator has been developed. This model enables the calculation of membrane performance for a given set of design and operational parameters. Preliminary data showing the performance of this novel permeable membrane support structure is also presented.

Keywords: hydrogen, separation, purification

Introduction

Palladium membrane based devices have the potential to provide low cost separation and purification of Hydrogen in a single step; however, due to the relatively high cost of palladium, fabrication and lack of reliability, practical applications using palladium membranes have been limited. Separation is needed to extract hydrogen from reformed fuel sources ranging from fossil fuels to renewable biomass. Purification of the extracted hydrogen is required to remove deleterious impurities that can reduce the lifetime of a proton exchange membrane (PEM) fuel cell. The PEM fuel cell is the device of greatest practical interest in realizing the benefits of distributed electrochemical power generation. The separation is typically done in a centralized fashion in which leading to significant challenges related to the problematic transport and storage of hydrogen. Given a low cost efficient separation technology, hydrogen separation can also be done at the point of use. Point of use hydrogen generation has distinct advantages which include avoiding the need to develop a hydrogen distribution infrastructure and also allowing the storage of liquid precursor fuels that are easily stored in traditional storage tanks.

Supported Thin Pd-alloy Membrane

Thinner membranes not only reduce the amount of costly palladium needed but also produce higher hydrogen throughput per surface area. These two effects combine to reduce the amount of palladium needed per unit of hydrogen flux by the square of the reduction ratio of the Pd membrane thickness which is the motivation behind a number of current state of the art studies.
Thinner membranes need to be supported by a rigid hydrogen permeable substrate which can be made either from porous metal or from ceramic material.

Performance impacted by the presence of the membrane substrate

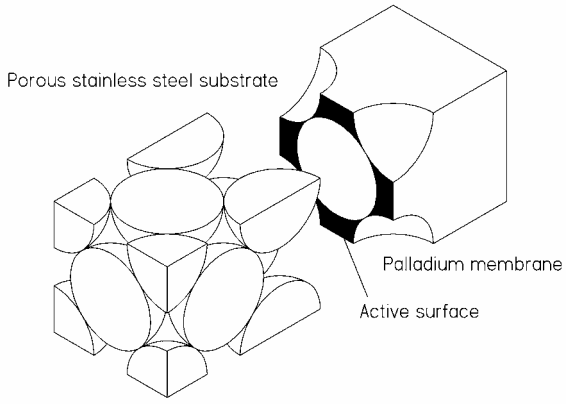

Figure 1. State of the Art substrate showing significantly reduced useful membrane area due to substrate blocking

The presence of a substrate, supporting a thin membrane, introduces a performance reducing factor for the composite structure. This is illustrated in figure 1 showing large part of a state of the art membrane surface being physically blocked by the substrate which reduces the area available for hydrogen transport. Figure 2 illustrates P&E's patent pending solution that provides a strongly supported membrane without obstructing significant parts of the surface area for hydrogen permeation. These features are obtained by placing a porous layer of palladium nanospheres in between the porous substrate and the solid palladium membrane. As becomes apparent in figure 2 the top layer of interconnected palladium spheres becomes an integral part of the solid membrane layer. Depending on the lattice structure of the substrate, the difference in transport capability ranges from a factor 20 to 40 for respectively a loosely packed cubic to dense hexagonal packed lattice. In reality the spheres will be compressed into each other, reducing the membrane area available for hydrogen transport even further.

It should be emphasized that P&E's solution avoids the introduction of new problems related to intermetallic diffusion and thermal expansion because the solid palladium alloy layer and the porous palladium alloy layer can be made of the same material. Also, differences in thermal expansion between the non-palladium substrate material and the porous palladium layer will be buffered because of the relative loose bond between these layers.

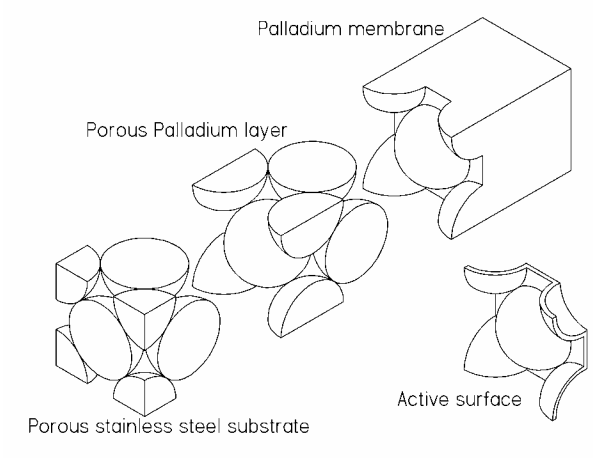

Figure 2. P&E structured composite membrane showing significantly increased useful membrane.

The interface between substrate and membrane is potentially problematic for a number of technical reasons, other than substrate blocking, such as:

- Bonding mechanism, inter-metallic diffusion, and robustness of adhesion strength
- Structural component differences in the coefficient of thermal expansion (without hydrogen)
- Hydrogen solubility, embrittlement, and coefficient of thermal expansion with hydrogen
- Pressure and thermal cycling behavior of permeability

Membrane test results using free-standing and supported membranes

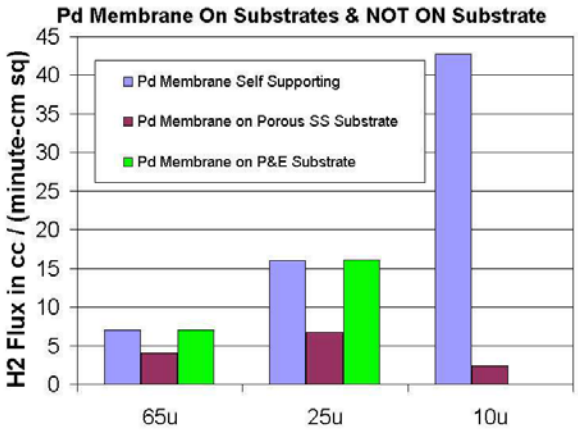

Figure 3. Data comparing H2 flux rates for membranes of three different thicknesses. The left bar at each thickness represents the flux rate of a free-standing membrane (10 µ data is calculated). The center bar represents the typical flux reduction which results from employing a porous SS support substrate. The right bars are flux rates measured for membranes supported with the subject novel nano-structured membrane support.

PATHWAYS TO BUILD A HYDROGEN ECONOMY INFRASTRUCTURE

V. Raman, Consultant

Allentown, PA

Building the infrastructure to support a fully developed hydrogen economy is an undertaking of massive proportions. However it does not need to be done all at once.

This build-out could be accomplished starting from the current relatively modest base infrastructure that supplies hydrogen for industrial applications today.

In the long term the production can transition from the fossil-based technologies of today to renewable energy based technologies thus eliminating greenhouse gas emissions.

Over the last 150 years or so ago the world's energy needs were met by transitioning from solid fuels like wood and coal to liquid fuels. Currently liquid fuels exceed the amount of solid fuels in use. This was followed by the introduction of gaseous fuels in the early 20th century. Gaseous fuels have been gradually increasing at the expense of both solid and liquid fuels. The primary gaseous fuel we use today is natural gas. Looking into the future, predictions are for the use of gaseous fuels to increase even more and for solid and liquid fuels to disappear over the next 150 years or so. Also the gaseous fuel of choice is expected to gradually change from natural gas to hydrogen.

This shift from solid to liquid to gaseous fuels also represents a shift to increasing hydrogen content or decreasing carbon. With increasing hydrogen content these fuels are more energetic and also burn cleaner releasing less carbon dioxide and other pollutants into the atmosphere. The use of hydrogen as a fuel will be the cleanest as it has no carbon. It simply produces water on combustion. The hydrogen economy or the use of hydrogen fuel is considered by many to be the next transition of global energy use.

Hydrogen can be produced using electrochemical, thermochemical, bacterial fermentation, thermolysis and photolysis of water. However many of these processes require further development to make them competitive.

Today hydrogen is produced most economically via steam reforming of natural gas in large plants. The majority of the hydrogen produced today is transported in dedicated pipelines to large refining and chemical manufacturers.

Hydrogen is used daily by many industries, including the petroleum industry and in manufacturing processes for producing chemicals, foods and electronics.

Today the only significant fuel use of hydrogen is for the NASA space shuttle.

Efforts underway now on fuel cells should lead to a variety of special niche applications where hydrogen fuel cells provide unique advantages in portable and stationary power needs as well as in This presentation will address the issues and challenges in building an infrastructure to support a hydrogen economy. The challenge in developing a hydrogen infrastructure to support these needs include:

- How best to leverage the existing industrial infrastructure to support the introduction of hydrogen and fuel cell products?
- Developing new products to meet the emerging demands of the fuel cell market. Since distribution costs play a dominant role in hydrogen prices today, new models for the production and delivery may be warranted in the emergence of a hydrogen economy.
- How to introduce renewable hydrogen into the expanding hydrogen infrastructure as the market develops and the economics warrant?

There are currently about 20 demonstration fueling stations in operation in the US to support testing and development. Various low cost innovative solutions are being developed such as the mobile fueler, which is modeled after the industrial tube trailer high pressure gas delivery system. This is proving to be very popular with the various car manufacturers who want low cost solutions to placing a limited number of vehicles in various diverse locations.

This presentation will shed some light on these issues. Pathways to leverage the current infrastructure with distributed production and fueling will be discussed. Capital utilization, safety, codes and standards, and consumer acceptance are critical components to achieving a success. These will be discussed in some depth as well.

METAL-ORGANIC FRAMEWORKS (MOFs): NEW MATERIALS DESIGNED FOR H_2 STORAGE

Omar M. Yaghi

Department of Chemistry, University of Michigan, Ann Arbor, MI 48103, USA

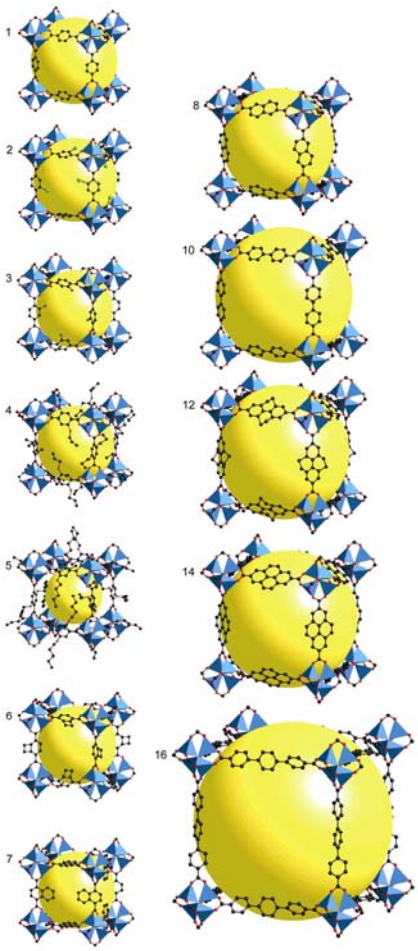

An outstanding challenge in the synthesis of crystalline solid-state materials is to alter chemical composition, functionality, and molecular dimensions systematically, that is, without changing the underlying topology. The insolubility of extended solids necessitates that their assembly be accomplished in only a single step. Thus, in order to design a target extended structure with the same precision practiced in organic synthesis, (i) the starting building blocks should have the relevant attributes necessary to assemble into the skeleton of the desired structure, (ii) the synthesis has to be adaptable to using derivatives of those building blocks to produce structures with the same skeleton but different functionalities and dimensions, and (iii) the products should be highly crystalline to facilitate their characterization by X-ray diffraction (XRD) techniques.

We have pursued the assembly of extended structures of metal-organic frameworks (MOFs) from molecular building blocks. In particular, in MOF-5, octahedral Zn-O-C clusters are linked by benzene struts to reticulate a primitive cubic structure (**1** in Fig.) and produce an exceptionally rigid and highly porous structure. Now we report the systematic design and construction of a series of frameworks having structures based on the skeleton of MOF-5, wherein the pore functionality and size have been varied without changing the original cubic topology. Several members of this series have pore sizes in the mesoporous range (>20 Å), and the lowest crystal density of any material reported to date.

The exceptionally high surface area and pore volumes observed for **6** coupled with its appropriately designed aperture made it an ideal candidate for methane and hydrogen storage. Indeed, the methane sorption isotherm was measured in the pressure range 0 to 45 atm and room temperature, and found to have an uptake of 240 cm^3 (STP)/g (155 cm^3/cm^3) at 36 atm. The H_2 isotherm showed that up to 4.5 % wt/wt could be stored at 78 K, and up to 2 % wt/wt at room temperature and 10 bar. The presentation will discuss synthesis of these compounds and their use for separation of large organics, and gas storage including the use of H_2 for fueling of cellular phones, laptops, and potentially automobiles.

Chemical Systems for Hydrogen Storage

G. J. Thomas, Consultant

Sandia National Laboratories

Hydrogen storage systems for use in hydrogen-fueled vehicles will require high energy density and high specific energy in order to achieve comparable performance to conventional gasoline-fueled vehicles. It is believed that this issue remains as one of the critical barriers to the development of fuel cell powered vehicles. With the president's initiative and increased funding levels in hydrogen and fuel cell development, there are a number of new and exciting areas of research which have emerged aimed at developing high density hydrogen storage media.

At the present time, essentially all hydrogen-fueled vehicles use either compressed gas or liquid hydrogen tanks for onboard storage. Both of these technologies are straightforward, relatively mature and are commercially available. Compressed gas systems have progressed rapidly over the last few years. These cylindrical tanks, constructed with high strength carbon fiber composite materials, are robust, lightweight and have been demonstrated at hydrogen pressures up to 700 bar. However, even at this pressure at ambient temperature, the volumetric density of the hydrogen is insufficient for long-term use. Liquid hydrogen storage has been advocated mainly by BMW and a number of their demonstration vehicles have employed tanks which were developed by Linde. The high energy cost of liquefying hydrogen has been stated as a key issue in its utilization as a fuel.

This presentation will focus on chemistry-based hydrogen storage methods, that is, hydrogen storage materials. Storage materials can be broadly classified as having reversible or non-reversible hydrogen behavior. Reversible materials absorb and desorb hydrogen from the gas phase based on the hydrogen gas overpressure and temperature. These materials can therefore be recharged *in-situ* onboard the vehicle by supplying hydrogen at the appropriate pressure. On the other hand, non-reversible systems require chemical processing, perhaps including intermediate phases and additional materials, to be recharged. In this case, the spent material (depleted of hydrogen) which could be in liquid or solid form, must be removed from the vehicle and reprocessed elsewhere. These materials are generally referred to as chemical hydrides. Although reversible systems would be the preferred method, both options are currently under consideration.

There are many materials which have reversible hydrogen properties. These include materials where the hydrogen is adsorbed to the surface and those where the material is absorbed into the bulk. Single wall carbon nanotubes and other nanostructured materials, such as metal organic frameworks (MOFs), are examples of adsorbed hydrogen systems being studied. Critical issues which must be answered with adsorbed systems are hydrogen capacity, volumetric density and hydrogen binding energies.

Materials where hydrogen is absorbed and chemically bound in the bulk offer the potential of having the highest volumetric density of hydrogen, surpassing even that of liquid hydrogen. Metal hydrides are the best known class of materials with this property and these have been extensively studied for more than 30 years. Although they exhibit good capacities and good kinetic properties, they are generally too heavy. Lighter weight hydrides typically have stronger covalent or ionic hydrogen bonds and hence require high temperatures for hydrogen release. Emphasis in this area of research has shifted in recent years to other materials. Complex hydrides, particularly those formed with Al-H or B-H complexes, offer higher hydrogen capacities, lighter weight over intermetallic hydrides and reduced hydrogen binding energies over covalent or ionic hydrides. However, only $NaAlH_4$, doped with Ti, has been demonstrated to be reversible at this time. Work on this and other complex hydrides, as well as effective dopant materials and processes to achieve reversible behavior and the desired kinetic and thermodynamic properties, is currently being pursued. A number of other alternative materials have also shown promising early results and are being proposed for further study, including imide-amides and amine borane systems.

In this overview presentation we will discuss inherent limitations of hydrogen storage concepts and briefly describe some of the specific chemical systems mentioned above. Emphasis will be on material performance relative to that required in storage applications.

START-UP OF AN AUTOTHERMAL REFORMER

S. Ahmed, R. Ahluwalia, S. Lee, S. Calderone, T. Harvey, K. Liao

Argonne National Laboratory, 9700 S. Cass Ave., Argonne, IL 60439

Abstract

The question of whether the hydrogen infrastructure or the fuel cell vehicle should come first has been debated for over a decade. This chicken-or-egg dilemma can be resolved with on-board fuel processors that can convert gasoline to hydrogen on demand. These on-board fuel processors have to meet many criteria for success in a demanding automotive application – a key requirement being the ability to start-up rapidly.

Argonne National Laboratory has been studying the feasibility of a fast-starting fuel processor (FP) by designing and testing an autothermal reformer (ATR) based fuel processor. The first step in this start-up process requires readying the ATR. With the FP start-up times targeted at 30 seconds, the constraints on the ATR for a smooth start-up transition are quite rigorous. This paper presents the experimental data of start-up protocols that begin the reactions in the partial oxidation mode and then switch to the autothermal reaction mode.

Introduction

The strategy for mass commercialization of fuel cell vehicles invariably brings up the question of whether the fuel cell vehicle or the hydrogen refueling infrastructure should come first. One solution around this dilemma is to use on-board fuel processors which can convert currently available fuels such as gasoline to hydrogen on demand. For commercial success of these vehicles, the revolutionary change in the power source should be transparent to the consumer, one element of which is that the fuel processor does not adversely contribute to the driving experience. One of those features is its ability to start-up rapidly.

The autothermal reforming process is recognized for its ability to reach operating temperatures quickly. However, the transition of a cold catalytic reactor to operating temperatures greater than 650°C within a few seconds requires synchronization of the balance of plant and careful control of the reaction parameters. A myriad of combinations are possible, each set introducing its own advantages and limitations, some of which are delineated in this paper. The experiments were conducted in the autothermal reaction zone of an integrated fuel processor [1].

Initiating the Catalytic Reactions

The catalytic autothermal reforming reaction is typically started in the partial oxidation mode (POX) by contacting the oxygen (air) and the fuel over the heated catalyst bed. Then as the exothermic reaction further heats up the catalyst bed, the reaction is switched to the autothermal mode by introducing water.

The start-up of our ATR catalyst consisted of the following steps, programmed as a sequence of logical steps using the LabView software. The fuel pump and the water pump were started to establish pressurized recirculation loops for each. The flows to each of their respective vaporizers were controlled to the desired setting with a pneumatic valve, a mass flow controller, and a PID control loop. A 3-way solenoid valve directed the flow from the vaporizer to either the ATR or back to their respective tank. The air flow was simpler (a compressor start-up was not necessary since our apparatus was connected to the house compressed air line) and consisted of a mass flow controller that directed the air through the nozzle into the ATR. Electrical heater coils placed above the catalyst bed were powered up to allow the catalyst bed to heat up, by a combination of radiation heat transfer and sensible heat transferred via the air stream that flowed past it and through the catalyst. Figure 1 shows the temperature rise measured on a heater coil and on the front face of the ATR catalyst. The test was performed with the heaters powered at 1.2 kW, while 5 L/min of air flowed past the heaters and into the catalyst structure.

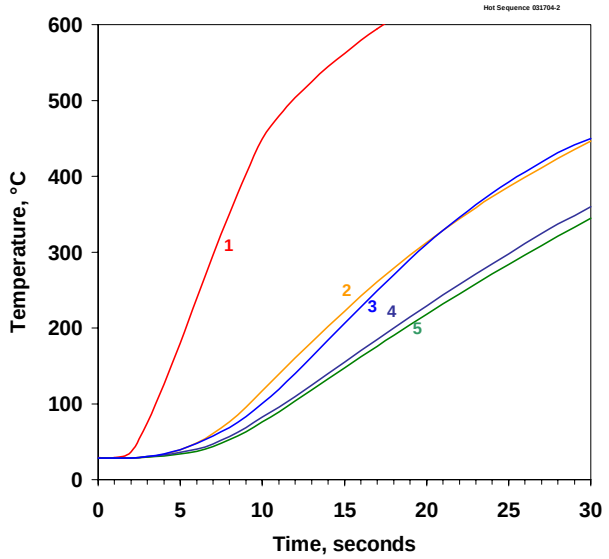

Figure 1. Temperature rise on a heater rod (1) and the ATR catalyst surface (2-5).

Ignition on the ATR catalyst depends on many conditions such as the catalyst formulation, structure, the composition, phase, and temperature of the fuel, and the air/fuel ratio, etc. Experiments were conducted to start the ATR operations using four different feed combinations. These were (1) vaporized fuel and air; (2) liquid fuel and air, followed by liquid water; (3) vaporized fuel and air, followed by steam; and (4) vaporized fuel and air, followed by liquid water. In all cases the fuel feed rate was maintained at 40 g/min. Liquid injections were achieved through a nozzle that delivered a fine spray over a catalyst bed with a diameter of 9.7 cm. The catalyst bed was 3.2-cm deep.

Results and Discussion

Figure 2 plots the feed rates of vaporized fuel, air, and water into the reactor as a function of time. The initial air flow rate corresponded to an O/C ratio of 0.56. Water was injected 40 seconds after the fuel to allow a sufficient depth of the catalyst zone to warm up such that the introduction of water would not quench the reactions entirely. Since water has a significant cooling effect, the air flow rate was increased to an O/C ratio of 0.92 and eventually to 1.07. The final steam-to-carbon (S/C) ratio was 1.28.

Figure 3 shows the temperatures of the catalyst at depths of 6-mm and 18-mm from the front face of the catalyst. The delay in temperature rise at the two locations is representative of the thermal mass of the catalyst and support that separates the two thermocouples. In 40 seconds the temperatures at the 6-mm and 18-mm locations had reached 856°C and 610°C, respectively. Introducing the water spray and the higher air flow rate brought the temperatures down to between 650-750°C. The effects of the air flow increases were more prominent on the downstream thermocouple.

Figure 4 shows the concentration of hydrogen and carbon monoxide measured by on-line analyzers. The introduction of water increases the hydrogen concentration to above 30%, while the CO

concentration drops below 4%. The presence of water has the desired effect of promoting the endothermic steam reforming reaction ($C_nH_m + H_2O \rightarrow CO + H_2$) and the mildly exothermic water gas shift reaction ($CO + H_2O = CO_2 + H_2$). The heat effects are reflected in the temperature responses seen in Figure 3.

Conclusions

Initiation of reforming reactions in a catalytic autothermal reforming reactor was conducted in a partial oxidation mode. It requires a combination of a heated catalyst surface and an appropriate air-to-fuel ratio. Introduction of water into the process has the desired effects of increasing the H_2 yield, reducing the CO yield, lowering the peak temperature, and reducing the potential for coke formation. The timing of the water injection (without quenching the catalyst bed) depends on the combination of feed proportions (O/C and S/C), the bed temperature profile, and the size and distribution of the liquid particles.

Acknowledgement. This work was supported by the Hydrogen, Fuel Cells, and Infrastructure Technologies Program of the U.S. Department of Energy, Office of Energy Efficiency and Renewable Energy, under Contract W-31-109-ENG-38.

Reference

1. Ahmed, S.; Ahluwalia, R.; and Lee, S.H.D., "Experimental Study to Determine Fast-Start Capability of On-Board Fuel Processors," 2003 Fuel Cell Seminar Abstracts, Miami Beach, FL, Nov. 2003.

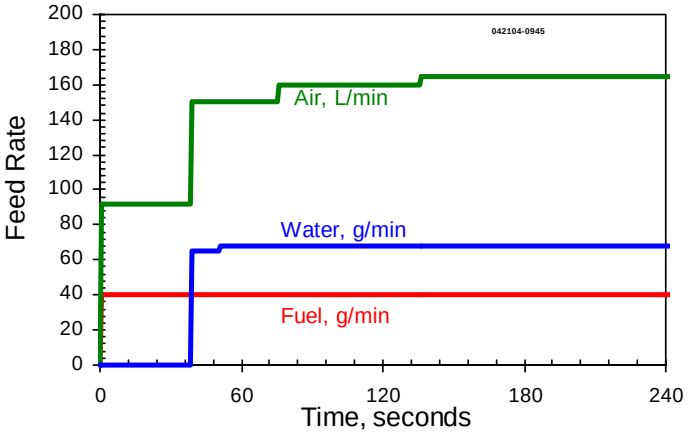

Figure 2. Feed rates into the autothermal reactor.

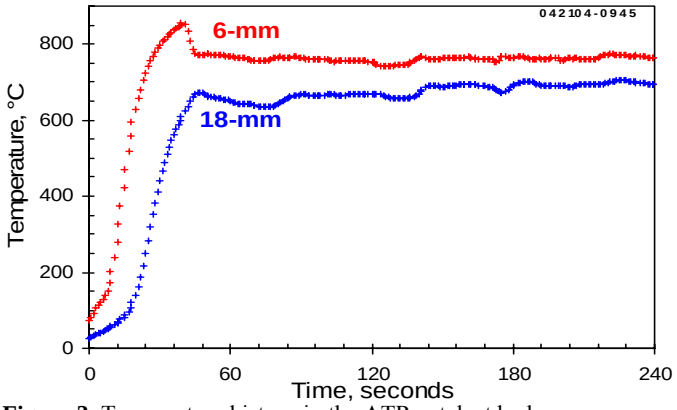

Figure 3. Temperature history in the ATR catalyst bed.

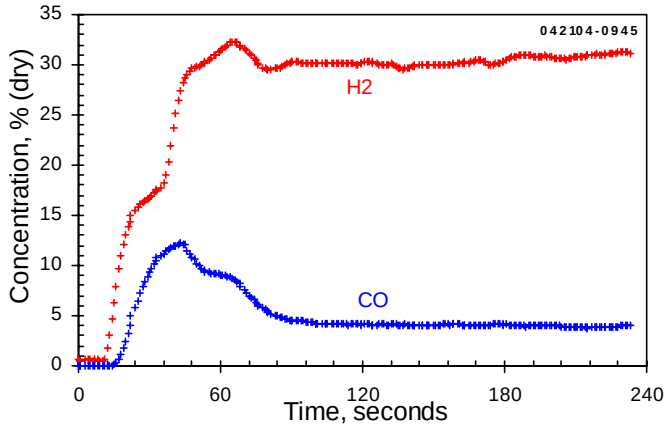

Figure 4. History of the hydrogen and carbon monoxide concentrations in the reformate from the ATR.

LIQUID HYDROGEN PRODUCTION VIA HYDROGEN SULFIDE METHANE REFORMATION

Cunping Huang and Ali T-Raissi

Florida Solar Energy Center
University of Central Florida
1679 Clearlake Road
Cocoa, FL 32922

Introduction

Hydrogen sulfide is a common contaminant in many of the world's natural gas (NG) wells. Approximately one-third of U.S. NG resources can be considered low or sub-quality gas not suited for pipeline shipment.[1] Hydrogen sulfide concentration in NG varies from traces to 90% by volume.[2] In natural gas processing hydrogen sulfide is viewed as a pollutant requiring treatment and removal. Presently, hydrogen sulfide is separated from hydrocarbon gases by amine adsorption and regeneration, producing acid gas containing 10-90% by volume hydrogen sulfide. When hydrogen sulfide concentration exceeds 40% the natural gas must be treated in the Claus plant, where a portion of hydrogen sulfide is burned to form sulfur dioxide. The gas then reacts with the main hydrogen sulfide stream to produce elemental sulfur and water. In this process, hydrogen in the hydrogen sulfide is converted into water vapor and wasted instead of being extracted as a clean energy source.

As an alternative to the Claus process, hydrogen sulfide can be removed by methods that produce elemental sulfur and hydrogen instead. For example, pyrolysis, thermochemical cycles, electrochemical and photochemical methods can be used to decompose H_2S directly. However, there are two drawbacks to direct decomposition of hydrogen sulfide for hydrogen production. Firstly, in the case of a hydrogen sulfide contaminated NG, the treatment process requires that H_2S be recovered from the sub-quality gas prior to its decomposition. In many cases, H_2S separation process requires considerable energy input, making utilization of the "sour" gas economically unfavorable. Secondly, H_2S decomposition produces only one mole of hydrogen per mole of H_2S reacted. A better approach is to reform H_2S and CH_4 already present in natural gas in a process analogous to steam reformation of methane as follows:

$$2H_2S + CH_4 = CS_2 + 4H_2 \quad \Delta H^0_{298K}=232.4 \text{ kJ/mole}$$

Hydrogen sulfide reformation of methane (HSRM) can generate two moles of hydrogen per mole of H_2S reacted. The main objective of this paper is to assess the merits of HSRM process with respect to the thermodynamics and chemical equilibrium considerations. Prior to the development of flowsheets, pinch point analyses are conducted to determine the necessary process conditions for zero carbon lay down based on the underlying HSRM chemistry. In addition, certain aspects of the process relevant to the liquid hydrogen production by cryogenic separation of constituent gases are discussed and compared to hydrogen membrane separation processes. The process energy requirements and efficiencies are also calculated using Aspen Technologies HYSYS^{TM} chemical process simulator.

Thermodynamics of hydrogen sulfide reforming of methane

The thermodynamic analyses were carried out using Aspen Technologies HYSYS^{TM} chemical process simulator. Since methane decomposition can result in carbon lay down that deactivates catalyst used for HSMR process, the analyses intended to find conditions that minimize carbon formation. This is done by pinch-point analyses. The yield of carbon, carbon disulfide and hydrogen are defined as the moles of product divided by the moles of methane input. The yield of carbon and carbon disulfide as a function of temperature during HSRM process are given in **Figure 1** and **2**.

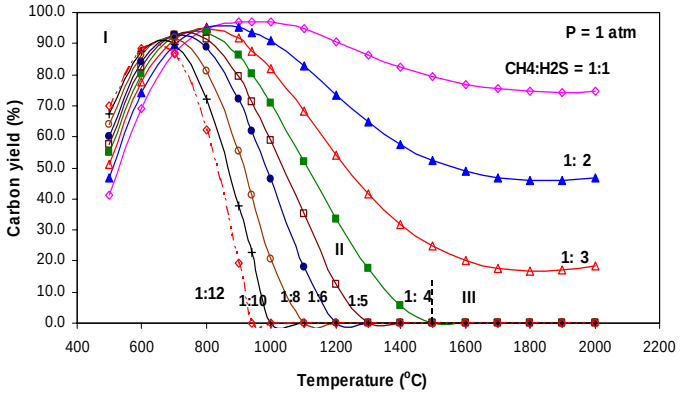

Figure 1. Carbon yields at various temperatures and CH_4 to H_2S molar feed ratios (Region I - CH_4 pyrolysis; Region II - excess CH_4 pyrolysis and HSRM zone; Region III - purely HSRM process).

In region III (HSRM), the hydrogen sulfide to methane feed ratio (x) does not have appreciable effect on the extent of CH_4 conversion. The major factor affecting methane conversion is temperature. When reaction temperatures exceed 800°C, methane conversion is practically 100% at all x values. The amount of carbon formed increases with increasing temperatures and has maxima as depicted in **Figure 1**. The temperature at which pinch-point occurs decreases with the increasing feed ratio x. For example, when x = 4, pinch point temperature is 1500°C, while it is 1000°C at x = 10. Carbon lay down can't be avoided if the hydrogen sulfide to methane feed ratio is lower than 4.

Total enthalpy (ΔH) change of HSMR process is calculated based on the enthalpy differences of products and reactants shown in **Figure 2** for one mole methane system.

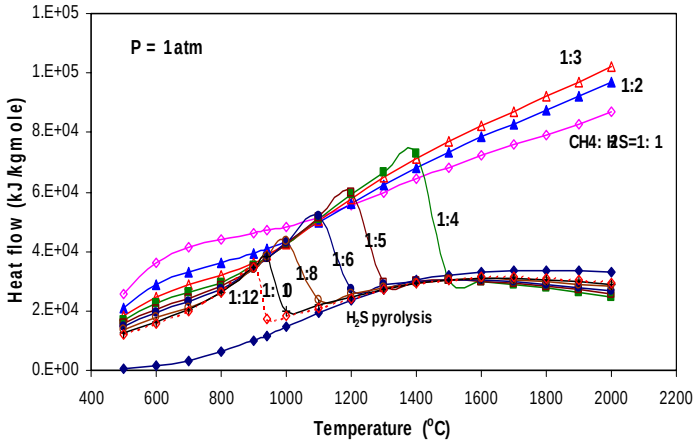

Figure 2. Total heat flow for HSRM process as a function of temperature and CH_4 to H_2S molar feed ratios.

It can be seen that ΔH is strongly dependent on both the temperature and hydrogen sulfide to methane feed ratio x. The required energies can be separated into two categories. Process energies required to carry out HSRM are much higher than those needed for hydrogen sulfide decomposition. At pinch-point temperature, the required energy drops from that for HSRM to a much lower value associated with the H_2S pyrolysis. As **Figure 2** indicates, HSRM is a highly

endothermic process and as such can be employed for storing energy in the form of chemical energy (*e.g.* hydrogen) from high temperature sources such as solar resource. The pinch-point temperatures and energy requirements for HSMR process are depicted in **Figure 3**. Increasing the hydrogen sulfide to methane ratio, x, reduces the pinch-point temperature, as does the total energy required for the HSRM process

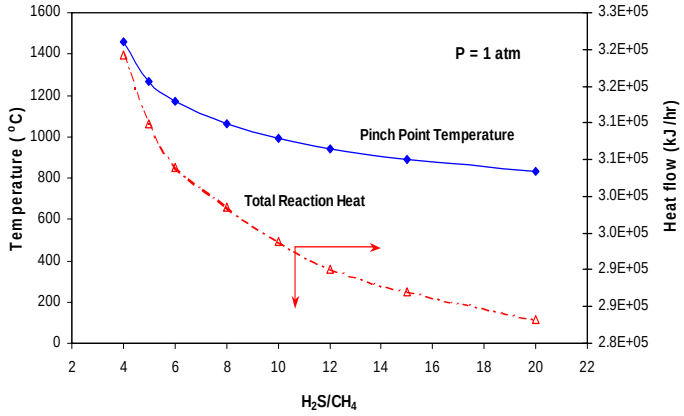

Figure 3. Pinch points temperature and total heat flow at various CH_4 to H_2S molar feed ratios.

Process flowsheet and efficiency calculations

Based on the thermodynamic analyses discussed above, three flowsheets based on cryogenic and membrane separation techniques were established for producing both liquid and gaseous hydrogen via HSRM process. All three flowsheets were set up at the pinch-point conditions for the HSRM process.

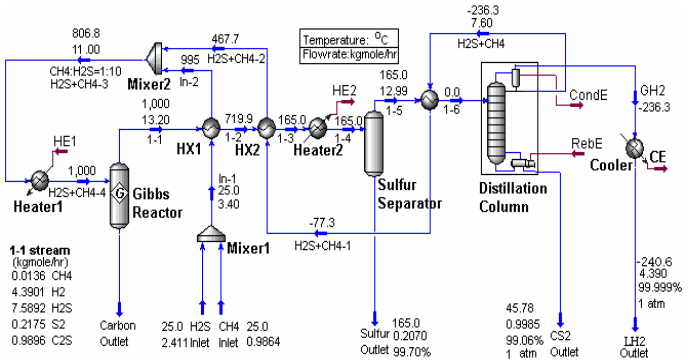

Figure 4. Process flowsheet for liquid hydrogen production via HSRM process.

A HYSYS™-based process flowsheet for liquid hydrogen production by cryogenic separation is shown in **Figure 4**. Hydrogen, sulfur diatomic gas and carbon disulfide are produced in a Gibbs reactor that operates under no carbon lay down condition. The gaseous mixture at the outlet of the Gibbs reactor is cooled to separate out sulfur, and the remaining gases are sent to a cryogenic distillation tower to recover hydrogen and carbon disulfide from the unreacted hydrogen sulfide and methane. The unreacted hydrogen sulfide and methane are mixed with fresh feed in a manner to maintain the initial H_2S to CH_4 feed ratio x and subsequently heated and sent back to the Gibbs reactor. Low temperature (-236.3 °C) gaseous hydrogen that exists distillation tower can be liquefied to by adding a small amount of cryogenic energy to reduce its temperature to -240.6 °C. One important advantage of the process is that hydrogen sulfide serves as both a reactant and as a working fluid for the cryogenic separation process. With H_2S recirculation, no other working fluid, such as nitrogen or helium, is necessary.

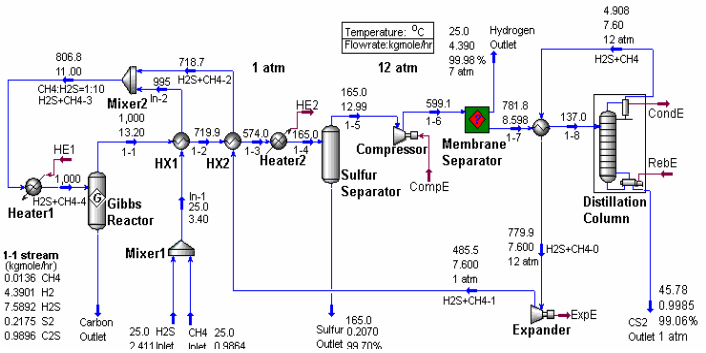

Figure 5. Gaseous hydrogen production via HSRM process paired with a membrane separation.

The HSRM process can be combined with a membrane separation technology for gaseous hydrogen production. Two types of membrane separation processes are developed based on the sequences of carbon disulfide and hydrogen separation. In one version depicted by the flowsheet of **Figure 5**, hydrogen separation occurs before that of carbon disulfide. After quenching the gas mixture exiting the Gibbs reactor, sulfur separates out of the main stream and the remaining gas mixture compressed to 12 atm (necessary for hydrogen separation through the membrane). The membrane separation efficiency assumed to be 100%. After hydrogen separation, the remaining gas mixture, consisting of hydrogen sulfide, methane and carbon disulfide, is sent to a distillation tower to separate the carbon disulfide from the mixture. The gas mixture is then expanded to 1 atm, mixed with fresh feed and sent back to the Gibbs reactor. The total required energy for both the cryogenic and membrane systems portions of the process are show in **Figure 6**.

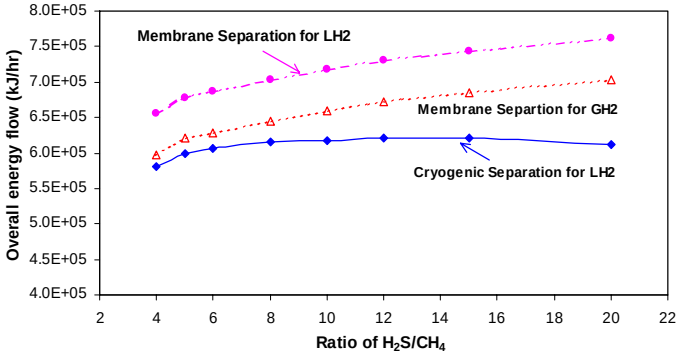

Figure 6. Overall energy requirements for hydrogen production via HSRM process

Acknowledgments. The authors are grateful for the financial support provided by the U.S. Department of Energy and NASA Glenn Research Center.

References

1. Hugman, R.H., Vida, E.H., Springer, P.S., Chemical composition of discovered and undiscovered natural gas in the United States. 1993 update. *GRI-93/0456* **1993.**
2. T-Raissi, A., Technoeconomic analysis of area II hydrogen production – Part 1. Final report fro DOE, **2002.**

HYDROGEN PRODUCTION BY STEAM REFORMING OF HYDROCARBONS

Niels R. Udengaard

Haldor Topsoe Inc.
17629 El Camino Real, Suite 300
Houston, Texas 77058

Introduction

The use of hydrogen for petrochemicals, fertilizers and as energy carrier in connection with renewable energy production will increase substantially in the next 5-10 years as even more stringent environmental legislation is enforced. Low sulfur gasoline and diesel fuels will become mandatory and harmful emissions will be reduced drastically. Hydrogen will be required by refiners and specialty chemical manufacturers to meet the global need for cleaner products. The growing fuel cell market will be dependant on hydrogen as a primary fuel source.

Hydrogen requirements vary widely. For small capacities below 0.1 MM SCFD, supply in cylinders or production by electrolysis may be preferable. Hydrogen production from methanol or ammonia cracking is suitable for small, constant or intermittent requirements as used in the food, electronics and pharmaceutical industries. For larger capacities hydrocarbons are used primarily as feedstock in the steam reforming process for production of hydrogen and synthesis gas.

The current production of hydrogen in North America is about 6000 MM SCFD, and the annual growth is expected to be above 4%. Most of this growth is for refineries for their production of ultra-low sulfur diesel and gasoline.

In spite of efforts to produce hydrogen by processes involving solar energy, wind energy, nuclear energy and biofuels, fossil fuels remain the most feasible feedstock in the near term, and for commercial scale production of pure hydrogen, steam reforming remains the most economic and efficient technology for a wide range of hydrocarbon feedstocks.

Steam Reforming Technologies

A typical layout of a hydrogen plant based on steam reforming including the following steps:

Natural gas feed is preheated in coils in the waste heat section of the reformer, and sulfur is removed over a zinc oxide catalyst. Process steam is added, and the mixture of natural gas and steam is further preheated before entering the tubular reformer. Here, conversion to equilibrium of hydrocarbons to hydrogen, carbon monoxide and carbon dioxide takes place over a nickel based reforming catalyst.

The gas exits the reformer and is cooled by steam production before entering the shift converter, typically a medium temperature shift. Over the shift catalyst more hydrogen is produced by converting carbon monoxide and steam to carbon dioxide and hydrogen. The shifted gas is cooled further to ambient temperature before entering the PSA unit. High purity hydrogen product is obtained, and the off-gas from the PSA unit is used in the reformer as fuel supplemented with natural gas fuel.

Combustion air for the tubular reformer burners can be preheated in coils in the reformer waste heat section. Part of the steam produced in the hydrogen plant is used as process steam, the excess steam is exported.

In many situations when natural gas is not available, higher hydrocarbons become the preferred feedstock for the reforming process. Many refineries also can benefit from flexibility in feedstock, taking advantage of the surplus of various hydrocarbon streams in the refinery.

Fired tubular reforming is generally the most competitive technology for capacities of up to more than 100 MM SCFD hydrogen.

Topsoe's latest development in steam reforming process technology is the advanced steam reforming process. The characteristics of this process are:

- High reformer outlet temperature
- Low steam to carbon ratio.
- High combustion air preheat (optional).
- Adiabatic prereforming (optional).
- High heat flux reformer.

Low steam to carbon ratios, typically 2.5, in hydrogen plants, reduce the mass flow through the plant and thus the size of equipment. The lowest investment is therefore generally obtained for plants designed for low steam to carbon ratios. However, a low steam to carbon ratio also increases the methane leakage from the reformer. This can be compensated for by increasing the reformer outlet temperature to typically 1690^{o} F in hydrogen plants. Furthermore, operating at a low ratio requires the use of non-iron containing catalyst i.e. a copper-based medium temperature shift catalyst in order to eliminate production of by-products in the shift section.

The installation of an adiabatic prereformer upstream of a tubular reformer has been found to be very advantageous in naphtha based plants and plant operating on fuel gases with higher concentrations of higher hydrocarbons. Since all higher hydrocarbons are converted over the prereformer catalyst, the inlet temperature of the gas inlet in the reformer can be increased to 1200^{o} and the reformer can be designed for higher heat fluxes. This reduces the size of the tubular reformer, resulting in direct capital cost reduction.

High combustion air preheat temperatures results in reduced fuel consumption and reduced steam production. The combustion air temperature can be used to adjust the steam export to a desired level. Temperatures of up to 1020^{o} F are industrially proven in a radiant wall reformer.

The Topsoe convection reformer (HTCR) is a new concept which combines the radiant and waste heat section of the conventional reformer in one relatively small piece of equipment, thereby optimizing heat transfer to the steam reforming reaction and avoiding the surplus energy (often seen as steam export) inherent in conventional plants.

HTCR based layout is an attractive option for smaller sized hydrogen plants.

Efficiency and Production Costs

With no steam export the theoretical energy consumption is 300 BTU/scf H_2 on LHV (lower heating value) basis. The industrial value for natural gas based plants is about 320 BTU/scf H_2 corresponding to 94% of the theoretical efficiency. At locations with high natural gas prices, the energy efficiency becomes critical. For a natural gas price of 4 USD/MM BTU, the feedstock and utility costs makes about 65% of total operating costs.

Catalysts and the Mechanism of Steam Reforming

The steam reforming process may appear straightforward from an overall consideration as the product composition is determined

by simple thermodynamics, but in reality it is a complex coupling of catalysis, heat transfer and mechanical design.

In recent years, there has been progress in steam reforming technology resulting in less costly and more efficient plants, in part because of better materials for reformer tubes, better control and understanding of carbon limits, and better catalysts and process concepts with high feedstock flexibility. This progress has been accompanied by a better understanding of the reaction mechanism.

The typical steam reforming catalyst contains nickel. The catalyst properties are dictated by the severe operating conditions in the reformer with high temperatures and steam partial pressures. Sintering is an important cause of deactivation of nickel-containing steam reforming catalysts. The most important parameters are the temperature and the atmosphere in contact with the catalyst. The catalyst support can affect the sintering in various ways by loss of surface area. The sintering ceases when the nickel particle size exceeds a given size. The maximum size increases with temperature.

The catalyst activity is rarely a limiting factor. The catalyst volume (space velocity) is fixed from the tubular reformer design. The equilibrium conversion at high reforming temperatures is achieved at even very high space velocities when extrapolating the intrinsic rates. In practice, however, the utilization of the activity (as expressed through the effectiveness factor) is smaller than 10% because of transport restrictions. It can be shown by computer simulations that the catalyst is not the limiting factor for the design of a tubular reformer. An increase of the heat flux and the load at a given exit temperature by a factor of two results in an increase in methane leakage by only 10%.

Recent studies of the fundamentals of the steam reforming reactions have lead to a more consistent understanding of the mechanism of the main reactions and the competing reactions for carbon formation. The dissociation of methane on nickel surfaces has been investigated extensively, and several details of the reaction pathway are known from fundamental studies, in-situ high resolution electron microscopy and theoretical calculations.

In-situ high resolution electron microscopy has provided new information on sintering mechanisms and for the importance of steps in nucleation of whisker carbon. Density Functional Theory calculations have quantified the energetics of methane activation and shown that activation barriers are smaller on surface steps where also carbon is the most stable surface species.

Conclusions

The demand for hydrogen is growing in many industries, particularly in the chemical and refining industries. Topsoe has been active in this field for more than 50 years and offers a wide range of advanced technologies for small and large capacities meeting the demand for low operating and investment costs.

For small plants, convection reforming in the form of compact, skid-mounted plants is available. This is a low investment alternative to conventional concepts using tubular reforming.

For medium and large-scale plants the predominant technology is steam methane reforming of hydrocarbons. Advanced steam reformer design allows high temperatures and low steam to carbon ratios for hydrogen production resulting in high energy efficiency and lower cost plants.

For very large hydrogen and syngas plants the oxygen reforming technology may be applied, such as autothermal reforming and oxygen fired secondary reforming. These technologies are especially attractive when cheap oxygen is available.

References

(1) Rostrup-Nielsen, J.R.; Sehested, J.; Norskov, J.K.; Hydrogen and Syngas by Steam Reforming, Academic Press, 2002.

(2) Dybkjaer, I.; Winter Madsen, S., Hydrocarbon Engineering, December/January 1997/98.

Logistic Reformation of Hydrocarbon Mixtures and Jet Fuels

Ivan C. Lee[1], Jakob J. Krummenacher[2], Brady Dreyer[2], and Lanny D. Schmidt[2]

[1] AMSRD-ARL-SE-DC
US Army Research Laboratory
2800 Powder Mill Road
Adelphi, MD 20904
And
[2]Department of Chemical Engineering and Materials Science
University of Minnesota
412 Washington Ave SE
Minneapolis, MN 55455

Abstract

Reformation of logistic fuels (diesel and jet fuel) has attracted a lot of attentions recently, mainly because a reformer can be integrated with fuel cells or internal combustion engines for power generation and/or emission control. Previous work in this group focused on the catalytic partial oxidation (CPOX) of a variety of heavy hydrocarbon including C8-C16. Here we will reformation results with both air and steam addition. This paper will focus on jet fuel , decane, and a binary mixture. All experiments are performed in a short contact time adiabatic reactor with a rhodium-coated monolithic catalyst. The addition of steam lowers the reformation temperature and reduces the undesired carbon deposition, while the fuel conversion remains above 90% in low fuel-to-air-ratio (i.e. syngas production regime).

Introduction

An integrated system of a fuel reformer and a fuel cell can provide portable and mobile power for battery chargers and scout vehicle silent watch. However, one of the key challenges is the hydrogen source.

The catalytic partial oxidation of heavy alkanes (C8 to C16) can produce H_2 and CO with >80% selectivities on Rh-based catalyst at short contact times operating autotheramlly [(1)- (3)]. Previously, all these experiments considered reformation in dry conditions. This paper focuses on jet fuel and hydrocarbon mixtures with steam addition. Steam addition with water-to-carbon ratio (H_2O/C) of 1 simulates the condition at which the reformer utilizes the recycle steam from solid oxide fuel cells.

Experimental

Material Synthesis. The catalyst sample were Rh/alumina on ceramic alumina monolith foams. The foams (1 cm thick) were coated with 5wt% γ-Al_2O_3 to roughen the catalyst surface and increase the surface area. The monolith with wash-coats were then coated with 5wt% Rh by soaking them in Rh(NO3)3 solution and by calcination.

Fuel Characterization. The jet fuel sample is a military JP-8. Sulfur Analysis of the jet fuel is performed on a Agilent gas chromatography (GC) with a Ionic/ Sievers sulfur chemiluminescence detector (SCD). The total sulfur content was determined by peak area summation on the SCD chromatogram.

Catalysis and Carbon Burn-off. Since JP-8 is a hydrocarbon mixture, the conversion of JP-8 was estimated by assuming that all molecules > C8 were jet fuel reactants. This gives a lower bound to the conversion, and the actual conversion is higher than the value reported here. Similar experiments on decane and decane-naphthalene mixture were also performed. The product gas analysis was performed with a GC.

Carbon burn-off experiment was performed after each CPOX experiment by feeding oxygen and nitrogen while the fuel and H_2O feed was shut off. The exothermic nature of the carbon burn off was recorded by changes in the catalyst bed face temperatures.

Results and Discussion

Figure 1 shows the chromatograms of a military JP-8. Area summation of sulfur peak in sulfur chromatogram indicates that the sulfur content of this jet fuel is 310ppmw.

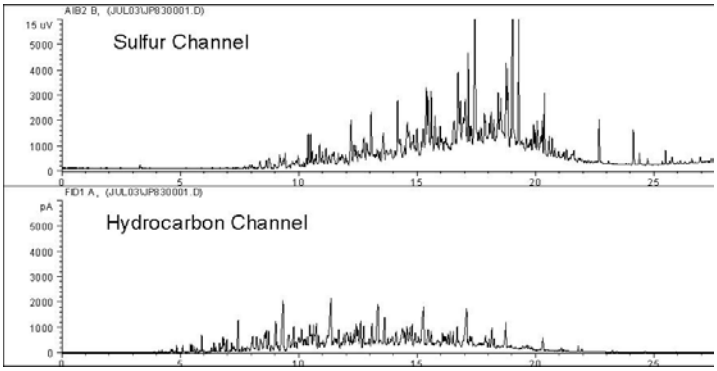

Figure 1. Analysis of a jet fuel that is being reformed in this study.

Figure 2 shows the jet fuel conversion and corresponding catalyst back face temperature at various C/O ratios. The conversion remains high at any C/O ratio when the reformer runs dry. The results also indicate that the steam addition (H_2O/C =1) lowers the catalyst back face temperature by 50 to 100 oC. At C/O = 1.3 and H_2O/C = 1.0, the catalyst back-face temperature is 770 ^{O}C and the conversion is 90%; at C/O = 1.5 and H_2O/C =1.0, the catalyst back-face temperature is 752 ^{O}C and the conversion is 65%. Apparently, catalyst temperature (as a result of steam addition) of 752^{O}C is too low to sustain high fuel conversion.

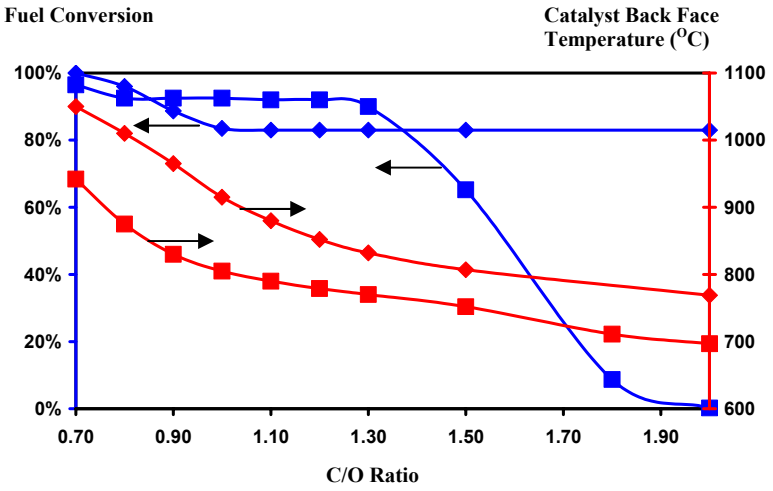

Figure 2. Fuel conversion and catalyst back face temperature of JP-8 catalytic partial oxidation. ∨ represents H_2O/C = 0, and ® represents H_2O/C = 1.

Figure 3 shows the selectivities to syngas (H_2 & CO), combustion products (H_2O & CO_2) and olefins for the JP-8 reformation at H_2O/C =0. The major products at low C/O ratio are H_2 and CO. When C/O > 1.0, the major products are olefins. Since the preferable products for solid oxide fuel cells are H_2 and CO, one would like to run C/O of 0.7 or 0.8 for fuel cell applications.

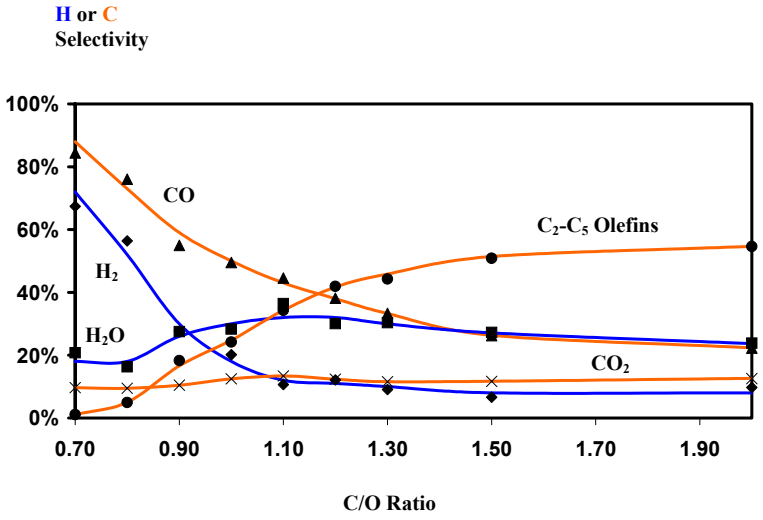

Figure 3. Product selectivities for catalytic partial oxidation of JP-8.

As aforementioned, one key benefit of steam addition is the reduction of reaction temperature. Another potential benefit is the reduction of carbon formation. Carbon burn-off results are shown in Figure 4. Smaller peak area for steam addition reformation implies less carbon formation.

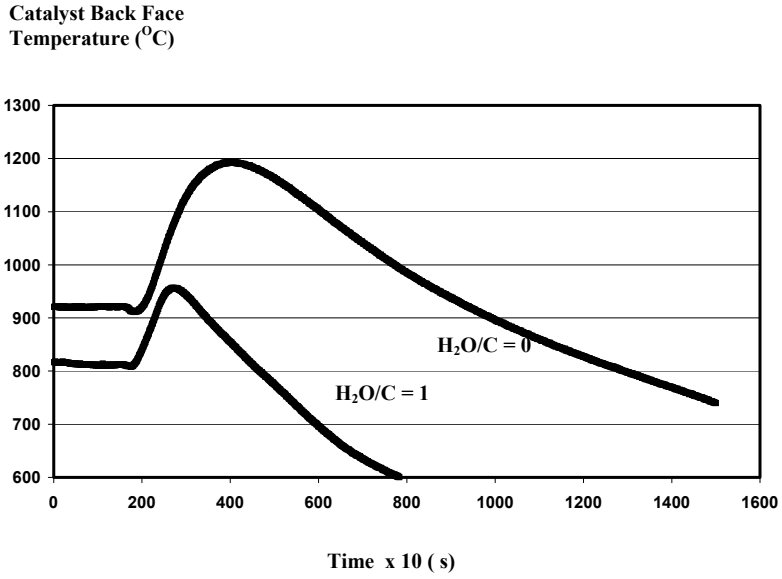

Figure 4. Carbon burn off curves (Exotherms) for JP-8 reformation at C/O ratio = 1.

Recently, Krummenacher and Schimdt have demonstrated that the selectivities of CO and H_2 formation are both above 80% [(1),(2)]. Here Figure 5 indicates that there is some extra hydrogen being stripped off from H_2O, which results in the hydrogen selectivity above 100%. Moreover, the CO selectivity is suppressed to 60%. This suggests that the steam addition also enhance the water-gas shift reaction.

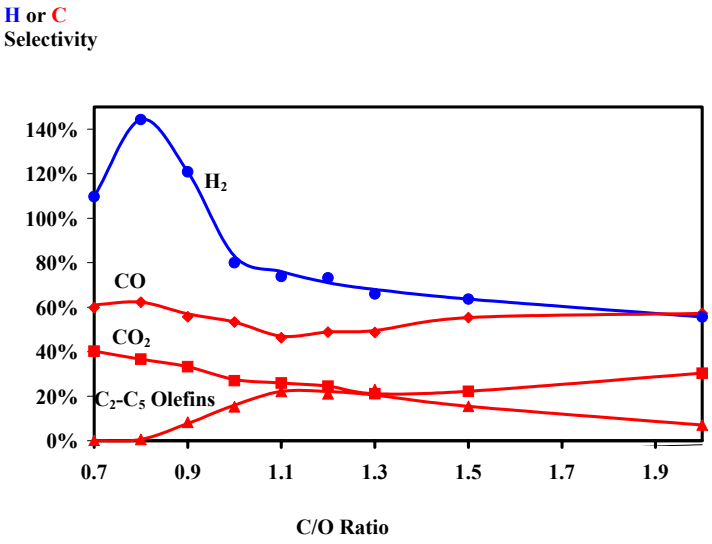

Figure 5. Product selectivities for decane reformation with steam addition (H_2O/C =1.0)

Additional steam addition experiments on binary mixtures such as decane-naphthalene were performed. The data analysis is underway.

Conclusions

These experiments demonstrate that a single monolithic reactor with Rh/alumina catalyst can operate under dry or steam condition. Steam addition lowers the reforming temperature and reduces the carbon formation. Low C/O ratio (0.7-0.8) favors hydrogen and carbon monoxide production. Steam addition also promotes the hydrogen production for decane reformation by stripping off hydrogen from water or by high temperature shift reaction.

Acknowledgement. This work was sponsored by the Army Research Laboratory Collaborative Technology Alliance in Power and Energy.

References

(1) Krummenacher, J. J., West, K. N. and Schmidt, L. D., *J. Catalysis* **2003**, *215*, 332.
(2) Krummenacher, J. J. and Schmidt, L. D., *J. Catalysis*, accepted.
(3) Subramanian, R., Panuccio, G.J., Krummenacher, J. J., Lee, I. C. and Schmidt, L.D., *Chem. Eng. Sci*., accepted

LOGISTIC FUEL TO HYDROGEN - FUEL PROCESSING USING MICROFIBROUS ENTRAPPED CATALYSTS AND SORBENTS FOR PEM FUEL CELL

Mukund Karanjikar, Bong-Kyu Chang, Yong Lu, Bruce Tatarchuk

Department of Chemical Engineering
Auburn University
Auburn, AL 36849

Introduction

Fuel cells offer a unique way to convert chemical energy of a fuel directly into electrical energy and is a renewable resource. Unlike most other fuel cell types, Polymer Electrolyte Membrane Fuel Cells (PEMFC) are suitable for small, low power applications. These can be scaled down to small size without sacrificing performance and are suitable for applications ranging from microwatts to hundreds of kilowatts. Other advantages are low noise signature, pure water as by-product and the ability to refuel rather than recharge or discard. PEMFC are preferred in many applications like mobile power generation units, man-portable power generators and on-board power generation for automotive propulsion.

The bandwidth requirement for new electronic appliances demands more energy density than the existing batteries can offer (1). Due to the high cost of primary batteries and the large weight of rechargeable batteries, fuel cell technology is being developed to provide a power source for the individual soldier, sensors, communication equipment and other various applications in the United States army (2).

PEMFC require hydrogen as a fuel to generate electricity.

Hydrocarbon reforming is widely regarded as the best means of hydrogen generation for PEM Fuel Cells.

Various fuels such as methane, methanol, ethanol, gasoline, diesel and JP8 are being considered for fuel cell applications. Diesel and JP8 have salient advantages over other fuels mainly high energy density, safe handling and logistics (3).

Present work deals with development of a bread-board fuel processor for JP8 fuel. The fuel processor has its main components to be reformer, post-reformer, H_2S removal, water gas shift, carbon dioxide removal, preferential oxidation and fuel filter units. Most of these units contain microfibrous entrapped catalysts and sorbents. Microfibrous materials is a new class of proprietary materials that offer advantages such as high contacting efficiency, very low pressure drop and efficient thermal management over conventional packed bed approach thereby making the whole processor very compact (4).

Experimental

Experimental Set-up. Figure 1 shows the schematic process flow diagram of the fuel processor. First reactor is steam reformer for JP8 fuel the outlet of which flows into post-former followed by H_2S removal reactor through intermediate gas storage tank by means of a compressor. After H_2S removal the reformate flows into high temperature water gas shift and low temperature water gas shift reactors followed by preferential oxidation of CO reactor. The reformate then flow through carbon dioxide removal absorption tower that has continuous circulation of alkaline absorbent. The reformate finally flows through fuel filter unit to remove trace quantities of all gases other than hydrogen before entering fuel cell.

Catalysts and Sorbents. Catalysts for reformer, post-former (precious metal) and water gas shift reaction (Fe-Cr and Cu-Zn) were obtained commercially from Sud-chemie Inc. Sorbent used for H_2S removal was a microfibrous entrapped ZnO sorbent. The liquid sorbent used for CO_2 removal was alkaline solution. The solid sorbent in the fuel filter for CO_2 removal was microfibrous entrapped lime based sorbent. The PROX catalyst was a microfibrous entrapped metalloxide promoted precious metal catalyst (5). The fuel filter had microfibrous entrapped sorbents for CO, CO_2, NH_3 and H_2S.

Preparation of Catalysts and Sorbents. The microfibrous entrapped catalysts and sorbents are prepared by wet-lay process followed by sintering at high temperature in presence of hydrogen. D. Cahela and B. Tatarchuk (6) discuss the process in details. This gives the support material for the catalyst /sorbent. The final catalysts/ sorbents were prepared using conventional incipient wetness method followed by calcination in air. Figures 2 shows SEM image of microfibrous entrapped PROX catalyst.

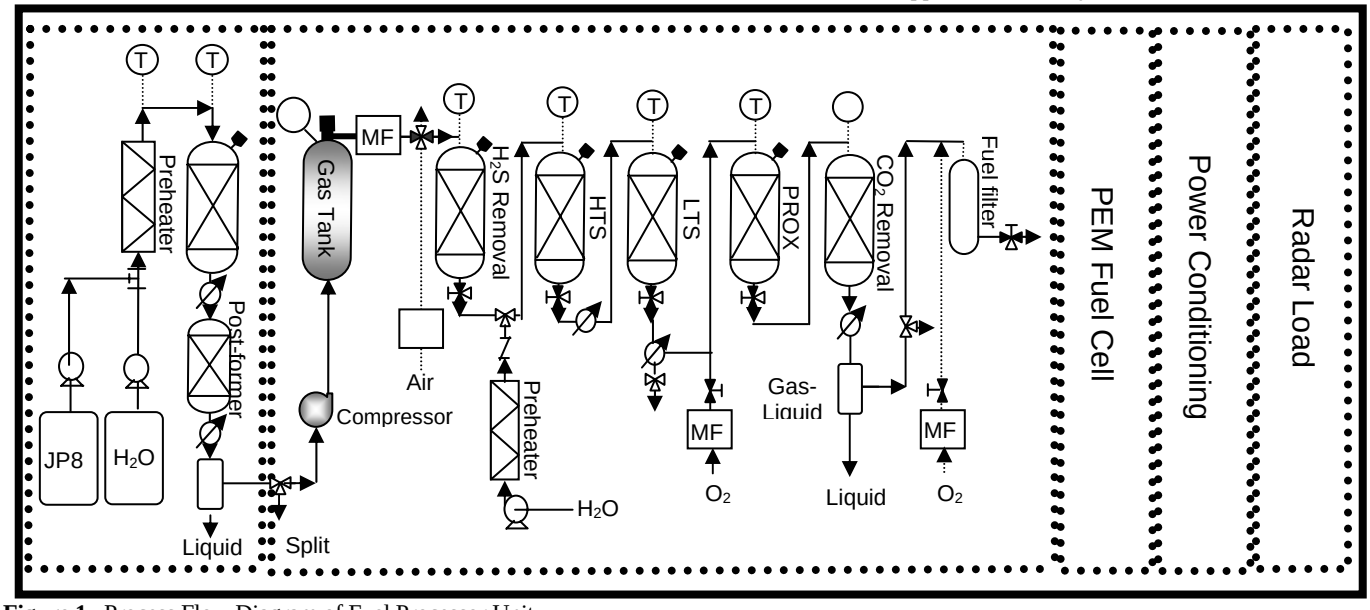

Figure 1. Process Flow Diagram of Fuel Processor Unit

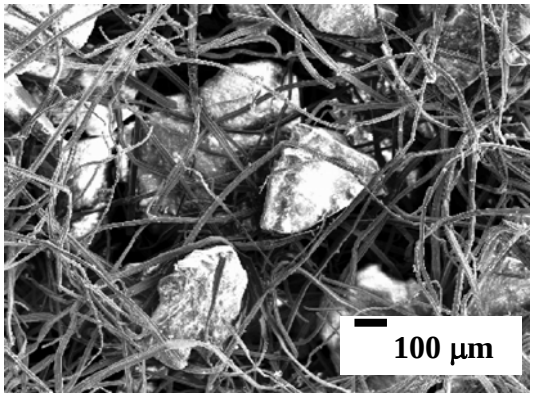

Figure 2. SEM of PROX catalyst support

Results and Discussion

Reformer and Post-former. The steam reforming of JP8 at 900°C and atmospheric pressure over the commercial catalyst gives reformate with composition 60 – 65% H_2, 18-22% CO_2, 8-12% CO, 5 – 12% C_1-C_3 and around 60 ppm H_2S. Post-former reduces the light hydrocarbons to below detection limits. The reforming and post-forming catalyst is sulfur tolerant hence the sulfur removal phase was employed after these stages.

Hydrogen Sulfide Removal. This section of the processor implements polishing sorbent concept. A composite bed consisting of the packed bed of 1-2mm Sud-Chemie ZnO extrudates followed by the above mentioned microfibrous entrapped ZnO/SiO_2 sorbent particulates has been demonstrated for H_2S removal from H_2 fuel stream. Figure 3 shows the breakthrough curves for 2vol% H_2S challenge in H_2 in single and composite beds at 400°C and a face velocity of 1.2cm/s (30mL(STP)/min dry gas flow rate). Two single beds, 7mm(dia.)×3mm(thick) microfibrous entrapped ZnO/SiO_2 (A) and 7mm(dia.)×7mm(high) packed bed of 1-2mm Sud-Chemie ZnO sorbent extrudates (B), provided breakthrough times (@1ppmv H_2S detection limit) of 5min and 28min, respectively. The breakthrough curve with small particulates (ZnO/SiO_2) alone is very sharp. But the breakthrough curve in packed bed with large particulates (B) is very sigmoidal. When the polishing sorbent was placed behind the packed bed (B+A), the outlet from the packed bed B, where the H_2S concentrations increased very slowly with the time on stream after the breakthrough point in bed B, was encountered immediately with the high contacting efficiency polishing sorbent A. As a result, a very large extension in gas life was obtained due to high contacting efficiency, compared to that either the polishing sorbent or the packed bed alone will do.

For this demonstration, 60 ppm H_2S in real reformate is reduced to less than 0.6 ppm at the outlet at 400°C and 30% water content.

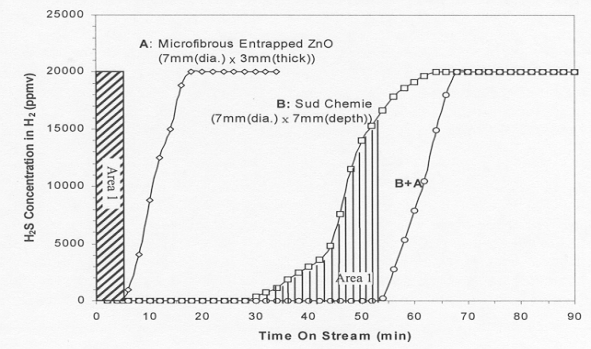

Figure 3. H_2S Adsorbent performance

Water Gas Shift Reactions. High temperature and low temperature water gas shift reactions operate respectively at 350 -400 and 180 -200 °C and atmospheric pressure. The inlet CO concentration of 10 -15% is reduced to around 0.75 - 1% in presence of microfibrous entrapped catalysts.

PROX Stage. The PROX reactor operates at 180 – 200 ° C and atmospheric pressure. The carbon monoxide content is reduced to less than 10 ppm at the exit of the reactor.

Figure 4 compares the performance of microfibrous entrapped catalyst with pellets of the size 1.5 – 2.5 mm.

CO_2 Removal Section. The absorption in alkaline solution reduces the CO_2 content from 35% to about 200 ppm at the outlet. The absorption unit is operated in a continuous circulating fashion.

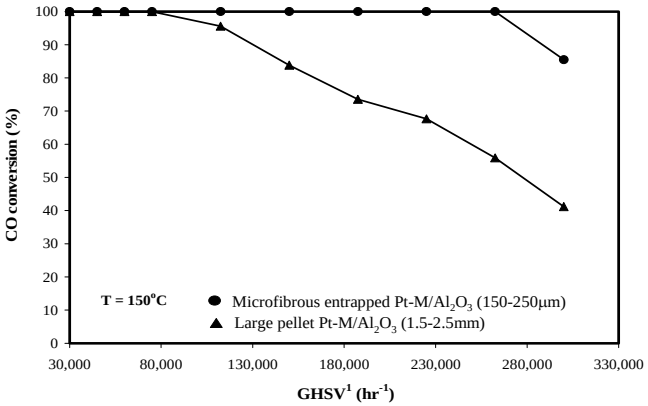

Figure 4. Comparison of microfibrous entrapped PROX catalyst with pellets

Fuel Filter Section. All the ppm level gases such as H_2S CO, CO_2, NH_3 and organic vapors are removed by means of various microfibrous entrapped sorbents. This unit operates at room temperature and atmospheric pressure.

Conclusion

1. Logistical fuel to radar power is possible by means of a fuel processor followed by PEM fuel cell.
2. Traditional processes are applicable for reformate clean-up processing technologies can be reduced in weight and volume by means of new materials such as microfibrous entrapped sorbents and catalysts and regenerable continuous – batch operation.
3. With additional process integration, mainly energy, the fuel processor can become an attractive means of hydrogen generation.

Acknowledgment. The financial support of SMDC – SMDTC is gratefully acknowledged.

References

1. C.K.Dyer, *J Power Sources*, 4675 (2000), 1-4
2. A.S. Patil, *Proceedings of 32nd Intersociety Energy Conversion Engineering Conference, (*1997) 793-795
3. C. Pereira, J-M. Bae, S. Ahmed, M. Krumpelt, *DOE Hydrogen Program Annual Review*, May 9, 2000, San Ramon CA
4. D Harris, D Cahela, B Tatarchuk, *Composites Part A*, 32, (2001)1117-1126
5. B.K. Chang, B. J. Tatarchuk, *Prepr. Pap. – Am. Chem. Soc., Div. Fuel. Chem*
6. D. Cahela and B. Tatarchuk, *Catalysis Today* , 69(2001) 33-39

HYDROGEN PRODUCTION FROM BIOMASS FEEDSTOCKS

Hyun-Seog Roh, David L. King, and Yong Wang[*]

Pacific Northwest National Laboratory, P.O. Box 999, Richland, WA 99352, USA

Introduction

Hydrogen attracts significant research interests because it is a clean fuel emitting only water without formation of greenhouse gases. Commercially, hydrogen has been produced from catalytic steam reforming of fossil fuels, for example, methane.[1] To reduce greenhouse gas emissions, the hydrogen should be derived from renewable energy sources such as bio-ethanol.[2-4] As a consequence, ethanol steam reforming has been studied, which gives potential alternative to hydrogen production.[4,5] For the purpose of H_2 production as a fuel in molten carbonate fuel cell (MCFC), ethanol steam reforming has been studied at the temperature range of 600 – 700°C, which is the operating temperature of anode in MCFC.[6-8] As for a steam/ethanol ratio, most researchers employ more than 8 to avoid carbon formation.[7-9]

In this paper, we have tested various supported Rh catalysts and the effects of metal composition, promoter, and support on the selectivity to intermediates, hydrogen, and CO/CO_2 were evaluated. For comparison, micro-channel reactor was employed at low temperatures (350 – 500°C) with a stoichiometric feed ratio (H_2O/EtOH = 3.0) to examine the benefits of efficient heat and mass transport comparing with conventional quartz tube reactor.

Experimental

Support materials employed in this study were γ-Al_2O_3 (99%, SASOL), ZrO_2 (99%, MEL Chemicals), and CeO_2-ZrO_2 (CeO_2: 17.5%, MEL Chemicals). The supports were pre-calcined at 800°C for 6 h in air. Supported Rh catalysts were prepared by the incipient wetness method using its nitrate source. In some cases, Pt was co-impregnated with Rh. The catalyst samples were calcined at 600°C for 6 h in air.

Catalytic activity measurements were conducted in a fixed-bed micro-tubular quartz reactor with an inner diameter of 4 mm at atmospheric pressure. Special cares were taken to eliminate the potential mass and transport limitations. SiC was employed as a diluent in a micro-tubular quartz reactor, otherwise stated. For comparison, catalytic performance was also tested in a micro-channel single reactor having a gap of 0.75 mm, which is a much shorter transport distance as compared to that in a micro-tubular reactor. Thermocouples were placed strategically throughout the reformer system. Prior to each catalytic measurement, the catalyst was reduced in H_2/N_2 (10% H_2 in vol.) at 350°C for 1 h. A stoichiometric steam to ethanol ratio of 3 and a weight hourly space velocity (WHSV) of 75,660 cm^3/g cat/hr were used in all experiments. The mixture of ethanol and water was fed using a syringe pump and was vaporized at 250°C in the vaporizer.[10] The reformate was chilled, passed through a ice-trap to condensate residual water and ethanol, and then flowed to the on-line gas chromatograph (GC) for analysis. The GC was a micro-GC (Agilent) and GC columns used in this study were Molesieve 5A and PoraPlot Q.

Results and Discussion

A thorough literature search on ethanol steam reforming indicates that the Rh based catalysts are most active, and ethanol steam reforming mechanisms are complex.[4,5,7-9] Cavallaro assumes that the ethanol is converted during the first stage into ethylene by dehydration or into acetaldehyde by dehydrogenation.[11] The acetaldehyde easily undergoes decarbonylation to form CH_4 and CO.

First, we studied the effect of support on product distribution. Ethanol conversion is relatively independent on Rh loading (over 3wt%) while methane selectivity increases with Rh loading. It is most likely that acidic supports favor the ethylene formation over methane formation. The ethylene selectivity over Rh/Al_2O_3 catalysts with various Rh loading is summarized in Table 1.

Table 1. Ethylene Selectivity with Temperature over Rh/Al_2O_3 Catalysts

Temp. (°C)	1%Rh	3%Rh	6%Rh	10%Rh
500	0.73	0.69	0.59	0.46
550	0.46	0.45	0.34	0.22
600	0.14	0.12	0.00	0.00
650	0.00	0.00	0.00	0.00

1%Rh catalyst showed higher than 70% ethylene selectivity at 500°C. The ethylene selectivity decreases with reaction temperature due to the fact that ethylene steam reforming is favorable at higher temperatures. It is also clear that the ethylene selectivity decreases with Rh loading. This is possibly due to the fact that the portion of Al_2O_3 in the catalyst decreases with Rh loading. In addition, the effects of support were also studied. 10%Rh/ZrO_2 showed 12% ethylene selectivity at 500°C, while 10%Rh/CeO_2-ZrO_2 exhibited no ethylene formation at the same condition. Instead, 10%Rh/CeO_2-ZrO_2 showed 43% CH_4 selectivity. Under the same condition, the selectivities to CH_4 over 10%Rh/ZrO_2 and 10% Rh/Al_2O_3 were 15% and 3%, respectively.

Table 2 summarizes the effect of Pt promotion on 3%Rh/CeO_2-ZrO_2 catalyst at 450°C.

Table 2. Promotion Effect of Pt on 3%Rh/CeO_2-ZrO_2 Catalyst at 450°C

Catalyst	X_{EtOH}	S_{CO}	S_{CO2}	S_{CH4}
3%Rh3%Pt	1.00	0.08	0.38	0.53
3%Rh	0.74	0.57	0.12	0.30

The addition of Pt to Rh based catalysts results in enhanced ethanol conversion. In addition, Pt plays a role in decreasing CO selectivity and enhancing both the formation of CH_4 and CO_2. The increased CH_4 selectivity is possibly due to the enhanced decarbonylation of CH_3CHO.[11] The increase of CO_2 selectivity is mainly due to the beneficial effect of CeO_2 to increase water gas shift reaction.

In order to demonstrate the potential advantages of microchannel reactors, a 3%Rh3%Pt/CeO_2-ZrO_2 catalyst was compared in both a micro-channel reactor and a conventional micro-tubular reactor. Here, micro-channel reactor has a gap of 0.75 mm, which is a much shorter transport distance as compared to that in a micro-tubular reactor with an inner diameter of 4 mm. To demonstrate the benefits of micro-channel reactor, the catalyst packed in the micro-channel reactor was not diluted with inert materials. In the case of micro-tubular quartz reactor, catalyst tests were executed both with and without catalyst dilution. The comparison of reaction results at 400°C are summarized in Table 3. Comparing the results of diluted quartz reactor with undiluted one, the former exhibited higher ethanol conversion than the latter. This is due to the enhanced heat transfer in the presence of SiC as diluents. The product distribution is similar to each other. As a result, the

[*] Corresponding author: yongwang@pnl.gov

hydrogen produced per ethanol fed of diluted quartz reactor is higher than that of undiluted one. At the same temperature, the ethanol conversion was 99% using micro-channel reactor but less than 80% with the undiluted quartz reactor. This clearly shows the benefit of micro-channel reactor in ethanol steam reforming. In another word, similar hydrogen productivity can be achieved in a microchannel reactor at a lower temperature. Lower temperature operations can directly translate into potential energy savings. In addition, the CO selectivity was decreased by employing micro-channel reactor resulting in high CO_2 selectivity.

Table 3. Comparison of Reaction Results on 3%Rh3%Pt/CeO_2-ZrO_2 Catalyst at 400°C

Reactor	X_{EtOH}	S_{CO}	S_{CO2}	S_{CH4}	H_2/EtOH
Micro-channel	0.99	0.33	0.25	0.40	2.10
Quartz (diluted)	0.97	0.44	0.11	0.44	1.65
Quartz (undiluted)	0.76	0.45	0.10	0.43	1.31

The CH_4 selectivity of micro-channel reactor was also slightly lower than those of quartz reactor with or without diluents. The reduced heat transfer distance was anticipated to be beneficial to the endothermic ethanol steam reforming.[10] Therefore, it is not surprising to see that the micro-channel reactor outperforms the micro-tubular reactor in terms of hydrogen productivity under the identical reaction conditions.

Table 4 shows the hydrogen produced per mole ethanol fed which are dependent on the reactor-type and reaction temperature.

Table 4. H_2/EtOH Depending on Reactor-Type with Reaction Temperature over 3%Rh3%Pt/CeO_2-ZrO_2 Catalyst

Reactor	350°C	400°C	450°C	500°C
Micro-channel	1.25	2.10	2.64	2.64
Quartz (diluted)	0.92	1.65	1.86	2.32
Quartz (undiluted)	0.79	1.31	1.73	2.29

The H_2/EtOH typically increases with reaction temperature because ethanol steam reforming is thermodynamically favorable at higher temperatures. However, it is clear that the productivity of H_2 is strongly dependent upon the reactor-type within the temperature range tested in this study. It should be noted that the productivity of H_2 at 450°C in the micro-channel reactor is even higher than that of 500°C with the quartz reactor regardless of the presence of diluents.

Conclusions

Ethanol steam reforming follows either dehydration to form ethylene or dehydrogenation to form CH_3CHO resulting in decarbonylation to form methane pathways. Acidic supports favor the ethylene formation over methane formation. Ethanol conversion is relatively independent on Rh loading (over 3wt%) while methane selectivity increases with Rh loading. Non acidic supports, such as CeO_2-ZrO_2, favors methane formation. Addition of Pt to Rh based catalysts increases both the formation of methane and CO_2 via water gas shift reaction. The micro-channel reactor outperforms the micro-tubular reactor in terms of hydrogen productivity under identical reaction conditions over 3%Rh3%Pt/CeO_2-ZrO_2 catalyst due to the reduced heat transfer distance, which is beneficial to the endothermic ethanol steam reforming.

Acknowledgement. This work was supported by Department of Energy's Office of Hydrogen, Fuel Cells, and Infrastructure Technologies. Most of work was performed in the Environmental Molecular Science Laboratory, a national scientific user facility sponsored by the U.S. Department of Energy's Office of Biological and Environmental Research and located at Pacific Northwest National Laboratory in Richland, WA.

References

(1) Rostrup-Nielsen, J. R. In *Catalysis, Science and Technology*; Anderson, J. R, Boudart, M., Eds; Springer: Berlin, 1984; Vol. 5.
(2) Huber, G. W.; Shabaker, J. W.; Dumesic, J. A. *Science* **2003**, *300*, 2075.
(3) Cortright, R. D.; Davda, R. R.; Dumesic, J. A. *Nature* **2002**, *418*, 964.
(4) Deluga, G. A.; Salge, J. R.; Schmidt, L. D.; Verykios, X. E. *Science* **2004**, *303*, 993.
(5) Liguras, D. K.; Kondarides, D. I.; Verykios, X. E. *Appl. Catal. B* **2003**, *43*, 345.
(6) Cavallaro, S.; Freni, S. *Int. J. Hydrogen Energy* **1996**, *21*, 465.
(7) Freni, S. *J. Power Sources* **2001**, *94*, 14.
(8) Cavallaro, S.; Chiodo, V.; Freni, S.; Mondello, N.; Frusteri, F. *Appl. Catal. A* **2003**, *249*, 119.
(9) Diagne, C.; Idriss, H.; Kiennemann, A. *Catal.Commun.* **2002**, *3*, 565.
(10) Palo, D. R.; Holladay, J. D.; Rozmiarek, R. T.; Guzman-Leong, C. E.; Wang, Y.; Hu, J.; Chin, Y.-H.; Dagle, R. A.; Baker, E. G. *J. Power Sources* **2002**, *108*, 28.
(11) Cavallaro, S. *Energy and Fuels* **2000**, *14*, 1195.

Hydrogen Production from Ethanol Using Low Energy Pulse Discharge at Ambient Temperature

Y. Sekine, M. Matsukata, E. Kikuchi, S. Kado, F. Haga***

Department of Applied Chemistry, School of Engineering and Science, Waseda University, Tokyo, Japan
*Department of Mechanical Engineering and science, Tokyo Institute of Technology, Tokyo, Japan
**Nissan, Yokosuka, Kanagawa, Japan

Introduction

Recently fuel cell is attracting attention. Especially, Polymer Electrolyte Membrane Fuel Cell (PEMFC) is one of the candidates. Because it is operated lower temperature than that of other fuel cell, and it has high performance in energy efficiency. Other reasons, clean exhaust gases, small size, light weight, fast start-up, rapid response and so on are also worthy of remark. So PEMFC is expected to serve as a fuel cell vehicle (FCV) and a home cogeneration system. But recent considerable Hydrogen production and transportation processes have many problems with the present technology (for example, The transportation and storage of Hydrogen), so it is need to research innovative technological methods to produce Hydrogen. So, we applied low energy pulse (LEP) discharge for this purpose. If LEP discharge used for reforming, reactions can be achieved at room temperature and atmospheric pressure. On the other hand, ethanol has a potential for being an alternative fuel replacing fossil fuels because ethanol can be produced from various renewable sources. So we tried to unify a supply and storage system with using liquid fuel (ethanol and water solution) and LEP discharge. And it was also attempted to design much smaller reformer, and improve energy efficiency.

Experimental

Figure 1-(a) shows our previous fuel delivery system. No catalyst was used, and argon was used as carrier gas. Gap distance of electrodes was fixed at 2.1 mm. Our previous reformer was flow type reactor, and the mixture of ethanol and water was supplied by chemical pump, and evaporated at 413 K. The reaction temperature was set at 393 K to prevent condensation into liquid.

On the other side, Figure 1-(b) shows our novel system. The bottom of carbon fiber bundle was soaked in ethanol solution contained in a small bottle. Present reformer was so attractive, because it was no need of heaters or pumps at all. This reformer used carbon fiber bundle as electrode. The solution could be pumped up to the top of the carbon fiber bundle by capillary action and supplied into discharge region. And, liquid fuel was evaporated by Joule heat which generate from internal resistance of electrode. The supplied fuel amount was controlled by the length and number of carbon fibers. The amount became larger in proportion to fiber length and fiber number. And the supplying fuel amount into the discharge region was about 30 cc min^{-1}, when the length was 7 cm and the number of carbon fiber was 84,000.

And a DC power supply (Matsusada precision inc. HARb-40R30) was used to produce the non-equilibrium pulsed discharge. All products were analyzed using a gas chromatography equipped with FID and TCD (Shimadzu GC14-B). The waveforms of current and voltage were observed by a digital signal oscilloscope (DSO):(Lecroy 9314C).

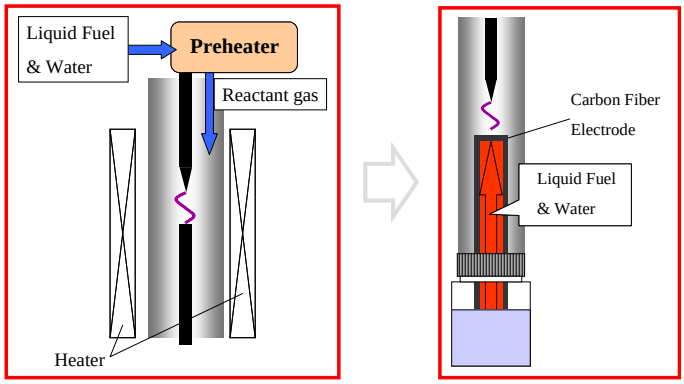

(a) previous system vapor phase reactor (b) present system liquid phase reactor

Figure 1. Schematic diagram of previous and present fuel delivery system to discharge region.

Results and Discussion

1) **Comparison of the vapor phase reaction and the liquid phase reaction.** Here, steam reforming of ethanol proceeded and hydrogen obtained as a main product. In addition to hydrogen, gases such as carbon monoxide, carbon dioxide, C2 compounds (mainly acetylene) and methane were produced. And the amount of produced gas increased in proportion to the increase of the gap distance of electrodes. But there is no influence of the gap distance of electrodes on the selectivity to product. So we discussed difference of H_2 formation rate before and after improvement. It was shown in Figure 2. They showed almost same trends. So the discharge energy loss in case of vapor phase reactor was partly utilized to vaporize ethanol solution in the case of liquid phase reactor. Moreover, it was possible to lessen the size of the reformer compact, and make the process more efficient, because of the needless to install such equipments as heaters to evaporate liquid fuel.

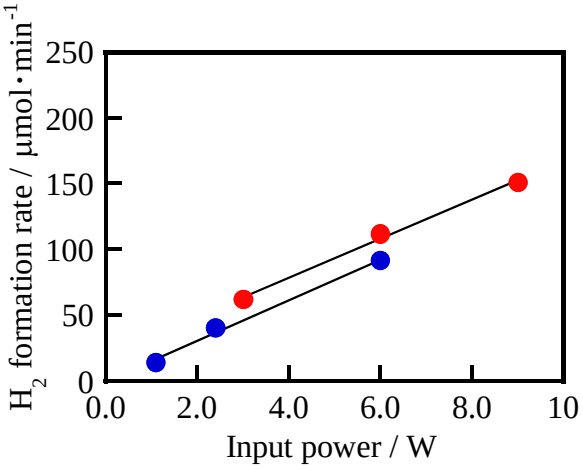

(●) Vapor phase reaction; mixture ratio, C_2H_5OH / H_2O = 1 / 1; gap distance of electrodes, 2.1 mm; temperature, 393 K; atmospheric pressure.
(●)Liquid phase reaction; mixture ratio, C_2H_5OH / H_2O = 1 / 1; gap distance of electrodes, 3.0 mm; room temperature; atmospheric pressure.

Figure 2. Comparison of previous and present reaction system

2) Effect of input power. In this section, we investigated effect of input power on ethanol consumption rate and carbon selectivity. The results of ethanol consumption rate and carbon selectivity are plotted against the input power in Figure 3. As shown in Figure 3, carbon selectivity was almost stable under any conditions.

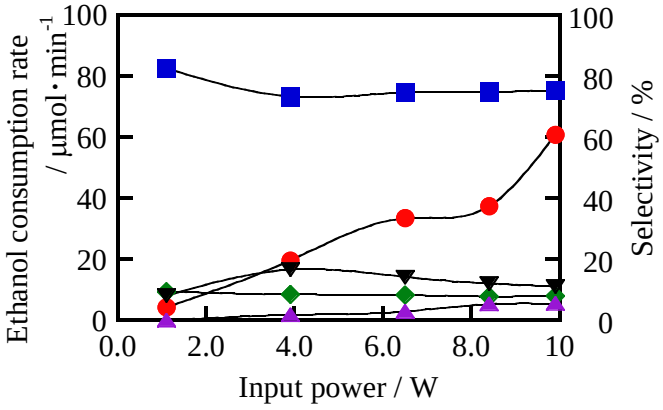

(●) ethanol consumption rate, (■) CO Sel., (◆) CH_4 Sel., (▲) CO_2 Sel., (▼) C2 Sel.
Conditions; mixture ratio, C_2H_5OH / H_2O = 1 / 1;
gap distance of electrodes, 3.0 mm; room temperature; atmospheric pressure.

Figure 3. Effect of input power on ethanol consumption rate and on Carbon selectivity.

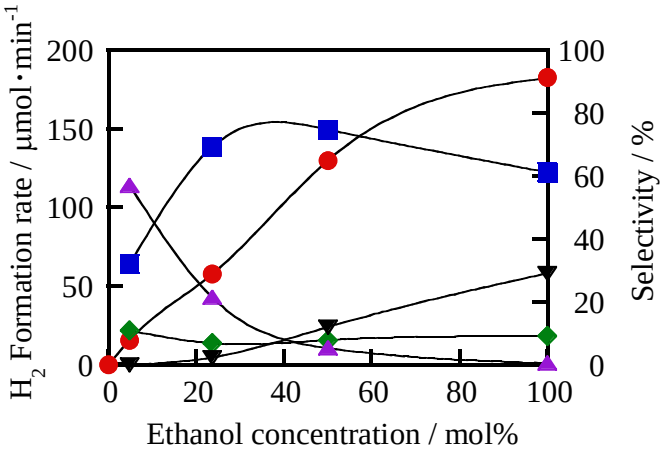

(●) ethanol consumption rate, (■) CO Sel., (◆) CH_4 Sel., (▲) CO_2 Sel., (▼) C2 Sel.
Conditions; input current 7.0 mA, gap distance of electrodes,
3.0 mm; room temperature; atmospheric pressure.

Figure 4. Effect of ethanol concentration on H_2 formation rate and on Carbon selectivity.

3) Effect of concentration of C_2H_5OH and H_2O. In this section, we investigated effect of concentration of ethanol and water. At first, H_2 and O_2 were not generated when H_2O concentration was 100 %. So the reaction of water electrolysis did not advance. Next, at the decomposition reaction of ethanol 100 %, small amount of carbon deposition were gradually formed, and it caused destabilization to stop the discharge. So the discharge couldn't be kept stable for a long time. On the other hand, when the reaction was handled in the case of steam reforming (0 < ethanol concentration < 100), the discharge could be stabilized for a long time and could be continued in steam reforming without stopping the reaction.

Figure 4 showed the results. The larger ethanol concentration is, the more produced H_2. And higher ethanol concentration field, C2 selectivity was rather high (it was about 30 %), compared to that of lower ethanol concentration field. So it seems to say that the reaction of which ethanol concentration is from 20 to 50 mol% is the highest efficiency at a present stage. Because C2 selectivity was not high, and carbon deposition was not observed.

4) Calculating result of Energy efficiency. Input power was regarded as the power consumption in the discharging space. And it was calculated from integration value which is current multiply by voltage, picked up from the waveforms of the oscilloscope. Here, input power (Ei) was calculated based on the following formula.

$$Ei = \sum_{t} \{(v_i + v_{i+1})/2\} \times \{(c_i + c_{i+1})/2\} \times (t_{i+1} - t) \times f \qquad (1)$$

On the other hand, output power was regarded as the difference of the standard enthalpy of formation between the amount of liquid fuel converted and the amount of compounds formed. Finally energy efficiency was calculated by making output power into the numerator and by making input power into the denominator.

And, if it's supposed that input and output power were calculated such way, energy efficiency was 41.7 % at the ethanol concentration of 50 %, the gap distance of electrode 3.0 mm. The efficiency in this experiment was exceeding that of the former way. Furthermore, this reformer has a potential to improve the efficiency by controlling Voltage and Current system.

Conclusions

We succeeded in improving the energy efficiency because the liquid phase reactor does not require a heater which is needed to vaporize the mixture of water and ethanol. Moreover any pump supplying the liquid into the reactor was not required. So the liquid phase reactor made the process scale reduced, and also made the device size compact without spoiling its function. Therefore, if the controlling Voltage and Current system makes more progress, we consider that this process would be very useful for room temperature hydrogen formation system.

References

(1) Kado, S., Y. Sekine and K. Fujimoto, ; "Direct synthesis of acetylene from methane by direct current pulse discharge" Chem Commun., 1999, 24 2485.
(2) Kado, S., K. Urasaki, Y. Sekine and K. Fujimoto, ; " Low temperature reforming of methane to synthesis gas with direct current pulse discharge method" Chem. Commun., 2001, 5 415.
(3) Martin K., B. Eliasson, U. Kogelschatz and A. Wokaun,; " CO2 reforming of methane by the combianation of dielectric-barrier discharge and catalysis," Phys. Chem. Chem. Phys., 2001, 3, 294-300.
(4) Nozaki, T., Y. Miyazaki, Y. Unno and K. Okazaki, ; "Energy distribution and heat transfer mechanisms in atmospheric pressure non-equilibrium plasmas" J. Phys. D: Appl. Phys. 34 (2001) 3383-3390.
(5) Nozaki, T., Y. Unno and K. Okazaki, ; "Thermal structure of atmospheric pressure non-equilibrium Plasmas" Plasma Source Sci. Technol. 11 (2002) 431-438.
(6) Sekine, Y., K. Urasaki, S. Kado, M. Matsukata, and E. kikuchi, ; " Nonequilibrium Pulsed Discharge: A Novel Method for Steam Reforming of Hydrocarbons or Alcohols" Energy Fuels, 2004, 18, 455-459.
(7) S.L. Yao, M. Okumoto, A.Nakayakma and E. Suzuki, ; " Influence of Rise Time of Pulse Voltage on the Pulsed Plasma Conversion of Methane," Energy Fuels, 2001,15,1295.
(8) Wonihl C., Y. beak, S. Moon, Y. C. Kim, ; "Oxidative coupling of methane with microwave and RF plasma catalytic reaction over transitional metals loaded on ZSM-5," Catal. Today 74 (2002) 207-223.

SOLID OXIDE FUEL CELL COMBUSTIBLE BY PLASMA SPOUTED BED GASIFICATION OF GRANULATED BIOMASS

Jerzy W. Jurewicz, Alan Lemoine

CREPE – Centre de Recherche en Énergie, Plasma et Électrochimie
Université de Sherbrooke,
Sherbrooke, Québec, Canada J1K 2R1

Introduction

In the search for both the most suitable and efficient methods of biomass gasification, the plasma spouted bed reactor, already tested[1,2] in this application exhibits, among other benefits, high transformation rates for solids to gases and the absence of tarry by products. This short report is a statement on our continuing research program and describes the most recent results where the research effort has been concentrated on process efficiency issues, including determining mass and energy balances.

Experimental

Raw Materials. The properties of the canola used as the raw material, were as follows: average grain size ≈ 1.5 mm, the moisture content of ≈8 %, ultimate analysis: mass composition of 56.43 ! 1 % carbon, 8.76 ! 0.2 % hydrogen, 23.43 ! 0.5 % oxygen, 7.34 ! 0.15 % nitrogen, 3.75 ! 0.1 % ash and traces of sulphur < 0.3 % and chlorine < 0.1 %. The heating value using the Dulong formula amounts to 28.23 MJ/kg.

Apparatus. The pyrolitic gasification tests were performed in an atmospheric-pressure bench scale plasma spouted bed apparatus (Fig.1).

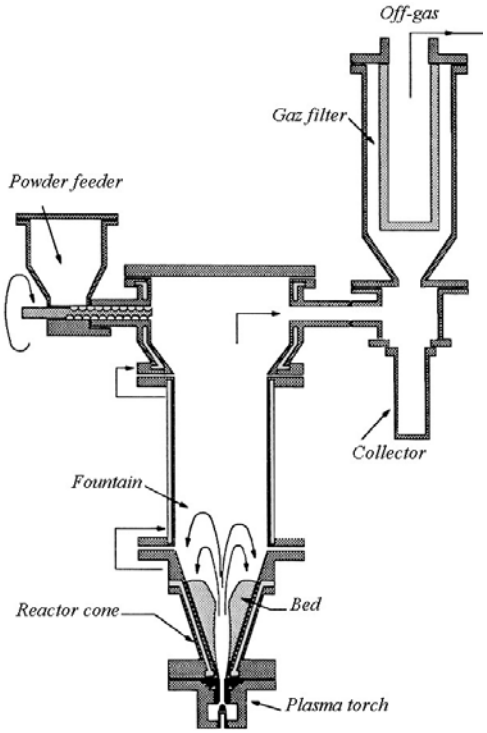

Figure 1. The schematic of the plasma spouted bed apparatus used in this study.

The stainless steel reactor, comprised a 150 mm cylindrical chamber part fitted to a conical (40°) base, protected with a thermal barrier ZrO_2 coating on the inside, and coupled with a standard DC plasma torch. The carbon dioxide was injected through three orifices at the periphery of the 4 mm torch nozzle. The seeds material was screw fed into the reactor from the sealed top.

Results and Discussion

Series of tests were performed to determine the effect of plasma power and injected carbon dioxide flow rate on product gas yield, its composition and overall energetic efficiency of the process.

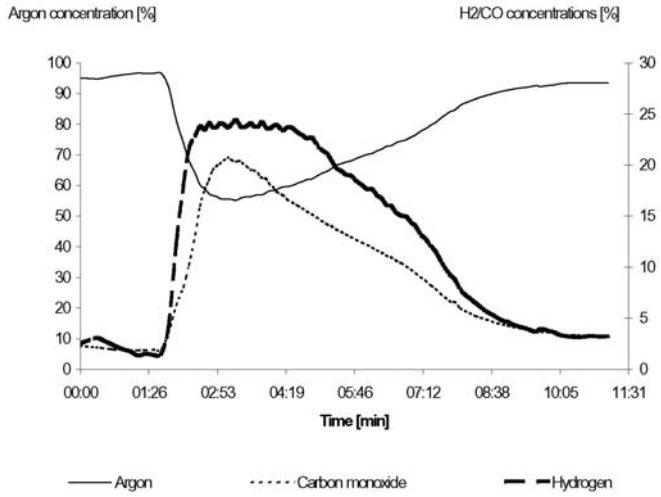

Figure 2. The variation of the off-gas composition during experiment for non-reactive plasma (without carbon dioxide).

Table 1. The Distribution of Solids (By Size Fraction) Remaining After the Run for Injected Power of 4,69 kW (% of Initial Load).

Size fraction	Reactor		Collector	Filter	Total
③m	Bottom	Walls			
$d_p > 425$	4,59	1,51	1,00	0,87	7,97
$425 > d_p > 212$	0,79	1,21	1,70	2,94	6,64
$212 > d_p > 150$	0,23	0,70	0,39	1,64	2,97
$150 > d_p > 125$	0,14	0,71	0,21	1,84	2,89
$125 > d_p > 90$	0,12	1,28	0,25	0,82	2,47
$90 > d_p > 45$	0,09	2,11	0,25	0,37	2,82
$45 > d_p$	0,00	1,50	0,08	0,00	1,59
Total	5,96	9,03	3,88	8,49	27,35

Due to the appreciable variation in off-gas composition for various applied plasma powers related to the different rate of pyrolysis for the input volatile matter (Fig.2), the total volume of gases produced for each pyrolytic gasification run was chosen as the mean for making comparison between the different runs (Table 2a,b,c). Time period of each experiment: 450 seconds.

Table 2a. Total Volume of Gas Produced per Gram of Canola Consumed During Complete Run for Injected Power of 3,58 kW.

Gas	Volume of gas produced per gram of canola consumed (L/g)			
	Spouting gas composition			
	Ar (plasma gas)	CO_2 Flowrate (Lpm)		
	30 Lpm	2,5	5	10
H_2	0.33	0.28	0.24	0.19
CO	0.16	0.26	0.37	0.46
CH_4	0.02	0.15	0.017	0.016
CO_2	0.03	-	-	-
C_2H_4	0.03	0.03	0.03	0.03
C_2H_2	0.13	0.08	0.08	0.06
Total	0.7	0.8	0.74	0.76

Table 2b. Total Volume of Gas Produced per Gram of Canola Consumed During Complete Run for Injected Power of 4,69 kW.

Gas	Volume of gas produced per gram of canola consumed (L/g)			
	Spouting gas composition			
	Ar (plasma gas)	CO_2 Flowrate (Lpm)		
	30 Lpm	2,5	5	10
H_2	0.33	0.39	0.38	0.31
CO	0.16	0.20	0.36	0.48
CH_4	0.02	0.02	0.02	0.02
CO_2	0.03	0.04	-	-
C_2H_4	0.03	0.03	0.03	0.03
C_2H_2	0.13	0.14	0.17	0.09
Total	0.7	0.82	0.96	0.93

Table 2c. Total Volume of Gas Produced per Gram of Canola Consumed During Complete Run for Injected Power of 5,88 kW.

Gas	Volume of gas produced per gram of canola consumed (L/g)			
	Spouting gas composition			
	Ar (plasma gas)	CO_2 Flowrate (Lpm)		
	30 Lpm	2,5	5	10
H_2	0.33	0.42	0.38	0.34
CO	0.16	0.21	0.33	0.43
CH_4	0.02	0.02	0.02	0.02
CO_2	0.03	0.04	-	-
C_2H_4	0.03	0.03	0.03	0.03
C_2H_2	0.13	0.13	0.11	0.09
Total	0.7	0.85	0.87	0.91

As seen from table 1a,b,c the increase in the plasma power and the introduction of carbon dioxide corresponds to the increased volume of gases produced during the same time period. The input seeds are exposed to higher temperatures resulting in liberation of more volatile matter and its increased decomposition rate, in addition to increased formation of carbon monoxide trough char oxidation by carbon dioxide.

Analysis of the overall energy efficiency values, which can reach 60% for the medium value plasma power of 9.4 kW and decrease for the highest plasma power value employed, indicates the necessity for further process optimization especially in respect of the reactor design (its volume versus the plasma jet length).

Table 2. Overall Energy Efficiency of the Process

Plasma power		CO_2 Flow rates			
Electric	Effective injected	0 lpm	2.5 lpm	5 lpm	10 lpm
[kW]	[kW]	[%]	[%]	[%]	[%]
6.5	3.58	58	53	59	56
9.4	4.69	54	59	57	60
12	5.88	48	51	50	52

Conclusions

The plasma spouted bed gasification of canola seeds is characterized by following advantages:

- Process is very fast – comparable with flash pyrolysis;
- Absence of tarry by products – at least at the process scale investigated;
- Very high overall energy efficiencies – up to 60 %, it is expected, that for continuous operation of such reactor the efficiency will increase further;
- High hydrogen and carbon monoxide contents in the gas product accompanied only by light hydrocarbons: methane, ethylene and acetylene with absence of sulphur;
- The possibility of employing medium temperature SOFC off-gas recycling into a plasma spouted bed gasifier is a very interesting option to consider for achieving future balanced energy needs.

Acknowledgement. The financial support of Natural Sciences and Engineering Research Council of Canada (NSERC) is gratefully acknowledged.

References

(1) Lemoine, A., - *MscA Thesis.*, **2001**, *Université de Sherbrooke.*
(2) Lemoine, A., Jurewicz J.W., *Proc. of International Symposium on Plasma Chemistry ISPC-15*, **2001**, pp. 2873-8.

THE LAB-SCALE SORBENT INJECTION TESTING ON MERCURY CAPTURE WITH FOLLOW-UP SOLID-GAS MIXTURE

Yan Cao, Kunlei Liu, Xin Liu, Hongmin Yang, John T. Riley and Wei-Ping Pan*

Institute for Combustion Science and Environmental Technology (ICSET)
Western Kentucky University, Bowling Green, KY 42101
Email: yan.cao@wku.edu,

Introduction

The DOE prefers the retrofitting of dry sorbent injection upstream of either an ESP or an fabric filter baghouse to further control mercury emission in coal-fired power plants.[1] This promising technology has the widest potential application for controlling mercury emissions in plants that are not equipped with FGD scrubbers, which includes 75% of all U.S. plants. However, unlike the successful carbon injection for mercury control in waste incinerators, which produces one or two orders of magnitude lower mercury emissions, sorbent injection used in coal-fired utility boiler faces many challenges. Large quantities of PAC must be injected, leading to high costs if high removal efficiency is required.[2] In this study, two new highly effective, low-cost mercury sorbents including IGCC char and woodceramic will be used to inject in the simulated duct in a lab-scale facility with a low pressure drop turbulence mixer to enhance the mass transfer of mercury capture process.

Experimental

At ICSET of WKU, a lab-scale demonstration facility on sorbent injection was setup to evaluate the some promising sorbents behavior on Hg capture efficiency. The lab-scale facility was designed and attempted to simulate real injection and reaction process inside the duct under the power plant conditions, the brief diagram is presented in Figure 1. It consists of a reactor pipe, ash free probe, Venture flow meter and educator. The educator was used to generator a vacuum at the end of system and intake flue gas into the system. A venture flow meter was used to measure the flow rate of gas inside the reactor. The concentrated Hg generated by Cavkit as well as sorbent were injected in the front of reactor. Two ash free probes were used to make sure no sorbent was sucked out of the system which might buildup a filter cake in the gas sampling process and adversely affecting the mercury reading on semi-continuous mercury monitor (SCMM). Mercury concentration changes through the system were monitored by SCEM. At system exit, a cotton trap was used for capture of used sorbent. The system was fully insulated to maintain the desired temperature range which is about 120-150 ^{o}C.

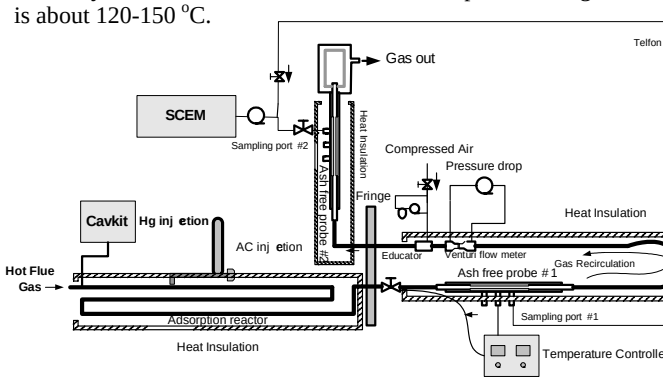

Figure 1. The Lab-Scale Testing Facility for Sorbent Injection Testing

Results and Discussion

The preliminary testing results using ceramics sorbents from chicken waste were shown in Figure 2. The testing was conducted at stack locations with two utility boilers with capacity of 165 and 450MWe, respectively. It was found that the mercury concentration in the flue gas at the outlet of the sorbent trap decreased dramatically when the sorbent was deployed.

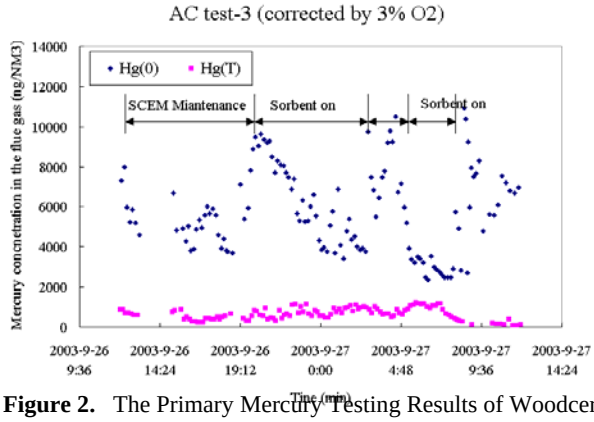

Figure 2. The Primary Mercury Testing Results of Woodceramics Prepared by WKU

The testing results of four sorbent injections showed that the maximum Hg removal efficiency of Eastern IGCC char could be as high as 78% using the S/Hg injection ratio of 12000 at a lower temperature (20 ^{o}C) and shorter residence time (0.13 s) as shown in Figure 3. The Hg removal efficiency of Eastern IGCC char decreases greatly (27%) after removal of the fine constitutes (< 45 um). To simulate the flue gas and ash under turbulent conditions inside the adsorption reactor, sorbent mixed with baked ash was used in the following tests. Eastern IGCC with medium sized particle diameter (100<dp<250um) was used, yielding 30% mercury removal efficiency at a lower carbon injection ratio (S/Hg: 1200). For Polk IGCC char with a similar particle size (100<dp<250um), about 60% mercury removal efficiency was reached at a higher carbon injection ratio (S/Hg: 12000) and a shorter residence time (0.13 s). For Woodcermics, less mercury removal efficiency was found at lower injection ratios, using a longer sorbent residence time. Increasing the injection ratio to 37000, an 80% mercury removal efficiency was found at 50 ^{o}C. Increasing the temperature to 104 ^{o}C and decreasing the injection ratio to 12000, greatly decreased the woodceramics mercury removal efficiency. The mercury removal efficiency decrease for all sorbents in the lab-scale demonstration testing was due to the lower gas velocity used (3m/s) which was far smaller than the actual flue gas velocity in a power plant. A smaller gas velocity decreases the turbulent gas flow rate and thus decreases the contact efficiency of sorbent and mercury in the flue gas.

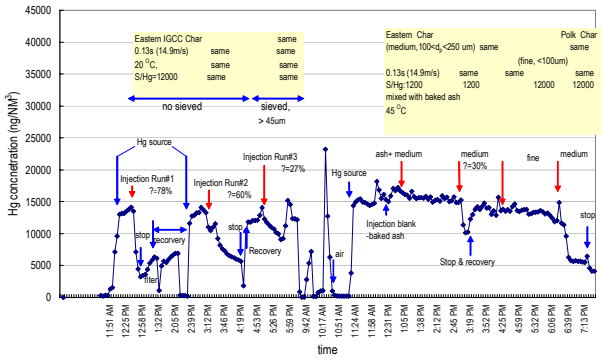

Figure 3. Mercury Removal Behavior Using IGCC Char.

Inserting an obstacle inside the adsorption reactor increased the mercury removal efficiency in the lab-scale demonstration testing. Considering the fact that the sorbent absorption rate is largely dependent on the contact efficiency of sorbent and mercury in the flue gas, a new designed Turbulence Generator was designed and used in the sorbent injection tests to strengthen gas-solid contacting efficiency. As shown in Figure 4., the elemental mercury removal efficiency by Polk IGCC char could reach 46% with Turbulence Generator adding in compared with 20% without the Turbulence Generator, a net increase of 26% at conditions of sorbent injection ratio of 3000, temperature of 120 ^{0}C and residence time of 3.5 s. As Eastern IGCC char injected in at same conditions, the elemental mercury removal efficiency increased only 5%. That means the Turbulence Generator does work on mercury removal, however, is also dependent on absorption capability of sorbent.

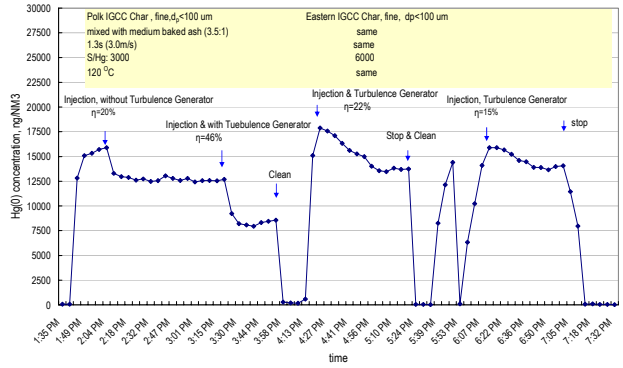

Figure 4. The effect of Turbulence Generator on mercury removal efficiency

Conclusions

At ICSET of WKU, a lab-scale demonstration facility on sorbent injection was setup to evaluate the some promising sorbents behavior on Hg capture efficiency including two type woodceramic sorbents and two types of IGCC chars. The mercury removal efficiency decrease for all sorbents in the lab-scale demonstration testing was due to the lower gas velocity used (3m/s) which was far smaller than the actual flue gas velocity in a power plant. A smaller gas velocity decreases the turbulent gas flow rate and thus decreases the contact efficiency of sorbent and mercury in the flue gas. After using turbulence mixer, even at a lower sorbent injection ratio (S/Hg: 3000) and a shorter residence time (1.3s), 69% mercury removal efficiency was achieved for Eastern IGCC char. Inserting an obstacle inside the adsorption reactor increased the mercury removal efficiency in the lab-scale demonstration testing.

References

1. Solicitation for Financial Assistance Application, DE-PS26-03NT41718, “Large Scale Mercury Control Technology Field Testing Program – Phase II”, DOE-NETL, **2003.**
2. Pavlish, J.H., Sondreal, E.A., Mann, M.D., Olson, E.S., Galbreath, K.C., Laudal, D.L., Benson, S.A., Fuel Processing Technology **2003**; 82:89-165.

NITROGEN ENRICHED ACTIVATED CARBONS AS ADSORBENTS AND CATALYSTS IN DESULFURIZATION TECHNOLOGIES

Andrey Bagreev [1], Svetlana Bashkova [2], Teresa Bandosz [1,2], Angel Menendez [3], Irina Dukhno [4], Yuriy Tarasenko [4]

[1] Department of Chemistry, The City College of New York
[2] The Graduate School of the City University of New York, New York, NY, USA
[3] Instituto National Del Carbon, INCAR (CSIC), Oviedo, Spain
[4] Institute for Sorption and Problems of Endoecology, Kiev, Ukraine

Introduction

Activated carbons (ACs) are widely used as adsorbents and catalysts in desulfurization technologies. Among AC applications in desulfurization are air purification from hydrogen sulfide and methyl mercaptan from waste water treatment plants [1-2], sulfur dioxide removal from flue gases [3-6], and deep desulfurization of gaseous fuel in fuel cell power plants [7]. Desulfurization efficiency is significantly improved when AC works not only as adsorbent of sulfur containing species, but also as a catalyst for selective oxidation of these compounds to less volatile ones which are then strongly adsorbed on a carbon surface. The catalytic properties can be improved by incorporation of nitrogen into the carbon matrix. This process results in an increase in the carbon basicity and polarity. Moreover, dramatic changes in catalytic properties of AC in electron transfer reactions take place.

The objective of this paper is to investigate the ability of nitrogen-containing AC for working as an oxidation catalyst and adsorbent for deep air purification from H_2S, CH_3SH and SO_2.

Experimental

Materials. Nitrogen enriched activated carbons were prepared by impregnation of carbons of different origins with melamine or urea followed by high-temperature treatment (HTT) in inert atmosphere at 850-950^{o}C. Among the precursors for nitrogen immobilization the following carbons were used: bituminous coal based carbons SBC (INCAR, Spain) and BPL (Calgon), wood based commercial carbon BAX-1500 (Westvaco) and experimental EBC (INCAR), as well as experimental fruit stone based carbon KAU (ISPE, Ukraine). Other series of ACs were prepared by pyrolysis of ion-exchange resin containing methylpyridinium and pyridinic nitrogen groups (SCN) and a porous styrene-divinylbenzene copolymer containing no hetero-elements (SCS). The nitrogen modification procedures were described in details elsewhere [8-11]. For comparison the results obtained on commercial catalytic carbon containing nitrogen, Centaur (Calgon), are also discussed. After nitrogen modification the additional letter U (urea) or M (melamine) are added to the names of the carbons. The exhausted carbons after the breakthrough tests are referred to with an additional letter, E.

Methods. The dynamic tests were carried out at room temperature to evaluate the capacity of the ACs for H_2S, CH_3SH and SO_2 removal [8-11]. Moist air (relative humidity 80% at 25^{o}C) containing 3000 ppm of H_2S, CH_3SH or SO_2 was passed through a column with 6 ml of adsorbent at 500 ml/min. The outlet concentrations of gases were monitored with electrochemical sensors. The tests were stopped at the breakthrough concentrations of 500 ppm for H_2S, 50 ppm for CH_3SH and 350 ppm for SO_2. The adsorption capacities of each carbon were calculated by integration of the area above the breakthrough curve (from the inlet concentration of gas, flow rate, breakthrough time), and carbon weight.

Sorption of nitrogen was used to characterize the porosity of adsorbents. Nitrogen isotherms were measured using an ASAP 2010 (Micromeritics) at -196 ^{o}C. Before experiments the samples were outgassed overnight at 120^{o}C under the vacuum of 10^{-5} Torr to a constant pressure. The isotherms were used to calculate the total specific surface areas (S_t), micropore volumes (V_{mic}), total pore volumes (V_t), average micropore sizes (L_{mic}) and pore size distributions using Density Functional Theory (DFT).

pH of carbon surface for initial and exhausted samples was estimated by placing 0.4g of carbon powder in 20 ml of water. The suspension was equilibrated during night and then its pH was measured. The amount of acidic and basic surface groups was determined by titration, with either 0.05N NaOH or 0.05N HCL.

In order to evaluate either the species present on the initial carbon surface or surface reaction products, thermal analysis was carried out using TA Instruments Thermal Analyzer. The instrument settings were: a heating rate of 10^{o}C/min in a nitrogen atmosphere, 100 ml/min flow rate. The products of CH_3SH oxidation were studied by GC/MS on Shimadzu GAS Chromatograph/Mass Spectrometer model QP5050 with XTI-5 column. The samples for GC/MS analysis were extracted from exhausted carbon samples using methanol.

The content of carbon, hydrogen, nitrogen, sulfur and oxygen was analyzed by LECO CNHS-932 and VTF900 instruments. In some cases XRF and EDX methods were used to determine the amount of sulfur adsorbed and the presence of metal impurities. The surface chemistry of nitrogen containing carbons was studied by XPS method (LEYBOLD LHS 11). The values of binding energy were calibrated with respect to C1s peak at 285.0 eV. The N1s envelopes were used to characterize different forms of nitrogen [12].

Results and Discussion

Modification of ACs with melamine and urea resulted in a significant increase in the nitrogen content (Table 1). Introduction of nitrogen also leads to changes in the surface chemistry of carbons. Indeed, after nitrogen doping all carbons became more basic than the initial counterparts, which is reflected as a rise of surface pH, absolute amount of basic functional groups and a relative carbon basicity expressed as a ratio of the number of basic groups to the total number of groups present on the surface.

Table 1. Nitrogen Content, pH of Carbon and Amount of Basic and Acidic Goups

Sample	N content %wt.	pH	Amount of groups, mmol/g		
			basic	acidic	basic/total
SBC	1.0	9.1	0.05	0.5	0.09
SBC-M	5.4	9.2	0.72	0.11	0.87
BPL	0.4	7.4	0.40	0.50	0.44
BPL-U	1.1	8.5	0.60	0.35	0.63
BPL-M	6.8	8.0	0.68	0.24	0.74
BAX	0.2	7.2	0.35	0.90	0.28
BAX-U	3.1	7.4	0.65	0.70	0.48
SCS	0	8.1	0.62	0.12	0.84
SCN	2.4	9.1	0.56	0.25	0.69

The development of nitrogen functionality for different types of nitrogen enriched carbon was extensively studied by X-ray photoelectron spectroscopy (XPS) [12-15]. It was found that the type of a carbon precursor and nitrogen modification agent result in the same surface functionalities when the treatment is done at

temperatures higher then 850°C [4,6,12-15]. During HTT of nitrogen-containing precursors, nitrogen atoms are incorporated into carbon rings and located at the edges of graphene layers as pyridinic (BE = 398.7 ev), pyrrolic (BE = 400.3 ev) and pyridone (BE = 400.5 eV), or in the interior as "quaternary" nitrogen (BE = 401.3 eV). When carbons are exposed to oxygen containing atmosphere the pyridine–N-oxides (BE= 403-405 eV) are formed. It is interesting to note that the energy state of "quaternary" nitrogen observed in N-carbons is very close to the state of real quaternary nitrogen in methylpyridinium group ($>N^+$-CH_3) of vinylpyridine resin - precursor used for preparation of polymeric carbon SCN type [12]. The pyridinic nitrogen contributes to one p_π-electron to the graphitic π-system, while pyrrolic and "quaternary"nitrogen contributes to two p_π-electrons to the graphitic π-system. These extra electrons delocalized over graphene layers can dramatically change catalytic properties of a carbon matrix in reactions involving electron transfer.

Modifications with nitrogen-containing species may also result in changes in the porous structure. For all initial and N-modified carbon samples the nitrogen adsorption isotherms were measured and then structural parameters were calculated [8-11]. All adsorbents have highly developed micro- and mesopore structure. The examples of the results are presented in Table 2. For majority of the samples after N-modification and HTT a 10 to 25% decrease in textural parameters is observed (Table 2). An exemption is the BAX-U sample whose precursor carbon (BAX) was prepared by chemical activation at 550 °C.

Table 2. Structural Parameters of Carbons Calculated from Nitrogen Adsorption Isotherms

Sample	S_t m^2/g	V_t cm^3/g	V_{mic} cm^3/g	L_{mic} nm
BPL	1000	0.71	0.40	1.16
BPL-U	883	0.67	0.34	1.17
BPL-M	811	0.70	0.31	1.19
BAX	1350	1.29	0.50	1.32
BAX-U	1087	0.80	0.40	1.15
SCN	973	0.83	0.43	1.07

The ability of N-containing ACs to work as oxidation catalyst and adsorbents for deep air purification from H_2S, CH_3SH and SO_2 was investigated in dynamic conditions. From the breakthrough curves the capacities for removal of sulfur-containing gases were calculated [8-11]. Examples of data for selected samples are collected in Table 3. In all cases a significant increase in the capacity is found for N-containing carbons compared to the initial ones, which suggests the feasibility of application of N-enriched ACs in desulfurization technologies [8-11].

Table 3.Amount of Gases Adsorbed and the pH of the Carbons

Sample	H_2S ads/pHE mmol/g	CH_3SH ads/pHE mmol/g	SO_2 ads/pHE mmol/g
SBC	0.74/4.4	6.17/4.7	-
SBC-M	7.44/2.0	7.92/3.5	-
BPL	0.12/7.9	2.50/6.9	-
BPL-M	10.1/1.8	9.19/3.7	-
BAX	0.26/4.2	0.58/6.8	0.53/2.2
BAX-U	7.94/2.0	6.25/4.9	1.09/1.9
SCS	0.76/3.9	-	0.84/2.3
SCN	5.88/1.4	9.38/2.9	4.95/1.3
Centaur	3.06	1.5	2.56

The process of SO_2 adsorption/oxidation has been studied extensively and such parameters as the porosity, surface chemistry, ash content and gas phase composition were taken into consideration [2-5,10,14-15]. It was found that in oxygen atmosphere and in the presence of water, SO_2 is adsorbed on the surface of AC, then oxidized to SO_3 by oxygen radicals and after hydration with adsorbed water it is condensed in pores as H_2SO_4 [2-5,10]. The presence of nitrogen-containing functional groups significantly enhances the adsorption capacity due to activation of molecular oxygen and creation additional basic sites for adsorption of oxidation products in molecular or ionic form. Figure 1 demonstrates the dependence of SO_2 adsorption measured in wet, dry and dry anaerobic conditions on the incremental basicity of surface in pores with sizes between 6.8 and 8.6 Å. The graph indicates that both the pore structure and surface chemistry are very important factors which should be taken into account in designing highly effective SO_2 adsorbents.

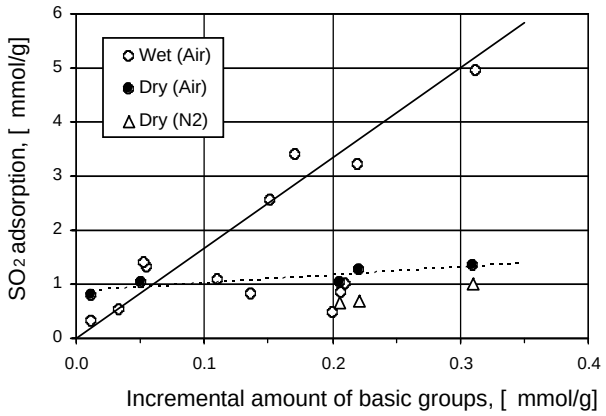

Figure 1. Dependence of SO_2 adsorption on the incremental basicity of surface in pores with sizes 6.8 and 8.6 Å. Lines show the trend in the data.

Caustic impregnated and virgin activated carbons are among most effective adsorbents for H_2S removal from different gas media at low temperatures [1-2]. It was found that presence of water and basic environment on ACs contributes to the dissociation of H_2S and facilitates its oxidation to sulfur and sulfur dioxide [1-2,8]. The proposed mechanism involves H_2S adsorption on the carbon surface, its dissolution in a water film, dissociation of adsorbed H_2S in the water film, surface reaction with adsorbed oxygen with formation of elemental sulfur or SO_2, and further oxidation of SO_2 to H_2SO_4 [1-2]. It was proposed that two types of active sites are probably responsible for catalytic action: one is the carbon active sites where molecular oxygen is adsorbed and activated, and the second ones are the small sulfur clusters or polysulfides where oxygen can also be chemisorbed. The oxidation products are adsorbed in carbon micropores. The reaction proceeds until all micropores or carbon active sites are filled with adsorbed sulfur or until low pH of oxidation products suppresses dissociation of H_2S.

The main feature of H_2S adsorption on N-containing ACs is its deeper oxidation (low pH of exhausted carbon) and higher removal capacity then on carbons without nitrogen (Table 3) [8,9]. To identify the products of H_2S adsorption/oxidation, thermal analysis in nitrogen was performed on the exhausted carbons. The results are presented as DTG curves with three main peaks (Fig. 2). First peak at 100°C represents desorption of water, second peak at 250°C is assigned to desorption of SO_2 and decomposition of H_2SO_4, and the third one at 400-450°C is related to the removal of elemental sulfur. From these data the selectivity for SO_2 oxidation was calculated as the molar ratio of SO_2 formed to total amount of sulfur adsorbed.

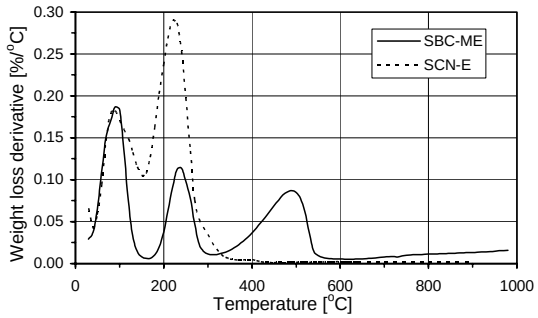

Figure 2. DTG curves in nitrogen for the samples after H_2S adsorption

To see the effect of nitrogen incorporation, the normalized capacity (with respect to the surface area of adsorbents) and selectivity for SO_2 oxidation was plotted versus the ratio of atomic content of nitrogen to carbon determined from elemental analysis (Fig. 3). Four series of N-modified carbons were chosen for this analysis. The results follow, in general, the same tend. While the specific capacity increases until the plateau is formed (saturation), the selectivity changes in the opposite direction. This is likely due to a limited accessibility of oxygen to sulfur active sites in the bulky crystals.

Adsorption/catalytic removal of methyl mercaptan on N-enriched activated carbons follows in general the same trend as the adsorption of hydrogen sulfide. The process is pH dependent and enhanced in the presence of water and oxidation proceeds due to the surface reaction between adsorbed CH_3SH and active oxygen radicals. N-dopping improves the catalytic activity. The oxidation products are adsorbed in carbon micropores [11,16]. In spite of these similarities CH_3SH adsorption has specific peculiarities: due to less water solubility and smaller dissociation constant the oxidation requires more basic conditions. Owing to higher bond energy in S-C then in S-H the reaction proceeds to dimethyl disulfide and methyl methanethiosulfonate formation at room temperature. Water and dimethyl disulfide compete for adsorption sites on the carbon surface. The dependence of the normalized CH_3SH breakthrough capacity on the N/C atomic ratio has the maximum in the capacity at N/C content of about 2% [11,16].

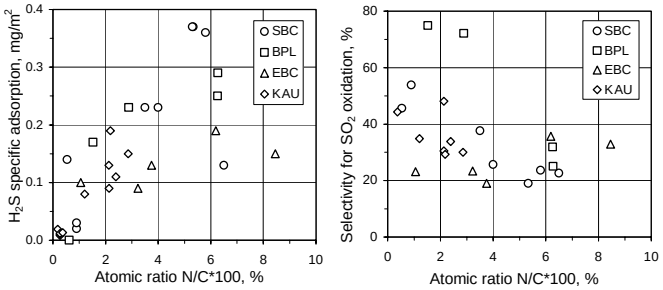

Figure 3. Dependence of the normalized H_2S breakthrough capacity (A) and the selectivity for SO_2 oxidation (B) on the N/C atomic ratio in the carbon matrices.

The observed improvement of adsorption-catalytic properties of nitrogen containing carbons in desulfurization reactions can be explained from the point of view of the electronic theory of catalysis. The extra π-electrons of pyrollic and quaternary nitrogen occupy the high-energy states in the conduction band. It is likely that from there they can be transferred to the adsorbed oxygen and superoxide ions O_2^- can be formed. Those superoxide ions can easily trigger the formation of OH* and HO_2* radicals in reaction with water. All of these species are much more reactive then molecular oxygen and may oxidize described above sulfur compounds, when they are adsorbed on carbon surface.

Conclusions

Nitrogen enriched activated carbons can be successfully used in desulfurization technologies to remove hydrogen sulfide, sulfur dioxide and methyl mercaptan from wet air at ambient temperatures. Nitrogen incorporation has a positive effect on adsorption capacities for all gases studied. Unique surface chemistry of these materials can dramatically change catalytic properties of a carbon matrix in reactions involving electron transfer.

Acknowledgement This research was supported by NATO Collaborative Linkage grant NATO EST CLG 978688.

References

(1) Bandosz, T.J.; *J. Colloid. Interface Sci*., **2002**,*246*,1.
(2) Bagreev, A.; Adib, F.; Bandosz, T.J.; *Carbon*, **2001**, *39*, 1897-1905.
(3) Mochida, I.; Korai, Y.; Shirahama, M.; Kawano, S.; Hada, T.; Seo, Y.; Yoshikawa, M.; Yasutake, A.; *Carbon*, **2000**, *38*, 227.
(4) Li, K.; Ling, L.; Lu, C.; Qiao, W.; Liu, Z.; Liu, L.; Mochida I.; *Carbon*, **2001**, *39*,1803.
(5) Raymondo-Pinero, E.; Cazorla-Amoros, D.; Salinas-Martinez de Lecea, C.; Linares-Solano, A.; *Carbon*, **2000**, *38*, 335.
(6) Raymondo-Pinero, E.; Cazorla-Amoros, D.; Linares-Solano, A.; *Carbon*, **2003**, *41*, 1925.
(7) Gardner, T.H.; Berry, D.A.; Lyons, K.D.; Beer, S.K.; *Fuel*, **2002,** *81*,2157.
(8) Adib, F.; Bagreev, A.; Bandosz, T.J.; *Langmuir*, **2000**, *16*, 1980.
(9) Bagreev, A.; Menendez, J.A.; Duhno, I.; Tarasenko, Y.; Bandosz, T.J.; *Carbon*, **2004**, *42*, 469.
(10) Bagreev, A.; Bashkova, S.; Bandosz, T.J.; *Langmuir*, **2002**, *18*, 1257.
(11) Bashkova, S.; Bagreev, A.; Bandosz, T.J.; *Langmuir*, **2003**, *19*, 6115.
(12) Lahaye, J.; Nanse, G.; Bagreev, A.; Strelko, V. ; *Carbon*, **1999**, *37*, 585.
(13) Pels, J.R.; Kaptejn, F.; Moulijn, J.A.; Zhu, Q.; Thomas, K.M.; *Carbon,* **1995**, *33*, 1641.
(14) Boudou, J.P. ; *Carbon*, **2003**, *41*,1955.
(15) Boudou, J.P.; Chehimi, M.; Simieniewska, T.; Bimer, J. ; *Carbon,* **2003**, *41*,1999.
(16) Bagreev, A.;Bashkova, S.; Bandosz, T.J. ; *Langmuir*, **2002,** *18*, 8553.

USE OF MACERAL CONTENT TO CHARACTERIZE STEAM COAL PERFORMANCE

Jane Chen[1], Shi Su[2] and, John H. Pohl[3]

1. University of Queensland, Brisbane, Australia, 2. CSIRO, Pullenvale, QLD, Australia, and 3. Virginia Tech/ARI, Alexandria,VA

Introduction

The maceral is the original vegetable matter laid down to form coal. Maceral content is measured under the optical microscope using reflectance and structure to identify the macerals and surface area (converted to volume) to quantify the maceral groups. Figure 1. shows the maceral groups for hard coals (as opposed to brown, younger coals). Macerals have been used for a long time to characterize the performance of coking coals.

The major maceral groups are vitrinite composed of woody structures, exinite (also called liptinite) composed of resins, and inertinite composed of highly altered charcoal. The maceral groups are further divided into maceral subgroups (2). Falcon and Snyman (3) show micrographs of the different submacerals.

Pohl (1) correlated most of the physical and chemical properties of coal with the maceral groups and the carbon content on a dry ash-free basis (C(daf)). The correlations included chemical content gross chacateristics such as volatile matter content of brown and black coals, chemical structure, and most physical properties. The nitrogen content, porosity, and surface area of the coal did not correlate well with the maceral groups and C(daf). In general, the maceral group accounts for the original vegetable matter and the carbon content accounts for geological alternation of the material. Figure 2. shows an example of the correlation for volatile matter of hard (black) coal.

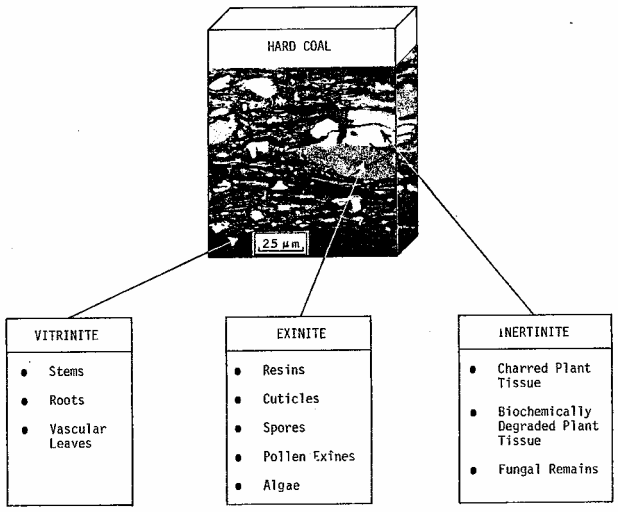

Figure 1. Maceral groups in coal. Heap, et al (1).

Pohl made attempts to correlate the maceral compositions of coals (1983-1986) with burnout of the coals measured in the Energy and Environmental Research Corp (EER) pilot scale furnace.

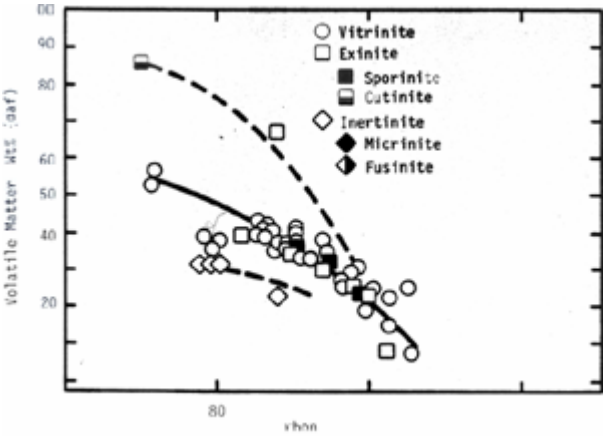

Figure 2. Correlation of volatile matter with carbon content for hard coals.(1).

The correlation used the amount of exinite plus ineritinite with a reflectance greater than 0.96. The correlation worked reasonably well, but had some problems. All maceral groups should be included. However, exinite was considered to rapidly volatilize (see Figure 2.) and burn quickly, and it was not considered necessary to include exinite in the correlation. The percent of vitrinite with reflectance greater than 0.96 worked reasonably well for USA coals where the major maceral group is vitrinite, but the correlation had to be done with percent of vitrinite and inernite with reflectance greater than 0.96 for Australian coals, where a majority of the maceral groups can be inertinite. Finally, the correlation could not differentiate between the burnout of different coals that had either 0 or 100 percent of the maceral material with reflectance greater that 0.96.

Chen, et al. (4) have recently made weight loss measurements during devolatilization and burning of single 100 um particles from pure vitrinite and some inertinite macerals groups. Chen identified the maceral groups under the optical microscope and dug out low ash 100 um pieces. The particles were suspended on a fine vibrating needle whose amplitude and frequency response were previously calibrated with glass spheres of known weight. A laser beam was spilt and used to heat the particle from two sides. We measured the particle temperature using two-color pyrometry and measured the change in amplitude and frequency continually through several hundred milliseconds until the particle completely burned. Five particles from each maceral were burned to statistically achieve an accuracy less than a factor of two for the rate of burning. Figure 3. shows the rate of weight loss in time for 5 particles each of coals with different rank (reflectance) dug from Australian Coals. Figure 3. indicates that at 80 percent burnout the rate of burning depends on the reflectance (rank) of the coal. Coals with low reflectance can have high rates of burning, while bituminous coals with reflectance near 1 can have low rates of burning. Preliminary data indicates different macerals of the same reflectance have the same burning rate and that the minimum in burning rate is a result of loss of surface area for bituminous coals.

Finally Su (6) used combinations of maceral concentrations to correlate the flame stability of pure and blends of Australian coals burned in the EER and Australia Coal Industry Research Laboratry (ACIRL) pilot scale furnaces.

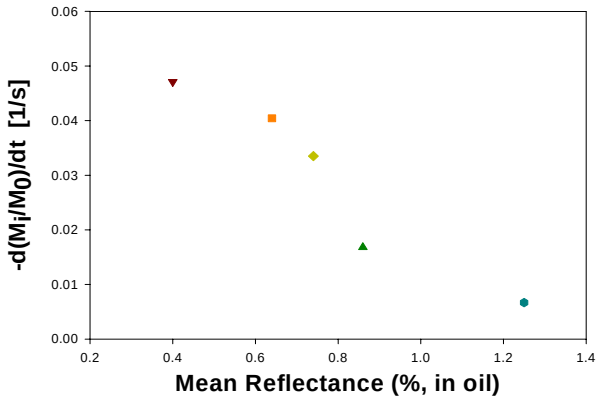

Figute 3. Vitrinite Maceral burning rate at 80 percent burnout. Chen, et al (4).

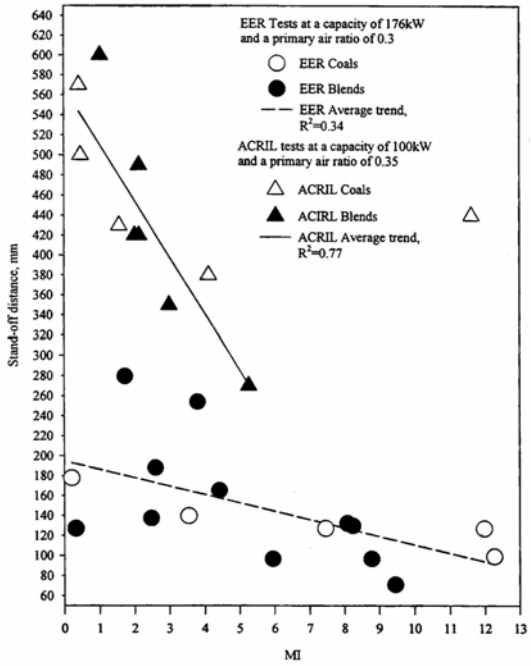

Figure 4. Correlation of Maceral Index (MI) with observed flame stability in two pilot scale furnaces. Su et a. (6)

The Maceral Index (MI) is:

$MI=(L+V/R^2/I^{1.25})*(HV/30)$

Where

MI=maceral index
L=volume percent of liptinite (exinite)
V=volume percent of vitrinite
R= vitrinite reflectance
I= volume percent inertinite
HV= high heating value in kcal/kg

Figure 5. shows the correlation of the maceral index with burnout. The correlation is excellent at high and low burnouts, but there is some scatter at burnouts around 99.5 percent and a few (5) points were not used to develop the empirical equation.

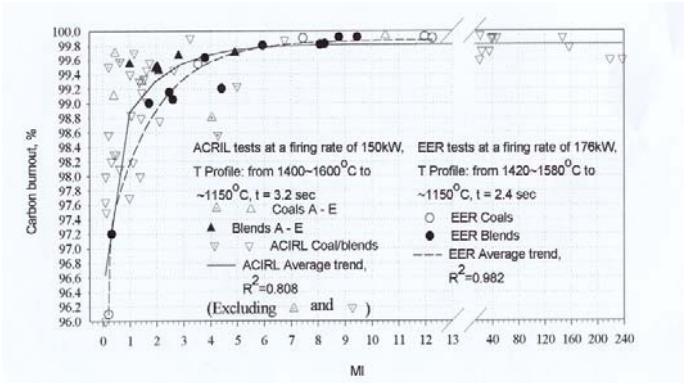

Figure 5. Correlation of Maceral Index (MI) with pilot scale burnout. A few points around 99 percent burnout were not included in developing the equation.

Conclusions

Maceral content appears to be a promising parameter to correlate coal properties and coal performance.

Acknowledgement. The authors wish to thank those who funded portions of the work at different times and places.:Electric Power Research Institute Palo Alto, CA, USA and Arun Metha, The Cooperativbe Research Centre for Black Coal Utilisation Research, Newcastle, NSW. Australia. We would also like to thank the places where this work was done: Energy and Environmental Research Co, Irvine, CA, USA, University of Queensland, Brisbane,QLD, Australia, and Australia Coal Industry Research Laboratory (ACIRL), Ipswich, QLD, Australia.

References

(1) Heap, M.P., J.C. Karmlich, D.W. Pershing, J.H. Pohl, W.F. Richter, and W.R.. Seeker, Effects of Coal Quality on Power Plant Performance and Costs, v.. 4 Review of Coal Science Fundamentals, Electric Power Research Institute, CS-4283, February 1986.

(2) Van Krevelen, D.W., Coal: Typology,-Physics,-Chemistry-Constitution, 3rd ed., Elsevier, Amsterdam, 1993);p. 39.

(3) Falcon, R.M..S., and C.P. Snyman, An Introduction to Coal Petrography: Atlas of Petrographic Constituents in the Bituminous Coals of Southern Africa, The Geological Society of South Africa, Johannesburg, South Africa.

(4) Chen, J., J.H. Pohl, V. Rudolph, and D. Harris, Combustion Rates of Single Maceral Particles from Australian Coals, Clean Power from Coal with Maximum Efficiency, China-Australian Workshop, Tiayuan, Shanxi, China, August 2001.

(5) J.H. Pohl and R. Payne, Pilot scale Evaluation of Mineral Matter on Boiler Performance, 2nd Annual Pittsburgh Coal Conference, Pittsburgh, PA, 1985, P.670.

(6) Su, S. J.H. Pohl, and D. Holcombe, Power Plant Performance of Blended Coals, 1st International Energy Conversion and Engineering Conference, AIAA, Portsmouth, VA, August 2003.

ENHANCED METHOD FOR PREDICTING THE PROPERTIES OF PETROLEUM FRACTIONS

Tareq A. Albahri

Chemical Engineering Dept. - Kuwait University
P.O.Box 5969 - Safat 13060, Kuwait
albahri@kuc01.kuniv.edu.kw

Introduction

The properties of petroleum and its fractions are usually determined experimentally in the laboratory. Several methods are available in the literature to predict these properties for petroleum fuels from their bulk properties such as the boiling point and the specific gravity for example. Although accurate enough, these methods are not suitable for incorporation into the molecularly explicit models for simulating the kinetics and dynamics of petroleum refining processes.

In previous work[1] we have developed a molecularly explicit characterization model (MECM) that allows for the simulation of the molecular composition of petroleum fractions using a pre-selected set of pure components. What is lacking, however, is the ability to predict the properties of the various streams as the molecular composition changes during processing by physical separation or chemical reaction. This work focuses on the development of such a property estimation method from the molecular composition of complex, multicomponent mixtures such as petroleum.

Technical Development

In our previous work on the simulation of light petroleum fractions[1] we have found that not all the properties of the petroleum fuel are required to be optimized against those from the pure components. In fact only the ASTM D86 Distillation, the PNA content and the RVP were sufficient to provide a feasible solution. All the other properties calculated form the bulk properties of the petroleum fraction and those from the pure components in them were almost alike. This lead us to believe that the properties of a petroleum fraction can be estimated from the above three properties alone.

The concept of the proposed model is that the global properties of a petroleum fraction such as the boiling point, the vapor pressure and the paraffins, naphthenes, and aromatics content must be equal to those calculated from the pure components contained in that petroleum fraction. When both bulk and pure component properties are available, the composition of the petroleum fraction may be predicted using optimization algorithms as simplified in Figure 1. The predicted composition of a limited set of pure components may then be used to predict the other properties of the petroleum fuel using appropriate mixing rules.

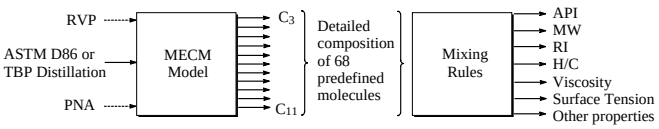

Figure 1. Simplified schematic representation of the proposed model.

Experimental values of the RVP and PNA are always desirable as inputs. However, when these are not available they may be predicted using methods available in the literature[2,3] making the ASTM D86 distillation or the true boiling point (TBP) the minimum model input required.

The internally calculated properties are the molecular weight, the Reid vapor pressure (RVP), the true vapor pressure at 100°F, the specific (API) gravity, the cubic average boiling point (CABP), the mean average boiling point (MeABP), the volumetric average boiling point (VABP), the weight average boiling point (WABP), the molar average boiling point (MABP), the Watson characterization factor (K_w), the refractive index, the carbon to hydrogen ratio (C/H), the kinematic viscosity at 100 and 210°F, the surface tension, the aniline point, the true and pseudo critical temperatures and pressures, the critical compressibility factor, the acentric factor, the freezing point, the heat of vaporization at the normal boiling point, the net heat of combustion at 77°F, the isobaric liquid heat capacity at 60°F, the isobaric vapor heat capacity at 60°F, the liquid thermal conductivity at 77 ºF, and the paraffins, naphthenes, and aromatics content. These properties are calculated for the petroleum fraction using well established methods in the literature or were developed specifically for this project[1].

The same properties are calculated from the pure component composition using the appropriate mixing rules from the literature. When the pure component properties are not available in databases they were estimated using group contribution methods available in the literature or were developed specifically for this project[1].

The difference between the values obtained from the two different methods for the true boiling point and the PNA content are minimized in the objective function the purpose of which is to calculate the values of x_i which is the mole fraction of the pure components in the petroleum fraction. This is shown in Equation 1 where both PNA and T_b of the pure components are a function of x_i. The composition of the light ends was determined using the RVP which is converted to the true vapor pressure at 100 °F and then using simple bubble point calculations.

The First line in the objective function represents the sum of errors in the boiling points of the pure components and the corresponding value on the true boiling point (TBP) curve. The pure component concentrations are determined by minimizing the following modified objective function,

$$S = \sum_{j=1}^{n} \left((Tb_j - T'b_j) \times W_o \times 100 / Tb_j \right)^2 + \left((PNA - PNA') \times W_1 \times 100 / PNA \right)^2 \quad (1)$$

where j is the index number of the molecule and n is the total number of molecules. PNA_i and PNA'_i refer respectively to the actual and predicted paraffin, naphthene, and aromatic content of the petroleum fraction. T_{bj} and T'_{bi} refer respectively to the boiling point of the pure component j and the corresponding value on TBP curve. W_1 and W_o are weighting factors and S is the objective function to be minimized.

An optimization algorithm based on the least square method was used to minimize the objective function while calculating the concentration of the pure components. The nonlinear regression algorithm minimizes the sum of the difference between the fuels bulk properties and those estimated from pure components. Using the Microsoft Excel Solver tool and the global optimization algorithm, convergence was achieved in less than one minute for all cases on a Pentium IV-1.7 GHz PC.

Discussion

The model was tested to predict the properties of 30 petroleum naphtha samples ranging in API from 35 to 91, IBP from 62 to 267 °F and FBP from 152 to 312 °F. Some of these results are shown in Table 1 and Figures 2 to 4. The MECM model proves to be a powerful tool for simulating the properties of petroleum fuels.

This work demonstrates that the complex nature of petroleum fuels may be modeled by a limited set of representative pure components using non-linear-regression optimization models. Considering the difficulty and limitations in predicting the properties of petroleum fuels in the currently used pseudo component techniques, the proposed method can be an effective alternative. The clear advantage of the model is its ability to compliment the molecularly explicit models for petroleum refining processing.

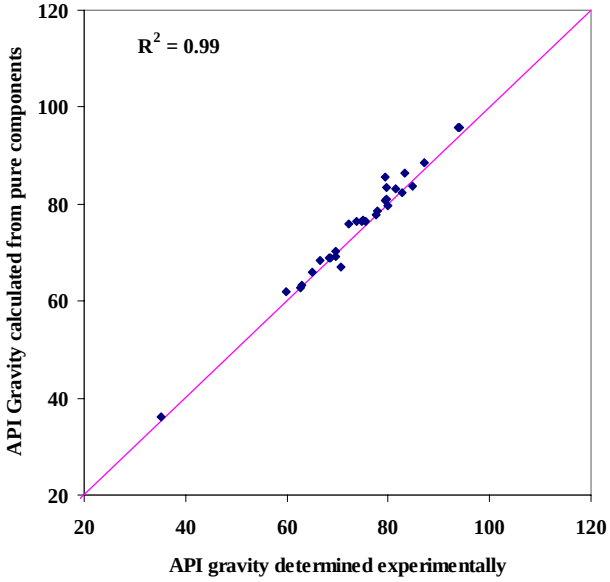

Figure 2. Bar plot for the predicted API gravity from pure components for 30 petroleum naphtha samples versus that calculated from global properties using published methods.

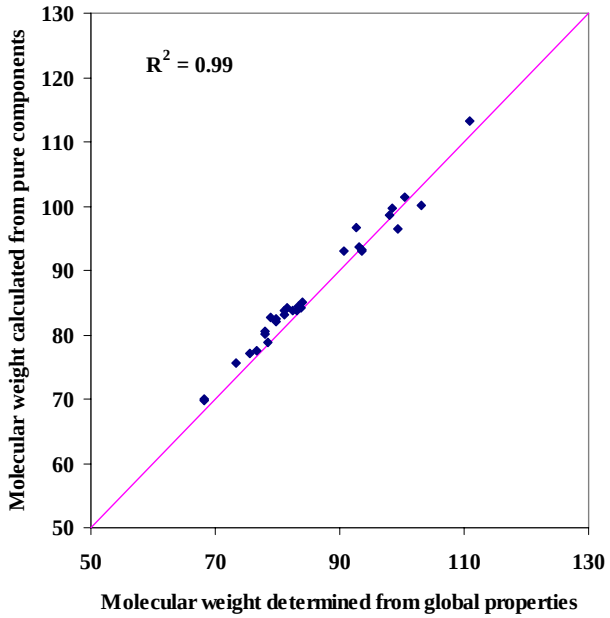

Figure 3. Bar plot for the predicted molecular weight from pure components for 30 petroleum naphtha samples versus that calculated from global properties using published methods.

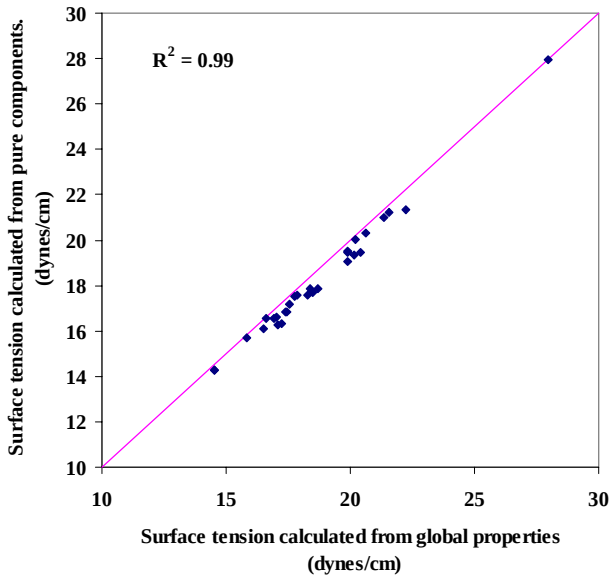

Figure 4. Bar plot for the predicted surface tension from pure components for 30 petroleum naphtha samples versus that calculated from global properties using published methods.

Table 1. Error analysis for some of the properties investigated

No.	Property	Av. % error	Corr. Coef.
1.	API gravity	2.67	0.995
2.	Cubic average boiling point	1.34	0.995
3.	Mean average boiling point	0.99	0.995
4.	Volume average boiling point	1.34	0.995
5.	Molar average boiling point	0.83	0.995
6.	Mass average boiling point	1.07	0.996
7.	Watson characterization factor	0.80	0.970
8.	Molecular weight	2.06	0.990
9.	Refractive index	0.21	0.993
10.	Hydrogen content	2.57	0.965
11.	Viscosity at 210 °F	4.04	0.960
12.	Viscosity at 100 °F	5.41	0.972
13.	Surface Tension	2.67	0.995
14.	Aniline Point	4.27	0.830
15.	Critical temperature	0.93	0.991
16.	Pseudocritical temperature	0.80	0.989
17.	Pseudocritical pressure	2.22	0.890
18.	Heat of vaporization	2.07	0.948
19.	Heat of combustion	0.80	-
20.	Freezing	5.38	-
21.	Acentric factor	3.13	0.946
22.	Critical compressibility factor	0.25	0.832
23.	Flash point	5.16	0.924

Acknowledgment

This work was supported by Kuwait University, Research Grant No. EC04/01.

References

[1] T. A. Albahri, Am. Chem. Soc., Div. fuel chem. prep., **2004**, 49(1), 327-328.
[2] M. R. Riazi & T. E. Daubert, Ind. Eng. Chem. Process Des. Dev., **1980**, 19 (2), 289-294.
[3] Jenkins, G. I. and white, M. M.. J. Inst. Petrol., **1969**, 55 (543), 153.

EFFECT OF ATMOSPHERES ON EVOLUTION OF SULFUR CONTAINING GASES DURING COAL PYROLYSIS

Qiang Zhou, Haoquan Hu, Quanrun Liu, Shengwei Zhu*

Institute of Coal Chemical Engineering, Dalian University of Technology, 129 street, Dalian 116012, P.R.China
* hhu@chem.dlut.edu.cn

Introduction

Coal is the main consumption energy in China, meanwhile it is also the main pollution contributor. Sulfur is a major factor in inhibiting the effective and extensive utilization of coal. So desulfurization is very necessary for improving coal quality and for protecting environment. Although many methods have been developed for coal desulfurization, an effective and economic process remains to be found.

Pyrolysis as an important intermediate stage in coal gasification, combustion and liquefaction etc, and a simple and effective method for clean conversion of coal has received many attentions. By pyrolysis both inorganic sulfur and organic sulfur can be removed, and most sulfur goes into gas phase in the form of sulfur containing gases (H_2S, COS, CH_3SH, CS_2 and SO_2, etc.) which is relatively easy to be recovered as sulfur. Thus knowledge of evolution of sulfur containing gases during pyrolysis is essential in finding optimum desulfurization method.

Numerous factors, including coal properties and pyrolysis conditions affect sulfur removal during the pyrolysis of coal[1,2]. Many studies about those have been done and some useful results have been obtained. Although gases derived from coal pyrolysis, such as N_2, H_2, CH_4, CO, CO_2 and so on, play important roles on the formation of sulfur containing gases, little effort has been done. The aim of this study was to investigate the effect of those gas components on the evolution of sulfur containing gases during coal pyrolysis.

Experimental

Coal Samples. Two Chinese coals, Yanzhou (YZ) and Datong (DT) coal, were used in the study. Air-dried samples were ground to -100 mesh before use. The proximate, ultimate and sulfur form analyses of two coals are listed in Table 1.

Table 1 Analyses of coals

Coal	Proximate (wt%)			Ultimate (wt%, daf)			Sulfur (wt%, db)			
	M_{ad}	A_d	V_{daf}	C	H	N	S_t	S_p	S_s	S_o*
YZ	5.9	27.7	44.8	81.4	5.7	1.3	3.6	1.7	0.1	1.8
DT	2.9	13.7	32.7	76.9	4.1	0.5	1.6	1.2	0.1	0.3

S_t: total sulfur; S_p: pyritic sulfur; S_s: sulfatic sulfur; S_o: organic sulfur. * By difference.

Pyrolysis. Pyrolysis was performed in an ambient pressure, vertical quartz micro-fixed bed reactor with inner diameter of 5mm; approximate 50mg sample placed in the reactor was heated from 25 to 1000°C with a heating rate of 5K/min under different pyrolysis atmospheres (90% N_2 mixed with 10% other selected gases, i.e. H_2, CO, CO_2 and CH_4). Air was removed from system by purging with pyrolysis atmospheres before each run. Gaseous products were all led to a gas chromatograph (GC) which was equipped with a 3m long glass column packed with 25% 1,2,3-tris(2-cyanoethoxy)propane and a flame photometric detector (FPD) to analyze sulfur-containing gases. To avoid the condensation of tar in the heating zone in the reactor, a high gas flow rate, 200cm^3min^{-1}, was used. Tar was trapped by quartz wool at outlet of the reactor. To avoid adsorption of sulfur containing gases by system, glass tube (i.d.=1mm) was used as conduit to connect reactor with GC. Total sulfur in coal was determined by Coulomb method (Testing Standard of China: GB214-77) and pyrite sulfur content was determined by ASTM D2492-80.

Results and Discussion

H_2S evolution. Figure 1 shows H_2S evolution during coal pyrolysis as function of temperature in different atmospheres. It can be seen that the evolution of H_2S during coal pyrolysis is affected by coal properties and pyrolysis conditions.

For DT coal, only one peak at about 525°C on H_2S evolution curve with two shoulders can be observed when pyrolyzed in N_2. According to the literatures[3,4], the peak is attributed to the decomposition of pyrite. The shoulder at lower temperature corresponds to the decomposition of aliphatic sulfur, and the shoulder at higher temperature is related to the decomposition of aromatic sulfurs. When YZ coal was pyrolyzed in N_2, two peaks, at about 425°C and 550°C, on H_2S evolution curve can be observed. As stated above, the first peak is related to the decomposition of aliphatic sulfur, and the second one is attributed to the decomposition of pyrite. Above 650°C, because of fixation of H_2S in mineral matter[5], almost no H_2S releases for both coals.

Compared with H_2S evolution in N_2, more H_2S evolves and more H_2S peaks are observed as coals were pyrolyzed in H_2. For DT coal, four H_2S peaks, at about 300, 525, 650 and 750°C, respectively, can be observed. According to the literature[6], the first peak results from decomposition of aliphatic sulfur, the second from decomposition of pyrite, the third and the last from decomposition of pyrrhotite and organic sulfur, such as thiophenes. The H_2S evolution of YZ coal is similar to that of DT coal, except the first peak shifts to higher temperature, which indicates the organic sulfur in thermally labile structures is mainly in the form of disulfides in YZ coal. And the effect of H_2 on the peak from pyrite decomposition is more pronounced, which results in a great difference between the peak in N_2 and that in H_2. This may be explained from the good swelling property of YZ coal which may trapped more sulfur from decomposition of pyrite, successively this trapped sulfur may transform into organic sulfur in N_2, thus less sulfur releases as H_2S. And the peaks of H_2S derived from decomposition of both pyrrhotite and thiophenes are integrated into a broad peak at about 725°C.

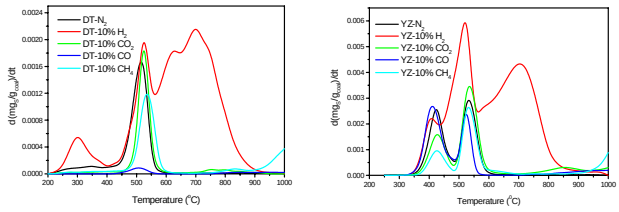

Figure 1. Effect of atmospheres on evolution of H_2S during coal pyrolysis

Compared with the effect of N_2 on H_2S evolution, CO prohibits H_2S evolution for DT coal, and has little effect for YZ coal at temperature below 650°C. Above 650°C, CO promotes H_2S evolution for both coals. This may be caused by the following reactions:

$$CO + FeS \rightarrow COS \quad [7]$$

$$COS + H_2 \rightarrow CO + H_2S \quad (\Delta G = -16.3 kJ/mol\ [8])$$

In CO_2, less H_2S releases below 500°C and more H_2S evolves at temperature region of 500 to 600°C than that in N_2. CO_2 reacts with

C (coal) to form CO at high temperature, so the evolution of H_2S in CO_2 is similar to that in CO.

In CH_4, less H_2S evolves than that in N_2 at temperature below 650°C; above this temperature, more H_2S evolves and the rate increases with increasing temperature. This may be resulted from the decomposition of CH_4 to form H_2[9], which promotes the decomposition of pyrrhotite and/or thiophenes to form H_2S.

COS evolution. It is known that COS derives from pyrite and organic sulfur[4,7]. The profiles of COS evolution during pyrolysis of two coals as a function of temperature in different atmospheres are presented in **Figure 2**.

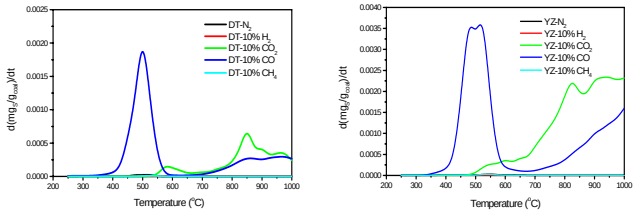

Figure 2. Effect of atmospheres on evolution of COS during coal pyrolysis

From **Figure 2** it can be seen that when coal was pyrolyzed in N_2, only a little COS evolved and mainly occurs in the temperature range of 450 to 600°C. Compared with the COS evolution in N_2, CH_4 and H_2 prohibits the formation of COS. This is because that H_2 may react with oxygen contained in coal to form water and consequently causes less CO formation, and that CO promotes the formation of COS, which will be discussed latter; meanwhile both H_2 and water can react with COS to form H_2S, all lead to less formation of COS. CH_4 may decompose to H_2 at relative low temperature in presence of coal, then it has similar effect as H_2.

Compared with the effect of N_2 on COS evolution, CO promotes the formation of COS and a COS evolution peak is observed at about 500°C, i.e. the pyrite decomposition temperature, for both coals, this shows that CO competes with H_2 to react with sulfur derived from the decomposition of pyrite. Above 650°C, the rate of COS evolution increases with increasing temperature. CO_2 also promotes the formation of COS, but at temperature below 575°C, the extent is not notable; above this temperature, more COS is formed than that in CO. This result indicates that the formation of COS is mainly related to CO in system and the effect of CO_2 is owing to the formation of CO by reaction of CO_2 with C (coal) at high temperature.

CH_3SH evolution. CH_3SH is mainly derived from the decomposition of organic sulfur in coal[2], so the evolution of CH_3SH also reflects the knowledge of decomposition of organic sulfur in coal. **Figure 3** shows the CH_3SH evolution rate profiles of the select coals in different pyrolysis atmospheres. From **Figure 3** it can be seen that the CH_3SH evolution during coal pyrolysis, just as H_2S evolution, is affected by not only pyrolysis conditions, but also coal properties. The evolution of CH_3SH mainly occurs in temperature range of 200 to 650°C, which indicates that the CH_3SH is mainly derived from the decomposition of organic sulfurs in the form as thiols, polysulfides, disulfides, dialkyl sulfides and alkyl-aryl sulfides etc.

As coal was pyrolyzed in N_2, two peaks, at around 275°C and 475°C, for DT coal and one peak, at around 475°C, for YZ coal can be observed. From the temperature of CH_3SH evolution peak, it can be concluded that there is some thiols, polysulfides and disulfides in DT coal, and some disulfides in YZ, respectively.

Compared with the evolution of CH_3SH in N_2, less CH_3SH evolves in H_2, which is caused by the promotion of H_2 on the decomposition of organic sulfur into H_2S. The other two atmospheres make CH_3SH peak shifts to high temperature.

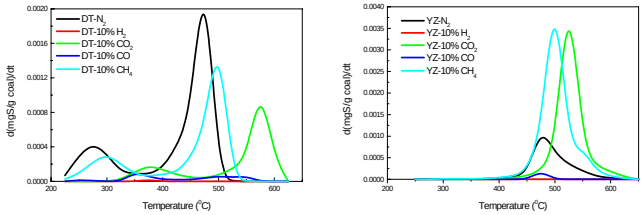

Figure 3. Effect of atmospheres on evolution of CH_3SH during coal pyrolysis

CS_2 evolution. The formation of CS_2 was also observed, but the effect of atmospheres on the formation of CS_2 is somewhat irregular. Some researchers assumed that CS_2 is derived from the reaction between pyrite and CH_4[1,10], no evidence proves CH_4 is essential for the formation of CS_2 in this study, but the evolution of CS_2 occurs in the temperature region of pyrite decomposition, which indicates that the decomposition of pyrite attributes to the formation of CS_2.

Little SO_2 was observed during pyrolysis of two coals in five atmospheres.

Conclusions

Compared with the evolution of sulfur containing gases in N_2, CO promotes the formation of COS; CO_2 prohibits the evolution H_2S at temperature below 500°C and shows similar effect on sulfur containing gases as CO does at above 500°C; CH_4 prohibits the evolution of H_2S more intensely than CO_2 at temperature below 650°C, but at higher temperature, more H_2S is formed; H_2 promotes the formation of H_2S and prohibits the formation of other sulfur containing gases.

Acknowledgement. This work was performed with the supports of the National Key Fundamental Research and Development Project of China (G1999022101).

References

(1) Khan, M. R. *Fuel*, **1989**, *68*, 1439.
(2) Hu, H.; Zhou, Q.; Zhu, S.; Krzack, S.; Meyer, B.; Chen, G. *Fuel Processing Technology*, **2004**, *85*(8-10), 849.
(3) Sugawara, K.; Enda, Y.; Kato, T.; Sugawara, T.; Shirai, M. *Energy and Fuels*, **2003**, *17*(1), 204.
(4) Ibarra, J. V.; Bonet, A. J.; Moliner, R. *Fuel*, **1994**. *73*(6): 933.
(5) Liu, Q.; Hu, H.; Zhou, Q.; Zhu, S.; Chen, G. *Fuel Processing Technology*, **2004**, *85*(8-10), 863.
(6) Piotr, R.; Steven, M.; Jan, Y.; Grazyna, G. *Fuel Process. Technol.* **2002**. *76*(2), 121.
(7) Furimsky, E.; Palamer, A. D.; Cheng, M. *The Canadian journal of chemical engineering*, **1991**. *69*, 869.
(8) Trewhella, M. J.; Grint, A. *Fuel*, **1987**, *66*(10), 1315.
(9) Breakman-Danheux, C.; Cypress, R.;Fontana A. *Fuel*, **1992**, *71*, 251
(10) Oh, M. S.; Burnham, A. K.; Crawford, R. W. Prepr. Pap. – *Am. Chem. Soc. Div. Fuel Chem.*, **1988**, *33*, 274.

EFFECT OF ATMOSHPERES ON SULFUR TRANSFORMATION DURING PYROLYSIS OF YIMA COAL

Qiang Zhou, Haoquan Hu, Quanrun Liu, Shengwei Zhu*

Institute of Coal Chemical Engineering, Dalian University of Technology, 129 street, Dalian 116012, P.R.China
* hhu@chem.dlut.edu.cn

Introduction

Desulfurization of coal is very necessary for improving coal quality and for protecting environment. Although many methods have been developed for coal desulfurization, an effective and economic process remains to be found.

Hydropyrolysis (HyPy), as an effective desfurfurization method, has received many attentions, but it's unprofitable to undertake industrial HyPy with pure hydrogen in the present energy market. Thus, it is necessary to use cheaper hydrogen-rich gas instead of pure hydrogen gas.

Some researchers have used coke-oven gas as hydrogen resource to study the sulfur removal and observed satisfying results[1]. However, little effort on the influence of pure components of coke-oven gas on sulfur transformation during coal pyrolysis has been done. The aim of this study was to study the effect of four main pure components of coke-oven gas, i.e. H_2, N_2, CH_4 and CO, on the behavior of sulfur during fixed-bed pyrolysis of Yima coal.

Experimental

Coal sample. A high sulfur Chinese coal, Yima coal (YM), ground to -100mesh, and dried in a vacuum oven at 100°C for 24hrs was used in the study. The analytical data are given in Table 1.

Table 1. Analyses of YM coal

Proximate (wt%)			Ultimate (wt%, daf)			Sulfur form (wt%, db)			
M_{ad}	A_d	V_{daf}	C	H	N	S_t	S_p	S_s	S_o *
5.9	27.7	41.3	80.1	5.3	1.2	2.4	1.5	0.1	0.8

S_t: total sulfur; S_p: pyritic sulfur; S_s: sulfatic sulfur; S_o: organic sulfur. * By difference.

Pyrolysis. Pyrolysis of coal was carried out in an ambient pressure, horizontal fixed-bed reactor (i.d. 18mm) under isothermal conditions at carried gas flow rate 400ml/min, residence time 20min and temperature from 350 to 900°C. About 2g coal samples were placed in a stainless steel boat and heated in furnace, preheated carried gas flowed through fixed-bed and carried out the volatilized matter. The heating time from ambient temperature to the desired is in about 2 minutes. After reaching the determined time, the boat was moved away from the furnace and let it cool down to the ambient temperature. To minimize the problem of the weight lose of char, the weight of char was calculated from the weight difference of boat and sample before and after pyrolysis of coal. The air was removed from the system by purging with nitrogen at the beginning of each run.

Analysis. The Coulomb method (Testing Standard of China GB214-77) was used to determine the total sulfur content in coal and residual chars, the sulfur form content was determined by the Gladfelter method[2]. The removal of total sulfur was calculated by the following expressions:

$$Desulfuriz\ ation\ ,\% = \left(\frac{S_{t,coal\,(d)} - S_{t,char\,(d)} \times Y_{char\,(d)}}{S_{t,coal\,(d)}}\right) \times 100 \qquad (1)$$

Where $S_{t,coal(d)}$, $S_{t,char(d)}$ is total sulfur content (dry base) of coal and char, respectively; $Y_{char(d)}$ is the yield of char (dry base) during pyrolysis.

Results and Discussion

Total sulfur. The total sulfur content in residual chars is shown in **Figure 1**. When Yima coal is pyrolyzed in H_2, the total sulfur content in residual char decreases with increasing temperature. The decrease mainly occurs in 350-450°C and 650-900°C regions, reaches 0.4 and 0.7wt%, respectively. In the region of 550-650°C, only 0.03wt% total sulfur decrease is occurred.

In N_2, the total sulfur content in chars increases from 2.25wt% at 350°C to 2.57wt% at 450°C firstly, and then decreases with increasing temperature at the range of 450 to 550°C. Above 550°C, the total sulfur content increases slowly from 2wt% to 2.17wt% at 900°C.

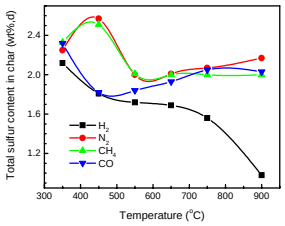

Figure 1. Total sulfur contents *vs* temperature in chars

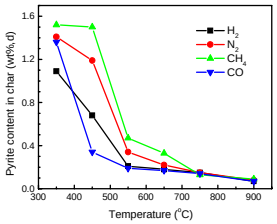

Figure 2. Pyrite sulfur contents *vs* temperature in chars

CO shows similar effect on total sulfur content change as H_2 does at temperatures below 450°C. Above this temperature, the total sulfur content continues to increase monotonously with increasing temperature, reaching 2.05wt% at 750°C, and then remains almost constant with increasing temperature.

The trend of total sulfur content change in residual chars obtained in CH_4 is similar as that in N_2 until temperatures up to 650°C. Above this temperature, the total sulfur content does not markedly change and becomes constant at about 2wt%.

Sulfate sulfur. Because the sulfate sulfur is only 3.78% of total sulfur in raw coal, it is not discussed in this study.

Pyritic sulfur. Figure 2 shows the effects of atmospheres on changes of pyritic sulfur content in residual chars during pyrolysis. It can be seen that H_2 and CO show similar effectiveness on decomposition of pyrite, while CH_4 shows similar effect as N_2 does.

The decomposition of pyrite mainly occurs at temperature region of below 550°C in atmospheres of H_2 and CO. In this region, the pyritic sulfur content decreases from 1.50% in raw coal to 0.21 at 550°C in H_2, and 0.19% in CO, respectively. At lower temperatures, H_2 shows more positive effect on the pyrite decomposition than that CO does.

Pyrite is more stable in the other two atmospheres, especially in CH_4. The mainly decomposition takes place in the temperature of 450 to 550°C for both atmospheres, and the decrease reaches 0.85 and 1.03wt% in N_2 and CH_4, respectively. At temperatures below 450°C, the content decreases slowly in N_2, and almost remains constant in CH_4 with increasing temperature.

Above 750°C, the pyritic sulfur in residual char is mainly affected by temperature, and only a little (<0.1wt%) remains in chars in all atmospheres at 900°C.

Organic sulfur. The influence of atmospheres on the organic sulfur content in residual chars during pyrolysis is given in **Figure 3.** It can clearly be seen that both temperature and atmospheres have significant effects on the decomposition of organic sulfur and transformation of inorganic sulfur into organic sulfur.

When coal pyrolysis in H_2 and temperature rise to 450°C, the organic sulfur content in residual char decreases from 0.76wt% in the raw coal to 0.57wt%, then increases with increasing temperature and reaches 0.66wt% at 650°C. Above this temperature, the content of organic sulfur in residual char decreases again and reaches 0.34wt%

at 900°C. The first decrease is caused by the decomposition of organic sulfur groups with low thermal stability, such as thiols and Polysulfides[3]. The considerable increase in organic sulfur is accompanied by the intensive decomposition of pyrite, which indicates the increase is from the transformation of inorganic sulfur. Other researchers also observed the increase of organic sulfur in char in hydrogen atmosphere [4]. The new-formed organic sulfur may have high thermal stability and is very difficult to decompose. The second decrease is caused by the decomposition of aromatic sulfurs[3]. The organic sulfur remains in residual char (0.34wt%) at 900°C may exist in condensed thiophenic species.

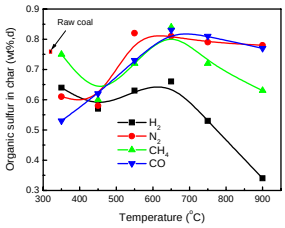

Figure 3. Organic sulfur content *vs* temperature in chars

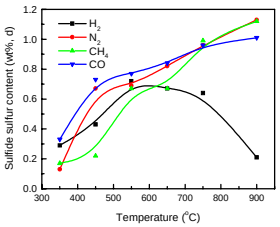

Figure 4. Sulfide sulfur content *vs* temperature in chars

The change of organic sulfur content in N_2 is similar to that in H_2 below 650°C, but the content is notable higher in N_2 than that in H_2 except at 350°C. At higher temperatures, the organic sulfur content remains almost constant in N_2. As mentioned above, the decomposition of pyrite in coal mainly occurs at 450 to 500°C in N_2, while in H_2 rich environment, this reaction starts at a relatively low temperature [5].

More organic sulfur persists in residual char in CH_4 than that in N_2 at temperatures below 450°C. Above 650°C, less organic sulfur remains in residual char in CH_4 than that in N_2. At high temperature CH_4 may decompose to H_2[6] and more ethene will be formed in the presence of CH_4 during coal pyrolysis[7]. Except for the promotion of H_2 on decomposition of organic sulfur, ethene also can react with H_2S or nascent sulfur derived in pyrolysis to form small molecule sulfur containing organic species and releases[8,9]; Meanwhile, ethene can react with organic matrix in residual char, which will decrease the coal conversion, all those lead to low sulfur content in chars.

At studied temperature range, the change of organic sulfur content in chars in CO is similar to that in N_2, but it seems that CO prohibits the transformation of pyrite sulfur to organic sulfur. CO promotes the decomposition of pyrite[1], while has little effect on coal pyrolysis, thus the relative ratio of organic free radical to nascent sulfur is lower in CO than that in N_2, so less nascent sulfur is trapped by free radical to form new stable organic sulfur in CO.

Sulfide sulfur. Figure 4 represents the sulfide sulfur content of residual chars obtained in different atmospheres. The sulfide sulfur content in char increases steadily with the progressive decomposition of the pyrite in H_2 up to 550°C, and then decreases with increasing temperature because of the decomposition of sulfide sulfur. At 900°C, only 0.21wt% sulfide sulfur persists in residual char.

The change of sulfide sulfur content in char obtained in other three atmospheres is similitude with each other, i.e. it increases with increasing temperature. By comparing **Figure 2** with **Figure 4**, it can be seen that the increase of the quantity of sulfide sulfur is corresponding to the extent of the decomposition of pyrite at temperatures below 650°C. Above this temperature, although the conversion of pyrite to ferrous sulfur is nearly complete, a further increase in sulfide sulfur is observed, which is caused by the reaction of hydrogen sulfide with alkali mineral [3,10].

Sulfur removal. The sulfur removal during coal pyrolysis is shown in **Figure 5**. It can be seen that the most effective temperature for sulfur removal of Yima coal in H_2, N_2, CH_4 and CO is 900, 550, 550 and 450°C, respectively. And the desulfurization reaches 75.5, 39.1, 38.4 and 44.0%, respectively.

In the early pyrolysis stage, below 550°C, in H_2, the desulfurization yield increases rapidly with increasing temperature from 17.1wt% at 350°C to 49.1wt% at 550°C, and then increases slowly with increasing temperature up to 750°C (59.0wt%), above 750°C, increases rapidly again, reaching 75.5wt% at 900°C. The rapid increase at temperature below 550°C is mainly caused by the decomposition of pyrite and organic sulfur groups of low thermal stability, see **Figure 2** and **Figure 3**, at temperature above 750°C is caused by the decomposition of organic sulfur and sulfide sulfur, see **Figure 3** and **Figure 4**, the slowly increase at middle temperature results from the transformation of inorganic sulfur into organic sulfur.

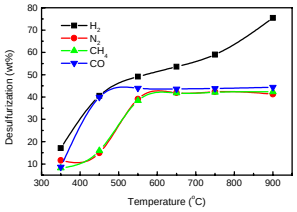

Figure 5. Effect of atmospheres on desulfurization

The desulfurization in other atmospheres are mainly caused by the decomposition of pyrite, so desulfurization mainly occurs at temperature 450-550°C for N_2 and CH_4, and 350-450°C for CO, respectively, which corresponds the temperature region of pyrite decomposition.

Conclusions

By analysis the sulfur form content changes in residual chars obtained in different atmospheres, the following conclusion can be drawn. The decomposition of pyrite mainly occurs at temperature region of below 550°C in atmospheres of H_2 and CO; in other two atmospheres, especially in CH_4, pyrite is more stable and the mainly decomposition temperature region is 450-550°C. The organic sulfur content in the residual char is the net effect of decomposition of organic sulfur species with low thermal stability and formation of new ones with high thermal stability by the reaction of hydrogen sulfide and/or nascent sulfur with organic matrix. Above 750°C, CH_4 can promote the decomposition of organic sulfur.

Acknowledgement. This work was performed with the supports of the National Key Fundamental Research and Development Project of China (G1999022101).

References

(1) Liao, H. Q.; Li, B. Q.; Zhang, B. J. *Fuel*. **1998**, *77*, 1643.
(2) Sugawara, T.; Sugawara, K.; Ohashi, H. *Fuel* 1988. *67*,1263.
(3) Grazyna, G. *Fuel*, **1995**. *74*, 356.
(4) Xu, W. C.; Kumagai, M. *Fuel*, **2003**. *82*, 245.
(5) Khan, M. R. *Fuel*, **1989**, *68*, 1439.
(6) Breakman-Danheux, C., Cypress, R., Fontana A., *Fuel*, **1992**, *71*, 251.
(7) Calkins, W. H.; Bonifza, C. *Fuel*, **1984**, *63*, 1716.
(8) Attar, A. *United States Patent* 4465493, August 14, **1984**.
(9) Hu, H.; Wu, X.; Zhu, S. Prepr. Pap. - *Am. Chem. Soc., Div. Fuel Chem.*, **2003**,*48*(1), 409.
(10) Liu, Q.; Hu, H.; Zhou Q.; Zhu S.; Chen G. *Fuel Processing Technology*, 2004, *85*(8-10), 863.

EFFECTS OF BOILER OPERATION ON WET FLUE GAS DESULPHURIZATION SYSTEM

Manyin Hu[1], Hezhong Tian[2], Bingwei Liu[1], Lidong Wang[1], Shuqin Wang[1]

1. School of Environmental Science and Engineering, North China Electric Power University, Baoding 071003, China
2. Department of Environmental Science and Engineering, Tsinghua University, Beijing 100084, China

1. Introduction

With the continuously rapid economy growth, coal-dominated energy consumption in China has caused very serious SO_2 and acid rain pollution. Northeastern Asia including China has become the third acid rain areas in the world. In 2000, total coal burning by utility boilers in China was about 600Mt, accounting for 60% of the total coal consumption. Coal fired power plants emitted more than 8Mt SO_2, contributing as high as 40% of the total SO_2 emissions in China [1]. Therefore, equipping with desulphurization installations to abate SO_2 emission from coal fired power plants is crucial for SO_2 and acid rain control in China.

Among all kinds of desulphurization processes, wet limestone-gypsum flue gas desulphurization (FGD) is the most popular process in power plant for its high efficiency, mature technique, as well as cheap and widely distributed limestone absorbent. In the early 2004, Chinese government promulgated new version of air pollutants emission standards for thermal power plant [2], newly modified SO_2 emission ceilings will lead to large amount of FGD installation.

Boiler operation conditions have a great impact on FGD performance, such as coal characteristics, excess air coefficient, boiler load, et al. In this paper, effects of these factors on FGD efficiency were analyzed and discussed, and mathematical expression of FGD efficiency was deduced. In addition, univariable and multivariable regression between FGD efficiency and some factors were carried out.

2. Factors influencing FGD performance

2.1 Coal characteristics. 2.1.1 Sulfur content

Coal sulfur content and the share of combustible components have a great impact on flue gas SO_2 concentration and FGD performance. High SO_2 concentration can improve kinetic reactivity velocity, but it is much less than the effects of SO_2 volume increase, so the desulphurization efficiency declined.

2.1.2 Coal element components

Different coal element configuration not only has impact on flue gas components and characteristics, also has effects on the flue gas rate and SO_2 concentration.

2.1.3 Coal low heating value (LHV)

Coal low heating value determined coal burning rate and produced flue gas rate. Thus, it can influence SO_2 concentration and FGD efficiency.

2.2 Gas velocity. Below the flooding velocity, gas velocity increase facilitate decreasing liquid diameter to increase the contact area, it is advantage to the SO_2 absorption. But when the gas velocity is above flooding velocity, it will make the contact of gas and liquid overbalance, which will decrease the efficiency [3].

2.3 Excessive air coefficient and air leak coefficient. The changes of excessive air coefficient of hearth exit and air leak coefficient of boiler flue directly affect the gas amount and make the SO_2 concentration and gas velocity change, and further affect the desulphurization efficiency.

2.4 Boiler load. Boiler load affects flue gas volume, gas velocity and SO_2 rate, which will make the desulphurization efficiency change.

3. Mathematical models

3.1 Desulphurization efficiency of wet FGD system. Desulphurization efficiency of wet flue gas desulphurization system can be expressed by the following equation:

$$\eta = \left[1 - C'_{SO_2} / C_{SO_2}\right] \times 100 \qquad (\%) \qquad (1)$$

Where, η is desulphurization efficiency (%), C'_{SO_2} and C_{SO_2} is the outlet and inlet SO_2 concentration of FGD (mg/Nm^3), respectively.

Desulphurization efficiency of wet FGD system is determined by liquid-gas ratio, pH value of slurry, inlet SO_2 concentration, etc. It is difficult to reveal completely the relationship between the desulphurization efficiency and the above factors, thus some hypotheses were given as following:

Air flow in the desulphurization tower was turbulence, SO_2 mixed completely by gas turbulence and diffusion, and SO_2 on any cross-section was evenly distributed. Gas velocity in scrubber tower was uniform distributed except at the boundary layer. SO_2 was absorbed completely when it came into the equipment.

The wet desulphurization tower sketch map was showed in Fig. 1, in which desulphurization tower diameter was r_b, the height was H, axes coordination was z, radial coordination was r, gas moved from down to up, absorber was sprayed from up to down.

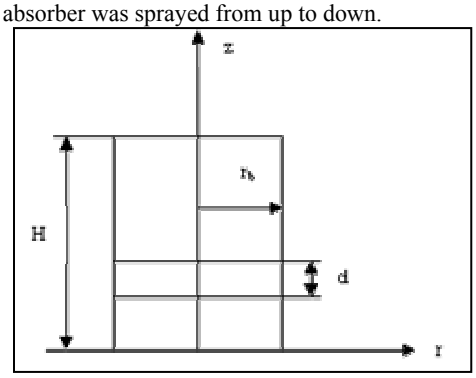

Figure 1. Sketch map of the desulphurization tower

In the z direction, any micro-volume (dv) was selected, whose section was $F(F=\pi \times r_b^2)$, length was dz, so $dv=Fdz=\pi r_b^2 dz$.

Where, F was tower cross-section area (m^2), r_b was scrubber tower diameter (m). Thus, SO_2 mass in the dv was:

$$M = C_{SO_2} dv = C_{SO_2} F dz \qquad (2)$$

Where C_{SO_2} was SO_2 concentration in dv（mg/m^3）. SO_2 mass absorbed by liquid in dt time in dv was:

$$dm = C_{SO_2} q \alpha dt dv \qquad (3)$$

Where q was absorbent spray rate in unit time (m^3/s·m^3), α was absorbing velocity coefficient (value of SO_2 concentration increasing amount in the liquid divided by flue gas SO_2 concentration).

As the SO_2 was absorbed by the absorbent liquid, its concentration in the elemental volume cell would decrease, the change was dC_{SO_2},

$$dC_{SO_2} = -dm/dv = -C_{SO_2} q\alpha dt \quad (4)$$

$$dC_{SO_2}/C_{SO_2} = -q\alpha dt \quad (5)$$

The boundary conditions were as follows:
$z=0,\ t=0,\ C_{SO_2} = C_{In}$; $z=H,\ t=t,\ C_{SO_2} = C_{Out}$.

Then, $$\int_{C_{Out}}^{C_{In}} \frac{1}{C_{SO_2}} dC_{SO_2} = -\int_0^t q\alpha dt \quad (6)$$

Then, following expression can be obtained:

$$C_{Out}/C_{In} = e^{-q\alpha t} \quad (7)$$

In which C_{out} and C_{In} were the outlet and inlet SO_2 concentration of desulphurization tower (mg/Nm^3), respectively.

$$t = H/u \quad (8)$$

Where, t was flue gas settling time(s), u was gas velocity (m/s), and H was tower height (m).

Introducing equation (3) into equation (2), we could get

$$C_{Out}/C_{In} = e^{-q\alpha H/u} \quad (9)$$

In the expression of $e^{q\alpha H/u}$, multiplying $\pi r b^2$ in denominator and numerator, respectively, and considering $\pi r b^2 u = Q$, $\pi r b^2 H = V$, thus:

$$\eta = 1 - C_{Out}/C_{In} = 1 - e^{-q\alpha V/Q} \quad (10)$$

In which, Q was flue gas rate (m^3/s), V was the effective tower volume (m^3), $V = F \cdot H$. Thus, equation (10) changed into the following form:

$$\eta = 1 - e^{-(L/Q)\alpha} \quad (11)$$

In which, L was absorbent spraying rate (m^3/s), while L/Q was liquid-gas ratio.

3.2 Outlet SO_2 concentration of desulphurization equipment. According to boiler combustion calculation, expression of the outlet SO_2 concentration of FGD equipment was as follows: [4]

$$C_{SO_2} = 2\times10^4 f S_{ar} / \left[V_y + (273+T)/273\right] \quad (12)$$

In which, f was the percent of coal sulfur which could burn (%), while S_{ar} was coal sulfur content in air received basis. T was flue gas temperature (□), and V_y was flue gas volume produced by a kilogram of coal burning (m^3/kg).

4. Calculation example and analysis

Element analysis of the calculated coal was shown in Tab. 1.

Table 1. Elemental composition of the calculated coals

Coal	Element composition, %							$Q_{ar,net}$ (kJ/kg)
	M_{ar}	A_{ar}	C_{daf}	H_{daf}	O_{daf}	N_{daf}	S_{daf}	
Xi-Shan Sub-bituminous	6.0	21.0	91.0	3.6	2.4	1.2	1.8	24720
Xu-Zhou Bituminious	10.0	15.0	82.3	5.4	8.8	1.9	1.6	24720
Huai-Nan Bituminious	6.0	21.0	81.9	5.4	10.3	1.5	0.9	24300
Jin-Zhushan Anthracite	7.0	24.0	92.5	3.2	2.6	0.8	0.9	22210

When t=80□, k=0.95, the produced SO_2 concentrations of different coal under different excess air coefficient (α) were shown in Tab. 2.

Table 2. SO_2 concentration under different α Unit: mg/m^3

α / coal kinds	1.4	1.5	1.6	1.7	1.8	1.9	2.0
Xi Shan sub-bituminous	2014	1883	1767	1665	1574	1493	1419
Xu Zhou bituminious	1878	1757	1650	1556	1471	1396	1328
Huai Nan bituminious	1076	1006	945	891	842	799	760
Jin Zhushan anthracite	1010	944	886	834	789	748	711

As can be seen from the above two tables, flue gas SO_2 concentrations produced by different coal under different excessive air coefficient differs to a fairly large extent.

By regressing with test data of wet liestone-gypsum flue gas desulphurization system of Luo-huang power plant in Sichuan province, relationship of SO_2 concentration, pH value, liquid-gas ratio(L/Q) and desulphurization efficiency were carried out, which was shown in equation (7)[5].

$$\eta = 1 - e^{1.069 - 75.3544 L/Q - 0.4983x + ky} \quad (13)$$

Where, x was the pH value, L/Q was liquid-gas ratio(m^3/m^3) $y = C_{SO_2} - 1100$ (mg/m^3); k was concentration coefficient, $k = -2.8896\times10^{-9} y + 1.7811\times10^{-4}$.

When x=5.0 and y=2270, the relation between desulphurization efficiency and liquid-gas ratio was shown in Fig. 2.

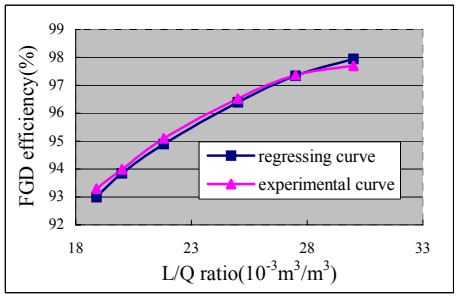

Figure 2. Relationship between FGD efficiency and L/Q

When x=5.0, L/Q=0.02, the relation between desulphurization efficiency and SO_2 concentration was shown in Fig. 3.

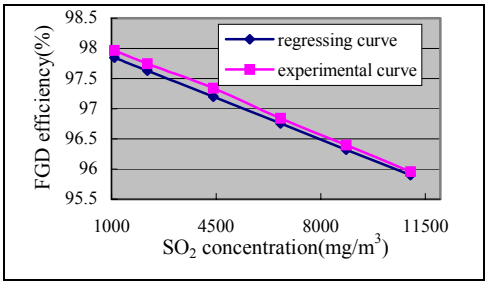

Figure 3. Relationship between FGD efficiency and SO_2 concentration

Both of the curves were well agreement with the experimental ones, and this implies that the equation could analyze and forecast the effect of boiler operation on wet flue gas desulphurization system.

5. Conclusions

Effect of power boiler combustion and operation on the wet limestone--gypsum desulphurization system was studied in this paper, and the mathematic model of FGD efficiency was established. By regression of the real FGD equipment experiment data, the relation between some factors and desulphurization efficiency was deduced. Simulation results demonstrated that these models will be very helpful for forecasting effect of power boiler burning and operation on FGD system, and supply instruction for wet desulphurization system design and operation.

References

1. Wang Z.X. countermeasures and suggestions on SO_2 discharge control for thermal power plant in China. Electric Power. 2002, 35(1): 60-63
2. GB13223-2003. Air pollutants emissions standards for thermal power plants. 2004.
3. Hao J.M., Ma G.D. Air Pollution and Control Engineering, Beijing: Higher Education Press, 1992, 330-331.
4. Fan C.Z. Power Boiler Theory, Beijing: Electricity Power Industry Press, 1985, 21-23.
5. Design construction and running of flue gas desulphurization equipment of Luo-Huang Power Plant, 1998, 10-13.

KINETICS OF OXYGEN DESORPTION/ADSORPTION IN SWNTs

U. K. Patel, R. Jalilian, S. Desai, J. Rivera, and G.U. Sumanasekera

Department of Physics, University of Louisville, KY 40292

Introduction

Very recently, much attention has been focused on the fundamental science and applications of carbon nanotubes in gas adsorption. Interest on this subject has been heightened by several observations of changes in the electrical conductance of SWNT via gas or chemical adsorption, and a clear interdependence of gas adsorption and transport properties is being established. For example, two research groups[1,2] have reported unusual sensitivity of the electrical resistivity and thermoelectric power (S) of SWNTs to the adsorption of oxygen. They have argued that SWNTs are easily doped with O_2 under ambient conditions, forming a weak charge transfer complex ($C^{+\delta}{}_pO_2{}^{\delta-}$), and adsorbed oxygen changes the sign of the thermopower[3]. Similar results have been observed for multiwall carbon nanotubes and activated carbon fibers. However, this conclusion has been contested *via* FET studies by Avouris and coworkers[4], who find that O_2 dopes the electrical contacts made to the SWNT, and not the wall. In a recent publication, Ulbricht el al.[5], argue that minority oxygen species located either at defect sites on the SWNT bundles or at tube-metal contacts in electronic devices are responsible for the observed p doping. In fact, several mechanisms may explain such phenomena. The gas molecules could affect transport properties indirectly, by binding to donor or acceptor centers in the substrate, or at the contacts, or directly, by binding to the nanotube. In the latter case, the gas could be physisorbed (bound by dispersive van der Waals forces) or chemisorbed (bound by formation of chemical bond resulting some charge transfer), and adsorption could take place either on perfect nanotube walls or at defect sites. Experimentally, a way to distinguish physisorption from chemisorption is to check for a linear relation between the thermoelectric power and the additional resistance induced by gas adsorption[6]. According to this criterion, O_2 is chemisorbed. However, a recent experimental study of the kinetics of oxygen adsorption and desorption on SWNT shows the estimated binding energy is low and consistent with physisorption of oxygen in molecular form. It also remains unclear whether atomic or molecular oxygen is responsible for the charge transfer.

Experimental

The sample used in our study was a commercial bucky paper made of SWNTs grown by laser ablation with an average diameter of 1.4 nm. After purification by refluxing in 2-3 M nitric acid, the tubes have been dissolved in a Sodium Lauryl Sulfate (SLS) surfactant solution. We studied the sample as received (contaminated with surfactant) and after annealing at 1200 ^{0}C at 10^{-7} Torr for 24 hrs to remove the surfactant. Two, Chromel-Au/7at.%Fe thermocouples (all 0.003" dia. wires) were attached to the edges of the sample with small amounts of silver epoxy to measure the thermoelectric power (TEP). The thermopower (*i.e*), Seebeck coefficient data were collected using a heat pulse technique[7]. The sample was placed in an apparatus equipped with a turbo molecular pump capable of evacuating to 10^{-7} Torr for in situ studies which can be heated to 600 K.

Results and Discussion

The thermopower curves during desorption of oxygen for the sample without surfactant at four different temperatures are shown in Fig. 1. The best fits for a double exponential of each graph is also shown in the figure. The fits with a single exponential with the experimental data do not show good agreement and deviate from the experimental data. Whereas, a two exponential function fits the experimental data quite well.

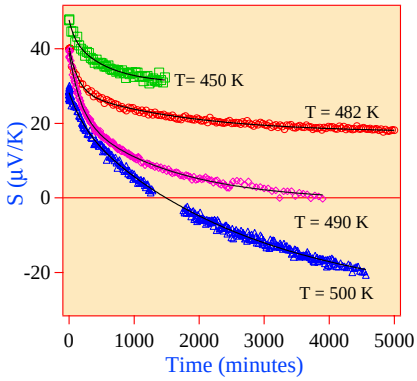

Figure 1. Thermopower versus time at four different temperatures for SWNTs sample free of surfactant during desorption of oxygen. Best fits with two exponentials are shown in solid lines.

The results of oxygen desorption kinetics of the SWNT sample containing surfactant are shown in Fig.2 for two dfferent temperatures. Again the data can be very well fitted with two exponentials.

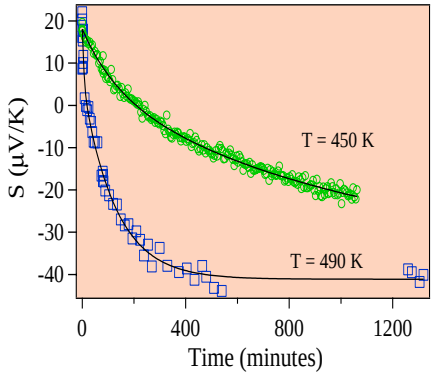

Figure 2. Thermopower versus time at two different temperatures for SWNTs sample contaminated with surfactant during desorption of oxygen. Best fits with two exponentials are shown in solid lines.

These observations show that oxygen has at least two adsorption sites available in SWNT bundles corresponding to the two exponentials. These two sites with different binding energies for oxygen adsorption results in different time constants**.** The comparison of the desorption graphs for the two samples with and without surfactant also reveals that the desorption of oxygen for the SWNTs containing surfactant is faster than that of annealed sample (free of surfactant) at a given temperature. This can be understood as due the wall defects induced on the nanotube walls during the purification process with nitric acid. Due to the presence of wall defects, oxygen can desorb relatively easily compared to the annealed sample. So, in the case of the sample without surfactant, the oxygen is tightly bound to the walls of the tubes compared to the sample with surfactant. Hence, the loosely bound oxygen molecules are relatively easy to be desorbed and result in shorter time for the thermopower to saturate compared to tightly bound oxygen in the case of annealed sample. From above data it is a marked difference that the SWNT free of surfactant with ambient doping with oxygen

has the positive thermopower of about 40 μV/K compared to the one containing surfactant having thermopower of only 20 μV/K. Moreover, in the case of the sample with surfactant, for a given temperature e.g., 490 K the thermopower saturates at a higher negative value of ~ – 40 μV/K compared to the saturated thermopower of ~ -4 μV/K for the annealed sample. This can be explained with the aid of band structure diagram of the SWNTs where in the simplest case, for a fully compensated sample with holes and electrons contributing equally gives zero thermopower for a symmetric band structure[8]. When the sample is doped with the oxygen, which is an acceptor, the Fermi energy moves towards the acceptors states and pinned at these acceptor levels. During the desorption, the Fermi energy E_F is pinned at the donor states presumably introduced by the wall defects. Recently, Larciprete et al.[9], have used photoemission spectroscopy to study the interaction between oxygen and nanotubes. They have found strong interaction of oxygen and nanotubes contaminated with surfactant and interpret the results as due to charge transfer from the nanotube to the Na-O complex. But they find weak interaction of oxygen with nanotubes free of surfactant.

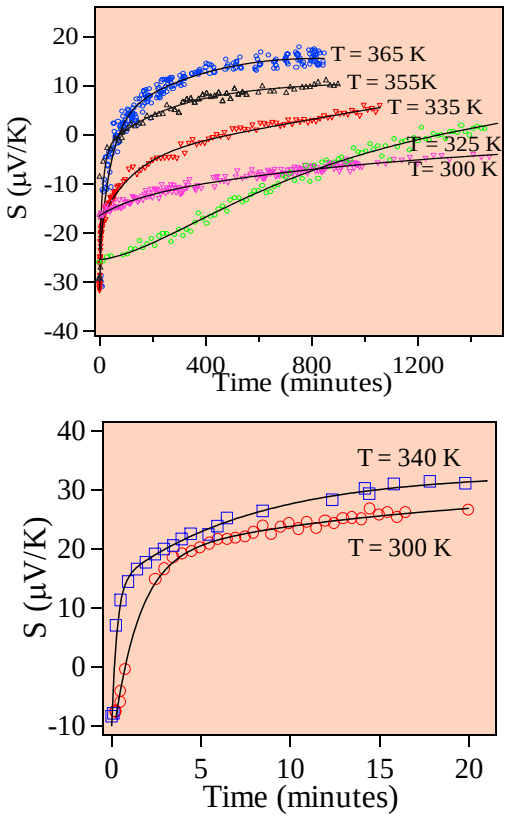

Figure 3. Time evolution of Thermopower during O2 adsorption at various temperatures for (a) SWNTs sample contaminated with surfactant (b) SWNTs free of surfactant. Best fits with two exponentials are shown in solid lines.

The thermopower curves for adsorption of oxygen for the two samples with and without surfactant are shown in Fig. 3 for different temperatures with best fits for two exponentials. The comparison of these two graphs shows that the adsorption of oxygen is faster in the case of the annealed sample compared to the sample contaminated with surfactant. This is due to presence of surfactant obstructing the diffusion of oxygen resulting delays in the adsorption**.**

The time constants extracted from desorption data reflect the strength of the oxygen-nanotube interaction with an activated behavior which requires an extra energy to desorb the oxygen molecule in excess of the binding energy. The temperature dependence of the time constants for the two adsorption sites can be used to estimate the difference between the binding energies of the two sites.

Conclusions

Our study on sensitivity of thermopower of bundles of SWNTs to adsorbed oxygen gas molecules reveal that there are at least two sites available for the adsorption of oxygen in the entangled bundles of nanotubes. The ends of the naotubes are believed to be closed, but wall damages can exist in the tubes. The faster kinetics of the desorption of oxygen in single wall carbon nanotubes contaminated with surfactant compared to the nanotubes free of surfactant is attributed to the wall damages induced by acid treatment during the purification process. The presence of surfactant obstructing the diffusion of oxygen during adsorption result in slower kinetics in the contaminated sample. The magnitude of the thermopower at the saturation for adsorption/desorption is consistent with the band structure analysis. The t emperature dependence of adsorption/desorption time constants allows us to compare the binding energy for the two adsorption processes.

Acknowledgement. This work was supported by funds from Department of Energy (Grant No: DE-FG02-00ER45832). We thank Profs. P. C. Eklund at Pennsylvania State University and S. Y. Wu at University of Louisville for useful discussions.

References

(1) Collins, P. G.; Bradley, K.; Ishigami, M.; Zettl, A., *Science*, **2000**, *287*, 1801
(2) Sumanasekera, G. U.; Adu, C. K. W.; Fang, S. L.; Eklund, P. C., *Phys. Rev. Lett*., **2000**, *85*, 1096
(3) Jhi, S-H; Louie, S. G.; Cohen, M. L., *Phys. Rev. Lett*, **2000**, *85*, 1710
(4) Derycke, V.; Martel, R.; Appenzeller, J.; Avouris, Ph., *Nano Letters*, **2001**, *1*, 9.
(5) Ulbricht H.; Moos, G.; and Hertelet al, *Phys. Rev. B*, **2002**, *66*, 075404 (2002)
(6) Adu, C. K. W.; Sumanasekera, G. U.; Pradhan, B. K.; Romero, H. E.; Eklund, P. C., *Chem. Phys. Lett*., **2001**, *337*, 31
(7) Sumanasekera, G. U.; Grigorian, L.; Eklund, P.C., Meas. Sci. Technol., **2000**, *11*, 273
(8) Romero,H. E.; Sumanasekera, G. U.; Mahan, G. D.; Eklund, P. C., *Phys. Rev. B*. **2000**, *65*, 205410.
(9) R. Larciprete, A. Goldoni, S. Lizzit, Nucl. Instr. and Meth. in Phys. Res. B, **2003**, *200*, 5

APPLICATIONS OF FUNCTIONALIZED SINGLE-WALLED CARBON NANOTUBES

Elena Bekyarova, Bin Zhao, Rahul Sen, Mikhail E. Itkis, Robert C. Haddon

Center for Nanoscale Science and Engineering, Departments of Chemistry and Chemical & Environmental Engineering, University of California, Riverside, California 92521-0403

Introduction

The outstanding materials properties of single-walled carbon nanotubes (SWNTs) have increased the level of interest in their applications. However, many of the potential applications of SWNTs are hindered by the difficulties in their processing. The chemical functionalization of SWNTs will play a key role in the realization of the promise of this material. The solubilization of SWNTs by attachment of long-chain molecules to the open ends of the nanotubes was the first step in brining SWNTs into the realm of molecular chemistry.[1] Rapid progress in development of methods for covalent attachment of various organic groups,[2-6] quantum dots[7] and biological molecules[8] has broadened the opportunities for applications of SWNTs. With the advancement in the chemistry of SWNTs it is now possible to tailor the electronic and chemical properties of SWNTs.[9,10]

Some of the important issues addressed by the chemistry of SWNTs involve dissolution of SWNTs and bundle exfoliation. The chemical functionalization of SWNTs has been shown to increase their solubility in organic solvents and facilitate their processing.[1,11,12] It has also been demonstrated that the chemical functionalization affects the SWNT rope size and results in exfoliation into smaller bundles and individual nanotubes. These issues are especially important for the fabrication of high-performance composite materials, controlled assembling of molecular electronics and development of ultra-high sensitive sensor devises.

Here, we outline chemical approaches to functionalized SWNTs with an emphasis on their application for high-performance composites and biosensors.

Functionalization of SWNTs with oligomers and polymers

SWNTs are considered to be the ideal reinforcing fibers due to their exceptional mechanical, electronic and thermal properties, low density and high aspect ratio. However, the incorporation of SWNTs into the polymer matrix is often problematic due to the chemical inertness of SWNTs. The covalent functionalization of SWNTs is a valuable route towards the development of high-performance composites. It provides homogeneously dispersed SWNTs incorporated in the polymer and a strong interfacial bonding between the polymer and SWNTs. We have applied chemically functionalized SWNTs to prepare a number of SWNT-polymer composite materials.

In one approach, poly (m-aminobenzene sulphonic acid), PABS, a conducting water soluble polymer, was covalently attached to chemically functionalized SWNTs (Scheme 1).

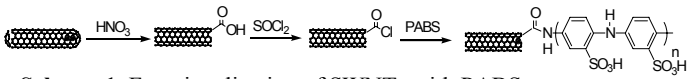

Scheme 1. Functionalization of SWNTs with PABS.

AFM analysis has shown that the PABS-functionalized SWNTs exist in small bundles of 2 to 6 nanotubes (Figure 1). The graft co-polymer (PABS-SWNTs) has high solubility in water (5 mg/ml),[12] which makes the material especially attractive for biological applications. In one study, PABS-funcionalized multi-walled carbon nanotubes have been used as a substrate for neuron growth and have shown an ability to control the neurite outgrowth.[13]

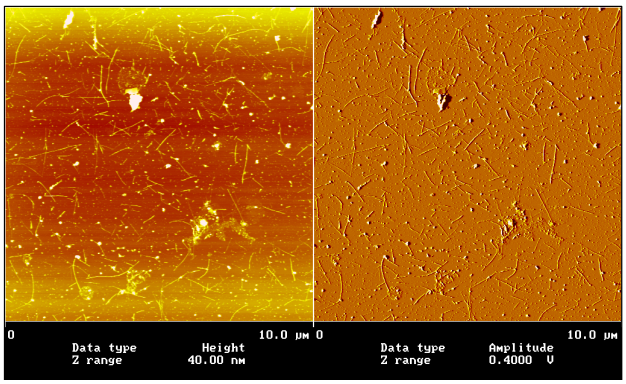

Figure 1. AFM image of SWNT-PABS showing bundles of 4-6 SWNTs.

In another study we have prepared SWNT-reinforced polyurethane (PU) and polystyrene (PS) membranes.[14] In our experiments we have used as-prepared (AP)-SWNTs and soluble ester-functionalized SWNTs (s-SWNT-$COO(CH_2)_{11}CH_3$, EST) in order to study the effect of the nanotube functionalization on the performance of the SWNT composites.

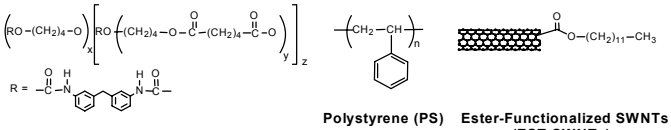

The membranes fabricated by electrospinning of the ester-functionalized SWNT-PU composite have shown enhanced mechanical properties (Table 1).[14] The increased strength exhibited by the polyurethane-SWNT-ester composites, may be due to improved dispersion of the SWNTs, but could also be a response to the polar functionalities in the SWNT-ester groups, to the opportunities offered by hydrogen bonding sites between the polymer and matrix or to amidation reactions between free amine in the polyurethane and the ester functionality in SWNTs.

Table 1. Mechanical Properties of Electrospun PU Membranes.

Electrospun membrane	Tensile strength, MPa	Tangent modulus, MPa
PU	7.02	6.96
AP-SWNT-PU*	10.26	21.86
EST-SWNT-PU*	14.36	24.32

* the SWNT:PU weight ratio is 1:100.

Functionalization of SWNTs with biomolecules

The functionalization of SWNTs with biological molecules is a relatively new direction in exploring the chemistry of SWNTs for biosensor applications. While both covalent[8,15,16] and non-covalent functionalization[17,18] with proteins, enzymes and DNA has been attempted, the covalent approach provides better stability and reproducibility of the devices fabricated from these materials.

One approach for covalent binding of proteins and enzymes utilizes the diimide-activated amidation of carboxylic acid-functionalized carbon nanotubes. We have functionalized purified SWNTs, produced by the arc-discharge method, with bovine serum albumin (BSA) as schematically illustrated in Scheme 2. The SWNT

purification process involves reflux of SWNTs in HNO_3, which terminates the open nanotube ends with carboxylic acid groups. The carboxylic groups can further undergo an amidation reaction with the amino acids of the protein.

EDC – 1-ethyl-3-(3-dimethylaminopropyl) carbodiimide hydrochloride

Scheme 2. Synthesis of BSA-functionalized SWNTs.

The BSA-functionalized SWNTs were separated from the free BSA molecules by dialysis against deionized water for 5 days. A typical AFM image of the BSA-functionalized SWNTs is given in Figure 3.

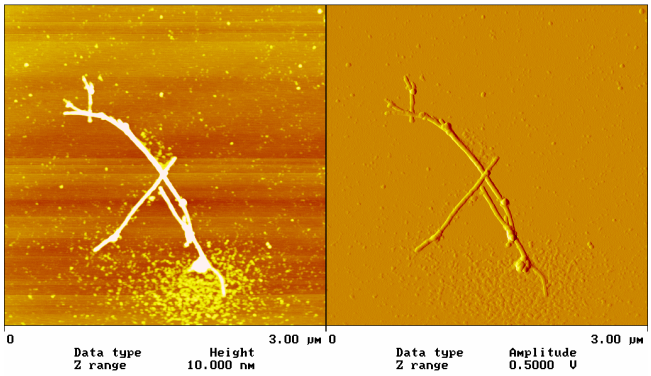

Figure 3. AFM image of BSA-functionalized SWNTs.

In order to test the biological activity of the attached the nanotubes BSA, the functionalized SWNTs were incubated in a solution of anti-BSA, developed in rabbit, for 1 hour to obtain a specific antibody-antigen interaction. The material was washed 5 times with a buffer solution (pH=7.4) and exposed to FITC-conjugated anti-rabbit IgG- for 20 min. Detection of analyte binding to the functionalized SWNTs was then performed by fluorescence and phase contrast microscopy (Figure 4).

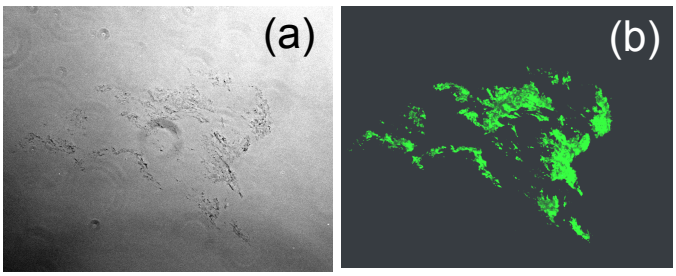

Figure 4. Phase contrast (a) and fluorescent (b) images of BSA-functionalized SWNTs.

The fluorescent image (Figure 4b) confirms the successful interaction between the BSA-functionalized SWNTs and the FITC-conjugated secondary antibody, which is an indication for the retained biological activity of the protein after the attachment to SWNTs. The fluorescent image reveals a feature similar to that observed in the phase contrast image (Figure 4a). A control test with non-functionalized SWNTs incubated in FITC-conjugated anti-rabbit IgG resulted in a dark image, which confirming the specific interaction between the BSA-functionalized SWNTs and anti-BSA. These specific interactions may be used for development of biosensors and controlled assembly of ordered nanostructures.

Conclusions.

The chemistry of SWNTs offers considerable scope for development of functional materials, structures and devices based on SWNTs. Further advance in our understanding the chemistry of SWNTs will make it possible to take full advantage of the remarkable properties of these materials and will help to tailor the properties of SWNTs for particular applications.

Acknowledgement. This work was supported by DOD/DARPA/DMEA under Award No. DMEA90-02-2-0216.

References

(1) Chen, J.; Hamon, M. A.; Hu, H.; Chen, Y.; Rao, A. M.; Eklund, P. C.; Haddon, R. C. *Science* **1998**, *282*, 95-98.
(2) Chen, Y.; Haddon, R. C.; Fang, S.; Rao, A. M.; Eklund, P. C.; Lee, W. H.; Dickey, E. C.; Grulke, E. A.; Pendergrass, J. C.; Chavan, A.; Haley, B. E.; Smalley, R. E. *J. Mater. Res.* **1998**, *13*, 2423-2431.
(3) Holzinger, M.; Vostrowsky, O.; Hirsch, A.; Hennrich, F.; Kappes, M.; Weiss, R.; Jellen, F. *Angew. Chem., Int. Ed.* **2001**, *40*, 4002-4005.
(4) Dyke, C. A.; Tour, J. M. *Nano Lett* **2003**, *3*, 1215-1218.
(5) Saini, R. K.; Chiang, I. W.; Peng, H.; Smalley, R. E.; Billups, W. E.; Hauge, R. H.; Margrave, J. L. *J. Am. Chem. Soc.* **2003**, *125*, 3617-3621.
(6) Dyke, C. A.; Tour, J. M. *J. Am. Chem. Soc.* **2003**, *125*, 1156-1157.
(7) Haremza, J. M.; Hahn, M. A.; Krauss, T. D.; Chen, S.; Calcines, J. *Nano Lett* **2002**, *2*, 1253-1258.
(8) Williams, K. A.; Veenhuizen, P. T. M.; de la Torre, B. G.; Eritja, R.; Dekker, C. *Nature* **2002**, *420*, 761.
(9) Niyogi, S.; Hamon, M. A.; Hu, H.; Zhao, B.; Bhowmik, P.; Sen, R.; Itkis, M. E.; Haddon, R. C. *Acc. Chem. Res.* **2002**, *35*, 1105-1113.
(10) Kamaras, K.; Itkis, M. E.; Hu, H.; Zhao, B.; Haddon, R. C. *Science* **2003**, *301*, 1501.
(11) Chen, J.; Rao, A. M.; Lyuksyutov, S.; Itkis, M. E.; Hamon, M. A.; Hu, H.; Cohn, R. W.; Eklund, P. W.; Colbert, D. T.; Smalley, R. E.; Haddon, R. C. *J. Phys. Chem. B* **2001**, *105*, 2525-2528.
(12) Zhao, B.; Hu, H.; Haddon, R. C. *Adv. Func. Mater.* **2004**, *14*, 71-76.
(13) Hu, H.; Ni, Y.; Montana, V.; Haddon, R. C.; Parpura, V. *Nano Letters* **2004**, *4*, 507-511.
(14) Sen, R.; Zhao, B.; Perea, D. E.; Itkis, M. E.; Hu, H.; Love, J.; Bekyarova, E.; Haddon, R. C. *Nano Lett.* **2004**, *4*, 459-464.
(15) Dwyer, C.; Guthold, M.; Falvo, M.; Washburn, S.; Superfine, R.; Erie, D. *Nanotechnology* **2002**, *13*, 601-604.
(16) Huang, W.; Taylor, S.; Fu, K.; Lin, Y.; Zhang, D.; Hanks, T. W.; Rao, A. M.; Sun, Y.-P. *Nano Lett.* **2002**, *2*, 311-314.
(17) Chen, R. J.; Zhang, Y.; Wang, D.; Dai, H. *J. Am. Chem. Soc.* **2001**, *123*, 3838-3839.
(18) Dieckmann, G. R.; Dalton, A. B.; Johnson, P. A.; Razal, J.; Chen, J.; Giordano, G. M.; Munoz, E.; Musselman, I. H.; Baughman, R. H.; Draper, R. K. *J. Am. Chem. Soc.* **2003**, *125*, 1770-1777.

GOLD AND ALLOY NANOPARTICLE CATALYSTS IN FUEL CELL REACTIONS

*Mathew M. Maye, Jin Luo, Li Han, Nancy Kariuki, Zia Rab, Navaid Khan, H. Richard Naslund and Chuan-Jian Zhong **

Department of Chemistry
State University of New York at Binghamton
Binghamton, NY 13902 (*cjzhong@binghamton.edu)

Introduction

Gold-based nanoparticles (1-5 nm) have recently emerged as highly active catalysts for many important catalytic reactions [1]. A major factor for their catalytic activity is related to the size- and composition-dependent properties of nanoparticles. We have investigated the preparation and catalytic properties of gold-based alloy nanoparticles supported on carbon materials [2,3]. One example involves the preparation of monolayer-capped AuPt nanoparticles for electrocatalytic oxidation of methanol and reduction of oxygen. To delineate the size and composition correlation of the catalytic properties, we employed an array of surface analytical techniques to probe the structural and morphological evolution and reconstitution of the nanoparticles upon catalytic activation. These techniques include; atomic force microscopy (AFM), transmission electron microscopy (TEM), surface infrared reflection spectroscopy (IRS), X-ray photoelectron spectroscopy (XPS), and thermogravimetic analysis (TGA) [3-5]. The combined results of these characterizations have provided insights into the viability of tailoring the nanostructured catalysts in terms of size and composition.

Experimental

Gold nanoparticles (Au) of 2-nm core size encapsulated with alkanethiolate monolayer shells (e.g. decanthiol, DT) were synthesized by the standard two-phase method [6]. Gold-platinum (AuPt) nanoparticles of 2-nm core size encapsulated with an alkanethiolate monolayer shell (AuPt) were synthesized by a modified two-phase method. The Au:Pt ratio in the nanoparticles controlled in synthesis and analyzed using the direct current plasma – atomic emission spectroscopy method.

Au and AuPt nanoparticles were loaded on XC-72 carbon black, and were treated in a tube-furnace under controlled temperatures and atmospheres. For catalytic activity measurements, suspensions of the catalysts (AuPt/C) with Nafion were quantitatively cast to the surface of the polished GC disk.

The cyclic voltammetry (CV) experiments were performed at room temperature. All experiments were performed in three-electrode electrochemical cells, and electrolytic solutions were deaerated with high purity argon or nitrogen before the measurement. All potentials are given with respect to the reference electrode of Ag/AgCl saturated KCl. The measurements were performed using a microcomputer-controlled potentiostat (M273, PARC).

Results and Discussion:

Figure 1 showed a set of IRS for DT capped Au. Before thermal activation at 250 ^{o}C (30 min, O_2) the C-H stretching bands from the encapsulating DT are detected. Upon thermal treatment, these bands disappeared to a level below the detection limit, demonstrating the removal of the organic shell. The shell removal can also be correlated with recent TGA and in-situ heating AFM characterization. The shell removal was also confirmed by XPS, which showed the removal of S species.

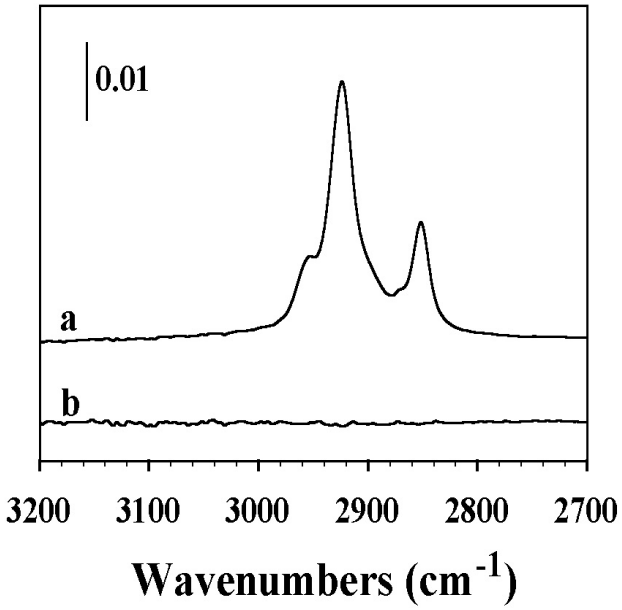

Figure 1. IRS spectra for DT-capped Au nanoparticles in the C-H stretching region before (a) and after (b) thermal treatment at 250 ^{o}C for 30 min.

By AFM characterization, we recently showed that at low surface coverages there were some degree of local aggregation of the Au nanoparticles depending on the nature of the substrate (from ~2 nm to 5~6 nm), but the resulting particle sizes are controllable. Similar results have also been observed with Au-containing bimetallic nanoparticles.

Figure 2 shows a set of CV data for the electrocatalytic reduction of oxygen at $Au_{81}Pt_{19}$/C catalyst in alkaline solutions. The catalyst were thermally treated, and the total metal loading was ~20% wt. The data were also compared with data for Pt/C catalyst (20%wt, E-tek) (not shown). Similar to the CV curve for the Au/C catalyst in the absence of oxygen (not shown), the observation of the oxidation-reduction wave of gold oxide at ~200 mV at the $Au_{81}Pt_{19}$/C catalyst in the O_2-free alkaline electrolyte is a clear indication of the presence of Au on the catalyst. The observation of the hydrogen reduction-oxidation currents at –200 mV in the O_2-free acidic electrolyte is strong evidence for the presence of Pt on the catalyst surface. In comparison with the data for Au/C catalysts, there are two important observations for the electrocatalytic activity of the AuPt nanoparticle catalysts. First, the ORR wave at the $Au_{81}Pt_{19}$/C catalyst is observed at about the same potential (+190 mV) as that for the Au/C in the alkaline electrolyte. We also note that a very small wave is detectable at –450 mV for the AuPt/C catalyst. Second, the ORR wave is highly dependent on the nature of the electrolyte. This

wave for $Au_{81}Pt_{19}$/C is observed at +350 mV in the acidic electrolyte, which is much more positive than that for the Au/C (+50 mV) in the same electrolyte. The result thus suggests that there is a significant fraction of Au on the bimetallic catalyst which keeps the nanoscale gold property unchanged in basic condition, but modifies the catalytic property of Pt in the acidic electrolyte.

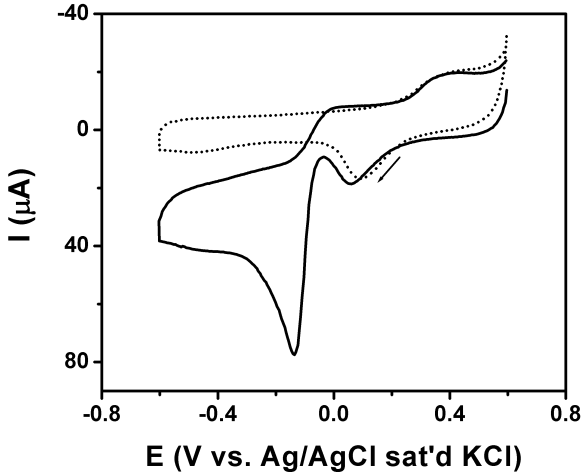

Figure 2. CV curves for a $Au_{81}Pt_{19}$/C catalyst (20%wt) on GC electrode (0.07 cm^2) in 0.5M KOH. The electrolytes were saturated with O_2 (solid curve) and Ar (dash curve). Scan rate: 50 mV/s.

The dependence of the electrocatalytic activity on the relative bimetallic composition of the catalyst is currently under investigation. We have shown that Au and AuPt nanoparticles that are highly active catalysts for fuel cell reactions can be prepared a combination of synthesis and processing strategies. The study of the tunability of the catalytic activities in terms of size and composition is part of our on-going investigation.

Acknowledgement

This work was supported in part by the National Science foundation, the Petroleum Research Fund administered by the American Chemical Society, and the GROW fund of the World Gold Council. M.M.M. thanks the Department of Defense for the National Defense Science & Engineering Graduate Fellowship support sponsored by ARO.

References

(1) Zhong, C.J.; Maye, M. M.; Luo, J.; Han, L.; Kariuki, N. N.; in "Nanoparticles: Building Blocks for Nanotechnology," Ed. By Rotello, V.M.; Kluwer. 2004. pp.113-144
(2) Zhong, C. J.; Luo, J.; Maye, M. M.; Han, L.; Kariuki, N. N.; in "Nanotechnology in Catalysis," Ed. Zhou, B.; Hermans, S.; Somorjai, G. A.; Kluwer, 2004; Vol 1., pp. 222-248.
(3) Luo, J.; Maye, M. M.; Lou, Y.; Han, L.; Hepel, M.; Zhong, C. J.; *Catal. Today*, **2002**, *77*, 127
(4) Maye, M.M.; Luo, J.; Lin, Y.; Engelhard, M.H.; Hepel, M.; Zhong, C.J.; *Langmuir*, **2003**, *19,* 125
(5) Maye, M.M.; Luo, J.; Han, L.; Kariuki, N. N.; Zhong, C.J.; *Gold Bull*., **2003**, *36*, 75
(6) Brust, M.; Walker, M.; Bethell, D.; Schiffrin, D. J.; Whyman, R. *J. Chem. Soc., Chem. Comm*. **1994**, 801.

HYDROFORMYLATION OF 1-OCTENE OVER CARBON NANOTUBE SUPPORTED COBALT CATALYST

Jieshan Qiu, Hongzhe Zhang, Xiuna Wang, Bing Yin

Carbon Research Laboratory, School of Chemical Engineering, Center for Nano Materials and Science, State Key Laboratory of Fine Chemicals, Dalian University of Technology, 158 Zhongshan Road, P.O .Box 49, Dalian 116012, China. E-mail: jqiu@dlut.edu.cn; Fax: +86-411-3633080

Introduction

The hydroformylation of higher olefins (also known as oxo process or carboxylation) is one important process for making value-added precursors or intermediates of chemicals and medicines, in which both homogeneous and heterogeneous catalysts have been extensively studied [1-4]. Recently, hydroformylation over carbon materials supported catalysts has drawn much attention [3-7], showing that carbon-supported catalysts are more active than the oxide-supported catalysts. Apart from the common knowledgement that carbon materials are a good electron-transfer agent, it is also found that carbon materials favor the carbonylation reactions because of their unique roles in the reactions, including to suppress dissociative hydrogen adsorption, to promote strong or multiple adsorption of CO and to inhibit dissociative CO adsorption [4]. These special characteristics of carbon materials are also important for hydroformylation reactions, which are governed by the molecular reaction of CO. Carbon nanotubes (CNTs) is a novel nano-sized carbon and is believed to be of potential as catalyst support for heterogeneous catalysis. Some studies about the hydroformylation of olefins over the CNTs-supported catalysts [5-7] have proved that the CNTs-supported catalysts are indeed quite active for the hydroformylation of olefins that involves a sequence of several competitive parallel and consecutive reactions. In the present work, the hydroformylation of 1-octene over CNT-supported cobalt catalysts were studied, and the variation of the activity and selectivity of the catalysts in different solvents and with the reaction time were analyzed. The reaction conditions were optimized with an aim of producing C_9-aldehyde selectively.

Experimental

The raw CNTs (RCNTs) was prepared by arc-discharge of high purity graphite electrodes, and was further treated by refluxing 65% HNO_3 at 120 ^oC for 8 h to obtain purified CNTs (PCNTs). Co/CNTs was prepared by incipient wetness impregnation technique with an aqueous solution of cobalt nitrate. After impregnation, the samples were dried overnight at 110 ^oC and calcined in air at 400 ^oC for 3 h, then, were reduced in flowing hydrogen at 400 ^oC for 6 h. Finally, the catalysts were passivated by 1% O_2 in N_2 at room temperature for 3 h. The reaction of 1-octene hydroformylation was conducted in a magnetically stirred autoclave with an inner volume of 100 ml and at 130 ^oC in high purity syngas (H_2/CO=1:1) with initial pressure being 5.0MPa. For each run, the reactor was loaded with 40 ml of solvent containing 13.4 mmol (15 g) of 1-octene and 100 mg of catalysts. After the reaction was finished, the products were analyzed using GC-MS (HP6890GC/5973MSD). Both the raw CNTs samples and the CNTs-supported catalysts were examined by transmission electron microscopy (TEM, JEOL JEM-2000EX, operated at 100 kV).

Results and Discussion

The solvent is an essential parameter that needs to be considered for liquid phase hydroformylation. The hydroformylation of 1-octene over 5.0 wt% Co/PCNTs were conducted in three different solvents, i.e. cyclohexane, acetone and ethanol, of which the data are presented in **Table 1.** It can be seen from Table 1 that in the case of cyclohexane, aldehydes are the only products, i.e. the selectivity of C_9-aldehyde is 100%, but the conversion of 1-octene is very low, only 9.37%. While in the case of acetone and ethanol solvent, the catalyst performance is improved significantly. For the acetone solvent, 52.3% 1-octene is converted with the selectivity of C_9-aldehyde being 95.30%. For the ethanol solvent, the conversion of 1-octene is 57.35% with the selectivity of C_9-aldehyde being only 9.21%, in this case condensation reactions take place that results in acetal products (C_{19}/C_{20}). Obviously, the acetone and ethanol solvents favor the reaction of 1-octene hydroformylation. This is in agreement with previously reported result [3]. This phenomenon may be attributed to the following factors: the reduction of cobalt catalyst is easier in ethanol than in cyclohexane; the formation of acetal and hemiacetals favors chem-equilibrium reaction that leads to aldehyde products, which help to speed up the reaction of hydroformylation; some solvent molecules may be adsorbed on the catalyst, which modifies the catalyst's surface.

Table 1. Effect of Solvents on Hydroformylation of 1-Octene[a]

Solvents	Conversion of 1-octene (%)	Selectivity (%)		
		C_9-aldehyde	C_9-alcohols	C_{19}/C_{20} acetal
Cyclohexane	9.67	100	0	0
Acetone	52.3	95.30	0	4.70
Ethanol	57.35	9.21	31.42	58.37

[a] reaction conditions: 130 ^oC, 5.0 MPa, 6 h.

Table 2. Effect of Reaction Time on 1-Octene Hydroformylation[a]

Time (h)	1-octene conversion (%)	C9-aldehyde Selectivity(%)	n/i
4	0	0	0
5	9.95	91.36	5
6	52.3	74.3	0.94
7	53.4	56.9	0.53
8	52.6	54.2	0.29

[a] reaction conditions: 130 ^oC, 5.0 MPa, 40 ml acetone

The variation of the 1-octene hydroformylation with the reaction time is shown in **Table 2.** It can be seen from Table 2 that the conversion of 1-octene increases as time increases, then levels off after 6 h, at the same time, the selectivity of C_9-aldehyde drops and the ratio of n/i becomes smaller as the reaction time increases. The detailed reason for this phenomenon is not clear at the moment. It is very likely due to the complex reaction scheme involved in the reaction system, in which some competitive and consecutive reactions take place. The decrease in the n/i ratio can be attributed to the steric effect for the insertion of CO in the second C atom of the 1-octene that is relatively difficult in comparison to the insertion of CO in the first C atom, which makes the formation of linear products go faster than the branched ones. However, the decrease of n/i ratio might also be due to the decrease of CO partial pressure as the reaction proceeds. More CO species on the metal catalysts at high pressures is favorable for the formation of linear products rather than branched ones.

In addition, a peculiar metal/support interaction between the cobalt crystallites and the CNT support could have a significant influence on the conversion of 1-octene and product selectivity in comparison to active carbon-supported catalyst. Such a hypothesis has been evidenced by the specific selectivity observed over graphite nanofiber-supported catalyst: a significant improvement in the selectivity has been reported by Baker and his colleagues [6] with the use of graphite nanofiber as support during the liquid phase hydrogenation of cinnamaldehyde.

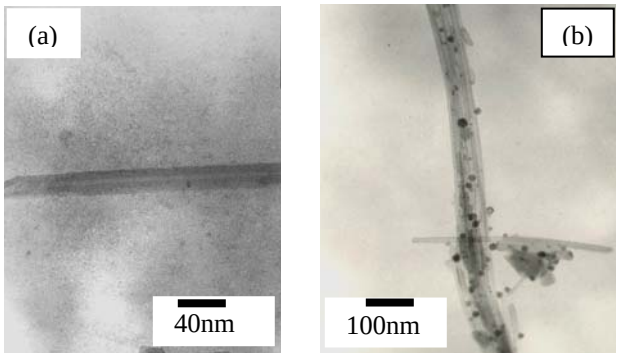

Figure 1. TEM images of CNTs samples; (a) the PCNTs, (b) the Co/PCNTs catalyst.

The CNTs materials before and after acid treatment were examined using TEM, and fairly clean CNTs and the agglomeration of few carbonaceous impurities in the bulk can be observed after purification treatment. It has been found that the outer diameters of PCNTs are in a range of 6-50 nm, and the inner diameters are in a range of 3-5 nm. The typical TEM image of the PCNTs sample is shown in **Fig. 1a**. The BET surface area of the CNTs, determined by nitrogen adsorption at 77 K, is about 22.5m^2/g.

Fig. 1b shows a typical TEM image of Co/PCNTs catalyst. From the TEM images, the size of metal catalysts and the size distribution can be measured and calculated. It can be seen clearly that the metal catalysts, the dark spots on the external surface of the tubes, are uniformly deposited on the surface of CNTs, though occasionally some large aggregates can also be seen. For Co/PCNTs catalysts, the size of metal Co particles are in a range of 10-15nm. The relatively homogeneous dispersion could be attributed to the relatively strong metal/support interaction between the metal salt precursor and the carbon nanotubes [6]. Baker et al reported that the distribution of metallic particles size on the graphite nanofibers was relatively wide, ranging from 1.5 nm to 43.5 nm, with an average size of *ca.* 7-10 nm; nickel particles were deposited on the external surface of the nanotubes; and the nickel supported on the nanofiber surface adopted a peculiar thin hexagonal morphology and almost no spheroidal particles were observed. This means that depending on the nature of the support, the morphology of the metal particles can be modified during the preparation step. The difference between the present work and Baker's work could be attributed to the different crystallinity of the two carbon supports, which could influence the formation of the final metal morphology.

Under the identical experiemtnal conditions, the performance of Co catalysts supported on CNTs and a kind of active carbon was also compared, of which the results are shown in Table 3. It can be seen from Table 3 that the CNTs-supported Co catalyst is more active than the AC supported Co catalyst. This might be due to the good crystallinity of the CNTs support, and it needs to be clarified in detail.

Table 3. Comparison of the Catalytic activity of PCNTs and Active carbon supported Co catalysts [a]

Catalyst	1-octene conversion (%)	C_9-aldehyde Selectivity(%)	n/i
Co/PCNTs	41.54	71.56	0.96
Co/AC	24.26	33.38	0.68

[a] reaction conditions: 130 ^oC, 5.0 MPa, 40 ml acetone

In summary, the performance of Co/CNTs for the 1-octene hydroformylation varies greatly in different solvents. Under the reaction conditions mentioned above, 6 h is suitable for the hydroformylation of 1-octene. Thus, for the liquid phase hydroformylation of 1-octene, rational design of catalysts and optimized reaction conditions are essential to the CNTs-supported catalysts. In this regard, more detailed work is needed.

Acknowledgment. This work was partly supported by the National Science Foundation of China (No. 29976006, 20376011), the Natural Science Foundation of Liaoning Province (No. 9810300701, 2001101003), the National Basic Research Program of China (Grant No. G2003CB615806) and the Ministry of Education of China.

References

(1) McDougall, J.K.; Simpson, M.C.; Green, M.J.; *J. Chem. Soc., Dalton Trans.* 1996, 1161.
(2) Qiu, X.; Tsubaki, N.; Sun, Shouli; Fujimoto, K.; *Catalysis Communications*. 2001, (2) 75.
(3) Li, B.T.; Li, X.H.; Asami, K.; Fujimoto, K.; *Chemistry Letters.* 2003, 32, 378.
(4) Kainulainen, T.A.; Niemelä, M.K.; Krause, A.O.I.; *Journal of Molecular Catalysis A: Chemical.* 1997, 122, 39.
(5) Planeix, J.M.; Coustel, N.; Coq, B.; Brotons, V.; Ajayan, P.M.; *J. Am. Chem. Soc.* 1994,116, 7935.
(6) Zhang, Y.; Zhang, H.-B.; Lin, G.-D.; Chen, P.; Yuan, Y.-Z.; Tsai, K. R.; *Appl. Catal. A.* 1999, 187, 213.
(7) Baker, R.T.K.; Laubernds, K.; Wootsch, A.; Paal, Z.; *J. Catal.* 2000, 193, 165.

ON THE HYDROGEN ON-BOARD STORAGE IN GRAPHITE NANOMATERIALS

Yury S. Nechaev[1] and T. Nejat Veziroglu

Clean Energy Research Institute, College of Engineering, University of Miami, Coral Gables, FL 33124; [1)] Fulbright grantee (Moscow)

Introduction

As is noted in study[1], there is the anomalous scattering and non-reproducibility of the known experimental data on the hydrogen gravimetric capability in carbon nanofibers and nanotubes (3 orders of magnitude, if the unique Rodriguez-Baker data[2] are included, and 2 orders, if without them), while there is a 'normal' scattering (within one order of magnitude) – for metallic hydrides (practically, in studies of the same researches).

According to our feeling, the main reasons of such a large difference in the results are related with a larger spectrum of the structure and sorption process peculiarities for the carbon nanomaterials (in comparison with metallic hydrides), depending on regimes of their synthesis, pre-treatment and hydrogenation, and also on their composition (particularly, with respect to metallic catalysts).

In this connection, some new significant results on diffusion, sorption and storage of hydrogen in graphites and novel carbon nanomaterials are discussed, which have been obtained on the basis of thermodynamic analysis[3-7] of the known experimental data, and their comparison with theoretical data[8] (*'ab initio'* molecular orbital (MO) studies of chemisorption of hydrogen atoms on graphite).

Results and Discussion

According to analysis[4-7], in many cases the main processes of hydrogen desorption both in an isotropic graphite[9] (TPD peaks I, II, III, IV) and in novel carbon nanomaterials with sp^2 hybridization can be characterized as trapping-with-diffusion rate-controlled processes with the diffusion activation enthalpies of $Q_I \approx 20$ kJ/mol ($H_{2(ads)}$), $Q_{II} = 120$ kJ/mol ($H_{2(ads)}$), $Q_{III} = 250$ kJ/mol ($H_{(abs)}$), $Q_{IV} \approx 365$ kJ/mol ($H_{(abs)}$), corresponding to the related desorption enthalpies (due to the reversible diffusant trapping by carbon chemisorption "sites"). The entropy (frequency) factors of the hydrogen diffusion coefficients in these materials have also been determined[4-7]: $D_{0I} \approx 0{,}003$ cm^2/s, $D_{0II} = 1800$ cm^2/s, $D_{0III} \approx 0{,}007$ cm^2/s, $D_{0IV} \approx 600$ cm^2/s.

TPD peak III in the isotropic graphite[9] is related with a dissociative chemisorption of H_2 gas molecules on carbon chemisorption sites localized in graphene layers in grains-crystallites, and corresponding to potential "HC- molecules" (within model[8] 'F', sp^3 rehybridization). The total process III is described by an absorption isotherm of the Sieverts-Langmuir type: $((X_{III}/X_{IIIm}) = K_{III}(P_{H2}/P^0_{H2})^{1/2} / [1+K_{III}(P_{H2}/P^0_{H2})^{1/2}]$, $K_{III} = \exp(\Delta S_{III}/R)\exp(-\Delta H_{III}/RT)$, where $P^0_{H2} = 1$ Pa, the absorption enthalpy of $\Delta H_{III} = -19$ kJ/mol ($H_{(abs..)}$); the absorption entropy of $\Delta S_{III} \approx -(14{,}7\text{-}15{,}4)R$; the largest potentially possible concentration of hydrogen atoms (H/C) in graphene layers of $X_{IIIm} = 0{,}5\text{-}1{,}0$, that is close to the hydrogen content in "a carbohydride-like bulk phase".

The process (III) includes the first stage (1) of hydrogen molecules dissociation to atoms with enthalpy of $\Delta H_{(1)} = 228$ kJ/mol ($H_{(gas)}$), the second stage (2) of hydrogen atoms dissolution between graphene layers with $\Delta H_{(III2)} \approx 0$, and the third stage (3) of hydrogen atoms chemisorption on "HC-sites" with $\Delta H_{(III3)} = -247$ kJ/mol($H_{(abs.)}$); $\Delta H_{III} \approx (\Delta H_{(1)}+\Delta H_{(III3)})$. Thus, TPD peak III in graphite[9] is related with the trapping-with-diffusion of hydrogen atoms in grains-crystallites, with the reversible diffusant trapping (chemisorption) by "HC-sites" in graphene layers; $Q_{III} \approx -\Delta H_{(III3)}$.

According to analysis[4-7], the concentration of hydrogen absorbed in graphene layers (TPD peak of III type) in nanostructured graphite[10] and in graphite nanofibers[2] can be close to the largest possible ("carbohydride-like") values (X_{IIIm}).

The sorption capability of TPD peak of III type in carbon nanofibers and mechanically prepared nanostructured graphite charged under P_{H2} = 1-10 MPa and room temperatures can be close to the values ($X_{III} \approx 0.5\text{-}0.8$), corresponding to the technical targets for hydrogen storage on-board fuel cell-powered vehicles; however, the near-zero "reversibility" (i.e., a very sluggish diffusion kinetics) of the process is not acceptable.

Ab initio MO calculations[8] (model 'F') give the chemisorption energy of hydrogen atoms in the graphene layers of about -195 kJ/mol (H_{abs}), i.e., the absolute value is considerably less than for $\Delta H_{(III3)}$. It points to the necessity of the further theoretical[11,12] and experimental studies (in the light of results[4-7]) of this contradiction, that has a significant importance in the connection with the graphene structure of carbon nanotubes and nanofibers.

TPD peak IV in isotropic graphite[9] is related with a dissociative chemisorption of H_2 gas molecules on 'armchair' and/or 'zigzag' edge carbon sites localized mainly near the grain boundary regions and corresponding to potential "HC-like molecules" (within model[8] 'C' and/or 'D' sp^2 hybridization). Total process (IV) is described [4-7] by a sorption isotherm of the Sieverts-Langmuir type , with $\Delta H_{IV} \approx -140$ kJ/mol ($H_{(abs..)}$); $\Delta H_{(IV3)} \approx (\Delta H_{IV} - \Delta H_{(1)}) \approx -Q_{IV}$. The sorption capacity and the diffusion kinetics ("reversibility") of this peak at room temperatures and technological pressures do not satisfy to the hydrogen vehicles target values.

TPD peaks II and I in isotropic graphite[9] are related with a dissociative-associative chemisorption of H_2 gas molecules on carbon sorption sites localized in the regions of grain-crystallites boundaries and boundaries (interfaces) of graphite filler grains, and corresponding to potential "H_2C-molecules" (within model[8] 'H' of 'zigzag' edge sp^3 rehybridization sites (for TPD peak II) and model[8] 'G' of 'armchair' edge sp^3 rehybridization sites (for TPD peak I), and also (another variant for peak I) - to potential "H_2C_2-molecules" (within model[8] 'F' of sp^3 rehybridization in graphene sites). Total process is described[4-7] by a sorption isotherm of the Henry-Langmuir type: $((X/X_m) = K(P_{H2}/P^0_{H2}) /[1+K(P_{H2}/P^0_{H2})]$, $K = \exp(\Delta S/R)\exp(-\Delta H/RT)$, with adsorption enthalpies and entropies values of $\Delta H_{II} \approx -Q_{II}$, $\Delta H_I \approx -Q_I$, $\Delta S_{II} \approx -31R$, $\Delta S_I \approx -23R$, and the largest potentially possible concentrations (H_2/C_{loc}) close to the hydrogen content in "a carbohydride-like adsorbed phase". TPD peaks II and I are related with the trapping-with-grain boundary diffusion of hydrogen molecules, with reversible trapping (chemisorption) of the diffusant by "$H_2C(H_2C_2)$ sites"; the apparent activation enthalpies of the hydrogen diffusion can be close to the desorption enthalpies.

The sorption capabilities (H/C_{tot}) of TPD peaks of II and I types in carbon nanostructures ($2\gamma_{II}X_{II}$ and $2\gamma_I X_I$, where γ_{II} and γ_I are the volume fractions of the sorption regions) can be close to the values (~0.8), corresponding to the technical targets for hydrogen storage on-board fuel cell vehicles; however, the near-zero "reversibility" (the diffusion kinetics) of the II type peak is not acceptable, and moreover, the nature, characteristics and conditions of the manifestation of the I type peak in carbon nanotubes and nanofibers have been insufficiently studied.

A specific physical (or physicochemical) multilayer hydrogen adsorption, with an anomalous high sorption capacity and adsorbate packing density ("peak V"), seems to be possible in graphite nanofibers[2], which (according to analysis[4-7]) could be "decorated" with "the carbohydride-like phases" (TPD peaks of the II and III types). There are serious reasons[4-7] to suppose that the sorption capacity and "reversibility" (kinetics) of this nearly unstudied

process ("peak V") can satisfy to the technique requirements for the hydrogen on-board storage in fuel cell-powered vehicles.

On chemiadsorption and chemiabsorption of hydrogen by isotropic graphite, mechanically nanostructured graphite and graphite nanofibers. As is noted in study[13], one of the main reasons for the negative discussion of the anomalous scattering and non-reproducibility of some known experimental data on the hydrogen gravimetric capability in carbon nanofibers and nanotubes is confusion in the gas storage concepts: physical adsorption, chemisorption, absorption and occlusion. As is also noted[13], physical adsorption and chemisorption are surface phenomena, and in absorption and occlusion, the material taken up is distributed through the body (bulk) of the absorbent.

According to our feeling, some additional aspects (concepts) must be taken into account on evaluating the storage capacity, as follows[4-7,11].

1. Absorption (in the sense of a true bulk solubility) can be attributed with the thermodynamic characteristics of the gas (adsorbat) interaction with the normal lattice of the absorbent, and it can be of a chemical nature; a situation of a dissociative chemiabsorption has obviously place for hydrogen sorption processes, corresponding to TPD peak of # III type in isotropic graphite, mechanically nanostructured graphite and graphite nanofibers. 2. Adsorption (especially, of a chemical nature) can be attributed with the thermodynamic characteristics of the gas interaction with the free surface regions (nanolayrs), both external and internal ones (as pore and cavity surfaces), grain boundary regions (nanolayers) or near dislocation nanoregions in the adsorbent bulk; a situation of a dissociative-associative chemiadsorption has obviously place for processes, corresponding to TPD peaks of # II type in the three materials mentioned above. 3. The sorption process, corresponding to the extremely anomalous 'peak' # V in the Rodriguez-Baker graphite nanofibers[2], might be related with a specific physico-chemical hydrogen adsorption[4-7], that is a subject of further studies.

On the nature of the catalyst activity of nanostructured graphite, under ball milling in hydrogen molecular gas atmosphere. As has been mentioned above, thermodynamic and diffusion characteristics of two hydrogen desorption processes (similar to the processes of TPD peaks # II and # III) are obtained from data[10] on mechanically prepared nanocrystalline graphite charged at P_{H2} = 1 MPa and about 300 K (under the ball milling). It's necessary to emphasize result[4-7], that the concentrations of both the chimiabsorbed and the chemiadsorbed hydrogen in the mechanically nanostructured graphite are of the same order as the largest possible (carbohydride-like) values and correspond to the extrapolated (equilibrium) values, those are obtained by the use of the isotherms noted above (for TPD peaks # II and # III).

Hence, it follows that the catalyst activity of the ball milling graphite results in the sufficiently fast kinetics of the intermediate step of H_2 dissociation, which occurs over the carbon catalyst. Such a high catalyst activity of the milling graphite is obviously caused by a high stationary concentration of the lattice defects in the material[14]; some of them are attributed with the formation of the dangling C-C sp^2 edge bonds of the zigzag-like or armchair-like types. The nature of the catalyst activity of the ball milling graphite is revealing by the comparison of the absolute values of the H_2 dissociation energy and the adsorption (absorption) energies of atomic hydrogen on the different carbon sites (C-H, C-2H bonds energies), and especially on the sites related with the deformation lattice defects (in the deforming graphite).

Conclusions

Thermodynamic analysis[4-7] of some known data on hydrogen sorption in by novel carbon nanomaterials allows us to suppose that the anomalous large scattering (up to three orders of the magnitude) in the experimental values of the hydrogen capacity at room temperatures and the technological pressures in the studies of different authors is mostly related with faintly studied physicochemical aspects (processes).

The presented results[4-7] are mainly of the conceptual and methodological significance, and they can serve as an effective basis both for the further fundamental and technological developments on using novel carbon nanomaterials in the field of hydrogen energy for vehicles. Such new results are important for optimizing and understanding the interaction between hydrogen and carbon materials[15].

There is a real possibility of revealing the true Rodriguez-Baker regimes of hydrogenation and/or synthesis of graphite nanofibers, providing the manifestation of the anomalous 'peak V', and their use for a radical solution of the urgent problem of the hydrogen on-board storage – a bottle neck in constructing fuel cell-powered non-pollution vehicles.

References

1. Hirscher M, Becher M, Haluska M, Chen X, Dettlaff-Weglikowska U, Roth S. *Abstracts of MH2002*, France; **2002**, 29.
2. Park C, Anderson PE, Chambers A, Tan CD, Hidalgo R, Rodriguez NM. *J. Phys. Chem. B*, **1999**,103, 10572-10581.
3. Nechaev YuS. *Physics Uspekhi*, **2001**, 171, 1251-1261.
4. Nechaev YuS, Alexeeva OK. *IJHE*, **2003**, 28, 1433-1443.
5. Nechaev YuS, Alexeeva OK. *Transactions of EHEC-2003*, Grenoble, France; **2003**, (CO2-43).
6. Nechaev YuS, Alexeeva OK, Hirschberg JG, Veziroglu TN.. *Transactions of the HYPOTHESIS V*, Porto Conte, Italy; **2003**.
7. Nechaev YuS, Alexeeva OK. *Chemistry Uspekhi*, **2004**.
8. Yang FH, Yang RT. *Carbon*, **2002;**, 40, 437-444.
9. Atsumi H, Tokura S, Miyake M. *J. Nucl. Mater*. **1988,** 155-157, 241-245.
10. Orimo S, Matsushima T, Fujii H, Fukunaga T, Maier G. *J. Appl. Phys.*, **2001**, 90, 1545-1549.
11. Stojkovic D, Zhang P, Lammert PE, Crespi VH. *Physical Review B*, **2003,** 68, 195406-1-195406-5.
12. Volpe M, Cleri F. *Surface Science*, **2003,** 544, 24-34.
13. Murata K, Kaneko K, Kanoh H, Kasuya D, Takahashi K, Kokai F, Yudasaka M, Iijima S. *J. Phys. Chem. B*, **2002,** 106, 11132-38.
14. Nechaev YuS. *Transactions (Izvestija) of the Russian Academy of Sciences, Physical Series*, **2001**, 65, 1399-1406.
15. Dillon AC, Heben MJ. *Appl. Phys. A*, **2001**, 72, 133-142.

ELECTRICAL CHARGE DISTRIBUTION STUDIES IN SWNT, C_{60}@SWNT, AND DWNT STRUCTURES

Jose Rivera[1], *G. U. Sumanasekera[1], S. Bandow[2], S. Iijima[2], P. C. Eklund[3].*

[1]Department of Physics, University of Louisville, KY 40292, U.S.A
[2]Department of Physics, Meijo University, Nagoya, Japan
[3]Department of Physics, Penn State University, University Park, PA 16802, U.S.A.

Introduction

Single walled Carbon nanotubes (SWNTs) have extremely interesting and unique chemical and physical properties. The interior space of SWNTs can be utilized for interesting applications such as one-dimensional array elements, drug delivery, and fluidics. C_{60} molecules have been inserted with high efficiency in the interior of SWNTs by vapor phase reaction of C_{60} with SWNTs to form peapods (C_{60}@SWNT). It has been found that high temperature annealing of peapods at 1200 ^{0}C result in coalescence among the C_{60} within the host SWNT. The DWNT is the latest well-ordered all-carbon structure to be found [1], following fullerenes, multiwalled and single-walled carbon nanotubes (MWNT, SWNT) [2], nanohorns [3], and peapods [1,4]. Recently, Chen et al., [5] have reported charge transfer properties between bromine and DWNTs using resonant Raman scattering. They have found that the most of the charge resides on the outer wall of the DWNT confirming a molecular Faraday cage effect.

Experimental

The SWNTs used in this study were prepared using high temperature pulsed laser vaporization (PLV) of a graphite target containing Fe/Ni (0.6%-0.6% atomic) catalysts. The chemical purification of the PLV derived material was carried out by refluxing in 70% HNO_3 for 8 h at 160 ^{0}C. The suspension was neutralized by centrifugal decantation with distilled water and finally with ethanol. Then the purified SWNTs were dried and heated in dry air at 420 ^{0}C for 20 min. This last treatment was found to be necessary for opening the tube ends to allow the dopants to easily creep into the nanotubes. The doping of C_{60} into the inner hollow space of SWNTs was carried out in a sealed glass ampoule at 400 ^{0}C for 24 h by vapor phase reaction of C_{60} with SWNTs. The DWNTs were synthesized by annealing the peapods at 1200 ^{0}C in a vacuum better than 10^{-6} Torr. During the high temperature annealing in vacuum, the C_{60} molecules are found to coalesce between adjacent molecules within the host SWNT. The fully packed C_{60} molecules inside the SWNTs are completely transformed into a tubular structure forming DWNTs. Each sample was vacuum-degassed *in situ* in the TEP apparatus at 500 K before exposing to potassium. The doping-induced change of the thermopower, or Seebeck coefficient S, and the four probe resistance *R* were studied in a quartz reactor with; 20-mm inner diameter; ~25 cm in length equipped with a 2 3/4-in. knife-edge flange sealed via a Cu gasket to a standard multipin feedthrough flange. For *in situ* transport measurements, two chromel–Alumel thermocouples and two additional Cu leads were attached with small amounts of silver epoxy to four corners of the 4 mm× 4 mm sample to measure the TEP and the DC four-probe electrical resistance simultaneously. The sample holder with the sample attached to the electrical leads was loaded into the glass reactor together with a small, break-seal ampoule containing potassium. The reactor was evacuated to 10^{-7} Torr using a turbo molecular pump and degassed at 500 K while the time evolution of both R and S were recorded. Then the reactor was cooled down to room temperature and isolated through a high vacuum valve. The alkali metal was then released by shaking the reactor and breaking the break-seal on the alkali metal-containing ampoule. The surface of the alkali metal remained shiny throughout the experiment indicating the absence of any significant amount of oxygen or water in the reactor. The reactor was positioned in a temperature gradient in a horizontal furnace and heated to vaporize the alkali metal. The temperature gradient was chosen to provide efficient transport of alkali metal from the ampoule to the sample, avoiding excessive condensation of the unreacted potassium layer on the surface of the sample. At any time during or after the doping, we were able to stop the reaction by cooling the furnace and then measure the temperature dependence of R and S between 500 and 77 K by lowering the reactor into a dewar of liquid nitrogen. Further doping could then be carried out by repositioning the reactor in the furnace. Three independent experiments were carried out for SWNTs, peapods, and DWNTs all derived from the same initial material of SWNTs.

Results and Discussion

Figure 1 shows a typical *in situ* variation of the resistance R normalized to the resistance of pristine SWNT mat R_0 with exposure time to K vapor. An initial drop in *R* was observed when the alkali-metal temperature reached 400 K. Further sharp drops in *R* indicated with arrows in Fig. 1 were observed when the furnace temperature was stepped up by another 10 °C. We have increased the furnace temperature in steps in order to be able to observe the diffusion kinetics.

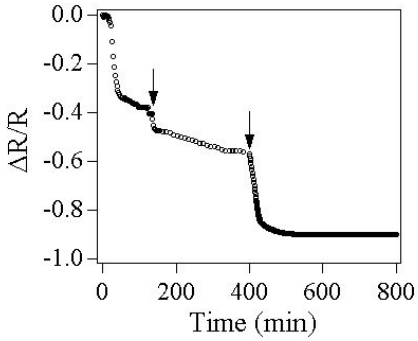

Figure 1. A typical *in situ* variation of four-probe dc resistance *R* of K-doped SWNT mats normalized to the *T*=400 K resistance of the pristine SWNT mat as a function of exposure time to K vapor.

The thermopower (S) of each air-exposed sample shows strong p-type behavior consistent with previous studies. Interestingly, in contrast to previous studies on SWNT materials, this p-type behavior of S remained essentially unchanged during degassing at 500 K in vacuum (<10^{-7} Torr). It has been shown previously [6] that the p-type behavior observed in air-exposed SWNTs can be easily driven n-type by in-situ degassing under these conditions. Further it has been shown that if the degassed SWNTs were exposed to oxygen at temperatures above 500 K, the thermopower is irreversibly changed to p-type, presumably due to strongly bound oxygen resulting in a C-O bond. It should be noted that the SWNTs used in this study are heated in dry air at 420 ^{0}C. For the peapod sample, the irreversible p-type behavior can be due to the same reason. Second possible explanation is that a small charge transfer between C_{60} and SWNTs can result in pinning the Fermi energy near the valance band edge independent of oxygen adsorption/desorption. Another possibility is that the the endohedral C_{60} blocks the oxygen molecules from desorbing out of peapods. The third scenario is more likely in explaining the irreversibility of p-type behavior in DWNTs. The annealing of peapod sample at 1200 ^{0}C in a vacuum <10^{-7} Torr

should be sufficient to remove all the oxygen adsorbed on the carbon surfaces. Any oxygen blocked by C_{60} could be trapped during the coalescence of the C_{60} molecules during the annealing.

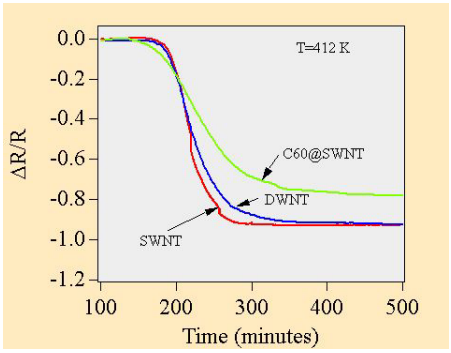

Figure 2. *In situ* variation of four-probe resistance *R* of K-doped SWNT, peapods, and DWNT mats normalized to the *T*=412 K resistance (before the doping started) as a function of exposure time to K vapor.

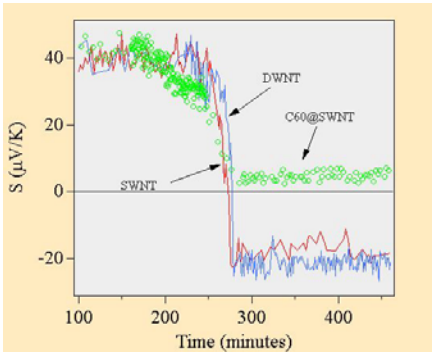

Figure 3. *In situ* variation of four-probe resistance *R* of K-doped SWNT, peapods, and DWNT mats normalized to the *T*=412 K resistance (before the doping started) as a function of exposure time to K vapor.

Fig .2 shows the K-doping effects of the resistance (normalized to the resistance of the undoped sample at T = 412 K) of the three samples, SWNT, peapods, and DWNT. They all show drastic drop of resistance of ~ 80-95 %. Interestingly SWNT and DWNT show almost the same change in resistance, while the change for peapod is somewhat less. Fig. 3 shows the concomitant results of the thermopower for the three samples during the K-doping. Again, SWNT and DWNT show very similar changes in TEP; starting ~ 40 μV/K, decreasing in magnitude, reversing the sign and eventually saturating ~ -20 μV/K. Most interestingly, the TEP of the peapod sample saturates only ~ 0 μV/K without reversing the sign.

Doping effects on both resistance and TEP suggest that the charge transfer properties between K and SWNT or DWNT are very similar consistent with the observations on charge transfer properties on Raman spectra of SWNTs and DWNTs. But peapods show entirely different behavior as can be expected due to the mediation of C_{60} during the charge transfer process. Raman studies on charge transfer in peapods have revealed competition between C_{60} and SWNTs during the charge transfer process. This behavior is not well understood and currently under theoretical investigation. A likely scenario is that the Fermi energy is pinned near the midpoint between the valence band and the conduction band due to the presence of C_{60}.

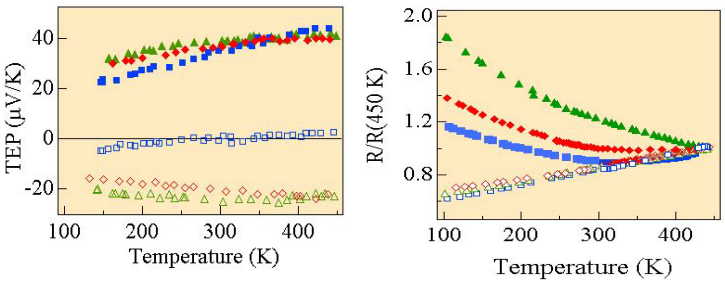

Figure 4 Temperature dependence of (a) Resistance R (b) TEP S before and after saturation doping with K for SWNTs, peapods, and DWNT mats.

Fig.4 shows the temperature dependence of the resistance and the TEP of the three samples before and after K-doping. Unfortunately, the low temperature data is for T > 100 K for obvious technical reasons. It is clearly seen that all three samples show typical temperature dependence of resistance and TEP characteristic of SWNTs before doping. After doping they show obvious metallic behavior.

Conclusions

In situ study of K-doping in SWNTs, C_{60}@SWNTs, and DWNTs has been done by monitoring resistance and thermopower. The data suggest that the charge transfer effects are similar in SWNTs and DWNTs, but drastically different in C_{60}@SWNTs. All three samples show p-type behavior before doping presumably due to oxygen doping. Degassing at 500 K under high vacuum is not sufficient to desorb oxygen suggesting stronger C-O bond.

References

(1) Bandow *et al.*, *Chem. Phys. Lett,* **2001**,. 337, 48
(2) Iijima S. and Ichihashi T., *Nature* (London), **1993**, 363, 603
(3) Iijima S. *et al.*, *Chem. Phys. Lett*. **1999**, 309, 165
(4) Smith B. W., Monthioux M., and Luzzi D. E., *Nature (London),* **1998**, **396**, 323
(5) Chen G. *et al*., Phys. Rev. Lett., **2003**, 90, 257403
(6) Sumanasekera *et al*., Phys. Rev. Lett., **2000**, 85, 1096

EFFECTS OF OXYGENATED SPECIES ON REFORMING GASOLINE RANGE HYDROCARBONS

John P. Kopasz, Laura Miller, Daniel Applegate, and Shabbir Ahmed

Chemical Engineering Division
Argonne National Laboratory
9700 S. Cass Ave
Argonne, IL 60439

Introduction

High octane rating and good reformability are important characteristics for a gasoline-type fuel that could be marketed to both internal combustion engine (ICE) and fuel cell (FC) vehicle owners. Aromatic components contribute to a high octane rating in the gasoline formulations currently produced for internal combustion engines. Unfortunately, aromatic components are difficult to reform because they require longer residence times in the reformer and, as a result, lower the kinetic rate of paraffin reforming.[1-3] An ideal solution would be an inexpensive, low toxicity, easily reformed component that could replace the aromatics, yet maintain a high octane rating in the fuel. The pump octane number (PON), which is an average of the research octane number (RON) and motor octane number (MON), is high for aromatics like toluene as well as for oxygenates like dimethylcarbonate (DMC), ethanol, and methyl *tert*-butyl ether (MTBE).[4] These oxygenates may improve reforming while maintaining high octane ratings, allowing a fuel with lower aromatic content to be used. This would also make desulphurization easier, since requirements for maintaining high octane aromatic components during hydrodesulphurization would be removed.

Experimental

The experiments were conducted using approximately 2 grams of 0.5 wt% Pt on $Ce_{0.8}Gd_{0.2}O_{2-\delta}$, packed as +25/-35 mesh granules. The reactor tube ID was 0.422 cm and the bed length 5 cm for a bed volume of 0.698 cm^3. The furnace settings used in these experiments ranged from 650-800°C, in 50° increments. GHSV's of 15000-150000 h^{-1} were achieved by using two flow settings (0.04 and 0.08 mL/min fuel) and sample ports at multiple locations in the bed. The fuels tested were binary mixtures of isooctane-xylene and isooctane-oxygenate, and ternary mixtures of isooctane-xylene-oxygenate. The H_2O:C molar ratio was fixed at 1.43. The O_2:C molar ratio was 0.4225 for the isooctane-xylene mixture. For dimethylcarbonate (DMC), the ternary mixture was run such that the overall O:C ratio (accounting for the oxygen in the DMC and water) was the same as that for the isooctane-xylene mixture (2.275). The binary isooctane-DMC mixture was run such that the O_2:C ratio (not accounting for the oxygen in the DMC) was 0.4225. Consequently, the oxygen potential in the reactor was higher for the binary isooctane-DMC mixture than for the other two fuels. The product gas was monitored with a residual gas analyzer (RGA) and the bed temperature was monitored with four thermocouples located at various points in the bed.

Results and Discussion

The ternary blend of 75% isooctane, 5% DMC, and 20% xylene showed improved hydrogen production after accounting for hydrogen which would be produced from the water-gas shift reaction compared to isooctane + 20% xylene over most of the parameter space investigated. A percent difference plot is shown in figure 1. The difference in the percent theoretical hydrogen (% theoretical H_2 = (moles H_{2out} + moles CO_{out})/[(total moles H in)/2-moles excess H_2O] where moles excess H_2O is the water excess or water formed from excess oxygen, and is calculated as (moles excess H_2O) = (total moles O)/2-(moles C). In this figure as well as the next, positive differences reflect an improvement due to DMC, while negative differences indicate better performance without DMC.

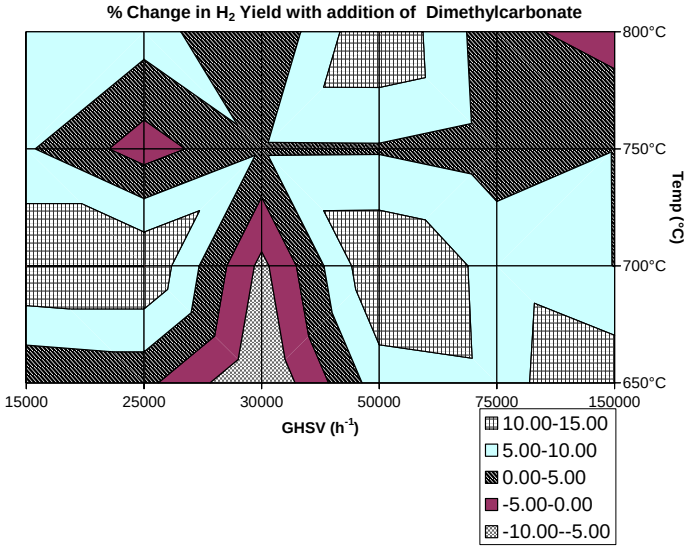

Figure 1. %Change in H_2 yield when adding dimethyl-carbonate to isooctane-xylene mixture.

A large portion of the parameter space investigated showed differences of ±5%, which are believed to be in the range of the error of the measurements. However, improvements in H_2 yield of greater than 5% were observed over a substantial portion of the parameter space. At 650˚C, improvements in H_2 yield upon addition of DMC generally increased with increasing GHSV. At 700˚C hydrogen yield was improved over almost the entire range of space velocities. At 800˚C, where reforming is most efficient, DMC's effect is greatest at a GHSV of 50,000h^{-1}. Looking at GHSV variations, DMC addition improves reforming most at a GHSV of 50,000h^{-1}. The largest absolute difference was at 700°C and a space velocity of 15000 h^{-1}, where the ternary mixture (with DMC) produced an additional 13% hydrogen over the binary mixture (no DMC).

Replacing all the xylene in an isooctane + 20% xylene solution with DMC provided mixed results. DMC increased the hydrogen yield over about half of the operating space, but decreased yields over about half the space. Increases were observed for GHSV in the range of 30,000 to 50,000 h^{-1} at lower temperatures, and shifted to higher GHSV at higher temperatures. To determine how DMC affected reforming kinetics, we looked at how DMC affected the concentration of butyl species, a major product from isooctane cracking, and methane. Methyl species generally decreased in concentration with increasing reaction time, while the butyl species increased with increasing reaction time for both isooctane + 20% xylene and isooctane + 20% DMC. In general, the reformate produced from the solution with DMC contained slightly higher methane content, but larger hydrocarbons, such as butyl species, were reduced. Data for the concentrations as a function of residence time were fit to pseudo-first order rate laws, and the natural log of the rate constants plotted versus the inverse temperature (see fig. 2).

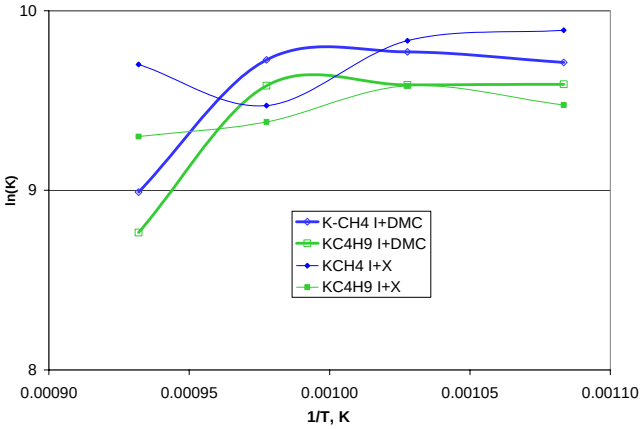

Figure 2. Effect of fuel composition on kinetics of methane decomposition and butyl formation during reforming

The first-order rate constants for methane decay and the net formation of butyl species from isooctane are practically independent of temperature from 650 to 750˚C when reforming isooctane + DMC, but drop sharply when the temperature is increased to 800˚C, suggesting a change in the rate controlling step between 750 and 800˚C. For isooctane + xylene, the rate constants decrease slightly with temperature from 650 to 750˚C, with a slight increase in the rate of methane decay at 800˚C. This suggests different mechanisms are responsible for fractionation and reforming of isooctane in isooctane + 20% xylene and isooctane + 20% DMC. The mass spectra for the DMC-containing mixtures showed no evidence of DMC remaining in the product. The product gas from all three mixtures produced mass spectra with very similar fragmentation patterns for unreformed isooctane.

Discussion

Dimethylcarbonate holds potential for replacing aromatic components of gasoline to improve reformability while maintaining high octane rating and low toxicity. As an oxygenate, DMC can also raise the P_{O2} in the reactor, which could further enhance reformability of the fuel. The results showed that there is a slight improvement to autothermal reforming when DMC is added at a 5 vol% level to a mixture of isooctane and xylene. The effect was largest at 700˚C. Results were mixed when the entire 20 vol% aromatic component was replaced with DMC in an 80:20 mixture with isooctane. Some combinations of temperature/GHSV showed improvement with DMC, while other combinations showed a drop in performance. Replacement of the xylene component with DMC did not significantly improve autothermal reforming as had been hoped. The increase in P_{O2} in the reactor did not have a major impact on hydrogen production or reforming products. The mass fragments observed in the RGA were similar for all three fuels, demonstrating that the DMC was being reformed, but suggesting that it did not substantially enhance the reforming of isooctane over the range of conditions investigated. Future experiments will pursue other fuel additives with the potential to enhance autothermal reforming.

Acknowledgement. This work was supported by the U.S. Department of Energy, Office of Hydrogen, Fuel Cells, and Infrastructure Technologies.

References

(1) Kopasz, J.P.; Miller, L. E.; Ahmed, S.; Devlin, P.;Pacheco, M. Society of Automotive Engineers Technical Paper Series, **2002**, 2002-01-1885.

(2) Kopasz, J.P.; Krause, T.R.; Ahmed, S.; Krumpelt, M. *Prepr. Pap. - Am. Chem. Soc., Fuel Chem. Div.* **2002**, 47(2), 489-491.

(3) Borup, R.; Inbody, M.A.; Tafoya, J. I.; Vigil, W. I.; Guidry, D. *Prepr. Pap. - Am. Chem. Soc., Fuel Chem. Div.* **2001**, *46(2)*, 547-548.

(4) Pacheco, M. A.; Marshall, C. L. Energy & Fuels, **1997**, 11, 2-29.

HIGH CONTACTING EFFICIENCY MICROFIBROUS ENTRAPPED PROX CATALYSTS FOR REFORMATE CLEANUP AND PEM FUEL CELL APPLICATIONS

Bong-Kyu Chang and Bruce J. Tatarchuk

Center for Microfibrous Materials Manufacturing (CM^3)
Department of Chemical Engineering
Auburn University, Auburn, AL 36849

Introduction

Preferential oxidation (PROX) of CO in H_2 is believed to be the most efficient way to remove CO from practical reformate for PEM fuel cells.[1] Pt/Al_2O_3 has long been known as a suitable catalyst for this purpose. However, preferential oxidation of CO in H_2 over Pt/Al_2O_3 occurs at temperatures above 150°C, and the maximum CO conversion takes place at around 200°C. The overall objective of this study is to develop a novel catalyst material for effective removal, particularly at low temperatures, of small amounts (1-2%) of CO present in H_2-rich gas such as practical reformate produced by partial oxidation or steam reforming of hydrocarbons for PEM fuel cells.

Conventional Pt/Al_2O_3 was promoted by cobalt ($Pt\text{-}Co/Al_2O_3$) in this study and the promoted catalysts demonstrate enhanced activity and selectivity compared with the un-promoted catalysts. In particular, CO conversion takes place at significantly lower temperature over $Pt\text{-}Co/Al_2O_3$ catalysts and the active reaction temperature window is enlarged to 25-200°C compared with a narrow window around 200°C over conventional Pt/Al_2O_3.

A high void and tailorable sintered microfibrous carrier consisting of 5vol% 4 and 8μm diameter Ni fibers is used to entrap 15vol% 150-250μm Al_2O_3 particulates. SEM images show the microstructures of the thin microfibrous entrapped alumina support particles. The alumina support particulates are uniformly entrapped into a well sinter-locked three-dimensional network of 4 and 8μm Ni fibers. Cobalt and platinum are then dispersed onto the microfibrous entrapped alumina support particles by impregnation method so as to prepare microfibrous entrapped $Pt\text{-}Co/Al_2O_3$ catalysts. The composite catalysts possess 80vol% voidage. A thin bed of microfibrous entrapped small catalyst (150-250μm) was investigated for preferential oxidation (PROX) of CO from practical reformate for PEM fuel cells. At equivalent bed volumes, microfibrous entrapped catalysts demonstrate superior catalytic activity compared to conventional packed beds of same and larger particles demonstrating ultra-high contacting efficiency provided by the microfibrous entrapped catalysts. A microfibrous entrapped H_2S sorbent layer was, then, placed upstream of a microfibrous entrapped PROX catalyst layer to remove both H_2S and CO from a sulfur-contaminated practical reformate stream. Operating in this fashion, an outermost H_2S sorbent layer promotes the activity maintenance of a secondary non-poison tolerant PROX CO catalyst, which ultimately serves to provide activity maintenance to CO-intolerant precious metal based MEA assemblies in PEM fuel cells.

Experimental

Preparation of Microfibrous Entrapped Catalyst. Traditional high speed and low cost paper making equipment and technique were used in this study to prepare microfibrous composite materials. In this process, 4 and 8μm diameter metal (Ni) fibers in a variety of compositions and alloys are slurried in an aqueous suspension with cellulose fibers and other selected particulates such as alumina support particles. The particle size of alumina support was 150-250μm (60-100 mesh). The resulting mixture is then cast into a preform sheet using a wetlay process and dried to create a sheet of preform material. Subsequent pre-oxidation in O_2 flow at 500°C for 1hr and sintering of the preform in H_2 flow at elevated temperature (900°C) for 30mins remove the cellulosic binder/pore former and entraps the selected support particulates within a sinter-locked network of conductive metal fibers. The resulting preform generally consists of 10-15vol% support particles, 5vol% metal (Ni) fibers, and 80-85vol% voidage. Finally, the microfibrous entrapped support particles such as alumina are impregnated with the metal salt precursor solutions as in the preparation of powder catalysts. Then, microfibrous entrapped catalysts are dried and calcined at desired temperatures.

Catalytic Activity and Selectivity Investigation. Practical reformate consists of 1% CO, 20% CO_2, 40% H_2, and balance N_2. Reaction products were analyzed using a HP6890 gas chromatograph equipped with a TCD detector. Water condenser was used to prevent water vapor from entering the gas chromatograph. Empty reactor without catalyst showed no CO conversion.

Catalyst Characterization Methods. For SEM (scanning electron microscopy), the samples were coated with carbon using SPI module carbon coater to avoid charge building inside the sample while performing SEM. The SEM images of microfibrous materials were obtained using a JEOL JSM 840 (20KV) SEM. The SEM images were recorded at magnification levels of 37 and 200 using an in-built digital camera. For XRD (X-ray diffraction) analysis, structural phases were determined for catalysts in an X-ray diffractometer using Cu Kα radiation. A continuous scan mode was used to collect 2θ data from 10° to 80° with a 0.02 sampling pitch and a 4°/min scan speed. X-ray tube voltage and current were set at 40kV and 40mA, respectively. For EDX (energy dispersive X-ray spectroscopy) analysis, catalyst sample was coated with carbon using SPI module carbon coater to avoid charge building inside the sample while doing EDX. EDX data for the catalyst was obtained using a JEOL JSM 840 (20KV) SEM/EDX.

Results and Discussion

Effect of Various Transition Metal Promoters. Figure 1 shows the effect of various transition metal promoters on the CO oxidizing activity and O_2 selectivity over $4.0wt\%Pt\text{-}X/Al_2O_3$ catalysts (X is a transition metal promoter) as a function of reaction temperature. All of these modified catalysts show enhanced low-temperature activity for CO oxidation versus un-promoted conventional Pt/Al_2O_3 catalyst. Fe, Co, and Mn are found to be effective promoters for conventional Pt/Al_2O_3 catalyst for enhanced CO oxidizing activity and O_2 selectivity at low temperatures. Fe- and Co-modified catalysts achieve complete CO conversion at room temperature to 50°C. Complete CO conversion means that no CO is detected from the outlet stream by the TCD used in this study and it indicates that CO conversion is 99.5 to 100% since CO sensitivity of the TCD used in this study is 50ppm. It is observed that cobalt (Co) is the best promoter for Pt/Al_2O_3 catalyst to achieve complete removal of trace amount of CO in H_2 gas at low temperatures.

Microfibrous Entrapped PROX Catalyst. Figure 2 shows a SEM image of the microstructures of the thin microfibrous entrapped Al_2O_3 support particulates, i.e., alumina support particles entrapped in the microfibrous metal (Ni) mesh after sintering at magnification level of 200, respectively. As shown in the **Figure 2**, the alumina support particles are uniformly entrapped into a well sinter-locked three-dimensional network of 4 and 8μm diameter Ni fibers. Approximately 80-85vol%, 5vol%, and 10-15vol% of the microfibrous materials are voidage, nickel fibers, and alumina support particles entrapped, respectively.

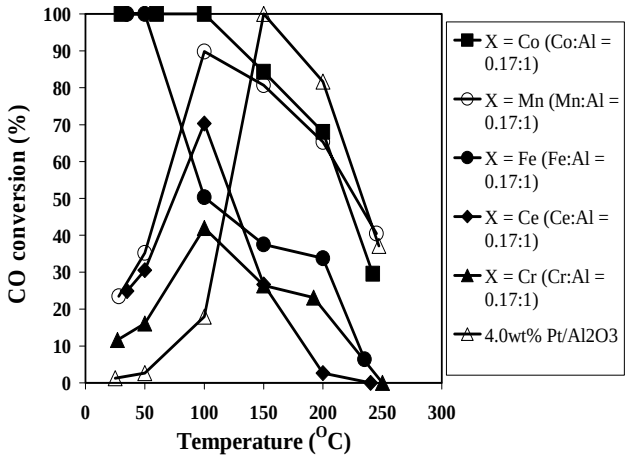

Figure 1. Effect of various transition metal promoters on CO oxidizing activity over 4.0wt%Pt-X/Al_2O_3 catalyst (X is a transition metal promoter) as a function of reaction temperature.

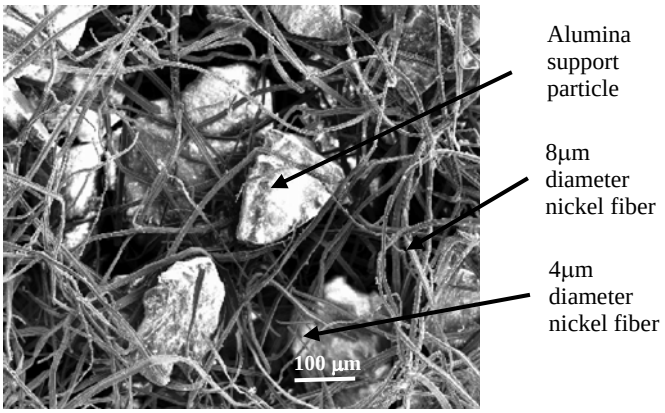

Figure 2. SEM image of 150-250μm γ-Al_2O_3 support particles entrapped in a mirometal fiber matrix of 4 and 8μm nickel fibers at magnification level of 200.

Figure 3 shows stability of microfibrous entrapped Pt-Co/Al_2O_3 catalysts at 70°C (PEMFC stack temperature) with effect of H_2O on the stability. Stability of PROX unit at PEM fuel cell stack temperature is important considering that PROX unit would be integrated into PEMFC stack if it is stable at stack temperature. 30% H_2O in the feed stream is the maximum amount of water which can be maintained in the vapor phase at 70°C which is the PEMFC stack temperature. As shown in **Figure 3**, at 70°C, 0% (no H_2O added), 10%, 20%, and 30% H_2O which are added in the dry practical reformates - which also correspond to 0%, 33%, 67%, and 100% of the saturation amount at 70°C, respectively - do not cause any negative effects on the stability of the microfibrous entrapped Pt-Co/Al_2O_3 catalysts mainly since none of the water vapor added in the feed stream does condense at 70°C. In other words, complete CO conversion activity over the microfibrous entrapped Pt-Co/Al_2O_3 catalysts is maintained for approximately a week without any catalytic deactivation in the presence of 0%, 10%, 20%, and 30% H_2O added in the dry feed stream at 70°C.

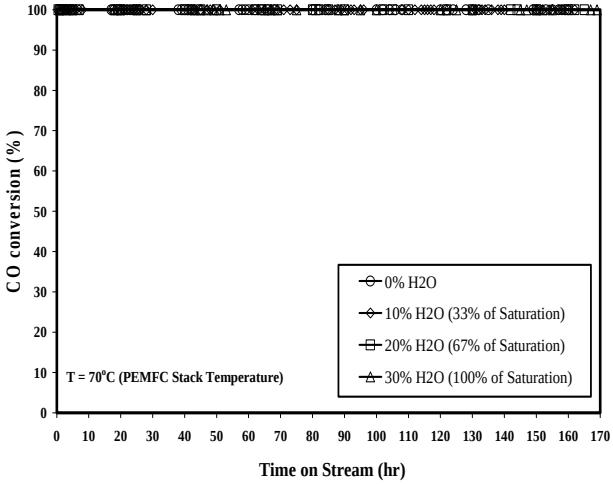

Figure 3. Stability of microfibrous entrapped Pt-Co/Al_2O_3 catalysts at 70°C (PEM fuel cell stack temperature) – Effect of H_2O.

Layering of Microfibrous Entrapped Reactive Media to Achieve Multiple Staged Chemical Reactions/Processes in Flow through Geometries of Millimeter Thickness. High contacting efficiency microfibrous media are used to entrap various reactive materials including; heterogeneous catalysts, electrocatalysts, sorbents, and various solid reactants. These media are then layered so as to permit multiple staged chemical reactions to be achieved within the space of a few millimeters of thickness. Layered media may be used alone or in combination with more traditional contacting schemes (i.e., packed beds, monoliths, etc) so as to be employed as polishing sorbents, polishing catalysts, or both. As a demonstrated example of this generic approach, a microfibrous entrapped polishing H_2S sorbent was placed upstream of a microfibrous entrapped polishing PROX CO catalyst to remove both H_2S and CO from a sulfur-contaminated practical reformate stream. Operating in this fashion, an outermost H_2S sorbent layer promotes the activity maintenance of a secondary non-poison tolerant PROX CO catalyst, which ultimately serves to provide activity maintenance to CO-intolerant precious metal based MEA assemblies.

The benefits and attributes of the above approach may be extended to a variety of entrapped materials and chemical processes. The enabling attribute is the high contacting efficiency afforded by microfibrous entrapment, and the thin layer design of these materials that permit facile and effective layering, packaging and sealing.

Figure 4 shows performance of the integrated bed of microfibrous entrapped ZnO/SiO_2 H_2S sorbent layer and Pt-Co/Al_2O_3 PROX CO catalyst layer at 25°C in the presence of 50ppmv H_2S in the feed. Total flow rate of the feed stream was 100ml/min and cross-sectional area of the microfibrous bed was 0.7854cm^2 making the face velocity 2.12cm/s. Complete CO conversion activity is maintained at least 35hrs without any catalytic deactivation over the microfibrous entrapped Pt-Co/Al_2O_3 PROX CO catalyst when H_2S does not present in the feed stream. CO conversion activity, however, starts dropping dramatically around 4hrs after 50ppmv H_2S is introduced in the feed stream together with CO mainly due to irreversible and permanent H_2S poisoning on the entrapped PROX catalysts. Finally, a microfibrous entrapped H_2S sorbent layer was placed upstream of a microfibrous entrapped PROX CO catalyst layer and the integrated H_2S and PROX CO removal units was investigated at 25°C in the presence of both 1% CO and 50ppmv H_2S in the feed stream. Thickness of the microfibrous entrapped H_2S sorbent layer and the microfibrous entrapped PROX catalyst layer

was approximately 2mm each making the total bed thickness 4mm. As it can be seen clearly in Fig. 30, complete CO conversion activity is recovered for approximately 27hrs before CO is detected in the outlet. H_2S is detected approximately 29hrs after introduction of 50ppmv H_2S in the feed stream, and it is the breakthrough time for the H_2S over the integrated system.

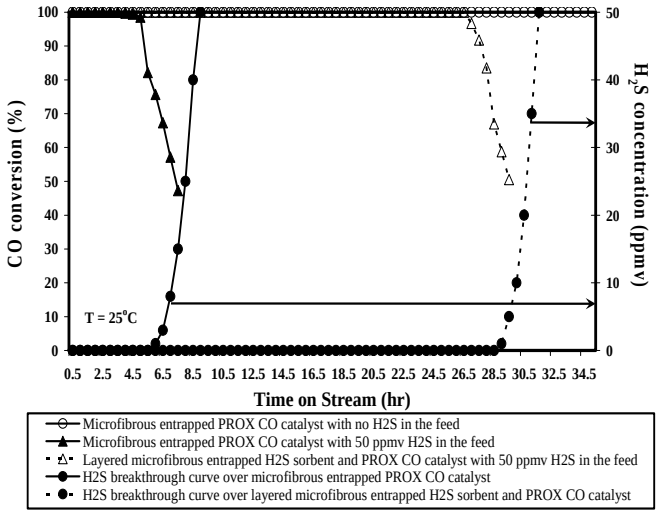

Figure 4. Performance of integrated bed of microfibrous entrapped ZnO/SiO_2 H_2S sorbent and Pt-Co/Al_2O_3 PROX CO catalyst at 25°C in the presence of 50ppmv H_2S in the feed stream.

Catalyst Characterization. Figure 5 shows the XRD patterns of Pt catalyst supported on alumina (4.7wt%Pt-Co/Al_2O_3) compared with those of mixtures of Pt (4.7wt%) and alumina powder. The strongest peak of Pt (111) which is not detected from the catalyst samples is detected at 2θ angle of 39.763° in standard sample of 4.7wt% Pt mixed with alumina powder. Pt (311) peak is also detected at 2θ angle of 81.286° in standard samples. XRD analysis indicates that nano-sized Pt and Co particles are highly dispersed on the alumina support.

Figure 6 shows the EDX spectrum of Pt-Co/Al_2O_3 (4.7wt% Pt, Co:Al = 0.04:1) catalyst. As seen in the figure, there are two peaks corresponding to Pt, two peaks to Co, one peak to Al, and one peak to O in the alumina support. The weight % of Pt obtained by EDS (4.1wt% Pt) is in good agreement with the calculated value (4.7wt% Pt) during the incipient-wetness impregnation process. The atomic ratio of Co:Al measured by EDX (0.034:1) is also in good agreement with the calculated atomic ratio (0.04:1).

Conclusions

Cobalt-promoted Pt/Al_2O_3 (Pt-Co/Al_2O_3) catalyst is significantly superior to un-promoted catalyst for preferential oxidation of CO in excess H_2. XRD patterns for Pt-Co/Al_2O_3 catalysts with different Pt and Co content verify the fact that nano-sized small Pt and Co particles are highly dispersed on the surface of alumina support. All the peaks observed in XRD experiments are from alumina supports. With the attachment of the energy dispersive X-ray spectrometer (EDX), however, the presence of Pt and Co particles is repeatedly verified and the precise elemental composition of catalysts can be obtained with high spatial resolution by scanning electron microscopy (SEM) and the values obtained by EDX show good agreement with the calculated values during the catalyst preparation.

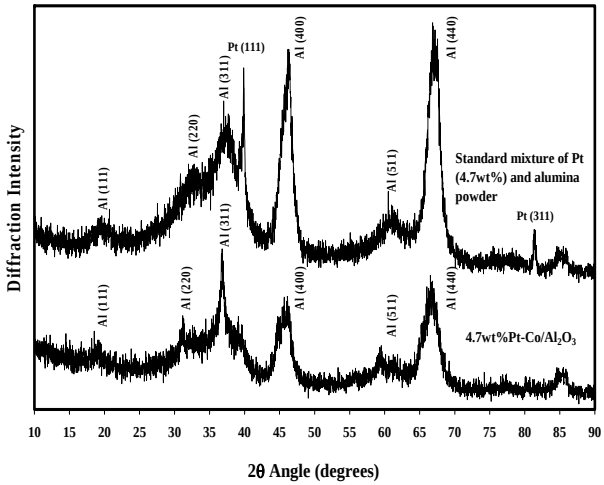

Figure 5. Comparison of XRD patterns of Pt catalyst supported on alumina (Pt-Co/Al_2O_3) with those of mixture of Pt and alumina powder: *4.7wt% Pt.*

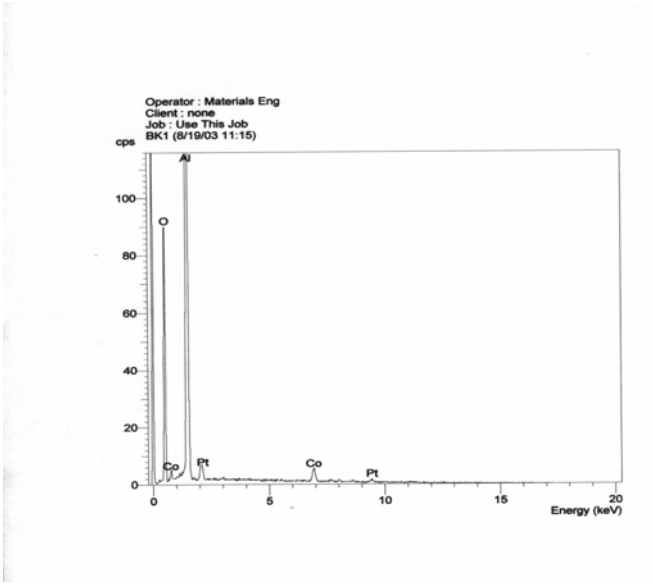

Figure 6. EDX spectrum of Pt-Co/Al_2O_3 catalyst.

High contacting efficiency microfibrous media can be used to entrap various reactive materials including heterogeneous catalysts, sorbents, and various solid reactants. Small particles of Pt-Co/Al_2O_3 catalysts (150-250μm) were entrapped in this study into the microfiber composite materials and investigated for preferential CO oxidation (PROX) reaction for PEM fuel cells. The microfibrous entrapped PROX catalysts demonstrate a long-term stability and high activity at temperature range of 25 (room temperature) to 150°C (PROX unit operating temperature). the nano-dispersed nature of Pt and Co particles combined with packaging of metal fibers and small support particles promotes high contacting efficiency in the microfibrous entrapped catalysts compared with conventional packaging of catalysts in packed bed of even same particle size.

These microfibrous media then could be layered so as to permit multiple staged chemical reactions to be achieved within the space of a few millimeters of thickness. As a demonstrated example

of this generic approach, a microfibrous entrapped polishing ZnO/SiO_2 H_2S sorbent was placed upstream of a microfibrous entrapped polishing $Pt\text{-}Co/Al_2O_3$ PROX catalyst to remove both H_2S and CO from a sulfur-contaminated practical reformate stream. Operating in this fashion, an outermost H_2S sorbent layer promoted the activity maintenance of a secondary non-poison tolerant PROX catalyst, which ultimately served to provide activity maintenance to CO-intolerant precious metal based MEA assemblies.

Acknowledgement. This work was performed under a U.S. Army contract at Auburn University (DASG 60-00-C-0070) administered through the U.S. Army Space & Missile Defense Command (SMDC).

Reference

(1) Sanchez, P. M. T., Ueda, A., Tanaka, K., and Haruta, M., *J. Catal.* **1997**, 168**,** 125.

MULTIFUEL CLEAN-UP CONSIDERATIONS FOR HIGH TEMPERATURE FUEL CELLS

Sai P. Katikaneni, Mohammad Farooque

FuelCell Energy, Inc.
3 Great Pasture Road
Danbury, CT 06813, USA
skatikaneni@fce.com
(203) 825-6067
Fax: (203) 825-6273

Carbonate fuel cells are new generation of power plants that provide electricity at very high efficiency and low environmental emissions. FCE's "direct carbonate fuel cell" operates on a variety of hydrocarbon fuels such as natural gas, digester gas, coal gas, diesel and HD-5. Conventionally, an external reformer is used to supply hydrogen rich gas to fuel cell. FuelCell Energy's DFC^{TM} technology has adopted an internal reforming approach that eliminates the need for an external reformer, resulting in increased efficiency, compactness, better thermal management and lower cost.

DFC operation on natural gas, peak shaving gas, HD-5, LPG/propane, digester gas, syngas, coal bed methane, and liquid fuels such as diesel, methanol and ethanol has been already demonstrated. Fuel clean-up and fuel processing operation varies based on the nature of fuel. However, the fuel thus supplied to the fuel cell has a two-step refinement approach. Step 1 involves fuel clean up system to remove impurities such as sulfur, halides, solid particulates, aromatic hydrocarbons, and oxygen. The second step is pre-reforming desulfurized fuel to knock out higher hydrocarbons in order to eliminate coke formation during reforming inside the fuel cell. Methane-rich gas obtained from pre-reformer is thus fed into fuel cell for internal reforming to produce hydrogen in DFC stacks which in turn is electrochemically converted to water, thereby producing DC power. At each stage of this operation, catalysts are used to facilitate production of desirable fuel cell fuel.

Fuel clean-up considerations vary with type of fuel and its constituents. The nature of impurities and their concentration will be considered to design suitable clean-up processor for each type of fuel for DFC applications. Table 1 indicates various fuels specification including type of impurities and their levels for designing clean-up processor. The impurities present in fuels will impact the performance of reforming catalysts, cell performance and overall life of fuel cell. Ni-based catalysts are used for internal reforming and prereforming of higher hydrocarbons. Nickel catalysts are sensitive for sulfur, chloride and particulate poisoning, thus, require impurity-free fuel for fuel cell applications. The tolerance level of these impurities on both catalyst and fuel cell components are significantly lower than conventional fuel processing operations. Also, the tolerance level is based on the type of impurity. Although worldwide standards favor a gradually lowering sulfur and other impurity levels in transportation fuels, it is necessary to further reduce the sulfur levels in fuel cells to sub-ppm levels prior to use in fuel cell power plants. Depending on the nature of fuel and impurity levels, an appropriate fuel clean-up process with suitable adsorbents/catalysts is required in DFC balance of power plant operation.

FCE has designed multi-fuel clean-up processor to meet DFC power plant tolerances for each type of impurities present in the fuel. These designs were based on either catalytic or adsorbent and selected based on type of fuel and impurity. Multi-fuels processed at FCE's tests have been able to reduce impurity levels (sulfur, halides, particulates and metals) to less than sub ppm levels. This presentation will discuss FCE's experience with multi-fuel clean-up considerations and primarily focusing on desulfurization of multi-fuels.

NANOSIZED CERIA BASED WATER-GAS SHIFT (WGS) CATALYST FOR FUEL CELL APPLICATIONS

Ranjan K. Pati[1], Ivan C. Lee[2], Deryn Chu[2], Sicong Hou[1], and Sheryl H. Ehrman[1]

[1]Department of Chemical Engineering, University of Maryland, College Park, MD 20770
[2]Sensors and Electron Devices Directorate, US Army Research Lab, Adelphi, MD 20783

Introduction

Cerium oxide (CeO_2) / ceria is an important inorganic material having the cubic fluorite type crystal structure (1). Ceria either in the pure form or doped with other metals (Cu, Ni, etc) / metal ions (Mg^{2+}, La^{2+}, Sc^{2+}, Gd^{3+}, Y^{3+}, Zr^{4+} etc.), potentially has a wide range of vast applications including gas sensors (2), electrode materials for solid oxide fuel cells (3) oxygen pumps, amperometric oxygen monitors and three way catalytic supports for automobile exhaust gas treatment (4).

In recent years, nanocrystalline particles of ceria have attracted much attention because of their improved physical and chemical properties compared to those of bulk ceria materials. Various solution-based techniques have been used for the preparation of pure ceria and transition metals, rare earth metals, or metal ions doped ceria materials, including coprecipitation (5), hydrothermal (6), microemusion (7), sol-gel (8), solution combustion (9) and electrochemical methods (10). These methods are either multi step and time-consuming or control of the product composition may be difficult.

In the present paper we report a single step alternative route for synthesizing CeO_2 based nanoparticles. The process involves the pyrolysis of aqueous solutions of the metal acetate without addition of any extra fuel in a methane oxygen flame.

Experimental

The precursors used were cerium acetate as the cerium source, copper acetate as the copper source, nickel acetate as the nickel source and iron acetate as the iron source. The precursors were dissolved in deionized water to make 0.3 M solutions of each. For the transition metal supported ceria, a series of solutions have been prepared starting from 5, 10, 20, 30 and 40 mole % of transition metal in ceria. The solutions were filtered through a membrane filter before filling the nebulizer. Liquid precursor feed was then atomized with compressed air resulting in a fine spray. In the reactor the flame was made by methane, oxygen and nitrogen. The gas flow controller controls the flow rate of the gas and precursors. After burning the fine spray, the particles were collected on a water-cooled surface by thermophoresis, which was kept on the top of the flame.

Characterization

The synthesized materials were then characterized by powder X-ray diffraction (XRD) using CuK_α (λ = 1.5408Å) for the phase analysis and crystal structure determination. Thermogravimetric analysis (TGA) was used to determine the amount of unwanted materials such as water and carbononaceous compounds in the sample. Atomic bonding was analyzed using Fourier transformed infrared spectroscopy (FTIR). Brunauer, Emmett and Teller (BET) gas absorption method was applied to investigate the surface area of the sample. Transmission electron microscopy (TEM) was used for the particle size analysis and surface morphology of the material. X-ray photoelectron spectroscopy (XPS) was utilized to determining the oxidation state of the transition metal used in the ceria system.

Results and Discussion

Thermogravimetric analysis was performed in air at a heating rate of 10ºC/min. The TGA curve (Figure1) for the pure ceria sample indicates that there were two stage of weight loss. The first weight loss (between 20 to 200ºC) was due the removal of water molecules, which probably come from the condensation of water molecule on the water-cooled surface. The second stage weight loss (between 300 to 600ºC) resulted from the burning and oxidation of carbon compounds (combustion by-product) likely from incomplete combustion of the metal acetate precursor, which is confirmed by FTIR. Similarly, the TGA of the as prepared Cu/CeO_2 showed the same weight loss behavior with the presence of more carbon in the sample.

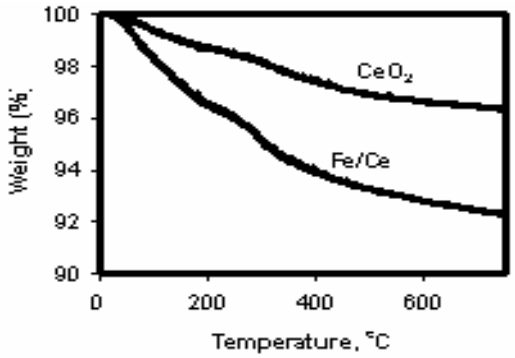

Figure 1. Thermogravimetric analysis (TGA) of as prepared pure CeO_2 and 40% Fe/CeO_2 powder

The X-ray diffraction patterns of transition metal doped CeO_2 are performed. The diffraction lines corresponding to the fluorite type structure and the d values agree well with those expected for CeO_2. The peaks corresponding to transition metal or oxides could not be detected even with the increase of transition metal content. This suggests that transition metal or its ion may not be substituted for Ce^{4+} in CeO_2. Increasing the transition metal content increases the line width compared to the pure CeO_2 and the absence of transition metal or its oxide phase suggest that the transition metal or its ions are dispersed on the surface of CeO_2.

X-ray photoelectron spectra of 40% Ni/CeO_2 in the Ce(3d) and Ni(2p) regions have been performed. The Ce(3d) spectrum with intense satellites identifies with Ce^{4+} in CeO_2 (9). No significant peak is observed in the Ce(3d) spectrum corresponding to Ce^{3+}. The XPS of as prepared Ni($2p_{3/2}$) shows that Ni is in the +2 oxidation state as seen from the Ni^{2+} ($2p_{3/2}$) binding energy as well as the satellite peaks. The Ni/CeO_2 catalyst after the water-gas shift treatment shows the zero oxidation state of Ni, which indicates the reduction of Ni^{2+} to Ni happens in the reducing atmosphere.

Transmission electron microscopic image of 40%Cu/CeO_2 is shown in Figure 2. The particles are spherical in size with particle size in the range of 3-5 nm. The absence of big particle suggests that the precursor droplets are vaporized completely in the flame. The selected area electron diffraction (SAED) pattern is indexed to polycrystalline CeO_2 in the fluorite structure and no line corresponding to Cu or any of the oxides of Cu is detected. This again suggests the dispersion of Cu^{2+} on the CeO_2 surface. A particle sizes obtained from Ni/CeO_2 and

Fe/CeO_2 are in the range of 3-10 nm. The BET surface area for the prepared sample is in the range of 127-163 m^2/g.

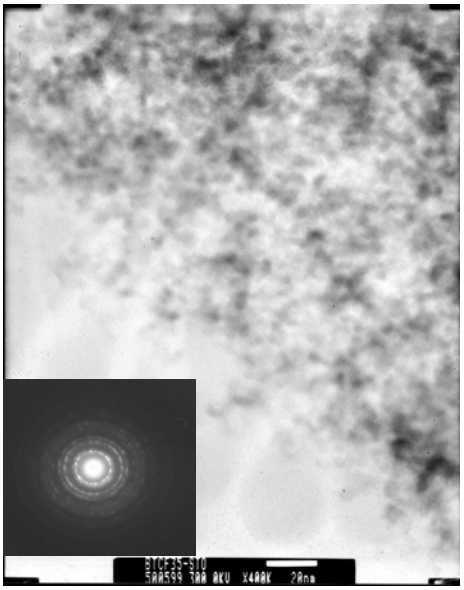

Figure 2. Transmission electron micrograph and the selected area electron diffraction pattern of the as prepared Cu/CeO_2 powder

WGS reaction has been done in a differential reactor with 5% CO, 5% H_2 in Ar and CO/H_2O=5. Figure 3 shows the comparative study of WGS activity of different catalysts. From the graph it is clear that pure ceria is not active because of the absence of any active site. 40% Cu/CeO_2 and annealed 40% Cu/CeO_2 show better activity compared to the other. The reason of the better activity for annealed 40% Cu/CeO_2 is probably the absence of carbon in the sample

Conclusion

Flame synthesis is an easy, single step method for the preparation of pure CeO_2 and the transition metal doped CeO_2 materials starting from aqueous solution of metal salts. From XPS it is clear that the transition metals in the CeO_2 are in an oxidized state and the metal ions may be on the surface of the CeO_2 lattice. The particle sizes of the synthesized materials are in the range of 3-10 nm and the BET surface area are in the range of 127-163 m^2/g. Catalysts prepared in the flame synthesis method are WGS active and Cu/CeO_2 is better so far.

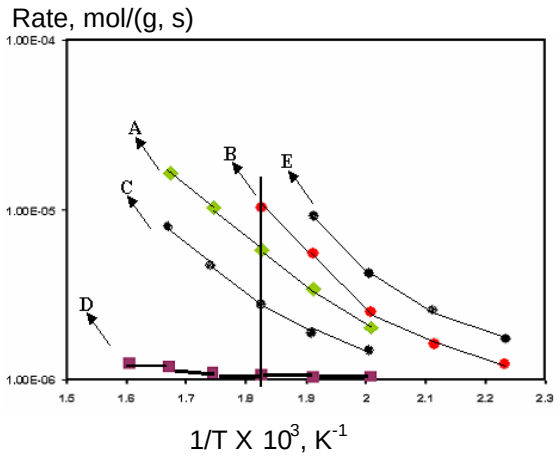

Figure 3. WGS activity of the prepared sample, (A) 15% Cu/CeO_2, (B) 40% Cu/CeO_2, (C) 40% Ni/ CeO_2, (D) pure CeO_2, and (E) 700^{0}C annealed 40% Cu/CeO_2.

Acknowledgement

We thank Amy Wingfield, Jason Repac, and Radhika Char for the help in making the materials, and Dr. Bindhu Varughese for the XPS measurements. Ranjan K. Pati and Sheryl H. Ehrman would like to thank U.S. Army Research Laboratory (ARL) for the financial and instrumental support through PEER program.

References

1. Hirano, M.; Inagaki, M. *J. Mater.Chem.*, **2000,** 10,473
2. Steele, B.C.H. *Solid State Ionics*, **2000,** 129, 95
3. Kubo, T.; Obayasi, H. *J.Electrochem.Soc.* **1975,** 122, 42
4. Fornasiero, P.; Balducci, G.; DiMonte, R.; Kaspar, J.; Sergo, V.; Gubitosa, G.; Ferrero, A. ; Maziani, G.; *J.Catal*., **1996**, 164, 173
5. Vanherle, J.; Horita, T.; Kawada, T.; Sakai, N.; Yokokawa, H. ; Dokiya, M., *J. Am. Ceram. Soc*., **1997** 80, 933
6. Hirano, M.; Kato, E., *J. Am. Ceram. Soc.*, **1999**, 82, 786
7. Martinez-Arias, A.; Fernandez-Garcia, M.; Ballesteros, V.; Salamanca, L.N.; Conesa, J.C.; Otero, C.; Soria, J., *Langmuir*, **1999**, 15, 4796
8. Li, L.; Lin, X.; Li, G.; Inomata, H., *J. Mater. Res*., **2001,** 16, 3207
9. Bera, P.; Aruna, S.T.; Patil, K.C.; Hegde, M. S., *J.Catal.*, **1999**, 186, 36
10. Zhou, Y.; Phillips, R.; Switzer, J.A., *J. Am. Ceram. Soc*., **1995**, 78, 981

ENERGETIC CATALYST-HYDROGEN PLASMA REACTION AS A POTENTIAL NEW ENERGY SOURCE

R. L. Mills, Y. Lu, M. Nansteel, J. He, A. Voigt, W. Good, B. Dhandapani

BlackLight Power, Inc., 493 Old Trenton Road,Cranbury, NJ 08512

Introduction

Theoretical Predictions. The basic spectral emission of pure helium and hydrogen light sources have been well known for about a century. Recently, however, unique vacuum ultraviolet (VUV) emission lines were found at predicted wavelengths and reported in numerous publications [1-5]. For example, extreme ultraviolet (EUV) spectroscopy was recorded on microwave discharges of helium with 2% hydrogen. Novel emission lines were observed with energies of $q \cdot 13.6\,eV$, $q = 1,2,3,7,9,11$. or $q \cdot 13.6\,eV$, $q = 4,6,8$ less $21.2\,eV$ corresponding to inelastic scattering of these photons by helium atoms due to excitation of $He(1s^2)$ to $He(1s^1 2p^1)$. These strong emissions are not found in any single gas plasma, and cannot be assigned to the known emission of any species of the single gases studied such as H, H^-, H_2, H_2^+, H_3^+, He, He_2^*, and He^+, known species of the mixture such as He_2^+, HeH^+, HeH, HHe_2^+, and HHe_n^+ and possible contaminants [1], or doubly excited states [6]. However the results can be explained by a novel catalytic reaction of atomic hydrogen [1-5] to lower-energy states given by Rydberg's equation

$$E_n = -\frac{e^2}{n^2 8\pi\varepsilon_o a_H} = -\frac{13.598\,eV}{n^2} \tag{1a}$$

where

$$n = \frac{1}{2},\frac{1}{3},\frac{1}{4},...,\frac{1}{p};\quad p \le 137 \text{ is an integer} \tag{1b}$$

replaces the well known parameter

$$n = 1,2,3,... \tag{1c}$$

for hydrogen excited states.

The theory reported previously [1-5, 7-12] predicts that atomic hydrogen may undergo a catalytic reaction with certain atoms, excimers, and ions which provide a reaction with a net enthalpy of an integer multiple of the potential energy of atomic hydrogen, $E_h = 27.2\,eV$ where E_h is one hartree. Specific species (e.g. He^+, Ar^+, Sr^+, and K) identifiable on the basis of their known electron energy levels are required to be present in plasmas with atomic hydrogen to catalyze the process. In contrast, species such as atoms or ions of Kr, Xe, Na, or Mg do not fulfill the catalyst criterion—a chemical or physical process with an enthalpy change equal to an integer multiple of E_h that is sufficiently reactive with atomic hydrogen under reaction conditions. The highly exothermic reaction involves a nonradiative energy transfer followed by $q \cdot 13.6\,eV$ emission or $q \cdot 13.6\,eV$ transfer to H to form extraordinarily hot H [1, 10-16] and a hydrogen atom that is lower in energy than unreacted atomic hydrogen that corresponds to a fractional principal quantum number given by Eq. (1b). That is, the $n = 1$ state of hydrogen and the $n = \frac{1}{\text{integer}}$ states of hydrogen are nonradiative, but a transition between two nonradiative states, say $n = 1$ to $n = 1/2$, is possible via a nonradiative energy transfer. A catalyst provides a net positive enthalpy of reaction of $m \cdot 27.2\,eV$ (i.e. it resonantly accepts the nonradiative energy transfer from hydrogen atoms and releases the energy to the surroundings to affect electronic transitions to fractional quantum energy levels). As a consequence of the nonradiative energy transfer, the hydrogen atom becomes unstable and emits further energy until it achieves a lower-energy nonradiative state having a principal energy level given by Eqs. (1a) and (1b).

Prior related studies that support the possibility of a novel reaction of atomic hydrogen which produces hydrogen in fractional quantum states that are at lower energies than the traditional "ground" ($n = 1$) state include extreme ultraviolet (EUV) spectroscopy [1-5, 9-12, 15, 17-24, 26-28], characteristic emission from catalysts and the hydride ion products [11-12, 17-20, 23-24], lower-energy hydrogen emission [1-5], chemically formed plasmas [9-12, 17-24], Balmer α line broadening [1, 2, 10-17, 20, 23-24, 26-27], population inversion of H lines [23-26], elevated electron temperature [13-15, 27], anomalous plasma afterglow duration [21-22], power generation [2, 4, 15, 20, 27, 29], and analysis of novel chemical compounds [20, 30-33].

$H(1/p)$ may react with a proton, and two $H(1/p)$ may react to form $H_2(1/p)^+$ and $H_2(1/p)$, respectively. The hydrogen molecular ion and molecular charge and current density functions, bond distances, and energies were solved previously [8] from the Laplacian in ellipsoidal coordinates with the constraint of nonradiation. The bond dissociation energy, E_D, of hydrogen molecular ion $H_2(1/p)^+$ was given as

$$E_D = p^2\,2.535\,eV + p^3\,0.118755\,eV \tag{2}$$

where p is an integer. The bond dissociation energy, E_D, of hydrogen molecule $H_2(1/p)$ E_D was given previously as

$$E_D = p^2\,4.151\,eV + p^3\,0.326469\,eV \tag{3}$$

The vibrational and rotational energies of fractional-Rydberg-state hydrogen molecular ion $H_2(1/p)^+$ and molecular hydrogen $H_2(1/p)$ are p^2 those of H_2^+ and H_2, respectively. Thus, the vibrational energies, E_{vib}, for the $\upsilon = 0$ to $\upsilon = 1$ transition of hydrogen-type molecular ions $H_2(1/p)^+$ are [8]

$$E_{vib} = p^2\,0.271\,eV \tag{4}$$

where p is an integer and the experimental vibrational energy for the $\upsilon = 0$ to $\upsilon = 1$ transition of H_2^+, $E_{H_2^+(\upsilon=0\to\upsilon=1)}$, is given by Karplus and Porter [34] and NIST [35]. Similarly, the vibrational energies, E_{vib}, for the $\upsilon = 0$ to $\upsilon = 1$ transition of hydrogen-type molecules $H_2(1/p)$ are [8]

$$E_{vib} = p^2\,0.515902\,eV \tag{5}$$

where p is an integer and the experimental vibrational energy for the $\upsilon = 0$ to $\upsilon = 1$ transition of H_2, $E_{H_2(\upsilon=0\to\upsilon=1)}$, is given by Beutler [36] and Herzberg [37]. The rotational energies, E_{rot}, for the J to $J+1$ transition of hydrogen-type molecules $H_2(1/p)$ are [8]

$$E_{rot} = E_{J+1} - E_J = \frac{\hbar^2}{I}\left[J+1\right] = p^2(J+1)0.01509\,eV \tag{6}$$

where p is an integer, I is the moment of inertia, and the experimental rotational energy for the $J=0$ to $J=1$ transition of H_2 is given by Atkins [38]. The p^2 dependence of the rotational energies results from an inverse p dependence of the internuclear distance and the corresponding impact on I. The predicted internuclear distances $2c'$ for $H_2(1/p)$ are

$$2c' = \frac{a_o\sqrt{2}}{p} \tag{7}$$

Experiments to Test the Theoretical Predictions. The reaction Ar^+ to Ar^{2+} has a net enthalpy of reaction of $27.63\,eV$; thus, it may serve as a catalyst to form $H(1/2)$. The product of the catalysis reaction, $H(1/2)$, may further serve as both a catalyst and a reactant to form $H(1/4)$ [2-3]. Also, the second ionization energy of helium is $54.4\,eV$; thus, the ionization reaction of He^+ to He^{2+} has a net enthalpy of reaction of $54.4\,eV$ which is equivalent to $2\cdot 27.2\,eV$. The product of the catalysis reaction, $H(1/3)$, may further serve as both a catalyst and a reactant to form $H(1/4)$ and $H(1/2)$ [2-3].

Since $H_2(1/2)^+$ is a resonant state of $H_2(1/4)^+$, the reaction designated

$$H(1/4)+H^+ \rightarrow H_2(1/4)^+ \tag{8}$$

wherein $H(1/4)$ reacts with a proton to form $H_2(1/4)^+$ is possible with strong emission through vibronic coupling with the resonant state $H_2(1/2)^+$. The energies, E_{D+vib}, of this series due to vibration in the transition state given previously [28] are

$$\begin{aligned} E_{D+vib} &= E_D\left(H_2(1/4)^+\right) - \left(\upsilon^* + \frac{1}{2}\right)2^2 E_{vib\,H_2^+} \\ &= 48.16 - \left(\upsilon^* + \frac{1}{2}\right)1.172\,eV \end{aligned} \quad , \quad \upsilon^* = 0,1,2,3... \tag{9}$$

where $E_D\left(H_2(1/4)^+\right)$ is the bond energy of $H_2(1/4)^+$ given by Eq. (2) and $E_{vib\,H_2^+}$ is the transition-state vibrational energy of H_2^+ given by Eq. (108) of Ref. [8]. In Eq. (9), υ^* refers to vibrational energies of the transition state which must have equal energy separation as a requirement for resonant emission [8, 28]. Thus, anharmonicity is not predicted. The series is predicted to end at 25.74 nm corresponding to the predicted $H_2(1/4)^+$ bond energy of 48.16 eV given by Eq. (2).

The present paper tests theoretical predictions [1-5, 7-12] that atomic and molecular hydrogen form stable states of lower energy than traditionally thought possible. Substantial spectroscopic and physical differences are anticipated. For example, novel EUV atomic, molecular ion, and molecular spectral emission lines from transitions corresponding to energy levels given by Eqs. (1a) and (1b), Eqs. (2) and (4), and Eqs. (3) and (5-7), respectively, are predicted. The atomic lines have been shown previously [1-4, 27] as well as a series of unique EUV lines assigned to $H_2(1/2)$ [4]. To test additional predictions, EUV spectroscopy was performed to search for emission that was characteristic of and identified $H_2(1/4)^+$ and $H_2(1/4)$. Low pressure plasmas are more highly ionized. Thus, we further investigated the emission of the $H_2(1/4)^+$ vibrational series given by Eq. (9) from microwave discharges of helium-hydrogen and argon-hydrogen mixtures.

The rotational energies provide a very precise measure of I and the internuclear distance using well established theory [34]. Neutral molecular emission was anticipated for high pressure argon-hydrogen plasmas excited by a 15 keV electron beam. Rotational lines for $H_2(1/4)$ were anticipated and sought in the 150-250 nm region. The spectral lines were compared to those predicted by Eqs. (5-6) corresponding to the internuclear distance of 1/4 that of H_2 given by Eq. (7). The predicted energies for the $\upsilon = 1 \rightarrow \upsilon = 0$ vibration-rotational series of $H_2(1/4)$ (Eqs. (5-6)) are

$$\begin{aligned} E_{vib-rot} &= p^2 E_{vib\,H_2(\upsilon=0\rightarrow\upsilon=1)} \pm p^2(J+1)E_{rot\,H_2} \\ &= 4^2 E_{vib\,H_2(\upsilon=0\rightarrow\upsilon=1)} \pm 4^2(J+1)E_{rot\,H_2} \\ &= 8.254432\,eV \pm (J+1)0.24144\,eV \end{aligned} \quad , \quad J = 0,1,2,3... \tag{10}$$

for $p=4$.

The product $H_2(1/p)$ gas predicted to liquefaction at a higher temperature than H_2 [28]. Helium-hydrogen (90/10%) plasma gases were flowed through a high-vacuum (10^{-6} Torr) capable, liquid nitrogen (LN) cryotrap, and the condensed gas was characterized by ^1H nuclear magnetic resonance (NMR) of the LN-condensable gas dissolved in $CDCl_3$. Other sources of hydrogen such as hydrocarbons were eliminated by mass spectroscopy (MS) and Fourier transform infrared spectroscopy (FTIR). The ^1H NMR resonance of $H_2(1/p)$ is predicted to be upfield from that of H_2 due to the fractional radius in elliptic coordinates [7-8] wherein the electrons are significantly closer to the nuclei. The predicted shift, $\frac{\Delta B_T}{B}$, for $H_2(1/p)$ derived previously [7-8] is given by the sum of that of H_2 and a relativistic term that depends on $p>1$:

$$\frac{\Delta B_T}{B} = -\mu_0\left(4-\sqrt{2}\ln\frac{\sqrt{2}+1}{\sqrt{2}-1}\right)\frac{e^2}{36a_0 m_e}\left(1+\pi\alpha(p-1)\right) \tag{11}$$

$$\frac{\Delta B_T}{B} = -(28.01+0.64(p-1))ppm \tag{12}$$

where for H_2 there is no relativistic effect and $p=$ integer >1 for $H_2(1/p)$.

The exothermic helium plasma catalysis of atomic hydrogen was shown previously [13-14] by the observation of an average hydrogen atom temperature of $180-210\,eV$ for helium-hydrogen mixed plasmas versus $\approx 3\,eV$ for hydrogen alone. Since the electronic transitions are very energetic, power balances of helium-hydrogen plasmas compared to control krypton plasmas were measured using water bath calorimetry to determine whether this reaction has sufficient kinetics to merit its consideration as a practical power source.

$2K^+$ to $K+K^{2+}$ and K to K^{3+} also provide a reaction with a net enthalpy equal to one and three times the potential energy of atomic hydrogen, respectively. The presence of these gaseous ions or atoms with thermally dissociated hydrogen formed a so-called resonance transfer (rt)-plasma having strong VUV emission with a stationary inverted Lyman population [9, 17, 19-24]. Significant line broadening of the Balmer α, β, and γ lines of 18 eV was observed, compared to 3-4 eV from a hydrogen microwave plasma

[17, 23-24]. Emission from rt-plasmas occurred even when the electric field applied to the plasma was zero [21-22]. Light output per unit power input up to 8600 times that of the control standard light sources as also observed from certain rt-plasmas [10-12]. The reaction was exothermic since excess power of 20 $mW \cdot cm^{-3}$ was measured by Calvet calorimetry [20]. An energetic catalytic reaction was proposed involving a resonant energy transfer between hydrogen atoms and $2K^+$ or K to form very stable novel hydride ions $H^-(1/p)$ called hydrino hydrides having a fractional principal quantum numbers $p = 2$ and $p = 4$, respectively. Characteristic emission was observed from K^{2+} and K^{3+} that confirmed the resonant nonradiative energy transfer of $27.2\,eV$ and $3 \cdot 27.2\,eV$ from atomic hydrogen to $2K^+$ and K, respectively. The product hydride ion $H^-(1/4)$ was observed spectroscopically at $110\,nm$ corresponding to its predicted binding energy of $11.2\,eV$ [17, 19, 20].

In addition to liquefaction at liquid nitrogen temperature, $H_2(1/p)$ gas was also isolated by decomposition of compounds found to contain the corresponding hydride ions $H^-(1/p)$. The total shift, $\frac{\Delta B_T}{B}$, was calculated previously [6, 20] for the hydride ions $H^-(1/p)$ having a fractional principal quantum number. The shift was given by the sum of that of ordinary hydride ion H^- and a component due to a relativistic effect:

$$\frac{\Delta B_T}{B} = -\mu_0 \frac{e^2}{12 m_e a_0 \left(1+\sqrt{s(s+1)}\right)} \left(1 + \alpha 2\pi (p-1)\right) = -\left(29.9 + 1.37(p-1)\right) ppm \quad (13)$$

where for H^- there is no relativistic effect and $p = \text{integer} > 1$ for $H^-(1/p)$. The experimental absolute resonance shift of tetramethylsilane (TMS) is -31.5 ppm relative to the proton's gyromagnetic frequency [39, 40]. The results of ^1H MAS NMR spectroscopy were given previously [20, 31-32] on control and novel hydrides synthesized using atomic potassium as a hydrogen catalyst wherein the triple ionization reaction of K to K^{3+}, has a net enthalpy of reaction of $81.7766\,eV$, which is equivalent to $3 \cdot 27.2\,eV$. The KH experimental shift of +1.3 ppm relative to TMS corresponding to absolute resonance shift of -30.2 ppm matched very well the predicted shift of H^- of -30 ppm given by Eq. (13). The ^1H MAS NMR spectrum of novel compound $KH*Cl$ relative to external tetramethylsilane (TMS) showed a large distinct upfield resonance at -4.4 ppm corresponding to an absolute resonance shift of -35.9 ppm that matched the theoretical prediction of p = 4. A novel peak of $KH*I$ at -1.5 ppm relative to TMS corresponding to an absolute resonance shift of -33.0 ppm matched the theoretical prediction of p = 2. The predicted catalyst reactions, position of the upfield-shifted NMR peaks, and spectroscopic data for $H^-(1/2)$ and $H^-(1/4)$ were found to be in agreement [7, 20].

The decomposition reaction of $H^-(1/p)$ is

$$2M^+H^-(1/p) \xrightarrow{\Delta} H_2(1/p) + 2M \quad (14)$$

where M^+ is a metal ion. NMR peaks of $H_2(1/p)$ given by Eqs. (11-12) provide a direct test of whether compounds such as $KH*I$ contain hydride ions in the same fractional quantum state p. Furthermore, the observation of a series of singlet peaks upfield of H_2 with a predicted integer spacing of 0.64 ppm provides a powerful means to confirm the existence of $H_2(1/p)$.

Since atomic hydrogen and K atoms are formed by reduction at the cathode of an aqueous K_2CO_3 electrolysis cell and K^+ ions present in the electrolyte as well as the K atoms contact the atomic hydrogen at the cathode, the catalysis of atomic hydrogen to fractional Rydberg states was also predicted to occur in these cells. The electrolysis reaction is supported by the observation of novel hydride compounds that were reported previously [33]. For example, after 10^4 hours of continuous aqueous electrolysis with K_2CO_3 as the electrolyte, highly stable novel inorganic hydride compounds such as $KH\,KHCO_3$ and KH were isolated and identified by time of flight secondary ion mass spectroscopy (ToF-SIMS). The existence of novel hydride ions was determined using X-ray photoelectron spectroscopy (XPS) and ^1H MAS NMR.

The energy given off during catalysis is much greater than the energy initially transferred to the catalyst, and the energy released is large as compared to conventional chemical reactions. For example, when hydrogen and oxygen gases undergo combustion to form water

$$H_2(g) + \frac{1}{2}O_2(g) \rightarrow H_2O(l) \quad (15)$$

the known enthalpy of formation of water is $\Delta H_f = -286\,kJ/mole$ or 1.48 eV per hydrogen atom. By contrast, each ($n = 1$) ordinary hydrogen atom undergoing a catalysis step to $n = \frac{1}{2}$ releases a net of $40.8\,eV$. Moreover, further catalytic transitions may occur: $n = \frac{1}{2} \rightarrow \frac{1}{3}, \frac{1}{3} \rightarrow \frac{1}{4}, \frac{1}{4} \rightarrow \frac{1}{5}$, and so on. Once catalysis begins, $H(1/p)$ atoms autocatalyze further in a process called disproportionation discussed previously [2-3, 7].

The power corresponding to the exothermic reaction to form H states given by Eqs. (1a) and (1b) was studied by measuring the temperature of the electrolyte of a K_2CO_3 electrolytic cell for a given input electrolysis power compared to the heat loss of the electrolyte using a resistive heater. For sodium, no electrocatalytic reaction of approximately $27.2\,eV$ is possible by the transfer of an electron between two Na^+ ions as is the case with K^+. Thus, Na_2CO_3 served as a control electrolyte. $H_2(1/p)$ formed from the product $H(1/p)$ has an internuclear distance of $1/p$ times that of H_2; thus, it is predicted to have a higher mobility through metals than H_2. This provided a means to enrich and isolate $H_2(1/p)$ by differential diffusion through a hollow nickel cathode. The collected gas was dissolved in dissolved in $CDCl_3$ and characterized by ^1H NMR which has the capability to measure the energy state of hydrogen according to Eqs. (11-12) with the elimination of hydrocarbons as the source of the peaks by FTIR. Since the ionization energy of $H_2(1/2)$ is about a factor of four times that of H_2 ($IP_1(H_2(1/2)) = 62.53\,eV$ versus $IP_1(H_2) = 15.426\,eV$) [7-8, 28], the mass spectral $m/e = 2$ ion current as a function of time was recorded while changing the

electron gun energy from 30 to 70 eV for ultrapure hydrogen and the gas collected electrolysis gases.

Experimental

To investigate the vibrational series of $H_2(1/4)^+$, EUV spectra (20-65 nm) were recorded on light emitted from microwave discharge plasmas of helium, argon, krypton, or xenon or a mixture of 10% hydrogen with each noble gas. Each ultrapure (99.999+%) test gas or mixture was flowed through a half inch diameter quartz tube at 100 mTorr maintained with a total gas flow rate of 10 sccm. The tube was fitted with an Opthos coaxial microwave cavity (Evenson cavity). The microwave generator was an Opthos Model MPG-4M generator (Frequency: 2450 MHz). The input power to the plasma was set at 40 W.

The spectrometer was a McPherson 4° grazing incidence EUV spectrometer (Model 248/310G) equipped with a grating having 600 G/mm with a radius of curvature of $\approx 1 m$ that covered the region $5-65\,nm$. The angle of incidence was 87°. The wavelength resolution was about $0.1\,nm$ (FWHM) with an entrance and exit slit width of $40\,\mu m$. A CEM was used to detect the EUV light. The increment was $0.01\,nm$ and the dwell time was $1\,s$.

Vibration-rotational emission of $H_2(1/4)$ was investigated using an electron gun described previously [41, 42] to initiate argon plasmas with 1% hydrogen in the pressure range of 450-1000 Torr. The plasma cell was flushed with oxygen, then pumped down, flushed with argon-hydrogen (99/1%), and filled with argon-hydrogen (99/1%). Krypton replaced argon in the controls, and argon, hydrogen, oxygen, nitrogen, water vapor, nitrogen-oxygen (50/50%), and argon or krypton with oxygen addition up to 100% oxygen served as further controls. The Ar^+ catalyst mechanism was tested by atmospheric-pressure-plasma-gas flow at 75 sccm and nonflow conditions. The electrons were accelerated with a high voltage of 12.5 keV at a beam current of $10\,\mu A$. The electron gun was sealed with a thin (300 nm thickness) SiN_x foil that served as a $1\ mm^2$ electron window to the cell at high gas pressure (760 Torr). The beam energy was deposited by hitting the target gases, and the light emitted by beam excitation exited the cell through a MgF_2 window mounted at the entrance of a normal incidence McPherson 0.2 meter monochromator (Model 302) equipped with a 1200 lines/mm holographic grating with a platinum coating. The resolution was $0.5\,nm$ (FWHM) at an entrance and exit slit width of $100\,\mu m$. The increment was $0.1\,nm$ and the dwell time was $1\,s$. The PMT (Model R8486, Hamamatsu) used has a spectral response in the range of 115-320 nm with a peak efficiency at about 225 nm. The emission was essentially flat for $200 < \lambda > 275\,nm$, but a notch in the response of about 20% existed in the short wavelength range with a minimum at 150 nm. Peak assignments were determined by an external calibration against standard line emissions.

Condensable gas from helium-hydrogen (90/10%) microwave plasmas maintained in the Evenson cavity was collected in a high-vacuum (10^{-6} Torr) capable, LN cryotrap described previously [28]. After each plasma run the cryotrap was pumped down to 10^{-5} Torr to remove any non-condensable gases in the system. The pressure was recorded as a function of time as the cryotrap was warmed to room temperature. Typically, about $45\,\mu moles$ of condensed gas was collected in a 2 hr plasma run. Controls were hydrogen and helium alone.

The mass spectra ($m/e = 1$ to $m/e = 200$) of ultrahigh purity (99.999+%) hydrogen (Praxair) control samples and samples of the condensable gas from the helium-hydrogen microwave plasmas were recorded with a residual gas analyzer.

Premixed He/H_2 (90/10%) was flowed from a supply bottle through a metering valve and a LN trap just upstream of a 700 mTorr Evenson microwave plasma. A second LN trap downstream of the plasma tube was used to remove any water vapor generated by the plasma. The plasma gas, devoid of impurities due to the LN traps, was flowed through a long capillary tube which was maintained in the temperature range ~12-17 K by a cryo-cooler described previously [28]. Residual gas was pumped from the capillary, condensable gas was collected over a period of several hours, and the system was evacuated to 10^{-5} Torr to remove any non-condensable gases in the system. Controls were hydrogen and helium alone. Two capillary valves were closed to trap any vaporizing gas as the cryo-cooler was stopped, and the tube was warmed to room temperature. Typically about 100 mTorr of gas was collected over a 24 to 48 hour period and then analyzed by mass spectroscopy and compared with the results for a control sample collected in the same way, except that no plasma was present.

Sealed ^1H NMR samples were prepared by collecting the condensed gas from the cryotrap in $CDCl_3$ solvent (99.99% Cambridge isotopes) in an NMR tube (5 mm OD, 23 cm length, Wilmad) maintained at LN-temperature which was then sealed as described previously [28]. Control NMR samples comprised ultrahigh purity hydrogen (Praxair) and the helium-hydrogen (90/10%) mixture with $CDCl_3$ solvent. The NMR spectra were recorded with a 300 MHz Bruker NMR spectrometer that was deuterium locked. The chemical shifts were referenced to the frequency of tetramethylsilane (TMS) at 0.00 ppm.

$KH*I$ that was prepared under long duration (two weeks) synthesis according to methods given previously [30-32], and about a one gram sample was placed in a thermal decomposition reactor under an argon atmosphere. The reactor comprised a 1/4" OD by 3" long quartz tube that was sealed at one end and connected at the open end with Swagelock™ fittings to a T. One end of the T was connected to the NMR tube containing $CDCl_3$ solvent, and the other end was attached to a turbo pump. The apparatus was evacuated to less than 1 milliTorr with the $CDCl_3$ maintained at LN temperature. The sample was heated to 200 °C under vacuum. A valve to the pump was closed, and the sample was heated in the evacuated quartz chamber containing the sample to above 600 °C until the sample melted. Gas released from the sample was collected in the $CDCl_3$ solvent, the NMR tube was sealed and warmed to room temperature, and the NMR spectrum was recorded. Using identical samples, the NMR-tube end of the collection apparatus was connected directly to the sampling port of a quadrupole mass spectrometer to test for hydrocarbon contamination. FTIR was also performed on the released gas for this purpose.

An NMR sample from $KH*I$ provided by BlackLight Power, Inc. was also prepared and analyzed at the Naval Air Warfare Center Weapons Division, Naval Air Warfare Center, China Lake, CA under the same procedure except that the $CDCl_3$ solvent was maintained at ice temperature during hydrogen gas collection, and the NMR spectrum was recorded with a 400 MHz instrument at China Lake. Control NMR samples of ultrapure hydrogen dissolved in $CDCl_3$ solvent were also prepared, and NMR spectra were

obtained under conditions matching those of the $KH*I$ -derived samples.

The excess power was measured by water bath calorimetry on helium-hydrogen (95/5%) plasmas maintained in a microwave discharge cell compared to control plasmas with the same input power as described previously [27]. The water bath was calibrated by a high precision heater and power supply. A high precision linear response thermistor probe (Omega OL-703) recorded the temperature of the 45 L water bath as a function of time for the stirrer alone to establish the baseline. The heat capacity was determined for several input powers, 30, 40, and 50 W ± 0.01 W, and was found to be independent of input power over this power range within ± 0.05%. The temperature rise of the reservoir as a function of time gave a slope in °C/s. This slope was baseline corrected for the negligible stirrer power and loss to ambient. The constant known input power (J/s), was divided by this slope to give the heat capacity in J/°C. Then, in general, the total power output from the cell to the reservoir was determined by multiplying the heat capacity by the rate of temperature rise (°C/s) to give J/s.

Since the cell and water bath system were adiabatic, the general form of the power balance equation with the possibility of excess power is:

$$P_{in} + P_{ex} - P_{out} = 0 \tag{16}$$

where P_{in} is the microwave input power, P_{ex} is the excess power generated from the hydrogen catalysis reaction, and P_{out} is the thermal power loss from the cell to the water bath. Since the cell was surrounded by water that was contained in an insulated reservoir with negligible thermal losses, the temperature response of the thermistor T as a function of time t was determined to be

$$\dot{T}(t) = \left(1.940\ X\ 10^5\ J/°C\right)^{-1} \times P_{out} \tag{17}$$

where $1.940\ X\ 10^5\ J/°C$ is the heat capacity for the least square curve fit of the response to power input for the control experiments ($P_{ex} = 0$). The slope was recorded for about 2 hours after the cell had reached a thermal steady state, to achieve an accuracy of ± 1%.

The power balance of the electrolysis of aqueous potassium carbonate (K^+/K^+ and K catalysts) was determined using single cell 350 ml silvered vacuum jacketed dewars and compared with the results with the replacement of K_2CO_3 with Na_2CO_3 as described previously [29]. A linear calibration curve was obtained. Two methods of differential calorimetry were used to determine the cell constant which was used to calculate the excess enthalpy. First, the cell constant was calculated during the experiment (on-the-fly-calibration) by turning an internal resistance heater off and on, and inferring the cell constant from the difference between the losses with and without the heater. Second, the cell constant was determined with no electrolysis processes occurring by turning an internal resistance heater off and on for a well stirred matched dewar cell, and inferring the cell constant from the difference between the losses with and without the heater.

The general form of the energy balance equation for the cell in steady state is:

$$0 = P_{appl} + Q_{htr} + Q_{xs} - P_{gas} - Q_{loss} \tag{18}$$

where P_{appl} is the electrolysis power; Q_{htr} is the power input to the heater; Q_{xs} is the excess heat power generated by the hydrogen catalysis reaction; P_{gas} is the power removed as a result of evolution of H_2 and O_2 gases; and Q_{loss} is the thermal power loss from the cell. When an aqueous solution is electrolyzed to liberate hydrogen and oxygen gasses, the electrolysis power $P_{appl}\ (= E_{appl} I)$ can be partitioned into two terms:

$$P_{appl} = E_{appl} I = P_{cell} + P_{gas} \tag{19}$$

An expression for $P_{gas}\left(= E_{gas} I\right)$ is readily obtained from the known enthalpy of formation of water from its elements:

$$E_{gas} = \frac{-\Delta H_{form}}{\alpha F} \tag{20}$$

(F is Faraday's constant), which yields $E_{gas} = 1.48V$ for the reaction

$$H_2O \rightarrow H_2 + \frac{1}{2} O_2 \tag{21}$$

The net Faradaic efficiency of gas evolution is assumed to be unity; thus, Eq. (19) becomes

$$P_{cell} = (E_{appl} - 1.48V) I \tag{22}$$

The cell was calibrated for heat losses by turning an internal resistance heater off and on while maintaining constant electrolysis and by inferring the cell conductive constant from the difference between the losses with and without the heater where heat losses were primarily conductive losses through the cap of the dewar. When the heater was off, the losses were given by

$$c(T_c - T_b) = P_{appl} + 0 + Q_{xs} - P_{gas} \tag{23}$$

where c is the conductive heat loss coefficient; T_b is ambient temperature and T_c is the cell temperature. When a new steady state is established with the heater on, the losses change to:

$$c(T_c' - T_b) = P'_{appl} + Q_{htr} + Q'_{xs} - P'_{gas} \tag{24}$$

where a prime superscript indicates a changed value when the heater was on. When the following assumptions apply

$$Q_{xs} = Q'_{xs};\ P_{appl} = P'_{appl};\ P_{gas} = P'_{gas} \tag{25}$$

the cell constant or heating coefficient a, the reciprocal of the conductive loss coefficient (c), is given by the result

$$a = \frac{T_c' - T_c}{Q_{htr}} \tag{26}$$

In all heater power calculations, the following equation was used

$$Q_{htr} = E_{htr} I_{htr} \tag{27}$$

The experiments were carried out by observing and comparing the temperature difference ($\Delta T_1 = T(electrolysis\ only) - T(blank)$) and ($\Delta T_2 = T(resistor\ heating\ only) - T(blank)$) referred to unit input power, between two identical dewars. The heating coefficients were calculated from

$$a_1 = \frac{\Delta T_1}{P_{cell}} \tag{28}$$

$$a_2 = \frac{\Delta T_2}{Q_{htr}} \tag{29}$$

Then, the excess power is given by

$$Q_{xs} = \frac{\Delta T_1}{a_2} - P_{cell} \tag{30}$$

or

$$Q_{xs} = P_{cell}\left(\frac{a_1}{a_2} - 1\right) \tag{31}$$

The heating coefficient was also determined "on the fly" by the addition of increments of ~0.1 W of heater power to the electrolytic cell where 24 hours was allowed for steady state to be achieved.

The temperature rise above ambient ($\Delta T_3 = T(electrolysis + heater) - T(blank)$) was recorded as well as the electrolysis power and heater power. The heating coefficient, a_3, in this case was given by the slope of the plot of ΔT_3 versus total input power ($P_{cell} + Q_{htr}$):

$$a_3 = \frac{\Delta T_3}{P_{cell} + Q_{htr}} \quad (32)$$

wherein the electrolysis heating power, P_{cell}, was kept constant. The heating coefficient a_3 and the temperature rise of the cell with electrolysis power only, ΔT_1, were used to determine the total cell power comprising $P_{cell} + Q_{xs}$. Then, Q_{xs} was determined by subtracting P_{cell}:

$$Q_{xs} = \frac{\Delta T_1}{a_3} - P_{cell} \quad (33)$$

The electrolyte solution was 200 ml of 0.57 M aqueous K_2CO_3 (Aldrich $K_2CO_3 \cdot 3/2H_2O$ 99±%) or 200 ml of 0.57 M aqueous Na_2CO_3 (Aldrich Na_2CO_3 A.C.S. primary standard 99.95 ±%).

The cathode and anode comprised 24 meters of 0.38 mm diameter coiled nickel wire (99.8 % Alfa, cold drawn, clean Ni wire). The electrodes were cleaned by placing them in a beaker of 0.57 M K_2CO_3/3% H_2O_2 for 30 minutes and then rinsing it with distilled water. The leads were inserted into Teflon tubes to insure that no recombination of the evolving gases occurred. The Faraday efficiency was determined by measuring the volume of the evolved electrolysis gases. The power was applied as 83.0 mA constant current at a measured 1.95 V. When Na_2CO_3 replaced K_2CO_3 the power was applied as 83.0 mA constant current at a measured 3.26 V.

For heat measurement and electrolysis gas collection, the cathode comprised a 170 cm long nickel tubing cathode (Ni 200 tubing, 0.159 cm O.D., 0.107 cm I.D., with a nominal wall thickness of 0.0254 cm, MicroGroup, Inc., Medway, MA). The cathode was coiled into a 3.0 cm long helix with a 2.0 cm diameter about the central Pt anode. The cathode was cleaned by placing it in a beaker of 0.57 M K_2CO_3/3% H_2O_2 for 30 minutes and then rinsing it with distilled water. The power was applied as 101 mA constant current at a measured 1.86 V. The anode was a platinum basket (Johnson Matthey) with a 0.38 mm Ni lead wire. The leads were inserted into Teflon tubes to prevent recombination, if any, of the evolving gases. The cathode-anode separation distance was 1 cm.

An ultrahigh-vacuum system was used to collected sealed ^1H NMR samples of the electrolysis gases from the hollow as described previously [29]. The NMR spectra were recorded with the 300 MHz Bruker NMR spectrometer that was deuterium locked. The chemical shifts were referenced to the frequency of tetramethylsilane (TMS) at 0.00 ppm. Hydrocarbon contamination in the samples was eliminated by mass spectroscopic analysis and by FTIR spectral analysis.

The mass spectra ($m/e = 1$ to $m/e = 200$) of ultrahigh purity hydrogen (Praxair) control samples and samples of the electrolysis gases collected in the hollow nickel cathode from K_2CO_3 and Na_2CO_3 cells were recorded with a residual gas analyzer. In addition, the ion current as a function of time of the mass to charge ratio of two ($m/e = 2$) was recorded while changing the electron gun energy from 30 to 70 eV for ultrapure hydrogen and the electrolysis gas from the hollow cathode connected directly to a needle valve on the sampling port mass spectrometer. The pressure of the sample gas in the mass spectrometer was kept the same for each experiment by adjusting the needle value of the mass spectrometer. The entire range of masses through $m/e = 200$ was measured before and after the determinations at $m/e = 1$ and $m/e = 2$.

Results and Discussion

EUV spectroscopy of Helium-Hydrogen and Argon-Hydrogen Plasmas. *Detection of Fractional Rydberg State Hydrogen Molecular Ion* $\mathbf{H_2(1/4)^+}$. In the case of the EUV spectra of helium, krypton, xenon, krypton-hydrogen (90/10%), or xenon-hydrogen (90/10%), no peaks were observed below 65 nm, and no spurious peaks or artifacts due to the grating or the spectrometer were observed. No changes in the emission spectra were observed by the addition of hydrogen to noncatalysts krypton or xenon. Only known atom and ion peaks were observed in the EUV spectrum of the helium and argon microwave discharge emission.

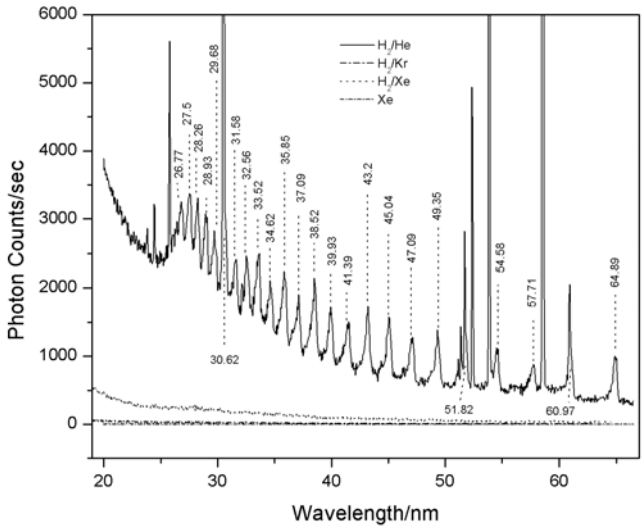

Figure 1. The EUV spectra (20-65 nm) of microwave plasmas of xenon and 10% hydrogen mixed with helium, krypton, and xenon. A vibrational pattern of peaks with an energy spacing of 1.18 eV was observed from the helium-hydrogen plasma having He^+ catalyst. The peaks matched Eq. (9) for $\upsilon^* = 0,1,2,3...24$. The series terminated at about 25.7 nm corresponding to the predicted bond energy of $H_2(1/4)^+$ of 48.16 eV given by Eq. (2). No emission was observed from the noncatalyst controls, krypton and xenon alone or with hydrogen. The sharp peaks in the spectrum were assigned to He I and He II.

The EUV spectra (20-65 nm) of the microwave plasmas of xenon and 10% hydrogen mixed with helium, krypton, and xenon are shown in Figure 1. No emission was observed from the noncatalyst controls, krypton and xenon. A characteristic vibrational series was observed for helium-hydrogen (90/10%), but at higher energies than any known molecule by about an order of magnitude. The series was not observed with helium alone as shown in Figure 2. The energies of the peaks observed in Figures 1 and 2 are plotted in Figure 3 as a function of peak number or integer υ^*. The slope of the linear curve fit in Figure 3 is 1.18 eV, and the intercept is 47.6 eV which matches the predicted series given by Eq.

(9) to within the spectrometer resolution of 1%. This energy separation matches the transition-state vibrational energy of the resonant state $H_2(1/2)^+$, and the series terminates at about 25.7 nm corresponding to the predicted bond energy of $H_2(1/4)^+$ of 48.16 eV given by Eq. (2). Thus, emission in this region was due to the reaction $H(1/4)+H^+ \rightarrow H_2(1/4)^+$ with vibronic coupling with the resonant state $H_2(1/2)^+$ within the transition state. The predicted emission at $E_{D+vib} = E_D\left(H_2(1/4)^+\right) - \left(\upsilon^* + \frac{1}{2}\right)2^2 E_{vib\,H_2^+}$ was observed for $\upsilon^* = 0,1,2,3...24$. All other peaks in the spectra were assigned to He I and He II.

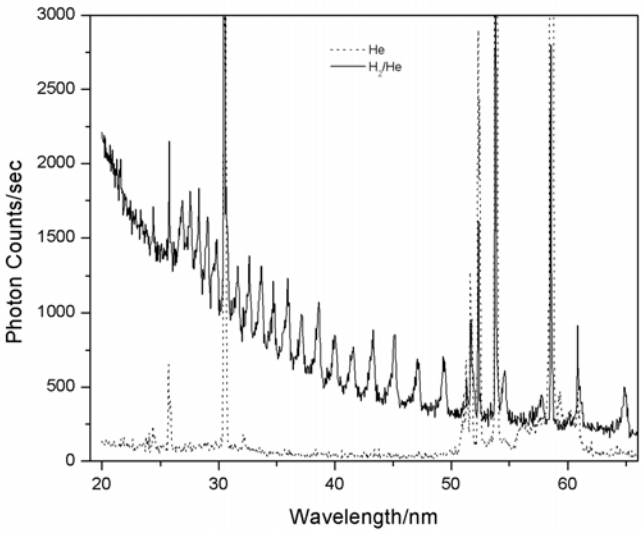

Figure 2. The EUV spectra (20-65 nm) of microwave plasmas of helium-hydrogen (90/10%) (solid) and helium alone (dashed). The vibrational series of peaks assigned to the reaction $H(1/4)+H^+ \rightarrow H_2(1/4)^+$ was observed from the helium-hydrogen plasma having He^+ catalyst and hydrogen, but not from helium alone. The sharp peaks in the spectrum were assigned to He I and He II.

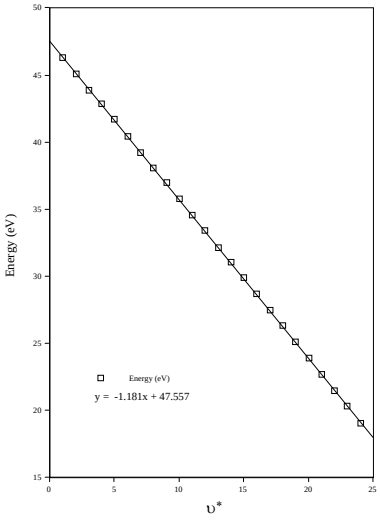

Figure 3. The plot of the energies of the peaks shown in Figures 1 and 2. The slope of the linear curve fit is 1.18 eV, and the intercept is 47.6 eV which matches the predicted emission given by Eq. (9) to within the spectrometer resolution of about 1%.

The EUV spectra (20-65 nm) of microwave plasmas of argon-hydrogen (90/10%) compared with argon alone are shown in Figure 4. The vibrational series of peaks with an energy spacing of 1.18 eV was observed from the argon-hydrogen plasma having Ar^+ catalyst with hydrogen. In contrast, the series was not observed without hydrogen. The peaks matched Eq. (9) for $\upsilon^* = 0,1,2,3...24$.

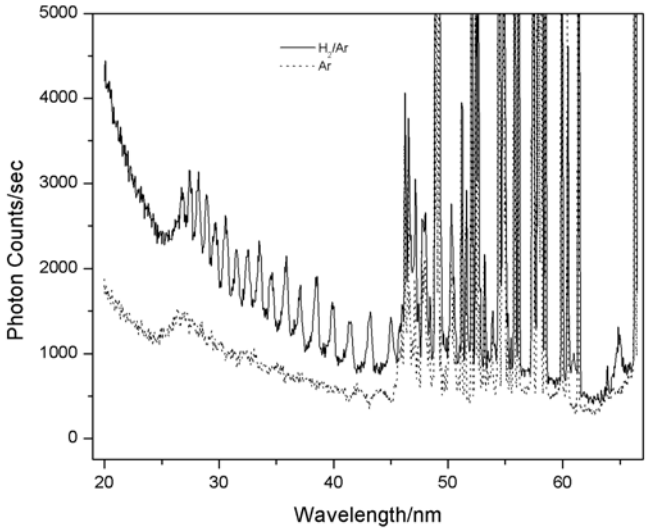

Figure 4. The EUV spectra (20-65 nm) of microwave plasmas of argon-hydrogen (90/10%) (solid) and argon alone (dashed). The vibrational series of peaks assigned to the reaction $H(1/4)+H^+ \rightarrow H_2(1/4)^+$ was observed from the argon-hydrogen plasma having Ar^+ catalyst and hydrogen, but not from argon alone. The sharp peaks in the spectrum were assigned to Ar II.

Detection of Fractional Rydberg State Molecular Hydrogen $\mathbf{H_2(1/4)}$**.** The observation of emission due to the reaction $H(1/4)+H^+ \rightarrow H_2(1/4)^+$ at low pressure (< 1 Torr) shown in Figures 1 and 2 indicates that $H(1/4)$ formed in the argon-hydrogen plasma. Molecular formation was anticipated under high-pressure conditions (~760 Torr). Thus, EUV spectroscopy of argon-hydrogen plasmas was performed to search for $H_2(1/4)$ from $H(1/4)$ formed by Ar^+ as a catalyst using a 15 keV electron beam to maintain the plasma and to collisionally excite vibration-rotational states of $H_2(1/4)$. The corresponding emission provides a direct measure of the internuclear distance; thus, this method provides the possibility of direct confirmation of $H_2(1/4)$.

The 100-350 nm spectrum of a 450 Torr plasma of argon containing about 1% hydrogen is shown in Figure 5. Lyman α was observed at 121.6 nm with an adjoining H_2 band, the third continuum of Ar was observed at 200 nm, O I was observed at 130.6 nm, and the $OH(A-X)$ band was observed at 309.7 nm. A series of sharp, evenly-spaced lines was observed in the region 145-185 nm. The only possibilities for peaks of the instrument width are those due to rotation or electronic emission from atoms or ions. The

series was not observed when krypton replaced argon or with any of the controls and could not be assigned to any known species [28].

The series matched the P branch of $H_2(1/4)$ for the vibrational transition $\upsilon = 1 \rightarrow \upsilon = 0$. P(1), P(2), P(3), P(4), P(5), and P(6) were observed at 155.0 nm, 160.2 nm, 165.8 nm, 171.1 nm, 178.0 nm, and 183.2 nm, respectively. The sharp peak at 147.3 nm may be the first member of the R branch, R(0). Since the vibration-rotational transitions of $H_2(1/4)$ are allowed with nuclear spin-rotational coupling, the vibrational rotational spectrum of $H_2(1/4)$ was predicted to comprise only the R(0) line and the P branch [28] in agreement with observations. The slope of a linear curve fit was 0.241 eV with an intercept of 8.21 eV which matches Eq. (10) very well for $p = 4$. Using Eqs. (6) and (7) with the measured rotational energy spacing of 0.24 eV establishes an internuclear distance of 1/4 that of the ordinary hydrogen species for $H_2(1/4)$. This technique which is the best measure of the bond distance of any diatomic molecule identifies and unequivocally confirms $H_2(1/4)$.

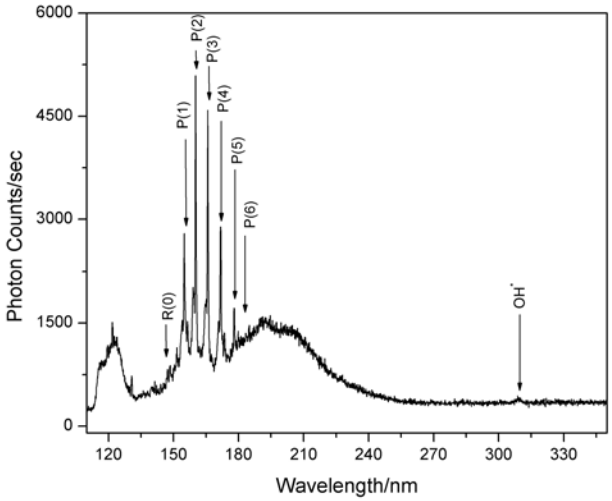

Figure 5. The 100-350 nm spectrum of a 450 Torr plasma of argon containing about 1% hydrogen and trace oxygen using a 15 keV electron gun. Lyman α was observed at 121.6 nm with an adjoining H_2 band, the third continuum of Ar was observed at 200 nm, O I was observed at 130.6 nm, and the $OH(A-X)$ band was observed at 309.7 nm. A series of sharp, evenly-spaced lines was observed in the region 145-185 nm. The series matched the P branch of $H_2(1/4)$ for the vibrational transition $\upsilon = 1 \rightarrow \upsilon = 0$. P(1), P(2), P(3), P(4), P(5), and P(6) were observed at 155.0 nm, 160.2 nm, 165.8 nm, 171.1 nm, 178.0 nm, and 183.2 nm, respectively. The sharp peak at 147.3 nm may be the first member of the R branch, R(0). The slope of a linear curve fit is 0.241 eV with an intercept of 8.21 eV which matches Eq. (10) very well for $p = 4$.

The Ar^+ catalyst mechanism was confirmed by atmospheric-pressure-plasma-gas flow at 75 sccm and nonflow conditions. Flow does not change known atomic and ionic line emission such as the O I line at 130.6 nm. In contrast, the series assigned to vibration-rotation of $H_2(1/4)$ was observed under static conditions; whereas, the series decreased to about 10% with flow indicating a reaction involving the formation of intermediates as predicted.

A possible confirmation of the lines identified in this study has been published previously. Ulrich, Wieser, and Murnick [42] compared the third continuum of argon gas with a very pure gas and a spectrum in which the gas was slightly contaminated by oxygen as evidenced by the second order of the 130 nm resonance lines at 160 nm. A series of very narrow lines at the instrument width having an intensity profile that was characteristic of that of a P-branch were observed in the 145-185 nm region. These lines shown in Figure 6 of Ref. [42] matched those in Figure 5. The slope of the linear curve fit was 0.24 eV with an intercept of 8.24 eV which matches Eq. (10) very well for $p = 4$. The series matches the predicted $\upsilon = 1 \rightarrow \upsilon = 0$ vibrational energy of $H_2(1/4)$ of 8.25 eV (Eq. (5)) and its predicted rotational energy spacing of 0.24 eV (Eq. (6)) with $\Delta J = +1; J = 1,2,3,4,5,6$ and $\Delta J = -1; J = 0$ where J is the rotational quantum number of the final state. With this assignment all of the peaks in Figure 6 of Ref. [42] could be identified; whereas, the evenly-spaced lines could not be unambiguously assigned by Ulrich et al [42]. The series was not observed in krypton and xenon plasmas. The determination of the presence of the common contaminant, hydrogen, in the argon plasmas is warranted in future studies.

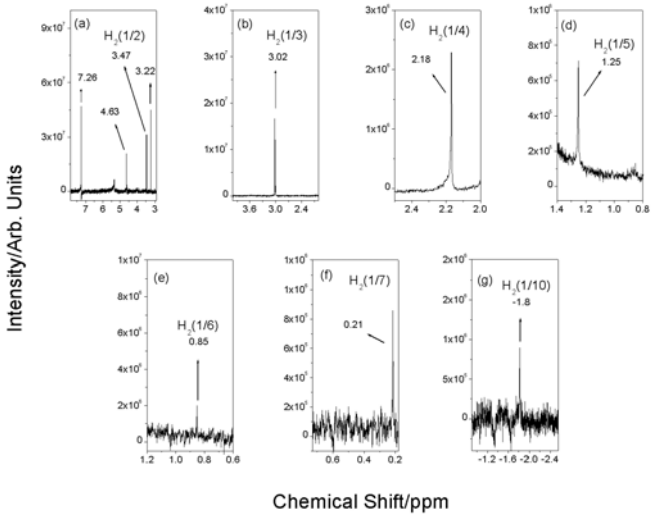

Figure 6 (a)-(g). ^1H NMR spectra on sealed samples of liquid-nitrogen-condensable helium-hydrogen plasma gases dissolved in $CDCl_3$ relative to tetramethylsilane (TMS). The solvent peak was observed at 7.26 ppm, the H_2 peak was observed at 4.63 ppm, and a singlet at 3.22 ppm matched silane. Singlet peaks upfield of H_2 were observed at 3.47, 3.02, 2.18, 1.25, 0.85, 0.21, and -1.8 ppm relative to TMS corresponding to solvent-corrected absolute resonance shifts of -29.16, -29.61, -30.45, -31.38, -31.78, -32.42, and -34.43 ppm, respectively. Using Eq. (12), the data indicates that p = 2, 3, 4, 5, 6, 7, and 10, respectively. The data matched the series $H_2(1/2)$, $H_2(1/3)$, $H_2(1/4)$, $H_2(1/5)$, $H_2(1/6)$, $H_2(1/7)$, and $H_2(1/10)$.

Isolation and Characterization of $H_2(1/p)$. *Cryotrap Pressure* Helium-hydrogen (90/10%) gas was flowed through the microwave tube and the cryosystem for 2 hours with the trap cooled to LN temperature. No change in pressure over time was observed when the dewar was removed, and the system was warmed to room temperature. The experiment was repeated under the same

conditions but with a plasma maintained with 60 W forward microwave power and 10 W reflected. In contrast to the control case, a liquid-nitrogen-condensable gas was generated in the helium-hydrogen plasma reaction since the pressure due to the reaction product rose from 10^{-5} Torr to 3 Torr as the cryotrap warmed to room temperature.

Mass Spectroscopy. The mass spectrum for the gases collected in the cryotrap from the He/H_2 (90/10%) plasma over the range $m/e=1$ to $m/e=200$ showed that the LN-condensable gas was highly pure hydrogen. The mass spectrum ($m/e=1$ to $m/e=200$) for the gases collected in the cryo-cooler from the He/H_2 (90/10%) plasma only showed peaks in the ($m/e=1$ to $m/e=50$) region. The $m/e=2$ peak was 40-50 times more intense than the $m/e=28$ (nitrogen), $m/e=32$ (oxygen), and $m/e=40$ (argon) peaks that were assigned to very trace residual air contamination. Whereas, without the plasma, the mass $m/e=2$ peak was present in only trace concentration ($\sim 10^{-10}$ Torr) compared with the air contaminant gases that were also present in low abundance ($\sim 10^{-9}$ Torr). Von Engel [43] gives the efficiency of production of various common ions at 70 eV and shows that the cross section for the formation of H_2^+ is 10% of that of air contaminants at the same partial pressure. Thus, hydrogen was ~500 times more abundant in the collected gas than air contaminants which may have originated through back-streaming in the mass spectrometer.

From the phase diagram of helium and hydrogen plotted from data given by Lide [44] and extended to lower pressures and temperatures using the Clausius-Clapeyron equation [45], it is not possible to condense ordinary hydrogen below ~50 Torr at 12-17 K. The condensation of a $m/e=2$ gas in the temperature range of 12-17 K at 700 mTorr that was not removed at 10^{-5} Torr indicates that a novel hydrogen gas formed in the plasma reaction between hydrogen and helium. The results are even more dramatic in the case of the condensation of a $m/e=2$ gas in the temperature range of 77 K using the LN cryotrap.

^1H NMR. The ^1H NMR on $CDCl_3$ showed only a singlet solvent ($CHCl_3$) peak at 7.26 ppm relative to tetramethylsilane (TMS) with small ^{13}C side bands. The ^1H NMR on ultrahigh purity hydrogen dissolved in $CDCl_3$ relative to tetramethylsilane (TMS) showed only singlet peaks at 7.26, 4.63, and 1.57 ppm corresponding to $CHCl_3$, H_2, and H_2O, respectively. The chemical shifts of the $CHCl_3$ and H_2O peaks matched the literature values of 1.56 and 7.26 ppm, respectively [46]. The error in the observed peaks was determined to be ± 0.01 ppm. The ^1H NMR spectroscopic results of the control prepared from the reagent helium-hydrogen mixture was the same as that of the high purity hydrogen control.

H_2 has been characterized by gas phase ^1H NMR. The experimental absolute resonance shift of gas-phase TMS relative to the proton's gyromagnetic frequency is -28.5 ppm [47]. H_2 was observed at 0.48 ppm compared to gas phase TMS set at 0.00 ppm [48]. Thus, the corresponding absolute H_2 gas-phase resonance shift of -28.0 ppm (-28.5 + 0.48) ppm was in excellent agreement with the predicted absolute gas-phase shift of -28.01 ppm given by Eq. (12).

The absolute H_2 gas-phase shift can be used to determine the solvent shift for H_2 dissolved in $CDCl_3$. The correction for the solvent shift can then be applied to other peaks to determine the gas-phase absolute shifts to compare to Eq. (12). The shifts of all of the peaks were relative to liquid-phase TMS which has an experimental absolute resonance shift of -31.5 ppm relative to the proton's gyromagnetic frequency [39, 40]. Thus, the experimental shift of H_2 in $CDCl_3$ of 4.63 ppm relative to liquid-phase TMS corresponds to an absolute resonance shift of -26.87 ppm (-31.5 ppm + 4.63 ppm). Using the absolute H_2 gas-phase resonance shift of -28.0 ppm corresponding to 3.5 ppm (-28.0 ppm - 31.5 ppm) relative to liquid TMS, the $CDCl_3$ solvent effect is 1.13 ppm (4.63 ppm - 3.5 ppm) which is comparable to that of hydrocarbons [46].

^1H NMR spectra on sealed samples of condensable helium-hydrogen plasma gases dissolved in $CDCl_3$ relative to tetramethylsilane (TMS) are shown in Figures 6 (a)-(f). The solvent peak was observed at 7.26 ppm, the H_2 peak was observed at 4.63 ppm, and a singlet at 3.22 ppm matched silane. Small ^{29}Si side bands were observed for the latter. The source was determined to be hydrogen-plasma reduction of the quartz tube. The peak was unchanged after three weeks at room temperature. No other silanes, silane decomposition species, or solvent decomposition species were observed even after one month of repeat NMR analysis. Since the plasma gases were first passed through an LN trap before the plasma cell, and the cryotrap was high-vacuum (10^{-6} Torr) capable, no hydrocarbons were anticipated. This was confirmed by mass spectroscopic and FTIR analysis that showed only water vapor in addition to silane as contaminants. Again, the source was determined to be hydrogen-plasma reduction of the quartz tube.

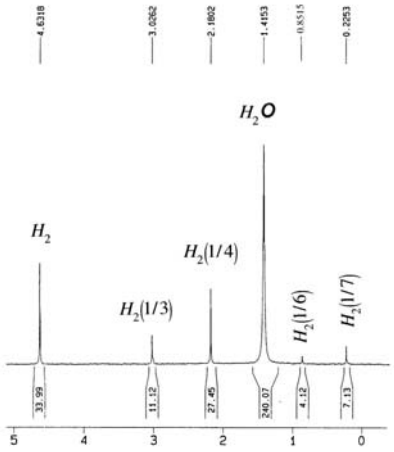

Figure 7. The ^1H NMR spectrum recorded at China Lake on gases from the thermal decomposition of $KH*I$ dissolved in $CDCl_3$ relative to tetramethylsilane (TMS). H_2 and H_2O were observed at 4.63 ppm and 1.42, respectively. Singlet peaks upfield of H_2 were observed at 3.02, 2.18, 0.85, and 0.22 ppm relative to TMS corresponding to solvent-corrected absolute resonance shifts of -29.61, -30.45, -31.78, and -32.41 ppm, respectively. Using Eq. (12),

the data indicates that p = 3, 4, 6, and 7, respectively. The data matched the series $H_2(1/3)$, $H_2(1/4)$, $H_2(1/6)$, and $H_2(1/7)$.

As further shown in Figures 6 (a)-(g), singlet peaks upfield of H_2 were observed at 3.47, 3.02, 2.18, 1.25, 0.85, 0.21, and -1.8 ppm relative to TMS corresponding to solvent-corrected absolute resonance shifts of -29.16, -29.61, -30.45, -31.38, -31.78, -32.42, and -34.43 ppm, respectively. Using Eq. (12), the data indicates that p = 2, 3, 4, 5, 6, 7, and 10, respectively. The data matched the series $H_2(1/2)$, $H_2(1/3)$, $H_2(1/4)$, $H_2(1/5)$, $H_2(1/6)$, $H_2(1/7)$, and $H_2(1/10)$. The molecules corresponding to the reaction product atom $H(1/3)$ with products from further transitions as given in Refs. [2-3] are in agreement with the observed molecules.

^1H NMR spectra were recorded at China Lake and at BlackLight Power, Inc. on ultrahigh purity hydrogen and gases from the thermal decomposition of $KH*I$ dissolved in $CDCl_3$ relative to tetramethylsilane (TMS). These samples were determined not to contain hydrocarbons by mass spectroscopy and FTIR analysis. Only the $CDCl_3$, H_2, and H_2O peaks were observed from the controls. As shown in Figure 7, novel singlet peaks upfield of H_2 were observed from a $KH*I$ -derived sample run at China Lake. The peaks at 3.02, 2.18, 0.85, and 0.22 ppm relative to TMS corresponded to solvent-corrected absolute resonance shifts of -29.61, -30.45, -31.78, and -32.41 ppm, respectively. Using Eq. (12), the data indicates that p = 3, 4, 6, and 7, respectively. The data matched the series $H_2(1/3)$, $H_2(1/4)$, $H_2(1/6)$, and $H_2(1/7)$. The observed products were consistent with those anticipated with the catalysis of *H* by *K* to form $H(1/4)$ and subsequent transition reactions [2-3, 8, 17, 20].

As shown in Figures 6 and 7, the observation of the series of singlet peaks upfield of H_2 with a predicted integer spacing of 0.64 ppm at 3.47, 3.02, 2.18, 1.25, 0.85, and 0.22 ppm identified as the consecutive series $H_2(1/2)$, $H_2(1/3)$, $H_2(1/4)$, $H_2(1/5)$, $H_2(1/6)$, and $H_2(1/7)$ and $H_2(1/10)$ at -1.8 ppm provides powerful confirmation of the existence of $H_2(1/p)$. Furthermore, the ^1H NMR spectra of gases from the thermal decomposition of $KH*I$ matched those of LN-condensable hydrogen. This provides strong support that compounds such as $KH*I$ contain hydride ions $H^-(1/p)$ in the same fractional quantum state p as the corresponding observed $H_2(1/p)$. Observational agreement with predicted positions of upfield-shifted ^1H MAS NMR peaks (Eq. (13)) of the compounds [8, 20, 30-32], catalyst reactions [17, 20, 23-24], and spectroscopic data [17] supports this conclusion.

The existence of novel alkaline and alkaline earth hydride and halido-hydrides were previously identified by large distinct upfield ^1H NMR resonances compared to the NMR peaks of the corresponding ordinary hydrides [20, 30-32]. Using a number of analytical techniques such as XPS and time-of-flight-secondary-mass-spectroscopy (ToF-SIMS) as well as NMR, the hydrogen content was assigned to $H^-(1/p)$, novel high-binding-energy hydride ions in stable fractional principal quantum states [8, 20, 30-32]. Upfield shifts of the novel hydride compounds matched those predicted for $H^-(1/2)$ and $H^-(1/4)$ (Eq. (13)). Novel spectral emission from $H^-(1/2)$ and $H^-(1/2)$, the predicted products from the potassium catalyst reaction and the supporting results of 1.) the formation of a hydrogen plasma with intense extreme ultraviolet (EUV) emission at low temperatures (e.g. $\approx 10^3\,K$) and an extraordinary low field strength of about 1-2 V/cm [9-12, 17-24] or without an electric field or power input other than thermal [21-22] from atomic hydrogen and certain atomized elements or certain gaseous ions that serve as catalysts, 2.) a high positive net enthalpy of reaction [20], 3.) characteristic predicted catalyst emission [17, 23-24], 4.) ~15 eV Doppler broadening of the Balmer lines [17, 23-24], and 5.) inversion of the Lyman lines [23-24] have also been reported previously.

Based on their stability characteristics, advanced hydride technologies are indicated. Hydride ions $H^-(1/p)$ having extraordinary binding energies may stabilize a cation M^{x+} in an extraordinarily high oxidation state as the basis of a high voltage battery. And, a rocketry propellant based on $H^-(1/24)$ to $H_2(1/24)$ may be possible with an energy release so large that it may be transformational. Significant applications also exist for the corresponding molecular species $H_2(1/p)$. The results of this study indicate that excited vibration-rotational levels of $H_2(1/4)$ could be the basis of a UV laser that could significantly advance photolithography.

Power Balance of the Helium-Hydrogen Microwave Plasma In addition to high energy spectral emission as shown in Sec. IIIA and previously [1-5], other indications of very energetic reactions are observed. For example, population inversion has been observed from plasmas which contain atomic hydrogen with the presence of a catalyst [23-26], and selective H broadening with a microwave plasma having no high DC field present was reported previously [13-15]. Microwave He/H_2 and Ar/H_2 plasmas showed extraordinary broadening corresponding to an average hydrogen atom temperature of $80-120eV$ and $110-130eV$, respectively. Whereas, pure hydrogen and Xe/H_2 microwave plasmas showed no excessive broadening corresponding to an average hydrogen atom temperature of <2 eV [13-15]. Only the H lines were Doppler broadened, and this result was shown to be inexplicable by any mechanism based on electric field acceleration of charged species. The observation of excessive Balmer line broadening in microwave driven plasmas as well as other hydrogen-mixed plasmas maintained in glow discharge [10-15] and RF discharge cells [14, 16] as well as unique chemically driven plasmas called resonant-transfer or rt-plasmas [17, 20, 23-24] requires a source of energy other than that provided by the electric field. The formation of fast H only in specific predicted plasmas was explained by a resonant energy transfer between hydrogen atoms and catalysts such as Ar^+ or He^+ of an integer multiple of the potential energy of atomic hydrogen, 27.2 eV [13-15]. Consistent with predictions, noncatalyst plasma mixtures such as Kr/H_2 and Xe/H_2 show no unique features. The observation of the $H_2(1/4)$ rotational lines reported in Sec. IIIAb from Ar/H_2 plasmas but not from Kr/H_2 and Xe/H_2 plasmas also matches predictions.

The excess power of the catalytic reaction was measured by water bath calorimetry. The water bath calorimeter is an absolute standard and indicated $P_{in} = 41.9 \pm 1W$ input power at the selected diode settings for all control plasmas. From these results, power input to the helium-hydrogen plasma was confidently known as the diode readings were identically matched for the controls. For

example, the *T(t)* water bath response to stirring and then with selected panel meter readings of the constant forward and reflected microwave input power to krypton was recorded. Using the corresponding $\dot{T}(t)$ in Eq. (17), the microwave input power was determined to be 41.9 ± 1 W. The *T(t)* response was significantly increased for helium-hydrogen (95/5%). From the difference in the *T(t)* water bath response, the output and excess power of the helium-hydrogen plasma reaction was determined to be 62.1 ± 1 W and 20.2 ± 1 W using Eq. (17) and Eq. (16) with the measured $P_{in} = 41.9 \pm 1W$. The sources of error were the error in the calibration curve (± 0.05 W) and the measured microwave input power (± 1 W). The propagated error of the calibration and power measurements was ± 1 W. Given an excess power of 20.2 W in 3 cm^3 and a helium-hydrogen (95/5%) flow rate of 10.0 sccm, the excess power density and energy balance were high, 6.7 W/cm^3 and -5.4×10^4 *kJ/mole* H_2 (280 *eV / H atom*), respectively.

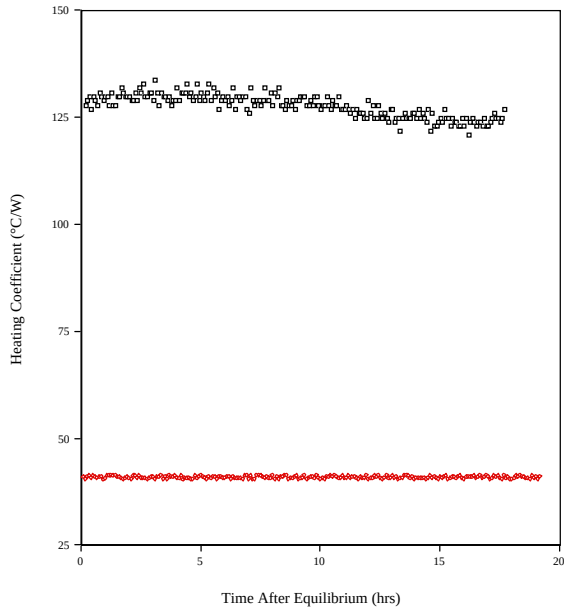

Figure 8. Plot of the heating coefficients versus time. (top) - K_2CO_3 electrolysis with a nickel wire cathode at 83.0 mA and 1.95 V, (bottom) - resistor working in K_2CO_3. The heating coefficient of the heater run (calibration) was 41°C/W.; whereas, the heating coefficient of the electrolysis run was 127 °C/W. The production of excess power of 81.8 mW was observed that was 3.1 times P_{cell} and 75% of P_{appl}.

Isolation and Characterization of $H_2(1/p)$ from Electrolysis Cells. ***Power Balance of the Electrolysis Cells.***

The temperature versus time results of the electrolysis of K_2CO_3 with a nickel wire cathode at 83.0 mA constant current and 1.95 V corresponding to an electrolysis resistive input power, P_{cell}, of 39.0 mW (Eq. (22)) and heater run of K_2CO_3 with 50 mW appear in Figure 8. The heating coefficient of the heater run (calibration) was 41°C/W.; whereas, the heating coefficient of the electrolysis run was 127°C/W. The production of excess enthalpy is observed. The higher the heating coefficient, the more heat released in the process. Using Eq. (31), the excess power, Q_{xs}, was determined to be

$$Q_{xs} = P_{cell}\left(\frac{a_1}{a_2} - 1\right) = 39.0\,\text{mW}\left(\frac{127}{41} - 1\right) = 81.8\,\text{mW} \qquad (34)$$

Thus, the experiment developed an extra 81.8 mW over the input power, P_{cell}, which corresponded to a total thermal power of 3.1 times P_{cell} and 75% of P_{appl}. The Faradaic efficiency of the production of gas by a K_2CO_3 cell and a control Na_2CO_3 cell was 100% within experimental error. The results of excess heat observed only from the K_2CO_3 cell could not be explained by recombination of electrolysis gases as shown previously [49, 50]. The observed heating coefficient of the electrolysis run when Na_2CO_3 replaced K_2CO_3 was 45 °C/W; whereas, the heating coefficient of the heater run (calibration) was 46 °C/W. The production of excess heat was not observed for the control as predicted. Similar excess heat results from K_2CO_3 electrolysis have been reported by Mills [49-51] and others [50, 52].

Neglect, for the moment that $H(1/2)$ can form a diatomic molecule $H_2(1/2)$ and subsequent transitions to lower energy states occur to a substantial extent. From Eqs. (1a) and (1b), 40.8 eV is released per H atom transition to the n = 1/2 quantum state due to catalysis by potassium ions which corresponds to 8 MJ/mole of H_2 [9, 17, 19-20]. In contrast, only 286 kJ is consumed by electrolyzing one mole of H_2O to produce one mole of H_2 (Eq. (15)). Thus, the excess power of 82 mW produced by the K_2CO_3 electrolytic cell as shown in Figure 8 (which also produces 0.43 μ moles of H_2 per second) could be accounted for by the conversion of at most 3.5% of the hydrogen atoms from the n = 1 state to the n = 1/2 state.

^1H NMR of Electrolysis Gases. ^1H NMR spectra on sealed samples of K_2CO_3 electrolytic gases dissolved in $CDCl_3$ relative to tetramethylsilane (TMS) are shown in Figures 9 (a)-(d). The solvent peak was observed at 7.26 ppm, the H_2 peak was observed at 4.63 ppm. No hydrocarbons were anticipated to permeate the nickel tube. This was confirmed by mass spectroscopic and FTIR analysis. For example, the FTIR spectra of the electrolysis gases in the region of the C-H stretching showed no evidence for hydrocarbons. As further shown in Figures 9 (a)-(d), singlet peaks upfield of H_2 were observed at 3.49[1], 2.17, 1.25, 0.86, and 0.21 ppm relative to TMS corresponding to solvent-corrected absolute resonance shifts of -29.14, -30.46, -31.38, -31.77, -and -32.42 ppm, respectively. Using Eq. (12), the data indicates that p = 2, 4, 5, 6, and 7, respectively.

The observed series has implications for the catalysis reactions and the corresponding rates of the formation of atoms $H(1/p)$ and the corresponding molecules $H_2(1/p)$ and their diffusion through the nickel tubing. The product of the catalysis of H by potassium ions is $H(1/2)$ corresponding to the peak at 3.49 ppm shown in Figure 9. Similarly, the product of catalysis of H by K is $H(1/4)$ corresponding to the peak at 2.17 ppm shown in Figure 9 which was the dominant peak. K as the principle catalyst with K_2CO_3 or

[1] The broad increase in the baseline in the region 3.25-3.75 ppm was an instrument artifact.

$K(m)$ as the source was also supported by the observation of characteristic catalyst emission and EUV emission from the corresponding hydride ion having an upfield-shifted ^1H MAS NMR peak at -4.4 ppm as discussed in Sec. IB. Since the products of the catalysis reaction have binding energies of $m \cdot 27.2eV$, they may further serve as catalysts by so called exothermic disproportionation reactions where one atom goes to a lower state (e.g. $n = \frac{1}{2} \rightarrow \frac{1}{3}, \frac{1}{3} \rightarrow \frac{1}{4}, \frac{1}{4} \rightarrow \frac{1}{5},$) while another goes to a higher state [2, 3, 7]. Thus, $H_2(1/p)$ molecules corresponding to the product atoms $H(1/p)$ from further transitions having $p > 2$ or $p > 4$ as given in Refs. [2-3] are anticipated as the reaction products.

As shown in Figures 9 (a)-(d), the observation of the series of singlet peaks upfield at 3.49, 2.17, 1.25, 0.86, and 0.21 ppm with an integer spacing of 0.64 ppm (except for the previously observed 3.02 peak shown in Figure 6) identified as the consecutive series $H_2(1/2)$, $H_2(1/4)$, $H_2(1/5)$, $H_2(1/6)$, and $H_2(1/7)$ provides powerful confirmation of the existence of $H_2(1/p)$.

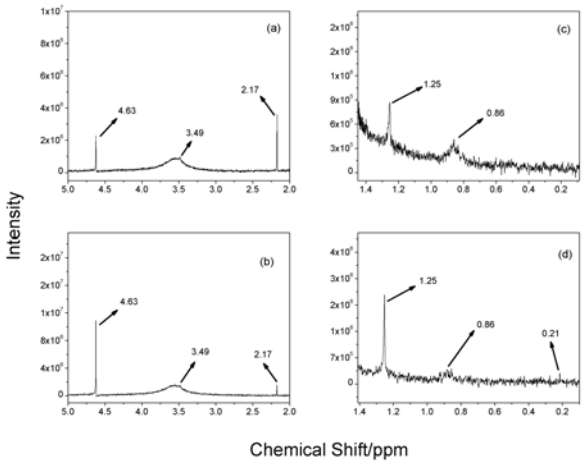

Figure 9. (a)-(d). ^1H NMR spectra on sealed samples of K_2CO_3 electrolytic gases dissolved in $CDCl_3$ relative to tetramethylsilane (TMS). The solvent peak was observed at 7.26 ppm, and the H_2 peak was observed at 4.63 ppm. Singlet peaks upfield of H_2 were observed at 3.49, 2.17, 1.25, 0.86, and 0.21 ppm relative to TMS corresponding to solvent-corrected absolute resonance shifts of -29.14, -30.46, -31.38, -31.77, and -32.42 ppm, respectively. Using Eq. (12), the data indicates that p = 2, 4, 5, 6, and 7, respectively. The data matched the series $H_2(1/2)$, $H_2(1/4)$, $H_2(1/5)$, $H_2(1/6)$, and $H_2(1/7)$.

Mass Spectroscopy of Electrolysis Gases. $H_2(1/2)$ was identified by mass spectroscopy as a species with a mass to charge ratio of two ($m/e = 2$) that has a higher ionization potential than that of normal hydrogen by recording the ion current as a function of the electron gun energy. The mass spectra of the K_2CO_3 and Na_2CO_3 electrolysis gases was obtained over the range $m/e = 1$ to $m/e = 200$. In both cases, the sample contained only hydrogen.

The relative changes in the $m/e = 2$ ion current while changing the electron gun energy from 30 to 70 eV indicated that the K_2CO_3 electrolysis gases has a higher ionization potential than ultrapure hydrogen and Na_2CO_3 electrolysis gases. Upon increasing the ionization potential from 30 eV to 70 eV, the $m/e = 2$ ion current for the controls increased by a factor of about 30%; whereas, the current for K_2CO_3 electrolysis gases collected under liquid nitrogen increased by a factor of about 10 under the same pressure condition as that of the controls.

Conclusion

In this study we made specific theoretical predictions regarding the exothermic reaction to form $H_2(1/p)$ and its characterization and tested them with standard, easily interpretable experiments. The results show that new states of hydrogen are formed by reaction of hydrogen atoms with He^+, Ar^+, and potassium ions and atoms that serve as catalysts but not with control atoms and ions as predicted. The observation of excess enthalpy and the same states of hydrogen, $H_2(1/p)$, from chemicals compound, plasma gases, and electrolysis cells demonstrates the hydrogen catalysis reaction occurs in liquid-solid interfacial environments as well as in the gas phase under a range of reaction conditions. The power results indicate that a new power source based on the catalysis of atomic hydrogen is not only possible, but it may be competitive with gas-turbine combustion. Furthermore, since the identified $H_2(1/p)$ byproduct is stable and lighter-than-air, it can not accumulate in the Earth's atmosphere. The environmental impact of handling fossil fuels and managing the pollution of air, water, and ground caused by the ash generated by fossil fuels or the radioactive waste from a nuclear plant may be eliminated.

Acknowledgments. Special thanks to D. E. Murnick and M. Salvermoser of Rutgers University for providing the 15 keV electron gun. D. C. Harris, Naval Air Warfare Center Weapons Division, Naval Air Warfare Center, China Lake, CA, is acknowledged for suggesting the method of identifying $H_2(1/p)$ by ^1H NMR using $CDCl_3$ solvent. D. C. Harris and L. Merwin are acknowledged for preparing and analyzing a $KH*I$ NMR sample.

References

(1) R. L. Mills, P. Ray, *J. Phys. D: Appl. Phys.*, **2003**, *36*, 1535.
(2) R. L. Mills, P. Ray, B. Dhandapani, M. Nansteel, X. Chen, J. He, *J Mol. Struct*., **2002**, *643* (1-3), 43.
(3) R. Mills, P. Ray, *Int. J. Hydrogen Energy*, **2002**, *27*, 301.
(4) R. L. Mills, P. Ray, J. Dong, M. Nansteel, B. Dhandapani, J. He, *Vib. Spectrosc*., **2003**, *31*, 195.
(5) R. Mills, P. Ray, *Int. J. Hydrogen Energy*, **2002**, *27*, 533.
(6) R. Brunch, P L. Altick, E. Trabert, P. H. Heckmann, *J. Phys. B: At. Mol. Phys*., **1984**, *17*, L655.
(7) R. Mills, *The Grand Unified Theory of Classical Quantum Mechanics*, September 2001 Edition, BlackLight Power, Inc., Cranbury, New Jersey, Distributed by Amazon.com; January (2003) Edition posted at www.blacklightpower.com.
(8) R. L. Mills, "The Nature of the Chemical Bond Revisited and an Alternative Maxwellian Approach," submitted.
(9) R. Mills, J. Dong, Y. Lu, *Int. J. Hydrogen Energy*, **2000**, *25*, 919.

(10) R. Mills, M. Nansteel, P. Ray, *IEEE Transactions on Plasma Science*, **2002**, *30*, 639.
(11) R. Mills, M. Nansteel, P. Ray, *New J. Phys*., **2002**, *4*, 70.1.
(12) R. Mills, M. Nansteel, P. Ray, *J. Plasma Phy.s*, **2003**, *69*, 131.
(13) R. L. Mills, P. Ray, B. Dhandapani, R. M. Mayo, J. He, *J. Appl. Phys.*, **2002**, *92*, 7008.
(14) R. L. Mills, P. Ray, B. Dhandapani, J. He, *IEEE Trans. Plasma Sci.*, **2003**, *31*(3), (2003), 338.
(15) R. L. Mills, P. Ray, *New J. Phys.*, www.njp.org, **2002**, *4*, 22.1.
(16) J. Phillips, C. Chen, "Evidence of Energetic Reaction Between Helium and Hydrogen Species in RF Generated Plasmas," submitted.
(17) R. L. Mills, P. Ray, *Int. J. Hydrogen Energy*, **2003**, *28*, 825.
(18) R. Mills, Int. J. Hydrogen Energy, **2001**, *26*, 1041.
(19) R. Mills, P. Ray, *Int. J. Hydrogen Energy*, **2002**, *27*, 183.
(20) R. Mills, P. Ray, B. Dhandapani, W. Good, P. Jansson, M. Nansteel, J. He, A. Voigt, "Spectroscopic and NMR Identification of Novel Hydride Ions in Fractional Quantum Energy States Formed by an Exothermic Reaction of Atomic Hydrogen with Certain Catalysts," in press.
(21) H. Conrads, R. Mills, Th. Wrubel, *Plasma Sources Sci. Technol*., **2003**, *12*, 389.
(22) R. Mills, T. Onuma, Y. Lu, Int. J. Hydrogen Energy, **2001**, *26*, 749.
(23) R. Mills, P. Ray, R. M. Mayo, *IEEE Trans. Plasma Sci.*, **2003**, *31* (2), 236.
(24) R. L. Mills, P. Ray, *J. Phys. D: Appl. Phys.*, **2003**, *36*, 1504.
(25) R. Mills, P. Ray, R. M. Mayo, *Appl. Phys. Lett*., **2003**, *82* (11), 1679.
(26) R. L. Mills, P. C. Ray, R. M. Mayo, M. Nansteel, B. Dhandapani, J. Phillips, "Spectroscopic Study of Unique Line Broadening and Inversion in Low Pressure Microwave Generated Water Plasmas," submitted.
(27) R. L. Mills, X. Chen, P. Ray, J. He, B. Dhandapani, *Thermochim. Acta*, **2003**, *406* (1-2) 35.
(28) R. L. Mills, Y. Lu, J. He, M. Nansteel, P. Ray, X. Chen, A. Voigt, B. Dhandapani, "Spectral Identification of New States of Hydrogen," submitted.
(29) R. Mills, B. Dhandapani, W. Good, J. He, "New States of Hydrogen Isolated from K_2CO_3 Electrolysis Gases,"submitted.
(30) R. Mills, B. Dhandapani, M. Nansteel, J. He, T. Shannon, A. Echezuria, *Int. J. Hydrogen Energy*, **2001**, *26*, 339.
(31) R. Mills, B. Dhandapani, N. Greenig, J. He, *Int. J. Hydrogen Energy*, **2000**, *25*, 1185.
(32) R. Mills, B. Dhandapani, M. Nansteel, J. He, A. Voigt, *Int. J. Hydrogen Energy*, **2001**, *26*, 965.
(33) R. Mills, E. Dayalan, P. Ray, B. Dhandapani, J. He, *Electrochim. Acta*, **2002**, *47*, 3909.
(34) M. Karplus, R. N. Porter, *Atoms and Molecules an Introduction for Students of Physical Chemistry*, The Benjamin/Cummings Publishing Company, Menlo Park, California, (1970), pp. 447-484.
(35) NIST Atomic Spectra Database, www.physics.nist.gov/cgi-bin/AtData/display.ksh.
(36) H. Beutler, *Z. Phys. Chem*., **1934**, *27B*, 287.
(37) G. Herzberg, L. L. Howe, *Can. J. Phys*., **1959**, *37*, 636.
(38) P. W. Atkins, *Physical Chemistry*, Second Edition, W. H. Freeman, San Francisco, (1982), p. 589.
(39) K. K. Baldridge, J. S. Siegel, *J. Phys. Chem. A*, **1999**, *103*, 4038.
(40) J. Mason, Editor, *Multinuclear NMR*, Plenum Press, New York, (1987), Chp. 3.
(41) J. Wieser, D. E. Murnick, A. Ulrich, H. A Higgins, A. Liddle, W. L. Brown, *Rev. Sci. Instrum.*, **1997**, *6* (3), 1360.
(42) A. Ulrich, J. Wieser, D. E. Murnick, Second International Conference on Atomic and Molecular Pulsed Lasers, *Proc. SPIE*, **1998**, *3403*, 300.
(43) A. von Engel, *Ionized Gases*, American Institute of Physics Press, New York, (1965), pp. 62-64.
(44) D. R. Lide, *CRC Handbook of Chemistry and Physics*, 76 th Edition, CRC Press, Boca Raton, Florida, (1995-6), p. 6-66 and p. 6-140.
(45) I. N. Levine, *Physical Chemistry*, McGraw-Hill Book Company, New York, (1978), pp. 174-175.
(46) H. E. Gottlieb, V. Kotlyar, A. Nudelman, *J. Org. Chem*., **1997**, *62*, 7512.
(47) C. Suarez, E. J. Nicholas, M. R. Bowman, J. Phys. Chem. A, **2003**, *107*, 3024.
(48) C. Suarez, "Gas-phase NMR spectroscopy," *The Chem. Educator*, 1998, 3 (2).
(49) R. Mills, W. Good, *Fusion Technol*., **1995**, *28*, 1697.
(50) R. Mills, W. Good, R. Shaubach, *Fusion Technol*., **1994**, *25*, 103.
(51) R. Mills, S. Kneizys, *Fusion Techno*l., **1991**, *20*, 65.
(52) J. Niedra, I. Meyers, G. C. Fralick, R. Baldwin, "Replication of the Apparent Excess Heat Effect in a Light Water-Potassium Carbonate-Nickel Electrolytic Cell," NASA Technical Memorandum 107167, February, (1996). pp. 1-20.; Niedra, J., Baldwin, R., Meyers, I., NASA Presentation of Light Water Electrolytic Tests, May 15, 1994.

PROTECTIVE COATINGS FOR Pd-BASED HYDROGEN SENSORS

Rodney D. Smith II, Roland Pitts, Se-Hee Lee and Edwin Tracy

National Renewable Energy Laboratory, 1617 Cole Blvd., Golden, CO 80401

Introduction

The ability to detect hydrogen gas leaks economically and with inherent safety is an important technology that will help facilitate commercial acceptance of hydrogen as a fuel source in various applications. The sensors used in these applications must be inexpensive enough for liberal deployment on a hydrogen powered vehicle, and they must be adequately responsive to provide early leak detection so that appropriate action can be taken before the explosive limit in air is reached. NREL has chosen to work on a fiber-optic sensor configuration that represents the best chance of meeting all of these goals (1-4). The fiber-optic approach is the only proposed sensor configuration that meets the criterion of being inherently safe and does not represent a possible ignition source as in other conventional sensor designs powered by electrical means.

The sensor consists of a hydrogen sensitive chemochromic coating at the end of an optical fiber. Chemochromic materials such as tungsten oxide (WO_3) can reversibly react with hydrogen and exhibit significant changes in their optical properties. A thin catalytic over-layer of palladium (Pd) acts as a dissociation catalyst forming atomic hydrogen, which subsequently reacts with the WO_3. Light from a central electro-optic control unit is projected down the optical fiber where it is either reflected from the sensor coating or is transmitted to another fiber leading to a remote optical detector. A change in the reflected or transmitted light intensity indicates the presence of hydrogen. A conceptual schematic of such a sensor is presented in Fig. 1.

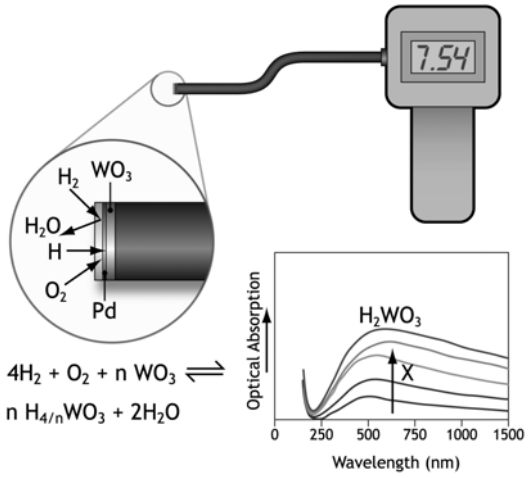

Figure 1. Schematic of fiber optic hydrogen sensor.

Efforts at NREL have been focused on developing a better understanding of the service lifetime and performance issues that will enable thin film hydrogen sensors to be commercialized. These issues have been addressed through real time reliability testing of sensor films as well as sensor fabrication with advanced materials to achieve improved durability in the presence of contaminants.

The main mode of degradation in thin film chemochromic hydrogen sensors is poisoning of the palladium (Pd) catalyst layer by airborne contaminants. Fouling of the Pd surface inhibits the dissociation of hydrogen on the catalyst surface, severely degrading the device. Several protective layers for the Pd film have been investigated, with varying degrees of success. These include films of amorphous carbon deposited by plasma enhanced chemical vapor deposition (PECVD) and spin coated nano-phase anatase titanium dioxide (TiO_2).

Of these, a colloidal suspension of nano-TiO_2 applied as a spin coating offers the best protection. Spin coating produces a thick (approximately 300 nanometers [nm]) porous film that does not impede the diffusion of hydrogen or oxygen to the underlying thin film stack.

The main function of the coating is to maintain the activity of the Pd catalyst surface by a photocatalytic cleaning mechanism. The coating is continuously exposed to ultraviolet (UV) radiation at 365 nm from a UV source. Interaction with UV light causes the TiO_2 particles to form hydroxide radicals on their surfaces from water vapor in the atmosphere. These radicals will subsequently oxidize any contaminants that are adsorbed on the TiO_2 surface. Any contaminants that may diffuse through the coating and occupy sites on the metal surface are also eventually oxidized, converted to a volatile species and escape from the film. Sensor operational lifetimes have been extended to 3 years with this photocatalytic coating. Unprotected sensors will degrade in days or weeks, depending upon the concentration of pollutants in the air.

The photocatalytic properties of TiO_2 have been studied extensively (5-8). TiO_2 has been used for many applications including organic and inorganic catalysis, self-cleaning coatings, and as semiconductor layers in dye sensitized solar cells. However, to the best of our knowledge this material has never been used to maintain the functionality of noble metal-based catalysts or other metal surfaces.

Experimental

Methods for fabrication and the apparatus for testing the sensor films have been described previously (4). Sensor films were deposited by thermal evaporation and all depositions were monitored with a quartz crystal deposition rate monitor. To calibrate the deposition rate monitor, film thicknesses were measured with a stylus profilometer.

Colloidal Anatase TiO_2 Films. TiO_2 colloids were synthesized by a hydrothermal process from an alkoxide precursor such as titanium isopropoxide. The resulting particle size was typically in the range of 15-30 nm. The TiO_2 suspension was then diluted in ethanol to obtain the proper consistency and spin coated at 2000 rpm on the evaporated thin film sensor stacks. The sensors were continuously exposed to 365 nm radiation from a UV pencil lamp under ambient air. Performance was measured periodically using a diode array fiber optic UV/VIS spectrophotometer (Ocean Optics model S2000).

Results and Discussion

TEM/SEM images of the TiO_2 particles and resulting spin coated thin film are presented in Figures 2 and 3. Experiments at NREL have indicated that variations in synthesis temperature, particle size or precursor purity do not significantly alter the effectiveness of the film for this application.

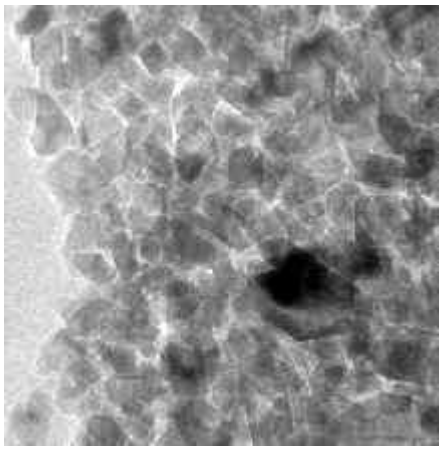

Figure 2. TEM image of colloidal TiO_2 synthesized at 230°C.

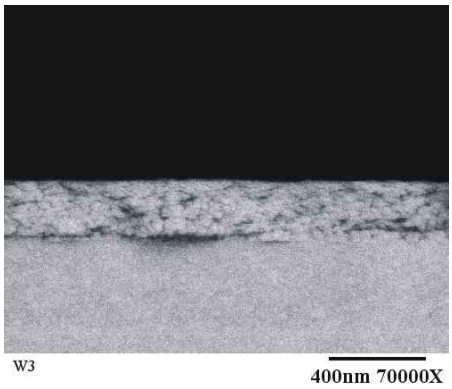

Figure 3. SEM image of spin coated colloidal TiO_2 thin film.

Figure 4 shows typical optical response data for a sensor with the TiO_2 coating. The sensor is still operational at the working detection limit of 0.1% hydrogen after almost 3 years. Figure 5 shows more recent response data for a similar sensor after 1 year of testing.

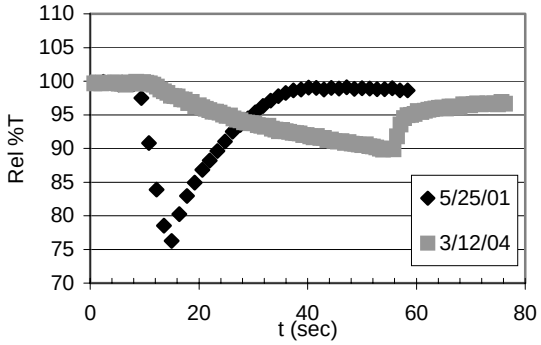

Figure 4. Optical response of thin film $WO_3/Pd/TiO_2$ sensor stack after 3 years of storage in ambient air (0.1% H_2/N_2).

This method of using a photocatalytic TiO_2 layer for prolonging catalyst lifetime could conceivably be carried out with other systems as well (patent filed). While the results presented here describe a continuous thin film of Pd that is protected from contamination,

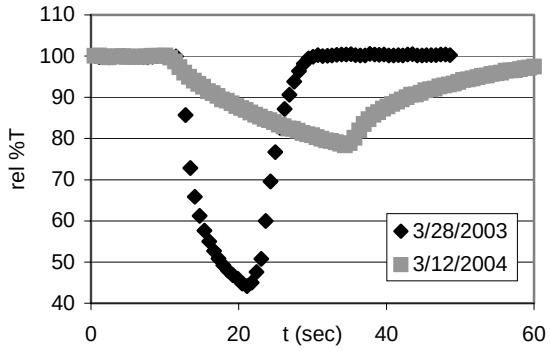

Figure 5. Optical response of thin film $WO_3/Pd/TiO_2$ sensor stack after 1 year of storage in ambient air (0.1% H_2/N_2).

protection could also be obtained on discontinuous metal films as well as metal islands on supported catalysts.

The TiO_2 coating should be equally effective at protecting Pd or other noble metal based catalysts used for hydrogen sensors, maintaining functionality of metal membranes used for hydrogen purification, and preventing poisoning or cleaning fouled supported catalysts used in fluidized beds.

Conclusions

Chemochromic hydrogen sensors have been developed at NREL to indicate the presence of hydrogen by a change in optical properties. Thin film stacks deposited on the end of fiber optic cables can be used to detect hydrogen economically and with inherent safety. The response of these and other Pd-based sensors tends to degrade over time due to the exposure of the catalyst surface to airborne contaminants. A photocatalytic TiO_2 coating has been developed for protection of the Pd catalyst that can prolong the working life of the Pd from days or weeks up to 3 years. This protective coating may have other possible applications where noble metal catalysts are used (fuel cell membrane assemblies, hydrogen separation membranes and industrial catalysts).

This advancement provides the opportunity to greatly simplify the sensor design and to further reduce cost. Future work will concentrate on optimization of the TiO_2 and modification of the technology for use with other systems.

Acknowledgement. This work was supported by the Hydrogen Program of the U.S. Department of Energy under Contract No. DE-AC-36-99-G010337.

References

(1) Benson, D. K., Tracy, C. E. and Bechinger, C. *Proceedings of the DOE Hydrogen Program Meeting Vol. II, Miami, FL,* **1996,** *pp. 605-624.*

(2) Benson, D. K., Tracy, C. E., Hishmeh, G. A., Ciszek, P. A., Lee, S. and Haberman, D. P. *Proceedings of the SPIE International Symposium on Industrial and Environmental Monitors and Biosensors, Boston, MA,* **1998,** *pp. 185-202.*

(3) Benson, D. K., Tracy, C. E. and Bechinger, C. U. S. Patent 5,708,735, **1998**.

(4) Smith II, R. D., Liu, P., Lee, S-H., Tracy, C. E. and Pitts, J. R *Am. Chem. Soc., Div. Fuel Chem.,*, **2002**, *47 (2), pp. 825-827.*

(5) *Photocatalysis Fundamentals and Applications*, Serpone, N. and Pellizetti, E., ed. John Wiley and Sons, New York, **1989**.

(6) Fujishima, A., Watanabe T. and Hashimoto, K.,*TiO_2 Photocatalysis: Fundamentals and Applications*, **1999**.

(7) Fox, M. A. and Dulay, M. T. *Chem. Rev.* **1993**, 93, pp. 341-357.

(8) M. Lisebigler, G. Lu and J. T. Yates Jr., *Chem. Rev.*, **1995**, 95, pp. 735-758.

PLASMATRON NATURAL GAS REFORMING

L. Bromberg, D.R. Cohn, K. Hadidi, A. Rabinovich, N. Margarit, N. Alexeev, A. Samokhin

MIT Plasma Science and Fusion Center
Cambridge MA 02139

Introduction

Low-current plasma discharges have been tested for reformation of natural gas. Experiments were carried out using both homogeneous (non-catalytic) and heterogeneous (catalytic) conditions at power levels of 200 and 700 W. Byproducts of the reforming process were hydrogen, CO, and light hydrocarbons. Hydrogen yields were around 40% for homogeneous conditions with 40% energy efficiency whereas for catalytic reforming it was 70% with an energy efficiency of 90%. In addition, the effect of stratification (inhomogeneous air/fuel mixtures) were investigated. This paper presents comparison between models and experiments carried out with air. Future papers will present results using oxygen-enriched air, and CO_2 enriched-air. Results of modeling that involves simple CFD simulations without combustion have been used to calculate the mixing time. The chemistry is modeled using the Partially Stirred Reactor and Perfectly Stirred Reactor options of Chemkin.

Plasma Reforming. Experimental results of plasma reformation and the reformation setup have been described before[1,2]. The experiments that were modeled were carried with commercial grade natural gas with a power of 250 W, and a flow rate of 0.3 g/s, with O/C ratio ~ 1.1. Although some of the experiments were carried out with a catalyst downstream from the plasma, the results commented in this paper were for homogeneous reforming.

Experimentally it was determined that strong stratification of the air fuel mixture in the plasma zone was required for reaction initiation. Premixed air/methane mixtures could not be started under the conditions tested.

Models for plasmatron methane reforming. To understand the plasmatron reformer several models were developed. They included PFR as well as Partially Stirred Reactor (PaSR).

Ignition delay in the presence of radicals

In order to determine the effect of radicals that are produced by the nonthermal plasma, calculations were performed using CHEMKIN 3.7 Plug Flow Reactor. Multiple radical concentrations were used, with the rest of the well-mixed air/methane mixture. Multiple temperatures were considered. The results from the calculations are shown in Table 1.

Three radical types were used: atomic oxygen (O), hydroxil (OH) radical, and atomic hydrogen (H) radicals, for initial temperatures from 600 to 1000 K. Shown in table 1 is the ignition delay, defined as the time for consumption of 10% of the fuel. However, the reaction, once it starts, is so fast (stiff chemistry) that the 10% assumption is not important.

The results in Table 1 indicate that even very large concentrations of radicals at low temperature do not substantially change the ignition delay. The radical concentration assumed in table 1 is very large, much larger that what could be expected for the conditions of the experiment. From the simulations it is clear the radicals recombine, raising slightly the air/methane temperature. This increase in temperature occurs very quickly (on the order of 10's of microseconds. The slightly increase in temperature is responsible for the relatively small effect in the ignition delay.

Table 1. Ignition Delay Time (In Seconds) For Various Radicals For Multiple Air/Methane Temperatures.

Methane homogeneous ignition delay time (s)

Initial Temperature	600 K	700 K	800 K	1000 K
No radicals	>1000	920	12.5	0.31
[O]=3e-4	>1000	195	4.3	0.23
[O]=3e-5	>1000	515	8.1	0.30
[OH]=3e-4	>1000	290	5.7	0.29
[H]=3e-4	>1000	240	4.9	0.25
[O]=[H]=3e-4	>1000	140	3.5	0.23

Model Using Partial Stirred Reactor

The plasma was modeled by using a high temperature zone that started local reaction and then through mixing carried the reactions to the rest of the air/fuel mixture.

To simulate the inhomogeneities, the PASR model[3] was used. The model allows for control of the mixing time. However, the code has limitation with respect to the number of input streams (two). This places a severe constrain in the capabilities of the model.

It is thought that the effect of the plasma is to raise the local temperature of the air/methane mixture in order to locally ignite the air/fuel mixture. The actual temperature of the local regions is not known. Possible energy distribution are shown in Figure 1. The plasma power requirement is shown in this Figure as a function of the temperature of the hot zone, with the fraction of the hot zone as a parameter. Different fractions of hot-zones (with respect to the total gas flow) are assumed: 1%, 5%, and 10%. As the temperature of the hot zone increases for a given hot-zone fraction, the power required increases. Because of changes of the heat capacity as a function of temperature, the lines are not quite linear (although approximately linear). When the fraction of hot particles increases, the power increases. Figure 1 was calculated for flow rates typical of the plasmatron operation, about 0.4 g/s methane and O/C = 1.

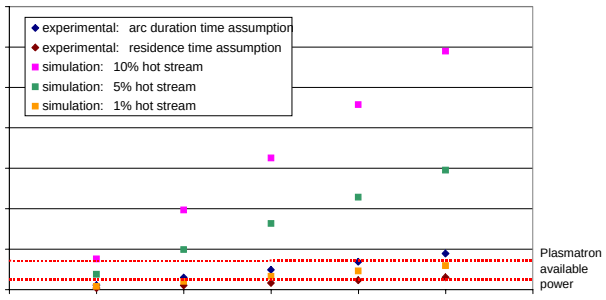

Figure 1. Power requirement as a function of the temperature of the hot zone, for several hot zone fractions.

Calculation of the PASR for the type of hot zone fraction and hot zone temperature shown in Figure 1 are given in Figure 2. These are the results of homogeneous mixture of methane and air, with a fraction of the zones at high temperature, for different ratios of mixing time to residence time, for different values of the hot zone temperature. It is assumed that 10% of the air/methane mixture is in the hot zone.

There is a maximum of the hydrogen production as a function of the ratio between the mixing time and the residence time. This can be understood by realizing that if the mixing is too fast, the hot zone enthalpy is divided with the rest of air/methane, with an increase in temperature but with little reaction. On the other hand, if the mixing time is too long, too many cold zones never get the energy required for reaction initiation, and conversion is poor.

The residence time in the plasmatron region in on the order of 1 ms. Calculations of the mixing time, by both back-of-the-envelope and CFD calculations (in the absence of chemistry), indicate that the mixing time in the plasmatron is on the order of 100 microseconds.

The results are in relatively good agreement with the experiments. However, the power required by the calculations is substantially larger than the one that is determined experimentally. While the calculations assumed about 2.5 kW power (10% as hot zone fraction with a temperature of about 5000 K), the experimental results are obtained at about one order of magnitude smaller powers.

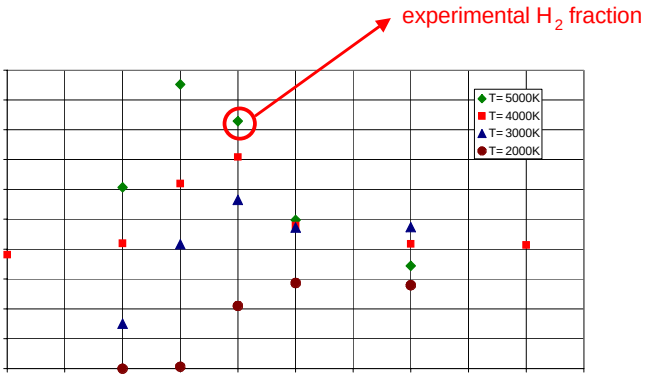

Figure 2. Hydrogen concentration (by mass) as a function of the ratio between the mixing time and the residence time, for residence time of 1 ms. Results are plotted for different temperatures of the hot zone.

Table 2 shows the results from the experiments as well as from the calculations. Because the PASR model in Chemkin does not calculate volume fractions, Table 2 shows mass concentrations. The first row shows the experimentally determined H_2, CO, H_2O and CO_2 mass fractions. The last three rows show the results for the PASR model assuming that a fraction of the particles in the PASR model are at 5000K. The fraction of particles at this temperature is varied from 1% to 10%.

The hydrogen mass concentration is comparable to those in the experiment. However, the measured concentrations of water (experimentally derived from mass balance) CO_2 are substantially higher than in the model.

In addition, the power required for good comparison in the experimentally and calculated values of the hydrogen mass balance (about 5% particles at 5000K) is substantially higher (~1500 W from Figure 1) than the power in the experiment.

We assume that the reason for the difference in the results is due to the limited capabilities of the PaSR model to handle non-uniform air/fuel mixtures,

A recently released version of CHEMKIN 4.0 has substantially enhanced PaSR modeling capabilities, Calculations will be carried out to determine whether better agreement between experiment and the model can be obtained. The greater flexibility in establishing particle distribution functions (PDF's) at user-defined temperatures allows the model to represent closer the experiment. Presently, our understanding of the process is that in a non-uniform air/natural gas mixture the plasma starts the reaction in zones that have O/C ratios that are favorable for reaction (i.e., near stoichiometric combustion). The heat generated in these zones increase the temperature, through mixing, of the other zones. Once hot, reaction in these zones can take place.

Summary

In order to understand the natural gas plasma reformation process, modeling has been undertaken. At the present time we believe that processing requires air/fuel stratification, combustion of a fraction of the fuel in regions of appropriated O/C rations, mixing with the unreacted mixture. This process generates combustion products with energy and fuel loss that may not be recoverable.

The nonthermal plasma processing is good, however, for initial processing of hydrocarbons fuels. Controlled preprocessing with the use of nonthermal plasmas could lead to a decrease in the amount of catalyst required for initial gas preheating, decreasing the problems with hot-spots in the catalyst bed (having the hot spot in the homogeneous zone), and decreasing the amount of carbon formation and decreased methane concentration and free oxygen in the reagents at the location of the catalyst.

Acknowledgement. Support for this work came from ChevronTexaco and ArvinMeritor.

References

(1) *Plasma Catalytic Reforming of Methane*, L. Bromberg, D.R. Cohn, A. Rabinovich and N. Alexeev, *Int. J. Hydrogen Energy* **1999** 24, 1131

(2) *Plasma Reforming of Natural Gas, L. Bromberg et a.*, submitted for publication, *Int Journal Hydrogen Energy.*

(3) Reaction Design, PASR Application User Manual, CHEMKIN Collection 3.7.1, 2003.

Table 2. Comparison of Mass Concentratatino of H_2, CO, H_2O and CO_2 Between Experiment and Calculations, For 250 W Plasma Power and O/C ~ 1, with Natural Gas.

O/C=1 t_{res}=1ms t_{mix}=0.1ms	Power input [kW]	H_2	CO	H_2O	CO_2
Exper. results	0.6	.60%	5.0%	7.0%	4.0%
10% particles @ 5000K	3	.80%	5.7%	1.8%	0.3%
5% particles @ 5000K	1.5	.45%	3.0%	1.0%	0.2%
1% particles @ 5000K	0.3	.03%	0.3%	0.1%	.05%

IN-SITU SPECTROSCOPIC STUDIES OF RHODIUM CATALYZED PRODUCTION OF HYDROGEN FROM DIMETHYLAMINE BORANE. HOMOGENEOUS OR HETEROGENEOUS CATALYSIS?

Yongsheng Chen, John Fulton, John Linehan & Tom Autrey

Fundamental Science Division
Pacific Northwest National Laboratory

Introduction

The US Department of Energy has recently issued a Grand Challenge in Hydrogen Storage.[1] The ambitious goals for volumetric and gravimetric densities and the controlled release of H_2 from materials at temperatures below 80 ºC contained within this Grand Challenge demand the discovery of new materials and catalysts. Our interests in discovery of novel materials for hydrogen storage have led us to examine the chemical and physical properties of amine borane complexes.[2] In previous work we have discovered that both the kinetics and thermodynamics for the dehydropolymerization of ammonia borane (NH_3BH_3) are perturbed when the material is coated into mesoporous silica.[3] These results piqued our interest for catalyst materials which would facilitate N-B bond formation with the concurrent release of hydrogen. Recent work from the Manners group suggested that colloidal rhodium catalyzes the release of hydrogen via dimerization of dimethylaminoborane in solution at room temperature.[4] However, whether the dehydrocoupling and release of hydrogen occurred by a heterogeneous catalytic or a homogeneous catalytic pathway was not conclusively identified. To help elucidate the mechanistic pathway we undertook an *in-situ* spectroscopy approach (XAFS/XANES) to help identify the active catalyst concurrent with ^{11}B NMR studies to follow the kinetics of the reaction. This study demonstrates the utility of *in-situ* XAFS and XANES to differentiate between heterogeneous and homogeneous reaction pathways.

Experimental

The catalyst precursor, $[Rh(1,5\text{-cod})(\mu\text{–}Cl)]_2$ (17mM) and Me_2NHBH_3 (1.1M) were prepared in a solution of toluene in an Ar-purged glove box. The reaction solution was immediately transferred into sealed, 4-cm long glass EXAFS (extended x-ray absorption fine structure spectroscopy) sample holders having Kapton windows on both ends or into a 5 mm NMR tube. The reaction was conducted at 25°C for over 3 hrs. The *in situ* Rh K-edge (23222 eV) EXAFS spectra were collected on the bending magnet beamline (PNC-CAT, Sector 20) at the Advanced Photon Source, Argonne National Laboratory. Data were analyzed using AUTOBK and IFEFFIT routines.[5] The kinetics of Me_2NHBH_3 disappearance were followed using $^{11}B\{^1H\}$ NMR spectroscopyrun unlocked on a Varian VXR-300 NMR spectrometer operating at 96 MHz. Caution: The reactions described release a large amount of H_2 gas and can be exothermic and the gas release can be violent. Proper safety precautions including but not limited to pressure release devices and personal safety equipment should be used.

Results and Discussion

In-situ characterization of the active transition metal catalyst: EXAFS spectroscopy of Rhodium complex. In order to clarify the identity of the active Rh species, a series of *in situ* EXAFS spectra were collected as the solution was evolving hydrogen gas. Upon the initial mixing of the catalyst precursor with the dimethylamine borane solution the initial XAFS spectra shows that the Rh complex rapidly evolves during the first stages of the reactions, undergoing a complete conversion to a new Rh compound in about 20 min. Further, from the heights of the XAFS absorption edges we determine that, during the first 40 minutes of the reaction, the amount of soluble Rh species remains constant (during which 60% of the reaction has occurred). Thus we conclude that the complex at this point corresponds to the active rhodium complex. The spectrum for the active complex in Figure 1 was acquired after 30 minutes of reaction where all Rh was completely soluble in the toluene. Finally, we observe that as the reaction proceeds beyond 40 min, the amount of soluble Rh then steadily decreases until it reaches about 20% of the starting concentration after about 3 hrs of reaction time.

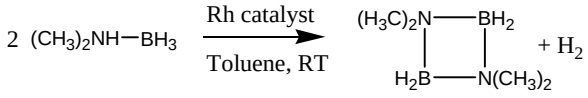

The EXAFS radial structure plot (RSP) for the active rhodium complex is shown in Figure 1, together with that for Rh(0) metal for comparison. The RSP is related to the probability of finding an atom at some radial distance from the central absorbing atom (Rh). The EXAFS backscattering amplitudes for high-Z atoms such as rhodium are uniquely different than those from the low-Z ligands around the rhodium. Hence we can uniquely identify the peak in Figure 1 at about 2.7 Å as belonging to Rh-Rh structures in the active rhodium complex.

As a first approximation, we know that the coordination number is proportional to the peak amplitude in the radial structure plot. The active complex has a Rh-Rh peak amplitude that is about 4 times smaller than that of bulk Rh(0) metal (12 first shell rhodiums). Furthermore, this peak for the active complex, is about 2 times smaller than that for a $Rh(0)_6$ metal cluster.[6] Preliminary EXAFS peak fitting to theoretical standards shows that the active metal contains no more than 4-6 metal atoms in a core cluster surrounded by ligands. As shown in Figure 1 the Rh-Rh distance for the $Rh(0)_6$ metal cluster is the same as for the bulk metal, whereas the one for the active complex is significantly longer by about 0.06 Å. This is evidence that the strong ligand-rhodium interactions in the complex decrease the Rh-Rh interaction and thereby increase the Rh-Rh

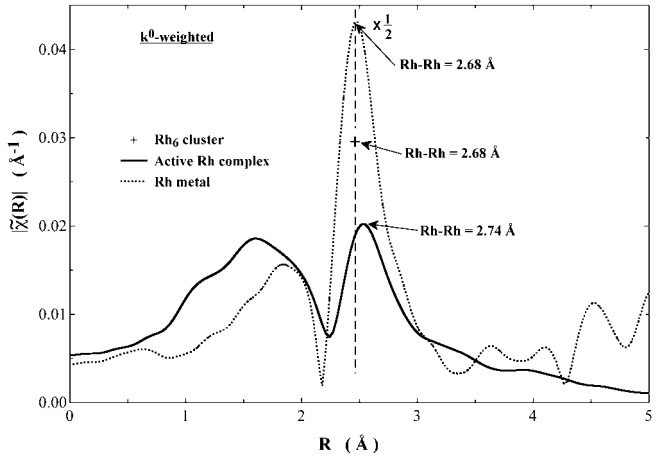

Figure 1. The radial structure plot for the active Rh complex at t=30 min (solid), and for Rh metal (dashed), both without phase corrections. The phase-corrected Rh-Rh distances are listed next to their respective peaks. The (----) vertical line and the (+) symbol locates the distance and amplitude respectively for a $Rh(0)_6$ cluster (from Ref. 6).

distances. The same effect is observed for the $Rh_6(CO)_{16}$ complex.[6] This EXAFS study concludes that the active Rh complex for $[Rh(cod)Cl]_2$ catalyzed Me_2NHBH_3 dehydrocoupling is most likely a Rh (0) cluster with no more than 4-6 core Rh atoms with strongly-bound external ligands. This cluster size is significantly smaller than the 2 nm Rh(0) particles suggested in previous studies.[4]

Kinetics of hydrogen formation in the Rh catalyzed coupling of dimethylamine borane. Solution phase ^{11}B NMR spectroscopy was used to follow the reaction kinetics of the catalyzed dehydrocoupling reaction of Me_2NHBH_3 in toluene to yield the cyclic dimer and hydrogen. In the NMR experiment the solid catalyst precursor and the solid amine borane complex were weighed into the same vial and the mixture taken into the glove box. When toluene was added to the $[Rh(1,5\text{-cod})(\mu\text{–Cl})]_2$/amine borane mixture the solution began to bubble immediately. As shown in Figure 2b the $^{11}B\{^1H\}$ NMR spectra at ca. 50% conversion shows the starting material and the product are the predominate species. The reaction does not appear to generate any significant amount of side products.

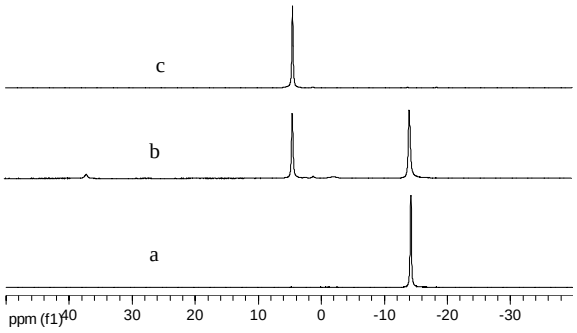

Figure 2. a) The $^{11}B\{^1H\}$ toluene solution NMR spectra of Me_2NHBH_3 (-14.2 ppm) b) at ca. 50% conversion, 30 minutes, c) complete conversion, 200 minutes. The product $[Me_2NBH_2]_2$ (4.4 ppm) grows in over time.

For the kinetic analysis, the area under each peaks was integrated at various times and provides the rates of disappearance of the starting material Me_2NHBH_3 and the appearance of the product dimer $[Me_2NBH_2]_2$. These results are shown in Figure 3.

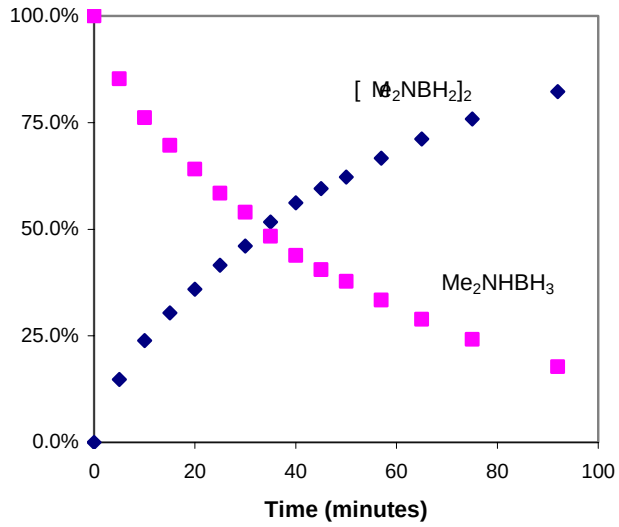

Figure 3. Time evolution of Me_2NHBH_3 disappearance/$[Me_2NBH_2]_2$ appearance in toluene in the presence of rhodium at room temperature as determined by $^{11}B\{^1H\}$ NMR.

Conclusions

The *in-situ* EXAFS experiments permit the observation of the transition metal species during the progression of the reaction. The predominant species observed during H_2 evolution does not appear to be colloidal but most likely is composed of 2 to 6 Rh atoms surrounded by tightly bound external ligands. This result is in contrast to previous conclusions that suggest the mechanism involves a heterogeneous catalyst.

We believe the combination of in-situ EXAFS spectroscopy to identify the active catalyst species and in-situ NMR spectroscopy to monitor kinetics provides a unique approach to answering the elusive question for many reported ambiguities, “Is it homogeneous or heterogeneous catalysis?”[7]

Acknowledgement. The authors wish to acknowledge support from the Laboratory Directed Research and Development Program at the PNNL and the Nano Science and Technology Initiative. Pacific Northwest is operated for the Department of Energy by Battelle. Use of the Advanced Photon Source was supported by the U. S. Department of Energy, Office of Science, Office of Basic Energy Sciences, under Contract No. W-31-109-ENG-38.

References

1 Hydrogen, Fuel Cells & Infrastructure Technologies Program, 2003 Merit Review and Peer Evaluation Meeting, May 19-22, 2003, Berkeley, CA.

2 Gutowski, M., Autrey, T., Prepr. Pap. - *Am. Chem. Soc., Div. Fuel Chem.*, **2004**, *49* (1), 275.

3 Autrey, T., Gutowska, A., Li, L., Linehan, J.C., Gutowski, M., Prepr. Pap. - *Am. Chem. Soc., Div. Fuel Chem.*, **2004**, *49* (1), 150.

4 Jaska, C. A.; Manners, I., *J. Am. Chem. Soc.* **2004**, *126*, 1334. and references cited therein.

5 Newville M. *J. Synchrotron Rad.* **2001**, *8*, 322.

6 Alexeev, O. S.; Panjabi, G.; Phillips, B. L.; and Gates, B. C. *Langmuir* **2003,** *19*, 9494.

7 (a) Dyson, P. J., *Dalton Trans.* **2003**, 2964. (b) Weddle, K. S.; Aiken III, J. D.; Finke, R. G. *J. Am. Chem. Soc.* **1998**, *120*, 5653.

NEW OXYGEN-EVOLVING COMPLEXES IN ARTIFICIAL PHOTOSYNTHESIS SYSTEM SPLITTING WATER INTO OXYGEN AND HYDROGEN

Xiaojun Peng,[1] Feng Shi,[1] Hongyang Li,[1] Rong Zhang,[1] Xiaoqiang Chen,[1] Licheng Sun, [2]* and Björn Åkermark[2]*

[1]State Key Laboratory of Fine Chemicals, Dalian University of Technology, 116012 Dalian, China.
[2]Department of Organic Chemistry, Arrhenius Laboratories, Stockholm University, 106 91 Stockholm, Sweden.

Introduction

Photosynthesis oxygen evolving through water oxidation performed in photosystem II (PSII) of plants and cyanobacteria. The key player in water oxidation is a triad composed of a multimer of chlorophylls (named P_{680}), a redox active amino-acid (named $Tyrosine_z$), and a Mn-cluster composed of 4 Mn ions of high valence (oxygen-evolving complex, OEC). [1] In the past decades, considerable attention has been paid to biomimic the structure of OEC,[2] which resides on the electron donor side of PSII. P_{680} is excited when it absorbs a photon, and transfer an electron to the acceptor system (pheophytin and two quinines Q_A and Q_B). We use the ruthenium(II) *tris*-bipyridine complex as photosensitizer, that plays the role of the P_{680} chlorophyll in PSII. And our former work [3] has been to use the principles of the nature PSII to construct supramolecular complexes in which a photosensitizer is linked to monomeric and dinuclear manganese complexes.

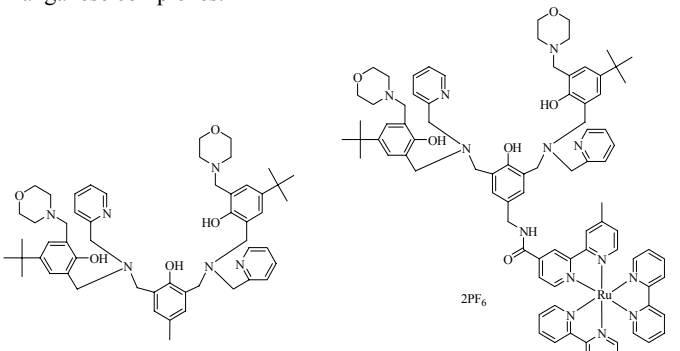

But until now, there are few well-defined molecules which act as catalysts toward water oxidation.[4] Among the very few water oxidation catalysts, the Ru^{III} dimmer and its derivatives are the only materials shown to perform water oxidation function through homogeneous chemical catalysis.[5] As a good alternative model for the electron donor side of photosystem II in green plants, we have prepared dinuclear ruthenium complex **2** and *tris*-nuclear ruthenium supramolecular complex. Introduction of phenolate groups into the ligand instead of some of the pyridyl groups in **1** or **2** can make them possible to coordinate two high valent Ru(III) ions. *tert*-Butyl groups in the ligand not only improves the solubility of complex,[6] but also increases their electron donating effect that may result in lower redox potentials for the Ruthenium. The two "out-standing" arms of morpholine on *tert*-butyl-phenol provide the function of anchoring water via a chain "N---H-O-H---N" by the hydrogen bound function between two nitrogen atoms in morpholine and two hydrogen atoms in H_2O.[7] It is a very important improvement for the reason that the decreasing distance between anchored water and reactive center Ru(III, III) benefits the following water oxidation with less external influence. They will also increase the solubility of the complex and electron donating effect as the *tert*-butyl groups. According to these ideas, two novel complex **1** and **2** in which {[(2-hydroxy-3-(morpholin-4-ylmethyl)-5-*tert*-butylbenzyl)(pyridyl-2-methyl)-amino]-methyl} arms are linked to the *ortho*-positions of the hydroxyl group have been synthesized. And complex **3** was prepared by refluxing the complex 1 and $Ru(DMSO)_4Cl_2$ in MeOH in the presence of NaOAc followed by addition of a saturated aqueous solution of $NaClO_4$.[8] The complex **4** was synthesized by the similar method. We have also studied the properties of these complexes, including electrochemical and photophysical properties. Moreover, we hope that the simplified and explicit model system may offer mechanic insight into elucidation of electron transfer coupled with proton transfer involved in photosynthetic water oxidation.

Results and Discussion

Absorption and Emission Properties. For the simple dinuclear ruthenium complex **3**, there is almost no absorption between 400~500 nm in the visible region and there are two weak absorptions at λ_{max} = 290 nm ($\varepsilon = 9.5 \times 10^3\ M^{-1}\cdot cm^{-10}$) and 340 nm ($\varepsilon = 4.5 \times 10^3\ M^{-1}\cdot cm^{-10}$). The UV-Vis absorption spectrums of complex **2** and **4** essentially have similar features to those of Ru *tris*-bipyridine compounds. The main absorption band between 400~500 nm arises from MLCT (the metal to ligand charge transfer M→π*L). The intense absorption peak at 288 nm is due to LC (a ligand center transition π→π*). In compound **2**, the emission maximum locates at 627 nm, is red-shifted compared to that of $Ru(bpy)_3$ and the radiative quantum yield (Φ_r) is 0.082 while the Φ_r of $Ru(bpy)_3$ is 0.062.[11] The red-shift of the MLCT band and the higher luminescence quantum yield compared to $Ru(bpy)_3$ are caused by the different ligands in the compounds. In **2**, the bipyridine ligand with an amide group has a lower energy than the unsubstituted ones, thus the MLCT state may involve this ligand that may result in the small red-shift of the MLCT band. Moreover, in the presence of ruthenium no change was observed in the absorption maximum and only a small red shift (<5 nm) in the emission maximum. However, the emission intensity was much lower for the *tris*-ruthenium compounds than for the corresponding ruthenium complex.

Electron transfer. All the complexes investigated were photooxidized in laser flash photolysis experiments in the presence of the external acceptor methyl viologen [$MV(PF_6)_2$]. Even the short-lived states of **4** could be effectively photooxidized to Ru^{III} if the concentration of viologen was high as 0.2 M. In complex **2** or **4**, the negative absorption at 400~500 nm is due to the $Ru^{(II)}$ ground state bleaching. Two positive absorption bands with the maximum at 600 and 398 nm, are assigned to the absorption of $MV^{\cdot+}$. Formation of the $MV^{\cdot+}$ indicates the oxidative quenching of the Ru(II) ^{3}MLCT excited state by MV^{2+}. According to the emission kinetics of Ru(II) ^{3}MLCT at 640 nm, giving a pseudo-first-order quenching rate constant of $2.5\times10^7\ s^{-1}$. The lifetime of 1.27 μs for complex **2**, so 97 % of photoexcited Ru(II) was oxidized to Ru(III) under such condition. And from the **Fig. 1**(a), we can see no decay of $MV^{\cdot+}$

absorption when the recovery of Ru(II) complete. This result shows that the regeneration of Ru(II) is due to the intramolecular electron transfer from the substituted phenols to the photooxidized Ru(III), rather than the electron recombination from the $MV^{\cdot+}$. The ET rate constant in complex **2** determined from the 470 nm trace was 2.5×10^6 s^{-1}, which is almost two orders of magnitude faster than the ET rate of *ca.* 10^4 s^{-1} in the compound without substitute on the tyrosine moiety. From the above results, we conclude that the introduction of an amine, morphine and a pyridine would increase the electron-donated ability of Ph-OH.

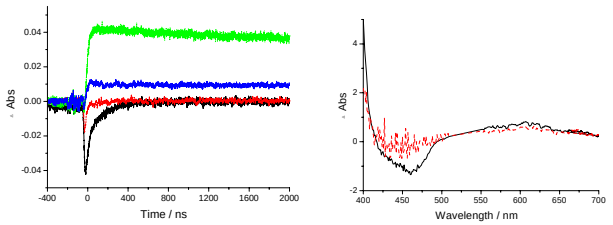

a b

Figure 1. Transient absorption changes after excitation at 532 nm for complex **2** and **4** in the presence of 200 mM methyl viologen (MV^{2+}): (a) increased absorption at 600 nm due to the formation of $MV^{\cdot+}$ (upper curves) and bleaching of the Ru(II) ground state at 470 nm (lower curves). (b) Transient absorption spectra at 100 ns after excitation for complex **2** and **4**. The spectra were normalized at 600 nm (the complex **4** spectra was multiplied by 2) to facilitate comparison of the spectra shapes.

In complex **4**, the Ru^{II} recovery was clearly much faster than the $MV^{\cdot+}$ decay. From a comparison of the signal amplitude in **Fig. 1**(a), it is clearly that most of Ru^{II} recovery occurred within the time of *ca.* 20 ns. According to fitting the kinetics of 470 nm trace, 80 % of the Ru^{II} recovery occurred with $k > 5.5 \times 10^7$ s^{-1}. We attribute this to intramolecular electron transfer from the $Ru_2^{III,III}$ moiety, probably generating the $Ru_2^{III,IV}$ or $Ru_2^{IV,IV}$ complex. The remaining, slower recovery seen at 470 nm occurred with the same rate as that in complex **2** ($k = 2.5 \times 10^6$ s^{-1}) may be the partly dissociation of Ru.
It is important to note in **Fig. 1**(b), the (normalized) transient absorption spectra at 400 ns after excitation for complex **2** and **4**, the very rapid Ru^{II} recovery in **4**, which is not observed in complex **2**, which lacks dinuclear Ru, suggested that electron transfer form the ruthenium complex moiety to the photogenerated Ru^{III} occurs with a rate constant of $k > 5.5 \times 10^7$ s^{-1}.

Electrochemistry. Electrochemical properties of **2, 3, 4** were studied by cyclic voltammetry (CV) and differential pulse voltammetry (DPV) in acetonitrile. DPV of **2** obtain the typical waves of the metal and the reduction of the three ligands in $Ru(bpy)_3^{2+}$ moiety: an quasi-reversible oxidation wave at $E_{1/2} = 0.986$ V *vs* $Fc^{+/0}$ (ΔE = 80 mV), due to Ru^{3+}/ Ru^{2+} for **2**, and three quasi-reversible reductive waves ($E_{pc1} = -1.601$ V, $\Delta E_1 = 38$ mV; $E_{pc2} = -1.862$ V, $\Delta E_2 = 21$ mV; $E_{pc3} = -2.142$ V, $\Delta E_3 = 38$ mV *vs* $Fc^{+/0}$ respectively) due to the three bipyridine ligands. In CV, the oxidation peaks of the three bipyridine ligands are smaller than the reduction peaks, but there are also three equal peak heights of redox waves in DPV. In addition to these waves, the peak at *ca.* 0.52 V *vs* $Fc^{+/0}$ obtained from DPV is probably related to the phenol oxidation since it is close to the reported peaks of phenol oxidation in $Ru(bpy)_3$-tyrosine compound in acetonitrile. [3a] The peak at *ca.* -1.0 V *vs* $Fc^{+/0}$ is due to an impurity present in the electrode which is adsorbed on to the electrode. The CV of complex **3** shows two reversible oxidation waves ($E_{1/2}$ = 0.554, 0.765 V *vs* $Fc^{+/0}$), and two reversible reduction waves ($E_{1/2}$ = -0.849, -1.099 *vs* $Fc^{+/0}$). DPV shows these well-resolved peaks. The compound **3** is a dinuclear ruthenium (III,III) complex, so these four voltammetric waves could be assigned to two subsequent oxidations ($Ru_2^{III,III} \rightarrow Ru_2^{III,IV}$ and $Ru_2^{III,IV} \rightarrow Ru_2^{IV,IV}$). In addition to these waves above, there are two small revisable peaks at 0.384 and 0.511 V *vs* $Fc^{+/0}$. These reactions may involve the oxidation of tertiary amine and phenol groups.

For the mononuclear $[Ru(bpy)_3]^{2+}$ complex **2**, the Ru^{II} to Ru^{III} is 0.906 V. This is decreased to -1.099 V for the $Ru_2^{II,II}$ to $Ru_2^{II,III}$ and -0.853 V for the $Ru_2^{II,III}$ to $Ru_2^{III,III}$. The difference for the redox potential may be due to the introduction of *tris*-phenolate group. And in complex **3**, the $Ru_2^{III,IV}$ can easily performed, the potential is only at 0.765 V. Furthermore, although the redox potentials of dinuclear Ru moiety in CV of complex **4** are not clear, the DPV have these four well-resolved peaks, which are close to the Ru moiety in complex **3**. The result also shows in the complex **4**, the Ru in the photosensitizer could oxide the dinuclear $Ru_2^{III,III}$ to $Ru_2^{III,IV}$ and $Ru_2^{IV,IV}$, which is important for the water oxidation.

Acknowledgment. This work was financially supported by the "973 program" Ministry of Science & Technology of China and National Natural Science Foundation of China (Project 20376010 and 20128005).

References

1. Sun, L.; Hammarström, L.; Åkermark, B.; Styring, S., *Chem. Soc. Rev.*, **2001**, *30*, 36-49.
2. a) Pecoraro, V. L.; Baldwin, M., Gelasco, A.; *Chem. Rev.*, **1994**, *94*, 807-826. b) Kitajima, N., Singh, U. P., Amagai, H., Osawa, M., Moro-oka, Y. J., *J. Am. Chem. Soc.*, **1991**, *113*, 7757-7758. c) Chen, C., Huang, D., Zhang, X., Chen, F., Zhu, H., Liu, Q., Zhang, C., Liao, D., Li, L., Sun, L.. *Inorg. Chem*., **2003**, *42*, 3540-3548. d) Mukhopadhay, S., Armstrong, W. H.. *J. Am. Chem. Soc*., **2003**, *42*, 3540-3548. e) Gupta, R., MacBeth, C. E., Young, V. G., Borovik, A. S.. *J. Am. Chem. Soc*., **2002,** *124*(7), 1136-1137.
3. a) Sun, L., Burkitt, M., Tamm, M., Raymond, M. K., Abrahamsson, M., LeGourrierec, B., Frapart, Y., Magnuson, A., Kenez, P. H., Brandt, P., Tran, A., Hammarström, L., Styring, S., Åkermark, B.. *J. Am. Chem. Soc.*, **1999**, *121*, 6834-6842. b) Sun, L., Raymond, M. K., Magnuson, A., LeGourrierec, B., Tamm, M., Abrahamsson, M., Kenez, P. H., Marttensson, J., Stenhagen, G., Hammarström, L., Styring, S., Åkermark, B.. *J. Inorg. Biochem.*, **2000**, *78*, 15-22. c) Abrahamsson, M. L. A., Baudin, H. B., Tran, A., Philouze, C., Berg, K. E., Raymond-Johansson, M. K., Sun, L., Åkermark, B., Styring, S., Hammarström, L.. *Inorg. Chem.*, **2002**, *41*(6), 1534-1544.
4. Yagi, M., Kaneko, M.. *Chem. Rev*., **2001**, *107*, 21-36. b) Ruttinger, W., Dismukes, G. C.. *Chem. Rev.*, **1997**, *97*, 1-18.
5. Ramaraj, R., Kiva, A.. *Chem. Lett.*, **1987**, *264*, 261-266. b) Binstead, R. A., Chronister, C. W., Ni, J., Hartshorn, C. W., Meyer, T. J.. *J. Am. Chem, Soc*., **2000**, *122*, 8464-8472.
6. Lomoth, R., Huang, P., Zheng, J., Sun, L., Hammarström, L., Åkermark, B., Styring, S.. *Eur. J. Inorg. Chem*., **2002**, 2965-2974.
7. White, D. J., Laing, N., Miller, H. A., Parson, S., Coles, S., Tasker, P. A.. *Chem. Commun.,* **1999**, 2077-2078.
8. Lomoth, R., Magnuson, A., Xu, Y., Sun, L. *J. Phys. Chem*., **2003,** *107*(22), 4373-4380.
9. Miller, H. A., Laing, N., Parsons, S., Parkin, A., Tasker, P. A., White, D. J.. *J. Chem. Soc. Dalton Trans*., **2000**, 3773-3782.
10. Adams, H., Bailey, N. A., Fenton, D. E., Papageorgiou, G. J.. *J.Chem. Soc. Dalton Trans.*, **1995**, 1883-1885.
11. Casper, J. V., Meyer, T. J.. *J. Am. Chem. Soc.,* **1983,** 105, 5583-5591.

NON-THERMAL PLASMA CATALYTIC CONVERSION OF METHANE TO SYN-GAS

Chiranjeev Kalra[1], Young Cho[1], Alexander Gutsol[1], Alexander Fridman[1], Tecle S Rufael[2]

[1] Drexel Plasma Institute, Drexel University, Philadelphia, PA19104
[2] ChevronTexaco Energy Technology Company, Houston TX 77042

Introduction

Syn-gas, a mixture of hydrogen and carbon monoxide, is used as a major intermediary for the production of hydrogen or other hydrogen based chemical compounds like ammonia, liquid fuels, solvents etc. Commercially syn-gas production from methane or lower hydrocarbons can be carried out in a number of ways: steam reforming, thermo-catalytic reforming, partial oxidation, etc. [1]. Syn-gas formed via endothermic reactions (steam and CO2 reforming) requires high-energy input. The simplest and most efficient way for the large scale production would be partial oxidation of hydrocarbons [1]. The partial oxidation of hydrocarbons in air is usually described by idealized equation as:

$$C_nH_mO_p + x\,(O_2 + 3.76N_2) \rightarrow n\,CO + m/2H_2 + 3.76(n/2\text{-}p)\,N_2 \quad [\text{when, } x = (n/2\text{-}p)] \quad (1)$$

Increase in x from (n/2-p), for rich mixtures, increases heat of reaction but at the same time produces carbon dioxide and water vapor thus reducing the amount of syn-gas generated. The oxygen to fuel ratio (x) determines the heat of the reaction and amount of syn-gas generated. For this process Nickel (Ni) has traditionally been used as catalyst, but problems concerning to bulky catalyst volume, catalyst poisoning and high maintenance costs have limited application to large scale industrial operations.

The use of highly active electrical discharges (plasmas) for this conversion has been experimented with and studied numerically during the last decade, but traditional plasma systems cannot simultaneously provide high power density, for large scale industrial output, and chemically selective conversion process [2]. Broader understanding of electrical discharge physics resulted in development of newer class of discharge systems, which fall in the category of transitional discharges, looks very attractive for the above application [3]. These are discharges with plasma parameters between those of the thermal and cold non-thermal discharges called the transitional non-thermal discharges, where the gas temperature increases considerably (2000 – 3000 K) but the discharges still are not in the thermal regime [4]. Gliding Arc is an example of such transitional discharges can be achieved in Gliding Arc (GA) reactor.

Experiments and Numerical Modeling of the Process

A large-scale laboratory experimental unit for Gliding Arc in Tornado (GAT) assisted syn-gas generation was developed at Drexel Plasma Institute. GAT is an advanced Gliding Arc (GA) system developed by the authors where GA plasma is stabilized inside a Reverse Vortex Flow, and has many advantages over traditional systems as reported in [5] and [6]. This unit had 3 important components: (1) GAT reactor with heat exchanger, (2) Power supply and (3) Instrumentation.

GAT reactor design [3], based on cylindrical geometry, generates transitional plasma in a volumetric continuous flow reactor providing uniform flow treatment. Reverse Vortex Flow (RVF), which is very similar to the natural tornado, is set up inside the reactor. It has a circular disc shaped electrode and a spiral electrode both are arranged such that they are locally parallel to the streamlines thus causing minimum disturbance to the gliding arc. These two electrodes in RVF are in effect diverging electrodes in the "plane" of the flow. Reverse vortex flow provides perfect thermal insulation of the discharge zone form the reactor walls at the same time intense convective cooling of the arc. Also there is a recirculation zone near the exit. Here the active species from the plasma zone are retained inside the reactor [5]. This recirculation is very important for plasma-catalytic reactions. Heat exchanger is employed for internal heat recuperation, as this conversion process is exothermic for methane. DC power supply from Voltronics (10kV, 1A maximum) is used to generate GA plasma inside the reverse vortex reactor. Inlet flow controllers, thermocouples to measure temperature at heat exchanger, and analyzers for CO, CO_2, H_2, GC/MS for hydrocarbons from C_1 – C_5 and out-flow meter complete the instrumentation of the apparatus.

The modeling was done in ChemKin using zero dimension assumption and GRI 2.11 mechanism of kinetic scheme with 65 species and 200 reactions, including low temperature reactions.

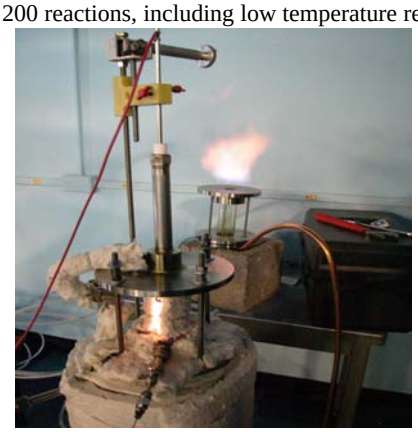

Figure 1. Experimental GAT reactor fired at equivalence ratio 4, in the background syn-gas produced is burned before disposal.

Results and Discussion

Experiments in different regimes were conducted. For same equivalence ratio, different flow rates and flow configurations were tried. The most optimal and stable of the cases is for tangential entry of methane and axial air inlet, with minimum flow rate of methane at about 0.35 L/S for the present system. In fact the Reverse Vortex configuration it self is very effective in flame stabilization and experiments for methane conversion with out any plasma power gave stable combustion zone, but not very good conversion to syn-gas. Temperatures reach as high as 750 K at entry to the plasma reactor. Tangential methane and axial air in reverse vortex form a rotating central column of plasma and flame. The zone is cooled by intense flow around it and is simultaneously insulated from any heat losses to the surrounding by the same reverse vortex. Tangential methane ensures dissociation of methane in plasma and not air thus ensuring no NOx emissions.

The data collected from experimental tests and analyzed for mass balance. The secondary data thus obtained: the conversion degree (methane conversion to syn-gas) and energy cost analysis were plotted vs. the equivalence ratio.

Conversion Degree is a good measure of the system performance and evaluation as shown in **Figure 2**. Numerical results (curve in fig 2) show that the conversion is best for equivalence ratio 3.0 to 3.6, and not 4.0. This is because of the fact that as we go to lower equivalence ratio we have higher heat in the system.

This heat helps achieve better conversion and reaction rates. Experimental points as shown in **Figure 2** are in good agreement with the numerical results.

Electrical Energy is added to the system in the form of plasma power. Plasma acts as a catalyst and thus this power should be optimized. We should not spend too much power on one hand and lesser power should not restrict the extent of reaction on the other.

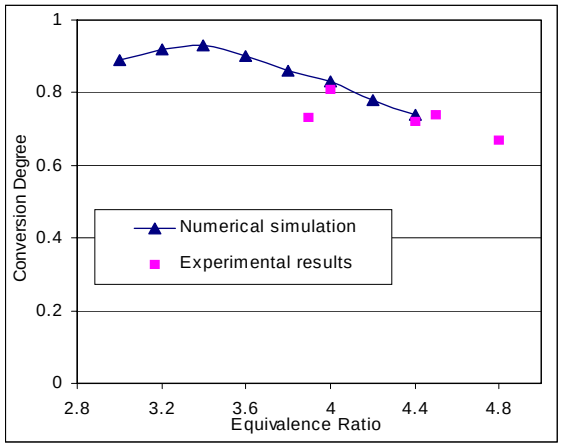

Figure 2. Conversion degree as a function of equivalence ratio

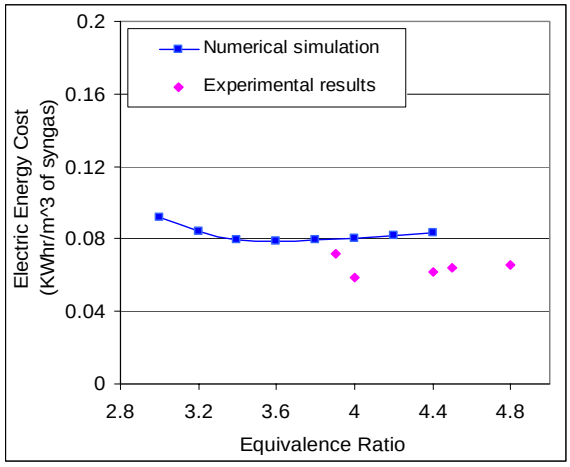

Figure 3. Electric Energy Cost as a function of equivalence ratio

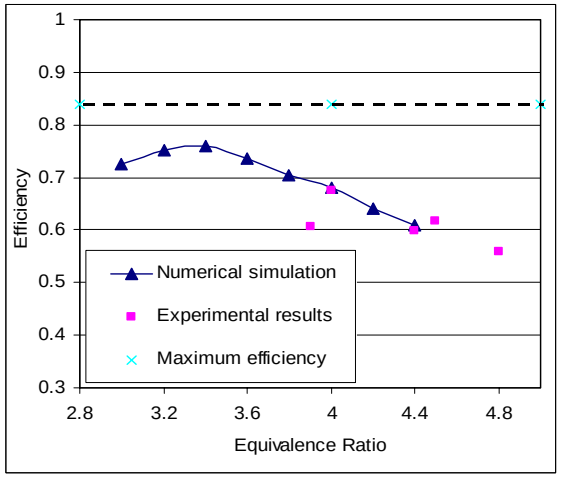

Figure 4. Efficiency as a function of equivalence ratio

As in **Figure 3,** At high equivalence ratio the heat of the system is low so more plasma power is required. But as we decrease the equivalence ratio we need lesser power and we achieve a minimum power level, which again rises as production rates start decreasing rapidly. Comparison with Experimental results reveal similar trend. Experimental values of power required are just lower this signifies the importance of reverse vortex geometry and positive impact of recirculation.

Total Energy cost: This represents the amount of energy spent to get 1-meter cube of syn gas. This includes electrical energy cost in KW-hr and the energy spent in the form of methane, which is a fuel, so can be interpreted in terms of KW-hr energy equivalent for producing 1 meter cube of syn-gas. Similarly the syn-gas produced is again a fuel so its equivalent in KW-hr is our output. The ratio of these energy equivalents spent and produced gives a very accurate efficiency of the system. Theoretically the maximum efficiency of such a system can never be more than 84%, because syn-gas gas lower heat value than methane. This efficiency as function of equivalence ratio is expressed in **Figure 4**. Energy cost is optimal between equivalence ratio 3.2 and 3.8.

Conclusions

Experimental system built for syn-gas production from hydrocarbon fuel was tested and evaluated based on various production parameters as stated above. Syn-gas was generated in this continuous volumetric flow reactor pilot plant at output of about 1.1 L/S. Electric energy spent in the process was as low as 0.06 KW-hr/m^ 3 of syn-gas. High chemical process selectivity is obtained using GAT. GC/MS analysis of the reactants shows no production of C2 to C5 hydrocarbon species.

The experimental system worked predominantly at higher equivalence ratio. This was due to the fact that since methane flow was driving the arc there was a lower limit to this flow rate. Lower equivalence ratio can be achieved by designing fine nozzle for gas injection. The system can run continuously without the need of any maintenance, as there are no consumables, electrode erosion or cooling requirements. In fact the reverse vortex burner stabilizes flame at very high equivalence ratio without any combustion support. In that case we have very low conversion to syn-gas and high soot formation. This result signifies the importance of selectivity of chemical processes that can be achieved by plasma catalysis.

References

(1) Jean Marie, Iulian Rusu, 2001 J. Phys. D: Applied Phys. 34, Pg. 2798-2803.

(2) Sobacchi M.G., Saveliev A.V, Fridman A.A, Kennedy L.A, Ahmed S, Krause T. 2002, International Journal of Hydrogen Energy 27, Pg. 635-642.

(3) C. S. Kalra, M. Kossitsyn, K. Iskenderova, A. Chirokov, Y. I. Cho, A. Gutsol, A. Fridman, Electronic Proceedings of 16th International Symposium on Plasma Chemistry, Taormina, Italy, June 22-27, 2003. ISPC-565.pdf.

(4) A. A. Fridman, L. Kennedy "Plasma Physics and Engineering" (Taylor & Francis, accepted for publication in 2003).

(5) Gutsol A. F. and Kalinnikov V. T. Reverse-Flow Swirl Heat Insulation of Plasma and Gas Flame. (High Temperature, Vol. 37, No. 2, 1999, pp. 172 - 179.)

(6) Gutsol A. Thermal Insulation of Plasma and Flame in Reverse Vortex. In: Progress in Plasma Processing of Materials 1999. Editors: Pierre Fauchais and Jacques Amouroux. Begell House, Inc., NY, 1999. (Proceedings of the Fifth International Thermal Plasma Processes Conference, St.-Petersburg, July 13-16, 1998) P. 81 - 86.

ACID LEACHING OF COAL AND COAL-ASH: KINETICS AND DOMINANT IONS

Mehtap Paul[a], Meryem Seferinoglu[b], Gul Asiye Ayçik[c], Åke Sandström[d], and Jan Paul[e]

[a]Turkish Atomic Energy Authority, Ankara Nuclear Research and Training Center, 06100 Besevler-Ankara, Turkey**.** *Present address:* Luleå University of Technology, Division of Process Metallurgy, 971 87 Luleå, Sweden.

[b]Luleå University of Technology, Division of Physics, 971 87 Luleå, Sweden *, Permanent Address:* MTA, Mineral Research and Exploration Directorate, 06520 Balgat-Ankara, Turkey

[c]Turkish Atomic Energy Authority, Ankara Nuclear Research and Training Center, 06100 Besevler-Ankara, Turkey

[d]Luleå University of Technology, Division of Process Metallurgy, 971 87 Luleå, Sweden

[e]Luleå University of Technology, Division of Physics, 971 87 Luleå, Sweden, phone +46-920-491973, fax +46-920-491074, email jan.paul@sirius.luth.se

Introduction

Acid leaching is an alternative to the conventional stabilization of ash by carbonatization or polymer induced coagulation/flocculation [1-3]. It has also been suggested that ash can replace limestone in biohydrometallurgical processing [4, 5]. Dissolved metals can be recovered from the effluent in the down-stream stages of a bioleaching process. Metals extracted at delocalized units, i.e., in separate acid leaching processes, precipitated and shipped to the main biohydrometallurgical plant as hydroxides or sulfides. The above scenario is threefold beneficial: (i) it saves limestone in the hydrometallurgical processing of sulfidic minerals, (ii) it recycles metals and (iii) it creates an inert solid ash residue. All three come with economic as well as environmental gains. The acid consumption in ash/water slurries (pH 1.0, initial S/L ratio 1:10) starts at a modest 5 L 1 M H_2SO4 per kg dry peat fly-ash and reaches 15 L /kg for bottom-ash from the combustion of wood chips and 18-24 L/kg for ash from lignites [4, 5]. Mn and Mg are regularly leached to near unity, but the yields of other dominant elements - K, Na, Al and Fe - vary, probably due to the presence of stable oxides.

The current work shows the time dependencies of acid consumption and elemental compositions in the aqueous phase for four ashes and the kinetics of acid consumption of an additional 10 coal-ashes and whole coals. Time dependent studies can link acid consumption to the dissolution of major ash components and correlate trace element extraction to the destabilization of certain major phases [6]. This is the topic of a subsequent paper [7]. The current work forms a platform to discuss residence times and process designs for an industrial process.

Experimental

Coals. 13 Turkish coals were selected [5]. The majority of the coals were also included in the MTA project 'Türkiye Linyitlerinin Teknolojik ve Kimyasal Özellikleri Envanteri Projesi' (*Eng. Project for the inventory of technological and chemical properties of Turkish lignites*) [8, 9].

Untreated Ashes. Ash from the combustion of sawmill residues was collected at the Fränsta plant (http://www.angeenergi.se) and used as received [4]. Ashes from lignite combustion of lignites were prepared from the untreated fuels as described [5]. 'As prepared' ashes were analyzed by ICP-AES/MS/SMS (Analytica AB, www.sgab.se, procedure MG-2 plus additional elements). Our untreated ashes resemble, with respect to the metal content, the primary fly-ash, rather than the secondary fly-ash, used in a previous leaching study of ash from a waste incineration unit [17].

Acid Consumption. Dry ash was mixed (solid : liquid 1 : 10, by weight) with deionized water (Millipore Milli-Q, >18 MΩcm) and the slurry stirred overnight (> 12 h). pH was reduced to 1.0 by the addition of 1 M H_2SO_4 (VWR International, *pro analysi*). pH was maintained by the subsequent additions of 1 M sulfuric acid. We report the accumulated acid vs. time.

The results of akin experiments with whole coals are also reported. The coals were dried in air for 24 h at 40 EC and ground in a ball mill [5]. We selected the 250-1000 µm fraction for the present experiments.

Time Dependence. A homogenized batch of ash was divided into 8 or 16 samples, each weighing around 5.0 g. Some experiments were also performed with batches of around 50 g ash. One sample, at a time, was mixed with deionized water (S/L 1:10) and stirred as described. Within minutes the pH was lowered to 1.0 and maintained by the subsequent additions of 1 M H_2SO_4. Leaching was terminated by the separation of effluent and solid residue after 30 min (Munktell OOR filter paper). Filtration was completed within 30-40 s. The volume of the effluent was measured and a sample taken aside for ICP-AES/MS/SMS analysis (Analytica AB, www.sgab.se, procedure V3a plus additional elements). The experiment was then repeated for a new stopping time, with a fresh sample from the homogenized batch. We report analyses of the aqueous phase after 30 min, 1 h, 2 h, 4 h, 8 h, 16 h and 32 h of leaching. The results are compared with the results from our previous screening study of maximum extraction, i.e., with the concentrations after 10 days of continuous leaching in sulfuric acid at pH 1.0 [4, 5].

Results

Time Dependence of Acid Consumption. The accumulated volume of 1 M H_2SO_4 is needed to maintain pH 1.0 in coal and coal-ash slurries at 25 EC. With initial solid / liquid ratios of 1:10, which represent an upper limit. We have not varied this ratio, but assume from literature that it can be reduced to ca. 1:5 without altering the data [18]. The results for whole coals are displayed after division with the fraction of non-combustible material. The 'ash' fractions were taken from our small-scale preparations rather than averaged bulk values [5]. The 'ash' fraction do carry some uncertainty and we find it superficies to base discussion on changes in the inorganic portion of coal during combustion solely on a comparison of absolute acid consumption values. The time dependencies of whole coals and coal-ashes are markedly different. Initially, the whole coals consume acid very rapidly, but the consumption cease after less than 1/2 a day. Coal-ashes are characterized by a smaller initial acid consumption, followed by a second slower stage, extending over several days.

Initially, significant gas quantities evolved when acid was added to the slurry with ash from Fränsta. This leads to enhanced agitation and is an indication of strong carbonatization in the untreated ash. Little gas evolved during the leaching of ash from Silopi, Yata□an and Tunçbilek.

Leaching of Elements. We have analyzed the behavior of four ashes in detail: one wood-ash (Fränsta), two lignite-ashes (Mu□la-Yata□an and Kütahya-Tunçbilek) and one asphaltite-ash (Silopi). Table 1 gives the concentrations of dominant elements in the

untreated. Our analysis is based on the concentrations of ions in the aqueous phase and anomalous values X > 1 stem from samples variations and analysis uncertainties. We neglect silicon/silicic acid in solution [4, 5, 19, 20].

Discussion

Acid is consumed when parts of the untreated ash are dissolved. There is a time dependence during the first 32 h of leaching. We derive the amounts of sulfuric acid and compare these with the measured amounts of sulfur in solution. We also calculate the corresponding amounts of consumed protons from the concentration of Ca^{2+}, Fe^{3+}, K^{+}, Mg^{2+}, Na^{+}, PO_4^{3-}, Al^{3+} and Mn^{2+} in solution. This is a simplified model for the neutralizing capacity of ash [21], but it works to illuminate the role of different ash components and some anomalous behavior.

Sulfur in the solid residue is very well correlated to the concentration of Ca, Ba and other elements forming insoluble sulfates [4], but the consumption of acid is poorly explained solely by the formation of sulfate residues. Fränsta has a high neutralizing capacity, but a low concentration of sulfur in solution due to the formation of gypsum - only 12 % of Ca is dissolved after extended times. Fränsta has literally no sulfur in the untreated ash. Other metals from major components - Fe, K, Mg, Na, P, Mn - are leached to between 80 - 100 %. Aluminum alone is leached to a lesser degree (68 %). This indicates the presence of stable, Al containing (complex) ceramics, possibly the result of the combustion process.

Yatagan has a high sulfur concentration in the untreated ash, and the concentration in the solid phase increases further by about 50 %, following leaching in sulfuric acid. Ca appears to form insoluble $CaSO_4$, with only 18 % dissolved. Other elements, notably Fe, K and Na, are leached to less than 50 %, again indicating stable oxides, and we note that clays and other stable minerals are mined with the organic phase. Mn and Mg are leached completely, as expected of the carbonates and simple oxides.

Tunçbilek is actually depleted of sulfur during leaching in sulfuric acid. Ca, not very abundant in the untreated material, is almost completely extracted during leaching. Significant portions of other elements - Fe, K, Na, Al - remain in the solid phase, a strong indication that stable minerals are mixed with combustible phases, in the fuel. The current ashing temperature, 550 EC, is suitable for trace element studies and does not promote the formation of mixed oxides during combustion [5, 22]. Mg and Mn are again leached to near completion.

Finally, Silopi untreated ash is rich in sulfur, and the level increases by 30 % during leaching. Ca is leached to 23 % and Mn and Mg to near unity, but Fe, K, Na and Al are only dissolved marginally. Again stable minerals (clays, feldspars etc.) [23], mined together with the organic material, may explain the low figures.

Coals vs. Coal-ashes. Positively identified is a different time dependence for the acid leaching of coals and coal-ashes. Initially, coals consume acid at a very high rate. Within the first few minutes 60-87 % of the acid is spent, so we could not resolve details of the time dependence for this portion of the experiments. We note that Mg and Mn are leached to high percentages and there is no apparent difference between coals and coal-ashes [5]. The remaining acid is consumed during the next 3-9 h. No acid was added to the coal slurries after 10 h. We interpret the above as the dissolution of relatively small grains of inorganic material supported on a very permeable organic matrix. This agrees with the dispersion of clay minerals as finely dispersed inclusions in the coal [24].

The maximum extraction of aluminum is always higher after ashing than in the ground whole coals [5]. We suggest the possibility that the organic phase shields aluminum containing oxides from the surrounding aqueous phase. It is known from catalysis that carbonaceous residues readily form on such surfaces [25, 26]. This translates to high surface energies and makes it plausible to suggest that the organic phase in coals wets the surfaces of minerals with a high aluminum or iron content.

Silopi asphaltites are different from lignites. Only 42 % of the total acid is consumed within the first minutes and the following slower period stretches over a much longer time than 10 h. The 'ash' content - 36 % - is higher than for any of the lignites [5], which makes it feasible that the leaching is influenced by ground minerals. A different and lower permeability may also influence the time dependence [27, 28]. Silopi asphaltites are known to be denser and less fissured than Turkish lignites (MTA Geology Dept.).

The data motivates a residence time of 10 h for coals with particle sizes in the 250-1000 μm range. 10 mm particles will increase the necessary residence time with a factor 2-5, i.e., to 1-2 days [29], but current lumps for domestic use in Turkey, 18-50 mm, may give inconveniently long leaching times.

Kinetics of Ash Leaching. The kinetics of acid consumption for ashes indicated an initially fast process, followed by a slower period, possibly extending longer than 10 days (14400 min). Below, we analyze acid consumption as well as the concentration of ions from dissolved major ash components - Ca, Fe, K, Mg, Na, P, Al and Mn - in the two regimes.

The neutralizing capacity of the ashes, phrased as the total charge of ions in solution can be seen as well as the parallel behavior of acid consumption and the total charge of Ca^{2+}, Fe^{3+}, K^{+}, Mg^{2+}, Na^{+}, PO_4^{3-}, Al^{3+} and Mn^{2+} ions. We choose to display values for 16 h as well as 32 h. Note that neither set includes the initial 30 minutes. It is clear that the dissolution of different solid components are responsible for the neutralizing capacity during the initial contact (< 30 min) and the extended leaching (30 min - 16/32 h). It is likewise clear that the ashes of wood and coals are different.

Fast Regime. The initial neutralizing capacity of ash from sawmill residues (Fränsta) is dominated by Ca, K and Mg. This is a general observation for biofuels: straw, hard- and softwood, and in particular bark [30, 31], but the high neutralizing capacity is not found in peat [4]. The observed gas evolution indicates a high concentration of carbonates in the untreated ash. Time dependent data for Ca, K and Mg shows that the concentration of these ions quickly reach stable values, corresponding to the very rapid dissolution of Ca, K and Mg compounds. Whereas K and Mg are stable in solution, calcium and sulfate ions favor gypsum formation. The atomic ratios for dissolved Fränsta ash in the initial period (< 30 min) were Fe/Al 1 : 6, K/Al 15 : 1 and Na/Al 2 : 3. This reflects the ratio between simple oxides and carbonates rather than the stoichiometry of complex ceramics. Complex ceramics with Al are expected to form at combustion temperatures above 800 EC [32].

Yatagan and Tunçbilek are similar with respect to major components and represent ash from lignite combustion. The initial neutralizing capacity comes from Ca, Mg and Al. Ca and Mg quickly reach stable concentrations, at intermediate levels, but the Al fraction in solution continues to increase. We suggest the possibility of a mixture of Ca, Mg and Al compounds in the untreated ashes, but note that particle size distributions as well as solubilities will effect the profile [33-36]. The tentative second phase containing Ca and Mg is hardly leached, but the second Al containing phase is dissolved at a slow pace.

Silopi ash constitutes its own entity, separate from bio-ash or ash from lignites. The initial neutralizing capacity comes from Ca and Mg. Mg is almost completely dissolved after a short contact time, but Ca reaches an intermediate level, suggesting the possibility of two calcium containing phases in the untreated ash, one stable and one easily dissolved.

Slow Regime. As the initial phase passes, the center of importance for the neutralizing capacity shifts to new compounds in the ashes. Mg and K are still important for sawmill residues (Fränsta), but many elements contribute with Mn dominating. Momade and Momade observed a similar profile for Mn leaching from manganese oxide ore, and extended the study to the positive effects of methanol addition (< 40 %), stronger acids (< 0.3 M), higher temperatures (< 170 EC) and smaller particles (< 32 μm) [37]. Manganese carbonates are abundant in coals [38], but our data suggests that other forms also are present in the ashes.

There is a time dependence for the fraction (X) of dissolved magnesium and aluminum, interpreted by the (simplified) solution to the Elovich equation [35, 37, 39]:

$$X = a \bullet \ln(t) + b \qquad (1)$$

Lignite-ashes from Yatagan and Tunçbilek constitute a separate group. Al and Fe are dominant contributors in the 30 min - 32 h regime and the time dependencies are well modelled by a SCM process [7]. We use the expression for a product layer / diffusion controlled process [34]:

$$1 - 3 \bullet (1-X)^{2/3} + 2 \bullet (1-X) = c \bullet t \qquad (2)$$

in agreement with previous studies [37] and note that self-inhibition by the precipitation of gypsum or $MnSO_4$ as diffusion barriers, have been reported [39-41]. The above expression gives a better fit than expressions for a surface controlled process [34]. We have not exploited more elaborate idioms [36, 39], nor models for surface reaction and diffusion controlled processes [34, 42].

We conclude that the neutralizing capacity of lignite-ash in the 30 min - 32 h regime is controlled by the dissolution of particles. During the first few hours magnesium is still dissolved, but this ceases, while iron and aluminum continue to be leached. Sodium and potassium are leached, but it is unclear if the ratio of cations in a tentative mineral with aluminum can be derived.

[36, 39], nor models for surface reaction and diffusion controlled processes [34, 42].

We conclude that the neutralizing capacity of lignite-ash in the 30 min - 32 h regime is controlled by the dissolution of particles. During the first few hours magnesium is still dissolved, but this ceases, while iron and aluminum continue to be leached. Sodium and potassium are leached, but it is unclear if the ratio of cations in a tentative mineral with aluminum can be derived.

The Fe/Al atomic ratio for dissolved Yatagan lignite-ash was 1:7 in the initial period (< 30 min) as well as during the extended leaching regime (30 min - 32 h). Only small amounts of potassium (K/Al 3:100) and sodium (Na/Al 2:100) were leached after the first 30 min. The Fe/Al ratio for dissolved Tunçbilek lignite-ash was 1:5 at all times, i.e., during the initial (< 30 min) as well as the extended (30 min - 32 h) leaching period. The K/Al ratio was 10:100 (approx.) and the Na/Al ratio 2:100 towards the end of the 'slow regime', down from K/Al 20:100 (approx.) and Na/Al 10:100 in the initial period. These values may be compared with the stoichiometries of common minerals [43].

The fixed Fe/Al ratio suggests dissolution of a clay mineral (illite) [24, 43-45]. We can not discern the presence of montmorillonites, a class of iron containing clays, which swell in water, due to their sheet-like structure. This makes them feasible as inherent (liquefaction) catalysts, either by sulfidation of the metals in the coal or by adsorbing metal ions from aqueous solutions, followed by treatment in H_2S [46].

The Fe/Al ratio of elements leached from Silopi asphaltite-ash changed from 1:10 during the initial (< 30 min) period to 1:2 after 32 h. The altered ratio infers that more than one mineral is leached, albeit with comparable yields. Mn and Mg follow similar profiles, but the ratio to Al is not constant, nor to Fe. We suggest a combination of clay and carbonate association [24, 43, 44]. The initial K/Al and Na/Al ratios for Silopi were both 1:5, but diverged to slightly higher potassium concentration and slightly lower sodium concentration after 16 h or 32 h. Na occurs in several minerals [43], but association is sometimes difficult to discern [45]. Potassium and sodium containing clays are abundant, but feldspars have also been observed [23].

Whereas carbonates are expected to contribute mainly in the 'fast regime', clays and feldspars dissolve slowly. Complex oxides, with well defined structures and stoichiometries, are formed at high temperatures and observed as narrow areas in phase diagrams. These structures have high resistance to leaching. The effect is well illustrated by aluminum minerals. Aluminum was extracted to near 100 % from Bayerite / $Al_2O_3 \bullet 3H_2O$ in sulfuric acid [36]. More complex aluminum/silicon oxides showed higher stability. Kaolinite / $Al_2O_3 \bullet 2SiO_2 \bullet 2H_2O$, one common clay mineral in coal [24], was leached effectively after calcination at 500-600 EC, i.e., conditions similar to the present ashing procedure [36]. Illite / $K_2O \bullet 3Al_2O_3 \bullet 6SiO_2 \bullet H_2O$ was leached to a lower percentage, again after calcination [36]. Finally, mullite / $3Al_2O_3 \bullet 2SiO_2$, the most stable aluminum silicate and a typical product after high temperature treatment, i.e., in ash residues from power plants, showed high resistivity to sulfuric acid leaching [36, 47]. Feldspars - alkali, (K, Na)$AlSi_3O_8$, and plagioclase, $NaAlSi_3O_8$ to $CaAl_2Si_2O_8$, - constitute additional, often stable minerals [43]. These minerals are observed as minority phases in coal [24]. We note that crystallinity is a key factor [48] and poor crystallinity/amorphous material [45] and prolonged wetting [49] may significantly alter extraction yields.

Mg and P are major contributors to the neutralizing capacity of Silopi asphaltite-ash and, together with manganese, dissolved to high percentages. Other elements - Al, Na, Fe and K - contribute less to the neutralizing capacity, but are still leached according to a SCM / diffusion model, except during the initial hour [7]. It appears that the initial regime extends to 1 h, compared with 30 min or less for the lignite-ashes. A similar knee was observed in the graphical representation of Al, Fe and Mg dissolution in sulfuric acid from waste incineration fly-ash [17].

We note that acid consumption during leaching of Silopi 'whole coal' was different than acid consumption during akin leaching of lignite whole coals and we suggest that more original mineral matter contribute for Silopi asphaltite-ash than for Yatagan and Tunçbilek lignite.

Whole Coal' Processing. Acid washing of whole coals is motivated when no aftertreatment of flue gases or ash residues is feasible, i.e., for domestic heating in less developed countries. Improved design of stoves is important (http://www.laowan.com), but the long lifetime of such units leaves no alternative to improved fuel quality [50]. Catalytic gas conversion [51, 52] is not a realistic option in the areas where low rank coals are the dominant fuel for domestic heating.

Our results show that 10 h of leaching (1 M H_2SO_4, 25 EC) gave a near complete removal of acid-consuming parts of 12 Turkish lignites (whole coals). The results were obtained for 250-1000 μm size particles. Literature indicates 2-5 times longer time for 10 mm particles [29]. Continued tests need to refine these claims in bench or pilot plant operations of feasible process designs [5, 53]. Current commercial lumps (in Turkey 18-50 mm) should be tested, but indications are that the necessary combustion tests must address the effects of an altered particle size distribution (to < 10 mm), as well as heating values and the quality of flue gases and ash residues. Simultaneous acid leaching and biodesulfurization of coal in the

bioleaching stage of a process for metal production from sulfidic concentrates may be of interest.

Acid washing of whole coals is also of interest for preprocessing before liquefaction. During coal liquefaction the coal structure is thermally decomposed in the presence of hydrogen. Atomic hydrogen terminate thermally broken carbon-carbon bonds. Atomic hydrogen is produced on metalsulfide (Mo, Co, Ni, W, Fe) catalysts and, pending the dispersion of the catalyst, either used directly or carried by a transporting molecule to the organic part. Catalyst precursors are commonly adsorbed as metal ions from aqueous solutions, thus preferentially on polar sites, and then sulfided.

Removal of a large fraction of the 'ash' part, by acid leaching, will remove many polar sites, apart from the organic structure, and thus shorten the diffusion path of atomic hydrogen. Removal of non-combustible phases will also enhance the permeability [54] during the liquefaction process, and limit the volume of solid residues. Acid preprocessing, followed by normal hydrotreatment, constitutes an alternative to unconventional supercritical processing [28].

Conclusions

Extraction kinetics indicated that lignites are ideally suited for direct acid leaching (H_2SO_4, pH 1.0, 25 EC). We estimate that 2 days constitute a suitable time for the preparation of 'clean' coals (< 10 mm) for domestic use. Asphaltites require considerably longer residence times.

Lignites are ideally suited for treatment in the biological oxidation stage of a hydrometallurgical process for the production of metals from sulfidic concentrates. The biocatalyzed oxidation of sulfidic minerals is also one and the same reaction as biodesulphurization of coals. Coals, washed in the bioleaching stage, will emerge with lower sulfur, 'ash' and trace element contents. The washed product is intended for domestic stoves. Two technical obstacles remain and need to be addressed: (i) the low neutralizing capacity of coal require 5-10 times larger masses compared with CaO and (ii) readsorption and precipitation onto the washed coal must be prevented.

Lignite- and asphaltite-ashes consume acid during ca. 10 days. We discern a 'fast regime' ending after 30 min and dominated by the release of Ca, Mg, K and Al ions, probably from carbonates and simple oxides, but possibly also from small particles or poorly crystalline complex minerals and oxides. A second, 'slow regime' for ashes is well modelled by a diffusion limited shrinking core (SCM) process. Several minerals contribute to the neutralizing capacity in this regime and we observe the leaching of Fe, Al, K, Na and Mn.

Acknowledgement. We thank our colleagues Agah Köker and Selami Toprak from MTA in Ankara for discussions on coal pretreatments. We also thank Ömer Ünver from TKI Türkiye Kömür Isletmeleri Kurumu *(Eng. Turkish Coal Enterprises*) for his continued interest in our work and Michael L. Smith, Anabolic Laboratories, Phoenix/AZ for his careful reading of the manuscript. Last, but not least, we acknowledge Vattenfall AB and Ånge Energi for their support of our project.

References

(1) Querol X., Uma□a J.C., Alastuey A., Ayora C., Lopez-Soler A., Plana F., Fuel 2001; 80; 801
(2) Chandler A.J., Eighmy T.T., Hartlén J., Hjelmar O., Kosson D.S., Sawell S.E., van der Sloot H.A., Vehlow J., Municipal Solid Waste Incinerator Residues, Study in Environmental Science 67 (Elsevier, 1997, Amsterdam)
(3) Katsuura H., Inoue T., Hiraoka M., Sakai S., Waste Management 1996; 16; 491
(4) Paul M., Sandström Å., Paul J., Journal of Hazardous Materials (submitted)
(5) Seferino□lu M., Paul M., Sandström Å., Köker A., Toprak S., Paul J., Fuel 2003; 82; 1721
(6) Harris W.R., Silberman D., Environ. Sci. Technol. 1983; 17; 139
(7) Paul M, Seferinoglu M., Aycik G.A., Sandström Å., Paul J., Fuel (submitted)
(8) MTA Enstitüsünce Bilinen Türkiye Yeralti Kaynaklari Envanteri, No.168, (MTA, Ankara, 1977), *in Turkish*
(9) Tuncal2 E., Çifci B., Yavuz N., Toprak S., Köker A., Ayçik H., Gençer A., Sahin N., Chemical and Technological Properties of Turkish Tertiary Coals, (MTA, 2002, Ankara)
(10) TMMOD, 2000'li Yillarda Ulusal Enerji Politikalari, TMMOD Elektrik Mühendisleri Odas2 Birli□i, December 1999, p.93, *in Turkish*
(11) Karayigit A.I., Whateley M.K.G., Int.J.Coal.Geol. 1997; 34; 131
(12) Gayer R.A., Karayigit A.I., Goldsmith S., Onaçak T., Rose M., Proceedings 8th Austalian Coal Science Conference, (Australian Institute of Energy, 1998, Toukley)
(13) Querol X., Alastuey A., Plana F., Lopez-Soler A., Tuncali E., Toprak S., Ocakoglu F., Köker A., Int.J.Coal.Geol. 1999; 41; 311
(14) Toprak S., Alpagut-Dodurga (Osmancik - Çorum) Bölgesi Çevresindeki Kömürlerin Olusum Ortamlari ve Özelliklerinen Belirlenmesi' (*Eng. Determination of depositional environments and properties of coals located in the vicinity of Alpagut-Dodurga (Osmanc2k - Çorum) region)*, Doctoral Thesis, (Hacettepe University, 1996, Ankara), *in Turkish*
(15) Atamer H., Derman D., Özdil G., 1975, Güneydogu Anadolu Bölgesi Asfaltit Küllerinden Molibden, Nikel, Vanadyumun ve Uranyumum Kazan2lmas2, M.T.A. Enstitüsü Teknoloji Dairesi Radyoaktif ve Nadir Metaller Teknoloji Servisi, Ankara, *in Turkish*
(16) Atamer H., Özdil G., Essiz R., Durmus H., 1979, Güneydogu Anadolu Bölgesi Asfaltit Küllerinden Molibden, Nikel ve Vanadyumun Kazanilmasi Amaciyla Liçing Ara□t2mas2, MTA 6636, M.T.A. Enstitüsü Teknoloji Dairesi Radyoaktif ve Nadir Metaller Teknoloji Servisi, Ankara, *in Turkish*
(17) Nagib S., Inoue K., Hydrometallurgy 2000; 56; 269
(18) Vitolo S., Seggiani M., Filippi S., Brocchini C., Hydrometallurgy 2000; 57; 141.
(19) Iyer R., Journal of Hazardous Materials B 2002; 93; 321
(20) Jia C.Q., Xiao J.Z., Orr R.G., J. Environ. Sci. Health, Part A: Toxic/Hazardous Substances & Environmental Engineering 1999; 34; 1013
(21) Jinying Y., Moreno L., Neretnieks I., J. Environ. Sci. Health, Part A: Toxic/Hazardous Substances & Environmental Engineering 1998; 33; 923
(22) Finkelman R.B., Palmer C.A., Krasnow M.R., Aruscavage P.J., Sellers G.A., Dulong F.T., Energy & Fuels 1990; 4; 755
(23) Karayi□it A.I., Querol X., Energy Sources 2002; 24; 703
(24) Stach E., Mackowsky M.Th., Teichmüller M., Taylor G.H., Chandra D., Teichmüller M., Stach's Textbook of Coal Petrology, 2nd Ed., (Gebrüder Borntraeger, 1975, Berlin), pp. 122
(25) Gray M.R., Zhao Y., McKnight C.M., Komar D.A., Carruthers J.D., Energy & Fuels 1999; 13; 1037

(26) Manju C.S., Lalithambika M., Nair V.N., Clays and Clay Minerals 2001; 49; 355
(27) Clarkson C.R., Bustin R.M., Int. J. Coal Geol. 1997; 33; 135
(28) Erol M., Demirel B., To□rul T., Çal2ml2 A., Fuel Proc. Technol. 1995; 41; 199
(29) Couch G.R., Advanced Coal Cleaning Technology, CR/44 (IEA Coal Research, 1991, London)
(30) Steenari B.M., Schelander S., Lindqvist O., Fuel 1999; 78; 249
(31) Obernberger I., Biedermann F., Widmann W., Riedl R., Biomass and Bioenergy 1997; 12; 211
(32) Steenari B.M., Lindqvist O., Biomass and Bioenergy 1998; 14; 67
Beloborodov V.V., Voronenko B.A., Inzhenerno-Fizicheskii Zhurnal 1997; 70; 685 (*in Russian*)
(33) Levenspiel O., Chemical Reaction Engineering, (John Wiley, 1999, New York)
(34) Stumm W., Morgan J.J., Aquatic Chemistry: Chemical Equilibria and Rates in Natural Waters, 3rd Ed., (Wiley, 1996, New York)
(35) Fernandez A.M., Ibá□ez J.L., Llavona M.A., Zapico R., in Light Metals, Proceedings of the 127th TMS Annual Meeting, Feb 15-19 1998, San Antonio, TX, USA, Ed. B, Welch, pp. 121
(36) Momade F.W.Y., Momade Z.G., Hydrometallurgy 1999; 54; 25
(37) Davidson R.M., Modes of Occurrence of Trace Elements in Coal - Results from an International Collaborative Programme, CCC/36, (IEA Coal Research, 2000, London)
(38) Seidel A., Zimmels Y., Chem. Eng. Sci. 1998; 53; 3835
(39) Seidel A., Sluszny A., Shelef G., Zimmels Y., Chem. Eng. J. 1999; 72; 195
(40) Momade F.W.Y., Hydrometallurgy 1996; 40; 123
(41) Ahmed I.B., Gbor P.K., Jia C.Q., 2000, Aqueous sulphur dioxide leaching of Cu, Ni, Co, Zn and Fe from smelter slag in absence of oxygen, Can. J. Chem. Eng. 2000; 78; 694
(42) Hurlbut C.S. Jr., Klein C., Manual of Mineralogy (after James D. Dana) 19th Ed., (John Wiley, 1977, New York)
(43) Berkowitz N., An Introduction to Coal Technology, 2nd Ed., (Academic Press, 1994, San Diego) pp. 46
(44) Palmer C.A., Filby R.H., Fuel 1984; 63; 318
(45) Artok L., Malla P.B., Komarneni S., Schobert H.H., Energy & Fuels 1993; 7; 430
(46) Schneider H., Okada K., Pask J., Mullite and Mullite Ceramics, (John Wiley, 1994, Chichester)
(47) Öhman L.O., Wågberg L., J. Pulp and Paper Sci. 1997; 23; J475
(48) Laiti E., Persson P., Öhman L.O., Langmuir 1998; 14; 825
(49) Unterberger S., Berger R., Maier H., Hein K.R.G., Norin B., Gaegauf C., Struschka M., Hyytiäinen H., 1998, Development of newly designed wood burning systems with low emissions and high efficiency, Final Report EU Joule III, Institute of Process Engineering and Power Plant Technology, University of Stuttgart, Germany
(50) Ferrandon M., Berg M., Björnbom E., Catalysis Today 1999; 53; 647
(51) Hannay D.P., Franklin H.N., Effect of design upon selective catalytic reduction system operation, in Proceedings of the 1997 International Conference on Power Generation, POWER-GEN, (PennWell, 1997, Tulsa) p.71
(52) Osborne D.G., Coal Preparation Technology, (Graham & Trottman, 1988, London)
(53) Güvenç A., Erol M., Çalimli A., Sarikaya Y., Fuel Processing Technol. 1994; 38; 211

Table 1. Concentrations in Untreated Ash

Element [mg/kg]	Fränsta/ sawmill residue	Yatagan/ lignite	Tunçbilek/ lignite	Silopi/ asphaltite
Ca	314510	187991	14296	162973
Fe	5511	40289	87428	32523
K	66632	5012	10787	26387
Mg	34732	25265	22310	26290
Na	2426	1313	1054	2404
P	5720	1044	1546	4890
Al	8682	55588	96353	38171
Mn	37931	803	1353	116
S	3920	118000	25400	97600

ACID LEACHING OF ASH FROM WOOD, ASPHALTITE AND LIGNITE COMBUSTION: TRACE ELEMENT OCCURRENCES

Gul Asiye Ayçik[c], Mehtap Paul[a], Meryem Seferinoglu[b], Åke Sandström[d], and Jan Paul[e]

[a]Turkish Atomic Energy Authority, Ankara Nuclear Research and Training Center, 06100 Besevler-Ankara, Turkey**.** *Present address:* Luleå University of Technology, Division of Process Metallurgy, 971 87 Luleå, Sweden.

[b]Luleå University of Technology, Division of Physics, 971 87 Luleå, Sweden *, Permanent Address:* MTA, Mineral Research and Exploration Directorate, 06520 Balgat-Ankara, Turkey

[c]Turkish Atomic Energy Authority, Ankara Nuclear Research and Training Center, 06100 Besevler-Ankara, Turkey

[d]Luleå University of Technology, Division of Process Metallurgy, 971 87 Luleå, Sweden

[e]Luleå University of Technology, Division of Physics, 971 87 Luleå, Sweden, phone +46-920-491973, fax +46-920-491074, email jan.paul@sirius.luth.se

Introduction

Trace element extraction, followed by metal recovery, offers a route to sustainable ash handling, and may become an alternative to conventional stabilization and deposition. Direct acid leaching at low pH is a most powerful first step, albeit additional steps, including strong bases or chelating agents [1-4], may be needed, if the solid residue should be cleaned of all environmentally harmful elements. The trace elements; Cd, Cu, Co, Ni, Th, U, V and Zn, are leached to high percentages in sulfuric acid (pH 1.0, initial S/L ratio 1:10 25 EC) [5, 6]. Biohydrometallurgical production of base metals, i.e., the bacteriological oxidation of dominant mineral sulfides, offers established procedures for the recovery of several metals and gives directions for others.

Data for maximum extraction [5, 6] need to be amended with the results of time dependent studies before residence times and process designs can be discussed. Time dependent studies can also correlate trace element extraction to the dissolution of dominant ions [7] and the destabilization of major phases. It is not trivial to reveal the chemical nature of trace elements in the untreated ash by direct physical observation [8], but correlation studies, optionally using several leachants [9], offer a feasible, albeit indirect, route.

Experimental

Ash from the combustion of sawmill residues was collected at the Fränsta plant (http://www.angeenergi.se) and used as received [5]. Ashes from the combustion of two lignites, Mu la-Yata an and Kütahya-Tunçbilek, and one asphaltite, Silopi (http://www.tki.gov.tr), were prepared from the untreated fuels as described [6]. The untreated ashes were analyzed by ICP-AES/MS/SMS (Analytica AB, www.sgab.se, procedure MG-2 plus additional elements). Table 1 displays trace element data. Data for dominant ions were reported in a previous communication [7].

Ash samples were divided, stirred in deionized water and forcefully leached at pH 1.0 by the addition of 1 M sulfuric [7]. The effluent was analyzed by ICP-AES/MS/SMS analysis (Analytica AB, www.sgab.se, procedure V3a plus additional elements). We report analyses of the aqueous phase after 30 min, 1 h, 2 h, 4 h, 8 h, 16 h and 32 h leaching. The results are compared with the results from our previous screening study of maximum extraction, i.e., with the concentrations after 10 days of continuous leaching in sulfuric acid at pH 1.0 [5, 6].

Results

Table 1 gives trace element concentrations in the untreated materials and the extracted fractions of the same ions during leaching in sulfuric acid can also be seen (H_2SO_4, pH 1.0, 25EC, Initial solid/liquid ratio 1:10). Akin data for dominant ions were disclosed in a previous publication [7]. Our analysis is based on the concentrations of ions in the aqueous phase and anomalous values X > 1 stem from samples variations and analysis uncertainties.

We excuse the Fränsta ash. Table 1 reveals low levels of literally all relevant trace elements and maximum extraction figures have been presented [5]. Fränsta ash is contaminated by some radioactive elements, particularly Cs-137 from softwood exposed to long-range pollutants (Chernobyl), but also natural Ra-226. We have investigated the possibility to leach these pollutants [11], albeit the activity of our sample was below 5000 Bq/kg, the legal limit for the use as forest fertilizer (http://www.ssi.se).

There is a time dependence of trace element extraction for lignite-ash (Mu la-Yata an and Kütahya-Tunçbilek) and asphaltite-ash (Silopi). We have deliberately chosen to display the data in the same SCM model as for the major components. The purpose was to compare profiles and identify patterns which will reveal the matrices surrounding particular trace elements, i.e., occurrences. One difference is that we include the values for 30 min leaching.

Discussion

Trace Element Leaching and Occurrences.

Arsenic. Maximum extraction yields between 27-81 % for ground coal and 24-77 % for coal-ash have been reported [6]. We note that only marginal quantities are leached from ash after the initial period. It has been suggested that As is associated with $CaSO_4$ [12] and our results do not contradict these findings.

Barium. Bariumsulfate is nearly insoluble and barium, dissolved from phases in the untreated ash, is readily altered to barite in the solid residue [5, 6]. We were able to observe the early stages of leaching from Silopi ash, despite the stability of $BaSO_4$. The plateau corresponds to 26 µg / L or 1 % extraction. Ba forms carbonates, but replaces also alkali metals or alkaline earths in Si/Al oxides [13]. The traces of sodium and barium are two of a kin, albeit many elements in show a similar increase during the first 4 h.

Cadmium. Silopi ash gave an approximate straight line in the entire regime. Cd associated with mineral sulfides will be altered during combustion. We note that cadmium is extracted to better than 90 % in most ashes, notably from waste incineration [5], but significantly less in whole coals [6]. The present data give 94 % Cd extraction for Silopi asphaltite-ash and 100 % for Fränsta / bio-ash, but only 30-40 % for lignite-ashes. This is at the low-end of compiled data for coal-ashes [6] and shows that dissolution continuous after 32 h, for cadmium, as well as for aluminum and iron [7], two possible host elements. Lignite combustion may also lead to the formation of insoluble spinels, akin to the formation of $ZnFe_2O_4$ from the oxidation of (Fe, Z)S or reactions between zinc oxide and hematite [14]. Association with iron or zinc containing oxides [9, 15], formed from FeS_2 or ZnS, may protrude as a similarity with Fe or Zn leaching. In conclusion, we need extended process times to deplete coal-ashes of cadmium. The rapid dissolution from waste-ashes is probably a result of surface association [16].

Cobalt. It is unclear if cobalt leaching follows a SCM model. Extraction reaches 29-44 % after 32 h, which is lower than 40-82 % after 10 days [6]. No occurrence is universally favored in literature [15], albeit association with clays has been suggested [9, 17].

Chromium. All ashes show smooth profiles but only Silopi approaches maximum extraction after 32 h i.e., the apparent plateau for Tunçbilek is artificial. The iron and aluminum profiles for Silopi ash, as well as the degree of completion [6, 7], mimic the chromium behavior, in all suggesting clay association, in agreement with literature [17]. Organic occurrences in 'whole coals' [9] and the heat during combustion, may lead to association with other oxides, apart from clay minerals. The above analysis applied anew, for Yata□an and Tunçbilek lignite-ashes, recognizes the close similarities between Cr and Fe/Al kinetics of leaching as well as the proximity to maximum extraction [6, 7]. During leaching (30 min - 16 h) the Cr / Fe atomic ratios were 1:420 (Yata□an), 1:53 (Tunçbilek) and 1:32 (Silopi). The Cr / Al ratios were 1:2900 (Y), 1:160 (T) and 1:380 (S), respectively. These values serve to illuminate the degree of doping, assuming solid solutions. In conclusion we suggest that Cr is found as a dopant in iron and aluminum oxides, i.e., probably in illite clays.

Cesium. Low concentrations are an obstacle for trustworthy data on Cs leaching of coal-ash, but measurements on radioactive Cs-137 in wood-ash indicated a very rapid process (< 30 min) with high extraction yields (>90 %) [11].

Copper. Silopi ash dissolution is well modelled by a diffusion controlled SCM process, but Yata□an and Tunçbilek give more scattered data. The common knee at 1 h is not obvious for Cu, but the near linearity of Al, Fe and Mn (>1 h) connect well to the straight line of Cu. Copper is most likely found as chalcopyrite in the whole coals [6, 9, 15]. This makes it logical to suggest that Cu is associated with Fe oxides in the ash. Copper forms very stable oxides with aluminum, but this is less likely considering the low ashing temperature, 550 EC [18, 19].

Mercury. Mercury is literally not dissolved in sulfuric acid, due to the low solubility of $HgSO_4$ [5, 6]. Other leachants must be amended to obtain mercury recovery.

Molybdenum. Molybdenum is present at unprecedented levels, 2290 mg/kg, in ash from Silopi asphaltites (Table 1). 79 % extraction is reached in 32 h. This is near the maximum value 88-90 % [4, 6]. The Elovich equation gives a straight line for Mo extraction, but a SCM model show the same steep onset as Fe and Al leaching. Al and Fe, in ash from Silopi, also reach near maximum extraction after 32 h [6, 7]. Mo is associated with organic material or sulfidic phases in coal and thus altered by ashing. The element is commonly present in solid solution with other sulfides, but high concentrations may also lead to a separate molybdenite (MoS_2) phase. Association with pyrite or chalcopyrite in the fuel suggests that Mo is primarily present as a dopant in ironoxides in the ash, but association with $CaSO_4$ in the ash has also been suggested [12]. The extraction of Mo is not affected by the combustion temperature (< 950 EC). Alternative leachants, natural waters or strong bases gave yields ranging from 10-30 %, but yields around 90 % can be obtained by pyrolysis followed by acid leaching [4].

Nickel. Nickel dissolution shows similar shapes for the three ashes. Silopi and Tunçbilek reach 17 % and 20 % extraction in 32 h, out of maximum yields of 31 % and 33 %, respectively. Surprisingly, Yata□an ash, with 24 % extraction after 32 h, reach 84 % dissolved nickel in 10 days [6]. 55 % extraction has been reported for Silopi ash in sulfuric acid, but literally no dissolution in natural waters and strong bases [4]. The shape of Ni extraction is also observed for Al and Fe dissolution and suggests association with clays [9]. Some differences persist regarding the ratio between initial leaching and 'slow phase' leaching, and we can not warrant that majority phases contain the same dopants in the two regimes. Apart from clays, both Al and Fe oxides may serve as matrices for Ni. Iron oxide association is more likely, after ashing at low or moderate temperatures, since bimetallic (bulk) oxides with aluminum require high temperature oxidation [18, 19]. A significant drop in the nickel extraction yield was observed after combustion of Silopi asphaltite at 850 EC, instead of 500 EC [4]. The lower yield was repeated for pyrolysis at 950 EC [4]. At lower combustion temperatures we merely observe alumina surface modifications and leaching of surface associated metals do not follow a SCM model.

Lead. Due to the low solubility of $PbSO_4$ [6, 20], only limited extraction of lead in sulfuric acid is observed, but reveals a smooth profile, albeit not a straight line, for Silopi asphaltite-ash. We obtain maximum extraction after 32 h treatment. Calcium alone of major components demonstrates similar characteristics [7]. Calcium dominates the neutralizing capacity for short contact times, but some contributions linger during the 30 min - 32 h period. Lead is mainly found as galena (PbS) in 'whole coals' [9]. We suggest the possibility that Pb^{2+} ions, after coal combustion, are substituted for Ca^{2+} ions in the untreated ash. This suggestion is well in line with the suggested association of Pb to $CaSO_4$ [12].

Tin. Sn is not leached and we note that SnO_2 is stable in sulfuric acid [5].

Thorium. The non-linear profile for Tunçbilek translates to a straight line in the Elovich model, but approximate linearity is also found for a range of other metals when X is plotted vs. ln(t) and the implications of the Elovich model are not clear [21]. 8 h of treatment almost completes the leaching process for all ashes and this mimics Ca [7] more than Al/Fe. Thorium is extracted to high percentages from Yata□an (90 %) and Elbistan (78 %) ashes [6], but also to modest levels in other lignite-ashes, notably Tunçbilek (32 %).

Uranium. The uranium concentration in untreated ash from Silopi is very high (Table 1), but also the two lignite-ashes show considerable radioactivity, from ^{238}U as well as ^{232}Th [11]. The main primary ore minerals are uraninite and pitchblende, often associated with mineral sulfides [13]. Ashing boosts the extraction yield of uranium dramatically and 79-94 % maximum dissolution is reported [6]. This points at the formation of uranyl - ions (UO_2^{2-}). Maximum extraction is reached after 8 h except for one odd value for Yata□an lignite-ash. This indicates association with calcium containing phases in the untreated ash, although we may not exclude surface association or even separate phases.

Vanadium. Vanadium is abundant in Silopi asphaltites and asphaltite-ash [6]. Combustion brakes the stable chelate of vanadyl-porphyrins and opens vanadium ions for extraction in acids. We do not reach maximum extraction after 32 h, but we recognize the SCM pattern of Al and/or Fe. Yields above 90 % were also observed after pyrolysis at 950 EC, which suggests a disintegrated porhyrin [4]. Alternative leachants, natural waters and strong bases gave yields below 10 %. We concede with literature [17] and suggest V association with clays (illite) in the ash, or possibly, with a separate phase of iron or aluminum oxide. Combustion temperatures below 950 EC have no effect on V extraction [4], which tells that no complex oxides were formed.

Zinc. The profile of zinc leaching from Tunçbilek is very similar to the profile of cadmium leaching and we note that the main occurrence of cadmium is as a substitutional defect in sphalerite [9, 15]. Extraction numbers between 70-90 % were reported for waste incineration ashes, but zinc bound as a trace element in minerals makes coal-ash a different material than ash from garbage combustion [20]. We note the possibility of spinel formation, $ZnFe_2O_4$, upon the combustion of lignites. The time dependence of waste-ash leaching [20] indicates that Zn is bound at the surface of fly ash particles, rather than as a dopant. It has been suggested that Zn is bound to $CaSO_4$ particulates [4].

Coal-Ash Treatment: **Residence Times and Process Design**. The above data may serve as input to full-scale plant studies on acid leaching [22-24]. Two additional concepts have been presented [5, 6]: (i) the use of ash for pH control in the biological oxidation of

sulfidic concentrates and (ii) a separate acid leaching process followed by metal recovery in the main bioleaching plant or a separate metallurgical unit. Conditions utilized in the present study (pH 1.0) mimic the biocatalyzed stage of a hydrometallurgical process for metal production from sulfidic minerals, albeit commonly used mesophilic organisms favor higher temperatures (40 EC).

The residence time of the biocatalyzed oxidation stage is 3-5 days, i.e., we will complete the fast phase of ash leaching and start the slow dissolution of more stable phases. This translates to 50-100 % lower concentrations of, for instance; Cd, U, Th and V, in the solid residue compared with the untreated ash. The issues that need to be addressed are twofold: (i) will the extracted elements hamper the biological activity and (ii) can the extracted elements be retrieved or removed economically with maintained quality of the main product, usually copper or zinc. We suggest that the recovery of Cd, Co, Cu, Ni and Zn is technically feasible and of potential economic value [6, 25, 26]. Mn and V may be amended at a higher cost. U and Th leaching are of interest to prevent the release of radioactive materials. A complete scheme for the acid leaching and recovery of Mo, V, Ni and U has been proposed [24]. In the present work we suggest that the washed ash will be mixed and deposited with mineral residues or the precipitates from the main biohydrometallurgical process [5, 6].

The residence times of intermediate (Fe/As) and final precipitation stages in a bioleaching process are around 2 h [5, 6]. pH is raised to 2.5 - 3.0 in the former and 7.0 in the latter. The usage of ash for pH adjustment in these stages needs to be addressed in further studies.

In a separate acid leaching plant we may choose the residence times independently of the requirements of parallel processes. We suggest the possibility to use acid leachate (excess sulfuric acid) from the bioleaching plant, but local feeds, from roasting or desulfurization units, coking plants or refineries, may determine the source of sulfuric acid. Acid leaching is simple and can be accommodated either at the power plant or the main hydrometallurgial plant [5, 6]. Leached elements can be shipped as precipitated hydroxides or sulfides to the main plant for metal recovery. Residues will be literally inert since no natural habitat will display a more acidic environment.

Further tests must be conducted with as received ash samples [6, 27]. Above we argued that the combustion temperature is critical, with higher temperature favoring more stable ceramics [28], but variations in fuel quality and additives from ash aftertreatment also affect leaching properties. Moreover, chlorine is found in ash from waste incineration both as a result of plastics in the fuel and as an additive [29]. Finally, it can not be taken for granted that stabilization by carbonatization or flocculation will reduce dissolution at low pH, which means that even deposits of stabilized ashes are an environmental hazard [6, 30].

Conclusions

Lignite- and asphaltite-ashes dissolve in sulfuric acid (initial S/L ratio 1:10, pH 1.0, 25 EC). We discern a 'fast regime' ending after 30 min and a second, 'slow regime' extending 10 days or more. The second stage is well modelled by a diffusion limited shrinking core (SCM) process.

High extraction yields of Th and U are observed during the initial 30 min of leaching. Ca, Ba and Pb readily precipitate as sulfates, but low levels of Ba and Pb dissolution were noticed. Extraction of the trace elements Cd, Co, Cr, Cu, Mo, Ni, V and Zn were observed during the second stage and linked to the dissolution of clays and other relatively stable complex minerals and oxides. 3-5 days of treatment may render an inert residue with 50-100 % lower concentrations of Cd, U, Th and V.

The recovery of Cd, Co, Cu, Ni and Zn is technically feasible using present hydrometallurgical processes. Additional measures are necessary for the recovery of Mn, Mo, Th, U and V, but schemes have been suggested and tested at bench or pilot scale. There is no need for additional extraction steps if direct acid leaching give high yields. Alternative acids, strong bases or complexing agents will be motivated if targeted elements remain in the solid residue. This is the case for Hg, Pb and Zr in the present study, due to the formation of insoluble sulfates.

Acknowledgement. We thank our colleagues Agah Köker and Selami Toprak from MTA in Ankara for discussions on coal pretreatments. We also thank Ömer Ünver from TKI Türkiye Kömür Isletmeleri Kurumu *(Eng. Turkish Coal Enterprises*) for his continued interest in our work and Michael L. Smith, Anabolic Laboratories, Phoenix/AZ for his careful reading of the manuscript. Last, but not least, we acknowledge Vattenfall AB and Ånge Energi for their support of our project.

References

(1) Harris W.R., Silberman D., Environ. Sci. Technol. 1983; 17; 139
(2) Nugteren H.W., Janssen-Jurkovícová M., Scarlett B., Fuel 2001; 80; 873
(3) Nugteren H.W., Janssen-Jurkovícová M., Scarlett B., J.Chem.Technol.Biotechnol. 2002; 77; 389
(4) Atamer H., Özdil G., Essiz R., Durmus H., 1979, Güneydogu Anadolu Bölgesi Asfaltit Küllerinden Molibden, Nikel ve Vanadyumun Kazanilmasi Amaciyla Liçing Ara∏t2mas2, MTA 6636, M.T.A. Enstitüsü Teknoloji Dairesi Radyoaktif ve Nadir Metaller Teknoloji Servisi, Ankara, *in Turkish*
(5) Paul M., Sandström Å., Paul J., Journal of Hazardous Materials (submitted)
(6) Seferinoglu M., Paul M., Sandström Å., Köker A., Toprak S., Paul J., Fuel 2003; 82; 1721
(7) Paul M, Seferinoglu M., Ayç2k G.A., Sandström Å., Paul J., Fuel (submitted)
(8) Camerani M.C., Somogyi A., Drakopoulos M., Steenari B.M., Spectrochim. Acta Part B 2001; 56; 1355
(9) Davidson R.M., Modes of Occurrence of Trace Elements in Coal - Results from an International Collaborative Programme, CCC/36, (IEA Coal Research, 2000, London)
(10) Levenspiel O., Chemical Reaction Engineering, (John Wiley, 1999, New York)
(11) Ayç2k G.A., Paul M., Smith M.L., Sandström Å., Paul J., Waste Management (manuscript)
(12) Querol X., Fernández-Turiel J.L., López-Soler A., Fuel 1995; 74; 331
(13) Hurlbut C.S. Jr., Klein C., Manual of Mineralogy (after James D. Dana) 19th Ed., (John Wiley, 1977, New York)
(14) López-Delgado A., Martín de Vidales J.L., Vila E., López F.A., J. Alloys and Compounds 1998; 28; 312
(15) Swaine D.J., Trace Elements in Coal, (Butterworth, 1990, London)

(16) Camerani Pinzani M.C., Somogyi A., Simionovici A.S., Ansell S., Steenari B.M., Lindqvist O., Environ. Sci. Technol. 2002; 36; 3165
(17) Palmer C.A., Filby R.H., Fuel 1984; 63; 318
(18) Centi G., Perathoner S., Applied Catalysis A: General 1995; 132; 179
(19) Trumble K.P., Acta Metallurgica et Materialia 1992; 40 SUPPL; S105
(20) Nagib S., Inoue K., Hydrometallurgy 2000; 56; 269
(21) Stumm W., Morgan J.J., Aquatic Chemistry: Chemical Equilibria and Rates in Natural Waters, 3rd Ed., (Wiley, 1996, New York)
(22) Katsuura H., Inoue T., Hiraoka M., Sakai S., Waste Management 1996; 16; 491
(23) Querol X., UmaƷa J.C., Alastuey A., Ayora C., Lopez-Soler A., Plana F., Fuel 2001; 80; 801
(24) Atamer H., Derman D., Özdil G., 1975, Güneydogu Anadolu Bölgesi Asfaltit Küllerinden Molibden, Nikel, Vanadyumun ve Uranyumum Kazan2lmas2, M.T.A. Enstitüsü Teknoloji Dairesi Radyoaktif ve Nadir Metaller Teknoloji Servisi, Ankara, *in Turkish*
(25) Jia C.Q., Xiao J.Z., Orr R.G., J. Environ. Sci. Health, Part A: Toxic/Hazardous Substances & Environmental Engineering 1999; 34; 1013
(26) Ahmed I.B., Gbor P.K., Jia C.Q., Can. J. Chem. Eng. 2000; 78; 694
(27) Steenari B.M., Schelander S., Lindqvist O., Fuel 1999; 78; 249
(28) Stach E., Mackowsky M.Th., Teichmüller M., Taylor G.H., Chandra D., Teichmüller M., Stach's Textbook of Coal Petrology, 2nd Ed., (Gebrüder Borntraeger, 1975, Berlin), pp. 122
(29) Chandler A.J., Eighmy T.T., Hartlén J., Hjelmar O., Kosson D.S., Sawell S.E., van der Sloot H.A., Vehlow J., Municipal solid waste incinerator residues, Study in Environmental Science 67 (Elsevier, 1997, Amsterdam)
(30) Wei M.C., Wey M.Y., Hwang J.H., Chen J.C., 1998, Stability of heavy metals in bottom ash and fly ash under various incinerating conditions, J. Hazard. Mater. 1998; 57; 145

Table 1. Concentrations in Untreated Ash

Element [mg/kg]	Fränsta/ sawmill residue	Yatagan/ lignite	Tunçbilek/ lignite	Silopi/ asphaltite
As	< 3	226	80.3	132
Ba	5840	409	422	297
Cd	5.3	2.43	0.457	123
Co	12.2	27.7	97.6	13
Cr	44	168	794	346
Cs	2.66	4.93	11.2	4.27
Cu	131	308	86	207
Hg	< 0.1	< 0.1	< 0.1	< 0.1
Mo	< 6	44.2	50	2290
Ni	21.5	111	2150	3030
Pb	22.8	187	79.2	22.8
Sn	< 20	< 20	< 20	< 20
Th	N/A	18	34.4	4.85
U	0.422	67.3	23.9	171
V	6.04	294	265	3990
Zn	1020	385	147	3890

THE STUDY OF HYDRODESULFURIZATION OF 4,6-DIMETHYLDIBENZOTHIOPHENE OVER PHOSPHORUS-ADDED NiMo/γ-Al_2O_3

Yongqiang Xu, Hongyan Shang, Chenguang Liu

Key Laboratory of Catalysis, CNPC
State Key Laboratory of Heavy Oil Processing
College of Chemistry & Chemical Engineering
University of Petroleum (East China),
Dongying, Shandong, 257061, China

Introduction

Deep hydrodesulfurization (HDS) of diesel oil has attracted much attention recently as the more and more strict environmental regulations. Among the sulfur compounds of diesel oil, dibenzothiophenes (DBTs, such as dibenzothiophene (DBT), 4-methyldibenzothiophene (4-MDBT), 4,6-dimethyldibenzothiophene (4,6-DMDBT)) are found the refractory compounds to HDS [1-4]. However, even now scientists have different ideas on the adsorption states of DBTs over the HDS catalysts and carriers [5-7], as a result, they proposed different HDS mechanism of DBTs. On the other hand, the reactive thermodynamics and kinetics of HDS of DBTs are still studied inadequately. Therefore, the studies of HDS of DBTs are the key subjects to the deep HDS of diesel oil.

The phosphorus-added hydrotreating catalysts were found have promoting effects on the HDS activity of these catalysts [8,9]. The reasons for that have various explanations. Kwak C. et al. [8] concluded that phosphorus modifies catalytic behavior in two ways: increase of active sites by enhanced metal dispersion and increase of Bronsted acidity. In this paper, the HDS of 4,6-DMDBT on phosphorus-added NiMo/γ-Al_2O_3 sulfide catalyst (P-NiMo/γ-Al_2O_3) was studied, moreover, the reaction network and mechanisms were advanced on the basis of GC, and GC-MS analyses of the reaction products.

Experimental

Material and Catalyst. 4,6-DMDBT was synthesized according to an improved method of literature [10]. Its purity is 99.6%, and its melting point is 153.5-154.1°C.

CoMo/γ-Al_2O_3 catalyst was prepared in the following way. γ-Al_2O_3(20-40 mesh) was impregnated with an aqueous solution of ammonium heptamolybdate, followed by drying at 120ºC for 5h, and calcinations in air at 500ºC for 5h. After that, it was impregnated with an aqueous solution of cobalt nitrates, dried and calcined as done above. The CoMo/γ-Al_2O_3 catalyst contains 16.1wt% MoO_3 and 3.4wt% CoO, CoO/(CoO+ MoO_3) (mol/mol)=1:3.5.

Phosphorus-added NiMo/γ-Al_2O_3 catalyst was prepared in the following way. The slurry of γ-Al_2O_3 mixed with P_2O_5 was extruded to form 1mm in diameter needle. Then it was dried in air at 120°C for 5h, and then crushed and sieved to get 20-24 mesh granules. The granules were calcined in air at 500°C for 5h. The phosphorus-added γ-Al_2O_3 was then impregnated with an aqueous solution of molybdenum oxide, nickel carbonate basic and phosphorus acid, followed by drying at 120ºC for 5h, and calcinations in air at 500ºC for 5h. The phosphorus-added NiMo/γ-Al_2O_3 catalyst contained 26wt.% MoO_3 and NiO, NiO /(NiO + MoO_3) (mol/mol)=1:3.5. The amount of phosphorus added to the catalyst was 3.5wt.%.

Reactor and Experimental Procedure. The HDS reaction was carried out in a fixed-bed flow microreactor, consisting of a 17mm i.d. stainless steel tube. 2ml of catalyst particles were diluted with quartz sand to 10ml, and then packed in the middle section of the tube, and the other sections were filled by quartz sand. The catalyst was presulfided before HDS reaction with 3wt%CS_2 in cyclohexane for 6h at 2.0MPa, 300°C, LHSV, $3h^{-1}$ and H_2/feed ratio (V/V), 200/1. After presulfidation, the reactant (1wt%4,6-DMDBT in decalin) was pumped into the reactor. 6h later, sampling of products was started at intervals of 30 min. the samples were immediately analyzed by gas chromatograph. Reaction pressure and temperature were then changed for studying the effects of them on HDS of 4,6-DMDBT. The reaction pressures used were 2.0, 1.5, 1.0MPa, while the reaction temperatures used were 300ºC, 280ºC, 260ºC.

Analysis. The samples were analyzed by Varian 3800 Chromatograph. The products were identified by GC-MS (Finnigan SSQ710).

Results and Discussion

The Analysis of Products of HDS and The Reaction Network. The products from reactions of 4,6-DMDBT and their yield at 300ºC under 2.0MPa over P-NiMo/γ-Al_2O_3 were shown in Table 1. The isomerization of 4,6-DMDBT to 3,6-DMDBT was found over P-NiMo/γ-Al_2O_3 as well as HDS. From Table 1, the speculated reaction network for HDS of 4,6-DMDBT is shown in Scheme 1.

Table 1 also shows the products from HDS of 4,6-DMDBT and their concentration at 300ºC under 2.0Mpa over sulfided CoMo/γ-Al_2O_3. It can be found that under the same reaction conditions, the conversion of 4,6-DMDBT over sulfided CoMo/γ-Al_2O_3 is much lower than that over P-NiMo/γ-Al_2O_3. That means the P-NiMo/γ-Al_2O_3 has higher 4,6-DMDBT-HDS activity than sulfided CoMo/γ-Al_2O_3. On the other hand, the ratio between cyclohexylbenzenes (CHBs) and biphenyls (BPs) in the products of HDS of 4,6-DMDBT over P-NiMo/γ-Al_2O_3, which approximately reflects the ratio of the rate of the desulfurization through hydrogenation (HYD) route to the direct desulfurization (DDS) route, is 3.05. But over sulfided CoMo/γ-Al_2O_3, it is 2.54, which means that P-NiMo/γ-Al_2O_3 has higher hydrogenation activity than CoMo/γ-Al_2O_3.

The concentrations of isomers such as 3,6-DMDBT, 3,4'-DMBP in the products of HDS of 4,6-DMDBT over P-NiMo/γ-Al_2O_3 are very low, which replies the high HDS activity of P-NiMo/γ-Al_2O_3 should not lie on its acidity, but on increase of active sites by enhanced metal dispersion.

Table 1. Concentration of HDS products of 4,6-DMDBT

Product	Concentration, wt.%	
	P-NiMo/Al_2O_3	CoMo/Al_2O_3
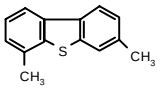	0.23	0.20
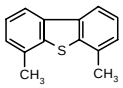	25.66	64.26
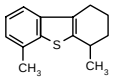 And its isomer	1.66	1.65
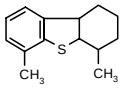	0.23	0.46
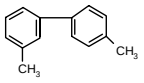	0.10	0.04
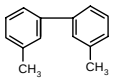	17.10	9.18
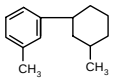 and its isomers	52.44	23.41
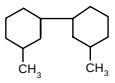 and its isomer	2.59	0.80

The Effect of Reaction Pressure And Reaction Temperature on HDS of 4,6-DMDBT. The concentration of products for HDS of 4,6-DMDBT under different reaction pressures at 300ºC is shown in Fig.1. Fig.1 illustrates that the reaction velocity of HYD routes in HDS of 4,6-DMDBT obviously decreases with the descending of reaction pressure. But the effect on DDS pathway is much smaller than that on HYD. As a result, the CHBs/BPs ratio descends greatly with the reducing of reaction pressure (as shown in Fig.2). It can also be found that the effect of reaction pressure on the transformation of 4,6-DMDBT is very obvious for the high selectivity of HYD route in the HDS reaction network of 4,6-DMDBT.

The concentration of products of HDS of 4,6-DMDBT at different reaction temperatures under 2.0MPa is shown in Fig.3. From Fig.3 it can be found that the reaction velocity of the HDS of 4,6-DMDBT and the DDS route, HYD route inside all obviously decrease with the descending of reaction temperature, which suggests that the HDS is not reach the thermodynamic equilibrium under the reaction conditions adopted in this experiment.

Conclusion

P-NiMo/γ-Al_2O_3 has higher 4,6-DMDBT-HDS activity and hydrogenation activity than sulfided CoMo/γ-Al_2O_3, which does not lie on its acidity, but on increase of active sites by enhanced metal dispersion. Effect of reaction pressure on the HYD route is higher than that on the DDS route for HDS of 4,6-DMDBT. Reaction temperature has obvious effect on all the HDS of 4,6-DMDBT and the DDS route, HYD route inside

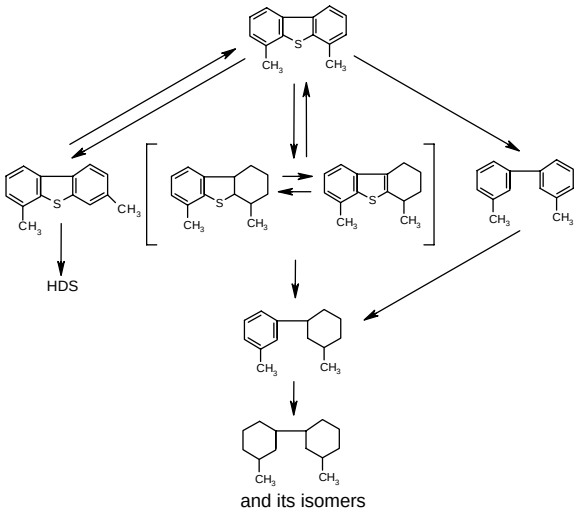

Scheme 1. Reaction network for HDS of 4,6-DMDBT on P-NiMo/γ-Al_2O_3.

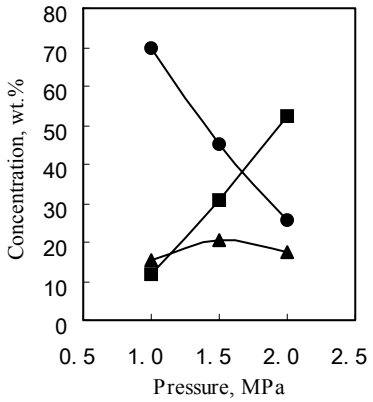

Figure 1. Concentration of hydrodesulfurization products of 4,6-DMDBT under different reaction pressure, ●4, 6-DMDBT, ▲ 3,3'-dimethylbiphenyl and 3,4'-dimethylbiphenyl, ■ 3,3'-dimethyldicyclohexyl

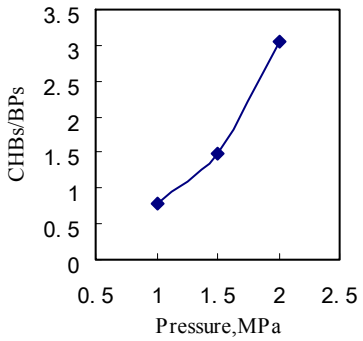

Figure 2. Ratio of dimethylcyclohexylbenzene to dimethylbiphenyl under different reaction pressure

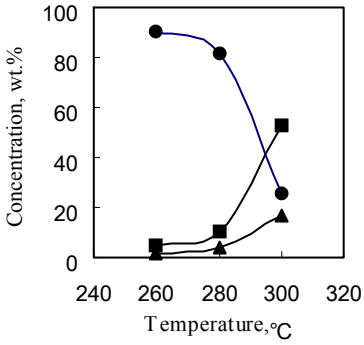

Figure 3. Concentration of HDS products of 4,6-DMDBT under different reaction temperatures, ●4, 6-DMDBT, ▲ 3,3'-dimethylbiphenyl and 3,4'-dimethylbiphenyl, ■ 3,3'-dimethyldicyclohexyl

References

(1) Amorelli A., Amos Y. D., Halsig C.P., et al., Estimate Feedstock Processsability [J], *Hydrocarb.Proc.*,1992, *71(6)*: 93-101.

(2) Shih S. S., Mizrahi S., Green L. A., et al., Deep Desulfurization of Distillates [J], *Ind. Eng. Chem. Res.*, 1992, *31*:1232-1235

(3) Kabe T., Ishihara A., Tajima H., Hydrodesulfurization of Sulfur-Containing Polyaromatic Compounds in Light Oil[J], *Ind. Eng. Chem. Res*., 1992, *31*: 1577-1580

(4) Schulz H., Bohringer W., Ousmanov F., et al.,, Refractory sulfur compounds in gas oils[J], *Fuel Processing Technology*, 1999, *61*: 5–41

(5) Macaud M., Milenkovic A., Schulz E.,et al., Hydrodesulfurization of Alkyldibenzothiophenes: Evidence of Highly Unreactive Aromatic Sulfur Compounds[J], *J. Catal.*, 2000,*193*:255-263.

(6) Kabe T., Qian W., Ishihara A., Study of Hydrodesulfurization of Dibenzothiophene on Ni-Mo/Al_2O_3, Mo/Al_2O_3,and Ni/Al_2O_3 Catalysts by the Use of Radioisotope ^{35}S Tracer[J], *J. Catal.*, 1994,*149*: 171-180.

(7) Laudau, M. V., Deep Hydrotreating of Middle Distillates from Crude and Shale Oils[J]. *Catalysis Today*, 1997,*36(4)*:393-429

(8) Kwak C., Kim M. Y., Choi K., et al., Effect of Phosphorus Addition on the Behavior of CoMoS/Al_2O_3 Catalyst in Hydrodesulfurization of Dibenzothiophene and 4,6-Dimethyldibenzothiophene[J], *Applied Catalysis A: General* 1999,185 (1): 19±27.

(9)Atanasova P., Lopez Cordero R., Mintchev L., et al., Temperature Programmed Reduction of the Oxide Form of PNiMo/Al_2O_3 Catalysts Before and After Water Extraction [J], *Applied Catalysis A: General* 1997, 159(1): 269-289.

(10) Kuchm-Caubere, C., Adach-Becker, S., Fort, Y. et. al., Expeditious and Efficient Syntheses of pure 4-Methyl and 4,6-Disubstituted Dibenzothiophene[J]. *Tetrahedron*, 1996,*52(27)*:9087-9092.

THE HYDRODESULFURIZATION OF 4-METHYLDIBENZOTHIOPHENE AND DIBENZOTHIOPHENE OVER SULFIDED Mo/γ-Al_2O_3

Yongqiang Xu, Chenguang Liu

Key Laboratory of Catalysis, CNPC,
State Key Laboratory of Heavy Oil Processing
College of Chemistry & Chemical Engineering
University of Petroleum (East China),
Dongying, Shandong 257061, China

Introduction

Deep hydrodesulfurization (HDS) of diesel oil has attracted much attention recently as the more and more strict environmental regulations. Among the sulfur compounds of diesel oil, dibenzothiophenes (DBTs, such as dibenzothiophene (DBT), 4-methyldibenzothiophene (4-MDBT), 4,6-dimethyldibenzothiophene (4,6-DMDBT)) are found the refractory compounds to HDS [1-4]. However, even now scientists have different ideas on the adsorption states of DBTs over the HDS catalysts and carriers [5-8], as a result, they proposed different HDS mechanism of DBTs. On the other hand, the reactive thermodynamics and kinetics of HDS of DBTs are still studied inadequately. Therefore, the studies of HDS of DBTs are the key subjects to the deep HDS of diesel oil.

Sulfided Mo/γ-Al_2O_3 catalyst has lower reactivity of catalysis than sulfided CoMo/γ-Al_2O_3 catalyst. But just because of this, most of the partly hydrogenated DBTs remain in the products, which are helpful to the studies of the HDS mechanism of DBT and 4-MDBT over Sulfided Mo/γ-Al_2O_3 catalyst.

Experimental

Material and Catalyst. DBT was synthesized by a modified procedure of the literature (9). Its purity is 99.7%, and its melting point is 98.2-98.4°C. 4-MDBT was synthesized according to an improved method of literature (10). Its purity is 94.6%, and its melting point is 63.6-63.7°C.

Mo/γ-Al_2O_3 catalyst was prepared in the following way. γ-Al_2O_3(20-40 mesh) was impregnated with an aqueous solution of ammonium heptamolybdate, followed by drying at 120ºC for 5h, and calcinations in air at 500ºC for 5h. The Mo/γ-Al_2O_3 catalyst contained 16.7wt%MoO_3.

Reactor and Experimental Procedure. The HDS reaction was carried out in a fixed-bed flow microreactor, consisting of a 17mm i.d. stainless steel tube. 5ml Mo/γ-Al_2O_3 catalyst (20-40 mesh) was packed in the middle section of the tube, and the other sections were filled by quartz sand. The catalyst was presulfided before HDS reaction with 3wt%CS_2 in cyclohexane for 6h at 2.0MPa, 300°C, LHSV, $3h^{-1}$ and H_2/feed ratio (V/V), 200/1. After presulfidation, the reactant (2wt%DBT or 2wt% 4-MDBT in toluene) was pumped into the reactor. 6h later, sampling of products was started at intervals of 30 min, the samples were immediately analyzed by gas chromatograph. Reaction pressure and temperature were then changed for studying the effects of them on HDS of DBT and 4-MDBT. The reaction pressures used were 2.0, 1.5, 1.0MPa, while the reaction temperatures used were 300ºC, 280ºC, 260ºC, 240ºC.

Analysis. The samples were analyzed by Varian 3800 Chromatograph. The products were identified by GC-MS (Finnigan SSQ710).

Results and Discussion

The Analysis of Products of HDS and The Reaction Network. The products from HDS of 4-MDBT and their yield at 300ºC under 2.0MPa over Mo/γ-Al_2O_3 are shown in Table 1. From that, the speculated reaction networks for HDS of 4-MDBT are shown in Scheme 1.

Table 2 shows the products from HDS of DBT and their concentration at 300ºC under 2.0Mpa over Mo/γ-Al_2O_3. From Table 2 and Table 1, it can be found that under the same reaction conditions, the conversion of 4-MDBT is slightly lower than that of DBT, and the molar ratio between cyclohexylbenzenes (CHBs) and biphenyls (BPs) in the products of HDS of 4-MDBT, which approximately reflects the ratio of the rate of the desulfurization through hydrogenation (HYD) route to the direct desulfurization (DDS) route, is 2.40. But to DBT, it is 0.97, which means that the HDS of 4-MDBT is essentially through the HYD route, while to DBT, the contributions of both routes are comparable. The methyl group in 4-MDBT molecule spatially hinds the "end on adsorption" of sulfur atom on the active sites of the catalyst, which depresses the DDS route and lead to the reduction of conversion of 4-MDBT. On the other hand, because the HYD route is also important to the HDS of DBT over Sulfided Mo/γ-Al_2O_3 catalyst, the difference between the conversion of DBT and 4-MDBT is not as obvious as that over Sulfided CoMo/γ-Al_2O_3 catalyst. Over Sulfided CoMo/γ-Al_2O_3 catalyst the HDS of DBT is essentially through the DDS route.

The Effect of Reaction Pressure on HDS of DBT and 4-MDBT. The concentration of products for HDS of DBT and 4-MDBT under different reaction pressures at 300ºC are shown in Fig.1 and Fig.2. The apparent kinetic orders of reaction pressure in different reaction among the HDS reactions are summarized in Table 3. Fig.1, Fig.2 and Table 3 illustrates that the reaction velocity of HYD routes in HDS of DBT and 4-MDBT obviously decreases with the descending of reaction pressure. But the effect on DDS is much smaller than that on HYD. As a result, the BPs/CHBs molar ratio increases greatly with the reducing of reaction pressure (as shown in Fig.3). Although the obviously difference exists between the transformation of DBT and that of 4-MDBT, it is found from Table 3 that the apparent kinetic orders of reaction pressure in HYD route in the HDS reaction network of DBT is similar with that of 4-MDBT. All of these imply that the reaction mechanisms of them may be similar.

Table 1. Concentration of HDS products of 4-MDBT

Product	Concentration, mol%
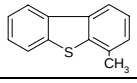	50.3649
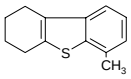	5.9015
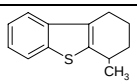	2.7141
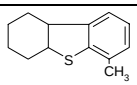	0.8139
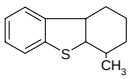	0.2748
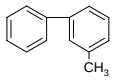	10.2775
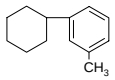	5.2329
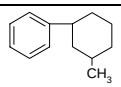	19.2945
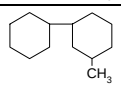	2.6525

The Effects of Reaction Temperature on HDS. The concentration of products of HDS of DBT and 4-MDBTat different reaction temperatures under 2.0MPa are shown in Fig.4 and Fig.5. From them it can be found that the reaction velocity of the HDS of DBT and 4-MDBT and the DDS routes, HYD routes inside all obviously decrease with the descending of reaction temperature, which suggests that the HDS is not reach the thermodynamic equilibrium under the reaction conditions adopted in this experiment. On the other hand, it is also found that the effects of reaction temperature on the DDS routes of the HDS of DBT and 4-MDBT are relatively weaker than that on the HYD routes, which lead to the BPs/CHBs molar ratio increases with the reducing of reaction temperature (as shown in Fig.6). This shows that the activation energy of the DDS routes is smaller than that of the HYD routes. At the same time, it can be found the effects of reaction temperature on conversion of DBT and 4-MDBT are different. The BPs/CHBs molar ratio in the products of HDS of 4-MDBT increases more slowly with the descending of reaction temperature than that of DBT. The reason speculated for that is the electron donor induction of the methyl group in 4-MDBT could promote the hydrogenation of the adjacent phenyl, leading to the reduction of activation energy of that. But that enhances the activation energy of the direct hydrogenolysis route for that's spatial restraining for the "end up adsorption".

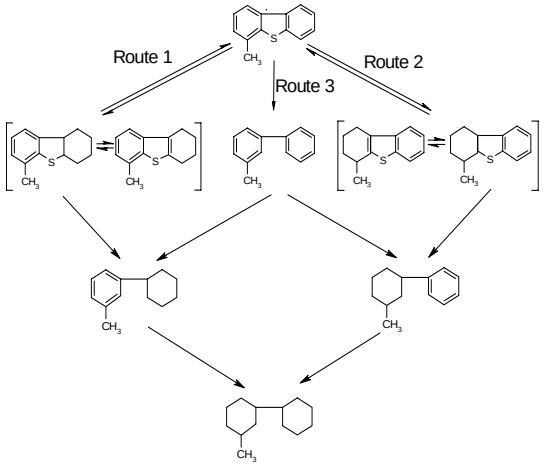

Scheme 1. Reaction network for HDS of 4-MDBT on Mo/γ-Al_2O_3, Route 1: hydrogenation route 1; Route 2: hydrogenation route 2; Route 3: hydrogenolysis route.

Table 2. Concentration of HDS products of DBT

Product	Concentration, mol%
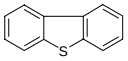	48.3679
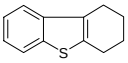	5.2465
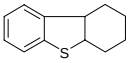	1.071
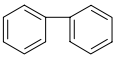	22.0872
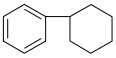	21.358
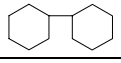	1.0265
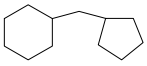	0.843

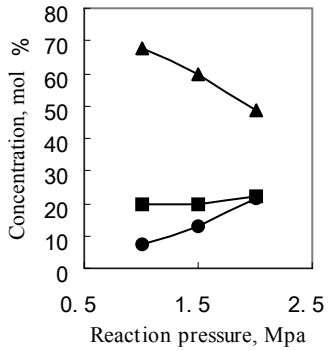

Figure 1. Concentration of HDS products of DBT under different reaction pressures, ▲DBT, ■biphenyl, ●cyclohexylbenzene

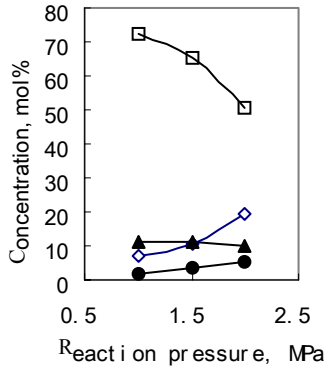

Figure 2. Concentration of HDS products of 4-MDBT under different reaction pressures, □4-MDBT, ○ (3- methyl-cyclohexyl)-benzene, ▲3- methyl-biphenyl, ●1-cyclohexyl-3-methyl-benzene

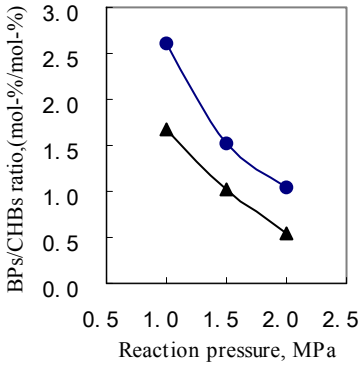

Figure 3. Molar ratio of BPs to CHBs under different reaction pressures, ●DBT, ▲4-MDBT

Table 3. Apparent Kinetic Orders of Reaction Pressure in Different Reactions

Reactant	DBT	4-MDBT
Conversion	0.66	0.83
Direct desulfurization route	0.18	0.15
Desulfurization route through hydrogenation	1.51	
HYD Route 1*		1.47
HYD Route 2*		1.36

*HYD route 1: to 1-cyclohexyl-3-methyl-benzene;
HYD route 2: to (3- methyl-cyclohexyl)-benzene

Conclusion

Comparing with sulfided CoMo/γ-Al_2O_3 catalyst, Sulfided Mo/γ-Al_2O_3 catalyst has lower reactivity of catalysis. As a result, most of the partly hydrogenated DBTs are detectable in the products. From that, the detail HDS mechanisms of DBT and 4-MDBT were proposed. over Sulfided Mo/γ-Al_2O_3 catalyst, the HDS of 4-MDBT occurs mainly through the HYD route. But to DBT, the contributions of both routes are comparable. The methyl group in 4-MDBT molecule spatially hinds the "end on adsorption" of sulfur atom on the active sites of the catalyst, which depresses the DDS route and lead to the reduction of conversion of 4-MDBT. However, the HYD route is also important to the HDS of DBT over Sulfided Mo/γ-Al_2O_3 catalyst, thus the difference between the conversion of DBT and 4-MDBT is not as obvious as that over Sulfided CoMo/γ-Al_2O_3 catalyst.

Descending reaction pressure evidently causes the descending of reaction rate of the hydrogenation routes of HDS of 4-MDBT and DBT. However, the reaction rate of the direct hydrogenolysis routes slightly ascends with the descending of reaction pressure. The effect of reaction pressure on the conversion of 4-MDBT is higher than that on DBT.

Reaction temperature has obvious effect on both the direct hydrogenolysis routes and the hydrogenation routes of HDS of 4-MDBT and DBT. However, the electron donor induction of the methyl group in 4-MDBT can promote the hydrogenation of the adjacent phenyl, leading to the reduction of activation energy of that. But that enhances the activation energy of the direct hydrogenolysis route for that's spatial restraining for the "end up adsorption".

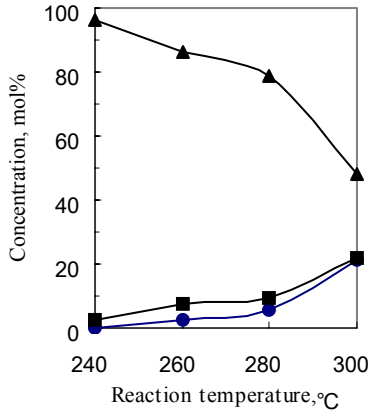

Figure 4. Concentration of HDS products of DBT under different reaction temperatures, ▲DBT, ■biphenyl, ●cyclohexylbenzene.

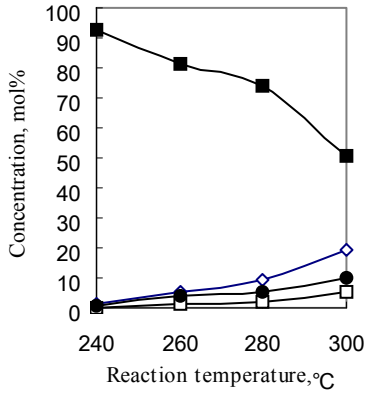

Figure 5. Concentration of HDS products of 4-MDBT under different reaction temperatures, ■4-MDBT, ○ (3- methyl-cyclohexyl)-benzene, ●3- methyl-biphenyl, □1-cyclohexyl-3-methyl-benzene

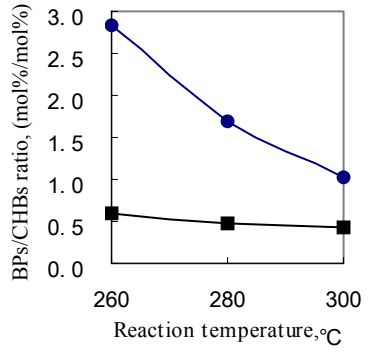

Figure 6. Molar ratio of BPs to CHBs under different reaction temperatures, ●DBT, ▲4-MDBT

References

(1) Amorelli A., Amos Y. D., Halsig C.P., et al., Estimate Feedstock Processsability [J], *Hydrocarb.Proc.*,1992, *71(6)*: 93-101.
(2) Shih S. S., Mizrahi S., Green L. A., et al., Deep Desulfurization of Distillates [J], *Ind. Eng. Chem. Res.*, 1992, *31*:1232-1235
(3) Kabe T., Ishihara A., Tajima H., Hydrodesulfurization of Sulfur-Containing Polyaromatic Compounds in Light Oil[J], *Ind. Eng. Chem. Res.*, 1992, *31*: 1577-1580
(4) Schulz H., Bohringer W., Ousmanov F., et al.,, Refractory sulfur compounds in gas oils[J], *Fuel Processing Technology*, 1999, *61*: 5–41
(5) Macaud M., Milenkovic A., Schulz E.,et al., Hydrodesulfurization of Alkyldibenzothiophenes: Evidence of Highly Unreactive Aromatic Sulfur Compounds[J], *J. Catal.*, 2000,*193*:255-263.
(6) Singhal, G. H., Espino R. L., Sobel J. E., Hydrodesulfurization of Sulfur Heterocylic Compounds: Reaction Mechanism[J], *J.Catal.*,1981,*67*: 446-456.
(7) Kabe T., Qian W., Ishihara A., Study of Hydrodesulfurization of Dibenzothiophene on Ni-Mo/Al_2O_3, Mo/Al_2O_3,and Ni/Al_2O_3 Catalysts by the Use of Radioisotope ^{35}S Tracer[J], *J. Catal.*, 1994,*149*: 171-180.
(8) Laudau, M. V., Deep Hydrotreating of Middle Distillates from Crude and Shale Oils[J]. *Catalysis Today*, 1997,*36(4)*:393-429
(9) Gilman, H. & Jcoby, A. L., Dibenzothiophene: Orientation and Derivatives[J]. *J. Org. Chem.*, 1938, *3*:108-119
(10) Kuchm-Caubere, C., Adach-Becker, S., Fort, Y. et. al., Expeditious and Efficient Syntheses of pure 4-Methyl and 4,6-Disubstituted Dibenzothiophene[J]. *Tetrahedron*, 1996,*52(27)*:9087-9092.
(11) Stanislaus A., Cooper, B. H., Aromatic Hydrogenation Catalysis: A Review[J], *Catalysis Reviews-Science and Engineering*, 1994, *36(1)*:75-123.
(12) Vasudevan P.T., A Review of Deep Hydrodesulfurization Catalysis[J], *Catalysis Reviews-Science and Engineering*, 1996, *38(2)*:161-188.